Rehydroxylation Dating: Assessment for Archaeological Application

Rehydroxylation Dating: Assessment for Archaeological Application

by

Gerard Thomas Barrett

[B.Sc. Experimental Physics, Trinity College, Dublin

M.Sc. Atomic and Molecular Cluster Physics, National Univ. of Ireland, Maynooth

M. Sc. Dating and Chronology, Queen's University Belfast, Belfast]

Submitted in accordance with requirements

for the awarding of the degree of

Doctor of Philosophy

on

30th April 2015

School of Geography, Archaeology and Palaeoecology

Faculty of Engineering and Physical Sciences

Queen's University Belfast

Contents

List of Figures

Chapter 2

Appendix B

Appendix C

Appendix D

Figure D.15: Arrhenius plot ($t^{1/4}$ model) for 130°C (blue), 500°C (red) and 500-130°C (green, RHX component) components of mass gain rates for *Joy* sample. Uncertainties are to 2σ.

Figure D.16: Arrhenius plot ($t^{1/n}$ model) for 130°C (blue), 500°C (red) and 500-130°C (green, RHX component) components of mass gain rates for *Joy* sample. Uncertainties are to 2σ.

Figure D.17: Arrhenius plot ($t^{1/4}$ model) for 130°C (blue), 500°C (red) and 500-130°C (green, RHX component) components of mass gain rates for *Cau* sample. Uncertainties are to 2σ.

Figure D.18: Arrhenius plot ($t^{1/4}$ model) for 130°C (blue), 500°C (red) and 500-130°C (green, RHX component) components of mass gain rates for *Bel* sample. Uncertainties are to 2σ.

Figure D.19: Arrhenius plot ($t^{1/n}$ model) for 130°C (blue), 500°C (red) and 500-130°C (green, RHX component) components of mass gain rates for *Bel* sample. Uncertainties are to 2σ.

Figure D.20: Arrhenius plot ($t^{1/4}$ model) for 130°C (blue), 500°C (red) and 500-130°C (green, RHX component) components of mass gain rates for *Tur* sample. Uncertainties are to 2σ.

Figure D.21: Arrhenius plot ($t^{1/n}$ model) for 130°C (blue), 500°C (red) and 500-130°C (green, RHX component) components of mass gain rates for *Tur* sample. Uncertainties are to 2σ.

Figure D.22: Arrhenius plot ($t^{1/4}$ model) for 130°C (blue), 500°C (red) and 500-130°C (green, RHX component) components of mass gain rates for *Ted* sample. Uncertainties are to 2σ.

Figure D.23: Arrhenius plot ($t^{1/n}$ model) for 130°C (blue), 500°C (red) and 500-130°C (green, RHX component) components of mass gain rates for *Ted* sample. Uncertainties are to 2σ.

Appendix E

Figure E.1: Mass gain curves, displaying the *Stage 1* region, of *Ann* sample. Sample aging at 25°C following heating at 130°C (blue) and 500°C (red).

Figure E.2: Mass gain curves, displaying the *Stage 1* region, of *Esp* sample. Sample aging at 25°C following heating at 130°C (blue) and 500°C (red).

Figure E.3: Mass gain curves, displaying the *Stage 1* region, of *Nic* sample. Sample aging at 25°C following heating at 130°C (blue) and 500°C (red).

Figure E.4: Mass gain curves, displaying the *Stage 1* region, of *Mac* sample. Sample aging at 25°C following heating at 130°C (blue) and 500°C (red).

Figure E.5: Mass gain curves, displaying the *Stage 1* region, of *Ria* sample. Sample aging at 25°C following heating at 130°C (blue) and 500°C (red).

Figure E.6: Mass gain curves, displaying the *Stage 1* region, of *Etr* sample. Sample aging at 25°C following heating at 130°C (blue) and 500°C (red).

Figure E.7: Mass gain curves, displaying the *Stage 1* region, of *Rom* sample. Sample aging at 25°C following heating at 130°C (blue) and 500°C (red).

Figure E.8: Mass gain curves, displaying the *Stage 1* region, of *Por* sample. Sample aging at 25°C following heating at 130°C (blue) and 500°C (red).

Figure E.9: Mass gain curves, displaying the *Stage 1* region, of *Rat* sample. Sample aging at 25°C following heating at 130°C (blue) and 500°C (red).

Figure E.10: Mass gain curves, displaying the *Stage 1* region, of *Cal* sample. Sample aging at 25°C following heating at 130°C (blue) and 500°C (red).

Figure E.11: Mass gain curves, displaying the *Stage 1* region, of *Lan* sample. Sample aging at 25°C following heating at 130°C (blue) and 500°C (red).

Figure E.12: Mass gain curves, displaying the *Stage 1* region, of *Joy* sample. Sample aging at 25°C following heating at 130°C (blue) and 500°C (red).

List of Tables

Table 8.3: Modelled remaining loose water (*model 2*), corrected for the mass of samples placed in beakers and used in dating trials and mass gain experiments.

Table 8.4: Results of Modelling of cooling curves using the relationship $T=ae^{-bt}+c$, where a=difference in initial and final temperature of the ceramic and c is the final temperature of the ceramic. Also included are the R^2 values and cooling coefficient for a whole brick.

Table 8.5: Table of relevant parameters used in mapping long regional reconstruction data to local data as part of temperature history construction for *Joy*. MAT = mean annual temperature. ATR = annual temperature range. b is sine model parameter (synchronisation term) and R^2 corresponds to sine modelling quality.

Table 8.6: Table of mean lifetime temperature, ELT values and simulated fractional mass gain values for all samples and both models.

Table 8.7: Table of age estimates based on ELTs and both the $t^{1/4}$ and $t^{1/n}$ models. Also included are OM/OC_w and T_w, conditions of OM/OC and temperature under which the age calculation will fall within the uncertainty bounds of the known age. m_{out} is the fractional mass the samples are estimated to be out by (relative to simulated mass gain using ELTs) for the dates to work.

Table 8.8: Examples of the effect of uncertainties in OM/OC ratio and the activation energy on the age range estimates. For $t^{1/4}$ model. Italicised and bold correspond to age ranges that overlap with known age.

Table 8.8: Examples of the effect of uncertainties in OM/OC ratio and the activation energy on the age range estimates. For $t^{1/4}$ model. Italicised and bold correspond to age ranges that overlap with known age.

Table 8.9: Examples of the effect of uncertainties in OM/OC ratio and the activation energy on the age range estimates. For $t^{1/n}$ model. Italicised and bold correspond to age ranges that overlap with known age.

Table 8.10: STETE – effects on simulated mass gain using *moderate* (Mod.) and *strong* (Str.) conditions. m_{sim} = simulated mass gain over lifetime of ceramic using temperature history. BC (80) = Brick Cooling (80=max. RHX temp.). 2d60=2 days heating at 60°C. 15d77=15 days at 77°C. 60c80=60 heat/cool cycles with max. temp of 80°C. m(dur_ELT)=additional mass gained over the duration of the STETE effects but at the ELT. m_{stete}=additional mass gain due to STETE effects. All masses are fractional.

Table 8.11: Extra age, t_{stete} , caused by STETE effects, using *moderate* (Mod.) and *strong* (Str.) conditions. t_{out}=number of years calculated dating ages are out by. BC (80) = Brick Cooling (80=max. RHX temp.). 2d60=2 days heating at 60°C. 15d77=15 days at 77°C. 60c80=60 heat/cool cycles with max. temp of 80°C.

Table 8.12: Increase in ELT caused by STETE effects, T_{stete}, using *moderate* (Mod.) and *strong* (Str.) conditions. T_{out}= increase in ELT required for successful dating of samples. BC (80) = Brick Cooling (80=max. RHX temp.). 2d60=2 days heating at 60°C. 15d77=15 days at 77°C. 60c80=60 heat/cool cycles with max. temp of 80°C.

Table 8.13: Table of corrected ages, working OM/OC and working ELT values for samples following STETE correction under *moderate* (*mod.*) and strong (*str.*) conditions. Bold = reasonable working condition. Bold and italicised = Plausible/borderline working condition.

Chapter 9

Table 9.1: Table of main FTIR peaks associated with organic matter, together with IR bond assignments, possible organic matter source, and associated references.

Table 9.2: Relationship between curvature and the ratio of the working mass gain rate, $a_{W,}$ and the mass gain rate at the ELT, a_{elt}.

Table 9.3: Age estimates using RHX activation energies calculated form the average of the 130C and 500C component activation energies.

Table 9.4: Summary of the drying conditions and presence of drying data in the literature.

Table 9.5: The STETE effects on the $t^{1/n}$ ages. t_{out} is the difference between the estimated and known age. t_{stete} is the additional age the STETE event would contribute (based on the additional mass the event adds to the simulated mass gain of the ceramic over its lifetime, m_{sim}). The STETE events are as follows: BC80 = brick cooling with maximum RHX temperature of 80°C, 2d60 = 2 days at 60°C, 60C80 = 60 heating/cooling cycles with maximum RHX temperature of 80°C. Note that yrs=0 correspondents to an additional age of <0.5 yrs.

Appendix A

Appendix B

Table B.8: Mineral identification of diagnostic FTIR peaks for *Por* samples. Qtz=Quartz, Ano=Anorthite, Rut=Rutile, Mic=Microcline, For=Forsterite, Wol=Wollastonite, Ens=Enstatite, Cal=Calcite, Geh=Gehlenite, Mus=Muscovite, Alb=Albite, Ort=Orthoclase.

Table B.9: Mineral identification of diagnostic FTIR peaks for *Rat* samples. Qtz=Quartz, For=Forsterite, Ano=Anorthite, Hem=Hematite, Ens=Enstatite, Ort=Orthoclase, Cor=Cordierite, Spi=Spinel, Dio=Diopside, Alb=Albite, Cal=Calcite, Cri=Cristobalite.

Table B.10: Mineral identification of diagnostic FTIR peaks for *Cal* samples. Qtz=Quartz, Ano=Anorthite, Cri=Cristobalite, Mul=Mullite, For=Forsterite, Wol=Wollastonite, Mic=Microcline, Enst=Enstatite, Geh=Gehlenite, Ort=Orthoclase, Cal=Calcite, Oli=Olivine, Dol=Dolomite.

Table B.11: Mineral identification of diagnostic FTIR peaks for *Lan* samples. Ens=Enstatite, Hem=Hematite, Mic=Microcline, Alb=Albite, Wol=Wollastonite, Qtz=Quartz, Rut=Rutile, Ort=Orthoclase, Ano=Anorthite, Cri=Cristobalite, Geh=Gehlenite, Cal=Calcite, Mul=Mullite, Dol=Dolomite, Oli=Olivine, For=Forsterite, Mus=Muscovite, Bio=Biotite.

Table B.12 Mineral identification of diagnostic FTIR peaks for *Joy* samples. Qtz=Quartz, Ano=Anorthite, Mul=Mullite, Ens=Enstatite, Mul=Mullite, For=Forsterite, Hem=Hematite, Wol=Wollastonite, Mic=Microcline, Geh=Gehlenite, Rut=Rutile.

Table B.13: Mineral identification of diagnostic FTIR peaks for *Cau* samples. Qtz=Quartz, Hem=Hematite, Alb=Albite, Mic=Microcline, Bio=Biotite, Cal=Calcite, Aug=Augite, Ens=Enstatite, Org=Organic.

Table B.14: Mineral identification of diagnostic FTIR peaks for *Bel* samples. Hem=Hematite, Alb=Albite, Qtz=Quartz, Mic=Microcline, Anh=Anhydrite, Bas=Bassanite, Gyp=Gypsum, Spi=Spinel, Bio=Biotite.

Table B.15: Mineral identification of diagnostic FTIR peaks for *Dow1* samples. Qtz=Quartz, Ano=Anorthite, Cri=Cristobalite, Geh=Gehlenite, Cal=Calcite, Dol=Dolomite, For=Forsterite, Ens=Enstatite, Oli=Olivine, Mic=Microcline.

Table B.16: Mineral identification of diagnostic FTIR peaks for *Dow2* samples. Qtz=Quartz, Mul=Mullite, Ano=Anorthite, Mic=Microline, For=Forsterite, Alb=Albite, Wol=Wollastonite, Cri=Cristobalite, Ill=Illite, Ana=Anatase, Ort=Orthoclase, Dio=Diopside, Geh=Gehlenite, Cal=Calcite, Dol=Dolomite, Ens=Enstatite, Bio=Biotite.

Table B.17: Mineral identification of diagnostic FTIR peaks for *Tur* samples. Qtz=Quartz, Mic=Microcline, Mul=Mullite, Spi=Spinel, Wol=Wollastonite, Ort=Orthoclase, Cri=Cristobalite, Cal=Calcite.

Table B.18: Mineral identification of diagnostic FTIR peaks for *Ted* samples. Qtz=Quartz, Mic=Microcline, Ort=Orthoclase, Dio=Diopside, Ana=Anatase, Cri=Cristobalite, Ano=Anorthite, Mul=Mullite, Hem=Hematite, Alb=Albite, Oli=Olivine, San=Sanidine, For=Forsterite, Cal=Calcite, Wol=Wollastonite, Mus= Muscovite, Geh=Gehlenite, Aug=Augite.

Glossary, Nomenclature and Notation

General

AE	Activation energy, the energy required for a chemical reaction to occur.
AETH	Activation energy temperature history approach, a method of RHX dating age estimation analysis that takes advantage of a well understood temperature history to provide more refined age estimates.
ATR	(Mean) Annual Temperature Range
BET	Brunauer-Emmett-Teller, a theory used to describe the physisorption of gas molecules on solids. BET analysis may also be used to refer to the determination of specific surface area (or pore volume) using gas sorption methods.
BJH	Barrett-Joyner-Halenda, an analysis method for the determination of pore volume and area distributions of porous solids based using sorption curves.
Ceramics	Used to refer to fired clay (mineral) ceramics.
Curvature	The degree $1/n$ in the $t^{1/n}$ model varies from 1/4, with $1/n < 1/4$ a negative (convex downward) curvature and $1/n > 1/4$ a positive (concave upward) curvature.
ECC	Environmentally controlled chamber.
ELT	Effective lifetime temperature, see *Section 3.7.*
FTIR	Fourier transform infrared spectroscopy.
GBA	Glove box arrangement.
MAT	Mean annual temperature.
MLT	Mean lifetime temperature, the average temperature across the ceramics lifetime.
OM/OC	Organic matter to organic carbon ratio, the ratio of the mass of organic matter to the mass of organic carbon.

p-XRF	Portable x-ray fluorescence.
RHX	Rehydroxylation, the chemical recombination of hydroxyls via the uptake of atmospheric moisture.
SB	Sample box, a modified lunch box used to store six samples (in beakers) with a layer of saturated salt solution to control the %RH.
SSA	Specific surface area, measured in m^2/g.
STETE	Short term elevated temperature events, short term events (hours to days) during which the ceramic experiences elevated temperatures (> 50°C) and gains mass rapidly due to the non-linearity of its Arrhenius temperature dependent mass gain rate.
TGA	Thermogravimetric analysis.
TG-MS	Thermogravimetric mass spectrometry.
XRD	X-ray diffractometry.

Components and Stages (curves)

130C	The 130°C component, the mass gain curve obtained following drying. May be used to refer more specifically to the *Stage 2* portion of this curve.
500C	The 500°C component, the mass gain curve obtained following heating. May be used to refer more specifically to the *Stage 2* portion of this curve.
RHXC	The RHX component of the 500C curve, i.e. the difference between *Stage 2* 500C and 130C components.
S1	Refers to *Stage 1* of the mass gain curve, more specifically the early stage of mass gain not associated with a $t^{1/4}$ or $t^{1/n}$ behaviour.
S2	Refers to *Stage 2* of the mass gain curve, linear as a function of $t^{1/4}$ or $t^{1/n}$.

Stage 1

m_d The dry mass of the ceramic. More, practically the initial mass recorded during *Stage 1*.

$m_{S1\text{-}130}$ The *S1* fractional mass gain of the 130C (500C) curve.

$m_{S1\text{-}avg}$ The average *S1* fractional mass gain of the 130C and 500C curves.

$t_{S1\text{-}130}$ The duration of *S1* for the 130C (500C) curve.

$t_{S1\text{-}avg}$ The average duration of *S1* for the 130C and 500C curve.

Stage 2

$a_{130\text{-}25}$ The (fractional) mass gain rate ($t^{1/4}$ or $t^{1/n}$, model specified) of *Stage 2* of the 130°C (500°C) mass gain curve aged at 25°C (35°C, 45°C), say.

$a_{RHX\text{-}25}$ The RHX-attributed (fractional) mass gain rate ($t^{1/4}$ or $t^{1/n}$, model specified) at 25°C (35°C, 45°C). $a_{RHX\text{-}25} = a_{500\text{-}25} - a_{130\text{-}25}$.

m_0 Initial or intercept mass from linear regression.

$m_{130\text{-}25}$ Initial (intercept) mass (fractional) of the *Stage 2,* $t^{1/4(n)}$, line. This is equivalent to the equilibrated mass of the sample less any mass gain related to *Stage 2,* $t^{1/4(n)}$, processes. 130 – denotes 130C curve, and 25 denotes aging temperature.

$m_{RHXC\text{-}25}$ The total mass (fractional) loss of the *RHXC* due to heating between 130°C and 500°C. In an idealised scenario this is the RHX mass, but in practice it is, at minimum, described by the following equation:

$$m_{RHXC} = m_{RHX} + m_{lw} + m_{om}$$

where m_{RHX} is the true mass of hydroxyls removed, m_{lw} is the mass of loose water (non- RHX or *S2* mass gain related) removed above 130°C, and m_{om} is the mass of organic matter (inferred based on organic carbon in this thesis) removed.

Note that it is estimated using $m_{RHXC\text{-}25} = m_{130\text{–}25} - m_{500\text{-}25}$. Therefore, it is calculated for a number of aging temperatures, with m_{RHXC} (aging temperature subscript absent) denoting the average of these values.

Activation Energy

E_{a130} The activation energy of the 130°C component.

E_{a500} The activation energy of the 500°C component.

E_{aRHX} The activation energy of the RHX component, calculated from the Arrhenius plot generated using the $m_{RHX\text{-}25,\ 35,\ 45}$ rates, i.e. not from subtraction of E_{a130} from E_{a500}.

ELT and Simulation

m_{sim} The simulated RHX mass gain.

SAT Surface air temperature – i.e. the instrumentally recorded air temperature near surface level

T_{atr} The annual temperature range (difference between the lowest and highest monthly average temperature).

T_{elt} The effective lifetime temperature.

T_{mean} The mean temperature over a specified period.

T_{mat} The mean annual temperature (average of monthly average temperatures).

T_{mlt} The mean lifetime temperature.

Dating

m_{RHX} The mass (fractional) attributed to long term $t^{1/4(n)}$ processes (RHX) due to heating between 130-500°C. This is the mass used in age calculations.

m_{lw} The mass (fractional) of loose water not removed during drying at 130°C.

m_{om} The mass (fractional) of organic matter removed during heating between 130-500°C, estimated based on the organic carbon present, m_{oc}, and an estimate of the organic mass to organic carbon ration (OM/OC).

OM/OC	The organic mass to organic carbon ratio (1.95 but with reasonable range of 1.4-2.5).
$t_{age\text{-}elt}$	The estimated age of the sample. Subscript denotes the temperature upon which the estimate is based. Where absent, the ELT is used.
t_A	The known age of the sample.

Discrepancies

OM/OC_w	The working OM/OC ratio – the ratio at which the estimated age agrees with the known age.
m_{out}	The discrepancy between the simulated RHX mass, m_{sim}, and the estimated RHX mass, m_{RHX}.
t_{out}	The discrepancy between the known age and the estimated age.
T_w	The working ELT – the ELT temperature at which the estimated age agrees with the known age.

STETE

m_{stete}	The additional mass gained due to STETE events over mass gained at the ELT.
t_{stete}	The additional age gained due to STETE events.
T_{stete}	The additional gain in the ELT due to STETE events.

Acknowledgments

This research was made possible through the aid of a Department for Employment and Learning (DEL) Ph.D. studentship for which I am very grateful. I am also most appreciative of the assistance provided by the School of Geography, Archaeology and Palaeoecology (GAP), at which this research was conducted.

I wish to give special thanks to my supervisor Prof. Paula Reimer (GAP, QUB) for her continual support and guidance during the period of my research. I also wish to thank Prof. Caroline Malone (GAP, QUB) for her advice (and aid in sourcing samples), as well as Dr. Moira Wilson (Univ. Manchester) for her counsel with regard to RHX dating.

Locating suitable samples was more difficult than expected and I wish to thank the following persons for their recommendations and assistance in this matter: Mr. Michael Barrett (Turlough), Dr. Joanne Curran (Consarc Design Group), Mr. Peter Francis (Ballynahinch), Ms. Audrey Gahan (Gahan and Long Arch. Serv. Ltd), Mr. Stephen Gilmore (Northern Arch. Cons. Ltd), Mr. Barrie Hartwell (GAP, QUB), Mr. Paul Logue (N. Ireland Environment Agency), Dr. Sara Pavía (Trinity College Dublin). Special thanks are offered to both Mr. Cormac McSparron and Mr. Ruairí Ó Baoill (Centre for Archaeological Fieldwork, QUB) for their often being a first port of call when dead ends, or indeed brick walls, were reached.

Many analytical techniques were applied as part of this work, all requiring varying levels of guidance and technical aid. Special thanks are extended to Mr. Pat McBride and Mr. John Meneely in the School of GAP, QUB, for their perpetual helpfulness, aid in sample and thin section preparation, and instruction on a variety of techniques. Acknowledgments are also given to the following individuals for their invaluable assistance: Mr. Peter Gray, Mr. Stephen Roper, and Mr. Jim McDonald (^{14}CHRONO Centre, QUB) for training and help in carbon content analysis; Dr. Jennifer McKinley (GAP, QUB) for guidance and the use of air-injection permeametry; Dr. John Caulfield (SPACE, QUB) for training and direction in the use of FTIR and Dr. Rory Flood (GAP, QUB) for guidance in the use of p-XRF; Mr. Mark Russell (SPACE, QUB) for his kindness in the carrying out of TG-MS analysis; and Mr.

William Harra, of the centre for Analytical Services and Environmental Projects (ASEP, QUB), for carrying out BET analysis.

Finally, I wish to offer enormous thanks to my love Aoife Cuddihy for her constant support, love, and encouragement, as well as to my family and friends for being themselves and always being there.

Abstract

Investigations are carried out into the mass gain behaviour of fired clay ceramics following drying (130°C) and reheating (500°C), and the application of these mass gain properties to the dating of archaeological ceramics using a modified rehydroxylation dating (RHX) methodology, a component based approach. Gravimetric analysis is conducted using a temperature and humidity controlled glove box arrangement (featuring a top-loading balance) on eighteen samples of varied known ages and contexts; this occurs following transfer from environmentally controlled chambers where subsamples of these samples are aged at three temperatures (25°C, 35°C, 45°C) following drying and reheating. The sample set consists principally of post-medieval bricks, but also includes some post-medieval pottery as well as both Etruscan and Roman ceramics. A suite of techniques are applied to characterise these ceramics, including XRD, FTIR, p-XRF, thin-section petrography, BET analysis, TG-MS and permeametry.

It is demonstrated that almost all samples exhibit issues with a prolonged and indefinite period of drying, exceeding two months at 130°C. Methods are presented for treating this issue as well as an interpretation of the processes involved. As well as this, one third of samples (abnormal samples) are shown to have problematic mass gain behaviour that is revealed to be correlated with high specific surface area/pore volume and the likely result of pore condensation issues.

It is confirmed that, as for reheating at 500°C, samples exhibit a two-stage mass gain behaviour following drying at 130°C, with the second of these stages continuing indefinitely and approximately *linear as a function of* $t^{1/4}$. *The first stage,* Stage 1*, is shown to have similar magnitude and duration following both drying and reheating, and is associated with physisorption of water on the surface and pores of the ceramic. The second stage,* Stage 2*, following both drying and reheating, is demonstrated to be better described by a* $t^{1/n}$ *model, where* 1/n *varies from* 1/6 - 1/2, *dependent on the sample; a correlation with the specific surface area/pore volume, connecting the diffusion mechanism of the process with the pore structure*

*of the ceramic, will be presented. As well as this, it is established that the curvature (*1/n *value of* $t^{1/n}$ *model*) *has similar values for all subsamples of a sample aged at different temperatures and following both drying and reheating. The mass gain in* Stage 2 *following drying is shown to have an Arrhenius temperature dependence with activation energies of the order of those for mass gain following reheating at 500°C; a notable difference from the activation energies of rehydroxylation will be demonstrated. It is hypothesised that* Stage 2 *mass gain following drying is due to the recombination of chemisorbed water previously removed during drying, and support for this argument is presented. The rate of* Stage 2 *mass gain following drying will be shown to have a linear relationship with the rate following reheating at 500°C, and it will be argued that the underlying mass gain processes (chemisorption/rehydroxylation) are either the same and governed by the heating procedure or, more likely, different chemisorption processes but with some fundamental and compositional relationship.*

For RHX dating, a component based approach is presented and applied. The results are inconclusive, with the estimated ages of most samples generally far too large, neither confirming the effectiveness of a component based approach nor the use of a $t^{1/4}$ *or* $t^{1/n}$ *model. The effects of a range of factors on the estimated ages are examined and discussed, including: uncertainties due to the experimental setup, data quality and resolution, uncertainty in the effective lifetime temperature (ELT), issues with the incomplete drying of samples, the presence of organic matter, the presence of problematic minerals, and the effects of short term elevated temperature events (*STETE*s). Of note, it is shown that organic matter contamination is present in significant quantities in all samples, regardless of retrieval context, and uncertainties in this quantity, particularly the organic matter to organic carbon ratio (OM/OC), have considerable effects on the estimated ages. The presence of gypsum is identified as a possible large source of uncertainty due to its dehydration and lower physisorption levels following reheating. The need for a better understanding of the nature of the drying processes and water not removed during drying is also highlighted. For samples with large activation energies, it is shown that STETEs, for example post-firing cooling of a brick or heating/cooling*

cycles during the use of a cooking pot, can add considerable quantities of (re)hydroxyl mass to the sample, detrimental to any dating estimations.

*Finally, two contrasting methods of dealing with uncertainty and certainty in the temperature history of a ceramic are proposed, with examples of their use presented: an age-temperature curve approach is recommended for the visual interpretation of the ages and age ranges of samples where the ELT is less certain; the activation energy temperature history (*AETH*) approach is recommended for use where the temperature history of a sample is very well understood.*

Chapter 1

Introduction

1.1 Fired Clay Ceramics in Archaeology

Fired clay ceramics are ubiquitous. For most people in the world, they form a vital technological component of everyday life; from sanitary ware to structural bricks, and from kitchenware to electrical insulators, their functions are wide-ranging and their use endemic. The raw sources for this technology are the equally abundant inorganic clays, for example kaolins and illites, found across much of the Earth's surface (see *Section 2.2*). When these clays are fired a sequence of physical and chemical processes occur throughout the clay matrix. Water molecules, loosely bound in the pores and capillaries, are driven off at temperatures exceeding 100°C. Then, at temperatures in the range 450-900°C, dehydroxylation occurs, a chemical process during which hydroxyls of the silicate-based clay molecules are lost through conversion to water molecules, which are subsequently evaporated following diffusion to the surface of the ceramic (Bellotto et al. 1995; Wang et al. 2002; Gualtieri and Ferrari 2006; Wilson et al. 2009). The end result is a strong, rigid material, known as a fired clay ceramic, typically used in the manufacture of pottery, bricks and tiles. Within the context of this thesis, when the term ceramic is used it refers to these fired clay ceramics specifically.

Modern reliance on fired clay ceramics, in particular pottery and brick, is nothing new, extending across history and deep into the prehistory of humankind; the earliest known deliberate firing of clays was at Dolni Věstonice, Czech Republic (Vandiver et al. 1989), where small figurines were formed, fired and sometimes exploded in fires about 30,000 cal. BP. However, it is not evident that the functional uses or advantages of this technology were realised, desired, or existed, at that time or for a subsequent period thereafter. A more purposeful advent for fired clay pottery began c. 12,000-18,000 cal. BP with its deliberate, possibly independent, development by hunter-gatherer communities in at least three regions of East Asia

(Japan, North China, and the Amur Basin in Russia) (Jordan and Zvelebil 2010). Evidence from this region may even suggest a possible appearance as early as 19,000 cal. BP, at Xianrendong Cave, China (Wu et al. 2012). The diffusion, indigenous creation and general adoption of this new fired clay technology across the rest of the world followed, however was not synchronous; used principally in the production of pottery it appears, for example, in North Africa c. 12,000-10,000 cal. BP (gatherer-cattle keeper communities, Huysecom et al. 2009; Jórdeczka et al. 2011), in the Near East c. 9,000-8,500 cal. BP (sedentary farmers, Gheorghiu 2009), in the British Isles of Western Europe c. 6,200-5,700 cal. BP (sedentary farmers, Sheridan 1995; Gibson 2002), in the Amazon Basin c. 7,500 cal. BP (hunter-gatherers, Roosevelt 1995) and across much of North America c. 3,000-1,500 cal. BP (farmers and sedentary hunter gatherers, Fagan 2011).

Pottery aside, another development in the function of fired clay ceramics, of particular relevance to this thesis, is the appearance of fired clay bricks. The first mud, sun-dried, bricks have been discovered in Jericho and date to c. 10,000-9,000 cal. BP; however, it is not until the Ubaid 3-4 period (c. 7,000-6,500 cal. BP) that fired clay bricks appear, albeit in rare, isolated contexts, with more common usage from the Uruk period (c. 5,000 cal. BP) onward (Campbell and Pryce 2003). Evidence from China may indicate the independent invention of fired clay bricks elsewhere as early as c. 5,500 cal. BP (Yang et al. 2014). And while its distribution and frequency of production is much more limited than is the case for pottery in prehistory, in the historic period bricks have become a staple and commonplace structural medium across many areas of the world.

With the above in mind, for much of the world fired clay ceramics span a significant period of social development from the Mesolithic to the present. Together with their ubiquity at habitation and ritual sites, their durability has made the study of ceramics a cornerstone of archaeological investigation (Renfrew and Bahn 2000) with the capacity for its dating, direct or indirect, critical to building chronologies of sites and understanding the social dynamics at work.

1.2 Dating of Ceramics

Several existing techniques can be used to date fired clay ceramics: radiocarbon dating, luminescence-based dating, and archaeomagnetic dating. These are both *direct*, luminescence and archaeomagnetic dating, in that they date when the ceramic was produced or exposed to a high temperature, and *indirect*, radiocarbon dating, in that they date closely associated material. These methods have their advantages yet also have limitations in their use, and in some contexts are not even applicable (see Bonsall et al. 2002 for a more detailed description of these methods and a review of their application).

Radiocarbon dating (see Bronk Ramsey 2008 for an overview) is used to indirectly date the ceramic, either through encrustations of food residues on the surface of the pot (Hedges et al. 1992; Nakamura 2001) or organic residues (lipids) that have been absorbed into the matrix of the ceramic during cooking or storage (Stott et al. 2003; Berstan et al. 2008). While the use of radiocarbon dating in this way can produce narrow age ranges, it relies on the original use of the ceramic in practices that will leave these residues and, furthermore, the survival of these residues in sufficient quantities. The use of encrustations can be complicated by the presence of carbon of differing ages, for example organic temper, carbon from the fire, and contaminants absorbed post-deposition. The lipids extracted as organic residues are less susceptible to contamination; however, the procedure is quite complex (Stott et al. 2001; 2003) and to be certain of satisfactory lipid identification and sufficient quantities of the lipid a large number of ceramic samples may be required (Berstan et al. 2008). Of course, with radiocarbon dating there is also the possibility of unsatisfactorily large age ranges when radiocarbon dates occur at plateaus in the calibration curve (Reimer et al. 2013).

Luminescence dating has the advantage of allowing direct dating of the fired clays in calendar years and has been used to date some of the earliest known pottery (Kuzmin et al. 2001; see Wintle 2008 for a review). However, there are several issues: the dating uncertainties, while capable of reaching ± 2%, are more likely to be in the range ± 5 – 10%; it can require a large number of samples per date and is

destructive; it does not work for all types of baked clays and certain environments are unsuitable (non-homogeneous, burial depth < 0.3m, low natural radiation); and date calculations depend on a dozen or so factors that require many assumptions about past environments, particularly the influence of environmental water and radiation dose rates, with not all sources of inaccuracy quantifiable (Aitken 1990; Bonsall et al. 2002; Duller 2008).

Archaeomagnetism is another direct dating technique. It works by mapping the thermoremanent magnetic signal, stored in the clays since firing, to a regional secular variation calibration curve (Sternberg 2008; Walker 2008). A major problem is it requires that the fired clay has not moved or that its original position and orientation since the time of heating is known. In practice, this generally limits the use of this method to dating kilns or firing sites (Reinders 1999; Riisager 2003). The technique is hindered by several other issues, including difficulties in the construction of regional secular calibration curves, in measurements of weakly magnetised materials, and in measurement of the local magnetic field in the vicinity of the fired clay itself (Walker 2008; Sternberg 2008).

Given the significance of pottery as a marker and descriptor of human development since prehistoric times and the limitations of the techniques described above, any alternative or complementary method for direct dating of fired clay ceramics would find instant use and be invaluable as an archaeological research tool.

1.3 Rehydroxylation Dating

An alternative approach to direct dating of archaeological ceramics, the rehydroxylation dating method (RHX), was first proposed following investigations into the expansive properties of fired clay bricks (Wilson et al. 2003) and has since undergone considerable investigation (for example, Savage et al. 2008a; Savage et al. 2008b; Tosheva et al. 2010, Bowen et al. 2011; Clegg et al. 2012; Bowen et al. 2013; Le Goff and Gallet 2014a, Numrich et al. 2015). Some of this research has led to its recent application to dating of bricks and tiles (Wilson et al. 2009), and archaeological pottery (Wilson et al. 2012).

As mentioned above, when inorganic clays are fired at temperatures in the range 450-900°C, dehydroxylation occurs and a hard ceramic is produced. This process, during which hydroxyls of the clay molecules are lost through conversion to water molecules with subsequent evaporation, is accompanied by a collapse of the crystal structure of the clays (Bellotto et al. 1995; Wang et al. 2002; Gualtieri and Ferrari 2006; Wilson et al. 2009). However, upon cooling, the reverse takes place; water from the environment is rapidly absorbed into the pores and capillaries, and rehydration/rehydroxylation occurs, albeit at a much slower rate, with moisture from the surrounding environment chemically recombining with the clay molecules (Heller et al. 1962; Shoval et al. 1991; Muller et al. 2000).

The rate at which the rehydration/rehydroxylation process takes place is dependent on the material, the original firing temperature and dwell time, the time elapsed since firing, and the ambient temperature of the ceramic (Wilson et al. 2009; Mesbah et al. 2010a; 2010b; Tosheva et al. 2010). The background and equations that govern this are discussed in greater detail in *Chapter 2* and *Chapter 3*. The result of rehydration/rehydroxylation is that the mass increases linearly as a function of $time^{1/4}$ since the ceramic was last fired, with the rate obeying an exponential Arrhenius type temperature dependence (Wilson 2009). Any subsequent reheating (> 500°C) is considered sufficient to zero or reset the mass to that of the as-fired state with the subsequent mass gain process repeating as before

and at the same rate, provided the temperature is the same as that during the lifetime of the ceramic (Wilson et al. 2009; Tosheva et al. 2010).

Rehydroxylation (RHX) dating is a gravimetric technique that exploits these properties of fired clays. In principle, by weighing a piece of ceramic, under controlled environmental conditions, before and after reheating, the mass the ceramic has gained since it was originally or last fired above 500°C can be estimated. Then the rehydration/rehydroxylation (mass gain) rate can be calculated by measuring the mass gain of this reheated sample as a function of time and in an aging environment (temperature) equivalent to that of the mean lifetime of the ceramic in its burial or depositional position. Knowing both the rate of mass gain and the mass gained during its lifetime, the elapsed time since the ceramic was fired can be calculated.

These basic principles have been developed and pioneered by Wilson et al. (2009; 2012) to successfully date bricks, tiles, and pottery up to 2000 years old, providing experimental evidence of the potential of RHX dating as a significant alternative and complementary tool for the direct dating of archaeological ceramic. However, these results have been questioned (Le Goff and Gallet 2014b) and further independent validation of its key properties and evidence of its successful application are required before it can be accepted by the archaeological community.

1.4 Thesis Motivation, Aim and Objectives

Motivation

Central to the RHX dating method are several assumed properties of fired clays, including: (1) the mass gain curve, associated with uptake of environmental moisture following firing/reheating, is a two-stage process with the second of these, *Stage 2*, described by a $time^{1/4}$ based relationship (Savage et al. 2008b); (2) the mass gain behaviour following reheating at a suitable temperature (500°C) is identical to that of the original freshly-fired sample provided the *aging* temperatures (environmental conditions under which the samples gain mass) are equal (Savage et al. 2008a, Tosheva et al. 2010); (3) the second stage process continues indefinitely, beyond the age of the ceramic (Wilson et al. 2003, Hall et al. 2011); (4) the second stage mass gain rate, as a function of $t^{1/4}$, is humidity independent and has an Arrhenius temperature dependence (Wilson et al. 2009), a property that plays a significant role in the mass gain over the lifetime of the ceramic (Barrett 2011, Hall et al. 2013). Provided these properties hold up to experimental testing and that two key quantities, the rate of mass gain as a function of $t^{1/4}$ and the mass gained due to rehydration/rehydroxylation over the ceramics lifetime, can be estimated with sufficient accuracy and precision, then successful calculation of the age of the ceramic are theoretically possible, as argued and suggested by the results of Wilson et al. (2009; 2012).

However, despite the promise suggested by these dating trials, very few ceramic fabrics of known age have been dated to a satisfactory level (11 based on Wilson et al. (2009; 2012)) and several significant issues have arisen with various aspects of the technique: the ages calculated are poor (Burokov et al. 2013; Numrich et al. 2015); the $t^{1/4}$ model is considered unsatisfactory (Bowen et al. 2011; 2013; Le Goff and Gallet 2014a; 2014b; 2015) with non-linearity in the second stage often evident (for example Savage et al. 2008a; 2008b; Bowen et al. 2011; Le Goff and Gallet 2014a); the equilibration following drying of samples is not observed (Le Goff and Gallet 2014a; 2014b); contaminants are problematic (Numrich et al. 2015); and considerable difficulties have been encountered with experimental determination

of the key variables involved (Bowen et al. 2011; Wilson et al. 2012; Le Goff and Gallet 2014a) as well as serious questions posed regarding the existing successful dating trials (Le Goff and Gallet 2014b).

The research undertaken by the author is motivated by the need to help clarify these issues through independent validation trials of several key properties of fired clays that are critical to RHX dating, whilst examining how these properties are affected by factors such as the chemical, mineralogical and morphological structure of the materials tested. Ultimately, it aims to test the viability of rehydroxylation dating as an archaeological technique, through the use of an analytical balance and glove box arrangement, in dating trials on a range of fired clay materials (principally post-medieval brick but including Roman and Etruscan material) of known age. These tests are conducted using a low-cost method that is centred on an analytical balance under controlled environmental conditions. The more specific aims and objectives are described in detail below.

Aims and Objectives

Aim:

To assess the exploitation of the rehydration/rehydroxylation characteristics of fired clays for the dating of archaeological fired clay ceramics. In particular, to independently examine the mass gain behaviour of fired clay ceramics, to verify that this behaviour has the necessary properties to permit dating, and to develop and test a methodology that exploits these properties to date fired clay samples of known age.

Objectives:

The objectives are split into two groups, *RHX Behaviour* and *RHX Dating*. The former is focussed on examination and validation of key properties of fired clays associated with their mass gain behaviour, the latter focussed on dating trials of ceramics of known age, both groups using the same set of samples. Of course, there is an element of crossover between the *RHX Dating* objectives into the *RHX*

Behaviour objectives with, for example, the level of success of dating trials providing more/less validation of key properties; this is addressed later in the thesis but experimentally the two areas are generally treated separately. The significance of some objectives will become clearer upon reading the *Background* and *Equation* chapters.

Group 1: RHX Behaviour – examination and validation of mass gain properties

1. To construct and validate an experimental setup centred on a temperature and humidity controlled glove box arrangement (GBA), and to develop a working methodology for subsequent rehydration/rehydroxylation experiments.
2. To examine the mass gain properties of fired clay samples (archaeological brick and pottery) following drying at 130°C and reheating at 500°C.

   Following drying at 130°C to examine the following:

   - Validate if the samples equilibrate to a constant mass and examine the factors affecting the rate of equilibration.
   - If the samples do not equilibrate, to examine the mass gain behaviour, determine how it can be explained and described, and examine the factors affecting it.
   - If the samples do not equilibrate, to also investigate the use of an alternative dating methodology (component based approach) to account for this.

   Following reheating at 500°C

   - To examine and validate the presence of a two-stage mass gain behaviour.
   - To examine the *Stage 1* behaviour and the factors affecting its magnitude and duration.
   - To examine the *Stage 2* behaviour and determine if it is better described by a $t^{1/4}$ model or a $t^{1/n}$, as well the factors affecting the mass gain rates.

- To examine the temperature dependence and validate that it has an Arrhenius behaviour (exponential). If so, determine the associated activation energies and investigate potential factors affecting them.

3. To examine the mass loss during heating between 130-500°C:
    - To investigate how well the total mass loss can be determined from mass gain data.
    - To determine the RHX mass loss from the total mass loss and examine the relationship between the two as well as the relationship with other factors.
    - To determine if organic matter (organic carbon) is present in samples from varied contexts, the magnitude of organic mass loss during reheating, and potential factors affecting its presence/magnitude, using carbon content analysis and Fourier transform infrared spectroscopy (FTIR), principally.
    - To examine if any mineralogical/chemical changes occur during reheating that might additionally contribute to the mass loss (or mass gain behaviour), using techniques such as X-ray diffractometry (XRD), FTIR, portable X-ray fluorescence spectrometry (p-XRF), and thin-section petrography.
4. To examine the nature of the loss of water and other products (CO_2, SO_2) using thermo-gravimetric analysis (TG-MS), and to use this information to help explain the variation in the mass gain behaviour of different samples.
5. To carry out mineralogical and elemental analysis for examination of how the mass gain behaviour might be affected both by different sample compositions and original firing conditions (temperature). The principle methods used include XRD, FTIR, p-XRF, thin section petrography and to a lesser extent TG-MS.
6. To carry out specific surface area, porosity and permeability tests to examine how the RHX method is affected by different surface and pore characteristics, principally using Brunauer-Emmett-Teller theory (BET) analysis (nitrogen sorption) and to a lesser extent thin section petrography and permeametry (air injection).

Group 2 – Dating

1. To carry out dating trials on a large set of samples using a new component-based approach, the samples consisting principally of a range of Irish post-medieval fired clay bricks of known age (spanning the period AD 1600 – 1900), as well as several samples of Etruscan and Roman ceramics.
2. To compare the results obtained using a $t^{1/4}$ and $t^{1/n}$ approach and to identify potential issues in their use.
3. To examine how the degree of success/failure of RHX dating is affected by a range of factors including:
    - Experimental setup and modelling issues
    - Temperature history uncertainties and the effects of short term elevated temperature events (STETEs, for example post-firing cooling of a brick)
    - Organic matter contaminants
    - Drying issues (prolonged drying and removal of loose water)
    - Mineralogical composition
    - Structural composition (surface area and porosity)
4. To propose and present the use of *age-temperature* curves, useful tools in examining the effect uncertainties in the effective lifetime temperature (ELT) have on the estimated age of a ceramic, particularly where the temperature history is less clear.
5. To propose and present the use of an activation energy temperature history (*AETH*) approach that makes use of a more detailed knowledge of the temperature history of a ceramic to refine the estimated ages.

The samples used are described in greater detail in the *Methods* chapters, however the reasoning behind focussing principally on post-medieval fired clay bricks are as follows:

- In order to be used as a construction material, post-medieval bricks are usually very well-fired (>800°C), above those temperatures

required for dehydroxylation of the clay minerals, thus avoiding any issues surrounding low-temperature partial firing (see *Chapter 2* for more on this).

- Bricks, unlike pottery, have not been used in storage or cooking and are thus likely to contain lower levels of organic contamination.
- Bricks allow for a greater quantity of less fragmented sample material from one source unit than pottery, say, and are also, especially in the case of post-medieval bricks, more readily available for destructive tests.
- The temperature history of bricks is better defined than more portable ceramics, with the period of functional use in one location and above ground longer than that of more fragile ceramics such as pottery. The RHX behaviour of exterior building bricks should better reflect local air temperature than ceramics which would normally be stored indoors.
- Later post-medieval bricks span a period in which instrumental records of temperature exist and these can be used to provide more accurate estimates of the bricks temperature histories (see *Chapter 2*).

1.5 Thesis Outline

This thesis generally conforms to a relatively conventional format for reporting scientific research (introduction, background, equations, method, results, discussion, and conclusion). Following on from the introduction, *Chapter 2* (*Background*) provides an introduction to clays and the effects of heat on clays, a brief review of research into rehydration and rehydroxylation of clays, a detailed review of rehydroxylation dating, and a small section on contaminants in archaeological ceramics.

Theory and equations are presented in *Chapter 3* (*Equations*). This section explains the equations that are central to rehydroxylation dating, as well as those which are more specific to the approach developed by the author. The mathematics behind simulations as well as other relevant theory and equations, such as those related to modelling of cooling/heating and drying of ceramics, are described.

The methods and results chapters are arranged and split in order to provide a more convenient and logical order of reading. In *Chapter 4* (*Experimental Method - Non-RHX Characterisation*) the methods of characterisation of the dating samples, excluding mass gain behaviour experiments conducted using the glove box arrangement, are described in full. This includes XRD, FTIR, p-XRF, thin-section petrography, TG-MS, carbon content analysis, permeametry, and BET analysis. *Chapter 5* (*Experimental Results – Non-RHX Characterisation*) will then present the results of this work.

The mass gain and dating methods are described in *Chapter 6* (*Experimental Method – RHX Behaviour & Dating)* with the results split into two chapters, *Chapter 7* (*Experimental Results – RHX Behaviour*) and *Chapter 8* (*Experimental Results – RHX Dating*).

The complete set of results will be discussed in *Chapter 9* (*Discussion*) with subsections devoted to non-RHX characterisation, RHX behaviour, and RHX dating but with a great deal of overlapping of the results discussed across these areas.

The thesis, its main findings and issues summarised, and with areas for future work outlined, will be concluded in *Chapter 10* (*Conclusion*).

Chapter 2

Background

2.1 Introduction

This chapter will provide a brief background to the composition of fired clay ceramics, particularly clay minerals, *Section 2.2*, followed by a description of the effects of heating on the components of the fired clay and its structure, *Section 2.3*. Rehydration and rehydroxylation occur following firing and these processes are reviewed in *Section 2.4*. The aforementioned sections will be concise and do not seek to provide a comprehensive review of the various aspects of fired clays described; this is beyond the scope of this thesis (references to more detailed work will be provided) and would add little greater insight in terms of understanding the remainder of the document. Instead, they are included to provide a more rounded picture and basic understanding of the nature of the materials and processes involved before RHX dating research is reviewed.

The core element of this chapter is a detailed critical review of work conducted on RHX dating up to the present, *Section 2.5*. All peer-reviewed research that has a particular RHX dating focus will be scrutinised and the main findings and points of interest/issue discussed. This will provide the reader with a complete understanding of the context into which the present work fits and the areas of contention that this work provides a contribution towards resolving.

Finally, *Section 2.6* will briefly discuss some major sources of contamination of ceramics and provide a short survey of work on organic matter to organic carbon ratios.

2.2 Ceramics and Clays

In this thesis, the expression *ceramics* refers to fired clay ceramics, with fired clay ceramics being the result of thermal transformations of a *clay*. A clay is composed of inclusions (inorganic minerals, organic matter) and clay minerals, and, depending on where the clay has been extracted from, the mixture and form of these components can vary considerably. This is because the formation of clay minerals results from a complex cycle of weathering, transportation, and diagenetic and hydrothermal alteration, *Figure 2.1*, that can be viewed as commencing and ending with the dissolution of rock minerals and rock mineral formation, respectively. The formation processes are described in other work of varying levels of detail, from introductory (Worrall 1986; Rice 1987; Fahrenholtz 2008) to intermediate and advanced (Kerr 1955; Keller 1964; Eberl et al. 1984; Velde 1992; Meunier 2005).

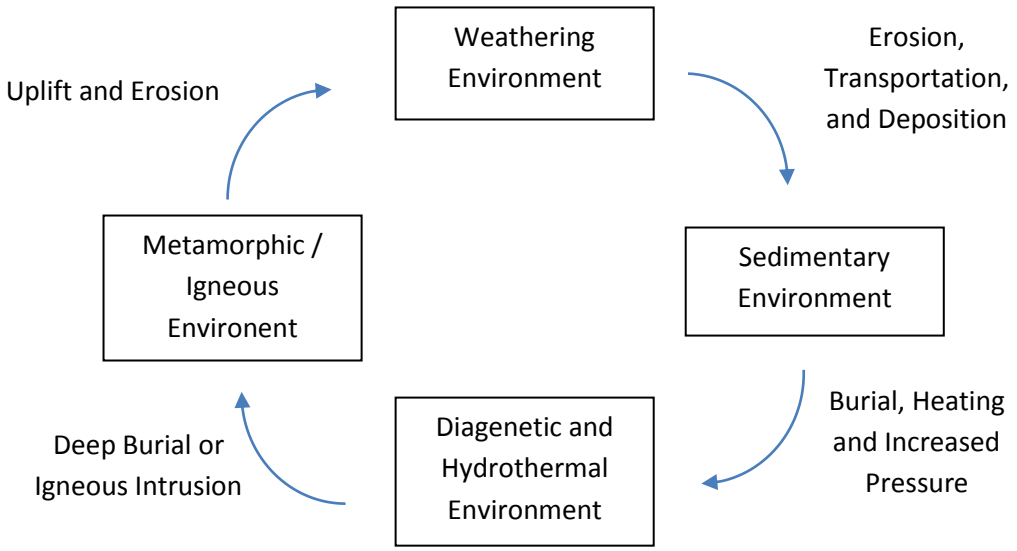

Figure 2.1: The clay cycle (based on Eberl et al. 1984, Figure 2, and Velde 1992, Figure 1.4)

A clay can be extracted from a source close to the point of clay mineral formation (*residual* or *primary*) or away from the source of clay mineral formation (*sedimentary* or *secondary*). The former is more likely to be low in organic content and iron minerals and rich in angular fragments of parent rock, particularly those composed of minerals more resistant to physical/chemical alteration, *Table 2.1,* the latter more homogenous and fine in texture, due to filtering during transportation,

with high organic and iron content and lower levels of impurities such as quartz and mica (Norton 1974; Rice 1987; Fahrenholtz 2008).

1	Quartz (most)	7	Mucovite Mica	13	Anorthite Feldspar (Ca)
2	Zircon	8	Orthoclase feldspar (K)	14	Apatite
3	Tourmaline	9	Garnet	15	Biotite mica
4	Magnetite	10	Albite feldspar (Na/Ca)	16	Hornblende (amphibole)
5	Ilmenite	11	Oligoclase feldspar (Na/Ca)	17	Augite (pyroxene)
6	Rutile	12	Andesine feldspar (Ca/Na)	18	Olivine (least)

Table 2.1: Resistance of rock-forming minerals to physical/chemical alteration, most to least (Rice 1987, Table 2.3).

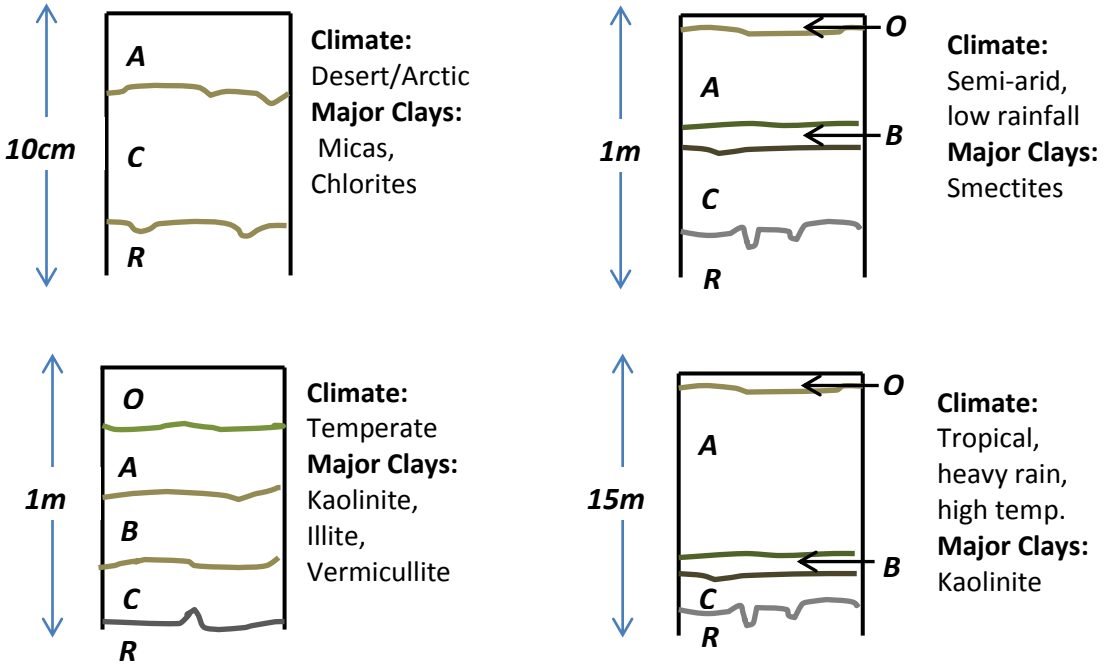

Figure 2.2: Weathering profiles in different climates. A = surface soil, B = clay layer, C = saprock (rocks undergoing alteration to clays), R = bedrock, O = organic matter. Based on Velde (1992, Figure 4.8).

The degree and type of clay mineral formed varies considerably with the manner (i.e. weathering, diagenesis) and context (i.e. temperature or arid climate) of formation, for example *Figure 2.2*.

The main clay minerals produced, and their groupings/classifications are presented in *Table 2.2*.[1] The classifications follow Brown and Nadeau (1984) and Moore and

[1] The general structure of clay minerals and the specifics of the clay mineral species find broad agreement in the present literature, although there is some variation in the ordering and classification (Brindley et al. 1951; Grim 1968; Norton 1974; Millot 1979; Brown and Nadeau 1984; Worrall 1986; Rice 1987; Moore and Reynolds 1997; Meunier 2005).

Reynolds (1997) and are based on the layer type, charge on the layers, and dioctahedral or trioctahedral occupation, described shortly.

Layer Type	Layer Residual Charge	Group	Subgroup	Tri- (T) or Di- (D) octahedral	Species
1:1	0	***Kaolin – Serpentine***	Kaolins	D	Kaolinite ($Al_2Si_2O_5(OH)_4$), dickite, nacrite, halloysite
			Serpentines	T	Chrysotile, antigorite, lizardite
2:1	0	***Talc-Pyrophyllite***	Talc	T	Talc
			Pyrophillite	D	Pyrophyllite
	0.2-0.6	***Smectite***	Smectites	T	Saponite, hectorite
				D	Montmorillonite ($(Al_{1.67}Mg_{0.33})Si_4O_{10}(OH)_2$), beidellite, nontronite
	0.6-0.9	***Vermicullite***	Vermicullites	T	Vermicullite
				D	Vermicullite
		Illite	Illite	D	Illite ($Al_{2-x}Mg_xK_{1-x-y}(Si_{1.5-y}Al_{0.5+y}O_5)_2(OH)_2$), Glauconite
	1.0	***Mica***	Micas	T	Biotite, phlogopite, lepidolite
				D	Muscovite, paragonite
	Variable	***Chlorite***	Chlorites	Mixed	Chlorite, donbassite
2:1	Variable	***Sepiolite – palygorskite***	Sepiolite	T	Sepiolite
			Palygorskite	D	Palygorskite

Table 2.2: Classification of clay minerals. Expressions for the elemental composition are provided for kaolinite, montmorillonite and illite, clay minerals used commonly in pottery and brick production. Following Brown and Nadeau (1984) and Moore and Reynolds (1997).

Clay minerals are hydrous alumino-silicates, with most classified as phyllosilicates (from Greek *phyllos,* "leaf"), or layered silicates, though some have a chain or lattice type structure (Rice 1987). They are so called because the atoms (cations, anion) in their structures are organised in sheet-like arrangements of one of two modular units: a sheet of corner-linked tetrahedral and a sheet of edge-linked octahedral.[2]

[2] Given there is some variation in the literature at the ordering and classification level, the following descriptions are heavily guided by the works of Brown and Nadeau (1984) and Moore and Reynolds (1997), for their clarity and mineralogical detail, and towards Rice (1987), who approaches the topic very much from the perspective of prehistoric/historic pottery manufacture.

The tetrahedral sheet is made up of tetrahedrons, *Figure 2.3 (left)*, arranged in a hexagon-like pattern, *Figure 2.3 (right)*. At the centre of the tetrahedron is a cation, dominantly Si^{4+}, but Al^{3+} substitutes for it regularly and Fe^{3+} to a much lesser extent. At each of the corners is a covalently (almost ionic) bonded oxygen (O) anion. This oxygen atom provides the bonding between the tetrahedrons of the sheet. In effect, each oxygen bonds to two silicon, satisfying its valence requirements. Each tetrahedron then shares three of its corners with three adjacent tetrahedrons, resulting in a formula of $(Si_2O_5)_n$ for the sheet (Kingery, Bowen and Uhlmann 1976, p. 77-80). The interlinked oxygens are called *basal* oxygens, while the remaining 'upward' pointing oxygens are called *apical* oxygens. The Si-O bond distance is about 1.62Å and the O-O distance is about 2.64Å. When substitution of the cation, Al replacing Si say, takes place these dimension will change accordingly (1.77Å for Al-O) (Moore and Reynolds 1997).

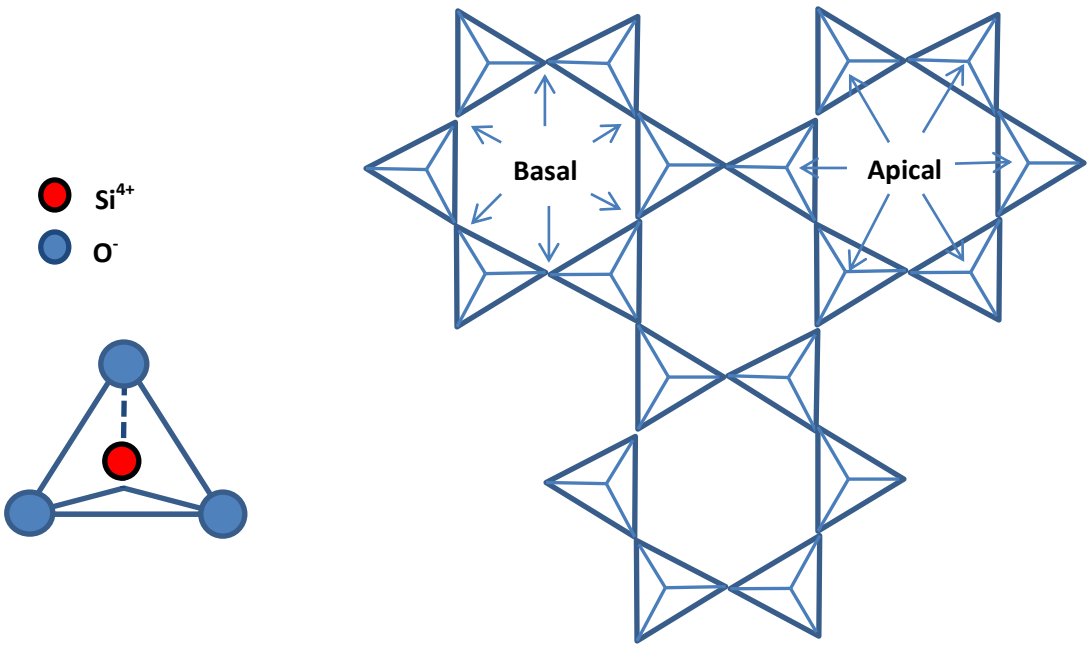

Figure 2.3: Left - centrally positioned cation (Si) tetrahedrally coordinated to four anions (oxygen). Right - Sheet of corner-linked tetrahedral.

The octahedral sheet is generally made up of edge-linked octahedrons, formed from a cation of aluminium, Al^{3+}, with two oxygens (O) and four hydroxyls (OH) equidistantly spaced about it, *Figure 2.4 (left)*. In place of Al can be found Mg^{2+} and to a lesser extent Fe^{2+} or Fe^{3+}. The oxygens and hydroxyls form the joints to

neighbouring octahedrons producing a sheet-like manifold, *Figure 2.4 (right)* with an effective chemical formula of $[AlO(OH)_2]_n$. There are two kinds of octahedral sheets. If all the octahedral have a central cation the sheet is called trioctahedral; if two-thirds are occupied the sheet is called dioctahedral.

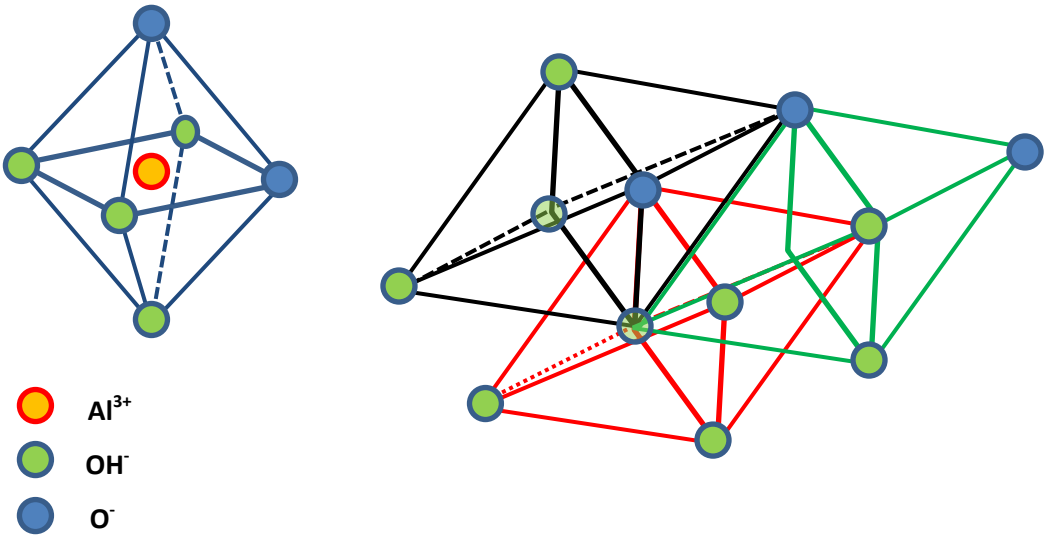

Figure 2.4: Left – cation, Al octahedrally coordinated with O and OH anions. Right – combination of three octahedrons (black, red, green) to form octahedral sheet.

These tetrahedral and octahedral sheets form the basic structural units of clays, of which there are approximately fifty mineral types (Rice 1987). This large array of clays can be obtained from these structural units using two main variations: (a) the manner in which these layers are combined with one another; (b) the cation substitutions within the tetrahedral and octahedral sites (accompanied by ion absorption in some cases).

Structural layers – 1:1 and 2:1

There are two fundamental units formed by stacking of tetrahedral and octahedral sheets, namely a 1:1 and 2:1 structure. A 1:1 structure, also referred to as a three layer structure is obtained by linking one octahedral sheet to one tetrahedral sheet, *Figure 2.5*. A strong bond (covalent) is formed by shared oxygens (the apical oxygen of the tetrahedral) between the two layers. This can be seen as occurring through bonding with the two oxygen ions in the octahedron's lower plane; the remaining

OH is not involved in the bonding but instead sits aligned with the hexagonal hole of the tetrahedral sheet (Moore and Reynolds 1997). The exposed surface of the octahedral sheet consists of hydroxyls only (Brown and Nadeau 1984). These are referred to as *outer hydroxyls* while the unbounded interior OH is referred to as the *inner* hydroxyl (Velde 1992; note - outer hydroxyls do not occur in the 2:1 structure).

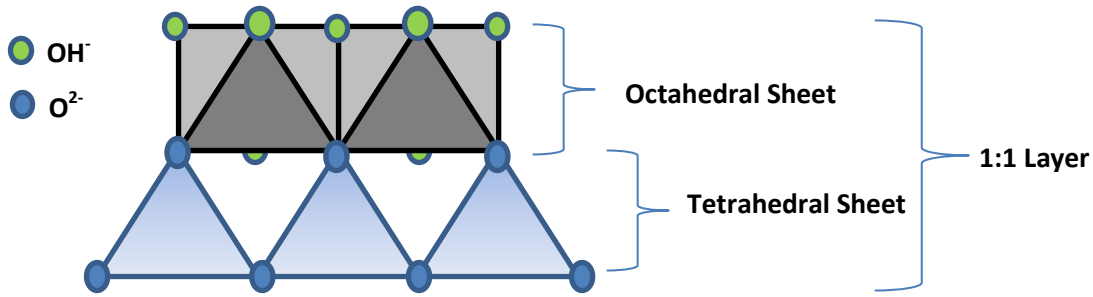

Figure 2.5: 1:1 structure corresponding to an octahedral sheet stacked upon a tetrahedral sheet, with oxygen forming the bonds.

Of course, a single 1:1 layer does not constitute a clay mineral crystal. To obtain this, layers are stacked on top of one another, *Figure 2.6* (for the kaolin clay group), with the resulting crystal held together by weaker hydrogen bonds acting between OH groups in the octahedral layer and oxygen in the next tetrahedral layer. This requires closer stacking of the layers than is observed in the 2:1 structures.

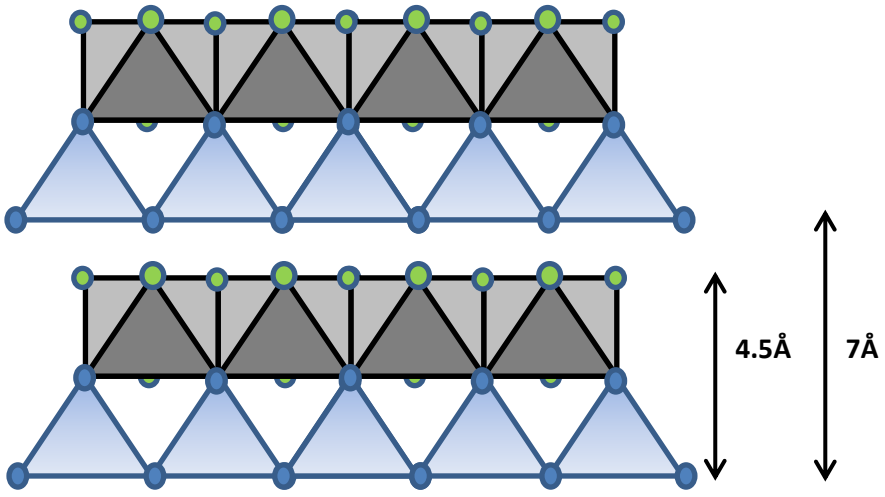

Figure 2.6: Stacking of 1:1 layer. Dimension corresponds to the clay mineral kaolinite.

A 2:1 layer, *Figure 2.7 (left)*, also referred to as a three layer structure, consists of two tetrahedral units to one octahedral unit and is formed by inverting a tetrahedral layer and placing it on top of the 1:1 structure already described. The covalent bond is again formed by apical oxygens from the tetrahedral sheet, this time replacing two of the hydroxyls on the upper layer of the octahedral sheet. The result is a tetrahedral – octahedral – tetrahedral sandwich. The remaining hydroxyls are 'floating'; they do not form any significant bonds with the sheets above or below, sitting instead in the hexagonal gaps of the tetrahedral sheet. A more accurate representation of the three-dimensional stacking is provided in *Figure 2.7 (right)* (Moore and Reynolds 1997, Figure 4.5). This shows that in reality the position of the hydroxyls is not the same for each octahedral and depends on its location relative to the above/below tetrahedron.

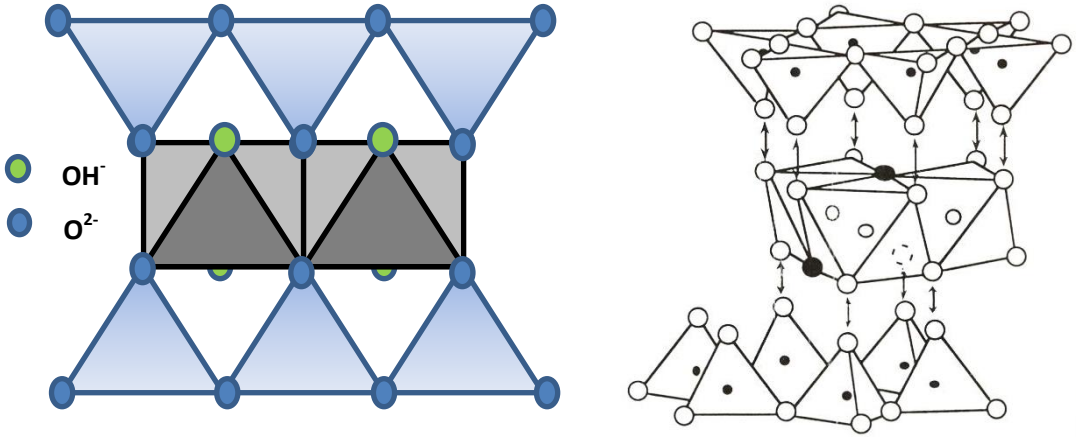

Figure 2.7: Left - 2:1 layer consisting of a tetrahedral-octahedral-tetrahedral sheet combination. Right – three-dimensional perspective of the stacking. Large black dots represent hydroxyls. (Image on right taken from Moore and Reynolds 1997, Figure 4.5).

Clay mineral crystals are formed by stacking these 2:1 layers on top of one another. The particulars of the arrangement depend on whether the basic 2:1 layer is electrically neutral or has a net charge. Briefly, if the layer is neutral, *Figure 2.8 (a)*, the layers are bonded very weakly by dispersive van der Waals forces, with the inter-layer alignment less well defined. Where charge is not neutral, balancing is maintained by inter-layer materials, for example individual cations or hydrated cations, *Figure 2.8 (b, c)*, that bond the layers electrostatically (Bailey 1980; Meunier 2005).

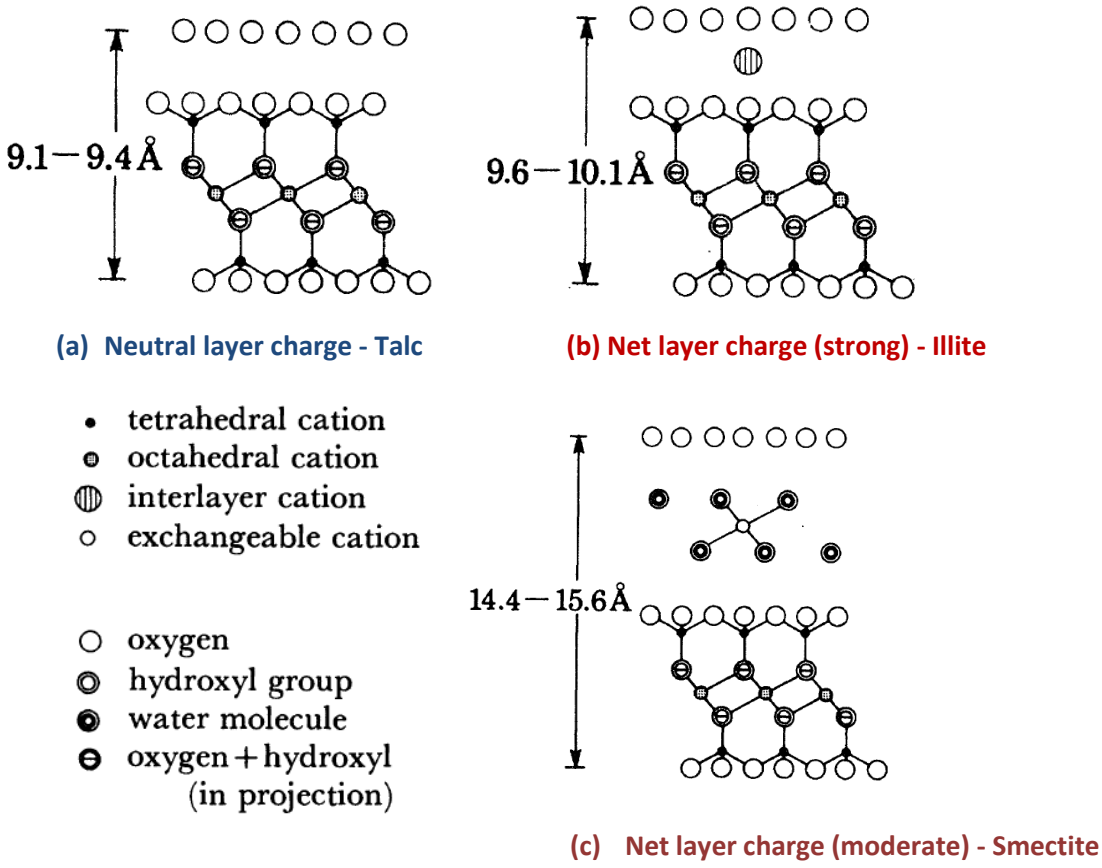

Figure 2.8: Structures for clay minerals with different residual charges on the 2:1 layer (from Bailey 1980).

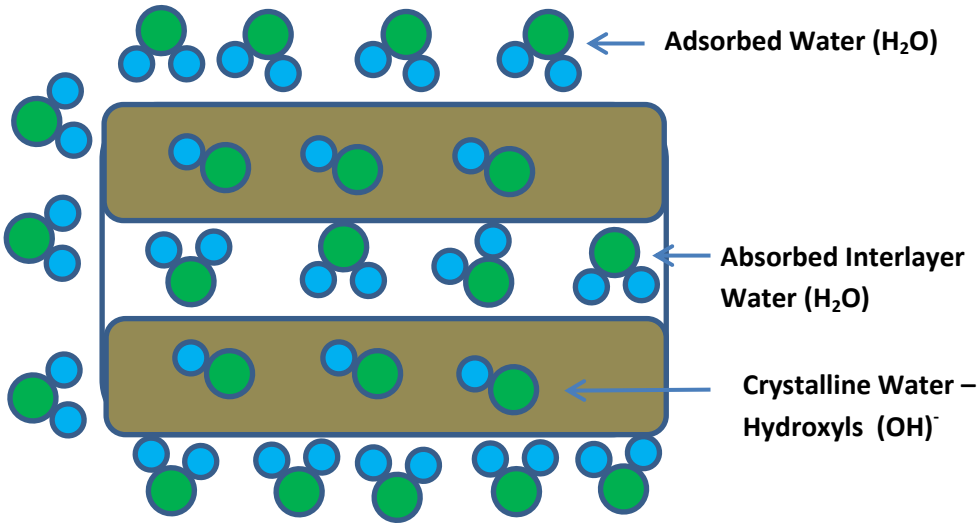

Figure 2.9: Types of water associated with swelling clays. Adsorbed water molecules fixed on clay particle surface. Absorbed water molecules loosely bound to cations between the crystal layers. Crystalline water, hydroxyls, is part of the structure of the clay. Based on Velde (1992, Figure 1.2).

On account of this sheet-like structure and their very fine grain size (<2µm), clay minerals have a very high surface area favourable to adsorption of large quantities of moisture. All clays attract water to their surface (adsorption), but some can incorporate it into their structure (absorption), *Figure 2.9*. [3]

In the context of this thesis, the most relevant clay minerals are those found in the raw clays used in ceramic production of archaeological pottery and brick. A wide range of clay compositions can be tolerated. This allows various sedimentary (or less refined residual) clays to be used with the dominant clay minerals present kaolins, illites, smectites and chlorites (Rice 1987; Dunham 1992).[4] These are not found in the idealised forms described above but instead are extracted from the ground as a combination of a mixture of clay mineral species, mineral inclusions (quartz, feldspars) and organic matter, that, depending on the particular deposit and formation process, are more suited to one function over another, and may need to be subjected to preparation (filtering, purification, tempering) for use.[5] Aside from this, a variety of *tempers* may be added to the clay to alter its behaviour during forming, firing and following firing; this can include mineral temper (sand, igneous rock), bone, shell, organic matter (grass, dung), flint, etc. (for range of materials used as temper and found in archaeological pottery see Rice 1987

[3] Clays that absorb interlayer moisture (and other ions) have the capacity to expand in volume; these are referred to as swelling clays, or more specifically *smectites*. The term *smectite* can lead to some confusion as it is often interchanged with the clay mineral type montmorillonite which is actually the most common mineral of the smectite group of clay minerals.

[4] For bricks, the composition can be quite varied; the clays tend to be high in alkalis and iron but low in alumina according to Grim (1962). No standard chemical composition can be given, due to the variety involved; however, most contain significant proportions of iron oxide (6-12%) and calcium oxide (6-11%) (see Worrall 1986, Table 15). High iron content gives the bricks their distinctive red colour; ferric oxide, Fe_2O_3, the normal product of firing produces yellow and red colouring. Under reduced (oxygen limited) conditions, ferrous oxide, Fe_3O_4, is formed, resulting in blue or black colours. Grain size, mixing, other constituents and firing temperature can also influence the colour (a summary of effects is provided by Worrall 1986, pg. 84-85). Despite having a coarseness due to being rich in mineral impurities, the clay minerals in bricks are actually quite fine grained, < 2µm. Shrinkage is highly variable depending on the size distribution of the clay minerals and impurities involved (Worrall 1986, Rice 1987). Also see Dunham 1992 for an excellent publication on the mineralogy of brick-making in the United Kingdom.

[5] Because of this, it is more common to describe clays using terms expressing their functionality as opposed to mineral species content. Major categories are china clays, ball clays, refractory clays, fire clays and brick clays. For a description of these categories see Norton (1974), Worrall (1986), Rice (1987), and Fahrenholtz (2008).

(notably Table 14.1); Barnett and Hoopes 1995; Gibson 2002; Jordan and Zvelebil 2010; Quinn 2013).

2.3 Heating and Firing of Clays

For a soft, non-durable, clay to be converted into a hard and rigid ceramic it must be heated to a minimum temperature at which the clay minerals commence dehydroxylation, in the temperature regime 450-600°C (Bellotto et al. 1995; Wang et al. 2002; Gualtieri and Ferrari 2006). Archaeological ceramics (pottery particularly) have firing temperature ranges that can vary considerably, 600-1300°C, (Rice 1987, Tite 1995; Pavía and Bolton 2000; Gibson 2002) with brick usually manufactured at a higher temperature range, typically 900-1200°C (Hammond 1981; Dunham 1992; Tite 1995; Pavía and Bolton 2000).

The raw clays used are composed of a mixture of clay minerals, inclusions (inorganic and organic) and temper (inorganic and organic) that, during heating and firing, undergo a range of processes (dehydration, dehydroxylation, oxidation, decomposition, mineral transitions and transformations) with the particular products formed, and the temperature of their formation, varying considerably with the composition of the clay, the rate and duration of firing, and the atmosphere of formation (Rice 1987).[6] The following is an outline description of the sequence of main thermal reactions that occur, *Figure 2.10* and *Table 2.3*; it is guided by similar descriptions in Rice (1987, pottery focussed) and Dunham (1992, brick focussed) but attempts to provide temperature ranges, as well as associated mineral transformations, that encompass those observed from a wider range of studies conducted on raw clays (not pure clay minerals) and archaeological ceramics (pottery and brick), referenced in *Table 2.3*.[7]

[6] Inclusions are defined as non-clay mineral components that are part of the raw clay when extracted from the ground. Temper is defined as non-clay mineral components added to the raw clay by the manufacturer.

[7] It is beyond the scope of the present work to go into the specific details of these studies; however, in *Chapter 9* greater detail and reference will be made to particular publications that are of particular note with regard to the findings of this thesis. The temperature ranges in *Table 2.3* highlight the variable that exists dependent on the original clay composition.

50-200°C – Loose water removal and gypsum dehydration:

The main process in this temperature range is the removal of any loosely-bound adsorbed or pore water from the clay. For 2:1 type clay minerals, particularly smectites, temperatures between 100-300°C may be required to remove more strongly bonded absorbed interlayer water, *Figure 2.9* (Grim 1968, Norton 1974; Rice 1987; Worrall 1986).

Where gypsum ($CaSO_4 \cdot 2H_2O$) is present, dehydration occurs in the range 120-160°C (Dunham 1992).

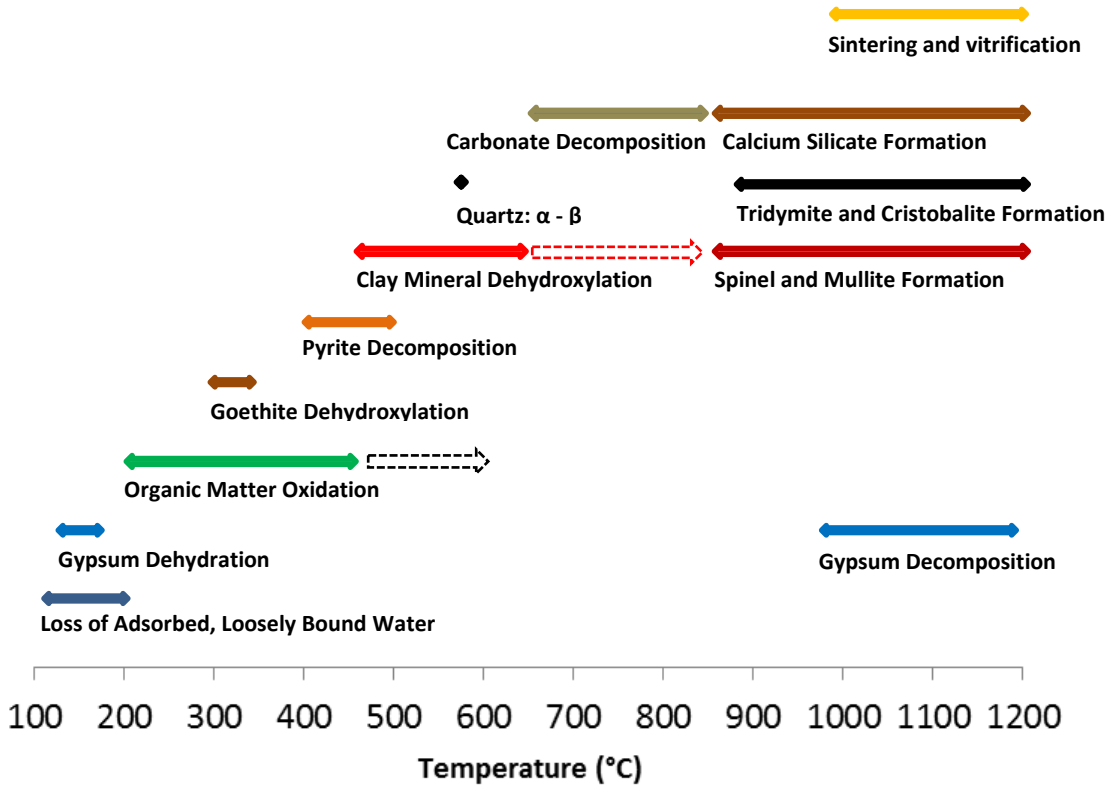

Figure 2.10: Main processes and approximate temperature ranges that occur on firing a clay. Dashed arrows indicate that under certain conditions the process may continue to higher temperatures.

200-450°C- Organic oxidation and goethite dehydroxylation:

Raw clays will typically have some level of organic matter present dependent on the type of clay and its context of extraction. The organic matter occurs principally in the form of coal, lignite, humic acids, bitumen and hydrocarbons that can easily

constitute up to several percent of the raw clay mass (Worrall 1956; Worrall 1986; Prentice 1990). Oxidation of these organics commences from 200°C-450°C, however longer heating times and higher temperatures exceeding 600°C may be required before carbon is completely removed from thicker samples (Ford 1967; Rice 1987).

Also very common in certain clays (ball clays, fireclays) is the presence of iron (hematite principally, Fe_2O_3), which can give the ceramic its red/orange colour when fired. If the iron is present in the form of the iron hydroxide mineral goethite (α-FeO·OH), then dehydroxylation occurs (transforms to hematite) at approximately 300-340°C (Gialanella et al. 2010).

450-650°C – Pyrite decomposition, quartz transition and clay mineral dehydroxylation:

Thermal oxidative decomposition of pyrite (FeS_2), if present in the raw clay, occurs most strongly over the temperature range 400-500°C with the ultimate production of hematite (Fe_2O_3) and SO_2 (see Cheng et al. 2013 for reaction details).

At a well specified temperature of 573°C, quartz changes phases from the alpha form to the beta form, with an accompanying volume expansion. This process is reversible on cooling (Rice 1987).

Arguably the most significant process that occurs during heating of raw clays is that involving dehydroxylation of the clay minerals. General accounts of these processes for the main clay minerals can be found in Grim (1962; 1968) and Brindley and Lemaitre (1987) with more detailed accounts for pure clay minerals in, for example, Heller et al. (1962), Bellotto et al. (1995), Wang et al. (2002), Gualtieri and Ferrari (2006). Dehydroxylation is the process by which the clay mineral losses its hydroxyls via the following set of reactions (Brindley and Lemaitre (1987):

$$1)\ OH^- \leftrightarrow H^+ + O^{2-}$$

$$2)\ H^+ + OH^- \leftrightarrow H_2O$$

The result is the release of water vapour and the loss of crystalline structure within the clay mineral. In raw clays, this process commences and is strongest in the temperature range 450-650°C, with kaolinite transforming to metakaolinite early, 450-550°C (e.g. $Al_2Si_2O_5(OH)_4 \rightarrow Al_2Si_2O_7 + 2H_2O$), smectite (montmorillonite) dehydroxylating at slightly higher temperatures, 550-650°C (e.g. $3[Al_2Si_4O_{10}(OH)_2] \rightarrow 3Al_2O_3.2SiO_2 + OSiO_2 + 3H_2O$), and illites commencing at 450-550°C but showing some persistent structure at temperatures up to 900°C (Grim and Bradley 1940, Worrall 1986; Rice 1987). It is evident from *Table 2.3*, that the temperatures can vary dependent on the composition of the raw clay but that by 850-900°C, under suitable heating regimes (rates and dwell times), considerable, if not complete dehydroxylation, is likely to have occurred for all clay minerals (Rice 1987, Dunham 1992); beyond this new mineral phases form from the dehydroxylated clays.

650-850°C – Carbonate decomposition

Carbonates, particularly calcium carbonate ($CaCO_3$) in the form of limestone, calcite, and shell, can occur as a natural inclusion or deliberately added temper in raw clays used for pottery/brick production (Rice 1987; Quinn 2013). When fired, calcium carbonate (and similarly dolomite, a calcium magnesium carbonate) decomposes to form lime (CaO) and carbon dioxide (CO_2).[8] This generally occurs over a reasonably narrow temperature span of, say, 100°C; however, as can be observed in *Table 2.3*, this can occur over a wide range from 650-900°C, dependent on the conditions of firing and the degree of crystallinity of the calcium carbonate (Shoval et al. 1993; Cardiano et al. 2004). Carbon dioxide is given off during this process.

850-1250°C – High temperature mineral formation and gypsum decomposition:

It is in this temperature range that a series of mineral transformations and the formation of new minerals occur. Again, the transformation temperatures and minerals formed are not entirely agreed upon in the literature, see *Table 2.3*, and is composition dependent. Generally, dehydroxylated clay minerals undergo

[8] Following firing, any remnant CaO is very hygroscopic and will pick up moisture to form calcium hydroxide ($Ca(OH)_2$). This in turn can slowly react with carbon dioxide to form recarbonated or recrystallized calcite, with smaller crystal size, poorer crystallinity, and the presence of impurities (Shoval 2003; Quinn 2013).

transformations to the mineral spinel first and at slightly higher temperatures to mullite (Brindley and Nakahira 1959; Grim 1968; Norton 1974; Worrall 1986). Quartz transitions to tridymite/cristobalite above 870°C and new calcium silicate mineral phases, e.g. gehlenite, wollastonite, anorthite and diopside, are formed above 800°C in clays rich in calcium; the breakdown of $CaCO_3$ at lower temperatures liberates CaO that can then be taken up for the formation of these calcium silicates (see Peters and Iberg (1978), Duminuco et al. (1998) and Cultrone et al. (2001) for details on calcium silicate formation).[9] It is in the temperature range 900-1200 that feldspars (K and Na) begin to melt freeing sources of SiO_2 and Al_2O_3 that can also be involved in the formation of the aforementioned high temperature mineral phases (Dunham 1992; Benedetto et al. 2002; Iordanidis et al. 2009; Rasmussen et al. 2012). Other high phase minerals that have been known to form at high temperatures, > 850°C, include forsterite and enstatite (Ford 1967; Dunham 1992; Maritan et al. 2006; Jordan et al. 2008; Rathossie and Pontikes 2010; Quinn 2013).

If gypsum is present, this will begin to dissociate in the range 1050-1200°C, releasing SO_2 in the form of gas and CaO that, again, can be involved in the formation of calcium silicates (Rice 1987; Pavía and Bolton 2000).

At the upper end of this temperature range and above, >1000°C, increased sintering (the fusing of mineral grains with melting) and vitrification (formation of glassy phases due to increased sintering) occur resulting in a reduction in porosity and possible bloating due to the trapping of gases within the ceramic (West 1969; Rice 1987; Quinn 2013).

The above temperature ranges and transitions provide a guide to the processes involved during heating and are not comprehensive. For more detailed and general discussions on the range of effects of heating on ceramics see Ford (1967) and Rice (1987).

Identification of the high temperature mineral phases presented in *Figure 2.10* and *Table 2.3* provides a means of estimating the maximum firing temperature (because

[9] The reactions that form the high temperature minerals may draw their compositional elements, say SiO_2 and CaO, from any available source, not exclusively the minerals described in the text, although these are the dominant sources.

of considerations of the effect of heating rate and dwell time, see Gosselain 1992) of the ceramic. There has been considerable debate surrounding the appropriateness of this estimation and its interpretation (Gosselain 1992; Livingstone Smith 2001; Tite 1995; 2008), yet it still remains important in understanding the fabrication method and technological choices of potters (Rice 1987; Quinn 2013). With RHX dating, the estimation of maximum firing temperature will be used in this work to estimate if the ceramic may have been under-fired, with insufficient dehydroxylation occurring, or, instead, over-fired to the point of having limited capacity for rehydroxylation (see Mesbah et al. (2010b) and Tosheva et al. (2010), reviewed in *Section 2.4*, for the effect of firing temperature on mass gain rates).

Temperature Stages and Major Processes	**Temperature Range (*maximum*) of Process**	**Process (*additional detail*)**	**Reference**
50-200°C **Loose Water removal 50-200°C** **Gypsum dehydration 120-160°C**	**50-200°C** 50-200°C 50-180°C *100°C* *125°C* *130°C*	**Removal of 'loose' water (adsorbed or pore water)** *Organic-rich clay* *Shell-rich clay*	 Rice (1987) Dunham (1992) Moropoulou et al. (1995) Maritan et al. (2006) Maritan et al. (2007)
	120-160°C 120-160°C 120-160°C *139°C*	**Gypsum dehydration**	 MacKenzie (1970) Dunham (1992) Cardiano et al. (2004)
200-450°C **Organic matter removal commencement 200-450°C** **Goethite dehydroxylation 300-330°C**	**200-450°C** 200-400°C 250°C 300-550°C *350-450°C* *550-650°C*	**Organic Matter Oxidation** *Commencement* *Commencement* *Shell-rich clay* *Organic-rich clay*	 Rice (1987) Dunham (1992) Maritan et al. (2007) Maritan et al. (2006) Moropoulou et al. (1995)

	450°C	*Completion*	Dunham (1992)
	500°C	*Completion*	Rice (1982
	300-340°C	**Goethite Dehydroxylation**	
	300°C		Moropoulou et al. (1995)
	325°C		Dunham (1992)
	320-340°C	*Powdered goethite (TGA/DTA)*	Gialanella et al. (2010)
450-650°C	**400-500°C**	**Pyrite Decomposition**	
	400-450°C	*Anhydrite formation possible*	Dunham (1992)
Pyrite decomposition	450°C		Ford (1967)
400-500°C	480°C		Prentice (1990)
	350-500°C		Bonamartini Corradi et al. (1996)
Quartz transition			
573°C	400-600°C	*Coal-derived pyrite*	Cheng et al. (2013)
	573°C	**α → β Quartz**	Rice (1987)
Clay dehydroxylation commencement			Ford (1967)
450-650°C			Prentice (1990)
	450-650°C	**Clay Dehydroxylation Commencement**	
	450-600°C	*General commencement*	Rice (1987)
	450-650°C	*Brick Clays*	Dunham (1992)
	400-500°C	*Ca-poor, illite/kaolinite clay*	Toledo et al. (2004)
	400-500°C	*Organic-rich, chlorite-rich*	Toledo et al. (2004)
	440-500°C	*Alluvial clay, kaolinite/illite*	Manoharan et al. (2011)
	400-600°C	*Can persist to 800°C*	Maniatis et al. (1982)
	500°C	*Kaolin*	Grim (1968)
	500-550°C	*Ca-rich, kaolinite*	Peters and Iberg (1978)
	500-550°C	*Ca-rich, iron-rich, chlorite*	Nodari et al. (2007)
	500-600°C	*Non-Ca, Kaolinitic clay*	Maggetti 1982
	500-650°C	*Organic-rich, chlorite-rich*	Maritan et al. (2006)
	500-650°C	*Chlorite*	Maritan et al. (2007)
	500-650°C	*Kaolinite → Metakaolinite*	Shoval (2003)
	540°C	*Organic-rich, chlorite-rich*	Maritan et al. (2006)
	550°C	*Non-carbonate, smectite/kaolinite clay*	Moropoulou et al. (1995)
	550-650°C	*Kaolinite, illite, smectite mixed clays*	Cultrone et al. (2001)
	600-800°C	*Smectite* → Meta-smectite	Shoval (2003)
	650-950°C	*Ca-rich, illite/montmorillonite*	Peters and Iberg (1978)

	650-670°C	*Ca-rich, Iron-rich, chlorite (XRD 001)*	Nodari et al. (2007)
	700°C	*Only illite clay survives, Ca-rich and Ca-poor clays*	Cultrone et al. (2001;2004)
	800°C	*Organic-rich, illite*	Maritan et al. (2006)
	800°C	*Clay minerals absent, brick clay*	Pavía (2006)
	850°C	*Illite (XRD 001) loss*, *Ca-rich, Iron-rich clays*	Nodari et al. (2007)
	850-900°C	*Shell-rich, illite*	Maritan et al. (2007)
	900°C	*Illite, Ca-rich/poor clays*	Cultrone et al. (2004;2005)
	<900°C	*Illitic clay breakdown*	Jordan et al. (2008)
	900-1000°C	*Illitic non-Ca clays*	Maggetti 1982
650-850°C	**650-850°C**	**Calcium/Magnesium Carbonate Decomposition**	
Carbonate Decomposition	650-900°C	*General range*	Rice (1987)
	650°C	*Calcite decomposition starts*	Dunham (1992)
	550-850°C	*Calcite –grains to fine grains*	Riccardi (1999)
	550-650°C	*Dolomite, Ca-rich clays*	Peters and Iberg (1978)
	600-700°C	*Ca-rich clay, fine-grained calcite*	Peters and Iberg (1978)
	650°C	*Polycrystalline (limestone,chalk)*	Shoval et al. (1993)
	650-750°C	*Calcite*	Quinn (2013)
	650-850°C	*Calcite*	Cardiano et al. (2004)
	700°C	*Ca-rich, Iron-rich, carbonate/non-carbonate clay, calcite and dolomite decomposition*	Cultrone et al. (2001)
	700-750°C	*Dolomite*	Maritan et al. (2007)
	750°C	*Ca-rich, iron-rich, dolomite*	Nodari et al. (2007)
	750°C	*Monocrystalline calcite*	Shoval et al. (1993)
	750-800°C	*Calcite tempered clays*	Cardiano et al. (2004)
	780-860°C	*Dolomite in clays*	Moropoulou et al. (1995)
	750-800°C	*Illitic calcareous clays, calcite*	Maggetti 1982
	800°C	*Calcite*	Shoval (2003)
	800°C	*Carbonate clay, calcite*	Cultrone et al. (2001)
	800,870°C	*Shell-rich clay, dolomite and calcite decomposition*	Maritan et al. (2007)
	800-900°C	*Clay (limestone inclusions)*	Shoval (1994)
	840°C	*Carbonate-rich clays*	Moropoulou et al.

	840°C	*Organic-rich clay, calcite*	(1995)
			Maritan et al. (2006)
	850°C	*Ca-rich, Iron-rich, calcite*	Nodari et al. (2007)
	850-950°C	*Peloponnese clays, calcite*	Rathossi and Pontikes (2010)
850-1250°C	**850-1100°C**	**Clay Minerals (dehydroxylated) form Spinel and Mullite**	
Clay Minerals → Spinel/Mullite	900°C	*Kaolinite → Spinel/Mullite*	Dunham (1992)
900-1100°C	950°C	*Metakaolin → Spinel*	Rice (1987)
	1050-1275°C	*Spinel → Mullite*	Rice (1987)
	900°C	*Illitic clay, spinel formation*	Jordan et al. (2008)
Quartz→ Tridymite/Cristobalite	900°C	*Organic-rich clay, spinel*	Maritan et al. (2006)
	900°C	*Non-calcareous clay, mullite*	Cultrone et al. (2004)
867-1250°C	900°C	*Brick, mullite/spinel*	Pavía (2006)
	900°C	*Mullite*	Cultrone et al. (2005)
Gypsum Breakdown 1050-1200°C	900°C	*Carbonate/non-carbonate clays, mullite formation*	Cultrone et al. (2001)
	900°C	*Illitic, non-calcareous, spinel*	Maggetti (1982)
Ca-rich Clays→ Calcium Silicates: Diopside/Wollastonite/ Gehlenite/ Anorthite	900°C	*Chlorite→ spinel, olivine, enstatite*	Dunham (1992)
	900-1000°C	*Illite → spinel/mullite*	Rice (1987)
	950°C	*Non-calcareous clays, kaolinite → mullite*	Maggetti (1982)
	950°C	*Metakaolinite → spinel*	Ford (1967)
	950°C	*Alluvial clay, spinel and mullite*	Manoharan et al. (2011)
	980°C	*Metakaolin → Al-spinel*	Moropoulou et al. (1995)
	1050°C	*Organic-rich, spinel*	Maritan et al. (2006)
	1050°C	*Illite → spinel/mullite*	Dunham (1992)
	1050-1100°C	*Illitic, non-calcareous, mullite*	Maggetti (1982)
	1100°C	*Spinel → mullite*	Ford (1967)
	1100°C	*Carbonate rich/poor clays, mullite formation*	Jordan et al. (2008)
	867-1250°C	**Quartz formation of tridymite/cristobalite**	
	867°C	*Quartz → tridymite*	Rice (1987)
	870°C	*Quartz → cristobalite*	Prentice (1990)
	870°C	*Quartz → cristobalite*	Ford (1967)
	1000-1100°C	*Bricks clays, cristobalite*	Dunham (1992)
	1050°C	*Kaolinitic non-calcareous clays, cristobalite formation*	Maggetti (1982)

	1100°C	*Ca-poor, illite/kaolinite clay, cristobalite formation*	Toledo et al. (2004)
	1150-1250°C	*Flint → cristobalite*	Ford (1967)
	1250°C	*Tridymite → cristobalite*	Rice (1987)
	1050-1200°C	**Gypsum Breakdown**	
	1050°C		Pavía and Bolton (2000)
	1200°C		Rice (1987)
	800-1050°C	**Ca-rich clays, formation of Gehlenite, Wollastonite, Anorthite, Diopside**	
	750-800°C	*Gehlenite*	Nodari et al. (2007)
	750-850	*Gehlenite*	Benedetto et al. (2002)
	800°C	*Gehlenite*	Cultrone et al. (2001)
	800°C	*Gehlenite*	Cultrone et al. (2004)
	800-900°C	*Limestone inclusion rich clay, gehlenite, anorthite, diopside*	Shoval (1994)
	850-900°C	*Brick clays, wollastonite, anorthite, diopside*	Dunham (1992)
	850°C	*Diopside and wollastonite*	Pavía (2006)
	850°C	*Gehlenite*	Riccardi et al. (1999)
	850°C	*Pelloponnese clays, gehlenite, anorthite, wollastonite*	Rathossi and Pontikes (2010)
	850-900°C	*Illitic clay, gehlenite, wollastonite, diopside, anorthite*	Maggetti (1982)
	860-1050°C	*Gehlenite*	Peters and Iberg (1978)
	860°C	*Wollastonite, diopside, anorthite*	Peters and Iberg (1978)
	900°C	*Anorthite*	Cultrone et al. (2001)
	900°C	*Gehlenite and diopside (organic-rich clay)*	Maritan et al. (2006)
	900-1000°C	*Gehlenite, wollastonite, diopside (blue clay Denmark)*	Rasmussen et al. (2012)
	950°C	*Gehlenite*	Jordan et al. (2008)
	1000°C	*Wollastonite and diopside*	Cultrone et al. (2004)
	1050°C	*Wollastonite*	Riccardi et al. (1999)

Table 2.3: The temperature ranges and associated processes that occur during firing of raw clays. Temperatures ranges are included from individual studies conducted on raw clays and archaeological ceramics, including pottery and brick. Italicised text provides additional detail and, where not self-explanatory, is of the general form *type of clay, result of process (i.e. new mineral formed).*

2.4 Rehydration and Rehydroxylation

Rehydration is a general expression that describes the uptake of molecular water in a ceramic following firing. This can include physical adsorption processes (physisorption) and chemical adsorption processes (chemisorption). Physisorption processes include molecular water adsorbed on the external surfaces and in the pore surfaces of the ceramic by van der Waals forces, molecular water that is held by capillary condensation (Laplace-type forces), and molecular water held by hydrogen bonding (involved in multi-layer adsorption and capillary condensation). Chemisorption processes are chemically bonded and in the case of fired clays this refers to rehydroxylation, a chemical (re)combination in which molecular water reacts with the remnant dehydroxylated clay in the ceramic matrix to form new hydroxide ions (see Lowell et al. (2004, Chapter 2) for more on the definitions and distinctions between physisorption and chemisorption and the forces involved).

The physisorption processes are not long term processes (although capillary condensation may take longer than surface adsorption) and respond quickly to changes in environmental conditions (the relative humidity, %RH); they can be described by various theories of adsorption, for example Langmuir theory, Brunauer, Emmett and Teller theory (BET), Barrett-Joyner-Halenda theory (BJH), with the level of adsorption governed largely by the ceramics' composition, pore structure geometry and size distribution, and the ratio of the partial vapour pressure (for water) to the equilibrium vapour pressure (i.e. the relative humidity) (Lowell et al. 2004, Chapter 4).

The chemisorption process of rehydroxylation is the long term process that is critical to RHX dating. Therefore, the remainder of this section will focus on this process, providing a summary account and brief history of significant research studies and advances into understanding rehydroxylation, up to the point at which RHX dating related studies commence (Wilson et al. 2003), examined in *Section 2.5*. A more detailed review is provided by Hamilton and Hall (2012).

Perhaps the earliest publication reporting rehydroxylation in fired clays is that of Washburn and Footit (1921), who describe mass gain in freshly fired brick and

associated this with rehydration of the 'burned' clay. [10] Schurect (1928), examined the crazing of ceramic glazes, and related the moisture expansion to the uptake of 'combined water'. Hence, these two rehydroxylation-driven processes, expansion and mass gain, have long been recognised; since then there have been several notable advances in understanding the underlying mechanism and kinetics involved via their study. A significant publication by Barrett (1937) examined the rehydration of fired brick clays (measuring the expansion and mass gain before and after autoclaving and for a brick which had been weathered for 60 years). Significant mass gain was observed in the autoclaved and weathered samples that was not associated with "free" pore water removed at 100°C but instead with a type of "bound" water that was most strongly removed by reheating close to 400°C; Barrett stated, "fired clay will pick up water at ordinary temperature, either on soaking or even on being left in a moist atmosphere. This moisture is not expelled by drying in an oven at 110°C, and so must be firmly held, presumably by "chemical" forces." The dependence of the level of rehydration with original firing temperature (finding a maximum at 850-950°C) was also demonstrated, finding parallels in much more recent work by Mesbah et al. (2010b) and Tosheva et al. (2010) (*Section 2.5*).

Increased interest in moisture expansion of ceramics occurred in the 1950s-1960s (e.g. Hueber and Milne 1955; Smith 1955; Norris et al. 1958; Young and Brownell 1959; Waters et al. 1960; Cole 1961; 1962a; Freeman and Smith 1967). The underlying cause of expansion was linked with the level of amorphous material within the ceramic (Smith 1955; Young and Brownell 1959), supported by the work of Norris et al. (1958), and this amorphous phase itself linked to the firing temperature (Young and Brownell 1959). A significant connection was made in the work of Cole (1961; 1962a; 1962b) who demonstrated that the expansion in fired clay products was correlated, roughly proportionally, with an increase in mass. More recent studies conducted on the long term expansion of large sets of bricks (Smith 1993; Zsembery et. al. 2004) have been valuable in demonstrating that the process does continue over long periods of time. Otherwise, before the moisture

[10] In the early literature the expression rehydroxylation is not used, with rehydration instead used to describe processes that would later be ascribed to rehydroxylation. It is following the work of Heller et al. (1962) that the term rehydroxylation becomes more commonplace.

expansion studies that commence with Wilson et al. (2003) and mark the advent of RHX dating research, see *Section 2.5*, there are few other notable contributions to understanding the underlying mechanism, rehydroxylation, from moisture expansion or mass gain studies.

Examination of the fired clay and clay minerals themselves has provided another source of understanding. Early publications demonstrated considerable, if not complete, rehydration of clay minerals under high steam pressures and temperatures (Van Nieuwenberg and Pieters 1929; Schachtschabel 1930, both cited by Barrett 1937 and Grim 1968). However, it was arguably the work of Grim and Bradley (1948), using differential thermal analysis (DTA), that was pivotal in providing more detailed evidence of dehydration and rehydration of a range of clay minerals (montmorillonite, illite, kaolinite, and halloysite) at room temperature and associating this strongly with rehydroxylation. The adsorption of molecular water was associated with a gain in hydroxyl groups and it was also demonstrated that the rehydroxylated ceramic could be dehydroxylated by reheating at lower temperatures than the original firing, the implication being that the structure of the fired clay is structurally dissimilar to that of the original raw clay.

Renewed interest appeared to have been generated by this publication and a series of work by various groups followed (for example Roy 1949; Hill 1953; Jonas 1955; Saalfeld 1955; Hill 1956; Roy and Brindley 1956; Dietzel and Dhekne 1957). Saalfeld (1955) and Dietzel and Dhekne (1957) carried out hydrothermal rehydration of metakaolin, reporting a reconversion to a poorly crystallised kaolinite form, with Dietzel and Dhekne (1957) also reporting dehydroxylation of rehydroxylated metakaolin occurring at lower temperatures than the original dehydroxylation, 500°C. Roy and Brindley (1956) also demonstrated a conversion from metakaolin to kaolinite by hydrothermal treatment for a range of temperature, pressure and time, showing that temperature is a dominant factor in the amount of conversion. Jonas (1955) examined the rehydroxylation of montmorillonite and found near complete regain of hydroxyls as well as that the rehydroxyls can be removed by heating at a lower temperature than the original firing temperature, suggesting a temperature of 500°C. Later, Heller et al. (1962) also observed rehydroxylation in clay minerals

but by using infra-red spectroscopy and XRD, in addition to DTA, their work permitted changes in OH bonding to be observed and structural alterations to be examined; the findings provide support for a rehydroxylation process and support the earlier work of Grim and Bradley (1948) in that rehydroxylation does not structurally return the ceramic to its original unfired structure.

This work conducted on clay minerals between 1920-1970 provided a body of work that established that a) rehydroxylation of ceramics takes place (and with it an associated mass gain) b) rehydroxylation is associated with fired clay minerals c) the ceramic does not structurally return to its pre-fired state, and d) the ceramic can be refired at lower temperatures, approximately 400-600°C, than the original firing temperature to dehydroxylated the rehydroxylated ceramic.

Despite more recent studies into the rehydroxylation of fired clay minerals (see Hurst and Kunkle 1985, Rocha and Klinowski 1991, Rocha et al. 1990; Muller et al. 2000a; 2000b; Molina-Montes et al. 2010), there appears little additional understanding of the underlying mechanism, particularly what governs its rate and temperature dependence (activation energy). As concluded by Hamilton and Hall (2012), dehydroxylation is assumed to proceed via the reaction of two adjacent OH groups to form a water molecule which is removed following diffusion to the ceramic surface (Grim and Bradley 1948; Brindley and Lemaitre 1987) with RHX presumably operating via the reverse mechanism.

How water molecules adsorbed in the pore structure diffuse to sites where RHX can occur is unclear; the time dependent (mass gain) behaviour has only recently been examined in any detail, discussed more in *Section 2.5*, but a $t^{1/4}$ or $t^{1/n}$ power law behaviour appears well supported (Wilson et al. 2003; Bowen et al. 2011; Le Goff and Gallet 2015). Hamilton and Hall (2012) associate this subdiffusion (relative to $t^{1/2}$ kinetics of classical diffusion) with transport processes that are constrained either spatially, i.e. narrow channels of diffusion, or temporally, i.e. blocking of routes of diffusion until a molecule with long residence times reacts and is removed from the path. They speculate that "the super-slow reaction which we observe in most fired clay ceramics occurs by transfer of OH^- ions between acceptor/donor

sites in such a way that the concentration of free water molecules is either small or zero, and by means of pathways which are extremely restricted."

This concludes a short summary of rehydration and rehydroxylation research into fired clays. The following section will discuss in detail RHX-dating related research which contributes to this knowledge while remaining focussed on archaeological application. This will start with the work of Wilson et al. (2003), before which, despite the observation of rehydroxylation in archaeological ceramics (Kingery 1974; Shoval et al. 1991), there was insufficient understanding of the long term kinetics involved and no serious consideration given to using these properties of rehydration and rehydroxylation of fired clays to date archaeological ceramics.

2.5 Rehydroxylation Dating

The following is a detailed chronological account and critical review of the research and developments in rehydroxylation dating to date. It focusses on research that either deals with rehydroxylation (RHX) dating of fired clay ceramics directly or explores aspects of the behaviour of fired clay ceramics with the dating technique in mind.

Despite the long-term recognition of moisture expansion and associated mass gain in fired clay ceramics, see *Section 2.4*, there was no "*unifying description of this expansion process in ceramics"* when the subject was researched by Wilson et al. (2003). It was from this piece of work that the potential for rehydroxylation dating was first proposed, and as such this work can be considered the advent of the field of research into RHX dating.[11] The work of Wilson et al. (2003) was originally concerned with the moisture expansion kinetics of bricks over long time scales, of interest for structural engineering reasons. They measured the dimensional changes of freshly fired brick samples (all of the same type) that were allowed to age under a range of environmental conditions over periods up to 104 days. The conditions, were diverse, from low (vacuum) to high (100%RH, water saturated, steam autoclaved) moisture content (vacuum), and from temperatures ranging from laboratory at 20°C to 186°C (autoclaving). Several mass gain measurements were also performed, using a top-loading balance. They also examined longer term expansion and the capacity for expansion of bricks of ages ranging from 20 to 2000 year old (Roman samples) by recording expansive strains before and after heating at 450°C for 2 hours followed by autoclaving at high temperatures (186°C).

[11] Work decades earlier by Enriquez et al. (1979) had drawn attention to an observable correlation between the magnitude of DTA peaks, corresponding to the release of lattice water hydroxyl groups and interpreted as due to rehydroxylation since original firing, and the age of Amazonian archaeological pottery up to several thousand years old; however, this was based on a well-defined DTA endothermic peak from 100-140°C (not deemed due to removal of physically adsorbed water which occurred over an extended temperature range below 100°C), and the observed relationship with the age of the ceramic does not appear to have been developed upon.

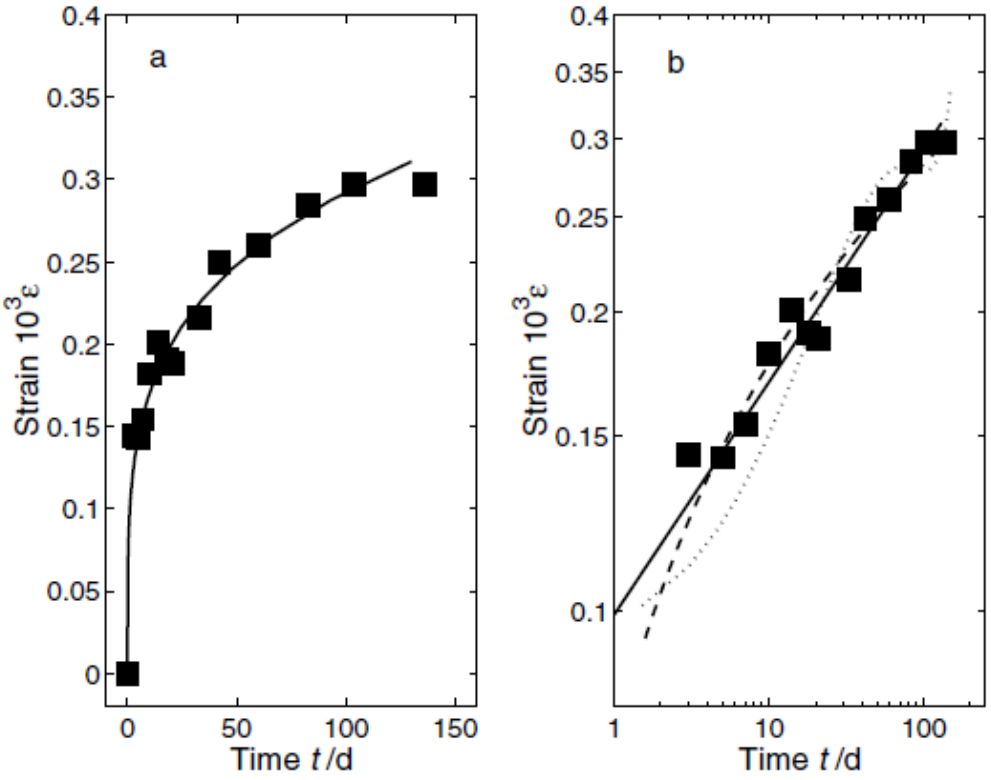

Figure 2.11: The expansion of a freshly fired brick, aging under ambient conditions (approximately 20°C, 50%RH) in the laboratory. The solid line is the power-law fit, $\epsilon = 9.9 \times 10^{-5}$ $(t/\mathrm{d})^{0.24}$. (a) Linear axes. (b) Log axes; logarithmic (dashed line) and polynomial (dotted line) regression fits are shown for comparison. From Wilson (2003, Figure 1).

Several significant findings came out of these tests: the expansion of the freshly fired bricks*, Figure 2.11*, was argued to be well described over longer periods by an approximate *time*$^{1/4}$ ($t^{1/4}$) power law, an improvement upon the commonly used logarithm function (Cole 1961); the mass increased proportionally with the expansion, *Figure 2.12*; the expansion was shown to be driven by uptake of environmental moisture (cessation of expansion under vacuum conditions); the authors also argue that provided some water is available the expansions are relatively insensitive to the environmental moisture conditions, *Figure 2.13*, being driven primarily by temperature. The last point is not entirely convincing as only for cases *B, C* and *E*, *Figure 2.13*, can the effects of moisture level on the expansion be compared for the similar temperature conditions. For these, it appears that the expansion is greater at 100%RH (*E)* than it is underwater (*C*), with both greater than the ambient condition at 50%RH (*B*). The differences may be due to experimental

uncertainties but might also suggest some sensitivity to moisture conditions. It is also interesting that, for cases *D* (underwater at 50°C) and *E* (100%RH at 20°C), the expansion is greater at the lower temperature than the higher temperature, with an explanation not provided by the authors. Of note also, is that the strain and fractional mass gain are modelled with a power law $t^{1/n}$ where n = 0.24 (strain) and 0.22 (mass), presumably because these provide a better fit, with the authors only suggesting an *approximate* $t^{1/4}$ model at this point.

The reason for the slow power-law expansive behaviour, as argued by Wilson et al. (2003), is diffusion of water molecules on a structure of low dimensionality (Mojaradi and Sahimi 1988; Lin et al. 1997; Ahn et al. 1999), where molecules cannot bypass one another and progress is hindered until chemisorption at reaction sites removes a molecule from the channel allowing further diffusion to occur. Traditionally, for molecules diffusing in three dimensions, the mean square displacement $\langle r^2 \rangle$ varies with t. When restricted to one dimension, it is proportional to $t^{1/2}$ (Harris 1965). This diffusion does not, however, involve reactions along the path, chemisorption reactions which, in the case of fired clay ceramic, are responsible for the $t^{1/4}$ behaviour. Wilson et al. (2003) further suggest that because the pores in fired clays are extremely large compared to the size of the water molecules, sites on the surface of the pores are almost immediately reacted, with the long term diffusion process that of water molecules moving through narrower channels and networks, of similar dimensions to the water molecule. They identify the chemisorption reaction responsible for the expansion and mass gain as rehydroxylation in the fired clays, discussed in *Section 2.4*.[12]

Another important set of results came from the second group of tests by Wilson et al. (2003); the older samples examined showed expansive strain that was consistent with the shorter term data and with their having continuously gained moisture over

[12] It was already well established that clays fired lightly, from 550°C up to 930°C, showed some rehydration or rehydroxylation when exposed to water vapour (Grim and Bradley 1948; Kingery 1974). Wilson et al. (2003) demonstrated that even bricks fired to considerably higher temperatures (1100°C) retain a capacity for rehydration and rehydroxylation. Shoval et al. (1991) associate the potential for rehydroxylation with the presence of amorphous matter in fired clays of ancient pottery; Wilson et al. (2003) comment on having synchrotron XRD data in agreement with this association.

long periods of time; firing at 450°C could be used to return the ceramic to its as-fired state according to the authors. Examination of Wilson et al. (2003, Figure 3) shows, however, that the freshly fired brick does not return to its original dimensions following firing; this would suggest that the firing temperature is either too low or not sustained for a long enough period. In later work by this group the temperature is raised to 500°C (Savage et al. 2008; 2008b).

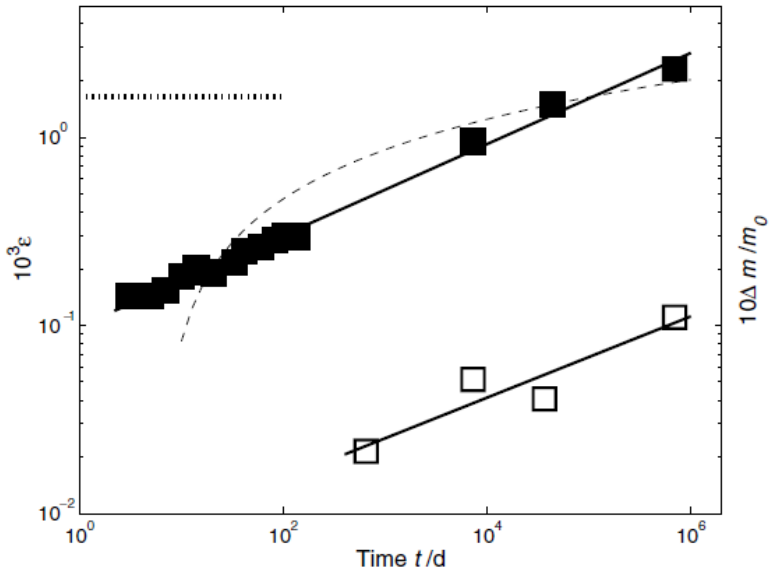

Figure 2.12: The total expansive strain, ϵ (solid squares), and fractional mass gain, $\Delta m/m_0$ (open squares), from the time of original manufacture of bricks. The power-law regression equations are $\epsilon = 9.87 \times 10^{-5}\ (t/\mathrm{d})^{0.24}$ and $\Delta m/m_0 = 5.7 \times 10^{-4}\ (t/\mathrm{d})^{0.22}$ where t is the time. The dashed curve is the best fit logarithmic function. From Wilson et al. (2003, Figure 4).

Despite some minor inconsistencies, this work was critical to future research into rehydroxylation dating. It showed that, after firing, there is a long term expansion in fired clay ceramics that could be well-described by an approximate and simple $(time)^{1/4}$ law, and that once reheated the same sample could be returned to the as-fired state; the authors provided further insight into the nature of the mechanisms involved (diffusion down channels of low dimensionality) and the chemical reactions (rehydroxylation) responsible for this power-law behaviour. The work showed that mass gain was proportional to this expansion, paving the way for future gravimetric methods. Tests on older samples demonstrated that there was the potential that this shorter term $(time)^{1/4}$ expansion/mass gain extended indefinitely over longer time scales, which, combined with the other findings,

pointed towards its potential as an archaeological dating technique. While not conclusive, the tests also revealed something of the nature of the temperature and moisture dependence of the expansion and mass gain.

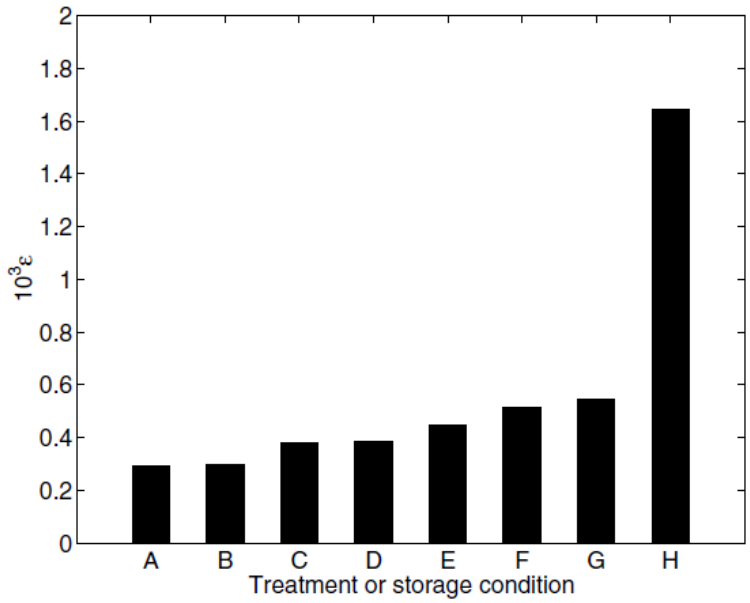

Figure 2.13: The expansion of freshly fired bricks subjected to different aging treatments. A: steaming at 100°C for 6 hours; B: aging in ambient laboratory conditions for 104 days; C: aging under water at 20°C for 104 days; D: aging under water at 50°C for 104 days; E: 100%RH at 20°C for 104 days; F: aging at 105°C in a ventilated oven for 104 days; G: alternate vacuum saturation with water and oven drying; H: steam autoclaving at 1.15 MPa, 186°C for 4 hours. From Wilson et al. (2003, Figure 2).

Developing upon this work, Savage et al. (2008a) examined both the expansion and mass gain of freshly fired clay bricks in the early stages, with particular focus on the initial 1.5 hours following firing. They stressed the absence of experimental research on diffusion into fired clays at this timescale. Expansive strain and mass gain were recorded for freshly fired bricks that were either (a) allowed to air cool as measurements were carried out or (b) vacuum cooled prior to exposure to environmental moisture and the commencement of measurements. They observed what appear to be two distinct stages of expansion/mass gain, with the first stage ending after approximately 1.5 hours, *Figure 2.14*. The authors believed both stages, *Stage 1* and *Stage 2* (using naming convention of this thesis) were well described by a $t^{1/4}$ based model, and see this as evidence that the same

fundamental mechanism is involved in both stages. To explain a two-stage process, the authors suggest that there is "a thin surface layer of material which has more open diffusion pathways, albeit of similar morphology, than the bulk of the solid" responsible for the first stage, with the second stage due to more constrained channels of diffusion, both stages "consistent with the hypothesis that the chemisorption process is a diffusion controlled rehydration reaction on a low-dimension structure", as reasoned in Wilson et al. (2003). The work also provides convincing evidence that the expansive strain and mass gain have the same underlying cause, with a linear relationship between the two presented, *Figure 2.15.*

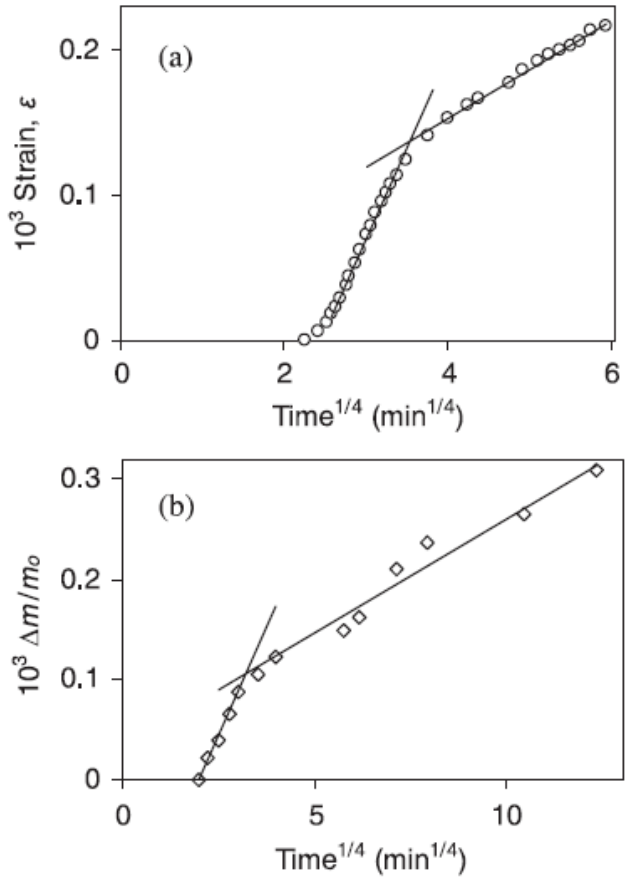

Figure 2.14: Expansive strain (top) and fractional mass gain (bottom) of air cooled bricks. From Savage et al. (2008a, Figure 2).

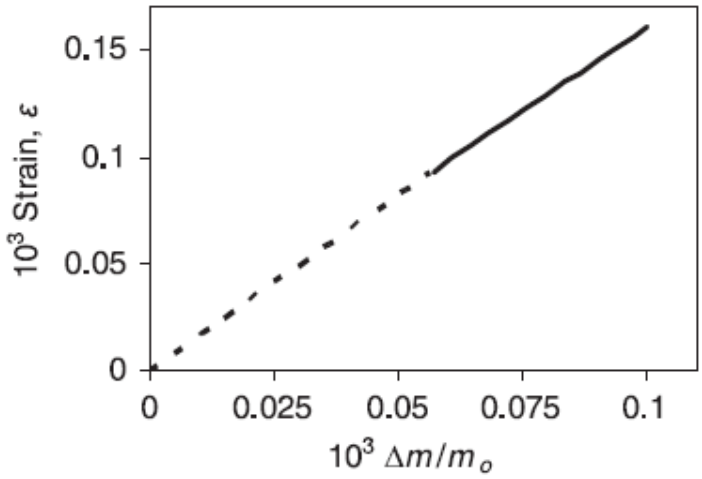

Figure 2.15: Expansive strain versus fractional mass gain for vacuum cooled bricks. Dashed line – first stage, solid line – second stage. From Savage et al. (2008a, Figure 3).

The results of Savage et al. (2008a) do suggest two distinct stages of expansion and mass gain, yet the assertion that they are both well described by the power law is less clear. Looking at the first stage, *Stage 1 (S1)* alone in Figure 1 and Figure 2 (*Figure 2.14 above*) from Savage et al. (2008a), it is not clear at what point in time it begins and ends and what criteria is used for defining this. The power law fit is more secure in the expansion plots due to more data points; however, omission or inclusion of additional points from one stage to the other would appear to render an equally apt linear fit, yet with a very different slope. Inspection by eye would even suggest that there is no first stage linearity for any sustained period and that assigning a $t^{1/4}$ model could be premature. For the second stage, the power law fit to the fractional mass data suffers from a lack of sufficient data points and is not convincing. On the other hand, for the expansion data the fits are much more conclusive, although selection of when this stage commences still appears somewhat arbitrary.

Another point of note is that the rates of mass gain and expansion were higher in both *Stage 1* and *Stage 2* of the air cooled test than in the vacuum cooled test. This is despite the fact that both were measured at ambient laboratory aging conditions. Savage et al. explain this as due to the vacuum cooled bricks having been initially

exposed to environmental moisture at a lower temperature than was the case for the air cooled brick, thus making them less chemically reactive. While this might explain the difference in the first stage rates, during which both sets of bricks were conditioning to laboratory conditions, it fails to explain why there is such a significant difference in rates for the second stage (where the rate is approximately 40% higher in the air cooled bricks). The second stage data was gathered over a period of 21 hours for the expansion data and 7 days for the fractional mass gain data. It is likely that for most of this time periods both sets of bricks would have had a temperature equal to that of the laboratory at 22°C and, accepting some difference due to compositional variation in the bricks, the expansion and mass gain rates should not differ greatly.[13]

In any case, Savage et al. (2008a) does demonstrate two stages of expansion/mass gain in the early post-firing stages and provides extra, if not conclusive, support for a second stage that can be described by the aforementioned $t^{1/4}$ power law. Perhaps more importantly, it demonstrates that the expansion and mass gain are linearly proportional to one another and therefore likely driven by the same underlying mechanism.

For the findings of Wilson et al. (2003) and Savage et al. (2008a) to find use in archaeological dating it would be necessary to demonstrate that under suitable firing conditions fired clay ceramics could be returned to the as-fired state and would then undergo mass gain and expansion in an identical way to the freshly fired ceramic. Savage et al. (2008b) went about examining this through comparison of the mass gain in freshly fired bricks with that of re-fired bulk and powdered samples. In two separate gravimetric tests they first examined the fractional mass gain for a freshly fired brick and for samples taken from that brick and subjected to two different reheating regimes, one where the temperature in the furnace was ramped gradually (10°C/min up to 500°C), and the other where the furnace was preheated to the same temperature before the sample was placed within, *Figure*

[13] The increased *Stage 1* and *Stage 2* might be associated with time-offset effects (Barrett 2013), discussed later, caused by additional mass gain during cooling. This would certainly result in an increase *Stage 1* mass gain and mass gain rate, and would cause a curvature effect in the *Stage 2* data that could affect the mass gain rates measured by Savage et al. (2008a).

2.16 and *Table 2.4*. In the second set of tests, they looked at how the fractional mass gain rates were affected in the reheating of different size fractions, produced by crushing of the original brick.

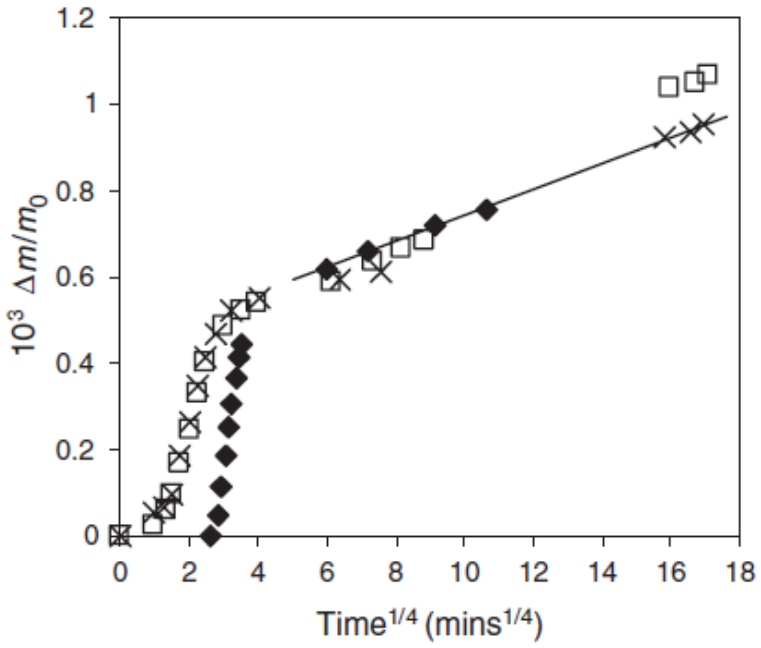

Figure 2.16: Fractional mass gain of a freshly fired brick (black diamonds) together with the fractional mass gain following reheating of two samples cut from the same brick and subjected to severe (×), and moderate (empty squares), reheating regimes. The straight line is the linear least square fit through the *Stage 2* data points for the freshly fired brick. From Savage et al. (2008b, Figure 1).

In the opinion of Savage et al. (2008b), the results of the first set of tests provide further support for the $t^{1/4}$ power law model (Wilson et al. 2003), with two distinct stages of mass gain apparent (Savage et al. 2008a) and strong similarities between the freshly fired and reheated samples. They also state that the "severity of the reheating regime does not appreciably affect the subsequent mass gain kinetics", while accepting notable differences in the gradients obtained between the freshly fired and reheated samples.

The authors consider the lower *Stage 1* gradients (*Table 2.4)* for reheated samples as resulting from incomplete removal of chemically combined water during heating, and hence a lower concentration of chemical recombination reaction sites available

following reheating, while they envisage the higher *Stage2* gradients for reheated samples as due to additional nano-scale damage upon reheating that permits easier diffusion of water molecules. However, there is no clear reason why either of these factors should exclusively/dominantly affect only one of the stages and not the other; if there is lower reactivity in *Stage 1*, might this not also be expected for *Stage 2*? And why does the nano-scale damage result in a greater fractional mass gain for the moderately, not severely, reheated sample?

	Gradients of fractional mass Gain ($\times 10^{-5}$ min$^{-1/4}$)		
Reheating regime	Stage I	Stage II	Fractional mass gain at the end of Stage 1
Freshly fired	60	3.0	0.055
Severe	32	3.3	0.049
Moderate	31	4.5	0.042

Table 2.4: Gradients of fractional mass gain for freshly fired brick, and samples from the same brick following severe and moderate reheating. From Savage et al. (2008b, Table 1).

Savage et al. (2008b) also comment on the total fractional mass gain in *Stage 1* as being 10-20% less for the reheated samples, however, from inspection of *Figure 2.16*, it is not clear where *Stage 1* and *Stage 2* begin and end, and the 10-20% difference seems less certain. Also, an over-confidence is expressed in the $t^{1/4}$ power law upon which these stages and their gradients are determined; the fits suffer from a shortage of data points (4-7) in *Stage 2*, and a less than clear linearity in *Stage 2* for the reheated samples; there actually appears to be a 'positive' curvature, discussed later, in the *Stage 2* data. The suggestion that the severity of the reheating regime does not "appreciably affect the subsequent mass gain kinetics" or that the reheating produces "a material having reaction kinetics essentially similar to those observed in the freshly fired ceramic" perhaps understates what appears to be a very significant effect on the observable mass gain rates estimated by Savage et al. (2008b) (*Table 2.4*).

The second set of tests, on the different fraction sizes, showed that both the first and second stage mass gain rates were significantly affected by particle size, *Table*

2.5. The *Stage 1* data showed a more extreme effect than that observed for *Stage 2*. For both, the mass gain rates increased with decreasing particle size, although the largest fraction (1.18-2.36mm) displayed *Stage 2* rates the same as those of the bulk sample. Savage et al. (2008b) associate the increase in *Stage 1* rates with decreasing particle size as due to more open nano-scale pathways near the surface of the ceramic, and draw parallels with the increased surface area measured (based on a spherical particle model). Indeed, there does appear to be a relationship between the two, however, this could also be inferred to be the case with regard to the *Stage 2* data. The effect of fraction size on the *Stage 2* rates is not considered by Savage et al. to be significant, "following the very large mass gain in *stage I*, the powders show long-term reactivity in *stage II* essentially identical to the bulk material". It must be pointed out, however, that this is not true; it is only the case for the largest fraction size, with the smallest fraction size having a rate nearly 50% greater than the bulk sample.

Size fraction (mm)	Surface area (cm^2 /g)	Stage I ($\times 10^{-5}$ $min^{-1/4}$)	Stage II ($\times 10^{-5}$ $min^{-1/4}$)	Fractional mass gain at the end of Stage I
1.18–2.36	16	1140	4.2	0.81
0.600–1.18	31	1240	5.3	0.89
0.150–0.300	125	1340	6.1	0.93
Solid brick	0.4	25	4.2	0.04

The surface areas of the powder fractions were calculated from a geometrical model assuming spherical particles.

Table 2.5: Gradients of *Stage 1* and *Stage 2* and the fractional mass gains at the end of *Stage 1* for different size fractions of crushed brick following reheating. From Savage et al. (2008b, Table II).

Savage et al. (2008b) do not discuss the implications of these tests on archaeological dating. Their tests do show some support for a two stage behaviour that is described by a power law model, and demonstrate, upon reheating, fractional mass gain rates very similar, but not quite identical, to the freshly fired material. Their research also suggests that the firing regime has an effect, if considered minor by the authors, worthy of more research, and that the increased

surface area with grinding and powdering impacts upon both stages of mass gain, more in *Stage 1* but also considerably in *Stage 2* (below a certain fraction size).

In Wilson et al. (2009) there appears the first application of the findings discussed above to archaeological dating. Exploiting the $t^{1/4}$ power law, they measured the mass gain kinetics and total mass gain since original firing of archaeological fabrics, and used this information to extrapolate the date of original firing of fired clay ceramics up to approximately 2000 years old. They attribute the mass gain to chemical rehydroxylation and first use the term 'rehydroxylation dating', claiming the method provides "an accurate self-calibrating method of archaeological dating". They also demonstrate the importance of environmental temperature on the mass gain rates, obtaining activation energies (*Section 3.3*) in line with those of chemical recombination.

The method used by Wilson et al. (2009) relies on several factors and assumptions: (1) the *Stage 2* mass gain rate is the same as that of the freshly fired ceramic, obeys a $t^{1/4}$ power law, and can be accurately measured; (2) the *Stage 1* mass gain is not associated with rehydroxylation and does not impact upon the method (3) the rehydroxylation-based mass gain since original firing can be determined by reheating methods; (4) the rehydroxylation rate is insensitive to water vapour pressure (RH) under moderate, normal environmental conditions; (5) and that the rehydroxylation rate is temperature dependent, requiring an estimate of the mean lifetime temperature of the ceramic since original firing.

As discussed above, the level of support for many of these factors had not been demonstrated without issue by preceding work: Savage et al. (2008b) does not provide conclusive support for either (1) or (2) above; estimation of the rehydroxylation-based mass gain (3) had not been tested; the insensitivity of the rehydroxylation rate to water vapour pressure, asserted by Wilson et al. (2009) to have been demonstrated by Wilson et al. (2003), is not accepted to have been the case by this author; and though a certain level of temperature dependence had been demonstrated (Wilson et al. 2003), it was only shown for a few disjointed temperatures, with additional issues pointed out above. Hence the factors and

assumptions requisite to the technique were far from certain when applied by Wilson et al. (2009), yet despite this their work went on to provide some of the strongest support to several of these points, specifically (1), (3) and (5).

The basic methodology of Wilson et al. (2009) involved measuring the mass of samples before (post heating at 105°C to remove capillary moisture) and after heating at 500°C (for 4 hours) to determine the final and initial (as-fired) masses. Then the fractional mass gain rate for *Stage 2* (rehydroxylation rate), *Figure 2.17*, was determined by weighing the 3-5g samples, over a period of 2-4 days in a microbalance, under conditions chosen to replicate the relevant environmental conditions (mean lifetime temperature and constant RH). This information was then used to estimate the age of the sample and compare it with assigned ages, *Figure 2.18.* Tests were also carried out across a range of temperatures to examine the temperature dependence of several samples, *Figure 2.19.*

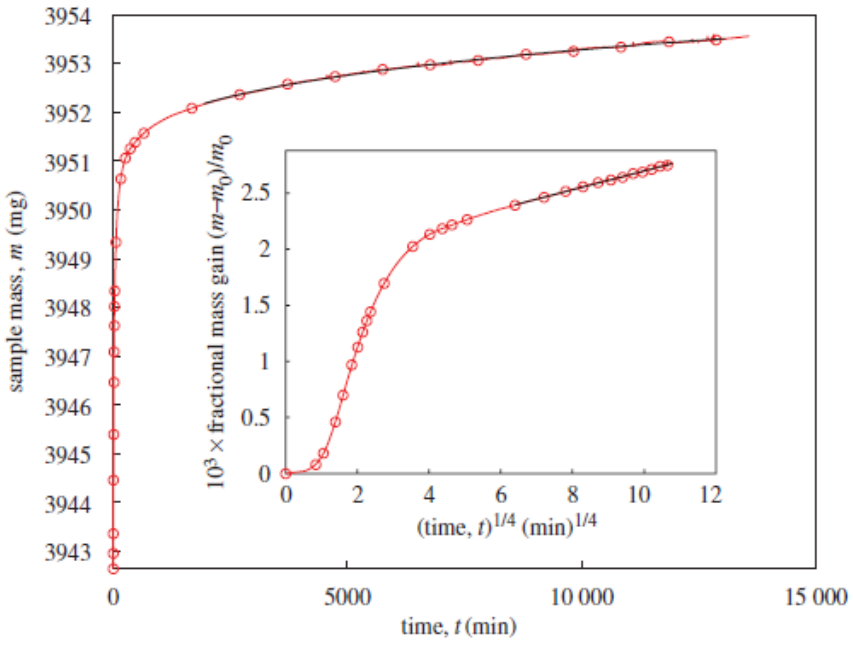

Figure 2.17: Rehydroxylation kinetics of reheated fired clay brick. Sample is a 14th century fired clay tile from St. Bride's Church London. Mass gain recorded for 25°C and RH of 35% over a period of 9.1 days. Heavy black line is the least squares fit of stage 2 data using power law (0.254 instead of 0.25 providing the best fit. From Wilson et al. (2009, Figure 1).

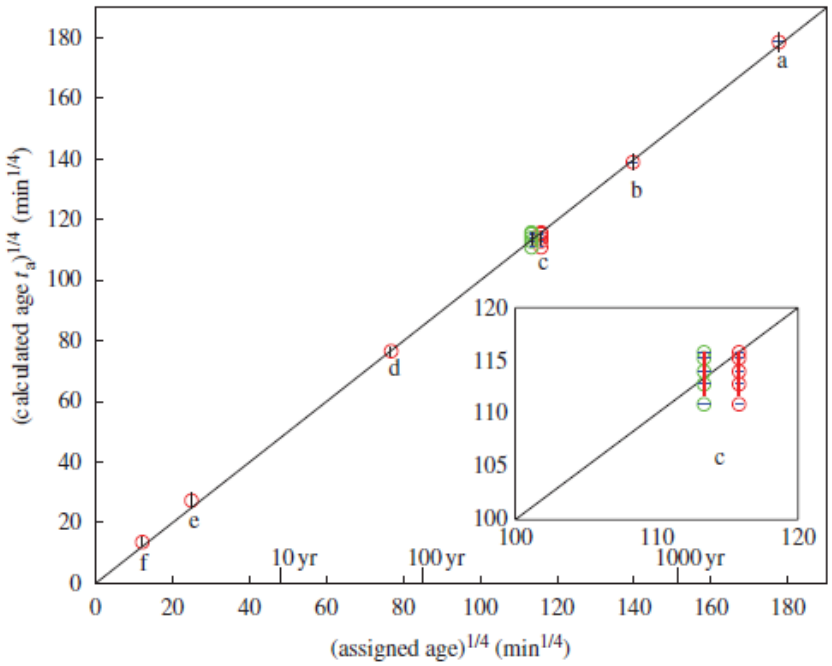

Figure 2.18: Comparison of calculated and assigned ages for fired clay and tile samples. Horizontal bars indicate the range of assigned ages; vertical bars show the probable error, ±1 s.d. based on statistics of replicate determinations. a: Roman paving brick (AD 50-160 assigned age). b: Westminster floor tile (AD 1250-1300 assigned age). c: Clay brick (AD 1664-1669 or 1690s possibly reconstruction). d: Clay brick (AD 1942). e: Chester Red clay brick (2005). f: Westminster floor tile (15 days after reheating). From Wilson et al. (2009, Figure 4).

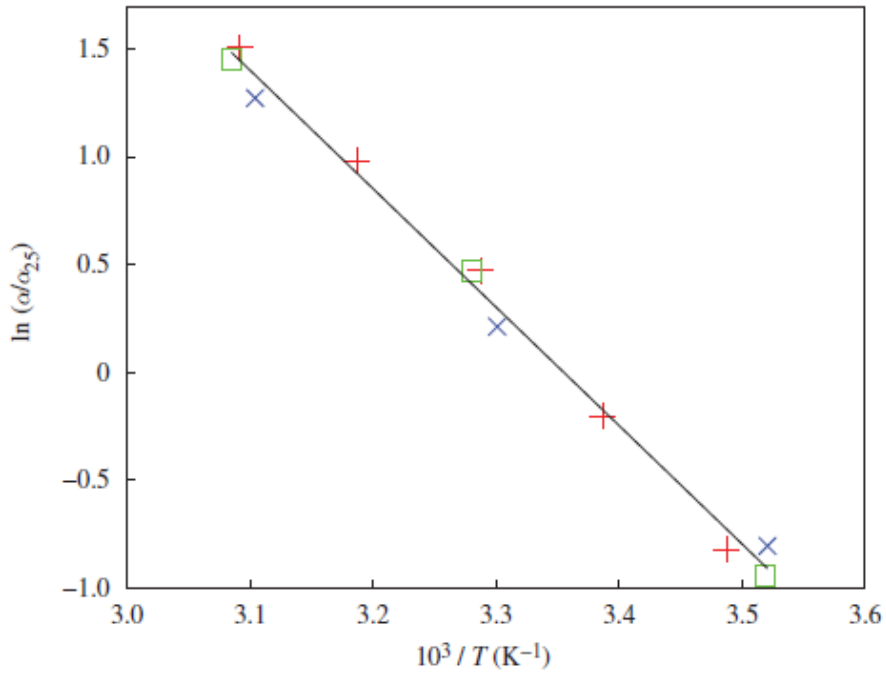

Figure 2.19: Arrhenius plot: effect of temperature on rehydroxylation mass gain rate. α: rehydroxylation fractional mass gain rate. α_{25} is the rate at 25°C. For three fired clay brick and tile samples. Red cross: Roman paving brick. Blue ×: Westminster clay tile (14th century). Green square: Clay brick (17th century). From Wilson et al. (2009, Figure 2).

Measurements of fractional mass gain, using this microbalance based method, produce curves, *Figure 2.17*, that provide strong support for a $t^{1/4}$ power law model. There remain questions over how to distinguish the beginning of the second stage, however. Tests of the temperature dependence successfully demonstrate, *Figure 2.19*, a well-defined Arrhenius behaviour (*see Chapter 3*) and produce activation energies of the same order as those associated with dehydroxylation reactions in kaolinite and illite (Bellotto et al. 1995; Gualtieri and Ferrari 2006). The three samples used in this test produce similar results and an average activation energy of 182 ± 5 kJ/mol. The most significant aspect of this paper are the dates obtained and how closely they agree with the assigned ages, *Figure 2.18*. They all appear to find excellent agreement with those assigned and almost all fall within the range of uncertainties. The uncertainties though are based only on repeatability, and in reality are probably much larger when experimental errors and uncertainties in temperature are accounted for. The oldest sample dated is a Roman paving brick, almost 2000 years old. The authors state that on the millennial time scale the rehydroxylated mass is only 1-2% of the sample mass and that this is considerably less than the ultimate rehydroxylation capacity based on known dehydroxylation estimates (Gualtieri and Ferrari 2006; Heide and Földvari 2006), potentially allowing samples at least 10,000 years old to be dated.

There are, however, a couple of issues with the ages obtained (aside from issues raised by Le Goff and Gallet (2014b) discussed later in this section). Simulations by the author (Barrett 2011, discussed below) have shown that where mean lifetime temperatures are used in calculating the ages in RHX it is necessary to correct for the effects of seasonal and annual temperature cycles (due to non-linearity in the Arrhenius temperature dependence). The result of this is that an age correction is required, a reduction in the range 10-13% being appropriate for samples from the

south-east of England. Were this correction made to the ages obtained by Wilson et al. (2009), their ages would be too young by the same percentages. [14]

The absence of any discussion on contaminants or their removal is also of note; the considerable effects of organic matter are described in Numrich et al. (2015), discussed below, and if present in even small quantities the dates will be affected.

Nonetheless, this work does demonstrate, with some success, the potential of a rehydroxylation-based gravimetric dating technique. It also provides strong support for a $t^{1/4}$ power law model of mass gain, and demonstrates the Arrhenius behaviour of the mass gain rate.

To understand at a more fundamental level one of the major factors affecting the reactivity or fractional mass gain/expansion rates of fired clay ceramics, Mesbah et al. (2010a) examined the effect of different initial firing durations (dwell time) on the subsequent rates. Using a very pure kaolinite clay mineral, subjected to first firing at temperatures of 1200°C and dwell times ranging from 2-12 hours they recorded the mass gain over periods of about 30 hours using a microbalance. XRD and SEM methods were also used to examine the amount of crystalline phase developed during firing, in an attempt to understand its relationship to the varying reactivity.

Their results clearly demonstrate, *Figure 2.20* and *Figure 2.21*, that the fractional mass gain rates in *Stage 2* decrease exponentially with firing time. This is correlated well with exponential increases in crystalline phases, *Figure 2.22,* observed in the XRD data (associated with growth of mullite and cristobalite minerals). The significance of this finding, in terms of RHX dating, is that for ceramics fired for shorter periods, there may be more reactivity to moisture sorption, resulting in a

[14] There could be several causes for this: the reheated rehydroxylation rates are higher than the as-fired rates resulting in the total mass gain since original firing occurring over a shorter period; the stage one non-rehydroxylation based mass gains are higher for the reheated samples, leading to an under-estimation of the rehydroxylation mass gain; the reheating temperature may be too low or the time too short resulting in incomplete dehydroxylation (the motivation for the temperature and time used are not discussed in any detail); the mean lifetime temperature estimate could be too high resulting in a larger rehydroxylation rate; and there is the possibility of systematic methodological errors in the weighing of samples.

greater mass gain over the lifetime of the ceramic and more pronounced rehydroxylation rates on reheating.

The fractional mass gain curves, produced as a function of $t^{1/4}$, do also provide supporting evidence for a two stage process with a linear second stage (note that Mesbah et al. (2010a) acknowledge the absence of any distinctly linear *Stage 1*). The *Stage 2* linearity looks reasonable; however, some slight (negative) curvature can be observed that proceeds for quite a portion of the measurements, *Figure 2.20*. The criteria for determining where this stage begins are also not clear. It must be emphasised that these tests are on freshly fired clays only and were not carried out on the reheated samples necessary for RHX dating.

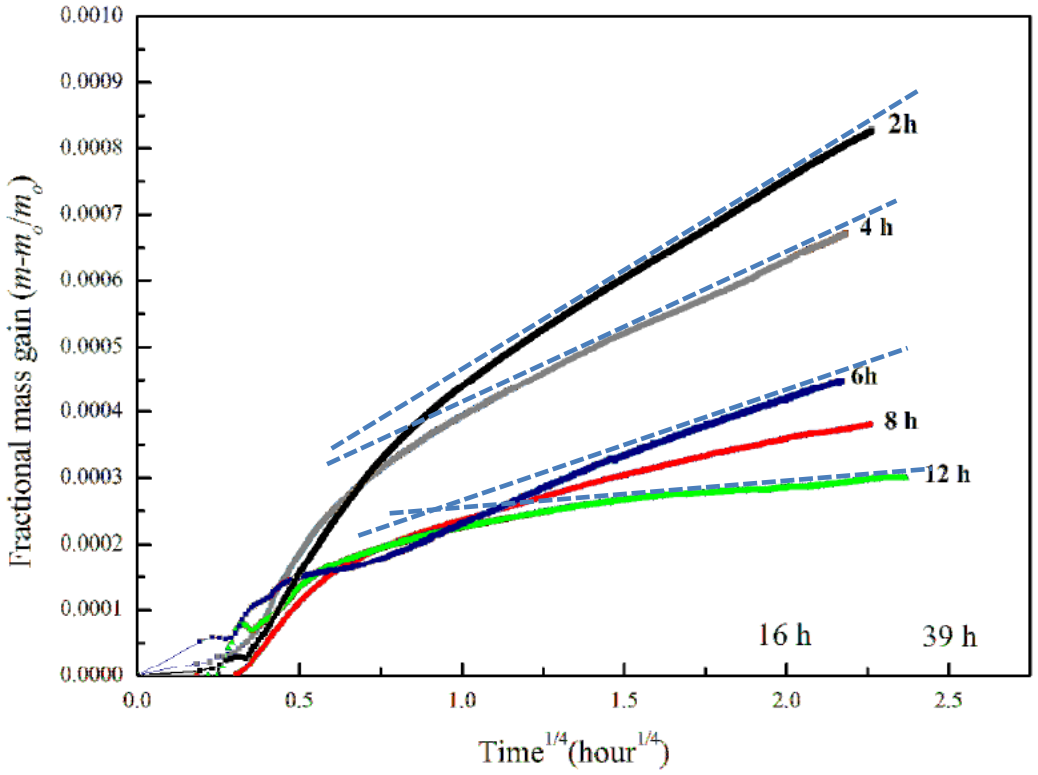

Figure 2.20: Fractional mass gain plotted against *time*$^{1/4}$ for kaolinite fired at 1200°C and sintered for times from 2 to 12 hours. From Mesbah et al. (2010a, Figure 1). Dashed straight lines added for comparison.

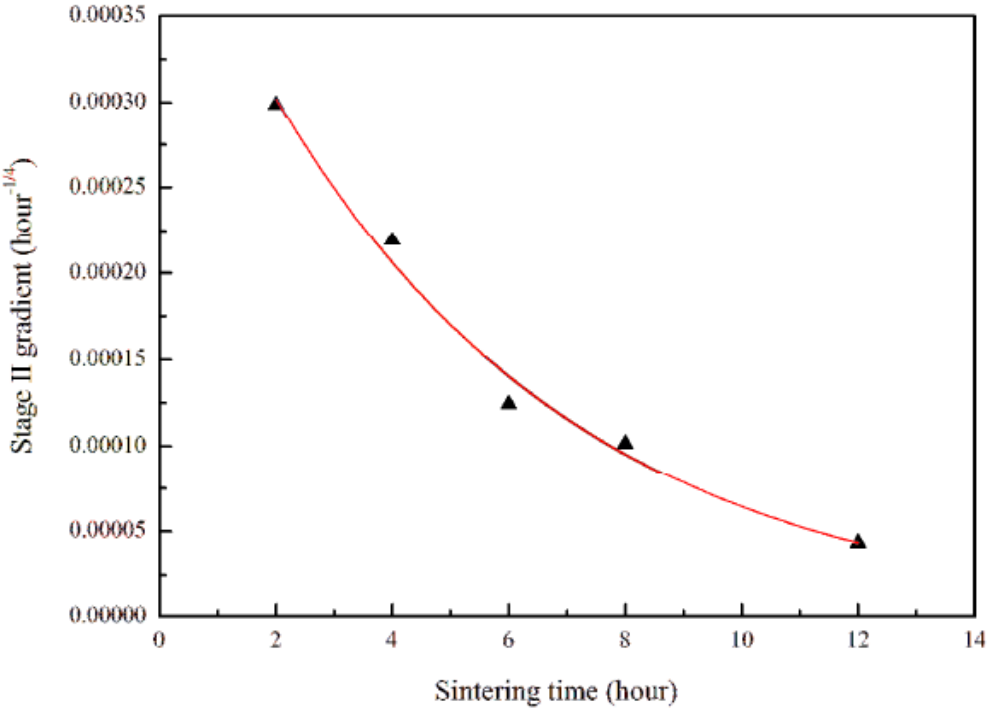

Figure 2.21: ***Stage 2*** **fractional mass gain rate plotted against sintering time for kaolinite fired at 1200°C. From Mesbah et al. (2010a, Figure 2)**

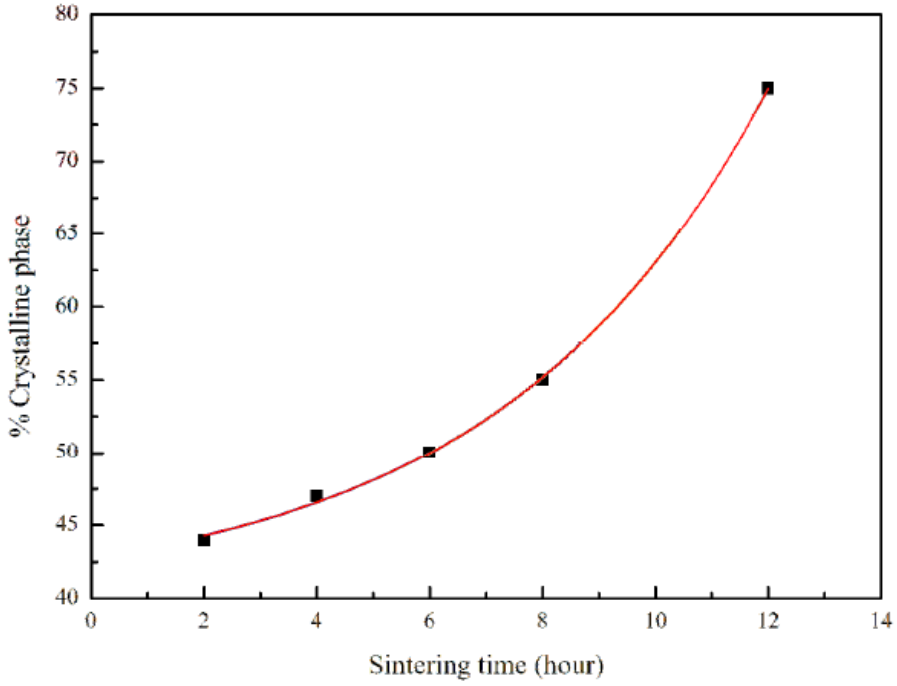

Figure 2.22: The percentage of crystalline phase developed during sintering of kaolinite at 1200°C as a function of sintering time. From Mesbah et al. (2010a. Figure 4).

In closely related work, Mesbah et al. (2010b) looked at the relationship between the firing temperature of kaolinite and the moisture reactivity, using gravimetric techniques, XRD and SEM. They explored the relationship for firing temperatures ranging from 700 – 1200°C. The tests conducted showed a clear reduction in *Stage 2* mass gain rates with increasing temperatures, *Figure 2.23* and *Figure 2.24*, and was also correlated with an increase in crystallinity. This was supported by XRD and strongly suggests that the reactivity of the fired clay is occurring in the amorphous phases of the ceramic, being more pronounced for lower temperatures.

The fractional mass gain curves again provide good support for an approximate $t^{1/4}$ power law describing the second stage mass gain for *freshly fired* kaolinite. Again, the criteria for deciding where this stage begins is not very clear, with the *Stage 1* to *Stage 2* transition less sharply defined for lower firing temperatures, *Figure 2.23*. Also, the *S1* mass gain decreases and has a shorter duration for higher firing temperatures. This may be associated with decreases in the sample surface area (Mesbah et al. 2010a).

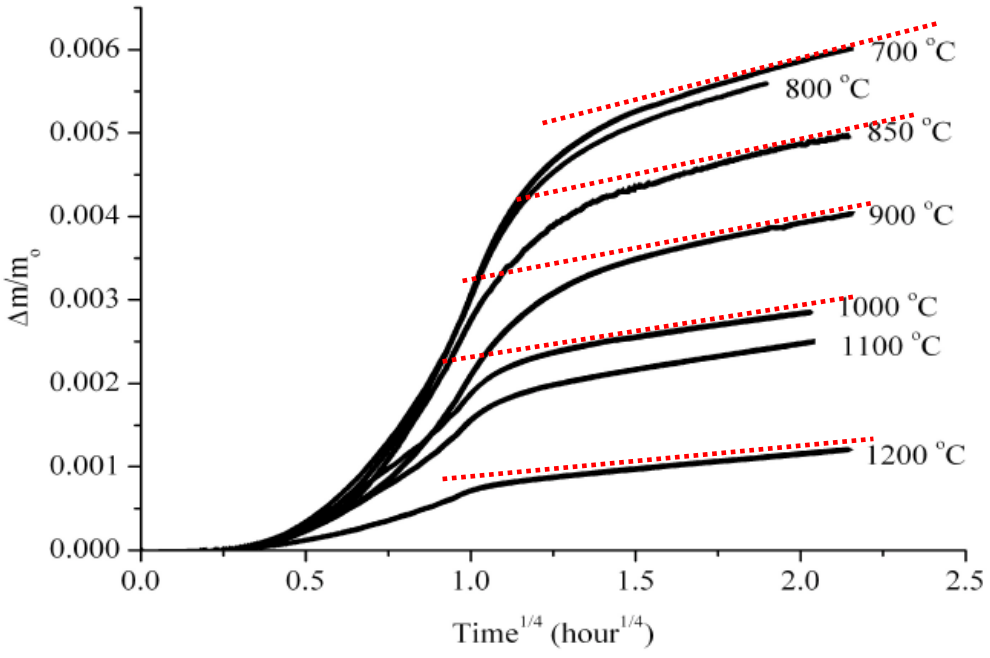

Figure 2.23: Variation of fractional mass gain with *time*$^{1/4}$ for kaolin samples fired at different temperatures. Dashed lines included to provide linear comparison. Developed from Mesbah et al. (2010b, Figure 1).

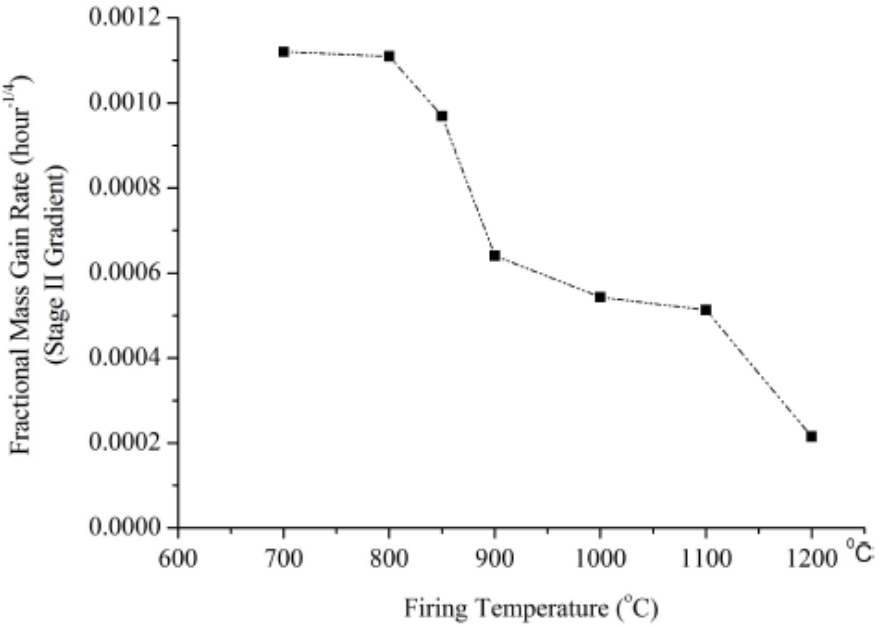

Figure 2.24: Variation of fractional mass gain (*Stage 2*) with firing temperature for fired kaolin. From Mesbah et al. (2010b, Figure 2).

While the works of Mesbah et al. (2010a; 2010b) provides useful insights into the effects of firing temperature and dwelling time on the fractional mass gain kinetics of a freshly fired kaolin, for application to RHX dating the reheating curves are equally important. Also, with fired clay ceramics the purity of the composition will rarely come close to that of pure kaolinites and the characteristics of fractional mass gain under firing and reheating could differ significantly. Tosheva et al. (2010) provide insight into these factors through gravimetric and Raman spectroscopy studies of fired and reheated terracotta. Two main tests were carried out. In the first, the effects of firing and reheating on mass gain rates were examined. Pieces of unfired terracotta (2.5g) were fired at a range of temperatures, from 800-1200°C, for 12 hours (ramp rate of 10°C/min) after reaching the desired temperature. The fractional mass gain was then recorded for 2-4 days. Samples were then reheated at 500°C and higher temperatures using the same heating rate and a dwell time of 4 hours (this reheating regime was chosen based on Wilson et al. (2009)). The mass gain behaviour was again recorded using a microbalance. Raman spectroscopy was carried out on disc shaped samples following firing at each temperature.

In the second set of tests the possibility of skipping *Stage 1* measurements was explored. Instead of immediate placement in the microbalance following firing or reheating, samples were instead placed in a desiccator under identical conditions (30°C and 75%RH) to those that would be used in the microbalance. After 3 days in this environment, the fired or reheated samples were transferred to the microbalance and mass gain measurements were carried out. This skipping of the *Stage 1* measurements was examined in order to speed up the throughput of tests and was referred to as the "conditioning" step.

The effect of firing temperature on fractional mass gain rate as a function of $time^{1/4}$ is demonstrated in *Figure 2.25* and *Figure 2.26*. In curves that demonstrate a clear two stage process, with linearity in the second stage, the gradients of *Stage 2* show an increase from 800°C to 1000°C followed by a sharp decrease with temperature to 1200°C. This differs from the work on pure kaolinite by Mesbah et al. (2010b) where a continuous decrease is observed over this range of temperatures, and demonstrates a difference in behaviour between pure and relatively natural clays (terracotta). Then again, it must also be stated that for Mesbah et al. (2010b) the samples were only held at the desired firing temperature for 4 hours as opposed to 12 hours for Tosheva et al. (2010); this may be a contributing factor. Of importance with respect to the *Stage 2* gradients, the authors specify using criteria based on the derivative of the data becoming constant to decide when *Stage 2* is underway.

While the *Stage 2* gradient has a maximum at 1000°C, both the fractional mass gain in *Stage 1* and the duration of *Stage 1* are at a maximum at 800°C and decrease for higher temperatures. The reasons for this are not discussed but, as for Mesbah et al. (2010a; 2010b), it appears likely to be associated with lower surface area/porosity as a function of firing temperature or dwell time, with the *Stage 2* behaviour appearing independent or driven dominantly by other processes. Raman spectroscopy failed to identify any particular phases in terracotta fired at 1000°C that might be responsible for the high mass gain rate, but this maximum is consistent with the findings of Barrett (1937) and Cole and Crook (1968) in examining moisture expansion of clays and firing temperature.

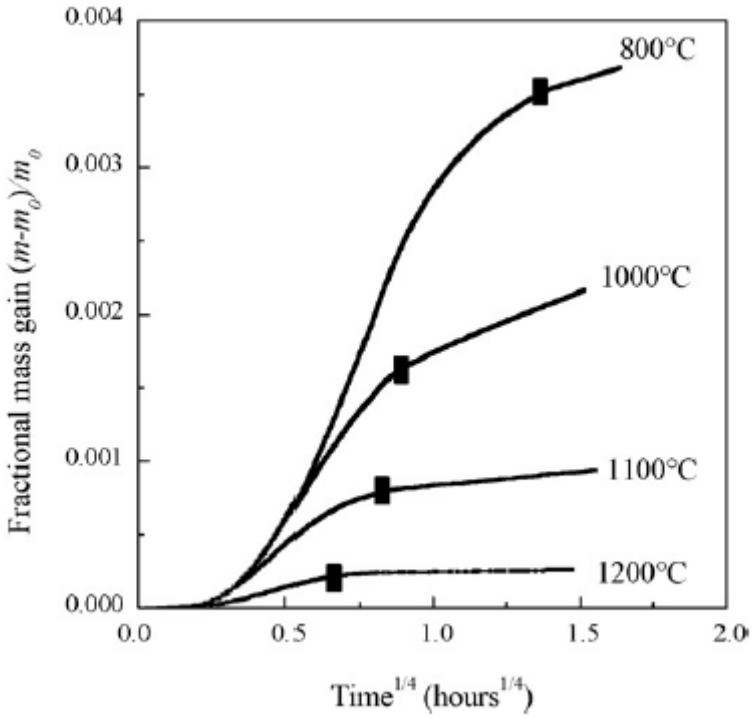

Figure 2.25: Fractional mass gain versus $t^{1/4}$ for terracotta samples fired at temperatures between 800°C and 1200°C and measured at 30°C and 60%RH. Smooth curves are made up of very closely spaced primary microgravimetric data points. From Tosheva et al. (2010, Figure 1).

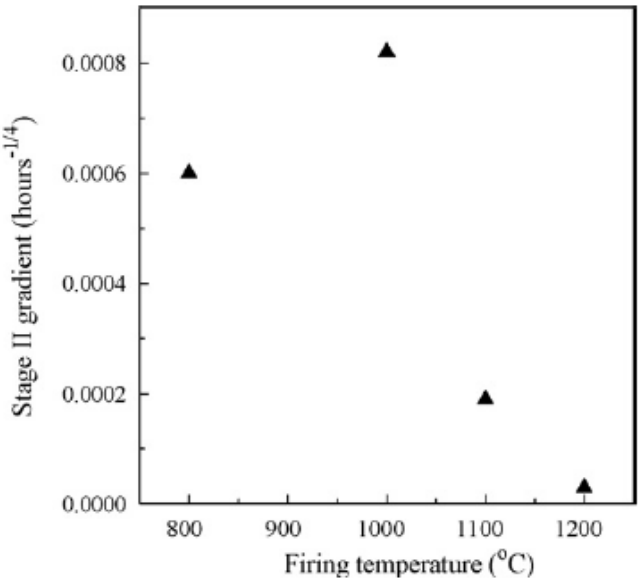

Figure 2.26: *Stage 2* gradients as a function of firing temperature for terracotta. From Tosheva et al. (2010, Figure 2).

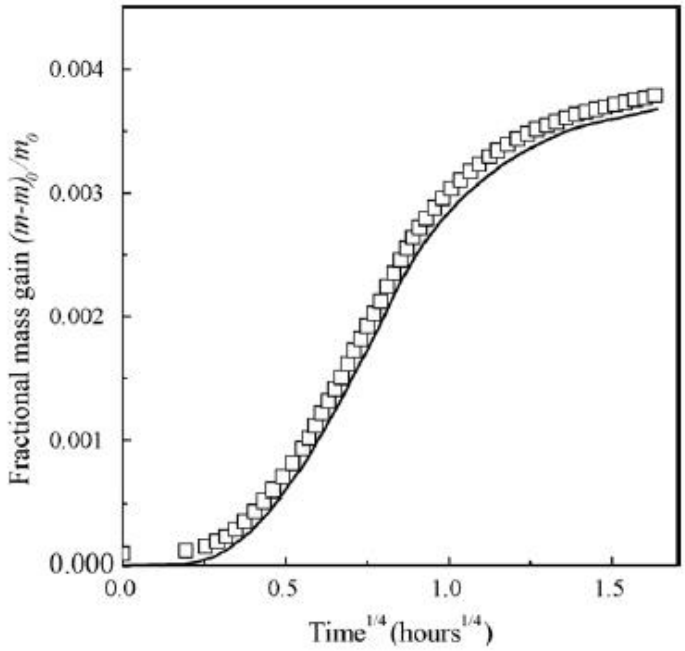

Figure 2.27: Fractional mass gain versus $t^{1/4}$ for fired terracotta. Solid line: freshly fired at 800°C and squares: the same sample following reheating at 500°C. From Tosheva et al. (2010, Figure 3).

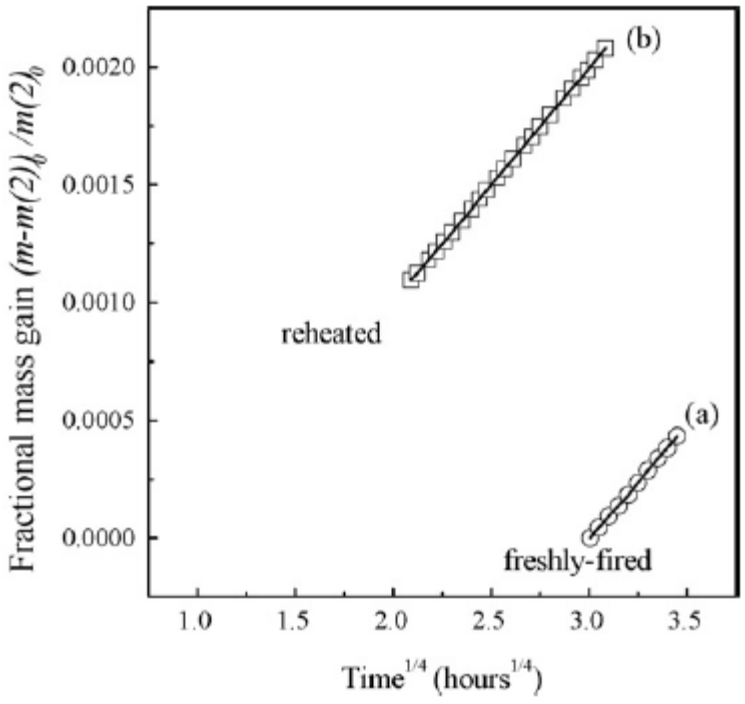

Figure 2.28: *Stage 2* fractional mass gain measured for: (a) terracotta fired at 1000°C and stored over saturated NaCl for 78 hours prior to measurements; (b) the same sample reheated at 500°C and placed directly into the microbalance chamber. $m(2)_0$ is the mass at the beginning of stage 2 measurements. From Tosheva et al. (2010, Figure 4).

For the reheated samples, the curves produced are almost identical to those of the as-fired samples, *Figure 2.27* (this is for the 800°C and 500°C reheated case; the authors claim similar results were obtained for all other reheating temperatures up to the original firing temperature, 800°C). Unfortunately, the curves shown in *Figure 2.27* only cover the *Stage 1* behaviour and while they support near identical mass gain behaviour across this period (6-7 hours) they, despite the affirmation of the authors, do not provide convincing evidence of identical *Stage 2* behaviour.

Using the 1000°C fired sample, they also performed reheating tests at a range of temperatures. They assert that reheating at any temperature below 1000°C did not change the *Stage 2* gradient (they do not comment on whether or not *Stage 1* is affected), whereas for reheating temperatures greater than the original firing temperature a reduction in the *Stage 2* gradient was observed. This they believe occurs because "reheating a ceramic at a temperature greater than the original firing temperature causes an increase in the amount of crystalline material, at the expense of amorphous material believed to be involved in the rehydroxylation process". Tosheva et al. (2010) also suggest the potential to exploit this finding to determine the original firing temperature of ancient fired clay ceramics (Tite 1969; Tite and Manianis 1975; Shoval and Beck 2005).

A problem is encountered fully accepting their assertion that the mass gain behaviour is the same in the reheated and freshly fired samples because the evidence they present for this, *Figure 2.27* and *Figure 2.28*, do not show the entire mass gain curve for both *Stage 1* and *2* of fired and reheated samples. The issue with *Figure 2.27* has been mentioned above. The problem with *Figure 2.28* is that, while it does present very linear *Stage 2* data with what appear to be identical gradients for freshly fired and reheated samples as a function of $t^{1/4}$, it would be preferable to have *Stage 2* curves that cover the same period and preferably both stages of mass gain.

It is also not clear how the reheating dwelling time is involved. Can any dwell time by used as long as the temperature is below that of the original firing and that it satisfies some minimum period to allow complete dehydroxylation (in line with original firing)? In any case, the findings from the first set of tests are significant as they indicate the importance of reheating below the original firing temperature, and the suitability of 500°C as a firing temperature (for the terracotta involved at least).

The second set of tests Tosheva et al. (2010), examining the possibility of skipping the *Stage 1* period, were successful, *Figure 2.28*. The fractional mass gain gradients (*Stage 1*) for the conditioning step sample agreed well with samples placed in the microbalance immediately after firing. By allowing *Stage 1* to be bypassed, the collection of *Stage 2* data necessary to RHX dating can be sped up.

The Raman micro-spectroscopy generally supported the microbalance tests with the spectra of as-fired and reheated samples similar, provided the reheating temperatures did not exceed the original temperature of firing. Along with this, the intensity of ratio between anatase and rutile in the sample appears closely related to the firing temperature, with the authors suggesting its possible application in determining the original firing temperature of some ceramics.

In summary, the findings of Tosheva et al (2010) provide support for the exploitation of the mass gain kinetics of fired clays in archaeological dating. This work provides evidence that the original mass gain curves following firing can be reproduced through reheating at 500°C, that these curves obey a $t^{1/4}$ power law, that the reheating temperature must not exceed the original firing temperature, and that the rehydroxylation rate varies considerably with firing temperature. The results also show that measurements during *Stage 1* can be avoided, and they highlight the potential use of the anatase/rutile ratio to determine the original firing temperature.

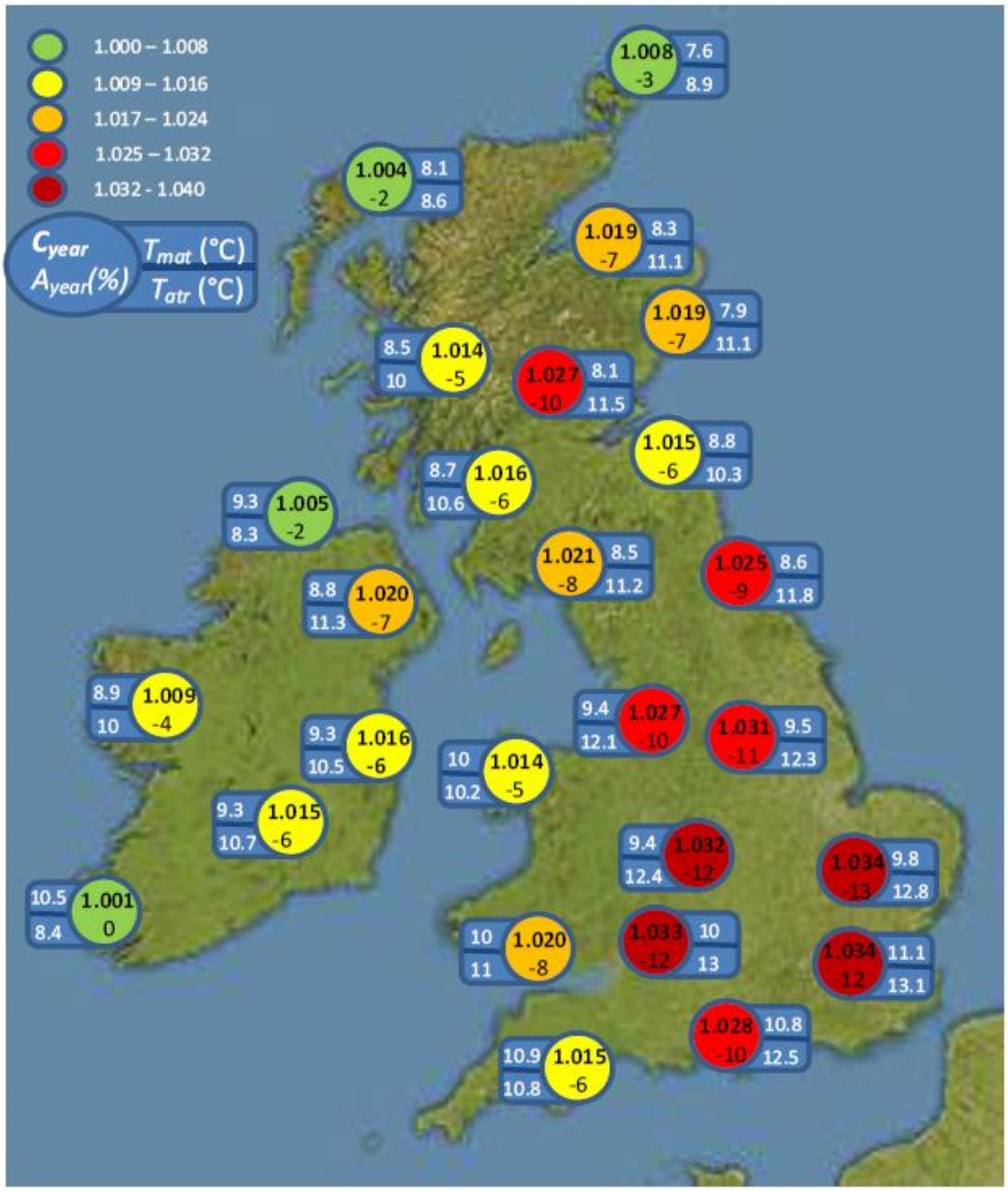

Figure 2.29: Annual correction factors, C_{year}, and age corrections, A_{year} (expressed as the percentage correction required to be applied to the age) for 26 sites across Ireland and Britain. Calculated for monthly temperature averages over the period 1961-1990. T_{mat} = mean annual temperature over the period. T_{atr} = mean annual temperature range over the period. Taken from Barrett (2011, Figure 4.37).

The implications of the non-linear temperature dependence of the RHX mass gain rate are first seriously addressed by Barrett (2011), in an examination of the effects of diurnal and annual temperature cycles on the rates used in dating calculations. It was demonstrated, using simulations involving short and long term instrumental records of surface air temperatures (SATs) from Ireland and Britain, that mass gain rates based on mean temperatures over a period of interest are unsuitable and that

these need to be corrected to account for the exponential temperature dependence of the mass gain rate that results in proportionately greater rates at higher temperatures. It was also demonstrated that the diurnal temperature effects are negligible on an annual timescale where the annual temperature range dominates the level of correction required. Examples were provided of the magnitude of such effects and the corrections required for a range of conditions, including spatial variation, *Figure 2.29*, and on an annual basis for long term records, *Figure 2.30*. This work does not contribute anything new with regard to the understanding of rehydroxylation mass gain behaviour but does draw early attention to this area of major concern with regard to dating calculations while demonstrating the magnitude of effects involved for a range of conditions, a topic returned to by Hall et al. (2013), discussed later.

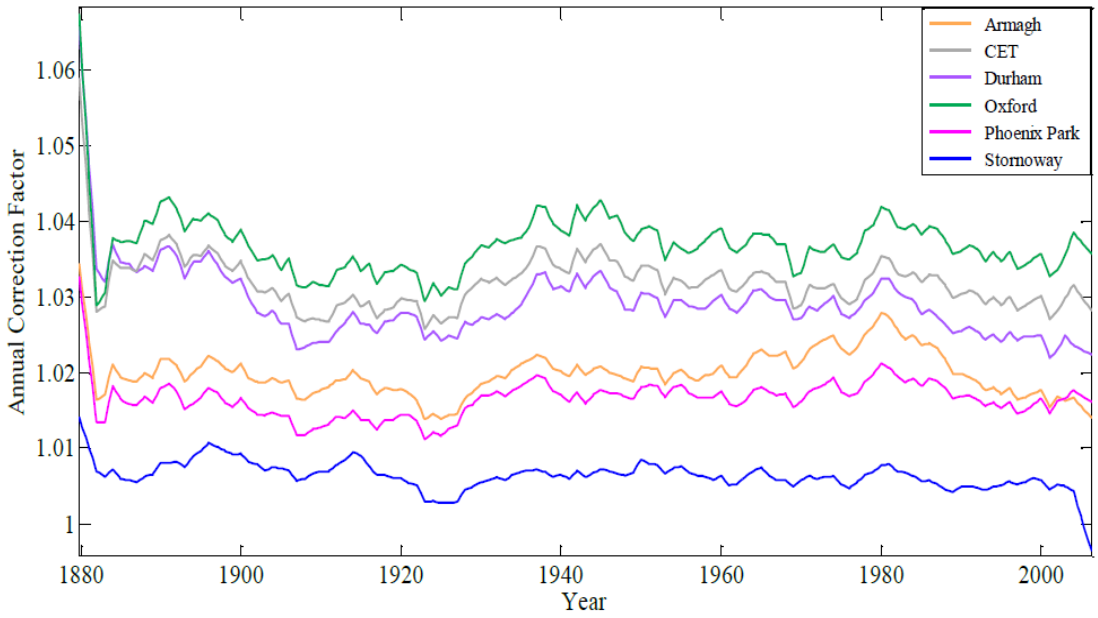

Figure 2.30: Smoothed (running average with window size = 11 years) annual correction factor produced from six monthly temperature records from Ireland and Great Britain. The correction factor is ratio of the actual mass gain rate calculated using the annual temperature variation data and the mass gain rate estimated using the mean annual temperature (MAT). From Barrett (2011, Figure 4.55).

At this point, the longest measurement evidence for long term $t^{1/4}$ behaviour is the expansive strain data of Wilson et al. (2003), extending over 104 days, and gravimetrically the data of Savage et al. (2008a) over approximately 6 weeks, both carried out on freshly fired bricks. The work of Hall et al. (2011) provided fresh and strong evidence for an approximate $t^{1/4}$ behaviour over longer periods. Hall et al.

(2011) re-examined existing long-term expansive (length and strain) measurements in bricks from four different sources and for a wide range of brick compositions. These measurements extended from 13 years to 58 years. Hall et al. (2011) showed that logarithmic fits that have long been used to describe the expansion (Cole and Birtwistle 1969) provide a poor fit over longer periods. They refitted the data using the $t^{1/4}$ power law and the fits obtained provide support for its validity, for example *Figure 2.31* and *Figure 2.32*, particularly considering a wide range of brick types was involved. Given the linear relationship between expansive strain and fractional mass gain (Savage et al. 2008a), this work also provides substantial support for mass gain having a (approximate) $t^{1/4}$ behaviour also. However, note that for the most comprehensive set of data, the 35 years moisture expansion for 318 Australian fired clay bricks, *Figure 2.31*, there appears to be a positive curvature; the more suitable use of a flexible $t^{1/n}$ model in describing the data used in Hall et al. (2011) is argued for by Le Goff and Gallet (2015), discussed later.

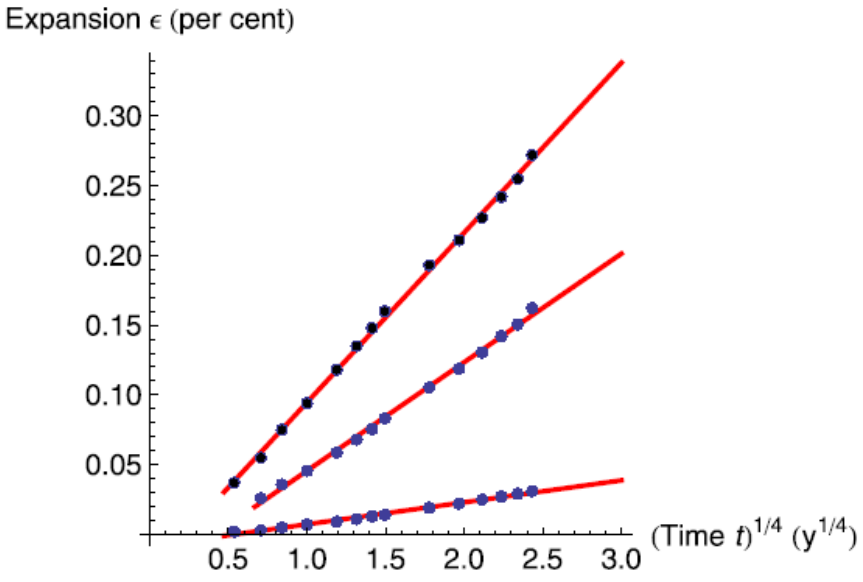

Figure 2.31: 35 years' moisture expansion of Australian fired clay bricks data of Zsembery et al. (2004) fitted to the power law model. The middle line represents the mean natural expansion of the entire set of 318 bricks. The top and bottom line represent subsets of this set based on steam autoclave properties discussed in Hall et al. (2011). From Hall et al. (2011, Figure 3).

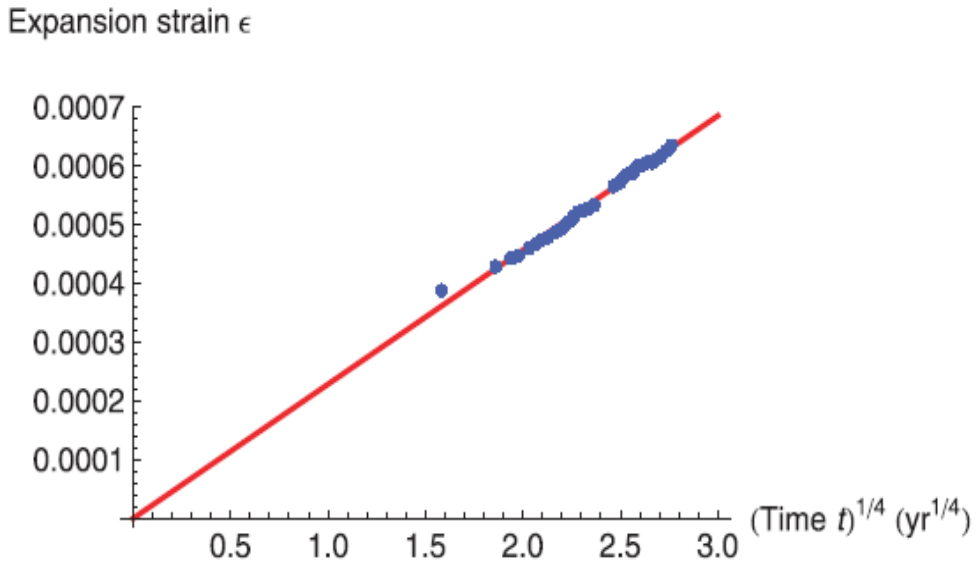

Figure 2.32: 58-year moisture expansion of National Physical Laboratory, U.K., standardizing bench (data of Cole 1967) fitted to the power law model. From Hall et al. (2011, Figure 6).

An alternative method of describing the long term mass gain kinetics was proposed by Bowen et al. (2011) who carried out gravimetric, XRD and TGA studies on 19th century pottery from Utah, U.S. In this study, using a top loading balance, Bowen et al. (2011) measured the fractional mass gain over several weeks for samples aged under three different temperature conditions (approx. -1°C, 23°C, 80°C). They argue that the mass gain kinetics were better described by a new empirical $t^{1/n}$-based formula instead of the $t^{1/4}$ power law, which they found issue with for several reasons, including fitting problems and the discrimination of *Stage 2*, *Figure 2.33*. Their empirical approach does indeed provide strong, if not perfect, fits to the data, *Figure 2.35*, and may allow for an alternative approach where complications arise with the $t^{1/4}$ power law or where the power law is just not suitable. Their model includes five parameters that require computation during modelling making it highly flexible but this level of flexibility could potentially lead to inappropriately strong fits. Aside from this, it requires studies to demonstrate that the kinetics of reheated ceramics described by their empirical equation are identical to the kinetics of freshly fired samples, and that suitable methods are available for estimating the rehydroxylation-based mass gain since original firing. Bowen et al. (2011) do not

provide any evidence or discussion regarding its application to dating of their ceramics.

They also argue that the power *n* has a temperature dependence and is better expressed as *n(T)*. However, their evidence for this, *Figure 2.34*, in which they plot *n* against *T* for all ten results obtained on various samples at various aging temperatures, is weak. This plot and its use is inappropriate and misleading as closer inspection reveals that only for a single sample, *sample 2*, was aging following dehydroxylation carried out at multiple temperatures (-1.3°C, 23°C and 80°C, name *low, room,* and *high,* respectively), and for this sample the difference in value of *n* for *low* (2.3±0.3) and *room* (3±1.0) (95% confidence level) conditions are not statistically significant enough to make any temperature dependent assertions. Along with this there were issues modelling the 80°C condition (requiring two additional parameters to the model), making its validity also questionable.

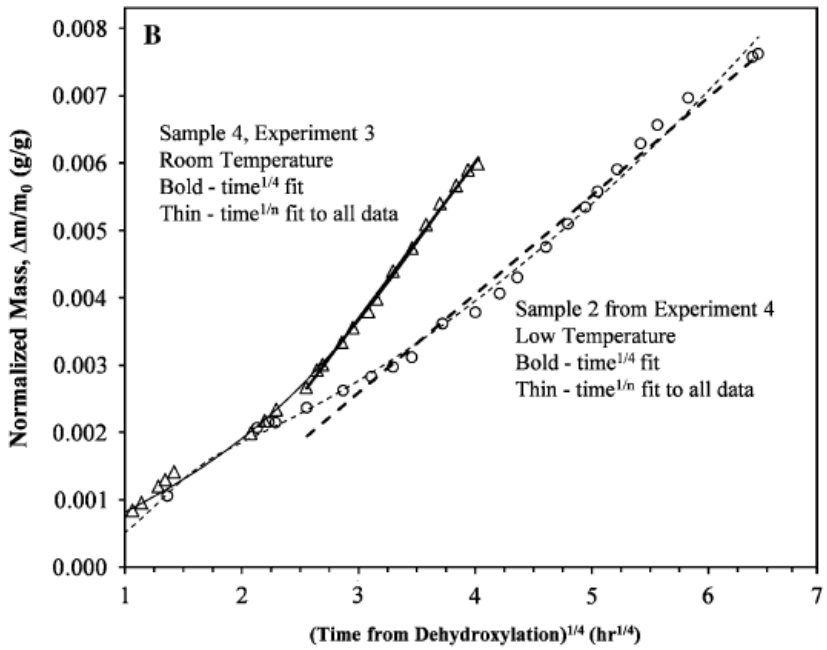

Figure 2.33: Rehydration/rehydroxylation mass gain curves plotted as a function of *time*$^{1/4}$, with theoretical fits according to power law of Wilson et al. (2009, dashed and bold line) and Bowen et al. (2011, dashed and thin). For Davenport pottery reheated at 650°C. From Bowen et al. (2011, Figure 4).

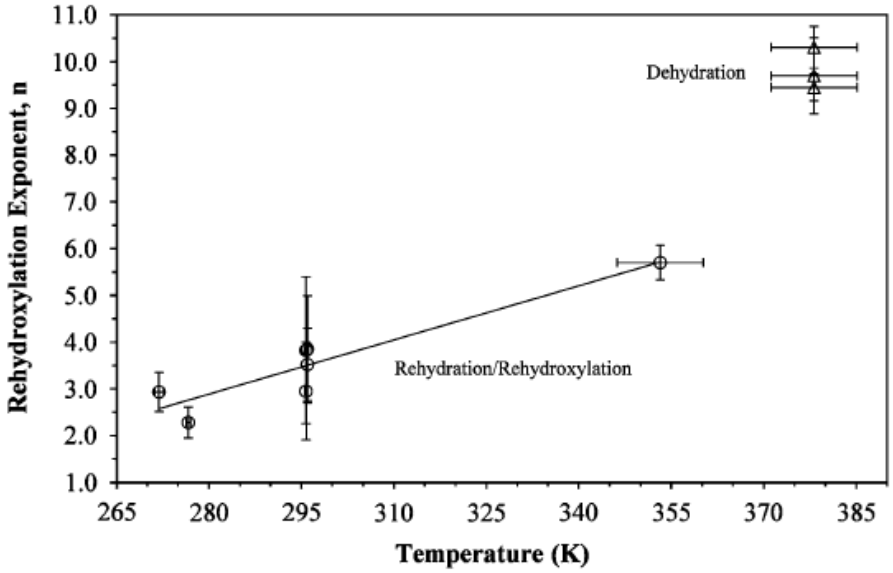

Figure 2.34: The temperature dependence of the rehydration/rehydroxylation (RHX) exponent, *n*. Circles represent rehydration/rehydroxylation processes and triangles represent dehydration. From Bowen et al. (2011, Figure 6).

Bowen et al. (2011) also believed that the firing temperature of Wilson et al. (2009, 500°C) would be insufficient for complete dehydroxylation of their samples and used a temperature of 650°C instead, associated with a peak in the TGA data. This is also quite different to that used by Tosheva et al. (2010), carried out on terracotta, where 500°C worked very well. The current author finds issue with what the conclusion by Bowen et al. (2011) that a peak at 640°C corresponds to major dehydroxylation. This may indeed be the case; however, given that a high level of calcite was detected in the XRD carried out, and that calcite decomposes at this temperature, *Section 2.3*, it seems odd that they did not carry out XRD on the samples following reheating to establish and eliminate calcite decomposition as a cause. Unfortunately, despite a sample also having been fired at 500°C, no information is given on the results from this sample or how well it compared with the 650°C fired samples (the authors own work, discussed in *Chapter 9*, will provide further evidence to support the likelihood of calcite being the cause).

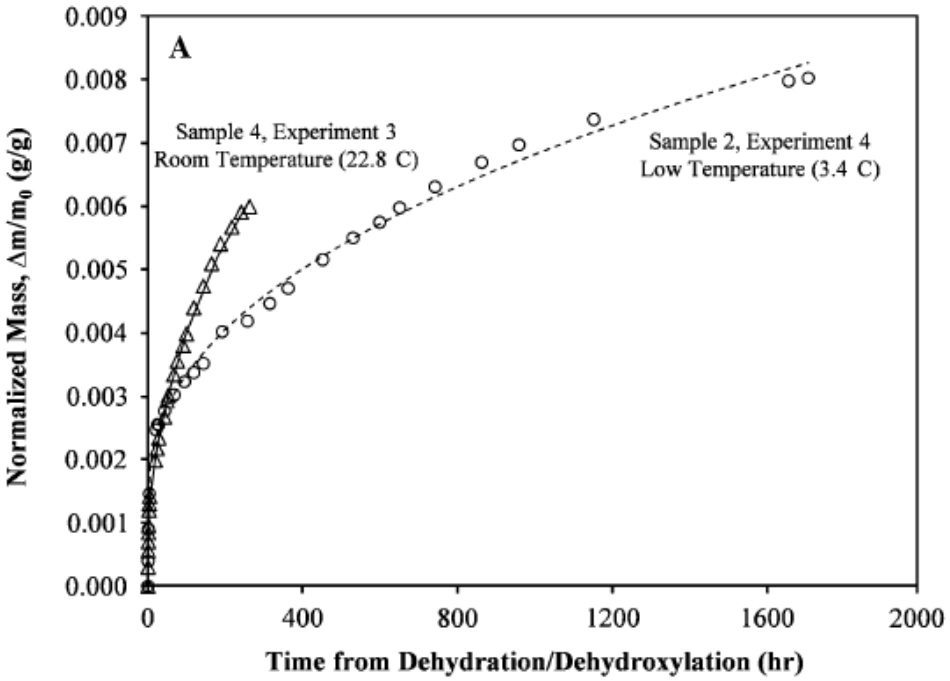

Figure 2.35: Rehydration/Rehydroxylation mass gain curves for Davenport pottery reheated at 650°C fit using empirical model of Bowen et al. (2011). From Bowen et al. (2011, Figure 4).

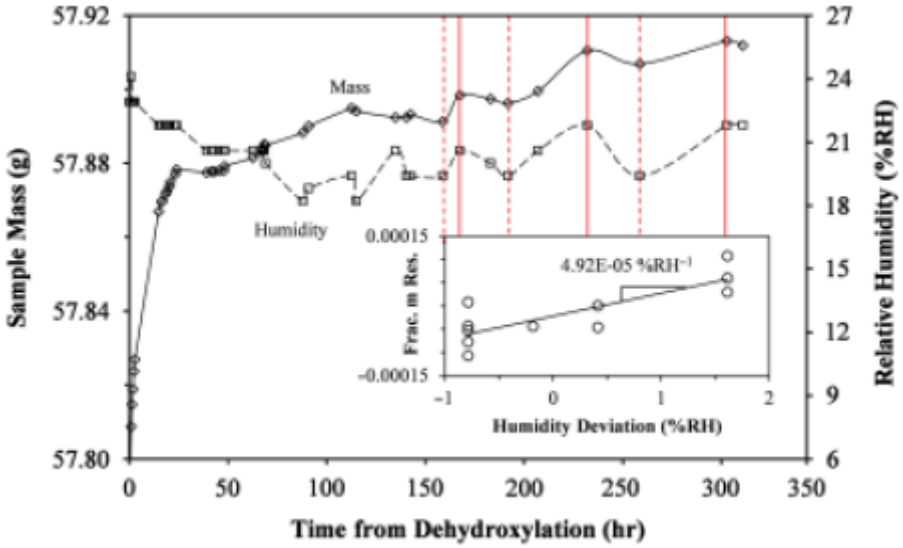

Figure 2.36: Correlation between fluctuations in humidity and observed mass from Bowen et al. (2011, Figure 7). The inset figure represents the effect of humidity fluctuations on the deviation from the empirically predicted mass postulated by Bowen et al. (2011).

An important aspect of Bowen et al. (2011) is that it involves a top loading balance approach instead of the microbalance approach of Wilson et al. (2009). Their work revealed considerable issues surrounding variation in the environmental conditions of measurement, drawing attention to the need for tighter control on RH. In *Figure 2.36* (Figure 7 of Bowen et al. (2011)) they show how the mass gain measurements carried out on a sample following reheating vary considerably with %RH fluctuations.

Other points of interest/issues with Bowen et al. (2011) include what appears to be a major misconception with regard to activation energy and temperature dependence and some contradictory information regarding the drying times at 110°C where slow and incomplete drying was observed.[15] Nevertheless, Bowen et al. (2011) does provide an alternative approach for describing the long term mass gain kinetics of fired clays that merits more attention.

Up to this point in RHX research, it had been assumed, based on the reheating temperatures and the activation energies involved in mass gain, that the main chemical mechanism involved in mass gain was rehydroxylation of amorphous phases in the fired clay (see Wilson et al. 2009). Yet this had not been explicitly examined through physical techniques in these studies. Clegg et al. (2012) used multiple instrumental methods (dilatometry, thermogravimetry-mass spectrometry (TG-MS), and variable temperature – diffuse reflectance infrared Fourier transform spectroscopy (VT-DRIFTS)) to investigate the role water plays in the expansion and

[15] Bowen et al. (2011) find issue with the Arrhenius temperature dependence of rehydroxylation argued for by Wilson et al. (2009). They present data that supports this, they argue, yet inspection of this data (Figure 4 from Bowen et al.) does not reveal any such issue. The mass gain rate is higher for the room temperature stored samples and lower for the low temperature stored samples. They also refer to the temperature dependence as "thermally activated" in the temperature range 13-50°C, suggesting a switching on/off of the power law behaviour in this range which is an incorrect interpretation of activation energy.
In drying the samples at 110°C to remove capillary moisture and physically bonded water, Bowen et al. state the duration of heating was such that the mass had reached a constant in about 20-30 hours. This contradicts later information where they describe slow moisture loss behaviour over the course of about 2 weeks, for a temperature just above 105°C. They describe this as dehydration/dehydroxylation without elaboration. Dehydroxylation can not be ruled out as Clegg et al. (2012) demonstrate that the temperature range over which it occurs may be quite wide for some materials. The issue of slow drying will be returned to in *Chapter 9.*

mass gain of fired clay ceramics. The temperature range over which adsorbed water molecules and hydroxyls are desorbed as fired clay is reheated and the nature of the moisture incorporated by the ceramic upon cooling were explored in detail.

Using dilatometry, they found that a major contraction of their brick sample occurred during heating between 200°C and 300°C, *Figure 2.37*. This agreed well with desorption of water shown by TG-MS, *Figure 2.38,* which has a maximum at 200-210°C (loss of physisorbed occurring at 95°C) and occurred continuously over a broad range of temperatures with no clear onset that could be assigned to dehydroxylation. The dilatometry test suggested that complete dehydroxylation had occurred by 500°C and that reheating is necessary above 330°C. An issue that is not clarified is how the heating rate and dwell times are involved and affect the process, an area that requires more research (i.e. could a lower temperature than 330°C be suitable if longer dwell times or heating rates are used).

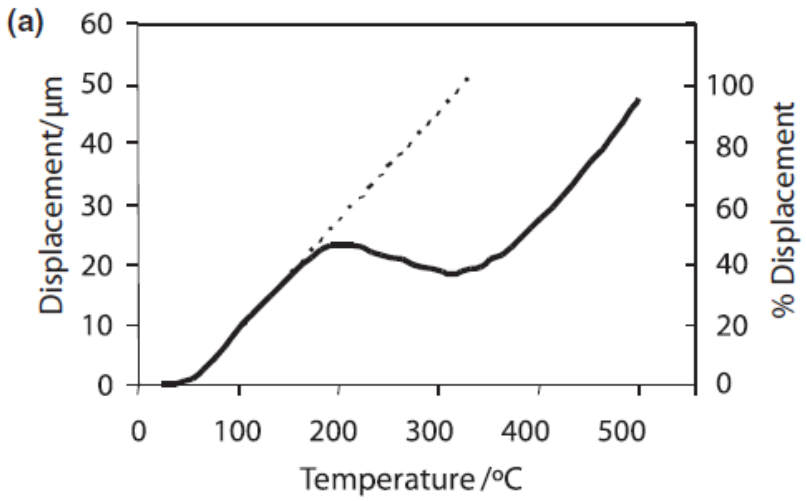

Figure 2.37: Dimension change versus temperature for Chester Red clay brick during heating to 500°C. Dotted line is extrapolation of expansion prior to 200°C. From Clegg et al. (2012, Figure 1).

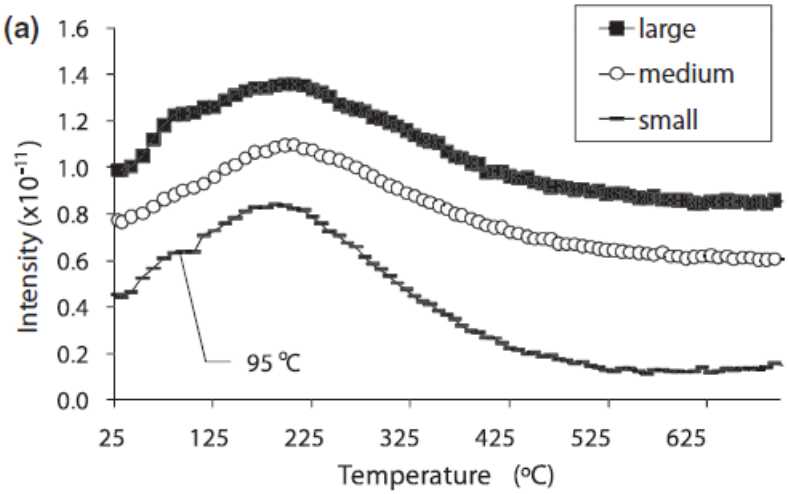

Figure 2.38: Mass chromatograms for the *m/z* = 18 ion obtained from TG-MS analysis of crushed GP brick, three size fractions. Curves offset for clarity. From Clegg et al. (2012, Figure 2).

The VT-DRIFTS results demonstrated that a wide range of structural OH groups are present, *Figure 2.39* and *Figure 2.40*. On heating, dehydration and dehydroxylation occurs across a wide range of temperatures with no clear commencing temperature for dehydroxylation evident. On subsequent cooling and aging, re-adsorption of moisture occurs and a spectrum with a very similar structure to the starting spectrum is obtained. Clegg et al. assign certain structural features to hydroxyls and others to water molecules that are physisorbed. However, this author is not convinced a clear distinction can be made, with similar increases in the intensity of the three major bands occurring during aging (compare the 16 hour and 50 day spectra of *Figure 2.40*). Indeed, Clegg et al. (2012) emphasize that "care must be exercised in the interpretation of infrared data" and admit that the processes involved in moisture induced expansion of clay bricks are still not resolved and "remain puzzling".

It is also worth noting (for later discussion) that for all bands, even the 3620cm^{-1} band most likely associated with (de/re)hydroxylation and others, 3450cm^{-1} and 3260cm^{-1}, associated with physisorption, there are notable increases in intensity during cooling in the temperature range 290-100°C which seems surprisingly high.

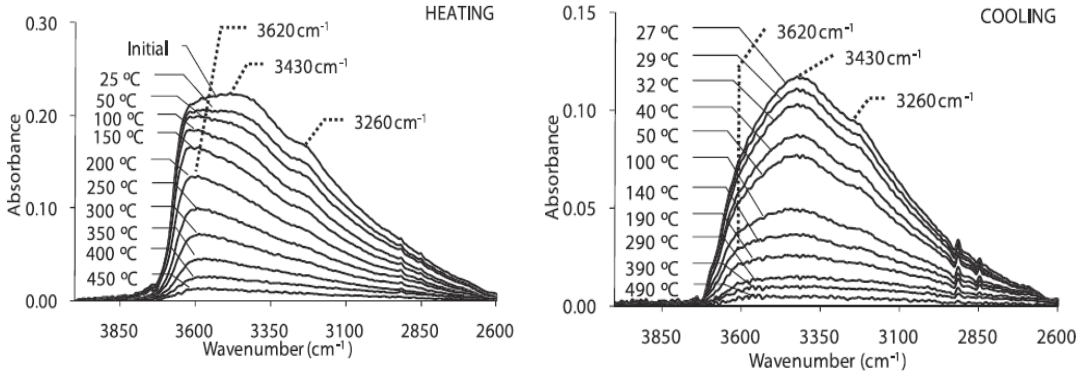

Figure 2.39: VT-DRIFTS Spectra from crushed GP brick (75-150µm fraction) during heating and cooling. Heating spectra collected under a flow of dry air; cooling spectra collected under a flow of moist air. From Clegg et al. (2012, Figure 3 and Figure 4).

Support for the two stage expansion/mass gain (Savage et al. 2008a) and the description of the second of these stages by an approximate $t^{1/4}$ power law (Wilson et al. 2003) is provided by a plot, *Figure 2.41*, of the area under the OH stretching band envelope (3800-2600cm^{-1}) versus $t^{1/4}$. Clegg et al. (2012) assert that first stage increases are caused by the formation of both structural hydroxyl groups and the sorption of molecules, with the second stage arising extensively, if not solely, from rehydroxylation. This may well be the case, but, given the difficulties in assignment of IR bands to hydroxyls or moisture alone, some uncertainty still remains.

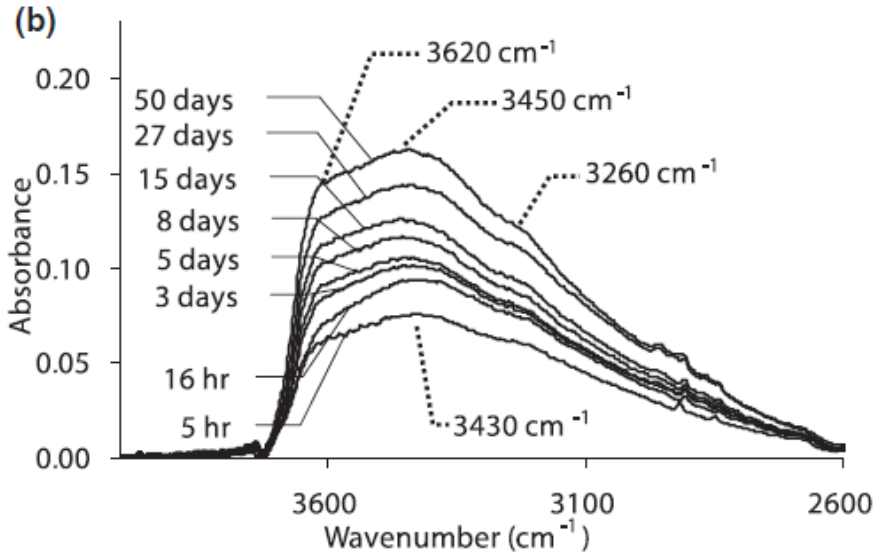

Figure 2.40: VT-DRIFTS spectra, following purging with dry nitrogen for 5 minutes, at 25°C for times up to 50 days from crushed Golden Purple Brick which had been heated to 500°C under a flow of dry nitrogen and allowed to cool to 25°C under a flow of moist air.

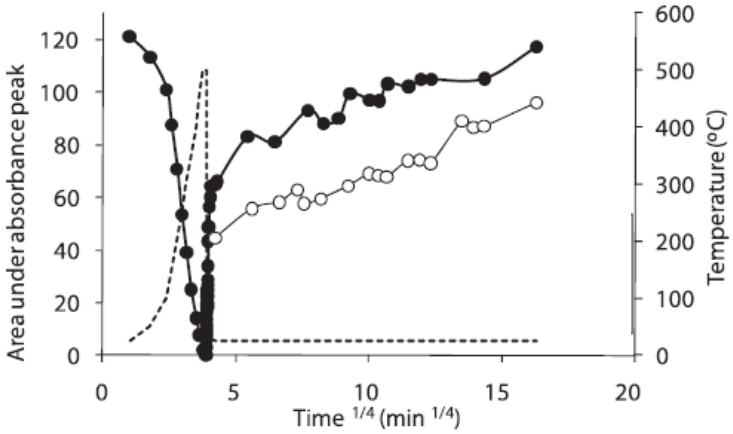

Figure 2.41: Area under OH stretching band envelope 3800-2600 cm^{-1} versus $time^{1/4}$ obtained from VT-DRIFTS spectra for GP brick. Upper line (black dot) and lower line (white dot) correspond to non-purged and purged (dry nitrogen) conditions, used to remove physisorbed moisture. Dotted line – temperature profile. From Clegg et al. (2012, Figure 7).

Moving away from the underlying chemistry of the rehydroxylation process, with Hall and Hoff (2012) we return to the related long-term expansion that was demonstrated in Hall et al. (2011). The main purpose of this article is to propose a definition of moisture expansivity in fired clay bricks that is based on the $t^{1/4}$ power-law model. Much of the data presented is from earlier work, Hall et al. (2011), yet there is some new data for the relationship between moisture expansivity and firing temperature (based on the work of Smith 1993) in several brick types, *Figure 2.42*. This shows how varied the moisture expansivity, and presumable the rehydroxylation rate, is for different materials and different firing temperatures, adding to the work of Mesbah et al. (2010b) and Tosheva et al. (2010), where similar patterns were observed.

Another important observation from Hall and Hoff (2012) comes from the moisture expansion of UK fletton bricks, *Figure 2.43*, where for bricks held under two different regimes, a fixed temperature of 18°C and relative humidities of 75% and 90%, the expansion data, as a function of $t^{1/4}$ is almost identical. This offers some of the strongest support for RH having a negligible role in the long term mass gain/expansion kinetics in agreement with the conclusion of Wilson et al. (2003).

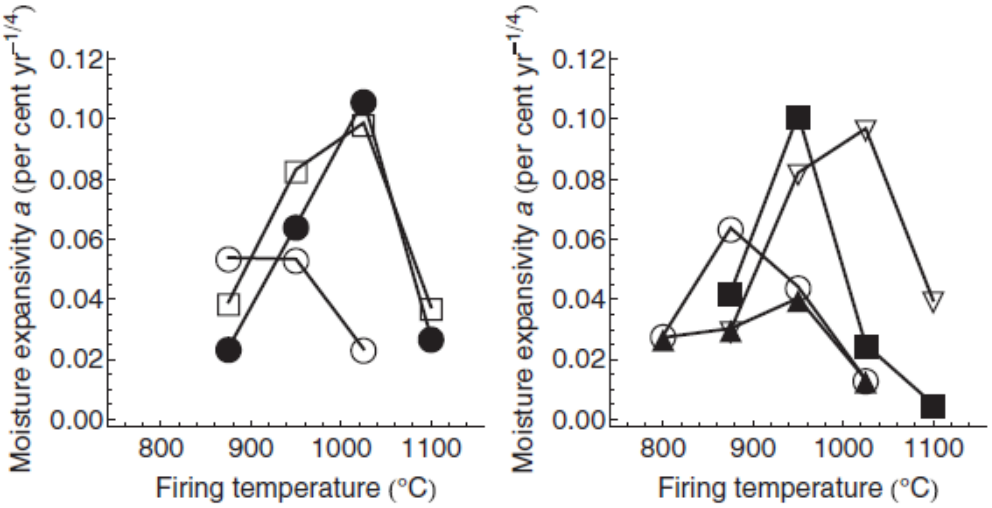

Figure 2.42: Relationship between moisture expansivity at 18°C and firing temperature, calculated from the 28-year expansion data of Smith (1993). Left: Oligocene clay (open squares); Keuper marl (62AS) (open circles); Devonian shale (filled circles). Right: London clay (open circles); Weald clay (filled squares); Keuper marl (62AT) (filled triangles); Carboniferous shale (open triangles). From Hall and Hoff (2012, Figure 2).

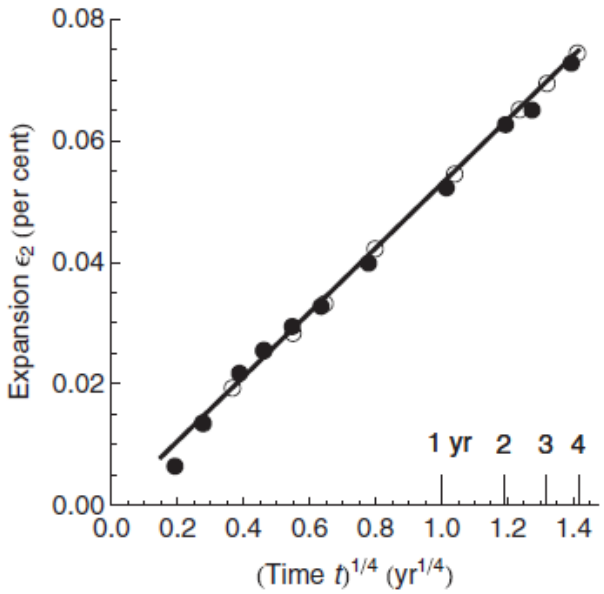

Figure 2.43: Four-year moisture expansion in UK fletton bricks (data from Smith (1974)). Controlled-environment expansion data at 18°C and at 75%RH (solid circles) and 90%RH (open circles). From Hall and Hoff (2012, Figure 4).

A detailed review of rehydroxylation research (predominantly non-dating oriented) into fired clay ceramics was carried out by Hamilton and Hall (2012), see *Section 2.3.* This is an important work in synthesising current understanding the dehydroxylation/rehydroxylation chemical recombination processes in (fired) clays and outlining open questions that need addressing.

With Wilson et al. (2012) we have a second publication that applies an RHX dating methodology with some degree of success, *Figure 2.44*. Wilson et al. (2012) date varied pieces of archaeological ceramic, all of which had been recovered by excavation. The work is significant in demonstrating that the RHX method can be applied to archaeological pottery and that the materials involved have $t^{1/4}$ mass gain behaviour, *Figure 2.45*. The work also presents a more detailed methodology over previous work (Wilson et al. 2009) with particular attention to the following areas: clear definition of the various mass components involved; a more rigorous method for defining/determining *Stage 2*; defining the effective lifetime temperature (ELT) and its use, see *Chapter 3*.

sample	ELT (°C)	m_a/α_m ($h^{1/4}$)	nominal RHX age 11°C (year)[a]	RHX age at ELT (year)[b]	RHX date AD	assigned date AD	comments
W1	10.5	42.29	365	387 ± 15	1624 ± 15	1605	
W2	10.5	43.52	409	434 ± 15	1577 ± 15	1605	
W3	10.5	42.88	386	420 ± 15	1599 ± 15	1605	
L1	9.1	56.08	1128	1284 ± 25	727 ± 60	560–660	[c]
S1	10.6	63.76	1886	1954 ± 30	59 ± 30	45–75	

[a]Calculated from m_a, α_m values of table 1, with 1 year = 24×365.25 h ($m_a/\alpha_m = y_a/\alpha$).
[b]Error in RHX age is combined uncertainty from nominal age and estimated ELT.
[c]Radiocarbon age (SUERC 33836): 1430 ± 35 BP, calibrated date 560–660 AD (95.4% probability).

Figure 2.44: Effective lifetime temperatures, RHX ages and assigned ages from Wilson et al. (2012, Table 3).

Wilson et al. (2012) define three types of water, *T0, T1, T2*, removed over the course of drying: *T0* is capillary/pore and adsorbed water removed during heating to constant mass at 105°C; *T1* is all molecular water (likely chemisorbed) removed between 105-500°C, typically 200-300°C, but not RHX water; *T2* is water attributed

to RHX. They also make it clear that the mass gain in *S1* is attributed to *T0+T1* type water. While clarification of definitions is useful, they do not explain why the distinction of a *Type 1* water is made and their reasoning for associating it with 200-300°C temperatures and *S1* mass gain.

There are some questions and both minor and major issues surrounding this work. Firstly, with regard to sample selection the authors state "the experimental data were obtained following a large number of exploratory experiments on a small group of well-sourced archaeological pottery samples" but do not elaborate clearly on what type of exploratory tests were conducted and how they guided sample selection. If there were samples that were not suitable, it would be valuable to know why.

Next, the samples were moved directly from the heating environment at 500°C to the weighing environment without being held for any period in desiccated/vacuum conditions to allow samples to cool to the aging temperature before exposure to moisture. If this is the case and if RHX mass gain commences during cooling at some temperature above the aging temperature, then a positive curvature (time-offset effect) should be observed in *Stage 2* (Barrett 2013, discussed shortly) but does not appear to be the case. This could be explained by rapid cooling of a single granule such that the effects are near negligible, but this requires demonstration. Aside from this, the period over which *Stage 2* is monitored is relatively short, approximately 16-50 hours; if low levels of curvature are present in the long term mass gain behaviour this might approximate to linear behaviour when only examined over such a short duration. Long term measurements (> 1 week) with their microbalance quality data would be more convincing evidence for long term linearity. Nonetheless, their method for *Stage 2* discrimination appears strong and there does not appear to be any reason over the period examined to suspect curvature.

The authors state uncertainties in the ELTs of all samples of ±0.2°C. This seem optimistic given, without considering the complexity of the temperature history, a) at best the uncertainties of long instrumental records that extend back only several

centuries are ±0.1°C (Butler et al. 2005), b) for samples that rely on long temperature reconstructions the uncertainties in these will certainly exceed ±0.2°C.[16]

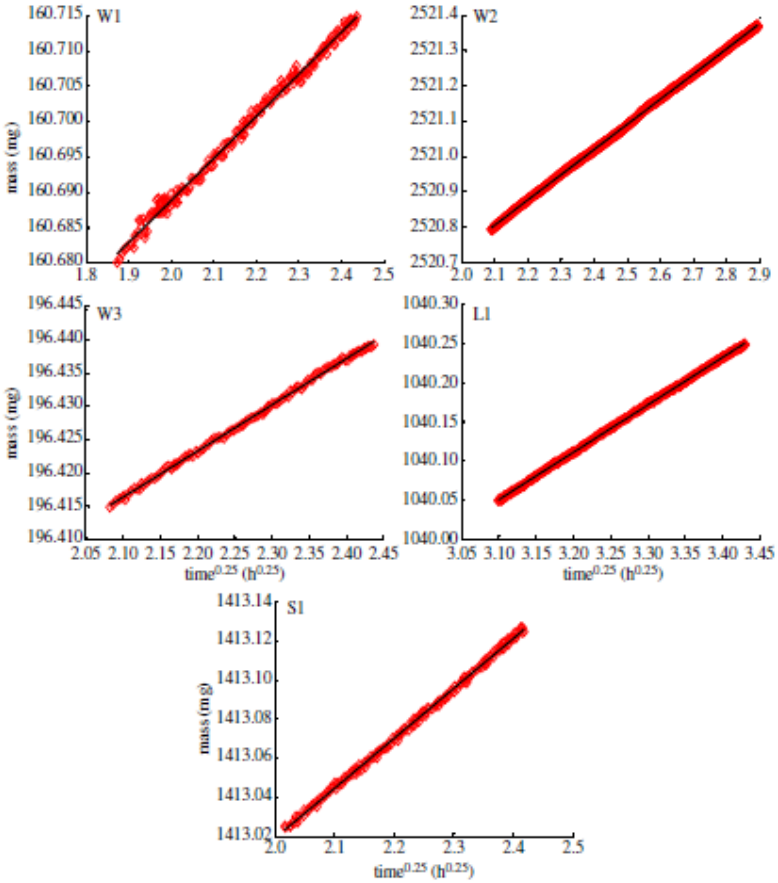

Figure 2.45: *Stage 2* data and modelled fits from Wilson et al. (2012).

Finally, a major issue arises with the validity of the dates, *Figure 2.44*, when the effects of organic contaminants are considered. All three samples were retrieved originally from burial contexts, yet carbon content was only measured for a single sample (Lambourn, L1). This is problematic as it is very difficult to accept that no contamination of organics occurred in the other samples (see *Chapter 9* for more on this) and if the magnitude of this contamination was only a fraction of that for L1 the dates would be adversely affected. Indeed, in Numrich et al. (2015), an issue

[16] For example in Luterbacher et al. (2004), used for the Wilson et al. (2012) Werra ware temperature reconstruction (W1,2,3), the standard errors (2σ) in the temperature reconstruction are of the order ±1°C for the period AD1500-1750 and ±0.5°C for the period AD1750-1880, decreasing afterwards with increased instrumental data.

with one of the dates (Werra-ware, W) arises when the carbon context is examined, discussed later.

Also, for L1, the mass of carbon (0.67%wt.) was subtracted in order to obtain the RHX mass gain (0.89%wt.). Yet no correction is made for the ratio organic matter/organic carbon, *Section 2.6*, typically of the order of 2.0. If the mass of carbon had been multiplied by this, the RHX mass would reduce to approx. 0.22%wt. and the dates estimated for L1 would be radically different and disagree hugely with the known age.

Therefore, while Wilson et al. (2012) does provided a tighter and possibly improved methodology there are significant doubts over the validity of the dates obtained, added to by the work of Goff and Gallet (2014b).[17]

The effect of mass gain during cooling following heating at 500°C is addressed by Barrett (2013). In experiments on modern brick samples Barrett demonstrates that if a ceramic commences gaining mass before it has cooled to a stable temperature (for subsequent mass gain measurements) this results in a pronounced *Stage 1* mass gain and a curvature in the *Stage 2* data as a function of $t^{1/4}$, *Figure 2.46*. This *time-offset* effect is equivalent to the ceramic having commenced gaining mass earlier than the start of measurements, hence the time offset. Using simulations, it was shown that mass gain curves generated for cooling and subsequent aging agreed well with those observed experimentally. The work highlights the need for removal of any mass gain during cooling or, instead, the use of a time-offset model in *Stage 2* to account for this, *Figure 2.47*. The work also provides support for an Arrhenius temperature dependence as well as drawing attention to the danger of finding linearity, depending on the region chosen for modelling, in *Stage 2* data that is actually curved. However, the work was conducted under the assumption of a $t^{1/4}$ behaviour; if $n \neq 4$ for the ceramics examined interpretation of the work is more complicated and less certain. Also, the work suffers from a lack of *Stage 1* data to support some of the assertions made regarding the time-offset effect explaining most of the *Stage 1* behaviour observed in other work.

[17] Also, no comment is made with regard to how well earlier dates worked (Wilson et al. 2009) despite not using the improved methodology.

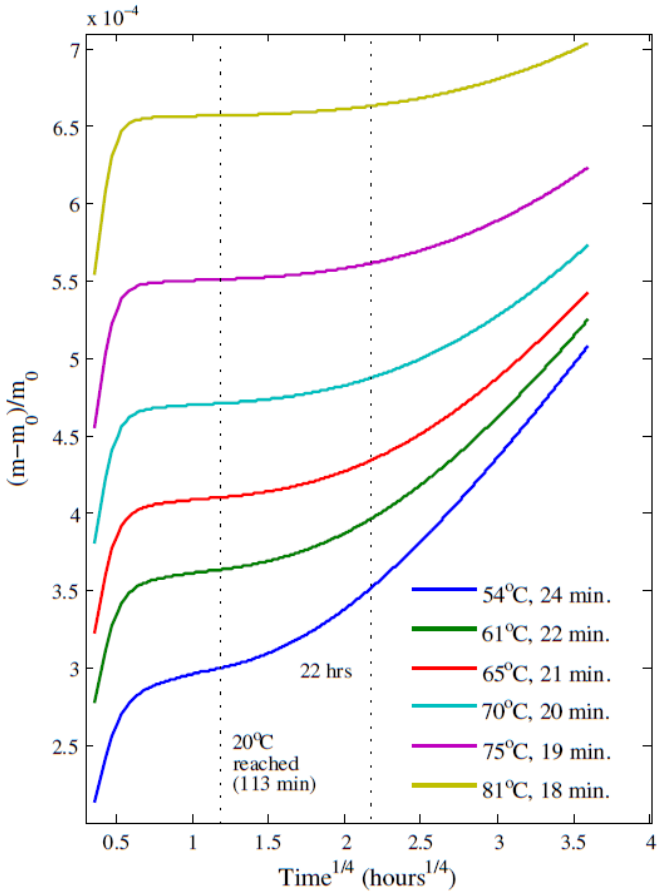

Figure 2.46: Simulation of the fractional mass gain curves of Chester Red brick samples during cooling for a range of commencement temperatures and periods since removal from the heating environment (500°C). The first dashed line corresponds to when samples reached thermal equilibrium at the aging temperature (20°C), the second dashed line the period after which mass gain measurements were carried out experimentally. From Barrett (2013, Figure 8).

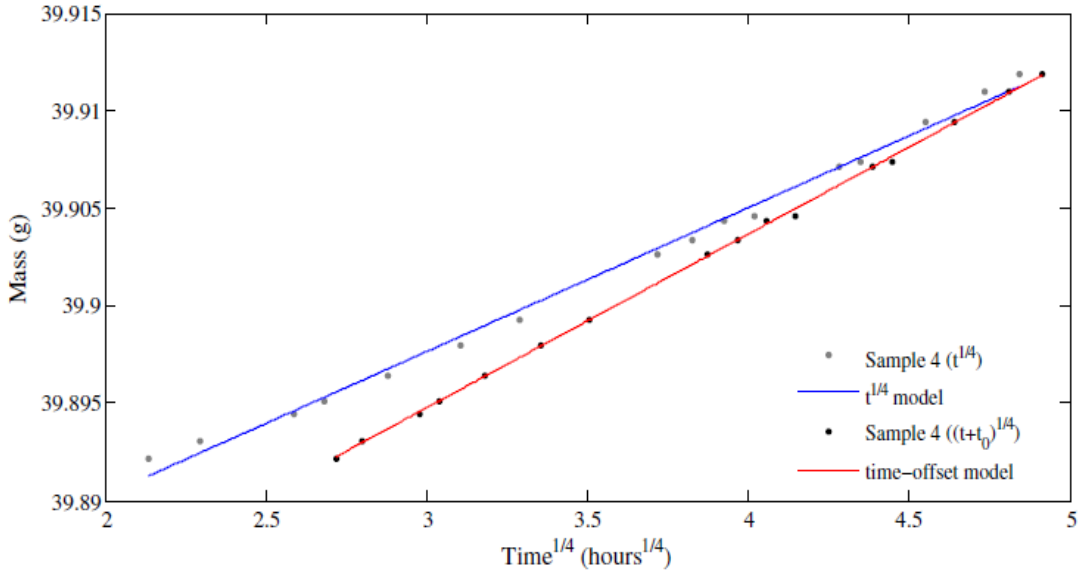

Figure 2.47: From Barrett (2013, Figure 2), the mass gain of a sample as a function of $t^{1/4}$ (blue) and $(t+t_0)^{1/4}$ (red) where t_0 is an offset of 33.7 hours obtained through modelling. With linear regressions provided.

Bowen et al. (2013) examined the mass gain behaviour of five archaeological pottery sherds of various sizes (1-1.8g) (that had undergone the same manufacture process and were assumed to be geochemically similar), as well as powdered fractions (100µm). They compared both the $t^{1/4}$ model and their own $t^{1/n}$ model for mass gain of the samples following firing at 500°C. For the $t^{1/4}$ model they observe varied mass gain behaviour with negative ("concave-down") curvature in all samples (as a function of $t^{1/4}$), *Figure 2.48*, and comment on how the spread in mass gain rates obtained "should not be observed, as rehydroxylation behaviour should theoretically be constant over this set of identical samples".

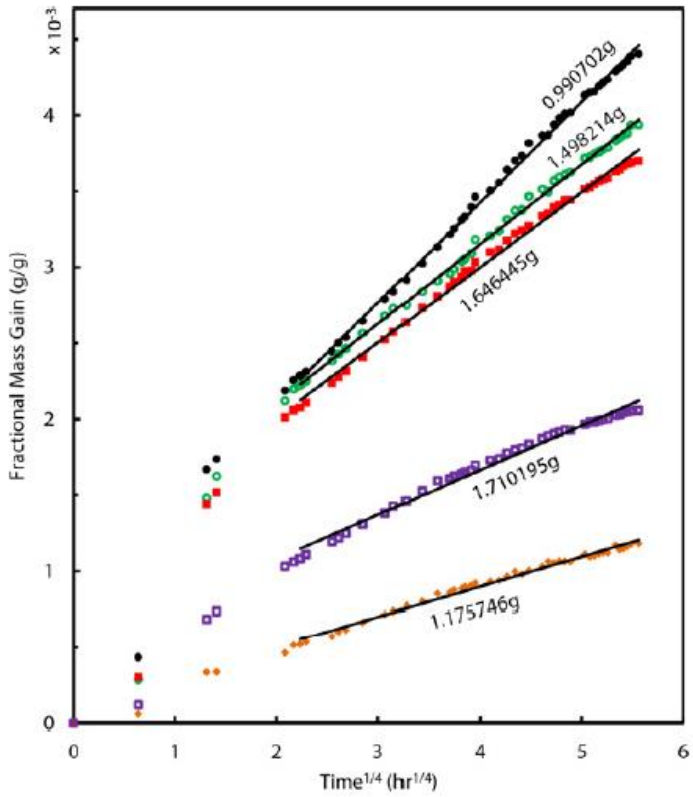

Figure 2.48: Mass gain curves from Davenport sherds as a function of $t^{1/4}$ with modelled linear fits of *Stage 2* included. From Bowen et al. (2013, Figure 3).

However, there are two issues with this. Firstly, they removed the first eight data points from their data to "preclude data from *Stage I*", yet they do not give a criteria for this number and given the downward curvature in their *Stage 2* data it

seems *Stage I* may still be proceeding; secondly, their statement that the behaviour should be constant over the samples is not tenable; just because the samples were manufactured the same way, were recovered from the same depositional context and have the same mineralogical composition, does not imply that the compositional component responsible for RHX behaviour is identical, and instead varied behaviour should perhaps be expected.

Modelling with the $t^{1/n}$ approach produced improved fits, *Figure 2.49*, with average *n* value of 3.92, yet there remained issues with more pronounced curvature obtained for larger sample size, curvature that their model could not account for, and the mass gain rates were again varied. They consider the possibility that the poorer modelling issues with larger samples is because of a longer *Stage 1* due to larger internal surface area of larger samples. They demonstrate, based on their $t^{1/n}$ modelling, that the duration of *Stage 1* is indeed correlated with sample size, *Figure 2.50*, yet then discount this result because the durations estimated are not of the same duration as the curvature. However, their logic is flawed and there is an issue with circular reasoning. They are trying to test if the prolonged *Stage 1* ("slow penetration of physically bonded water") is the cause of their $t^{1/n}$ model inadequately describing the data. Yet, they then estimate the duration of *Stage 1* from models which are inadequate in dealing with prolonged *Stage 1* to begin with, and then argue that the duration estimated from these models do not match up to the duration of the curvature in the observed data. It seems more reasonable that their estimates of the *Stage 1* duration, *Figure 2.50*, reflect (but are not identical to) the true duration and actually support the argument of prolonged physisorption for larger samples. This is backed up by their results on powdered samples, where their $t^{1/n}$ modelled provided very good fits, for which a shorter *Stage 1* is obtained and the authors state that "powdering may have partially opened the meso- and micropore networks, allowing for relatively rapid penetration of atmospheric water".

Bowen et al. (2013) also compare the rates obtained from powder fractions and sherds and consider the similarities between the groups "outstanding", despite the same authors considering the modelling results of the sherds poor for larger

samples. The mass gain rates are indeed of the same order which supports the possibility of powdering samples without drastic effects, yet it is not clear that the behaviour is unchanged by this process; the two powder samples may only have "differed by a statistically insignificant amount" but this is because the uncertainties are very large (of the order of 20%) and, in any case, it is not meaningful to compare rates that are measured in different units (they both have different time units $h^{1/n}$, because n differs from 3.03 to 3.42 between the two samples), as Bowen et al. have done.

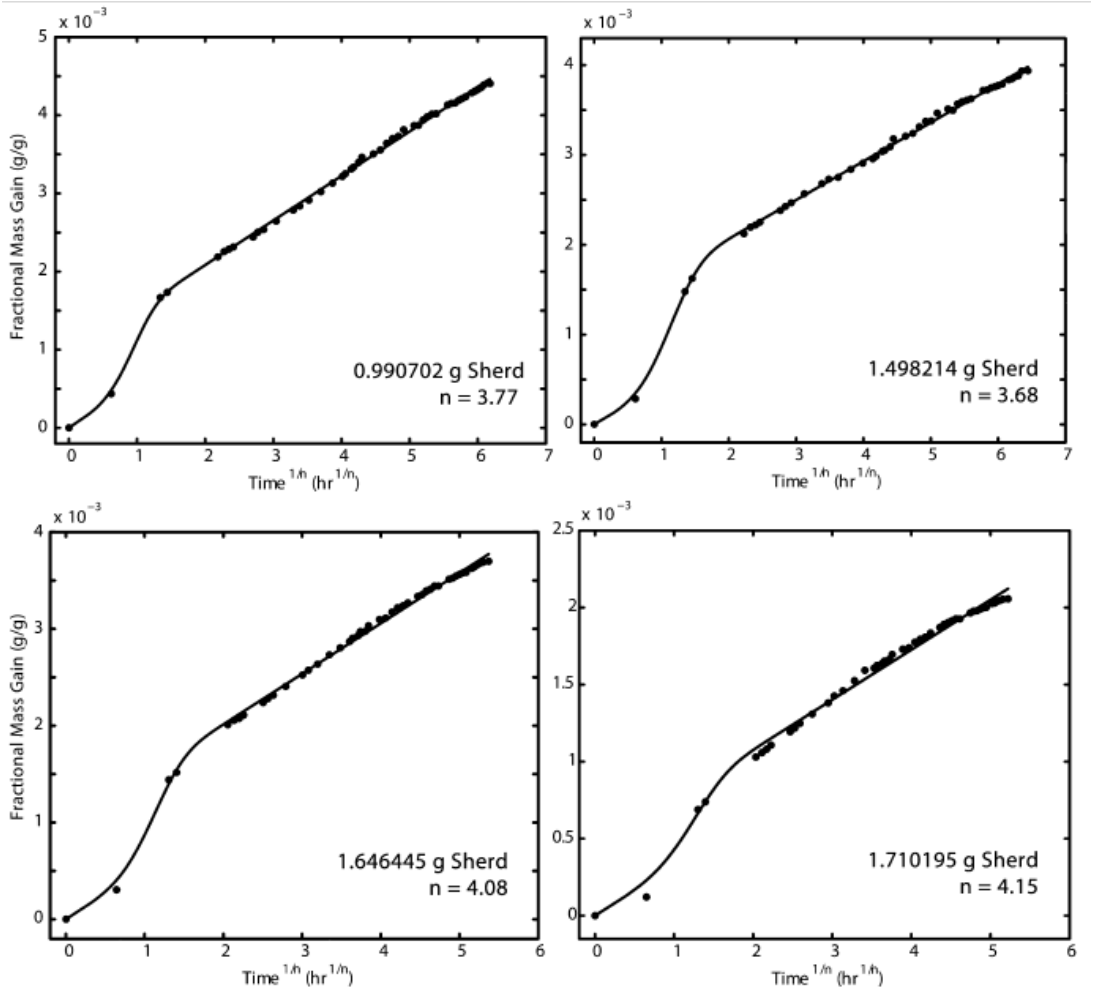

Figure 2.49: Fitting results for Davenport sherds using generalised $t^{1/n}$ model. From Bowen et al. (2013, Figure 4).

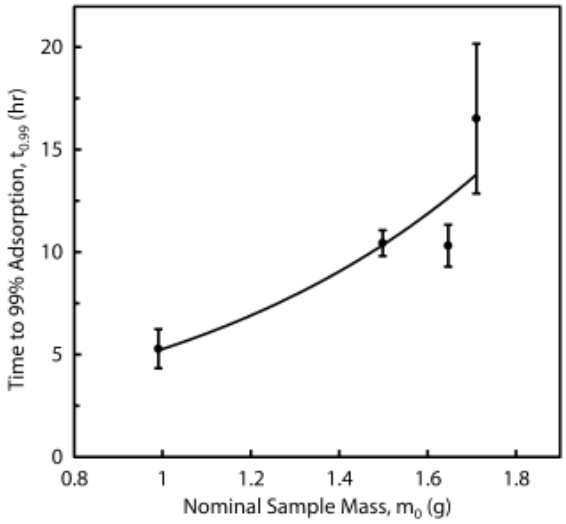

Figure 2.50: Characteristic adsorption times for Davenport ceramic as a function of nominal sample mass based on use of generalised $t^{1/n}$ modelling. Error bars correspond to one standard deviation. From Bowen et al. (2013, Figure 6).

Nonetheless, the work of Bowen et al. (2013) does demonstrate the possible value of a more flexible $t^{1/n}$ model and the need for homogenisation of samples to remove variations that might exist if multiple sherds or even portions of a single sherd are used in RHX tests. The work also appears to demonstrate a possible relationship between the *Stage 1* magnitude/duration and sample size, and of the value of using smaller samples in minimising *Stage 1* effects.

Burakov and Nachasova (2013) carried out rehydroxylation dating tests, together with an archaeomagnetic study, on a range of archaeological ceramics from a variety of contexts using a similar methodology to Wilson et al. (2009) involving a $t^{1/4}$ approach. The correspondence between the rehydroxylation dates and assigned ages are poor, with the RHX ages often far too old, *Figure 2.51*. Burakov and Nachasova (2013) believe that their archaeomagnetic analysis reveal a significant factor causing these deviations, an unaccounted for mass of hydroxides which are removed during heating and that originated because of a process of weathering of magnetite in the ceramics (formation of goethite). They conclude that "the factors causing deviations between the rehydroxylation datings and the true values are revealed, and a method is suggested for their correction. This

method provides estimates close to the true age of the material". However, under closer scrutiny this does not hold up. Of the eleven samples dated, only one (Granada, Alhambra, brick) provides an age within a century of the known age. The authors state that the three samples from the *8th century* Castillo de Gibralfaro fortress (*3s*, *6s* and *7s*) showed that all the bricks had been renovated and date to the 18th-20th century yet provide no evidence from other sources to support this. They argue that the sample *1s*, from the same site, produces a date of 1935 in agreement with the other samples from this site, if it is assumed that "half the amount of water lost under heating to 500°C is associated with iron hydroxides", but they provide no solid justification for this figure. Similarly for sample *3b* (Greenwich brick) the authors first estimate, unconvincingly, that the mass of water lost due to magnetite hydroxides is 20-40mg, yet then, by "assuming that 40mg of 65mg water lost by the sample when heated to 500°C relates to hydroxides", calculate an age in agreement with that expected, without addressing the fact that this is a very selective use of the upper bound estimate of 20-40mg.

The deviations in the sample *1b* (Roman pavement brick) and the Germonossa sample are attributed to heating of the brick to above 330°C at a later period, during which the sample "lost most of the gained water" or "the sample lost all the capillary water and 90% of the chemically bound water", respectively. But they do not explain how a figure of 90% was arrived at, and if this was the case the resulting RHX age would be younger than the assigned age for both samples, not older as is the case.

There is no adequate explanation given for the deviations of the remaining samples, yet the possibility of higher effective lifetime temperatures than used in calculations is suggested and possibly the case for *1063* (Pantikapaion).

A final issue with this work is that their samples were all aged at a temperature of 25°C and without any estimation of the activation energy of each sample. Instead they use the Wilson et al. (2009) estimate of 182kJ/mol (the current author has concluded this based on reverse calculation of their *Equation 2*) for all samples. This is inappropriate as the activation energy needs to be estimated on a sample by

sample basis because it will differ based on the composition of the samples (different activation energies have been reported in Wilson et al. (2012), Barrett (2013), and Clelland et al. (2014)).

Sample no., monument	Archaeological dating	Rehydroxylation dating
3s Malaga, Castillo de Gibralfaro	not available	1901 ± 15
6s Malaga, Castillo de Gibralfaro	"	1958 ± 2
7s Malaga, Castillo de Gibralfaro	"	1715 ± 35
1s Malaga, Castillo de Gibralfaro	"	790 ± 250 1935
121, Granada, Alhambra, brick	16–17 centuries	1535 ± 35
1b London, brick from the Roman mosaic pavement	75 ± 75	−385
1063 Pantikapaion, clay daub piece from the stove	190 ± 10	−880
610 Germonassa, ceramics	860 ± 60	−1450
123, Granada, Cartuja, brick from an oven	100 ± 10	−10050
125 Granada, Cartuja, ceramics	90 ± 10	−11210
3b, Greenwich, brick	not available	−10980 1725

Figure 2.51: Assigned ages and rehydroxylation dating estimates of ages taken from Burakov and Nachasova (2013, Table 1). Minus sign corresponds to B.C. and lower age in rehydroxylation dating field corresponds to corrected age (see original text).

The work of Burakov and Nachasova (2013) is unconvincing in its attempts to explain discrepancies between assigned ages and rehydroxylation dates (and does not address the possibility of other contaminants being removed, i.e. organics) yet does highlight a possible magnetite hydroxide issue that may need to be addressed

in future.[18] It does also provide one very good example of $t^{1/4}$ behaviour (Burakov and Nachasova (2013), Figure 2).

The insensitivity of the *Stage 2* mass gain rate to environmental moisture levels (%RH, say) had been assumed in studies to date based on suggestive evidence in several publications (Wilson et al. 2003, Hall and Hoff 2012, Wilson et al. 2013), yet conclusive evidence remained lacking. In Drelich et al. (2013) this issues is tackled. Following heating at 500°C, samples of Davenport pottery and modern Houghton brick were aged at a constant temperature while changes to the moisture levels were made to examine the effects on the *Stage 2* mass gain rate. In the first test, a sample of modern brick underwent a step change from 20-28%RH. The observed effect was a step change in the mass followed by a *Stage 2* mass gain rate that appeared unaffected, *Figure 2.52*. The step change was attributed to difference in the amount of capillary water condensing in the pores.

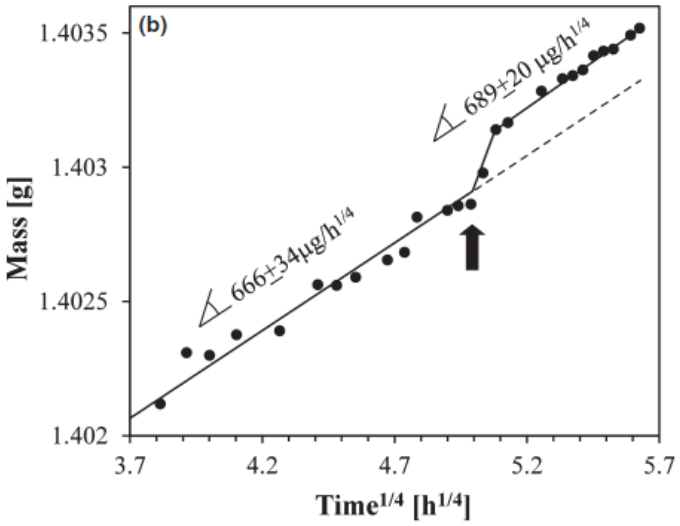

Figure 2.52: Mass gain as a function of $t^{1/4}$ for modern Houghton brick sample with arrow indicating change in %RH from 20-28%. From Drelich et al. (2013, Figure 1).

[18] Note: it can be argued that if the process of hydroxylation of magnetite is completed in *Stage 1*, it will not affect the RHX mass gain estimate and thus not affect the dates (because the methodology for RHX mass gain calculation avoids this). If it proceeds into *Stage 2,* it will either be evident as a non- linear $t^{1/4}$ behaviour or as a linear $t^{1/4}$ behaviour. If, as is the case for Burakov and Nachasova (2013, Figure 2) where *Stage 2* is linear, it is the latter AND if the process can be assumed to be long term, then the RHX mass gain rate estimate will include a magnetite rehydroxylation component which will actually take care of the component of magnetite hydroxides in the RHX mass estimate, again eliminating any adverse effect on the dates.

In a second test, Davenport pottery was stepped from 20%RH to 40%RH and back to 20%RH, *Figure 2.53*. A step change increase in mass occurs with the shift to 40%RH followed by a decrease on reversion to 20%RH; however, the mass does not return to the original mass level at 20%RH. The authors suggest this may be the result of a hysteresis in water capillary condensation. Unfortunately, the mass gain rates could not be compared before and after the step because of issues with modelling a non-linear *Stage 2* (as a function of $t^{1/4}$), yet the authors conclude that the changes in humidity do not appear to impact rates of mass gain in the long-term. On observation of the same data, the present author considers this test inconclusive; a step change in mass has occurred that, while attributed to a hysteresis effect, could equally be argued as the result of a greater mass gain rates during the period at 40%RH and which might not result in a significant change in the apparent mass gain rate upon reversion to 20%RH.

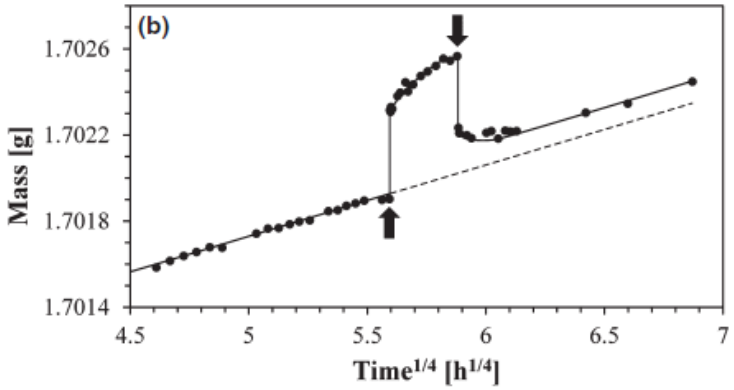

Figure 2.53: Mass gain as a function of $t^{1/4}$ for Davenport pottery, with step change from 20%RH to 40%RH and back to 20%RH. From Drelich et al. (2013, Figure 2).

In the final test carried out, a sample of the modern brick is put through several cycles of aging, drying at 110°C, soaking in water, removal of excess water, and aging again, *Figure 2.54* and *Figure 2.55* (some sample broke off during the second soaking cycle, hence the abrupt drop). The authors are of the opinion that the drying and soaking events have no effect on the long term underlying $t^{1/4}$ behaviour stating "during each cycle, the sample tended to restore the nominal *m* versus *t* correlation (as was observed before and drying or soaking events)." and the slopes as a function of $t^{1/4}$ were similar for each aging stage.

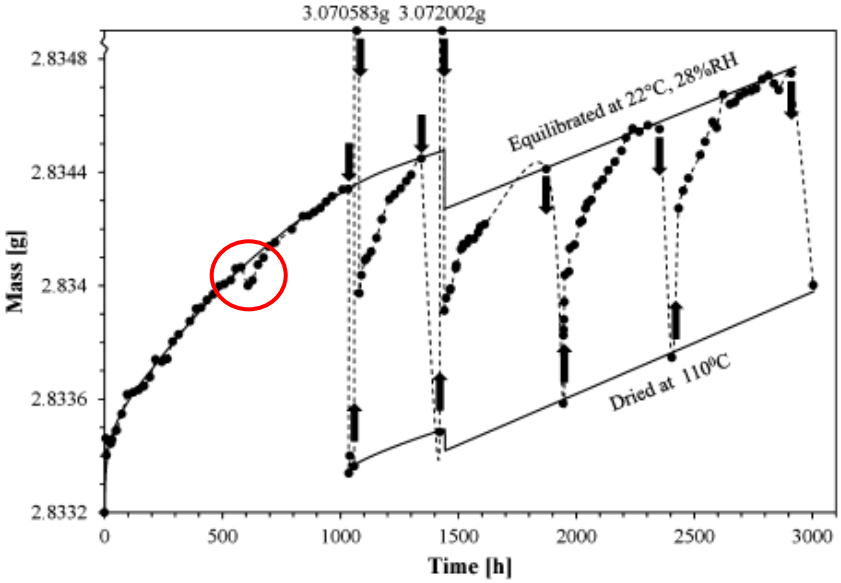

Figure 2.54: Mass gain versus time curve for modern brick sample during cycles of aging, drying, soaking in water and aging. From Drelich et al. (2013, Figure 3). Note the data is as a function of time. Also, a red circle was added by present author to highlight transition from 20%RH to 28%RH.

Stage	Sample treatment	Time sequence (h)	Slope for $m = f(t^{1/4})$ ($\mu g/h^{1/4}$)
I	Rehydroxylation: 22°C, 20% R.H.	0–651	350 ± 20
II	Rehydroxylation: 22°C, 28% R.H.	651–1033	390 ± 60
III	Drying: 110°C	1033–1059	–
IV	Soaking in water: 22°C	1059–1060	–
V	Rehydroxylation: 22°C, 28% R.H.	1060–1343	900 ± 160
VI	Drying: 110°C	1343–1421	–
VII	Soaking in water: 22°C	1421–1422	–
VIII	Rehydroxylation: 22°C, 28% R.H.	1422–1873	810 ± 50
IX	Drying: 110°C	1873–1945	–
X	Rehydroxylation: 22°C, 28% R.H.	1945–2353	770 ± 620
XI	Drying: 110°C	2353–2405	–
XII	Rehydroxylation: 22°C, 28% R.H.	2405–2911	570 ± 260
XIII	Drying: 110°C	2911–3005	–

Figure 2.55: Portion of Table I from Drelich et al. (2013) showing the cycles carried out on modern Houghton brick and the mass gain rates obtained for periods of aging.

The first point to be made is why the transition from 20%RH to 28%RH (red circle in *Figure 2.54*) has the opposite behaviour to that in *Figure 2.52*, when both are for the same material and humidity level transitions; Drelich et al. (2013) state that "the effects during these two stages were almost identical to those discussed in relation to Fig. 1 [*Figure 2.52 above*]" but clearly the step change in one is an increase and in the other a decrease. A second point to be contested is that the

mass gain behaviour continues unaffected by the drying and soaking events. It can be observed in *Figure 2.54* that Drelich et al. (2013) have superimposed two lines, one marked "equilibrated at 22°C, 28%RH", the other "dried at 110°C", appearing to suggest linearity. Yet this data is presented as a function of t not $t^{1/4}$; if the mass gain rate is linear as a function of t this would suggest non-linear increases as a function of $t^{1/4}$. It is then difficult to argue conclusively that the drying and soaking cycles do not affect the *Stage 2* mass gain behaviour. Indeed, looking at the rates presented by Drelich et al. (2013), *Figure 2.55*, it could be argued either way; however, as the authors explain, there were a lack of suitable data points for well modelled mass gain rates and the uncertainties are very large. The present author would argue that if samples were heated from 22°C to 110°C and cooled from 110°C to 22°C during a heating cycle then, because of the accelerated mass gain at higher temperatures due to the non-linear Arrhenius temperature dependence (Barrett 2013), additional mass gain above that expected at 22°C must have occurred and this is reflected in the data. This does not argue against the possibility of humidity and moisture levels having a negligible effect but does suggest a flaw in the methodology of the experiment with the results not entirely conclusive. Nonetheless, the work overall does provide some support to the argument that any effects on the *Stage 2* mass gain rates due to changes in humidity or moisture level are perhaps minor or negligible.

The effect and influence of temperature on rehydroxylation dating of archaeological pottery is given rigorous treatment by Hall et al. (2013), building on previous work by Barrett (2011). This work deals comprehensively with the theoretical elements involved surrounding the RHX rate temperature dependence, before examining the influence of varying environmental temperature on the RHX mass gain through simulations. They define the *effective lifetime temperature* (ELT), see *Chapter 3*, and demonstrate how this can calculated for a given lifetime temperature history with examples of its application for long temperature records. They examine how the effects of burial can be accounted for and describe how age uncertainties are affected by temperature history and effective lifetime temperature.

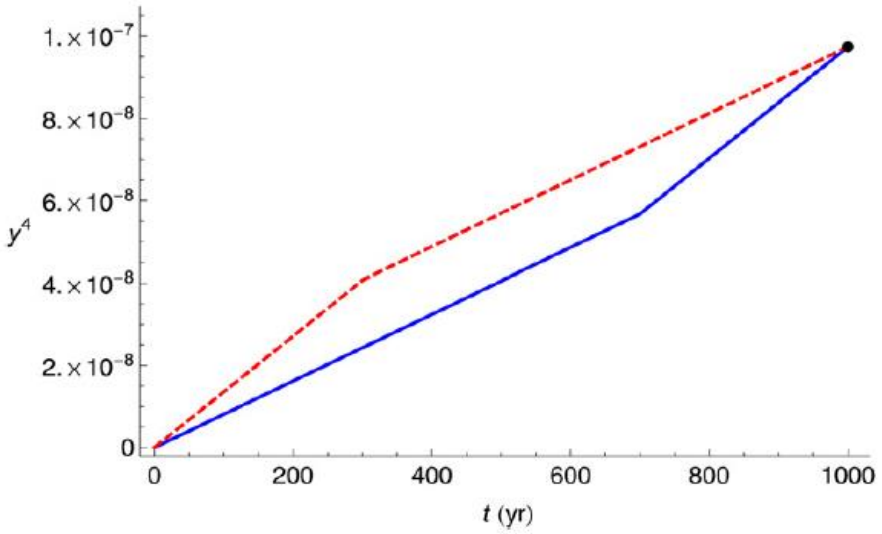

Figure 2.56: The effect of a step change of temperature on the final fractional mass gain. The fractional RHX mass gain *y* is plotted as y^4. The solid blue line corresponds to a history of 700 years at 10°C followed by 300 years at 15°C with the dashed red line corresponding to the order of these events reversed. Taken from Hall et al. (2013, Figure 2).

Of particular note is the implication from simulation work that if the lifetime temperature history of the ceramic is considered as a set of discrete temperature events (demonstrated by Hall et al. in terms of temperature switches) the final mass gain across all events is independent of the ordering of the sequence; according to Hall et al. (2013) "this is a remarkable result, which has the important consequence that in constructing temperature history equal attention must be given to all parts of the temperature history". For a step change of temperature this is shown in *Figure 2.56* (Hall et al. Figure 2).

With Shoval and Paz (2013) the possibility of using thermal analysis methods (thermogravimetric analysis (TGA), differential thermogravimetric analysis (DTG), differential scanning calorimetry (DSC)) and, in particular, the percentage mass loss estimates from TGA during heating to estimate the age of ancient pottery samples (7000BP – present) was examined. TGA, DTG and DSC were used to identify two regimes of mass loss, the first, from room temperature to 350°C attributed to dehydration, the second, from 350-600°C, attributed to dehydroxylation. Using existing TGA data, they estimated the percentage mass loss in both regimes. They then carried out regressions of the age of the individual pottery samples (for 45

samples) versus the % mass loss values for both regimes as well as the average age of samples from the same period versus the average % mass loss, again for both regimes, dehydration and dehydroxylation, *Figure 2.57*.

Shoval and Paz (2013) also examined the correlation between the average age of samples from the same period and the combined mass loss due to dehydration and dehydroxylation (room temperature-600°C). Strong correlations were found for all combinations. In particular, where the samples of similar period were averaged, the relationship was very strong and almost identical for the dehydration and dehydroxylation regime (R^2 = 0.82) and slightly better for the dehydration and dehydroxylation regimes combined (R^2 = 0.82). The authors do not explain why this might be the case, given that they have previously attributed dehydroxylation to the regime 350-600°C and would expect this to be the regime that correlates with the ceramic age. The current author believes the results suggest mass loss associated with rehydroxylation may occur across a much broader heating regime, commencing well below 350°C. Examination of the TGA examples they present (Figure 1 of Shoval and Paz (2013)) reveals a continual and gradual mass loss above 100°C with an increase in mass loss commencing c. 350-400°C, which they attribute to dehydroxylation. However, this is the temperature regimes at which organic matter/carbon begins to be strongly removed, *see Section 2.3*; given the samples examined are pottery mostly used in cooking/storage, and excavated from burial contexts, it seems likely that the mass loss commencing at 350-400°C reflects a strong, if not complete, organic matter/carbon component and that instead dehydroxylation has occurred more gradually over a wider range of temperatures.[19]

Also of note is that the results of Shoval and Paz (2013) present a correlation between mass loss and *t,* not $t^{1/4}$. This is not discussed by the authors.

The results of Shoval and Paz (2013) do convincingly demonstrate that the mass loss due to dehydration/dehydroxylation shows a general increase over time and

[19] Note, in the examples provided by Shoval and Paz (2013, Figure 1), there are no clear exothermic peaks in the DSC curves that might be associated with burning off of organic matter. On the other hand, the presence of endothermic peaks suggestive of dehydroxylation are not particularly convincing either.

supports long term processes being involved. It also suggests a sharp distinction between dehydration and dehydroxylation regimes may be unsuitable with perhaps dehydroxylation proceeding over a wide temperature range.

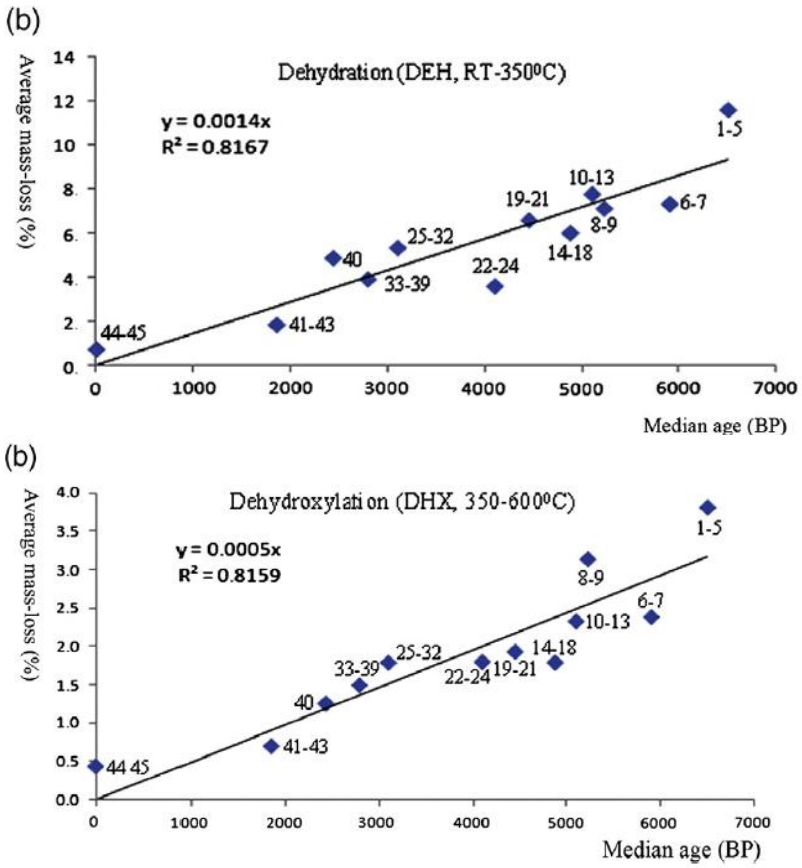

Figure 2.57: From Shoval and Paz (Figure 2b and 3b) the relationship between TGA derived average % mass loss and average median age for samples grouped according to period. Top- for dehydration regime, room temperature to 350°C. Bottom – for dehydroxylation regime, 350-600°C.

The publication of Le Goff and Gallet (2014a) is an important addition to existing RHX research. Using a specially constructed setup that permits continuous mass gain measurements of 10 samples under controlled temperature and humidity conditions, they carried out the dating methodology of Wilson et al. (2013) on a large set of archaeological ceramics (60 samples of varied origin). They found that no fragments provided satisfactory RHX dating results; samples collected from the same fired clay fragment "rarely show the same mass-gain behaviour", often resulting in dissimilar age estimates, and highlighting the care needed in sample

selection/homogenisation. The duration of heating at 105°C and 500°C are critical parameters that need to be better understood, with Le Goff and Gallet emphasising that while the *Stage 2* fractional mass gain behaviour was not observably affected by repeated heating at these temperature shifts (decreases) in the initial and average mass levels were. They also observed that the mass gain behaviour in *Stage 2* appears to obey a $t^{1/4}$ model when applied to a suitable region of the curve; however, it was demonstrated that a $t^{1/n}$ model could be argued to be equally satisfactory for a range of values (3-6), where $n \neq 4$, provided a suitable portion of the curve is used.

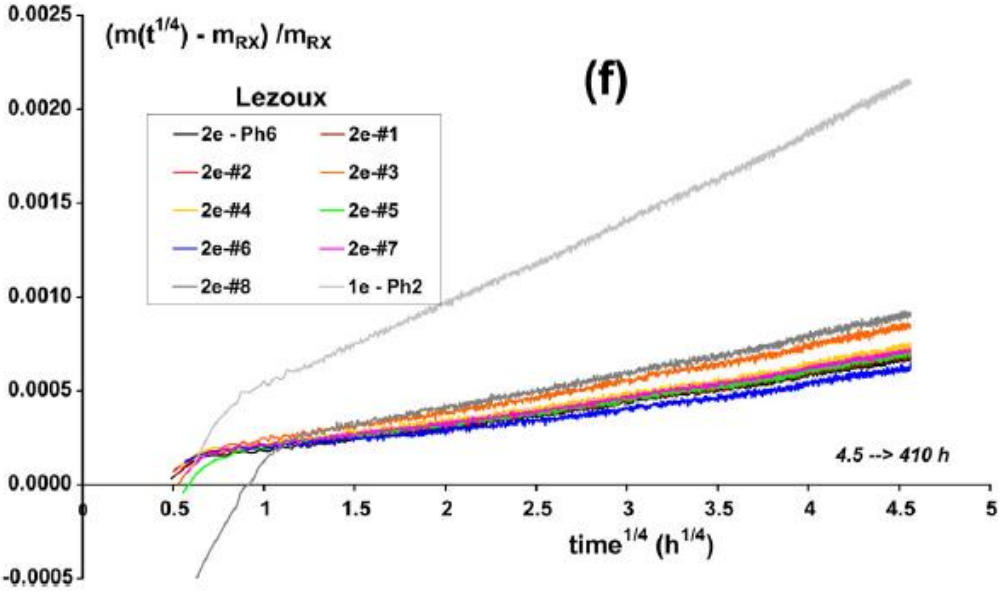

Figure 2.58: Portion of image from Le Goff and Gallet (2014a, Figure 4), showing the fractional mass gain of Lezoux, samian ware fragments following heating at 105°C as function of $t^{1/4}$.

The effect of running samples at two different %RH values (32% and 42%) was also shown not to affect the *Stage 2* behaviour, supporting moisture level insensitivity of rehydroxylation. A significant finding was that after heating at 105°C the samples did not equilibrate to a constant mass even after a prolonged period of measurement (weeks) – in fact the mass gain behaviour was observed to be similar to that following heating at 500°C, *Figure 2.58*, appearing to obey an approximate $t^{1/4}$ power law, the authors admitting that a "slow diffusion process" may be ongoing. No issues with magnetite mineral alteration during heating (Burakov and Nachasova 2013) were observed.

Le Goff and Gallet (2014a) is a rigorous piece of research with few areas for criticism and it addresses many significance issues that will be returned to in the current work. However, it is commented that the presence of contaminants that might be removed during heating is not discussed and that attempts to prevent/reduce additional mass gain during cooling (to minimise associated curvature effects, Barrett 2013) are not carried out. Issues with the dating results being too young possibly arising because of not using the component based approach proposed in this work, *Section 3.6*, and the use of drying times that are far too short will feature in the thesis discussion, *Chapter 9*.

Factors affecting the early-stage mass gain are examined by Wilson et al. (2014), who look at the behaviour of samples with low and high specific surface area (SSA) following heating at 500°C under aging conditions of varied temperature and relative humidity. They define high surface area material as that which has a convex downward curvature (negative) as a function of $t^{1/4}$ and associate this behaviour with a very slow *Stage 1* to *Stage 2* transition, *Figure 2.59*.[20] The *Stage 1* mass gain is attributed to a combination of *T0* physisorbed water (removed at 105°C) and *T1* chemisorbed water (removed between 105-500°C). According to the authors, for mass gain curves obtained at 11°C and 60%RH, and 50°C and 20%RH, the *Stage 1* mass gain is much greater for the sample at the lower *absolute humidity* (11°C and 60%RH) because of greater levels of physisorption (*T0*) at lower temperatures, whereas *Stage 1* at the higher temperature condition results in a more rapid uptake of chemisorbed water (*T1*) (suggesting a rate for this process that is temperature dependent), and a reduction in physisorbed water. The implication of this, according to Wilson et al. (2014) is that running samples at higher temperatures and humidities would reduce the magnitude and, more importantly, duration of *Stage 1*, in samples of large SSA; accepting, however, that this may not be practical for RHX dating purposes.

[20] Wilson et al. (2014) make a distinction between the time to end of *Stage 1* and the time to onset of linear *Stage 2,* with a transitionary period in between, the result of their interpretation of the processes involved. However the current author is not entirely in agreement with their interpretation and prefers to defines *Stage1* as lasting until commencement of *Stage 2*.

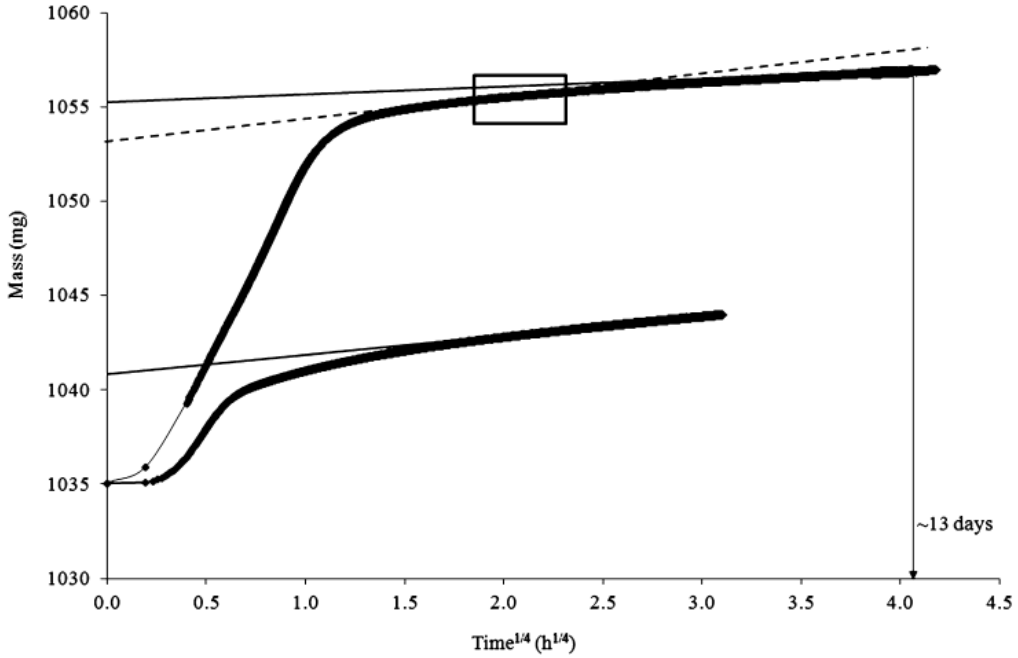

Figure 2.59: Mass gain curves of high SSA sample of loomweight following heating at 500°C. Top curve – aging at 11°C and 60%RH. Bottom curve – aging at 50°C and 20%RH. Lines corresponding to modelling results discussed in original publication. (Taken from Wilson et al. 2014, Figure 2).

However, the introduction of *T1* water is still not fully justified. It could be argued that all *Figure 2.59* does is demonstrate that the level of adsorbed *T0* is governed by %RH (as is theoretically (BET theory) the case for simple adsorption on porous solid surfaces, see Lowell et al. 2004 (*Chapter 2, Chapter 4)* and that a greater quantity of *T0* requires a greater period of time to diffuse and reach all internal surfaces. The interpretation of the two curves is made more complicated because Wilson et al. (2014) did not carry out the experiment with one variable, temperature or humidity, held constant while the other is varied, which might have clarified matters.

The low surface area samples are associated by Wilson et al. (2014) with a concave (positive upward) curvature as a function of $t^{1/4}$, *Figure 2.60*. Again, the duration of *Stage 1* occurred at an earlier time (with lower magnitude) for higher temperatures conditions (50°C and 10%RH as opposed to 11°C and 50%RH), highlighting the benefits of running samples at higher temperatures. The curvature is explained by Wilson et al. (2014) by first subtracting the $t^{1/4}$ behaviour, obtained from modelling

the linear portion at the end of the mass gain curve, from the overall mass gain curve, and superimposing the %RH values recorded during measurement, *Figure 2.61*. The resulting *T01* (combined *T0* and *T1*) behaviour has a maximum peak followed by a slow decrease to equilibrium, according to the authors, that is correlated with the fluctuations in RH measurements and the time taken for the RH to reach its set point; "the sample becomes 'over-wet' and exceeds its eventual equilibrium mass. This excess water must be lost by drying, and this occurs more quickly at the higher measurement temperature". Therefore, the authors believe the curvature observed in the data is an artefact of measurement conditions, and its reduction is aided by having a constant flow of drying gas in their microbalance chamber.

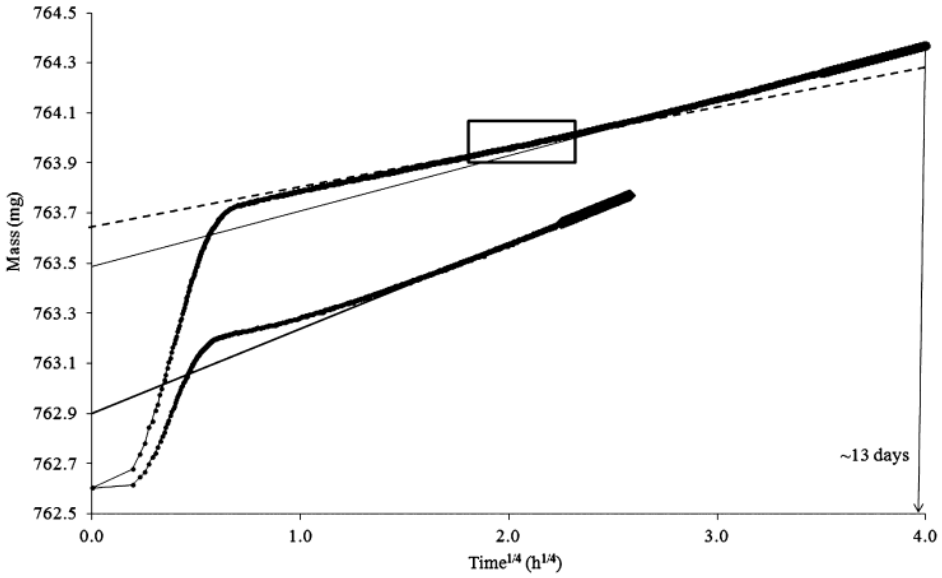

Figure 2.60: Mass gain curves of low SSA sample of samian-ware following heating at 500°C. Top curve – aging at 11°C and 50%RH. Bottom curve – aging at 50°C and 10%RH. Lines corresponding to modelling results discussed in original publication. (Taken from Wilson et al. 2014, Figure 4).

A few comments need to be made regarding the Wilson et al. (2014) interpretation of a positive *Stage 2* curvature as being an artefact of the measurement procedure. The authors suggest that the peak in *T01* component occurs with increased physisorption of *T0* to match the increase in %RH above its set point while the apparatus tries to reach equilibrium, hence 'over-wetting'. It must be emphasised, however, that the curvature exists when the data is presented as a function of $t^{1/4}$ and that its existence is only as 'real' as this model is appropriate. Also, it must be

considered as to why this effect is not observed for high SSA samples which would be expected to be more sensitive to %RH fluctuations? This is not discussed by the authors.

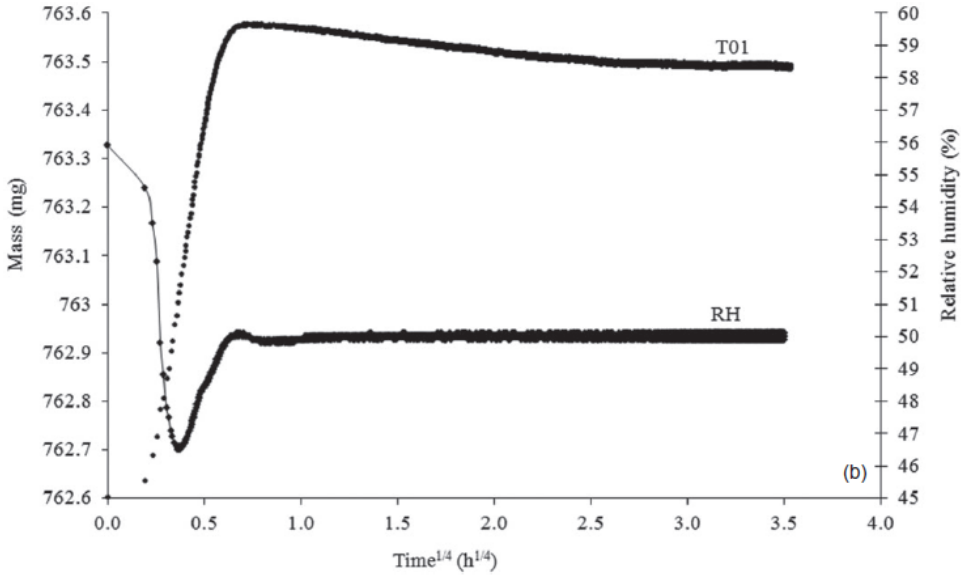

Figure 2.61: The *T01* component of the low SSA sample, 11°C and 50%RH, together with the %RH during measurements. From Wilson et al. (2014, Figure 6).

The fluctuations in %RH above the set value associated with causing this effect are only of the order of 0.25%RH, *Figure 2.61*. If this is indeed the cause, then later fluctuations in %RH, some appearing to be half the magnitude of the original %RH 'bump', would also be expected to cause large effects; such issues are not observed but the implication of this explanation would be that unless the experimental apparatus can control %RH to near negligible levels of fluctuation then uncontrollable curvature of the data will result.

Also, if the *T01* maximum is correlated with the over-shoot in %RH, then the response of the former to the increase in the latter appears almost instant, suggesting a physical adsorption response not involving slow diffusion processes (i.e. capillary effects); if this is the case it seems to take a remarkably long duration (39-150 hours to commencement of *Stage 2*) for the process to be reversed, considering how quickly the %RH drops down to a constant value.

Finally, Wilson et al. (2014) recommend measurements are carried out under a constant flow of gas to speed up drying and minimise the duration yet do not provide any experimental evidence to demonstrate this actually works. Therefore, interpretation by Wilson et al. (2014) of the positive curvature as being an artefact of the measurement process is opposed by the current author and results from the current work will be presented to argue strongly against this in *Chapter 9*. Indeed, work by Le Goff and Gallet (2014b) also argues again the interpretation of Wilson et al. (2014).

Wilson et al. (2014) also present data that demonstrates a correlation between the specific surface area and both the duration of *Stage 1* (by their definition) and time to onset of a linear *Stage 2*. This correlation provides a means of assessing the likely duration of *Stage 1* and curvature behaviour of a sample before mass gain measurements are conducted, *Figure 2.62*.

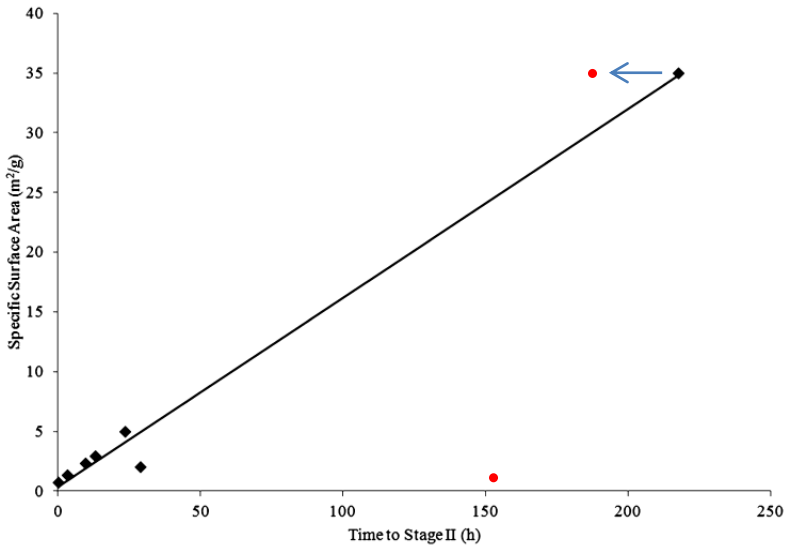

Figure 2.62: Specific surface area versus time to the commencement of *Stage 2*. From Wilson et al. (2014). Red data points are included by the present author and correspond to approximate location of data points omitted from use by Wilson et al. (from Table 2). Also the data point with a SSA of 35m^2/g is presented as having a time to *Stage 2* of 187 hours, not 210-220 hours, in Table 2 of Wilson et al. (2014).

The data used in this plot does not agree completely with the table (Table 2 of Wilson et al.) of data from which it is taken; a data point is omitted without explanation and one appears to be assigned an incorrect value, weakening the correlation when included. The plot is also biased positively by the single large SSA sample. Nonetheless, the data does suggest a correlation is may exist and this will be returned to in *Chapter 9*.

In summary, the publication of Wilson et al. (2014) and their interpretation of the results is dependent on the adequacy of a $t^{1/4}$ model and is not without issue. This aside, the nature of *Stage 2* curvature, negative or positive, is shown to be associated with samples of high or low SSA, respectively, and a possible correlation between the duration of *Stage 2* and the SSA is highlighted together with a means of reducing the duration of *Stage 2* by aging at higher temperatures.

In Clelland et al. (2014) a temperature-step method is reported for measurement of the sample activation energy. In theory this method removes the need for a series of separate mass gain measurements at different temperatures, each following heating at 500°C, by instead changing the aging temperature at set time intervals during a single mass gain measurement, keeping %RH constant, *Figure 2.63*. This also avoids repeated waiting for *Stage 1* to reach completion, with it occurring only once in this approach. Activation energy results for a range of material, estimated using this approach, are presented and compared with activation energies estimated from separate experiments. Reasonable agreement is found, with activation energies ranging from 50-120kJ/mol. Interestingly, multiple subsamples of a single sample (W1,2,5) produced significant variation (82.7, 68.2, 63.2kJ/mol) emphasising the effect of inhomogeneity in the sample.

There are some points worth nothing with regard to the mass gain curve presented and how well it agrees with the theoretical curves. There appear 'blips' at the points at which a transition to a new temperature occurs. These are related by Clelland et al. (2014) to transient increases in the %RH of 8.8% and 7.3% while the microbalance chamber stabilises to new temperatures. However, should this not result in 'over-wetting' effects due to an increase in physisorption of *T0* water that

the same research group argue for being the cause of positive curvature in Wilson et al. (2014)?

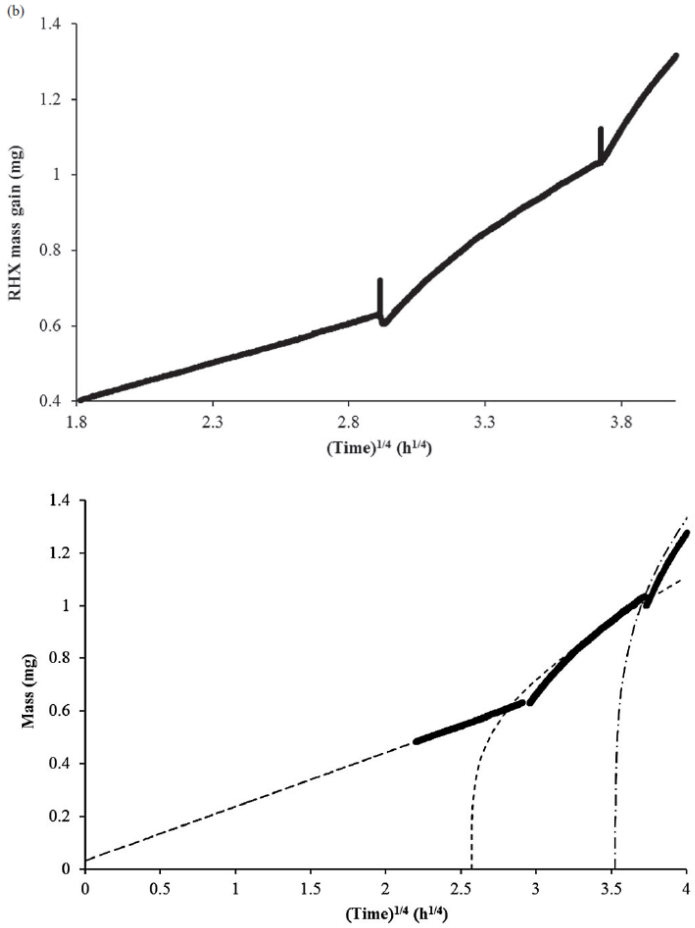

Figure 2.63: Top: Mass gain of sample at 9.5, 24.8 and 38.4°C used in temperature step method for activation energy calculation (from Clelland et al. (2014, Figure 2). Bottom: For same sample, a comparison between the experimental and theoretical data (from Clelland et al. (2014, Figure 4).

During the transition to new temperatures, Clelland et al. (2014) argue that the level of physisorption does not vary because the %RH is kept constant, yet this conflicts slightly with the assertions by the same group in Wilson et al. (2014) that the *T0* water adsorption is heavily influenced by temperature with "the capacity for *T0* adsorption is, however, reduced at higher temperatures" (perhaps they do not clarify well enough if the other variable %RH is allowed to vary in relation to this). Indeed, examination of the data, *Figure 2.63*, suggests that after the transition to a new temperature the mass may have actually decreased.

A difference between the experimental and theoretical curves, *Figure 2.63*, at early periods following the change in temperature, is apparent with the measured values of mass slightly less than the predicted values. This is explained as the result of "thermal lag as the sample equilibrates with the new chamber temperature". However, this does not make sense for three reasons: 1) if the sample is gaining mass at a lower temperature than expected in theory then the gradient of the curve immediately following the transition to the new temperature should be less in the experimental data than the theoretical prediction, but this is not the case; 2) the theoretical line should agree/cross the final data point at 9.5°C, regardless of any transition effect, yet his is not observed; 3) any thermal lag will result in a time offset effect (Barrett 2013) which in this case would appear not as a difference between the experimental and theoretical data in the early stages but instead as a deviation in the central portion of the period at 24.9°C with the experimental data lower and less curved.

These points raise some questions that need addressing in relation to the temperature step approach. Nonetheless, Clelland et al. (2014) obtained a good Arrhenius plot and reasonable activation energies supporting its application and possible future merit in speeding up activation energy estimations.

The publication of Le Goff and Gallet (2014b) looks at dating trials carried out on Syrian medieval ceramic fragments as well as re-examining previous data sets obtained by Wilson et al. (2009, 2012, 2014). The dating results highlighted issues with variability in two samples from a single sherd and multiple sherds from an identical context, with varied ages produced that are generally far too young, *Figure 2.64*. They also demonstrate a further issue in how the ages vary depending on the period of the mass gain curves over which the mass gain rate is estimated. An issue with their date estimates may be the result of not using a component-based approach which will be dealt with in detail in *Chapter 9*. Also the apparent stabilisation of the ages toward the end of some of the measurements may be the result of estimation of the mass gain rate over shorter duration during which the curvature is approximately linear with changes masked by statistical fluctuations in the data.

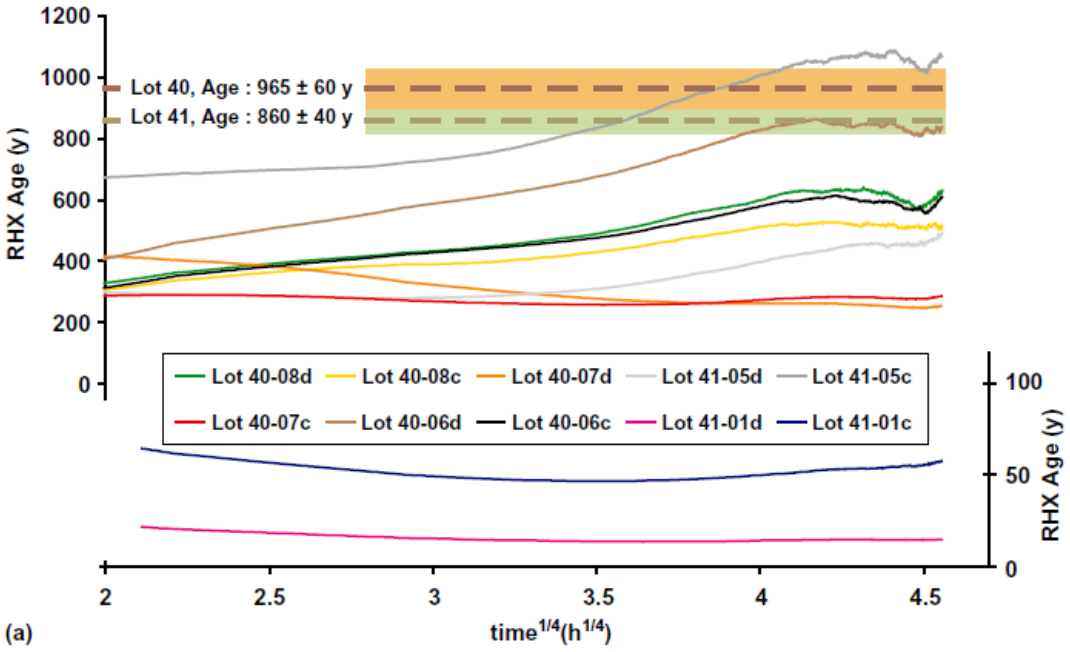

Figure 2.64: Variation in estimated ages of Syrian medieval ceramics from two context of known age (dashed lines) with period over which mass gain rates were estimated over (computed using intervals that decreased progressively up to the end of the experiments.) Taken from Le Goff and Gallet (2014b).

As in previous work (Le Goff and Gallet 2014a) they find that following heating at 105°C stabilising of the mass does not occur, as suggested by Wilson et al. (2009; 2012), with, instead, prolonged mass gain as a function of $t^{1/n}$, with n close to 4. They also provide sound arguments for why the curvature observed as a function of $t^{1/4}$ is indeed real and not the cause of measurement related RH conditions (Wilson et al. 2014) or time-offset effects (Barrett 2013). If the behaviour is not $t^{1/4}$ this adds additional reasons for their dates not working out.

Also, in a revaluation of data from Wilson et al. (2009; 2012), Le Goff and Gallet (2014b) demonstrate that stabilisation of mass following heating at 105°C did not occur, as Wilson et al. (2012) affirmed, and that mass gain rates used in Wilson et al. (2009) were highly selective. Both these results cast additional and serious doubts, on top of those already made in this chapter, on the validity of RHX dating trials carried out by the group of Wilson et al. The work of Le Goff and Gallet (2014b) does not invalidate the potential of the technique but instead stresses complexities in the method that still need further attention.

The universality of the $t^{1/4}$ power law in describing *Stage 2* mass gain is seriously questioned again in an ensuing publication by Le Goff and Gallet (2015). They reanalyse long-term moisture expansion datasets previously used to verify the suitability of this model (Wilson et al. 2003; Hall et al. 2011).

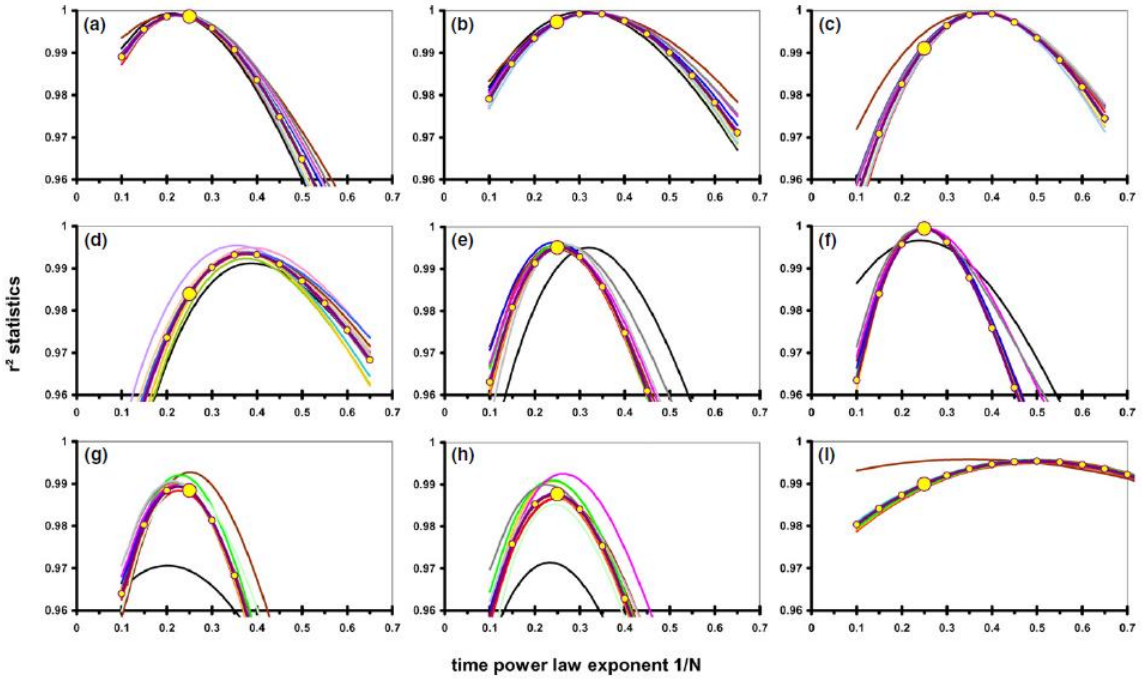

Figure 2.65: From Le Goff and Gallet (2015, Figure 1), the optimisation of the exponent *1/n* when the $t^{1/n}$ model is applied to nine expansion datasets used by Hall et al. (2011). Variations in r^2 are as a function of *1/n*. Large yellow dot corresponds to *1/n = 1/4*. For more details see original text.

The results present very strong evidence that the data sets obey a $t^{1/n}$ power law, but with the *1/n* value varying between 1/2 – 1/4, not strictly 1/4, for example *Figure 2.65*; this has considerable implication for the dating methodology and its validity as used by Wilson et al. (2009; 2012). The authors state that "the kinetics of moisture expansion (or of the mass-gain variations) in fired clay ceramics may naturally vary between a behaviour governed by a Brownian process ($t^{1/2}$ power law) and a behaviour controlled by a one-dimensional diffusion process ($t^{1/4}$ power law)."

Aside from issues with the kinetic equations governing mass gain behaviour, there is also the matter of determining the RHX mass gain without influence from the mass of contaminants that are also burnt off in the heating process. Wilson et al. (2012)

comment on the possible presence of organic contaminants and carry out a single measurement of the carbon content without any corrections for the organic/matter to organic carbon ratio but otherwise it is given little mention (Hamilton and Hall 2012). With Numrich et al. (2015, in press) the issue of the effect of organic carbon on rehydroxylation dating is given special attention. These non-refractory compounds are found in environmental contamination, and will be removed at temperatures between 200-500°C, *Section 2.3*, leading to a poor determination of the RHX mass. Numrich et al. (2015) carried out the general dating methodology of Wilson et al. (2012) on two samples of an archaeological brick (medieval) as well as elemental analysis of the carbon content present for a wider range of samples. Because it was only possible to age the samples at laboratory temperatures (22.9 ± 0.5°C) the age calculations were calculated using an effective lifetime temperature off 10°C and an activation energy 83kJ/mol, taken as a rough estimate based on typical literature values (Wilson et al. 2012; Hall et al. 2013). The resulting age estimates were thousands of years too old (estimated at 22,200 and 62,400 years). Carbon content analysis showed that the mass of organic material (using an OM/OC ratio of 2 based on the assumption of humic acids being the most likely contaminant) in the brick was of a significant level (0.55% or 0.41%) and removing this from the RHX mass reduced the ages of the samples considerably (2,865/14,734 years using 0.55% or 5,367/22,411 years using 0.41%). The authors stress that there are numerous uncertainties that could be reflected in these erroneously large dates, including unknown activation energy or ELT, as well as the CO_2 providing only a rough estimate of the organic carbon mass. Along with this, the current author would highlight that the OM/OC ratio may also deviate from a value of 2, see *Section 2.6*.

The carbon content was also measured and notable for Iron Age samples from Megiddo and a piece of Werra earthenware that featured in Wilson et al. (2012). Interestingly, the authors corrected the data from Wilson et al. (2012, who did not carry out any carbon content analysis on this sample) and demonstrate that the

estimated age shifts (from AD1577-1624 to AD 1767-1784) outside of agreement with the assigned age of AD 1605.[21]

To investigate the potential removal of organic carbon before RHX tests, Numrich et al. (2015) tested several wet chemistry pre-treatments (acid/base leaching, wet oxidation) and measured the carbon content afterwards. All approaches reduced the carbon content, with the oxidation (H_2O_2) treatments providing very positive results. However, no treatment was successful in removing all carbon contaminants for all samples and this is a reason why the authors recommend pre-treatment cleaning of RHX samples before mass gain tests with samples that still display large carbon content following this treatment being discarded. The authors also highlight that the effects of these treatments on the mineralogy or morphology of the ceramic is not clear and potentially could affect the hydroxyl content adversely, an area that would need more research.

This work of Numrich et al. (2015) is significant in highlighting the need for the presence of contaminants to be examined for all samples prior to RHX dating and for providing a set of potential pre-treatment approaches that could be used to remove organic carbon contamination, provided the (re)hydroxyls that have been gained over the samples lifetime and the mass gain behaviour are not affected by these treatments.

This concludes a chronological account and critical review of RHX dating related work up to the present. Beginning with the first work to recognise the potential application of a long term expansion/mass gain in fired clay bricks to archaeological dating (Wilson et al. 2003), it describes research that provided early evidence for a two stage expansion/mass gain process in freshly fired and reheated clay ceramics (Savage et al. 2008a; 2008b) that is described in the second stage by a $t^{1/4}$ power law model over shorter (Savage et al. 2008a; 2008b) and longer (Wilson et al. 2009; Hall et al. 2011) periods. The kinetics were shown to be dependent on the environmental temperature (Wilson et al. 2003; Wilson et al. 2009; Clelland et al.

[21] This, along with the issue of not using an organic matter/organic carbon ratio to correct the Anglo-Saxon loomweight casts serious doubt on 4/5 successfully dated samples by Wilson et al. (2012) with the remaining samian-ware sample also questionable given that no carbon content was recorded.

2014) with environmental moisture (RH) having a negligible effect (Wilson et al. 2003; Hall and Hoff 2012; Drelich et al. 2013). It was shown with varying degrees of success, that the as-fired mass gain/expansion can be reproduced upon reheating at suitable temperatures (Savage et al. 2008b; Wilson et al. 2009; Tosheva et al. 2010), with the effects of firing temperature and sintering time playing an important role in the original and reheated mass gain/expansion kinetics also demonstrated (Mesbah et al. 2010a; 2010b; Tosheva et al. 2010).

The underlying mechanism was attributed to rehydroxylation of amorphous phases within the fired clay (Wilson et al. 2009; Tosheva et al. 2010; Clegg et al. 2012), the slow kinetics associated with diffusion along low dimensional channels within the ceramic fabric (Wilson et al. 2003; 2009). These mechanisms were examined in detail using a range of instrumental techniques (Clegg et al. 2012) which, along with providing support for rehydroxylation taking place, highlighted the complexity and difficulties involved in completely understanding the process. The effect of sample size and the need for homogeneity in the use of multiple samples was also demonstrated (Bowen et al. 2013; Le Goff and Gallet 2014a; 2014b).

The effects of temperature on the RHX method is critical and this has been examined from a more theoretical perspective (Barrett 2011; Hall et al. 2013) with the possible adverse effects of accelerated mass gain during cooling highlighted (Barrett 2013). Also critical are the possible issues due to removal of contaminants other than (re)hydroxyls during heating; the effect of organic carbon was examined by Numrich et al. (2015) with methods for its minimisation/removal suggested.

The application of RHX dating to archaeological fabrics has also carried out by a number of groups (Wilson et al. 2009; 2012; Bowen et al. 2011; Burakov and Nachasova 2013; Le Goff and Gallet 2014a; 2014b), with varied levels of success and only Wilson et al. (2009; 2012) obtaining accurate results on a combined set of 15 samples. However, serious issues have been highlighted in the work of Wilson et al. (Le Goff and Gallet 2014a; 2014b). The suitability of a $t^{1/4}$ model, instead of a more general $t^{1/n}$ model, has also been questioned (Bowen et al. 2011; 2013; Le Goff and Gallet 2014a; 2014b) and re-evaluation of long term moisture expansion data used

to validate the $t^{1/4}$ approach (Wilson et al. 2003; Hall et al. 2011) has revealed that a more generalised $t^{1/n}$ may provide more appropriate modelling (Le Goff and Gallet 2015).

Hence, there still remain many areas of contention and aspects of the fractional mass gain and expansion of fired clay ceramics, together with its application to dating archaeological ceramics that need to be explored, validated or developed further.

A qualitative summary (based on the current author's interpretation of the existing literature) of the level of evidence and support for key properties of the mass gain in fired clay ceramics is provided in *Table 2.6* with a summary of the materials and conditions of gravimetric studies presented in *Table 2.7*.

Table 2.6: Summary of the evidence given in work-to-date to support the core requirements of the RHX dating technique. Up/down arrow: positive/negative support for requirement, based on current author's opinion. Single arrow = weak support; double arrow = moderate support; triple arrow = strong support. Question mark = unclear. Where both up and down arrows are given this suggests that the support depends on how the work is interpreted.

	Second stage $t^{1/4}$		$t^{1/4}$ Long Term		Temperature; Arrhenius Behaviour	
	Fired	Re-heated	Fired	Re-heated	Fired	Re-heated
Wilson et al. (2003)	↑		↑	↑	??	
Savage et al. (2008a)	↑↑					
Savage et al. (2008b)	↑↑	↑↑				
Wilson et al. (2009)	↑↑	↑↑↑	↑↑		↑	↑↑↑
Mesbah et al. (2010a)	↑↑↑					
Mesbah et al. (2010b)	↑↑↑					
Tosheva et al. (2010)	↑↑↑	↑↑				
Barrett (2011)						
Hall et al. (2011)	↑↑↑		↑↑↑			
Bowen et al. (2011)		↓↓				↑
Clegg et al. (2012)		↑				
Hall and Hoff (2012)	↑↑↑		↑↑↑		↑↑	
Wilson et al. (2012)	↑↑	↑↑↑	↑↑			↑
Barrett (2013)		↑↑		↑		↑↑↑
Bowen et al. (2013)		↓↓		↓		
Burakov & Nachasova (2013)		↑	↑			
Drelich et al. (2013)		↓		↓		
Shoval & Paz (2013)			↑			
Le Goff & Gallet (2014a)		↑↑↓↓		↑		
Wilson et al. (2014)		↑				
Clelland et al. (2014)		↑				↑↑
Le Goff & Gallet (2014b)		↑↑↓↓↓				
Le Goff & Gallet (2015)	↓↓↓	↓↓	↓↓↓	↓↓		
Numrich et al. (2015)						

	Humidity insensitive (S2)		Reheated =Freshly fired	Rehydrox. Mass Gain Determinable
	Fired	Re-heated		
Wilson et al. (2003)	↑		↑	??
Savage et al. (2008a)				
Savage et al. (2008b)			↑↑	
Wilson et al. (2009)			↑↑	↑↑
Mesbah et al. (2010a)				
Mesbah et al. (2010b)				
Tosheva et al. (2010)			↑↑↑	
Barrett (2011)				
Hall et al. (2011)				
Bowen et al. (2011)		↓		↑
Clegg et al. (2012)				
Hall and Hoff (2012)	↑↑↑			
Wilson et al. (2012)	↑↑		↑↑	↑↑

Barrett (2013)				
Bowen et al. (2013)				
Burakov & Nachasova (2013)			↑	↑
Drelich et al. (2013)		↑↑		
Shoval & Paz (2013)				↑
Le Goff & Gallet (2014a)		↑↑		
Wilson et al. (2014)		↓		
Clelland et al. (2014)				
Le Goff & Gallet (2014b)				
Le Goff & Gallet (2015)				
Numrich et al. (2015)				↓

Table 2.7: Summary of material that has undergone gravimetric (microbalance or top-loading balance) fractional mass gain following firing (fresh) or reheating as well as notable experimental details and conditions.

Material	Reference	Fired (F) Reheated (R)	Firing/Reheating Temperature-Heating Rate-Dwell Time	Sample Size	Aging Conditions	First stage duration	Total test duration
Brick – Chester Red (carbonaceous shale and Etruria marl mixture)	Savage et al. (2008a)	F	1040°C (heated over 35 hours) – held for 4 hours	Brick – 2.3 Kg	22°C, 50%RH	< 2.5 hours	3 weeks
	Savage et al. (2008b)	R	500°C (preheated) – 7 hours	Bulk – 210mm ×240mm×10mm	22°C, 50%RH	< 4 hours	2 - 3 weeks
				1.18-2.36mm (500-700g)			
				0.6-1.18mm (500-700g)		?	
				0.150-0.300, (500-700g)		?	
	Wilson et al. (2009)	R	500°C for 4 hours	Brick	22°C, 50%RH	?	15 days
Brick – mixture of carbonaceous shale and Little Flint fireclay.	Savage et al. (2008b)	F	Fired to 1035°C over 39 hour period (35hrs heating, 4 hrs dwell time).	Brick – 2.3Kg	22°C, 50%RH	< 4 hours	2 weeks
		R	500°C - 10°C/hour – 16hours	Bulk – 80mm×60mm×15mm			8 weeks
		R	500°C (preheated) – 16hours	Bulk – 80mm×60mm×15mm			
Roman Paving Brick (AD 50-160)	Wilson et al. (2009	R	500°C for 4 hours	3-5g	11°C, 14°C, 30°C. 50°C. 30%RH	?	2-4 days
Westminster Clay Tile (AD 1250-1300)							
Clay Brick (King Charles II Building, AD 1664-1669)							
Clay Tile (St. Bride's, AD 1350-1390)					25°C, 35%RH	< 7 hours	9.1 days
Clay Brick (Whitefriars priory, AD 1942 heated)					11°C, 30%RH	?	2-4 days
Kaolinite	Mesbah et al. (2010a)	F	1200°C, 10°C/min, for 2,4,6,8,12 hours	2g pressed powder	30°C, 55%RH	< 5 hours	< 2 days
	Mesbah et al. (2010b)	F	700-1200°C, 10°C/min, for 4 hours	4.5g pressed powder		< 5 hours	

Terracotta	Tosheva et al. (2010)	F	800-1200°C, 10°C/min, for 12 hours	2.5g	30°C, 60%RH	< 5 hours	2-4 days
		R	500°C, (and some to 1000°C), 10°C/min, for 4 hours				
Davenport Pottery (Utah, 19th century)	Bowen et al. (2011)	R	500°C/650°C for 4/12 hours, respectively	32 – 96g	-2 to +3°C, 20-24°C (20-28%RH), 80°C,	?	2-10 weeks
Anglo-Saxon loomweight, AD 560-660 Samian-ware pottery, AD45-75 Werra-ware pottery, AD1605	Wilson et al. (2012)	R	500°C, not specified	0.1-2.5g granules	8-11°C and 30%RH Higher Temps for E_a calculation not stated	13-92 hrs	35-140 hours approx.
Chester Red Modern Brick (9 pieces)	Barrett (2013)	R	500°C, 5°C/min, held for 74 hrs.	Bulk cubes of 30-40g	20,30,40°C at 75%RH	<22 hrs	24 days
Davenport Pottery 19th Century	Bowen et al. (2013)	R	500°C for 4-5 hrs	Five sherds 1-2g Powdered sherds <100µm	22°C and 18-20%RH	5-20hrs (according to Bowen et al. but possibly much longer, i.e. 100-1000hrs	40 days
4 samples from Malage, Castillo de Gibralfaro, 8th century AD Granada, Alhambra, brick, 16-17th century AD Roman Paving brick, London, AD 75 Pantikapaion clay daub, AD 190 Germonossa ceramics, AD 860 Granada, Cartuja, brick, AD 100 Granada, Cartuja, ceramics, AD 90 Greenwich	Burakov and Nachasova (2013)	R	500°C for 4 hrs	1-15g	25°C and 60-72%RH	7 days	3 months (approx.)

brick, ---							
Davenport Pottery Modern Houghton Brick	Drelich et al. (2013)	R	500°C for 4-5 hrs	1.4-2.8g	22°C and 20%RH – 28%RH step (Houghton) 22°C and 20-40-20%RH step (Davenport) Complex cycle of aging, drying, soaking (Houghton)	40-120 days	
Bois d'Espense ceramics, AD 1785-1815 Ancy-le-Franc ceramics, AD1797-1807 Ecouen castle, pavement brick, AD1549-1551 Hospices de Beaune, brick, AD1448-1452 Roman samian ware, 2nd century AD	Le Goff & Gallet (2014a)	R	105°C for 4/16 or 66/51 hrs 500°C for 72/68 hrs	2-3g	13°C and 32%RH (42%RH for some tests)	<1 hr for samian-ware approx. <24 hrs for other samples	7-16 days for 105°C 22-26 days for 500°C
Material from previous studies: Anglo-Saxon loomweight Samian-ware	Wilson et al. (2014)	R	500°C	160mg – 4g	11°C and 60/50 %RH, 50°C and 20%RH	End of *Stage 1* 1-4 hrs Start of *Stage 2* 4-187 hrs	Max of 13 days.
Scotland Street Brick	Clelland et al. (2014)	R	500°C to constant	<1g	9.5, 24,8, 38.4°C in sequence	10.5 hrs	10 days
Syrian Medieval Ceramic	Le Goff and Gallet (2014b)	R	500°C for 67 hours	2-3g	16°C and 31%RH	<24 hrs	21 days
Medieval Brick, Landesmuseum, AD 1000 2 samples from this brick	Numrich et al. (2015)	R	500°C for 72 hours	2-4g	23°C and 60%RH	Not clear, <24 hrs?	100 days

2.6 Contamination and the Organic Matter/Organic Carbon Ratio

Following firing, a ceramic will be exposed to a range of sources of contamination, both during its period of use and in its post-use buried context. A source of contamination can be defined as a substance that comes into temporary or permanent contact with the ceramic and results in a) alteration of the ceramics composition without any new material added or b) alteration of the ceramics composition with new material added.

During its period of use, sources of ceramic contamination for pottery can include residues associated with storage or cooking (Berstan et al. 2008; Evershed 2008) and soot deposits resulting from cooking (Nakamura et al. 2001; Rice 1987, p. 235), as well as contamination from general handling and environmental conditions.

For brick, if structural or ornamental, the period of use could be considered as that for which the building is still standing; in this case the sources of contamination can include rainwater, wind-borne particles (aerosols), biological growths (algae/fungae), and lime leeching. Rainwater can cause dissolution of salts (i.e. calcium/magnesium sulphate, sodium chloride) along the pores in the brick, with the solution potentially removed to the surface during subsequent drying. Re-crystallisation of the salts can then occur at the surface or elsewhere within the brick; dissolution/re-crystallisation of salts is a process that features strongly in weathering of brick or stone (Goudie et al. 1997; Warke and Smith 2000; Pavía and Bolton 2000; Smith et al. 2008; Curran et al. 2010). Sulphuric acid in rainwater may also react with calcium in the brick to produce gypsum (Pavía and Bolton 2000; Curran et al. 2010). Lime ($Ca(OH)_2$) can leech onto bricks from the surrounding mortar and, if this reacts with carbon dioxide in the atmosphere, calcium carbonate may form on the brick (Pavía and Bolton 2000).

Sources of post-use (i.e. burial) contamination may include secondary calcite, transported and crystallised in the ceramic pores by groundwater solutions (Pavía and Bolton 2000; Quinn 2013). Soluble minerals in the ceramic such as calcite and gypsum can be dissolved by acidic groundwater and removed or deposited/re-crystallised elsewhere within the ceramic; this is particularly the case for carbonate

inclusions (calcite, limestone, and shell) that have decomposed to CaO during the original firing (Quinn 2013). Groundwater solutions could also carry nitrates or phosphates, from human burials or fertilisers (Pavía and Bolton 2000), as well as organic matter (i.e. humic acids) into the pores of the ceramic.

Contaminants of particular relevance with regard to RHX dating are those which when heated between 105-500°C result in a decrease in mass in the ceramic. With reference to *Section 2.2*, contaminants of note in this regard are gypsum, which dehydrates between 120-160°C and results in a loss of mass associated with water vapour removal, and organic matter, which can commence oxidation at temperatures above 200°C, resulting in a decrease in mass associated with carbon dioxide removal as well as the removal of other organic compound components such as hydrogen (i.e. as H_2O) and nitrogen (i.e. as NO_2).

The quantity of organic matter in the ceramics will be examined as part of this thesis, and will be based on quantitative analysis of the organic carbon present. Therefore, a correction factor is required to convert the mass of organic carbon present to the mass of organic matter present. This is known as the organic matter to organic carbon ratio, OM/OC. A brief survey of research focussed on estimation of this ratio for organic matter from a range of environments (aerosol-borne, soil, peats, clays) is presented in *Table 2.8*. This survey, while not comprehensive, demonstrates that the OM/OC ratio can vary considerably but for all studies falls within the range 1.0-3.0. Notable attention can be given to the work of Pribyl (2010) who in a review of 26 existing publications on the OM/OC ratio for soils conclude that "a consideration of the possible variation in organic matter composition predicts a range of factor values between 1.4 and 2.5". This range is not greatly at odds with the OM/OC ratios ranges from other environments listed in *Table 2.8*, and is treated by the current author as an adequate, if not ideal, reflection of the range of OM/OC ratios of organic matter contaminants in ceramics, aerosol-borne or burial-related.

Environment/Source	OM/OC typical value	OM/OC range
Aerosol		
Ruthenberg et al. 2014	1.69	1.4-2.15
El-Zanan et al. 2009	1.92	1.52-2.32
Phillips et al. 2014	1.5 (urban)	not clear
	2.0 (rural)	not clear
Turpin and Lim 2001	1.6 (urban)	1.4-1.8
	2.1 (non-urban)	1.9-2.3
Soil		
Pribyl 2010 (*Review*)	Soil	
Soil	2.0	1.4-2.5
Humin	-	1.49-1.61
Humic Acid	-	1.70-1.85
Fulvic Acid	-	1.96-2.44
Carbohydrate	-	2.22-2.5
Lipids	-	1.27-1.45
Amino Acids	-	1.54-3.0
Peats		
Klingenfuß et al. 2014		
Own Work	1.73-2.41 (dependent on peat type)	1.64-2.97
Review of existing work	-	1.55-2.31
Clays		
Worrall 1955		
Ball Clays	1.56	1.51-1.61
Fireclays	1.26	1.15-1.37

Table 2.8: A short survey of the organic matter to organic carbon ratios from publications focussed on different environments/sources of organic matter.

Chapter 3

Equations

3.1 Introduction

This chapter provides a description of the equations and theory that are drawn upon within later sections of this thesis, notably the mass gain behaviour equations and those used as part of the dating methodology adopted by the author. The previous chapter has described the background to these equations and discussed the assumptions involved in their use; hence, they will be presented below, together with the notation followed throughout the remainder of the thesis, without detailed discussion. Also, to avoid confusion, mass gain processes related to heating between 110-500°C are generally referred to as RHX-related, although this attribution will be discussed in more detail in *Chapter 9*.

3.2 Mass Gain Behaviour

Following firing of a clay to a hard ceramic, or subsequent reheating above 500°C, the ceramic gains mass in two distinct stages (Savage et al. 2008a), *Stage 1* (*S1*) and *Stage 2* (*S2*), *Figure 3.1*. The *S1* mass gain can be attributed to a combination of non-rehydroxylation related processes of uptake of water (physisorption and possible chemisorption - see *Chapter 2* discussion of *S1* behaviour) together with rehydroxylation processes, whereas *S2* is attributed to rehydroxylation processes alone (Wilson et al. 2009). The rate of rehydroxylation-driven (fractional) mass gain, *y(t)*, in *S2* is described by a $time^{1/4}$ power law (Wilson et al. 2003), and governed by the following equation (Wilson et al. 2009):

$$y(t) = \frac{m(t) - m_0}{m_0} = a(T)t^{1/4} \quad (1)$$

with *m(t)* the sample mass, m_0 the intercept mass of the *S2* mass gain, *a* the rehydroxylation mass gain rate (fractional, *T* = temperature dependent), and *t* the elapsed time since firing/reheating, see *Figure 3.1*. It is this equation that is critical in estimating the age of the ceramic as part of RHX dating.

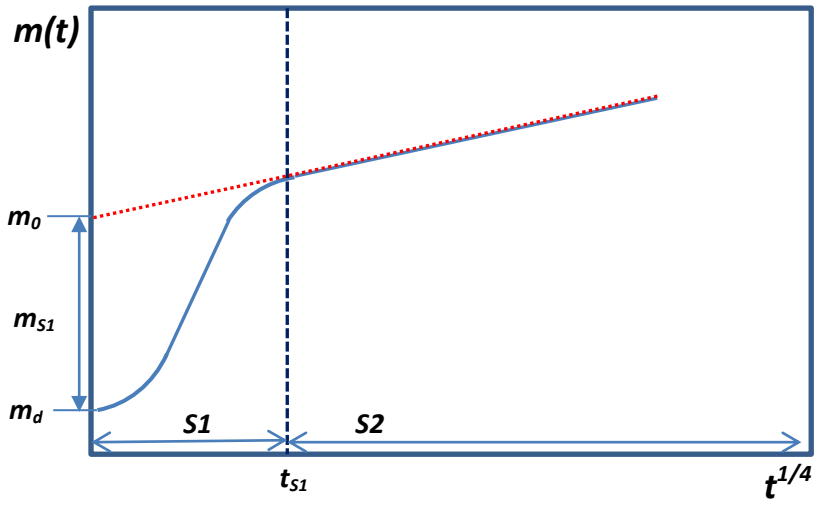

Figure 3.1: Mass gain behaviour and notation following firing/reheating of clay/ceramic.

For purposes of normalisation and comparison, fractional masses and fractional mass gain rates are generally used; for a variable *X,* the fractional form is $X=(X/m_0)$ with normalisation carried out relative to m_0, the *S2* intercept mass of the 500°C mass gain curve, generally.

The *S1* behaviour is mainly described by the following variables: m_{S1}, the (fractional) mass gained during *S1*, and t_{S1}, the duration of S1 (*Figure 3.1*). For m_{S1} the mass gain is estimated using:

$$m_{S1} = m_0 - m_d \qquad (2)$$

[$m_{S1} = (m_0 - m_d)/m_0$, fractional case]

where m_d, is the dry mass of the ceramic (i.e. the ceramic mass less any adsorbed, absorbed or RHX water). For calculations and comparisons this is expressed normalised relative to m_0, unless stated otherwise.

3.3 Temperature Dependence

The rehydroxylation rate, *a*, has been demonstrated to follow an Arrhenius temperature dependence (Wilson et al. 2009). This, together with the magnitude of estimated activation energies, suggests a process that is chemically determined with a rate described by the following equation (Hall and Hoff 2012; Hall et al. 2013):

$$a(T) = Ae^{-\frac{E_a}{4RT}} \tag{3}$$

where *A* is a pre-exponential factor, E_a, is the activation energy, *R* is the gas constant, and *T* is the temperature of the ceramic. The pre-exponential factor, as well as the activation energy, will be material dependent.

If the mass gain rate, *a*, can be estimated for a range of temperatures, then the activation energy can be calculated using the following expression:

$$\ln\left(\frac{a}{a_0}\right) = -\frac{E_a}{4RT} + \frac{E_a}{4RT_0} \tag{4}$$

where a_0 is a rehydroxylation reference rate at some reference temperature T_0. Plotting the natural log of the normalized mass gain rate (normalised relative to the reference rate) as a function of the inverse temperature and then carrying out a linear regression, permits the activation energy to be calculated from the slope. This plot is referred to as an Arrhenius plot in this document. Once the activation energy is known, the mass gain rate at any temperature can be estimated by rearranging (4) to give:

$$a(T) = a_0 \exp\left[-\frac{E_a}{4RT} + C\right] \tag{5}$$

where $C = E_a/4RT_0$. Note that *C* is the intercept of the Arrhenius plot and this is what is used in *Equation 5* for calculations later in this document.

3.4 $t^{1/n}$ - Model

The use of a $t^{1/4}$ model and, more specifically, the adherence of the power to 1/4 has been questioned in other work (Bowen et al. 2011; 2013), where instead a relaxation on the constraint of the power is suggested. Instead, a *S2* behaviour better described by a $t^{1/n}$ model is suggested. In this work, this model is also tested, requiring very basic modification of *Equation 1* and *Equations 3* (with adjustment to equations deriving from these also) required:

$$y(t) = \frac{m(t) - m_0}{m_0} = a(T)t^{1/n} \quad (6)$$

$$a(T) = Ae^{-\frac{E_a}{nRT}} \quad (7)$$

$$\ln\left(\frac{a}{a_0}\right) = -\frac{E_a}{nRT} + \frac{E_a}{nRT_0} \quad (8)$$

Where *1/n* > 1/4, the *Stage 2* mass gain behaviour will display a 'positive' (upward concave) curvature if plotted as a function of $t^{1/4}$. Where *1/n* < 1/4, the *Stage 2* mass gain behaviour will display a 'negative' (downward convex) curvature if plotted as a function of $t^{1/4}$.

3.5 Age Equation

If the rehydroxylation-related mass gained, m_{RHX}, over the lifetime of the ceramic (or since last heated above 500°C), can be estimated (*Section 3.6*), together with the mass gain rate at a suitable effective lifetime temperature (ELT) (*Section 3.7*), then rearrangement of *Equation (1)* allows the age, *t*, of the ceramic to be calculated:

$$t = \left(\frac{m_{RHX}}{a(T_{elt})}\right)^4 \quad [4 \rightarrow n \text{ for } t^{1/n} \text{ model}] \quad (9)$$

3.6 Dating Approach and Components

General Approach

The following is an outline of the general dating approach suggested and applied (in a variant form) by Wilson et al. (2009; 2012), with *Figure 3.2* a visual guide. To be in a position to estimate the age of a ceramic the quantity, m_{RHX} and $a(T_{elt})$ are the key variables to be obtained.

1. The ceramic is dried to constant mass at 105-115°C, removing any capillary/pore moisture.
2. Then the sample is placed in an environmentally controlled (RH and temperature) chamber where it is weighed until it has equilibrated (adsorbed moisture) to a constant mass, m_f , the 'final' mass. The environmental conditions must be the same as those which the ceramic will be weighed under following reheating at 500°C such that the adsorbed moisture is the same in both. [The temperature can be set to the ELT, which removes the need for the use of any activation energy calculations OR the experiment can be run at a number of different temperatures to allow an activation energy and mass gain rate at any temperature to be determined.]
3. The sample is then heated to 500°C for several hours to dehydroxylated the sample and return it to its as-fired state.
4. The sample is then aged in the environmental conditions (ELT ideally) mentioned above, while being periodically weighed as it gains mass (rehydroxylates) for a sufficient duration of *Stage 2*.
5. A linear regression is carried out on the *Stage 2* mass gain, as a function of $t^{1/4}$, from which the mass gain rate at the ELT, a_{elt}, and the intercept mass, m_0, the 'initial' mass, are obtained.
6. The mass attributable to RHX-related processes can then be calculated from as $m_{RHX}=m_f - m_i$. Together with a_{elt}, the age of the ceramic can then be estimated using *Equation 9*.

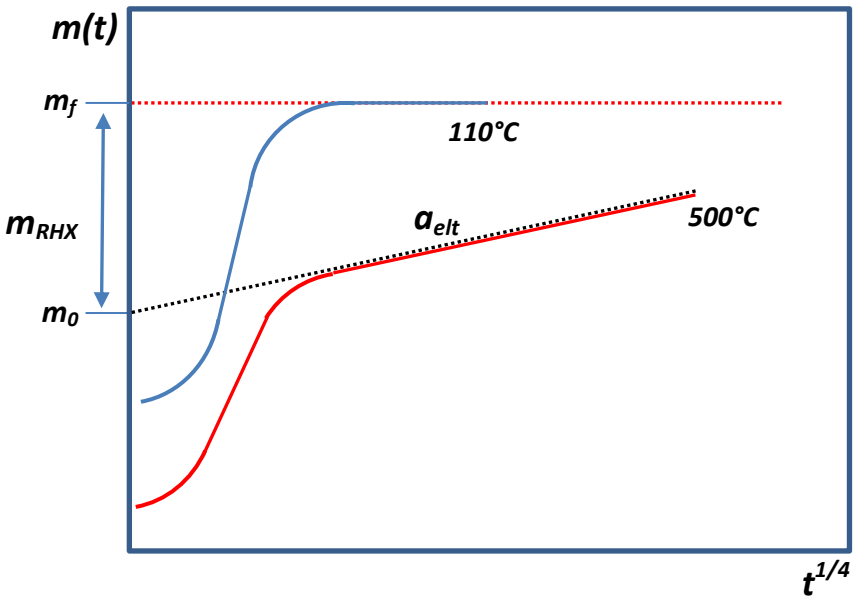

Figure 3.2: Illustration of the general dating approach; mass gain and equilibration following drying to constant mass at 110°C (blue); rehydroxylation related mass gain following heating at 500°C (red).

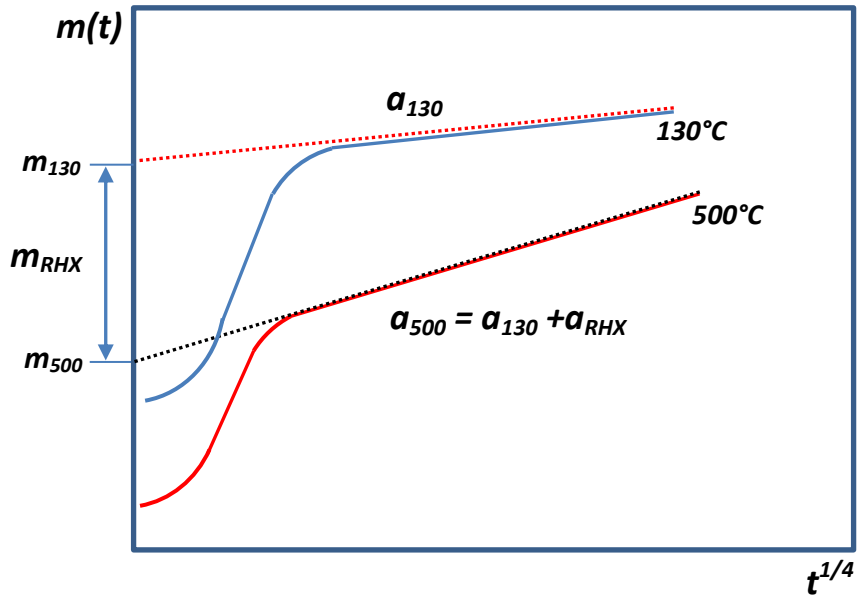

Figure 3.3: Illustration of the component-based dating approach; mass gain following drying to constant mass at 130°C (blue); mass gain following heating at 500°C (red). The *Stage 2* linear mass gain following heating at 500° is the sum of two components, the mass gain due to processes related to heating to 130°C and the processes related to heating between 130-500°C (RHX-attributed processes).

Component Based Approach

In the course of experiments it was found that during equilibration following the initial drying (see *Method* and *Discussion* for issues surrounding this) stage (at 130°C), samples were exhibiting a behaviour that was characteristically similar to that following heating at 500°C, i.e. two main stages of mass gain, with the latter appearing to closely follow a $t^{1/4}$ power law, albeit with a lower gradient than that observed for 500°C, (see *Figure 3.3* for illustration of behaviours observed and relevant variables; actual curves are presented in *Chapter 7*). This unexpected behaviour following low temperature heating prompted a revised dating approach to that described above and is based on the following observations and assumptions (the behaviour and approach will be discussed at length in *Chapter 9*):

1. Heating at low temperatures (110-130°C) followed by aging/equilibrating at moderately high %relative humidity (75%) results in a two-stage mass gain behaviour, with *S2* following a $t^{1/4}$ (or $t^{1/n}$) equation.
2. The mass gain rate for this low temperature 130°C component, referred to from now on as 130C, follows an Arrhenius temperature dependence with activation energies not dissimilar to those associated with de/rehydroxylation (see *Chapter 7*).
3. The mass gain curve following heating at 500°C (500C component henceforth) is assumed to be the sum of a 130C component and an RHX component, the former due to processes related to uptake of moisture following moisture removal during heating at 130°C, the latter due to processes related to rehydroxylation following dehydroxylation between 130°C and 500°. (The similarity in behaviour suggests that there may be shared processes across both temperature regimes, however for the present those between 130°C and 500° are treated as RHX, and those below 130°C are referred to otherwise).
4. The RHX mass gain rate (rate due to moisture removal between 130-500°C), α_{RHX}, can be obtained by a simple subtraction of the 130C mass gain rate, α_{130}, from the 500C mass gain rate, α_{500}. This assumes the 130C component follows the same $t^{1/4}$ or $t^{1/n}$ behaviour as the 500C component.

5. Similarly, the RHX mass (mass of moisture removed between 130-500°C), m_{RHX}, can be obtained by subtracting the 130C intercept, m_{130}, from the 500C intercept, m_{500}. This mass is interpreted as the mass gained during the lifetime of the ceramic by mass gain rates associated with processes associated with heating at > 130°C.

With these assumptions (the validity of which will be discussed later in *Chapter 9*) a modified dating approach was developed that was not dependent on a full understanding of the mechanism involved in the behaviour observed; the particular chemisorption/physisorption/rehydroxylation mechanisms involved, was not critical as long as the process itself was long term and that a component of mass (gained over the lifetime of the ceramic) could be calculated and assigned to an associated long term component of mass gain rate which would then permit an estimated age to be calculated.

Based on the above assumptions, the following approach was taken to dating the ceramic:

1. The sample is dried to constant mass at 130°C.
2. The mass gain curve of 130C is recorded during aging at a particular temperature (ELT ideally) and %RH.
3. From a linear regression on *S2* of this curve, the intercept, m_{130}, and the mass gain rate, a_{130}, are obtained.
4. The sample is fired at 500°C.
5. The mass gain curve of 130C is recorded during aging at a particular temperature (ELT ideally) and %RH.
6. From a linear regression on *S2* of this curve, the intercept, m_{500}, and the mass gain rate, a_{500}, are obtained.
7. The difference in behaviour of 130C and 500C is attributed to RHX processes. Therefore, the RHX mass gain rate, a_{RHX}, is obtained by subtracting the rates, i.e. $a_{RHX} = a_{500} - a_{130}$, considered valid where both curves present linear *S2* behaviour as a function of $t^{1/4}$. Similarly the RHX

mass, m_{RHX}, is treated as the difference between the intercepts of $t^{1/4}$ regressions carried out on *S2* of both curves.

8. Provided the mass gain curves were obtained at the ELT the age of the ceramic can be estimated using *Equation 9*.

The following equations are followed:

$$a_{RHX} = a_{500} - a_{130} \quad (10)$$

$$m_{RHX} = m_{130} - m_{500} \quad (11)$$

with variables previously described.

Instead of acquiring mass gain curves at a single ELT temperature, it is considered more suitable to run three suitably prepared subsamples at different aging temperatures (25°C, 35°C, and 45°C) following 130°C heating and 500°C heating. The activation energies, E_{a130}, E_{a500}, and E_{aRHX}, can then be estimated permitting the sample age to be calculated for any lifetime temperature. Another benefit is that the RHX mass, m_{RHX}, can be estimated independently three times.

3.7 ELT – Effective Lifetime Temperature

The mass gain rate's temperature dependence is exponential. This non-linearity has significant implications when mass gain over a period of time during which there is temperature variation is involved; use of the mean temperature over the period is not accurate as the mass gain will be weighted more heavily towards periods of higher temperatures. These temperature effects have been examined in previous work (Barrett 2011; 2013; Hall et al. 2013).

A significant case where an alternative to the use of a mean temperature is required is encountered when dating the ceramic using *Equation 9*. A suitable mass gain rate, that accounts for the weighted nature of the temperature dependence over the lifetime of the ceramic is required, $a(T_{elt})$, where T_{elt} is the *Effective Lifetime Temperature* (ELT) (using terminology from Hall et al. 2013). Over a period of temperature variation, t_a, composed of n discrete time intervals t_1, t_2,…t_n, and

associated temperatures T_1, T_2,…T_n, the ELT is a unique temperature which, when substituted into *Equation 1*, provides a mass gain (via the mass gain rate a_{elt}) over the period t_a, $m(t_a)$, that is equivalent to the sum of the mass gained over the discrete time and temperature intervals:

$$a(T_{elt})t_a^{1/4} = m(t_a) = m(t_1)+m(t_2)+....+m(t_n) \quad (12)$$

Therefore, if the mass gain, $m(t_a)$, over a temperature profile (of period t_a, say) can be simulated, then the mass gain rate at the ELT, $a(T_{elt})$, can be easily estimated through rearrangement of *Equation 10*. The ELT itself can then be obtained using *Equation 5*.

3.8 Simulating Mass Gain

As discussed above, it is often necessary or desired to simulate the mass gain of a ceramic for a particular temperature history profile. In this thesis, a step change approach was utilised (see Hall et al. 2013 for further detail). This iterative approach calculates the total mass gain at each additional time increment along the temperature history profile of a sample, and is described below for a profile of three sequential temperature periods T_0, T_1, T_2, that are bound and separated by the times 0, t_1, t_2, t_3 (*Figure 3.4)*.

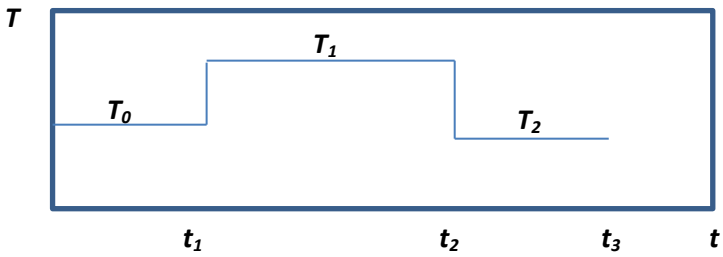

Figure 3.4: Temperature history with three periods of different temperature.

The steps in simulating the total mass gain, m_0, m_1, m_2, across this simple temperature history are as follows:

1. Calculate the mass gain rate at T_0:

$$a(T_0) = a_0 \exp[-\frac{E_a}{4RT_0} + C]$$

2. Calculate the mass gain across T_0:

   $m_0 = a(T_0)t_1^{1/4}$

3. Calculate the mass gain rate for temperature T_1, as above (step 1)
4. Calculate the effective time, t_1', at the start of T_1:

   $t_1' = (m_0/a(T_1))^4$

   This is the time it would take for mass gain m_0 to have occurred at temperature T_1.
5. Add the duration of T_1 to the effective time t_1' to obtain t_2'

   $t_2' = t_1' + (t_2 - t_1)$

6. Calculate that total mass gain at the end of T_1:

   $m_1 = a(T_1)(t_2')^{1/4}$

7. Repeat steps 3-6 to calculate the mass gain at the end of T_2.

This approach can be extended for any length of sequence.

3.9 Activation Energy Temperature History (AETH) Approach

An issue with calculation of the age of a sample that rely on knowledge of the effective lifetime temperature is that calculation of a suitable single ELT normally relies on a suitable estimation of the age of the ceramic to begin with. Beyond validation of the RHX method, the age of the sample will in general be unknown and providing a precise range of years for calculating a suitable ELT will be undesired. For this and other reasons listed below, the author proposes the use of an activation energy-temperature history driven approach (*AETH*) which works as follows.

1. Mass gain curves and associated variables are calculated for samples at a minimum of three different temperatures in order to estimate the RHX activation energy, E_{aRHX}, and provide multiple estimates of the lifetime RHX

mass gain, m_{RHX}. Ideally one of the three temperatures would be a standard temperature used by all RHX groups for comparison of sample behaviour. The activation energy estimation is critical as it is required for simulations of mass gain at any temperature in the temperature history record.

2. A temperature history record is constructed that spans all conceivable initial firing years for the sample, with upper and lower temperature history curves also constructed to allow for uncertainties.
3. The mass gain across the lifetime of the sample, m_{sim}, is simulated for an earliest possible firing year and repeated for later firing years at regular intervals; for a single firing year, m_{sim} is calculated by generating the mass gain as a function of the temperature history from the firing year to present. In this way an *AETH* curve, that presents the simulated lifetime mass gain as a function of firing year, can be generated. Upper and lower bound *AETH* curves can also be generated using the upper and lower temperature history curves (and accounting for other uncertainties, for example that of the activation energy).
4. An estimate of the age of the sample can then be carried out by examining where m_{RHX}, obtained experimentally finds agreement with m_{sim} on the *AETH* curve. Use of the uncertainty in m_{RHX} together with the upper and lower bound *AETH* curves will permit an age-range estimate for the sample.

The benefits of such an approach are as follows:

1. No prior knowledge (within reason) of the age of the ceramic is required. The ELT does not need to be estimated avoiding the requirement of a good estimate of the age of the ceramic to begin with.
2. By using a standard set of temperatures and always calculating an activation energy, inter-lab comparisons of behaviour are simpler and alternative temperature history driven approaches/models can be examined independently. (Use of standard temperatures does not require restriction to the above approach, but would not be the case where the age of the sample is estimated solely for ELT).

3. For an archaeological ceramic, the *AETH* approach offers no future constraint on the age of the sample. Updated knowledge of the temperature history can be used to instantly recalculate the age-range estimates without any need for further mass gain tests. If the age of the sample is calculated based on a mass gain curve generated for a single ELT, this flexibility is not present and samples may need to be re-run at different temperatures.
4. Running the sample at a minimum of three different temperatures, while more time-consuming, provides several measures of the RHX mass and confidence in the temperature dependent behaviour.

3.10 Cooling and Heating Equations

The cooling or heating profiles of samples were modelled using solutions of Newton's law of cooling or heating (Arpaci et al. 2000) of the form:

$$T(t) = T_0 \pm (T_i - T_0)e^{-bt} \quad (13)$$

where for a heating (-) or cooling (+) sample, $T(t)$ is the temperature as a function of time, T_0 is the temperature of the environment (final temperature the sample is cooling/heating towards), T_i is the initial temperature of the sample, and b is a constant that describes the rate of heating or cooling (referred to in text as the heating/cooling coefficient).

3.11 Drying Equations

Modelling of the drying of ceramics during heating at low temperatures (110-130°C) was carried out using two empirical equations that describe the mass, m, after a period, t:

Equation 1 (Power Law)

$$m(t) = a(t^{-b})+c \quad (14)$$

where *a* is the mass rate, *b* is the power of the model, and *c* is the final dry mass of the ceramic.

Equation 2 (Exponential)

$$m(t) = ae^{-bt} + c \tag{15}$$

where *a* and *b* (drying constant) are coefficients that determine the rate of moisture loss and *c* the final dry mass of the ceramic.

The former of these models was trialled based on the emphasis of the prevalence of $t^{1/2}$ transport processes in ceramic materials (Brosnan and Robinson 2003, p.69). However, it was found that the ½ power was a poor descriptor of the behaviour observed; hence the power constraint was relaxed.

The latter of these two models is derived from Lewis' (1921) thin-layer equation:

$$\frac{dX}{dt} = b(X - X_e) \tag{16}$$

where *X* is the moisture content, X_e is the equilibrium moisture content (i.e. 0 for an idealised dry ceramic) and *b* is the drying constant. Lewis (1921) considered that during drying of porous and hygroscopic materials, the rate of loss of moisture is proportional to the difference between the moisture content and the moisture content when the material is at equilibrium (dry) with the drying environment. This *thin-layer* equation assumes that the conditions of drying (humidity, temperature) are constant throughout the material during drying. Forms of this equation are often used in fundamental modelling of drying (see Pakoswki and Mujumbar (2006). According to Marinos-Kouris and Maroulis (2006, p.100):

"[Equation 14] constitutes an effort toward a unified description of the drying phenomena regardless of the controlling mechanism. The use of similar equations in the drying literature is ever increasing. It is claimed, for example, that they can be used to estimate the drying time as well as for the generalization of the drying curves.

The drying constant K [b above] is the most suitable quantity for purposes of design, optimization, and any situation in which a large number of iterative model

calculations are needed. This stems from the fact that the drying constant embodies all the transport properties into a simple exponential function, which is the solution of [Equation 14] under constant air conditions"

3.12 Temperature Sinusoidal model

To model annual temperature cycles, a sinusoidal-based model (Arnold 1960; Baskerville and Emin 1969) was used:

$$T(t) = T_{MAT} + \frac{1}{2}(T_{ATR})\sin(2\pi(\frac{t+b}{t_{year}}) \quad (17)$$

where T_{MAT} is the mean annual temperature, T_{ATR} is the annual temperature range, b is a time shift to synchronise with the start of the year, and t_{year} is the period of the year in the appropriate units. The temperature values can be modelled as part of the fitting procedure.

Chapter 4

Experimental Method – Non-RHX Characterisation

4.1 Introduction

A suite of non-RHX (mass gain) related experiments were carried out to examine the samples' structure (porosity, permeability, surface area), composition (mineralogical, elemental, organic), original firing temperature, and the effect of heating on these and other characteristics. The objective was not to provide a rigorously detailed charactisation of each sample using all of these methods; this was beyond the scope of this thesis and unnecessary. Instead, a general understanding of the nature of the samples that might shed light on any associated RHX mass gain behaviour was sought. A diagram of the methods applied and the various aspects they permitted investigation of is presented below in *Figure 4.1*. A full description of how these methods were applied is provided in subsequent sections.

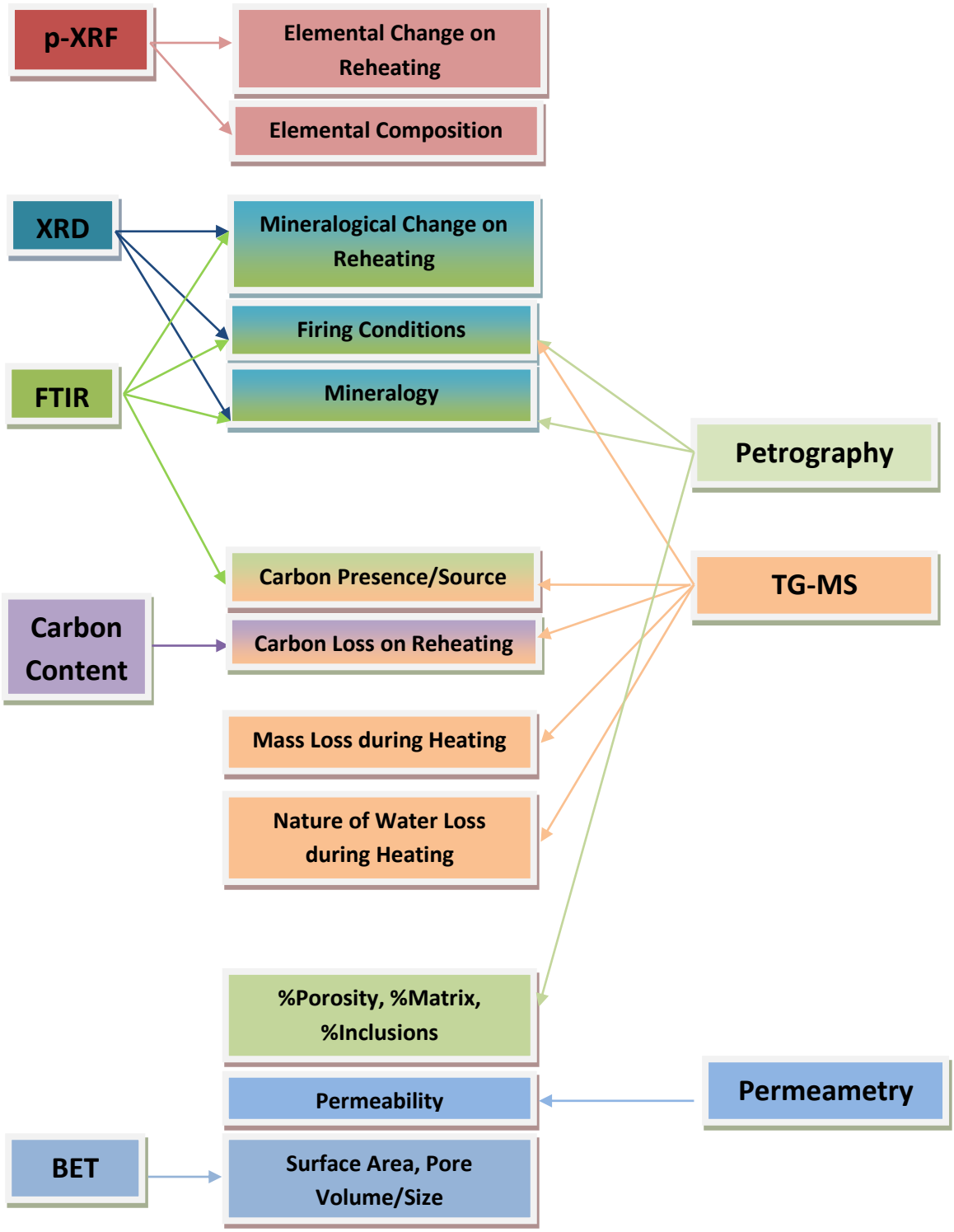

Figure 4.1: Methods used as part of non-RHX examinations of the samples structure, composition and behaviour under heating. The characteristic each method provides information on is indicated.

4.2 X-Ray Diffraction (XRD)

XRD (Moore and Reynolds 1997) was carried out to examine the mineral composition and look for any change in the mineralogy post reheating at 500°C. The original mineralogy could also be used to infer conditions of original firing when considered together with petrography, FTIR and TG-MS results (see *Section 2.3* and *Section 9.2.1*).

Analysis was carried out on powdered (<63μm) subsamples of both dried (130°C for 3 months) and heated (500°C for 18hrs) dating samples. Approximately 1-2 g of powder, enough to fill a 16mm diameter holder of depth 2.4mm, was required per subsample. The powder was compressed until it lay uniformly flat and flush within the holder. These holders were then placed in the XRD analyser.

X-ray diffractometry was then carried out with a *PANalytical X'Pert Pro* system using Cu-Kα radiation. Scans were run over the range 3-63° (2θ) with a step size of 0.0170 (2θ) and scan step time of 120s (total scan time of 58 minutes per sample). The sample stage was configured to spin during each scan. The energy and current settings of the XRD were 40kV and 40mA, respectively.

Analysis of the XRD spectra was carried out using the powder pattern analysis tool *PANalytical X'Pert Highscore Plus* (Highscore 2015). The spectra had the following treatments carried out in the following order: background removal; smoothing (quantic polynomial over a window size of n=15); peak search (using the minimum of the 2nd derivative method and a minimum peak significance of 15 counts); convert FDS to ADS correction; search and match algorithm to identify the possible minerals present using the in-built *International Center for Diffraction Data* (ICDD) library *PDF2* (ICDD 2015). Identification of minerals present was based on both peak and profile matching with the library spectra available. During selection/exclusion of the mineral phases interpreted as present, semi-quantitative analysis based on reference intensity ratio (RIR) values was carried out using *X'Pert Highscore Plus* (this uses the normalised RIR method of Chung (1974)).

Tables of the interpreted minerals present in each sample were compiled.

4.3 Fourier Transform Infrared Spectroscopy (FTIR)

The FTIR method (Russell and Fraser 1994) was used to examine the mineralogy, initial firing conditions, mineralogical change on heating at 500°C, and the presence/absence and nature of organics present.

FTIR analysis was carried out using a *PerkinElmer Spectrum One*. For each dating sample, two powdered subsamples (< 63 µm) were prepared into pressed pellets, a sample that had previously been dried at 130°C (3 months) and a sample that had been fired at 500°C (for 18 hours). This was achieved by mixing approximately 2-5mg of sample with 40-100mg of potassium bromide (KBr – transparent in infrared radiation) and compressing the pellet in an evacuated die under high pressure (10 tons) to form a pressed disc of diameter 13mm and thickness <1mm. These discs were then dried in an oven at 130°C for a minimum of 3 hours to remove any loosely bound surface adsorbed water before being placed in a desiccated jar to cool. Scans were then run on room temperature samples, following positioning in the *Spectrum One.* These scans were run over the wavenumber range 450cm^{-1} – 4000cm^{-1} (before each scan a background scan was also taken). The *Spectrum One* software was used to carry out a baseline correction on each of the scans.

Using *MATLAB*, the second derivative of the FTIR spectrum and a smoothed version of this second derivative (using *cftool* and a smoothing spline with smoothing parameter 0.0133) were acquired. The main absorption peaks were identified through comparison of the FTIR scan and its 2nd derivative with the mineral identification carried out largely over the region 1500-450cm^{-1} using tables compiled from the following references (Benedetto et al. 2002; Chukanov 2014; Russell and Fraser 1994; van der Marel and Beuterspacher 1976).

Tables of the possible minerals identified and their perceived likelihood were combined for each sample. Also, in conjunction with the XRD results, a table of the presence/absence of mineral phases associated with moderate to high firing temperatures was compiled. This is based on mineral transformations and firing temperature considerations, discussed in *Section 2.3.*

Special attention was also paid to the region 3000-2800cm^{-1} where absorption peaks associated with organics were compiled and tabulated.

4.3 Portable X-Ray Fluorescence Spectroscopy (p-XRF)

Portable X-Ray fluorescence spectroscopy (Bain et al. 1994; Potts and West 2008) was carried out to provide a swift assessment of the elemental composition of the samples and examine for any possible elemental alteration upon heating. It was carried out using a portable *Bruker S1 Turbo^{SD} LE* energy dispersive analyser (rhodium, Rh, source). Analysis was carried out on dating samples that had been dried at 130°C (3 months) and powdered to <63µm, and powdered dating samples reheated at 500°C (for a period of > 18 hours).

The powdered samples were placed in a plastic cylindrical container of height 23mm and diameter 24mm which had a taut Mylar thin film (for XRF, 3µ thick) as a base. The powder was added until a thickness of approximately 10mm was achieved and the contact layer between the sample and the Mylar sheet was tight and even. The p-XRF was placed in a table-top holder such that the examination window on its nose was pointing upright and vertical. A sample table upon which to place the container and sample was positioned upon the nose of the p-XRF (this does not obstruct the examination window) and the container with sample was positioned on this, covering and sitting directly above the examination window. A safety shield was then positioned over the sample and sample table. Scans were set running by a remote trigger attached to the p-XRF. A PDA control interface to the p-XRF was used for setting up the scans and recording the spectra obtained.

The scans were set up for 'Dual Mode' running and 'Fundamental Parameter' quantification. 'Dual Mode' involves running the p-XRF at 15kV (no filter) for 1 minute (analysis of light elements, Cu and below) and at 40kV (Ti and Al filters) for 1 minute (analysis of heavier elements, Ti to Ag). 'Fundamental Parameter' was the method of quantification (% weight) carried out by the PDA software (see Markowicz (2008) for details on the fundamental parameter approach. This is a theoretical quantification method and may not be as accurate as using an empirical

calibration but is suitable for the present study where all samples have undergone the same analysis procedure and quantification approach and are only being compared internally with one another).

Tables of the quantified results were prepared only for the non-reheated samples as there were no statistically significant differences with the reheated sample results.

4.5 Petrography and Image Analysis

Petrography

Thin section petrography (Quinn 2013; Reedy 2008) was carried out on all samples to examine forming methods and firing conditions, as well as general mineralogy and composition (voids, matrix, mineral).

Thin section preparation followed those outlined by Quinn (2013). For each dating sample, a normal and blue-dyed thin section was prepared from the bulk material, in this case mostly cubes of brick that had been dried at 60°C for 1 month. First, a small block of material was cut from the brick/sherd using a diamond-tipped rotary saw lubricated with water. These blocks were then impregnated with a two-part epoxy resin by placing the block in a small plastic cup, covering it with resin, placing the cup in a suitable evacuation chamber and then pumping out the air; for the blue-dye thin sections, at this stage blue dye was mixed into the resin. Following impregnation, the block was then polished manually on one surface using carborundum (SiC powder, 600 grit) to ensure a smooth surface for bonding with the glass slide. Following polishing the resin block was rinsed to remove any carborundum.

The block was bonded onto the frosted side (600 grit carborundum) of a glass slide (48 x 28 mm) using a two-part epoxy resin, care being made to ensure no air bubbles were trapped between the contact surfaces. Once glued, most of the ceramic block was cut off using the diamond tipped saw, leaving only a few millimetres of material remaining glued to the slide. The thin section was then

further thinned through use of a lapping machine (*Logitech*) that took the sample thickness down to 50-100µm. Following this, the sample was polished down to a thickness of 30µm by hand polishing; this is achieved by polishing until the appearance of first-order white interference in the quartz minerals under cross polarised microscope. Once 30µm was reached, the thin section was rinsed off again and allowed to dry before a cover slip of glass was applied, again with epoxy resin.

Samples were examined under plane and cross polarised light (PPL/XPL, respectively) using a petrographic microscope and magnification generally ranging from x10-x40. The characterisation of the ceramic strongly follows suggestion by Quinn (2013, Chapter 4) and mineral identification was informed using standard reference resources (MacKenzie and Guilford 1980; 1982; Adams et al. 1984).

Image Analysis of Thin Section

Images of the blue-dyed thin sections were taken using an *Olympus CX-41* microscope with a *CUC 30* camera attachment. Under plane polarised light, ten images of 715 x 530 µm (x10 magnification) were taken from random locations across the slide.

Image processing was then carried out using *GIMP 2.8.10* to obtain loose estimates of the percentage porosity and percentage mineral inclusions in the thin section. The % porosity/inclusions were obtained through the ratio of pixels associated with pores/inclusions (i.e. the blue dye of the pores and the white-greys of quartz-feldspars) to that of the number of pixels in the entire image. This involved using the 'select by colour' tool in GIMP to highlight all areas of the image of a suitable colour range (chosen by eye for each image) and recording the pixel count provided by the software for this colour range and for the entire image. This process was carried out for all 10 images of each dating sample. The average % porosity and % inclusion value was then calculated for each sample with the % matrix obtained by subtracting the sum of these two values from 100% for each sample.

For *Por*, *Dow1* and to a lesser extent *Dow2*, there had been some saturation of the slide with blue dye so the measurements were less reliable. Other issues include the subjectivity involved in ensuring that all the pores/inclusions within a particular colour range are highlighted. Nonetheless, the method can provide a loose guide to the visual sample composition.

4.6 Surface Area Analysis

Brunauer-Emmett-Teller (BET) analysis was carried out to examine the nature of the specific surface area (S.S.A. based on BET theory) and pore size/volume (based on Barrett-Joyner-Halenda (BJH) theory) of all samples (see Lowell et al. 2004, *Section 4, 5 & 8*).

This was carried out by the facility *Analytical Services and Environmental Projects (ASEP)* at QUB using a *Micromeretics Tristar II 3020* automated gas adsorption analyser, with nitrogen as the adsorption gas. Approximately 0.5-0.8g of granulated sample (3.35-2mm sieved fraction) was submitted for analysis for each dating sample. This followed heating of the sample at 500°C for 24 hours to remove most bulk moisture and combustibles from the sample that might interfere with the adsorption/desorption processes. Mathematical analysis of the sorption curves was also carried out by *ASEP*.

Issues were encountered with samples *Rat* and *Tur* where sorption of nitrogen was particularly poor and complete sorption curves could not be recorded for estimation of all surface area related characteristics (*Cal* also presented poor sorption curves due to low surface area).

4.7 Permeametry

The permeability of samples was examined using air-injection probe permeametry (Hurst and Goggin 1995).

These tests were carried out on samples of dating material that had been dried in an oven at 80°C for 2 months to remove bulk moisture. For bricks samples, a minimum of 10 cubes of standardised dimensions 4x4x4cm were used (where sufficient material was available); otherwise, multiple measurements were taken from different faces/positions on a cube (ideally, longer cores of material would be used. For pottery (*Downshire*) and non-brick samples (*Etruscan/Roman*) such standardisation was not possible and multiple measurements were taken from a scatter of locations on the available material.

Permeametry tests were carried out using a *New England Research TinyPerm II* portable air-injection permeameter. Following retraction of the plunger, the rubber nozzle of the *TinyPerm II* was pressed against a flat and smooth surface of the sample. Then the plunger was depressed completely and held in place until the vacuum reading of the *TinyPerm II* reached 0. The response function (based on pressure and volume within the plunger during a reading) is computed by the permeameter's microcontroller and was recorded for each measurement. This 'TinyPerm II Value' was converted into permeability (mD) using a calibration provided by *New England Research.* The average permeability and standard deviation was calculated for each sample. For measurements where the vacuum had not reached zero or acceptably close to zero within a period of 20 minutes, the material was considered virtually impermeable. This was the case for both *Downshire* pottery samples (*Dow1/2*). Also, there was not enough remaining material to carry out permeametry tests on the Castle Caulfield sample (*Cau*).

4.8 Carbon Content

Carbon content analysis was carried as a part of estimating the mass of organic matter/carbon removed during heating of dating samples between 130-500°C, mass that if unaccounted for could affect estimates of the RHX mass gain over the ceramics lifetime.

Carbon content analysis was carried out at the ^{14}*CHRONO Center* at QUB. For each dating sample, carbon content analysis was carried out on two subsamples of approximately 0.5g powdered form (<63µm); one sample that had been dried at 130°C and another that had been fired at 500°C (because combustion in this method could only take place at 850°C the difference in carbon content between these two samples was required – see below). The sample to be analysed was placed in a pre-baked quartz-glass tube together with copper oxide (0.5-0.6g, provides an oxygen source) and strips of silver (0.5g, removes halides) The tube was then evacuated and sealed (melted by blowtorch) before being heated at a temperature of 850°C for a period of 8 hours.

Following combustion, the trapped CO_2 was measured by opening the sample into a pre-evacuated cryogenic separation line. Water and non-condensables in the sample were removed using a water trap (ethanol and dry ice slush) and liquid nitrogen (to freeze/condense the CO_2 and then pump away any non-condensables), respectively. The remaining gas pressure, due to CO_2 in a specific volume of the line was then recorded. This gas pressure was then converted into a mass of carbon using an empirical equation from the laboratory's calibration. The ratio of the mass of carbon to the original mass of the sample was used to calculate the %wt C (carbon).

For each dating sample, this provided two values, the %wt C for the sample dried at 130°C (corresponding to mass m_{c130+}) and the %wt C for the sample heated at 500°C (corresponding to mass m_{c500+}). To obtain the %wt C removed from a sample during heating between 130-500°C (m_c) the following equation was used:

$$m_c = m_{c130+} - m_{c500+}$$

The use of m_c in estimation of the organic matter present is described in *Section 6.7.2.1*

4.9 Thermogravimetric Mass Spectrometry (TG-MS)

Thermogravimetric-mass spectrometry was carried out to examine the mass loss and associated mass products during heating of samples to, and beyond, 500°C. From this inferences could be made regarding the nature of the mass loss involved in RHX dating as well as the original conditions of firing of the sample.

This was carried out using a *Netzsch TG 209 F1 Libra* thermo-microbalance in series with a *Pfeiffer Thermostar* mass spectrometer. Approximately 30-40mg of powdered dating sample (<63µ) was used. The samples had previously been dried at 130°C and stored in a desiccated environment for a period of three months. The sample was placed in an Al_2O_3 crucible within the *TG 209* and heated from 25°C to 1000°C at a rate of 20°C/min under a constant flow of nitrogen at 50mL/min. Mass spectrometry was carried out for ions of mass number 18 (H_2O), 44 (CO_2) and 64 (SO_2), liberated during the heating process. Sampling of the mass and ion current (mass spectrometry) was carried out for each °C increment in temperature.

Analysis (identification of events and structures) of the mass loss curve, its first derivative, and ion fragment curves was carried out with Microsoft *Excel* after smoothing (moving average with n = 11).

Chapter 5

Experimental Results – Non-RHX Characterisation

5.1 Introduction

This chapter presents the results of non-RHX related experiments, methods described in *Chapter 4*. For several of these approaches, for example XRD, FTIR, a very large set of graphs and tables were generated. Unless particularly instructive, the bulk of these are presented instead in the *Appendices*, with illustrative examples and summary tables provided below.

5.2 XRD

The spectra and detailed tables of peak and mineral identification are provided in full in *Appendix A*.

Tables 5.1-5.3 summarise the results of XRD analysis. *Table 5.1* and *Table 5.2* provide the semi-quantitative mineral composition (based on reference intensity ration (RIR) results) for all major minerals identified together with mineral phases associated with high-temperature firing. In *Table 5.3* is a description, for each sample, of any significant differences between the non-reheated and the reheated samples' spectra (reheated with respect to original firing). A more complete summary table of high-temperature mineral phases identified using both XRD and FTIR, and the confidence in their presence is presented later in *Section 5.4*.

An example set of XRD spectra of the non-reheated and reheated *Ann* samples are provided overlaid in *Figure 5.1*. There are no significant differences between these two spectra. In *Figure 5.2* an example spectrum, for *Dow1*, is presented that highlights peaks interpreted as belonging to high temperature mineral phases useful in firing temperature estimation, *Section 2.3*. In this figure, and those in the appendix, where a single mineral is assigned to a peak, often the peak is a

superposition of reflections from the crystal faces of many minerals; the single mineral assignation is used to highlight what is interpreted as the strongest contributing mineral or a mineral of particular interest. Also, all mineral identification is interpretative to some degree and was always carried out in consideration of the results from FTIR and petrography and vice-versa.

Table 5.1: Semi quantitative (RIR method) mineral composition of sample based on XRD – part 1. XXX = 41-60%; XX = 21-40%; X = 11-20%; xxx = 6-10%; xx = 1-5%, x = ≤1%. Mineral phases associated with high-temperature are grouped.

	Ann	Esp	Nic	Mac	Ria	Etr	Rom	Por	Rat
Quartz	XX	X	xxx	XXX	XX	XX	XXX	XX	XXX
Plagioclase	X		X	xxx	xxx	xxx	xx		xx
Alkali	XX	XX	X	XX	X	XXX	XX	X	x
Hematite	xx	xx	xx	xx	xx	x	x		xx
Anatase						x			
Rutile		xx	xx	x				x	x
Mica	X	X				xxx	X		
Calcite			x		x	xxx	xx	xx	
Dolomite				x					
Pyroxene	X	X	xxx		X	xx	xxx		xxx
Olivine			xxx	xx		xx		xx	
Bassanite				x					
Marcasite								x	
High Temperature									
Cristobalite			x	x	x			x	x
Tridymite				xx					
Spinel	xx		xx	xx	xx			xx	x
Mullite			xx		xx				
Anorthite		X	X		xxx			X	xxx
Diopside			xxx		xxx			xxx	X
Gehlenite			x		x			xx	X
Wollastonite								xxx	
Forsterite		xx							
Cordierite									xx

Table 5.2: Semi quantitative (RIR method) mineral composition of sample based on XRD – part 2. XXX = 41-60%; XX = 21-40%; X = 11-20%; xxx = 6-10%; xx = 1-5%, x = ≤1%. Mineral phases associated with high-temperature are grouped.

	Cal	Lan	Joy	Cau	Bel	Dow1	Dow2	Tur	Ted
Quartz	XX	XX	XX	XXX	XXX	X	X	XXX	XXX
Plagioclase	xxx	xxx	X	xxx	xxx				xx
Alkali	XX	X	X	X	XX		XX	XX	XX
Hematite	xx	x	xx	xx	x			x	xx
Anatase				x	x		x	x	x
Rutile			x	x					
Mica		xxx		x	xxx	X			
Calcite	x	x		x		xx	xxx	x	x
Dolomite		x				xx			
Pyroxene	xxx	xx	xxx			X			
Olivine			xx			X	xxx		xx
Bassanite					x				
Marcasite									
High Temperature									
Cristobalite	x	x		x			x	x	
Tridymite				xx					
Spinel	xx	xx	x	x	x		x	xx	
Mullite			xx						x
Anorthite	X	X	xxx				X		X
Diopside		xxx				XX	XX		xxx
Gehlenite	x	xx	x			x			x
Wollastonite	xx	xx	xx			X			xxx
Forsterite									
Cordierite	xx								

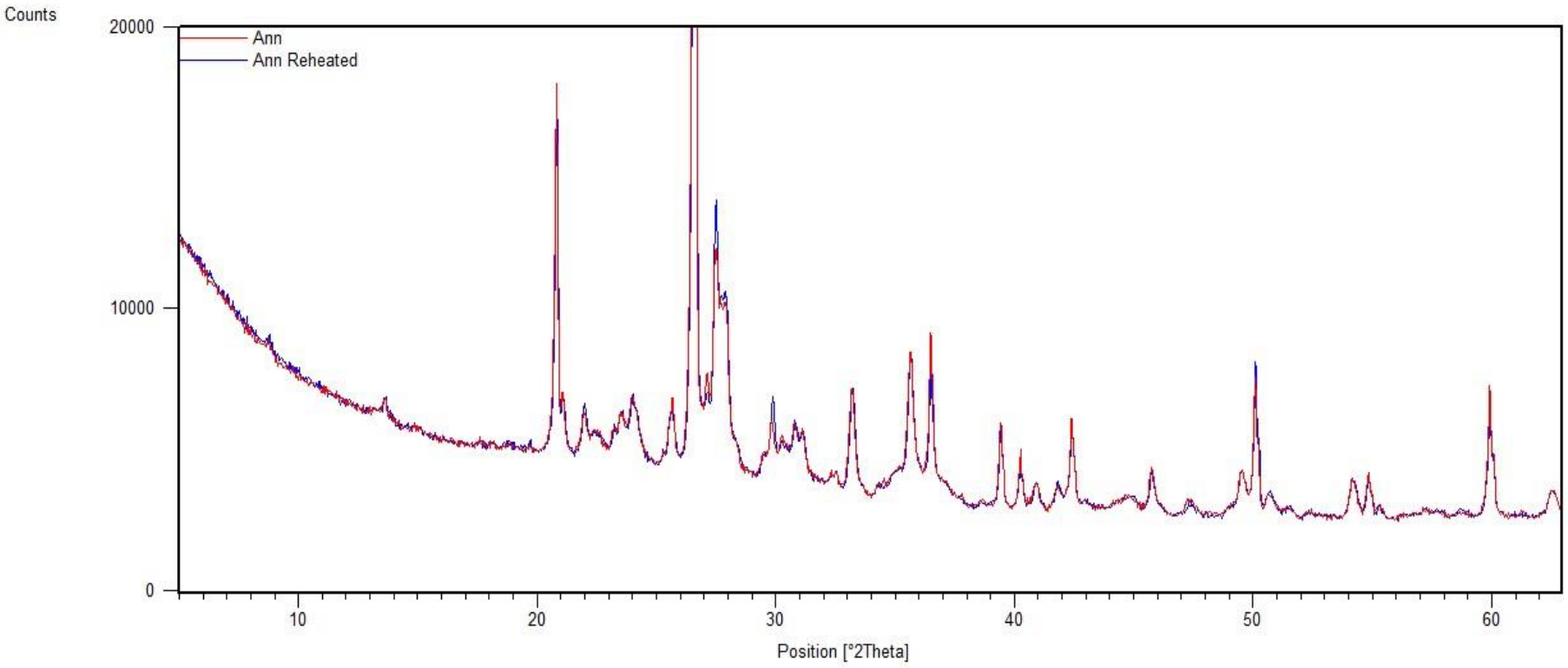

Figure 5.1: XRD spectra of Annadale sample without (red) and with (blue) reheating at 500°C.

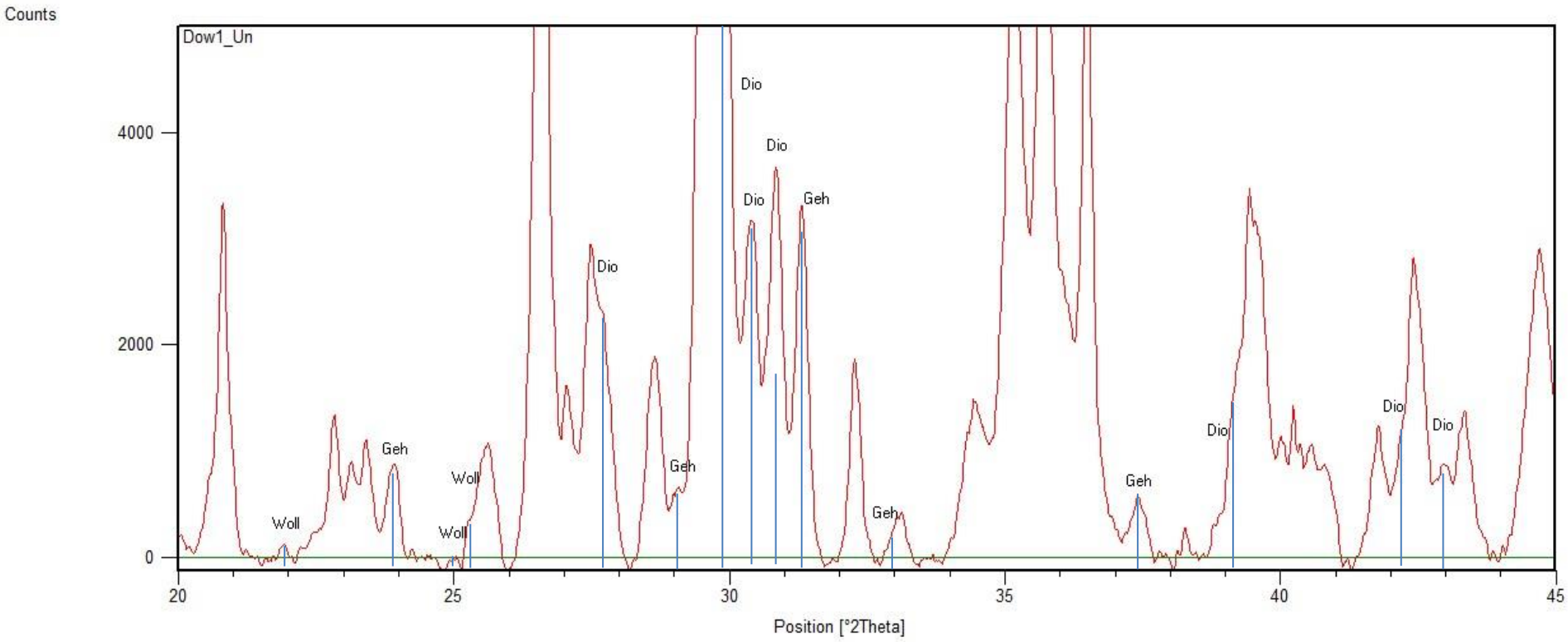

Figure 5.2: XRD spectrum of non-reheated *Dow1*, highlighting peaks attributed to high temperature related mineral phases. Wol=Wollastonite; Geh=Gehlenite; Dio=Diopside.

Table 5.3: Differences between the XRD spectra of non-reheated and reheated (500°C) samples. Sampling variation differences are those associated with minor differences in the composition of the two powder fractions used and most likely due to inhomogeneity of the larger powdered fraction from which they are sampled.

	Differences between XRD spectra of non-reheated and reheated samples.
Ann	No significant difference.
Esp	No significant difference.
Nic	No significant difference.
Mac	The overlapping spectra are presented in Figure 5.3. Significant differences exist; the non-reheated sample has peaks at 14.7°, 29.7° and 31.8° (2θ) that are either non-existent or very weak in the reheated sample spectrum, whereas the reheated sample spectrum has peaks at 25.4°, 38.6°, 48.6° and 52.3° (2θ) that are either non-existent or significantly weaker in the non-reheated sample. The former non-reheated peaks have been identified as bassanite (hemihydrate) reflections and the latter reflections in the reheated samples are attributed to anhydrite (using ICDD PDF2 peak identification library). Differences in the two spectra are attributed to the level of hydration of sulfates within the ceramic. Other minor differences are considered statistical.
Ria	No significant difference.
Etr	The XRD spectra of the non-reheated and reheated Etruscan samples are provided overlapped in Figure 5.4. The major differences are the presence of peaks at 31.4°, 51.3° and 51.4° (2θ)) in the non-reheated samples that are non-existent or very weak in the reheated samples, as well as peaks at 27.5° and 27.9° (2θ)), which are significantly stronger in the reheated samples. The peaks at 27.5°, 27.9° and 31.4° are attributed to feldspar reflections (albite, microcline and albite, respectively) with those at 51.3° and 51.4° more difficult to identify but most likely anomalous albite reflections. These reflections are confirmed to have no association with clay minerals, pyrite/sulphate minerals or iron minerals.
Rom	No significant difference.
Por	No significant difference
Rat	The only notable difference (*Figure A.15, Appendix A*) between the samples was a larger, sharper peak at 28° (2θ) in the reheated sample. This position corresponds to a reflection due to anorthite and the difference in magnitude is attributed to sampling variation or inhomogeneity.
Cal	There are some minor differences in the non-heated and reheated spectra for *Cal* (*Figure A.17, Appendix A*). A large peak appears at 27.45° (2θ) in

	the reheated sample. This is attributed to a microcline/anorthite reflection due to sampling variation or inhomogeneity.
Lan	A minor difference between the spectra is the presence of a small peak at 39° (2θ) in the non-reheated sample (*Figure A.19, Appendix A*). This is attributed to a wollastonite reflection and appears in only the non-reheated sample due to inhomogeneity in the samples. There are no other significant differences.
Joy	The only difference of note between the non-reheated and reheated spectra is a small peak at 28° (2θ) in the reheated sample that is attributed to an albite reflection not present in the non-reheated sample (*Figure A.21, Appendix A*).
Cau	No significant differences.
Bel	There are strong differences in the *Bel* non-reheated and reheated spectra (*Figure A.25, Appendix A*). The following peaks are present in the non-reheated and either absent or very low-level in the reheated sample: 14.6°(2θ), 29.6°(2θ), 31.8°(2θ). These can all be identified with bassanite (hemihydrate). For the reheated sample, peaks not present in the non-reheated sample are: 24.1°(2θ), 25.4°(2θ), 31.3°(2θ), 38.6°(2θ), 40.8°(2θ) and 41.6°(2θ). These can all be identified with anhydrite. The differences are similar to those recorded for *Mac*.
Dow1	No significant difference.
Dow2	No significant difference.
Tur	No significant difference.
Ted	No significant difference.

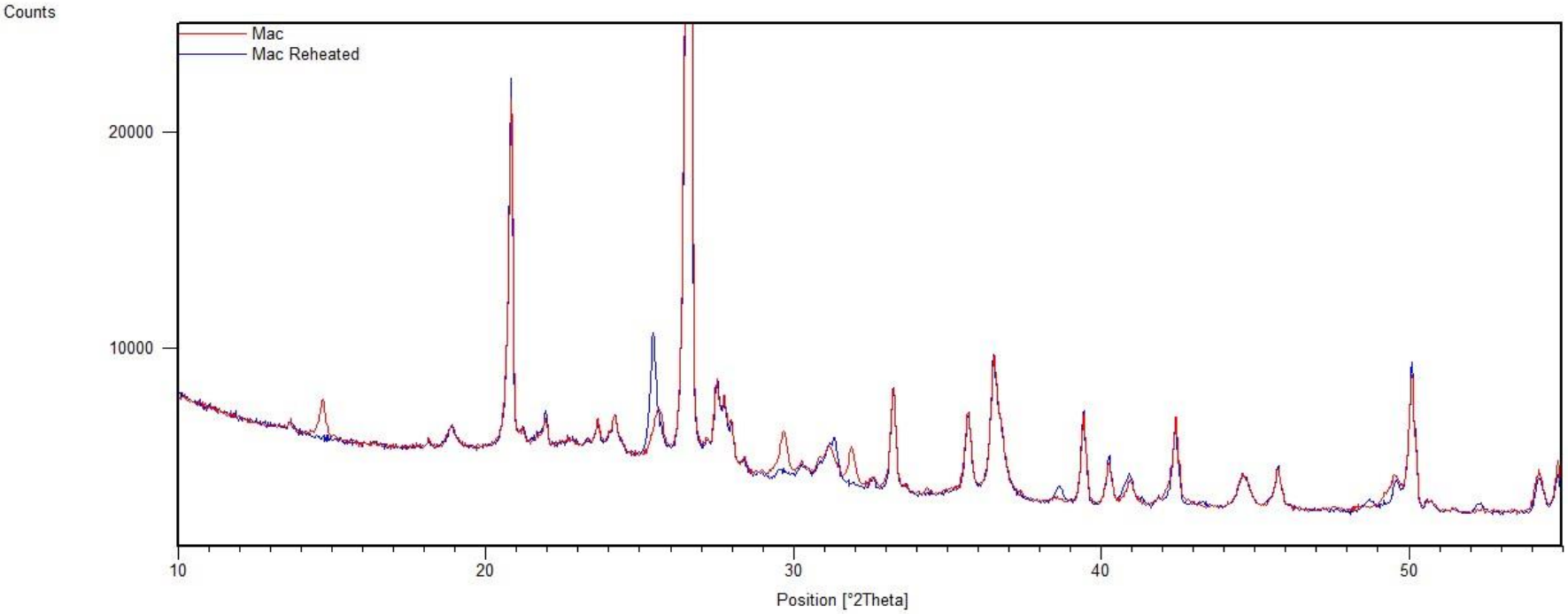

Figure 5.3: XRD spectra of *Mac* sample without (red) and with (blue) reheating at 500°C. Region constrained to 10-55° (2θ).

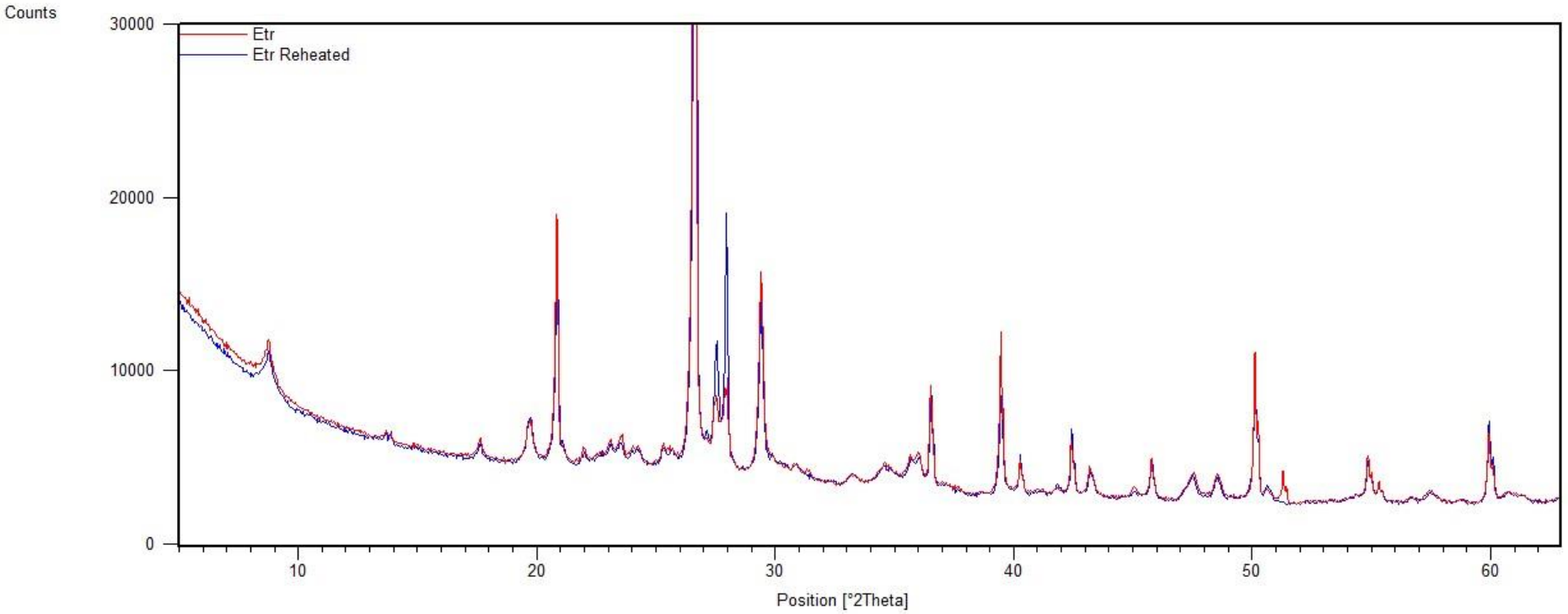

Figure 5.4: XRD spectra of *Etr* sample without (red) and with (blue) reheating at 500°C.

5. 3 FTIR

The complete set of spectra and tables of absorption peak-mineral interpretations are provided in *Appendix B*. This section will present a summary of the FTIR mineral identification results and any notable differences between the non-reheated and reheated (500°C) subsamples, together with results from organics peak identification in the region 2800-3000cm^{-1}. The results are not quantitative and confidence in the mineral identification was aided through consideration of XRD and petrography results.

The mineral interpretation based on FTIR, together with assessments of the likelihood of presence (based on consideration of number of mineral peaks present together with XRD and petrography), are presented in *Table 5.4* and *Table 5.5*. Differences between the non-reheated and reheated subsamples are described in *Table 5.6*.

Examples of the spectra obtained are provided in *Figures 5.5-5.8. Figure 5.5* presents the entire spectra (non-reheated and reheated) for *Mac*. *Figure 5.6* presents the same spectra over a region significant in mineral identification (450-900cm^{-1}) and that exhibits notable differences for *Mac,* see *Table 5.6* for description of these. *Figure 5.7* presents the non-reheated spectra over the region 450-1500cm^{-1} and highlights the 2nd derivative used in peak identification. The last of this set, *Figure 5.8*, presents an example, *Mac*, of the region 2800-3000cm^{-1} used in organics identification.

The results of analysis of the region 2800-3000cm^{-1} for organics are presented in *Table 5.7,* and *Figures 5.9-5.12*. *Table 5.7* presents, for all samples and for reheated and non-reheated spectra, the peak positions (cm^{-1}) and a subjective assessment of the strength of those peaks. It also attempts to group the observed peaks. *Figure 5.9* and *Figure 5.10* present the peak position and their possible ranges as a function of wavenumber for non-reheated and reheated samples. Using the peak position ranges in *Figure 5.9* and *Figure 5.10,* the number of samples with organic peaks at wavenumbers from 2840-2980cm^{-1} is presented in *Figure 5.11*. This data is smoothed with a running average (*n=9*) in *Figure 5.12*. Assignment of organics to

these peaks is discussed in *Section 9.2.1.* For all samples (reheated and non-reheated) a peak at 1384cm^{-1} (nitrate) was also identified.

Table 5.4: Summary of minerals and likelihood of presence based on FTIR analysis – part 1. XXX = very likely/certainly present. XX = likely present. X = possibly present. Likelihood of presence is based on consideration of number of peaks identified associated with mineral as well as consideration of XRD and petrography data.

	Ann	Esp	Nic	Mac	Ria	Etr	Rom	Por	Rat
Quartz	XXX	XXX	XXX	XXX	XXX	XXX	XXX	XXX	XXX
Plagioclase	X		XXX	X	XXX		X	XX	XX
Alkali	XXX	XXX	XXX	XXX	XXX	XXX	XXX	XXX	XX
Hematite	X		XX	XX	XXX	XX	XX		X
Anatase								X	
Rutile		X	X	XXX	XXX			X	
Mica	XXX			X	X	X	X	X	
Calcite			XXX			XXX	XXX	XXX	X
Dolomite									
Pyroxene	XXX	XXX	XX		XX		X	X	X
Olivine		XXX		XX	X	XX	XX		
Bassanite Anhydrite Gypsum				XXX					
Marcasite									
High Temperature									
Cristobalite				X					X
Tridymite				XX					
Spinel	X		X						
Mullite			XX	X					
Anorthite		XXX	XX	X	XX			XXX	XXX
Diopside		XXX	XX		X				XXX
Gehlenite			XX		XX			XX	
Wollastonite			X		X			XX	
Forsterite			XX					X	
Cordierite									X

Table 5.5: Summary of minerals and likelihood of presence based on FTIR analysis – part 2. XXX = very likely/certain present. XX = likely present. X = possibly present. Likelihood of presence is based on consideration of number of peaks identified associated with mineral as well as consideration of XRD and petrography data.

	Cal	Lan	Joy	Cau	Bel	Dow1	Dow2	Tur	Ted
Quartz	XXX	XXX	XXX	XXX	XXX	XXX	XXX	XXX	XXX
Plagioclase	XX	X	X	X	XXX		X		XXX
Alkali	XXX	XXX	XXX	XXX	XXX	X	XX	XXX	XXX
Hematite		XX	XX	XXX	XX				XXX
Anatase							XX		X
Rutile		XXX	X						
Mica		X	X	X	X		X		
Calcite	XXX	XXX		X		XXX	XXX	XXX	XXX
Dolomite	X	XX				X	XX		
Pyroxene	X	X	XX	X	X	XXX	X		X
Olivine						XX			
Bassanite Anhydrite Gypsum					XXX				
Marcasite									
High Temperature									
Cristobalite	X	X				XX	X	X	X
Tridymite									
Spinel					XX			X	
Mullite			XX				XX	X	XXX
Anorthite	XXX	XXX	XX			XX	XXX		XXX
Diopside							XX		XX
Gehlenite	XX	XX	XX			X	XX		X
Wollastonite	XX	XXX	XX				X	XX	X
Forsterite	XX	X					XX		X
Cordierite									

Table 5.6: Differences between the FTIR spectra of non-reheated and reheated (500°C) samples.

	Differences between FTIR spectra of non-reheated & reheated samples.
Ann	No significant differences.
Esp	No significant differences.
Nic	No significant differences.
Mac	There are some significant differences between the non-reheated and reheated *Mac* samples, *Figure 5.5*. The reheated sample has peaks at 575cm^{-1} and 614cm^{-1} that are either very weak or not present in the non-reheated samples as well as a peak at 677cm^{-1} that appears to be greater in magnitude and shifted from 673cm^{-1} in the non-reheated sample. The non-reheated sample has a peak at 633cm^{-1} that is not present in the reheated sample together with the previously mentioned shifted peak at 673cm^{-1}. The following minerals can be attributed to the aforementioned peaks: Anhydrite = 575, 614, 617, 673, 677cm^{-1}; Bassanite = 633cm^{-1}. The change upon reheated is associated with dehydration of sulfates (gypsum)
Ria	No significant differences.
Etr	Minor differences spectra (*Figure B.22*) can be attributed to subsample variation: peaks at 478cm^{-1} and 538cm^{-1} in the non-reheated correspond to quartz and microcline bands with a questionable band at 622cm^{-1} in the reheated sample attributable to anorthite or cristobalite.
Rom	No significant differences.
Por	No significant differences.
Rat	No significant differences.
Cal	No significant differences.
Lan	No significant differences.
Joy	No significant differences.
Cau	No significant differences.
Bel	There are a number of significant differences between the two spectra, *Figure B.54* (*Appendix B*). Peaks at 663cm^{-1}, 669cm^{-1} and 1154cm^{-1} in the non-reheated samples are consistent with bassanite, gypsum and bassanite, respectively. Peaks at 613cm^{-1} and 678cm^{-1} in the reheated sample are attributed to anhydrite. There are no other significant differences between the spectra aside from those associated with variations in adsorbed moisture and atmospheric carbon dioxide (see discussion).
Dow1	There is some variation in the main calcite peak, 1420-1450cm^{-1}, which appears narrower in the reheated sample, *Figure B. 57* (*Appendix B*).
Dow2	As for *Dow1*.
Tur	No significant differences.
Ted	No significant differences.

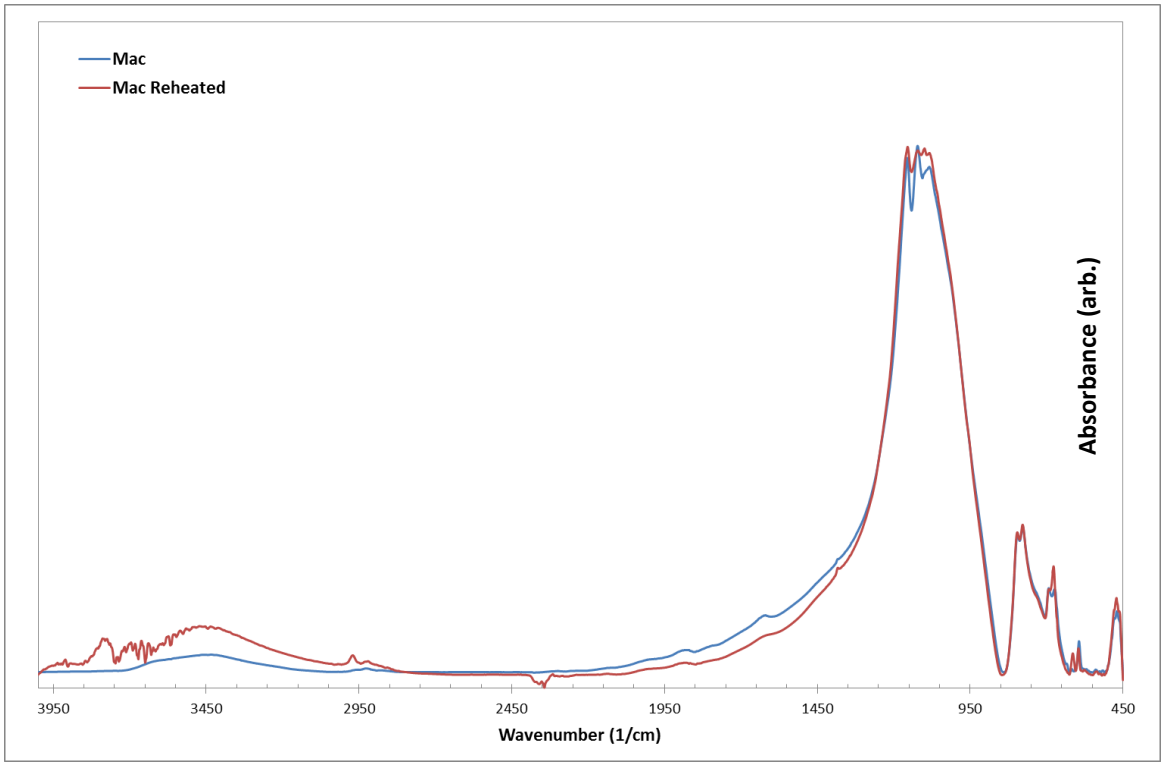

Figure 5.5: FTIR Spectra of non-reheated (blue) and reheated (red) *Mac* sample. See *Appendix B* for peak positions and minerals.

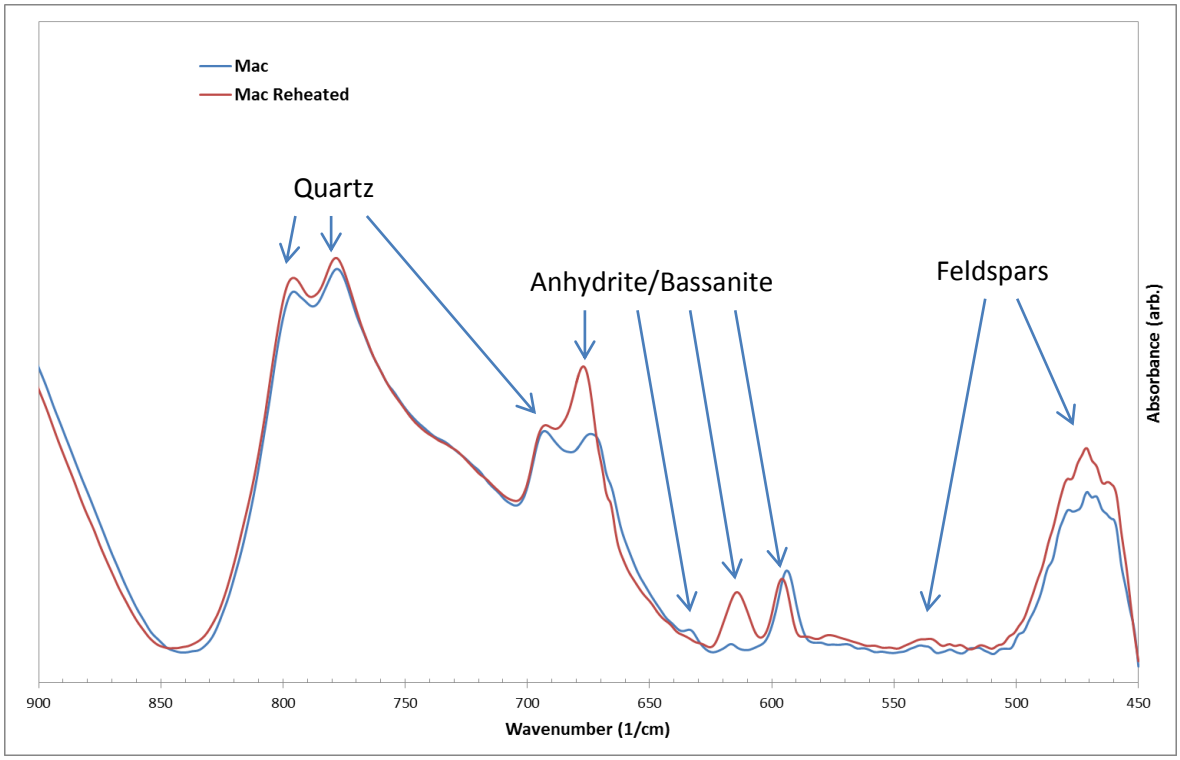

Figure 5.6: FTIR spectra of non-reheated (blue) and reheated (red) *Mac* sample over the region 450-900(1/cm). Gypsum associated peaks (anhydrite/bassanite) are highlighted together with some examples of quartz and feldspars (full list *Table B.4, Appendix B*).

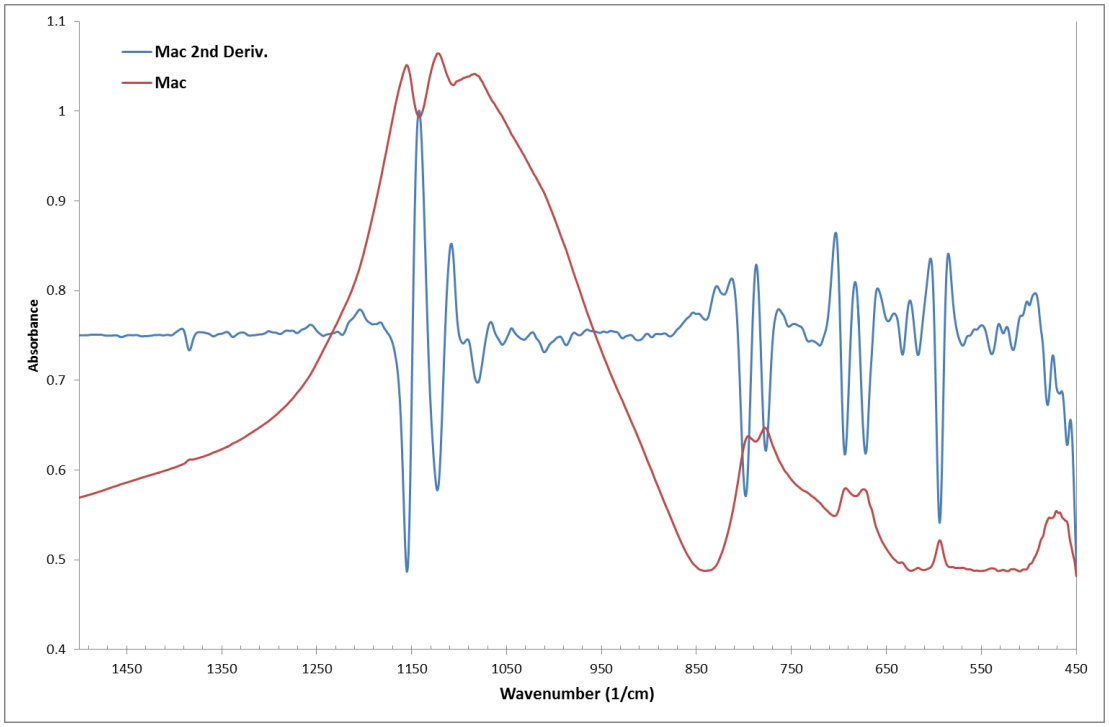

Figure 5.7: FTIR spectrum of non-reheated *Mac* sample over region 450-1500 (1/cm) with smoothed second derivative overlaid.

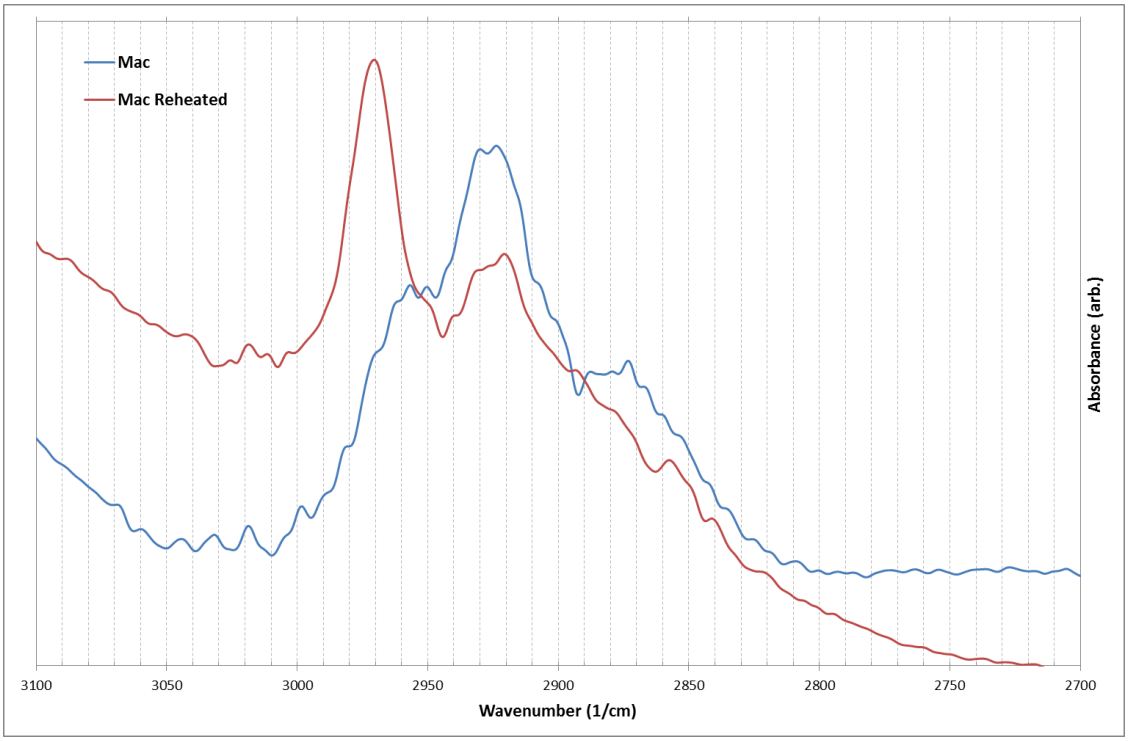

Figure 5.8: FTIR spectra across region of interest in organic identification for *Mac* (non-reheated and reheated). Peaks in the ranges 2850-2860cm^{-1}, 2920-2930cm^{-1}, 2950-2970cm^{-1} are typical for most samples (*see Table 5.7* for more detailed positions for all samples).

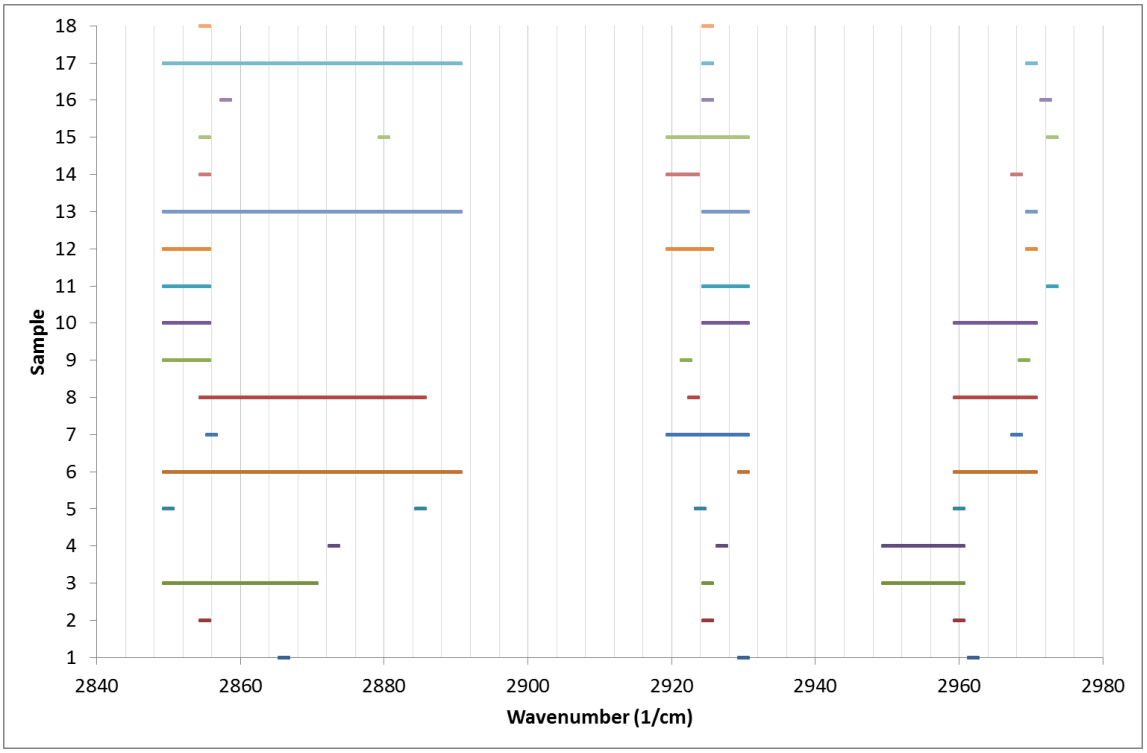

Figure 5.9: Peak positions of organics in non-reheated samples, see *Table 5.7*. Sample numbers correspond as follows: (1) Ann, (2) Esp, (3) Nic, (4) Mac, (5) Ria, (6) Etr, (7) Rom, (8) Por, (9) Rat, (10) Cal, (11) Lan, (12) Joy, (13) Cau, (14) Bel, (15) Dow1, (16) Dow2, (17) Tur, (18) Ted.

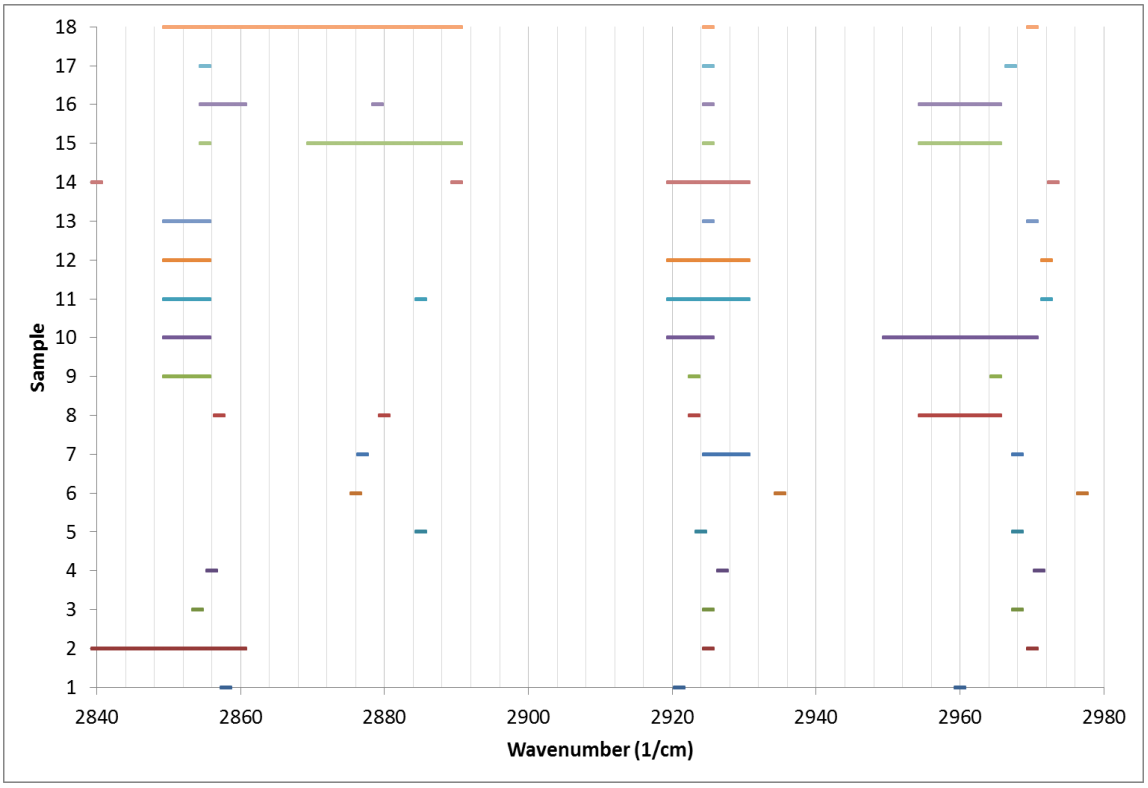

Figure 5.10: Peak positions of organics in reheated samples, see *Table 5.7*. Sample numbers correspond as follows: (1) Ann, (2) Esp, (3) Nic, (4) Mac, (5) Ria, (6) Etr, (7) Rom, (8) Por, (9) Rat, (10) Cal, (11) Lan, (12) Joy, (13) Cau, (14) Bel, (15) Dow1, (16) Dow2, (17) Tur, (18) Ted.

Table 5.7: FTIR peaks positions in organics regions 2800-3000cm^{-1} for dating samples, both non-reheated and reheated. Colour denotes relative strength of peaks: green=weak; gold=moderate; red=strong. Average values and standard deviations are based on midpoints of ranges.

	Non-Reheated				Reheated			
Ann	2866		2930	2962	2858		2921	2960
Esp	2855		2925	2960	2840-2860		2925	2970
Nic	2850-2870		2925	2950-2960	2854		2925	2968
Mac	2873		2927	2950-2960	2856		2927	2971
Ria	2850	2885	2924	2960		2885	2924	2968
Etr	2850-2890		2930	2960-2970		2876	2935	2977
Rom	2856		2920-2930	2968		2878	2925-2930	2968
Por	2855-2885		2923	2960-2970	2857	2880	2923	2955-2965
Rat	2850-2855		2922	2969	2850-2855		2923	2965
Cal	2850-2855		2925-2930	2960-2970	2850-2855		2920-2925	2950-2970
Lan	2850-2855		2925-2930	2973	2850-2855	2885	2920-2930	2972
Joy	2850-2855		2920-2925	2970	2850-2855		2920-2930	2972
Cau	2850-2890		2925-2930	2970	2850-2855		2925	2970
Bel	2855		2920-2923	2968	2840	2890	2920-2930	2973
Dow1	2854	2880	2920-2930	2973	2855	2970-2890	2925	2955-2965
Dow2	2858		2925	2972	2855-2860	2879	2925	2955-2965
Tur	2850-2890		2925	2970	2855		2925	2967
Ted	2855		2925	2965	2850-2890		2925	2970
Avg.	2859.5	2882.5	2925.4	2965.8	2855.3	2881.9	2925.2	2967.3
Std. Dev.	7.7	2.5	2.5	5.4	5.9	4.9	2.8	5.2

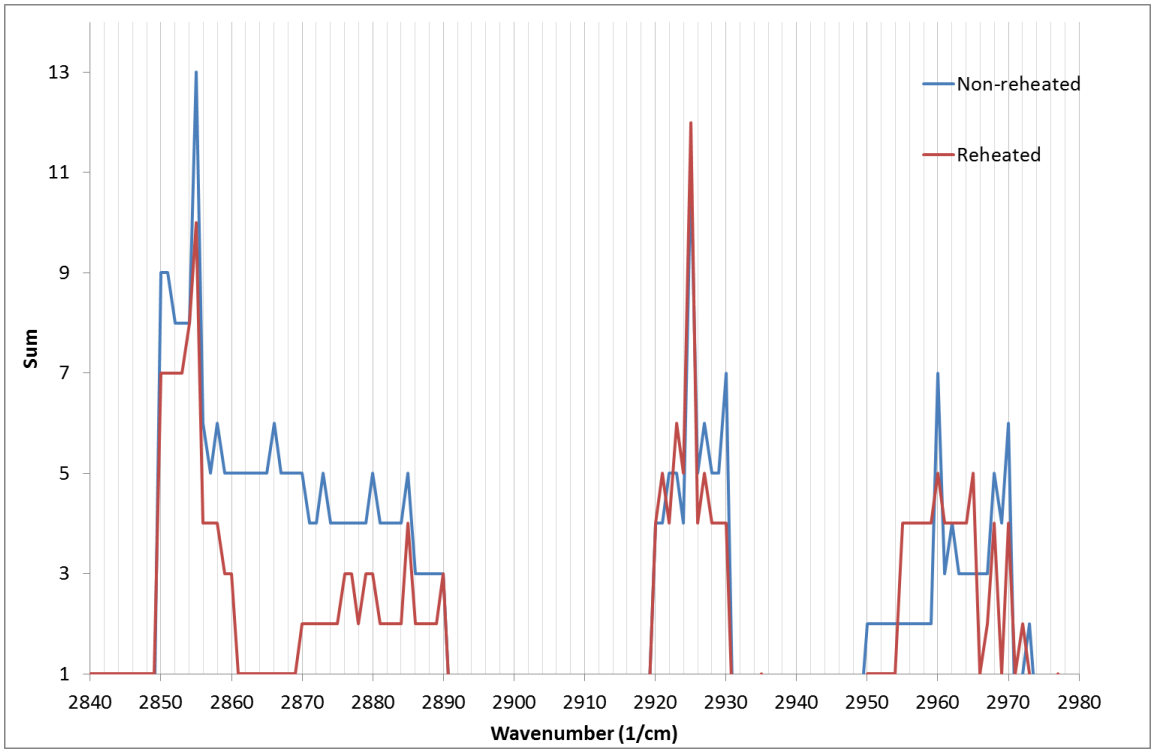

Figure 5.11 Number of samples with organics peaks at wavenumbers from 2840-2980cm^{-1}, for both non-reheated (blue) and reheated (red).

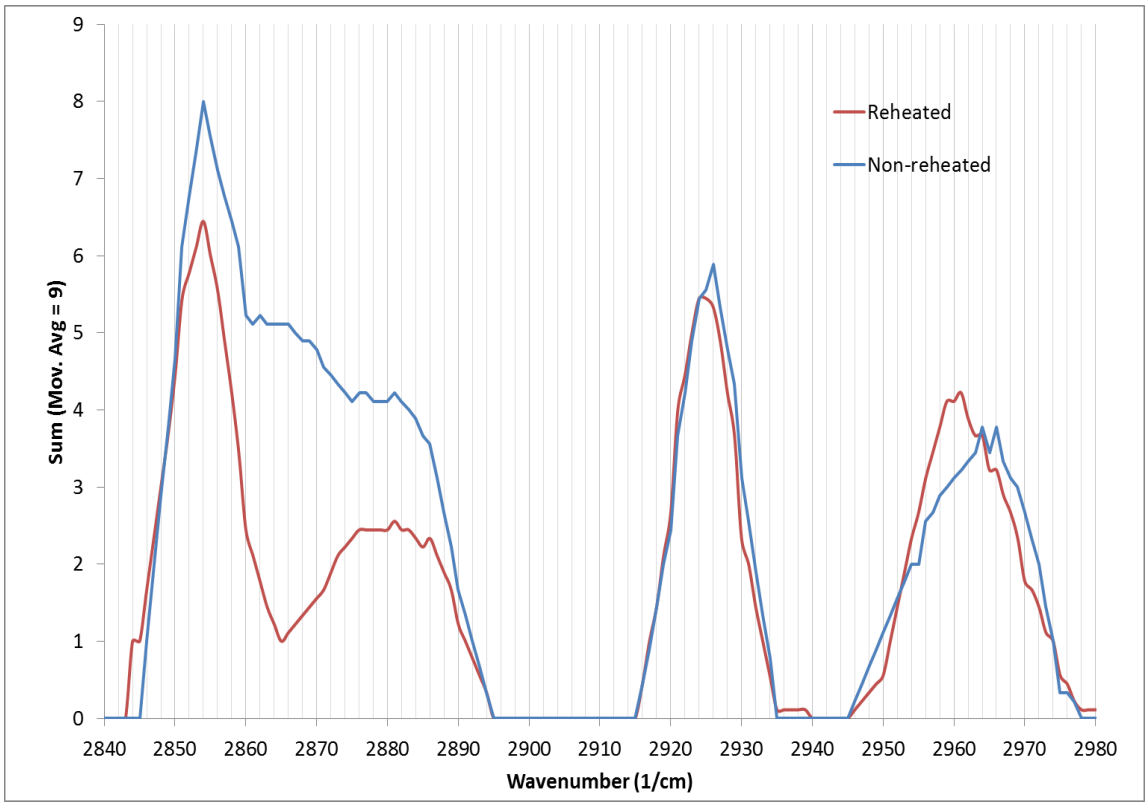

Figure 5.12: Moving average (n=9) of number of samples with organics peaks at wavenumbers from 2840-2980cm^{-1}, for both non-reheated (blue) and reheated (red).

5.4 Firing Temperature Deduction - XRD and FTIR

Information regarding the firing temperature of clay ceramics can be interpreted from XRD and FTIR data (*Section 2.3,* and *Section 9.2.1* for discussion) based on the presence/absence of suitable mineral phases formed at specific temperatures. A summary table of these minerals and their identification in dating sample material, using both XRD and FTIR, is presented in *Table 5.8*. A qualitative confidence in the mineral's presence is also expressed (use of 'present' in this table implies as much confidence as is considered achievable).

Table 5.8: Summary of presence/absence of minerals, obtained from XRD (top line – red) and FTIR (bottom line – blue) analysis, used in firing temperature deduction. Cc=Calcite, Kao=Kaolinite, Ill=Illite, Cri=Cristobalite, Tri=Tridymite, Spi=Spinel, Mul=Mullite, Geh=Gehlenite, Dio=Diopside, Wol=Wollastonite, Ano=Anorthite, For=Forsterite, Ens=Enstatite, Cor=Cordierite. XRD: x=possible, xxx=likely, X=present.FTIR: x=possible, xxx=likely, X=very likely/present.

	Cc	Kao	Ill	Cri	Tri	Spi	Mul	Geh	Dio	Wol	Ano	For	Ens	Cor
Ann			x	x		xxx			x		x		xxx	
			x			x							xxx	
Esp				x					x		xxx	xxx	xxx	
									X		X	X		
Nic	x			xxx		xxx	xxx	X	X		X	X	xxx	
	X					x	xxx	xxx	xxx	x	xxx	xxx	x	
Mac				x	xxx	x	xxx			x				
				x	xxx		x				x			
Ria	x			xxx		X	xxx	xxx	xxx	x	xxx		xxx	
								xxx	x	x	xxx		xxx	
Etr	X													
	X													
Rom	X											x	x	
	X													
Por	X			xxx		X	x	X	X	xxx	X	xxx	x	
	X							xxx		xxx	X	x	x	
Rat				xxx		X		xxx	xxx		X	x	xxx	xxx
	x			x					X		X		x	x
Cal	x			xxx		X		xxx	x	xxx	X	x	X	X
	X			x				xxx		xxx	X		x	
Lan	x		x	x		xxx	x	xxx	xxx	xxx	xxx		x	
	X							xxx		X	X	x	x	
Joy						X	xxx	X		X	X	X	xxx	
							xxx	xxx		xxx	xxx	x	xxx	
Cau	x		x	X	xxx	X	x					xxx	x	
	x												x	
Bel			x			X	x							
						xxx							x	
Dow1	X							X	X	xxx		X	xxx	x
	X			xxx				x			xxx		X	
Dow1	X		x	x		X	xxx	xxx	X		X	x	x	
	X					x	xxx	xxx	xxx	x	X		x	
Tur	x			X		X	x			x				
	X			x		x	x			xxx				
Ted	x			x	x		X	xxx	xxx	xxx	xxx	xxx	x	
	X			x			X	x	xxx	x	X	x	x	

5.5 Petrography

The results of petrographic analysis and ceramic characterisation are provided in *Table 5.9* and *Table 5.10*. The characterisation is guided by, and uses the terminology of, Quinn (2013, Chapter 4). These tables describe the minerals identified and their estimated abundance, together with the level of sorting (i.e. well, poor), shape (i.e. angular, rounded) and size of the typical mineral grains (inclusions) within the ceramic fabric. A brief description of the visible pore type shape (channels, vesicles) and size (micro (mi)=<0.05mm, meso (me)=0.05-0.5mm) is included. Also provided are estimates of the %inclusions, %pores and %matrix based on image analysis of the blue dyed slides.

Examples of the thin section image analysis are provided in *Figures 5.13-15*. Ranking of the %inclusion, %porosity, and %matrix are provided in *Figures 5.16-18,* respectively.

Finally, a table was compiled of observations that may be instructive with regard to the forming and firing conditions of the ceramics, *Table 5.11*.

Table 5.9: Petrographic analysis results – part 1. Minerals: Qtz=Quartz, Fel=Feldspar (Mic=Microcline, Plg=Plagioclase, An=Anorthoclase, O=Orthoclase), Cal=Calcite, Crt=Chert, Cdy=Chalcedony, Lim=Limestone, Oli=Olivine, Pyr=Pyroxene (ort=orthopyroxene, dio=diopside), Mus=Muscovite, Bio=Biotite, Rut=Rutile, Amp=Amphibole, Cri=Cristobalite. Abundance: T=Trace, ?=Possible/Uncertain, x= < 5%, xx=5-15%, xxx=16-30%, X=31-50%, XX=51-70%, XXX=71-100%. Sorting: w=well sorted, m=moderately sorted, p=poorly sorted, v=very, bi=bimodal. Shape: a=angular, sa=sub-angular, r=rounded, sr=sub=rounded, v=very. Pore type: vu=vughs, vo=voids, ch=channels, ve=vesicles el=elongate, ir=irregular, me=meso, mi=micro.

	Ann	**Esp**	**Nic**	**Mac**	**Ria**	**Etr**	**Rom**	**Por**	**Rat**
Mineral Abund.									
Qtz	XXX	XX	XX	XXX	XX	XX	X	XX	XXX
Fel	x (Plg)	xx (Plg, Mic, An)	xx (Plg)	xx (Plg, O?)	X (Plg, Mic)	X (Plg, Mic)	X (Plg, Mic)	xxx (Mic)	xxx (Plg)
Mica	xx	X	-	xx (Mus, Bio?)	xx (Mus, Bio?)	x	xx (Mus, Bio)	xx (Mus?, Bio)	T (Bio)
Cal	T	?	x	-	T	xx	xx	?	x
Oli	-	?	-	-	?	-	-	-	-
Pyr	-	?	xx?	x	?	T (Ort)	T (Dio?)	-	-
Crt Cdy	T	T	T	-	-	T	-	-	-
Rut	-	-	-	-	?	-	-	-	-
Amp	-	-	-	-	?	-	-	-	-
Lim	?	-	-	-	-	xx	-	-	-
Cri	-	-	-	-	-	-	-	T?	T?
Sorting	w-m	w-m	p	(bi) 1. m 2. m	p	vp	p	w	w
Shape	sa-a	sa-a	sa	(bi) 1. sr 2. r	sa	va-sa	sr-sa	sr-r	va
Grain Size (mm)	0.064-0.128	0.032-0.064	0.096-0.192	(bi) 1. 0.008-0.032 2. 0.16	0.064-0.128	0.16-0.32	0.16-0.24	fine-medium silt	0.0064-0.016
Pore Type	el-me-vu/vo	el-me-vu	el-me-ch/vu/ve	mi-ve & me-vu	el-me vu/vo & mi-ve	el-me-ch & el-me-vu	el-me-ch (aligned)	mi-ve	mi-ch
%Incl.	10.78	13.81	9.59	15.44	21.96	15.03	20.47	4.94	18.7
%Pore	0.52	0.61	1.69	3.16	7.93	11.55	1.05	11.55	13.03
%Matrix	88.7	85.58	88.71	81.4	70.11	78.64	78.64	83.51	68.27

Table 5.10: Petrographic analysis results – part 2. Minerals: Qtz=Quartz, Fel=Feldspar (Mic=Microcline, Plg=Plagioclase, An=Anorthoclase, O=Orthoclase), Cal=Calcite, Crt=Chert, Cdy=Chalcedony, Lim=Limestone, Oli=Olivine, Pyr=Pyroxene (ort=orthopyroxene, dio=diopside), Mus=Muscovite, Bio=Biotite, Rut=Rutile, Amp=Amphibole, Cri=Cristobalite. Abundance: T=Trace, ?=Possible/Uncertain, x= < 5%, xx=5-15%, xxx=16-30%, X=31-50%, XX=51-70%, XXX=71-100%. Sorting: w=well sorted, m=moderately sorted, p=poorly sorted, v=very, bi=bimodal. Shape: a=angular, sa=sub-angular, r=rounded, sr=sub=rounded, v=very. Pore type: vu=vughs, vo=voids, ch=channels, ve=vesicles el=elongate, ir=irregular, me=meso, mi=micro.

	Cal	Lan	Joy	Cau	Bel	Dow1	Dow2	Tur	Ted
Mineral Abund.									
Qtz	X	XX	XX	X	XXX	XXX	XXX	XXX	X
Fel	X (Plg, Ort)	X (Plg, Mic)	xxx (Plg, Mic)	xx (Mic, Plg, Ort)	xx (Plg, Mic, Ort)	? (Mic)	x (Plg)	xx (Plg, Mic)	X (Plg, Ort, Mic)
Mica		xx (Mus)	x (Bio)	x (Mus, Bio)	x (Mus, Bio)	x (Bio)	T	T (Bio)	x (Bio)
Cal	x	x	?	T	-	x	x	?	T
Oli		?	?	T	-	x	-	-	?
Pyr	x	x	x	x	x	x	x	?	?
Crt Cdy	T	-	T?	T	-	x	-	xx	T
Rut	-	-	-	?	-	-	-	-	-
Amp	-	-	-	-	-	-	-	-	-
Lim	-	-	-	-	?	-	-	-	-
Cri	-	-	-	-	-	-	-	-	-
Spi	-	-	-	-	?	-	-	-	?
Sorting	vp	m	p	p	m-p	w	m	p (bi)	m-p
Shape	sr-r	sr	r-va	sr-a	sr-r	r-sr	r	a	sa
Grain Size (mm)	0.16-0.32	0.08-0.16	0.16-0.016	0.16-0.016	0.24-0.48	0.08	0.16-0.24	bi 1. 0.016-0.048 (fine fraction) 2. 0.16-0.32	0.08-0.16
Pore Type	el-me-ch& el-me-vu	me-ve	el-mi-ch	ir-me-vu	el-me-ch (aligned)	mi-ve	mi-ve	ir-me-vu & ir-me-ve	el-mi-ch
%Incl.	17.52	16.57	14.13	17.48	20.16	2.43	3.28	6.92	17.94
%Pore	8.04	1.38	3.86	0.91	2.95	10.35	5.03	7.97	2.13
%Matrix	74.44	82.05	82.01	81.61	76.89	87.22	91.69	85.11	79.93

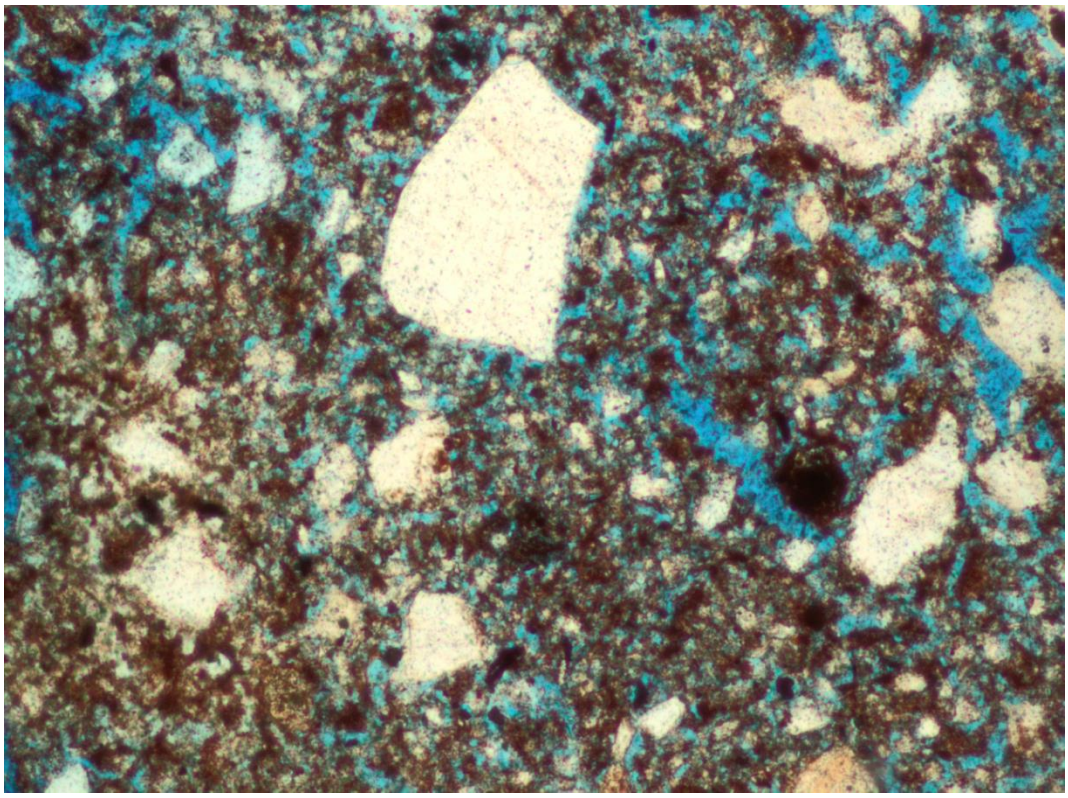

Figure 5.13: Thin section image (image width=0.715mm) of *Rat* brick before image analysis to determine %porosity and %inclusions. Blue dye corresponds to pores.

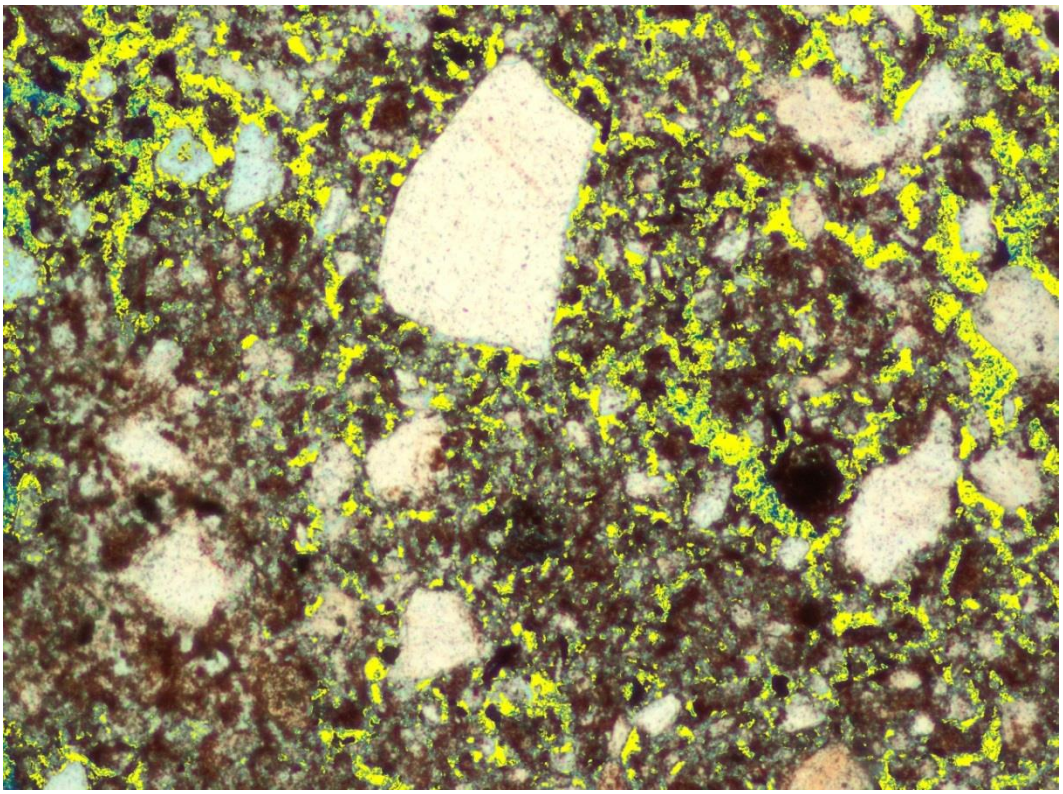

Figure 5.14: Thin section image of *Rat* brick with image analysis to pixel count %porosity (yellow).

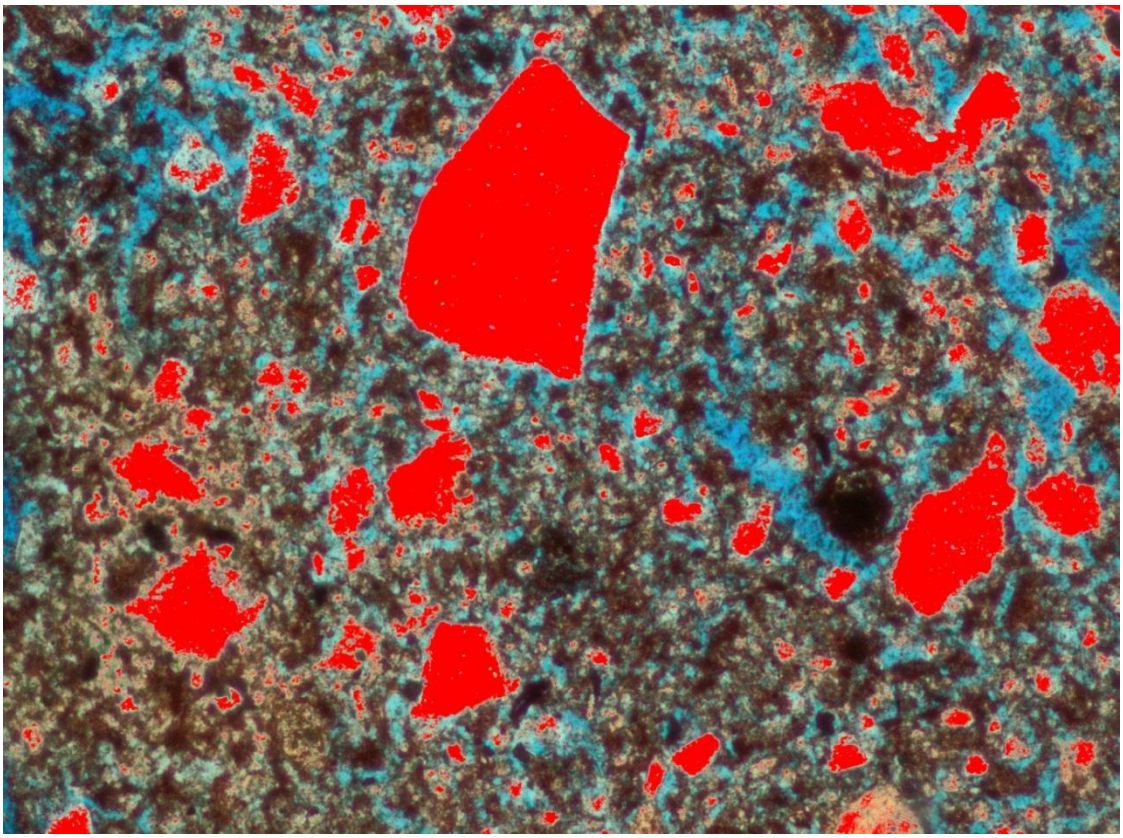

Figure 5.15: Thin section image of *Rat* brick with image analysis to pixel count %inclusions (red).

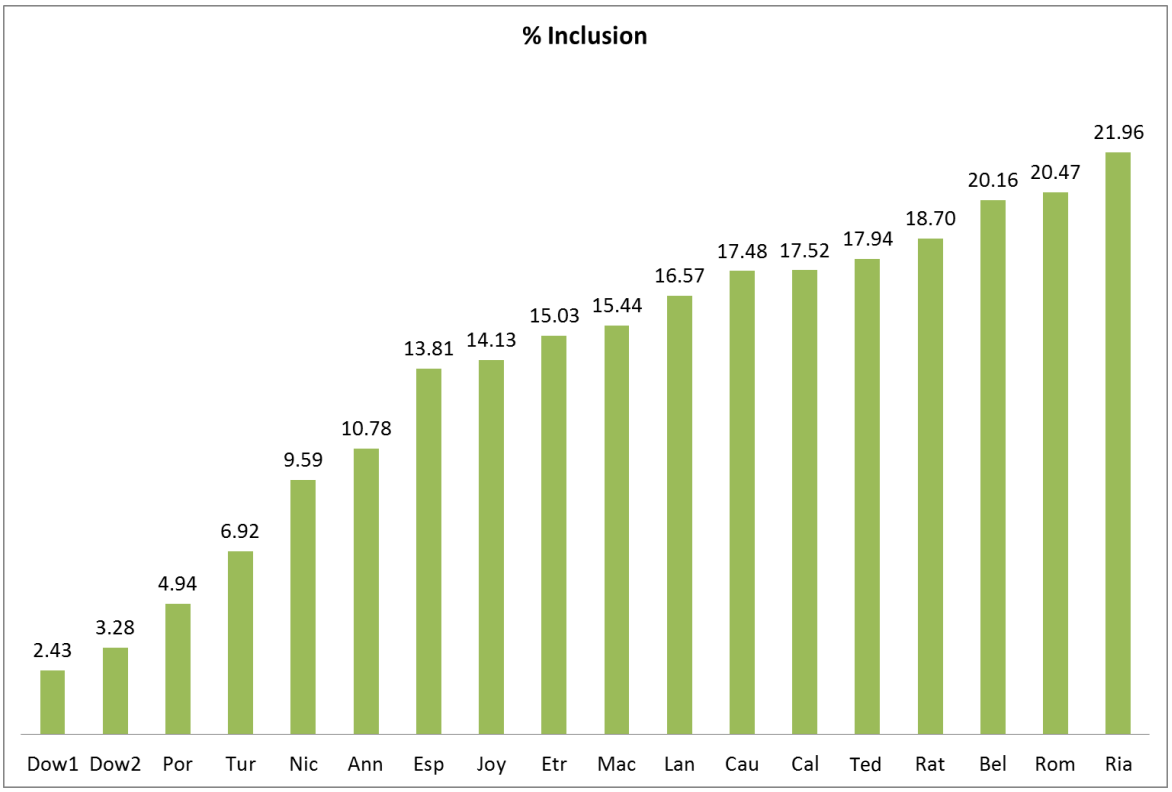

Figure 5.16: % Inclusions (visible) of RHX dating samples, estimated from petrography image analysis.

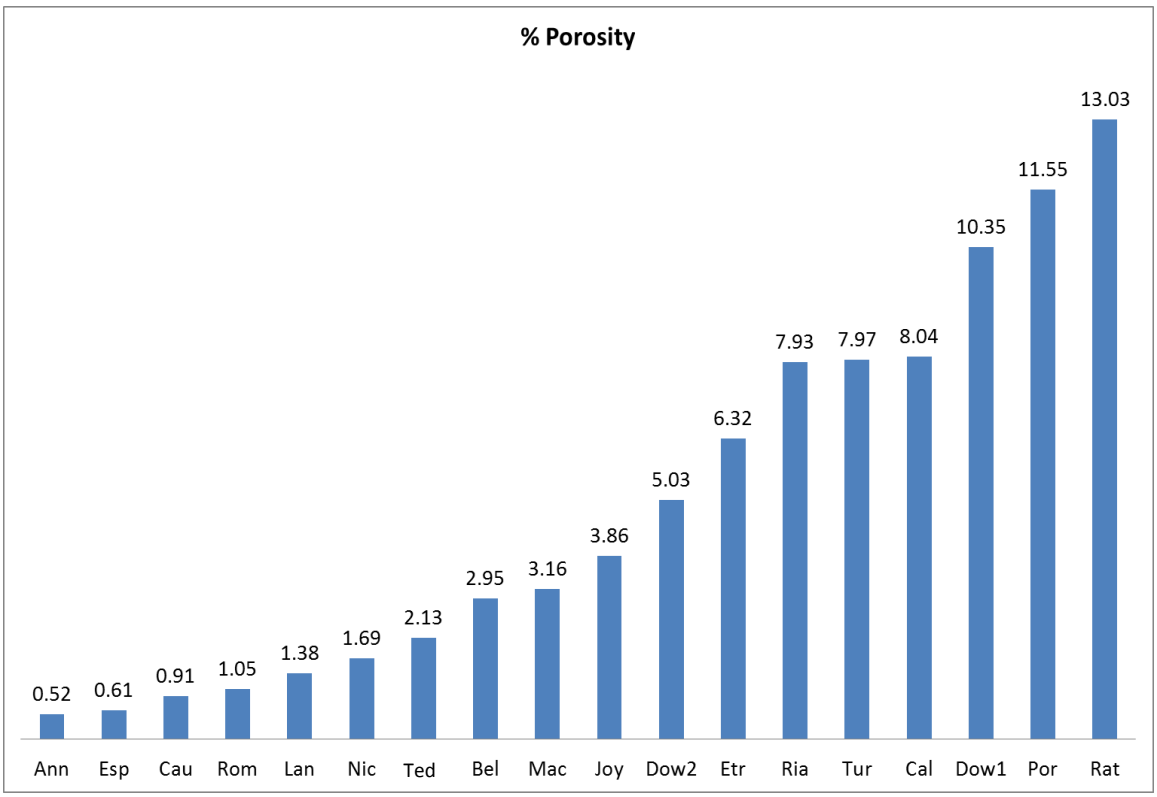

Figure 5.17: % Porosity (visible) of RHX dating samples, estimated from petrography image analysis.

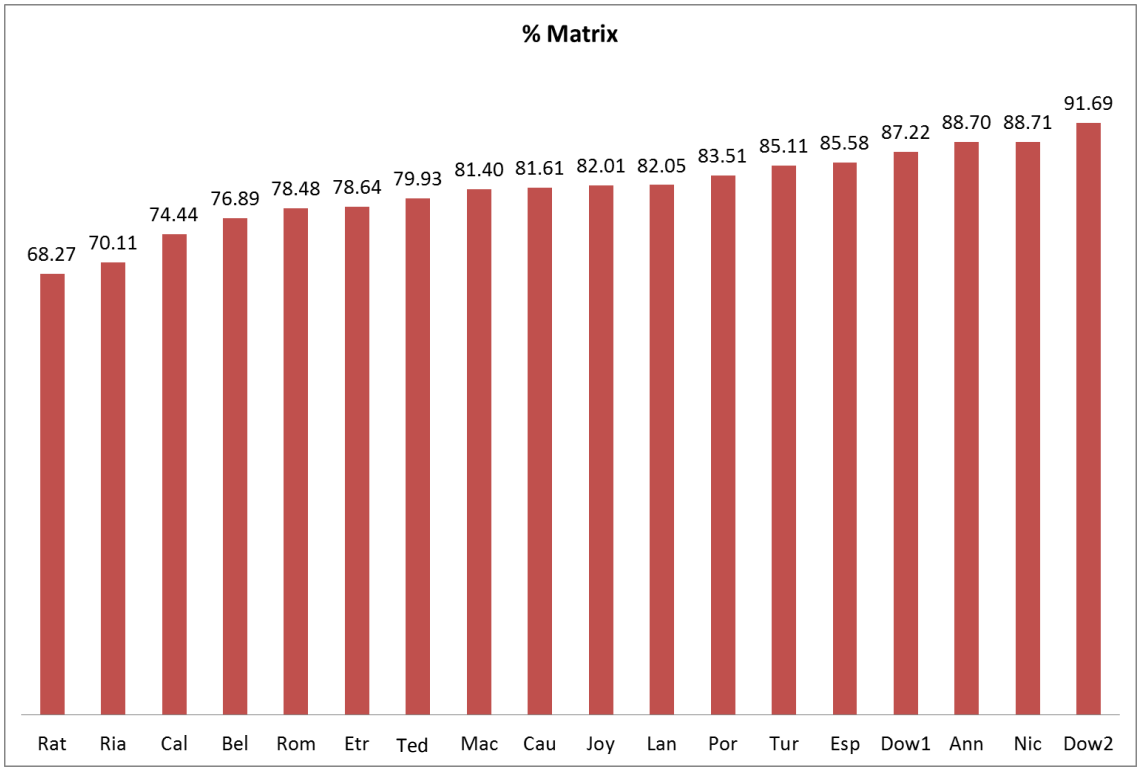

Figure 5.18: % Matrix of RHX dating samples, estimated from petrography image analysis.

Table 5.11: Petrographic notes on firing-related evidence and other points of interest.

Sample	Firing Evidence	Other Notes
Ann	• Thermally altered minerals • Isotropic matrix	• Pores: elongate voids/vughs, typically formied in long cracks or around inclusions • Micaceous clay? • Micritic calcite, possibly recrystallised
Esp	• Isotropic • Thermally altered minerals (including mica)	• Some large sand added • Micaceous clay? • Basaltic rock fragments • Possible micritic calcite in pores, but not certain
Nic	• Significant vitrification • Bloating • Very isotropic matrix • Blotched olive appearance (breakdown of calcareous clay? Quinn (2013, p. 191))	• Mineral identification difficult due to melting – possible degraded pyroxenes common. • Secondary micritic calcite in pores
Mac	• Degraded minerals • Very isotropic matrix • Vitrification & bloating • Possible biotite breakdown	• Bimodal: (1) fine sandy/silty clay matrix with (2) larger rounded sand temper • Possible precipitated gypsum. • No calcite evident
Ria	• Degraded feldspars/micas • Isotropic • Bloating & vitrification	• Poorly mixed heterogeneous clay • Calcite present
Etr	• Moderately active matrix • Calcite/limestone breakdown • No bloating or other mineral degradation	• Limestone tempered with some rock fragments > 1mm • Calcite appears primary – in mineral chunks
Rom	• Fossils/shell look dull/degraded but there is some 'fresh' looking calcite. • Optically moderately active	• Fossiliferous marl • Shell fragments • Igneous rock fragments • Quartzite
Por	• Isotropic • Black/brown isotropic pellets with diffuse boundaries – olive blotches – calcareous breakdown • Possible diopside • Possible cristobalite • Inactive biotite	• Cristobalite? • V. fine well-sorted (calcareous) clay • Feldspars too fine to determine type
Rat	• Degraded calcite • Possible cristobalite • Quite isotropic • Slight melting/vitrification • Slight bloating	• Appears to have some rounded calcite-like pellets of 0.16-0.32mm • Rich in very angular crushed quartz/feldspar temper

		• Dense network of micro channels
Cal	• Isotropic • Bloating/melting • Degraded feldspar/minerals • Olive blotching	• Sand/Sandstone temper • Calcite present both primary and secondary (micritic)
Lan	• Degraded calcite/pyroxene • Optically active (because of mica?) • No bloating	• Sand tempered mica rich clay • Secondary micritic calcite
Joy	• Feldspar melting • Pyroxene alteration • Calcined flint? • Moderately isotropic (micas)	• Igneous rock fragment • Sand tempered • Traces of secondary micritic calcite
Cau	• Altered biotite • Moderately Isotropic • Degraded calcite (sparitic/reformed)	• Poorly mixed heterogeneous clay • Microcline rich • Sparitic calcite
Bel	• Possible spinel • Altered pyroxenes/feldspars/biotite • Possible degraded limestone?	• Precipitated gypsum in pores • No obvious calcite
Dow1	• V. isotropic (black smudgey areas) • Altered microcline (reddish)? • Decomposed calcite	• Well-refined calcium rich clay • Micritic calcium quantity hard to visually estimate
Dow2	• Possible thermally altered pyroxenes • Decomposition of calcite (sparitic and micritic remnant)	• Calcium-rich clay
Tur	• V. isotropic with olive blotches and completely black smudges • Minor bloating evidence	• V. mixed clay - highly variegated with bands of silt • Possible micritic secondary calcite
Ted	• Isotropic matrix • Possible spinel • Possible altered pyroxenes/olivine	• Certain secondary micritic calcite in pores • Possibly some primary

5.6 p-XRF

The elemental compositions (quantified using fundamental parameters method) of the non-reheated samples are presented in *Table 5.12* and *Table 5.13*. The reheated compositions were identical (within 1σ uncertainties) and have thus been omitted (for example the reheated sulphur content for *Mac* and *Bel* are 1.51 ± 0.02% and 1.28 ± 0.02%, respectively, as compared to values of 1.51 ± 0.02% and 1.3 ± 0.02% for their respective non-reheated counterparts).

A ranking of samples according to calcium content (CaO) is provided in *Figure 5.19*.

Table 5.12: Elemental composition (%wt.) of samples using p-XRF and fundamental parameter quantification–part 1.

	Ann	Esp	Nic	Mac	Ria	Etr	Rom	Por	Rat
SiO_2	42.20	40.10	36.80	47.00	47.50	38.80	42.80	46.20	51.20
TiO_2	1.01	0.94	0.77	1.03	0.98	0.75	0.68	0.70	0.77
Al_2O_3	10.2	10.60	10.40	8.54	9.74	11.20	10.80	7.92	7.57
Fe_2O_3	7.40	7.54	6.60	6.36	6.92	6.69	5.88	3.79	4.71
MnO	0.13	0.14	0.11	0.05	0.11	0.16	0.09	0.11	0.077
MgO	4.59	4.07	6.36	4.07	3.77	1.48	3.63	4.08	2.77
CaO	3.80	7.13	9.90	2.93	1.04	9.72	6.42	9.40	1.80
K_2O	3.31	3.16	3.31	2.67	3.01	2.39	2.29	2.41	2.07
P_2O_5	0.21	0	0.25	0	0.17	0.34	0	0.46	0.19
S	0	0	0	1.51	0	0	0	0	0
Cl	0.002	0.01	0.007	0	0	0.008	0.002	0.055	0

Table 5.13: Elemental composition (%wt.) of samples using p-XRF and fundamental parameters quantification–part 2.

	Cal	Lan	Joy	Cau	Bel	Dow1	Dow2	Tur	Ted
SiO_2	49.80	37.40	49.10	51.50	49.30	26.10	32.60	60.50	49.40
TiO_2	0.84	0.89	1.31	1.23	1.09	0.64	0.67	0.61	1.32
Al_2O_3	9.57	9.50	11.30	11.60	10.50	7.83	10.40	8.28	12.20
Fe_2O_3	5.75	7.03	8.45	7.22	7.29	5.05	6.13	3.16	7.58
MnO	0.08	0.12	0.15	0.05	0.05	0.22	0.18	0.012	0.09
MgO	0.09	4.50	4.15	1.18	2.25	3.95	5.99	2.63	3.65
CaO	5.53	4.50	0.59	0.79	2.25	14.60	15.40	0.61	0.53
K_2O	2.55	3.03	2.37	1.93	2.10	3.42	3.86	2.68	2.82
P_2O_5	0.18	0	0.16	0.14	0.16	0.39	0.53	0	0.13
S	0	0	0	0	1.30	0	0	0	0
Cl	0	0.0128	0	0.0171	0	0.0161	0.0266	0	0

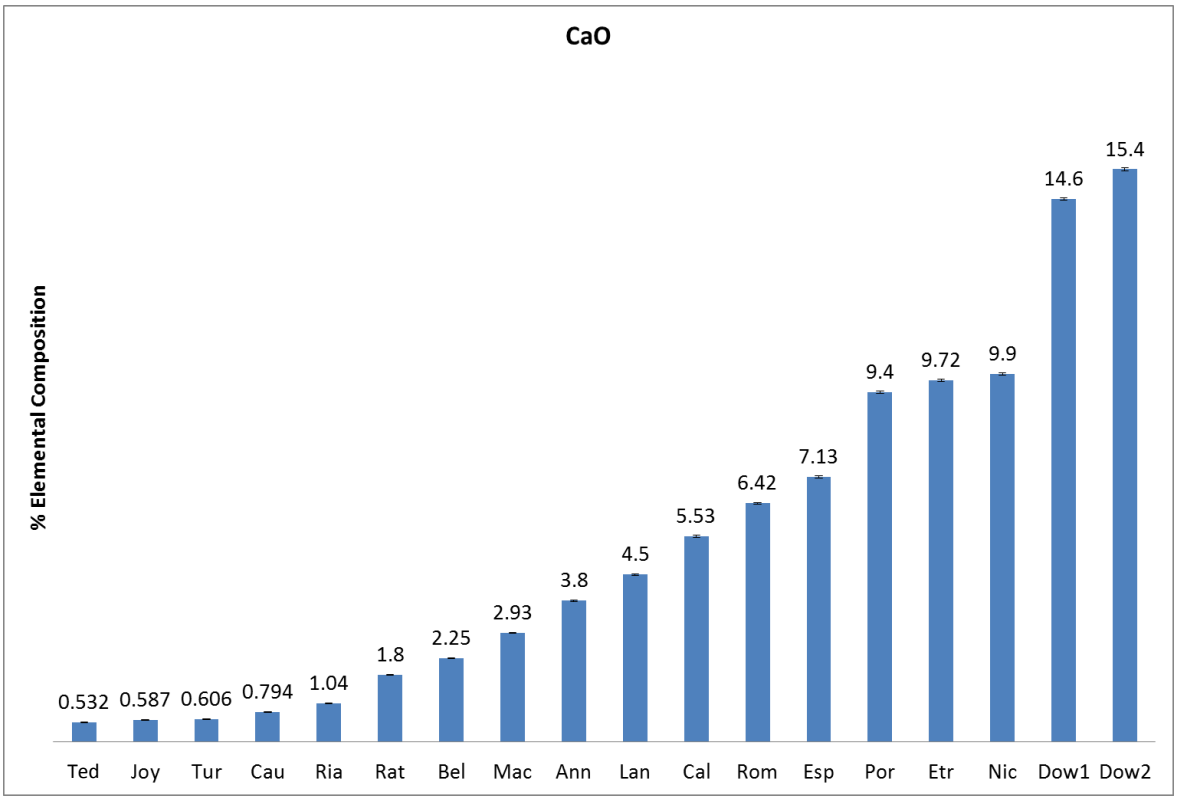

Figure 5.19: Calcium (oxide) content (%wt) of RHX dating samples from p-XRF analysis. Error bars (1σ) included.

5.7 Permeametry

The results of probe permeametry are presented in *Table 5.14*. The results were not particularly uniform; it can be observed from the standard deviation that there is quite a large variation across the 10 measurements conducted. Samples *Dow1,* and *Dow1* had permeability values too low to be measured with this technique (>20 minutes holding time with no sign of measurement completion) and *Lan* was borderline, permitting only two measurements to be conducted. Also not enough material was available for multiple runs on *Rom* and *Cau*.

A ranking of the permeability is provided in *Figure 5.20* below.

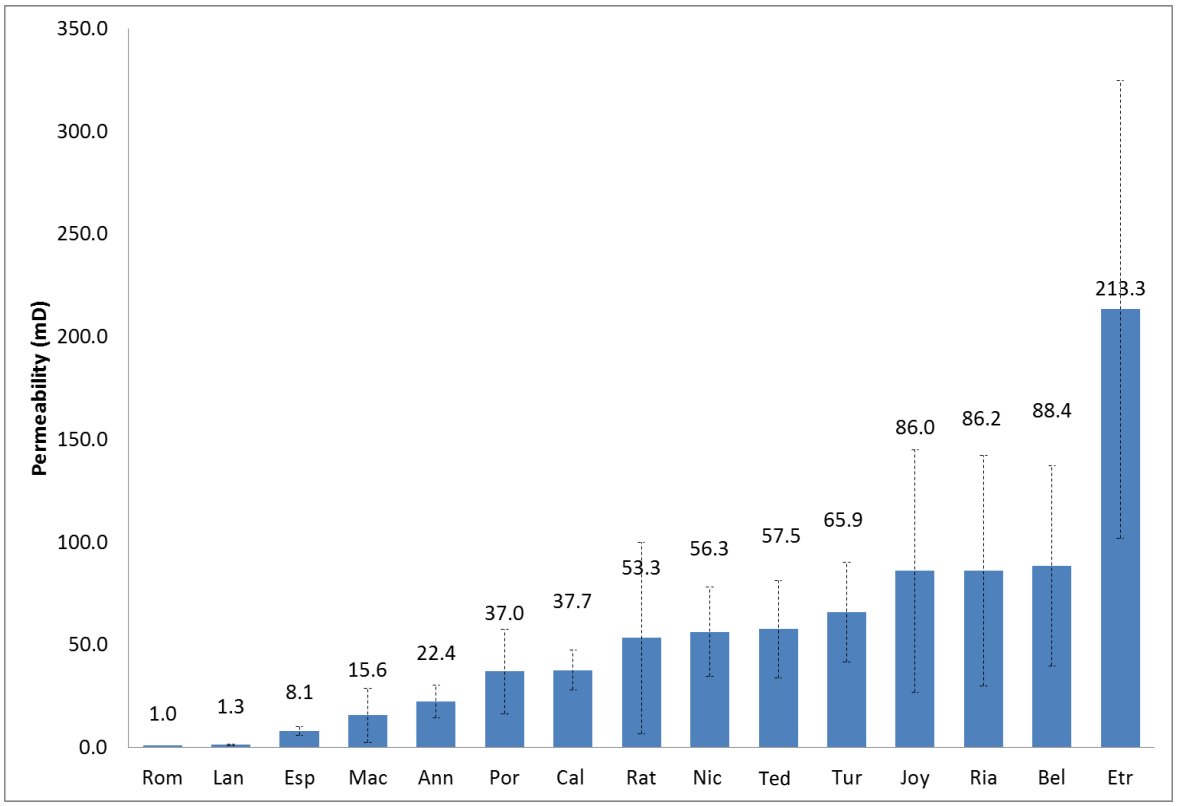

Figure 5.20: Probe permeametry results for samples (error bars (1σ) included). Note that *Rom* and *Lan* are based on only 1 and 2 measurements, respectively, due to shortages of material (*Rom*) and long (>20min) holding times.

Table 5.14: Probe permeametry analysis results.

Sample	Permeability (mD)	Std. Dev. (mD)	No. of Measurements	Notes
Ann	22.4	7.8	10	
Esp	8.1	2.1	10	
Nic	56.3	21.8	10	
Mac	15.6	13.2	10	
Ria	86.2	56.1	11	
Etr	213.3	111.4	12	
Rom	1.0		1	Not enough sample for multiple measurements
Por	37.0	20.7	10	
Rat	53.3	46.6	12	
Cal	37.7	9.6	10	
Lan	1.3	0.5	2	>20 min
Joy	86.0	58.9	10	
Cau				Not enough sample
Bel	88.4	48.6	12	
Dow1				>20 min
Dow2				>20 min
Tur	65.9	24.3	10	
Ted	57.5	23.5	10	

5.8 BET

The specific surface area determinations (using BET and BJH theory) are presented in *Table 5.15*.[1] Ranking of the samples based on BET S.A. is shown in *Figure 5.21*. Example nitrogen adsorption/desorption curves are presented in *Figure 5.22,* with the remainder included in *Appendix F.*

Complete analysis of *Rat* and *Tur* was not possible due to issues with poor nitrogen adsorption because of very low surface areas (to a lesser extent the sorption curves of *Cal* and *Joy* are also less well behaved due to low surface areas).

BJH analysis of pore volume and pore size is presented in *Table 5.16*, with sample ranking based on pore volume and pore width provided in *Figure 5.23* and *Figure 5.24,* respectively.

Table 5.15: Surface area results based on BET nitrogen sorption. BJH results calculated for adsorption and desorption curves.

	Specific Surface Area (m^2/g)		
	BET (S.A)	**BJH S. A. (adsorption)**	**BJH S. A. (desorption)**
Ann	1.05	0.74	0.56
Esp	2.12	1.51	1.14
Nic	1.19	0.77	0.45
Mac	1.36	1.04	1.09
Ria	0.48	0.28	0.20
Etr	14.73	14.52	16.71
Rom	5.21	3.67	6.40
Por	14.87	12.56	15.57
Rat	-	-	-
Cal	0.32	0.06	0.09
Lan	24.25	25.57	46.72
Joy	0.43	0.11	0.13
Cau	6.14	5.16	5.03
Bel	3.64	3.02	2.89
Dow1	16.33	15.10	19.62
Dow2	15.51	13.28	18.59
Tur	0.09	-	-
Ted	0.95	0.31	0.28

[1] A plot of the BET surface area and the BJH surface area results in $R^2 = 0.99$, showing that they are very highly correlated; henceforth, it is the BET surface area that is used in discussions involving the surface area.

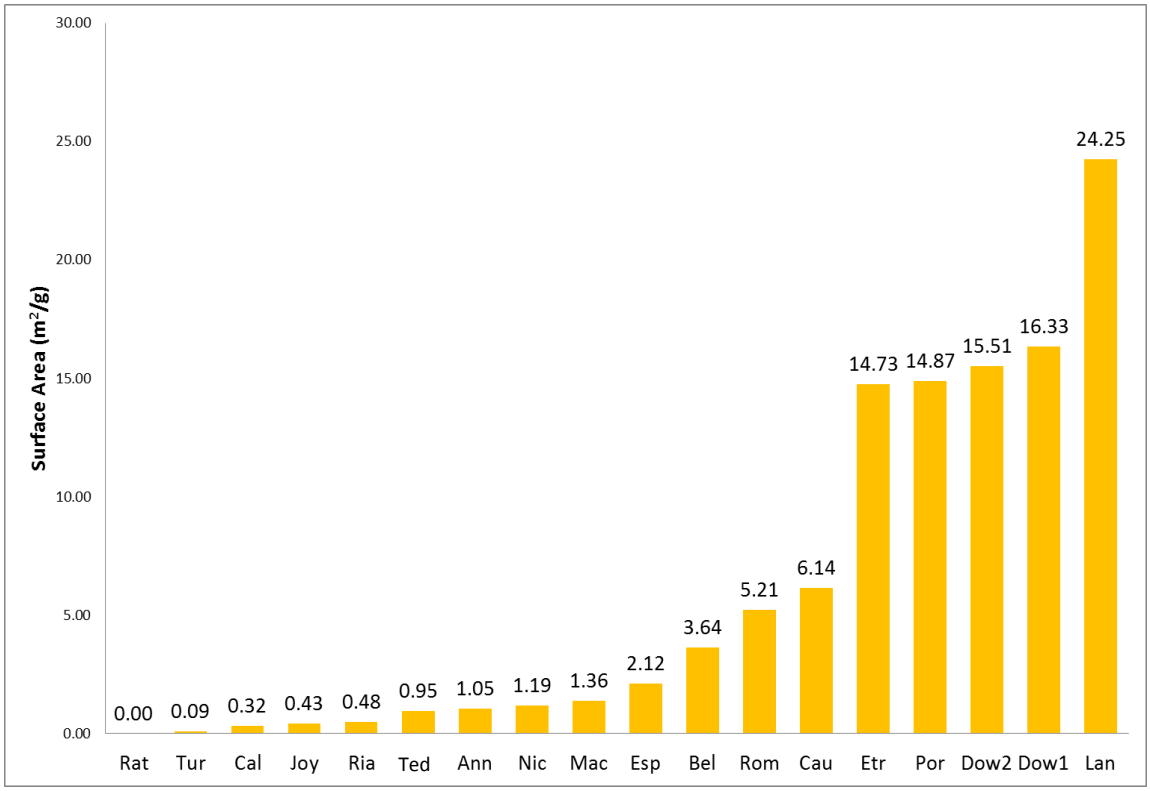

Figure 5.21: BET surface areas of samples. Value of 0.0 for *Rat* corresponds to null result.

The sorption curves displayed two clear types of behaviour (aside from *Rat* and *Tur* for which complete curves could not be obtained): adsorption and desorption curves that display a clearly defined hysteresis, as shown in *Figure 5.22 (a)* for sample *Etr*; and curves that display no clearly defined hysteresis, *Figure 5.22 (b)* for sample *Esp*. The former behaviour was observed for samples *Etr, Rom, Por, Lan, Dow1/2*, and to much lesser extent *Cau* (possibly *Bel* also), with the latter behaviour observed for the remaining samples (*Rat* and *Tur* excluded, and the curves of *Cal* and *Joy* also poor due to low adsorption levels). All sorption sets display a desorption curve that is at a slightly higher level than the adsorption curve (less easily observed in the high surface area samples). The sorption behaviour will be discussed in *Section 9.2.1.*

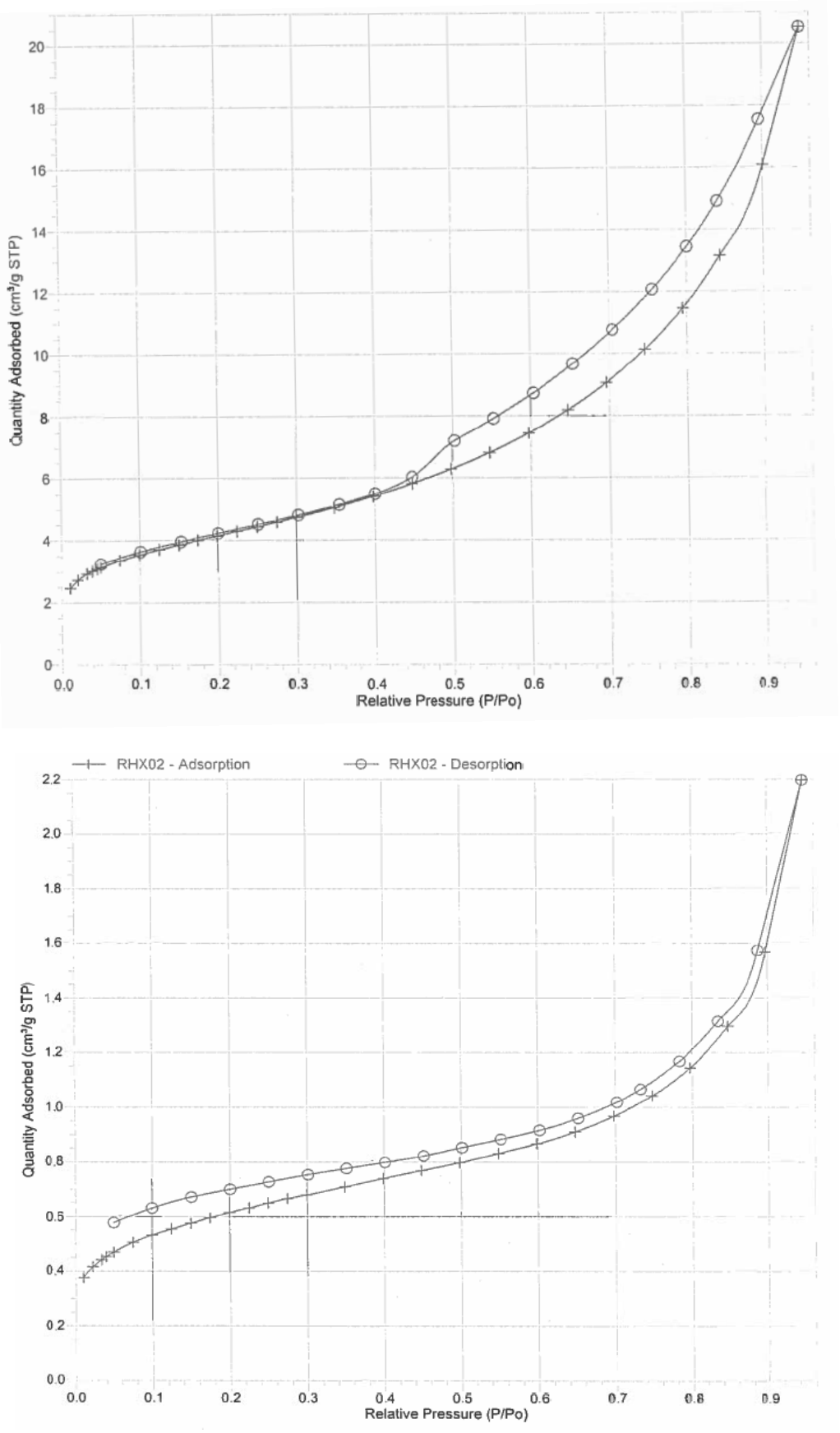

Figure 5.22: Sorption curves of (top) sample *Etr* with high specific surface area (14.73m^2/g) and exhibiting hysteresis effects and (bottom) sample *Esp* with low specific surface area (2.12m^2/g) and not exhibiting this hysteresis effect.

Table 5.16: BJH analysis results for pore volume and pore size of dating samples based on adsorption and desorption curves.

	Pore Volume (cm^3/g)		Pore Size (angstrom)	
	BJH Vol. (adsorption)	BJH Vol. (desorption)	BJH Ads. Av. Pore Width (4V/A)	BJH Des. Av. Pore Width (4V/A)
Ann	0.001339	0.001178	72.09	84.34
Esp	0.003104	0.002782	82.09	97.61
Nic	0.001831	0.001562	94.69	139.66
Mac	0.003477	0.003410	133.68	124.92
Ria	0.000700	0.000635	100.30	124.76
Etr	0.031048	0.032102	85.51	76.86
Rom	0.013111	0.013732	142.94	85.80
Por	0.024141	0.024616	76.86	63.24
Rat	-	-	-	-
Cal	0.000236	0.000389	153.30	182.13
Lan	0.049413	0.050137	77.29	42.93
Joy	0.000426	0.000529	156.67	168.82
Cau	0.013222	0.013051	102.45	103.85
Bel	0.007808	0.007662	103.54	106.12
Dow1	0.047806	0.048831	126.66	99.57
Dow2	0.043380	0.044785	130.62	96.36
Tur	-	-	-	-
Ted	0.001150	0.001074	148.99	153.41

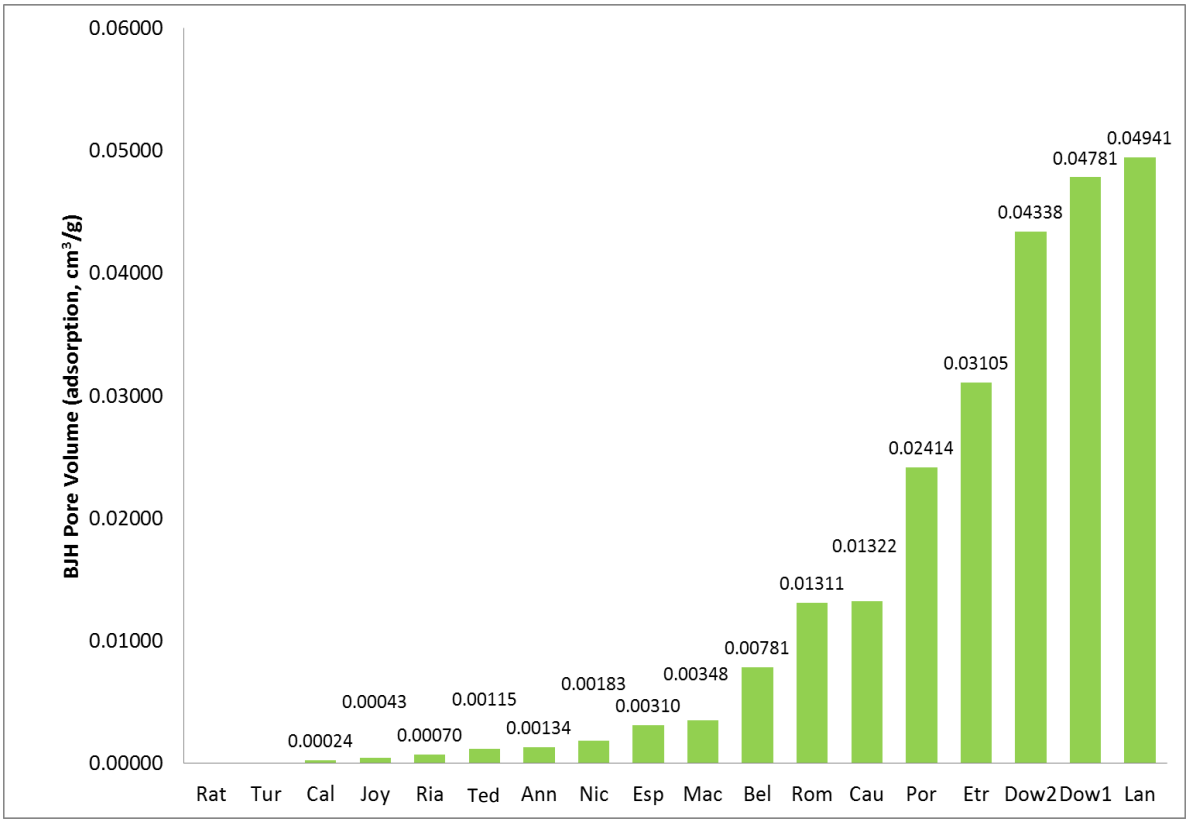

Figure 5.23: BJH pore volume (adsorption) of dating samples. No values could be calculated for *Rat* and *Tur*.

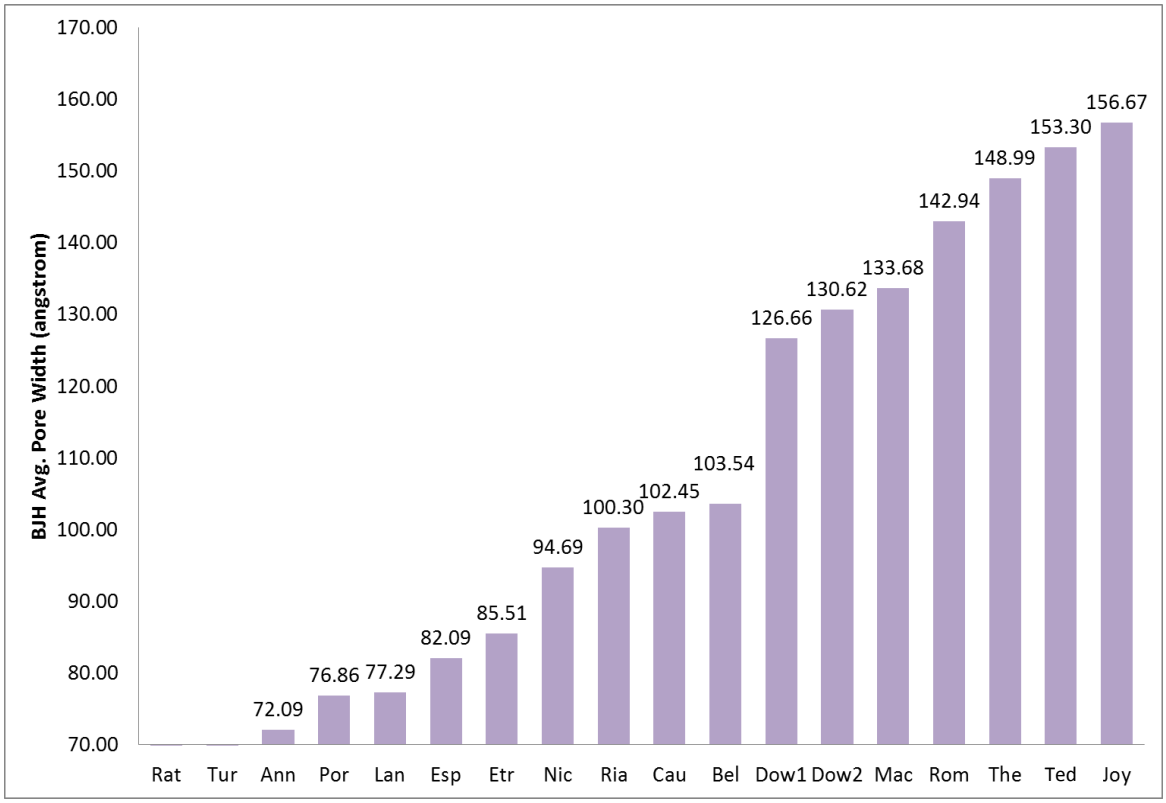

Figure 5.24: BJH average pore width (adsorption) for dating samples. No values could be calculated for *Rat* and *Tur*.

5.9 Carbon Content

The results of carbon content analysis are provided in *Table 5.17* and *Table 5.18*. *Table 5.17* presents the %wt. of carbon combusted (850°C) in sample fractions that were originally dried at 130°C (corresponding to m_{c130+}) and heated at 500°C (corresponding to m_{c500+}, see *Section 4.8*). The difference between these two percentages, presented in *Table 5.18* and ranked in *Figure 5.25*, provides the %wt. carbon (corresponding mass m_c) estimated to be evolved during reheating of samples from 130-500°C as part of the RHX dating procedure adopted in this thesis.

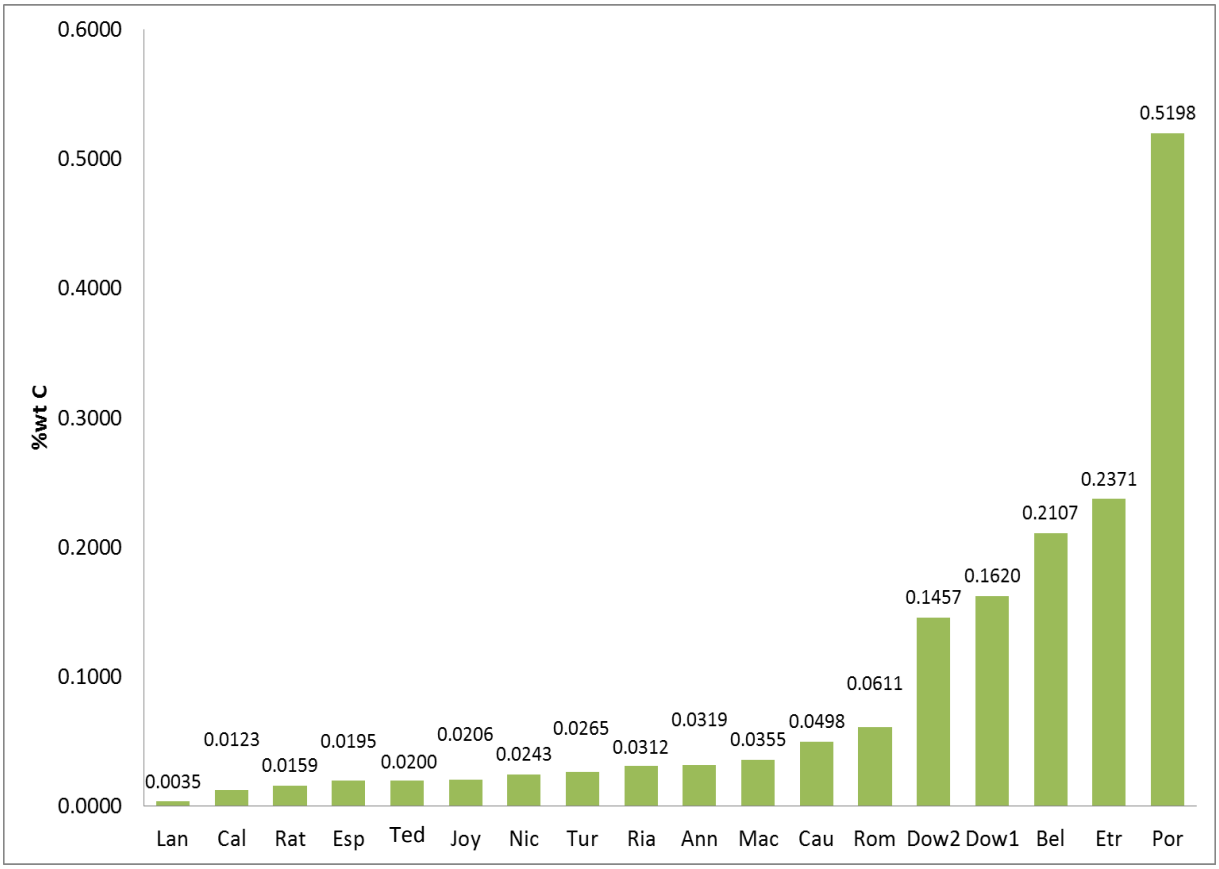

Figure 5.25: Percentage weight of carbon removed from dating samples during firing at 130-500°C.

Table 5.17: Carbon content results for all samples. m_{c500+} = samples pre-heated at 500°C. m_{c130+} = preheated at 130°C.

	Sample Mass (g)	Carb. Cont. (g)	%wt.
Ann m_{c500+}	0.4591	0.000174	0.0379
Ann m_{c130+}	0.5011	0.000341	0.0698
Esp m_{c500+}	0.5138	0.000245	0.0490
Esp m_{c130+}	0.5277	0.000352	0.0685
Nic m_{c500+}	0.5028	0.000962	0.1965
Nic m_{c130+}	0.4936	0.001060	0.2208
Mac m_{c500+}	0.4761	0.000090	0.0189
Mac m_{c130+}	0.581	0.000316	0.0544
Ria m_{c500+}	0.5623	0.000299	0.0531
Ria m_{c130+}	0.5531	0.000467	0.0843
Etr m_{c500+}	0.4681	0.006107	1.3047
Etr m_{c130+}	0.4027	0.006209	1.5418
Rom m_{c500+}	0.4594	0.001691	0.3682
Rom m_{c130+}	0.475	0.002039	0.4292
Por m_{c500+}	0.5554	0.003588	0.6460
Por m_{c130+}	0.4208	0.004906	1.1658
Rat m_{c500+}	0.5437	0.000209	0.0384
Rat m_{c130+}	0.5147	0.000280	0.0543
Cal m_{c500+}	0.5068	0.000406	0.0801
Cal m_{c130+}	0.6698	0.000619	0.0923
Lan m_{c500+}	0.4515	0.001389	0.3076
Lan m_{c130+}	0.5479	0.001704	0.3111
Joy m_{c500+}	0.5325	0.000191	0.0359
Joy m_{c130+}	0.4437	0.000251	0.0565
Cau m_{c500+}	0.3908	0.000471	0.1205
Cau m_{c130+}	0.4788	0.000815	0.1703
Bel m_{c500+}	0.414	0.000107	0.0259
Bel m_{c130+}	0.4896	0.001159	0.2366
Dow1 m_{c500+}	0.4599	0.005583	1.2140
Dow1 m_{c130+}	0.4563	0.006279	1.3760
Dow2 m_{c500+}	0.402	0.007929	1.9725
Dow2 m_{c130+}	0.4701	0.009957	2.1181
Tur m_{c500+}	0.5177	0.000110	0.0213
Tur m_{c130+}	0.4912	0.000235	0.0478
Ted m_{c500+}	0.442	0.000326	0.0738
Ted m_{c130+}	0.4529	0.000425	0.0937

Table 5.18: Percentage weight of carbon removed from samples during heating at 130-500°C (corresponding to m_c)

	%wt C
Ann	0.0319
Esp	0.0195
Nic	0.0243
Mac	0.0355
Ria	0.0312
Etr	0.2371
Rom	0.0611
Por	0.5198
Rat	0.0159
Cal	0.0123
Lan	0.0035
Joy	0.0206
Cau	0.0498
Bel	0.2107
Dow1	0.1620
Dow2	0.1457
Tur	0.0265
Ted	0.0200

To examine if there is any correlation between m_c and the *CaO* content (possible $CaCO_3$ proxy) of the samples, a regression was carried out between the two. This produced a poor correlation with R^2 = 0.20. Similarly, the relationship between m_c and BET S.A. and BJH pore volume produce correlation of R^2 = 0.22 and R^2 = 0.14.

5.10 TG-MS

The full set of TG-MS curves are presented in *Appendix C*. A summary of the TG-MS features observed are presented in *Table 5.19*. To highlight the main heating events described in this table, the TG-MS curves for *Esp* are presented in *Figure 5.26-28*: *Figure 5.26* presents the TG %wt. loss curve during heating together with the 1st derivative used to aid identification of features; *Figure 5.27* presents the mass spectrometry curve (monitored as ion current) for mass 18 (used as a proxy for H_2O) overlaid on the TG curve; *Figure 5.28* presents the MS curve for mass 44 (CO_2), similarly. In *Figure 5.26*, the curve is split into zones, labelled *A-G*. These correspond to approximate temperature regions where particular events are observed across most (but not all) samples (summarised in *Table 5.19*). For *Mac* event *D* is not present. The events are as follows:

A-D: ***H_2O Associated Features***

These occur between 50-500°C.

Event *A* is visible in all samples except *Ted*.

Events *B, C, D* mostly occur in pairs with *B&D* most common.

A: *50-100°C* – mass loss in TG curve associated with H_2O removal in MS curve.

B: *100-180°C* – mass loss in TG curve associated with H_2O removal in MS curve.

C: *210-280°C* – mass loss in TG curve associated with H_2O removal in MS curve.

D: *300-380°C* – mass loss in TG curve associated with H_2O removal in MS curve.

E-G: ***CO_2 Associated Features (see Discussion)***

These features occur over the region 200-800°C.

200-600°C – organic carbon.

550-800°C – inorganic carbon (calcium carbonate related).

E: *200-300°C* – onset of organic CO_2 mass loss.

F: *400-500°C* – organic CO_2 peak ('increasing' implies peak not clear due to overlap with inorganic peak.

G: *600-750°C* – inorganic CO_2 peak (calcite).

Of note were several observations:

1) Events related to water loss above 110°C (adsorbed, chemisorbed, RHX) are generally very broad features and lack clear sharp boundaries.
2) Very low intensities of *Event A* for *Rat* and *Tur* (and hard to even discern for *Ted*) were observed.
3) A split in *Event G* into two regimes, 570-660°C and 710-750°C, is apparent, the latter regime occupied by sample *Etr, Rom, Por, Dow1, Dow2*. Samples *Nic* and *Bel* at 690°C and 680°C appear intermediate between the two.
4) All samples had loss of organic carbon.
5) No inorganic carbon peak was observed for *Mac.*
6) The presence of SO_2 was observed for *Mac* and *Bel* with SO_2 removal occurring above 650-700°C.

Table 5.19: Summary of TG-MS analysis. Significant peaks (corresponding to events *A-D*) where weight loss is attributed to H_2O loss are colour coded according to strength of visible structure (all numbers are in °C). Onset of organic CO_2 mass loss (event *E*) and organic CO_2 maximum (event *F*) are included ('increasing' implies no clear peak and overlap with inorganic calcite-related peak) together with position of inorganic carbon (calcite-related) peak (event *G*). The presence/absence of SO_2 removal is also provided.

	H_2O peaks (yellow = weak, orange = medium, red =strong)				CO_2 onset	Organic CO_2 max.	Inorganic CO_2 max.	SO2 (a=absent; p=present)
Event	***A***	***B***	***C***	***D***	***E***	***F***	***G***	
Ann	70	130	-	310	250-300	450-500	620	a
Esp	60-70	110	260-270	-	250-300	increasing	610-620	a
Nic	50	-	210-230	-	250-300	400	690	a
Mac	90	-	-	310-320	200-250	410-420	trace	p
Ria	50	120-160	-	320-330	250-300	450-500	610-620	a
Etr	90	-	240	-	200-250	increasing	730-740	a
Rom	90-100	-	230-240	-	250-300	450-500	740-750	a
Por	60-70	-	-	310-340	250-300	increasing	710-720	a
Rat	60	160-170	-	350	250-300	450-500	600-610	a
Cal	60	140	-	340-350	300-350	430-450	630-640	a
Lan	90	-	210	350-400	300-350	increasing	640-650	a
Joy	60	150	-	310-320	250-300	-	630	a
Cau	70	130-140	270-280	-	250-300	450-500	640-650	a
Bel	90-100	-	250-300	-	230-250	480	680	p
Dow1	80-90	-	200-250	340-390	250-300	370	730-740	a
Dow2	95-110	-	-	350-400	250-300	480-530	750	a
Tur	60-70	140-160	-	310-330	250-300	450-500	570-580	a
Ted	-	170-180	-	290-310	270-300	450	650-670	a

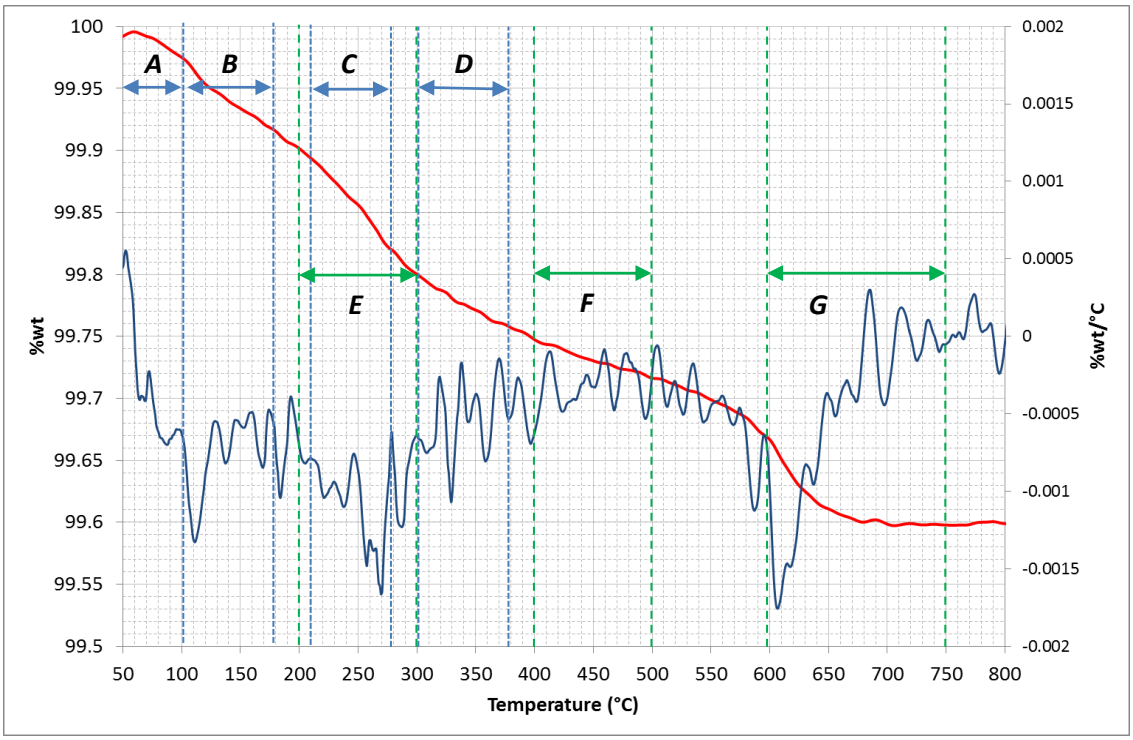

Figure 5.26: TG mass loss curve (red) and first derivative curve (blue) for *Esp*. Regions *A*-*G* follow those described in the text.

Figure 5.27: TG mass loss curve (red) and mass 18 (H_2O) mass spectrometry curve (blue) for *Esp*. Events *A*, *B* and *C* marked. Position of event *B* is based on strong derivative at 110°C in *Figure 5.26*.

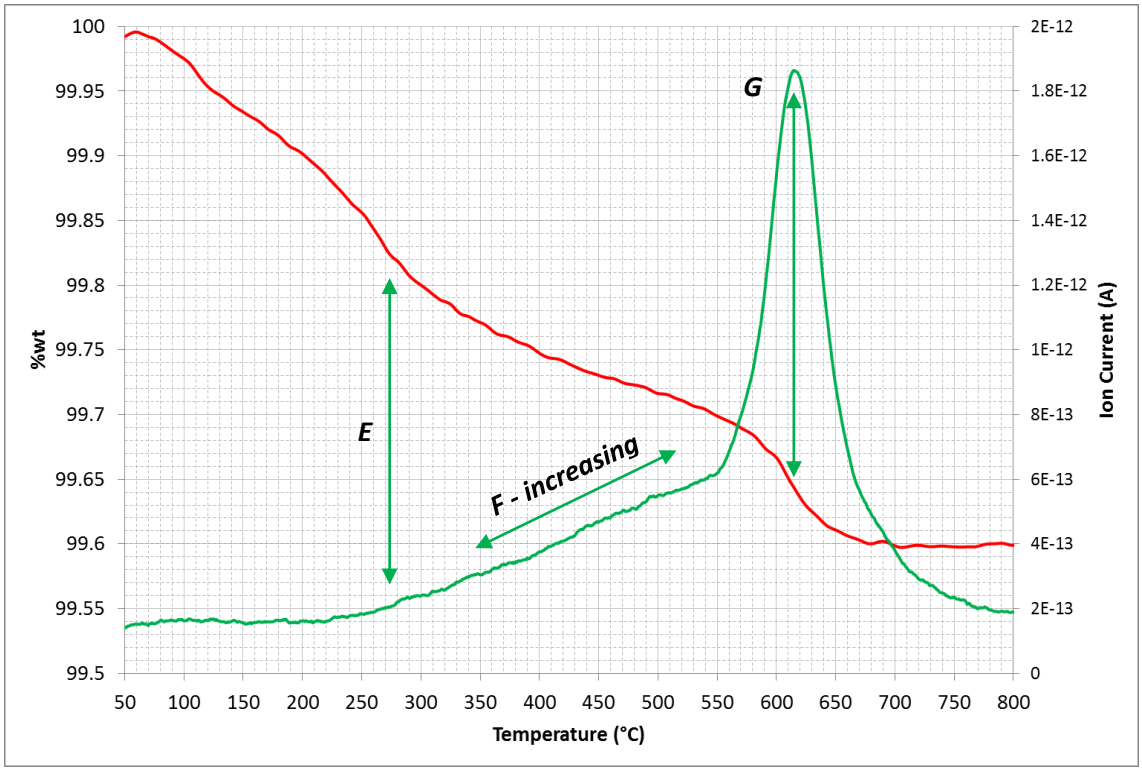

Figure 5.28: TG mass loss curve (red) and mass 44 (CO_2) mass spectrometry curve (green) for *Esp*. Events *E-G (see text)* are highlighted.

The mass loss (%wt) over various temperature regimes are presented in *Table 5.20*. Also included are the %wt loss over 130-500°C with the %wt carbon content estimate (*Section 5.9*) removed. Some ratios of interest, i.e. %wt loss carbon/total %wt loss (130-500°C, TG-MS), are also included.

The ranking of the samples based on %wt loss over 50-130°C and 130-500°C are presented in *Figure 5.29* and *Figure 5.30,* respectively. Then, in *Figure 5.31,* the ratio of H_2O derived %wt loss between the 50-130°C temperature range and the 130-500°C temperature range (achieved by subtracting the %wt carbon from the latter) is displayed for all samples. To examine the correlation between the water loss below 130°C and between 130-500°C the %wt loss in these regimes (with %wt C removed for the latter) were plotted against one another and a linear regression carried out, *Figure 5.32*. This shows a strong correlation with $R^2 = 0.87$.

The percentage ratio of the %wt C to the %wt loss over 130-500°C is presented in *Figure 5.33* with values ranging from 0.33% for *Lan* to 39% for *Por*.

The relationship between the BET S.A. and the TG %wt loss over 50-130°C is presented in *Figure 5.34,* showing a high correlation, R^2 = 0.90.

Table 5.20: TG analysis of %wt loss over various temperature ranges. Includes %wt loss with %wt carbon from carbon content analysis removed where indicated.

	%wt Loss TG						
	50-130°C	**130-200°C**	**200-500°C**	**130-500°C**	**130-500°C (*less %wt C*)**	**(%wt C/%wt loss (130-500°C)) x 100**	**%wt(50-130°C) /%wt(130-500°C) (*less %wt C*)**
Ann	0.018	0.036	0.185	0.221	0.190	14.419	0.097
Esp	0.045	0.045	0.185	0.230	0.211	8.466	0.213
Nic	0.089	0.146	0.402	0.548	0.524	4.428	0.171
Mac	0.222	0.054	0.323	0.377	0.341	9.421	0.651
Ria	0.026	0.043	0.337	0.379	0.348	8.242	0.074
Etr	0.761	0.437	1.726	2.163	1.926	10.959	0.395
Rom	0.353	0.214	0.807	1.022	0.961	5.977	0.368
Por	0.548	0.235	1.089	1.324	0.804	39.263	0.682
Rat	0.007	0.024	0.183	0.207	0.191	7.708	0.035
Cal	0.024	0.046	0.218	0.263	0.251	4.671	0.094
Lan	0.467	0.259	0.812	1.071	1.067	0.326	0.437
Joy	0.040	0.052	0.322	0.374	0.353	5.503	0.114
Cau	0.107	0.104	0.368	0.472	0.423	10.547	0.254
Bel	0.290	0.117	0.472	0.589	0.378	35.790	0.767
Dow1	0.707	0.372	1.265	1.637	1.475	9.893	0.479
Dow2	0.657	0.397	1.599	1.996	1.851	7.297	0.355
Tur	0.015	0.033	0.276	0.308	0.282	8.603	0.053
Ted	0.039	0.072	0.302	0.374	0.354	5.336	0.110

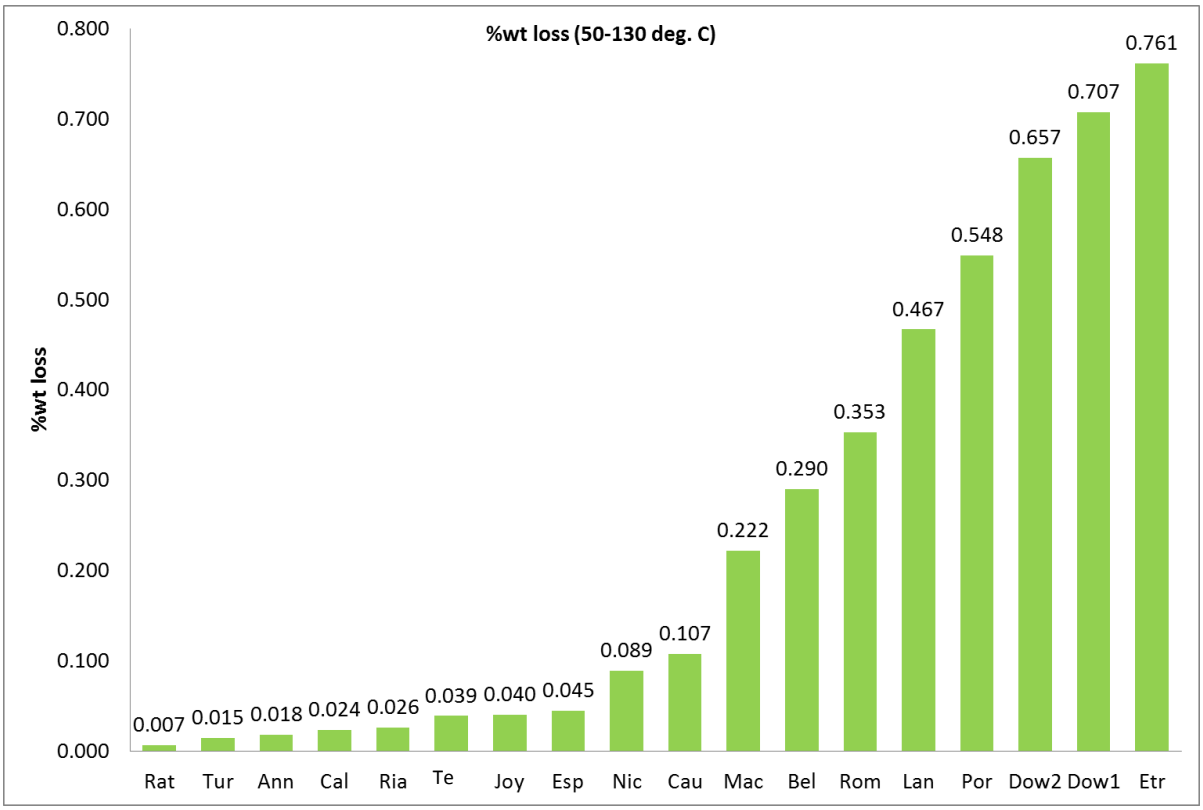

Figure 5.29: TG-MS %wt loss over the temperature range 50-130°C for dating samples.

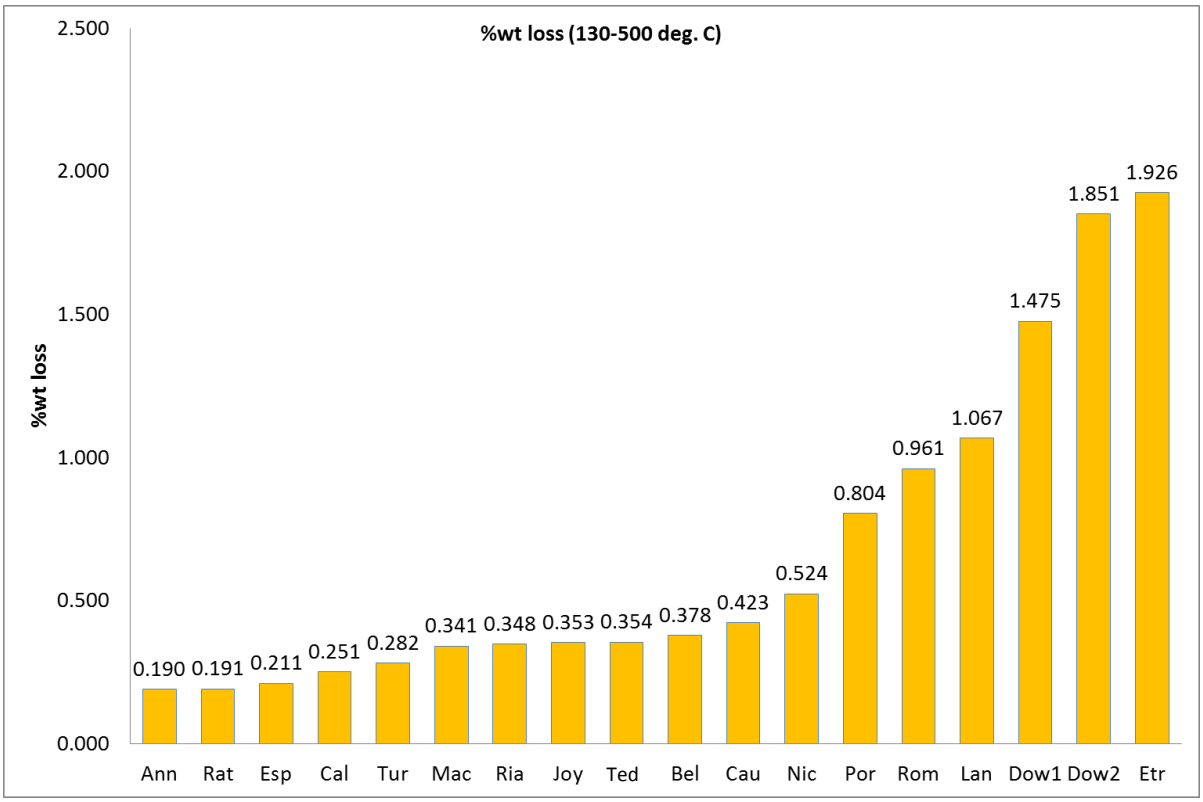

Figure 5.30: TG-MS %wt loss over the temperature range 130-500°C for dating samples. %wt carbon has been subtracted.

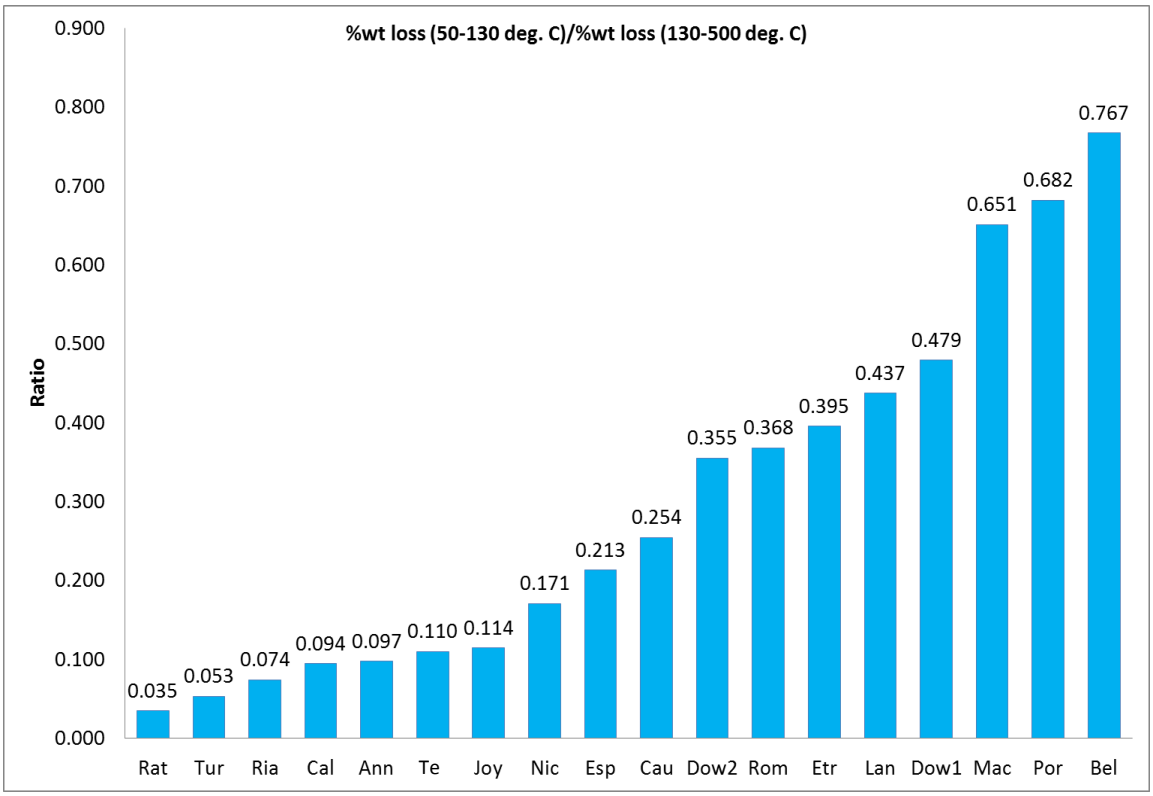

Figure 5.31: Ratio of H_2O derived %wt loss between 50-130°C and 130-500°C (%wt C removed).

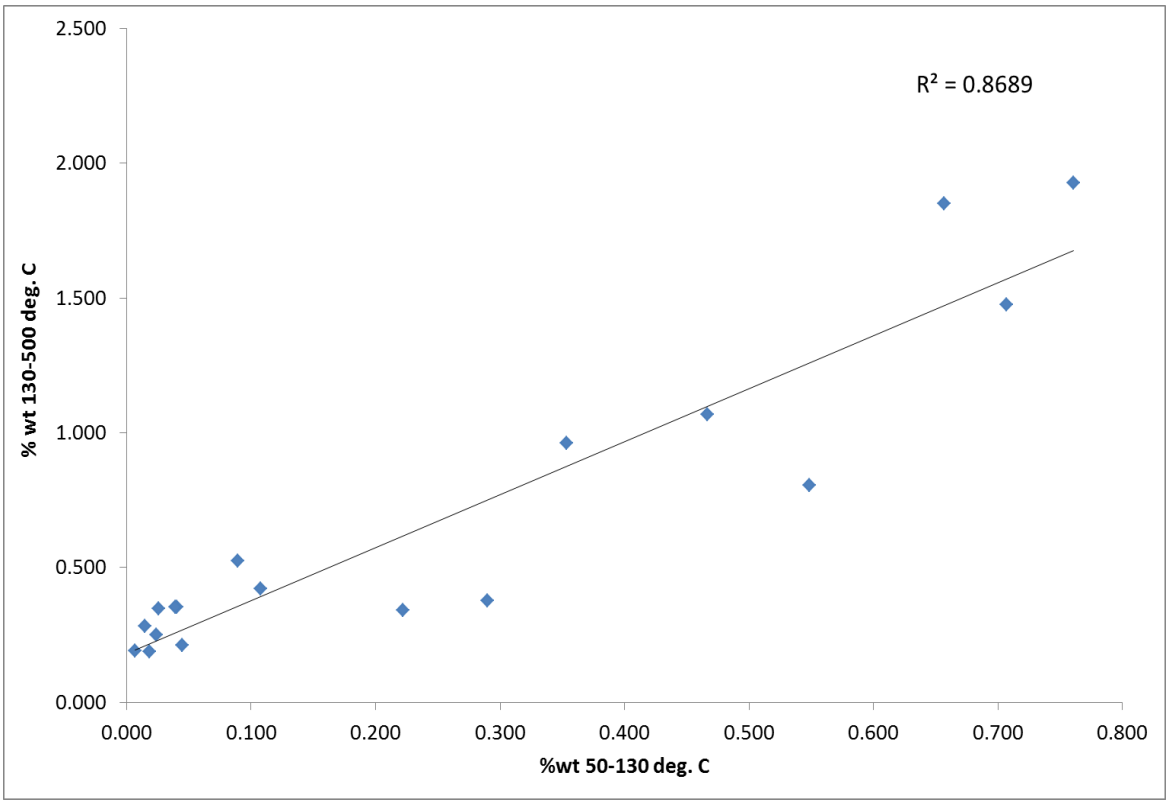

Figure 5.32: %wt loss over the range 50-130°C versus % wt loss over the range 130-500°C (% wt C removed). These %wt loss values are attributed to H_2O removal.

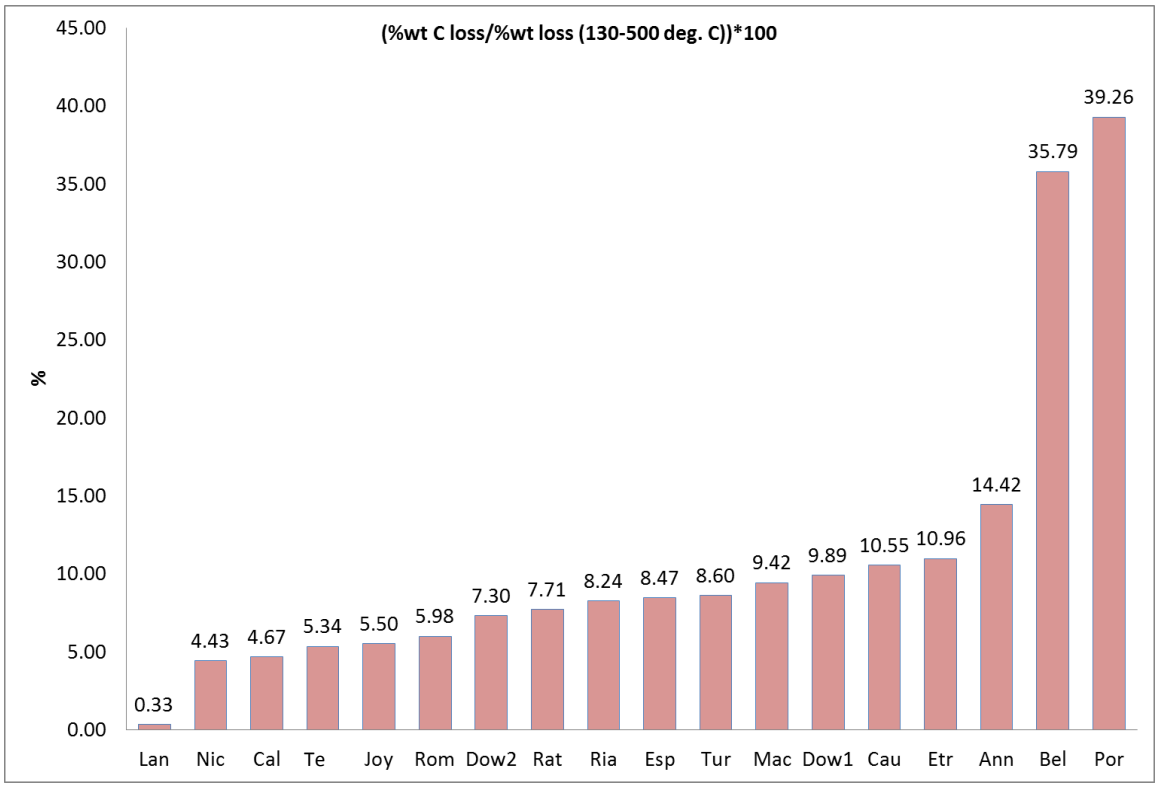

Figure 5.33: % of wt loss over the range 130-500°C that can be attributed to carbon loss.

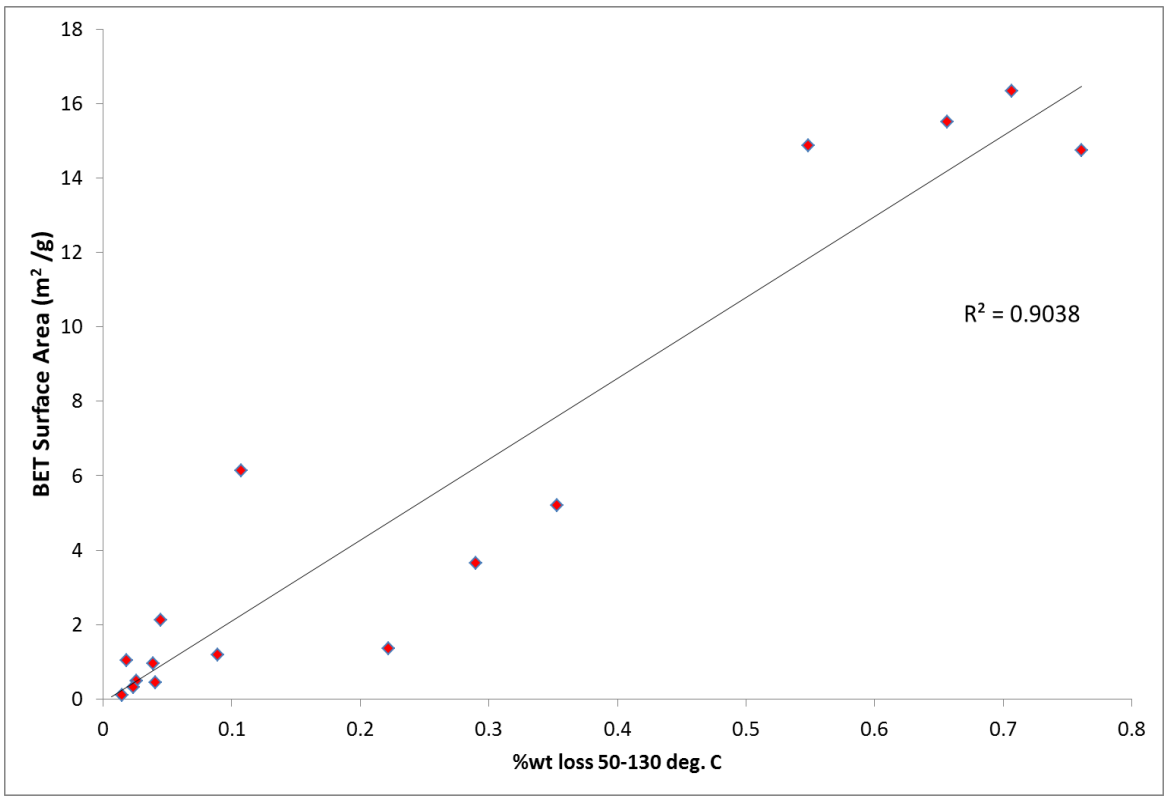

Figure 5.34: %wt loss over the temperature range 50-130°C versus BET surface area. Samples Rat and Lan are not included as the former produced no S. A. value and the latter was considered an outlier (very high S.A. values outside the range considered reliable with BET analysis).

Chapter 6

Experimental Method – RHX Behaviour & Dating

6.1 Overview

6.1.1 Experiment Summary

This chapter provides a detailed description of experiments used to examine the mass gain behaviour of fired clay ceramics, validate key properties required for archaeological dating, and to test the application of the RHX method to dating samples of known age. An outline of the method is now provided with the detailed procedure presented in subsequent sections.

For both validation and dating, eighteen samples of varied ages and contexts were selected. They included a mix of post-medieval pottery and bricks, as well as pieces of Roman tile and Etruscan pottery. Each sample had 3 subsamples, in granulated form, prepared for the application of mass gain tests and the dating approach described in *Section 3.6 (component based approach)*. Samples were dried at 130° to remove any loose water. The subsamples were each placed in different environmentally controlled cabinets (ECC) at three aging temperatures 25°C, 35°C, 45°C, where they gained mass under constant (75%) relative humidity conditions. Periodic measurement of the mass gain was carried out via transfer of the samples between the ECCs and an RH and temperature controlled glove box arrangement (GBA) with top-loading analytical balance. Before placement in the ECC, following drying (and reheating at 500°C) the 25°C subsample of each sample was weighed in the GBA, for a duration of 6-8 hours to record the *S1* behaviour, and then transferred to its ECC for subsequent mass gain and periodic measurements.

The samples were then reheated in a furnace at 500°C and, as followed the 130°C drying stage, the subsequent mass gain of the three samples aging at different temperatures was monitored using the glove box arrangement. Note that all

samples were allowed to cool in desiccated conditions following drying/reheating before being exposed to air in GBA or ECC cabinet container conditions.

The mass gain curves of both the 130°C stage and the 500°C stage were analysed using a $t^{1/4}$-based approach and a $t^{1/n}$-based approach with key properties, for example the fractional mass gain rate and activation energy, assessed.

Estimates were carried out of various sources of additional non-RHX mass loss, for example organic matter removed during firing and possible moisture not removed during initial 130°C heating. Using temperature histories, constructed for each sample with instrumental and proxy records, together with mass gain properties obtained from modelling of the mass gain curves, simulations were written to generate the lifetime mass gain of the ceramics and to estimate an effective lifetime temperature values that accounted for the effect of annual surface air temperature cycles.

The ages and age ranges of the samples were estimated for a range of ELTs and the effect of particular sources of error and uncertainty (OM/OC ratio, activation energy (AE) uncertainty, short-term elevated temperature events) were considered.

Finally, an illustrative example of the application of the activation energy temperature history (*AETH*) approach was carried out on a single sample, *Joy*.

Below, in *Figure 6.1*, is a diagram of the methodological stages, described in detail in the following sections.

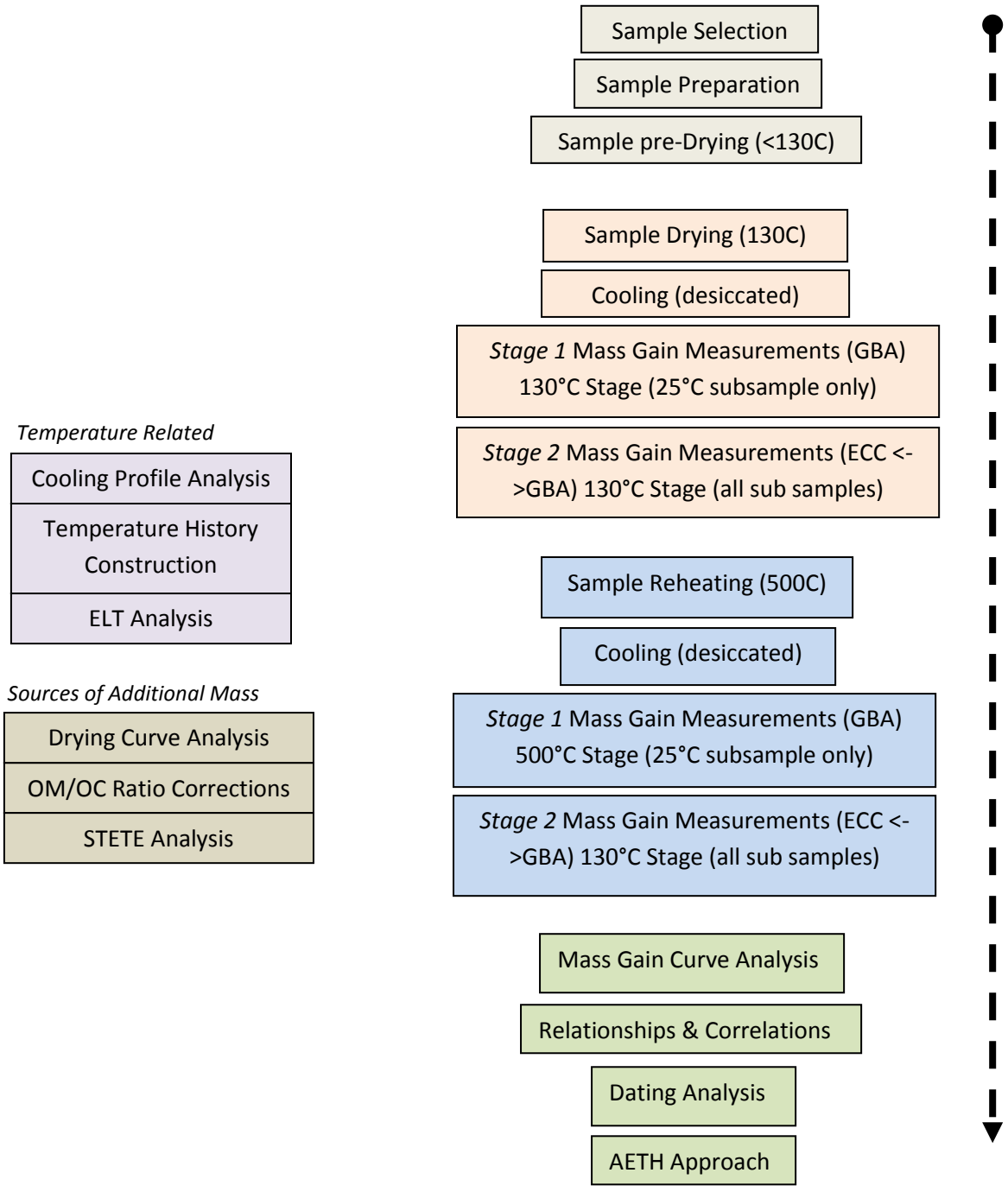

Figure 6.1: Methodological stages in RHX behaviour and dating experiments.

6.1.2 Chapter Outline

The remainder of the chapter will expand on the above summary and proceed as follows.

Firstly, *Section 6.2* will describe the samples selected, the reasons for their selection and detail any points of interest or issues that are considered relevant. Following this, *Section 6.3* will describe the experimental setup, principally the glove box arrangement (GBA), together with a description of the general procedure used in carrying out a mass gain measurement with this setup. This leads into *Section 6.4* which deals with the actual mass gain measurement experiments carried out. It describes all the stages involved: preparation, drying, cooling, reheating and mass gain measurements.

The procedure used to analyse the mass gain curves and calculate the variables that are relevant to both the mass gain behaviour and dating calculations are described in *Section 6.5*. Also necessary for the archaeological dating calculations are estimated of the ELTs of the samples. These are based on simulations derived from both constructed temperature histories and the properties of the samples obtained from the mass gain curves. Construction of the temperature histories and calculation of the ELTs are elaborated upon in *Section 6.6.*

The methods used in the dating estimates and their treatment are provided in *Section 6.7* This includes accounting for various sources of additional or non-RHX mass, the creation of age-temperature curves, and examining the effect of various sources of uncertainty on the age ranges of the samples.

A description of the *AETH* approach, a proposed more suitable method for calculating the age of the samples, is included in *Section 6.8.* Finally, a brief description of the correlation of the mass gain properties with one another and with the results from non-mass gain experiments is presented.

6.2 Samples

6.2.1 Selection, Age, Location and Context

The samples selected and a set of relevant details are provided in *Table 6.1* and *Table 6.2.* The samples are generally referred to by a three letter abbreviation used in labelling/tracking the samples (i.e. *Ann* for *Annadale*) during experiments. The collection is made up of 18 samples of brick (14) and pottery (4) with known ages that range from approximately 2300 years old to 110 years old. They come from a mixture of contexts with 9 retrieved from buried contexts and 9 retrieved from non-buried structural contexts. The decision to work with a large group of samples instead of a more focussed smaller group was motivated by a desire to examine if any effects observed in experiments are isolated or anomalous and also to add statistical weight to correlation between different properties.

The temperature history of the ceramics is mixed; Etruscan and Roman ceramics are more portable and likely to have experienced more movement during the period of their use whereas the structural bricks have been retrieved from their original position (9) or in their original but buried context (5). The two pieces of pottery wasters (*Downshire*) were never used and retrieved close to their original firing kiln.

The lifetime temperature of most samples is expected to be dominated by local surface air temperature (SAT) conditions, however, some samples are likely to have experienced elevated temperatures, during the lifecycle of the pot or building for example, which may result in an effective lifetime temperature above that of air temperature. For example, *Ria* was retrieved as a flooring brick located a short distance from a fireplace and an elevated ELT may be expected. In *Table 6.2,* a strength is attributed to the possibility of elevated ELTs due to internal temperature conditions or other short term elevated temperature events (STETEs); this is a subjective assignment and intended only as a loose guide or marker of samples that may be more strongly affected.

The sample set is dominated by post-medieval bricks (14/18). This was deliberate for the following reasons (previously stated in *Chapter 1*):

1. The temperature history will be less complex for a non-portable structural ceramic and is also likely to be more strongly governed by surface air temperatures where the brick is external.
2. The samples will not have been used for storage and be free of organic or non-organic residues which may affect pottery samples (but not necessarily clear of other contaminants).
3. The quantity of material available for destructive testing will, in general, be greater.
4. Bricks are generally very well fired (c. 1000°C) and thus more likely to have undergone complete or less questionable levels of dehydroxylation.
5. Instrumental records and temperature reconstructions with less uncertainty can be used on samples that are post-medieval.
6. The known ages are often recorded with small uncertainties.

The selection of a mixture of samples from burial/non-burial contexts and samples with ELTs that are governed by SATs and lifetime temperatures above those governed by air temperatures or elevated by the use-phase of the building was motivated by the following:

1. The use of buried/non-buried samples permits the examination of how well these two contexts perform under application of the dating method and to observe if there are any noticeable differences between the behaviour of the two groups which may be ascribed to specific burial/non-burial conditions.
2. The selection of samples with diverse ELTs (or a range factors affecting the ELTs) permits examination of how the date calculations are affected by different lifetime temperature effects and to ascertain if the method is still feasible where such lifetime conditions exist.

Details of the burial depth are not included because, as will be discussed in greater detail in *Section 9.4.2*, the mean surface air temperature and the ELT (estimated from the surface air temperature record and without burial depth effects) provide

reasonable bounds on the lower and upper ELT experienced by the ceramic, respectively (ignoring STETE effects).

The geographical distribution of Irish bricks and pottery are displayed in *Figure 6.2,* with the distribution of known ages for post-medieval samples are plotted in *Figure 6.3.*

Table 6.1: List of samples and relevant details, including sample ID and type (tile, brick ceramic), known age, source of the sample/known age, geographical location, and local context of sample.

Sample ***Sample ID*** **Type**	**Age (AD/BC)** **Age (BP)**	**Source** **(ref.)**	**Location**	**Local Context**
Annadale *Ann* Brick	AD 1890-1917 110±14	Stephen Gilmore NAC (Gilmore 2010)	Ormeau Rd Belfast, Co. Antrim, N. Ireland	Not clear
Castle Espie *Esp* Brick	AD 1867-1879 141±6	Stephen Gilmore NAC (Gilmore 2010)	Castle Espie, Co. Down, N. Ireland	Not clear
St. Nicholas *Nic* Brick	AD 1614 398±2	Barrie Hartwell (Ó Baoill 2008)	Carrickfergus, Co. Antrim, N. Ireland	Church window, transept.
Ballymacarrett *Mac* Brick	AD 1784-1788 228±2	Audrey Gahan (Gahan and Long) (Keery 2010)	Ballymacarret Townland, East Belfast, Co. Antrim, N. Ireland	Red brick corridor into glass works building (Gahan, pers. comm.)
Rialto *Ria* Brick	AD 1650-1700 339±25	Stephen Gilmore NAC (pers. comm.)	Rialto Theatre Site, Derry City, Co. Londonderry, N. Ireland	Floor before fireplace of domestic building
Etruscan *Etr* Pottery	400-200 BC 2300±100	Caroline Malone (pers. comm.) ongoing work	Montelabate, Gubbio-Perugia, Italy	Excavation
Roman *Rom* Pottery	AD 100-300 1800±100	Caroline Malone (pers. comm.)	Montelabate, Gubbio-Perugia, Italy	Excavation
Portumna	AD 1618	Sara Pavia	Portumna, Co.	Structural from castle

Por Brick	398±2	(Pavía et al. 2000)	Galway, Rep. Ireland	
Rathfarnham *Rat* Brick	AD 1771 245±2	Sara Pavía (Pavía 2006)	Rathfarnham, Co. Dublin, Rep. Ireland	Structural (external) from domestic building
Caledon *Cal* Brick	AD 1823-1840 182±9	Joanne Curran (Consarc) (pers. comm)	Caledon, Co. Tyrone, N. Ireland	Structural (external) from Water Mill
Lanyon *Lan* Brick	AD 1848 168±2	Joanne Curran (Consarc) (Moody 1959)	Queen's Uni. Belfast, Co. Antrim, N. Ireland	Structural (external) from University building
Mountjoy *Joy* Brick	AD 1600-1605 412±2	Paul Logue permission (NIEA) (Jope 1960)	Brockagh, Coalisland, Co. Tyrone, N. Ireland	Structural from Castle
Caulfield *Cau* Brick	AD 1611-1619 399±4	Paul Logue permission (NIEA) (Jope 1958)	Castlecaulfield, Dungannon, Co. Tyrone, N. Ireland	Fireplace lining brick or structural (internal)
Bellaghy *Bel* Brick	AD 1617-1622 395±3	Barrie Hartwell (Brannon 2010)	Bellagy, Co. Derry, N. Ireland	Bawn wall (external)
Downshire 1 Downshire 2 *Dow1/2* Potter Wasters	AD 1787-1796 222±5	Peter Francis (Francis 2001)	Ballymacarret, Belfast, Co. Antrim, N. Ireland	Pottery wasters
Turlough *Tur* Brick	AD 1750-1820 229±35	Georgian style	Turlough, Co. Mayo, Rep. Ireland	Interior Brick of domestic building (from kitchen)
Tedford's *Ted* Brick	AD 1650-1700 339±25	Peter Francis (pers. comm – Exc.Ie. (2015))	Central Belfast City, Co. Antrim, N. Ireland	Structural

Table 6.2: List of samples and relevant details, including relevant comments on use and context, retrieved from buried or original (i.e. structural wall) context, and probability of elevated ELTs based on potential exposure to elevated temperatures during lifetime use. Interior conditions is refers generally to a structural brick (external) that may have experienced some elevated temperatures due to thermal diffusion from the indoors environment.

Sample ***Sample ID*** **Type**	**Other Comments**	**Buried (Y/N)** **(N -> retrieved from original use context)**	**Probability of elevated ELTs (above SAT) (w=weak, m=medium, s=strong) (*possible source of elevated ELT*)**
Annadale *Ann* Brick	Unused brick produced during last phase of use of the brickworks factory. Likely stored outside.	Y	w
Castle Espie *Esp* Brick	Unused brick produced during last phase of use of the brickworks factory. Likely stored outside	Y	w
St. Nicholas *Nic* Brick	Structural wall	N	m (*affected by interior church conditions*)
Ballymacarrett *Mac* Brick	Looked in poor (over-fired) condition	Y	m (*affected by interior building conditions*)
Rialto *Ria* Brick	Hand made brick. High-fired (over-fired)	Y	s (*proximity to fireplace*)
Etruscan *Etr* Pottery		Y	-
Roman *Rom* Pottery		Y	-
Portumna *Por* Brick		N	w (*affected by interior conditions*)
Rathfarnham *Rat*		N	w (*interior condition*)

Brick			
Caledon *Cal* Brick		N	w (*interior condition*)
Lanyon *Lan* Brick		N	w
Mountjoy *Joy* Brick		N	w
Caulfield *Cau* Brick		N	m (*possible chimney heat effects*)
Bellaghy *Bel* Brick		N	w
Downshire 1 Downshire 2 *Dow1/2* Potter Wasters	Probably dumped (possibly inside kiln and repeatedly fired)	Y	w
Turlough *Tur* Brick		N	m (*interior kitchen conditions*)
Tedford's *Ted* Brick		Y	w (*interior building conditions*)

Figure 6.2: Location of Irish brick and pottery samples used in dating trials together with known ages. Included are colour coded markers that indicate the following interpretation of the samples lifetime conditions and recovery position:

- - Sample located internally in building. Recovered from original position.
- - Sample originally located internally in building. Recovered from buried position.
- - Sample structural and exposed to external air temperatures. Recovered from original position.
- -Sample structural and originally exposed to external air temperature. Recovered from buried context.

(map: d-maps.com)

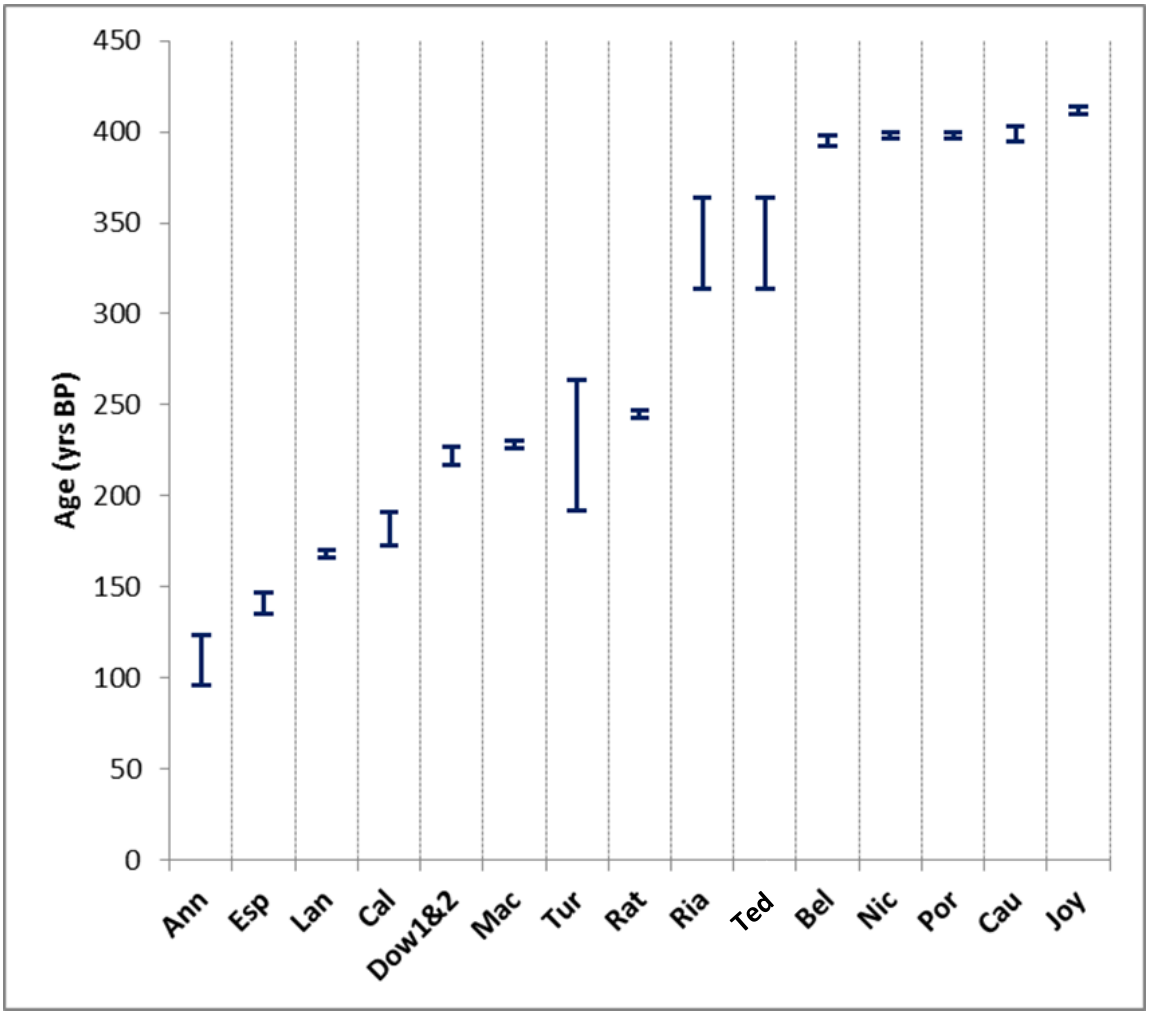

Figure 6.3: Known ages of post-medieval brick and pottery samples used in dating experiments.

6.3 Setup and General Approach

6.3.1 General Experimental Setup

The basic setup used to carry out RHX related experiments involved three main working areas: an oven/furnace for drying/reheating of samples; a controlled (temperature and humidity) environment for aging of samples as they gain mass; and a controlled environment (temperature and humidity) for carrying out periodic mass gain measurements of samples that are aging.

For controlled drying (130°C) and reheating/firing (500°C) an oven and furnace (*Carbolite AAF1100*) were used, respectively. For storage of aging samples post-drying/reheating, three temperature controlled cabinets were used (a temperature and humidity controlled *Binder* cabinet and two *LMS* incubator cabinets).

Figure 6.4: Glove box arrangement (GBA) used for periodic measurement of mass gain of samples following transfer from environmental control chambers (ECC) where aging at a constant temperature is taking place. Temperature and humidity are controlled within the GBA.

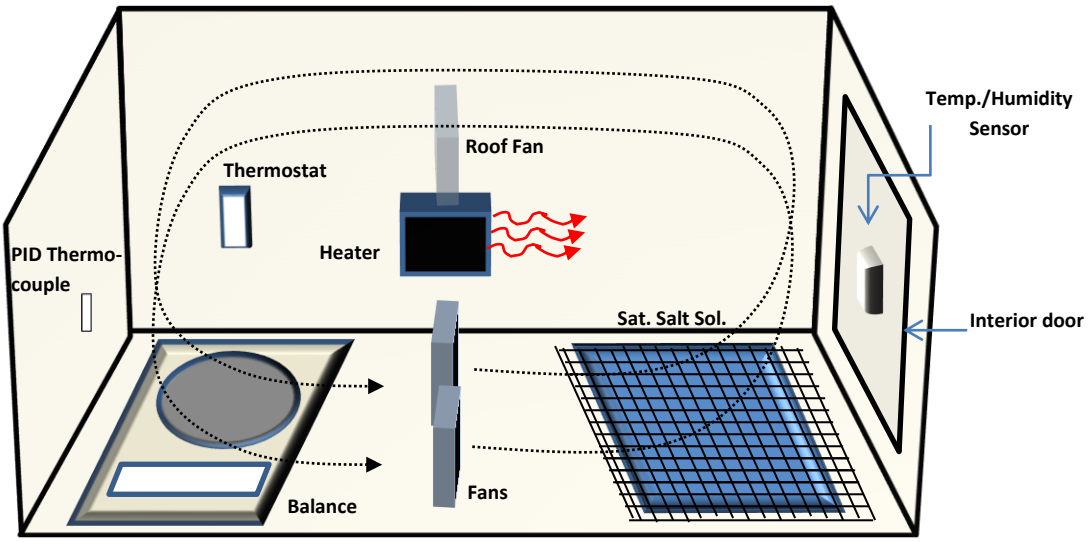

Figure 6.5: Schematic of interior chamber of glove box arrangement. Dotted lines represent circulation of air for distribution of heat and movement of air over saturated salt solution.

Periodic mass gain measurements were carries out using a *Sartorius CPA225D* analytical balance (100g capacity, 0.01mg precision). This was located in a glove box arrangement (GBA), designed and constructed to control the temperature and humidity conditions during mass gain measurement, *Figure 6.4* and *Figure 6.5.* The GBA permitted repeatable temperature (±0.5°C) and humidity (±1%RH) conditions. The temperature was controlled by a heater mounted at the rear of the glove box and regulated by a PID temperature controlled, with the humidity controlled by circulating air over a tray of saturated salt solution of NaCl (74-76%RH, Greenspan 1976). The GBA consists of an inner chamber (featuring balance, heater, salt solution) where measurements are carried out and a small outer chamber which acts as a buffering zone between room conditions and those of the inner chamber during transfer of samples. The temperature and humidity were fixed at 25°C and 75%RH during mass measurements. The temperature was dictated by the GBA only permitting heating, therefore requiring a temperature that would always be above room temperature. The %RH was based on trials of both saturated solutions of NaCl and MgCl (31-33%) with the former proving more manageable and stable, as well as equilibrating quicker following opening of GBA to environmental room conditions.

During the procedure, from final drying through to final mass gain measurements following heating at 500°C, the granulated samples were stored in Pyrex beakers. During aging, these beakers were stored in sealed sample boxes (SB). These sample boxes were custom adapted plastic 'lunch boxes' which had a layer of saturated salt solution (NaCl) at their base to maintain constant RH within the container. The beakers (6 per sample box) were isolated at their base from contact with the salt solution, via internal plastic holders, but open to air conditions within the sample box otherwise. The sample box was sealed and not exposed to the air conditions within the heated environment chambers. When transferred to the glove box (described below) the container was opened for equilibration of the samples to the new environment and to remove and weigh the beakers.

6.3.2 Comment on General Mass Gain Measurement Procedure

As described in *Section 3.6* and outlined above, for dating of a single sample three sub-samples are aged at three different temperatures following both drying and reheating. During aging in the environmental chambers (i.e. in the sample boxes stored in incubator cabinet) the samples must be transferred to the GBA periodically for a mass measurement to be carried out. This involves taking a sample that has equilibrated to a particular temperature and humidity, during aging and storage in the ECC, and transferring it to weighing conditions in the GBA that may differ in both temperature and humidity. The quantity of adsorbed moisture on the surface of the samples will depend on both the temperature and level of moisture in the atmosphere (%RH). Therefore, while the mass gain rate is considered independent of %RH (Wilson et al. 2003; 2009) it was necessary to fix the %RH conditions in both the samples boxes and GBA using saturated salt solutions. This means that conditions determining the level of adsorbed moisture on the ceramic in both environments were fixed before transfer and measurement. Transfer from one environment to the other for mass gain measurements would still involve re-equilibration of the sample to the new environment, i.e. a period of uptake or loss of adsorbed moisture.

To ensure that the quantity of adsorbed moisture contributing to the total mass of the weighed sample was as constant as possible mass gain measurements were

carried out under controlled timing conditions. The sealed sample box was transferred to the GBA where its lid was removed and the samples were exposed and permitted to re-equilibrate to the GBA conditions for a set period before measurement. Provided the level of adsorption is largely independent of the level of dehydroxylation/rehydroxylation, this should ensure that, though the sample may not have fully equilibrated to the GBA conditions at the point of measurement, the same percentage equilibration will have taken place for each measurement and the mass contribution for each measurement will be constant and not interfere with the dating procedure.

The conditions in the GBA were fixed at 25°C and 75%RH while the conditions in the ECs were 25°C, 35°C, 45°C and 75%RH. Therefore, the samples aging at 25° provided a set of samples where equilibration effects between the EC and GBA are near-negligible.

-

6.4 Mass Gain Measurements

6.4.1 Sample Preparation

The objective of the sample preparation was to obtain three granulated subsamples for each sample, with the three subsamples as similar in composition as possible, being taken from a pseudo-random distribution across the larger sample block. Pre-drying (<130°C) was carried out to slowly remove any large quantities of bulk pore or capillary moisture that, if removed more rapidly at higher temperatures, during drying could cause structural changes within the ceramic.

Approximately 12 cubes of roughly 2.5 x 2.5 x 2.5 cm (20-40g) were wet-cut (de-ionised water) using a diamond-tipped rotary saw from larger brick samples (generally whole or near-whole). These cubes were cut from a single face perpendicular to the long axis of the brick in order to represent the composition through and across the brick. For the pottery samples, the sherds were wet-cut into more manageable pieces for the next stages. Following wet-cutting, the samples were dried for 2 days at approximately 60°C. This was to remove wet-cutting moisture and also to begin pre-drying of the samples to removed abundant surface/pore moisture. This stage of heating was not considered likely to contribute any significant mass gain in the context of the long lifetime of the ceramic and based on considerations of the maximum temperature of rehydroxylation (Barrett 2013).

The outer layer of cubed subsamples was wet-grinded to remove several millimetres of the surface layers most likely exposed to environmental contaminants. The subsamples were briefly rinsed with de-ionised water and returned to the drying cabinet. The temperature in the drying cabinet was increased to 85-90°C as part of further pre-drying which was carried out over a period of 15 days.

During this period, cubed sub-samples were granulated by hand using a chisel and sieved to extract granules of size 2-5.6mm (approx. 0.05-0.15g). This size was deemed suitable for sufficient mixing when later split into three portions for the

25°C, 35°C and 45°C dating subsamples. For a single sample, the granules prepared from all cubed subsamples were stored together and thoroughly mixed. The Downshire pottery samples were not granulated as (a) the quantity of available material was limited and (b) the composition and texture of the sherds appeared very homogenous. Therefore, three non-granulated blocks were deemed sufficient.

A final cleaning was carried out. Sub-samples were rinsed thoroughly with de-ionised water, placed in an ultrasonic bath for 2 minutes to remove any remaining loosely bound contaminants, rinsed a final time with de-ionised water, before being spread out on aluminium trays for the drying stage.

6.4.2 Drying Stage

The objective of the drying stage is to remove any non-hydroxyl related moisture from the ceramic (i.e. pore or capillary bulk moisture) by weighing the sample to constant mass as it dries. However, it was concluded during experiments that even after 61-66 days drying of granulated samples at 130°C, constant mass was not reached and would not be reached in a reasonable period of time. It was instead necessary to record the mass loss curves under drying and at a later stage account for the loose water not removed via modelling of these curves.

The aluminium trays of granulated samples were placed in an oven at 130°C and dried over a period of 2 months. On a near daily basis, the trays were removed and weighed on a top-loading balance under room conditions of 20 ± 1 °C and 78 ± 3 %RH. Samples were weighed under a rigid timing regime, the first tray following 15 minutes removal from oven, the remaining 17 trays at 1 minute intervals subsequent to this. On the final day of drying, each sample was assigned three beakers into which a portion of granules (approximate mass 15-25g) was placed. The numbering etched on the beaker could be traced throughout all subsequent measurements (all empty beakers had been previously weighed in the GBA following 20 minutes equilibration to GBA conditions). The beakers were returned to the oven for the final day of drying.

6.4.3 130°C Stage

This stage is used to examine the *Stage 1* behaviour of the 25°C samples and to record the mass gain curves for samples following heating at 130°C. This mass gain curve is required to estimate the initial mass mass of the ceramic before dehydroxylation and to estimate mass gain rates that, assuming an Arrhenius-type behaviour, can be used to calculate the mass gain rate at any temperature.

Before the 130°C mass gain stage, all beakers (still drying) were assigned future sample boxes for storage in ECCs and transfer to GBA. The 54 beakers were comprised of 3 sets (3 aging temperatures) of 18 samples. Each of these three sets was then divided into 3 sample box assignations (6 beakers per sample box). The sample boxes were prepared; NaCl salt solution was placed at the base of each and they were left to equilibrate in their assigned ECCs until use.

When the drying stage was complete, in groups of 6, the 25°C subsample beakers were moved immediately from the oven into a desiccated container to minimise mass gain during cooling, i.e. time-offset effects (Barrett 2013). Following cooling for 1hr 15min at room temperature, the beakers were transferred in a sealed empty sample box into the GBA. The GBA was set to 25°C and 75%RH, the future aging conditions of the beakers (Note that for this and all subsequent GBA measurements, the glove box was allowed a minimum of 2 hours to equilibrate to its set temperature and humidity conditions before any weighing was carried out). Once in the GBA the lid was removed from the sample box and the fans in the sample box were switched on for 2 minutes (for speeding up return to weighing conditions in the GBA following opening/closing to outside room conditions). Fans were then switched off and the beakers were weighed repeatedly over a period of 6-7 hours, during which *Stage 1* behaviour was observed to have completed in a majority of samples.

The groups of 6 beakers were then placed in the assigned sample boxes and moved to the corresponding 25°C environment chamber. Over a minimum period of two months, these samples were moved, initially on a daily basis with broader spacing in the interval of measurement later on, to the GBA for weighing. This involved

conditioning the GBA for two hours before measurement. Then the samples, one sample box at a time were moved into the GBA for mass measurements. The lid of the sample box was removed and the fans were switched on for 4 minutes. Then the beakers were completely removed from the sample boxes and allowed a further 11 minutes equilibration before each was weighed. A standardised weight (20g) was measured at the end of each of these sequences to check for any drift in the balance. Following weighing, the beakers were returned to their SBs, which was then sealed and removed to the ECC.

For the 35°C and 45°C, the method is very similar. The *Stage 1* monitoring is not carried out, however. Instead, following drying the beakers were allowed 15 minutes cooling in desiccated conditions before transfer to SBs and placement in the SBs. Again, over a minimum of two months the mass gain was monitored via transfer to the GBA. The GBA procedure is identical except that the beakers were permitted an additional 10 minutes equilibration time within the GBA before measurement. The timings used were based on previous trials carried out on Chester Red brick samples (Barrett 2013).

6.4.4 500°C Stage

The following stage is carried out to 'reset' the mass of the ceramic to its original as-fired dehydroxylated mass and to obtain a mass gain curve that can be used to calculate this mass as well as the mass gain rates at a range of temperatures.

Following completion of mass gain measurements for the 130°C stage, the beakers then move to the 500°C stage. Beakers, six at a time, were place in the furnace. The temperature was ramped to 500°C, at a ramp rate of 1°C/min, and then left to heat the ceramic for a period of approximately 72 hours (based on literature review values, *Chapter 2*, and on preliminary trials that involved firing and weighing of *Mac* and *Ria* bulk samples at 6-12 hour intervals on room condition top-loading balance). The furnace was then allowed to cool down to 200°C before removal of the beakers. The remaining procedure is identical to that following 130°C drying with the *Stage I* monitored again only for the 25°C samples and all samples undergoing mass gain

measurements via transfer between the ECCs and GBA over a period of at least two months.

6.4.5 Cooling Temperature Profile

The cooling temperature profile was recorded to provide an indication of the initial temperature of the ceramics once exposed to environmental moisture following removal from the desiccated container (and placement in GBA or ECC) after drying/heating.

This experiment was carried out after completion of the mass gain curve measurements. The 25°C sub-sample was selected for each sample and assumed to have near-identical thermal characteristics to the 35°C and 45°C sub-samples. All sub-sample beakers were placed on aluminium trays for ease of movements and heated in the oven at 150°C for > 1 hour. When removed from the oven (three subsamples per tray at a time), surface temperature probes (thermistors) were quickly placed into the centre of each of the beakers of granules, and the tray was then placed in the same desiccated container used in mass gain measurements. The temperature of samples and the air temperature in the container were logged using a *Grant Squirrel 1000 Series* datalogger (±0.2°C) over the next 1hr 30mins. When data was acquired for all subsamples, the analysis was carried out using *Excel*.

6.5 Mass Gain Analysis

6.5.1 *Stage 1* Behaviour

The main characteristics of interest in *Stage 1* are the fractional mass gain across the duration of *S1*, the duration of *S1,* and the ratios/difference between the 130°C and 500°C components.

Curves displaying the *S1* behaviour (as a function of $t^{1/4}$) were generated using *Excel*. From these the approximate duration of *S1* was estimated visually and in consideration of the regression results carried out as part of modelling the curves (see following section). The fractional mass gain during *S1* is calculated from the difference in the intercept, $m_{130/500}$, acquired through modelling of the *S2* mass gain rates (see below) and the initial mass gain measurement recorded for *S1*, m_d. The ratios and differences between the 130°C and 500°C mass gain curves were then easily obtained.

6.5.2 Mass Gain Rates ($t^{1/4}$ and $t^{1/n}$ approaches) and Intercepts

The objective was to calculate the mass gain rate and intercept parameters over the *S2* data using a $t^{1/4}$ model, *Equation 1 Section 3.2*, and to calculate the mass gain rate, power (*1/n*) and intercept values for the $t^{1/n}$ model, *Equation 6* (*Section 3.4*), over the *S2* region also (See *Chapter 3* for a further description of these models and the relevant parameters).

The mass gain curves were analysed using *MATLAB R2012a* with the aid of custom-written code *bestfit* and *bestfitn* (*Appendix G*). The *bestfit* program was used to carry out $t^{1/4}$ modelling and *bestfitn* was used for $t^{1/n}$ modelling. At the core of these programs is the use of the *MATLAB* function *fit*, which in the case of *bestfit* was used to carry out regressions using a linear least square approach and a Trust Region algorithm (Moré and Sorensen 1983). For *bestfitn,* the fitting method is non-linear least squares with the same algorithm. Computation by *MATLAB* of confidence bounds on coefficients produced from the fits are based on

$$C = b \pm t\sqrt{s^2}$$

where *b* are the coefficients produced, *t* depends on the confidence level (95%), and is calculated using the inverse of Student's *t* cumulative distribution function, and s^2 is the mean squared error.

For a sequence of *N* data points (in reality 40-80 data points) the custom code (*bestfit* and *bestfitn*) carries out a linear/non-linear least squares fit on all data points, then for each subsequent fit removes an additional *p* data points (incrementing 1 for each cycle) from the start of the sequence leaving only *N-p* data points for regression, until only 10 data points remain (chosen as an arbitrary minimum number of data points required). The best-fit R^2 and *RMSE* values are provided for each set of data points the regression is carried out on. The program also outputs the mass gain rates, powers and intercepts of each model as a function of the number of data points removed, *p*, from the start of the series. This permits the effects of subtraction of early data points to be visually examined. The program can also choose the most suitable *Stage 2* region based on the best R^2 value obtained. From the fit carried out over the data points in this *S2* region, the most suitable mass gain rate, intercept and power (where applicable) are also provided.

For $t^{1/4}$ modelling, it was decided to restrict *Stage 2* to the period over which ECC-GBA measurements were carried out, i.e. removing the GBA measurements carried out on 25°C aging samples. For most samples, final modelling was carried out over the entire period of ECC-GBA weighing. Exceptions occurred where *bestfit* suggested a significantly improved alternative period based on R^2 values. This method and its issues are discussed in detail in *Section 9.3.3.*

For $t^{1/n}$ modelling, *bestfitn* was run across all measurement data and used to find the most appropriate *S2* and best fit for each of the six data series associated with each sample. Each best fit provided a value for *1/n*. The average of these six *1/n* values per sample was averaged. This average value was then used as a constant fixed *1/n* value, *r,* say. Then a $t^{1/r}$ model was applied to the sample, as for $t^{1/4}$ except across all data. This fixing of *1/r* was necessary for attempts at dating samples using a $t^{1/n}$ approach so that, for example, the mass gain rates were all in the same units. For samples *Etr, Por, Lan, Dow1, Dow2* (and *Rom* to some extent)

attempts to model the mass gain curves using a $t^{1/n}$ approach were unsuccessful with meaningless values of *1/n* (i.e. <0) produced for a majority of the curves per sample.

All mass gain rates were converted into fractional mass gain rates for comparison and dating calculations, where the intercept mass, m_{500}, is used for normalisation. Calculation of the RHX mass gain rate, a_{RHX}, is described in *Section 3.6*.

6.5.3 Lifetime Mass Gain (RHX mass gain)

Based on the differences in the intercepts from the 130°C and 500°C components, the mass loss due to heating between 130°C and 500°C, $m_{RHXC\text{-}25/35/45}$, can be estimated, see *Section 3.6*, for each aging temperature. The average of these three values was then taken to be m_{RHXC}. (The uncertainty was taken as the greater of the following two: (a) the standard deviation of the three values or (b) the average difference between m_{RHXC} calculated using the 95% confidence interval values and that of the best fit value.) The mass gain values were converted into fractional mass gain values using the intercept mass from the 500°C component.

To obtain the fractional mass loss attributable to rehydroxylation alone, m_{RHX}, the mass of loose water, m_{lw}, not removed during initial drying, needs to be subtracted, as does the mass of organic matter, m_{om}, removed during firing. Their calculation is discussed later with their removal requiring only a simple subtraction.

The above method was applied for both the $t^{1/4}$ and $t^{1/n}$ models.

6.5.4 Activation Energy

A description of how the activation energy is calculated is presented in *Section 3.3.* The procedure for calculating the activation energy of the 130°C and 500°C components are as follows for each component. The fractional mass gain rates were normalised with respect to the 25°C rate. Then a natural log was carried out on each of these. The three log normalised values produced for each of the 130°C and 500°C components then had a linear (least squares) regression carried out using the *LINEST* function in *Excel*. From this the slope, intercept and uncertainties are

provided. The slope, intercept and its uncertainties can then be used to estimate the activation energy and its uncertainty using *Equation 5* in *Section 3.3***.**

To calculate the activation energy due to the RHX component alone, first the fractional mass gain rates due to the 130°C components must be subtracted from their 500°C counterparts. The three values produces are used in the same manner as above to estimate the activation energy.

The above calculations were carried out for both the $t^{1/4}$ and the $t^{1/n}$ approaches.

6.6 Temperature History and Estimated Lifetime Temperature (ELT)

6.6.1 Temperature History Construction

In principle, calculation of the ELT requires as detailed a temperature history record of the sample as is possible. For most of the samples in this study, mobility during their lifetime would have been limited. It was decided, as a first approximation, to limit the temperature history to that of the surface air temperature (SAT) in the immediate locality of the sample over its lifetime. Construction of temperature histories, even in this most simplistic of approaches were still quite involved, as described below, and used the instrumental and reconstructed records listed in *Table 6.3*.

The general approach taken is illustrated in *Figure 6.6* and *Figure 6.7.* For the sample site, a modern local short instrumental record is used as a baseline for calibration/tuning of longer records. Then a longer regional instrumental record is calibrated against the local short instrumental record over the period of the short record such that the long record has the same mean annual temperature (MAT) and mean annual temperature range (ATR). This involves the addition of a constant shift factor to the monthly temperatures to calibrate the mean annual temperature and the multiplication of the difference between the monthly temperature and the mean annual temperature (of a given year) by a scale factor to correct the annual temperature range.

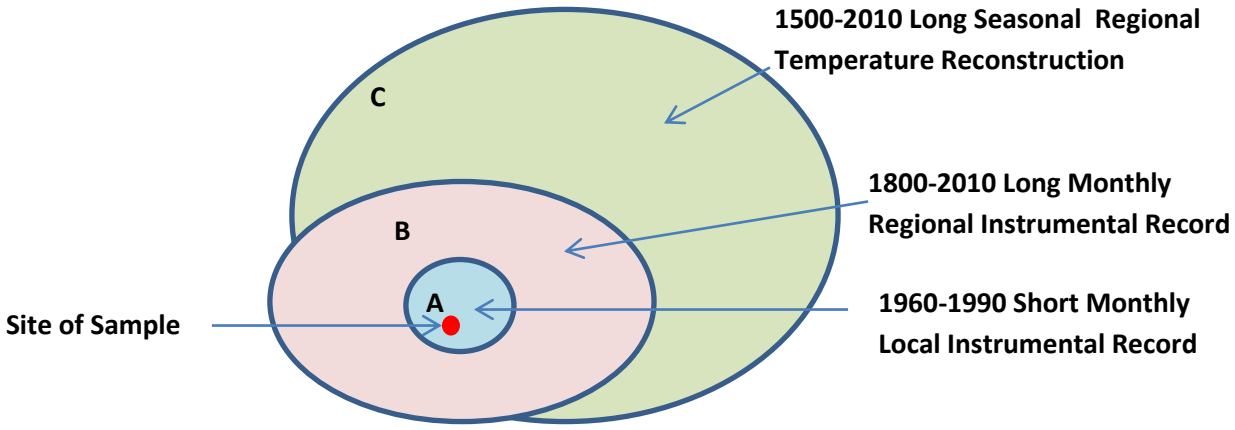

Figure 6.6: Example diagram of site and its relationship to records used in local SAT temperature history reconstruction. There is geographical overlap of all three groups: short local instrumental record, long regional instrumental record and long regional temperature reconstruction. The long records are tuned/calibrated to the short local record,

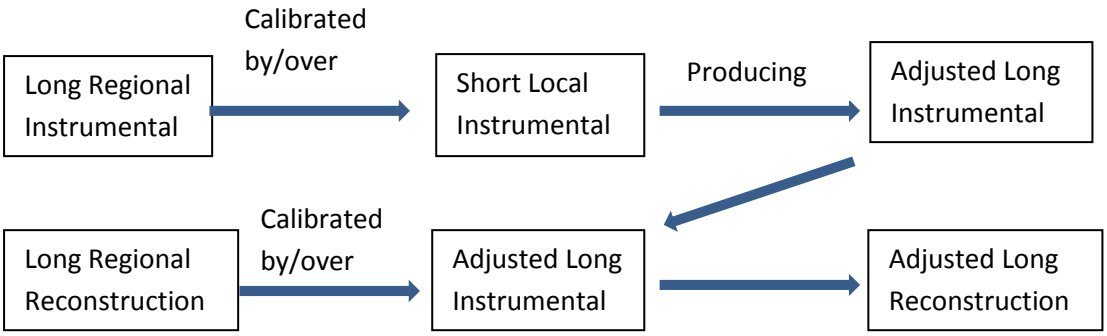

Figure 6.7: Construction of temperature history records by calibration of longer regional instrumental/reconstruction records by shorter more local/accurate instrumental records.

Once the long instrumental record has been mapped (adjusted) onto the local short instrumental data, then, if the instrumental series covers the period of the known age of the ceramic, the monthly data must be converted into daily temperature data, described below.

Where the long instrumental records do not extend back far enough, long seasonal temperature reconstruction records were used (Luterbacher et al. 2004). These were calibrated against and over the period of the previously adjusted long temperature records, again by shifting the MAT and scaling the mean ATR. The ATR for all records was estimated by fitting of the sine function *Equation 17*, described in *Section 3.12*, to the mean monthly/seasonal data over the period of the given record using the *fit* function in *MATLAB*. Following calibration of the long seasonal temperature reconstruction, this adjusted data must then be converted into daily temperature data.

To convert the monthly/seasonal data into daily data, on a year by year basis the tuned data series were fit using the sine function, *Equation 17*. The coefficients from this fit were then used to generate daily data on a year by year basis.

The mappings and data series used in constructing the temperature histories are provided below in *Table 6.3*.

Due to issues with the *Etr* and *Rom* samples, discussed later, it was not necessary to reconstruct long temperature histories. Nonetheless, daily temperature data was generated from the Luterbacher et al. (2004) 500 year old reconstruction to examine the likely scale of effects associated with the ELT.

Table 6.3: List of data series used in temperature history reconstruction, together with references and relevant geographical/grid location information.

	Long Regional Instrumental (monthly)	Short Local Instrumental (monthly)	Met. Office data-specific grid location(RC)	Long Regional Reconstruction: Luterbacher et al. (2004) (Y/N) (Years Applied over)	Long./Lat. of Luterbacher et al. (2004) data series used
Ann	Armagh 1796-2002 Butler et al. (2005)	Met Office (2015) 5km Gridded 1961-1990	144,69	N	
Esp	Armagh 1796-2002 Butler et al. (2005)	Met Office (2015) 5km Gridded 1961-1990	145,72	N	
Nic	Armagh 1796-2002 Butler et al. (2005)	Met Office (2015) 5km Gridded 1961-1990	142,69	Y (1614-1796)	5.75W/54.75N
Mac	Armagh 1796-2002 Butler et al. (2005)	Met Office (2015) 5km Gridded 1961-1990	144,69	Y (1784-1796)	5.75W/54.75N
Ria	Armagh 1796-2002 Butler et al. (2005)	Met Office (2015) 5km Gridded 1961-1990	134,51	Y (1650-1796)	7.25W/55.25N
Por	Galway 1861-2000 ECA&D (2015)	No adjustment	\	Y (1618-1861)	8.25W/53.25N
Rat	Phoenix Park 1881-2005 ECA&D (2015)	No adjustment	\	Y (1771-1881)	6.25W/53.25N
Cal	Armagh 1796-2002 Butler et al. (2005)	No adjustment <12km away	\	N	
Lan	Armagh 1796-2002 Butler et al. (2005)	Met Office (2015) 5km Gridded 1961-1990	144,69	N	
Joy	Armagh 1796-2002 Butler et al. (2005)	Met Office (2015) 5km Gridded 1961-1990	144,60	Y (1600-1796)	6.75W/54.75N
Cau	Armagh 1796-2002 Butler et al. (2005)	Met Office (2015) 5km Gridded 1961-1990	145,57	Y (1611-1796)	6.75W/54.75N
Bel	Armagh 1796-2002 Butler et al. (2005)	Met Office (2015) 5km Gridded 1961-1990	138,61	Y (1617-1796)	6.75W/54.75N
Dow1	Armagh 1796-	Met Office (2015)	144,69	Y (1787-1796)	5.75W/54.75N

Dow2	2002 Butler et al. (2005)	5km Gridded 1961-1990			
Tur	Galway 1861-2000 ECA&D (2015)	Wheeler and Mayes (1997) 1961-1990	Claremorris	Y (1750-1861)	9.25W/53.75N
Ted	Armagh 1796-2002 Butler et al. (2005)	Met Office (2015) 5km Gridded 1961-1990	144,69	Y (1650-1796)	5.75W/54.75N

6.6.2 Simulation and ELT Estimation

The mass gain of a ceramic over its lifetime for a given starting (firing) year was simulated using *AETH5,* a code written for *MATLAB* (*Appendix G*). The critical input required for this simulation was the SAT temperature history described above, the initial year, and the mass gain rate and activation energy data obtained from modelling of the mass gain curves. The method used for generating the mass gain as a function of time is detailed in *Section 3.8*. This was carried out for both a $t^{1/4}$ and $t^{1/n}$ model. The mass gain was also calculated for each year of the ceramics lifetime using the mean lifetime temperature (MLT) since firing.

Using the simulated mass gain, $m_{sim,}$ and the known age of the sample, t_a, along with *Equation 9* (*Section 3.5*)**,** the ELT was calculated. A plot of the ELT as a function of time since firing was also generated by *AETH5*.

Because of issues with poor activation energy plots or modelling of $t^{1/4(n)}$, ELTs were not estimated for *Por* or *Dow2* for either model or additionally for *Etr, Dow, Lan* and *Cal* with the $t^{1/n}$ model.

Also, for comparison between m_{sim} and m_{RHX}, m_{sim} needed to be adjusted to account for the gap in time between when the temperature history ended and when the ceramic was refired by the author. The simulated mass was recalculated with *Equation 1* using a mass gain rate determined at the ELT obtained from simulations as well as the known age of the ceramic at the point of re-firing. This is reasonable assuming the ELT will have varied very little over the gap between the end of the temperature history and the present; minor variation is supported by simulations of the ELT as a function of ceramic age, presented in *Chapter 8*.

6.7 Dating

6.7.1 Overview

Calculating the age of a ceramic using the RHX method requires knowledge of the amount of rehydroxylation that has taken place over the lifetime of the ceramic, an estimate of the lifetime temperature of the ceramic, and knowledge of the mass gain rate at that temperature. The above sections have described how these values were evaluated. The following section describes how dating was carried out with this information.

6.7.2 Additional Mass Sources

From modelling of the mass gain curves a measure of the mass removed upon heating between 130°C and 500°C, m_{RHXC}, was acquired. However this mass is the sum of several components, including hydroxyls, m_{RHX}, combustible organic matter, m_{om}, and loose water, m_{lw}, not fully removed during drying. A description of methods applied to account for these factors is provided below.

6.7.2.1 Organic Matter to Organic Carbon (OM/OC) Correction

In order to estimate the organic matter removed from the ceramic during firing, the carbon content was estimated first (*Section 4.8*). Before the age of the ceramic could be calculated, an estimate of the organic matter mass, m_{om}, was subtracted from m_{RHXC} (all calculations are fractional, in this case the carbon content was normalised as a fraction of the weight of the ceramic use in the carbon content experiment). This used the relationship:

$m_{OM} = OM/OC \times m_c$, where OM/OC is the organic matter to organic carbon ration and m_c is the fractional mass of carbon estimated for the sample.

For age calculation, a standard value of 1.95 for OM/OC, based on considerations discussed in *Section 2.6*, was used across all samples. For assessment of the effect of variation in the *OM/OC* a range of 1.4-2.5 was used (*Section 6.7.4)*.

6.7.2.2 Loose Water Modelling (Drying Stage)

As mentioned above, the drying stage (60 days @ 130°C) was insufficient for complete removal of loose water. Modelling of the drying curves was carried out using the fitting toolbox *cftool* in *MATLAB* to predict the amount of loose water, m_{lw}, not removed during drying but presumed to have been removed during heating at 500°C. Two models of drying were trialled, a power law, *Equation 14* (*Section 3.11*) and exponential law, *Equation 15* (*Section 3.11*).

The *goodness-of-fit* results of these two approaches are presented in the results section; however the power model proved unsatisfactory (see *Discussion*) and the exponential model was selected for complete modelling and calculation of the m_{lw} values. This model was used to estimate the completely dry mass of the sample trays and the mass at 61, 62, 63 and 66 days (when groups of samples were removed for commencement of mass gain measurements), with the difference between these two amounting to the potential remaining moisture that could be removed upon heating at 500°C. Uncertainties at the 95% confidence level were calculated from the upper and lower bounds on the model coefficients estimated by *MATLAB*. The total potential remaining moisture of the tray of granulated sample (less the tray mass) was split into potential remaining moisture per beaker of sample in the same ratio as the mass of the tray of sample was split into beakers of sample for mass gain tests.

6.7.3 Short Term Elevated Temperature Event (STETE) Modelling

Previous work has demonstrated that, due to the exponential temperature dependence of the mass gain rate, short term events (i.e. cooling following firing) can result in significant mass gain (Barrett 2013) in a ceramic, with consequences for the dating technique, notably a curvature of $t^{1/4}$ data or additional, unaccounted for, mass gain in a sample. Attempts to avoid the time-offset effect (curvature), caused by mass gain during cooling, involved cooling the sample in a desiccated container following drying/heating and the results and discussion of this will be provided later in the thesis. This aside, the possibility that other short term (the order of minutes to days) elevated (significantly above SAT and room temperature)

temperature events (STETE) that have taken place during the sample lifetime may have led to sources of additional mass gain (above those expected at ELT order temperatures) were examined.

These investigations were carried out only on samples that had permitted date calculations (see next section). Four possible STETE events were selected for simulation: (a) initial cooling of the ceramic post original firing, the pre-drying stages that involved (b) two days held at 60°C and (c) a more prolonged period (15 days) at 77-79°C (85-90° according to knob setting on cabinet but later re-examined and corrected), and (d) 60 heating/cooling cycles during removal from the oven for balance measurements while drying to constant mass.

Before the effects could be simulated, a temperature profile for each event was required. For simulating (b) and (c), this was not necessary, and for simulating (d) heating and cooling curves were generated from data obtained from the cooling profiles, *Section 6.4.5,* using *MATLAB* and *Equation 13* (*Section 3.10*). Because the samples for simulation (a) were all brick, a whole test brick was fired and its cooling response was recorded and modelled, as described in *Section 6.4.5*.

With no evidence available to indicate what upper temperature rehydroxylation can proceed to, a lower estimate of 80°C and a higher estimate of 95°C were selected. For event (c) a lower estimated of the cabinet temperature of 77°C and 79°C upper estimate were used.

To estimate the cumulative additional mass gain of all STETE effects, over that expected by the ELT alone, simulations were run using *MATLAB* with methods previously described (*Section 3.8*). The total mass gain from simulations involving the temperature history (used in the ELT estimation above) was used as the initial mass condition. Then, in sequence, each of the above effects was added (generated) onto this mass. This cumulative approach is valid, as Hall et al. (2013) demonstrate that the ordering of events bears no effect on the total mass gained (this was also tested by the author). The additional mass gain due to STETE events, m_{STETE}, was obtained by subtracting the total simulated mass of the temperature

history and STETE events from the mass gain due to temperature history (ELT) alone (extended in length by the period of duration of STETE events).

The STETE event effect simulations were carried out for two sequences of the events:

1. Moderate: temperature history, cooling ceramic (80°C max), 2 days 60°C, 15 days 77°C, 60 heating and cooling cycles (80°C max)
2. Strong: temperature history, cooling ceramic (95°C max), 2 days 60°C, 15 days 79°C, 60 heating and cooling cycles (95°C max)

The additional age and elevated ELT temperature caused by this additional STETE mass was calculated using standard RHX equations, described in *Chapter 3.* Plotted comparisons with values from age calculations were carried out in *Excel.*

The STETE effects were calculated only for the $t^{1/4}$ model as preliminary trials of the $t^{1/n}$ model presented much less significant effects and no strong correlation with mass gain discrepancies in the date calculations.

6.7.4 Age Calculation and Age-Temperature Curves

Following subtraction of the effects of organic matter and loose water, the mass of hydroxyls removed during reheating was obtained, m_{RHX}. This, together with the rehydroxylation mass gain rates and activation energies, was used in *Equation 9* to calculate the estimated age of the ceramic, t_{age}, for a range of temperatures from 7-24°C in 0.5°C, and including the ELT. Age-temperature curves (plots of the age as a function of temperature) were generated using *Excel*.

To examine the effect of uncertainty in the organic matter/organic carbon ratio on the calculated ages, age-temperature curves and age estimates were also generated under conditions of the OM/OC ratio, used to calculate the subtracted organic matter mass m_{om}, varying from 1.4 to 2.5.

To examine the magnitude of uncertainty in the dates caused by uncertainties in the activation energies, age-temperature curves were also generated using the upper and lower limit (1σ) confidence intervals of the activation energy

Quantities associated with how far removed the calculated ages were from the known ages, t_A, as well as the magnitude these quantities need to be for agreement, within the known age range, were also calculated. These include the quantity the RHX mass gain is out by for the dates to agree (difference between the mass of hydroxyls and the simulated mass), m_{out}, the value the organic matter/organic carbon ratios needs to be for the dates to agree, OM/OC_w, and the ELT for which the estimated dates work, T_w.

Finally the ages of the samples, t_{age}, and above 'working condition' values, were re-calculated following subtraction of the mass effects associated with STETE.

6.8 Activation Energy Temperature History (AETH) Method

The proposed *AETH* approach has been presented in *Section 3.9*. It involves estimating the age of the ceramic through matching the simulated mass gained over the ceramics lifetime with that estimated experimentally. This is achieved by generating the mass gain curves and total mass gain of the ceramic from a range of initial years (firing years) in the temperature history record to the present. The range and step size of the initial years is selected to span the expected age. From the curve of mass gained as a function of initial year, it is possible to select the initial year that provides a best match with the known experimental mass gained.

To demonstrate the application of the approach it was applied to the sample *Joy* for an idealised m_{RHX} and with the curve generated from experimental data. Code was written (*AETH5*) to generate total fractional mass gain versus starting year curves (AETH curves) with confidence intervals generated also. For *AETH* curve generation, the temperature history (SAT) curve was used, together with an upper and lower temperature history curve. These upper and lower curves are obtained by addition/subtraction of the uncertainties/errors in the reconstruction and instrumental records. Using the normal temperature history curve, over the period AD1500 to the start of the instrumental record, uncertainty estimates (1σ based on Luterbacher et al. (2004)) are added or subtracted (upper/lower temperature curve). From the beginning of the instrumental records to the present, the instrumental error (±0.1°C) is added or subtracted.

The uncertainties from Luterbacher et al. (2004) are not provided on a gridded basis - a best estimate of the uncertainties (2σ) over the winter and summer periods are obtained from the publication, particularly *figure 1*, and some of the text. The following uncertainty estimates are used: Winter AD1500-1750 = ± 1.3°C, AD1750-1880 = ± 0.6°C; Summer AD1500-1750 = ± 0.7°C, AD1750-1880 = ± 0.3°C (note that these are considered optimistic by Luterbacher et al. (2004)). Based on these, it was decided that a suitable estimated of the standard uncertainty (1σ) across the year would be of the order of ± 0.5°C for the period AD1500-1750 and ± 0.25C for the period AD1750-1880.

The lower bound *AETH* curve is generated using the upper bound activation energy and the lower temperature curve, with the opposite the case for the upper bound *AETH* curve. In future work, a more rigorous treatment is required that takes full account of the propagation of errors, but for demonstration of the approach the above is considered satisfactory.

The *AETH* curves for *Joy* were generated for a range of starting (firing) years from AD1500-1900 at intervals of 50 years. The ELTs and uncertainties, as a function of starting (firing) year were also generated.

The age of the ceramic, and range of uncertainty, was obtained by taking the point of intercept of an idealised experimentally measured mass gain, m_{RHX}, with the *AETH* curve, and its upper and lower bounds. This method and its result is illustrated in *Figure 8.37, Section 8.5*.

6.9 Mass Gain Properties' Correlations

Basic plots and analysis to examine the correlation of mass gain and dating variables amongst themselves and amongst variables from the non-mass gain experiments were carried out in *Excel.* Where relationships were examined, the general approach was to check for linear relationships via linear (least square) regressions, with the coefficient of determination, R^2, the main variable for assessment of correlation. Where necessary, the validity of a linear relationship was further examined by carrying out hypothesis testing (*t*-test, two tailed) that the slope of the regression is zero (the null hypothesis); *p*-values were estimated, with values of < 0.05 corresponding to the null hypothesis being rejected (< 5% probability) and a (linear) relationship being probable.

Chapter 7

Experimental Results – RHX Behaviour

7.1 Mass Gain Curves

Presented below in *Figures 7.1-7.18* are the mass gain curves acquired for all samples following heating at 130°C and 500°C and aging at temperatures of 25°C, 35°C and 45°C. The mass curves are presented following having been normalised with respect to m_0, the intercept mass from modelling of each of the curves using the $t^{1/4}$ model; this permits presentation of all samples on one plot. These plots are also presented as a function of $t^{1/4}$ and over the period of transfer to/from ECCs to GBA for weighing. A linear fit is applied to curves across the region displayed with the exception of *Etr*, *Rom*, *Por*, *Lan*, *Dow1/2*, where such fits were unsuitable. The results of modelling these curves are presented in *Sections 7.2-7.4.* The *Stage 1* curves are presented later in the chapter, *Section 7.6.1*.

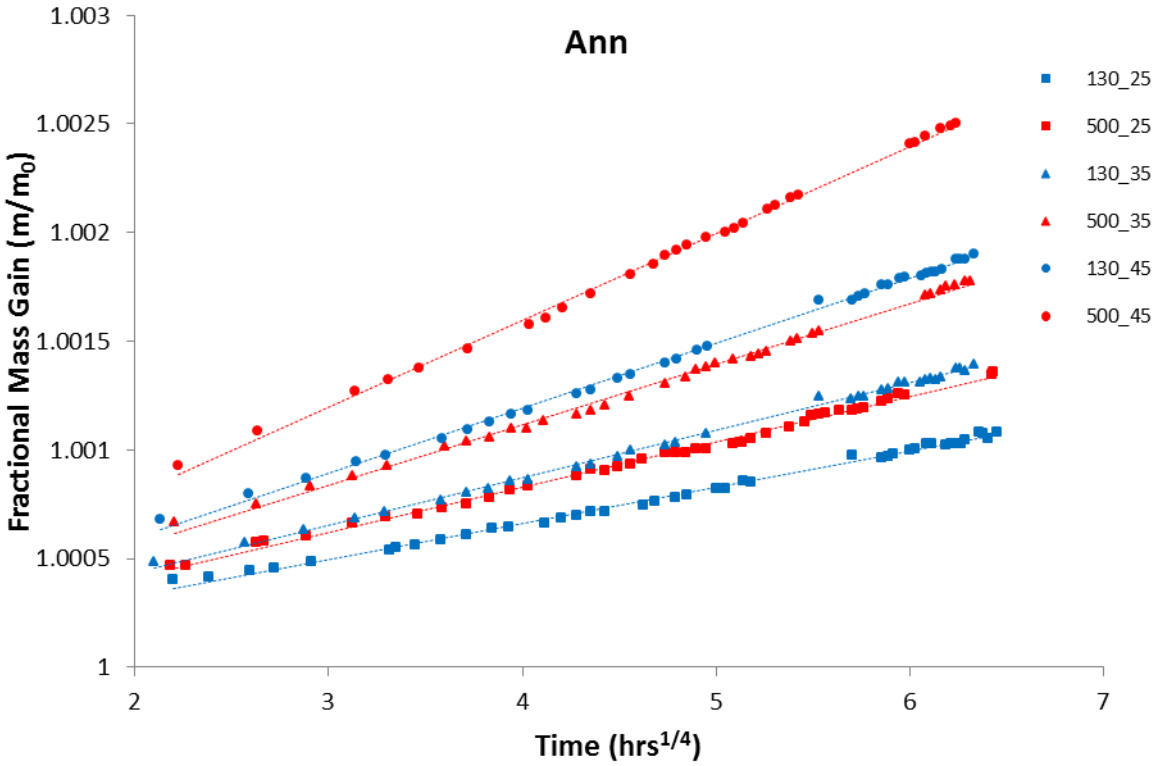

Figure 7.1: Fractional mass gain curves of *Ann* samples, following heating at 130°C (blue) and 500°C (red) and aging at temperatures of 25°C (square), 35°C (triangle), and 45°C (circle), presented across the period of ECC-GBA transfer and weighing. Imposed dashed lines correspond to linear fits across this period.

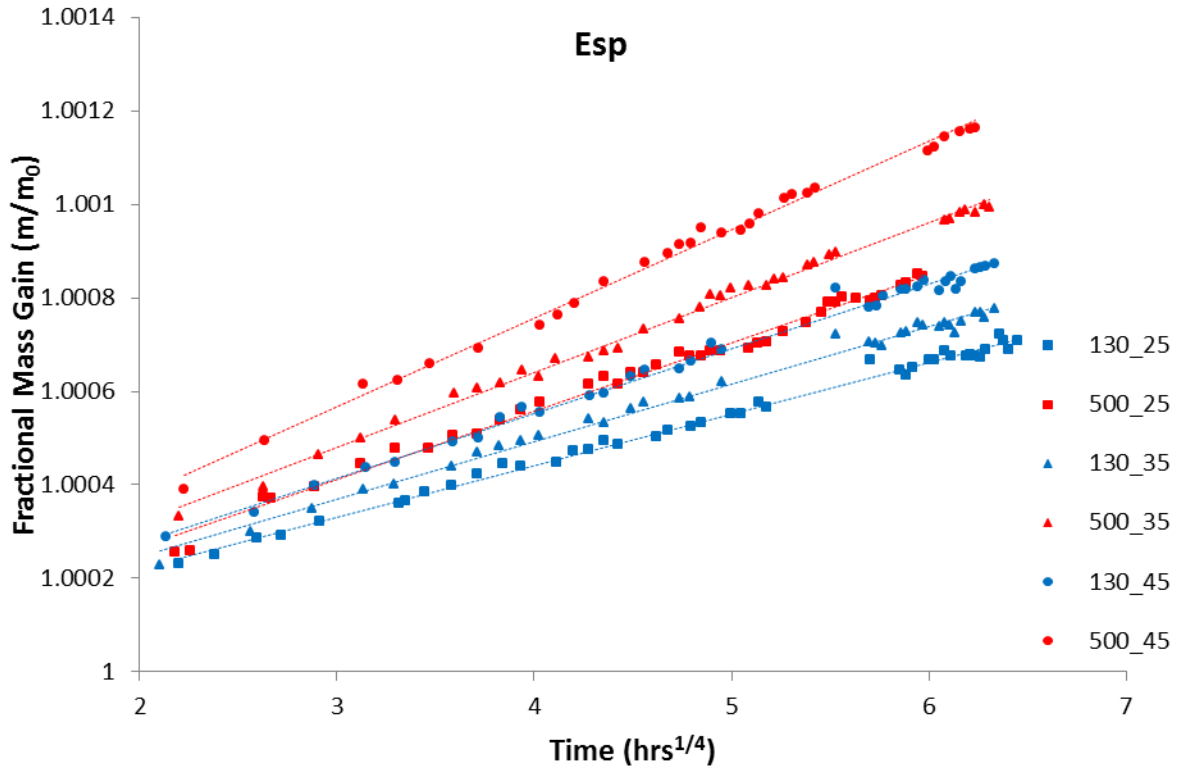

Figure 7.2: Fractional mass gain curves of *Esp* samples, following heating at 130°C (blue) and 500°C (red) and aging at temperatures of 25°C (square), 35°C (triangle), and 45°C (circle), presented across the period of ECC-GBA transfer and weighing. Imposed dashed lines correspond to linear fits across this period.

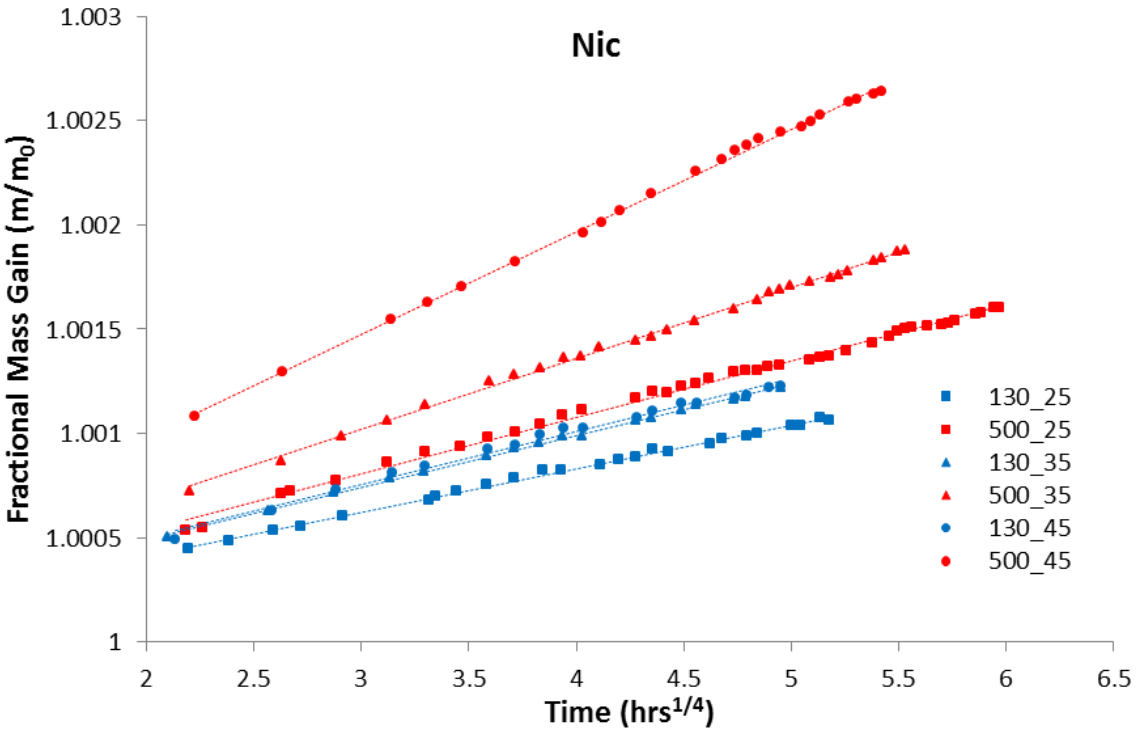

Figure 7.3: Fractional mass gain curves of *Nic* samples, following heating at 130°C (blue) and 500°C (red) and aging at temperatures of 25°C (square), 35°C (triangle), and 45°C (circle), presented across the period of ECC-GBA transfer and weighing. Imposed dashed lines correspond to linear fits across this period.

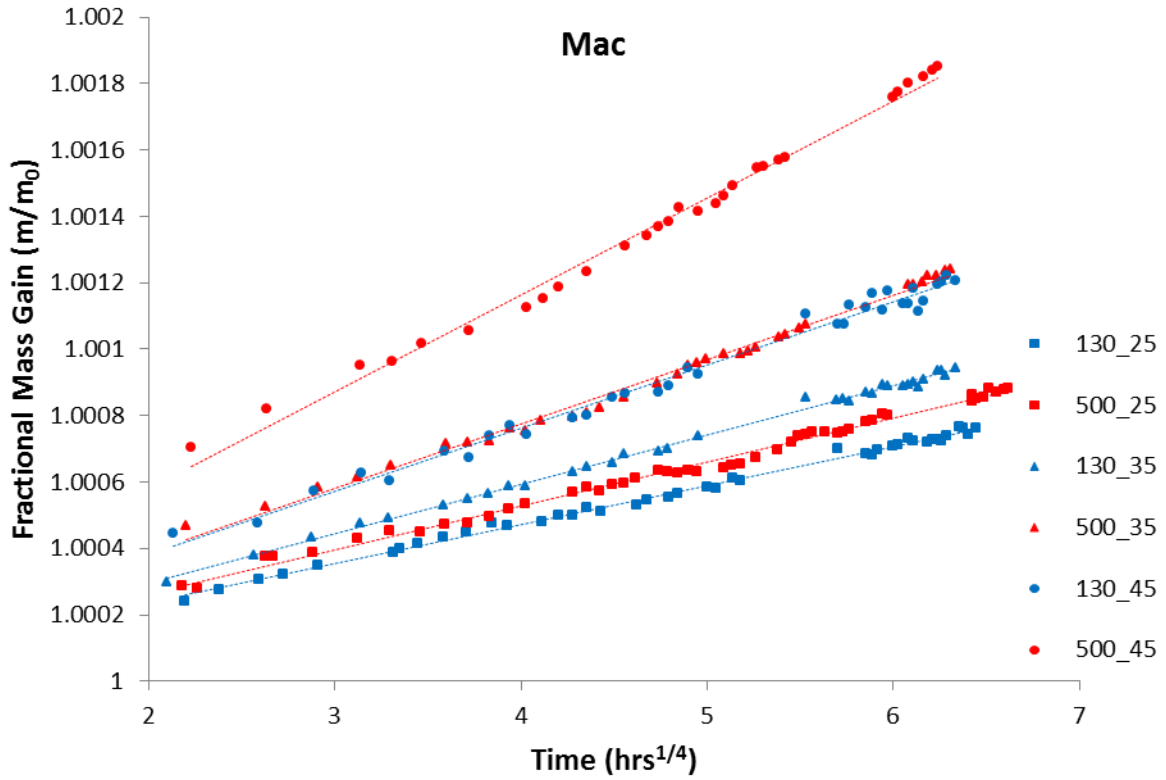

Figure 7.4: Fractional mass gain curves of *Mac* samples, following heating at 130°C (blue) and 500°C (red) and aging at temperatures of 25°C (square), 35°C (triangle), and 45°C (circle), presented across the period of ECC-GBA transfer and weighing. Imposed dashed lines correspond to linear fits across this period.

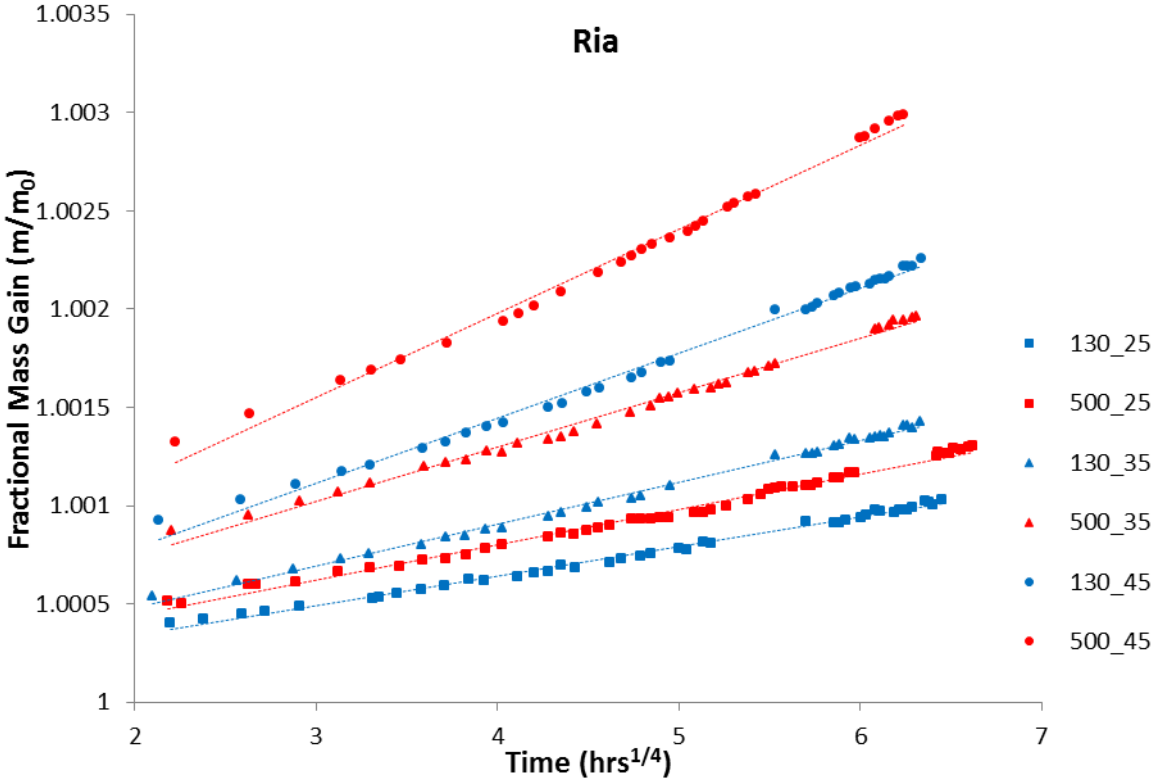

Figure 7.5: Fractional mass gain curves of *Ria* samples, following heating at 130°C (blue) and 500°C (red) and aging at temperatures of 25°C (square), 35°C (triangle), and 45°C (circle), presented across the period of ECC-GBA transfer and weighing. Imposed dashed lines correspond to linear fits across this period.

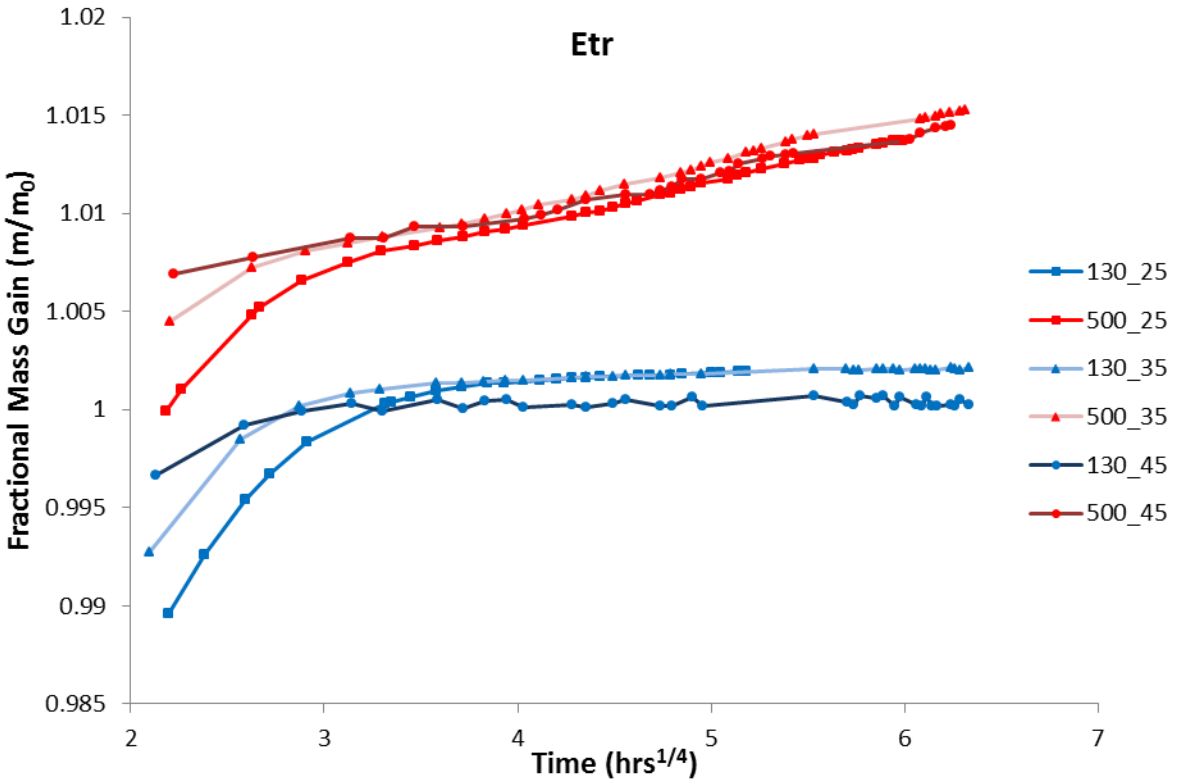

Figure 7.6: Fractional mass gain curves of *Etr* samples, following heating at 130°C (blue) and 500°C (red) and aging at temperatures of 25°C (square), 35°C (triangle), and 45°C (circle), presented across the period of ECC-GBA transfer and weighing. Interpolated lines included for visual purposes.

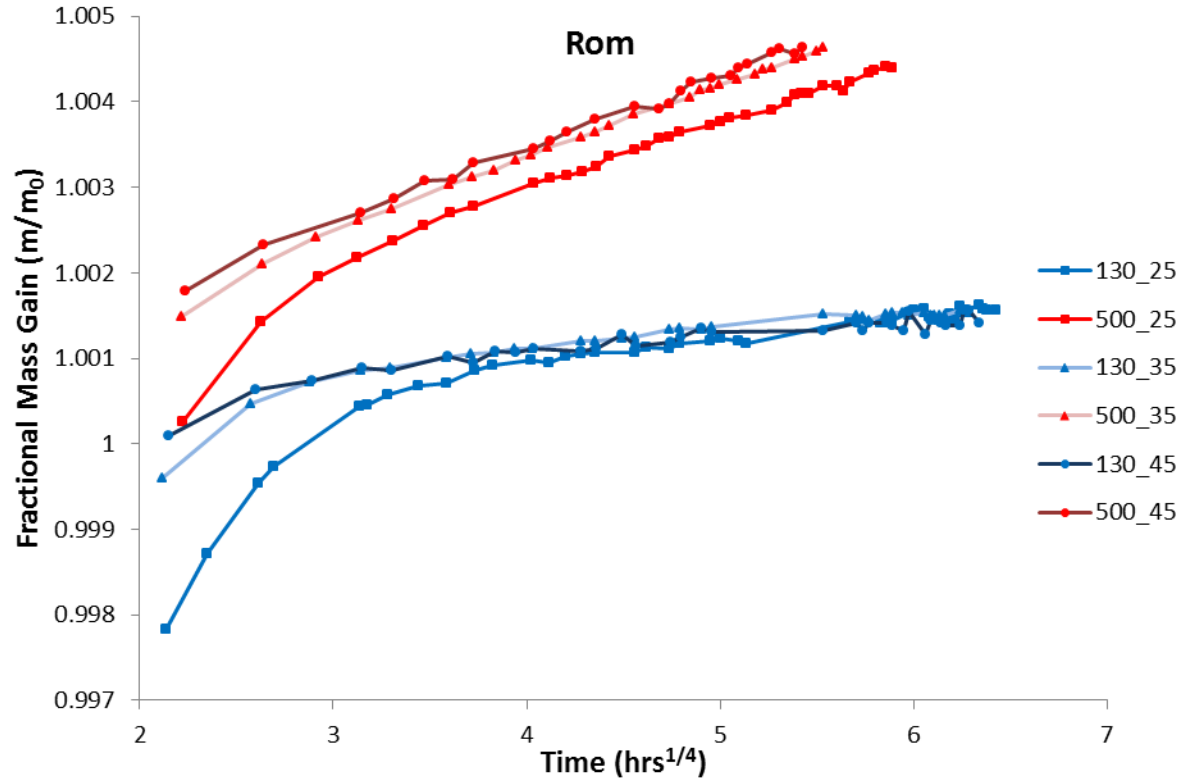

Figure 7.7: Fractional mass gain curves of *Rom* samples, following heating at 130°C (blue) and 500°C (red) and aging at temperatures of 25°C (square), 35°C (triangle), and 45°C (circle), presented across the period of ECC-GBA transfer and weighing. Interpolated lines included for visual purposes.

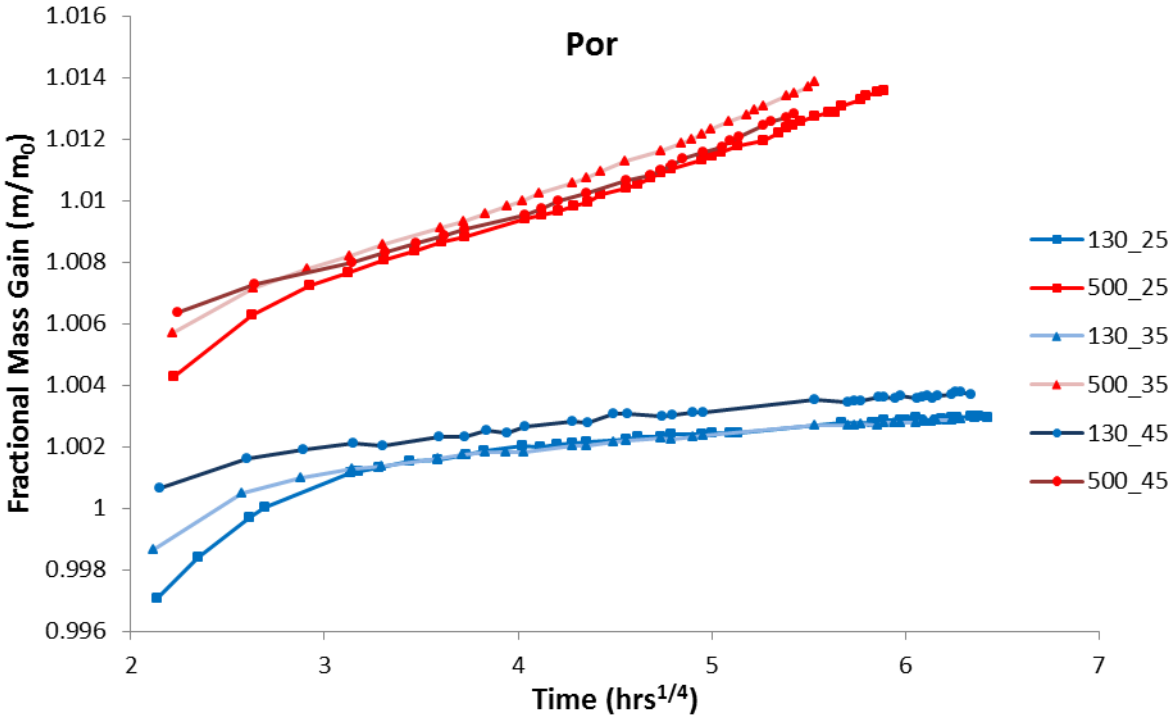

Figure 7.8: Fractional mass gain curves of *Por* samples, following heating at 130°C (blue) and 500°C (red) and aging at temperatures of 25°C (square), 35°C (triangle), and 45°C (circle), presented across the period of ECC-GBA transfer and weighing. Interpolated lines included for visual purposes.

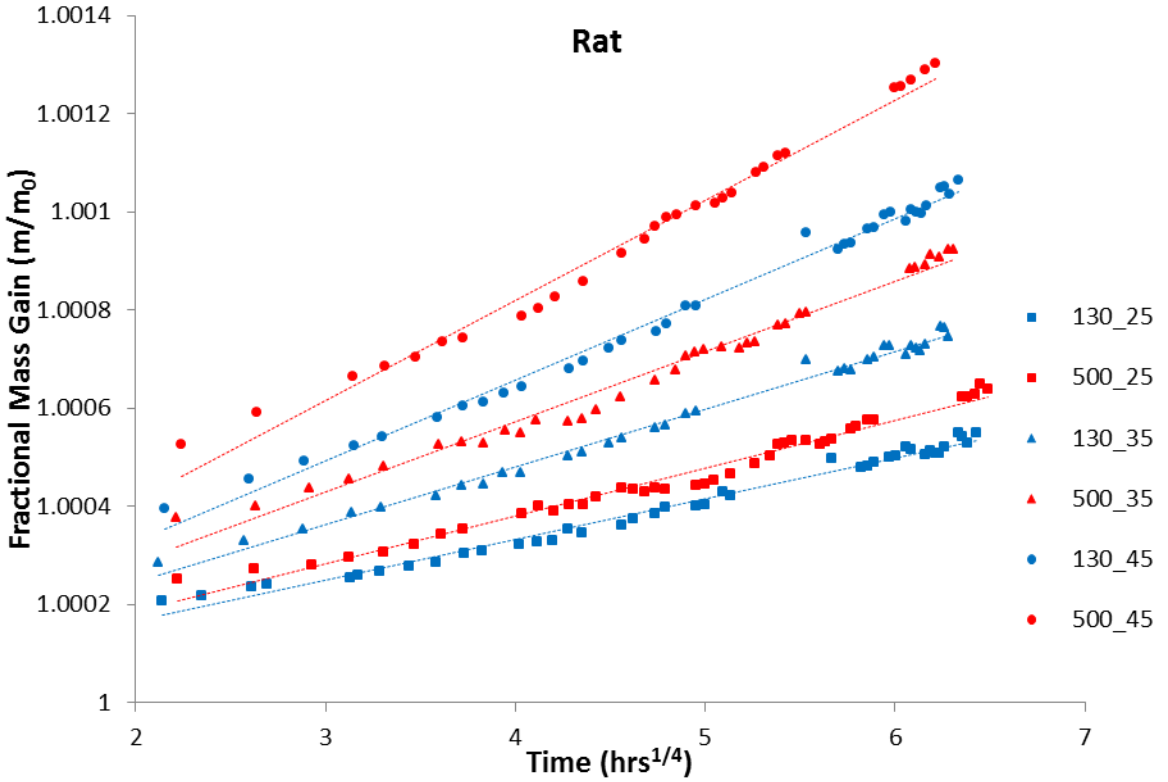

Figure 7.9: Fractional mass gain curves of *Rat* samples, following heating at 130°C (blue) and 500°C (red) and aging at temperatures of 25°C (square), 35°C (triangle), and 45°C (circle), presented across the period of ECC-GBA transfer and weighing. Imposed dashed lines correspond to linear fits across this period.

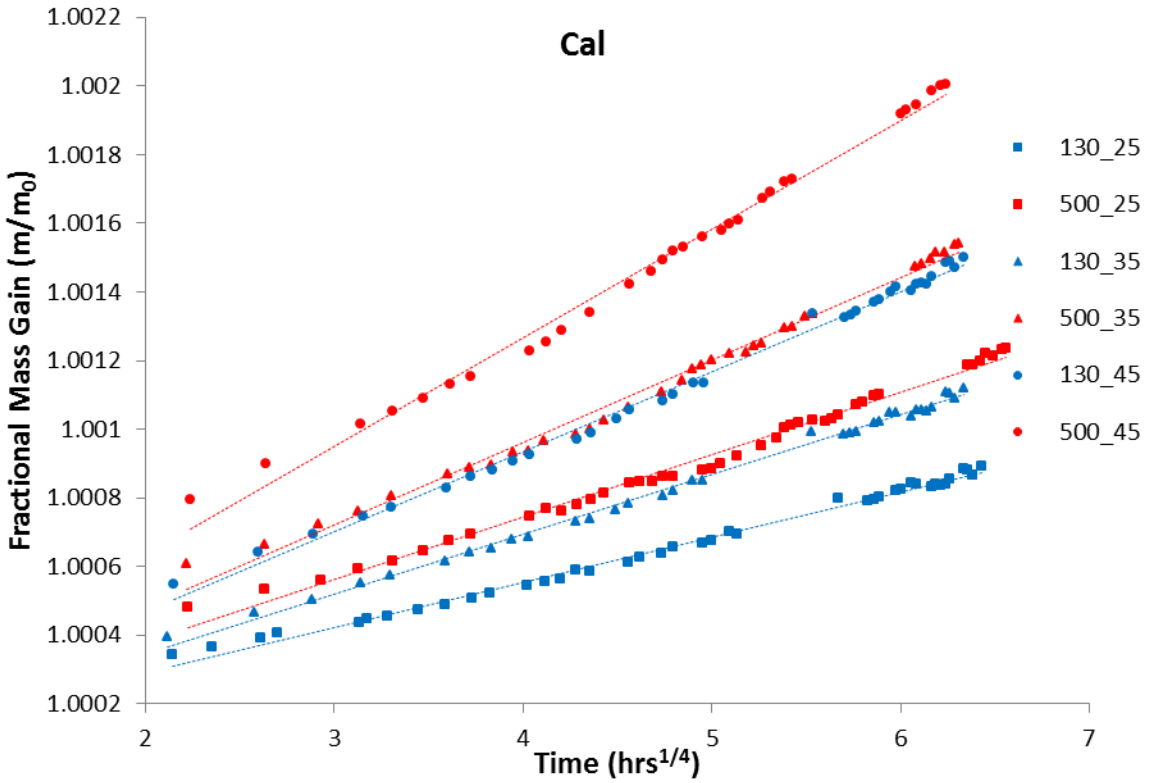

Figure 7.10: Fractional mass gain curves of *Cal* samples, following heating at 130°C (blue) and 500°C (red) and aging at temperatures of 25°C (square), 35°C (triangle), and 45°C (circle), presented across the period of ECC-GBA transfer and weighing. Imposed dashed lines correspond to linear fits across this period.

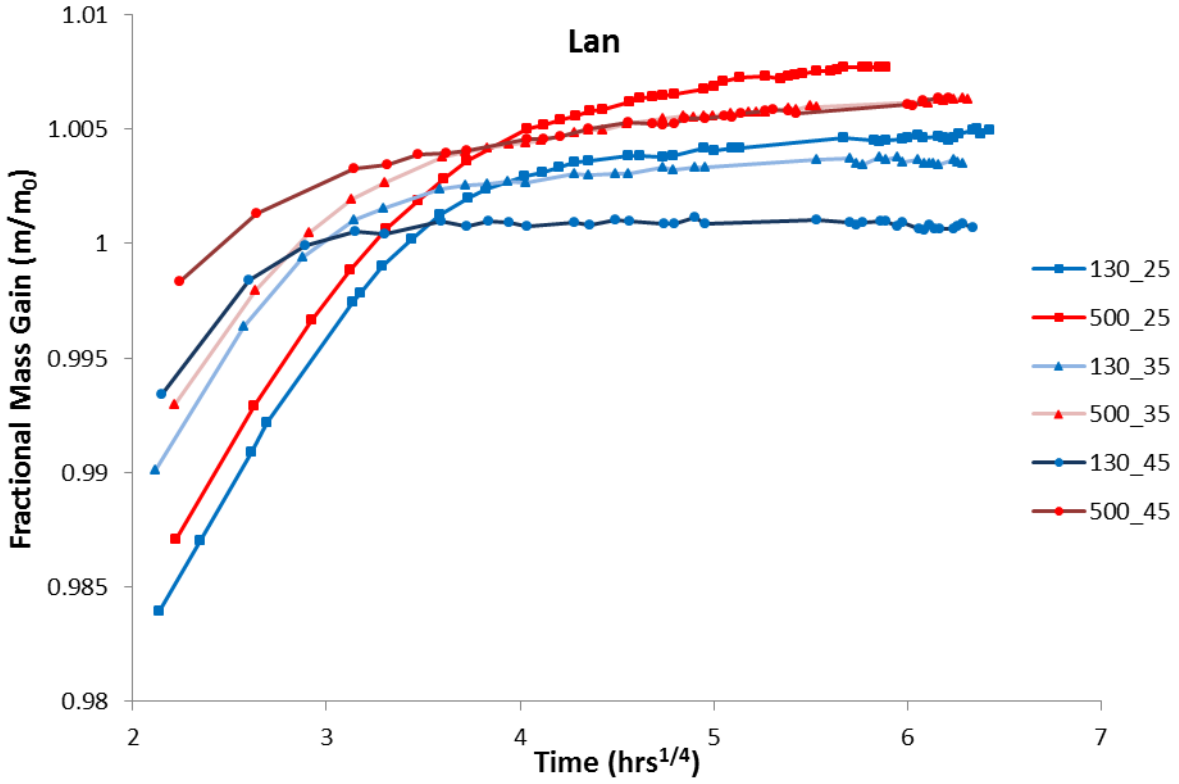

Figure 7.11: Fractional mass gain curves of *Lan* samples, following heating at 130°C (blue) and 500°C (red) and aging at temperatures of 25°C (square), 35°C (triangle), and 45°C (circle), presented across the period of ECC-GBA transfer and weighing. Interpolated lines included for visual purposes.

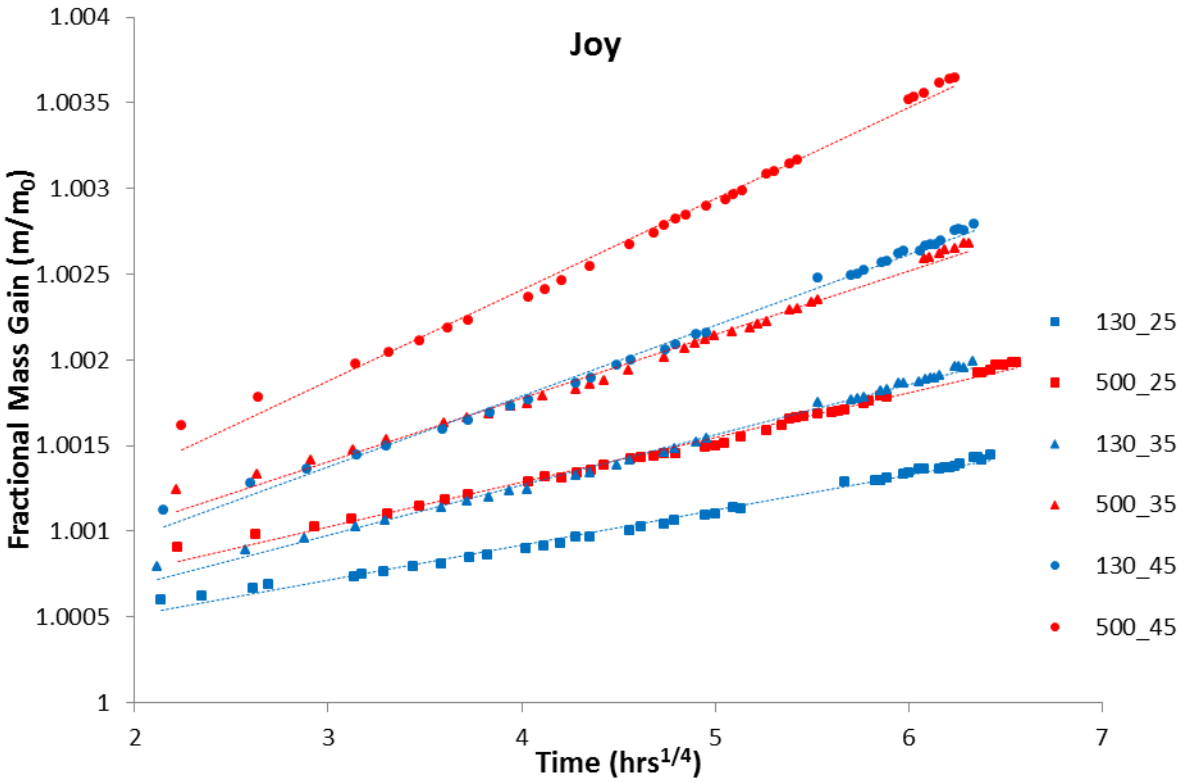

Figure 7.12: Fractional mass gain curves of *Joy* samples, following heating at 130°C (blue) and 500°C (red) and aging at temperatures of 25°C (square), 35°C (triangle), and 45°C (circle), presented across the period of ECC-GBA transfer and weighing. Imposed dashed lines correspond to linear fits across this period.

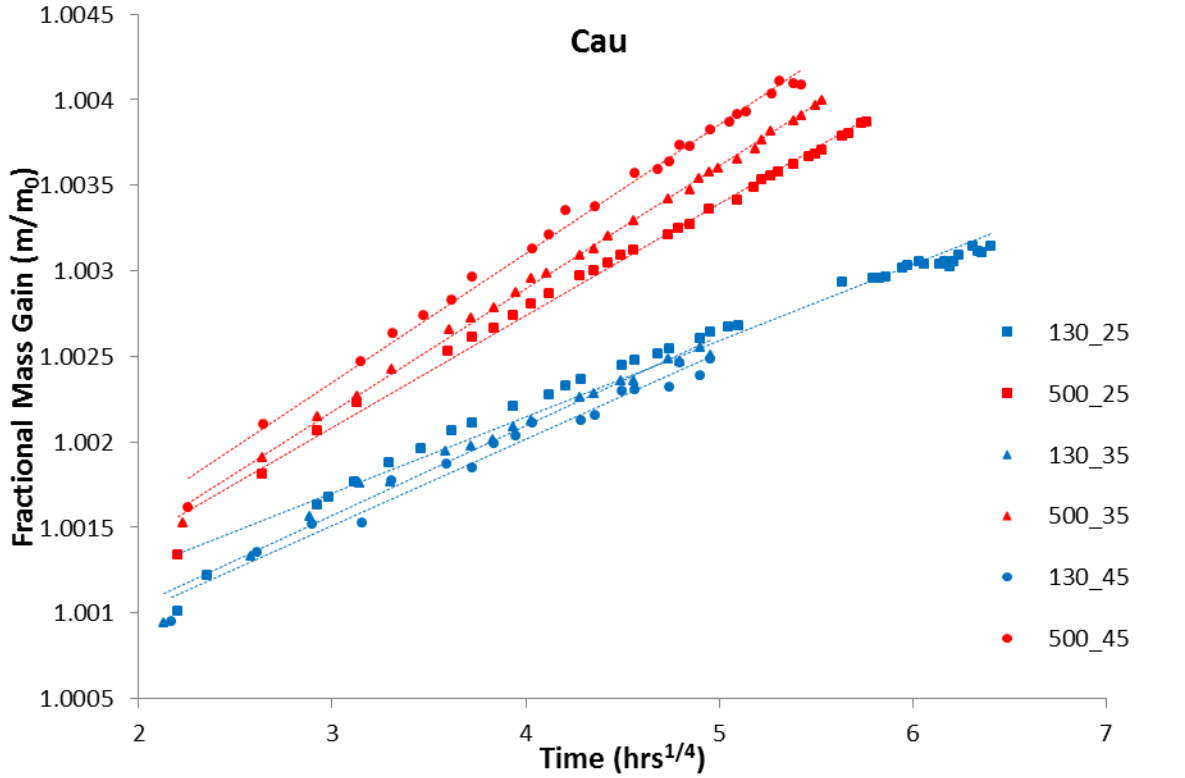

Figure 7.13: Fractional mass gain curves of *Cau* samples, following heating at 130°C (blue) and 500°C (red) and aging at temperatures of 25°C (square), 35°C (triangle), and 45°C (circle), presented across the period of ECC-GBA transfer and weighing. Imposed dashed lines correspond to linear fits across this period.

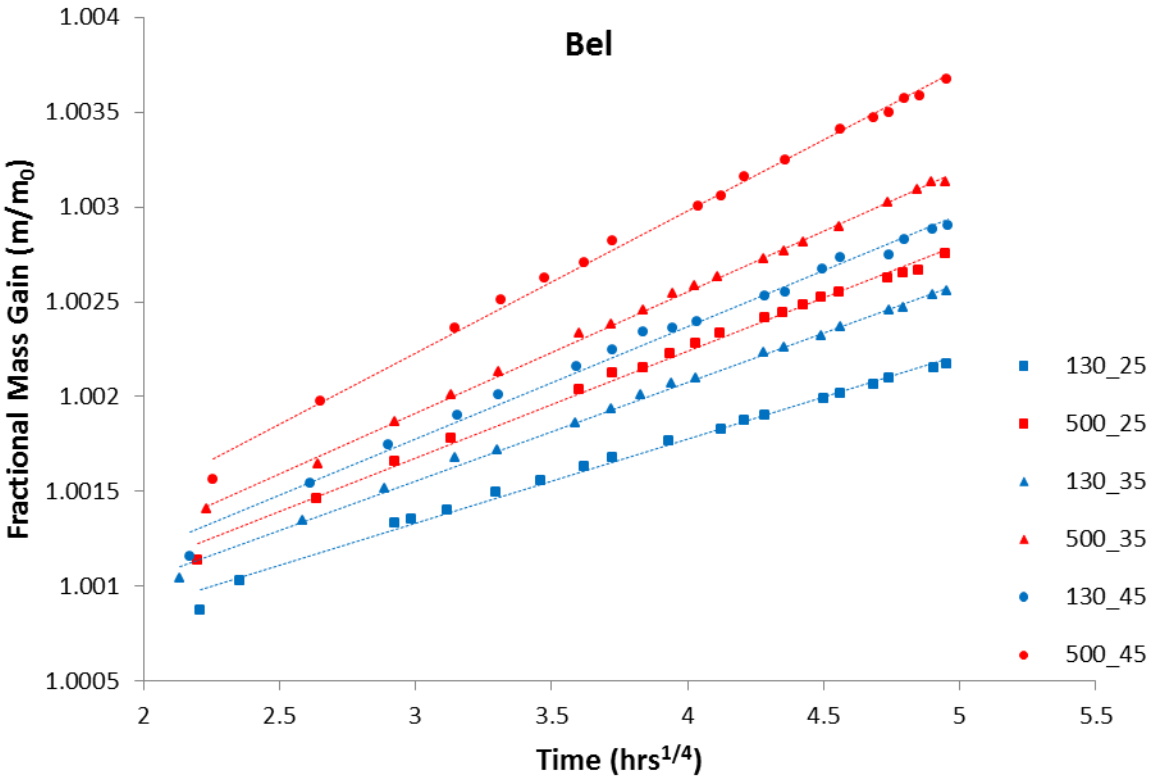

Figure 7.14: Fractional mass gain curves of *Bel* samples, following heating at 130°C (blue) and 500°C (red) and aging at temperatures of 25°C (square), 35°C (triangle), and 45°C (circle), presented across the period of ECC-GBA transfer and weighing. Imposed dashed lines correspond to linear fits across this period.

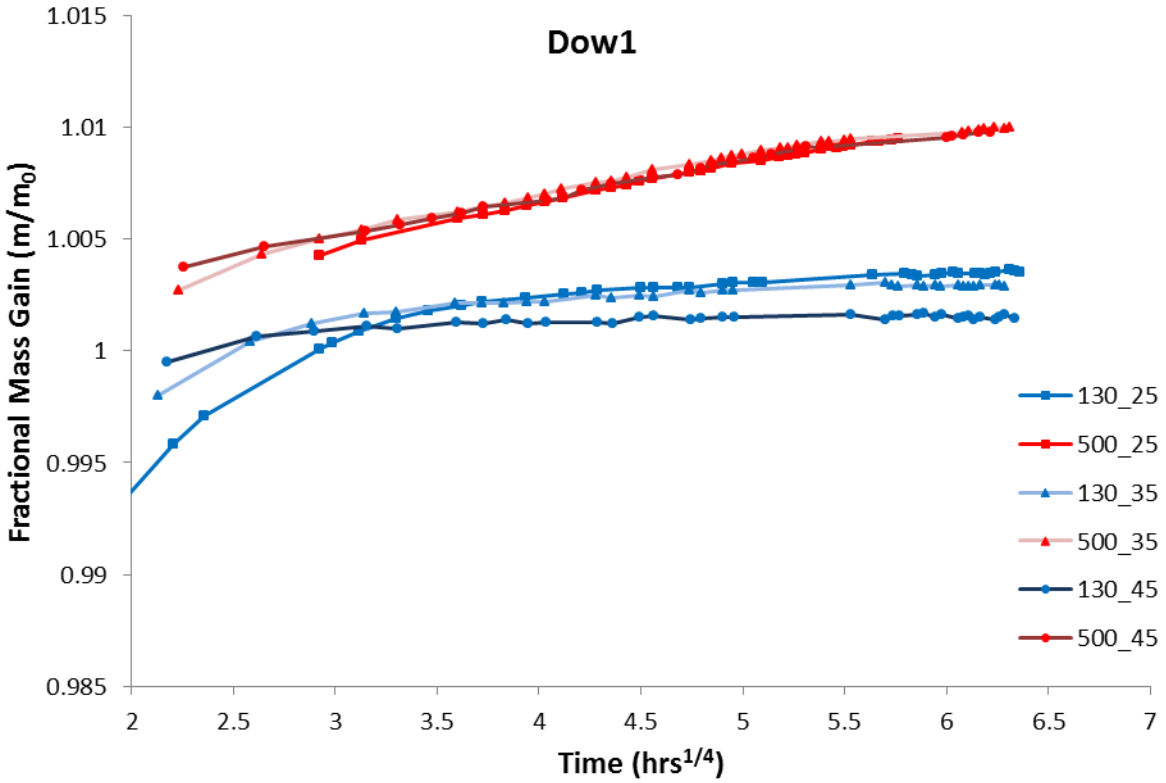

Figure 7.15: Fractional mass gain curves of *Dow1* samples, following heating at 130°C (blue) and 500°C (red) and aging at temperatures of 25°C (square), 35°C (triangle), and 45°C (circle), presented across the period of ECC-GBA transfer and weighing. Interpolated lines included for visual purposes.

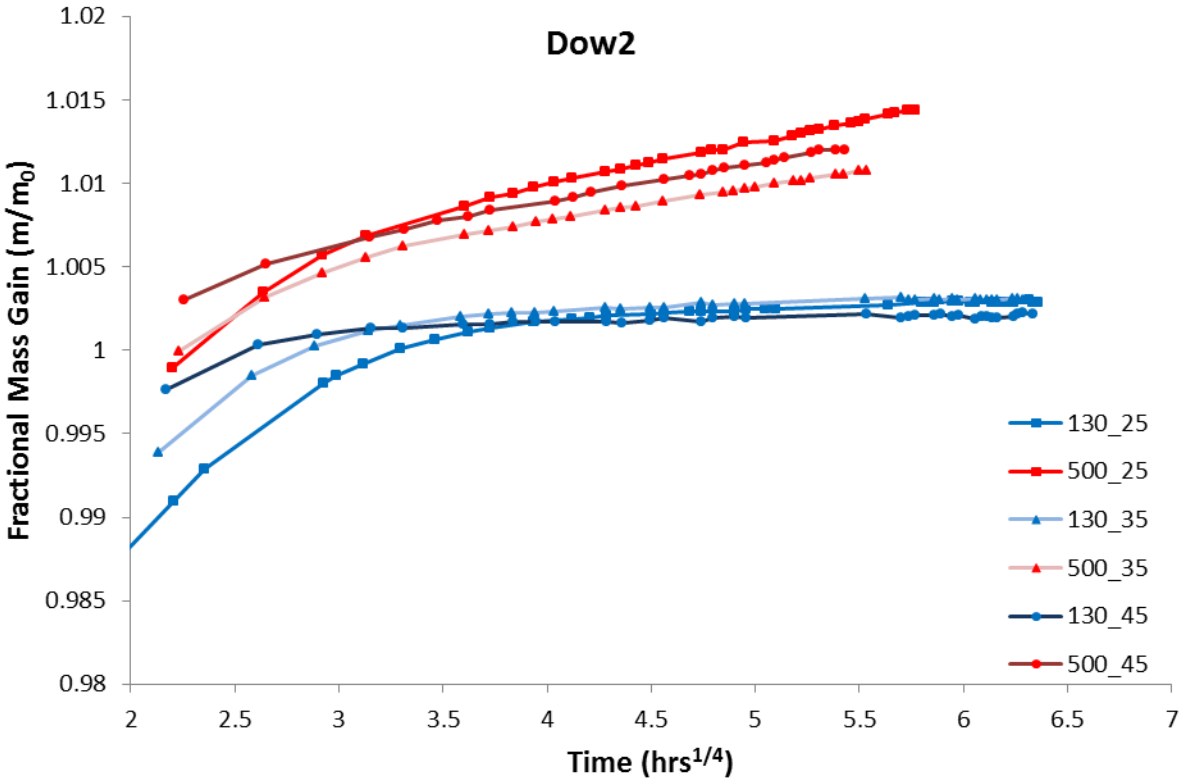

Figure 7.16: Fractional mass gain curves of *Dow2* samples, following heating at 130°C (blue) and 500°C (red) and aging at temperatures of 25°C (square), 35°C (triangle), and 45°C (circle), presented across the period of ECC-GBA transfer and weighing. Interpolated lines included for visual purposes.

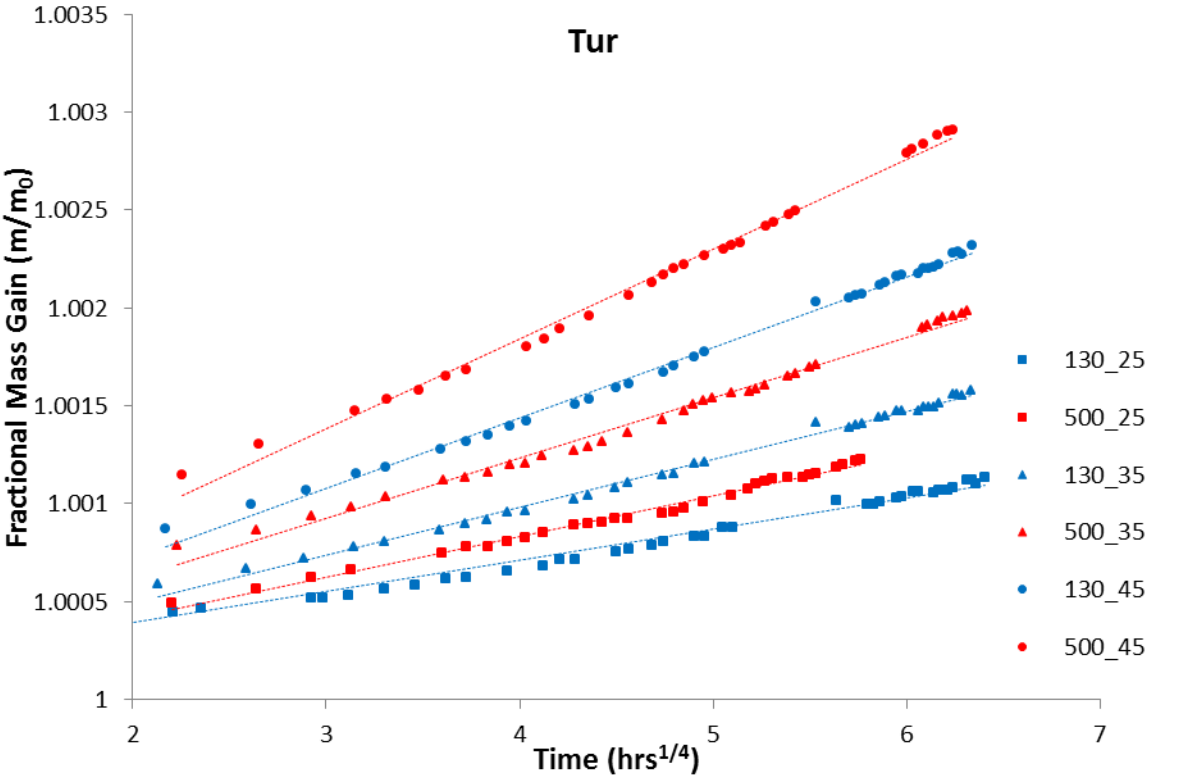

Figure 7.17: Fractional mass gain curves of *Tur* samples, following heating at 130°C (blue) and 500°C (red) and aging at temperatures of 25°C (square), 35°C (triangle), and 45°C (circle), presented across the period of ECC-GBA transfer and weighing. Imposed dashed lines correspond to linear fits across this period.

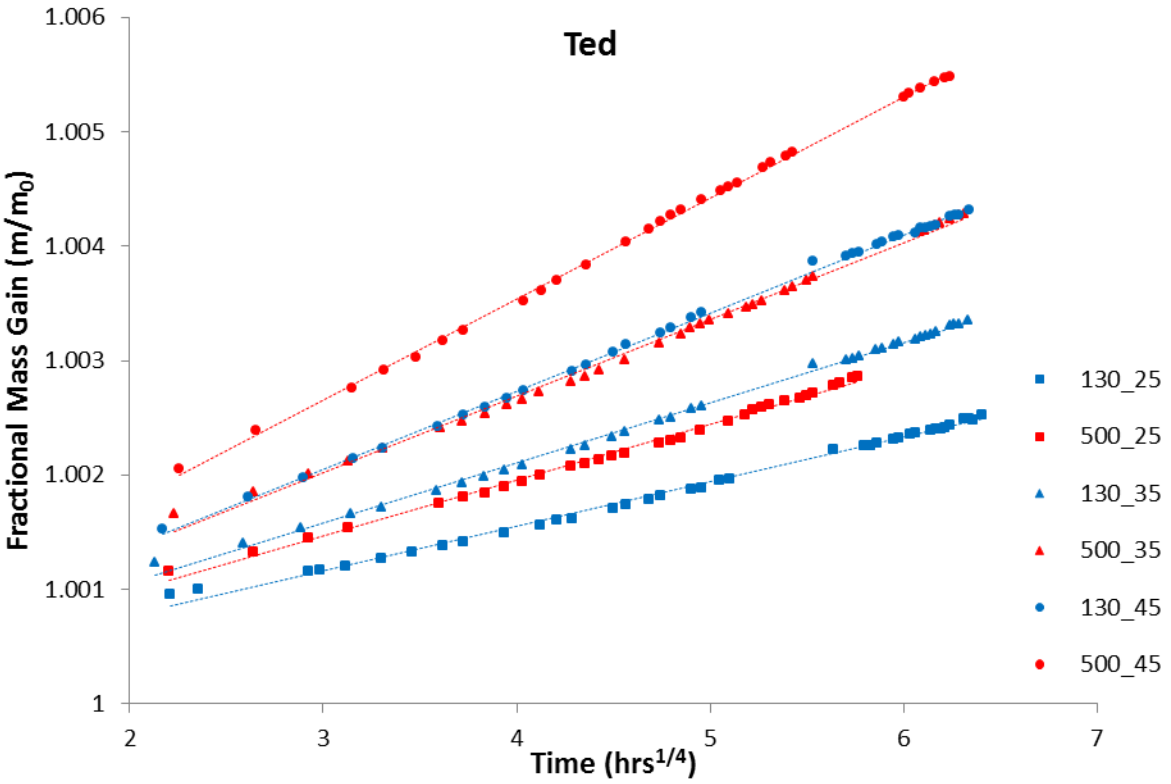

Figure 7.18: Fractional mass gain curves of *Ted* samples, following heating at 130°C (blue) and 500°C (red) and aging at temperatures of 25°C (square), 35°C (triangle), and 45°C (circle), presented across the period of ECC-GBA transfer and weighing. Imposed dashed lines correspond to linear fits across this period.

7.2 Mass Gain Curve Modelling

The results (parameters) of mass gain modelling, using both the $t^{1/4}$ and $t^{1/n}$ models and *MATLAB* code *bestfit* and *bestfitn,* are presented in later sections. An example of the application of *bestfit* to sample *Ann* (applied to all mass gain data) is provided in *Figures 7.19-7.23* with an example of the application of *bestfitn* to the same sample displayed in *Figures 7.23-7.29.* Note that *bestfit* is applied to data as a function of $t^{1/4}$ whereas *bestfitn* is applied to data as a function of *t*.

In *Figure 7.19,* the linear regression which provided the best R^2 value (*Figure 7.20*) following application of *bestfit* to $Ann_{130\text{-}25}$ is presented (corresponding to starting the regression on the 11th datapoint). The R^2 and *RMSE* values, as a function of initial datapoint are presented in *Figure 7.20* and *Figure 7.21*, respectively. It can be observed that once past *S1* the R^2 is the more sensitive of the two with regard to changes in the data series. Variation of the parameters fit as part of the regression (intercept and slope) are presented in *Figure 7.22* and *Figure 7.23* and demonstrate the effect slight curvature in the *Ann S2* data (as a function of $t^{1/4}$) has on the mass gain rate and initial mass determination.

For application of *bestfitn* ($t^{1/n}$) to *Ann,* the same properties as for *bestfit* are presented in *Figures 7.23-7.27* with the addition of *Figure 7.29* that shows the variation in *1/n* with initial data point.

Provided in *Table 7.1* are the goodness-of-fit (expressed using R^2 and *RMSE* values) values from final modelling together with the period over which the models were applied for both models. Samples with notably poor fits ($R^2 < 0.98$) are emphasised in red and samples for which modelling could not be acceptably carried out are marked *NA*. In this table the modelling results for $t^{1/n}$ ('pre-fixed') are for modelling each curve independently, and with that each *1/n* value independently. After this was carried out an average was taken and the curves were remodelled with this *1/n* value (see *Method, Section 6.5.2*). This goodness-of-fits for this stage of modelling are presented in *Table 7.2*.

The modelled values are presented in later sections.

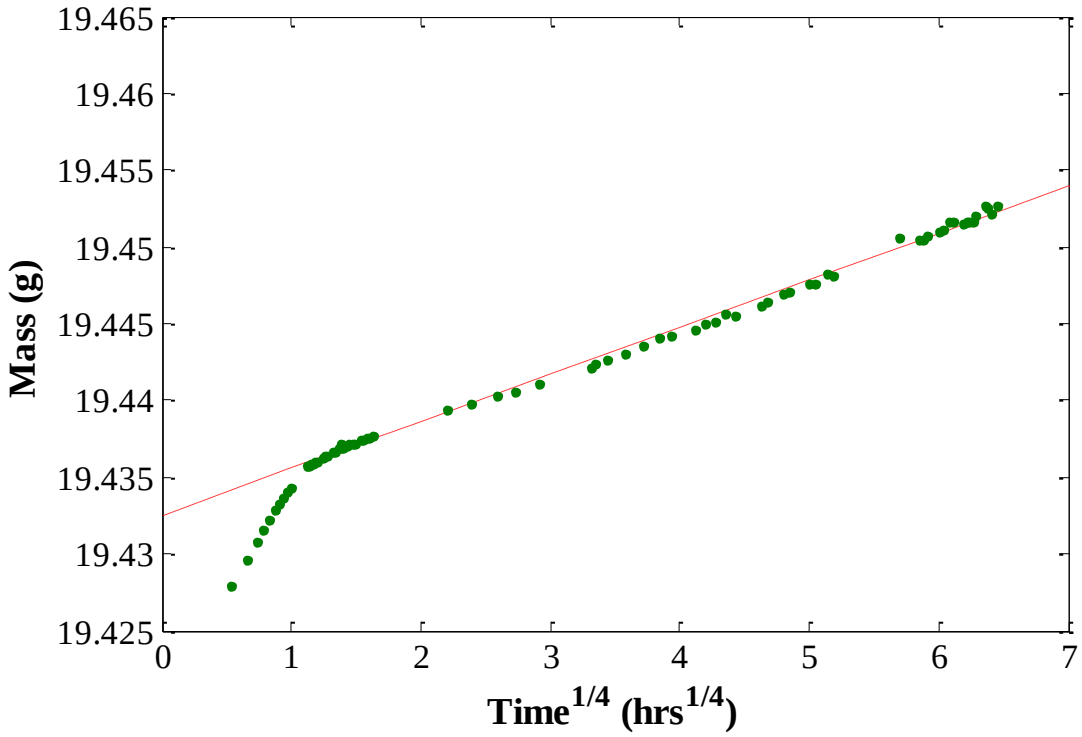

Figure 7.19: Example of application of *bestfit* to *Ann* 130°C 25°, showing the best fit line (starting at 11th datapoint) based on maximum R^2 from regressions carried out with incremental removal of first point in data series.

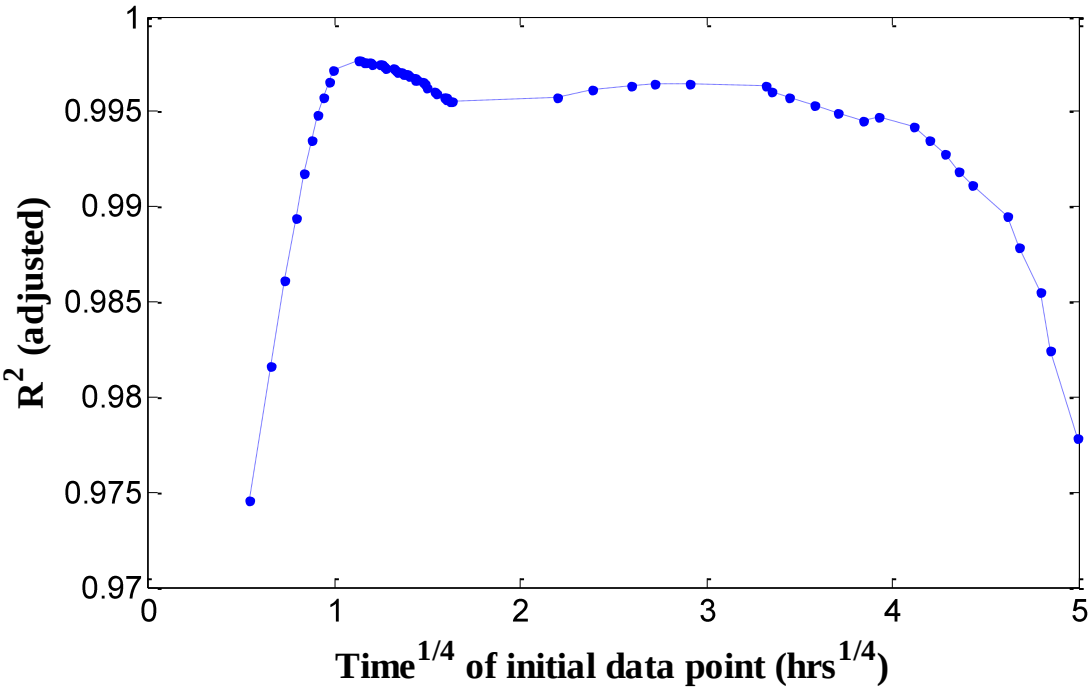

Figure 7.20: R^2 value as a function of time of initial data point in series from application of *bestfit* to *Ann* 130°C 25°C.

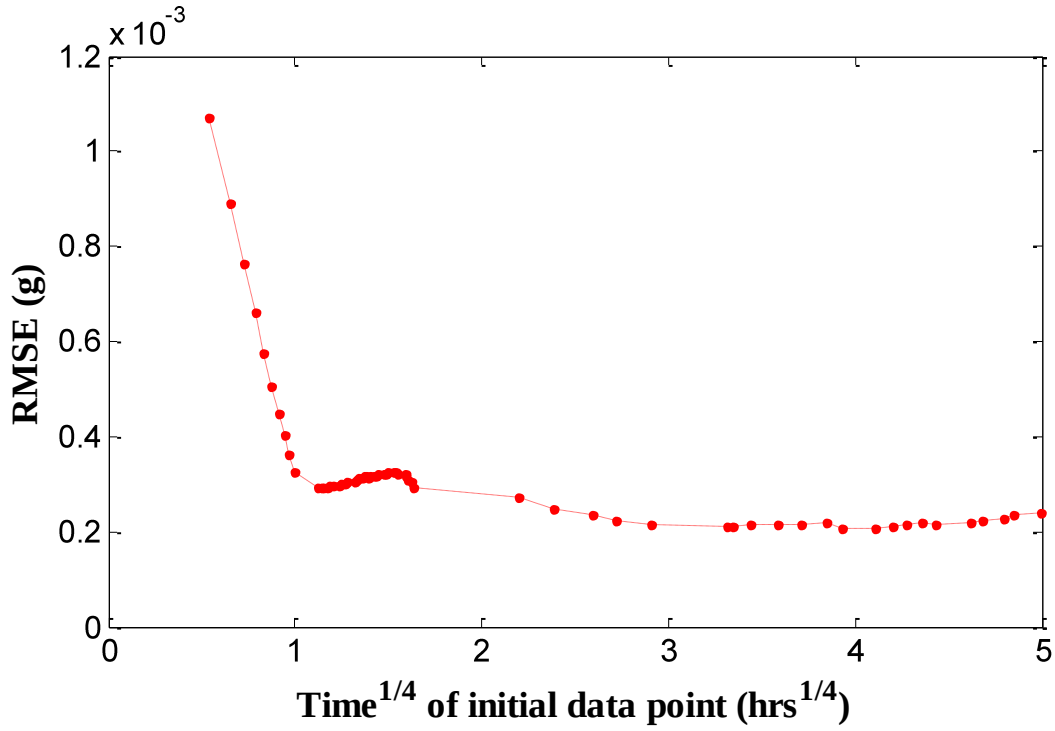

Figure 7.21: ***RMSE*** **value as a function of time of initial data point in series from application of** ***bestfit*** **to** ***Ann*** **130°C 25°C.**

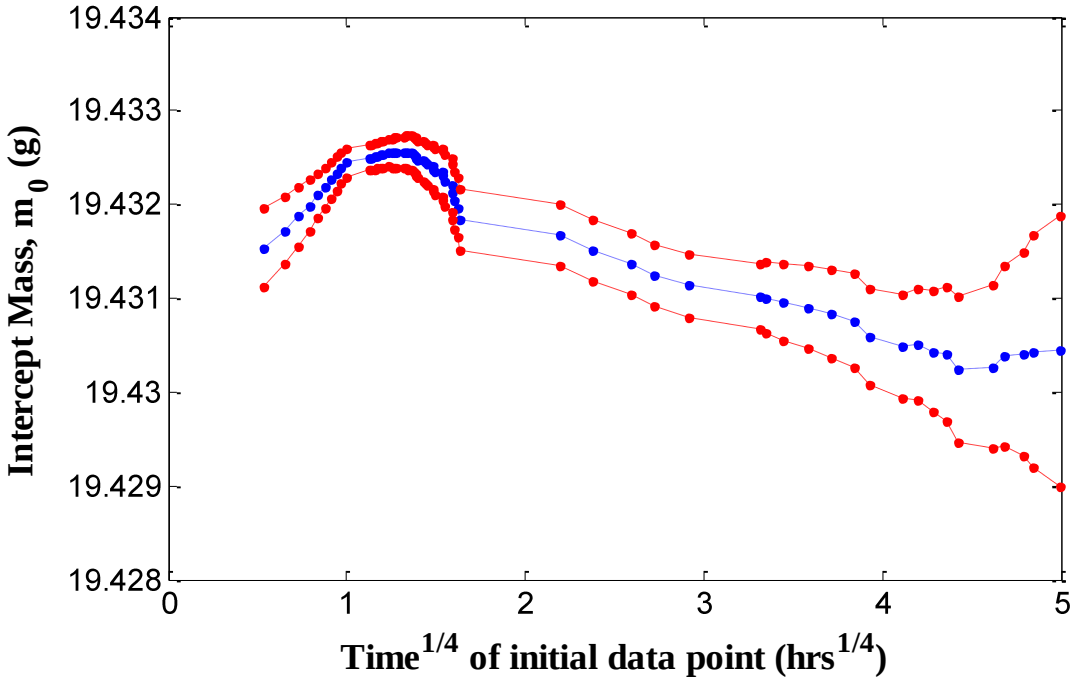

Figure 7.22: Intercept mass, m_0 (blue), as a function of time of initial data point in series from application of ***bestfit*** **to** ***Ann*** **130°C 25°C. Also included are 95% confidence intervals (red).**

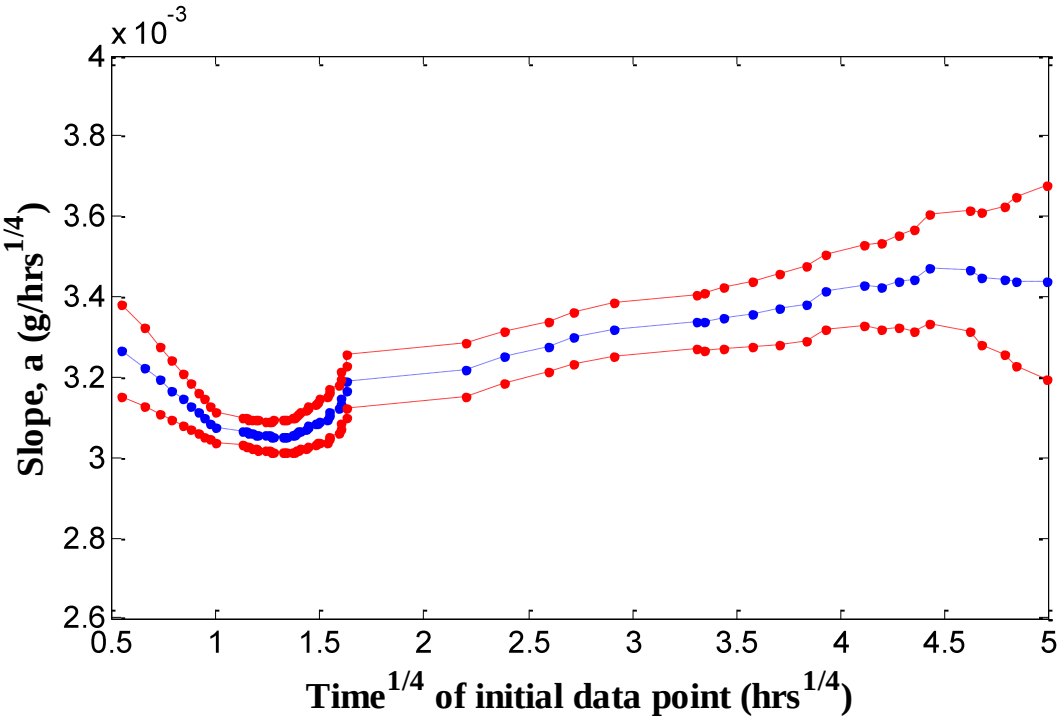

Figure 7.23: Slope, *a* (blue), as a function of time of initial data point in series from application of *bestfit* to *Ann* 130°C 25°C. Also included are 95% confidence intervals (red).

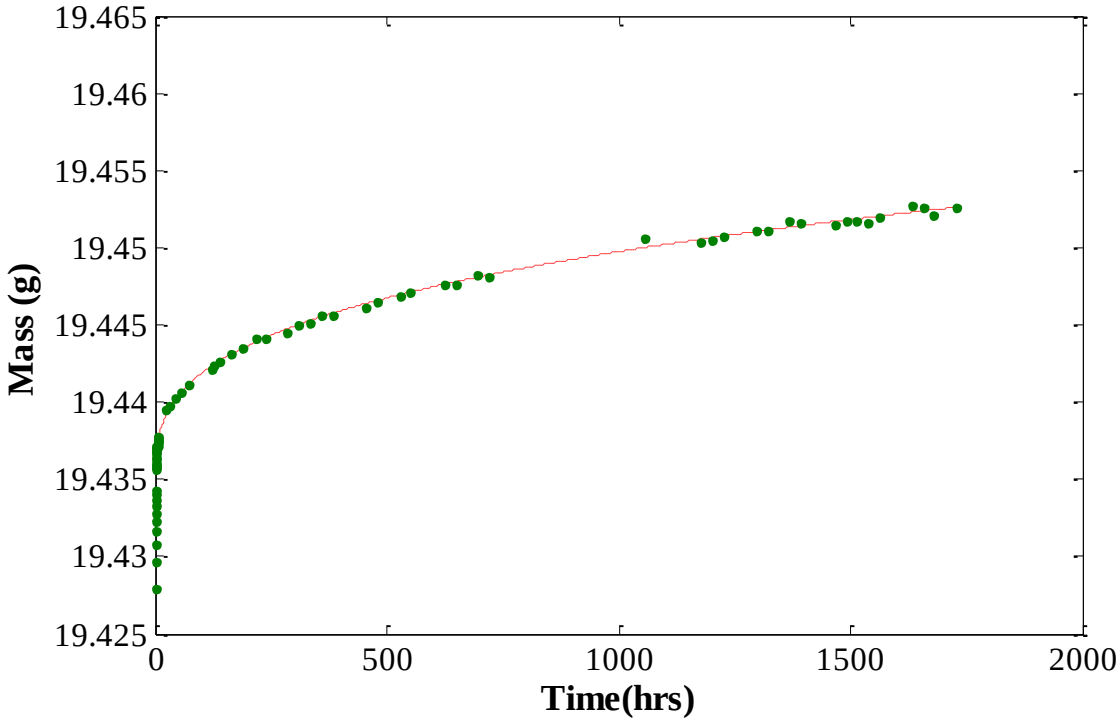

Figure 7.24: Example of application of *bestfitn* to *Ann* 130°C 25°, showing the best fit line (starting at 23rd datapoint) based on maximum R^2 from regressions carried out with incremental removal of first point in data series. For 1/n=0.31.

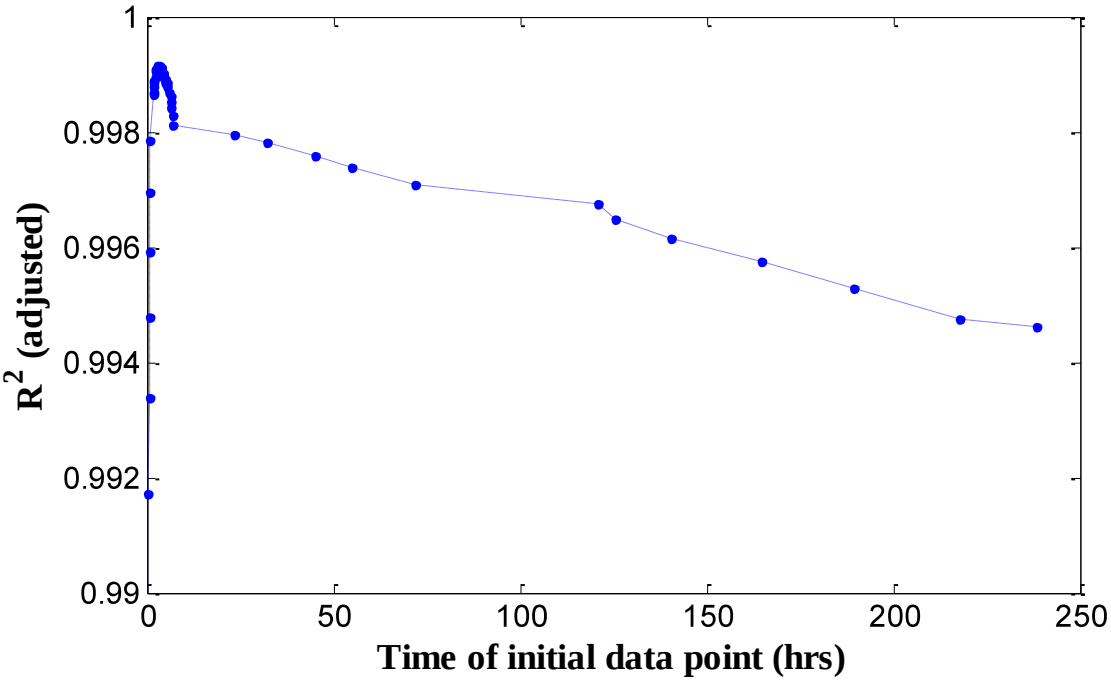

Figure 7.25: R^2 **value as a function of time of initial data point in series from application of *bestfitn* to *Ann* 130°C 25°C.**

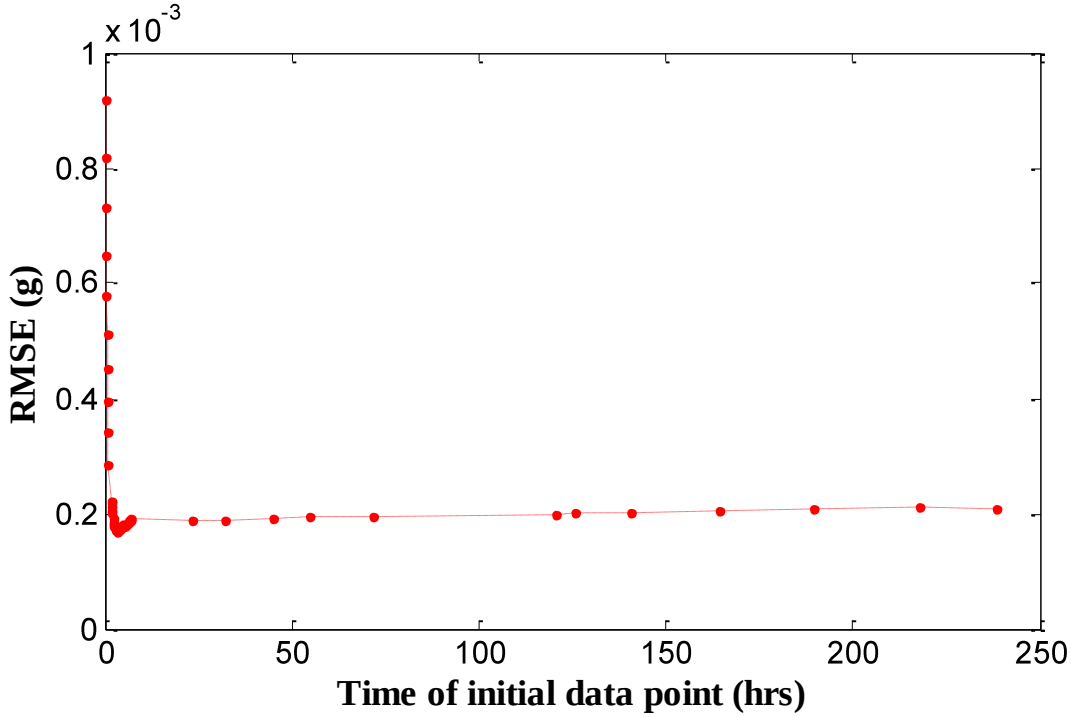

Figure 7.26: ***RMSE*** **value as a function of time of initial data point in series from application of *bestfitn* to *Ann* 130°C 25°C.**

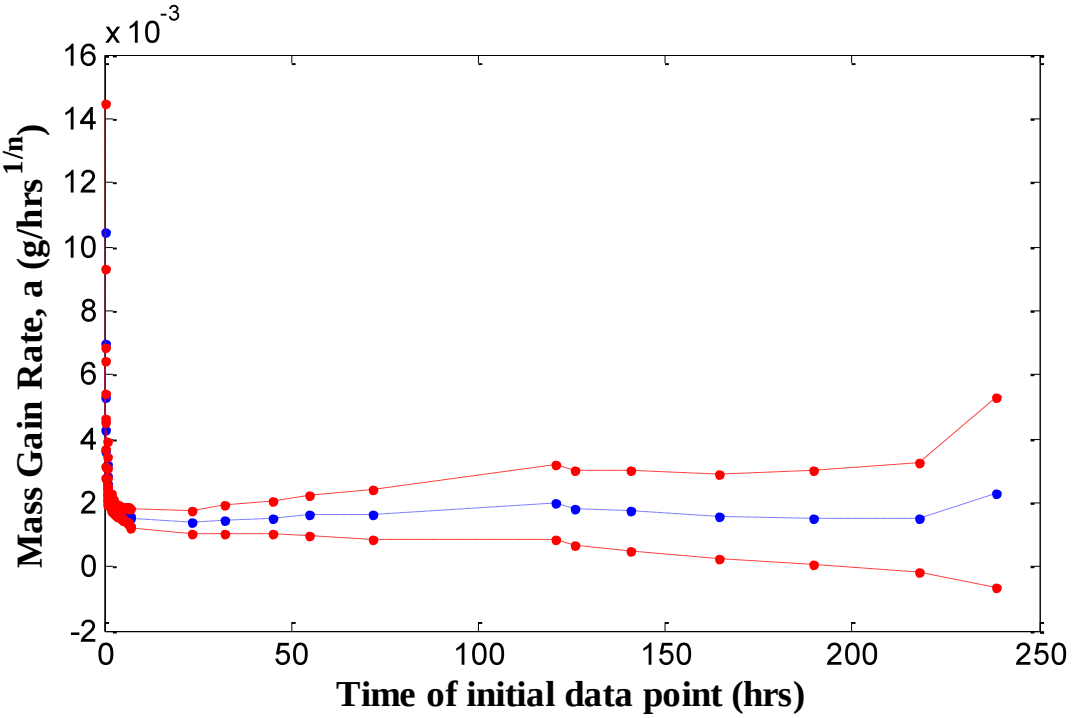

Figure 7.27: Slope, *a* (blue), as a function of time of initial data point in series from application of *bestfitn* to *Ann* 130°C 25°C. Also included are 95% confidence intervals (red).

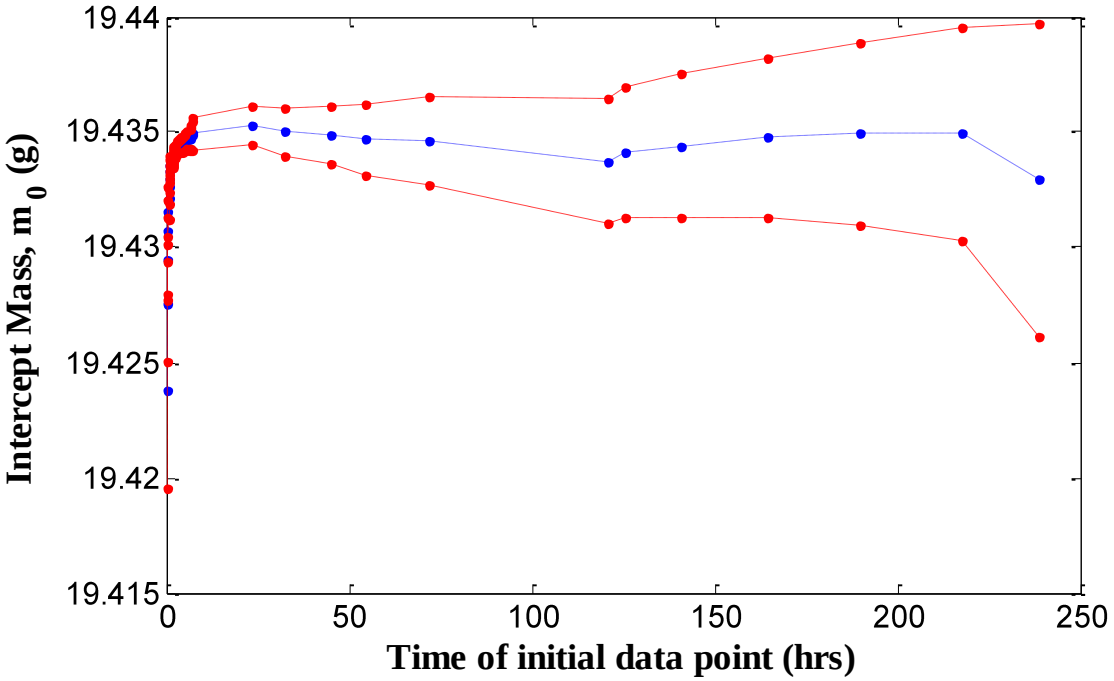

Figure 7.28: Intercept mass, m_0 (blue), as a function of time of initial data point in series from application of *bestfitn* to *Ann* 130°C 25°C. Also included are 95% confidence intervals (red).

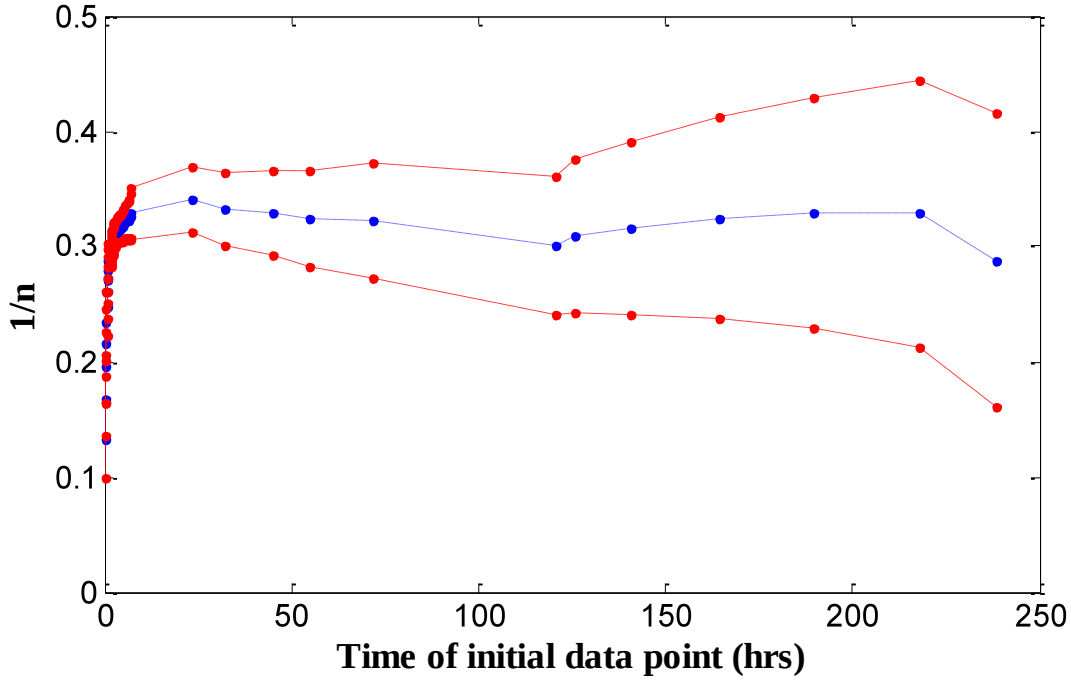

Figure 7.29*: 1/n*, as a function of time of initial data point in series from application of *bestfitn* to *Ann* 130°C 25°C. Also included are 95% confidence intervals (red).

Table 7.1: Goodness-of-fit values (R^2, *RMSE*) from modelling of data over most suitable period for both $t^{1/4}$ and $t^{1/n}$ approaches. Red font implies fits with poor R^2 values. *NA* implies unsuitable for modelling.

	$t^{1/4}$			$t^{1/n}$ *(pre-fixed)*		
Sample	**Period (hrs)** **130°C 25°C** **130°C 35°C** **130°C 45°C** **500°C 25°C** **500°C 35°C** **500°C 45°C**	**R^2** **130°C 25°C** **130°C 35°C** **130°C 45°C** **500°C 25°C** **500°C 35°C** **500°C 45°C**	***RMSE* (g)** **130°C 25°C** **130°C 35°C** **130°C 45°C** **500°C 25°C** **500°C 35°C** **500°C 45°C**	**Period (hrs)** **130°C 25°C** **130°C 35°C** **130°C 45°C** **500°C 25°C** **500°C 35°C** **500°C 45°C**	**R^2** **130°C 25°C** **130°C 35°C** **130°C 45°C** **500°C 25°C** **500°C 35°C** **500°C 45°C**	***RMSE* (g)** **130°C 25°C** **130°C 35°C** **130°C 45°C** **500°C 25°C** **500°C 35°C** **500°C 45°C**
Ann	>24 >24 >24 >24 >24 >24	0.996 0.998 0.998 0.996 0.996 0.998	0.00027 0.00026 0.00033 0.00030 0.00038 0.00038	>24 >24 >24 >24 >24 >24	0.998 0.998 0.999 0.997 0.999 0.999	0.00019 0.00022 0.00023 0.00024 0.00019 0.00022
Esp	>24 >48 >24 >24 >24 >24	0.994 0.992 0.992 0.993 0.995 0.994	0.00022 0.00028 0.00031 0.00023 0.00025 0.00031	>24 >24 >24 >47 >24 >24	0.994 0.995 0.993 0.993 0.997 0.996	0.00021 0.00022 0.00029 0.00023 0.00021 0.00027
Nic	>24 >24 >24 >24 >24 >24	0.997 0.998 0.989 0.996 0.998 0.999	0.00020 0.00018 0.00038 0.00036 0.00027 0.00027	>24 >24 >24 >47 >24 >24	0.998 0.999 0.998 0.998 0.998 0.999	0.00017 0.00012 0.00017 0.00026 0.00024 0.00023
Mac	>24 >24 >24 >24 >24 >24	0.995 0.997 0.987 0.993 0.992 0.991	0.00021 0.00021 0.00041 0.00027 0.00037 0.00044	>24 >24 >24 >47 >24 >24	0.995 0.997 0.988 0.994 0.997 0.998	0.00021 0.00021 0.00040 0.00023 0.00021 0.00023
Ria	>121 >117 >166 >24 >335 >264	0.995 0.997 0.998 0.993 0.998 0.999	0.00022 0.00022 0.00031 0.00027 0.00016 0.00018	>24 >24 >24 >47 >24 >24	0.998 0.999 0.999 0.997 0.999 0.999	0.00018 0.00019 0.00026 0.00021 0.00020 0.00022
Etr	>335 >164 >70 >240 >190 >264	0.995 0.979 0.074 0.997 0.997 0.982	0.00016 0.00046 0.00410 0.00129 0.00150 0.00259	NA	NA	NA
Rom	>193 >97 >45 >145 >72 >25	0.931 0.990 0.925 0.996 0.999 0.994	0.00060 0.00032 0.00122 0.00067 0.00035 0.00137	>193 >97 >70 >73 >48 >24	0.965 0.991 0.898 0.997 0.999 0.994	0.00090 0.00029 0.00123 0.00067 0.00033 0.00130
Por	>193 >190	0.959 0.990	0.00084 0.00071	NA	NA	NA

	>46 >289 >190 >265	0.972 0.998 0.997 0.992	0.00154 0.00076 0.00146 0.00175			
Rat	>24 >24 >24 >24 >24 >24	0.986 0.992 0.992 0.977 0.981 0.987	0.00027 0.00024 0.00038 0.00032 0.00041 0.00052	>24 >40 >24 >24 >24 >24	0.994 0.997 0.997 0.986 0.995 0.997	0.00011 0.00008 0.00064 0.00023 0.00022 0.00025
Cal	>96 >24 >24 >73 >24 >24	0.996 0.996 0.995 0.992 0.991 0.992	0.00021 0.00026 0.00041 0.00033 0.00049 0.00064	>24 >24 >24 >24 >24 >24	0.997 0.998 0.998 0.997 0.998 0.998	0.00020 0.00020 0.00026 0.00023 0.00022 0.00029
Lan	>311 >165 >98 >313 >168 >97	0.933 0.960 0.362 0.956 0.967 0.972	0.00144 0.00124 0.00289 0.00303 0.00238 0.00262	NA	NA	NA
Joy	>53 >165 >166 >481 >335 >265	0.997 0.998 0.998 0.996 0.999 0.999	0.00021 0.00026 0.00032 0.00023 0.00018 0.00019	>24 >24 >24 >24 >24 >24	0.999 0.999 0.999 0.998 0.999 0.999	0.00020 0.00023 0.00032 0.00024 0.00022 0.00028
Cau	>24 >24 >24 >24 >24 >24	0.975 0.980 0.973 0.988 0.997 0.992	0.00130 0.00105 0.00111 0.00103 0.00052 0.00089	>30 >45 >24 >96 >49 >24	0.999 0.994 0.983 0.999 0.999 0.997	0.00032 0.00047 0.00089 0.00025 0.00029 0.00049
Bel	>24 >24 >24 >24 >24 >24	0.992 0.997 0.991 0.994 0.999 0.995	0.00065 0.00044 0.00090 0.00065 0.00033 0.00078	>73 >46 >24 >23 >24 >24	0.999 0.999 0.997 0.999 0.999 0.999	0.00014 0.00022 0.00047 0.00032 0.00026 0.00041
Dow1	>192 >98 >47 >168 >73 >26	0.963 0.945 0.820 0.995 0.997 0.997	0.00084 0.00123 0.00175 0.00123 0.00121 0.00142	NA	NA	NA
Dow2	>338 >166 >71 >240 >243 >146	0.954 0.961 0.841 0.998 0.999 0.997	0.00036 0.00062 0.00099 0.00076 0.00035 0.00059	NA	NA	NA
Tur	>24 >24 >24 >24	0.990 0.995 0.996 0.991	0.00043 0.00044 0.00056 0.00037	>24 >24 >24 >24	0.998 0.999 0.999 0.996	0.00012 0.00019 0.00012 0.00025

	>24	0.991	0.00066	>24	0.998	0.00023
	>24	0.994	0.00077	>24	0.999	0.00024
Ted	>24	0.996	0.00068	>24	0.999	0.00013
	>24	0.998	0.00058	>24	0.999	0.00010
	>24	0.999	0.00052	>48	0.999	0.00015
	>24	0.996	0.00064	>24	0.999	0.00025
	>24	0.996	0.00091	>24	0.999	0.00025
	>24	0.999	0.00058	>24	0.999	0.00033

Table 7.2: Goodness-of-fit values (R^2, *RMSE*) from final modelling of $t^{1/n}$ data using fixed *1/n* value on all curves. Included is period over which modelling was carried out.

		$t^{1/n}$ *(1/n fixed)*		
Sample	**Fixed 1/n value**	**Period** **130°C 25°C** **130°C 35°C** **130°C 45°C** **500°C 25°C** **500°C 35°C** **500°C 45°C**	R^2 **130°C 25°C** **130°C 35°C** **130°C 45°C** **500°C 25°C** **500°C 35°C** **500°C 45°C**	*RMSE* **130°C 25°C** **130°C 35°C** **130°C 45°C** **500°C 25°C** **500°C 35°C** **500°C 45°C**
Ann	0.327	>24	0.998	0.00019
		>24	0.998	0.00023
		>24	0.999	0.00024
		>24	0.997	0.00024
		>24	0.999	0.00020
		>24	0.999	0.00025
Esp	0.191	>24	0.994	0.00021
		>24	0.995	0.00023
		>24	0.993	0.00029
		>24	0.992	0.00027
		>24	0.997	0.00021
		>24	0.996	0.00027
Nic	0.198	>24	0.998	0.00016
		>24	0.999	0.00012
		>97	0.993	0.00021
		>47	0.998	0.00022
		>24	0.998	0.00024
		>24	0.999	0.00028
Mac	0.317	>47	0.993	0.00021
		>48	0.996	0.00023
		>24	0.988	0.00039
		>47	0.994	0.00023
		>24	0.996	0.00025
		>24	0.996	0.00029
Ria	0.387	>24	0.997	0.00018
		>24	0.998	0.00021
		>24	0.999	0.00026
		>24	0.997	0.00023
		>24	0.999	0.00019
		>24	0.999	0.00022
Etr	NA	NA	NA	NA
Rom	0.139	>24	0.935	0.00058
		>97	0.992	0.00029

		>45	0.931	0.00118
		>73	0.997	0.00071
		>48	0.999	0.00040
		>25	0.994	0.00134
Por	NA	NA	NA	NA
Rat	0.450	>24	0.993	0.00012
		>24	0.998	0.00008
		>24	0.997	0.00012
		>24	0.992	0.00021
		>24	0.995	0.00022
		>24	0.997	0.00024
Cal	0.376	>24	0.997	0.00020
		>24	0.997	0.00022
		>24	0.998	0.00026
		>24	0.997	0.00024
		>24	0.998	0.00023
		>24	0.998	0.00029
Lan	NA	NA	NA	NA
Joy	0.392	>24	0.999	0.00020
		>24	0.999	0.00024
		>24	0.999	0.00033
		>24	0.998	0.00024
		>24	0.999	0.00026
		>24	0.999	0.00027
Cau	NA	NA	NA	NA
Bel	0.160	>31	0.999	0.00016
		>20	0.999	0.00027
		>46	0.997	0.00042
		>23	0.999	0.00032
		>49	0.999	0.00025
		>49	0.999	0.00040
Dow1	NA	NA	NA	NA
Dow2	NA	NA	NA	NA
Tur	0.443	>79	0.997	0.00012
		>24	0.999	0.00012
		>47	0.999	0.00012
		>48	0.995	0.00026
		>24	0.998	0.00023
		>49	0.999	0.00022
Ted	0.375	>0.5	0.999	0.00014
		>24	0.999	0.00012
		>47	0.999	0.00016
		>24	0.999	0.00025
		>24	0.999	0.00026
		>49	0.999	0.00044

7.3 *Stage 2* Mass Gain

7.3.1 Mass Gain Rates

The mass gain rates (not fractional) for both models are presented in *Table 7.3* ($t^{1/4}$), *Table 7.4* ($t^{1/n}$ pre-fixed), and *Table 7.5* ($t^{1/n}$ fixed). Also included are the 95% confidence intervals.

The fractional mass gain rates from the $t^{1/4}$ model are displayed in *Figures 7.30-7.32* for the 25°C aging temperature. These provide a ranking of $a_{130\text{-}25}$, $a_{500\text{-}25}$, and $a_{RHX\text{-}25}$ components for all samples. For *Figure 7.33,* the *abnormal* samples (*Etr, Rom, Por, Lan, Dow1/2*) have been removed (see *Discussion* on 'abnormal samples' but briefly it refers to those sample for which mass gain curves displayed very poor $t^{1/4}/t^{1/n}$ behaviour or no Arrhenius temperature dependence). The relationship between the different aging temperature components is displayed in the later activation energy plots with other relationships and correlations in the following *Section 7.3.2*. Ranking of the $t^{1/n}$ model are not meaningful where different *1/n* values are involved but the relationship of the rates, per sample, is provided in the activation energy section also.

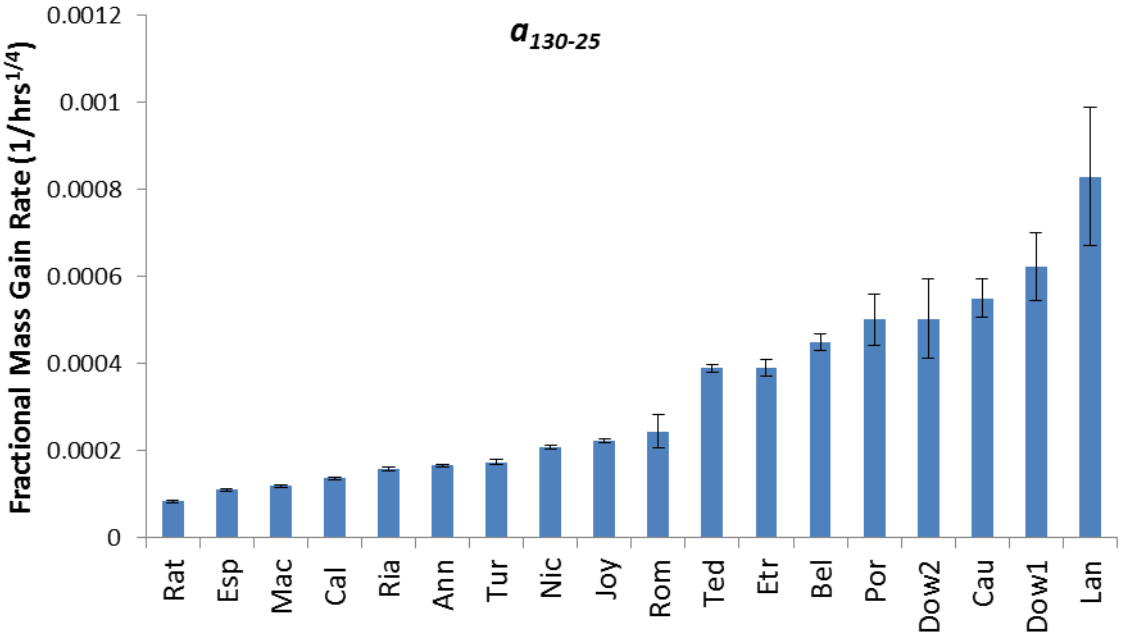

Figure 7.30: Fractional mass gain rate following 25°C aging of 130°C heated samples ($t^{1/4}$ model), including 95% uncertainties.

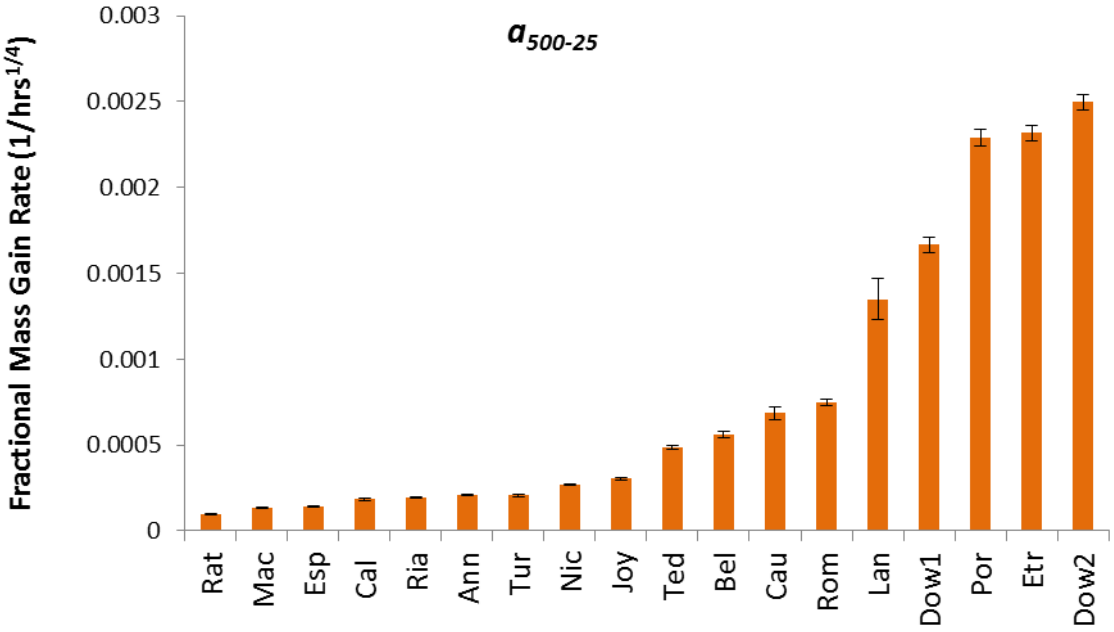

Figure 7.31: Fractional mass gain rate following 25°C aging of 130°C heated samples ($t^{1/4}$ model), including 95% uncertainties.

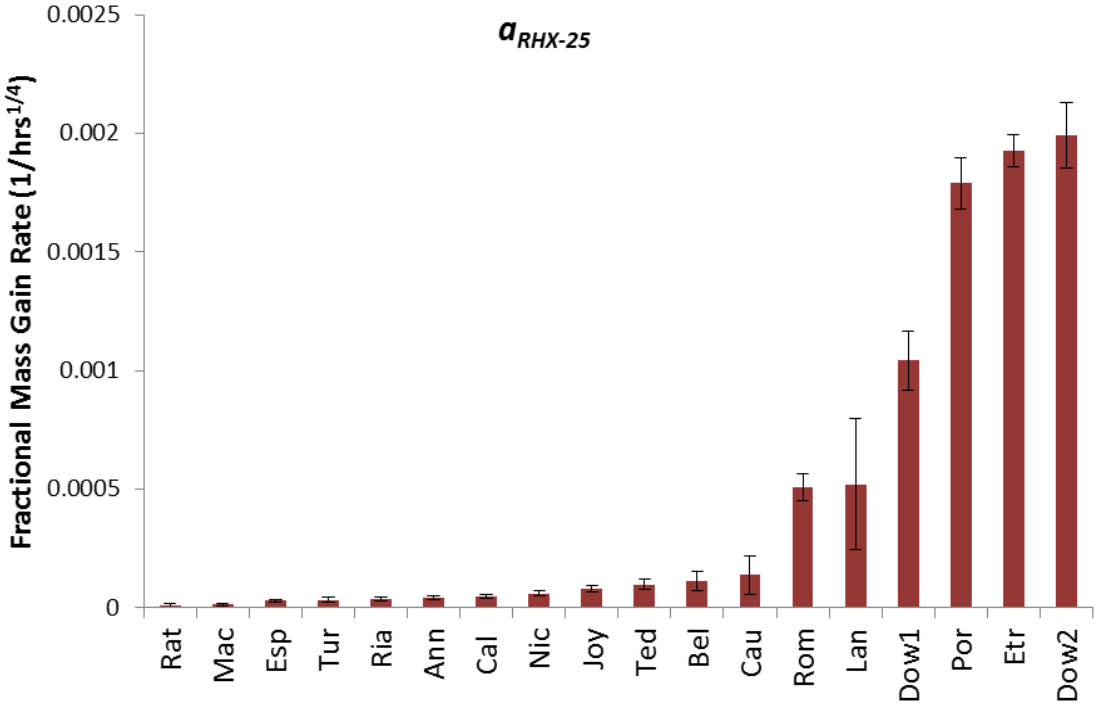

Figure 7.32: Fractional mass gain rate for RHX 25°C aging component of samples ($t^{1/4}$ model), including 95% uncertainties.

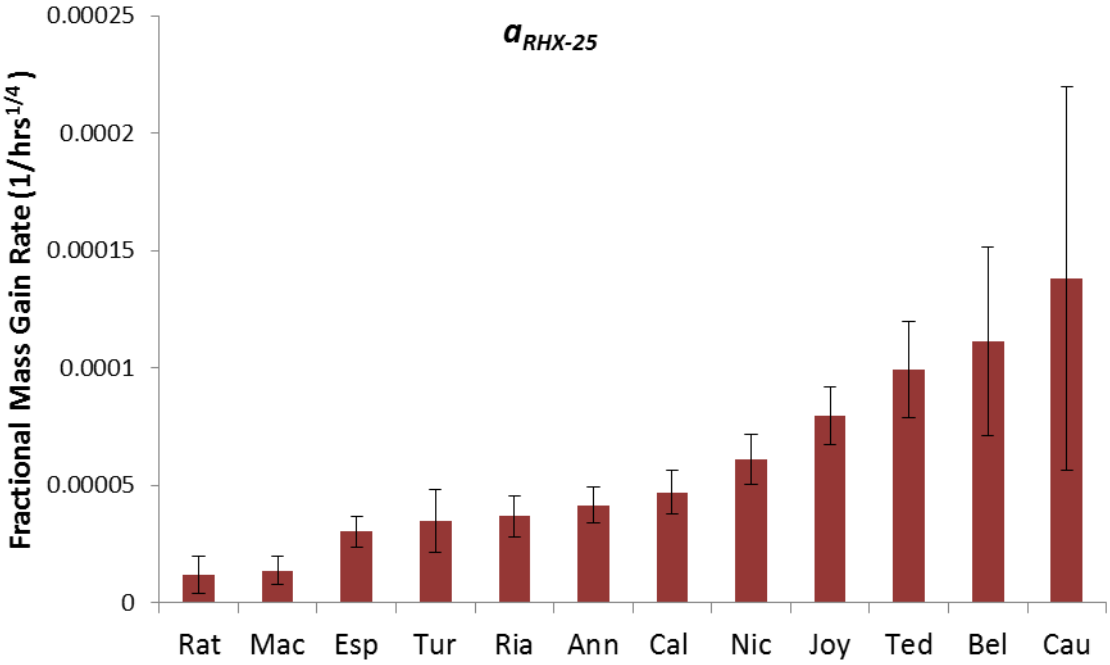

Figure 7.33: Fractional mass gain rate for RHX 25°C aging component of samples ($t^{1/4}$ model), including 95% uncertainties. Abnormally behaved samples have been removed.

Table 7.3: Modelled mass gain rates (*S2*) for $t^{1/4}$ approach. Also included are 95% confidence intervals.

$t^{1/4}$ Model	130°C			500°C		
Sample	**25°C Mass Gain Rate (95% confidence Interval) ($g/hrs^{1/4}$)**	**35°C Mass Gain Rate (95% confidence Interval) ($g/hrs^{1/4}$)**	**45°C Mass Gain Rate (95% confidence Interval) ($g/hrs^{1/4}$)**	**25°C Mass Gain Rate (95% confidence Interval) ($g/hrs^{1/4}$)**	**35°C Mass Gain Rate (95% confidence Interval) ($g/hrs^{1/4}$)**	**45°C Mass Gain Rate (95% confidence Interval) ($g/hrs^{1/4}$)**
Ann	0.0032188 (0.0031521 0.0032856)	0.0042219 (0.0041491 0.0042947)	0.0058880 (0.0057944 0.0059817)	0.0040247 (0.0039435 0.0041060)	0.0054011 (0.0052813 0.0055208)	0.0078756 (0.0077412 0.0080100)
Esp	0.0021293 (0.0020765 0.0021820)	0.0025561 (0.0024768 0.0026354)	0.0028092 (0.0027217 0.0028966)	0.0027121 (0.0026359 0.0027883)	0.0033202 (0.0032413 0.0033991)	0.0038340 (0.0037216 0.0039463)
Nic	0.0038718 (0.0037785 0.0039652)	0.0047925 (0.0046731 0.0049119)	0.0043615 (0.0041258 0.0045972)	0.0050043 (0.0048982 0.0051105)	0.0065565 (0.0064396 0.0066733)	0.0084730 (0.0083424 0.0086035)
Mac	0.0023021 (0.0022502 0.0023540)	0.0029324 (0.0028727 0.0029921)	0.0028966 (0.0027802 0.0030131)	0.0025666 (0.0025022 0.0026311)	0.0038067 (0.0036892 0.0039242)	0.0044052 (0.0042467 0.0045638)
Ria	0.0028998 (0.0028301 0.0029696)	0.0041144 (0.0040280 0.0042009)	0.0073393 (0.0072086 0.0074700)	0.0035753 (0.0034826 0.0036680)	0.0057359 (0.0056311 0.0058407)	0.0099122 (0.0098003 0.0100242)
Etr	0.0070301 (0.0066752 0.0073851)	0.0069871 (0.0063006 0.0076735)	0.0012735 (-0.0001011 0.0026481)	0.041793 (0.040974 0.042612)	0.044842 (0.043655 0.046028)	0.044323 (0.041103 0.047542)
Rom	0.0047764 (0.0040264 0.0055264)	0.0053503 (0.0050325 0.0056682)	0.0059985 (0.0050920 0.0069050)	0.014745 (0.014392 0.015098)	0.015941 (0.015754 0.016128)	0.019194 (0.018536 0.019852)
Por	0.0089678 (0.0079055 0.0100300)	0.0086832 (0.0082895 0.0090768)	0.0124417 (0.0113093 0.0135740)	0.0410405 (0.0401615 0.0419194)	0.0444930 (0.0433404 0.0456457)	0.0442566 (0.0421583 0.0463549)
Rat	0.0017433 (0.0016759 0.0018107)	0.0022396 (0.0021666 0.0023127)	0.0033476 (0.0032401 0.0034551)	0.0019903 (0.0018898 0.0020908)	0.0026698 (0.0025395 0.0028001)	0.0041701 (0.0039859 0.0043543)
Cal	0.0029770 (0.0029070 0.0030470)	0.0032893 (0.0032163 0.0033622)	0.0047685 (0.0046530 0.0048840)	0.0040004 (0.0038737 0.0041271)	0.0045370 (0.0043837 0.0046903)	0.0064511 (0.0062249 0.0066772)
Lan	0.0164541 (0.0133158 0.0195925)	0.013137 (0.011440 0.014835)	0.004000 (0.001113 0.006887)	0.0268214 (0.0244570 0.0291857)	0.0210998 (0.0193708 0.0228288)	0.0215333 (0.0198584 0.0232081)
Joy	0.0044327 (0.0043495 0.0045160)	0.0061271 (0.0060174 0.0062369)	0.0090886 (0.0089535 0.0092237)	0.0060140 (0.0058566 0.0061713)	0.0083598 (0.0082419 0.0084778)	0.0120948 (0.0119727 0.0122169)
Cau	0.0095382 (0.0087717 0.0103047)	0.0087802 (0.0081333 0.0094271)	0.0082569 (0.0075620 0.0089519)	0.0119383 (0.0112861 0.0125906)	0.0120835 (0.0117749 0.0123920)	0.0126713 (0.0120788 0.0132637)
Bel	0.0086748 (0.0082912 0.0090583)	0.0095745 (0.0093041 0.0098448)	0.0112690 (0.0107081 0.0118298)	0.0108304 (0.0104404 0.0112204)	0.0116708 (0.0114741 0.0118675)	0.0140083 (0.0135172 0.0144994)
Dow1	0.0097245 (0.0085098 0.0109393)	0.0088209 (0.0075948 0.0100470)	0.0052305 (0.0039346 0.0065264)	0.0259877 (0.0252589 0.0267166)	0.0271503 (0.0265024 0.0277982)	0.0276292 (0.0269415 0.0283169)
Dow2	0.0060560	0.0066399	0.0035653	0.0300568	0.0219747	0.0191807

	(0.0049454 0.0071666)	(0.0057927 0.0074872)	(0.0027108 0.0044199)	(0.0294902 0.0306233)	(0.0216406 0.0223089)	(0.0187126 0.0196488)
Tur	0.0033152 (0.0032028 0.0034276)	0.0048488 (0.0047242 0.0049734)	0.0069316 (0.0067706 0.0070925)	0.0039795 (0.0038377 0.0041212)	0.0060764 (0.0058699 0.0062830)	0.0088290 (0.0085587 0.0090993)
Ted	0.0080803 (0.0079023 0.0082584)	0.0102184 (0.0100525 0.0103843)	0.0141529 (0.0140057 0.0143001)	0.0101416 (0.0098937 0.0103895)	0.0130092 (0.0127220 0.0132964)	0.0182749 (0.0180699 0.0184798)

Table 7.4: Modelled mass gain rates for $t^{1/n}$ approach (pre-fixed). Also included are 95% confidence intervals.

$t^{1/n}$ Model (pre-fixed)	130°C			500°C		
Sample	**25°C Mass Gain Rate (95% confidence Interval) ($g/hrs^{1/n}$)**	**35°C Mass Gain Rate (95% confidence Interval) ($g/hrs^{1/n}$)**	**45°C Mass Gain Rate (95% confidence Interval) ($g/hrs^{1/n}$)**	**25°C Mass Gain Rate (95% confidence Interval) ($g/hrs^{1/n}$)**	**35°C Mass Gain Rate (95% confidence Interval) ($g/hrs^{1/n}$)**	**45°C Mass Gain Rate (95% confidence Interval) ($g/hrs^{1/n}$)**
Ann	0.0013745 (0.0010235 0.0017255)	0.0025842 (0.0018882 0.0032801)	0.0032605 (0.0025823 0.0039387)	0.0020861 (0.0015316 0.0026407)	0.0021831 (0.0017849 0.0025812)	0.0033788 (0.0025058 0.0042519)
Esp	0.0033954 (0.0018132 0.0049776)	0.0084062 (0.0038455 0.0129669)	0.0049102 (0.0019835 0.0078369)	0.0030145 (0.0010636 0.0049653)	0.0066019 (0.0041030 0.0091009)	0.0080692 (0.0042065 0.0119320)
Nic	0.0078800 (0.0042113 0.0115488)	0.010087 (0.006387 0.013788)	0.044650 (0.000184 0.089117)	0.0074875 (0.0046894 0.0102856)	0.010373 (0.007004 0.013741)	0.010596 (0.007360 0.013833)
Mac	0.0027421 (0.0015682 0.0039160)	0.0033467 (0.0020338 0.0046595)	0.0016197 (0.0004498 0.0027896)	0.0009274 (0.0005257 0.0013291)	0.0011529 (0.0008235 0.0014822)	0.0012620 (0.0008869 0.0016371)
Ria	0.0009158 (0.0006586 0.0011730)	0.0015763 (0.0011850 0.0019675)	0.0019210 (0.0015383 0.0023036)	0.0006834 (0.0004834 0.0008833)	0.0013871 (0.0011121 0.0016621)	0.0022518 (0.0019349 0.0025688)
Etr	NA	NA	NA	NA	NA	NA
Rom	0.0039713 (-0.0075868 0.0155295)	0.067437 (-0.252493 0.387367)	0.105343 (-1.753032 1.963718)	0.119684497 (0.022532659 0.216836336)	0.031765 (0.023295 0.040235)	0.035463 (0.010154 0.060773)
Por	NA	NA	NA	NA	NA	NA
Rat	0.0002510 (0.0000985 0.0004035)	0.0004484 (0.0001673 0.0007296)	0.0006431 (0.0003396 0.0009465)	0.0003139 (0.0001657 0.0004621)	0.0003912 (0.0002259 0.0005565)	0.0008122 (0.0005417 0.0010828)
Cal	0.0009567 (0.0006688 0.0012446)	0.0015627 (0.0010762 0.0020492)	0.0017884 (0.0012766 0.0023003)	0.0009759 (0.0007160 0.0012359)	0.0011054 (0.0008322 0.0013786)	0.0017157 (0.0012835 0.0021478)
Lan	NA	NA	NA	NA	NA	NA
Joy	0.0010170 (0.0008056 0.0012284)	0.0019848 (0.0015725 0.0023971)	0.0028712 (0.0023115 0.0034309)	0.0012627 (0.0010026 0.0015228)	0.0015065 (0.0012780 0.0017351)	0.0030060 (0.0025777 0.0034344)
Cau	1.168560 -2.750549 5.087670	0.066178 -0.070408 0.202764	0.177413 -0.646546 1.001372	0.010539 0.006462 0.014617	0.014075 0.009835 0.018315	0.0260175 0.0082417 0.0437933

Bel	0.011910 (0.007152 0.016669)	0.0138320 (0.0071061 0.0205579)	0.0945375 (0.0003176 0.1887574)	0.0274009 (0.0203974 0.0344044)	0.0205306 (0.0162042 0.0248570)	0.0628620 (0.0364680 0.0892561)
Dow1	NA	NA	NA	NA	NA	NA
Dow2	NA	NA	NA	NA	NA	NA
Tur	0.0002849 (0.0001730 0.0003967)	0.0010704 (0.0007578 0.0013829)	0.0011706 (0.0007938 0.0015474)	0.0011562 (0.0006653 0.0016470)	0.0011580 (0.0007911 0.0015249)	0.0020673 (0.0015280 0.0026066)
Ted	0.0016377 (0.0013643 0.0019111)	0.0030236 (0.0026951 0.0033520)	0.0058507 (0.0047932 0.0069082)	0.0034858 (0.0029048 0.0040669)	0.0037878 (0.0031852 0.0043903)	0.0098816 (0.0082522 0.0115109)

Table 7.5: Modelled mass gain rates for $t^{1/n}$ approach (fixed). Also included are 95% confidence intervals.

$t^{1/n}$ Model (1/n-fixed)	**130°C**			**500°C**		
Sample	**25°C Mass Gain Rate (95% confidence Interval) ($g/hrs^{1/n}$)**	**35°C Mass Gain Rate (95% confidence Interval) ($g/hrs^{1/n}$)**	**45°C Mass Gain Rate (95% confidence Interval) ($g/hrs^{1/n}$)**	**25°C Mass Gain Rate (95% confidence Interval) ($g/hrs^{1/n}$)**	**35°C Mass Gain Rate (95% confidence Interval) ($g/hrs^{1/n}$)**	**45°C Mass Gain Rate (95% confidence Interval) ($g/hrs^{1/n}$)**
Ann	0.0015078 (0.0014864 0.0015293)	0.0019782 (0.0019481 0.0020084)	0.0027571 (0.0027252 0.0027891)	0.0019163 (0.0018856 0.0019471)	0.0025416 (0.0025125 0.0025707)	0.0037178 (0.0036749 0.0037607)
Esp	0.0039582 (0.0038647 0.0040517)	0.0047529 (0.0046330 0.0048729)	0.0052230 (0.0050698 0.0053763)	0.0051428 (0.0049984 0.0052872)	0.0061564 (0.0060357 0.0062770)	0.0070867 (0.0069101 0.0072633)
Nic	0.0064131 (0.0062848 0.0065414)	0.0078690 (0.0077361 0.0080019)	0.0067742 (0.0064700 0.0070783)	0.0083248 (0.0081954 0.0084542)	0.0110227 (0.0108533 0.0111921)	0.0141884 (0.0139632 0.0144135)
Mac	0.0011540 (0.0011247 0.0011833)	0.0014805 (0.0014451 0.0015158)	0.0014861 (0.0014287 0.0015435)	0.0012929 (0.0012620 0.0013238)	0.0019629 (0.0019221 0.0020037)	0.0022803 (0.0022262 0.0023344)
Ria	0.00076134 (0.00074924 0.00077345)	0.0010885 (0.0010722 0.0011049)	0.0018955 (0.0018754 0.0019157)	0.0009121 (0.0008975 0.0009266)	0.0014086 (0.0013918 0.0014255)	0.0024863 (0.0024636 0.0025090)
Etr	NA	NA	NA	NA	NA	NA
Rom	0.016466 (0.013962 0.018971)	0.017702 (0.016761 0.018643)	0.019305 (0.016514 0.022096)	0.053373 (0.052351 0.054395)	0.053744 (0.053095 0.054393)	0.062287 (0.060197 0.064377)
Por	NA	NA	NA	NA	NA	NA
Rat	0.0003009 (0.0002901 0.0003117)	0.0003995 (0.0003895 0.0004095)	0.0005891 (0.0005739 0.0006043)	0.0003354 (0.0003259 0.0003450)	0.0004464 (0.0004351 0.0004578)	0.0007012 (0.0006868 0.0007156)
Cal	0.0008602 (0.0008456 0.0008747)	0.0009872 (0.0009685 0.0010059)	0.0014304 (0.0014078 0.0014529)	0.0011792 (0.0011597 0.0011986)	0.0013728 (0.0013514 0.0013942)	0.0019620 (0.0019313 0.0019926)
Lan	NA	NA	NA	NA	NA	NA
Joy	0.0011304 (0.0011171 0.0011436)	0.0015975 (0.0015785 0.0016166)	0.0023622 (0.0023362 0.0023881)	0.0014106 (0.0013928 0.0014284)	0.0020269 (0.0020042 0.0020497)	0.0030621 (0.0030356 0.0030886)

Cau	NA	NA	NA	NA	NA	NA
Bel	0.0209964 (0.0207439 0.0212489)	0.0236670 (0.0232556 0.0240783)	0.0271255 (0.0263432 0.0279078)	0.0273858 (0.0270688 0.0277029)	0.0295127 (0.0292030 0.0298224)	0.0339834 (0.0334036 0.0345632)
Dow1	NA	NA	NA	NA	NA	NA
Dow2	NA	NA	NA	NA	NA	NA
Tur	0.0006388 (0.0006214 0.0006562)	0.0009391 (0.0009236 0.0009546)	0.0013100 (0.0012918 0.0013282)	0.0007595 (0.0007401 0.0007788)	0.0011173 (0.0010982 0.0011364)	0.0016457 (0.0016218 0.0016695)
Ted	0.0027282 (0.0026922 0.0027642)	0.0035094 (0.0034832 0.0035356)	0.0050824 (0.0050417 0.0051230)	0.0034549 (0.0034223 0.0034875)	0.0043424 (0.0043031 0.0043817)	0.0063483 (0.0062640 0.0064325)

7.3.2 Rate Relationships and Correlations

500C vs 130C

The relationship between the 130C and 500C components of mass gain rate are displayed below in *Figures 7.34-7.40.* The first of these, *Figure 7.34*, shows the mass gain rate (fractional) $a_{130\text{-}25}$ versus the mass gain rate (fractional) $a_{500\text{-}25}$ for all samples and using the $t^{1/4}$ model. The correlation (R^2 = 0.47) between the two is poor. However, in the remaining *Figures 7.35-7.40*, the *abnormal samples* are removed from the $t^{1/4}$ set and the *abnormal* plus *Cau* (due to issues with conformity of *1/n* discussed later) samples are removed from the $t^{1/n}$ set. It can be observed that a very strong relationship exists between the 130C rates and their 500C counterparts at the same aging temperature.

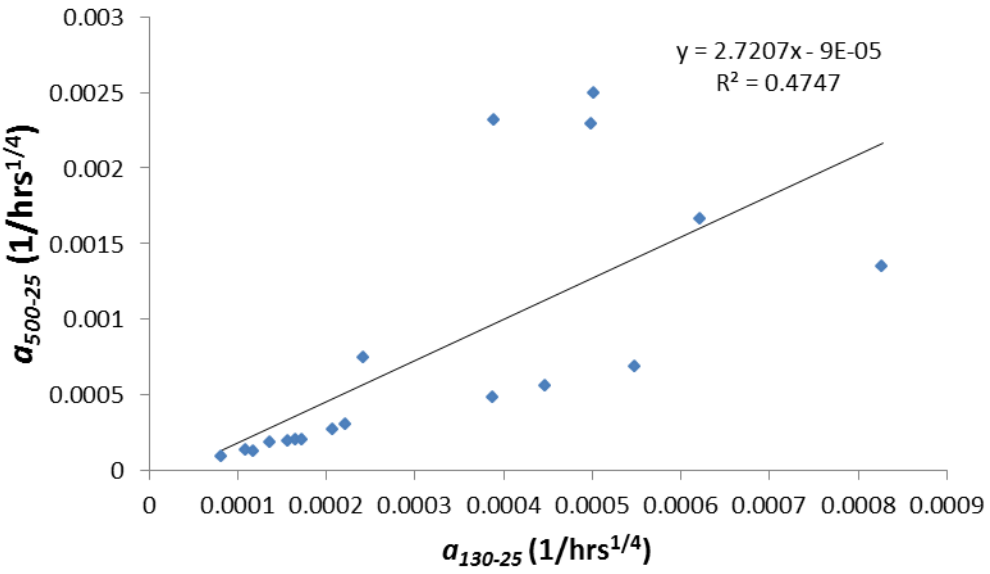

Figure 7.34: Mass gain rate of 130°C component (25°C aging) versus 500°C component (25°C aging) for all samples. Using $t^{1/4}$ model.

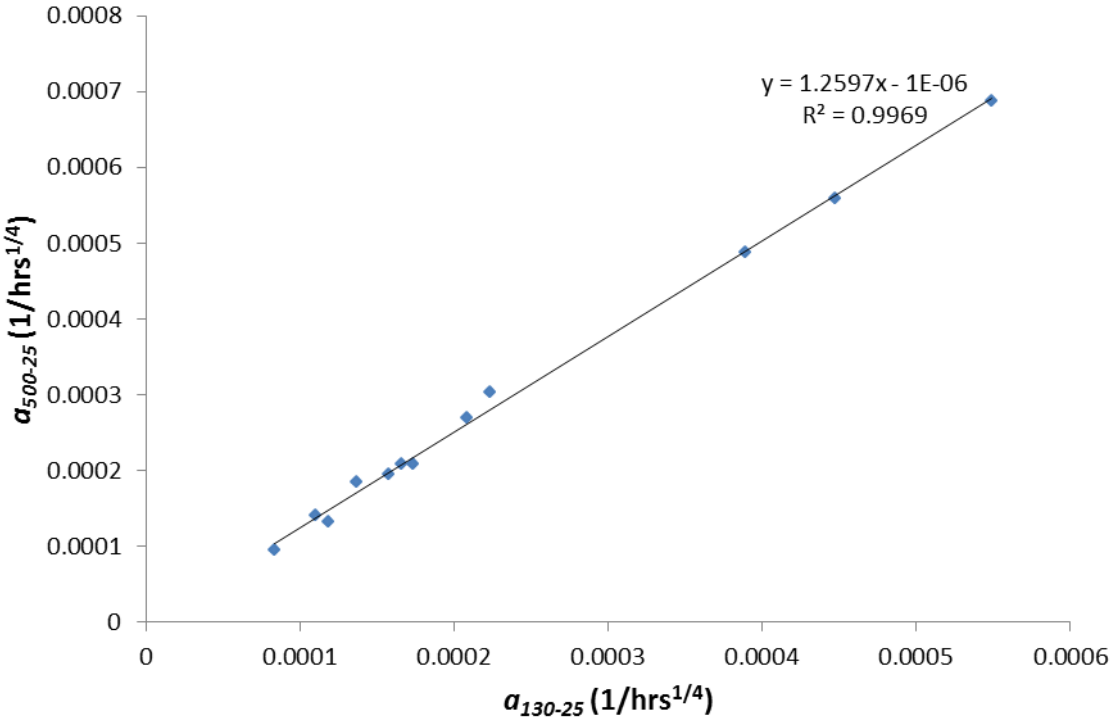

Figure 7.35: Mass gain rate of 130°C component (25°C aging) versus 500°C component (25°C aging) with abnormal six samples excluded. Using $t^{1/4}$ model.

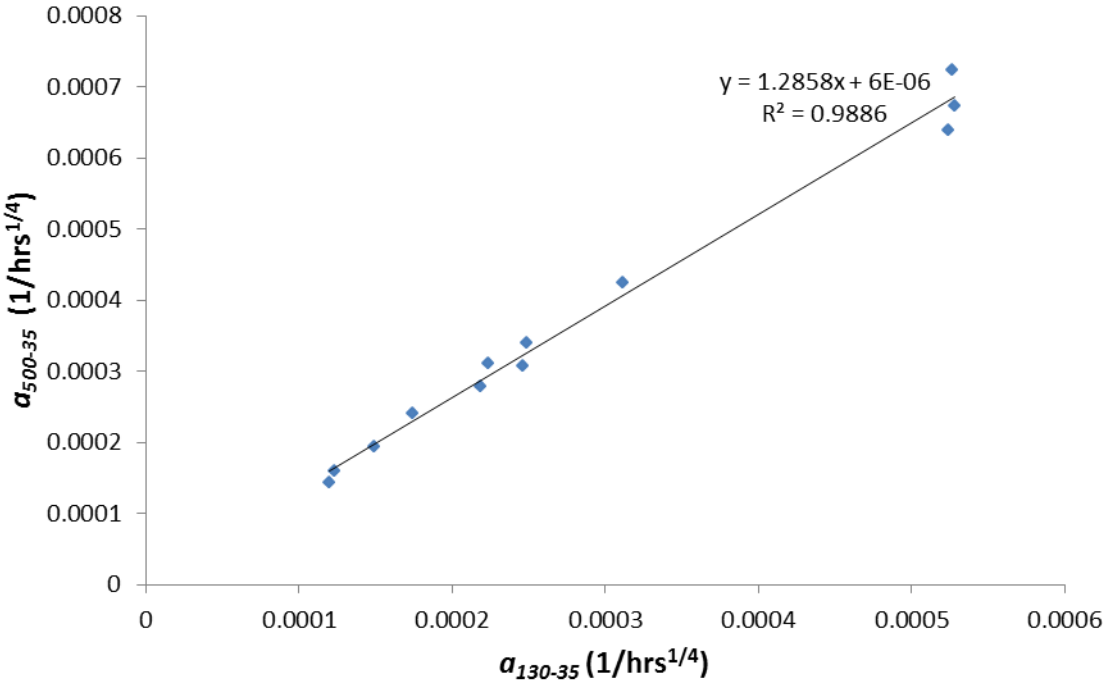

Figure 7.36: Mass gain rate of 130°C component (35°C aging) versus 500°C component (35°C aging) with abnormal six samples excluded. Using $t^{1/4}$ model.

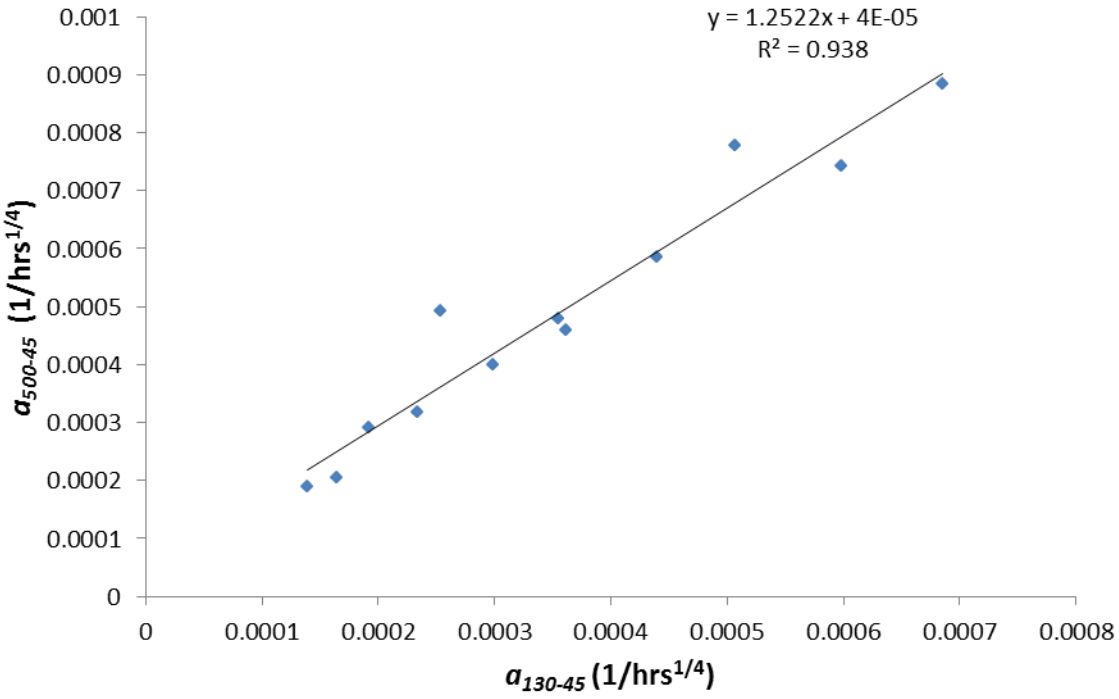

Figure 7.37: Mass gain rate of 130°C component (45°C aging) versus 500°C component (45°C aging) with abnormal six samples excluded. Using $t^{1/4}$ model.

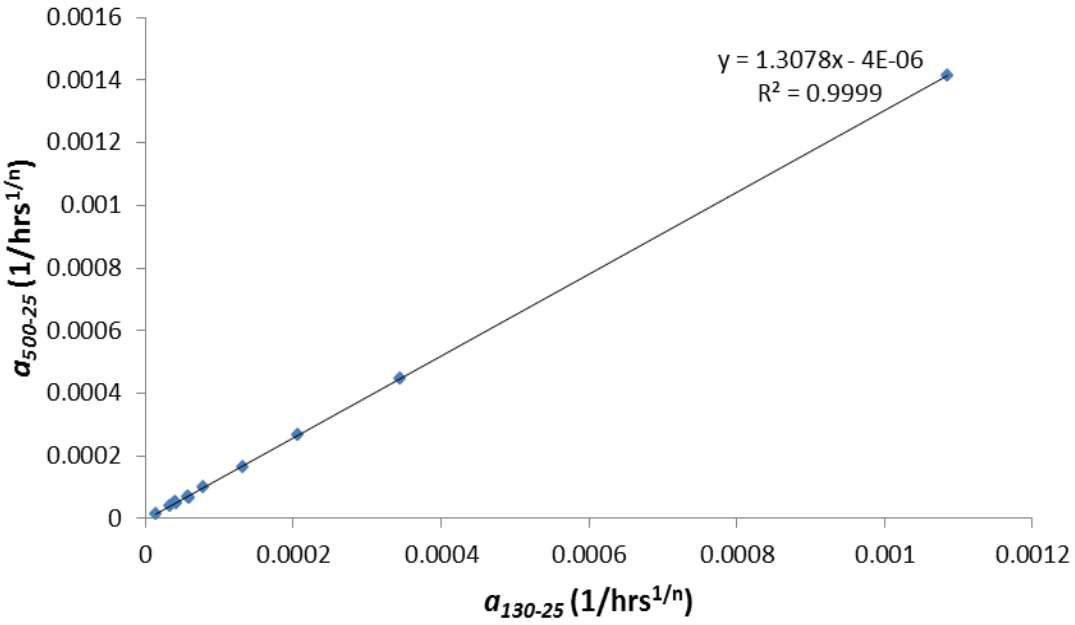

Figure 7.38: Mass gain rate of 130°C component (25°C aging) versus 500°C component (25°C aging) with abnormal samples (+ *Cau*) excluded. Using $t^{1/n}$ model.

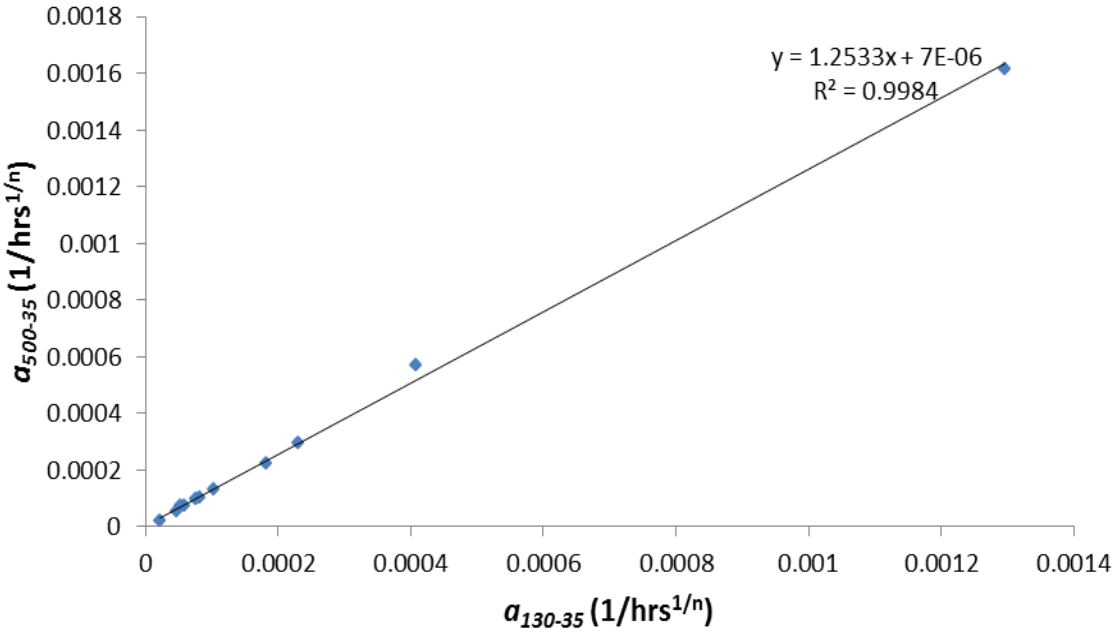

Figure 7.39: Mass gain rate of 130°C component (35°C aging) versus 500°C component (35°C aging) with abnormal samples (+*Cau*) excluded. Using $t^{1/n}$ model.

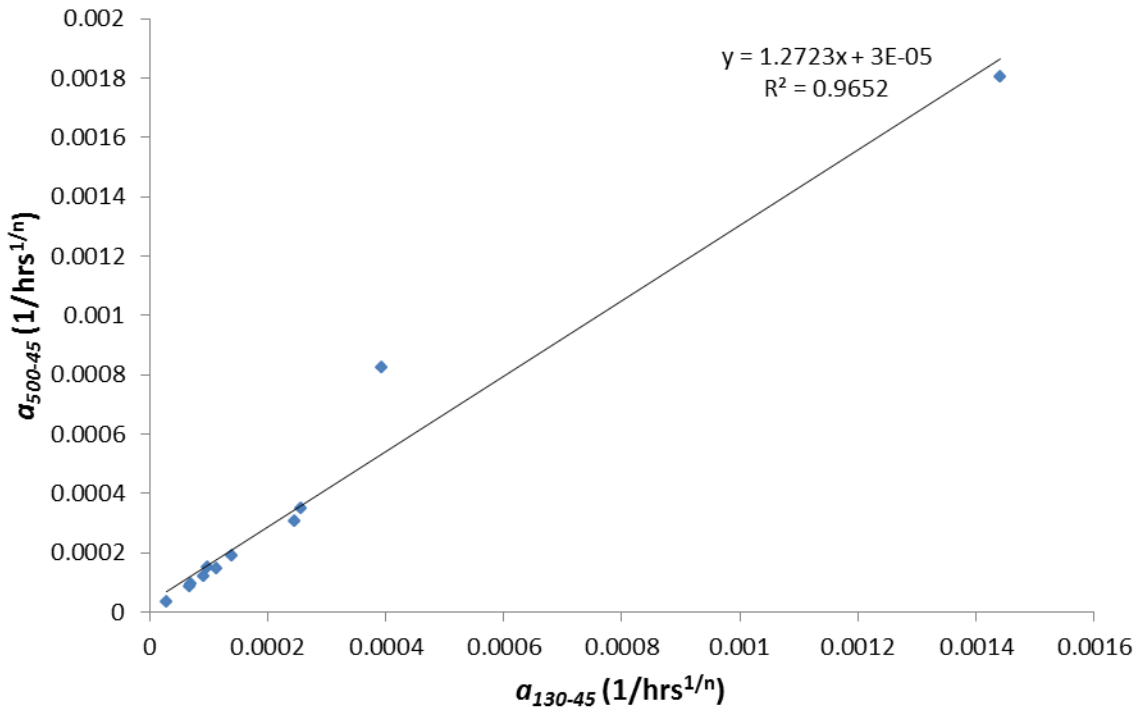

Figure 7.40: Mass gain rate of 130°C component (45°C aging) versus 500°C component (45°C aging) with abnormal samples (+*Cau*) excluded. Using $t^{1/n}$ model.

BET S.A. vs. $a_{130/RHX}$

The relationships between BET S.A. and mass gain rates were examined and for the $t^{1/4}$ model are presented in *Figure 7.41* and *Figure 7.42* for $a_{130\text{-}25}$ and $a_{RHX\text{-}25}$, respectively. The abnormal samples are excluded. Similar plots, *Figures 7.43* and *Figure 7.44*, are included for the $t^{1/n}$ model, this time with *Cau* additionally removed. It can be observed that, for all plots, while the correlation is not particularly strong and much of the variance is unexplained, R^2 = 0.53-0.78, some relationship is probable, p = 0.0072-0.0003 (enhanced by an outlier in the $t^{1/n}$ model).

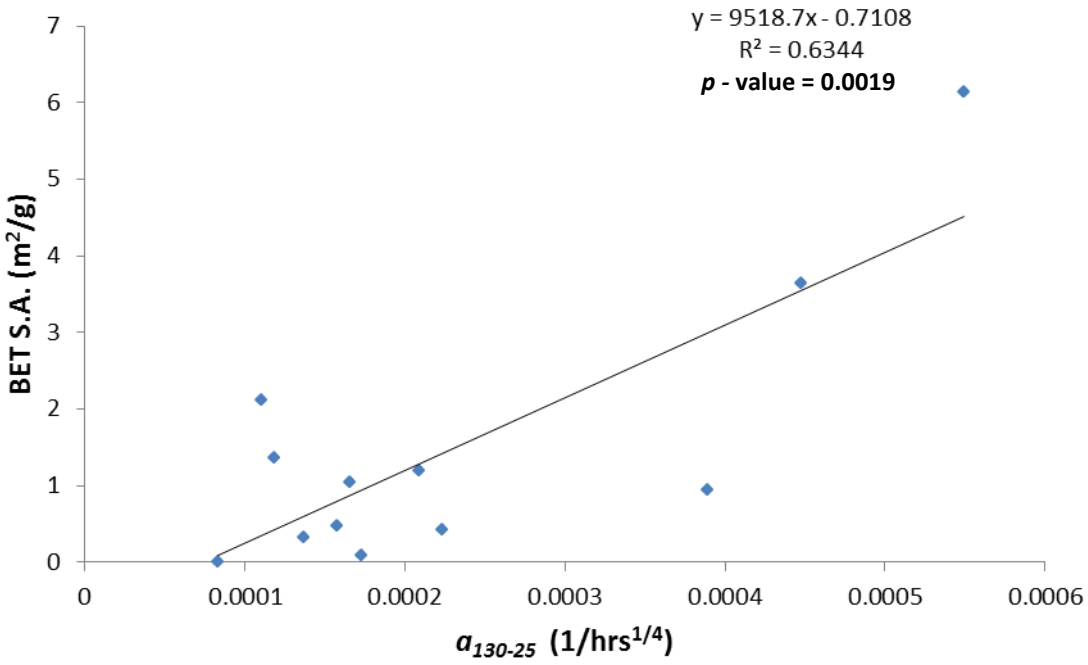

Figure 7.41: Mass gain rate of 130°C component (25°C aging) versus BET surface area of samples, excluding abnormal samples. Using $t^{1/4}$ model.

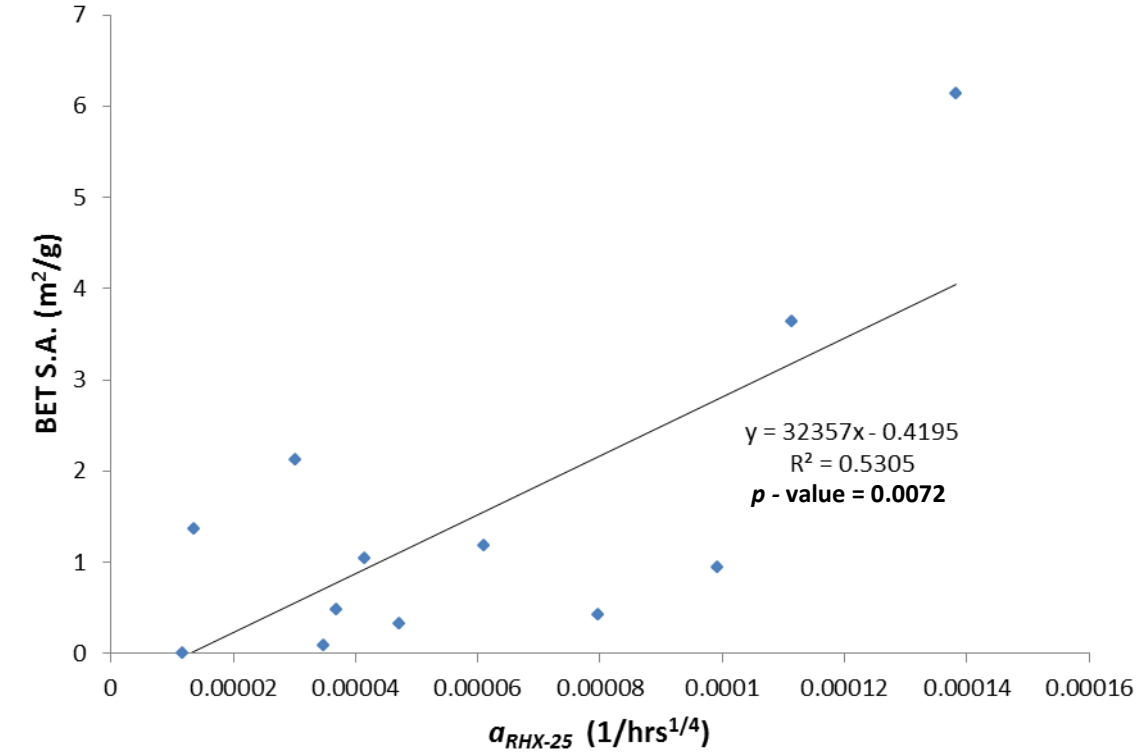

Figure 7.42: Mass gain rate of RHX component (25°C aging) versus BET surface area of samples, excluding abnormal samples. Using $t^{1/4}$ model.

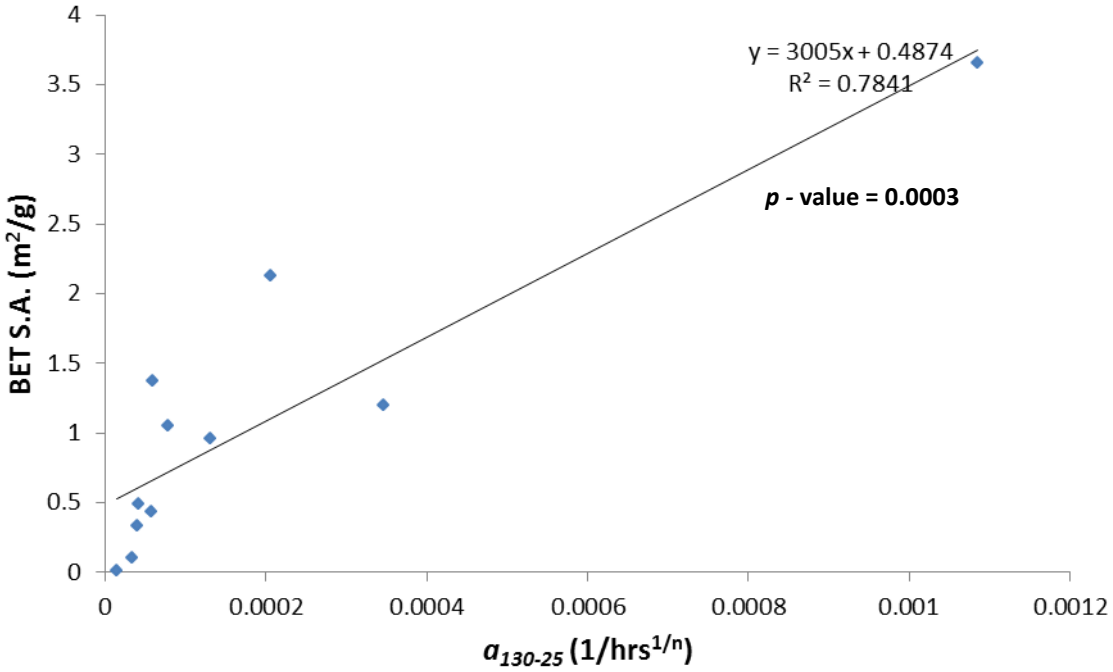

Figure 7.43: Mass gain rate of 130°C component (25°C aging) versus BET surface area of samples, excluding abnormal (+*Cau*) samples. Using $t^{1/n}$ model.

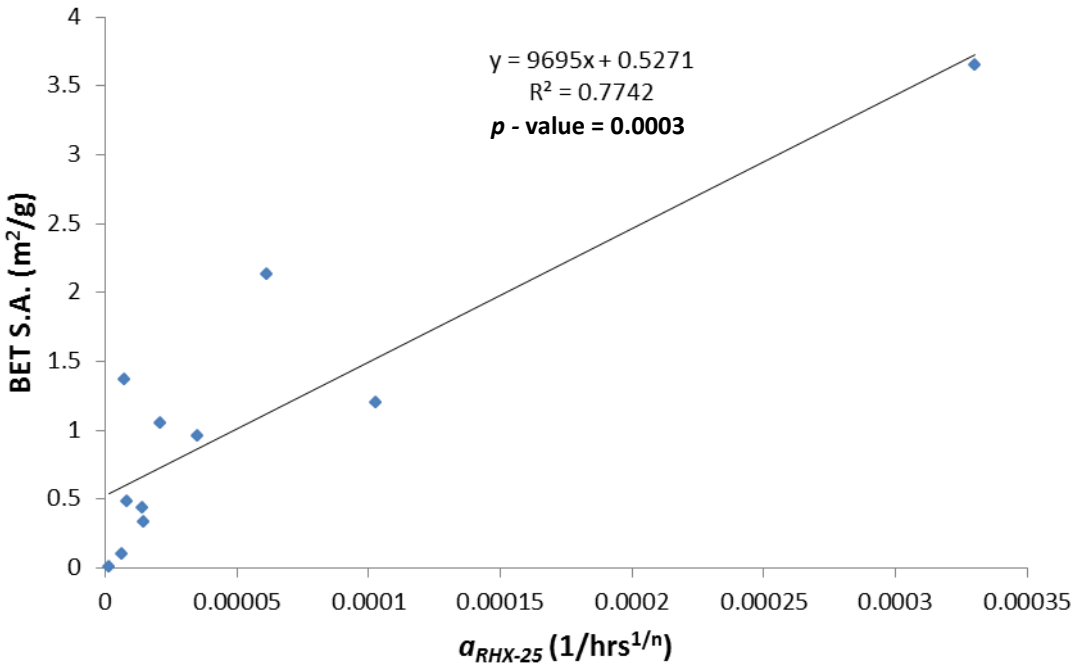

Figure 7.44: Mass gain rate of RHX component (25°C aging) versus BET surface area of samples, excluding abnormal (+*Cau*) samples. Using $t^{1/n}$ model.

S1 Mass Gain vs. (S2) Mass Gain Rate

The *S1* results are presented in *Section 7.6*. The following, *Figure 7.45* and *Figure 7.46* present the results of an examination of the correlation between the mass gain observed in *S1,* m_{S1}, and the *S2* mass gain rate, $a_{RHX\text{-}25}$, for both the $t^{1/4}$ and $t^{1/n}$ models. Abnormal samples (+ *Cau* for $t^{1/n}$) have been excluded. For the $t^{1/4}$ model, the correlation between the two properties is weak, R^2 = 0.23, and the null hypothesis can not be rejected, p = 0.1149. For the $t^{1/n}$ model, the correlation is improved and statistically significant, R^2 = 0.62 and p = 0.0042; however, if the sample *Bel* is removed (because of issues with *S1* mass gain, see *Discussion*) the correlation is very poor and not statistically significant, R^2 = 0.08, p = 0.419.

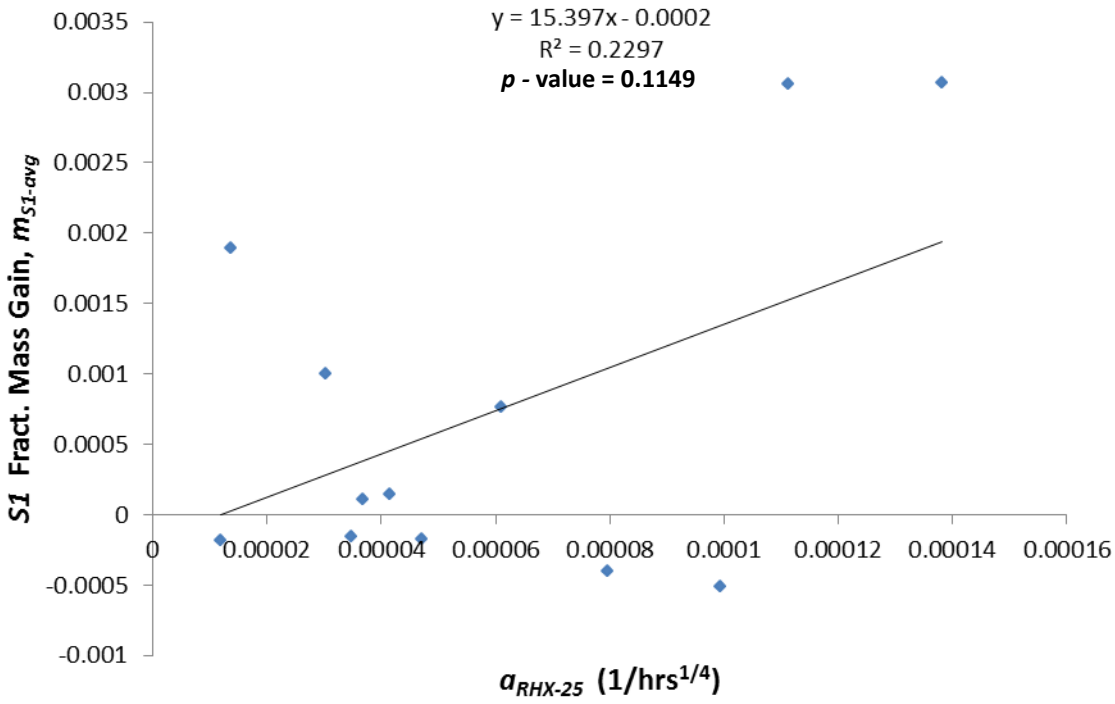

Figure 7.45: Mass gain rate (25°C) of RHX component versus S1 (avg.) fractional mass gain (excluding abnormal samples). For $t^{1/4}$ model.

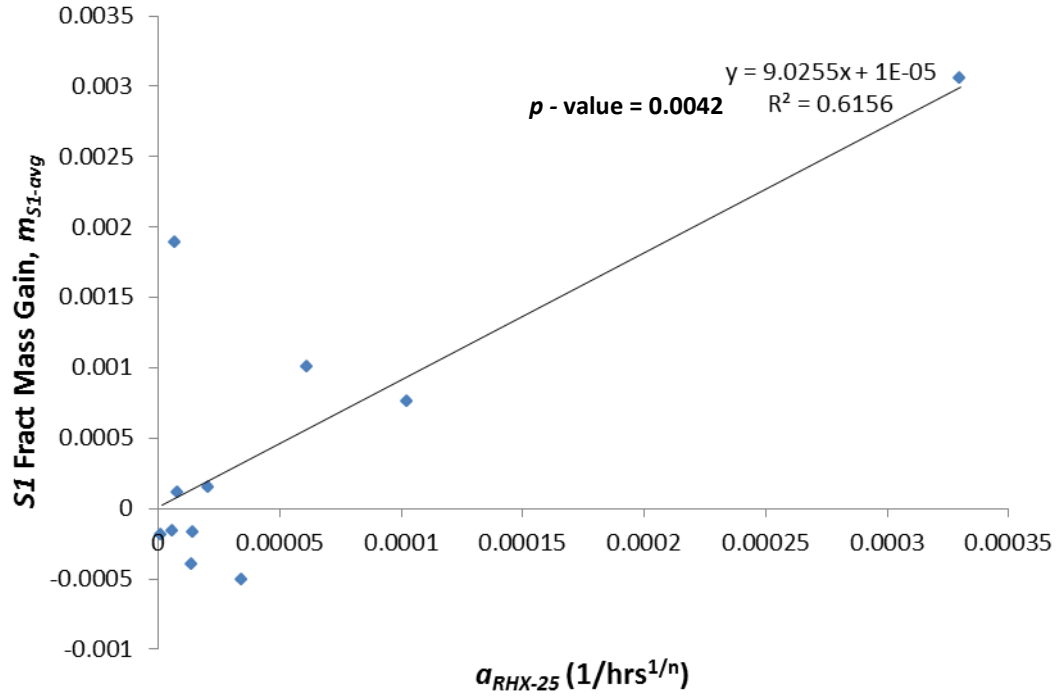

Figure 7.46: Mass gain rate (25°C) of RHX component versus S1 (avg.) fractional mass gain (excluding abnormal and *Cau* samples). For $t^{1/n}$ model.

7.4 Masses

7.4.1 Mass Values

The intercept masses obtained from modelling, for $t^{1/4}$ and $t^{1/n}$, are provided in *Table 7.6-7.8*. A table of the total fractional mass loss, m_{RHXC}, together with the fractional mass loss attributed to loose water, m_{lw}, organic matter, m_{om}, and RHX processes, m_{RHX}, is also provided for the $t^{1/4}$ and $t^{1/n}$ models, in *Table 7.9* and *Table 7.10*, respectively. The results of estimation of m_{lw} are presented in *Section 8.1* with m_{om} computed from carbon content results presented in *Section 5.9* and a multiplicative factor of 1.95 (OM/OC ratio).

For the $t^{1/4}$ model, ranking of the total fractional mass loss (with and without abnormal samples), m_{RHXC}, and the RHX attributed mass loss, m_{RHX}, are provided in *Figure 7.47, Figure 7.48* and *Figure 7.49*. In *Figure 7.50* and *Figure 7.51*, the fractional mass losses attributed to loose water and organic matter, respectively, are given as a percentage of the total fractional mass loss. Corresponding plots for the $t^{1/n}$ model are presented in *Figures 7.52-7.55*.

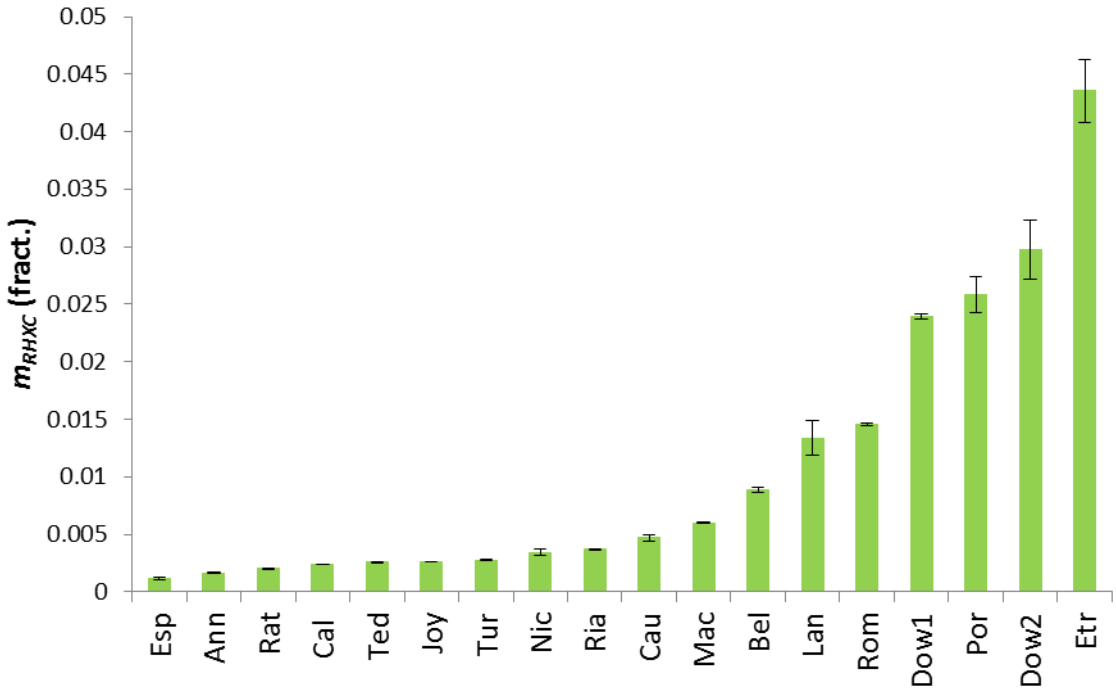

Figure 7.47: Ranking of total fractional mass loss due to heating between 130°C and 500°C. For $t^{1/4}$ model. Uncertainties are to 1σ.

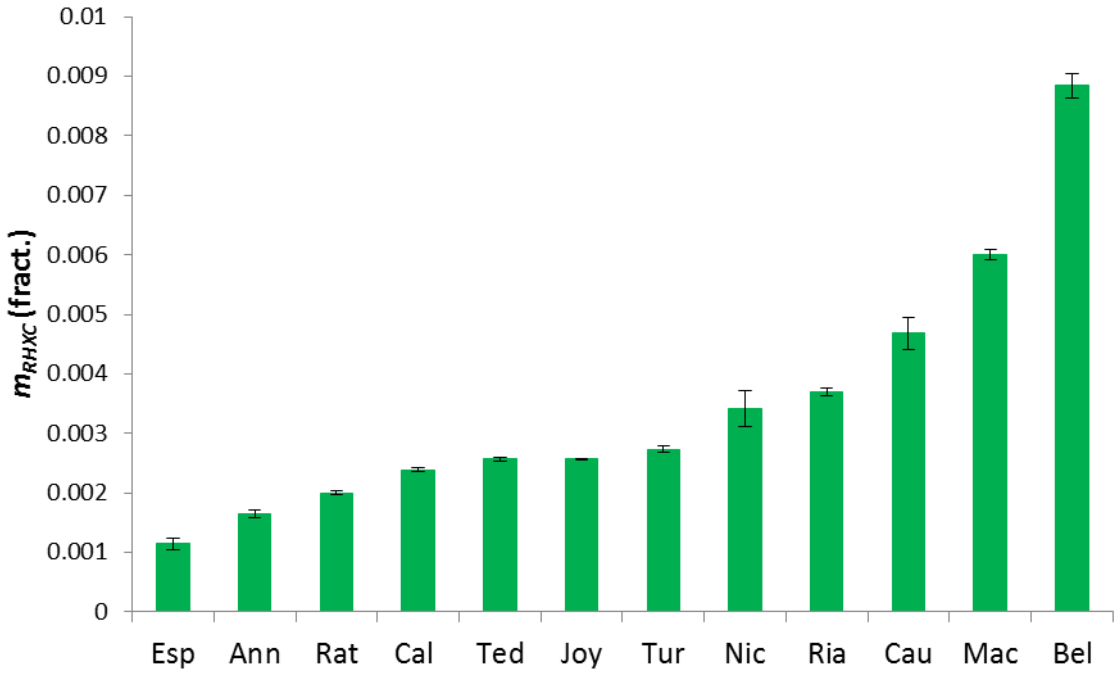

Figure 7.48: Ranking of total fractional mass loss due to heating between 130°C and 500°C with abnormal samples removed. For $t^{1/4}$ model. Uncertainties to 1σ.

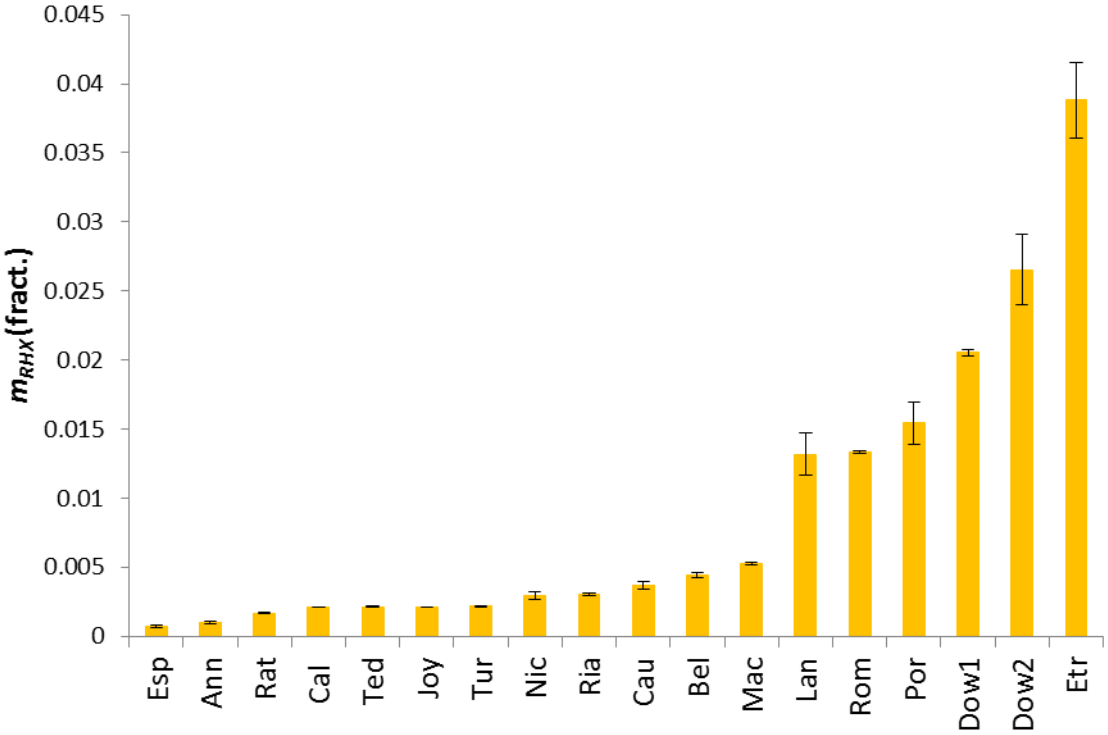

Figure 7.49: Ranking of fractional RHX-attributed mass loss due to heating between 130°C and 500°C. For $t^{1/4}$ model. Uncertainties to 1σ.

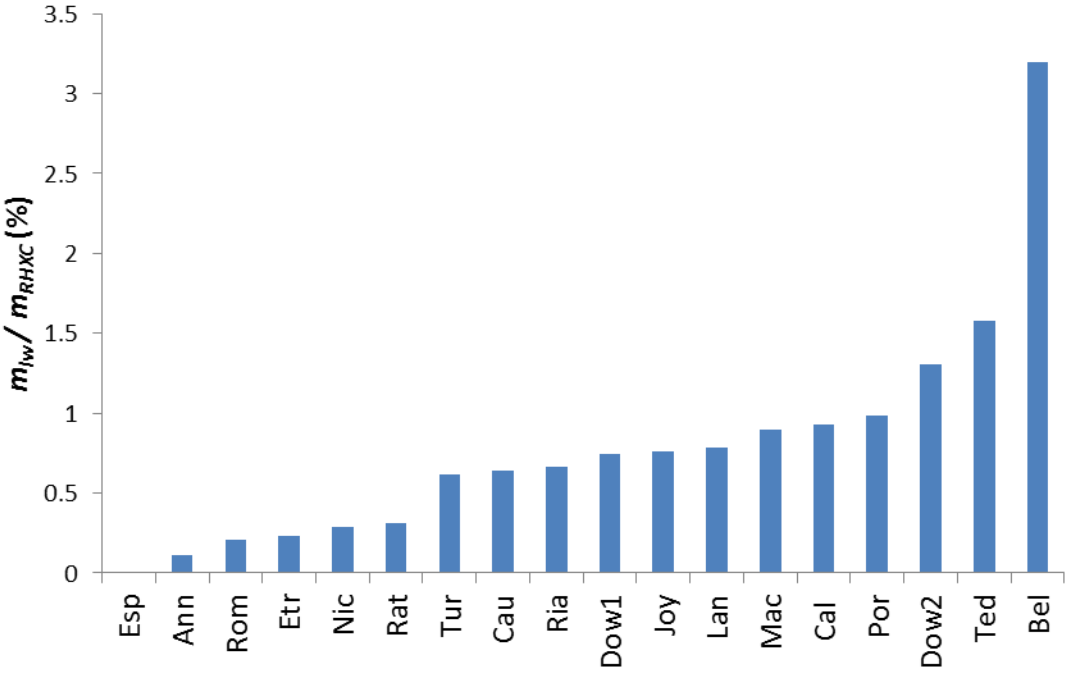

Figure 7.50: The mass of remaining loose water, m_{lw}, as a % of total fractional mass loss, m_{RHXC}, upon heating between 130°C and 500°C. For $t^{1/4}$ model.

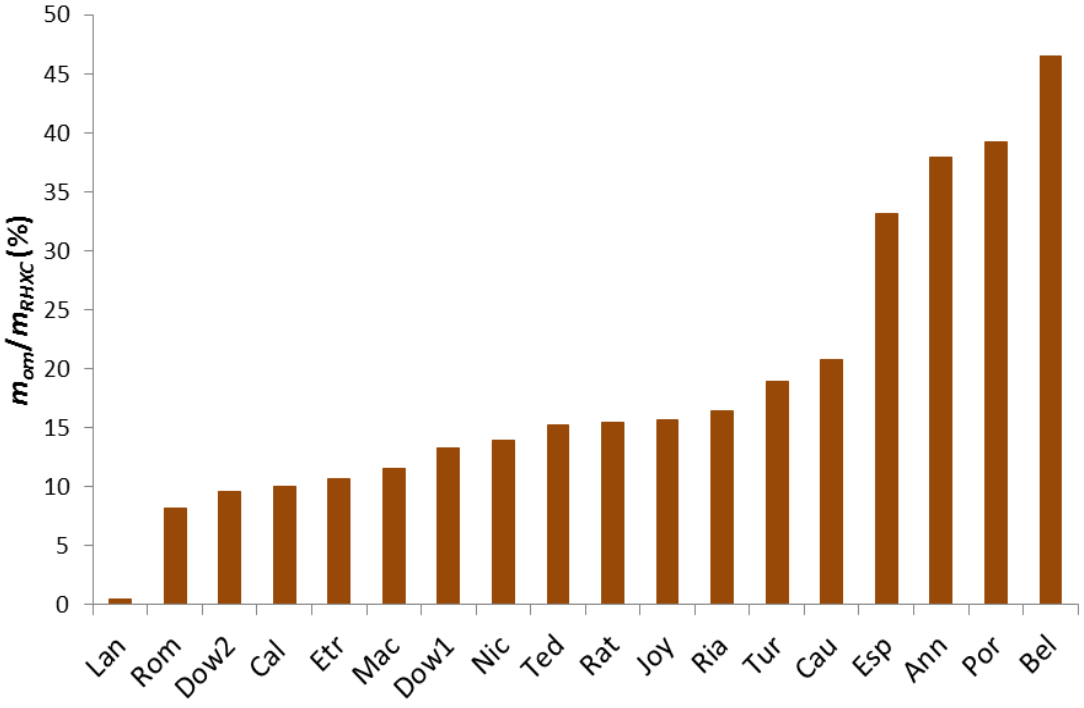

Figure 7.51: The mass of organic matter (computed using m_c and an OM/OC ratio of 1.95), m_{om}, as a % of total fractional mass loss, m_{RHXC}, upon heating between 130°C and 500°C. For $t^{1/4}$ model.

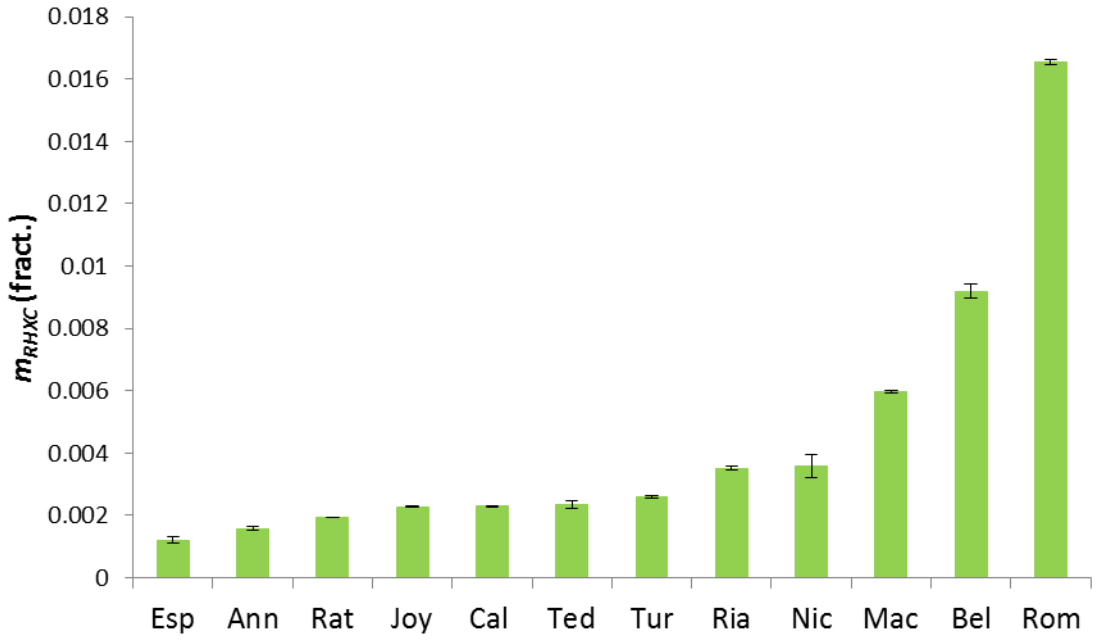

Figure 7.52: : Ranking of total fractional mass loss due to heating between 130°C and 500°C. For $t^{1/n}$ model. Uncertainties are to 1σ.

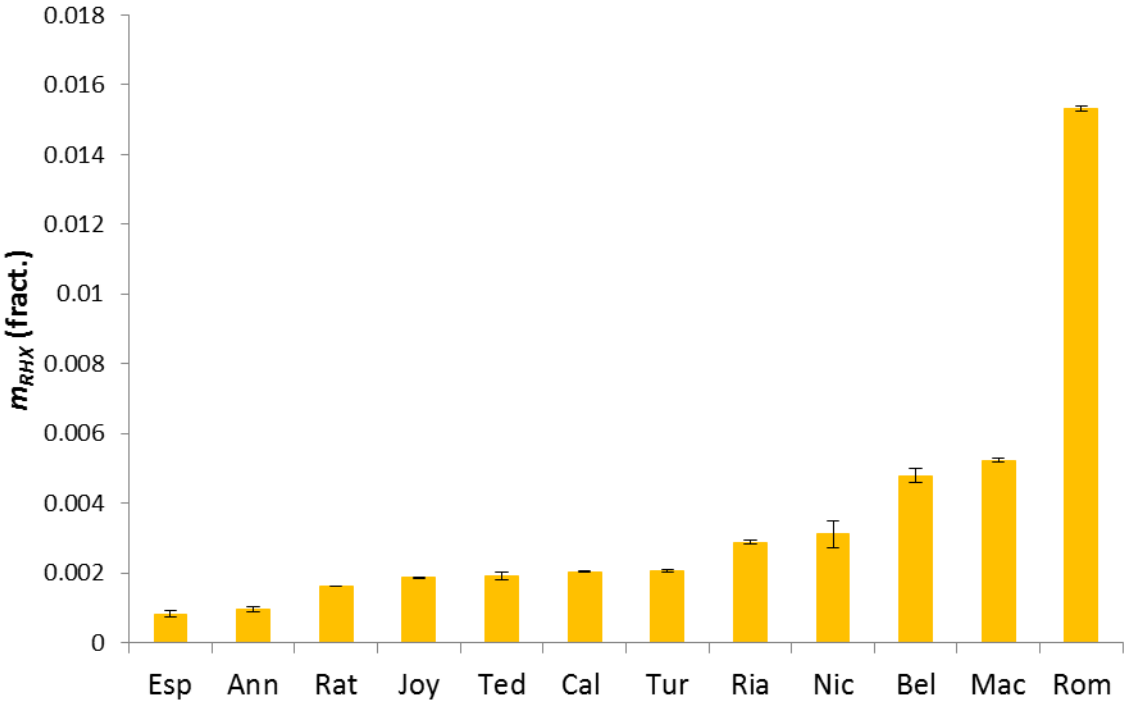

Figure 7.53: Ranking of fractional RHX-attributed mass loss due to heating between 130°C and 500°C. For $t^{1/n}$ model. Uncertainties to 1σ.

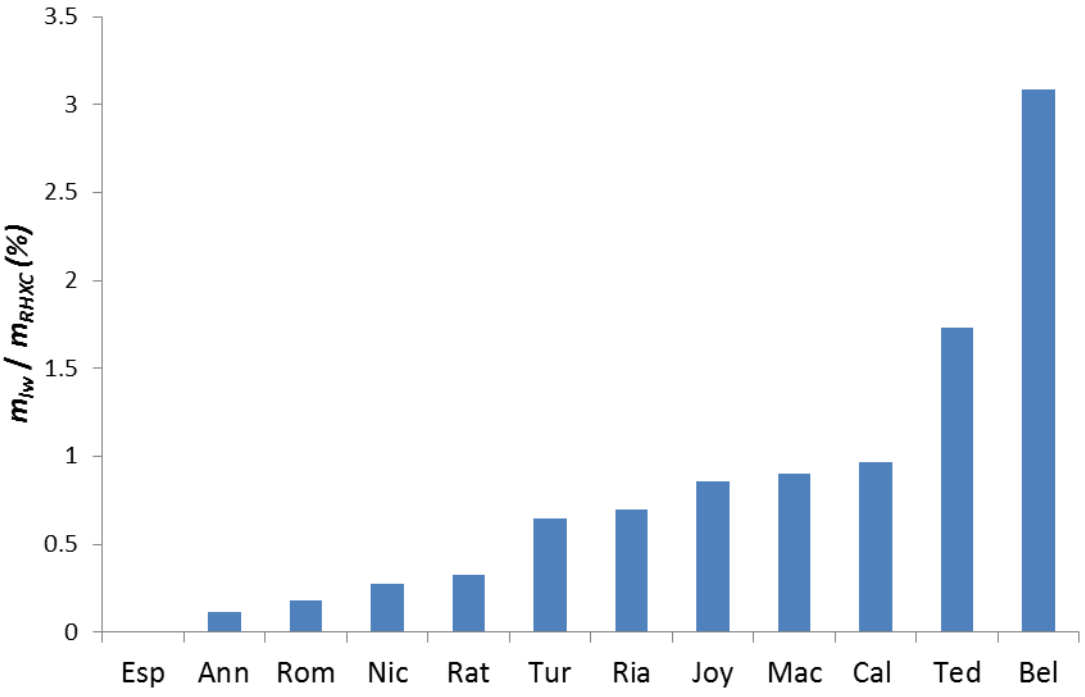

Figure 7.54: The mass of remaining loose water, m_{lw}, as a % of total fractional mass loss, m_{RHXC}, upon heating between 130°C and 500°C. For $t^{1/n}$ model.

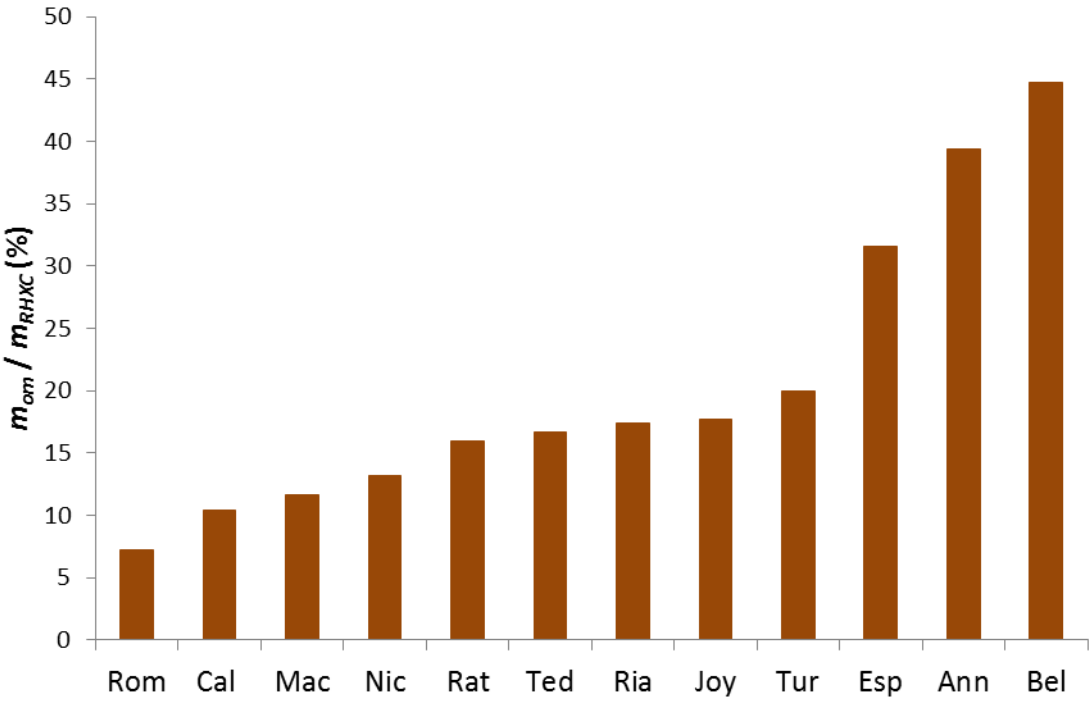

Figure 7.55: The mass of organic matter (computed using m_c and and OM/OC ratio of 1.95), m_{om}, as a % of total fractional mass loss, m_{RHXC}, upon heating between 130°C and 500°C. For $t^{1/n}$ model.

Table 7.6: Modelled intercept mass for $t^{1/4}$ model. Included are 95% confidence intervals.

$t^{1/4}$ Model	130°C			500°C		
Sample	**25°C Intercept mass, m_0 (95% confidence Interval) (g)**	**35°C Intercept mass, m_0 (95% confidence Interval) (g)**	**45°C Intercept mass, m_0 (95% confidence Interval) (g)**	**25°C Intercept mass, m_0 (95% confidence Interval) (g)**	**35°C Intercept mass, m_0 (95% confidence Interval) (g)**	**45°C Intercept mass, m_0 (95% confidence Interval) (g)**
Ann	19.43169 (19.43134 19.43201)	19.37671 (19.37634 19.37707)	19.74814 (19.74767 19.74862)	19.39899 (19.39860 19.39938)	19.34624 (19.34566 19.34682)	19.71522 (19.71457 19.71587)
Esp	19.29053 (19.29026 19.29079)	20.73420 (20.73380 20.73461)	20.30118 (20.30074 20.30163)	19.26656 (19.26620 19.26692)	20.71053 (20.71015 20.71091)	20.27976 (20.27921 20.28030)
Nic	18.63148 (18.63110 18.63185)	19.33869 (19.33822 19.33916)	17.29784 (17.29690 17.29878)	18.56532 (18.56482 18.56582)	19.27930 (19.27878 19.27982)	17.23570 (17.23512 17.23628)
Mac	19.53693 (19.53667 19.53719)	19.78013 (19.77982 19.78043)	15.21389 (15.21330 15.21448)	19.42174 (19.42142 19.42207)	19.66217 (19.66160 19.66274)	15.12157 (15.12080 15.12234)
Ria	18.42199 (18.42162 18.42235)	18.47240 (18.47194 18.47285)	20.79053 (20.78983 20.79123)	18.35507 (18.35457 18.35556)	18.40462 (18.40405 18.40518)	20.71242 (20.71184 20.71300)
Etr	18.77128 (18.76958 18.77297)	18.56316 (18.56022 18.56611)	19.27839 (19.27126 19.28552)	18.04068 (18.03646 18.04490)	17.77239 (17.76673 17.77805)	18.43659 (18.42101 18.45217)
Rom	19.92486 (19.92147 19.92825)	19.29881 (19.29747 19.30015)	22.63231 (22.62862 22.63600)	19.64120 (19.63945 19.64296)	19.01961 (19.01875 19.02046)	22.30657 (22.30366 22.30948)
Por	18.38072 (18.37592 18.38551)	18.46193 (18.45992 18.46395)	19.31660 (19.31199 19.32121)	17.91338 (17.90906 17.91771)	17.97263 (17.96713 17.97813)	18.86019 (18.85003 18.87034)
Rat	20.96705 20.96671 20.96738	18.71172 18.71135 18.71210	20.35837 20.35783 20.35892	20.92581 20.92532 20.92630	18.67447 18.67384 18.67511	20.31695 20.31606 20.31784
Cal	21.79549 (21.79513 21.79584)	18.94071 (18.94034 18.94108)	20.41125 (20.41067 20.41184)	21.74362 (21.74300 21.74425)	18.89592 (18.89518 18.89667)	20.36201 (20.36092 20.36310)
Lan	20.10597 (20.09118 20.12076)	19.32801 (19.32064 19.33538)	19.91697 (19.90480 19.92914)	19.86251 (19.85032 19.87471)	19.08523 (19.07706 19.09340)	19.62098 (19.61334 19.62862)
Joy	19.89434 (19.89389 19.89479)	19.69844 (19.69786 19.69903)	20.72914 (20.72842 20.72987)	19.84356 (19.84267 19.84445)	19.64772 (19.64709 19.64835)	20.67599 (20.67536 20.67663)
Cau	17.43754 (17.43455 17.44054)	16.76862 (16.76604 16.77119)	16.37628 (16.37350 16.37905)	17.36173 (17.35909 17.36437)	16.68821 (16.68696 16.68946)	16.29714 (16.29474 16.29954)
Bel	19.54302 (19.54152 19.54452)	18.42979 (18.42871 18.43086)	19.01833 (19.01610 19.02057)	19.36738 (19.36577 19.36898)	18.27146 (18.27066 18.27225)	18.85247 (18.85045 18.85449)
Dow1	15.97214 (15.96662 15.97765)	15.93229 (15.92713 15.93746)	16.65301 (16.64773 16.65829)	15.60260 (15.59904 15.60615)	15.56122 (15.55826 15.56419)	16.26064 (16.25760 16.26369)
Dow2	12.43586 (12.43058	11.56350 (11.55982	8.83145 (8.82790	12.04262 (12.03978	11.25103 (11.24941	8.58350 (8.58131

	12.44115)	11.56718)	8.83499)	12.04545)	11.25266)	8.58569)
Tur	19.19756 (19.19699 19.19813)	19.75655 (19.75592 19.75718)	19.24218 (19.24136 19.24300)	19.14635 (19.14569 19.14701)	19.70182 (19.70082 19.70282)	19.18969 (19.18839 19.19099)
Ted	20.81774 (20.81684 20.81864)	19.39786 (19.39702 19.39871)	20.71028 (20.70954 20.71103)	20.76401 (20.76285 20.76516)	19.34769 (19.34630 19.34908)	20.65814 (20.65716 20.65913)

Table 7.7: Modelled intercept mass for $t^{1/n}$ model (pre-fixed). Included are 95% confidence intervals.

$t^{1/n}$ Model (pre-fixed)	**130°C**			**500°C**		
Sample	**25°C Intercept mass, m_0 (95% confidence Interval) (g)**	**35°C Intercept mass, m_0 (95% confidence Interval) (g)**	**45°C Intercept mass, m_0 (95% confidence Interval) (g)**	**25°C Intercept mass, m_0 (95% confidence Interval) (g)**	**35°C Intercept mass, m_0 (95% confidence Interval) (g)**	**45°C Intercept mass, m_0 (95% confidence Interval) (g)**
Ann	19.43530 (19.43444 19.43615)	19.37974 (19.37829 19.38119)	19.75310 (19.75163 19.75458)	19.40258 (19.40137 19.40379)	19.35264 (19.35164 19.35365)	19.72369 (19.72175 19.72562)
Esp	19.28853 (19.28618 19.29088)	20.72604 (20.72038 20.73169)	20.29791 (20.29367 20.30215)	19.26605 (19.26282 19.26929)	20.70553 (20.70204 20.70902)	20.27342 (20.26813 20.27870)
Nic	18.62589 (18.62115 18.63062)	19.33147 (19.32680 19.33614)	17.25222 (17.20599 17.29844)	18.56186 (18.55768 18.56605)	19.27355 (19.26876 19.27834)	17.23242 (17.22755 17.23729)
Mac	19.53620 (19.53429 19.53811)	19.77944 (19.77727 19.78160)	15.21630 (15.21376 15.21884)	19.42526 (19.42415 19.42637)	19.66769 (19.66673 19.66864)	15.12810 (15.12699 15.12922)
Ria	18.42649 (18.42579 18.42720)	18.47800 (18.47702 18.47898)	20.80348 (20.80233 20.80462)	18.36242 (18.36167 18.36317)	18.41600 (18.41516 18.41684)	20.73189 (20.73089 20.73290)
Etr	NA	NA	NA	NA	NA	NA
Rom	19.92533 (19.90042 19.95024)	19.22734 (18.89350 19.56117)	22.52361 (20.62324 24.42398)	19.50716 (19.40031 19.61401)	18.99528 (18.98362 19.00694)	22.28281 (22.24845 22.31717)
Por	NA	NA	NA	NA	NA	NA
Rat	20.97032 (20.96980 20.97083)	18.71559 (18.71473 18.71644)	20.36413 (20.36325 20.36501)	20.92962 (20.92898 20.93026)	18.67972 (18.67901 18.68043)	(20.32435 20.32336 20.32533)
Cal	21.80001 (21.79923 21.80079)	18.94404 (18.94291 18.94518)	20.41724 (20.41592 20.41857)	21.75049 (21.74963 21.75135)	18.90330 (18.90241 18.90418)	20.37200 (20.37066 20.37333)
Lan	NA	NA	NA	NA	NA	NA
Joy	19.90273 (19.90207 19.90340)	19.70801 (19.70690 19.70913)	20.74362 (20.74208 20.74515)	19.85693 (19.85606 19.85780)	19.66622 (19.66540 19.66703)	20.69867 (20.69736 20.69997)
Cau	16.26259 (12.34053 20.18465)	16.70281 (16.55728 16.84834)	16.19475 (15.36017 17.02933)	17.36747 (17.36011 17.37484)	16.68575 (16.67900 16.69250)	16.27980 (16.25603 16.30357)
Bel	19.53947 (19.53248	18.42416 (18.41456	18.92208 (18.82283	19.34458 (19.33565	18.25891 (18.25296	18.79143 (18.76146

	19.54645)	18.43375)	19.02132)	19.35352)	18.26487)	18.82140)
Dow1	NA	NA	NA	NA	NA	NA
Dow2	NA	NA	NA	NA	NA	NA
Tur	19.20453 (19.20403 19.20503)	19.76437 (19.76351 19.76522)	19.25471 (19.25347 19.25596)	19.15201 (19.15063 19.15339)	19.71266 (19.71147 19.71386)	19.20400 (19.20243 19.20558)
Ted	20.83128 (20.83049 20.83207)	19.41193 (19.41114 19.41273)	20.72503 (20.72264 20.72743)	20.77702 (20.77552 20.77853)	19.36662 (19.36501 19.36823)	20.67290 (20.66956 20.67623)

Table 7.8: Modelled intercept mass for $t^{1/n}$ model (fixed). Included are 95% confidence intervals.

$t^{1/n}$ Model (1/n-fixed)	**130°C**			**500°C**		
Sample	**25°C Intercept mass, m_0 (95% confidence Interval) (g)**	**35°C Intercept mass, m_0 (95% confidence Interval) (g)**	**45°C Intercept mass, m_0 (95% confidence Interval) (g)**	**25°C Intercept mass, m_0 (95% confidence Interval) (g)**	**35°C Intercept mass, m_0 (95% confidence Interval) (g)**	**45°C Intercept mass, m_0 (95% confidence Interval) (g)**
Ann	19.43498 (19.43480 19.43517)	19.38105 (19.38078 19.38131)	19.75422 (19.75394 19.75450)	19.40295 (19.40270 19.40319)	19.35179 (19.35155 19.35203)	19.72324 (19.72289 19.72359)
Esp	19.28772 (19.28740 19.28803)	20.73082 (20.73041 20.73123)	20.29747 (20.29694 20.29799)	19.26257 (19.26211 19.26304)	20.70616 (20.70576 20.70656)	20.27478 (20.27419 20.27536)
Nic	18.62782 (18.62743 18.62820)	19.33434 (19.33395 19.33473)	17.29512 (17.29419 17.29605)	18.56064 (18.56019 18.56108)	19.27264 (19.27209 19.27319)	17.22728 (17.22655 17.22801)
Mac	19.53931 (19.53907 19.53955)	19.78307 (19.78277 19.78336)	15.21659 (15.21612 15.21706)	19.42435 (19.42409 19.42460)	19.66568 (19.66537 19.66600)	15.12558 (15.12517 15.12600)
Ria	18.42693 (18.42677 18.42708)	18.47930 (18.47909 18.47952)	20.80355 (20.80329 20.80382)	18.36157 (18.36138 18.36176)	18.41593 (18.41573 18.41614)	20.73120 (20.73092 20.73147)
Etr	NA	NA	NA	NA	NA	NA
Rom	19.90817 (19.90236 19.91398)	19.28183 (19.27973 19.28393)	22.61452 (22.60844 22.62060)	19.58373 (19.58128 19.58618)	18.96703 (18.96554 18.96853)	22.24896 (22.24420 22.25372)
Por	NA	NA	NA	NA	NA	NA
Rat	20.97016 (20.97002 20.97030)	18.71568 (18.71555 18.71581)	20.36429 (20.36409 20.36448)	20.92953 (20.92935 20.92972)	18.67950 (18.67929 18.67971)	20.32477 (20.32451 20.32503)
Cal	21.80027 (21.80010 21.80045)	18.94549 (18.94526 18.94572)	20.41820 (20.41793 20.41848)	21.74987 (21.74963 21.75010)	18.90250 (18.90226 18.90274)	20.37129 (20.37094 20.37163)
Lan	NA	NA	NA	NA	NA	NA
Joy	19.90240 (19.90223 19.90257)	19.70909 (19.70884 19.70934)	20.74504 (20.74470 20.74539)	19.85647 (19.85624 19.85670)	19.66457 (19.66429 19.66485)	20.69850 (20.69818 20.69882)
Cau	NA	NA	NA	NA	NA	NA
Bel	19.52705 (19.52643	18.41088 (18.40990	18.99793 (18.99603	19.34460 (19.34376	18.24676 (18.24595	18.82644 (18.82493

	19.52767)	18.41187)	18.99984)	19.34544)	18.24757)	18.82794)
Dow1	NA	NA	NA	NA	NA	NA
Dow2	NA	NA	NA	NA	NA	NA
Tur	19.20307 (19.20284 19.20329)	19.76473 (19.76454 19.76491)	19.25427 (19.25405 19.25450)	19.15321 (19.15290 19.15351)	19.71279 (19.71252 19.71307)	19.20545 (19.20510 19.20580)
Ted	20.82814 (20.82783 20.82845)	19.41082 (19.41061 19.41103)	20.72681 (20.72648 20.72714)	20.77710 (20.77678 20.77743)	19.36521 (19.36485 19.36558)	20.68101 (20.68021 20.68180)

Table 7.9: Table of relevant mass values for $t^{1/4}$ model. All values are fractional with uncertainty estimates (Δ) based on the standard deviation of the three mass loss values per sample.

$t^{1/4}$	m_{RHXC}	Δm_{RHXC}	m_{lw}	m_{om}	m_{RHX}	Δm_{RHX}
Ann	0.0016431	0.0000598	0.0000019	0.0006221	0.0010192	0.0000594
Esp	0.0011479	0.0000937	0.0000000	0.0003803	0.0007676	0.0000937
Nic	0.0034164	0.0002916	0.0000098	0.0004739	0.0029327	0.0002908
Mac	0.0060118	0.0000879	0.0000539	0.0006923	0.0052657	0.0000947
Ria	0.0037000	0.0000644	0.0000245	0.0006084	0.0030671	0.0000679
Etr	0.0435501	0.0027074	0.0000993	0.0046235	0.0388274	0.0027225
Rom	0.0145750	0.0001214	0.0000302	0.0011915	0.0133533	0.0001254
Por	0.0258378	0.0015280	0.0002552	0.0101361	0.0154466	0.0015250
Rat	0.0020014	0.0000346	0.0000063	0.0003101	0.0016850	0.0000355
Cal	0.0023912	0.0000247	0.0000222	0.0002399	0.0021292	0.0000255
Lan	0.0133545	0.0015170	0.0001053	0.0000683	0.0131809	0.0015230
Joy	0.0025704	0.0000113	0.0000195	0.0004017	0.0021492	0.0000140
Cau	0.0046803	0.0002720	0.0000301	0.0009711	0.0036790	0.0002748
Bel	0.0088441	0.0002057	0.0002828	0.0041087	0.0044526	0.0001912
Dow1	0.0238867	0.0002254	0.0001772	0.0031590	0.0205504	0.0002360
Dow2	0.0297713	0.0025586	0.0003881	0.0028412	0.0265421	0.0025344
Tur	0.0027293	0.0000521	0.0000169	0.0005168	0.0021956	0.0000538
Ted	0.0025683	0.0000385	0.0000406	0.0003900	0.0021377	0.0000371

Table 7.10: Table of relevant mass values for $t^{1/n}$ model. All values are fractional with uncertainty estimates (Δ) based on the standard deviation of the three mass loss values per sample.

$t^{1/n}$	m_{RHXC}	Δm_{RHXC}	m_{lw}	m_{om}	m_{RHX}	Δm_{RHX}
Ann	0.0015779	0.0000700	0.0000019	0.0006221	0.0009540	0.0000694
Esp	0.0012052	0.0000938	0.0000000	0.0003803	0.0008250	0.0000938
Nic	0.0035864	0.0003695	0.0000098	0.0004739	0.0031027	0.0003695
Mac	0.0059680	0.0000492	0.0000539	0.0006923	0.0052219	0.0000566
Ria	0.0034968	0.0000595	0.0000245	0.0006084	0.0028640	0.0000552
Rom	0.0165314	0.0000888	0.0000303	0.0011915	0.0153096	0.0000875
Rat	0.0019409	0.0000037	0.0000063	0.0003101	0.0016245	0.0000038
Cal	0.0022983	0.0000220	0.0000222	0.0002399	0.0020363	0.0000198
Joy	0.0022753	0.0000337	0.0000195	0.0004017	0.0018541	0.0000308
Bel	0.0091784	0.0002265	0.0002832	0.0041087	0.0047866	0.0002117
Tur	0.0025933	0.0000469	0.0000169	0.0005168	0.0020597	0.0000466
Ted	0.0023419	0.0001214	0.0000406	0.0003900	0.0019114	0.0001185

7.4.2 Mass Relationships and Correlations

m_{RHXC} vs. m_{RHX}

The relationship between the total fractional mass loss, m_{RHXC}, and the RHX-attributed mass loss, m_{RHX}, are presented, for the $t^{1/4}$ model, in *Figure 7.56* for all samples, in *Figure 7.57 (left)* with abnormal samples removed, and in *Figure 7.57 (right)* with *Bel* additionally removed (outlier in *Figure 7.57 (left)*). These graphs show a strong correlation between the two as is expected but highlights possible issues with *Bel*.

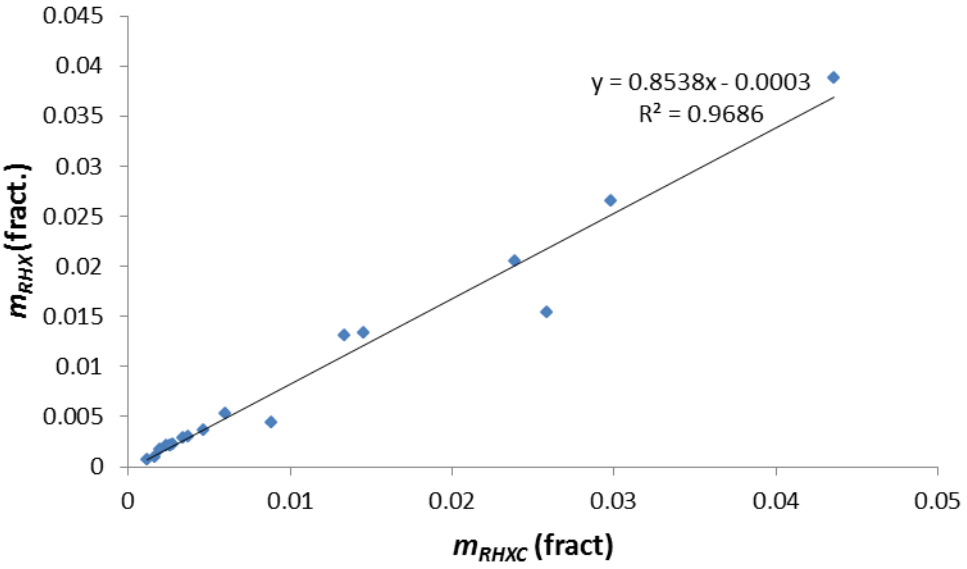

Figure 7.56: Relationship between total fractional mass loss and RHX attributed mass loss. For the $t^{1/4}$ model.

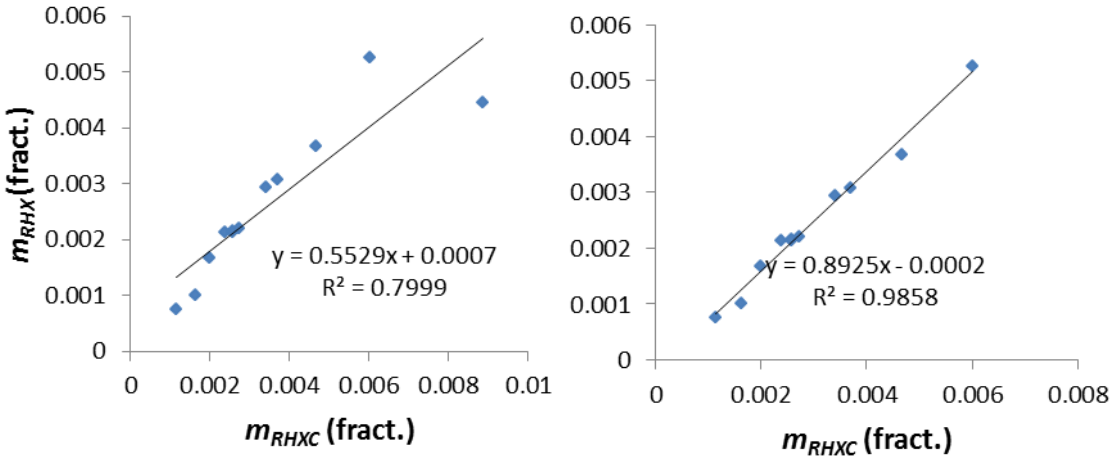

Figure 7.57: Relationship between total fractional mass loss and RHX attributed mass loss with abnormal samples removed (left) and with additional *Bel* sample removed (right). For the $t^{1/4}$ model.

Similarly, the relationships between the total fractional mass loss and the RHX attributed mass loss for the $t^{1/n}$ model are presented (with anomalous samples and anomalous plus *Bel* removed) in *Figure 7.58*, below. A strong correlation is also evident.

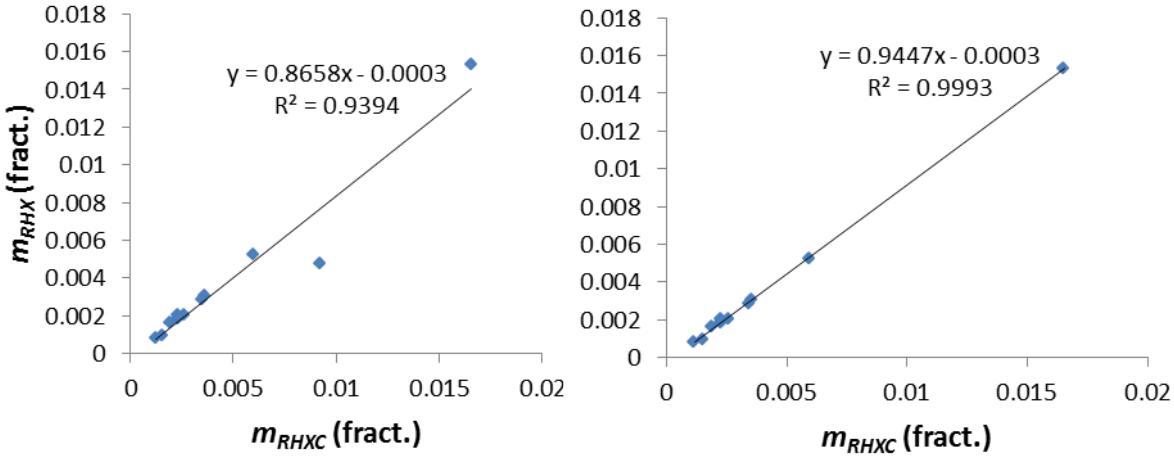

Figure 7.58: Relationship between total fractional mass loss and RHX attributed mass loss with anomalous samples removed (left) and with additional *Bel* sample removed (right). For $t^{1/n}$ model.

S1 m_{S1} vs. m_{RHX}

The relationship between the RHX fractional mass and the fractional mass gain during *S1* is presented in *Figure 7.59 (left)* for the $t^{1/4}$ model and *Figure 7.59 (right)* for the $t^{1/n}$ model. Abnormal samples are excluded in both. The level of correlation between the two properties for either model is not convincing, R^2 = 0.46 and 0.65, but the null hypothesis is rejected, p = 0.0157 and 0.0028. However, if samples with problematic *S1* behaviour, *Mac* and *Bel*, are removed (see *Discussion*), the correlations are weak, R^2 = 0.2 and 0.04, and the statistical significance of the relationships are low, p = 0.1959 and 0.6008, for the $t^{1/4}$ and $t^{1/n}$ models, respectively.

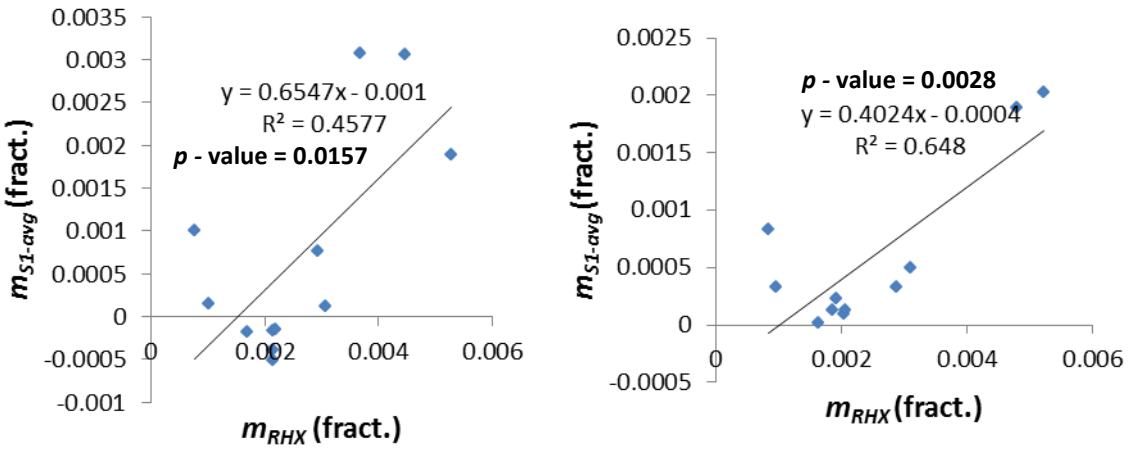

Figure 7.59: Relationship between *S1* fractional mass gain and the RHX fractional mass for $t^{1/4}$ model (*left*) and $t^{1/n}$ (*right*). Abnormal samples are excluded for both.

BET S.A. vs. m_{RHX}

The relationship between the BET S.A. and the RHX fractional mass are presented in *Figure 7.60* for both models (again abnormal samples excluded). The correlations are weak, R^2 = 0.17 and 0.22, and the relationship can not be treated as significant, with p = 0.1793 and 0.1505.

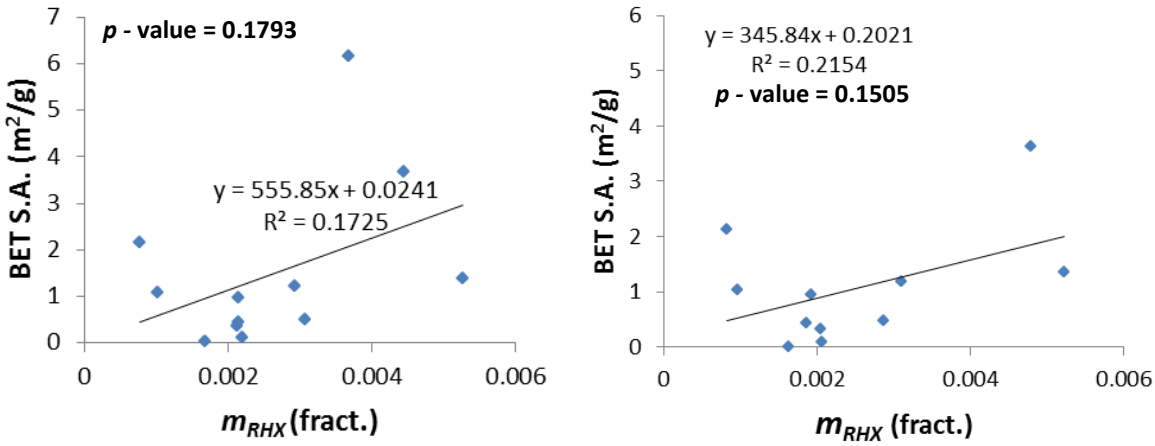

Figure 7.60: Relationship between BET S.A. and the RHX fractional mass for $t^{1/4}$ model (*left*) and $t^{1/n}$ (*right*). Abnormal samples are excluded for the former.

TG-MS vs. m_{RHXC}

To examine the validity of the total fractional mass estimate it was plotted against the TG-MS mass loss, the high correlation expected was confirmed. This is presented in *Figure 7.61* for all samples and the $t^{1/4}$ model.

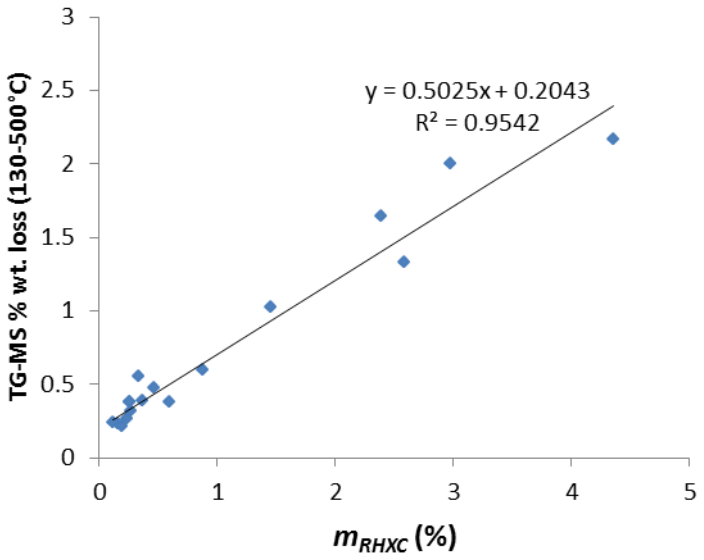

Figure 7.61: Relationship between TG-MS %wt. loss (130-500°C) and the estimated total mass loss (expressed as %) from mass gain experiments and using $t^{1/4}$ model.

In *Figure 7.62*, the *S1* fractional mass (avg.) is added to the total fractional mass and this value is then correlated against the TG-MS % wt. loss. An improved R^2 = 0.98 results. This is discussed in *Chapter 9*.

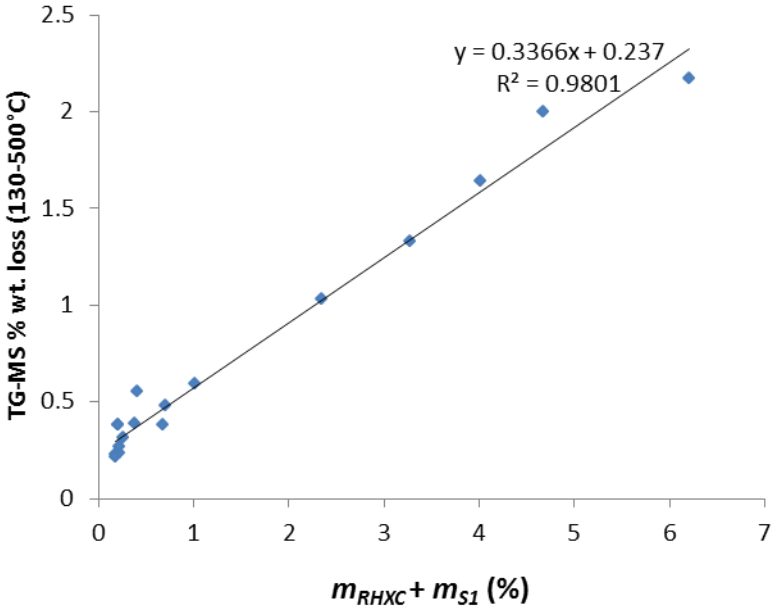

Figure 7.62: Relationship between TG-MS %wt. loss (130-500°C) and the sum of the estimated total mass loss and *S1* mass (expressed as %) from mass gain experiments and using $t^{1/4}$ model.

7.5 Activation Energy

7.5.1 Activation Energies

The Arrhenius plots used in activation energy calculations are presented in *Appendix D*. Examples are provided for *Ann* and *Joy* in *Figure 7.63* and *Figure 7.64,* respectively. The linearity of the various components (130C, 500C and RHX) plots is clear. However, this is not the case for all samples. In *Table 7.11* and *Table 7.12* the results of activation energy calculations are presented for all samples together with the uncertainties (2σ) and the R^2 value for $t^{1/4}$ and $t^{1/n}$ approaches. Samples for which the linearity was poor are highlighted in red and samples for which linear plots were completely unsuitable are marked void. It can be observed that the quality of the fits is in general slightly better for the $t^{1/4}$ model (see *Discussion*).

Bar chart plots of the sample activation energies for the 130C and 500C components are displayed in *Figure 7.65* and *Figure 7.66* (for samples where activation energies could be obtained for both components). For the $t^{1/4}$ model, *Figure 7.65*, it can be observed that the activation energies are very similar for both components with the exception of *Nic* and *Mac* where differences of > 40kJ/mol are observed. Similar behaviour is observed for the $t^{1/n}$ activation energies, *Figure 7.66*. In general, the 500C component activation energy appears to be greater than that of the 130C component but when the uncertainties are considered (provided to 2σ) there is overlap of the possible activation energy range for all samples, excluding *Nic* and *Mac* for $t^{1/4}$ and $t^{1/n}$ (borderline *Ann* and *Ria* for *1/n* also).

The RHX activation energies are provided in *Figure 7.67* and *Figure 7.68*, for $t^{1/4}$ and $t^{1/n}$ models, respectively. Also included are the 2σ uncertainties. In terms of typical behaviour, the average activation energies (and standard deviation) are as follows for $t^{1/4}$ model: $E_{a130}(avg) = 70 \pm 35$ *kJ/mol;* $E_{a500}(avg) = 77 \pm 40$ *kJ/mol;* $E_{aRHX}(avg) = 109 \pm 74$ *kJ/mol*. The large spread in values accounts for the large standard deviation. If abnormal samples are excluded, the values are: $E_{a130}(avg) = 78 \pm 31$ *kJ/mol;* $E_{a500}(avg) = 86 \pm 35$ *kJ/mol;* $E_{aRHX}(avg) = 137 \pm 70$ *kJ/mol*. For $t^{1/n}$ the values are as follows: $E_{a130}(avg) = 58 \pm 14$ *kJ/mol;* $E_{a500}(avg) = 67 \pm 26$ *kJ/mol;* $E_{aRHX}(avg) =$

101 ± 78 kJ/mol. With abnormal samples removed, this becomes: E_{a130}*(avg) = 58 ± 14 kJ/mol;* E_{a500}*(avg) = 72 ± 19 kJ/mol;* E_{aRHX}*(avg) = 109 ± 75 kJ/mol*.

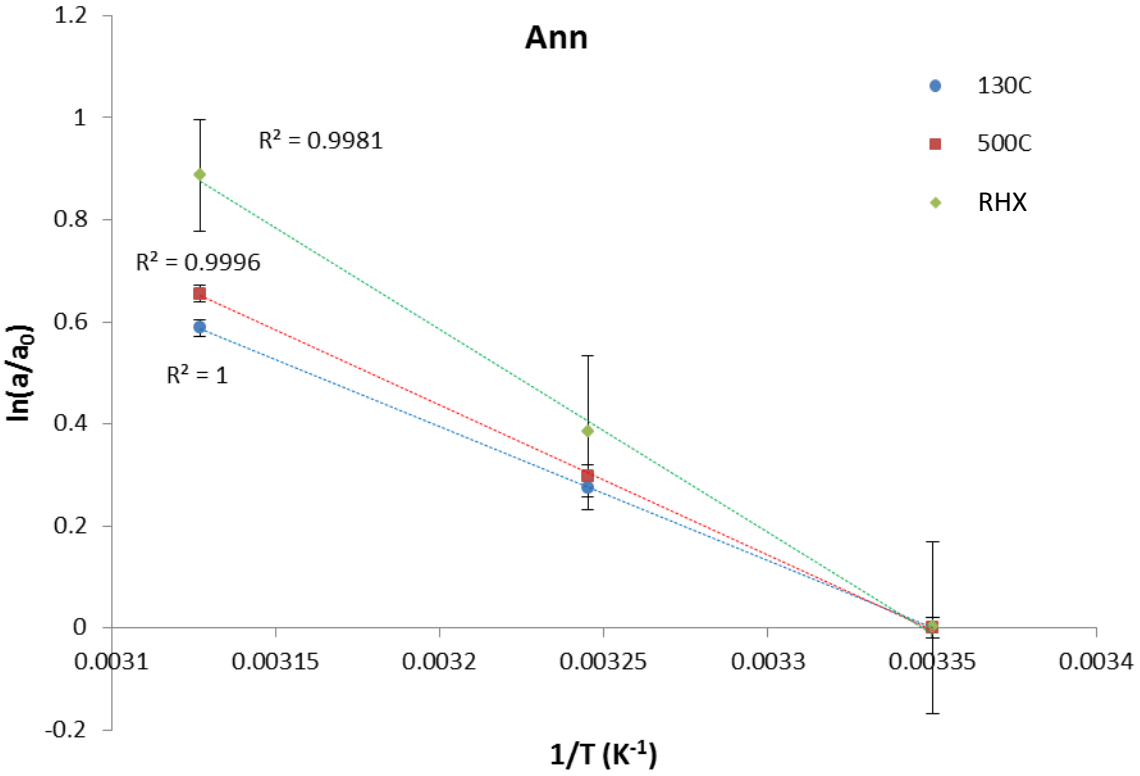

Figure 7.63: Arrhenius plot ($t^{1/4}$ model) for 130°C (blue), 500°C (red) and RHX (green, RHX component) components of mass gain rates for *Ann* sample. Uncertainties are to 2σ.

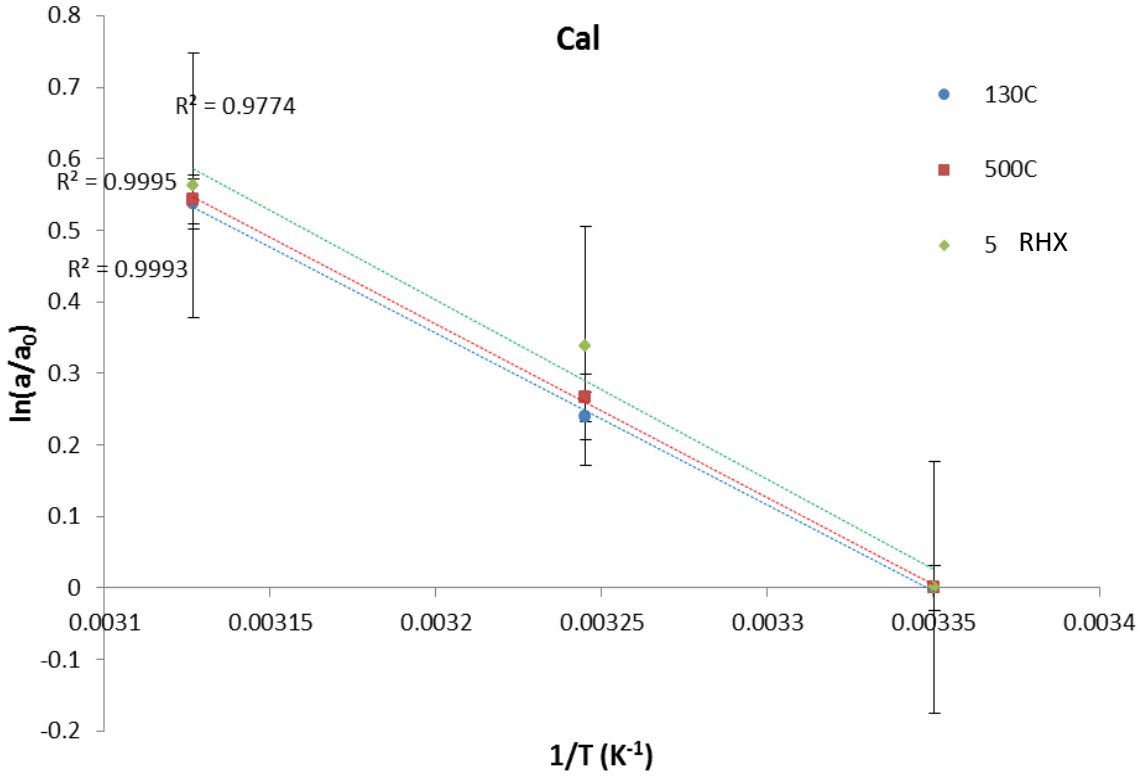

Figure 7.64: Arrhenius plot ($t^{1/4}$ model) for 130°C (blue), 500°C (red) and 500-130°C (green, RHX component) components of mass gain rates for *Cal* sample. Uncertainties are to 2σ.

Table 7.11: Activation energy and uncertainties (2σ) together with R^2 value of Arrhenius plot linear fits ($t^{1/4}$ model). Red font marks samples with poor quality fits. o = samples for which fits were not suitable.

$t^{1/4}$	E_{a130} (kJ/mol)	ΔE_{a130} (kJ/mol)	R^2	E_{a500} (kJ/mol)	ΔE_{a500} (kJ/mol)	R^2	E_{aRHX} (kJ/mol)	ΔE_{aRHX} (kJ/mol)	R^2
Ann	87.49	0.88	0.999	97.58	3.91	0.999	132.14	11.59	0.998
Esp	33.59	1.43	0.999	43.95	3.00	0.999	76.61	14.72	0.99
Nic	28.29	29.04	0.791	89.73	17.27	0.991	204.35	81.10	0.962
Mac	71.42	1.32	0.999	117.59	3.42	0.999	294.94	84.57	0.98
Ria	120.42	11.30	0.998	133.51	16.16	0.996	179.31	103.20	0.923
Etr	o	o	o	o	o	o	28.53	3.37	0.997
Rom	14.39	33.76	0.421	20.04	15.78	0.866	22.68	7.08	0.976
Por	42.03	56.78	0.687	24.51	o	o	33.82	o	o
Rat	101.25	14.93	0.995	114.21	15.67	0.995	182.90	30.41	0.993
Cal	79.96	4.27	0.999	80.83	3.61	0.999	83.33	25.32	0.977
Lan	o	o	o	o	o	o	82.82	163.77	0.505
Joy	100.66	5.20	0.999	97.70	10.25	0.997	89.08	24.71	0.981
Cau	o	o	o	18.32	2.11	0.997	99.86	14.59	0.995
Bel	42.83	7.26	0.993	42.31	0.26	0.999	40.23	32.63	0.859
Dow1	o	o	o	o	o	o	41.55	3.06	0.999
Dow2	o	o	o	o	o	o	o	o	o
Tur	109.41	1.94	0.999	118.15	7.14	0.999	155.34	31.87	0.99
Ted	83.95	13.49	0.994	88.17	13.80	0.994	103.64	15.51	0.994

Table 7.12: Activation energy and uncertainties (2σ) together with R^2 value of Arrhenius plot linear fits ($t^{1/n}$ model). Red font marks samples with poor quality fits. o = samples for which fits were not suitable.

$t^{1/n}$	E_{a130} (kJ/mol)	ΔE_{a130} (kJ/mol)	R^2	E_{a500} (kJ/mol)	ΔE_{a500} (kJ/mol)	R^2	E_{aRHX} (kJ/mol)	ΔE_{aRHX} (kJ/mol)	R^2
Ann	66.76	0.55	0.999	73.57	5.00	0.999	95.67	18.49	0.991
Esp	43.93	1.95	0.999	52.53	8.58	0.993	78.86	41.20	0.936
Nic	23.50	45.95	0.511	114.41	18.56	0.993	270.01	90.89	0.972
Mac	59.01	0.02	1	95.81	5.55	0.999	232.53	79.76	0.971
Ria	76.14	3.89	0.999	84.73	3.76	0.999	119.10	36.50	0.977
Etr	o	o	o	o	o	o	o	o	o
Rom	o	o	o	6.89	16.18	0.42	6.65	2.08	0.976
Por	o	o	o	o	o	o	o	o	o
Rat	57.72	12.82	0.988	63.22	7.40	0.997	100.17	28.17	0.981
Cal	56.84	1.82	0.999	56.85	5.03	0.998	56.86	13.46	0.986
Lan	o	o	o	o	o	o	o	o	o
Joy	65.84	6.21	0.998	69.45	5.92	0.998	82.77	5.56	0.999
Cau	o	o	o	o	o	o	o	o	o
Bel	65.57	24.11	0.967	56.43	10.15	0.992	23.51	41.14	0.567
Dow1	o	o	o	o	o	o	o	o	o
Dow2	o	o	o	o	o	o	o	o	o
Tur	60.03	3.85	0.999	64.74	1.02	0.999	86.10	23.00	0.982
Ted	62.14	6.25	0.997	60.84	2.42	0.999	55.80	12.94	0.987

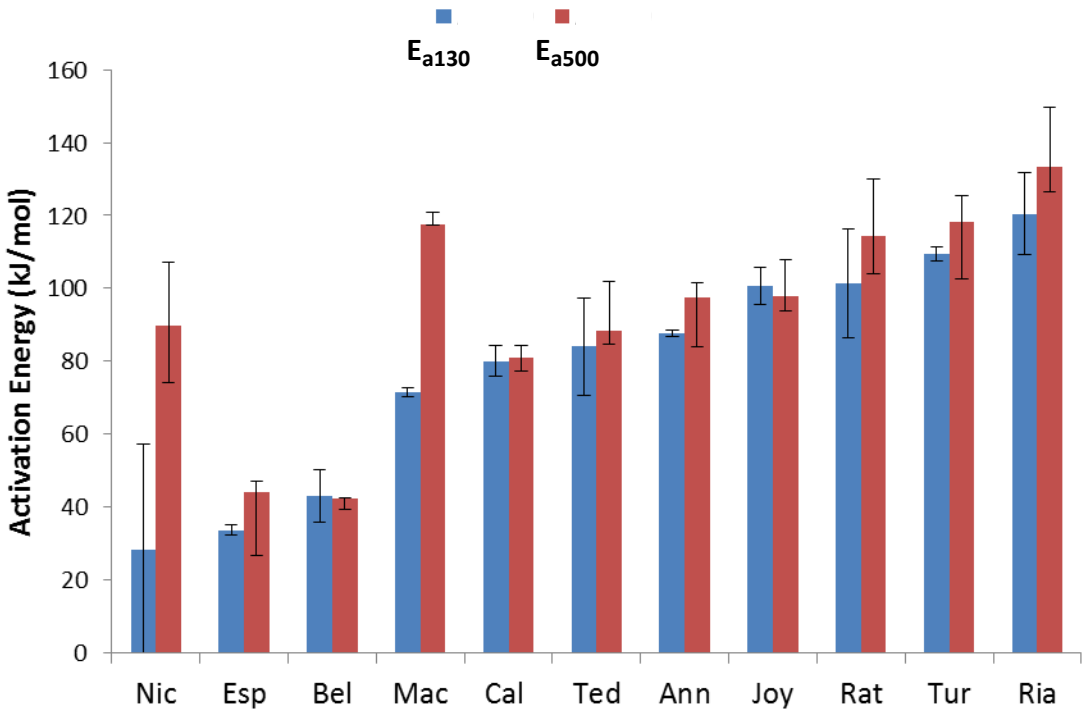

Figure 7.65: Activation energies calculated for 130°C (blue) and 500°C (red) components, for $t^{1/4}$ model. Included are the 2σ uncertainties. For samples where activation energies could be obtained for both components.

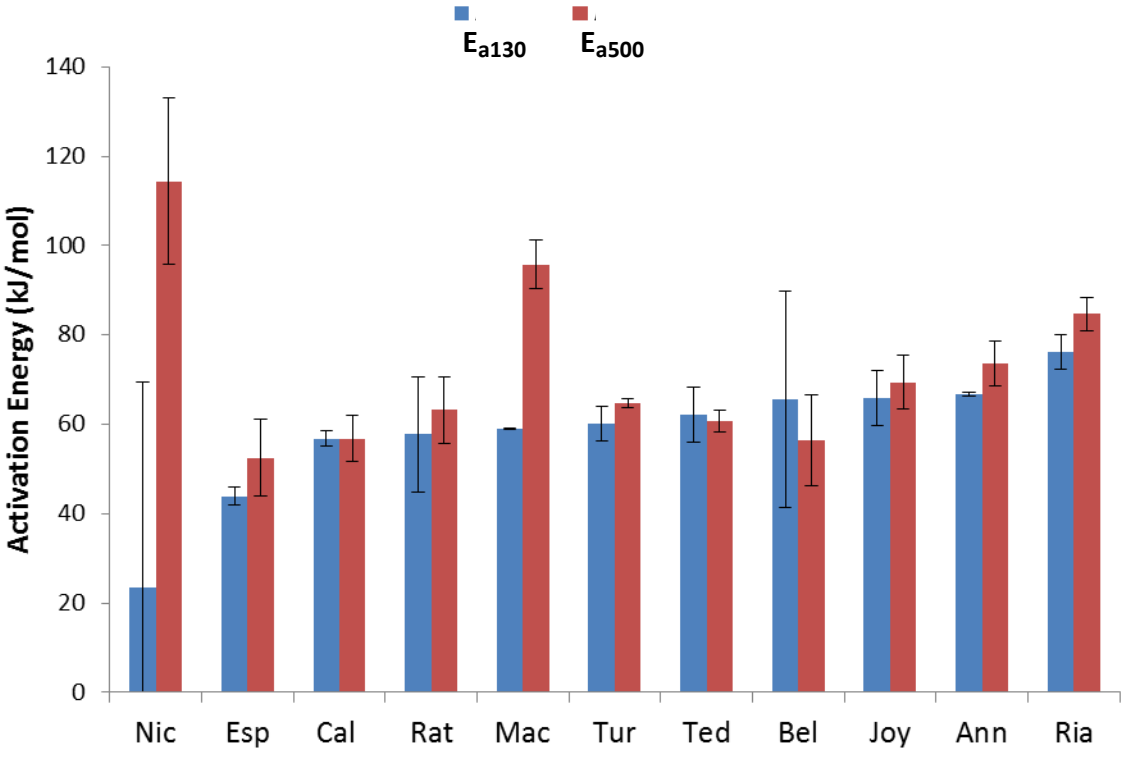

Figure 7.66: Activation energies calculated for 130°C (blue) and 500°C (red) components, for $t^{1/n}$ model. Included are the 2σ uncertainties. For samples where activation energies could be obtained for both components.

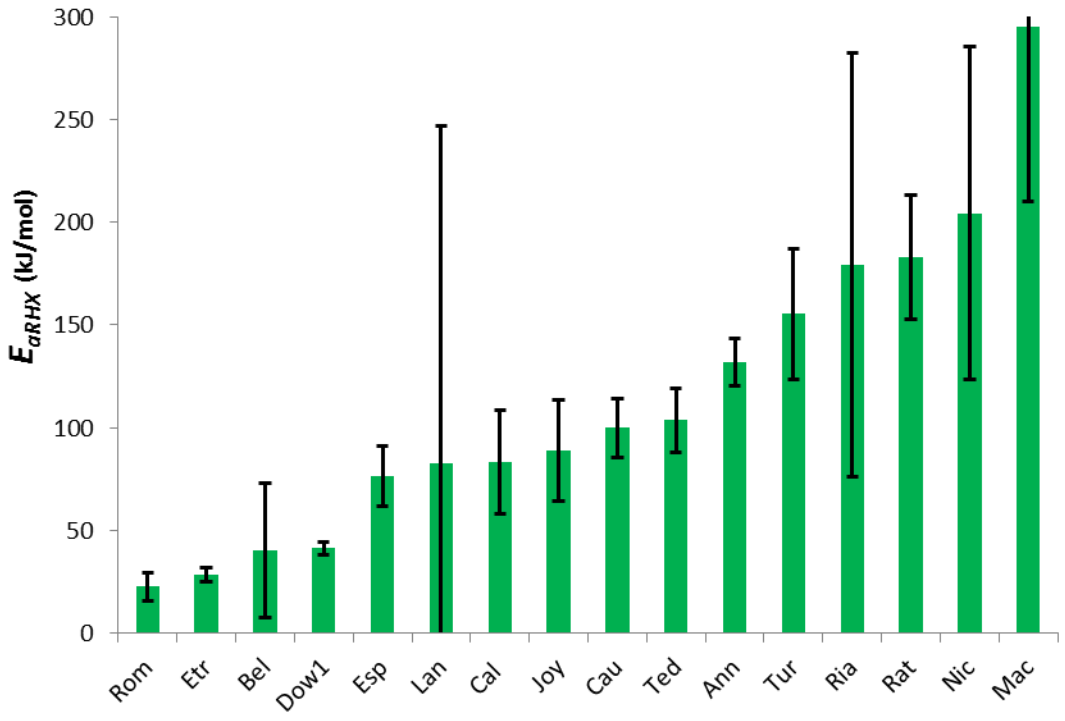

Figure 7.67: RHX activation energy and uncertainties (2σ) for $t^{1/4}$ model. Uncertainty in *Mac* cut off for scaling purposes.

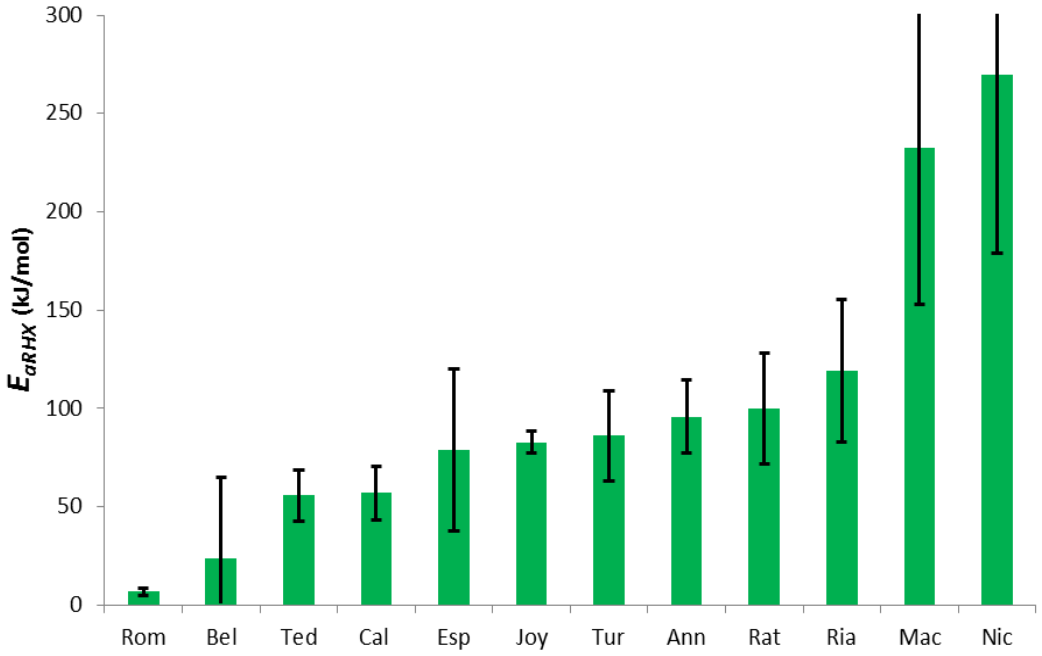

Figure 7.68: RHX activation energy and uncertainties (2σ) for $t^{1/n}$ model. Uncertainties in *Bel, Nic,* and *Mac* are cut off for scaling purposes.

7.5.2 Activation Energy Relationships and Correlations

Activation Energies

The relationship between the 130C activation energy and the 500C activation energy, for the $t^{1/4}$model, are presented in *Figure 7.69* with abnormal samples excluded (*left*) and additionally with *Nic* and *Mac* excluded (because of unusually large disparity in *Figure 7.65 and* R^2 issues with *Nic*, *Table 7.11*). In the latter a clear and strong correlation between the two is observed, R^2 = 0.98. Similar plots are presented in *Figure 7.70* for the $t^{1/n}$. The correlation is much weaker, R^2 = 0.68, but still significant, p = 0.0065.

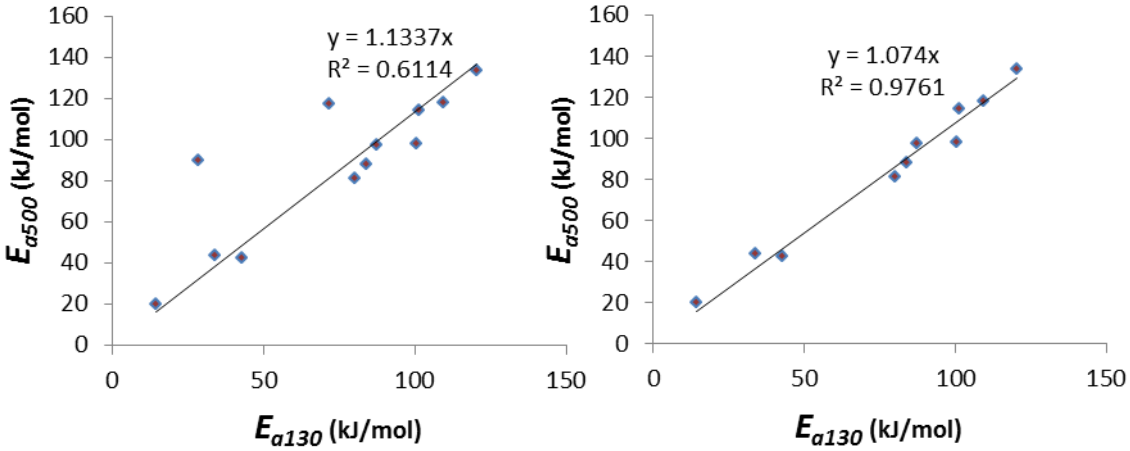

Figure 7.69: Relationship between 130°C and 500°C components of activation energy for samples excluding abnormal samples (left) and additionally *Nic* and *Mac* (right). For the $t^{1/4}$ model.

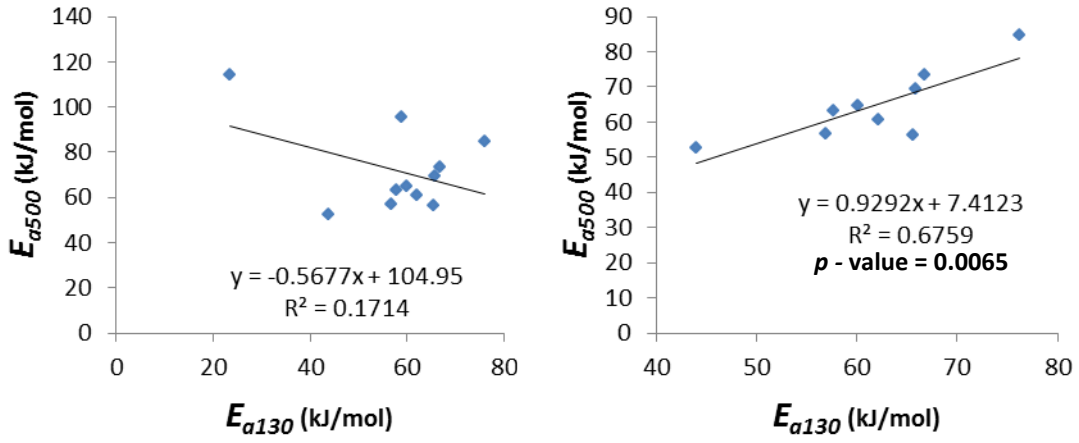

Figure 7.70: Relationship between 130°C and 500°C components of activation energy for samples excluding abnormal samples (left) and additionally *Nic* and *Mac* (right). For the $t^{1/n}$ model.

The relationship, $t^{1/4}$ model, between the RHX activation energy and the 130C activation energy are presented in *Figure 7.71* for (left) all samples where activation energies could be estimated and (*right*) for samples with poor R^2 values (< 0.9) removed (*Nic, Por, Rom, Bel* and *Mac* (treated as outlier)). A possible weak correlation between the two activation energies is observed for the latter, R^2= 0.52 and p = 0.043.

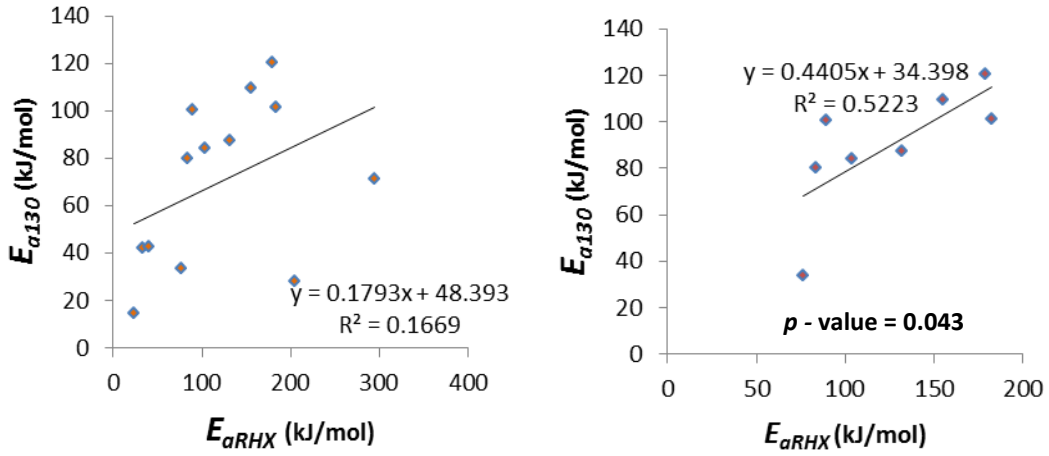

Figure 7.71: Relationship between RHX activation energy and 130C activation energy for all possible samples (*left*) and with *Mac, Nic, Rom, Bel* and *Por* removed (*right*). For $t^{1/4}$ model.

Corresponding plots for the $t^{1/n}$ model produced no correlation with R^2 = 0.0009 for all possible samples, and R^2 = 0.013 where *Nic, Rom* and *Bel* were removed because of poor Arrhenius plot linearities.

7.6 *Stage 1*

7.6.1 *S1* Curves

The full set of *S1* mass gain curves is presented in *Appendix E*. These are presented as a function of $t^{1/4}$. Several examples of the different types of behaviour observed are presented below. These are all normalised with respect to m_0 ($m_{130\text{-}25}$ or $m_{500\text{-}25}$ for respective curves) for display purposes.

The first of these, *Figure 7.72*, presents the mass gain curve for *Ann* and is typical of 'well-behaved' samples that exhibited reasonably linear $t^{1/4}$ behaviour and an Arrhenius temperature dependence. Typical of most well behaved (and abnormal) samples, the *S1* mass gain m_{S1} is of a very similar order for both the 130C and 500C components. Also, the duration, t_{S1} = approx. 1.5 hours, typical of well-behaved samples where *S1* has normally completed within 24 hours (the actual mass gain and duration will be dealt with in subsequent *Section 7.6.2*).

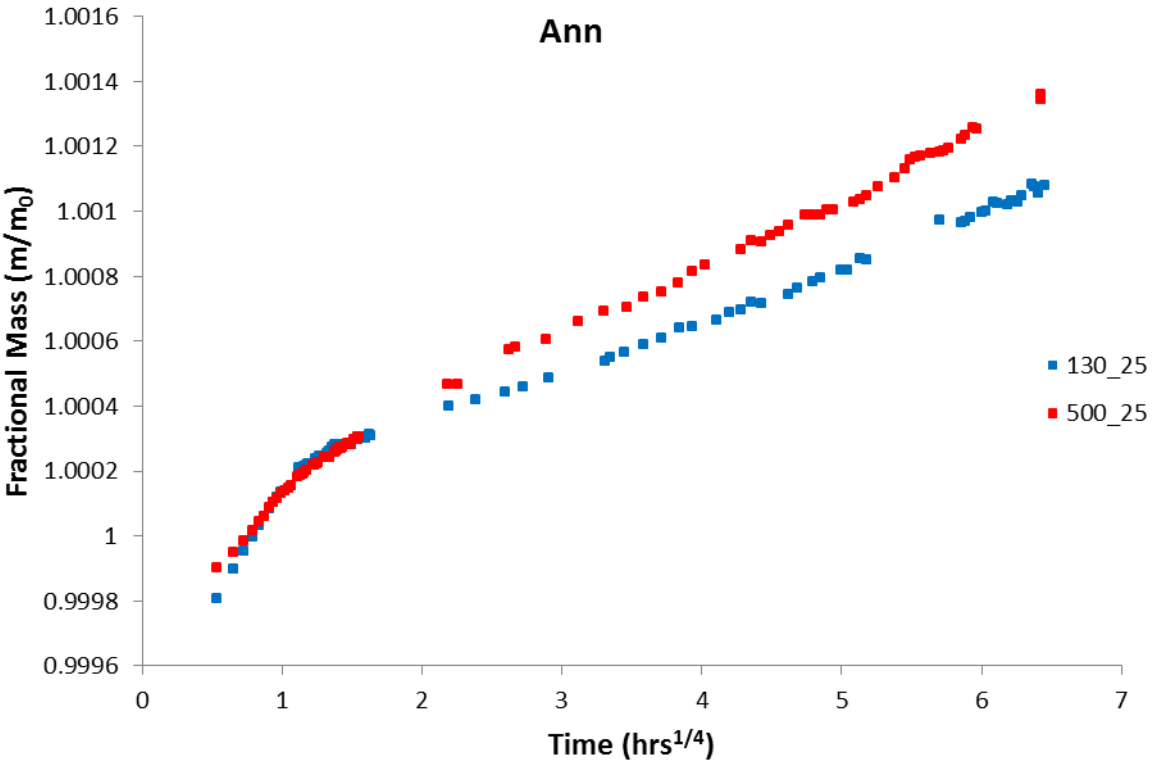

Figure 7.72: Mass gain curves, displaying the *Stage 1* region, of *Ann* sample. Sample aging at 25°C following heating at 130°C (blue) and 500°C (red).

The next example, *Figure 7.73*, is for *Rom*, and abnormal sample that displays very long *S1* duration, 165-195 hours, typical of samples with poor linearity and Arrhenius temperature dependence. Also, the magnitude is very large, approx. 1% of ceramic mass, with abnormal samples typically of this order, whereas well-behaved samples are normally less than 0.1% (see *Section 7.6.2*).

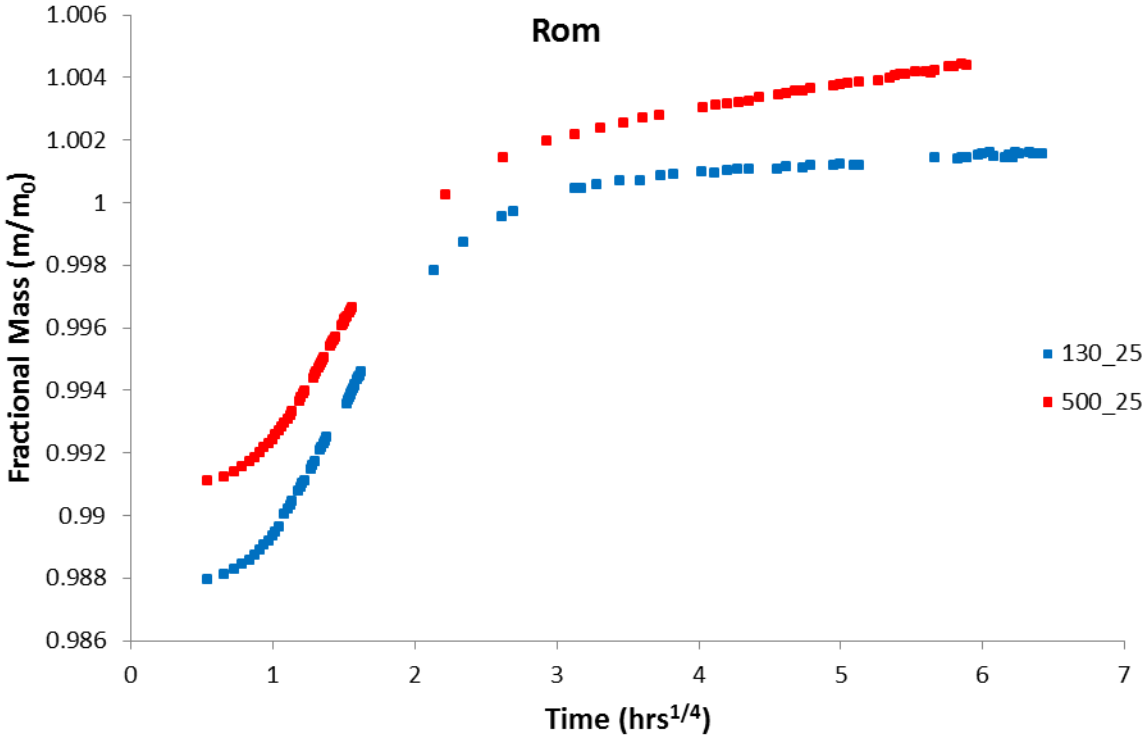

Figure 7.73: Mass gain curves, displaying the *Stage 1* region, of *Rom* sample. Sample aging at 25°C following heating at 130°C (blue) and 500°C (red).

The final two examples, *Figure 7.74* and *Figure 7.75*, are for *Rat* and *Mac*, respectively. *Rat* is unusual because it exhibits no *S1* behaviour; this sample also had issues with nitrogen adsorption as part of BET tests. The *S2* curvature can be observed as quite positively strong also (*Section 7.1*).

Mac, like *Bel* (see *Appendix E*) shows *S1* behaviour that is significantly greater in magnitude (of the order X4) for the 130C component than for the 500C component. Estimation of the *S1* mass gain is problematic (see *Discussion*) but the other samples display *S1* behaviour that is very similar for both components.

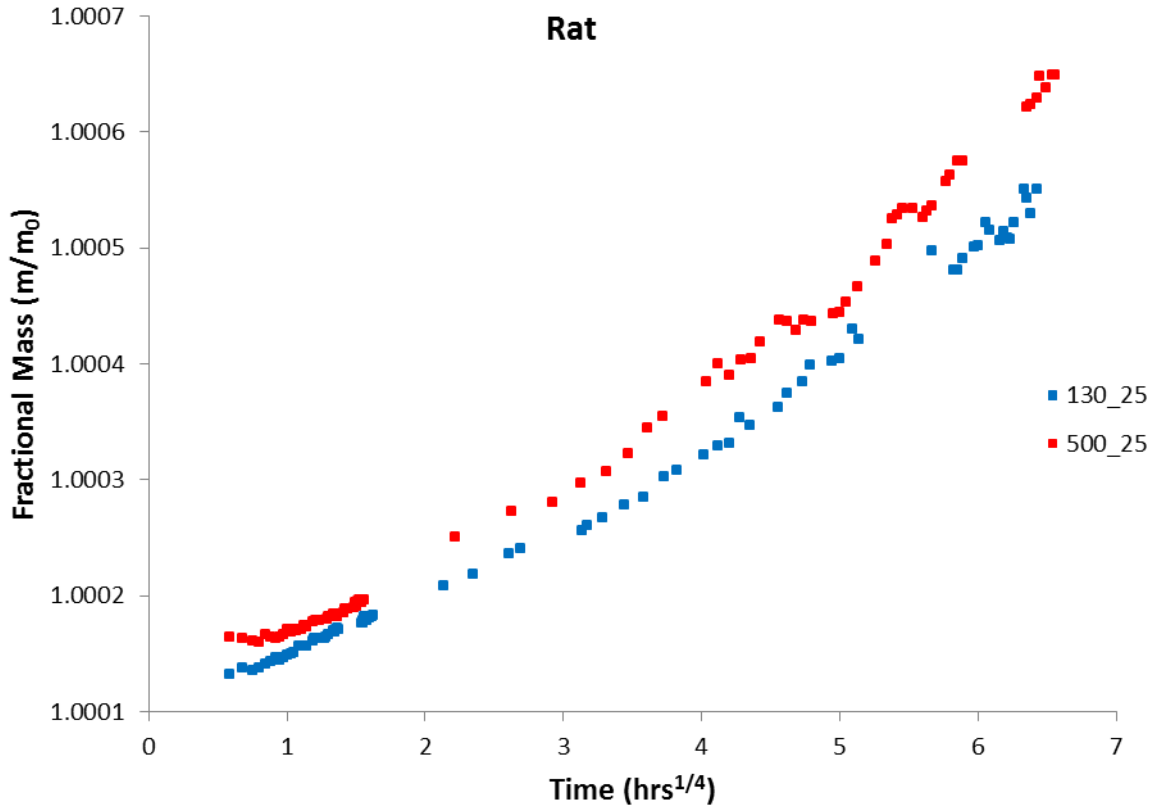

Figure 7.74: Mass gain curves, displaying the *Stage 1* region, of *Rat* sample. Sample aging at 25°C following heating at 130°C (blue) and 500°C (red).

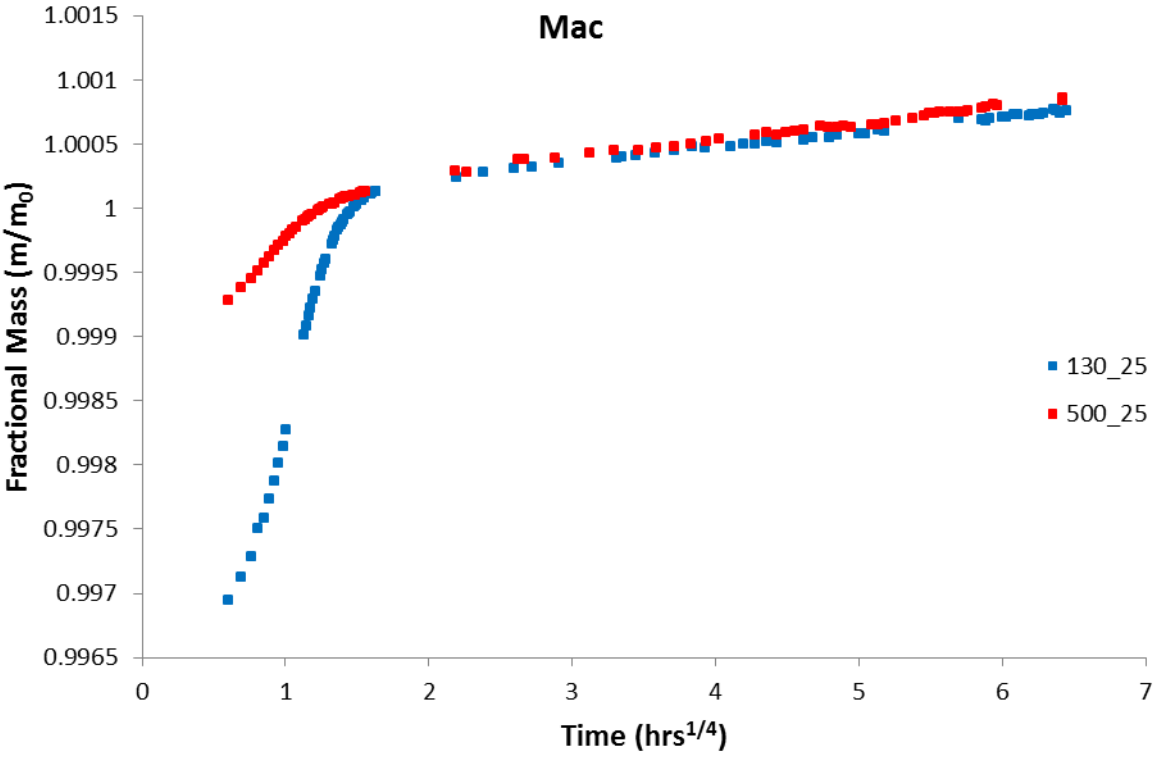

Figure 7.75: Mass gain curves, displaying the *Stage 1* region, of *Mac* sample. Sample aging at 25°C following heating at 130°C (blue) and 500°C (red).

7.6.2 *S1* Mass and Duration

Mass

The values of *S1* fractional mass, m_{S1}, for both components (130°C and 500°C) and both models are provided in *Tables 7.13* and *Table 7.14*. Negative mass values are a consequence of a combination of curvature effects and small *S1* mass (when $m_0 < m_d$, see *Figure 3.1* and *Figure 7.74*) and are suitable as a measure for comparison with other samples.

For the $t^{1/4}$ model, a comparison of the *S1* mass of both components is provided in *Figure 7.76* (all samples) and *Figure 7.77* (left - abnormal samples excluded, right – see below) and the average *S1* mass value is ranked in *Figure 7.78* and *Figure 7.79*. In *Figure 7.77 (right)* the samples *Mac* and *Bel* are removed for reasons discussed in the previous section (abnormally large difference in 130C and 500C *S1* behaviour) and *Cau* is removed as an outlier. For the case of all samples the correlation is strong, R^2 = 0.94, with a slope of 0.72, suggestive of a systematic difference in the ratio of the two. However, with abnormal samples and the additional samples removed the correlation is still high, R^2 = 0.95, with a slope close to unity (0.95).

Similarly, for the $t^{1/n}$ model, a comparison of the *S1* mass of both components is shown in *Figures 7.80* and the average value is ranked in *Figure 7.81*. For *Figure 7.80 (left)* all samples are included for which *S1* mass could be estimated. For *Figure 7.80 (right)* problematic samples *Mac* and *Bel* are removed, together with *Rom* (abnormal sample). The correlations from both of these, R^2 = 0.86 (all) and R^2 = 0.82 (samples removed), are reasonable, but the former is clearly enhanced by an outlier. The latter provides an unsatisfactory slope (0.71) or ratio between the components of *S1* mass gain. However, removal of a further outlier, *Nic*, improves the value of R^2 to 0.99 and the slope to 0.88, closer to unity. Issues with *S1* calculations and comparisons based on $t^{1/n}$ model will be dealt with in the *Discussion*.

From the figures that rank the samples, *Figure 7.78* and *Figure 7.81*, it is clear that for $t^{1/4}$ the abnormal samples (*Lan, Etr, Dow1/2*, *Por, Rom*) have significantly greater

S1 mass gain (and also for *Rom*, the only abnormal sample for m_{S1} is calculated using $t^{1/n}$). The samples with very low (or negative) mass gains in *S1* are those which are well-behaved (i.e. *Ted, Joy, Rat, Cal, Tur*).

Table 7.13: *Stage 1* fractional mass for 130C and 500C components (25°C aging) together with average value. For the $t^{1/4}$ model.

$t^{1/4}$	$m_{S1\text{-}130}$	$m_{S1\text{-}500}$	$m_{S1\text{-}avg}$
Ann	0.0002344	0.0000674	0.0001509
Esp	0.0010129	0.0009997	0.0010063
Nic	0.0009134	0.0006095	0.0007615
Mac	0.0030745	0.0007159	0.0018952
Ria	0.0001748	0.0000496	0.0001122
Etr	0.0321960	0.0184989	0.0253474
Rom	0.0120426	0.0089078	0.0104752
Por	0.0149146	0.0068267	0.0108707
Rat	-0.0001635	-0.0002040	-0.0001837
Cal	-0.0001381	-0.0001982	-0.0001681
Lan	0.0325883	0.0293222	0.0309553
Joy	-0.0003069	-0.0004888	-0.0003978
Cau	0.0038353	0.0023028	0.0030690
Bel	0.0048373	0.0012858	0.0030616
Dow1	0.0220664	0.0161798	0.0191231
Dow2	0.0270802	0.0170217	0.0220510
Tur	-0.0002083	-0.0001054	-0.0001568
Ted	-0.0004068	-0.0006013	-0.0005041

Table 7.14: *Stage 1* fractional mass for 130C and 500C components (25°C aging) together with average value. For the $t^{1/n}$ model.

$t^{1/n}$	$m_{S1\text{-}130}$	$m_{S1\text{-}500}$	$m_{S1\text{-}avg}$
Ann	0.0003625	0.0003018	0.0003322
Esp	0.0008673	0.0007930	0.0008301
Nic	0.0006809	0.0003074	0.0004941
Mac	0.0031964	0.0008498	0.0020231
Ria	0.0003325	0.0003241	0.0003283
Rom	0.0114177	0.0059994	0.0087085
Rat	0.0000164	0.0000130	0.0000147
Cal	0.0000848	0.0001093	0.0000970
Joy	0.0000991	0.0001615	0.0001303
Bel	0.0038103	-0.0000351	0.0018876
Tur	0.0001397	0.0001242	0.0001320
Ted	0.0002392	0.0002206	0.0002299

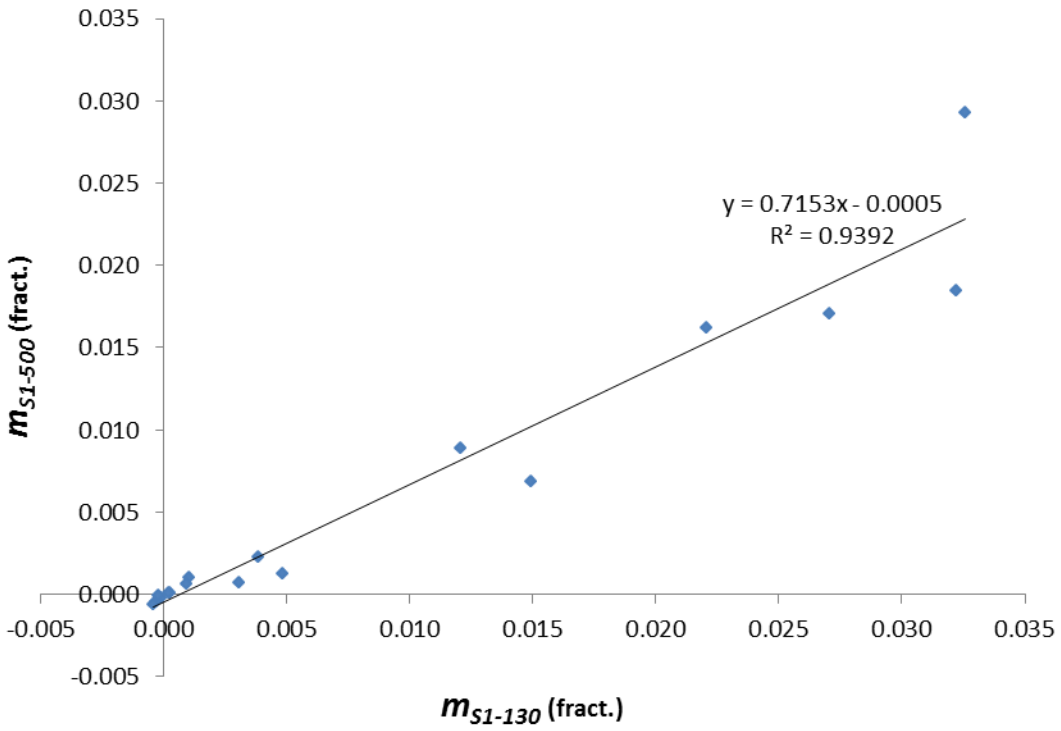

Figure 7.76: Comparison of *S1* fractional mass for 130C and 500C components. For $t^{1/4}$ model and all samples.

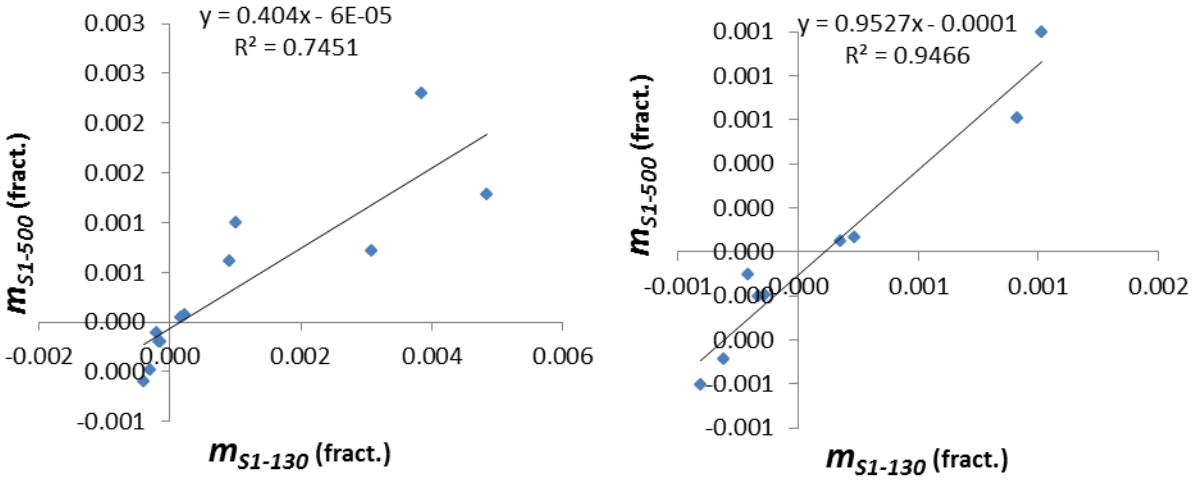

Figure 7.77: Comparison of *S1* fractional mass for 130C and 500C components with abnormal samples removed (left) and additionally with *Mac, Cau, and Bel* removed (right). For the $t^{1/4}$ model.

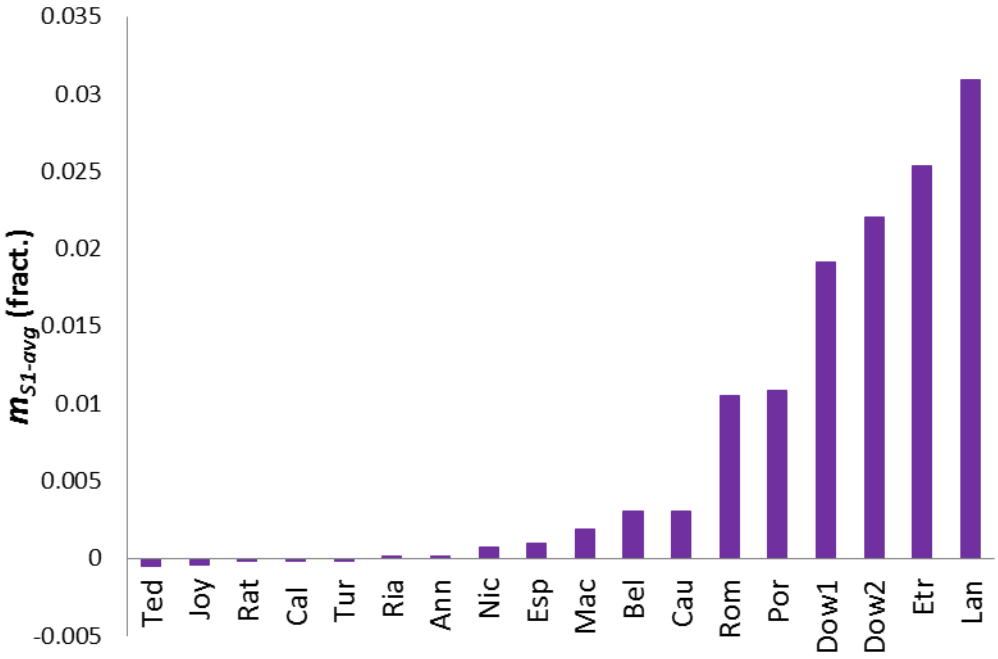

Figure 7.78: *S1* fractional mass (avg.) for all samples and for the $t^{1/4}$ model.

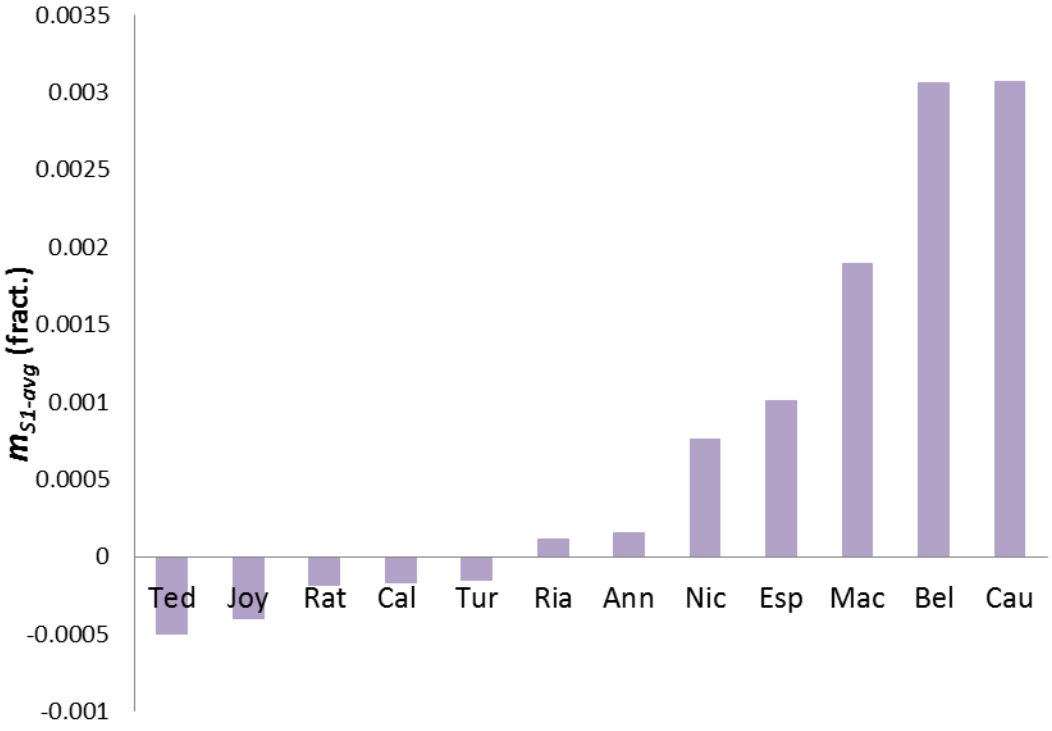

Figure 7.79: *S1* fractional mass (avg.) with abnormal samples excluded and for the $t^{1/4}$ model.

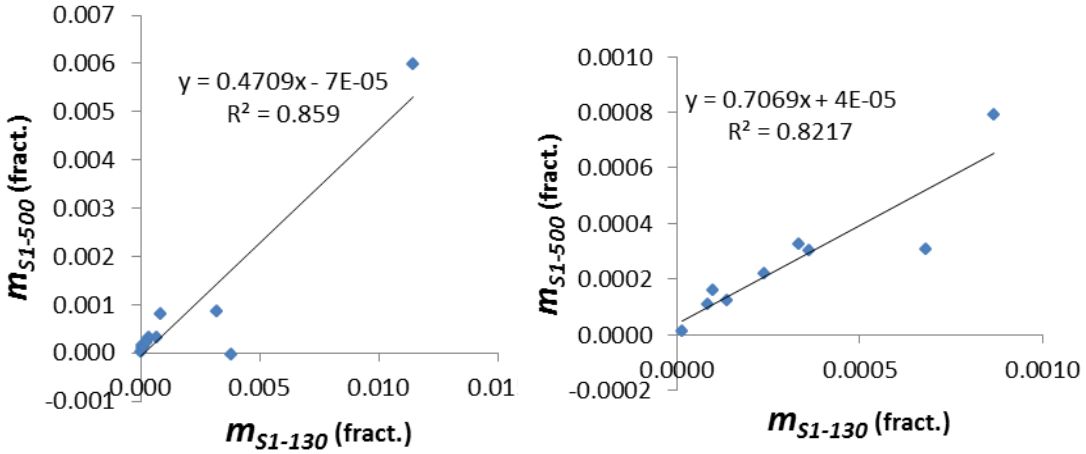

Figure 7.80: ***S1*** **fractional mass comparison of 130C and 500C components for all samples (left) and with samples *Mac*, *Rom*, and *Bel* removed (right). For the $t^{1/n}$ model. Note, for the image on the right, if the outlier *Nic* is removed the R^2 value increases to 0.986 and the slope to 0.88.**

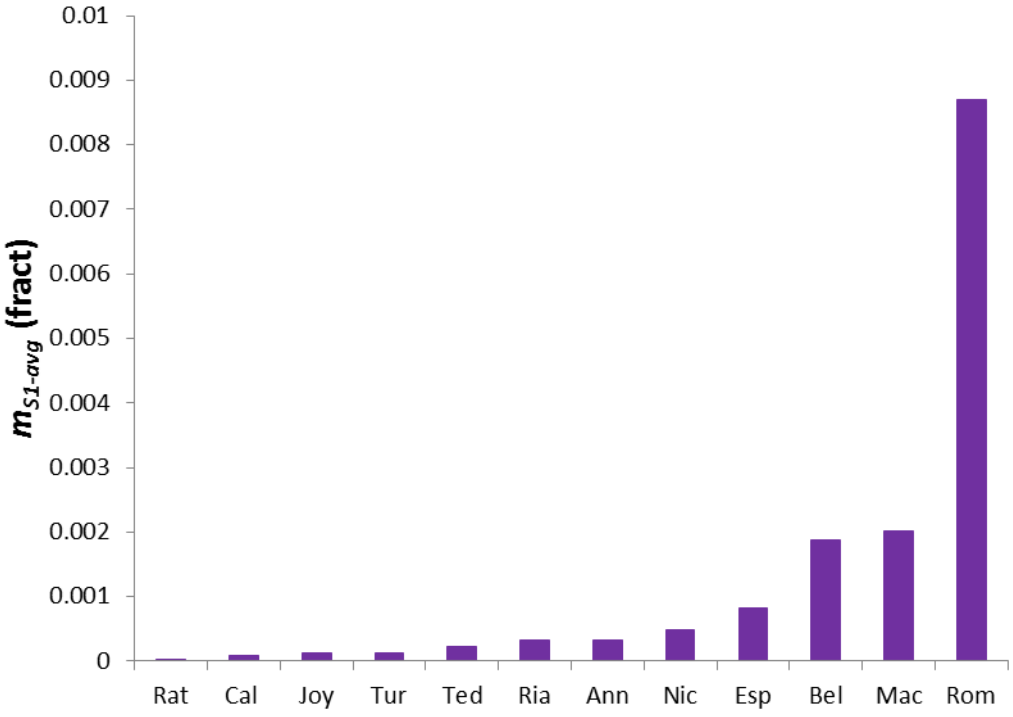

Figure 7.81: ***S1*** **fractional mass (avg.) for all samples and the $t^{1/n}$ model.**

Duration

Estimates (visual based on curves and in consideration of modelling results) of the duration of *S1,* t_{S1}, are presented in *Table 7.15* and *Figure 7.82* for $t^{1/4}$. It can be observed that some samples not treated as abnormal also have long *S1* durations, *Cau* and *Bel*. Estimations of *S1* durations for $t^{1/n}$ were not carried out due to difficulties dealing with the variation of *1/n* and curve behaviour on a sample by sample basis and because it would not be expected to differ greatly from the $t^{1/4}$ approach (assuming *S1* behaviour is independent of the power law *Stage 2* behaviour).

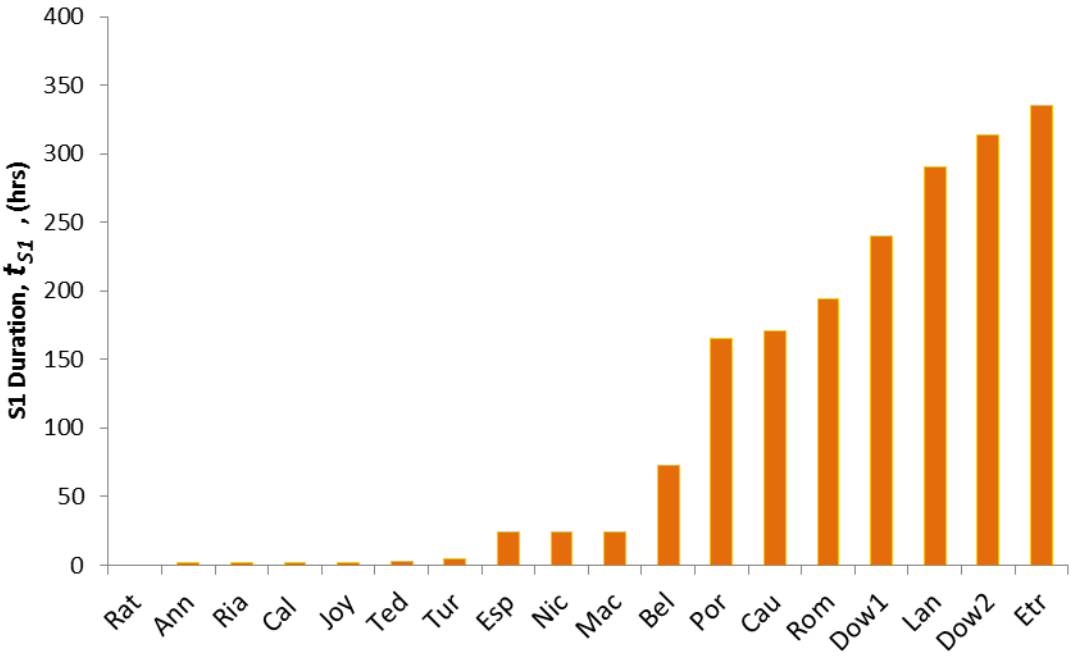

Figure 7.82: Duration (max) of *S1* for all samples and for the $t^{1/4}$ model.

Table 7.15: Estimated range of duration and maximum duration of *Stage 1* mass gain.

$t^{1/4}$	t_{S1} Range (hrs)	t_{S1} Max (to upper 0.5hrs)
Rat	0	0
Ann	1.5	1.5
Ria	1.05-1.65	1.5
Cal	1.0-2.0	2
Joy	1.5-2.0	2
Ted	2.0-3.0	3
Tur	2.5-5.0	5
Esp	>7 <24	24
Nic	>7 <24	24
Mac	>7 <24	24
Bel	30-73	73
Por	140-165	165
Cau	140-171	171
Rom	165-194	194
Dow1	192-240	240
Lan	260-290	290
Dow2	289-314	314
Etr	310-335	335

7.6.3 *Stage 1* Relationships and Correlations

***Stage 1* and BET S.A.**

The relationship between the *S1* mass (avg.) and the BET S.A. are presented in *Figure 7.83* and *Figure 7.84* for the $t^{1/4}$ and $t^{1/n}$ models, respectively. For the $t^{1/4}$ model, good correlations are observed for all samples, R^2 = 0.91, and with abnormal samples removed, R^2 = 0.78, suggesting some dependence between the two variables but more clearly emphasised for abnormal samples due to larger surface area and *S1* fractional mass values. Further removal of samples *Mac* and *Bel* improves the correlation to R^2 = 0.91.

For the $t^{1/n}$ model the correlation is stronger where samples *Mac, Rom,* and *Bel* are removed, R^2 = 0.89, instead of for all samples, where R^2 = 0.77 (appearing to be biased by outlier).

For all samples and for the $t^{1/4}$ model, the correlation between the maximum *S1* duration, t_{S1}, and the BET S.A. is presented in *Figure 7.85*. There is significant scatter but a strong correlation, R^2 = 0.82., considering the rough nature of estimation of the duration.

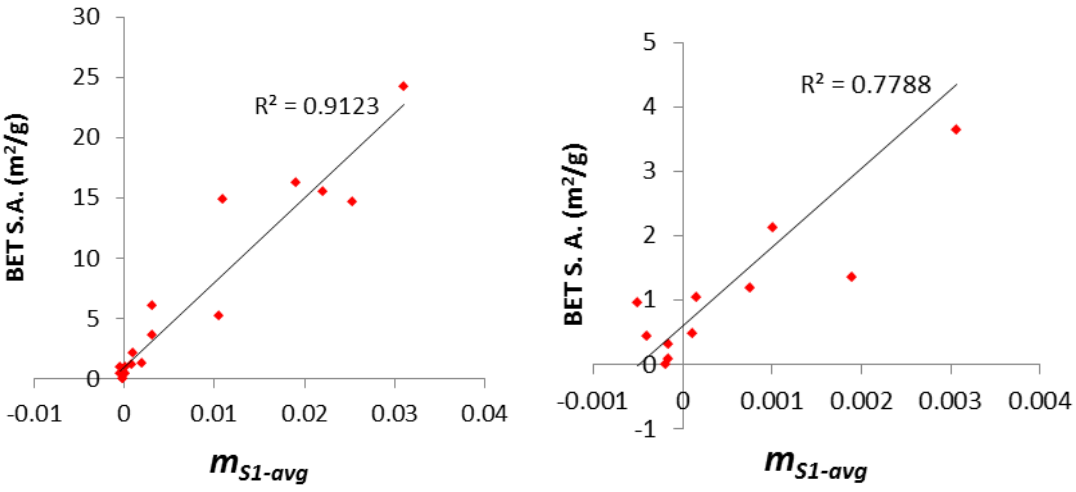

Figure 7.83: *S1* fractional mass gain versus BET S. A. for all samples (left) and with abnormal samples removed (right). For $t^{1/4}$ model.

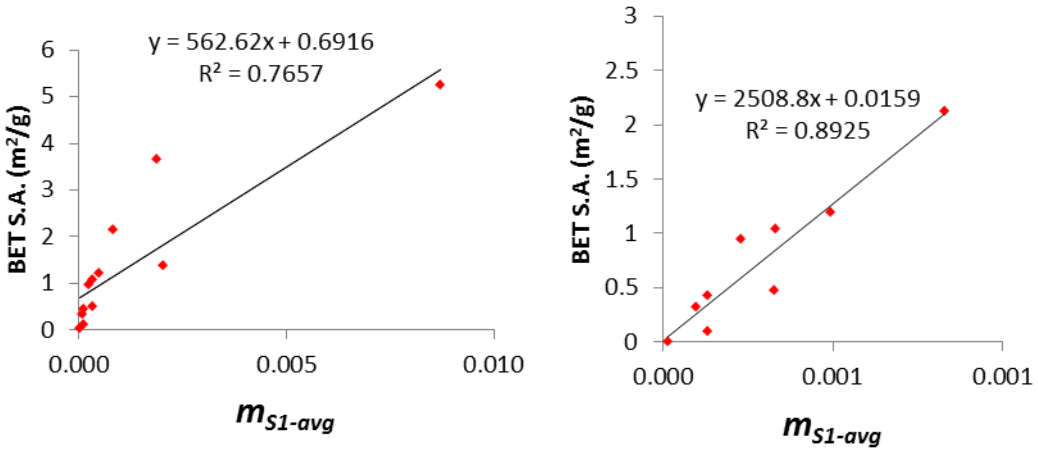

Figure 7.84: *S1* fractional mass gain versus BET S.A. for all samples (left) and with samples *Mac, Rom* and *Bel* removed (right). For the $t^{1/n}$ model.

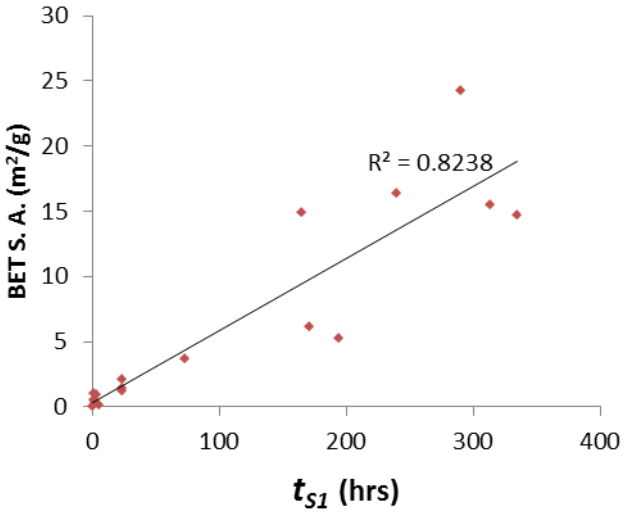

Figure 7.85: Duration (max.) of *S1* versus BET S.A. for the $t^{1/4}$ model.

S1 Duration and Mass

A strong relationship between the *S1* duration and the *S1* mass gain would be expected and this is supported in *Figure 7.86*, where a good correlation, R^2 = 0.89, is observed.

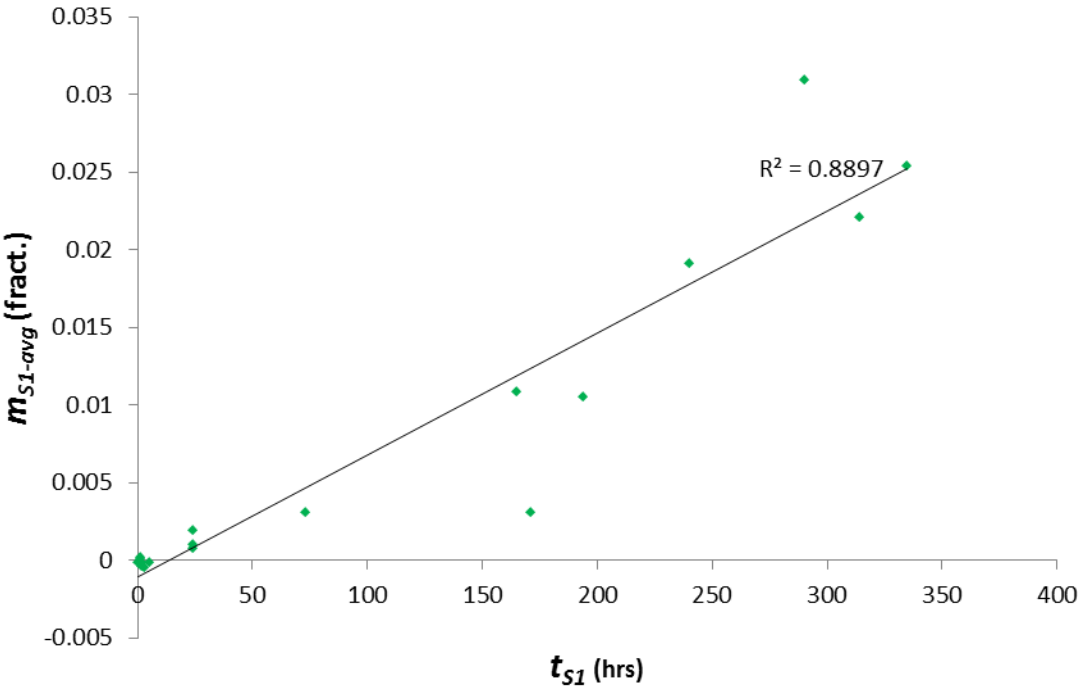

Figure 7.86: Relationship between duration and magnitude of *Stage 1*, for the $t^{1/4}$ model and for all samples.

TG-MS and *S1* mass gain

Further correlations were examined between the *S1* mass, for 130C and 500C components, and the TG-MS %wt. loss for different heating regimes, 50-130°C and 130-500°C without and with abnormal samples removed. The results for the $t^{1/4}$ model are presented in *Figure 7.87* (130C) and *Figure 7.88* (500C). The $t^{1/n}$ results are not included but exhibited similar behaviour.

It can be observed that for all samples and both the 130C and 500C components a strong correlation exists between the *S1* mass and TG mass loss for both heating regimes. However, with the abnormal samples removed the correlation between the *S1* mass and the TG mass loss in the 130-500°C regime is poor and the null hypothesis can not be rejected, with p = 0.198 and 0.1057.

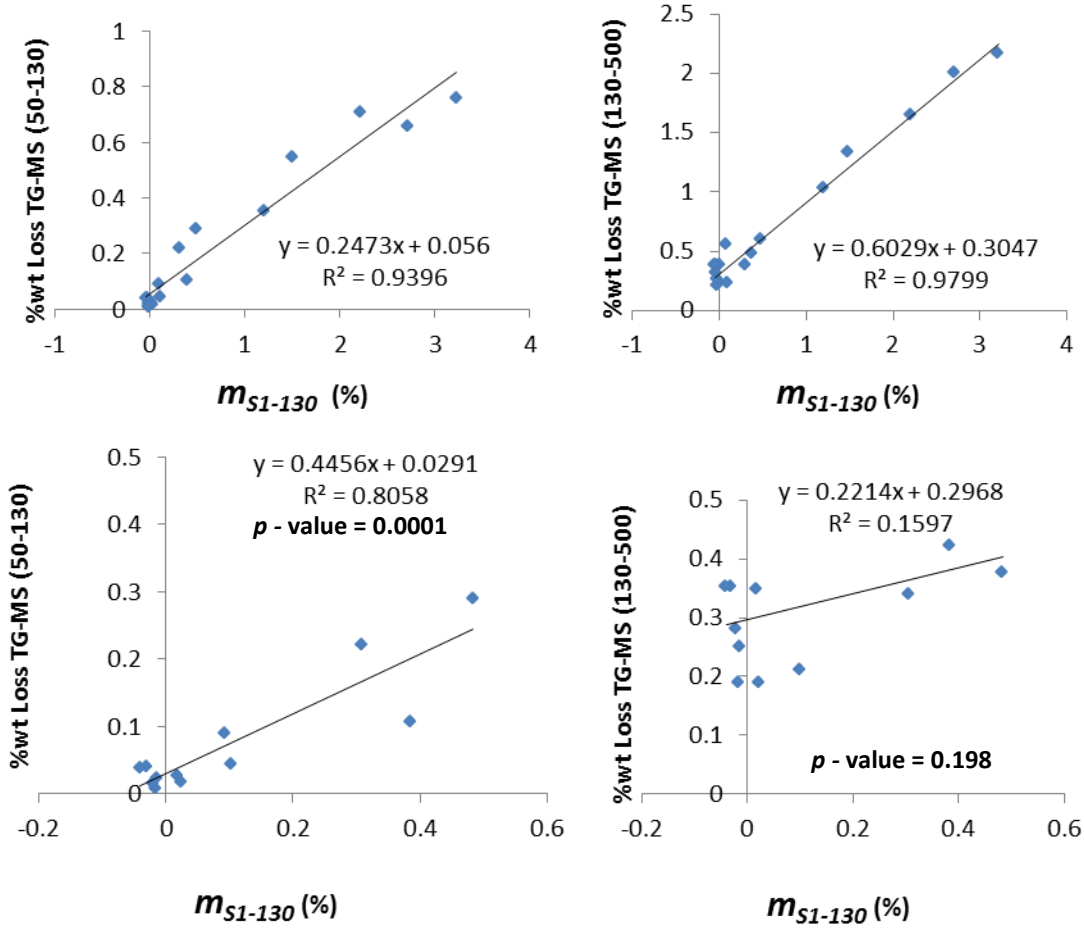

Figure 7.87: Relationship of *S1* fractional mass (130°C) to TG-MS mass loss for all samples (top) and with abnormal samples excluded (bottom) for 50-130°C range (left) and 130-500°C range (right).

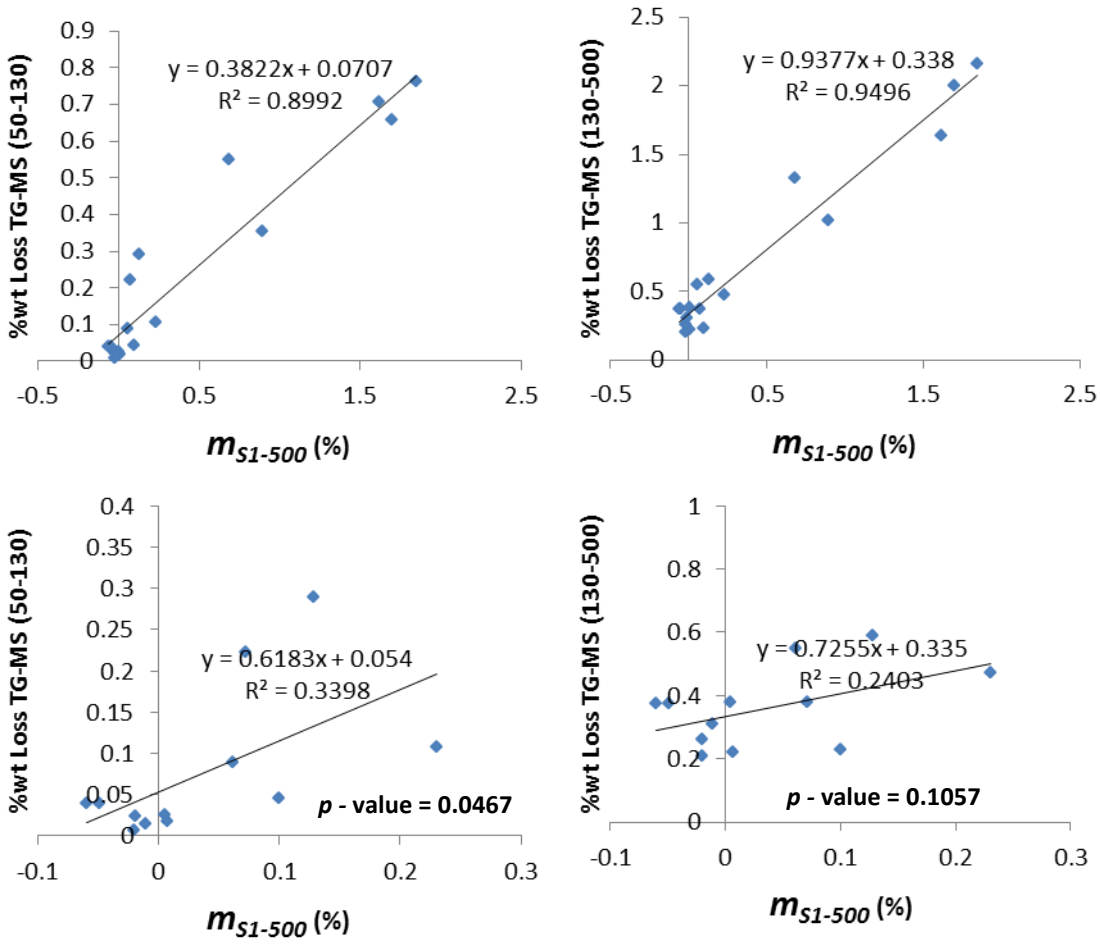

Figure 7.88: Relationship of *S1* fractional mass (500°C) to TG-MS mass loss for all samples (top) and with abnormal samples excluded (bottom) for 50-130°C range (left) and 130-500°C range (right).

With abnormal samples removed, a strong correlation between the *S1* mass gain and the TG mass loss in the 50-130°C regime is apparent for the $m_{S1\text{-}130}$ case, R^2 = 0.81 and p = 0.0001, but for the $m_{S1\text{-}500}$ case this correlation is much less certain, R^2 = 0.34 and p = 0.0467. This difference between the components is resolved by the removal of samples *Mac* and *Bel* from the data set (see *Discussion*), in which case the correlations for the $m_{S1\text{-}130}$ and $m_{S1\text{-}500}$ cases become R^2 = 0.68 and 0.60, respectively, with p–value = 0.0034 and 0.0083, respectively.

7.7 Curvature: 1/n variation

7.7.1 Curvature Results

This section presents the results of $t^{1/n}$ modelling, in particular the *1/n* parameter values obtained and their use as a measure of the 'curvature' of the *S2* mass gain curve as a function of $t^{1/4}$. Where *1/n* = 0.25, there is no curvature but deviations from this value result in positive, where *1/n* > 0.25, or negative, where *1/n* < 0.25, curvature. For samples where modelling was unsuccessful (*Etr, Por, Lan, Dow1/2*) the curvature can still be interpreted visually as positive or negative using the mass gain curves.

The modelled *1/n* results are presented in *Table 7.17*, toward the end of the section. Below, in *Table 7.16* is a summary of the average *1/n* results (average of 25°C, 35°C, 45°C modelled curves) for both the 130C and the 500C components, as well as a combined average (all six modelled curves). If the *1/n* values for a component (or between the different components) displayed a wide range of values suggestive of no common behaviour the group is considered 'non-conforming' (nc) and averaging is not carried out.

Uncertainties are based on the standard deviation of these averages.

A summary of the curvature (+, - , 0 where curvature is uncertain) for each curve is also included in the table.

The average value of *1/n* for all curves and samples is 0.29, with 8/12 well behaved samples having a certain positive curvature. A more negative curvature is more symptomatic of samples that are less well behaved (see *Discussion*).

In *Figure 7.89*, a chart compares the average curvature values (*1/n*) of the samples together with the uncertainties. It can be seen that the curvature is predominantly positive and there is reasonably strong conformity in the behaviour for each sample.

Table 7.16: Curvature values – *1/n* modelled values of curves. '+' = positive curvature, '-' = negative curvature, '0' = uncertain curvature. 'nc' = non-conforming, i.e. 1/n behaviour for different curves not in agreement. '---' = modelling issues. Uncertainties based on standard deviations.

	Curvature 130C (25,35,45)	**Curvature** 500C (25,35,45)	**1/n** 130C (avg.)	**Δ1/n** 130C	**1/n** 500C (avg.)	**Δ1/n** 500C	**1/n** 130C+500C (avg.)	**Δ1/n** 130C+500C
Ann	(+,+,+)	(+,+,+)	0.32	0.02	0.34	0.02	0.33	0.02
Esp	(-,-,-)	(-,-,-)	0.18	0.03	0.2	0.03	0.19	0.06
Nic	(-,-,-)	(-,-,-)	0.18	0.01	0.21	0.02	0.2	0.04
Mac	(-,-,+)	(+,+,+)	0.26	0.04	0.37	0.02	0.32	0.14
Ria	(+,+,+)	(+,+,+)	0.37	0.02	0.41	0.02	0.39	0.05
Etr	(0,0,0)	(0,0,0)	---	---	---	---	---	---
Rom	(+,-,-)	(-,-,-)	0.13	0.13	0.15	0.06	0.14	0.18
Por	(-,-,-)	(+,+,+)	---	---	---	---	---	---
Rat	(+,+,+)	(+,+,+)	0.45	0.02	0.45	0.02	0.45	0.04
Cal	(+,+,+)	(+,+,+)	0.35	0.02	0.4	0.01	0.38	0.06
Lan	(-,-,-)	(-,-,-)	---	---	---	---	---	---
Joy	(+,+,+)	(+,+,+)	0.38	0.02	0.41	0.02	0.39	0.05
Cau	(-,-,-)	(-,-,-)	0.04	0.04	0.22	0.04	nc	nc
Bel	(-,-,-)	(-,-,-)	0.16	0.08	0.15	0.04	0.16	0.11
Dow1	(-,-,-)	(-,-,+)	---	---	---	---	---	---
Dow2	(-,-,-)	(-,-,-)	---	---	---	---	---	---
Tur	(+,+,+)	(+,+,+)	0.47	0.06	0.41	0.03	0.44	0.1
Ted	(+,+,+)	(+,+,+)	0.39	0.04	0.36	0.04	0.37	0.08
Average			**0.28**		**0.32**		**0.29**	

Table 7.17: Modelled *1/n* values for all curves using $t^{1/n}$ model. Uncertainties are to 95%. *NA* implies that modelling was unsuccessful.

$t^{1/n}$ Model (pre-fixed)	130°C			500°C		
Sample	**25°C 1/n (95% confidence Interval)**	**35°C 1/n (95% confidence Interval)**	**45°C 1/n (95% confidence Interval)**	**25°C 1/n (95% confidence Interval)**	**35°C 1/n (95% confidence Interval)**	**45°C 1/n (95% confidence Interval)**
Ann	0.340 (0.312 0.368)	0.301 (0.272 0.330)	0.312 (0.289 0.334)	0.320 (0.291 0.350)	0.347 (0.327 0.367)	0.343 (0.313 0.374)
Esp	0.205 (0.162 0.248)	0.143 (0.101 0.185)	0.197 (0.142 0.251)	0.239 (0.175 0.304)	0.185 (0.151 0.218)	0.179 (0.137 0.221)
Nic	0.178 (0.135 0.222)	0.174 (0.140 0.208)	0.063 (0.015 0.111)	0.208 (0.173 0.243)	0.204 (0.173 0.235)	0.227 (0.196 0.258)
Mac	0.233 (0.191 0.274)	0.237 (0.198 0.275)	0.311 (0.233 0.389)	0.356 (0.308 0.404)	0.380 (0.347 0.413)	0.387 (0.353 0.422)
Ria	0.369 (0.337 0.401)	0.348 (0.320 0.376)	0.388 (0.366 0.411)	0.422 (0.388 0.456)	0.392 (0.369 0.415)	0.402 (0.385 0.418)
Etr	NA	NA	NA	NA	NA	NA
Rom	0.278 (-0.009 0.564)	0.058 (-0.150 0.266)	0.042 (-0.563 0.647)	0.086 (0.040 0.132)	0.184 (0.160 0.208)	0.189 (0.122 0.255)
Por	NA	NA	NA	NA	NA	NA
Rat	0.474 (0.393 0.555)	0.433 (0.352 0.514)	0.438 (0.376 0.501)	0.458 (0.402 0.514)	0.466 (0.415 0.517)	0.433 (0.393 0.472)
Cal	0.368 (0.334 0.402)	0.328 (0.294 0.363)	0.355 (0.323 0.387)	0.402 (0.371 0.432)	0.405 (0.376 0.434)	0.396 (0.366 0.425)
Lan	NA	NA	NA	NA	NA	NA
Joy	0.402 (0.378 0.426)	0.365 (0.342 0.389)	0.368 (0.346 0.390)	0.403 (0.379 0.426)	0.425 (0.407 0.443)	0.392 (0.376 0.409)
Cau	0.007 (-0.015 0.029)	0.077 (-0.036 0.190)	0.035 (-0.103 0.172)	0.251 (0.213 0.290)	0.232 (0.202 0.262)	0.174 (0.114 0.234)
Bel	0.211 (0.172 0.250)	0.209 (0.161 0.257)	0.073 (0.020 0.127)	0.160 (0.138 0.182)	0.192 (0.172 0.211)	0.113 (0.084 0.143)
Dow1	NA	NA	NA	NA	NA	NA
Dow2	NA	NA	NA	NA	NA	NA
Tur	0.544 (0.490 0.598)	0.423 (0.385 0.461)	0.455 (0.413 0.497)	0.389 (0.338 0.440)	0.436 (0.396 0.475)	0.412 (0.380 0.445)
Ted	0.432 (0.411 0.454)	0.389 (0.375 0.403)	0.353 (0.331 0.375)	0.369 (0.349 0.389)	0.386 (0.367 0.406)	0.319 (0.300 0.338)

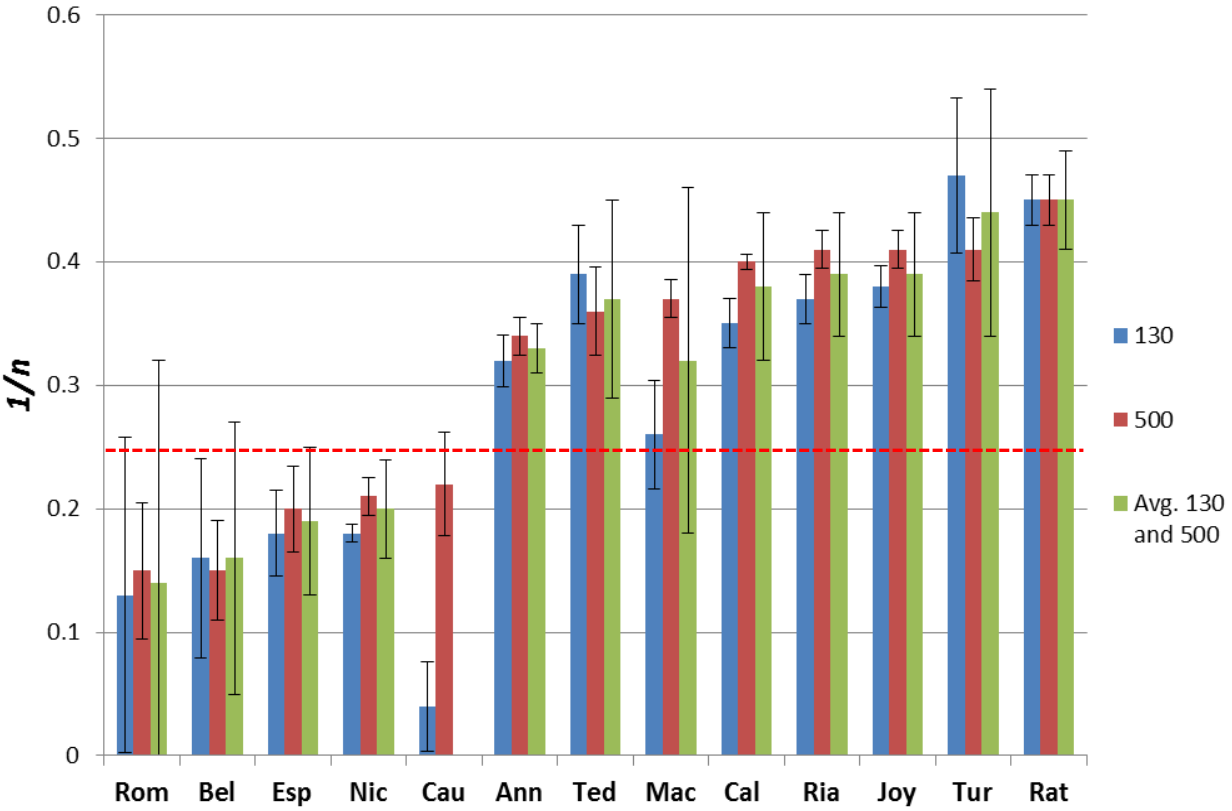

Figure 7.89: Curvature of samples based on *1/n* values for 130°C component (average of 3 aging temperatures) and 500°C (component (average of 3 aging temperature) and both components (average of 3+3 curves). Red line indicates 1/n=0.25. Uncertainties based on standard deviation of averages.

7.7.2 Curvature Relationships and Correlations

BET S.A. vs. Curvature

The relationship between BET S.A. and curvature (*1/n (avg.)*) is presented in *Figure 7.90* (*Rom* excluded). There is a correlation of R^2 = 0.76, and an inverse proportionality. This is in agreement with less well-behaved or abnormal samples having high surface areas and low curvature values. If samples with *1/n* < 0.25 are removed the correlation improves to R^2 = 0.89.

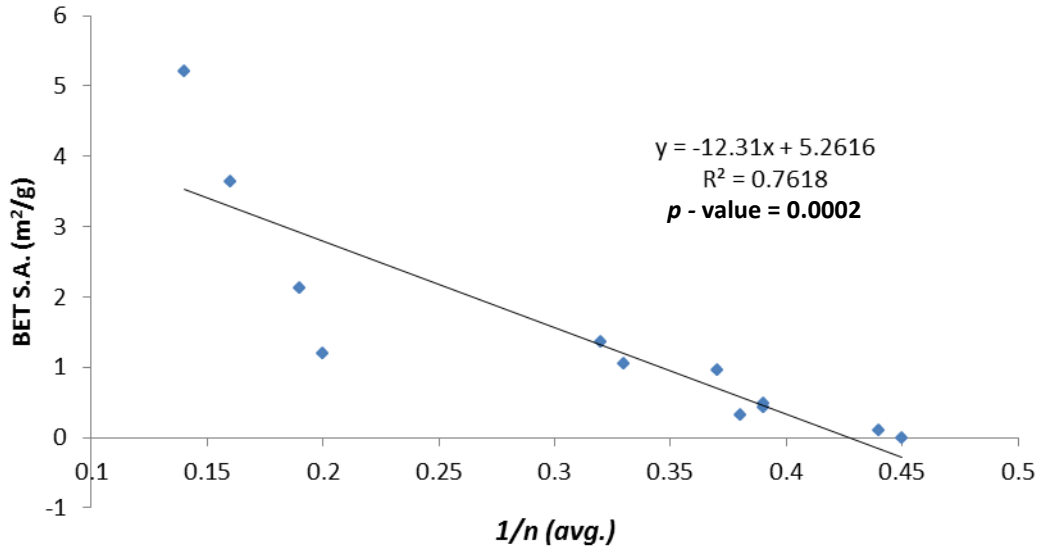

Figure 7.90: Relationship between the BET S.A. and curvature of samples.

S1 mass vs. Curvature

The relationship between *S1* mass and curvature is presented in *Figure 7.91 (left)* for abnormal samples excluded and *Figure 7.91 (right)* for samples *Mac* and *Bel* additionally excluded. The null hypothesis is rejected and a reasonable level of correlation is evident.

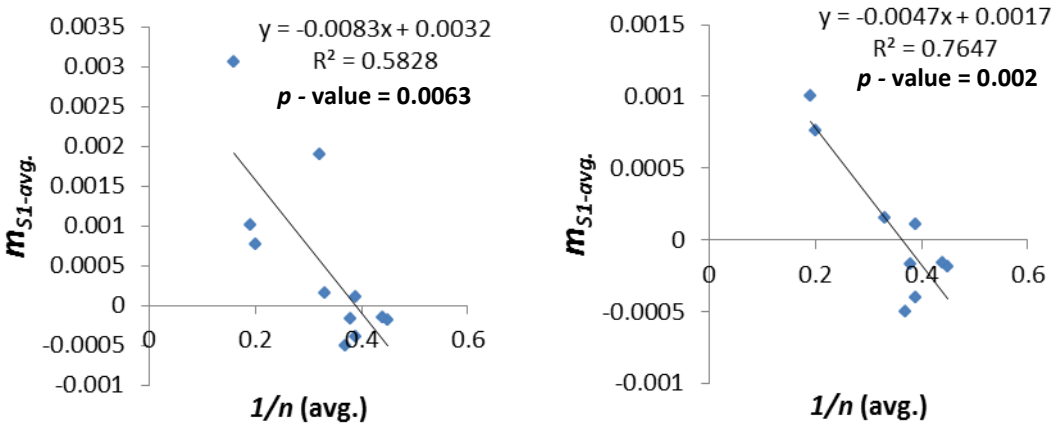

Figure 7.91: Relationship between the *Stage 1* mass ($t^{1/4}$) and the curvature for (*left*) all possible samples, excluding *Rom,* and *(right)* with *Mac* and *Bel* additionally removed.

Chapter 8

Experimental Results – RHX Dating

8.1 Drying: Curves, Models and Estimated Loose Water

The results of modelling to determine the quantity of loose water, m_{lw}, not removed during drying at 130°C are presented in this section. Two modelling approaches were applied, a power-based model (*model 1*) and exponential-based model (*model 2*).

The results of the latter exponential model were selected for use in RHX behaviour and dating calculations and will be the focus of this results section; *model 2* provided better goodness-of-fit results, *model 1* could not be successfully applied to a number of samples and produced estimates of the fractional mass of loose water that were, in several cases, greater than the total fractional mass loss determined from the mass gain curves (see *Discussion* for more).

Also, to further examine the validity, for both models the modelled loose water content, as a fraction of the modelled dry mass, was correlated against properties of the ceramic that would be expected to have a strong relationship with moisture content (% wt. TG-MS between 50-130°C, BET S.A. and pore volume). The results of linear regressions are presented in *Table 8.3.* They provide stronger support for use of *model 2*.

Goodness-of-fit results of the application of both models to the drying mass curves are presented in *Table 8.1*. Differences between the two models are minor but *model 2* is stronger in 10 instances versus 6 for *model 1*.

Two examples of the modelled fits of the drying curves are presented in *Figure 8.1* and *Figure 8.2*, for *Joy* and *Lan*, respectively. *Figure 8.3* presents an example of *model 2* applied to *Ria* together with the 95% confidence intervals. The large scatter in the quality of data is clear in all examples presented and is dealt with in the *Discussion*.

The fractional mass of loose water modelled (*model 2*), m_{lw}, has already been presented in *Section 7.4.1, Table 7.9*. Below in *Table 8.2* the non-fractional mass estimated, using *model 2,* to be remaining in each of the subsamples used in mass gain experiments are presented. It is from these values that the fractional mass value, m_{lw}, was estimated.

Finally, for comparison, *Figure 8.4* displays the modelled remaining loose water (*model 2*) as a percentage of the modelled final dry mass after 60 days of drying at 130°C. Samples are arranged in order of dryness and 95% uncertainties are included. It is notable that many of the samples with largest values are samples classed as abnormal in the previous chapter (*Etr, Lan, Dow1/2, Por*) as well as *Mac* and *Bel* which have been noted previously also.

Table 8.1: Assessment, for both drying models, of the level of correlation (R^2) between the remaining water content (as a fraction of the estimated dry mass) and various proxies for the potential moisture content of the sample. From linear regressions carried out across all dating samples.

versus	TG-MS 50-130°C %wt loss	*BET Surface Area*	*Pore Volume*
Model 1 (R^2value)	0.11	0.04	0.10
Model 2 (R^2value)	0.53	0.38	0.43

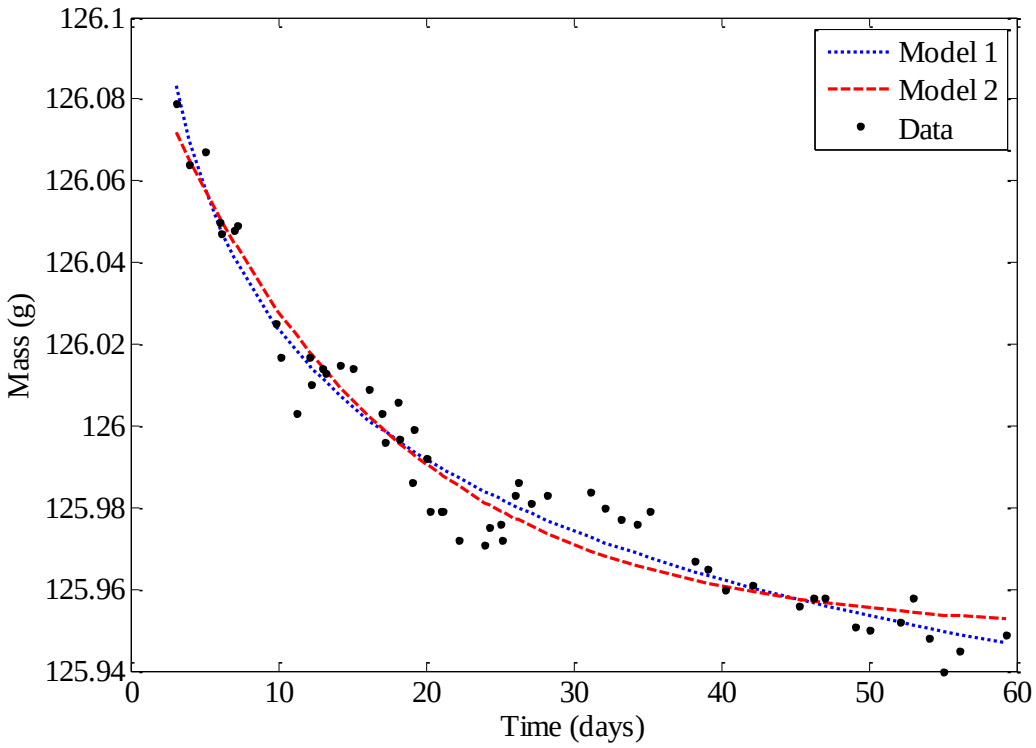

Figure 8.1: Drying mass curves for *Joy* with two models applied. Red dashed = exponential model; blue dotted = power model.

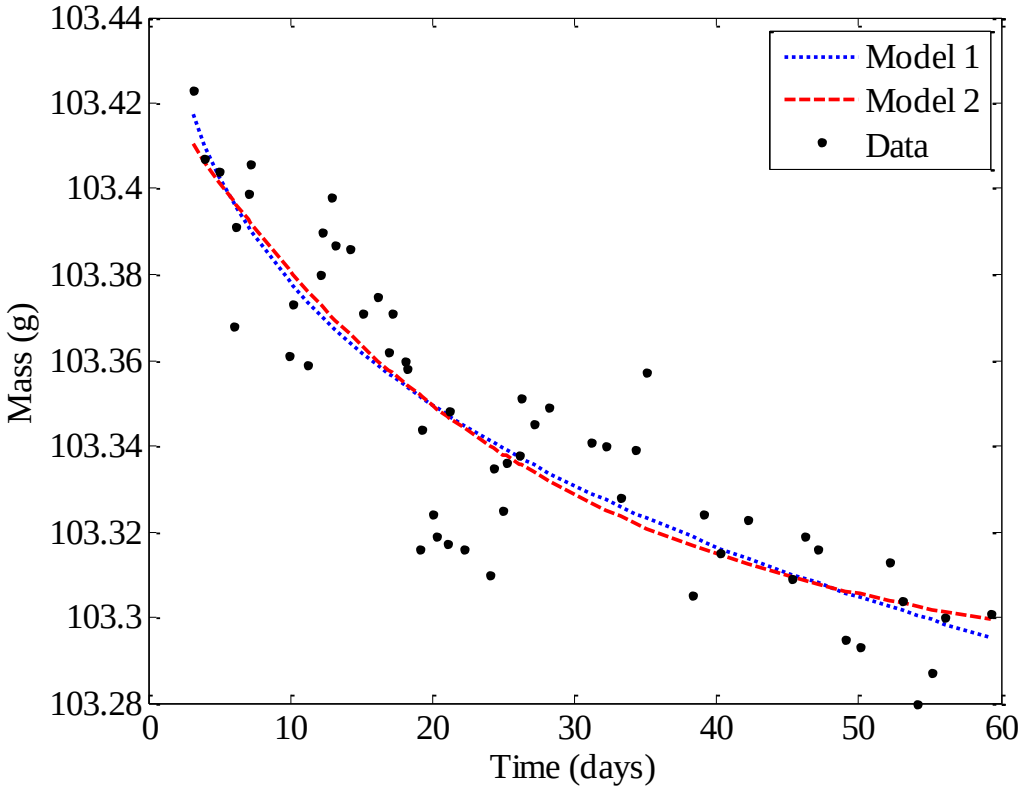

Figure 8.2: Drying mass curves for *Lan* with two models applied. Red dashed = exponential model; blue dotted = power model.

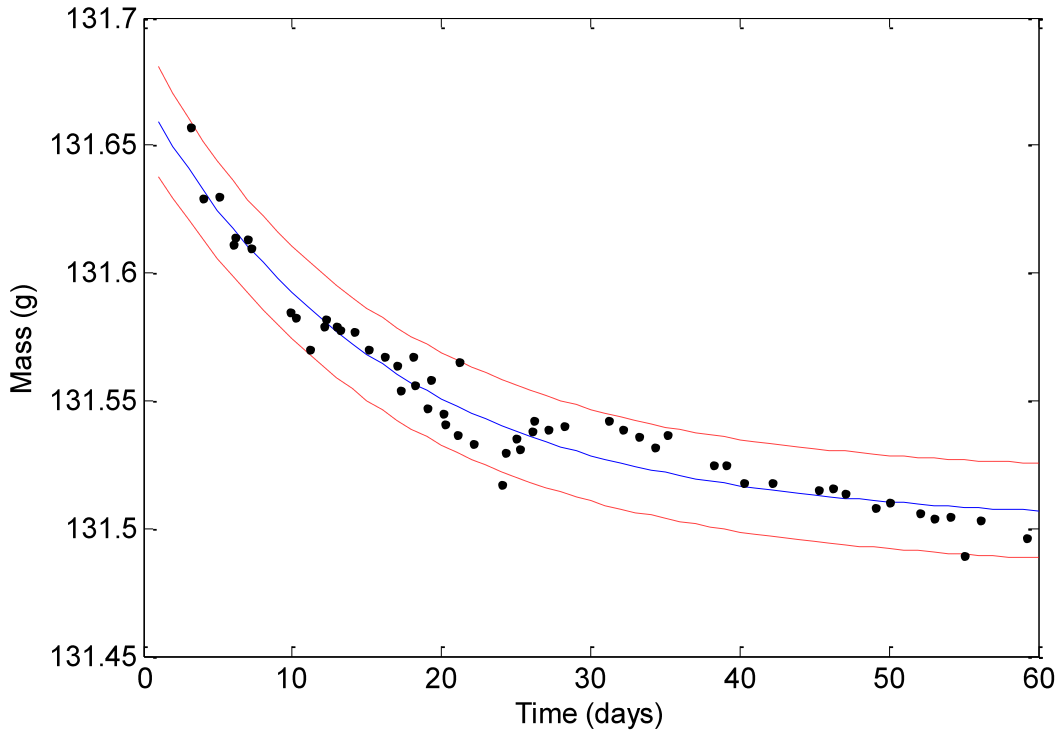

Figure 8.3: Drying mass curve of *Ria* with *model 2* fit and 95% confidence intervals.

Table 8.2: Comparison of goodness-of-fit estimates for two models applied to drying curves of dating samples.

	Model 1 $(m(t)=a(t^b)+c)$		*Model 2* $(m(t)=a(exp^{-bt})+c)$	
	R^2	*RMSE (g)*	R^2	*RMSE (g)*
Ann	0.67	0.008	0.66	0.008
Esp	0.16	0.006	0.17	0.006
Nic	0.72	0.008	0.71	0.008
Mac	0.90	0.009	0.93	0.009
Ria	0.96	0.008	0.95	0.008
Etr	0.81	0.025	0.90	0.025
Rom	0.82	0.016	0.82	0.016
Por	0.90	0.017	0.94	0.017
Rat	0.89	0.006	0.89	0.006
Cal	0.95	0.007	0.94	0.007
Lan	0.72	0.016	0.79	0.016
Joy	0.96	0.008	0.95	0.008
Cau	0.78	0.008	0.83	0.008
Bel	0.90	0.013	0.93	0.013
Dow1	0.81	0.017	0.89	0.017
Dow2	0.91	0.009	0.93	0.009
Tur	0.92	0.009	0.91	0.009
Ted	0.86	0.008	0.91	0.008

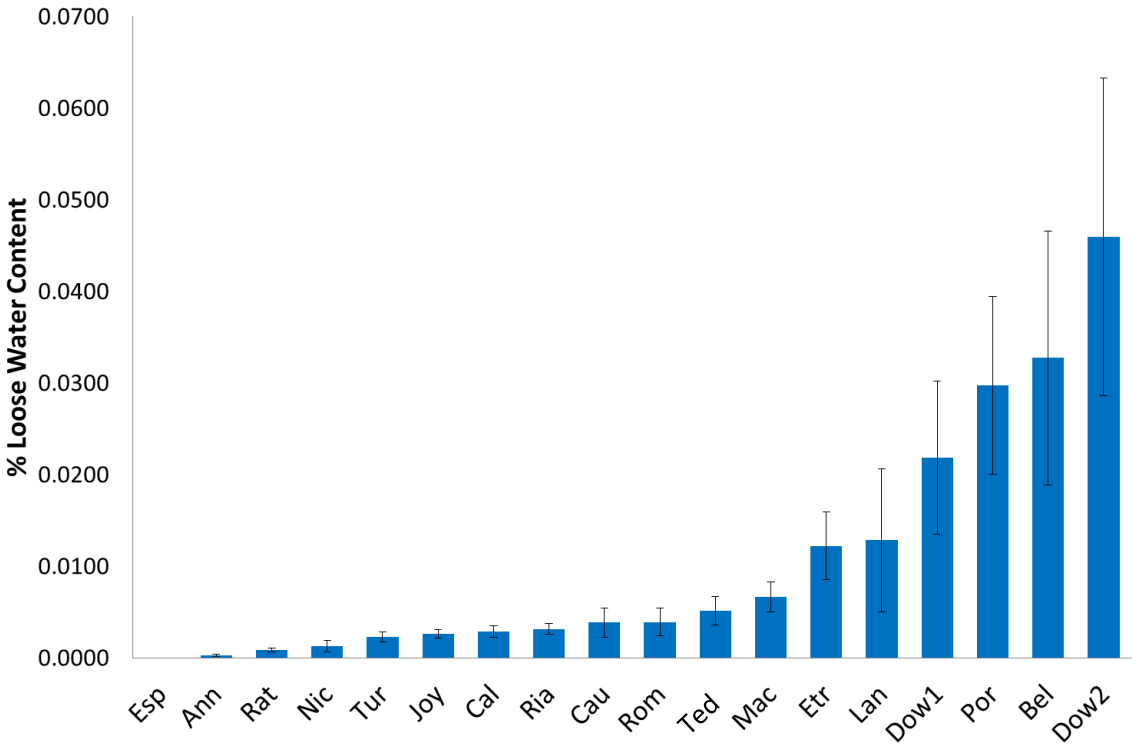

Figure 8.4: The modelled loose water content, as a percentage of the modelled dry mass of samples (*model 2*), remaining after 60 days drying at 130°C. Arranged in order of dryness and with 95% confidence intervals.

Table 8.3: Modelled remaining loose water (*model 2*), corrected for the mass of samples placed in beakers and used in dating trials and mass gain experiments.

	25°C		35°C		45°C	
	m_{lw} (g)	2σ (g)	m_{lw} (g)	2σ (g)	m_{lw} (g)	2σ (g)
Ann	0.0049	0.0084	0.0047	0.0134	0.0048	0.0137
Esp	0.0001	0.0014	0.0001	0.0015	0.0001	0.0015
Nic	0.0406	0.2650	0.0419	0.2751	0.0371	0.2437
Mac	0.0747	0.2301	0.0750	0.2330	0.0577	0.1793
Ria	0.0617	0.0891	0.0614	0.0893	0.0694	0.1009
Etr	0.0190	0.0229	0.0179	0.0224	0.0186	0.0233
Rom	0.2602	2.6280	0.2519	2.5490	0.2958	2.9932
Por	0.0497	0.1050	0.0490	0.0938	0.0515	0.0984
Rat	0.0189	0.0351	0.0167	0.0313	0.0182	0.0341
Cal	0.2703	2.0197	0.2346	1.7553	0.2529	1.8917
Lan	0.0254	0.0783	0.0240	0.0753	0.0248	0.0777
Joy	0.0542	0.0703	0.0533	0.0696	0.0561	0.0733
Cau	0.0238	0.0800	0.0227	0.0770	0.0222	0.0752
Bel	0.0446	0.0936	0.0415	0.0882	0.0429	0.0911
Dow1	0.0281	0.0538	0.0275	0.0536	0.0288	0.0562
Dow2	0.4314	3.3203	0.4011	3.0918	0.3065	2.3627
Tur	0.0609	0.1536	0.0624	0.1581	0.0608	0.1540
Ted	0.0553	0.1964	0.0512	0.1831	0.0547	0.1955

8.2 Cooling: Curves, Models and Behaviour

Modelling of cooling curves was carried out to estimate the temperature of the samples after removal from desiccated containers following removal from the oven/furnace and also to provide coefficients of cooling that could be used in modelling of particular temperature events.

The cooling curves of all samples following removal from an oven at 150°C are presented in *Figure 8.5*. The modelling results, i.e. the cooling coefficient *b*, are presented in *Table 8.4* (included in this table is a result for a generic whole brick that is used in *STETE* simulations). The average value for the cooling coefficient for dating samples is $b = 0.112 \pm 0.006$ (s^{-1}).

The temperatures of the samples following 15 minutes (desiccated container period for samples aging at 35°C and 45°C) and 1 hour 15 minutes since removal from the oven (samples aging at 25°C) are presented in *Figure 8.6* and *8.7*. Following 15 minutes the sample temperatures range from 36.75-44.6°C. Following 1 hour 15 minutes the temperatures range from 23.10-24.25°C. The variation in the range of temperature after a period of cooling can be shown to be strongly correlated (R^2 = 0.88) with the room ambient temperature, *Figure 8.8*.

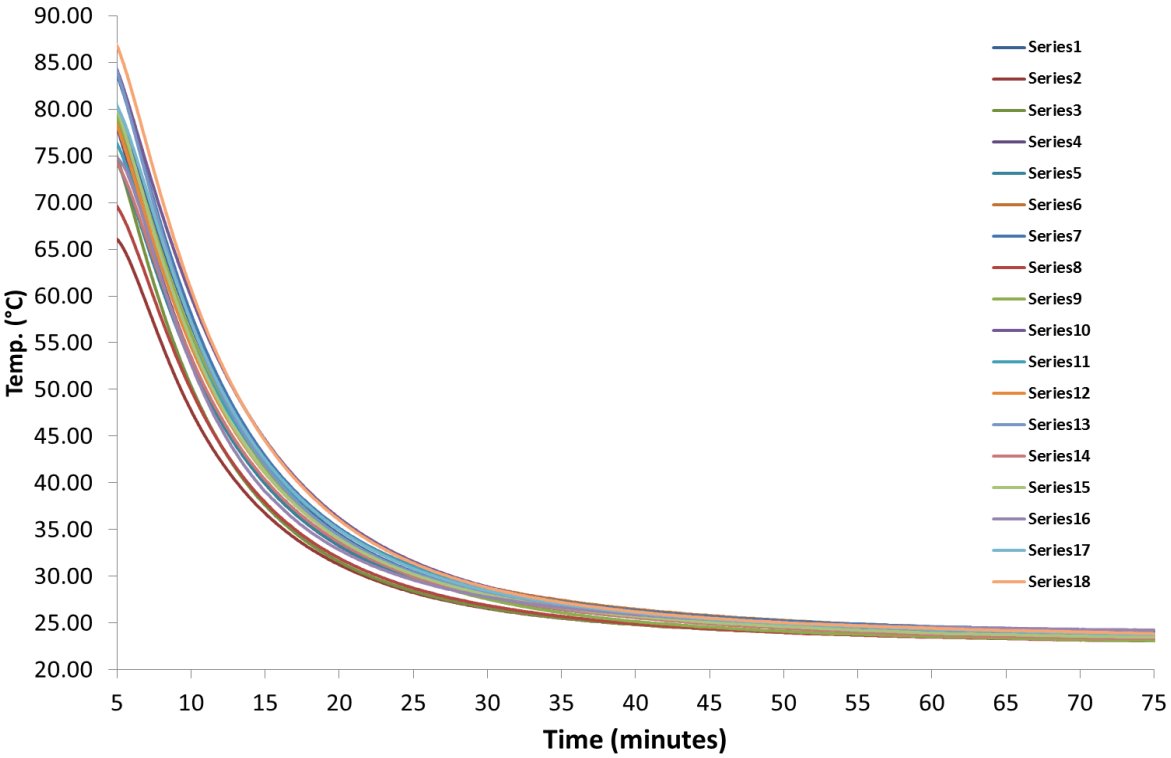

Figure 8.5: Cooling curves of dating samples following removal from oven at 150°C. Series 1 – Series 18 = *Ann, Esp, Nic, Mac, Ria, Etr, Rom, Por, Rat, Cal, Lan, Joy, Cau, Bel, Dow1, Dow2, Tur, Ted.*

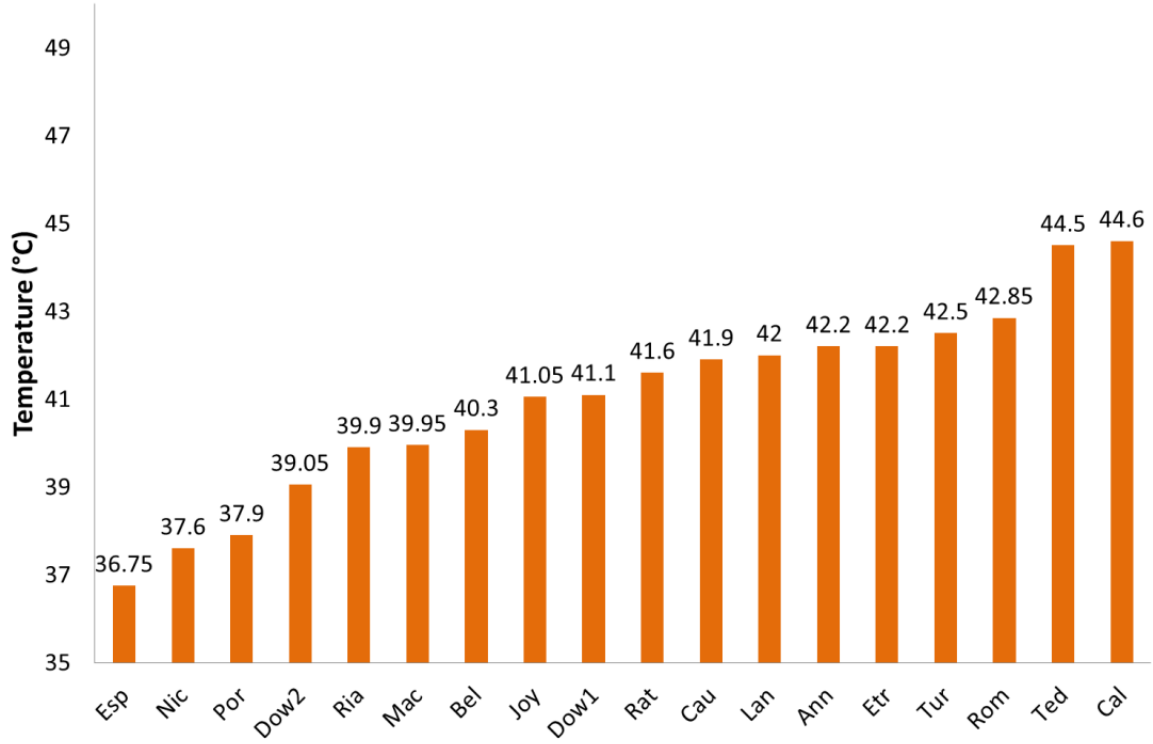

Figure 8.6: Temperature of dating samples following 15 minutes cooling after removal from oven at 150°C.

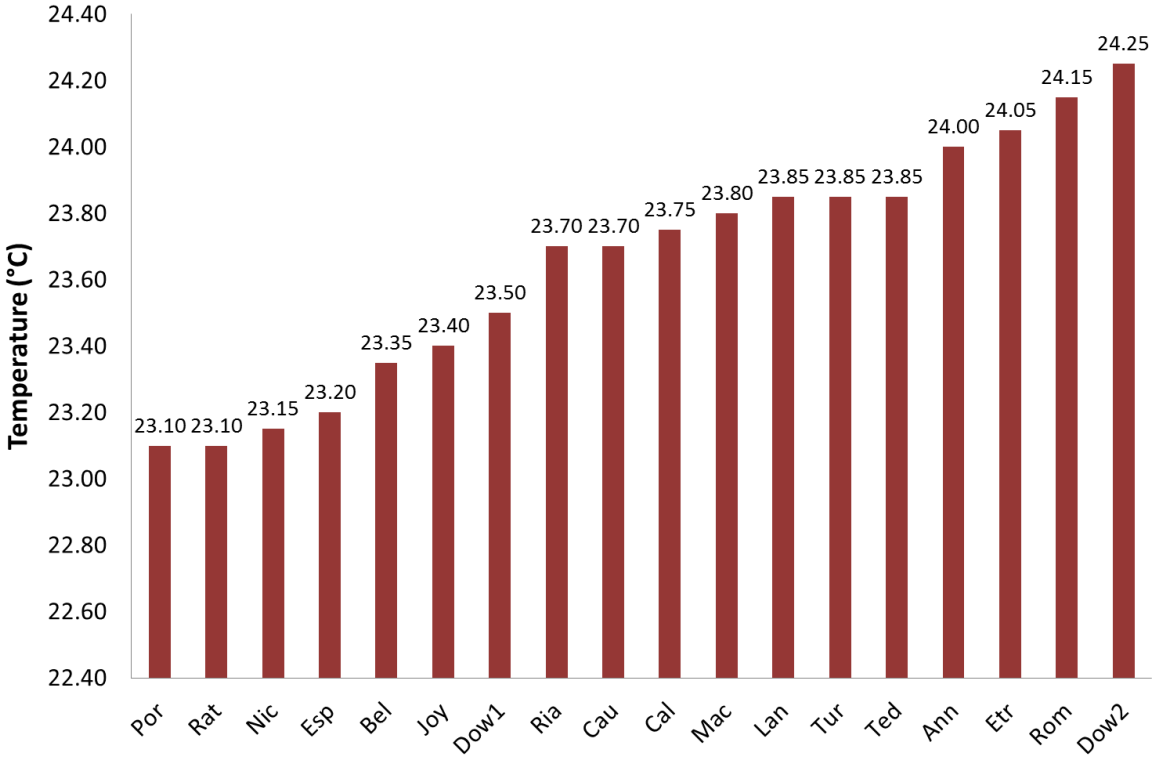

Figure 8.7: Temperature of dating samples following 1 hour 15 minutes cooling after removal from oven at 150°C.

Table 8.4: Results of Modelling of cooling curves using the relationship $T=ae^{-bt}+c$, where a=difference in initial and final temperature of the ceramic and c is the final temperature of the ceramic. Also included are the R^2 values and cooling coefficient for a whole brick.

	R^2	$b\ (s^{-1})$
Ann	0.9976	0.113
Esp	0.9973	0.1136
Nic	0.9946	0.1235
Mac	0.9952	0.1167
Ria	0.9966	0.1143
Etr	0.9943	0.1062
Rom	0.9949	0.1118
Por	0.9963	0.1139
Rat	0.9973	0.1099
Cal	0.9973	0.1043
Lan	0.9965	0.1037
Joy	0.9943	0.1091
Cau	0.9931	0.1146
Bel	0.9949	0.1082
Dow1	0.9939	0.1113
Dow2	0.9937	0.1249
Tur	0.9956	0.1094
Ted	0.9966	0.1095
Brick	0.9992	0.0192

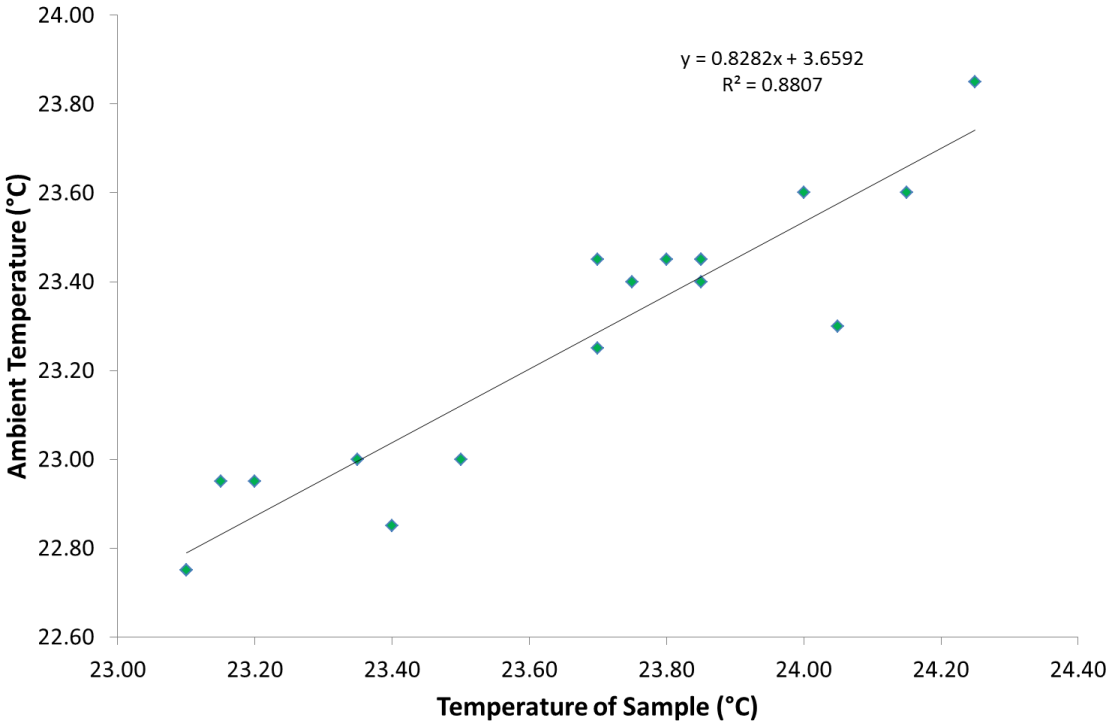

Figure 8.8: Correlation between the dating sample temperature after 1hr 15m cooling with the ambient measurement temperature.

8.3 Effective Lifetime Temperatures (ELTs)

To demonstrate how the ELTs were calculated, starting with SAT-based temperature history construction, to simulated mass gain curves, to ELT curves, the sample *Joy* will be used as an example. The ELTs produced and other relevant relationships for all samples will be presented in *Section 8.3.4* below.

8.3.1 Surface Air Temperature (SAT) History Construction Example

The temperature history for *Joy* (AD1600-2002) was constructed using three temperature records (see *Section 6.6.1* for all details and references):

(A) Met office 5km 1961-1990 gridded monthly SAT data (144,60 grid location) (short monthly instrumental - local)
(B) Armagh 1796-2002 instrumental SAT data (long monthly instrumental - regional)
(C) Luterbacher 1500-2002 (6.75W/54.75N) (long seasonal reconstruction - regional)

The steps in construction are described as follows (relevant values for the first two steps are summarised in *Table 8.5*):

Step 1: (B) mapped to (A)

MAT and ATR were calculated for (A) and (B) over the longest common period (1961- 1990) and an adjusted (B) was produced, (B'), by adding a shift factor to (B) and multiplying the difference between the monthly mean and annual mean of (B) by a scale factor.

Step 2: (C) mapped to (B')

The same process as the previous mapping was used except with (C) and (B'). The Luterbacher et al. (2004) record, (C), was adjusted with shift and scale factors to produce an adjusted record (C').

Step 3: (B') and (C') combined

The *Joy* sample required a record from AD1600 to present (or as close as permitted by the records) so the following portions of the adjusted records were combined:

(C') 1600-1795 & (B') 1796-2002

Step 4: Daily Record Generation

From the composite record, on a year by year basis, a sine model was fit, and using the parameters of this fit a daily temperature record was generated per year. A portion of the daily temperature curve generated from the adjusted Luterbacher et al. (2004) seasonal data is presented in *Figure 8.9*. The complete daily SAT curve over the lifetime of *Joy* was then used for ELT calculations.

Table 8.5: Table of relevant parameters used in mapping long regional reconstruction data to local data as part of temperature history construction for *Joy*. MAT = mean annual temperature. ATR = annual temperature range. *b* is sine model parameter (synchronisation term) and R^2 corresponds to sine modelling quality.

		Sine Modelling					
Step 1	***MAT (°C)***	***ATR (°C)***	***b***	***R^2***			
(A) Met (1961-1990) (144,50)	8.98	10.88	1.78	0.99	**Arm->Met (B) → (A) Calibration**	**Shift Factor (MAT) (+) (°C)**	**Scale Factor (ATR) (*)**
(B) Armagh (1961-1990)	9.21	11.31	1.73	0.99		-0.23	0.96
Step 2							
(B') Armagh (1796-2002)	8.77	10.49	1.76	0.99	**Lut->Arm' (C)→(B') Calibration**	**Shift Factor (MAT) (+) (°C)**	**Scale Factor (ATR) (*)**
(C) Lut (1796-2002)	8.01	9.83	1.76	1.0		0.76	1.07

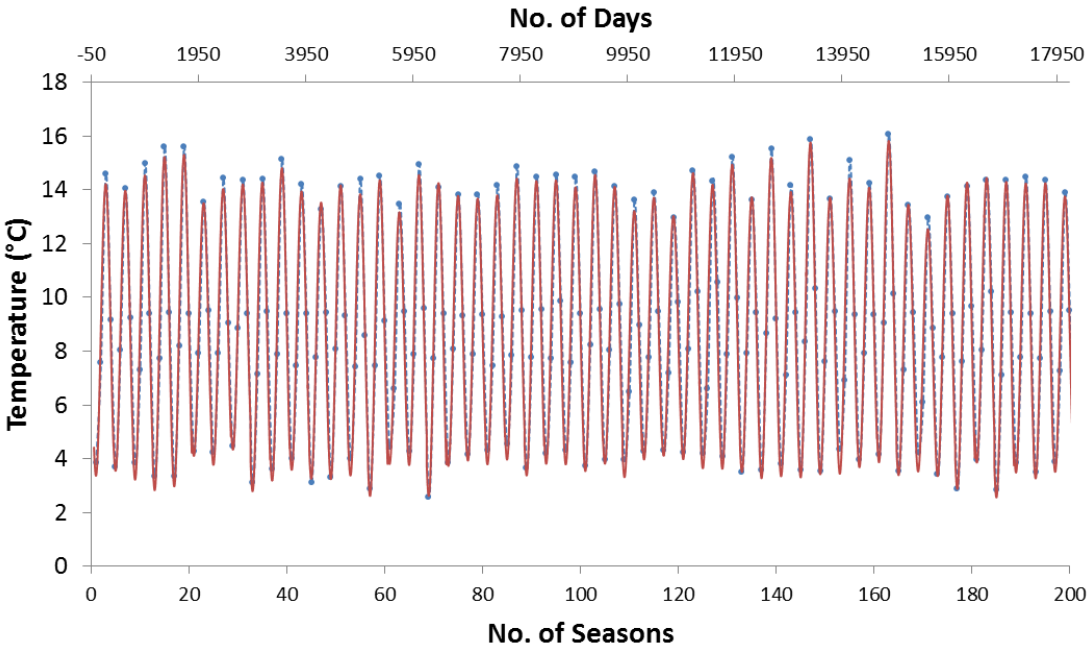

Figure 8.9: Portion (50 years) of Luterbacher et al. (2004) reconstruction record (blue dots) adjusted to local records (Armagh adjusted to Met Gridded) for purposes of *Joy* SAT temperature history reconstruction. Red line is daily data generated on a yearly basis via parameters of a sine model previously fitted to seasonal data on a yearly basis also.

8.3.2 Simulated Mass Gain Curve and ELT Curve Example

Using the constructed SAT temperature histories together with the activation energies and mass gain rates obtained in *Chapter 7*, the fractional mass gain as a function of time, across the lifetime of the ceramic, could be simulated. This was carried out for all samples using both the $t^{1/4}$ model and the $t^{1/n}$ model. The simulated mass gain results will be presented later in *Section 8.3.3*.

An example simulated mass gain curve for *Joy* using the $t^{1/4}$ model is presented in *Figure 8.10*. The activation energy and mass gain rates used are those presented in *Chapter 7*. This figure presents both the fractional mass gain generated from the constructed SAT temperature history and the fractional mass gain based on the mean lifetime temperature (MLT) of the ceramic as a function of time. Greater fractional mass gain based on the temperature history simulation is clear.

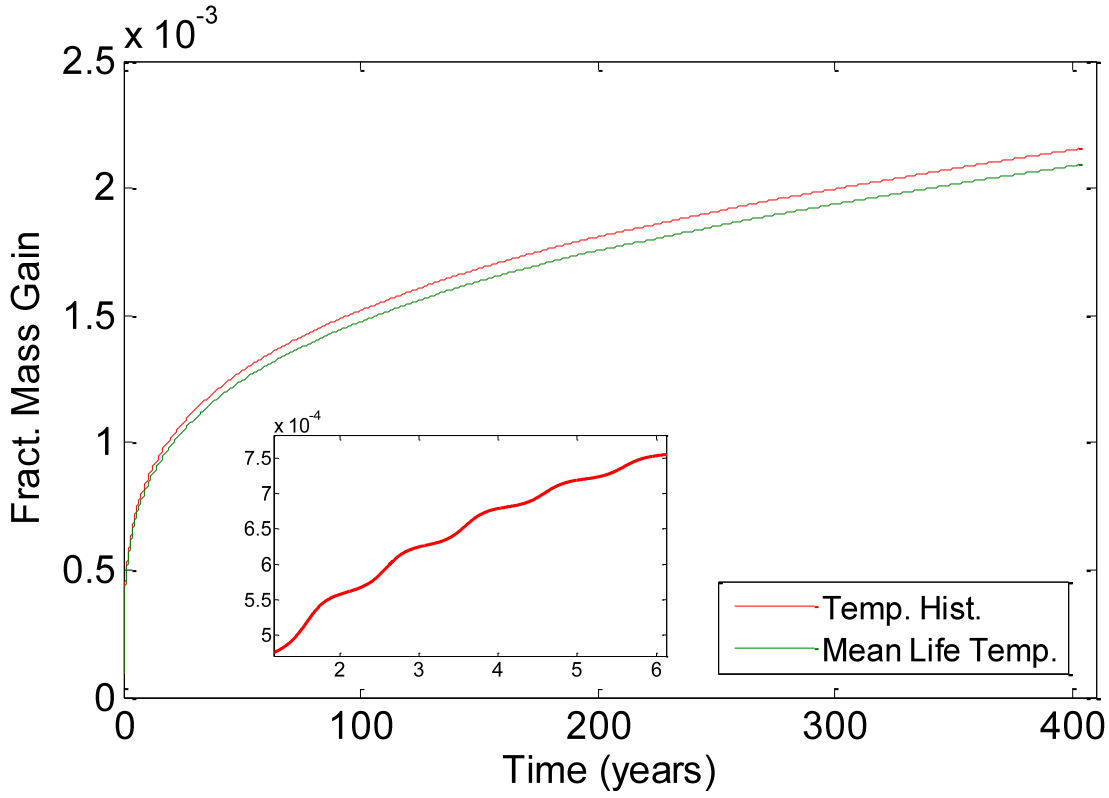

Figure 8.10: Simulated fractional mass gain as a function of time since firing based on SAT temperature history (red) and mean lifetime temperature (green) for *Joy* using the $t^{1/4}$ model. An early portion of the simulated curve is enlarged to highlight annual temperature cycle effects.

The effective lifetime temperatures (ELTs) were calculated for all samples as described in *Section 3.7* and *Section 6.6.2*, with the results in the following section. For each simulated mass gain curve, a curve of the ELT as a function of the age of the ceramic could also be generated. An example, for *Joy*, is presented in *Figure 8.11*. Also present is the mean lifetime temperature curve as a function of the age of the ceramic. The difference between the ELT and the mean lifetime temperature is clear. Also evident is that the ELT shows only minor variation (< 0.1°C increase) over the last 50 years of simulation.

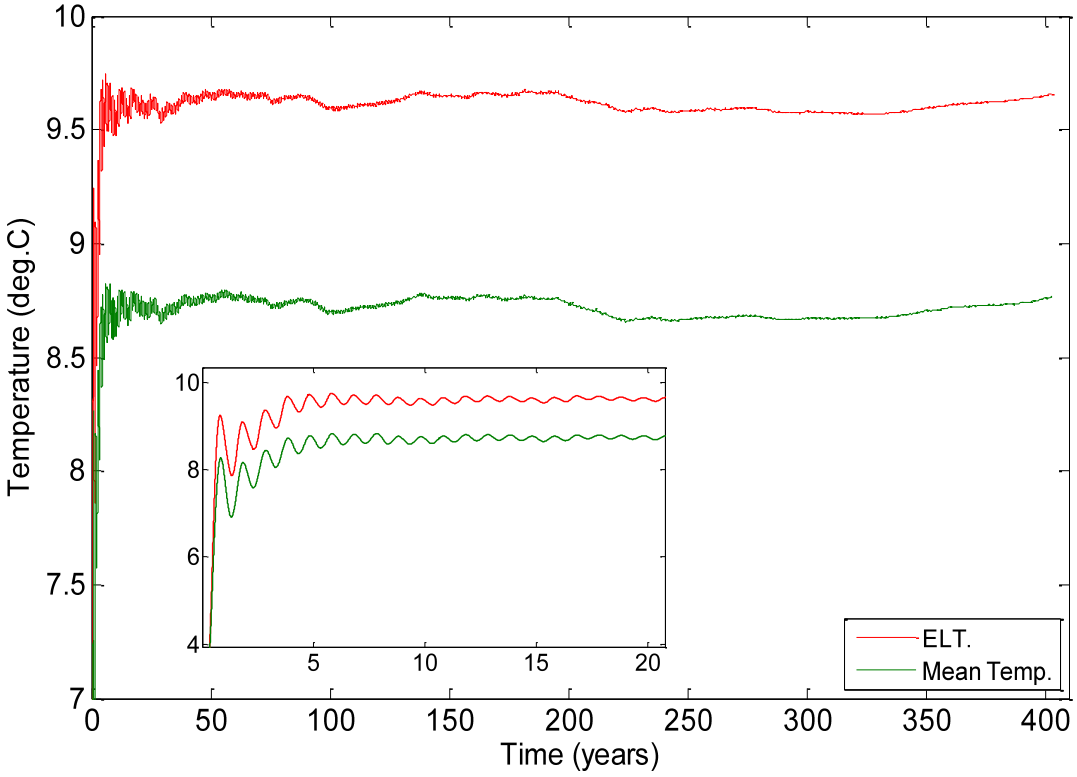

Figure 8.11: The ELT (red) and mean temperature (green) as a function of the year since firing of the sample *Joy* for $t^{1/4}$ model. Insert is enlarged portion of the early period, highlight the effects of annual temperature cycles.

8.3.3 ELTs and Simulated Mass Gain

The ELTs estimated for all samples using both the $t^{1/4}$ and $t^{1/n}$ models are presented in *Table 8.6*. Also included are the mean lifetime temperatures and the simulated fractional mass gains, m_{sim}.

The difference between the ELT, T_{elt}, and the mean lifetime temperature, T_{mlt}, varies from 0.37-2.47°C (*Bel* and *Mac*, respectively) for $t^{1/4}$ and from 0.05-2.26°C (*Rom* and *Nic*) for $t^{1/n}$. This difference is demonstrated in *Figure 8.12* to be very strongly correlated with the *RHX* activation energy, E_{aRHX}, and its impact on the exponential temperature dependence of the RHX mass gain rate. In this figure the difference between the ELT and mean lifetime temperature is plotted against the RHX activation energy, with a linear regression then carried out. The correlation is so good for both models, R^2 = 0.98 for $t^{1/4}$ and R^2 = 0.99 for $t^{1/n}$, that knowledge of the RHX activation energy alone could be used to correct the mean lifetime temperature towards the ELT.

Table 8.6: Table of mean lifetime temperature, ELT values and simulated fractional mass gain values for all samples and both models.

	T_{mlt} (°C)	($t^{1/4}$) T_{elt} (°C)	($t^{1/n}$) T_{elt} (°C)	($t^{1/4}$) m_{sim}	($t^{1/n}$) m_{sim}
Ann	9.41	10.66	10.33	0.00064645	0.00096475
Esp	9.3	9.99	10.01	0.00065409	0.00062761
Nic	9.05	10.89	11.31	0.00085179	0.00066702
Mac	9.13	11.6	11.22	0.00013332	0.00018126
Ria	8.96	10.59	10.09	0.00066466	0.00101439
Etr	11.46	12.08	o	o	o
Rom	11.46	11.93	11.51	o	o
Por	o	o	o	o	o
Rat	9.18	10.93	10.19	0.00018326	0.00198785
Cal	9.12	9.98	9.7	0.00108915	0.00257523
Lan	9.29	10.09	o	o	o
Joy	8.77	9.67	9.6	0.0021678	0.00254794
Cau	8.31	9.31	o	0.00343004	o
Bel	8.45	8.82	8.65	0.00366225	0.00326202
Dow1	9.13	9.53	o	o	o
Dow2	o	o	o	o	o
Tur	8.55	9.96	9.35	0.00057699	0.00156922
Ted	9.13	10.18	9.69	0.00239632	0.00572952

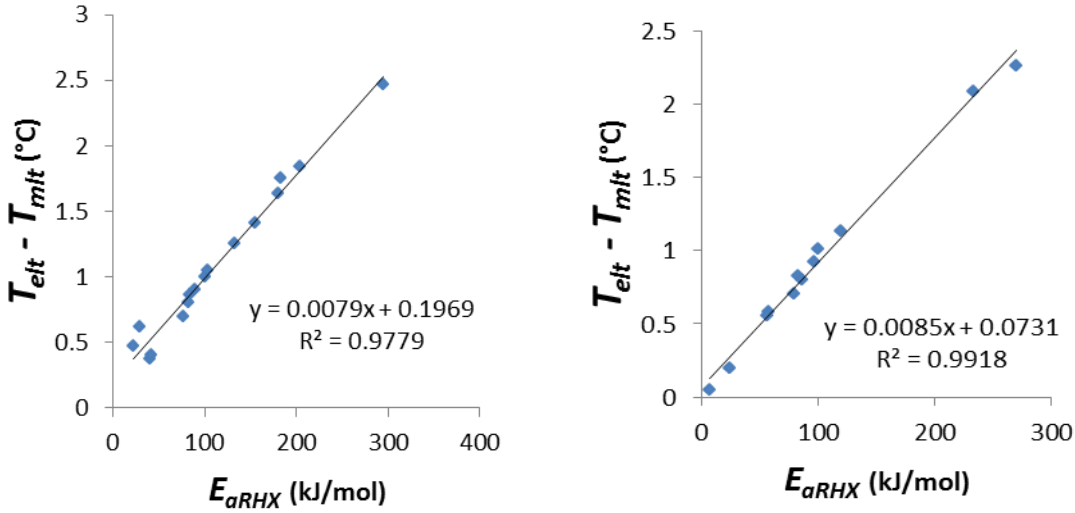

Figure 8. 12: Relationship between RHX activation energy and the difference between ELT and mean lifetime temperature for $t^{1/4}$ model (left) and $t^{1/n}$ model (right).

8.4 RHX Dating

8.4.1 Age-Temperature Curves

The age-temperature curves for samples upon which dating trials were carried out are presented in *Figure 8.13-8.25.* For each plot a curve for $t^{1/4}$ and $t^{1/n}$ are included as well as markers for the associated ELTs and known age ranges of the samples; the age calculations are presented in the following section. The age-temperature curves demonstrate both wide variety in the level of agreement between the experimental ages and the known ages (generally poorly) and the sensitivity of the age to the estimated ELT. This will be elaborated upon in the *Discussion*.

Ann

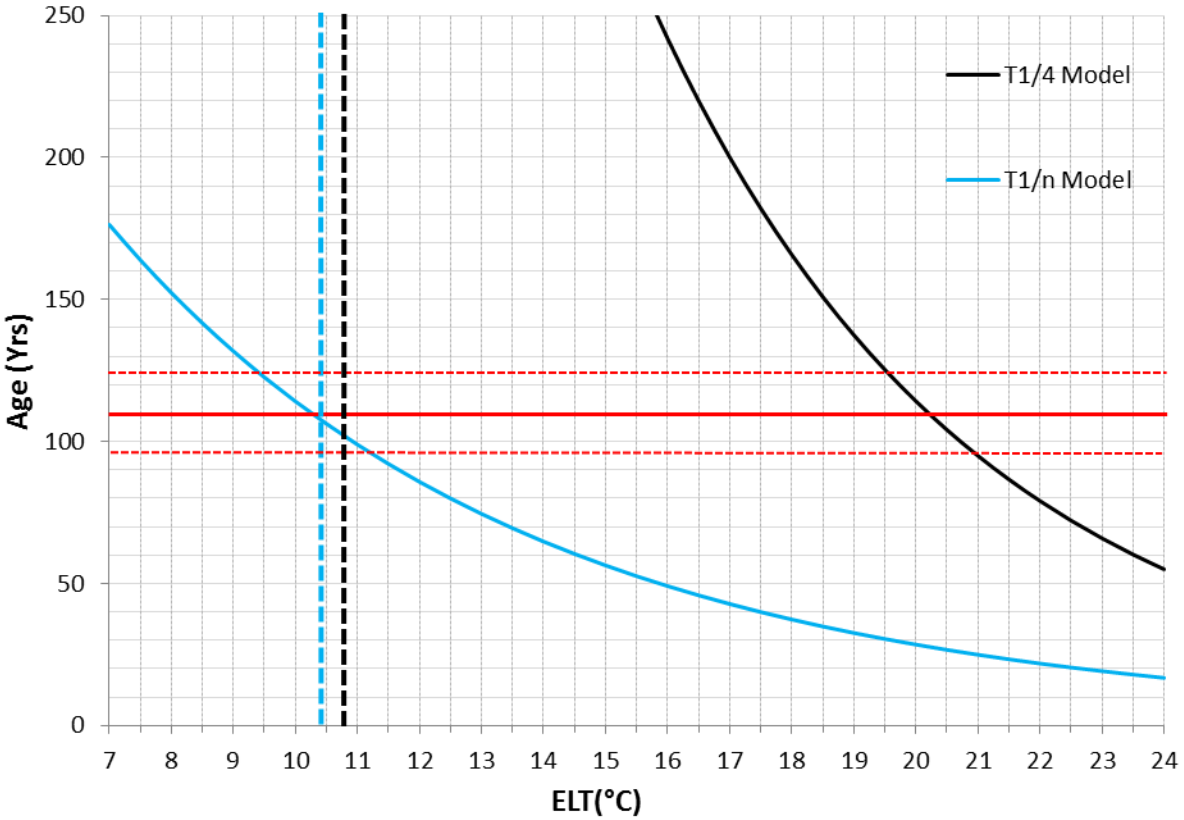

Figure 8.13: Age-temperature curves for *Ann*. Solid black line – $t^{1/4}$ model. Solid blue line – $t^{1/n}$ model. Solid red line (dashed pair) – known age midpoint (known age bounds). Dashed black – ELT of $t^{1/4}$. Dashed blue – ELT of $t^{1/n}$.

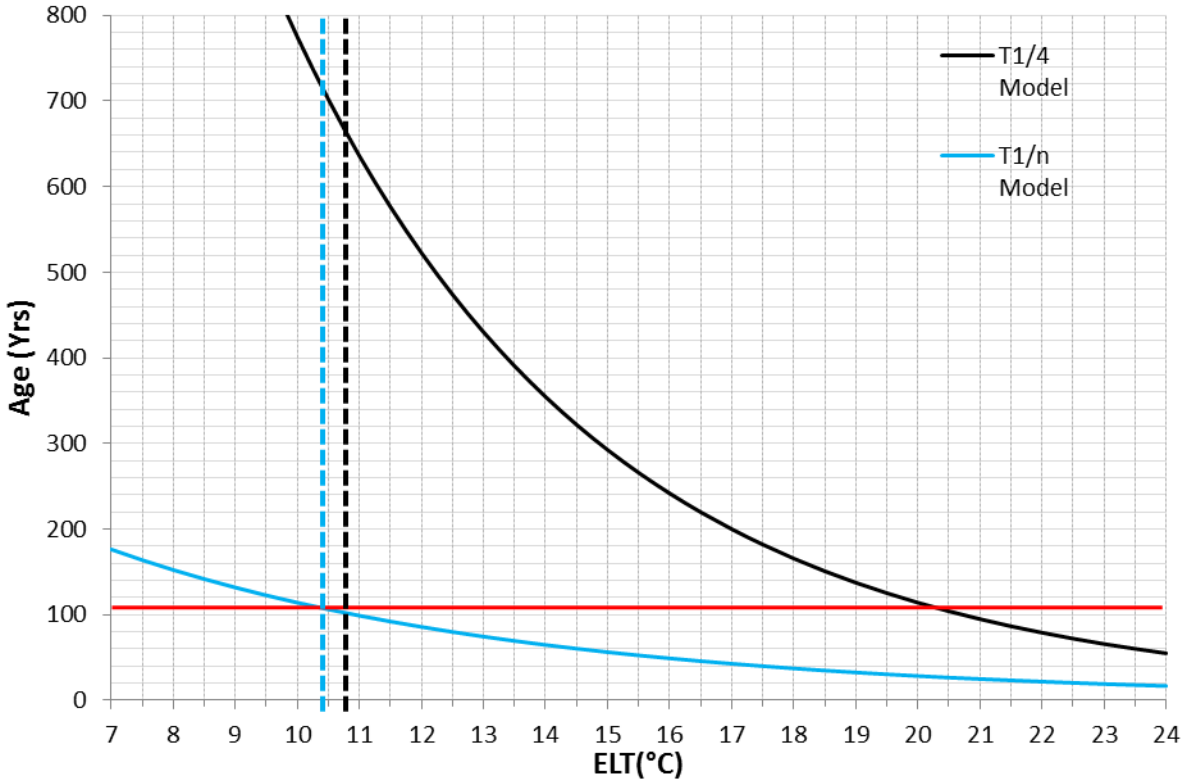

Figure 8.14: Age-temperature curves for *Ann,* scaled to observe $t^{1/4}$ curve. Solid black line – $t^{1/4}$ model. Solid blue line – $t^{1/n}$ model. Solid red line (dashed pair) – known age midpoint (known age bounds). Dashed black – ELT of $t^{1/4}$. Dashed blue – ELT of $t^{1/n}$.

Esp

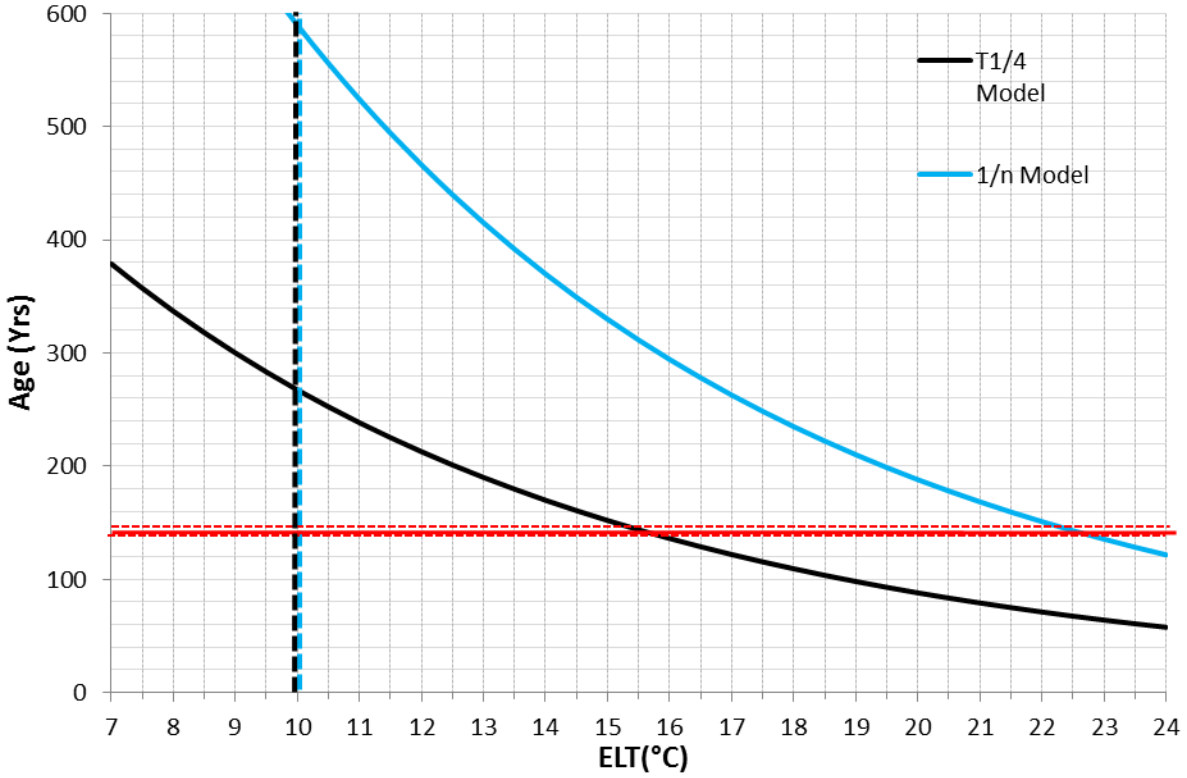

Figure 8.15: Age-temperature curves for *Esp*. Solid black line – $t^{1/4}$ model. Solid blue line – $t^{1/n}$ model. Solid red line (dashed pair) – known age midpoint (known age bounds). Dashed black – ELT of $t^{1/4}$. Dashed blue – ELT of $t^{1/n}$.

Nic

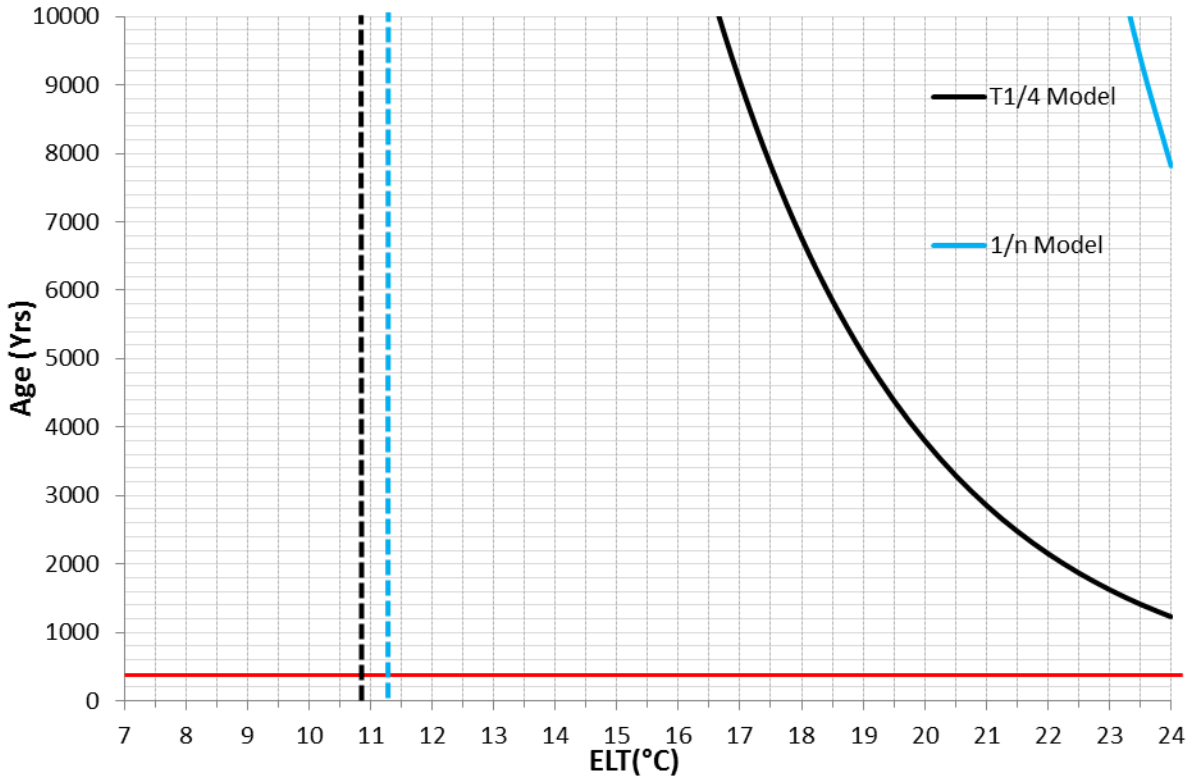

Figure 8.16: Age-temperature curves for *Nic*. Solid black line – $t^{1/4}$ model. Solid blue line – $t^{1/n}$ model. Solid red line (dashed pair) – known age midpoint (known age bounds). Dashed black – ELT of $t^{1/4}$. Dashed blue – ELT of $t^{1/n}$.

Mac

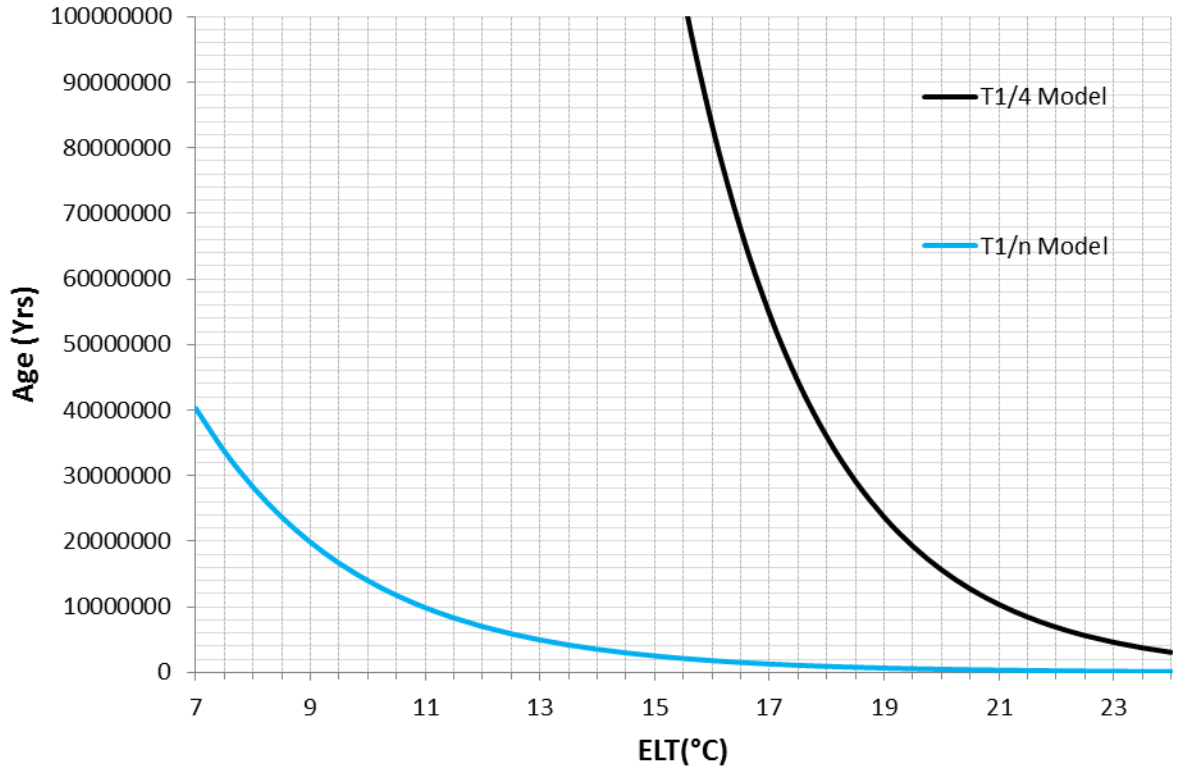

Figure 8.17: Age-temperature curves for *Mac*. Solid black line – $t^{1/4}$ model. Solid blue line – $t^{1/n}$ model. Solid red line (dashed pair) – known age midpoint (known age bounds).

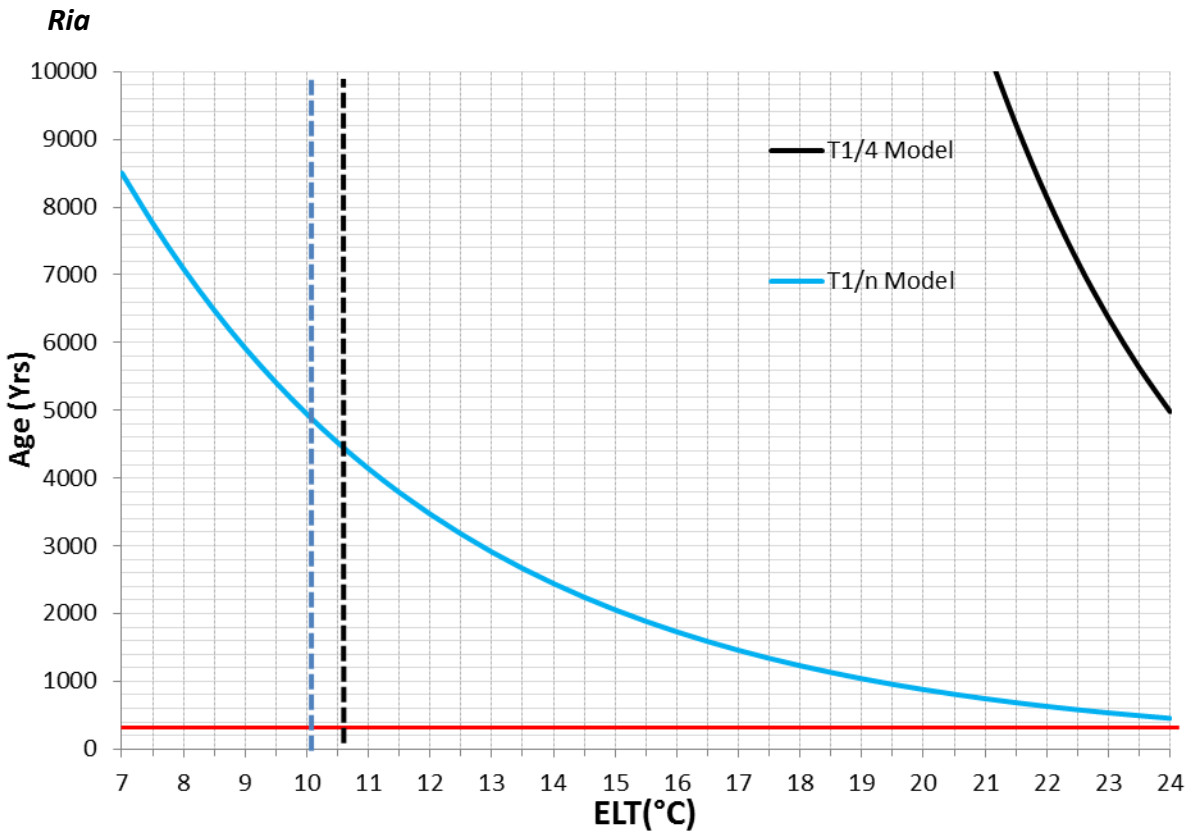

Figure 8.18: Age-temperature curves for *Ria*. Solid black line – $t^{1/4}$ model. Solid blue line – $t^{1/n}$ model. Solid red line (dashed pair) – known age midpoint (known age bounds). Dashed black – ELT of $t^{1/4}$. Dashed blue – ELT of $t^{1/n}$.

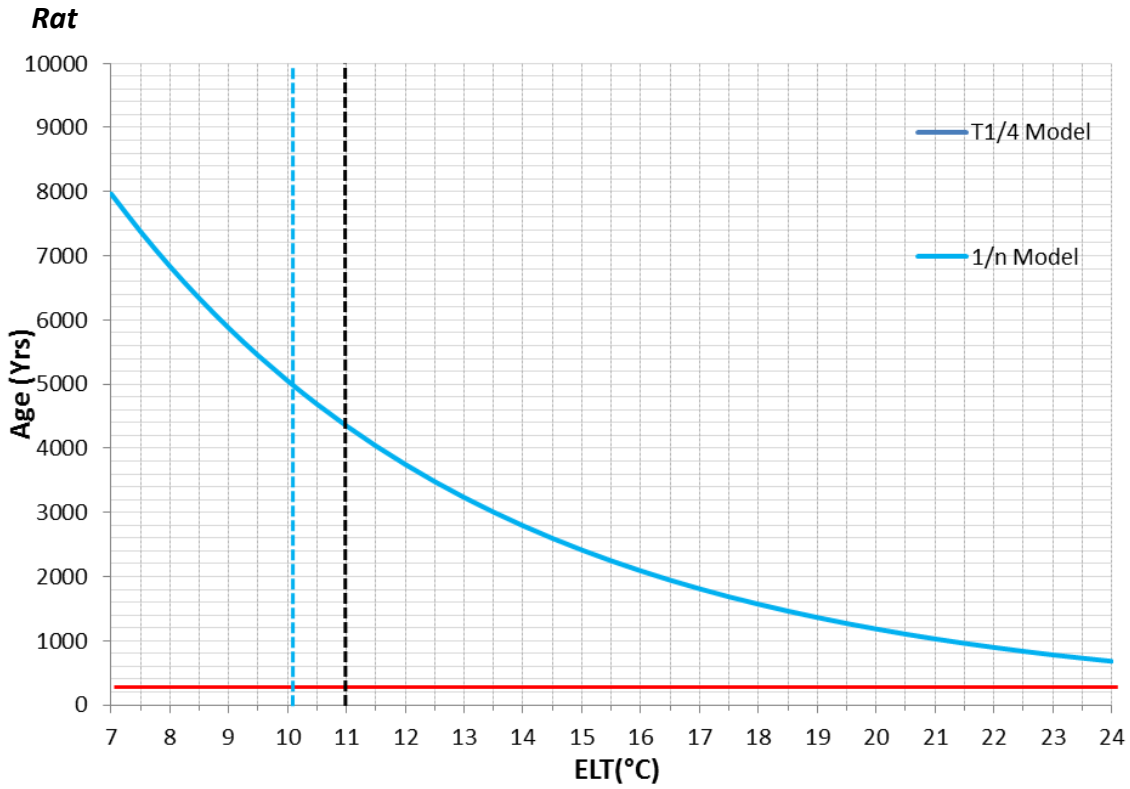

Figure 8.19: Age-temperature curves for *Rat*. $t^{1/4}$ model is off the scale. Solid blue line – $t^{1/n}$ model. Solid red line (dashed pair) – known age midpoint (known age bounds). Dashed black – ELT of $t^{1/4}$. Dashed blue – ELT of $t^{1/n}$.

Cal

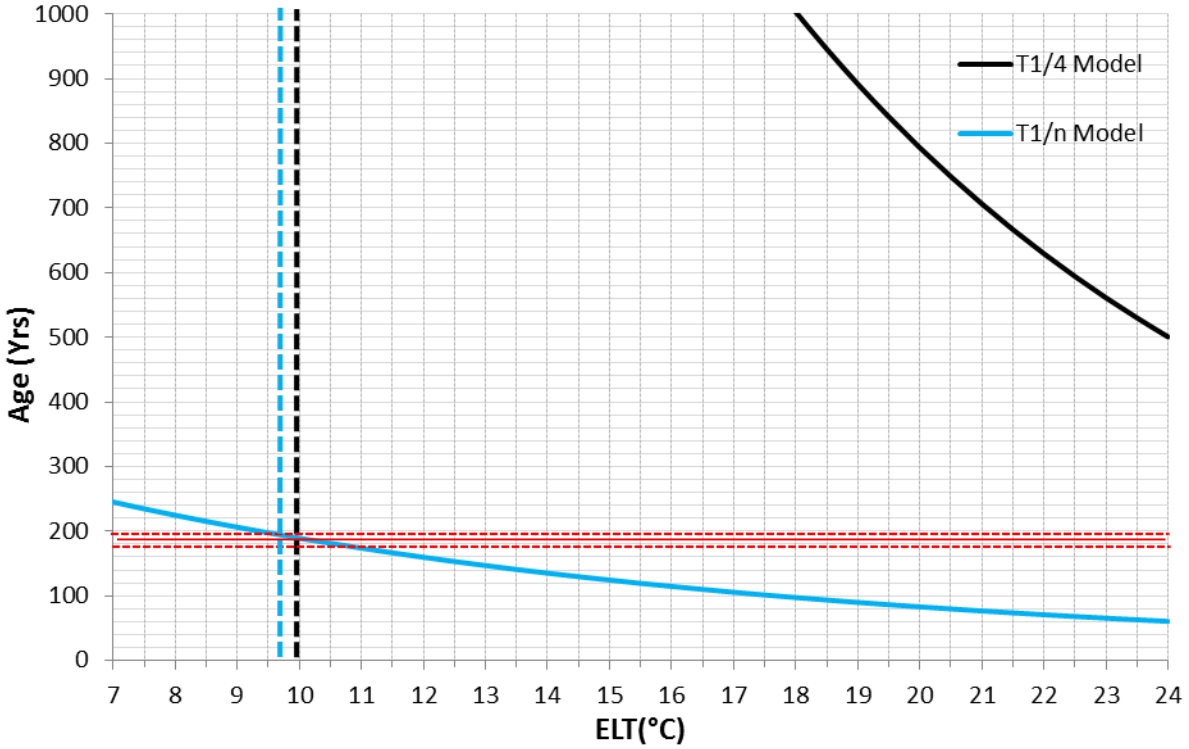

Figure 8.20: Age-temperature curves for *Cal*. Solid black line – $t^{1/4}$ model. Solid blue line – $t^{1/n}$ model. Solid red line (dashed pair) – known age midpoint (known age bounds). Dashed black – ELT of $t^{1/4}$. Dashed blue – ELT of $t^{1/n}$.

Joy

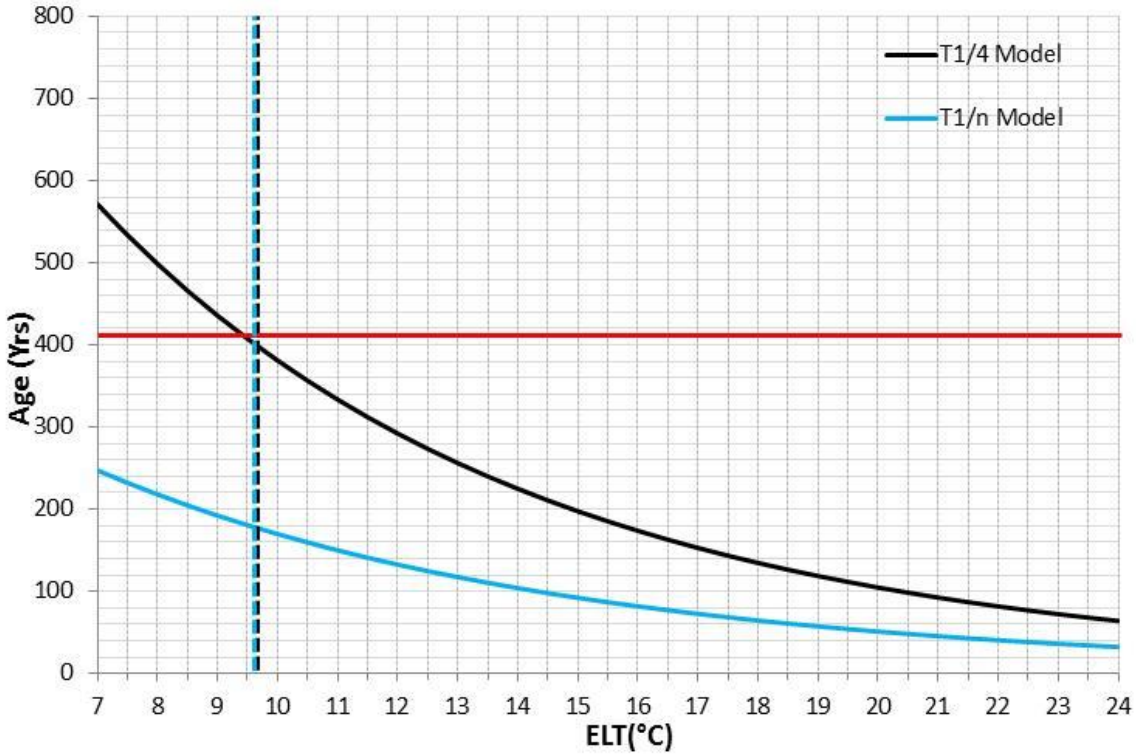

Figure 8.21: Age-temperature curves for *Joy*. Solid black line – $t^{1/4}$ model. Solid blue line – $t^{1/n}$ model. Solid red line (dashed pair) – known age midpoint (known age bounds). Dashed black – ELT of $t^{1/4}$. Dashed blue – ELT of $t^{1/n}$.

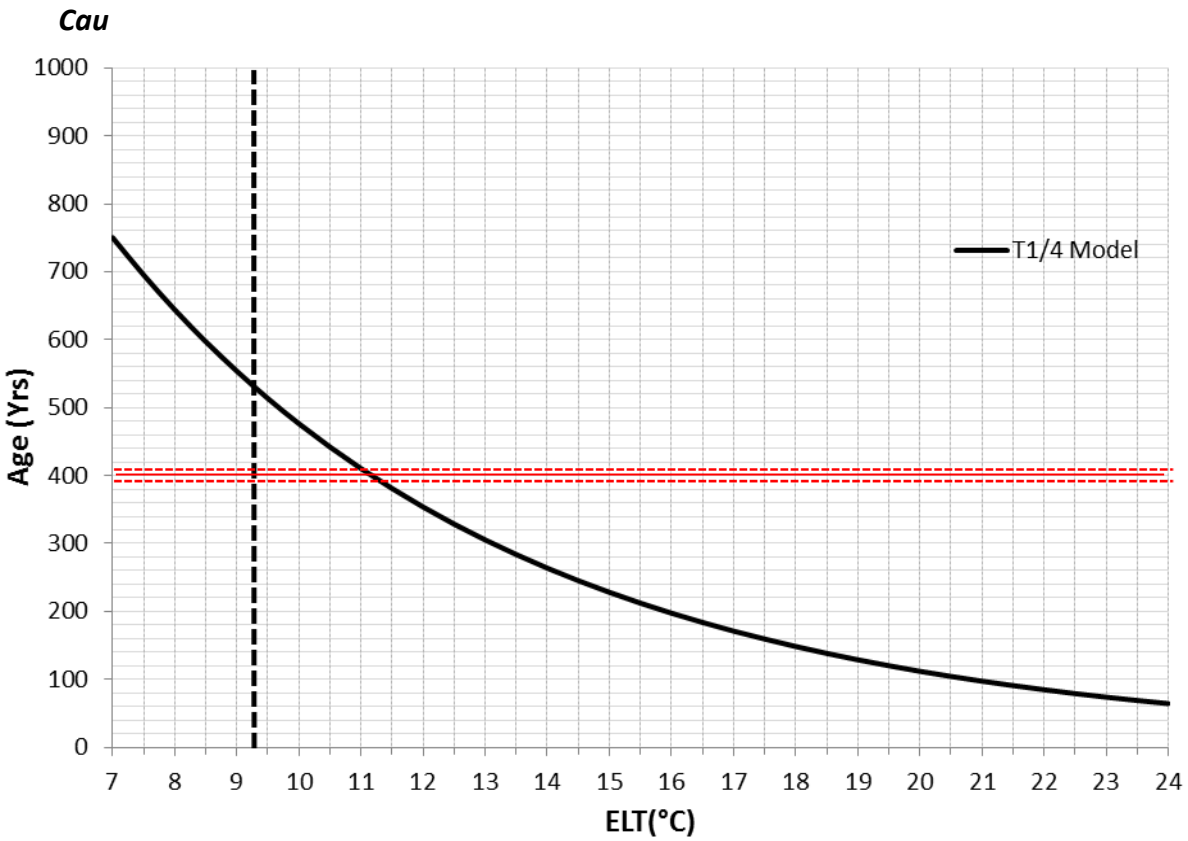

Figure 8.22: Age-temperature curves for *Cau*. Solid black line – $t^{1/4}$ model. Solid red line (dashed pair) – known age midpoint (known age bounds). Dashed black – ELT of $t^{1/4}$.

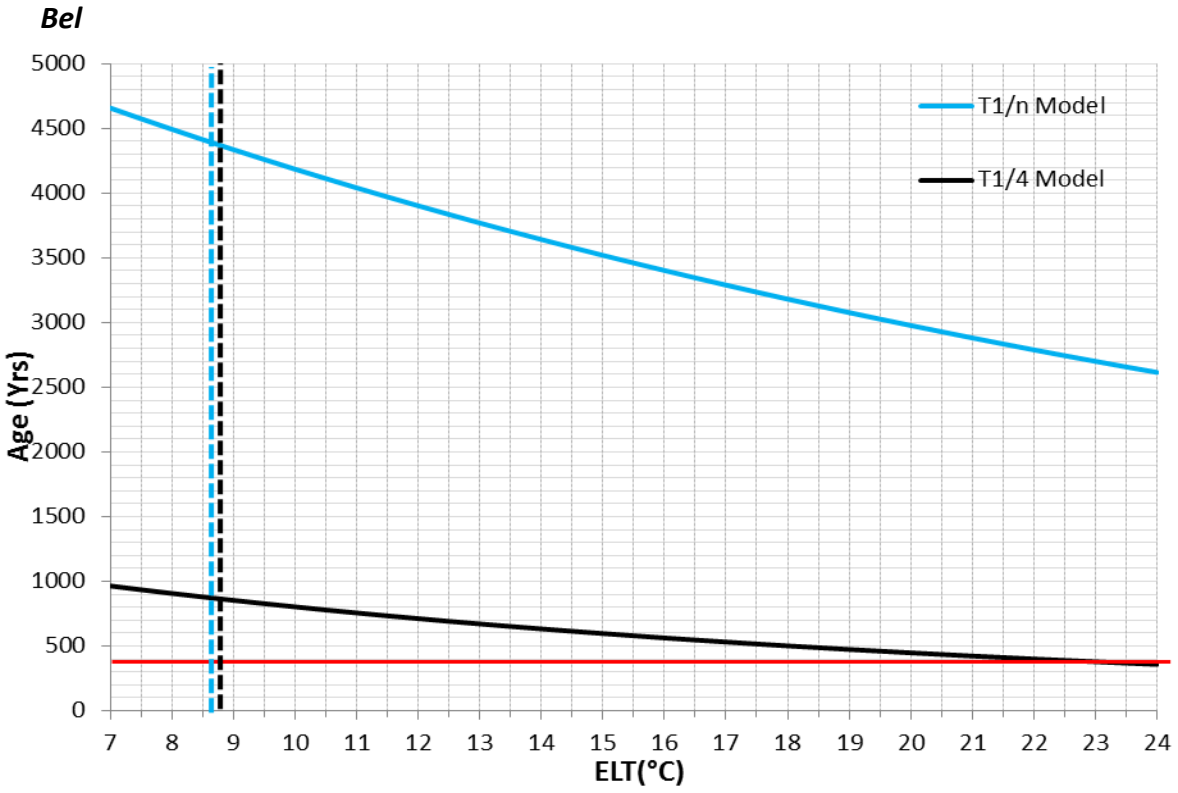

Figure 8.23: Age-temperature curves for *Bel*. Solid black line – $t^{1/4}$ model. Solid blue line – $t^{1/n}$ model. Solid red line (dashed pair) – known age midpoint (known age bounds). Dashed black – ELT of $t^{1/4}$. Dashed blue – ELT of $t^{1/n}$.

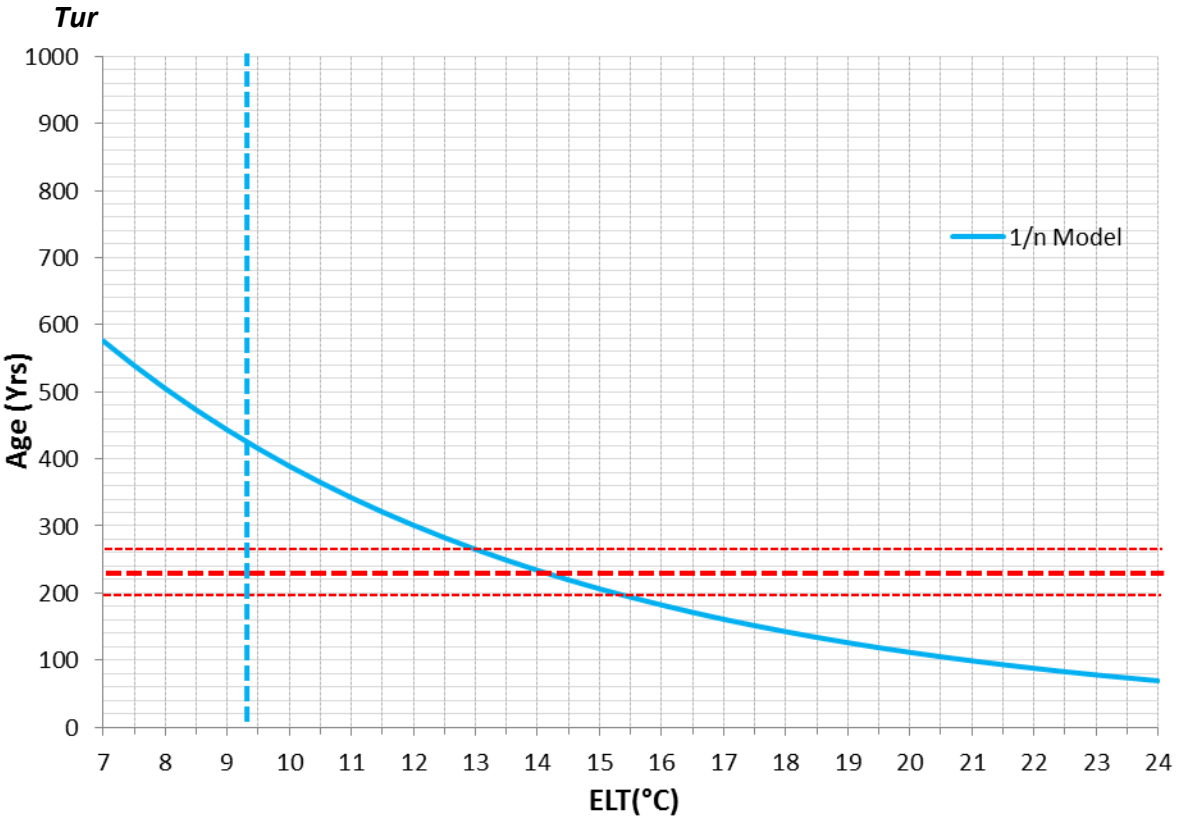

Figure 8.24: Age-temperature curves for *Tur*. Solid black line – $t^{1/4}$ model (off scale). Solid blue line – $t^{1/n}$ model. Solid red line (dashed pair) – known age midpoint (known age bounds). Dashed black – ELT of $t^{1/4}$. Dashed blue – ELT of $t^{1/n}$.

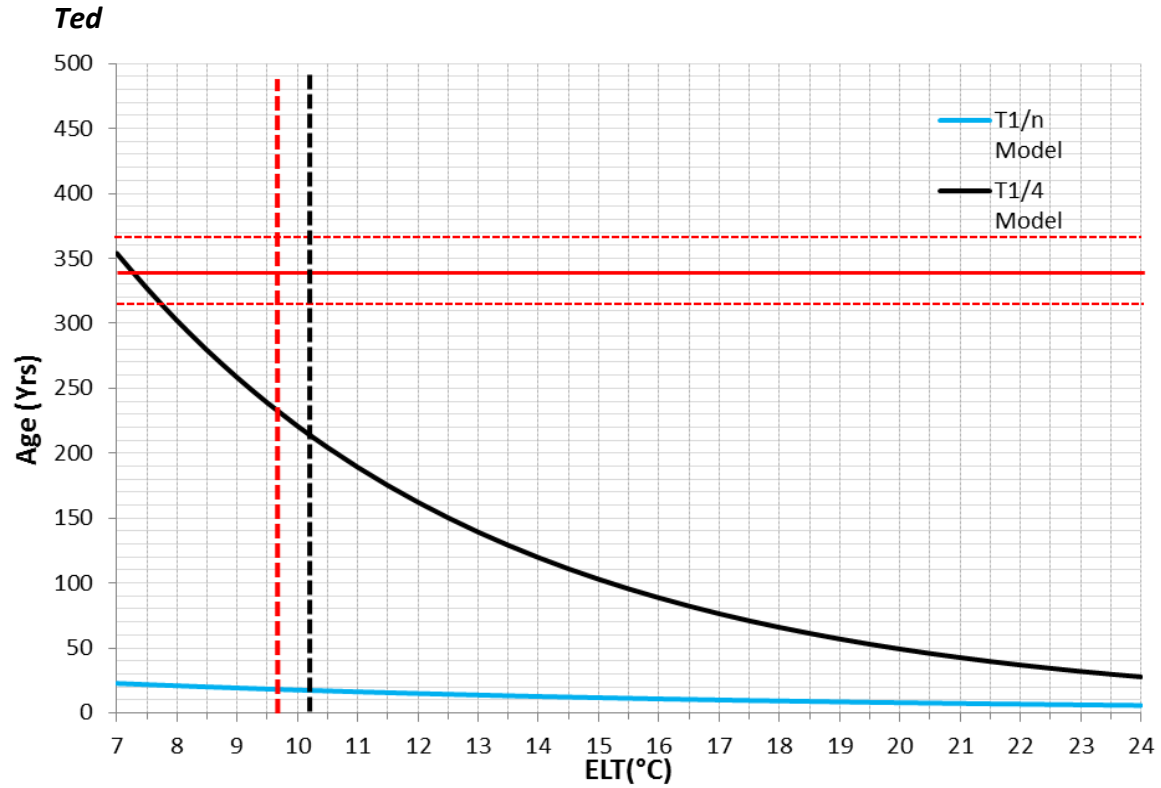

Figure 8.25: Age-temperature curves for *Ted*. Solid black line – $t^{1/4}$ model. Solid blue line – $t^{1/n}$ model. Solid red line (dashed pair) – known age midpoint (known age bounds). Dashed black – ELT of $t^{1/4}$. Dashed blue – ELT of $t^{1/n}$.

8.4.2 Age Estimates and Uncertainty Effects

The age estimates of all datable samples, for both models, are presented in *Table 8.7*. Also presented are the working temperature, T_w, and the working OM/OC ratio, OM/OC_W; these are minimum/maximum values required for the estimated age to fall within the uncertainty limits of the known age. The fractional mass the samples are estimated to be 'out' by, m_{out}, are also presented (difference between m_{sim} and m_{RHX}).

Table 8.7: Table of age estimates based on ELTs and both the $t^{1/4}$ and $t^{1/n}$ models. Also included are OM/OC_w and T_w, conditions of OM/OC and temperature under which the age calculation will fall within the uncertainty bounds of the known age. m_{out} is the fractional mass the samples are estimated to be out by (relative to simulated mass gain using ELTs) for the dates to work.

		$t^{1/4}$				$t^{1/n}$			
	Known Age (Yrs)	**Age Estimate (Yrs)**	OM/OC_W	T_W (°C)	m_{out}	**Age Estimate (Yrs)**	OM/OC_W	T_W (°C)	m_{out}
Ann	**110 ± 14**	**680**	3.12	20.2	0.0003727	**109**	1.94	10.1	-0.0000108
Esp	**141 ± 6**	**268**	2.53	15.7	0.0001135	**589**	2.96	22.6	0.0001974
Nic	**398 ± 2**	**55965**	10.51	28.1	0.0020809	**1024358**	12.03	32.1	0.0024357
Mac	**228 ± 2**	**555199409**	16.41	49.7	0.0051324	**9148913**	16.15	45.6	0.0050406
Ria	**339 ± 25**	**153820**	9.65	35.4	0.0024025	**4869**	7.85	26.0	0.0018496
Rat	**245 ± 2**	**1752430**	11.39	47.7	0.0015017	**4910**	9.5	31.7	0.0012032
Cal	**182 ± 9**	**2660**	10.4	33.2	0.0010400	**194**	2.35	10.5	0.0000484
Joy	**412 ± 2**	**399**	1.86	9.4	-0.0000179	**179**	<1	3.0	-0.0007211
Cau	**399 ± 4**	**528**	2.45	11.2	0.0002490				
Bel	**395 ± 3**	**864**	2.32	22.3	0.0007904	**4390**	2.675	97.1	0.0015246
Tur	**229 ± 35**	**48052**	8.06	34.9	0.0016187	**423**	3.8	14.2	0.0004905
Ted	**339 ± 25**	**215**	<1	7.3	-0.0002586	**18**	<1	-21.0	-0.0038182

The effects of uncertainty in the OM/OC ratio and the RHX activation energy on the estimated age of the samples are provided in *Table 8.8* and *Table 8.9*. These cover age estimation conditions where OM/OC varies from 1.4 – 2.5, the activation energy ranges from $E_{aRHX}+1\sigma$ to $E_{aRHX}-1\sigma$, as well as both combined. In bold are highlighted the conditions for which the estimated age range overlaps with the known age range. The known ages and estimated ages with the above uncertainties are plotted in *Figure 8.26-8.28* (large estimated ages have been cutoff for visual purposes).

Table 8.8: Examples of the effect of uncertainties in OM/OC ratio and the activation energy on the age range estimates. For $t^{1/4}$ model. Italicised and bold correspond to age ranges that overlap with known age.

$t^{1/4}$		Age Range (Yrs) (OM/OC)		Age Range (Yrs) (+/- σE_{aRHX})		Age Range (Yrs) (OM/OC+σE_{aRHX})	
	Known Age (Yrs)	OM/OC (2.5)	OM/OC (1.4)	$-\sigma E_{aRHX}$	$+\sigma E_{aRHX}$	OM/OC (2.5) $-\sigma E_{aRHX}$	OM/OC (1.4) $+\sigma E_{aRHX}$
Ann	**110±14**	319	1283	563	821	265	1549
Esp	**141 ± 6**	***147***	***452***	209	342	***115***	***577***
Nic	**398 ± 2**	46440	66885	15118	207161	12546	247585
Mac	**228 ± 2**	477321093	642239904	146945777	2097687937	126333562	2426549592
Ria	**339±25**	122179	191242	28561	828418	22686	1029959
Rat	**245 ± 2**	1415987	2145539	1073622	2860419	867501	3502076
Cal	**182 ± 9**	2337	3014	1744	4057	1532	4598
Joy	**412 ± 2**	***321***	***489***	***263***	***604***	***211***	***742***
Cau	**399 ± 4**	***388***	***704***	412	678	***302***	***903***
Bel	**395 ± 3**	***258***	***2178***	490	1522	***147***	***3840***
Tur	**229±35**	36508	62139	28231	81789	21449	105766
Ted	**339±25**	174	263	166	278	***135***	***339***

Table 8.9: Examples of the effect of uncertainties in OM/OC ratio and the activation energy on the age range estimates. For $t^{1/n}$ model. Italicised and bold correspond to age ranges that overlap with known age.

$t^{1/n}$		Age Range (Yrs) (OM/OC)		Age Range (Yrs) (+/- σE_{aRHX})		Age Range (Yrs) (OM/OC+σE_{aRHX})	
	Known Age (Yrs)	OM/OC (2.5)	OM/OC (1.4)	$-\sigma E_{aRHX}$	$+\sigma E_{aRHX}$	OM/OC (2.5) $-\sigma E_{aRHX}$	OM/OC (1.4) $+\sigma E_{aRHX}$
Ann	**110±14**	***59***	***182***	***80***	***148***	***43***	***247***
Esp	**141 ± 6**	284	1115	296	1170	***143***	***2216***
Nic	**398 ± 2**	820437	1267480	241745	4342090	193586	5371703
Mac	**228 ± 2**	8113299	10271317	2565101	32631307	2274744	36634569
Ria	**339±25**	4150	5660	2655	8929	2263	10378
Rat	**245 ± 2**	4343	5517	3080	7827	2724	8794
Cal	**182 ± 9**	***177***	***212***	***155***	***244***	***141***	***266***
Joy	**412 ± 2**	152	208	163	196	138	228
Cau	**399 ± 4**						
Bel	**395 ± 3**	774	17058	2140	9009	***377***	***35002***
Tur	**229±35**	359	494	286	627	***242***	***731***
Ted	**339±25**	16	21	15	23	12	26

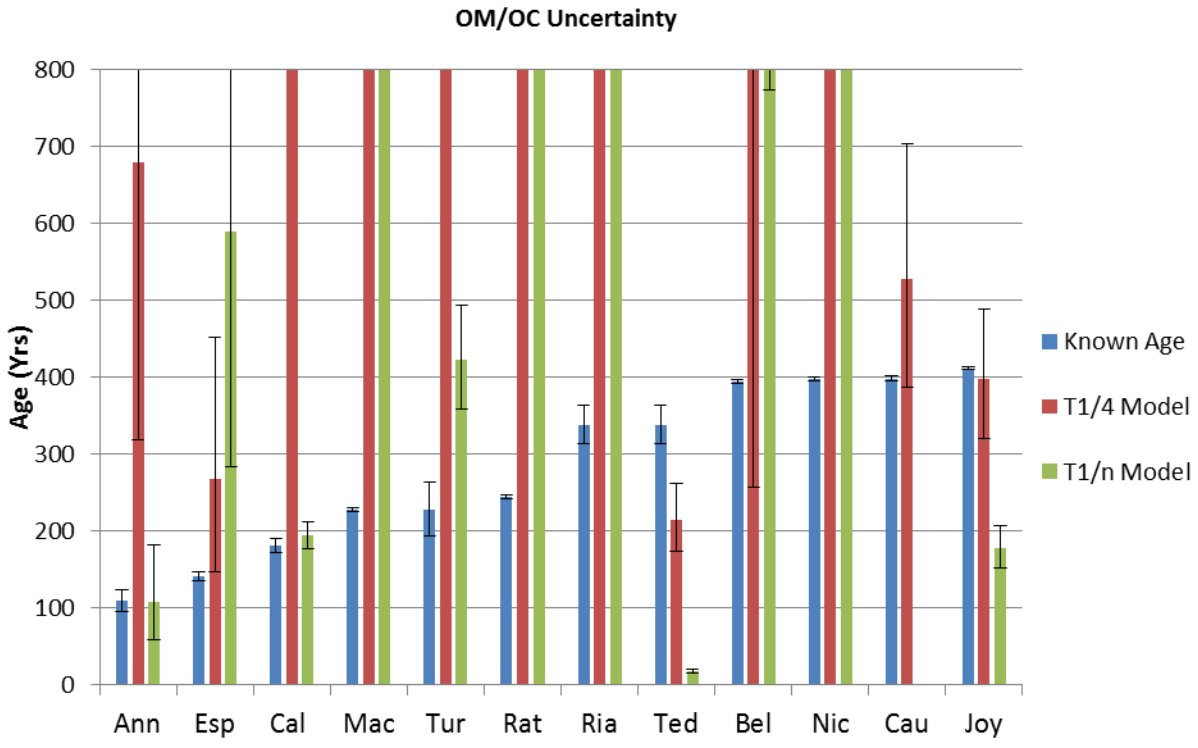

Figure 8.26: Plot of known ages (blue) and age estimates for $t^{1/4}$ model (red) and $t^{1/n}$ model (green), together with age ranges (black error bars) based on OM/OC uncertainties (OM/OC = 1.4-2.5). Cut off at 800years.

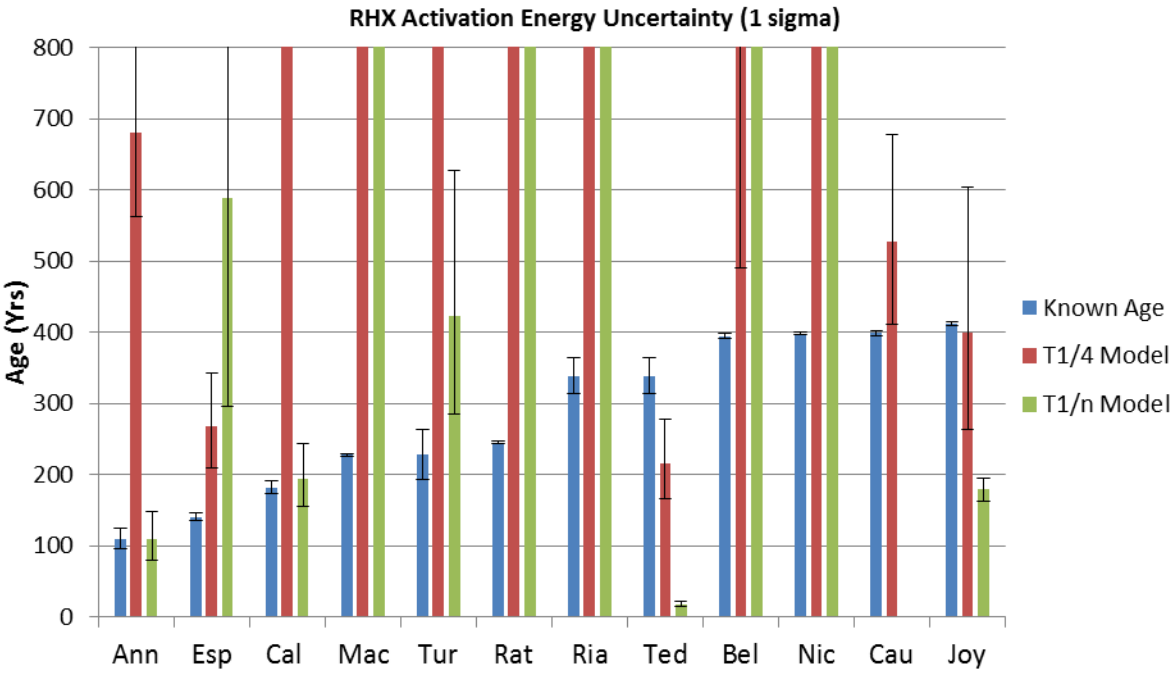

Figure 8.27: Plot of known ages (blue) and age estimates for $t^{1/4}$ model (red) and $t^{1/n}$ model (green) together with age ranges (black error bars) based on RHX activation energy uncertainties (1σ). Cut off at 800years.

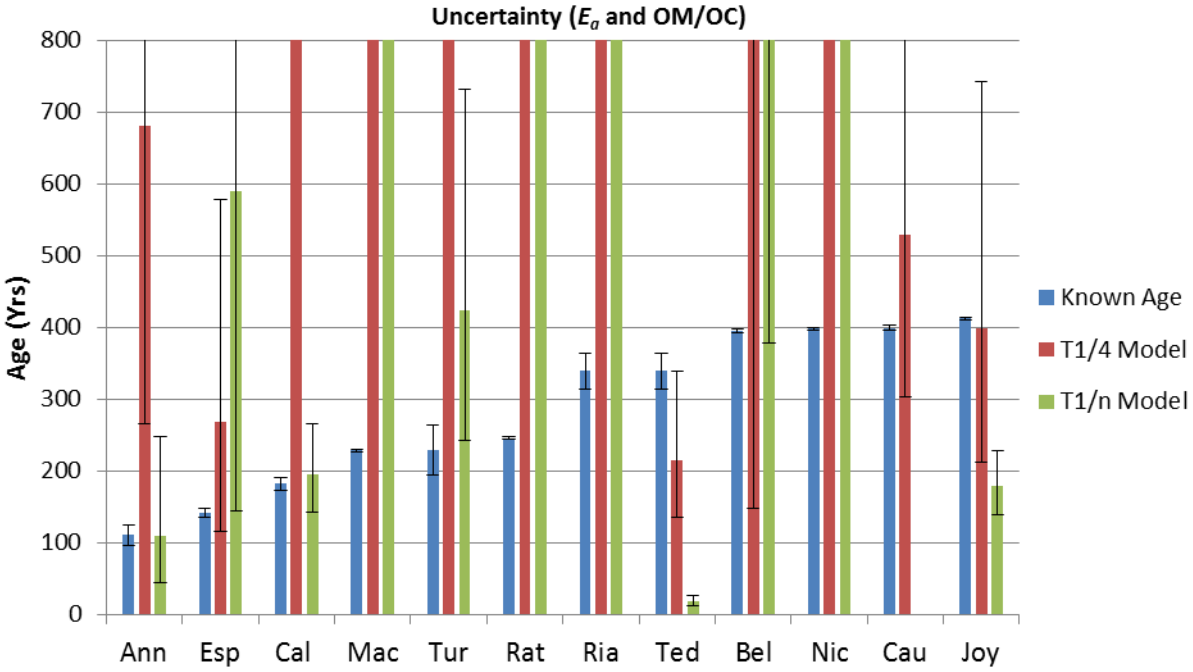

Figure 8.28: Plot of known ages (blue) and age estimates for $t^{1/4}$ model (red) and $t^{1/n}$ model (green) together with age ranges (black error bars) based on E_{aRHX} uncertainties (1σ) and OM/OC ratios (1.4-2.5). Cut-off at 800 years.

The effect uncertainties in the OM/OC ratio and RHX activation have on the age-temperature curves are illustrated with two examples, *Ann* and *Joy*, presented in *Figure 8.29* and *Figure 8.30* (for $t^{1/4}$). It can be observed that the uncertainties become more pronounced at temperatures more distant from the aging temperatures of 25°C, 35°C, 45°C at which experiments were conducted.

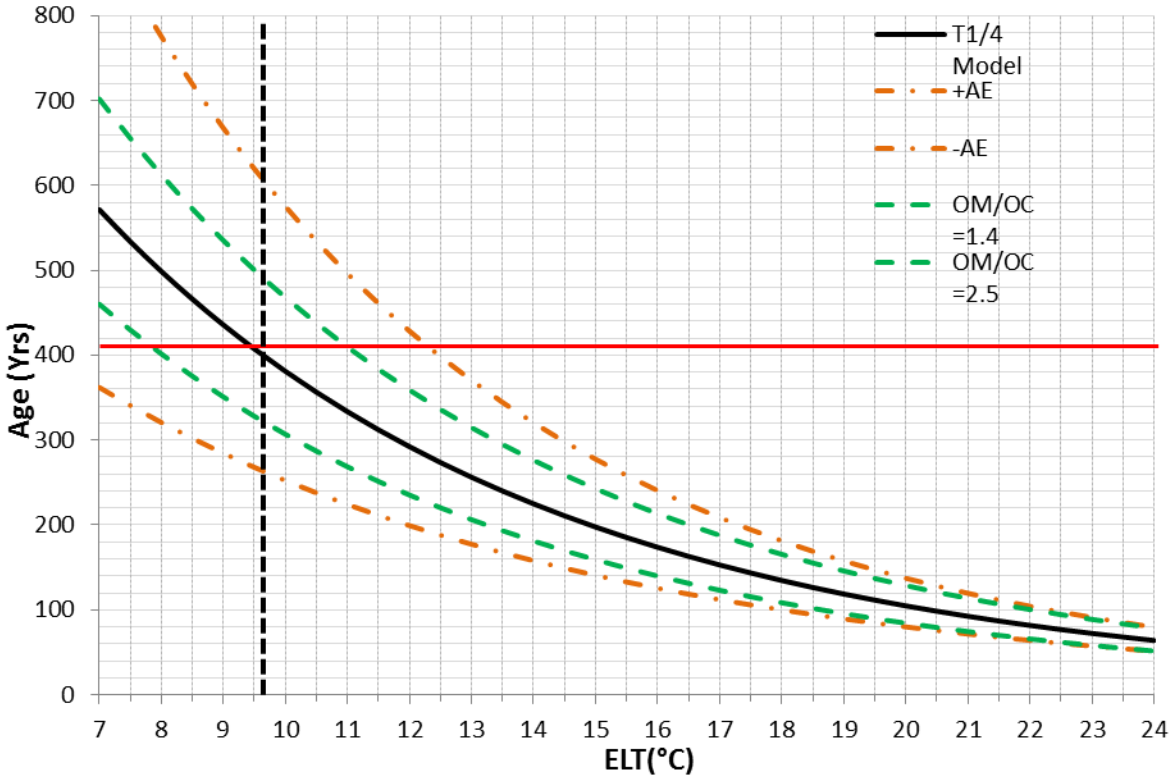

Figure 8.29: Effect of uncertainties in RHX activation energy (1σ, orange/brown dot-dash) and OM/OC ratio (1.4-2.5, green dash) on the age temperature curves of *Joy*.

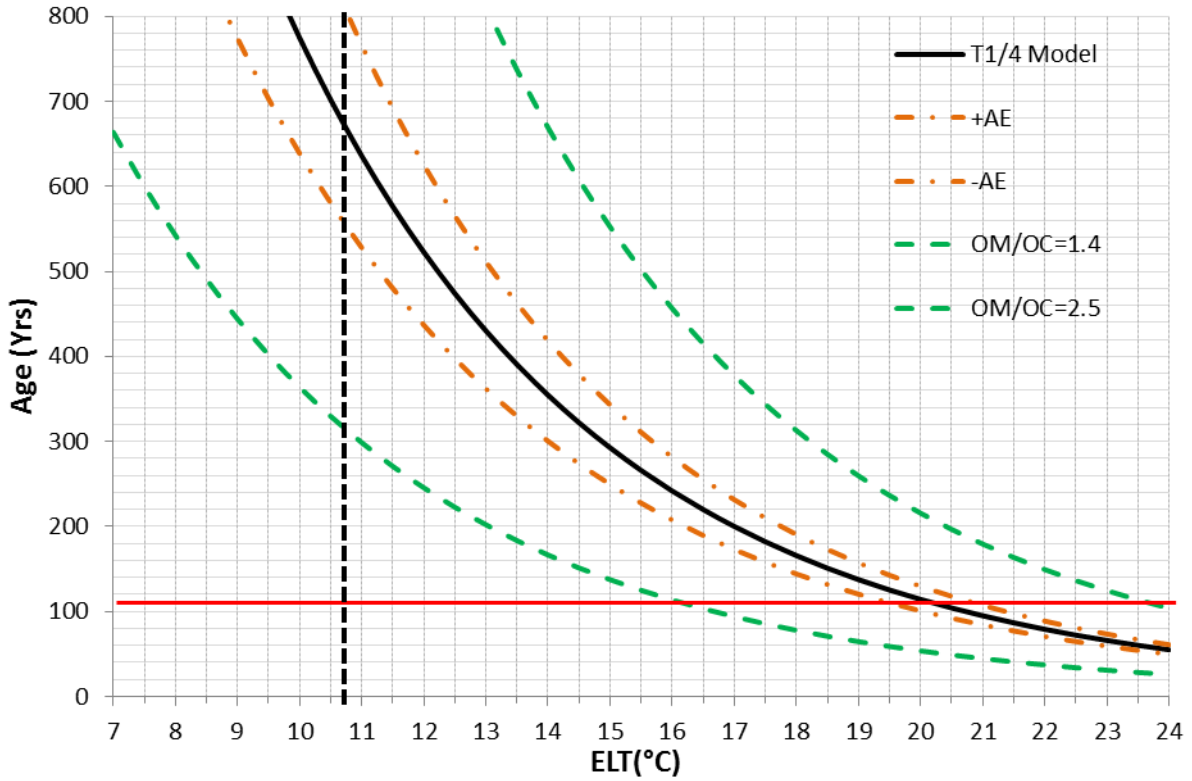

Figure 8.30: Effect of uncertainties in RHX activation energy (1σ, orange/brown dot-dash) and OM/OC ratio (1.4-2.5, green dash) on the age temperature curves of *Ann*.

The age and age range estimations produce mixed results when compared with the known ages. The results are summarised in the following points and will be dealt with in detail in the *Discussion*:

- 12/18 samples were used to calculate dates.
- 8/12 samples produce a *feasible** age using $t^{1/4}$ **OR** $t^{1/n}$.
- 5/8 samples provide agreement **ONLY** for $t^{1/4}$.
- Of 5/8 ($t^{1/4}$):
    - 4/5 work **ONLY** within the OM/OC uncertainty range (*Esp, Joy, Cau, Bel*).
    - 1/5 work **ONLY** within the RHX activation energy uncertainty range (*Joy*).
    - 5/5 work within activation energy **AND** OM/OC range (*Esp, Joy, Cau, Bel, Ted*)
    - 2/5 have good T_w (*Joy, Cau*)
    - 2/5 have plausible T_w (*Esp, Ted*)
    - 1/5 unreasonable T_w (*Bel*)
- Of 3/8 ($t^{1/n}$)
    - 2/3 work within OM/OC range **AND** AE range (*Ann, Cal*)
    - 1/3 **ONLY** works within full uncertainty range (OM/OC and E_{aRHX}) (*Tur*)
    - 2/3 have good T_w (*Ann, Cal*)
    - 1/3 have plausible T_w (*Tur*)

*Feasible: age range estimate (under conditions of uncertainty in OM/OC, RHX activation energy, or both) falls within limits of known age.

8.4.3 Mass Discrepancies and Relationships

To examine the large discrepancies in many of the estimated ages, the discrepancy between m_{RHX} and m_{sim}, m_{out} was considered as the most likely source. This discrepancy, when expressed as a percentage of the total fractional mass, m_{RHXC}, or the RHX fractional mass, m_{RHX}, is considerable, *Figure 8.31* and *Figure 8.32*. The mass discrepancy, m_{out}, was examined against m_{lw} and m_{om} to see if it might be linked to any systematic errors in their calculation that might lead to miscalculations of m_{RHX}. The relationships are presented in *Figure 8.33* and *Figure 8.34,* and it is clear that there are no statistically significant correlations (the null hypothesis can not be rejected for any case).

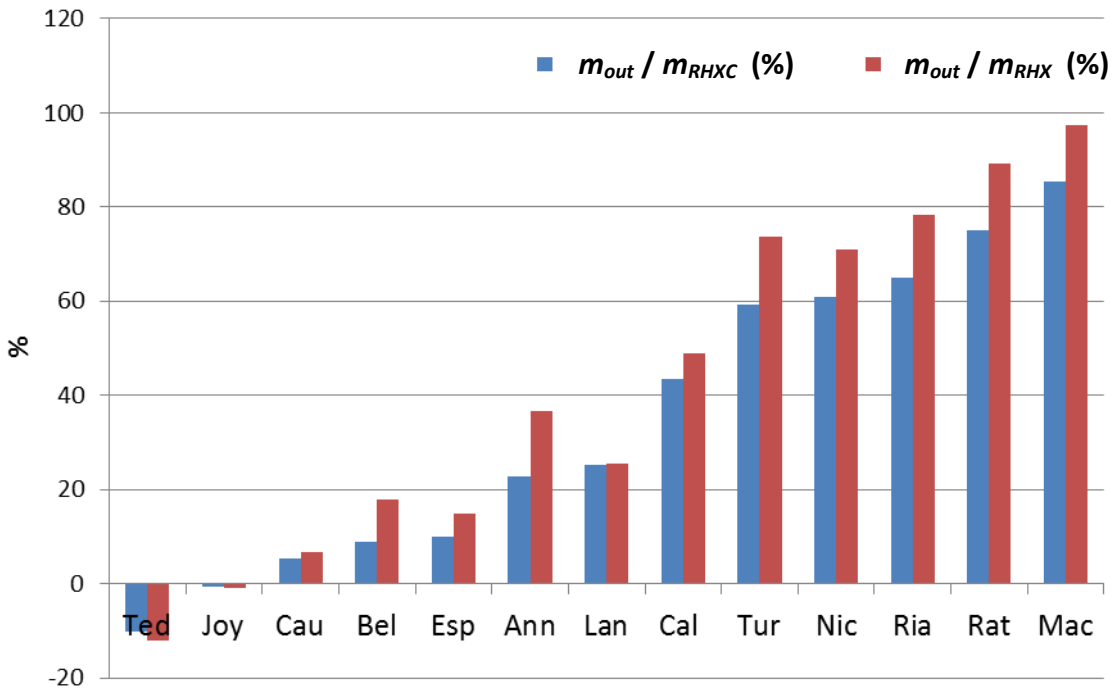

Figure 8.31: For $t^{1/4}$ model the mass discrepancy, m_{out}, as a percentage of the RHX fractional mass (red), m_{RHX} , and the total fractional mass (blue), m_{RHXC} .

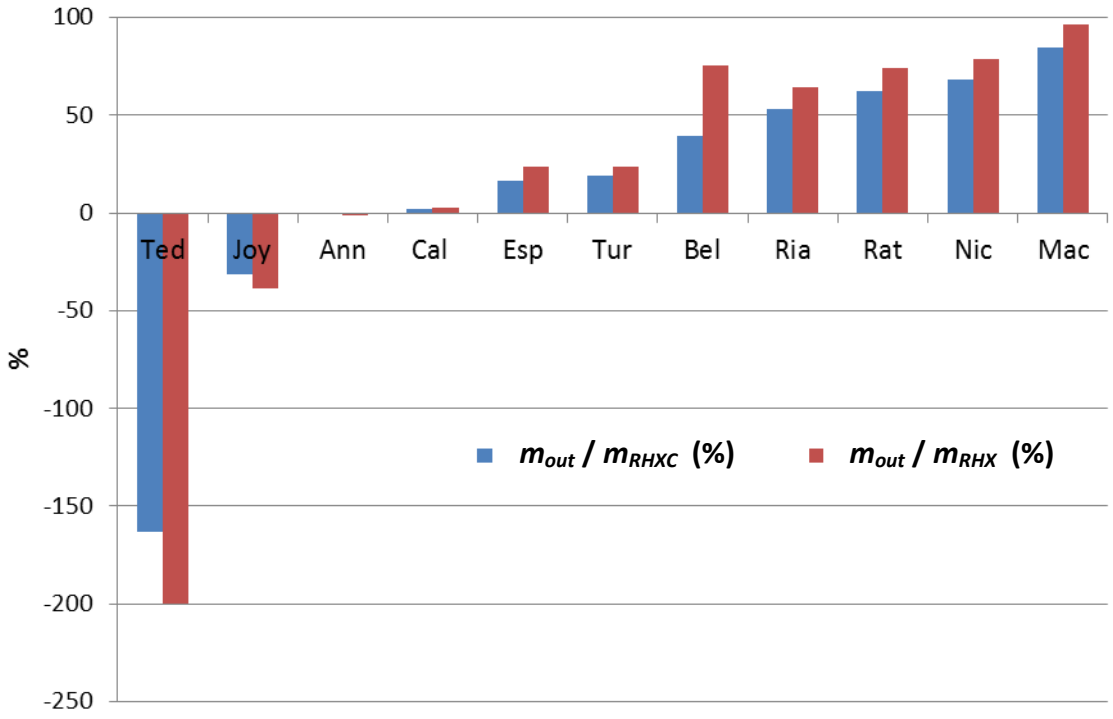

Figure 8.32: For $t^{1/n}$ model the mass discrepancy, m_{out}, as a percentage of the RHX fractional mass (red), m_{RHX} , and the total fractional mass (blue), m_{RHXC} .

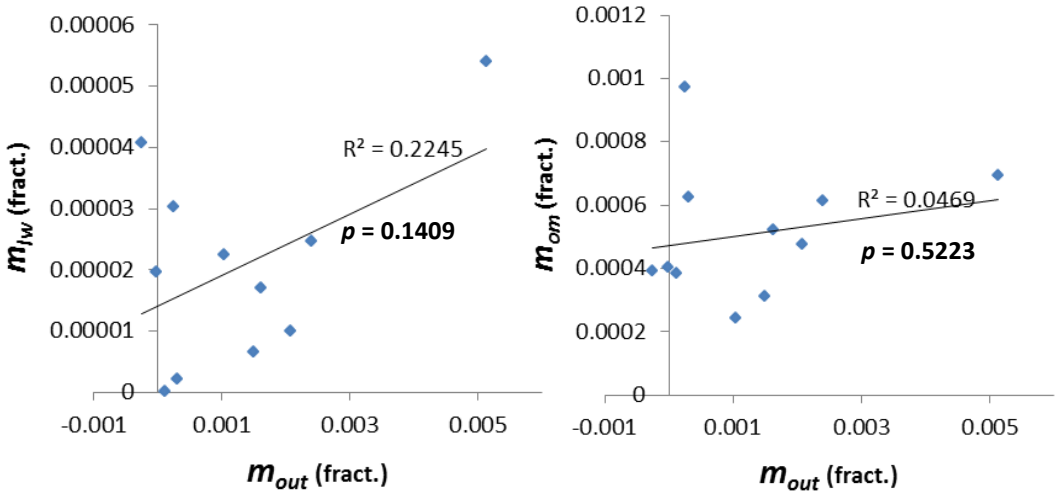

Figure 8.33: Plots of the mass discrepancy versus the estimated loose water removed, m_{lw}, and the estimated organic matter removed, m_{om}. For the $t^{1/4}$ model.

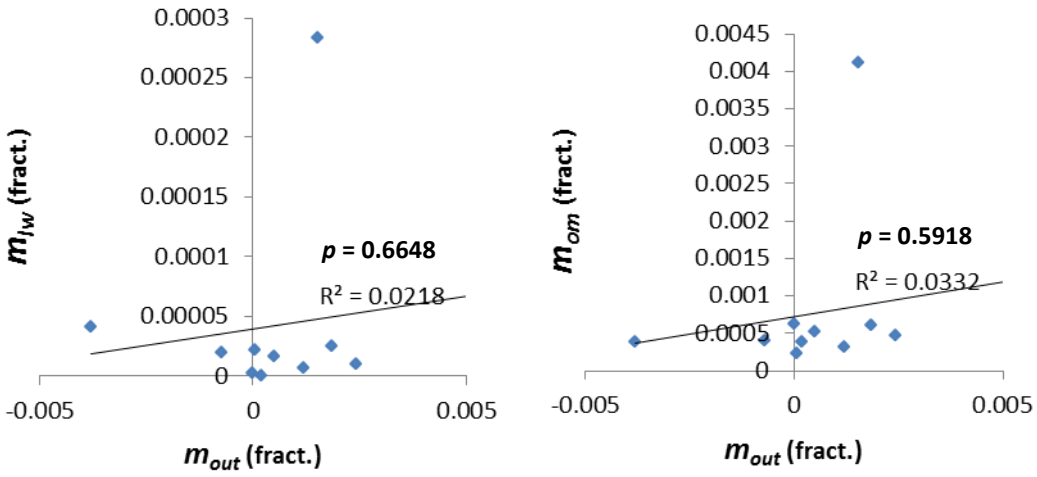

Figure 8.34: Plots of the mass discrepancy versus the estimated loose water removed, m_{lw}, and the estimated organic matter removed, m_{om}. For $t^{1/n}$ model.

8.5 Short Term Elevated Temperature Events (STETEs)

8.5.1 STETE Effects

Possible sources of 'additional' mass, above that expected for mass gain at ELTs are STETEs, such as cooling of a brick after firing or repeated heating and cooling of a pot during cooking. To examine the effect of STETEs on the calculated dating ages, simulations were run comprehensively for the $t^{1/4}$ model only; preliminary tests were carried out for the $t^{1/n}$ model, mentioned later in *Section 9.4.2,* but because the activation energies for this approach are substantially lower than for the $t^{1/4}$ model the effects of STETEs were significantly less (near negligible) for most samples.

For the simulations, the effects were additive, i.e. built onto the sequence of previous effects. The sequence was carried out for moderate and strong conditions, as described in *Section 6.7.3*. The cumulative mass gain values from simulations are presented in *Table 8.10*.

The potential extra age, t_{stete}, caused by the extra mass gain, m_{stete}, of these events are presented in *Table 8.11,* with the age the dating calculations were out by (*Section 8.3*), t_{out}, included for comparison. The additional quantities these effects would raise the ELTs by, T_{stete}, are provided in *Table 8.12* with the difference between the working temperature and ELT from dating calculations, T_{out}, included for comparison also.

It can be observed from *Table 8.11* that, in terms of the order of magnitude of the age effects, there are strong similarities between the STETE effects and discrepancies in the dating calculations. This is further supported by plotting $log_{10}(t_{out})$ against $log_{10}(t_{extra})$ and carrying out a linear regression which produce moderately strong correlations of R^2 = 0.83 (*moderate* and *strong* case)[1].

[1] A linear relationship produced from a regression on the log values of t_{out} and t_{extra} is equivalent to: $t_{extra} = a t_{out}^{m}$, where $a = 10^{C}$, m = slope, C = intercept, both obtained from the linear regression on the *log* values. Therefore where $m \rightarrow 1$, $t_{extra} = a t_{out}$. In the case of plots discussed, $m = 1.09$ and 1.14

Also clear from the tables is the strong relationship between the activation energy and the magnitude of STETE effects; for activation energies under 100kJ/mol, the effect is minor for most STETE events. The effect of the different events (brick cooling, heat cycling, etc.) will be taken up in the *Discussion.*

Table 8.10: STETE – effects on simulated mass gain using *moderate* (Mod.) and *strong* (Str.) conditions. m_{sim} = simulated mass gain over lifetime of ceramic using temperature history. BC (80) = Brick Cooling (80=max. RHX temp.). 2d60=2 days heating at 60°C. 15d77=15 days at 77°C. 60c80=60 heat/cool cycles with max. temp of 80°C. m(dur_ELT)=additional mass gained over the duration of the STETE effects but at the ELT. m_{stete}=additional mass gain due to STETE effects. All masses are fractional.

Mod.	m_{sim}	m_{sim} +BC (80)	m_{sim} +BC (80) +2d60	m_{sim} +BC (80) +2d60 +15d77	m_{sim} +BC (80) +2d60 +15d77 +60c80	m_{sim} + m(dur_ELT)	m_{stete}
Ann	0.0006464	0.0006477	0.0006776	0.0012806	0.0012862	0.0006468	0.0006395
Esp	0.0006541	0.0006541	0.0006550	0.0006772	0.0006777	0.0006544	0.0000233
Nic	0.0008518	0.0009483	0.0013498	0.0049801	0.0050069	0.0008521	0.0041548
Mac	0.0001333	0.0007382	0.0009594	0.0050066	0.0050448	0.0001334	0.0049114
Ria	0.0006647	0.0006800	0.0008245	0.0025139	0.0025265	0.0006649	0.0018616
Rat	0.0001833	0.0001902	0.0002445	0.0007886	0.0007926	0.0001833	0.0006092
Cal	0.0010891	0.0010892	0.0010910	0.0011393	0.0011403	0.0010896	0.0000507
Joy	0.0021678	0.0021679	0.0021704	0.0022423	0.0022437	0.0021686	0.0000751
Cau	0.0034300	0.0034302	0.0034384	0.0037141	0.0037191	0.0034313	0.0002878
Bel	0.0036623	0.0036623	0.0036630	0.0036663	0.0036664	0.0036636	0.0000028
Tur	0.0005770	0.0005806	0.0006395	0.0015536	0.0015609	0.0005772	0.0009837
Ted	0.0023963	0.0023965	0.0024038	0.0026623	0.0026667	0.0023972	0.0002695
Str.	m_{sim}	m_{sim} +BC (95)	m_{sim} +BC (95) +2d60	m_{sim} +BC (95) +2d60 +15d79	m_{sim} +BC (95) +2d60 +15d79 +60c95	m_{sim} + m(dur_ELT)	m_{stete}
Ann	0.0006464	0.0006529	0.0006822	0.0012813	0.0013011	0.0006468	0.0006544
Esp	0.0006541	0.0006541	0.0006551	0.0006806	0.0006810	0.0006544	0.0000267
Nic	0.0008518	0.0014678	0.0016354	0.0055069	0.0056673	0.0008521	0.0048151
Mac	0.0001333	0.0019674	0.0019855	0.0058016	0.0063108	0.0001334	0.0061775
Ria	0.0006647	0.0007894	0.0008932	0.0027441	0.0028034	0.0006649	0.0021385
Rat	0.0001833	0.0002357	0.0002705	0.0008625	0.0008819	0.0001833	0.0006986
Cal	0.0010891	0.0010893	0.0010911	0.0011473	0.0011492	0.0010896	0.0000596
Joy	0.0021678	0.0021680	0.0021705	0.0022552	0.0022582	0.0021686	0.0000896
Cau	0.0034300	0.0034307	0.0034389	0.0037665	0.0037779	0.0034313	0.0003465
Bel	0.0036623	0.0036623	0.0036630	0.0036665	0.0036666	0.0036636	0.0000030
Tur	0.0005770	0.0006024	0.0006560	0.0016740	0.0017013	0.0005772	0.0011241
Ted	0.0023963	0.0023970	0.0024043	0.0027113	0.0027219	0.0023972	0.0003247

Table 8.11: Extra age, t_{stete} , caused by STETE effects, using *moderate* (Mod.) and *strong* (Str.) conditions. t_{out}=number of years calculated dating ages are out by. BC (80) = Brick Cooling (80=max. RHX temp.). 2d60=2 days heating at 60°C. 15d77=15 days at 77°C. 60c80=60 heat/cool cycles with max. temp of 80°C.

Mod.	E_{aRHX} (kJ/mol)	t_{out} (years)	t_{stete} BC (80) (years)	t_{stete} BC (80) +2d60 (years)	t_{stete} BC (80) +2d60 +15d77	t_{stete} BC (80) +2d60 +15d77 +60c80
Ann	132.15	570	0.8	22.8	1584.8	1614.8
Esp	76.61	127	0.0	0.7	20.8	21.2
Nic	204.35	55567	213.6	2112.8	464981.0	475057.0
Mac	294.94	555199181	214176.5	611495.0	453734399.0	467734684.0
Ria	179.31	153481	32.5	463.7	69083.0	70483.0
Rat	182.90	1752185	39.2	531.6	83814.0	85526.0
Cal	83.33	2478	0.0	1.1	35.8	36.6
Joy	89.08	-13	0.0	1.7	59.4	60.6
Cau	99.86	129	0.1	3.6	149.1	152.0
Bel	40.23	469	0.0	0.1	1.5	1.2
Tur	155.34	47823	5.8	116.4	11815.0	12044.2
Ted	103.64	-124	0.1	4.1	177.1	180.5
Str.	**E_{aRHX} (kJ/mol)**	**t_{out} (years)**	**t_{stete} BC (95) (years)**	**t_{stete} BC (95) +2d60 (years)**	**t_{stete} BC (95) +2d60 +15d79**	**t_{stete} BC (95) +2d60 +15d79 +60c95**
Ann	132.15	570	4.5	26.4	1588.4	1696.0
Esp	76.61	127	0.0	0.8	24.0	24.5
Nic	204.35	55567	3112.9	5014.1	695380.0	780032.0
Mac	294.94	555199181	10819208.0	11223588.0	818105403.0	1145421875
Ria	179.31	153481	335.6	767.1	98221.0	107014.0
Rat	182.90	1752185	425.8	918.5	120029.0	131249.0
Cal	83.33	2478	0.1	1.2	42.0	43.5
Joy	89.08	-13	0.1	1.8	70.4	72.9
Cau	99.86	129	0.3	3.9	180.7	187.7
Bel	40.23	469	0.0	0.1	1.6	1.3
Tur	155.34	47823	43.1	153.7	16007.9	17091.2
Ted	103.64	-124	0.4	4.3	216.2	224.9

Table 8.12: Increase in ELT caused by STETE effects, T_{stete}, using *moderate* (Mod.) and *strong* (Str.) conditions. T_{out}= increase in ELT required for successful dating of samples. BC (80) = Brick Cooling (80=max. RHX temp.). 2d60=2 days heating at 60°C. 15d77=15 days at 77°C. 60c80=60 heat/cool cycles with max. temp of 80°C.

Mod.	E_{aRHX} (kJ/mol)	T_{out} (°C)	T_{stete} BC (80) (°C)	T_{stete} BC (80) +2d60 (°C)	T_{stete} BC (80) +2d60 +15d77	T_{stete} BC(80)+2d60 +15d77 +60c80
Ann	132.15	9.5	0.04	0.96	14.57	14.67
Esp	76.61	5.7	0.00	0.05	1.20	1.22
Nic	204.35	17.2	1.42	6.17	25.24	25.33
Mac	294.94	38.1	16.56	19.26	37.52	39.25
Ria	179.31	24.8	0.34	3.25	21.36	21.44
Rat	182.90	36.8	0.55	4.29	23.16	23.24
Cal	83.33	23.2	0.00	0.05	1.44	1.47
Joy	89.08	-0.3	0.00	0.04	1.00	1.02
Cau	99.86	1.9	0.00	0.06	2.12	2.16
Bel	40.23	13.5	0.00	0.00	0.05	0.05
Tur	155.34	25.0	0.11	1.77	18.08	18.17
Ted	103.64	-2.9	0.00	0.08	2.73	2.77
Str.	**E_{aRHX} (kJ/mol)**	**T_{out} (°C)**	**T_{stete} BC (95) (°C)**	**T_{stete} BC (95) +2d60 (°C)**	**T_{stete} BC (95) +2d60 +15d79**	**T_{stete} BC(95)+2d60 +15d79 +60c95**
Ann	132.15	9.5	0.20	1.09	14.58	14.93
Esp	76.61	5.7	0.00	0.05	1.37	1.40
Nic	204.35	17.2	7.33	8.83	26.82	27.27
Mac	294.94	38.1	26.94	27.04	39.25	40.25
Ria	179.31	24.8	2.59	4.48	22.88	23.25
Rat	182.90	36.8	3.74	5.83	24.70	25.09
Cal	83.33	23.2	0.00	0.05	1.67	1.72
Joy	89.08	-0.3	0.00	0.04	1.17	1.21
Cau	99.86	1.9	0.01	0.06	2.58	2.58
Bel	40.23	13.5	0.00	0.00	0.05	0.05
Tur	155.34	25.0	0.74	2.22	19.53	19.85
Ted	103.64	-2.9	0.01	0.08	3.21	3.31

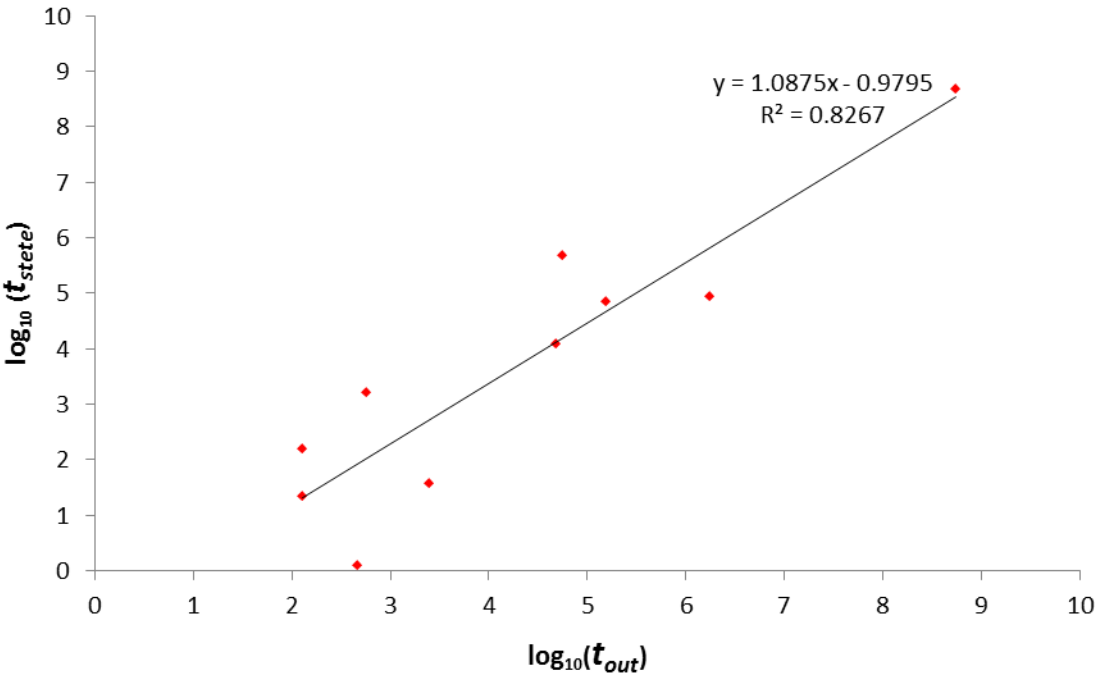

Figure 8.35: For *moderate* STETE conditions, t_{out} (from dating calculation) versus t_{stete} (from STETE simulations) using logarithms for scaling purposes. *Joy* and *Ted* removed because it is not possible to take the log of their negative values.

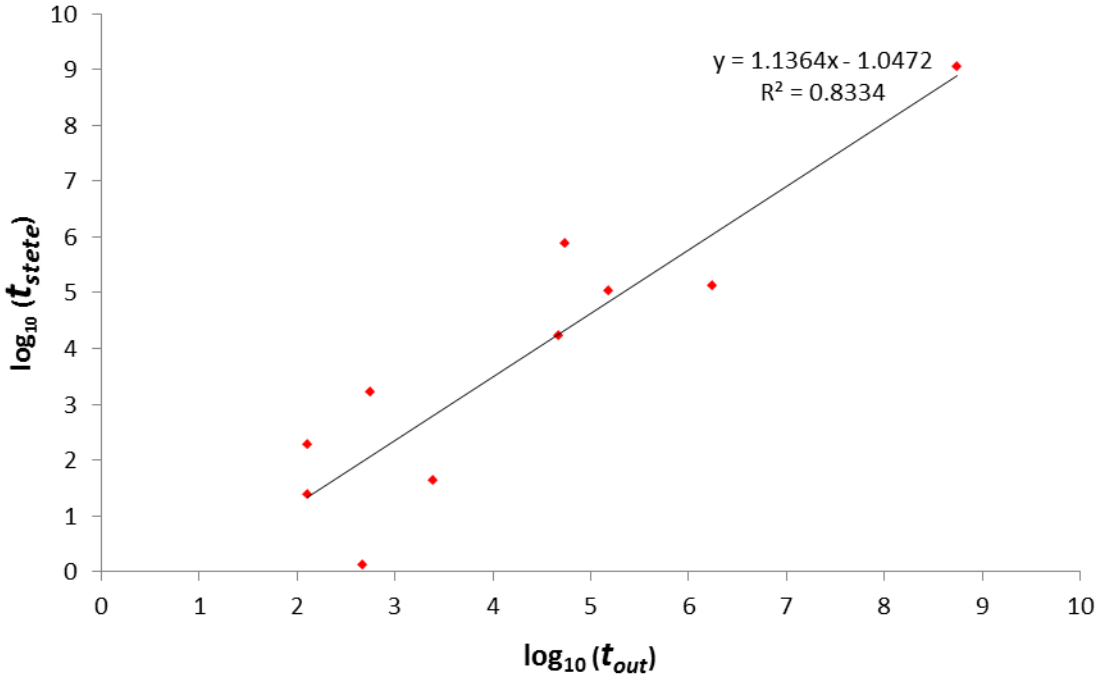

Figure 8.36: For *strong* STETE conditions, t_{out} (from dating calculation) versus t_{stete} (from STETE simulations) using logarithms for scaling purposes. *Joy* and *Ted* removed because it is not possible to take the log of their negative values.

8.5.2 STETE Dating Corrections

The dating estimates were re-calculated after subtraction of the mass gain associated with STETE effects, m_{stete}, from the RHX mass, m_{RHX}. This was carried out for both STETE conditions, *moderate* and *strong*. The corrected ages and new set of working conditions are presented in *Table 8.13* (again this was carried out only for the $t^{1/4}$ model). Values for *Nic* were not possible because of the magnitude of m_{stete} being greater than m_{RHX}, and similarly for the *strong* condition with *Mac*.

Table 8.13: Table of corrected ages, working OM/OC and working ELT values for samples following STETE correction under *moderate* (*mod.*) and strong (*str.*) conditions. Bold = reasonable working condition. Bold and italicised = Plausible/borderline working condition.

	Known Age (Years)	t_{age} (Years)	STETE Corrected Age (Years) (*Mod.*)	STETE Corrected Age (Years) (*Strong*)	OM/OC_w (*Mod.*)	OM/OC_w (*Str.*)	T_w (°C) (*Mod.*)	T_w (°C) (*Str.*)
Ann	110	680	13	11	**1.2**	**1.1**	0.9	0.1
Esp	141	268	237	232	**2.4**	**2.4**	**14.2**	**14**
Nic	398	55965	-	-	-	-	-	-
Mac	228	555199409	11373	-	**2.58**	-	20.8	-
Ria	339	153820	3671	1293	***3.65***	**2.77**	***19.5***	***15.5***
Rat	245	1752429	291160	205830	7.56	7	39.5	38
Cal	182	2660	2415	2374	9.9	9.9	31.8	32
Joy	412	399	345	336	**1.5**	**1.45**	**8.4**	**8.2**
Cau	399	528	382	356	**1.9**	**1.74**	**9.1**	**8.6**
Bel	395	864	862	861	**2.32**	**2.32**	22	22.1
Tur	229	48052	4461	2726	***4.3***	***3.75***	22.6	20.5
Ted	339	215	125	111	<1	<1	4.4	3.6

For corrected samples 7/12 can be said to work under reasonable values of OM/OC_w with a further 1/12 sample borderline (*Tur*). For T_w, 3/12 samples can be considered as having reasonable temperatures, with a further 1/12 being plausible (*Ria*). Again these are considered with the other variables (ELT, OM/OC) fixed and combinations of variation of the two may permit some further improved results. For example, for *Ted*, with OM/OC=1 and T=8.5°C the calculated age, 314 years, falls within 339±25 years.

8.6 Activation Energy Temperature History (AETH) Example

The *AETH* curves generated for *Joy* are presented in *Figure 8.37*. An idealised m_{RHX} is used to illustrate how the approach would work. The curves are generated from experimental data. In this example the estimated age of the sample would be AD1602 or, if the confidence bounds are considered, AD1540-1655, using an intercept approach.

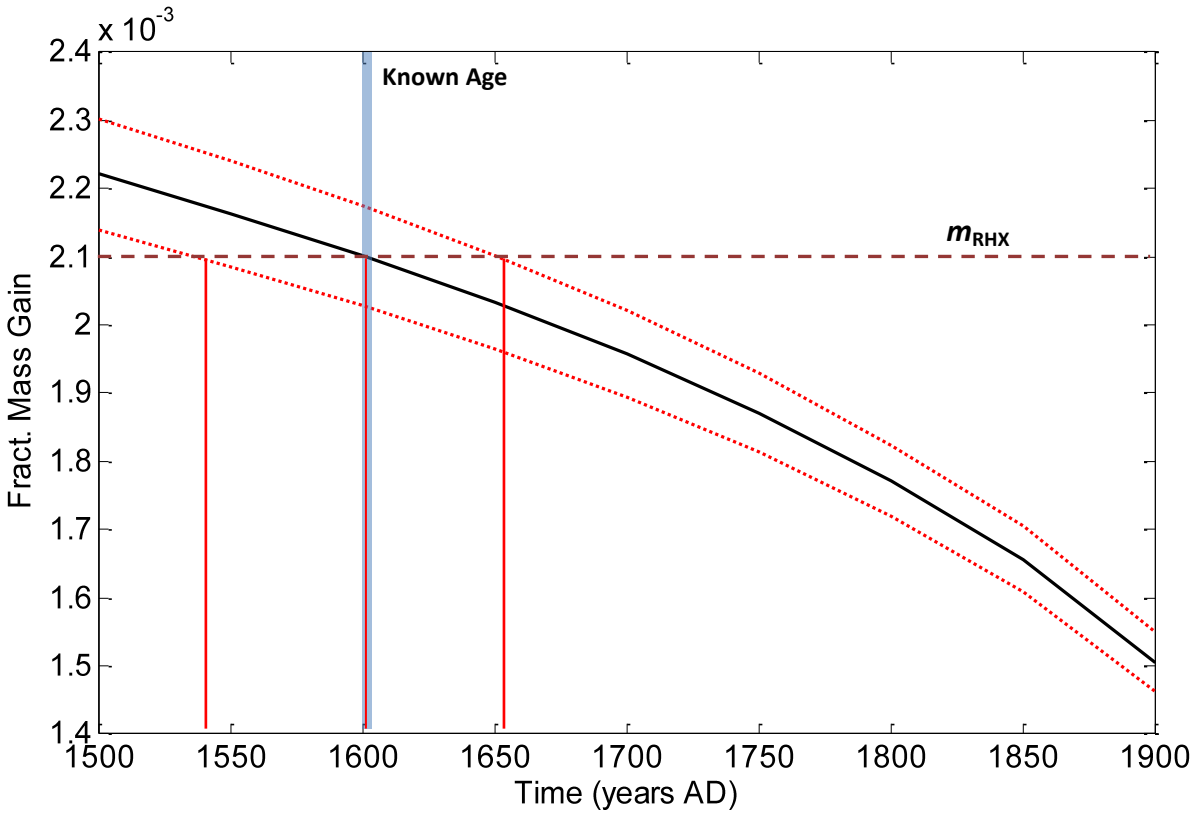

Figure 8.37: *AETH* curve generated for *Joy*, using $E_{\alpha RHX}$ = 89±12 kJ/mol (1σ) and α_{25} = 7.9865x10^{-5} (1/hrs$^{1/4}$). Upper and lower bounds are based on curves generated using the 1σ upper and lower bounds of activation energy as well as the 1σ upper and lower bound temperature history curves. Superimposed are the known age of the sample (blue) and an idealised m_{RHX} to highlight how the approach would work.

Chapter 9

Discussion

9.1 Introduction

This chapter will be divided into subsequent sections that examine and discuss the findings of the non-RHX characterisation results, the RHX behaviour results, and the RHX dating results.

Non-RHX characterisation, discussed in *Section 9.2*, will deal with the results of *Chapter 5*, and will convey the key findings and the significance of these in relation to RHX behaviour and dating. Issues surrounding these findings and their interpretation will also be debated.[1] The discussion will generally be restricted in scope to those findings that stand alone within the context of the suite of non-RHX experiments, with some other non-RHX characterisation results discussed in relation to RHX behaviour and dating results only in later sections.[2]

The RHX behaviour discussion, *Section 9.3*, will examine how well the RHX behaviour results of *Chapter 7* (in consideration of the non-RHX and Dating results of *Chapter 5* and *Chapter 8*) validate key RHX properties required for dating, and present new findings of relevance to understanding the mass gain behaviour of fired clays and its application to the dating of ceramics. The section will look at the overall mass gain behaviour first, then the *Stage 1* and *Stage 2* behaviours in more detail.

[1] This section will only deal with characterisation results that are deemed to have significance in relation to understanding of the RHX behaviour and dating technique; for example the complete mineralogical, elemental and petrographic results contain a broad spectrum of information useful for other angles of research, for example the nature of post-medieval brick production in Ireland, yet only a subset of these results, of relevance within the scope of this thesis, will be elaborated upon.

[2] Where a finding requires consideration of both non-RHX and RHX experimental results, this will be withheld and discussed in subsequent RHX behaviour and dating sections, *Section 9.3* and *Section 9.4*.

The dating results will be discussed in *Section 9.4*. It will examine how well the component based approach worked for both models, the factors affecting/limiting the method, and the implications the work has for RHX as a dating technique. As well as these, the use of age-temperature curves and the *AETH* approach will be discussed.

9.2 Non-RHX Characterisation

9.2.1 Findings, Implications and RHX Significance

Firing Temperature

The results from XRD, FTIR and petrography suggest that all samples, with the exception of *Etr* and *Rom,* were likely fired at temperatures exceeding 850°C; this is indicated by the presence of high-temperature mineral phases (e.g. cristobalite, spinel, gehlenite), *Figure 2.10,* in the XRD and FTIR data, *Table 5.8*, as well as the presence of an isotropic matrix, indicative of the breakdown of the clay minerals, and degraded minerals such as feldspars and micas, both indicative of temperatures > 800°C, in the petrographic analysis, *Table 5.11* (Quinn 2013). Many of the samples (*Nic, Mac, Ria, Rat, Cal,* and *Tur*) also present petrographic evidence of bloating, sintering and vitrification, suggesting temperatures > 1000°C (Quinn 2013). Therefore, it is likely that the all samples, *Etr* and *Rom* excluded, underwent considerable, if not complete, dehydroxylation of the clay minerals present, described in *Section 2.3*.

The samples *Etr* and *Rom* presented little evidence of high-temperature mineral phases in the XRD and FTIR data. Under microscope, the matrix was moderately optically active, suggesting complete dehydroxylation had not occurred (Quinn 2013), but there was some evidence of calcite breakdown which might imply temperatures exceeding 650°C were attained, *Section 2.3*.

Heating at 500°C – Mineralogical Changes

The differences between the reheated (500°C) and non-reheated (dried at 130°C) XRD and FTIR spectra, *Table 5.3* and *Table 5.6,* respectively, are negligible or associated with sample variation (*Etr*) for all samples, with the exception of *Mac* and *Bel*. This implies that reheating does not significantly alter the mineralogy in any detectable way. No notable differences were observed in the p-XRF data either, *Section 5.6*.

For *Mac* and *Bel,* the changes are associated with the presence and dehydration of hydrated calcium sulfates (gypsum $CaSO{\cdot}2H_2O$, bassanite $CaSO{\cdot}0.5H_2O$) to anhydrite (*CaSO)*, that occurs in the temperature range 120-160°C (Dunham 1992). For *Mac* and *Bel,* the presence of gypsum was also detected, precipitated in the pores, by petrography, *Table 5.11*, with sulphur, *S*, detected in the p-XRF, *Table 5.12*, and the emission of SO_2 at temperatures exceeding 650-700°C, attributable to gypsum decomposition, in the TG-MS data, *Table 5.19* The significance of the presence of gypsum on the mass gain behaviour and dating results will be returned to.

Also of note is that no mineralogical changes associated with goethite dehydroxylation, *Section 2.3*, were observed and, hence, no related mass loss issues (Burakov and Nachosova 2013).

Calcium Carbonate (Calcite) Presence

It is possible, using XRD, FTIR, petrography or TG-MS, to identify the presence of calcium carbonate in all samples, except *Mac*. In the XRD and FTIR data, *Table 5.8,* calcite is detected in all samples except *Ann, Esp, Mac, Joy* and *Bel*; however, using petrography, low levels and traces of calcite were additionally observed for *Ann, Joy* and possibly *Esp*, *Table 5.11*. The presence of carbonates in all samples, with *Mac* a likely exception, is also demonstrated by the occurrence of well-defined CO_2 peaks in the temperature range 580-750°C associated with carbonate decomposition, *Section 2.3*. This peak is also distinct from a lower CO_2 structure associated with organics, discussed below. The reasons for the carbonates not being detected in

the XRD and FTIR for certain samples appears to be related to its very low levels; in the TG-MS curves, *Appendix C,* the ratios of the magnitude of the carbonate peak to that of the organics (300-500°C) for samples *Ann, Esp,* and particularly *Bel* (not observed in XRD, FTIR or petrography) are very low when compared to samples that were easily detected using XRD and FTIR, e.g. *Etr, Rom, Por*. The very low presence and absence of calcite in *Mac* and *Bel,* respectively, might be explained by the presence of gypsum in these two samples, which can be produced by the reaction of sulphuric acid and calcite during weathering (Prentice 1990).

The magnitude and nature of the carbonates present are also of interest. From XRD, the samples with the highest levels are *Etr, Rom, Por, Dow1* and *Dow2*, in the range 1-10%, *Table 5.1*. Significant levels are also strongly detected in the FTIR spectra of these samples, *Table 5.5* and are reflected in a high CaO content (6-15%) based on p-XRF analysis, *Figure 5.19*. The nature of the calcite can be examined by looking at the petrography notes, *Table 5.11*, the p-XRF results for CaO, *Figure 5.19*, and the TG-MS carbonate peak location, *Table 5.19*. The samples with a strong XRD calcite presence appear to be more likely to have a either a strong occurrence of primary calcite (in obvious mineral blocks or shells), *Table 5.11*, as for example with *Rom* and *Etr*, or are likely to result from the firing of a calcareous clay (*Por, Dow1, Dow2*), *Table 5.11* (evident also in a high *CaO* level*, Figure 5.19,* and a yellow/beige/white colour unique to these samples and associated with calcium rich clays (Rice 1987; Prentice 1990)). The TG-MS data, *Table 5.19*, suggests that the carbonate decomposition, *Event G,* occurs over a range of temperatures, 580-750°C, but may be split into two regimes, 570-660°C and 710-750°C, with the latter composed of the group *Etr, Rom, Por, Dow1* and *Dow2*, the same samples that have high calcite compositions. It has been shown (Shoval et al. 1993; 2003) that the decarbonation process can occur at temperatures higher than 750°C for monocrystalline calcite, and at lower temperatures than 650°C for more polycrystalline (sparitic/micritic) material. Therefore, it might be inferred that the samples that display high calcite composition and fall into the decarbonation regime 710-750°C may be samples that either a) had significant primary calcite (monocrystalline) pre-firing and underwent firing at insufficiently high temperatures

for decomposition to occur (*Etr, Rom*) or b) had significant levels of primary calcite pre-firing, such that despite firing at high enough temperatures for the formation of high temperature mineral phases, total carbonate decomposition did not take place (*Por, Dow1, Dow2)*; *Dow1* and *Dow2* had exceptionally high *CaO* content (14.6% and 15.4%, with *Nic, Etr, and Por* next highest on 9.9%, 9.72% and 9.4%), *Figure 5.19*, potentially aiding the survival of some primary calcite. For the samples *Por, Dow1* and *Dow 2,* the calcite observable under microscope was at best sparitic/micritic in appearance and often appeared to be imbedded in the matrix of the ceramic (for these samples the clays used were fine and pores were generally not large enough to be observed clearly under microscope and to discern a primary/secondary nature to the calcite). In any case, there appears to be some connection between the high decarbonation temperature and the nature of the high calcium carbonate samples.

It also follows that the samples in the TG-MS regime 570-660°C are more likely to be composed of sparitic/micritic calcite. Indeed, half of all samples, not including the high calcite samples above, almost exclusively contained micritic calcite (very fine grains that appears almost like a sparkling powder) which may be either primary, if the result of recrystallization of samples originally decomposed during firing, see *Section 2.3*, or secondary, e.g. if carried in by groundwater. For some samples (*Esp, Nic, Ted, Cal, Lan, Joy, Tur, Ted*) secondary calcite seems very likely with its presence in pores particularly obvious for certain samples, i.e. *Ted, Nic, Esp*. For the remaining samples, where not in clear mineral form or a calcareous clay, it is perhaps safest to assume that a mixture of primary and secondary calcite is present.

The significance of the above calcite related discussion will be returned to later in the discussion.

Carbon Content

The carbon content was significant for all samples, regardless of the context the samples were retrieved from, *Table 5.18*, varying from 0.0035 – 0.5198 %wt. It is worth noting that the highest levels were obtained for the samples *Por, Etr, Bel,*

Dow1, Dow2, Rom, Cau (0.52-0.05 %wt) and this will be returned to later. From the TG-MS, *Table 5.19* and *Appendix C*, it is clear that at heating temperatures from 200-300°C mass loss associated with CO_2 removal occurs, *Event E,* corresponding to commencement of the removal of organics, *Section 2.3*. This removal appears to peak or plateau in the range 400-500°C, *Event F*, however is not complete until higher temperatures. This is supported by the FTIR data, *Figure 5.9-5.12* and *Table 5.7,* where the presence of organics peaks in region 2800-3000cm^{-1} is still strongly detected even after reheating of powdered samples (<63µm) at 500°C for 18 hours. This is an area of concern for RHX dating where it is essential that the carbon removed during heating at 500°C equates to that measured as part of carbon content analysis.

From the FTIR identification in the region 3000-2800cm^{-1}, four main bands are identified as present in both the non-reheated and reheated samples, *Table 5.7* and *Figure 5.9-5.12.*[3] A possible band at 2860-2870cm^{-1}, present only in the non-reheated sample of *Figure 5.11* and *Figure 5.12,* appears to be only an effect of the broad absorption band ranges assigned to samples in *Figure 5.9* and *Figure 5.10* because of uncertainty in the peak; therefore, this peak is not real. The remaining four peaks, summarised below in *Table 9.1,* together with infrared bond assignments and organic source interpretations, are made up of the dominant bands, 2845-2860cm^{-1}, 2920-2930cm^{-1}, and 2950-2975cm^{-1} and a lesser band at 2870-2890cm^{-1}. These bands are identified as due to bonds associated with organic matter (CH bonds), specifically aliphatic stretching and bending bonds, *Table 9.1* (identified using Larkin 2011). According to Larkin (2011) the aliphatic stretching bonds often appear as a pair of doublets (in phase, out of phase) and it appears that two sets of doublets are observed in the present work, *Table 5.1,* one associated with *R-*CH_3 stretching and the other associated with *R-*CH_2*-R* (*R* is an unspecified group/molecule attached).

Possible organic sources are included in *Table 9.1* together with references for their identification at these bands; however, no source could be assigned to the band at

[3] This region of CH absorption was selected because it is absent of mineral interference and not subject to the subjectivity issues associated with other regions and discussed by Reeves (2012).

2870-2890cm^{-1} and the source for the remaining bands is by no means certain. The organic matter in soils is often characterised by a double absorption band at 2855cm^{-1} and 2930cm^{-1} (e.g. Madari et al. 2006; Vergnoux et al. 2011; Reeves III 2012), yet with no peak at 2950-2975cm^{-1} identified by these authors. Fernandes et al. (2010) provide FTIR spectra of the organic matter, humic and fulvic, in some soils and peats; again the double peak at 2855 cm^{-1} and 2930 cm^{-1} is evident yet any peak at 2950-2975cm^{-1} is absent. Chen et al. (2012) carried out FTIR on a suite of coals varying from peat to anthracite and again the double peaks at 2857cm^{-1} and 2927cm^{-1} were observed without any third peak apparent (this is supported by similar work by Tian et al. 2010). In this regard, the strong triplet of peaks observed in this study may be more characteristic of a triplet of peaks identified by van der Marel and Beuterspacher (1976) at 2950cm^{-1}, 2920cm^{-1}, and 2850cm^{-1}, found in peat, black peat, brown coal, lignite, hard coal and bitumen. The presence of substances derived from the peat-to-anthracite formation group is certainly possible for raw clays (Dunham 1992), yet it seems unlikely, given the high firing temperatures interpreted for most of the samples, that much, if any, of these substances would survive firing. It is conceivable that in a reduced (oxygen deprived) firing environment within the kiln (or even within the brick) carbon-rich coke may have been produced and that the major absorption triplet observed in the data could be explained by similar triplet of peaks at 2860cm^{-1}, 2930cm^{-1}, and 2970cm^{-1}, observed in coke (Guisnet and Magnoux 2001). The use of coke as a fuel in the firing of bricks (in clamps and kilns) is/was not uncommon (Hammond 1981; Brunswick 1990; Pavía and Bolton 2000) and this could also be a source of contamination, particularly post-firing.

From the above, it can not be clarified whether the source of the organics is humic-related substances or derived from part of the peat-to-anthracite formation pathway. From TG-MS, the organics are predominantly being burnt off at temperatures well below the original firing temperature, i.e. less than 500°C and certainly not above 800°C, suggesting that the source of organics removed during the RHX methodology are more likely to be post-firing contamination from burial or air-borne/rain precipitated processes, presumably humic-related substances. That

the source of organic matter is likely to be post-firing contamination may be supported by findings from BET analysis, discussed later.

Wavenumber cm^{-1} (n=non-reheated,r=reheated)	**IR bond Assignment (Larkin 2011)**	**Suspected/Potential Source Organic**	**Reference**
1. Peak =2854 (n,r) Range=2845-2860	Aliphatic R-CH_2-R Stretching (in phase)	Humic/Fulvic Acids Peat-Anthracite (coke)	Vergnoux et al. 2011 Reeves III 2012 Madari et al. 2006
2. 2880 (n,r) 2870-2890	Aliphatic R-CH_3 Stretching (in phase)	Not Clear	--
3. 2925 (n,r) 2920-2930	Aliphatic R-CH_2-R Stretching (out of phase)	Humic/Fulvic Acids Peat-Anthracite (coke)	Vergnoux et al. 2011, van der Marel et al. 1976 Reeves III 2012 Madari et al. 2006
4. 2960,2970 (n,r) 2950-2975	Aliphatic R-CH_3 Stretching (out of phase)	Hard Coal, Brown Coal, Coke	van der Marel et al. 1976 Guisnet and Magnoux 2001

Table 9.1: Table of main FTIR peaks associated with organic matter, together with IR bond assignments, possible organic matter source, and associated references.

Specific Surface Area and Pore Volume

The specific surface area varied considerably, *Figure 5.21*, within the set of samples, from extremely low, for example *Rat* for which sufficient adsorption did not take place to estimate the surface area, and *Tur,* with a value of 0.09m^2/g, to a very high value for *Lan* of 24.25m^2/g. The highest values are obtained for the samples, in order of magnitude, *Lan, Dow1, Dow2, Por, Etr, Cau, Rom*, *Bel* (24.25, 16.33, 15.51, 14.87, 14.73, 6.14, 5.12, 3.64, respectively (m^2/g)) and this ordering of the samples is very similar in the pore volume (BJH) estimates, *Figure 5.23*. A large difference/gap between samples >14m^2/g and <7m^2/g distinguishes samples of high and moderate surface area; the lowest ten samples have surface area below 2.5m^2/g. The magnitude of the specific surface area will affect the samples sensitivity to %RH conditions and have considerable effects on the sorption behaviour. For the majority of samples the adsorption and desorption curves are

broadly identical, with the desorption curve slightly higher in magnitude[4], *Figure 5.22 (a)*; however, for the samples *Lan, Por, Etr, Dow2, Dow1, Rom* (in order of the magnitude of the effect) and to a much lesser extent *Cau*, and possibly *Bel*, a hysteresis effect is evident, *Figure 5.22 (b)*. This type of hysteresis is consistent with pore condensation taking place in mesoporous (2-50nm) samples (Lowell et al. 2004, Section 4.4) and suggests that for samples where the BET S. A. exceeds $5m^2/g$ (*Rom*) condensation effects may be an issue in mass gain measurements.[5] This is an issue that will be returned to in relation the RHX mass gain experiment discussions.

The surface area and pore volume characteristics are also interesting because samples with higher surface area and pore volume, with the exception of *Lan*, also have the highest calcite and carbon contents, discussed above. The BET surface area is also highly correlated (R^2 = 0.90) with the percentage of water removed in the TG-MS heating regime 50-130°C, *Figure 5.34,* with the greatest quantities of water loss also occurring for the samples with highest surface area and pore volume, *Figure 5.29*. This suggests that high pore volume and surface area may be associated with, and permit, greater uptake of environmental moisture (groundwater, rain), and with it sources of carbon and calcite contamination, supporting an argument that much of the micritic/sparitic calcite in the samples is secondary and the carbon content is derived from organics of humic origin.[6]

[4] This low magnitude 'open' hysteresis may be associated with chemisorption or with changes in the volume of the adsorbent, trapping molecules adsorbed in pores (Lowell et al. 2004, p. 44-45). The former seems likely, considering that samples are heated to 350°C immediately prior to gas adsorption; this will likely dehydroxylated the samples to some extent, discussed in greater detail later in the chapter, and presumably render it more reactive to molecular uptake via chemisorption (although it is not clear to what extent this is likely under nitrogen). If the sample is still cooling down, it is plausible that contraction of the pore structure could also lead to trapping of molecules.

[5] Pore condensation may be avoidable at low %RH but discerning how low this needs to be is not certain. The second point of inflection (a positive upturn, increase in gradient) of the adsorption curve could be used as an indicator. For the present set of data, a relative pressure (P/P_0) of < 0.3-0.4 (30-40%RH) would appear suitable, where nitrogen is the adsorbate; corrections for air may be required.

[6] The lower calcite and carbon content for *Lan* may be related to the bricks original context; it was never buried and was retrieved from an elevated and very sheltered location.

Water Loss and TG-MS

The TGA curves from TG-MS analysis, *Appendix C,* are similar to those obtained in other studies of fired clay ceramics, displaying a strong mass loss between 50-150°C with a more gradual mass loss at higher temperatures (e.g. Drebushchak et al. 2005; Bowen et al. 2011; Shoval and Paz 2013). Combined with the TGA first derivative data and the TG-MS data for mass 18 (H_2O), a much more detailed picture of the mass loss associated with water is obtained. Structures associated with water loss can be loosely grouped into four events (*A, B, C, D*), *Table 5.19 Section 5.10*, not all found in each sample. These structures are generally very broad and sometimes may not be clearly identifiable if there is significant overlap from other more prominent peaks. Exceptions are *Mac* and *Bel*, which exhibit very narrow well defined peaks at 90-95°C, *Figure C.11* and *Figure C.42*; because of their unique presence for these two samples, they are associated with removal of adsorbed water associated with gypsum.[7]

Event A peaks at 50-100°C corresponds to the removal of surface adsorbed and pore water, see *Section 2.3*. This is supported by a) its presence for all samples, *Ted* excluded due to a very low level, b) the observation that for the abnormal[8], high surface area, samples (*Etr, Rom, Por, Lan, Dow1/2*) it is the only certain structure in the temperature range 50-200°C, and c) for samples with very low surface area, and hence less physisorbed moisture, i.e. *Rat*, *Tur* and *Ted*, *Event A* has a very low magnitude and tends to occur at a lower temperature, i.e. 50-70°C. That this event can be clearly linked to physisorption processes (adsorption, capillary condensation), via the BET analysis, permits events at higher temperatures to be associated with chemisorption processes.

Event B peaks at 100-180°C (typically 130-160°) and is not interpreted as present in the six high surface area, abnormal, samples. It is also not clearly present in *Nic,*

[7] This is not dehydration of gypsum/bassanite to anhydrite which must occur at higher temperatures; this will be discussed further with respect to *Stage 1* mass gain later in the chapter.

[8] The samples *Etr, Rom, Por, Lan, Dow1, Dow2* are referred to as 'abnormal' by the author based on their poor $t^{1/4}$ mass gain behaviour. These samples may also be referred to as 'badly-behaved' for similar reasons, with the remaining samples constituting the well-behaved samples, although the distinctions are not always so clear. This will be discussed later in the chapter.

Mac and *Bel*, but, particularly for *Mac* and *Bel,* its presence could be masked by the large desorption peak at lower temperatures. *Event B* is certainly much more clearly associated with well-behaved low surface area samples and is tentatively termed low temperature chemisorbed (LTC) water to distinguish it from higher temperature chemisorbed (HTC) water events, described shortly. This could be connected with the *Type1* water of Wilson et al. (2012; 2014), which they refer to as a type of weakly chemisorbed water, but they consider this water to be removed in the temperature range 200-300°C (for no obvious reason, see *Section 2.5*) and also associate it with *Stage 1* mass gain, which will be argued against later in this chapter. Therefore, the present author does fully agree with such a connection.

Event C (210-280°C) and *Event D* (300-380°C) are the most likely events associated with dehydroxylation. Only one of the two events occurs for each sample, with the exception of *Lan* and *Dow1* for which the assignment of *Event C* is not even certain, *Figure C.33* and *Figure C.46*. Certainly, for samples where *Event C* or *Event D* are very well-defined structures only a single event occurs, *Table 5.19*. It might be more appropriate then to interpret the behaviour as that of a single chemisorbed process (rehydroxylation) that can have a maximum temperature of moisture removal (dehydroxylation) over a broad range, 200-400°C. Without doubt, the water loss associated with this process appears to occur over a very wide range of temperatures in the TG-MS data, see all curves in *Appendix C*, the start and end of which can not be easily defined, and this agrees with a similar observation from TG-MS analysis in Clegg et al. (2012, Figure 2). Water removal continues at temperatures above 500°C; it is not clear how the rate of heating used in TG-MS may effect this; perhaps powdered samples, <63µm, heated at 20°C/min do not have sufficient time for removal of all possible water at a particular temperature before a temperature increment occurs.

In any case, from the TG-MS, a physisorbed process and at least two chemisorbed processes (high temperature and low temperature) can be interpreted, the higher temperature chemisorbed process likely associated with dehydroxylation. The temperatures these events occur at appear to vary considerably with the sample,

the boundaries between events are not sharply defined, and wide temperature ranges are evident.

In terms of the magnitude of mass loss, as mentioned earlier, this is greatest for the anomalous samples, *Figure 5.29* and *Figure 5.30*, over both the temperature range 50-130°C and 130-500°C. When the weight loss over both these temperature ranges were plotted against one another (with the %wt. carbon removed), *Figure 5.32*, a strong correlation is observed, R^2 = 0.87; given the water loss below 130°C was shown to be correlated with the BET S. A., *Figure 5.34*, it can also then be inferred that water loss at 130°C-500°C has a significant contribution that is related to the surface area and pore volume. Some of this may be the result of prolonged drying times required to remove all possible water below 130°, discussed later, with this water still undergoing removal while the temperature is incrementing to higher values; hence capillary/pore water still being removed at higher temperatures. Also, the strong correlation between BET S. A. and water loss between 50-130°C, and the strong correlation between water removed at 50-130° and 130-500°, is biased heavily by the anomalous samples for which much larger water capacity and pore condensation are probable; inspection of *Figure 5.34* and *Figure 5.32* makes it clear that if these data points (the five/six highest) are removed from the plots the strong correlation will cease to exist. This matter will be returned to when discussing the RHX mass gain behaviour.

9.3 RHX Behaviour

9.3.1 General Mass Gain Behaviour

Overall Behaviour

From observation of the *Stage 1* (*Section 7.6*), *Stage 2* (*Section 7.1* and *Appendix E*) and activation energy plots (*Section 7.5* and *Appendix D*), the samples can be split into two groups based on their mass gain behaviour, a *normal* (12 samples, i.e. *Ann* and *Esp*) and an *abnormal* (6 samples, *Etr, Rom, Por, Lan, Dow1, Dow2*) group; the samples *Cau,* and to some extent *Bel*, are treated as *normal* but their behaviour is borderline and sometimes problematic, discussed later. The characteristics distinguishing the groups are now outlined, with more detailed discussions following later.

Normal samples have the following general characteristics:

- They have two stages of mass gain, *Stage 1* and *Stage 2,* for example *Figure 7.72* for *Ann*. The first, *Stage 1*, features a more rapid increase that has normally reached completion within 24 hours and often considerably less (<5 hours for 7/12 normal samples, *Table 7.15*). The second, *Stage 2*, is *approximately* linear as a function of $t^{1/4}$, and is on-going after a period of two months.
- The *Stage 2* mass gain rate has an Arrhenius (exponential) temperature dependence, for example *Figure 7.63* for *Ann*.
- This behaviour (two stage, approximate $t^{1/4}$ *Stage 2*, Arrhenius temperature dependence) is observed following heating at both 130°C and at 500°C, but the mass gain rates and activation energies are not identical for both, for example *Figure 7.1* for *Ann*.

Abnormal samples have the following general characteristics:

- They display very long *Stage 1* durations, t_{S1} *Table 7.15*, typically exceeding one week, and the magnitudes of *Stage 1*, m_{S1}, are also notably large, *Figure 7.78*.

- The *Stage 1* duration is shorter at higher aging temperatures, for example *Figure 7.6* for *Rom*.
- Long term *Stage 2* behaviour is observed following heating at 130°C and 500°C, but for the 130°C case, the curves tend to flatten and possibly tend towards a constant equilibrium value, for example *Figure 7.16* for *Dow1* but uncertainties associated with the quality of the data make this less clear.
- The long term *Stage 2* behaviour following heating at 500°C appears to be broadly linear as a function of $t^{1/4}$, however the curves at different aging temperatures appear to converge on a similar mass gain rate, with no clear temperature dependence observable (also the case for the 130C component), see for example, *Figure 7.6* for *Etr*.
- The mass gain curves of abnormal samples also feature greater levels of random scatter. This can be observed directly from the curves but also in the *RMSE* values of the modelled curves, *Table 7.1*, and the modelled drying curves, *Table 8.2*, where the magnitudes are greater for abnormal samples. This scatter is associated with an increased sensitivity in these samples with higher specific surface area, discussed in the previous section, to any fluctuations in environmental conditions during measurements.

Abnormal Samples

The abnormal samples are considered poorly behaved with respect to the study of RHX mass gain behaviour and dating in this study, for a number of reasons. The large scatter in the experimental mass gain data for these samples means that the quality of the data to be used in modelling is poor to begin with. The uncertainty of any clear temperature dependence, due to curves that appear to converge to a similar behaviour (possibly obscured by the effects of scatter), as well as difficulties modelling *Stage 2* due poor to quality data and a smaller set of data points because of the prolonged *Stage 1* behaviour, meant that dating trials were not carried out on these samples. Also, because of the prolonged negative curvature of *Stage 1,* $t^{1/n}$ modelling of the mass gain curves was problematic, with the distinction of a transition to *Stage 2* very hard to identify with any confidence; modelling could only be carried out for *Rom*.

The large levels of scatter in the abnormal sample data can be associated with the large specific surface areas recorded for these samples, discussed above, providing them with a greater capacity for physisorption of moisture, and with that a greater mass change for any slight variation in environmental conditions during the weighing procedure; in principle then, this scatter could be reduced through a more refined experimental setup. However, the prolonged *Stage 1* and the similar behaviour of *Stage 2* for different aging temperatures are still troublesome. Running samples at higher aging temperatures does shorten the duration of *Stage 1*, in agreement with Wilson et al. (2014). However, Wilson et al. (2014) associated this with a *T1* chemisorbed water, typically removed between 200-300°C, but this is not supported in the present study where a very similar magnitude, and reduction in the duration, of *Stage 1* is observed in samples heated at both 130°C and at 500°C. Because the complete *Stage 1* mass gain could only be recorded at 25°C in the present study, it is not possible to conclude whether or not the reduced duration with aging temperature is due to the *Stage 1* mass gain occurring at a faster rate (i.e. chemisorption) or due to the *Stage 1* mass gain being reduced (i.e. less physisorption at higher temperatures with a duration that is related to the time taken for physisorption to reach all internal pore surfaces via diffusion), and therefore requiring less time. That the *Stage 1* mass gain is the result of physisorbed water, as well as there existing a strong correlation between the magnitude and duration of *S1* for a particular temperature, will be demonstrated in *Section 9.3.2,* and this suggests the shorter duration of *S1* at higher temperature is more likely associated with the magnitude of physisorption.[9]

The *Stage 2* behaviour of the *abnormal* samples is interesting. The flattening and possible equilibration of the mass gain curves following heating at 130°C is what would be conventionally expected (Wilson et al. 2009; 2012), however later work and re-examination of previous studies by Le Goff and Gallet (2014a; 2014b) suggest that the behaviour observed in the present study for normal samples (on-

[9] This is also supported by BET theory of adsorption where the fraction of a monolayer of moisture adsorbed is proportional to a factor *C,* with $C=Ae^{B/RT}$, where the relevant parameter *T* = temperature; this equation is simplified from Equation 4.22 of Lowell et al. (2004, page 21). Therefore at higher temperatures, there is a reduced level of physisorption. Of course, the level of reduction is important and will depend on the other parameters involved.

going *approximate* $t^{1/4}$ behaviour) may actually be more apt. From the TG-MS data, no clear *Event B*, a peak associated with the removal of water between 100-180°, was observed for the abnormal samples. It is conceivable that this peak may be associated with the removal of weakly chemisorbed moisture that under goes recombination in the normal samples. More attention will be devoted to this interpretation later. The reasons for the possible absence or low levels of this peak in the abnormal samples can only be speculated upon; these samples have been associated with low firing temperatures or a short duration of firing (absence of high temperature mineral phases and incomplete decomposition of calcite) and this is supported by their high surface area and pore volume, which decrease with higher temperatures and durations of firing (Rice 1987; Quinn 2013, Mesbah et al. 2010a). If so, perhaps there is a level of clay mineral breakdown that occurs at higher firing temperatures and duration (for example illite is known to persist to very high temperatures, see *Table 2.3, Section 2.3*), the breakdown of which is associated with this low temperature chemisorption event, not found in significant levels in the abnormal samples. This requires future examination.

The common behaviour of the 500C components for different aging temperatures suggests that environmental conditions other than temperature may dominate the rate of mass gain. The six abnormal samples (and to a very small extent *Cau*) displayed sorption curves, discussed above, consistent with pore condensation (capillary type forces), that are not observed in the normal samples. Therefore, a clear link between the abnormal samples and condensation effects in samples with high specific surface area and pore volume is evident. It seems plausible then that the issues observed with these samples are associated either with capillary condensation processes during aging in the ECs or capillary condensation issues arising from the ECC-GBA transfer, or both.

Capillary condensation will occur if the vapour pressure, P, exceeds some threshold equilibrium value in the pore (the equilibrium vapour pressure), P_e, that is below the saturation vapour pressure of the bulk liquid, P_0, i.e. at some % RH below 100% RH (% RH is the ratio of the vapour pressure to the saturation vapour pressure). For

idealised cylindrical pores, this threshold value is described by the Kelvin equation of the form (Lowell et al. 2004; equation 4.62):

$$ln(P_e/P_0) = (-2\gamma V)/(rRT)$$

where γ is the water surface tension, *r* is the pore radius, *V* is the molar volume of the condensed water, and *T* is the temperature, and the equation corresponds to a capillary at equilibrium. From this, an increase in temperature from 25 → 45°C, will result (all other condition being equal) in an increase in the volume of condensed water of only approximately 6%. Hypothetically, if this increase is reflected in a similar increase in the rate of capillary condensation, this would not be detectable with the setup used, where, because of the noise in the data, the uncertainties associated with modelling of the mass gain rates for abnormal samples were of the order of 5-10%, *Table 7.3*. This may also explains why any temperature dependence in the mass gain curves is not clearly evident, clouded perhaps by noisy data and condensation effects.

In any case, the present work highlights the value of carrying out BET analysis on the samples; in future it could be used to avoid abnormal sample issues by careful selection of %RH below the threshold value, or instead using the sorption curves for selection of more suitable samples of lower specific surface area.

The remainder of the discussion chapter will focus on results associated with the normal samples, though reference to abnormal samples will be made.

Normal Samples

The general characteristics of normal samples are outlined above, with detailed discussions of these properties in subsequent sections. These samples are considered well-behaved, in that their mass gain curves and behaviour permits estimation of mass gain rates, mass gain, and activation energies which can then be used to provide estimates of the age of the sample. It can be observed, *Stage 2* curves in *Section 7.1*, that the samples exhibit mass gain curves which are clearly

distinguishable from one another as a function of aging temperature but also as a function of the 130C or 500C components, defined in *Chapter 3*. The behaviour is approximately $t^{1/4}$ but there is still an obvious curvature present, which will be discussed later.

There are some problematic normal samples. *Cau* has already been noted above for its high surface area, condensation potential, and high carbon content; in the mass gain curves there is a prolonged negative curvature, which can be associated with an on-going *Stage 1*, and a convergence of the mass gain behaviour for different temperatures, *Figure 7.13*, both symptomatic of the abnormal samples. It was considered borderline and treated as normal, with modelling and dating carried out as for the other samples, yet there is clearly an issue, particularly with the 130C components, *Figure 7.13* and the associated activation energy, *Figure D.17*, and such problems will be returned to where relevant. Similarly, *Bel* may be problematic due to possible condensation issues, discussed above, as well as problems, shared with *Mac*, associated with the presence of gypsum. The sample *Nic* needs to be treated with caution also, particularly with respect to dating, as the 130C components, *Figure 7.3*, display very little temperature related differences. Otherwise, its *Stage 2* mass gain behaviour appears quite good. It may just be related to a very low temperature dependence of the mass gain rate for the 130C component, however, as noted above, *Nic* is the *normal* sample for which *Event B*, associated with low temperature chemisorption, is most clearly absent or minimal (the presence for *Mac* and *Bel* is uncertain). Also, the activation energy estimated for the 130C component is only 28.29kJ/mol ($t^{1/4}$ model), *Table 7.11*, the lowest obtained for normal samples where the average was 78kJ/mol. It also had an unusually large difference (> 40kJ/mol, also the case for *Mac*) with regard to its 500C component activation energy*, Figure 7.65*.[10]

The presence, following drying at 130°C, of a long-term *Stage 2* mass gain that is *approximately* linear as a function of $t^{1/4}$ and certainly linear as a function of $t^{1/n}$, as well as the demonstration of an Arrhenius temperature dependence are important

[10] A lowest activation energy and large difference with respect to the 500C component were also the case when using the $t^{1/n}$ model.

findings. To date, an on-going mass gain, approximately linear as a function of $t^{1/4}$, following drying has only been reported by Le Goff and Gallet (2014a; 2014b). The work of Wilson et al. (2009; 2012) had reported that their data equilibrated following drying at 105°C and this was required as part of the dating methodology. Yet in Le Goff and Gallet (2014b), re-examination of the work of Wilson et al. (2009; 2012) demonstrated that equilibration has not occurred and that mass gain was indeed on-going. The present work provides independent evidence to support Le Goff and Gallet (2014a; 2014b). As well as this, this work provides the first evidence that the behaviour is chemically driven, with a clear Arrhenius temperature dependence for the 130C component, *Appendix D*, and activation energies of an order similar to those obtained for the 500C component (average for normal samples 78 ± 31 kJ/mol (130C) and 86 ± 35 kJ/mol (500C), respectively, *Section 7.5.1*). These normal samples, excluding *Nic* and possibly *Mac* and *Bel* (due to gypsum issues), with strong 130C components, also displayed clear evidence of *Event B* in the TG-MS data. This event (peaking in the range 100-180°C) is not due to removal of physisorbed water and it is now suggested that it might be a low-temperature chemisorption event which is reversible to some extent during post-heating mass gain, resulting in the 130C component observed and with a corresponding activation energy of average value 78kJ/mol for the present set of samples. This might also contribute to explaining the issue of prolonged drying of samples with low surface area and pore volume, *Section 8.1*, where even after two months of heating at 130°C, mass loss was on-going. A temperature of 130°C, below the peak removal temperatures recorded in the TG-MS (typically 130-160°C), will remove the chemisorbed molecules at a less than optimal rate and this may result in a very slow on-going mass loss process. Interestingly, this is arguably supported by fact that the only normal sample to fully dry was *Esp* for which *Event B* was low in magnitude (detectable in the derivative curve of *Figure C.4*) and with a peak water removal temperature of 110°C, the lowest for samples where *Event B* was certain and well below the drying temperature of 130°C used in mass gain tests. This argument can be countered by the prolonged drying of abnormal samples; however, these samples have a considerably greater capacity for water

(high surface area and pore volume) and drying may be prolonged for this reason also. More discussion on this matter is carried out later.

To deal with this behaviour following heating at 130°C, the component based dating approach had to be developed; its merits and issues will be discussed in *Section 9.4.1*.

A more detailed discussion of the mass gain behaviour in each stage will now follow. Unless these is a notable difference between results associated with one model over the other ($t^{1/4}$ or $t^{1/n}$), the default results discussed will be for the $t^{1/4}$ model; this avoids unnecessary repetition. The merits of, and differences, between the models will be dealt with in *Section 9.4.1 and Section 9.4.2*.

9.3.2 *Stage 1* Behaviour

The mass gain curves generally consist of two stages, as first demonstrated by Savage et al. (2008a; 2008b). The first of these, *Stage 1*, consists of a relatively rapid mass gain, *Section 7.6.2* and *Appendix E*, which has generally concluded within twenty four hours, and less than seven hours for the seven fastest samples, *Table 7.15*. A number of useful findings come from examination of the *Stage 1* behaviour.

Firstly, the mass gain behaviour (magnitude and duration) in *Stage 1*, *Appendix E*, is very similar between the 130C and 500C components for all samples (normal and abnormal) with the exception of *Mac* and *Bel*. This is supported by strong correlations (R^2 = 0.95 and a slope of 0.95) between the *S1* fractional mass gain of both components when the problematic samples (*Cau, Mac, Bel*) are removed, *Figure 7.77 (right)*.[11] Slight differences in the curves are expected because of variation of conditions during weighing.[12]

This similarity in *Stage 1* for the 130C and 500C components suggests that the process responsible for this stage of mass gain is due to water removed below 130°C, with heating between 130-500°C having little or no effect (aside from for *Mac* and *Bel* which will be discussed). The process responsible for this can then be attributed to physisorption on this evidence alone. This is demonstrated very clearly by the sample *Rat* for which no *Stage 1* mass gain is evident; this sample had negligible adsorption properties preventing any BET specific surface area to be obtained, discussed in *Section 9.2.1*, as well as an almost non-existent *Event A* (associated with removal of physisorbed water) in the TG-MS data, providing further and extremely strong support for *Stage 1* being the result of physisorption

[11] This is with the $t^{1/4}$ model. With the $t^{1/n}$ model, the correlation is also strong, with R^2=0.99 with problematic samples (*Mac, Rom, Bel, Nic*) removed. The slope is 0.88.

[12] Samples are introduced to the glove box arrangement following cooling in a desiccated container; given the rapid response of *Stage 1* once exposed to moist air, any slight variation in the timing of manual manipulation of sample boxes and samples, as well as subtle variations in the GBA environment during the very early period of measurement, could significantly affect the level of physisorption that has taken place by the time the first measurement of mass (used in the calculation of m_{S1}, the *Stage 1* mass gain) is recorded. Hence, the *Stage 1* mass gain measurements are approximate, will vary slightly between the 130C and 500C components, and will be less than the true magnitude. Nonetheless, very similar magnitudes and duration between the 130C and 500C components at aging temperatures of 25°C are evident.

process associated with heating below 130°C. Indeed, a strong relationship (R^2 = 0.91) was recorded between the BET surface area and the average *Stage 1* mass gain for all samples (normal and abnormal), *Figure 7.83* (when abnormal samples and *Mac* and *Bel* are removed the correlation remains 0.91).[13] Therefore, the argument by Wilson et al. (2012; 2014) that *Stage 1* is associated with both physisorbed (*T0*) and weakly chemisorbed (*T1*) water, the later removed during heating at 200-300°C, is refuted. The strong relationship between *Stage 1* mass gain and specific surface area does provide additional and stronger support for the assertion of Wilson et al. (2014, Figure 7), that there is a correlation between the specific surface area and duration of *S1* (see *Chapter 2*).

The magnitude and duration of *S1* for the $t^{1/4}$ are presented in *Figure 7.78, 7.79* and *7.82*. As expected, the abnormal samples have considerably larger values of mass gain, *Figure 7.78* than the normal samples (at least 3 times greater than the next highest, *Cau, Bel,* and *Mac*) with a similar situation observed for the duration, t_{S1}, *Figure 7.82*. Again, this is in agreement with physisorption process associated with the high surface area of these samples. A reasonably good correlation was found between the magnitude and duration for all samples, *Figure 7.86*, with R^2 = 0.89, further supporting prolonged durations of *S1* resulting from large levels of physisorption of high surface area/pore volume samples. The mechanisms limiting the rate at which this process can become complete are not clear. Note that the *S1* duration results are approximate at best and based on visual interpretation of a range and maximum duration of *S1*; this is not ideal but considered adequate for the above inferences.[14] The durations are in agreement with the broad ranges observed in previous studies, *Table 2.7*.

Examination of the relationship between the *S1* mass gain and the %wt. loss from TG-MS, for both the 50-130°C and 130-500°C, *Figure 7.87* and *Figure 7.88*, is also

[13] This is for the $t^{1/4}$ model; similarly strong correlations are observed for the $t^{1/n}$ model, *Figure 7.84*.

[14] Estimation of the duration based on the use of *bestfit* to estimate the point at which *Stage 2* commenced was considered but rejected; it was found that accepting the suitability of the modelled results in locating the position of the *Stage1 – Stage 2* transition ultimately involved a subjective visual assessment of the mass gain curve in any case, and this visual assessment was generally considered as good, if not better than the *bestfit* results.

revealing. For all samples (normal and abnormal) the relationship between $m_{S1\text{-}130}$ and both heating regimes is very strong, R^2 = 0.94 (50-130°C) and 0.98 (130-500°C). This is not the case when the abnormal samples are removed, with R^2 = 0.81 (50-130°C) and a much poorer R^2 = 0.16 (130-500°C), with respective *p*-values of 0.0001 (null hypothesis rejected) and 0.198 (null hypothesis not rejected). This suggests that during TG-MS heating physisorbed water is still being significantly removed in samples with a high capacity for this water (abnormal samples) above 130°C, whereas for normal samples it is removed below 130°C and there is little or no reflection of this in the TG-MS 130-500°C regime. The poorer relationship for normal samples with the 50-130°C regime, is believed to be because a percentage of the water loss in this regime is associated with removal of chemisorbed water (*Event B*), discussed previously and later, and this is not reflected in the physisorbed *Stage 1* mass gain. The findings are similar for $m_{s1\text{-}500}$ (see *Figure 7.88* and associated text).

The samples *Mac* and *Bel*, *Figure E.4* and *Figure E.14,* respectively, have *Stage 1* behaviour that differs greatly between the 130C and 500C components. The 130C mass gain is greater than the 500C by an order of approximately 4 for both samples. This difference must be associated with the presence and dehydration of calcium sulfates, discussed *Section 9.2,* in these samples. The resulting anhydrite must have a capacity for physisorption that is only ¼ of that for the gypsum/bassanite heated at 130°C. Intriguingly, the ratio of water held in gypsum ($CaSO{\cdot}2H_2O$)) to that held in bassanite ($CaSO{\cdot}0.5H_2O$) is 4. Unfortunately, XRD and FTIR were not carried out on samples before and after heating at 130°C – this could be examined in future work.

This difference in *Stage 1* for *Mac* and *Bel* is problematic and highlights an issue with gypsum in samples that has not previously been raised in relation to RHX dating. If a quantity of water is removed during heating between 130-500°C and is not regained during *Stage 1*, it will be present in the estimate of the RHX mass gain (see *component based approach* in *Chapter 3*) and result in an incorrectly large estimate of this quantity. This appears to be the case with *Mac* and *Bel* and will be returned to in *Section 9.4.2*.

9.3.3 *Stage 2* Behaviour

Modelling

Modelling was carried out with the aid of *bestfit* and *bestfitn* and restricted to data recorded during ECC->GBA transfer (approx. >24 hours after heating), excluding the *Stage 1* related measurements for aging temperature 25°C, and ensuring that curves for all aging temperatures could be modelled over the same period if suitable. Fits were carried out on the data series as a function of the number of data points removed from the start of the data series, and R^2 was principally used to select the best quality fit. This approach is similar to that used by Le Goff and Gallet (2014a; 2014b). The results in *Section 7.2* show the typical results obtained when *bestfit* and *bestfitn* are applied to a complete data series.

For the $t^{1/4}$ model, using *bestfit*, the best R^2 values were generally obtained for modelling over the entire period, >24 hours, of ECC-GBA measurements, *Table 7.1*. For normal samples, the only major exceptions to this were *Ria* and *Joy* where later starts points produced significantly stronger R^2 values and were instead used. For abnormal samples the long duration of *Stage 1* inevitably meant that modelling was carried out commencing at later starting times. The goodness-of-fit values obtained from modelling the normal samples were very high, with $R^2 > 0.99$ for most fits, and the *RMSE* typically less than 0.30-0.40mg.[15] The R^2 and *RMSE* values do not appear to have any notable dependence on the component or aging temperature either, supporting there being no issue associated with transfer between an ECC and the GBA when the former is at a higher temperature. Observation of the linear fits across the entire ECC-GBA transfer period, displayed in *Section 7.1*, also demonstrate the strength of the fits on samples modelled over this period (for example *Ann, Esp, Nic, Mac, Rat*). For the abnormal samples, the goodness-of-fits are relatively poor by comparison, highlighted red in *Table 7.1,* and this might be associated with a prolonged *Stage 1,* which reduces the number of data points

[15] The precision of the balance is 0.01mg. Preliminary tests of the GBA involving transfer of empty Pyrex beakers, typical mass 30g, from the EC-> GBA for weighing (as for mass gain measurements), showed a repeatability of ±0.12mg (1σ). Therefore, reflects the order of magnitude of the lowest *RMSE* likely obtainable through modelling.

available for modelling, as well as the unsuitability of these samples due to possible condensation effects, discussed earlier.

However, it is clear from the mass gain curves in *Section 7.1* that, while the mass gain behaviour of normal samples is well described by a $t^{1/4}$ model, there is clearly some curvature that remains inadequately described by this model. In this regard, there are a number of issues with the experimental setup, the application of *bestfit*, and finding suitable criteria for selecting the period over which to carry out regressions on well-behaved samples. The application of *bestfit* to $Ann_{130\text{-}25}$, *Figure 7.19-7.23* is used to highlight these issues which were present for all normal samples.

One issue is the sensitivity of the data to environmental conditions and the temporal resolution at which measurements were carried out. Because measurements were carried out at intervals greater than 1 day,[16] and because the mass can fluctuate considerably with variations in measurement conditions (particularly %RH, see Bowen 2011; Drelich et al. 2013), the data series consist of only several dozen data points that can be affected considerably by small fluctuations in %RH in the weighing environment (controlled to ±1% RH) as well as by variation in the efficiency of the manual transfer and timing procedure. The result of this is that the modelled results, based on consecutive removal of the first data point, are not smooth and continuous but can be quite disjointed when plotted as a function of initial data point, *Figure 7.20-7.23*. The effect becomes more pronounced as the number of data points decreases and this is reflected in increased uncertainties in the modelled results, *Figure 7.22* and *Figure 7.23*. Related to this, the R^2 value (despite using an *adjusted*-R^2 value which compensates for statistical effects), *Figure 7.20*, will inevitably drop off quite rapidly in the later stages as the statistics worsen. This can occur at a period where the *RMSE*, a measure of the difference between the modelled and experimental data, is at an optimum, compare *Figure 7.21* with *Figure 7.20*. At the same time, the intercept

[16] Because the data was being modelled as a function of $t^{1/4}$ and because the increase in mass day-to-day reduces as time goes on, measurements were generally carried out at increasing intervals, i.e. greater than daily, at later stages of measurement. Otherwise, when plotted as a function of $t^{1/4}$ the data will become biased towards later periods

mass and slope values, *Figure 7.22* and *Figure 7.23,* respectively, which had previously appeared to vary continuously, are now arguably reaching a constant value. The slope (mass gain rate) reaching a constant value is a condition for selecting *Stage 2* that has been used by Wilson et al. (2009; 2012); however in the present data this occurs when the statistics are poor, the R^2 is at a minimum, and the uncertainties are at a maximum. This apparent linearity with both fewer data points and modelling over reduced (and later) periods of the curve may just be an artefact of the curve itself having an approximate linearity over smaller time intervals. In any case, the above arguments do highlight the issues encountered in modelling the data and selecting the period over which to calculate the mass gain rate. It emphasises the need for good environmental control and particularly the value of an improved temporal resolution in future studies.

Using the optimisation of the R^2 value, it is clear that there is curvature that is not accounted for, with the mass gain rate and intercept, *Figure 7.22* and *Figure 7.23,* not constant at the point of optimum R^2. However, this approach was considered the most reasonable way of proceeding. The R^2 values were very strong, demonstrating that the data, without describing the curves perfectly, provides an approximation that in the absence of other approaches (for example the $t^{1/n}$ model described shortly) is quite good. Also, the data was not of good enough quality to provide suitable evidence that at any point the mass gain rate and intercept will indeed reach a constant value, i.e. that the curvature is just a short term effect, an artefact of the experimental procedure (Wilson et al. 2014). Wilson et al. (2014), *Section 2.5*, interpret positive curvature as being the result of an initial increase in mass, 'over-wetting', associated with an increase in the %RH of the weighing environment while it attempts to equilibrates, followed by a slower decrease in mass as the sample dries off this excess water. However, this was refuted by Le Goff and Gallet (2014b) where curvature was observed despite no such issues with %RH. Similarly, in the present work subsamples of a sample that were initially aged in the glove box environment (*Stage 1* measurements at 25°C) and subsamples of the same sample that were initially aged in sample boxes (different aging temperatures, 35°C, 45°C) show no significant differences in the level of curvature,

suggesting it is not an artefact of the experimental method. The samples do, however, differ in curvature from other samples, some displaying positive and some displaying negative curvatures of varying magnitudes, that were aged in the same sample boxes or in the glove box at the same time; if the effect was related to fluctuations in %RH in the environment a systematic curvature across samples exposed to this might be expected. As well as this, during *Stage 1* weighing in the GBA, no significant fluctuations in %RH, notably beyond the ±1 %RH standard limits of the apparatus, were observed. Therefore, explanation for positive curvature by Wilson et al. (2014) is not accepted. Without good reason to suspect that the positive curvature would end, modelling based on optimisation of R^2, usually over the entire ECC-GBA period of measurement, was considered, if not ideal, the most acceptable approach. For samples with negative curvature, R^2 optimisation was still considered the most objective method in the absence of higher resolution and better quality data.

For modelling using the $t^{1/n}$ fits, improved R^2 and *RMSE* values were obtained, *Table 7.1* and *Table 7.2*. The benefits of the flexibility of this model are illustrated in its application to $Ann_{130\text{-}25}$, *Figure 7.24-7.29*. It fits the data very well, *Figure 7.24*, and accounts for any curvature. The R^2 value is well-behaved and appears to decrease linearly with decreasing data points, *Figure 7.25*. The *RMSE* value is approximately constant from the point at which the optimum R^2 value is obtained. As well as this the parameters modelled (mass gain rate, intercept, *1/n*) all display relatively constant values from the point at which R^2 is optimised, *Figure 7.27-7.29*. This is very positive as it provides strong support for the use of R^2 as the criteria for modelling but also because the $t^{1/n}$ model clearly describes the data very well, particularly in providing parameters that appear constant with removal of data points from the series. An issue is that the uncertainties in the modelled values are greater than for the $t^{1/4}$ model because of the increased flexibility of the model. For example the percentage uncertainty in the mass gain rate modelled for $Ann_{130\text{-}25}$ using the $t^{1/4}$ model is 2%, whereas for the $t^{1/n}$ model it is 26%, greater by an order of 10 (calculated using the 95% intervals in *Table 7.3*). This is an enormous difference with the implications for any dating related calculations obvious.

Presumably, this could be refined with improved experimental control and a high resolution series of data, but to what extent is not clear. Certainly, it will likely be poorer than the $t^{1/4}$ because of the additional parameter that is modelled.

In any case, the results suggest that more trust can be placed in the use of R^2 optimisation in the selection of the most suitable region to model over when $t^{1/n}$ modelling is used. Again, for normal samples this tended to be the entire region of ECC-GBA measurement. Except for *Rom*, which did not model very well, the abnormal samples could not be modelled in any acceptable manner (for example, the regressions would only provide fits where *1/n* was negative, particularly for the 130C components); this supports the unsuitability of these samples or, alternatively, the suitability of a $t^{1/n}$ model for their description.

It may be recalled, *Section 6.5.2*, that the $t^{1/n}$ model was applied first to estimate a value of *1/n* for all six curves associated with a sample. Then the average *1/n* value, say *1/r*, was used (*fixed*) to remodel the curves as a function of $t^{1/r}$. The goodness-of-fit values were similar to those obtained for previous *1/n* modelling, *Table 7.2*, but by virtue of reducing the number of flexible parameters in the modelling and using a value of *1/n* that better describes the data than *1/4*, the percentage uncertainty is significantly reduced, even below that of the $t^{1/4}$ model, *Table 7.5*. For application of $t^{1/r}$ to $Ann_{130\text{-}25}$, the percentage uncertainty is 1.3%. This suggests that initial modelling to refine the *1/n* value followed by subsequent modelling with this refined value provides better fits and lower uncertainties than a $t^{1/4}$ approach. Of course, the suitability of this depends on the confidence that can be given to subsamples conforming to the same $t^{1/n}$ behaviour. This will be discussed further below.[17]

[17] Note that for sample *Cau* (borderline abnormal) the *1/n* values for the six curves were too varied; no average was estimated, and no *1/r* modelling was carried out.

Rates and Relationships

Because the mass gain rates modelled as a function of $t^{1/4}$ have the same time units, comparison of the rates was possible for both the 130C component (25°C) and 500C component (25°), *Figure 7.30* and *Figure 7.31.* For abnormal samples, more confidence is expressed in the 500C component, with issues associated with the 130C component discussed earlier. The highest rates were observed for the samples with high surface area and condensation issues (*Dow2, Etr, Por, Dow1, Lan, Rom*) with normal samples *Cau* and *Bel* also having high rates.

Similarly, for the RHX mass gain rates the abnormal samples had estimated values that were exceptionally high in comparison to the normal samples rates, *Figure 7.32*, greater by an order of at least 3, with the normal samples sharing more similar values, *Figure 7.33*. The (fractional) mass gain rates obtained for normal samples are of a similar order as those obtained in previous studies, 0.00001-0.00015hrs$^{-1/4}$ (Wilson et al. 2012; Bowen et al. 2013).

The relationship between the mass gain rates of normal samples and their specific surface area, *Figures 7.41-7.44*, showed a moderate level of correlation and statistical significance, R^2 = 0.53-0.78, p = 0.0072-0.0003. This relation may be suggestive of a connection between the mass gain rates and the ready availability of chemisorption sites on the external and pore surfaces of the ceramics; however, more rigorous investigation is required to confirm this.

The RHX mass gain rate was correlated with the *S1* mass gain, *Figure 7.45-7.46*, and poor correlations and no statistically significant relationships were observed (R^2 < 0.23, p = 0.1149, for $t^{1/4}$).[18] This provides support for the argument that the 130C and RHX mass gain rates are independent of the *Stage 1* mass gain processes associated with the specific surface area and pore volume.

[18] The $t^{1/n}$ correlation was better but driven by the outlier *Bel*. This behaviour for *Bel* may be suggestive of it being problematic. It is the sample with the next highest surface area, after abnormal and *Cau*, and from the sorption curves some very low levels of hysteresis were observed, the only normal sample aside from *Cau* for which it might be argued to be significantly present.

In *Section 7.3.2* the relationship between the 130C mass gain rates, $\alpha_{130\text{-}25/35/45}$, and the 500C mass gain rates, $\alpha_{500\text{-}25/35/45,}$ at each aging temperature were examined. The findings were unexpected and could be very significant in terms of understanding the relationships between the two mass gain processes. When the relationship was examined for all samples and for the $t^{1/4}$ model a poor correlation was observed, R^2 = 0.47, *Figure 7.34*. However, with the abnormal samples removed (and additionally *Cau* for $t^{1/n}$ because of modelling issues discussed earlier), the correlations between both components of mass gain rate were extremely strong (ranging from R^2 = 0.94-1.00) at all aging temperatures, and for both models, *Figure 7.35-7.40*. As well as this, the ratios (slope of the linear fits) between $\alpha_{500\text{-}25/35/45}$ and $\alpha_{130\text{-}25/35/45}$ rates were very similar for each of the three aging temperatures, (ratios of 1.26, 1.29, 1.25, for $t^{1/4}$ model, and 1.31, 1.25, 1.27, for $t^{1/n}$). A strong relationship between the processes responsible for mass gain following heating at 130°C and 500°C appears to very clearly demonstrated, and this relationship appears to be independent of the sample. In the opinion of the author there are two plausible interpretations of this:

1) Mass gain following heating at 130°C is due to recombination of water associated with a low temperature chemisorption event, *Event B* discussed earlier, and mass gain following heating at 500°C is due to recombination of water associated with this event plus recombination due to a high temperature chemisorption event, *Event C/D* (rehydroxylation). The rates of mass gain are proportional to the number of low/high temperature chemisorption sites available for recombination, with *Event C/D* having approximately 25-31% (from ratios above) of the sites available for *Event B*. This relationship holds across 12 samples, suggesting both chemisorption events are associated with a single compositional component (for example a fully/partially dehydroxylated clay mineral) in which the ratio of high and low temperature chemisorption sites is structurally determined and approximately constant, with this compositional component present in all samples (but it is not required that it is present in the same quantities).

2) Heating at both 130°C (prolonged) and 500°C remove water associated with both *Event B* as well as *Event C/D,* i.e. all chemisorbed water below 500°C. The rate of mass gain is related to the number of chemisorbed sites available following heating, with the ratio of available sites for the 130C component and the 500C component dependent on the heating temperature and duration or, more specifically (speculatively), the cumulative thermal energy in the system during heating. In the case of the present experiment, the ratio of 1.25-1.31 is constant for all samples because all samples experienced the same heating procedure at 130°C and 500°C.

The author prefers the first interpretation, however both can be questioned. For example, the first interpretation, the constant ratio of *Event C/D* to *Event B* is not well-supported by the TG-MS H_2O curves, *Appendix C* and see *Table 5.19* and *Table 5.20,* where the magnitude of *Event C/D* is generally larger, sometimes considerably, than *Event B*. TG-MS experiments with different heating rates could be used to examine if the rate has any effect on the structures observed and their magnitudes; a much slower heating rate might provide better resolution of the peaks.

For the second interpretation, some simple chemical calculations and assumptions[19], suggest that the constant rate between the 130C and 500C

[19] Let the rate of mass removal of water associated with *Event B, b,* and *Event C/D, c* say, be described by the following expressions:

$b = A(T)e^{(Eb/RT)}$, $c = A'(T)e^{(Ec/RT)}$, where *A/A'* are constants, and *Eb* and *Ec* are negative activation energies.

Then during heating at 130°C or 500°C the total rate of removal, *r,* will be a combination of the two:

$$r(T) = A(T)e^{(Eb/RT)} + A'(T)e^{(Ec/RT)}$$

If the mass of water is removed as a linear function of time, i.e. $w(t) = rt$, then the total amount removed, w_T, at a particular temperature *T* for a period *t* can be expressed as:

$$w_T(t) = (A(T)e^{(Eb/RT)} + A'(T)e^{(Ec/RT)})t$$

or, if heating at 130°C for a period t_{130} and at 500°C for a period t_{500}, the following equations hold:

$w_{130} = (A(130°C)e^{(Eb/R130)} + A'(130°C)e^{(Ec/R130)})t_{130}$ *(continued on next page)*

components is only likely if activation energies and pre-exponential factors which determine the chemical rate of removal, are very similar across all samples, but this was not the case with the activation energies recorded. This calculation may be over-simplified and the question can not be resolved without a better understanding of the rates of dehydration and the related activation energies of the present set of samples.

In theory, it should be possible to test the second interpretation by examining the ratio of the mass gain rates following heating at the same temperatures but for different periods. Under the second interpretation, by increasing the duration of heating at 130° but keeping that of 500°C constant, the 130°C rate should tend towards the 500°C rate; this would not be expected for the first interpretation.

Of course, the above arguments are only interpretative, and it may well be the case that a mixture of both, or indeed neither, is more apt. Regardless, the findings are very significant in highlighting that a clear relationship does exist that is independent of the samples.

$w_{500} = (A(500°C)e^{(Eb/R500)} + A'(500°C)e^{(Ec/R500)})t_{500}$, the temperature in °C for the present.

The ratio of w_{130} to w_{500} is not easily simplified, but if we assume that *Event B* is completely removed, with total water loss W_b, for heating at 130°C and 500°C, then the equations reduce to,

$w_{130} = W_b + A'(130°C)e^{(Ec/R130)}t_{130}$

$w_{500} = W_b + A'(500°C)e^{(Ec/R500)})t_{500}$

Then, it can be observed that the ratio of w_{500}/w_{130} can only be constant for a range of samples provided the pre-exponential factors, *A'(T),* and the activation energies, E_c, are the same for all samples.

Masses and Relationships

The difference between the modelled intercept masses of the 500C and 130C mass gain curves, *Table 7.6* and *Table 7.7*, was used to estimate the total fractional mass loss, m_{RHXC}, at the three different aging temperatures. The average of these as well as the standard deviations are presented in *Figure 7.47* (all samples) and *Figure 7.48* (normal samples) for the $t^{1/4}$ model (values differ for the $t^{1/n}$ model but the findings discussed are the same). The main points to note are that the abnormal samples have the highest values, in agreement with the suspected removal of large quantities of physisorbed or loose water and organic matter, discussed earlier and supported by the modelled % mass of loose water removed, *Figure 8.4* and the % mass of carbon removed, *Figure 5.25*.

For the normal samples, it can be observed that the highest samples are *Bel, Mac,* and *Cau*, samples that have issues with either gypsum dehydration or possible high surface area/condensation and modelling issues, and this high total mass loss may reflect these problems. In any case, for normal samples the total fractional mass loss varied from approx. 0.1-1% mass of the sample (of note, perhaps, it is lowest for *Esp,* the only sample to dry fully, *Figure 8.4,* at 130°C). Following subtraction of the modelled loose water removed and the organic matter removed, the ranking varies only slightly, *Figure 7.49*, with the estimated RHX mass loss, m_{RHX}, still of the order of 0.08-0.5%, *Table 7.9*.

Significantly, the component based approach assumes that the total fractional mass loss should be the same for each aging temperature (provided the samples are well homogenised), and this is supported very well by the small standard deviations obtained for the three values, *Table 7.9*, of the order of approximately 1-3% of the estimated mass loss.

The contribution loose water, m_{lw}, not removed during 130°C drying and organic matter, m_{om}, have towards the total mass loss is highlighted in *Figure 7.50* and *Figure 7.51* for the $t^{1/4}$ model (same order of magnitude for $t^{1/n}$. The loose water can typically contribute between approx. 0.25-1.5% of the total fractional mass loss (0% for *Esp* and up to 3.5% for *Bel*), with organic matter much more problematic

(assuming an OM/OC ration of 1.95), typically from 8-20% of the total fractional mass loss but with several samples contributing between 35-50%. Therefore any uncertainty in this estimate will have appreciable effects on the age estimation, discussed later.

The total mass loss and the RHX mass loss would be expected to have a strong correlation, and this is reflected in *Figure 7.56-7.58*.[20] The RHX mass, m_{RHX}, relationship with *Stage 1* mass gain, m_{S1}, and BET S. A., showed no statistically significant correlations, see *Figure 7.59* and *Figure 7.60* and associated text, supporting its independence from these properties. Correlations between the TG-MS weight loss regime 130-500°C and the total fractional mass loss were high (R^2 = 0.95) as would be expected, *Figure 7.61*, but improved when the *Stage 1* mass gain, m_{S1}, was added to the total fractional mass loss, m_{RHXC}, *Figure 7.62*. This is consistent with the delayed removal of physisorbed water at higher temperatures, discussed earlier, and also, perhaps, reflected in the fact that the TG-MS %wt. loss is significantly less than the total fractional mass loss (approximately 50% of the magnitude).

Activation Energies and Relationships

Arrhenius temperature dependences (demonstrated with Arrhenius plots) and activation energies in the range 40-182kJ/mol have previously been reported (Wilson et al. 2009; Wilson et al. 2012; Barrett 2013; Clelland et al. 2014). Estimated from the mass gain rates following heating at 500°C, this behaviour and the associated activation energies has been interpreted as supporting a chemically driven rehydroxylation process in the ceramic (see Wilson et al. 2009; Clelland et al. 2014). There has, however, been no previous examination of the temperature dependence of the $t^{1/4}$ or $t^{1/n}$ -based behaviour following heating at low drying temperatures, i.e. 130°C. This has been examined in the present study, together with the 500C component and RHX component temperature dependences. The

[20] *Bel* is treated as an outlier in some of these plots; it has a high loose water and organic matter fraction which may again be symptoms of a problematic or abnormal sample.

Arrhenius plots, *Appendix D,* and the tabulated results in *Table 7.11* and *Table 7.12*, provide strong support for an Arrhenius temperature dependence for all components of the vast majority of the normal samples; the samples *Nic*, *Cau* had problematic or poor fits associated with poor 130C mass gain curves, discussed earlier, and *Bel* also produced a poor Arrhenius plot for the RHX activation energy.[21] The R^2 values are typically greater than 0.99 for normal samples with activation energy uncertainties varying considerably from 1-20% typically for the 130C and 500C components, but generally exceeding this for the RHX component (typically >20-25%); the effect of uncertainties in the RHX activation energy on dating results will be returned to. The uncertainties result from the cumulative effect of uncertainties in the modelled mass gain rates of the 130C and 500C, inhomogeneity in the subsamples used at different aging temperatures, and the small number of aging temperatures used. The modelling issues have already been discussed. The need for homogeneity of samples has been addressed previously (Bowen et al. 2013; Le Goff and Gallet 2014a; Clelland et al. 2014), and given the linearity of the Arrhenius plots and the convergent RHX mass values for different aging temperatures, a very good level of homogenisation is believed to have been achieved. The use of more than three aging temperatures is not very practical. Improvements in the quality of the mass gain curves and modelling procedure, therefore, appears to be the best avenue for refinement of the activation energy uncertainties.

In any case the activation energies obtained for normal samples are as follows (average and standard deviation of the sample values): E_{a130}(avg) = 78 ± 31 kJ/mol; E_{a500}(avg) = 86 ± 35 kJ/mol; E_{aRHX}(avg) = 137 ± 70 kJ/mol. For t1/n the values are as follows: E_{a130}(avg) = 58 ± 14 kJ/mol; E_{a500}(avg) = 67 ± 26 kJ/mol; E_{aRHX}(avg) = 101 ± 78 kJ/mol. These values are all in agreement with previously obtained values, and if obtaining activation energies of this order following heating at 500°C can be associated with a chemisorption process such as rehydroxylation (for example Wilson et al. 2009; 2012), then this could equally be argued to be the case for the 130°C heating case, which has been associated with a chemisorption process above.

[21] The temperature dependence was observed for both the $t^{1/4}$ and $t^{1/n}$ model.

If the mass gain rate of the 500C component is interpreted as a combination of the 130C mass gain rate and the RHX mass gain rate, then the activation energy of the 500C must be interpreted as reflecting the average behaviour associated with these two components. Its activation energy values is very similar to that of the 130C component, *Figure 7.65, Figure 7.66*, *Figure7.69* and *Figure 7.70*, and this may not be surprising considering, as demonstrated earlier, the 130C mass gain rate is the dominant contributor to the 500C mass gain rates used in its estimation. What is clear is that there appears to be a significant difference between the 130C activation energy and the RHX activation energy which is on average notably higher (59kJ/mol for $t^{1/4}$ and 43kJ/mol for the $t^{1/n}$). This may argue in favour of two different chemisorption processes being involved, the low temperature *Event B* and the high temperature *Event C/D*, discussed previously. Examination of the relationship between the 130C activation energy and the RHX activation energy, *Figure 7.71*, may suggest a weak relationship, R^2 = 0.52 and p = 0.043, for the $t^{1/4}$ model but more conclusive evidence is required.

Curvature and a $t^{1/4}$ or $t^{1/n}$ Model

An area of contention in RHX dating is the issue of whether or not the *Stage 2* mass gain is better described by a $t^{1/4}$ model (Wilson et al. 2009; 2012; 2014; Hall et al. 2011) or by a more general $t^{1/n}$ model (Bowen et al. 2011; 2013; LeGoff and Gallet 2014a; 2014b; 2015). The arguments surrounding this have been discussed in detail in *Chapter 2* and will not be repeated in depth; however, Wilson et al. (2014) argue that *Stage 2* is truly linear as a function of $t^{1/4}$ with negative curvature in the data the result of either prolonged *Stage 1* mass gain due to physisorption and chemisorption processes and positive curvature an artefact of the measurement procedure and associated with an initial increase in %RH while the setup equilibrates, mirrored in the mass gain data and followed by a slow decrease as excess water dries off. This explanation of positive curvature has been rejected by Le Goff and Gallet (2014b) where such issues did not affect the setup used, and the explanation has similarly been rejected by the present author based on related

arguments discussed above. The interpretation that chemisorbed water is involved in the *Stage 1* mass gain (but not $t^{1/4}$ or $t^{1/n}$ related), and thus a contributor to the negative curvature has also been argued against earlier, with the present author of the opinion that physisorbed water (possibly including pore condensation effects) is the sole contributor, accepting that this may result in a prolonged *Stage 1*.[22]

A possible cause of positive curvature is accelerated mass gain while a sample is exposed to air during cooling post-heating (Barrett 2013); this results in an additional mass gain during *Stage 1* and a curvature in *Stage 2*, a so-called *time-offset* effect. For the present set of tests, this effect can be largely rejected for the following reasons:

1) Samples were cooled in a desiccated container (where minimal %RH levels were recorded) following firing to minimise/remove such effects.
2) Samples aged at 25°C were first exposed to moist air at approx. 23-24°C, *Figure 8.7*. Assuming no mass gain occurred during desiccation, then first exposure at these temperatures would result in no positive curvature, but possible a very mild negative curvature. This is not observed for samples aged at 25°C, where a mixture of positive and negative curvatures were recorded in samples cooled in the same group.
3) Samples aged at 35°C and 45°C were first exposed to moist air at approx. 36-45°C, *Figure 8.6*. Assuming no mass gain occurred during desiccation, then first exposure at these temperatures should result in a systematic positive curvature in the 35°C aged samples, and a systematic negative curvature in the 45°C aged samples. This is not observed: samples cooled in the same group display a mixture of behaviours and the subsamples aged at different temperatures conform in their level of curvature, *Table 7.17* and *Figure 7.89*.
4) If the desiccator is permitting mass gain during cooling, the 25°C aged samples would be expected to have more pronounced and systematic positive curvature than other aging temperature samples the due to a

[22] During *Stage 1*, for both the 130C and 500C components a $t^{1/4}$ or $t^{1/n}$ mass gain is also taking place. However, when *Stage 1* is attributed to physisorption, *Stage 1* is referring to the rapid mass gain not associated with the $t^{1/4}$ *or* $t^{1/n}$ processes, and its magnitude is defined by the difference between their intercept masses and the initial recorded mass of the ceramic following firing (see *Figure 3.1*).

longer time spent gaining mass above the aging temperature (see Barrett 2013). This is not supported by the evidence, *Table 7.17*, with again a mixture of behaviour observed for samples cooled as a group, and subsamples at different temperatures conforming in their *1/n* behaviour.

5) Sample *Rat* has significant positive curvature with no *Stage 1* increase which would be indicative of a *time-offset* effect.

Therefore, *time-offset* effects, due to mass gain while the sample is equilibrating to the aging temperature, are not the cause of, and are unlikely to contribute significantly to, the curvature observed in the samples.

From examination of the curvature results in *Section 7.7.1* (*Table 7.16*, *Table 7.17, Figure 7.89*), it seems clear that the curvature in the samples is real, varying from approx. *1/6* (0.16 for *Bel*) to approx. *1/2* (0.45 for *Rat*) for the average *1/n* value of samples. The curvature is generally positive (>*1/4*) for well-behaved normal samples. Only samples *Rom, Bel, Nic, Cau, and Esp* are <1/4; with the exception of *Esp*, issues with the other samples have been highlighted at one point or another throughout the discussion and they all may be affected by long *S1* duration.

Perhaps the strongest support for the curvature being real is that, with the exception of *Mac* and *Cau*, the *1/n* values for the different heating temperatures (130C and 500C components) and aging temperatures of the subsamples agree very well with one another, while at the same time differing from other samples that experienced identical treatment and aging conditions. The range of *1/n* values, from approx. *1/6-1/2* for all samples and from approx. *1/5-1/2* with problematic samples *Rom, Bel, Nic, Cau* excluded, agrees well with those observed in previous work; Le Goff and Gallet (2014a; 2015) provide convincing evidence that the mass gain behaviour may be better described by a $t^{1/n}$ model with *1/n* varying from *1/6-1/3* (Le Goff and Gallet 2014a) or *1/4-1/2* (Le Goff and Gallet 2015, based on expansion data re-examination).

The relationships of the level of curvature, *1/n* with the BET surface area, and *S1* mass gain, were examined, *Figure 7.90* and *Figure 7.91,* respectively. There is a strong correlation with the specific surface area, $R^2 = 0.76$ ($p = 0.0002$), increasing to

R^2 = 0.89 when only positive curvature samples are used. There is also a significant relationship with the *S1* mass gain, particularly when the samples *Mac* and *Bel* are removed, R^2 = 0.77 (p = 0.002). This relationship between curvature and surface area has previously been discussed by Wilson et al. (2014), however, they explained the curvature as due to other effects, discussed previously. What the relationship certainly does is provide a connection, via the specific surface area, between the $t^{1/n}$ diffusion mechanism associated with mass gain and the pore structure of the ceramic. More work is needed to provide additional support for this finding and to elucidate why samples with lower surface area and lower pore volume might have higher *1/n* values that can be associated with freer diffusion within the available pore structure of the ceramic body, i.e. a more Brownian-type $t^{1/2}$ diffusion (the connection between surface area and the levels of physisorbed water may be involved).

In light of the above discussion, as well as the improved modelling of the mass gain curves provided by the $t^{1/n}$ model (greater R^2 values and reduced *RMSE* values) discussed earlier, there does not appear to be a good argument against supporting the hypothesis that the mass gain in fired clay ceramics obeys, or is more adequately described, by a $t^{1/n}$ model with *1/n* varying dependent on the diffusion pathways, more specifically the pore structure, of the sample.[23]

[23] The results of application of both models to the dating of ceramics is discussed in the next section, but these results do not provide convincing evidence in support of either model.

9.4 RHX Dating – Component Based Approach

9.4.1 Component Based Approach

Components Based Approach and Dating Results: $t^{1/4}$ and $t^{1/n}$ comparison

The use of a component based approach, *Section 3.6*, was necessitated by the behaviour following heating at 130°C discussed above. The main principle of this approach (that the 130C and RHX components are additive leading to the 500C component) is supported by the quality of the linear Arrhenius plots and RHX activation energies, E_{aRHX}, acquired using the RHX mass gain rates estimated from the difference in the components (130C and 500C) for three different aging temperatures. As well as this, the agreement in the estimates of the RHX mass, m_{RHX}, for the three different aging temperatures, discussed previously, also support this component driven approach. Of course, the decisive support for any dating approach is how well the estimated age agrees with the known age of a sample. For the twelve samples on which dating was carried out, the results are presented in *Tables 8.7-8.9* (with the age-temperature curves presented in *Section 8.4.1*) and summarised at the end of *Section 8.4.2*.

The results are mixed for both models, with some samples providing age estimates which agree well with the known ages, for example *Joy* ($t^{1/4}$, known age 412yrs, estimated age 399yrs) and *Cal/Ann* ($t^{1/n}$, known ages 110/182, estimated ages 109/194) but other samples for which the estimates are extremely poor, for example *Mac, Nic* (500Myrs and 56kyrs, respectively for $t^{1/4}$, 9Myrs and 1Myrs, respectively for $t^{1/n}$). Without uncertainties in the OM/OC ratio and activation energy considered, the estimated ages are generally too old, but perhaps less pronounced for the $t^{1/n}$ model. [24]

With some uncertainties (OM/OC ratio and activation energy) considered, it is possible to discuss the results based on how well the estimated age ranges agree

[24] A full propagation of error and uncertainty treatment was not carried out due to the large number of factors involved and difficulties in quantifying their effects within the scope of the present work. In future work, as the uncertainties involved are better understood and the problematic issues resolved/minimised, as well as with improved resolution and quality of mass gain data, more rigorous treatments will be applied. For the present explorative work, this is not considered a pressing concern.

with the known age ranges of the samples, see aforementioned tables and *Figure 8.26-8.28*. For the $t^{1/4}$ model, agreement between the estimated and known ages is the case for 5/12 samples (*Esp, Joy, Cau, Bel, Ted*) with 4/5 of these (*Esp, Joy, Cau, Bel*) feasible when the OM/OC range is permitted to vary from 1.4-2.5 (see *Chapter 2*), 1/5 (*Joy*) feasible for the RHX activation energy uncertainty range, and *Ted* only feasible if both uncertainties are considered.[25]

For the $t^{1/n}$ model, 3/12 samples (*Ann, Cal, Tur*) produce feasible ages under certain uncertainty conditions. Within the OM/OC uncertainty range 2/3 are feasible (*Ann*, *Cal*) with *Tur* only finding agreement when the full range of uncertainties is permitted. For some of these feasible samples the age range is considerable when the uncertainties are considered, for example 258-2178yrs for *Bel* with OM/OC=1.4-2.5 ($t^{1/4}$), whereas for others the effects are relatively small, for example 177-212yrs for *Cal* with OM/OC =1.4-2.5 ($t^{1/n}$). The reasons will be discussed later; however, for samples where large uncertainties are required for agreement this is clearly less satisfactory.

There is also the matter of the effective lifetime temperature (ELT). As part of this set of dating trials, an estimate based only on the surface air temperature was used, but in reality some samples may have experienced elevated temperatures during their lifetime, particularly *Ria* due to its close proximity to a fireplace and *Tur* which was an internal brick from a kitchen, see *Table 6.2*. In this regard, considering the working temperature, T_w (an ELT for which the dates would find agreement), it appears that *Joy* and *Cau* have good T_w (9.4°C and 11.2°C, respectively) with *Esp* and *Ted* just about plausible (15.7°C and 7.3°C, respectively) and *Bel* very unlikely (22.3°C) for the $t^{1/4}$ model. For $t^{1/n}$, both *Ann* and *Cal* are good (T_w = 10.1°C and 10.5°C, respectively) and *Tur* is plausible (14.2°C). However, the above working temperatures are based on other factors remaining fixed or not considered, for example the OM/OC is fixed at 1.95; if this is permitted to vary, the working temperature can also be permitted to find a more acceptable value.

[25] The term *feasible* is used to suggest that agreement/overlap between the estimated age range and the known age range of the sample has occurred.

As well as the above factors affecting the date ranges, there is the issue of samples which have previously been considered problematic, *Cau* and *Nic* for issues with their 130C mass gain behaviour and poor Arrhenius plots, and *Mac* and *Bel* for issues with *Stage 1* differences and the possible removal of gypsum related moisture. When these are removed and samples with unreasonably large uncertainties are ignored, then for the $t^{1/4}$ model only *Esp, Joy,* and possibly *Ted,* provide good or feasible agreement, and for the $t^{1/n}$ model *Ann* and *Cal* seem to be the only positive results. In light of this, if the problematic samples *Nic, Mac, Cau, Bel*, are not considered, the dating results can be summarised as providing reasonable results for approximately two of out eight samples for which no potential problems associated with high surface area/pore condensation or gypsum dehydration were evident. The working samples also differ with the model, $t^{1/4}$ or $t^{1/n}$, used, despite previous arguments favouring the $t^{1/n}$ model.

The generally large ages and associated positive mass discrepancies, m_{out} (the difference between the RHX mass estimate and the simulated (expected) mass), may suggest an overestimate of the RHX mass m_{RHX},[26] an underestimation of the mass gain rates, or an over estimation of the activation energy (which would result in an underestimation of the mass gain rate at lower temperatures).

An underestimation of the mass gain rate is plausible for the $t^{1/4}$ modelling of samples with positive curvature, where regressions were generally carried out over the entire period of ECC-GBA measurements. As discussed earlier and displayed in *Figure 7.23* for *Ann*, if a sample has positive curvature the modelled mass gain rate increases as the period over which the curve is modelled is reduced (by incremental removal of the earlier data points). From the example of *Ann*, the mass gain rate increases by approx. 0.0002g/hrs$^{1/4}$, or 6% of the original rate. For the $t^{1/4}$ model, the mass gain rate required for the estimated and known ages to agree, a_w, can be estimated as a ratio of the mass gain rate at the ELT, a_{elt}. Based on the above, it would be expected that the greater the curvature the more pronounced this ratio will be. The ratio is presented below in *Table 9.2* and the correlation between it and the curvature in *Figure 9.1*. The ratios are generally far too large (positive or

[26] Note that for the $t^{1/n}$ model the mass discrepancy is negative for 3/8 non-problematic samples.

negative) to be explained as the result of modelling the wrong portion of the curve and there is no correlation with the curvature. Also the ratio should be <1 for samples such as *Esp* and *Bel* with negative curvature (accepting that *Bel* is a problematic sample). Such issues with rates should not be applicable to the $t^{1/n}$ model for which large ages were also recorded.

	$1/n$	a_w/a_{elt}
Ann	0.33	1.58
Esp	0.19	1.17
Nic	0.2	3.44
Mac	0.32	39.5
Ria	0.39	4.61
Rat	0.45	9.20
Cal	0.38	1.96
Joy	0.39	0.99
Bel	0.16	1.22
Tur	0.44	3.80
Ted	0.37	0.89

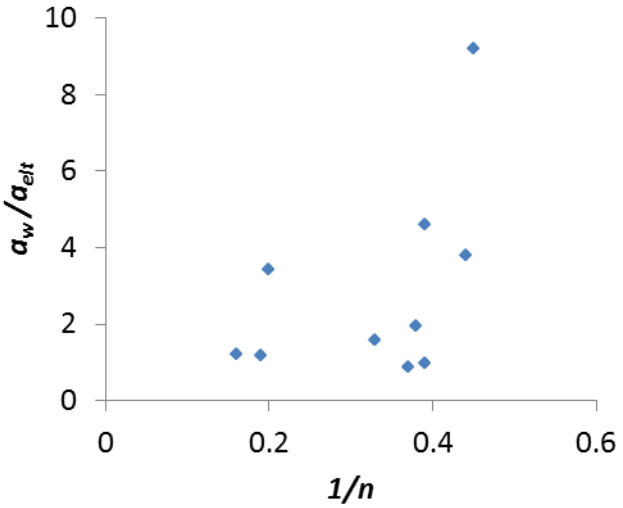

Table 9.2 and Figure 9.1*:* Relationship between curvature and the ratio of the working mass gain rate, a_w, and the mass gain rate at the ELT, a_{elt}.

An underestimation of the mass gain rate could result from overestimation of the RHX activation energy (or slope of the Arrhenius plot). The quality of the Arrhenius plots for the RHX activation energies do not generally suggest any systematic issues (problems with *Cau, Nic,* and *Bel* aside). Nonetheless, for the $t^{1/4}$ model, with which the activation energies are higher than the $t^{1/n}$ model and the *Stage 2* modelling may be less appropriate, the age estimates were re-calculated using activation energies that were the average of the 130C and 500C activation energies in order to explore the effects. Presented in *Table 9.3*, it can be observed that the issue of large ages is not resolved. Therefore, while issues with poor-estimation of mass gain rates and activation energies could be a contributor, the more likely source of issues with large ages is an overestimation of the RHX mass gain, either through

some fundamental flaw in the component based approach, modelling issues or components of mass that are not accounted for or incorrectly estimated.

Issues with estimation of the RHX mass, m_{RHX}, may be the dominant source of disagreement between the estimated and known ages. These issues will be reflected in the mass discrepancy, m_{out} (difference between the RHX mass and the simulated RHX mass). This is generally positive and with a magnitude that is a significant fraction of the total/RHX fractional mass estimate, *Figure 8.31* and *Figure 8.32*, ranging anywhere up to almost 100% (*Mac*). For the $t^{1/n}$ model, significant negative mass discrepancies were estimated for *Ted* and *Joy* (of the order of approx. 200-30%), *Figure 8.32*. These charts demonstrate that the estimated RHX mass, m_{RHX}, must be out by considerable amounts for the age estimates to work.

$t^{1/4}$	E_a (avg. 130C and 500C) (kJ/mol)	Age (yrs)
Ann	93	287
Esp	39	111
Nic	90	4115
Mac	95	15843939
Ria	127	77786
Rat	108	401647
Cal	80	2771
Joy	99	535
Bel	42	787
Tur	114	21658
Ted	86	148

Table 9.3: Age estimates using RHX activation energies calculated form the average of the 130C and 500C component activation energies.

Attempts to correlate the mass and age discrepancies with various factors and sources of uncertainty will be discussed throughout the remains of the chapter. However, the many factors involved and their varied effects complicate matters considerably, making it very difficult to attribute the issues in dating to specific causes with any certainty. Nonetheless, what the following discussions will do, as the above discussion has touched on, is emphasise how sensitive RHX dating (and

this is not just restricted to the component based approach) is to these factors, and demonstrate that unless these factors can be remove, minimised or very well quantified, then assessment of the validity of RHX dating using various approaches and models will remain inconclusive or clouded. In the present work these factors and sources of uncertainty can be outlined as follows:

1) Experimental (Mass Gain Data and Modelling)
    a. Procedure (aging temperatures and homogeneity of samples)
    b. Quality of Data (environmental control and resolution of data)
    c. Modelling (appropriate model, $t^{1/4}$ or $t^{1/n}$, rates and activation energy)
2) Temperature History and Effective Lifetime History (ELT)
3) Organic Matter
4) Drying and Loose Water
5) Gypsum Dehydration
6) Short Term Elevated Temperature Effects (STETE)

This is not intended to be a comprehensive list of factors/issues in RHX dating, instead representing factors affecting the estimated ages that are examined and dealt with in the present work. For example, no issue with goethite dehydration (Burakov and Nachasova (2013) was encountered and this source of issues is not discussed. There are no doubt additional sources of uncertainty which will arise in future work.

To summarise, for the present study, where at the outset eighteen samples were selected, only two samples provided good dates for either mass gain model (these samples differing for each model). Six samples were identified early on as problematic due to very high surface area and possible pore condensation (capillary) issues. Issues in a further four samples can be associated with the dehydration of gypsum (*Mac* and *Bel*), discussed below, high surface area and poor activation energy estimation (*Cau*), and the absence of *Event B* in TG-MS as well as 130C component and activation energy estimation issues (*Nic)*. The remaining eight

samples were well-behaved with no obvious problematic behaviour. The most likely reasons for issues with these samples are discussed below.

To conclude, the dating trials do not provide conclusive support for either the $t^{1/4}$ or $t^{1/n}$ model, and the use of a component based approach can not be validated or discredited, being strongly affected by many sources of uncertainty. Therefore, the validity of the component based approach remains unclear; however the presence of a 130C component with a *Stage 2* behaviour similar to that of a 500C component means that the dating methodology used in previous studies (for example Wilson et al. 2009; 2012; Le Goff and Gallet 2014a; 2014b) is unlikely to have been appropriate and needs to be altered. The present author believes that the component based has potential and provides a means of proceeding that merits further examination in more refined experiments where other sources of uncertainty have been eliminated, marginalised, or quantified.

9.4.2 Factors and Issues

Setup, Data, and Modelling

The samples were aged at temperature 25°C, 35°C, 45°C, the lowest of which is approximately 15°C above the ELTs of the samples. The result of this is that the uncertainty in the estimated mass gain rates, calculated using the temperature dependence (Arrhenius plots) and activation energies modelled at the higher aging temperatures, increases with distance away from the aging temperatures, and the effect on the age estimate uncertainties increases also, *Figure 8.29* and *Figure 8.30*.[27] Unfortunately the experimental setup used did not permit this, but clearly it would be advantageous to have run additional samples near the ELT as carried in other studies (for example Wilson et al. 2009; Clelland et al. 2014; Le Goff and Gallet 2014a; 2014b). The benefits of running at higher aging temperatures are a shorter *Stage 1*, previously discussed, as well as an improved ratio of the mass gain rate to noise (due to fluctuations in environmental conditions). As well as this a wider temperature range over which the activation energy is estimated provides a better confidence in the temperature dependence and it holding through over a wide range of temperatures.

Uncertainties in the activation energies are quite large and have been mentioned before. They results from uncertainties in the estimated mass gain rates, due inhomogeneity in the subsamples, data quality, modelling, and the number of temperatures used in the Arrhenius temperature dependence plots. Inhomogeneity is not considered to be a major issue in the present set of samples where subsamples were composed of > 100 granules (15-25g with each granule weighing approx. 0.05-0.15g) that had been well mixed prior to separation. This is also generally supported by Arrhenius plots and convergent fractional mass loss estimates. As well as this, the amount of material available for destructive use is a luxury that will not be the case for dating of individual or precious sherds so this is an area where refinement may be limited by material available.

[27] The equation used in estimating the uncertainty in the rate at lower temperatures is a standard confidence interval equation, see Montgomery and Runger 2011, page 422.

The quality of the data could be improved with an enhanced setup that does not require ECC-GBA transfer, removing timing and equilibration issues in the GBA, as well as continuous mass gain measurements as collected in other work (for example Wilson et al. 2009 and Le Goff and Gallet 2014a). The use of greater than three aging temperatures might be possible but could well be limited by samples material; the present work has been very comprehensive in this regard by having sufficient material to run 18 samples at three different aging temperatures, not matched in the existing literature. In future work, an ideal setup would involve at least three environmentally controlled chambers where samples are weighed continuously, with one set near the aging temperature and the remaining two at higher temperatures. The improved data quality of such a setup would also enhance the modelling results; the use of a $t^{1/n}$ model does describe the data better but has its own issues – increasing the number of parameters modelled also increases the uncertainties, discussed previously. However, as demonstrated, if multiple mass gain curves are used to refine the *1/n* value to a fixed *1/r* value, the modelling can be enhanced.[28]

Temperature History and Effective Lifetime Temperatures

The local temperature histories were compiled using surface air temperature records and reconstructions, for example *Joy* in *Table 8.5* and *Figure 8.9*. These were then used to simulate the mass gain and ELT over the lifetime of the ceramic, *Figure 8.10* and *Figure 8.11* for *Joy*. The results, compiled in *Table 8.6,* demonstrate the variation in ELT for each sample and mass gain model; the difference between the mean lifetime temperature (MLT), T_{mlt}, and the ELT, T_{elt}, can be quite small, for example the ELT is larger by +0.2°C for *Bel* ($t^{1/n}$), or large, for example +2.47°C for *Mac* ($t^{1/4}$).[29] The effect such a difference or, indeed, any uncertainty in the ELT, can

[28] Note, that a more rigorous statistical treatment would be required to account for uncertainty in *1/r* but the overall uncertainty of the $t^{1/n}$ modelled parameters should be improved when multiple curves are used to refine *1/n*.

[29] This difference is generated by the Arrhenius temperature dependence of the sample whereby over a period of temperature variation (i.e. annual temperature cycle) higher temperatures have a proportionately larger mass gain than lower temperatures.

have on the estimated ages can be examined through the age-temperature curves, *Section 8.4.1*. For example, for *Ann* ($t^{1/n}$), *Figure 8.13*, the estimated ages at ELTs of 9°C and 10°C are approx. 130yrs and 115yrs, respectively. For this same pair of ages, for *Joy* ($t^{1/4}$) the ages are approx. 440yrs and 380yrs, respectively, *Figure 8.21*. For *Cau* ($t^{1/4}$), the ages are approx. 550yrs and 480yrs, respectively. It evidently depends considerably on the gradient of the age-temperature curve at the point of interest. These few examples are typical (for samples that produced more reasonable ages) and highlight uncertainties that are of the order of 10-15% of the age of the ceramic per 1°C uncertainty. It is difficult to put an estimate on the uncertainty in the ELT, but where temperature reconstructions are used and where the temperature history of the ceramic is well described by surface air temperatures, then the present author is of the opinion that a minimum uncertainty of ±0.5°C is likely (discussed with regard to Wilson et al. 2012 in *Chapter 2*). This suggests minimum uncertainties of ±5% should be expected at best with the dating technique.

Again, the estimation of the temperature history was an involved process, yet this was without consideration of the effect of burial conditions, internal building thermal effects, and storage conditions. A rigorous temperature history reconstruction for all samples was beyond the scope of the present work and merits future examination. Nonetheless some comments can be made. The effect of burial condition has been examined by Hall et al. (2013); it is clear that burial dampens the effects of thermal oscillations (i.e. the diurnal and annual temperature cycles which are the source of the difference between the ELT and the MLT, see Barrett (2011)) with the ELT drifting towards the mean lifetime temperature of the ceramic for deeper burial. Therefore, the actual ELT of a sample that has been buried can be considered approximately bound by the mean lifetime temperature (lower bound) and the ELT estimated from surface air temperature records/reconstructions (upper bound), both of which can be examined both on the age-temperature curves, discussed below, and in relation to the estimated working temperature, T_W, already discussed. For other factors, such as possible elevated temperatures associated the context of a brick, the use of age-temperature curves

permits interpretations regarding these additional factors to be made, at least in term of likely, plausible, or unacceptable working ELTs, T_W, particularly where the temperature history is slightly ambiguous or temperature history reconstructions are unavailable.

A useful finding, perhaps, comes from examination of the relationship between the difference between the ELT and the MLT, $T_{elt} - T_{mlt}$, and the RHX activation energy, E_{aRHX}, *Figure 8.12*. There is a strong linear relationship between the two, (R^2 = 0.98/0.99), with the activation energy a clear predictor of the difference in temperatures. This relationship could, where a mean lifetime temperature is known, provide a useful shortcut for estimating the ELT without running any simulations or carrying out any unnecessarily complicated calculations.

In any case, variation in the ELT can contribute significantly to the age estimation of the ceramic and where possible should be given detailed examination. Otherwise, the use of age-temperature curves, and calculation of working temperatures for the ELT, can provide a useful means of examining if the estimated ages seem realistic. In the present work, some discrepancy in the age estimates of certain samples (buried or likely to have experienced elevated temperatures) may be partially attributed to issues in the ELT estimation but, as discussed in terms of working temperatures, uncertainties in ELTs do not generally explain the issues with the dates.

Organic Matter

The organic matter (with OM/OC at 1.95) has already been discussed in relation to its presence in all samples, and generally in significant quantities, say 10-50% of the estimated total fractional mass loss. Experimentally, it is not ideal that for each sample only a single estimate of the carbon content was carried out using two measurements of the carbon content of two subsamples, one of which had been previously heated to 500°C.[30] These subsamples were taken from a well-mixed

[30] This was constrained by the large number of samples, 36, which needed to be prepared and analysed. Ideally, the carbon content of the subsamples used in mass gain experiments would be captured during heating at 500°C; if conducted on the three subsamples, this would also provide some useful information on the homogeneity of the samples and uncertainty in the carbon content.

powder of the remaining granules from which the dating subsamples were taken. Hence, the samples used in carbon content analysis are expected to be well homogenised and representative of the dating samples in their carbon content.[31] Nonetheless, variation is to be expected, and with only a single estimate carried out per sample the repeatability of carbon content measurements and the associated uncertainty can not be estimated. As well as this there will be sources of uncertainty in the procedure used (described in *Chapter 4*) for its estimation. However, the author worked under the assumption that the uncertainties in the carbon content, associated with subsample variation and the experimental method, would be minor when compared with that associated with the organic matter to organic carbon ratio; the range of the OM/OC uncertainty used was 1.4-2.5, based on considerations in *Chapter 2*, and this range (which equates to a percentage uncertainty of 28% in the mass of organic matter (based on OM/OC ratio of 1.95 used in age estimates)), was considered broad enough to encompass and take account of any sources of uncertainty in the carbon content.[32]

This range of uncertainty used for the OM/OC ratio has a considerable effect on the estimated ages of the samples, *Table 8.8, Table 8.9*, and *Figure 8.2*, causing an uncertainty in the age range of a minimum of 35yrs (for *Cal* and $t^{1/n}$) but more typically on the order of at least 100 years for samples where the age estimates are in closes agreement with the known ages. For example, with the best sample using the $t^{1/4}$ model the uncertainty associated with the OM/OC ratio leads to an age range for *Joy* of 321-489 years. If the mid-point in the range is used[33] this can be re-written as 405±84 years, or a percentage uncertainty of 20%. For the best samples using $t^{1/n}$, the age range in *Ann* is 59-182 years, or 120±60 years, a percentage uncertainty of 50%. The effects can be quite considerable, then, but does not explain the issue of large ages in many samples.

[31] The XRD, FTIR, and XRF analysis has demonstrated that the subsamples were almost identical mineralogically and in elemental composition. The analysis for reheated and non-reheated were carried out on different subsamples but the spectra and compositional results are almost identical.

[32] The use of 1.4-2.5 is, itself, a subjective one and based on a short survey of the literature, but greater ratios are possible.

[33] The age estimate based on an OM/OC of 1.95 was 399yrs old. However, the effects of uncertainties on the age are not symmetric, because the age is proportional to mass^4, see Chapter 3 Equation 9.

The possibility that the mass discrepancy, m_{out}, resulted from a systematic issue in the estimation of the organic matter mass was checked, *Figure 8.33 (right)* and *Figure 8.34 (right)*; however no significant relationships (p = 0.5223 and 0.5918) were found, suggesting that a multiplicative error in the OM/OC ratio is not a major source of uncertainty in the dating estimates. In reality, the OM/OC ratio is likely to vary from sample to sample (without necessarily varying the average OM/OC), and this variation will be reflected to some extent in the mass discrepancy, m_{out}; this in turn complicates correlating the mass discrepancy with other sources of uncertainty, for example loose water or STETE effects, discussed further below.

It is clear then that the presence of organic matter is a serious issue for RHX dating, as previously stated by Numrich et al. (2015), not alone because of the magnitude in which it can occur, but also because it has been found to be present in significant quantities in all samples (only *Lan* had very low levels), whether the samples were buried during their lifetimes or just exposed to atmospheric conditions. This ubiquitous presence of organic matter raises questions surrounding good RHX dates obtained in previous studies where the presence of organic matter was either not examined or treated in a very limited fashion (Wilson et al. 2009; 2012, see *Chapter 2*). It also may be a contributor to poor dates obtained in other studies where the organic matter was not quantified (for example Burakov and Nachasova 2013; Le Goff and Gallet 2014a; 2014b). As proposed by Numrich et al. (2015), in all future dating work, analysis of the presence of organic matter needs to be carried out and if suitable quantification is not possible, then its removal using methods described by Numrich et al. (2015) may be necessary.[34]

Loose Water and Components

The RHX dating method used by Wilson et al. (2009; 2012) required drying of the samples (105-110°C) to constant mass to remove any capillary or adsorbed water

[34] As stated by Numrich et al. (2015) this is provided the wet chemistry methods used do not alter the composition, hydroxyl content, or mass gain behaviour in any detrimental way.

(loose water).[35] However, unexpected issues were encountered with what seemed like a trivial stage in the dating procedure. Mass loss due to drying was still occurring even after 60 days of heating at 130°C, for example *Figure 8.1 - 8.3*, this despite significant pre-drying having been carried out, *Section 6.4.1* and *Section 6.4.2*.[36] As the duration of complete drying was indefinite, and due to time constraints, it was decided that the only way to proceed would be to attempt to model any additional mass loss due to loose water which would subsequently occur upon heating at 500°C. This mass could then be subtracted from the total mass loss, on the assumption that the mass of loose water is not associated with long-term RHX processes, i.e. is not due to removal of hydroxyls that have been gained over the lifetime of the ceramic. The question of whether or not this is appropriate will be returned to.

Two models (power-based and exponential-based) were applied to the mass loss curves, *Figure 8.1-8.2*, with the quality of the regressions variable in quality, *Table 8.2*. Differences between the goodness-of-fits of both models are minor (the exponential model being better in 10 versus 6 cases) and do not provide clear support for the selection of either model; a better distinction might be made with improved quality data, however the issue with drying was not expected when the experiment was designed and this has been problematic. Control of environmental conditions during removal from the oven for weighing was inadequate to prevent large fluctuations in the mass, associated with the level of physisorption taking place; this is reflected in the *RMSE* values of the models, *Table 8.2*, where samples with high surface area (*Etr, Rom, Por, Lan,* etc) have the largest fluctuations, see for example *Figure 8.2* for *Lan*. A more refined procedure is recommended in future.

The correlation of the modelled remaining mass of loose water with properties with which it would be expected to be associated, for example surface area and pore volume, was examined, *Table 8.1;* these results favour the exponential model.

[35] It might be better to use the expression physisorbed water, however the expression loose water is retained to refer specifically to the water removed during drying.

[36] Indeed, the elevated drying temperature of 130°C was selected over 105-110°C to speed up drying because preliminary tests suggested it might be an issue.

The exponential model was selected for the reasons above and also because the power-based model was problematic; for a number of samples the modelled mass of remaining loose water exceeded the mass loss due to heating at 500°C obtained from mass gain experiments, and for several samples regressions using the power-based model produced parameter values that were nonsensical (i.e. a final 'dry' mass that exceeded the initial mass of the drying curve). As well as this, the use of a power model was motivated by a $t^{1/2}$ behaviour suggested by Brosnan and Robinson (2003); however, the model could only be successfully applied with the power constraint relaxed (*1/n* instead). The exponential model is more satisfactory in its interpretation, *Section 3.11*, with the rate of moisture removal being proportional to the level of moisture remaining.[37]

While the exponential model was selected for use, the authors emphasises that this was borne out of pragmatism and the appropriateness of this model requires more investigation; the quality of the fits produced, for *Figures 8.1-8.3*, were less than satisfactory, and the confidence intervals were also very large, for example *Figure 8.3* and *Figure 8.4*. Nonetheless, its use was deemed the only way to proceed. That the modelled remaining loose water was generally greatest for the high surface area samples, *Figure 8.4*, is somewhat reassuring and would also explain the greater correlation of this model with the surface area, pore volume and TG-MS data, *Table 8.1*, the inference being that for high surface area samples a significant quantity of physisorbed water is still being removed when heated at 500°; for normal, low surface area samples, this has previously been shown to be unlikely.

This prolonged drying is clearly an issue for RHX dating; its possible presence in previous work was examined, with the conditions of drying and evidence for constant mass or long drying times summarised in *Table 9.4*. For the majority of dating trials, the samples were dried at 105-110°C until the samples reached constant mass (Wilson et al. 2009; 2012) or for a fixed duration expected to be long enough to dry out the samples but without a strong rational for selection of drying times ranging from a few hours to a few days (Bowen et al. 2013; Burakov and Nachasova 2013; Numrich et al. 2015). These trials were for samples that are of

[37] This also makes sense if a chemisorbed process is being considered.

typical size 0.5-10g, greater than the size of the individual granules used in the present work (maximum size of approx. 0.3g). For experiments where a fixed duration was used without drying to constant mass being recorded, there is no certainty the samples actually did dry out. For the experiments where samples were stated as drying to constant mass (Wilson et al. 2009; 2012), no evidence or data to support this is presented. There is support for the findings of the present work in the publications of Bowen et al. (2011) and Le Goff and Gallet (2014a; 2014b). Bowen et al. (2011, Figure 3) produced drying curves that demonstrated that after a period of 2 weeks drying at 100°C constant mass had still not been achieved, *Figure 9.2*, however, they do not pursue the matter much further and this was for relatively large samples, 32-96g.

Publication	**Sample Size**	**Drying Temp. (°C)**	**Duration (°C) (Reason)**	**Drying Data Presented (Y/N)**
Wilson et al. (2009)	3-5g	105	To constant mass	N
Bowen et al. (2011)	32-96g (sherd)	110	20-30hrs However, incomplete drying after 2 weeks)	Y
Wilson et al. (2012)	0.5-4.0g	105	To constant mass ('few hours' to 'several days')	N
Bowen et al. 2013	1-2g	110	30-50hrs No reason	N
Burakov and Nachasova (2013)	1-15g	105	12hrs	N
Le Goff and Gallet (2014a)	2-3g	105	4 and 16hrs for one group 66 and 51hrs for one group Issue with duration of raised, additional mass loss with repeated heating	N Mass gain curves demonstrating variation in mass level with drying temp. 95/105°C and duration
Le Goff and Gallet (2014b)	2-3g	105	11hrs and 14 days	N Mass gain curves demonstrating increase in mass gain rate ($t^{1/4}$) with prolonged drying
Numrich et al. (2015)	2-4g	110	48hrs	N

Table 9.4: Summary of the drying conditions and presence of drying data in the literature.

Le Goff and Gallet (2014a; 2014b) draw attention to the need for better understanding of the effects of drying temperature and duration, finding that for longer drying times or higher temperatures there is an additional/greater mass loss

(observable in a shift in the subsequent mass gain curves to lower mass, see Figure B of Le Goff and Gallet (2014a)). Unfortunately, they do not record the mass of the samples as a function of drying time, so again it is not possible to know if, even for the longest drying times used, 14 days, complete drying occurred.

In any case, from the above, there is a lack of evidence in the literature that drying to constant mass is actually achieved, with instead evidence that it is instead prolonged (Bowen et al. 2011) and poorly understood Le Goff and Gallet (2014a; 2014b). The present work suggests that drying is a non-trivial issue that requires future attention, with more refined mass loss curves and a deeper examination of appropriate modelling necessary

It has been discussed and suggested earlier in this chapter that the 130C component of mass gain is associated with the slow removal of chemisorbed water (*Event B*) during drying. This interpretation has implications for the use of the modelled remaining loose water, m_{lw}, which was subtracted from the total fractional mass, m_{RHXC}, as part of the dating methodology. This was carried out under the traditional assumption that drying at 105-110°C is only removing physisorbed water (adsorbed, pore) (Wilson et al. 2009; 2012). However, this assumption was based on the assertions that equilibration of the mass did occur following drying (Wilson et al. 2009; 2012). The present work and the work of Le Goff and Gallet (2014a; 2014b) show that this is not the case and that the previous assertions were not supported experimentally (Le Goff and Gallet 2014b). Instead, the mass gain obeys a long term $t^{1/n}$ behaviour in the second stage. If the mass gain rate of this $t^{1/n}$ behaviour is interpreted as resulting from removal of chemisorbed water, and if it is chemisorbed water that is being removed in the drying curves of the normal samples, *Section 8.1*, then it is questionable if the modelled remaining moisture, m_{lw}, should indeed be removed from the total fractional mass loss during heating between 130-500°C. The following hypothetical arguments can be applied:

1. The mass gain rate of the 130C component is proportional to the amount of chemisorbed water removed (reflected in the amount of drying that has occurred for normal samples). Additional drying (if not complete) will result

in removal of more chemisorbed water and will be reflected in an increased 130C component mass gain rate as the potential number of sites available for chemisorption increases. This is supported by Le Goff and Gallet (2014b, Figure C - supplementary data), *Figure 9.3*, where increasing the duration of heating results in an increase in the mass gain rate.

2. The remaining chemisorbed water, not removed, but that could potentially be removed at 130°C is equivalent to the modelled loose water, m_{lw}. This will be removed upon heating at 500°C and will result in the contribution of a component of mass gain rate, a_{lw}, to the mass gain rate of the 500°C component, a_{500}.
3. The 500C mass gain rate, a_{500}, can then be seen as comprising of three components, the 130C component mass gain rate, a_{130}, the rehydroxylation component mass gain rate, a_{RHX}, and the contribution of the loose water chemisorbed sites, a_{lw}, with $a_{500} = a_{130} + a_{RHX} + a_{lw}$. Ideally, subtraction of the 130C mass gain rate, a_{130}, from the 500C mass gain rate, a_{500}, as part of the component based approach, is intended to leave the long term RHX mass gain rate, a_{RHX}. However, under the above arguments subtraction of the two components of mass gain rate will now leave a_{500}-$a_{130} = a_{RHX} + a_{lw}$
4. For the component based method to work, the mass gain rate, a_{RHX}, used in age calculations must have an associated mass estimate, m_{RHX}, the quantity of mass gained over the lifetime of the ceramic as a function of $t^{1/4}$ ($t^{1/n}$) due to the mass gain rate a_{RHX}. This mass is estimated from the difference in the intercepts of the modelled *Stage 2* mass gain curves, *Section 3.6*, i.e. $m_{RHX} = m_{130} - m_{500}$.
5. Therefore, for the mass gain rate $a_{RHX} + a_{lw}$ to work in dating estimations, it should be used in conjunction with $m_{RHX} + m_{lw}$, obtained from the difference in the intercepts, $m_{130} - m_{500}$; if m_{lw} is subtracted, as when treated as physisorbed water, then the mass m_{RHX} is inappropriately associated with the rate $a_{RHX} + a_{lw}$. In principal then, m_{lw} should not be subtracted where loose water is considered as due to chemisorption and associated with a long term mass gain rate.

The above line of arguments is plausible under the following assumptions: a) the *Stage 2* mass gain rate following heating at 130°C is due to removal of chemisorbed moisture; b) this *Stage 2* mass gain rate is long term (as for rehydroxylation); c) the mass loss associated with removal of this chemisorbed water is equivalent to mass gain which has occurred over the lifetime of the ceramic as a function of $t^{1/4}$ ($t^{1/n}$) and at the associated mass gain rate.

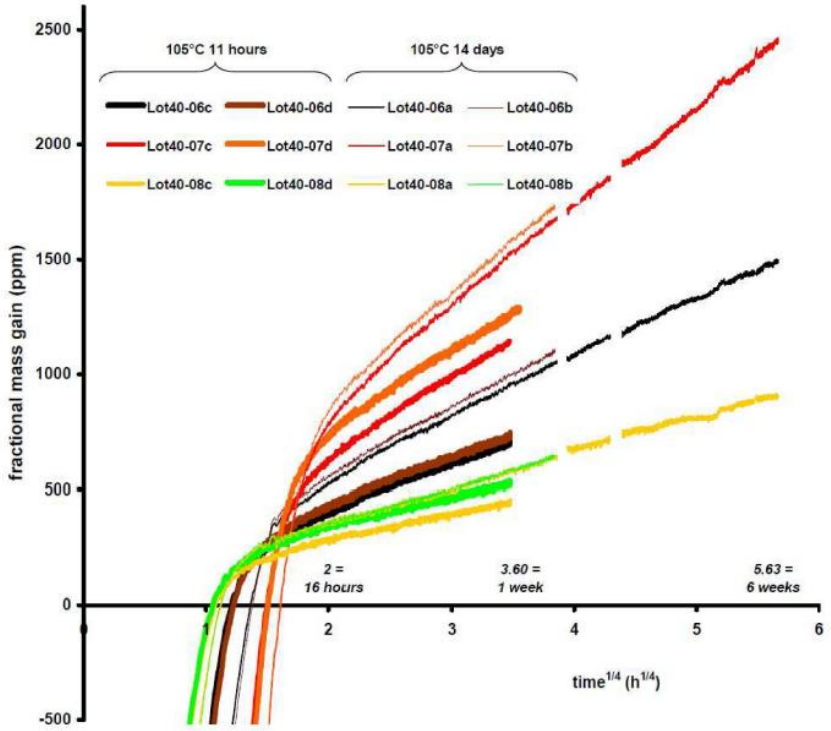

Figure 9.3: The effect of duration of heating at 105°C on the subsequent mass gain behaviour. From Le Goff and Gallet (2014b, Figure C - supplementary data). From each sample (colour) there is a thin (11 hours heating) and thick (14 days heating) line.

If the arguments above are valid, then one effect would be that by subtracting the loose water, m_{lw}, the mass used in the dating calculation would be too small, reflected in a negative mass discrepancy, and the ages would also be too small. As discussed above, the opposite is generally the case, with the mass discrepancies, m_{out}, positive, and the age too large. Any systematic issue with subtraction or the use of m_{lw} is also not reflected in correlations of it against m_{out}, *Figure 8.33 (left)* and *Figure 8.34 (left)* where p = 0.1409 and 0.6648 for the $t^{1/4}$ and $t^{1/n}$ models, respectively. However, given the estimated mass of loose water is only a very small contribution of the total fractional mass loss, typically 0.25-2% (*Figure 7.50*), it

might not be surprising that issues with its subtraction are not obvious in the ages estimates or mass discrepancy values; indeed, the mass of loose water, m_{lw}, is usually of an order of <1% of the mass discrepancy. Therefore, while a correction to the component based approach may be necessary to take account of the chemisorbed interpretation of the loose water, the absence of this correction is likely to have only a minor effect on the estimated ages (maximum of 10% of the age) of the samples relative to other issues, and does not explain the large discrepancies observed.[38]

This section has highlighted that drying of samples is not trivial and can be a prolonged process for which high quality mass loss data and appropriate modelling are required if the mass of loose water needs to be subtracted. If the loose water is associated with a long term chemisorption process, as discussed above, then an estimation of the loose water is not necessary and no subtractions of it need be carried out. However, this is an area that needs to be further investigated in order to clarify whether or not the 130°C component continues indefinitely as does the RHX component.

Gypsum

The presence of gypsum and its dehydration during heating at 500°C for samples *Mac* and *Bel* have previously been discussed. Associated with this was the observation of a large difference between the *S1* mass gains, m_{S1}, of the 130C and 500C components (25°C aging), *Figure E.4* and *Figure E.14*, a difference not found in the other samples, *Figure 7.77* and *Figure 7.80*. There are then two possible issues associated with gypsum. Firstly, there is a mass of water loss during dehydration of gypsum when the samples are heated between 130-500°C; this mass loss, if not associated with long term $t^{1/4}$ recombination following heating (as for loose water), will be included falsely in the total fractional mass estimate, m_{RHXC},

[38] It can be shown the if there is an uncertainty dm, in the mass, m, then the uncertainty, dt in the age estimate t is given by $(t+dt)/t = ((m+dm)/m)^4$. For the case of loose water contributing a maximum of 2% of the total fractional mass (of which the RHX mass is approx. 90%, typically), this corresponds to a variation in the estimated age of approximately $(1.022)^4 = 9\%$.

resulting in an erroneous increase in the age estimate. Secondly, if the level of physisorption is reduced following the conversion of gypsum/bassanite to anhydrite, then the magnitude of this difference will also be reflected as an increase in the total fractional mass estimate (the estimation of the total fractional mass requires that the level of physisorption is the same for both the 130C and 500C components).

In the present work, there is no estimate available for the mass loss due to dehydration but an estimate for the change in physisorption level is available. This is worth commenting on in terms of the magnitude of the effect it might have on the age estimates, particularly considering that *Mac* has the highest mass discrepancy (0.00513 and 0.00504, fractional mass for $t^{1/4}$ and $t^{1/n}$ models, respectively) of all samples for both models and *Bel* is the second highest for the $t^{1/n}$ model (0.00079 and 0.00152 for $t^{1/4}$ and $t^{1/n}$ models respectively). As stated previously, the estimates of m_{S1} are only approximate, but the differences between the 130C (the larger gain) and the 500C components, $m_{S1\text{-}130} - m_{S1\text{-}500}$, are as follows: for *Mac,* 0.00236 ($t^{1/4}$) and 0.00235 ($t^{1/n}$); for *Bel*, 0.00355 ($t^{1/4}$) and 0.00385 ($t^{1/n}$). The magnitude is clearly of a similar order to that observed for the mass discrepancies of these samples, particularly for the $t^{1/n}$ model, and therefore, gypsum dehydration, even only considering its effects on physisorption, may be a very significant contributor to issues encountered with the estimated ages of these samples. More focussed work on the hydration properties of anhydrite and gypsum in fired clays following heating is required; however, screening of samples for the presence of gypsum is recommended in future RHX work and methods for its removal should be explored if its presence is unavoidable.

STETE effects and Correction

The RHX mass gain rate has an exponential temperature dependence with the magnitude governed strongly by the activation energy. Because the mass gain rate is proportionately higher at higher temperatures than lower temperatures, this temperature dependence is responsible for the need to estimate ELTs instead of

average lifetime temperatures because of effects such as diurnal and annual temperature cycles (Barrett 2011), or burial and other lifetime events (Hall et al. 2013). It also means that if a sample experiences elevated temperatures (> 50°C for instance) for even a brief period of time it will gain mass at a considerably greater rate than at a lower temperature of say 10-20°C. This mass will be 'stored' in the RHX mass estimate of the sample, m_{RHX}, and could falsely lead to an over-estimate of the age of the sample, unless the event has been taken account of in the ELT estimation. Barrett (2013) has demonstrated that accelerated mass gain during cooling of a sample post-heating can lead to a considerable mass gain and an associated curvature effect in the $t^{1/4}$ behaviour (this would also effect $t^{1/n}$ behaviour similarly), again driven by the exponential temperature dependence.

However, it is not clear at what upper temperature limit the RHX mass gain rate can proceed up to before it has effectively ceased and the removal of physisorbed (and possibly chemisorbed moisture) is instead dominating the behaviour. Barrett (2013) estimated, based on the curvature in his samples' mass gain curves, that RHX mass gain had commenced in the temperature range 56-58°C during cooling post-heating. However, this was before curvature of the samples or a $t^{1/n}$ behaviour was considered likely to be real, discussed above. If a fraction of the positive curvature is due to the $t^{1/n}$ behaviour, then the effect due to mass gain during cooling is reduced and the commencement temperature will be less than 56-58°C.[39] The present work shows that the mass gain rate behaves normally for a reasonably large set of samples up to at least 45°C and Wilson et al. (2009) has observed typical mass gain behaviour at 50°C. There has, otherwise, been no work done to examine at what temperature the mass gain becomes restrained, however Bowen et al. (2011) had issues with the mass gain behaviour of a sample aged at 80°C (behaviour could not be described by their generalised $t^{1/n}$ equation) and this could be telling.

If the process of chemisorption requires some level of physisorbed moisture to be present (i.e. an increased residence time of water molecules near reactive sites), then it can be assumed that RHX mass gain will have completely ceased by 105-

[39] The inherent curvature of the sample could be negative but given previous discussions and work a positive curvature is much more likely.

110°C. Earlier arguments suggest that removal of chemisorbed moisture also seems likely at these temperatures, supporting the cessation of chemisorption mass gain at some lower temperature. For 10/12 normal samples, a maximum rate of removal of physisorbed water occurs by 70°C in the TG-MS data, *Table 5.19*, and this may be telling if the removal of physisorbed water is indeed critical to the cessation of RHX mass gain.

Therefore, the best evidence available suggests rehydroxylation mass gain may cease or be limited by the temperature range 55-70°C. Yet the evidence is not convincing and more investigation into this is necessary. In light of this, the effects of short term elevated temperature events (STETE) were investigated with rehydroxylation permitted up to temperatures of 80°C and 95°C.

STETE effects were explored for the $t^{1/4}$ model under two conditions, moderate and strong (described fully in *Chapter 6*). The effects examined included mass gain during cooling of a brick following initial firing (BC80/95) and possible effects during heating of the sample as part of the present work (2 days heating at 60°C (2d60), 15 days heating at 76.5 or 78.5 (15d77/79), and 60 heating/cooling cycles during weighing of drying curves (60C80/95)).[40] The results are presented in *Table 8.10-8.12*. The arguments in the following discussion of these results are undertaken on the hypothesis that RHX mass gain continues up to temperatures of 80-95°C. If this is not the case, the effects will be less pronounced and some of the arguments are less applicable with regard to dating issues.

The effects on the estimated age, described by the extra age t_{stete} are considerable, *Table 8.11*.[41] The brick cooling effect adds very little extra age to many samples (<1 year for *Ann, Esp, Cal, Joy, Cau, Bel, Ted*) but as the RHX activation energy increases beyond 150kJ/mol, the effects becoming increasingly more pronounced, adding 43

[40] The use of a pre-drying stage at 76.5-78.5° was originally expected to be carried out at 85-90°C, at a temperature well above that for which RHX mass gain was expected to have ceased (55-60°C based on Barrett 2013). However, it was later discovered that the temperature on the dial of the heating cabinet was not accurate and 85-90°C actually corresponded to 76-5-78.5°C.

[41] Note that this extra age is cumulative, with the effect of a single event obtained just by subtraction of the extra age from the set of events without it. For example, the extra age added by the event 60C80 for *Ann* (moderate) is 1615-1585 = 30 years.

years to *Tur* (155kJ/mol), 426 years to *Rat* (183kJ/mol), 3112 years to *Nic* (204kJ/mol), and 10 million years to *Mac* (295kJ/mol) (all for the *Strong* STETE case but the *Moderate* case is similar). If RHX mass gain is permitted to proceed up to 80-95°C, this tells us that for samples with high RHX activation energies, the period of brick cooling following firing could add a considerable mass to the sample, resulting in very poor dating results. Bearing in mind that bricks that are fired in batches in either clamps or kilns may have a much slower rate and period of cooling with this effect then likely to be even more pronounce (this may also be the case for pottery). This, together with any inability to assess the original firing conditions, could make the dating of some bricks (and possibly pottery) particularly problematic.

For the pre-drying stages, the two days at 60°C show similar trends with significant effects only for samples with activation energies exceeding 130-150kJ/mol (20 years added to *Ann*, 132kJ/mol). The effects of heating for 15 days at 76.5-78.5°C are extreme but perhaps significant in that the order of magnitude of the extra age added is similar to that of the age discrepancy, t_{out}, between the estimated and known ages of many of the samples (for example *Ann, Esp, Mac, Ria, Rat, Cau, Tur*). The order is far too great for *Nic* and too small to explain the issues with *Cal* or *Bel*. These results highlight that (pre-)drying of samples at low temperatures (60°) or inadequately high temperatures (75-80°C) can both have notable and problematic effects for the dating of samples, particularly the latter. If RHX mass gain proceeds to these temperatures without limitation, then the agreement between the order of magnitudes, *Figure 8.35* and *Figure 8.36*, of t_{stete} and t_{out} for the $t^{1/4}$ model, suggest that the use of pre-drying stages at these temperatures was flawed and has had a considerable effect on the estimated sample ages.[42] More positively, if this is the case, the use of these pre-drying stages has permitted the extreme effects of STETEs to be clearly demonstrated and possibly provided evidence that RHX mass gain proceeds to 70-80°C. This also has implications for any archaeological ceramics or museum pieces which have undergone any drying at elevated

[42] These figures use t_{STETE} of all effects but the other effects (BC, 2d60, 60C) are negligible compared to the 15d77/79 effects.

temperatures; their use in RHX dating must be avoided unless the conditions and durations of storage can be extremely well defined.

After the 15d77/79 event, the effect of 60 heating/cooling cycles has the greatest effect. It contributes a similar magnitude of additional age as the two days at 60°C, and is again significant for samples with activation energies exceeding 130-150kJ/mol. This heating/drying was necessitated by repeated measurements of the sample mass during drying; in future it could be avoided by weighing of the sample as it dries (some form of thermo-gravimetric analysis where suitably large sample size is permitted).[43]

The estimated ages of the samples ($t^{1/4}$) were corrected by removal of the mass gain associated with the STETEs, *Table 8.13*, in order to get a picture of the magnitude of improvement that might be expected. Considering the estimates of the magnitude of STETE effects are considerably affected by uncertainties in the maximum temperature of rehydroxylation (and even if this is the same for all samples), uncertainties in the duration of events, and particularly in the precise temperature of the 15d77/79 event, the associated corrections should be considered rough at best. There is a general improvement, with most of the exceptionally high ages reducing considerably (*Nic* to the point of 0 age). Considering the magnitude of reduction of samples, and the difference between the correction using the *Moderate* or *Strong* conditions (driven primarily by the difference in 76.5°C and 78.5°C), it is plausible that the remaining discrepancies for *Nic, Mac, Ria, Rat, Tur* may be related to uncertainties in the STETE estimates. Note that *Nic* was problematic in terms of activation energy estimation and perhaps should be excluded from considerations. Otherwise, the sample *Cal*, undergoes no significant improvement, and *Ann* and *Ted* are reduced below the known ages, but again uncertainties in the STETE estimations (and the variation or rehydroxylation conditions sample to sample) could play a major role in this. Following the corrections, 7/12 samples provide an age estimate inside the age range of the

[43] Any approach that involves removing the sample from the heating environment will be problematic given the 130C component of mass gain will commence chemisorption as soon as exposed to moisture at a lower temperature.

known samples if the OM/OC ratio is permitted to vary from 1.1-2.7, an improvement on the uncorrected situation where only 4/12 found agreement.[44] The results support STETE effects being a plausible source of major discrepancies in the RHX dates using the $t^{1/4}$ model.

The STETEs were examined in detail for the $t^{1/4}$ model because many of the samples have activation energies high enough for significant effects to be observed; for the $t^{1/n}$ model the activation energies are notably lower with only *Nic* (problematic activation energy estimation) and *Mac* having high activation energies (>130kJ/mol) so a full STETE treatment was not carried out. However, some results for the $t^{1/n}$ model are included below in *Table 9.5* and worth commenting on.

The STETE events are in two groups, one only consisting of the 15d77/79 events, and the other the cumulative effects of BC80, 2d60 and 60C80. It can be observed that the brick cooling, heating for two days, and heating/cooling cycles, have very minor effects for 9/11 samples (<6 years for 8 samples, 23 years for *Ria*) and are particularly large for samples with very high activation energies (*Nic* and *Mac,* the activation energy of the former being questionable).

For the 15d77/79 event, the effects, while significantly less pronounced than the $t^{1/4}$ model, are considerable nonetheless. Aside from *Cal*, *Ted* and *Bel* (all < 5 years additional age), there are moderate effects observed for *Esp, Joy*, *Tur* (24-56 years), strong effects for *Ann, Ria* and *Rat* (110-771 years), and extremely large effects for *Nic* and *Mac* (122myrs and 6myrs, respectively). If the sample *Nic, Mac* and *Bel* are excluded, it is clear that for the remaining samples with high age estimates *Esp, Ria, Rat, Tur*, the STETE effects, while contributing significantly to the age discrepancy, are not large enough to fully explain the issues observed. As well as this the STETE effects push *Ann* (a previously good dating results) and *Joy* away from their known ages. Note, it does not contribute to issues with *Bel,* and for *Mac,* while a considerable contribution, is not adequate to cover the full age discrepancy; for these samples, it is plausible that the age discrepancy may be caused by two large

[44] In this case the OM/OC ratio was permitted vary from 1.4-2.5. Loosening the constraint to 1.0-3.0 does not change the number of samples finding agreement.

sources of issue, gypsum dehydration and STETE events, with the former the dominant issue in *Bel*. In conclusion, the STETE effects due to 15 days heating at 76.5-78.5°C are significant for the $t^{1/n}$ model, but are less pronounced than for the $t^{1/4}$ model, and are not likely to fully explain the issues with age estimates for most samples.

To summarise, if RHX mass gain proceeds to high temperatures, i.e. greater than 60°C, the effects of STETE events could be considerable, particularly if the RHX activation energies exceed 130-150kJ/mol. For activation energies below this, STETE effects only become considerable at higher temperatures, i.e. > 75°C, and for long durations of the event, i.e. days. In the present work, STETEs provide a plausible explanation for a large part of the age discrepancies observed for the $t^{1/4}$ model, however, for the $t^{1/n}$ model while a considerable contributor it is not sufficient to explain the full range of age estimation issues. Better understanding of the upper temperature range and environmental conditions under which RHX can proceed is required before certainty can be attributed to the above findings.

The implications for RHX dating may be significant, particularly for samples with high activation energies. The early period of a sample post-firing could potentially contribute very significant quantities of RHX mass which in turn could have detrimental effects on the estimated ages. The same problems may also arise from other short term elevated temperature events, for example heating and cooling cycles in cooking pots, again contributing considerable error into the dates if not accounted for.[45]

[45] Ceramics with evidence of use in cooking/heating should probably be avoided as organic residues are likely to contribute significantly to the organic matter and carbon content of the sample (Evershed 2008), however, there may be cases where these are the only samples available for dating.

$t^{1/n}$	E_{aRHX} (kJ/mol)	Known Age (yrs)	t_{out} (yrs)	t_{stete} BC80+2d60+60C80 (yrs)	t_{stete} 15d77 (yrs)	t_{stete} 15d79 (yrs)
Ann	95.67	110	-1	5	89	110
Esp	78.86	141	448	1	24	28
Nic	270.01	398	1023960	2128225	72125062	122320699
Mac	232.53	228	9148685	104272	3875769	6108360
Ria	119.10	339	4530	23	611	771
Rat	100.17	245	4665	6	131	159
Cal	56.86	182	12	0	4	5
Joy	82.77	412	-233	3	35	41
Bel	23.51	395	3995	0	1	1
Tur	86.10	229	194	2	47	56
Ted	55.80	339	-321	0	4	5

Table 9.5: The STETE effects on the $t^{1/n}$ ages. t_{out} is the difference between the estimated and known age. t_{stete} is the additional age the STETE event would contribute (based on the additional mass the event adds to the simulated mass gain of the ceramic over its lifetime, m_{sim}). The STETE events are as follows: BC80 = brick cooling with maximum RHX temperature of 80°C, 2d60 = 2 days at 60°C, 60C80 = 60 heating/cooling cycles with maximum RHX temperature of 80°C. Note that yrs=0 correspondents to an additional age of <0.5 yrs.

9.4.3 Age-Temperature Curves and AETH Approach

Age-Temperature Curves and AETH Approach

The use of age-temperature curves, *Figure 8.13-8.25*, and the activation energy temperature history (*AETH*) approach, *Figure 8.37*, while not particularly useful in the present work due to the range of issues previously discussed, are presented as potentially very useful tools for the interpretation of RHX dating ages and their more accurate estimation. Both approaches have different strengths in their application.

Age-temperature curves are best applied to samples where the temperature history is less clear. Presenting the age estimate as a function of the ELT, they permit visual interpretation of the likely range of ages possible, as well as the likely age for a range of different, but plausible, ELTs. These curves also have the advantage that if additional temperature history information arises at a future point all that is required is an alteration of the ELT with the new age estimable from the existing age-temperature curve.

The *AETH* approach covers the opposite scenario. Where the temperature history is better understood this can be used, in principle, to provide a more accurate estimate of the age of a ceramic. By running a simulation of the mass gain of the ceramic as a function of years before present, and determining where this finds best agreement with the experimentally determined mass gain, an age range for the ceramic can be determined that takes account of the subtle variations of the temperature history as well as uncertainties in the temperature history and mass gain estimates; this should, in principle, be more accurate than making a single estimate of the ELT (requiring an approximate age in the first place) and then calculating the age of the ceramic based on this.

Again, these approaches are presented in the hope that with further refinement of the RHX dating method, they can be better applied and developed in future studies.

Chapter 10

Conclusion

10.1 Thesis Objectives, Findings and Interpretations

The aim of this work was to independently examine both the mass gain behaviour of fired clay ceramics, in particular certain key properties required for RHX dating, and the application of a RHX dating methodology (component based approach) to archaeological ceramics of known age. Using mass gain measurements, involving transfer of samples between environmentally controlled cabinets and a glove box arrangement following drying (130°C) and reheating (500°C), the mass gain behaviours of a large set of varied samples (predominantly post-medieval brick) from varied contexts were examined. The results of modelling of this mass gain data were further used to examine key behavioural properties and also in the application of a component-based dating methodology to the samples. As well as this, a suite of characterisation techniques were carried out on the samples, including XRD, FTIR, p-XRF, petrography, BET analysis, TG-MS, and carbon content analysis, with the results of their application combining with the mass gain data to provide a better understanding of the factors affecting both the mass gain behaviour and the age estimates obtained from dating.

The use of the glove box arrangement, a large set of varied samples, and a wide range of techniques has been fruitful, permitting a large set of mass gain curves of varied behaviours to be obtained which could then be examined against a range of characteristics (for example mineral composition, surface area, carbon content, TG-MS curves, firing temperature); this would not have been possible without the ECC-GBA transfer approach which permitted large numbers of samples to be run, as well as the decision to run a large number of samples to begin with. The resulting findings have been very positive with many significant new discoveries made as well as strong and independent validation of properties that had previously been debated. The key findings and interpretations are summarised below into two groups, *RHX Behaviour* and *RHX dating.*

RHX Behaviour – Key Findings and Interpretations

- *Drying of samples is prolonged and indefinite:*

  All samples exhibited a sustained period of drying (130°C) without completion after 60 days. For *normal* samples this is interpreted as due to the slow removal of chemisorbed water, and is supported by the only *normal* sample which appeared to have dried having a very minor water loss peak associated with this chemisorption process in the TG-MS data. This is an issue which has generally gone unreported in previous work and requires greater attention.

- *Poorly behaved samples due to high surface area and possible condensation effects:*

  The mass gain curves permitted samples to be split into twelve *normal,* well-behaved, samples and six *abnormal,* poorly-behaved, samples. The latter had poor mass gain curves with large scatter and were associated with possible capillary condensation issues either due to the high %RH (75%) at which experiments were run or due to transfer between high %RH but different temperature conditions during aging and weighing. The *abnormal* samples had higher specific surface area (and pore volume) than *normal* samples, > $5m^2/g$, and exhibited hysteresis effects in their nitrogen sorption curves during BET analysis. These samples also exhibited higher levels of calcite and organic matter content, an implication being that sources of secondary contaminants are higher in samples with greater surface area/pore volume. It was proposed that surface area analysis could be used in future to screen for problematic samples or aid in the selection of suitable %RH conditions in which to age samples.

- *Two-stage mass gain following drying, with similar behaviour to that following reheating at 500°*:

  Following heating at 130°C, all normal samples exhibited a two-stage mass gain behaviour with *Stage 1* of very similar magnitude and duration to the *Stage 1* following heating at 500°C, and *Stage 2* behaving in the same manner to that following heating at 500°C also, having a $t^{1/n}$ behaviour but

with a lower mass gain rate. This provides considerable support to related findings by Le Goff and Gallet (2014a; 2014b).

- *The Stage 1 mass gain is due to physisorbed water:*

  The *Stage 1* mass gain (not associated with $t^{1/n}$ behaviour) for both the 130°C and 500°C mass gain curves was found to be caused by physisorbed water, evident in its correlation with surface area/pore volume, its similar magnitude following 130°C and 500°C heating, and its connections with the removal of physisorbed water in TG-MS data. The duration of *Stage 1* was also found to be correlated with its magnitude and also with the specific surface area of the sample.

- *The Stage 2 mass gain of the 130°C component has an Arrhenius temperature dependence, and is associated with a (low temperature) chemisorption event:*

  The *Stage 2* mass gain behaviour was found to have an Arrhenius temperature dependence for both the 130°C and 500°C mass gain curves. The average activation energy of the 130°C (78kJ/mol or 58kJ/mol, model dependent) process was slightly lower than that following heating at 500°C (86kJ/mol or 67kJ/mol), but significantly lower than the estimated RHX activation energy (137kJ/mol or 101 kJ/mol), but all were in ranges previously associated with rehydroxylation (see Clelland et al. 2014). The interpretation is that the *Stage 2* mass gain following drying at 130° is due to chemisorbed water removed during heating. This is supported by a related water removal event in the TG-MS data, distinct from lower temperature physisorption and a higher temperature event associated with dehydroxylation.

- *The Stage 2 mass gain rates of the 130°C and 500°C curves are linearly related, with a fundamental connection between the underlying chemisorption events suggested:*

  A strong linear relationship (R^2 = 0.94-1.00) was found between the mass gain rate of the 130°C component and the 500°C component. This was the case for each of the three aging temperatures, with the ratio between the rates approximately 1.25-1.30. This demonstrates a very significant

connection between the two processes. Two interpretations were proposed: a) the chemisorption event associated with 130°C has a fundamental relationship to that associated with 500°C heating, with both events having an almost constant ratio of chemisorption sites across different samples, and suggesting some fundamental compositional component is present across all samples; b) heating at both 130°C and 500°C removes all forms of chemisorbed water, albeit at lower rates of removal for 130°C, with the ratio of the mass gain rates, associated with active chemisorption sites, governed by the heating temperatures and durations, common to all samples. The former of these interpretations is preferred.

- *The 130°C component Stage 2 mass gain is interpreted as due to the removal and subsequent recombination of low temperature chemisorbed water, distinct from a higher temperature rehydroxylation event:*

  Stage 2 mass gain following heating at 130°C is suggested to be due to the removal of water associated with a low temperature chemisorption event, and this event is likely distinct from a higher temperature chemisorption event associated with rehydroxylation. This is supported by differing activation energies and two distinct processes in the TG-MS data; however, some fundamental connection between the two processes is suggested by the strong linear relationship between the mass gain rates at different aging temperatures.

- *A component-based approach was developed applied to isolate RHX components necessary for dating, in light of the on-going 130°C component:*

  A component-based approach, with 130C, 500C and RHX component, was developed to take account of this 130°C mass gain behaviour, the core principle being that the *Stage 2* mass gain rate following heating at 500°C can be treated as due to the addition of the 130C mass gain rate and an RHX mass gain rate. The RHX mass gain rate, RHX mass, and activation energy can be calculated following simple algebraic manipulation to extract the RHX components. The resulting good quality Arrhenius plots for the RHX activation energy and the agreement in the total RHX mass loss estimated

for three different aging temperatures provide support for the principles of this approach.

- *Strong support for a $t^{1/n}$ model:*

  Strong support was found for the use of a $t^{1/n}$ model to describe the *Stage 2* mass gain behaviour of samples, with *1/n = 1/6-1/2,* dependent on the sample and supporting other work (Le Goff and Gallet 2014a; 2014b; 2015). Evidence of curvature in the mass gain data as a function of $t^{1/4}$ was present in all samples and shown not to be associated with experimental conditions or mass gain during cooling. The curves were found to be better modelled with a $t^{1/n}$ approach. Furthermore, the curvature for all six subsamples of a sample were found to agree very well in term of their modelled *1/n* values, despite having experienced different aging conditions (while at the same time having distinctly different *1/n* values to other subsamples which experienced identical aging conditions). A relationship was observed between the level of curvature and the surface area/pore volume of the sample suggesting a connecting between the diffusion mechanism and the pore structure; no notable relationship was found between the mass gain rates and the surface area/pore volume supporting their independence from these characteristics.

RHX Dating – Key Findings and Interpretations

- *Generally poor dating results with large ages – inconclusive support for the component-based approach or the use of a $t^{1/4}$ vs. $t^{1/n}$ model:*

  The estimated ages generally compared poorly with the known ages of the samples. Out of twelve samples dated only two can be said, for either model used, to have provided good agreement and these differed with the model used. The age estimates were generally too large. Many factors were shown to be plausible contributors to these issues and a range of their potential effects on the estimated ages was demonstrated; these factors included the presence of contaminants (organic matter), gypsum, issues with loose water not removed during drying, temperature history uncertainties, and the effects of short term elevated temperature events.

However, it was often not possible to attribute the age estimation issues to these factors with certainty and the results must remain inconclusive.

- *The need for better environmental control and higher temporal resolution data:*

  The sensitivity of samples to environmental conditions caused a considerable level of noise in the data of some samples. This noise is problematic and its effects on the modelled data can be significant – a more continuous and automated recording of the mass gain under better controlled environmental conditions would improve the statistics and data. As well as this, one aging temperature should be run close to the ELT, which was not possible with the present setup.

- *Temperature history a minor contributor to dating issues but significant source of uncertainty in the estimated ages:*

  It was found that 1°C uncertainties in the effective lifetime temperature can lead to typical uncertainties of the order of 10-15% of the age of the ceramic for well-behaved samples. This is a significant contribution and highlights the need for a good understanding of the temperature history, if possible. The magnitudes of the uncertainties in the ages associated with the ELT uncertainties were not major contributors to the problematic large ages in the present work.

- *RHX activation energy a predictor of the difference between the ELT and mean lifetime temperature (MLT):*

  For the present set of samples, with ELTs estimated from surface air temperature instrumental records and temperature reconstructions, it was demonstrated that a very strong linear relationship between the RHX activation energy and the difference between the ELT and the MLT could be used to predict the ELT based on the mean lifetime temperature of the ceramic. This provides a quick and provisional means of estimating the ELT without any complex calculations or simulations.

- *Organic matter was present in all samples in significant quantities and is a serious problem for RHX dating:*

  All samples investigated, whether retrieved from a standing building or a burial context, had significant quantities of carbon present, attributed to the presence of organic matter, most likely contaminants like humic-subtances or coke. This organic matter contributed anywhere between 10-50% of the total mass loss during heating at 130-500°C. Because of large uncertainties in the organic matter to organic carbon ratios used to estimate the organic matter mass, the uncertainties in the age ranges of samples were considerably affected, varying from 20-50% of the age of the best behaved samples. Therefore, the presence of organic matter is a very serious source of uncertainty in RHX dating and, unless the organic matter to organic carbon ratio can be refined, samples with high levels of carbon should be screened or have attempts made at the organic matter's removal, as suggested in previous work (Numrich et al. 2015). The uncertainties due to organics were not of an order to explain the large age issues with samples.

- *Loose water not removed during drying is an issue if due to physisorbed water but less so if associated with a long term chemisorption effect:*

  Modelling of loose water not removed during drying was problematic but an exponential model was preferred and applied. This loose water was found to contribute up to 2% of the total mass loss during heating at 130-500°C. If attributed to physisorbed water (adsorbed or pore water) uncertainties in this quantity will be reflected in the RHX mass estimate and contribute to issues in the age estimates to a maximum of approximately 10% of the estimated age. This is a considerable amount and clearly the quantity needs a refined method of estimation for future RHX dating. If, alternatively the loose water is due to removal of chemisorbed water, provided the chemisorption process is long term (lifetime of the ceramic), it has been argued that no subtraction may be necessary with the effect taken care of by the use of a component based approach. In any case, uncertainties in the quantity or its interpretation were only minor contributors to issues with the dating results.

- *Gypsum is a potential problem in brick samples:*

  For two samples of brick, gypsum (or less hydrated form bassanite) was found to be present. It was revealed by XRD and FTIR that dehydration to anhydrite occurred during heating at 130-500°C and this was associated with a lower level of *Stage 1* physisorption (of approximately one quarter that observed for the 130°C mass gain). The removal of water during heating as well as a lower level of physisorption will contribute both to an overestimation of the RHX mass and the age of the ceramic. It was shown that this issue with gypsum can explain partially, if not completely, the issue of large ages for these two samples.

- *Short term elevated temperature effects (STETE) are potentially the major source of age estimation issues and a considerable problem for the dating of samples with high RHX activation energies:*

  It was found that short term elevated temperature events, such as the period of cooling of a ceramic post-firing or repeated heated/cooling of a pot as part of cooking, could contribute significant quantities of mass gain and additional age to a ceramic, particularly for activation energies exceeding 130kJ/mol. For the present work, the effects were less pronounced for the $t^{1/n}$ model, where lower RHX activation energies were obtained for the samples. For both models, the pre-drying of samples for two weeks was shown to have potentially been a major contributor to the large age estimate issues. However, this was not definitively demonstrated and is dependent on RHX mass gain proceeding to high temperatures > 75°C, an area that requires future work and clarification. Nonetheless, for archaeological dating of samples with moderate to high activation energies, exposure to elevated temperatures even for a very short duration may lead to problematic dating results.

- *The proposed use of age-temperature curves and the AETH approach:*

  Two methods were proposed for dealing with contrasting levels of understanding of the temperature history of a ceramic. The age-temperature curves were presented and argued to be a useful tool for visual interpretation of the age, or uncertainties in the age of a ceramic where the

effective lifetime temperature is less well understood. The activation energy temperature history (*AETH*) approach was presented as a means of refining the age of a sample by making more thorough use of a better understood temperature history.

The above findings demonstrate that the present work has made a significant contribution to our understanding of both the mass gain behaviour of fired clay ceramics and the issues involved in the application of RHX dating to fired clay ceramics of archaeological origin.

10.2 Future Work

More dating trials are required to examine if the component-based approach offers a viable method of RHX dating. As part of these trials and future work, sources of uncertainty need to be further examined and minimised: a) samples should be selected with very clear and simple temperature histories, with external, in-situ, bricks spanning a period of instrumental temperature records preferred; b) STETE effects (drying below 100° heating/cooling cycles) and samples with high activation energies for which STETEs might be expected to have occurred should be avoided until the maximum RHX mass gain temperatures and conditions are better understood through future studies; c) samples should be screened for the presence of organic matter, with a focus on dating samples where the content is low or absent – more work needs to be conducted to examine if pre-treatment removal of organics has an effect on the mass gain dynamics and (re)hydroxyl content of a sample, and to examine methods of suitable estimation of the organic matter to organic carbon ratio; d) samples should be screened for the presence of problematic minerals such as gypsum or goethite, with further work conducted into quantifying their effects; e) surface area analysis should be carried out, where possible, to avoid potential condensation issues and to select suitable %RH conditions at which to run experiments; f) the drying of samples needs focussed research that examines the relationship between the *Stage 2* mass gain rate

following drying at a wide range of temperatures and durations (ideally using in-situ thermogravimetric analysis) – the association of the 130°C *Stage* 2 mass gain component with both a chemisorption event (for example low temperature dehydroxylation) and a long term process needs further validation; g) further validation that the $t^{1/n}$ behaviour, i.e. *1/n*, is the same for all aging temperatures and components of a sample is needed – this requires a more refined experimental setup with continuous measurements and better environmental control (with one low aging temperature).

These are just some of the areas the author would highlight as requiring immediate attention and is not intended to be comprehensive. The present work has contributed significantly to understanding RHX behaviour, and both major and minor issues with the RHX dating method; it is the hope of the author that pursuing this research further, along the lines suggested, will culminate in the development of a viable and valuable dating method for archaeological ceramics.

References

Adams, A. E., MacKenzie, W. S. and Guilford, C. 1984. *Atlas of Sedimentary Rocks under the Microscope.* Longman. Harlow.

Ahn, J., Kopelman, R. and Argyrakis, P. 1999. Hierarchies of nonclassical reaction kinetics due to anisotropic confinement. *Journal of Chemical Physics*. **43** 1999

Aitken, M. J. 1990. *Science-based Dating in Archaeology.* Longman Inc. New York.

Arnold, C. Y. 1960. Maximum-minimum temperatures as a basic for computing heat units. *Proceedings of the American Society of Horticultural Science.* **76** 682-692

Arpaci, V. S., Selamet, A. and Kao, S. 2000. *Introduction to Heat Transfer.* Prentice Hall. New Jersey. p. 19

Bailey, S. W. 1980. Structures of layer silicates. In Brindley, G. W. and Brown, G. (eds.). *Crystal Structures of Clay Minerals and their X-ray Identification.* Mineralogical Society. London. 1-124

Bain, D. C., McHardy, W. J. and Lachowski, E. E. 1994. X-ray fluorescence spectroscopy and microanalysis. In Wilson, M. J. (ed.) 1994. *Clay Mineralogy: Spectroscopic and Chemical Determinative Methods.* Chapman and Hall. London. 260-299

Barnett, W. K. and Hoopes, J .W. (eds.) 1995. *The Emergence of Pottery: Technology and Innovation in Ancient Societies.* Smithsonian Institution Press. Washington.

Barrett, L. R. 1937. The rehydration of fired brick clays. *Transactions of the Ceramic Society.* **6** 201-216

Barrett, G., 2011. *Rehydroxylation Dating: Investigating the Effects of Diurnal and Annual Temperature Cycles Within Ireland and Great Britain*. School of Geography, Archaeology and Palaeoecology, Queen's University Belfast. Unpublished M.Sc. thesis.

Barrett, G. T. 2013. Rehydroxylation dating of fired clays: an improved *time-offset* model to account for the effect of cooling on post-reheating mass gain. *Journal of Archaeological Science*. **40** 3596-3603

Baskerville, G.L. and Emin, P. 1969. Rapid estimation of heat accumulation from maximum and minimum temperatures. *Ecology.* **50** 514-517

Belloto, M., Gualtieri, A., Artoli, G. and Clark, S. M. 1995. Kinetic study of the kaolinite-mullite reaction sequence. Part I: Kaolinite dehydroxylation. *Physics and Chemistry of Minerals.* **22** 207-214

Benedetto, G. E. de, Laviano, R., Sabbatini, L. and Zambonin, P. G. 2002. Infrared spectroscopy in the mineralogical characterization of ancient pottery. *Journal of Cultural Heritage*. **3** 177-186

Berstan, R., Stott, A. W., Minnitt, S., Bronk Ramsey, C., Hedges, R. E. M. and Evershed, R. P. 2008. Direct dating of pottery from its organic residues: new precision using compound-specific carbon isotopes. *Antiquity.* **82** 702-713

Bonamartini Corradi, A., Leonelli, C., Manfredini, T., Pennisi, L. and Romagnoli, M. 1996. Quantitative determination of pyrite in ceramic clay raw materials by DTA. *Thermochimica Acta*. **287** 101-109

Bonsall, C., Cook, G., Manson, J. L., and Sanderson, D. 2002. Direct dating of Neolithic pottery: progress and prospects. *Documenta Praehistorica.* **XXIX** 47-59

Bowen, P. K., Ranck, H. J., Scarlett, T. J. and Drelich, J. W. 2011. Rehydration / rehydroxylation kinetics of reheated XIX-century Davenport (Utah) Ceramic. *Journal of the American Ceramic Society.* **94** 2585-2591

Bowen, P. K., Drelich, J. and Scarlett, T. J. 2013. Modeling rehydration/rehydroxylation mass-gain curves from Davenport ceramics. *Journal of the American Ceramic Society.* **96** 885-891

Brannon, N. 2010. The bawn at 'Vintners Towne'. *Battles, Boats & Bones: Archaeological Discoveries in Northern Ireland 1987-2008.* W&G Baird for the Northern Ireland Environment Agency, Belfast. 97-101

Brindley, G. W. and Lemaitre, J. 1987. Thermal, oxidation and reduction reactions of clay minerals. In Newman, A. C. D. (ed.). *Chemistry of Clays and Clay Minerals. Mineralogical Society Monograph No. 6.* Longman Scientific & Technical. 319-371

Brindley, G. W. and Nakahira, M. 1957. Kinetics of dehydroxylation of kaolinite and halloysite. *Journal of the American Ceramics Society.* **40** 346-350

Bronk Ramsey, C. 2008. Radiocarbon dating: revolutions in understanding. *Archaeometry.* **50** 249-276

Brown, G. and Nadeau, P. 1984. Crystal structures of clay minerals and related phyllosilicates [and discussion]. *Philosophical Transactions of the Royal Society of London A*. **311** 221-240

Brunswick, R. W. 1990. *Brick Building in Britain.* Victor Gollancz Ltd. London.

Burokov, K. S. and Nachasova, I. E. 2013. Archaeomagnetic study and rehydroxylation dating of fired-clay ceramics. *Izvestiya, Physics of the Solid Earth.* **49** 105-112

Butler, C. J., García Suárez, A. M., Coughlin, A. D. S. and Morrell, C. 2005. Air temperatures at Armagh observatory, Northern Ireland, form 1796 to 2002. *Internation Journal of Climatology.* **25** 1055-1079

Campbell, J. W. and Pryce, W. 2003. *Brick, A World History*. Thames & Hudson. London.

Cheng, H., Liu, Q., Huang, M., Zhang, S., Frost, R. L. 2013. Application of TG-FTIR to study SO_2 evolved during the thermal decomposition of coal-derived pyrite. *Thermochimica Acta.* **555** 1-6

Chukanov, N. V. 2014. *Infrared Spectra of Mineral Species – Extended Library*. Springer. London.

Chung, F. H. 1974. Quantitative interpretation of X-ray diffraction patterns, I. Matrix flushing method of quantitative multicomponent analysis. *Journal of Applied Crystallography.* **7** 513-519

Clegg, F., Breen, C., Carter, M. A., Ince, C., Savage, S. D. and Wiilson, M. A. 2012. Dehydroxylation and rehydroxylation mechanisms in fired clay ceramics: a TG-MS and DRIFTS investigation. *Journal of the American Ceramic Society.* **95** 416-422

Clelland, S-J., Wilson, M. A. and Carter, M. A. 2014. RHX dating: measurement of the activation energy of rehydroxylation for fired-clay ceramics. *Archaeometry.* doi: 10.1111/arcm.12118

Cole, W. F. 1961. Moisture expansion relationships for a fired kaolinite-hydrous mica-quartz clay. *Nature*. **192** 737-739

Cole, W. F. 1962a. Moisture expansion of a ceramic body and its internal surface area. *Nature.* **196** 431

Cole, W. F. 1962b. Possible significance of linear plots of moisture expansion against log of a time function. *Nature.* 1962. **196** 431-433

Cole, W. F. 1962c. Moisture expansion characteristics of a fired kaolinite-hydrous mica-quartz clay. *Journal of the American Ceramic Society.* **45** 428-434

Cole, W. F. 1967. Changes in a 50 m mural tape standardizing base. *The Engineer.* **223** 769-770

Cole, W. F. and Crook, D. N. 1968. High temperature reactions of clay mineral mixtures and their ceramic properties. IV. Dimensional and weight changes on refiring and the pore size distribution of fired kaolinite-muscovite-quartz mixtures with 25wt. % quartz. *Journal of the American Ceramic Society.* **51** 79-84

Cole, W. F. and Birtwistle, R. 1969. Kinetics of moisture expansion of ceramic bodies. *American Ceramic Society Bulletin.* **48** 1128-1132

Cultrone, G., Rodriguez-Navarro, C., Sebastion, E., Cazalla, O. and de la Torre, M. J. 2001. Carbonate and silicate phase reactions during ceramic firing. *European Journal of Mineralogy.* **13** 621 634

Cultrone, G., Sebastián, E., Elert, K., de la Torre, M. J., Cazalla, O. and Rodriguez-Navarro. 2004. Influence of mineralogy and firing temperature on the porosity of bricks. *Journal of the European Ceramic Society.* **24** 547-564

Cultrone, G., Sebastián, E. and de la Torre, M. J. 2005. Mineralogical and physical behaviour of solid bricks with additives. *Construction and Building Materials.* **19** 39-48

Curran J., Warke P., Stelfox D., Smith B. and Savage J. 2010. *Stone by Stone: A Guide to Building Stone in the Northern Ireland Environment.* Appletree. Belfast.

Dietzel, A. and Dhekne, B. 1957. Rehydration of metakaolin. *Berichte der Deutschen Keramischen Gesellschaft.* **32** 150

Drelich, J., Bowen, P, K. and Scarlett, T. J. 2013. Effect of humidity instability on rehydroxylation in fired clay ceramics. *Journal of the American Ceramic Society.* **96** 1047-1050

Duller, G.A.T. 2008. *Luminescence Dating: Guidelines on using Luminescence Dating in Archaeology*. English Heritage Publishing. Swindon.

Duminuco, P., Messiga, B. and Riccardi, M. P. 1998. Firing process of natural clays. Some microtextures and related phase compositions. *Themochimica Acta.* **321** 185-190

Dunham, A. C. 1992. Developments in industrial mineralogy: I. The mineralogy of brick-making. *Proceedings of the Yorkshire Geological Society.* **49** 95-104

Eberl, D. D., Farmer, V. C. and Barrer, R. M. 1984. Clay mineral formation and transformation in rocks and soils [and discussion]. *Philosophical Transactions of the Royal Society London A.* **311** 241-257

ECA&D. 2014. European Climate Assessment & Dataset. [Online]. *http://eca.knmi.nl/* [accessed 29th November 2014]

El-Zanan, H. S., Zielinska, B., Mazzoleni, L. R. and Hansen, D. A. 2009. Analytical determination of the aerosol organic mass-to-organic carbon ratio. *Journal of Air Waste Management Association.* **59** 58-69

Enriquez, C. R., Danon, J. and Beltrão, M. Da C. M. C. 1979. Differential thermal analysis of some Amazonian archaeological pottery. *Archaeometry*. **21** 183-186

Evershed, R. P. 2008. Experimental approaches to the interpretation of absorbed organic residues in archaeological ceramics. *World Archaeology.* **40** 26-47

Exc. Ie. 2015. 1997:004 – Tedford's, Donegall Quay, Belfast, Co. Antim. [Online] Available from: *http://www.excavations.ie/report/1997/Antrim/0002547/* [accessed 30th January 2015]

Fagan, B. 2011. *The First North Americans: An Archaeological Journey.* Thames & Hudson. New York.

Fahrenholtz, W. G. 2008. Clays. In Shackleford, J. F. and Doremus, R. H. (eds.). *Ceramics and Glass Materials: Structure, Properties and Processing.* Springer. New York. 111-135

Ford, W. G. 1967. *The Effect of Heat on Ceramics.* MacLaren and Sons Ltd. London.

Francis, P. 2001. *A Pottery by the Lagan: Irish Creamware from the Downshire Pottery, Belfast, 1787-c.1806.* W & G Baird Ltd for the Institute of Irish Studies, Queen's University Belfast, in association with the National Museums and Galleries of Northern Ireland, Belfast.

Freeman, I. L. and Smith, R. G. 1967. Moisture expansion of structural ceramics. I. Unrestrained expansion. *Transactions of the British Ceramic Society*. **66** 13-35

Gheorghiu, D. (ed.) 2009. *Early Farmers, Late Foragers, and Ceramic Traditions: On the Beginning of Potter in the Near East and Europe.* Cambridge Scholars Publishing. Newcastle. UK.

Gialanella, S., Girarde, F., Ischia, G., Lonardelli, I., Mattarelli, M. and Montagna, M. 2010. On the goethite to hematite phase transformation. *Journal of Thermal Analysis and Calorimetry*. **102** 867-873

Gibson, A. M. 2002. *Prehistoric Pottery in Britain and Ireland.* Tempus. Stroud. UK.

Gilmore, S. 2010. The building of Belfast: archaeological investigations at Annadale and Castle Espie. In Murray, E. and Logue, P. *Battles, Boats & Bones: Archaeological Discoveries in Northern Ireland 1987-2008.* W&G Baird for the Northern Ireland Environment Agency, Belfast. 73-79

Gosselain, O. P. 1992. Bonfire of the enquiries. Pottery firing temperatures in archaeology: what for? *Journal of Archaeological Science.* **19** 243-259

Goudie A. S. and Viles H. A. 1997. *Salt Weathering Hazard*. Wiley & Sons. Chichester.

Greenspan, L. 1976. Humidity fixed points of binary saturated aqueous solutions. *Journal of Research of the National Bureau of Standards- A, Physics and Chemistry*. **81A** 89-96

Grim, R. E. 1962. *Applied Clay Mineralogy.* McGraw-Hill. New York.

Grim, R. E. 1968. *Clay Mineralogy.* 2nd Edition. McGraw-Hill. New York.

Grim, R. E. and Bradley, W. F. 1940. Investigation of the effect of heat on the clay minerals illite and montmorillonite. *Journal of the American Ceramic Society.* **23** 242-248

Grim, R. E. and Bradley, W. F. 1948. Rehydration and dehydration of the clay minerals. *American Mineralogist.* **33** 50-59

Gualtieri, A. F. and Ferrari, S. 2006. Kinetics of illite dehydroxylation. *Physics and Chemistry of Minerals.* **33** 50-59

Gualtieri, A. F. 2007. Thermal behaviour of the raw materials forming porcelain stoneware mixtures by combined optical and *in situ* x-ray dilatometry. *Journal of the American Ceramic Society.* **90** 1222-1231

Hamilton, A. and Hall, C. 2012. A review of rehydroxylation in fired-clay ceramics. *Journal of the American Ceramic Society*. **95** 2673-2678

Hall, C. and Hoff, W. D. 2012. Moisture expansivity of fired-clay ceramics. *Journal of the American Ceramic Society.* **95** 1204-1207

Hall, C., Hamilton, A. and Wilson, M.A. 2013. The influence of temperature on rehydroxylation [RHX] kinetics in archaeological pottery. *Journal of Archaeological Science*. **40** 305-312.

Hall, C., Wilson, M. A. and Hoff, W. D. 2011. Kinetics of long-term moisture expansion in fired-clay brick. *Journal of the American Ceramic Society.* **94** 3651-3654

Hammond, M. 1981. *Bricks and Brickmaking.* Shire Publications Ltd. Oxford.

Harris, T. E. 1965. Diffusion with "collisions" between particles. *Journal of Applied Probability.* **2** 323

Hedges, R. E. M., Tiemei, C. and Housley, R. A. 1992. Results and methods in the radiocarbon dating of pottery. *Radiocarbon.* **34** 906-915

Heide, K. and Földvari, M. 2006. High temperature mass spectrometric gas-release studies of kaolinite $Al_2[Si_2O_5(OH)_4]$ decomposition. *Thermochimica Acta.* **446** 106-112

Heller, L., Farmer, V. C., MacKenzie, R. C., Mitchell, B. D. and Taylor, H. F. W. 1962. The dehydroxylation and rehydroxylation of trimorphic dioctahedral clay minerals. *Clay Minerals Bulletin.* **5** 56-72

Highscore. 2015. PANalytical X-ray diffraction software website. [Online] *http://www.panalytical.com/Xray-diffraction-software/HighScore-with-Plus-option.htm.* [accessed 10th June 2015].

Hill, R. D. 1953. The rehydration of fired clay and associated minerals. *Transactions of the British Ceramic Society*. **52** 589-613

Hill, R. D. 1956. Studies on rehydrated and refired kaolinite minerals. *Transactions of the British Ceramic Society*. **55** 441-456

Hueber, H. V. and Milne, A. A. 1955. Expansion and deterioration of ceramic bodies. *Nature*. **176** 509

Hurst, A. and Goggin, D. J. 1995. Probe permeametry: an overview and bibliography, *AAPG Bullet.* **79** 463–473

Hurst, V. J. and Kunkle, A. C. 1985. Dehydroxylation, rehydroxylation, and stability of kaolinite. *Clays and Clay Minerals.* **33** 1-14

Huyesecom, W., Rasse, M., Lespez, L., Neumann, K., Fahmy, A., Ballouche, A., Ozainne, S., Maggetti, M., Tribolo, Ch. and Soriano, S. 2009. The emergence of pottery in Africa during the tenth millennium cal BC: new evidence from Ounjougou (Mali). *Antiquity.* **83** 905-917

ICDD. 2015. International Centre for Diffraction Data PDF-2 Database Website. [Online] *http://www.icdd.com/products/pdf2.htm.* [accessed 10th June 2015].

Iordanidis A., Garcia Guinea J. and Karamitrou Mentessidi G. 2009. Analytical study of ancient pottery from the archaeological aite of Aiani, Northern Greece. *Materials Characterization*. **60** 292–302

Jope, E. M. 1958. Castlecaulfield, Co. Tyrone. *Ulster Journal of Archaeology.* **21** 101-107

Jope, E. M. 1960. Moyry, Charlemont, Castleraw, and Richhill: fortification to architecture in the North of Ireland 1570-1700. *Ulster Journal of Archaeology.* **23** 97-123

Jordan, M. M., Montero, M. A., Meseguer, S. and Sanfeliu, T. 2008. Influence of firing temperature and mineralogical composition on bending strength and porosity of ceramic tile bodies. *Applied Clay Science.* **42** 266-271

Jordan, P. and Zvelebil, M. (eds.) 2010. *Ceramics Before Farming: The Dispersal of Pottery among Prehistoric Eurasian Hunter-Gatherers.* Left Coast Press Inc. California.

Jórdeczka, M., Królik, H., Masojć, M. and Schild, R. 2011. Early Holocene pottery in the Western Desert of Egypt: new data from Nabta Playa. *Antiquity.* **85** 99-115

Keery, S. 2010. The Ballymacarett glasshouses in East Belfast. *Battles, Boats & Bones: Archaeological Discoveries in Northern Ireland 1987-2008.* W&G Baird for the Northern Ireland Environment Agency, Belfast. 68-73

Keller, W. D. 1964. Processes of origin and alteration of clay minerals. In Rich, C. I. and Kunze, G. W. (eds.). *Soil Clay Mineralogy: A Symposium.* University of North Carolina Press. Chapel Hill. 3-76

Kerr, P. F. 1955. Formation and occurrence of clay minerals. In Pask, J. A. and Turner, M. D. (eds.). *Clays and Clay Technology, Proceedings of the First National Conference on Clays and Clay Technology.* California Division of Mines. San Francisco. 19-32

Kingery, W. D. 1974. A note on the differential thermal analysis of archaeological ceramics. *Archaeometry.* **16** 109-112

Kingery, W. D., Bowen, H. K. and Uhlman, D.R. 1976. *Introduction to Ceramics. 2nd Edition.* John Wiley. New York.

Klingenfuß, C., Roßkopf, N., Walter, J., Heller, C. and Zeitz, J. 2014. Soil organic matter to soil organic carbon ratios of peatland soil substrates. *Geoderma.* **235-236** 410-417

Kollmann, M. 2003. Single-file diffusion of atomic and colloidal systems: asymptotic laws. *Physical Review Letters.* **90** 180602

Kuzmin, Y. B., Hall, S., Tite, M. S., Bailey, R., O'Malley, J. M. and Medvedev, V. E. 2001. Radiocarbon and thermoluminescence dating of the pottery from the early Neolithic site of Gasya (Russian Far East): initial results. *Quaternary Science Review*. **22** 961-966

Le Goff, M. and Gallet, Y. 2014a. Evaluation of the rehydroxylation dating method: insights from a new measurement device. *Quaternary Geochronology*. **20** 89-98

Le Goff, M. and Gallet, Y. 2014b. Evidence for complexities in the RHX dating method. *Archaeometry*. doi: 10.1111/arcm.12137

Le Goff, M. and Gallet, Y. 2015. Experimental variability in kinetics of moisture expansion and mass gain in ceramics. *Journal of the American Ceramic Society*. **98** 398-401

Lewis, W. K. 1921. The rate of drying of solid materials. *Indus. Eng. Chem. – Sympos. Drying.* **3 (5)** 42

Lin, A. L., Kopelman, R. and Argyrakis, P. 1997. Diffusion-controlled elementary reactions in tubular confinement: extreme nonclassicality, segregation, and anomalous scaling laws for dimensional crossovers. *Journal of Physical Chemistry A.* **101** 802

Lin, B., Meron, M., Cui, B. and Rice, S. A. 2005. From random walk to single-file diffusion. *Physical Review Letters*. **94** 216001

Livingstone Smith, A. 2001. Bonfire II: the return of pottery firing temperatures. *Journal of Archaeological Science.* **28** 991-1003

Lowell, S., Shields, J. E. and Thomas, M. A. 2004. *Characterization of Porous Solids and Powders: Surface Area, Pore Size and Density.* Kluwer Academic Publishers. Dordrecht.

Luterbacher, J., Dietrich, D., Xoplaki, E., Grosjean, M. and Wanner, H. 2004. European seasonal and annual temperature variability, trends and extremes since 1500. *Science.* **303** 1499-1503

Mackenzie, R. C. 1970. *Differential Thermal Analysis 1 and 2. 1st Edition.* Academic Press. London.

MacKenzie, W. S. and Guilford, C. 1980. *Atlas of Rock-forming Minerals in Thin Section*. Longman. London.

MacKenzie, W. S. and Guilford, C. 1982. *Atlas of Igneous Rocks and their Textures*. Longman. Harlow.

Maggetti, M. 1982. Phase analysis and its significance for technology and origin. In Olin, J. S. and Franklin, A. D. (eds.) *Archaeological Ceramics.* Smithsonian Institution Press. Washington D. C. 121-133

Maniatis, Y., Katsonas, A. and Caskey, M. E. 1982. Technological examination of low-fired terracotta statues from Ayia Irina, Kea. **24** 191-198

Manoharan, C., Sutharsan, P., Dhanapandian, S., Venkatachalapathy, R. and Mohamed Asanulla, R. 2011. Analysis of temperature effect on ceramic brick production from alluvial depositis, Tamilnadu, India. *Applied Clay Science.* **54** 20-25

Marinos-Kouris, D. and Maroulis, Z. B. 2006. Basic process calculations and simulations in drying. In Mujumbar, A. S. (Ed.) *Handbook of Industrial Drying (3rd Edition)*. CRC Press. Florida. p. 81

Maritan, L., Mazzoli, C. and Freestone, I. 2007. Modelling changes in mollusc shell internal microstructure during firing: implications for temperature estimation in shell-bearing pottery. *Archaeometry.* **49** 529-541

Maritan, L., Nodari, L., Mazzoli, C., Milano, A. and Russo, U. 2006. Influence of firing conditions on ceramic products: experimental study on clay rich in organic matter. *Applied Clay Science.* **31** 1-15

Mesbah, H., Wilson, M. A. and Carter, M. A. 2010a. Effect of prolonged sintering time at 1200°C on the phase transformation and reactivity with moisture of fired kaolinite. *11th International Conference on Ceramic Processing Science.* 27th August 2010.

Mesbah, H., Wilson, M. A. and Carter, M. A. 2010b. The role of the kaolinite-mullite reaction in moisture mass gain in fired kaolinite. *CIIMTEC Ceramic Congress.* Italy. 6-11th June 2010.

Met Office. 2015. The British Meteorological Office. [Online]. *http://www.metoffice.gov.uk* [accessed 20th January 2015]

Meunier, A. 2005. *Clays.* Springer. Berlin.

Mojaradi, R. and Sahimi, M. 1988. Diffusion-controlled reactions in disordered porous media II. Nonuniform distribution of reactants. *Chemical Engineering Science.* **43** 2995

Molina-Montes, E., Donadio, D. Hernández-Laguna, A. and Sainz-Diáz, C. I. 2010. Exploring the rehydroxylation reaction of pyrophillite by *ab initio* molecular dynamics. *Journal of Physical Chemistry B*. **114** 7593-7601

Montgomery, R. W. and Runger, G. C. 2011. *Applied Statistics and Probability for Engineers – 5th Edition.* Wiley. New York.

Moody, T. W. and Beckett, J. C. 1959. *Queen's Belfast 1845-1849: the History of a University.* Faber & Faber, London.

Moore, D. M. and Reynolds, Jr., R. C. 1997. *X-Ray Diffraction and the Identification and Analysis of Clay Minerals.* 2nd Edition. Oxford University Press. Oxford.

Moré, J. J. and Sorensen, D. C. 1983. Computing a Trust Region Step. *SIAM Journal on Scientific and Statistical Computing.* **3** 553-572

Moropoulou, A., Bakolas, A. and Bisbikou, K. 1995. Thermal analysis as a method of characterizing ancient ceramic technologies. *Thermochimica Acta.* **269/270** 743-753

Muller, F., Drits, V. A., Plançon, A. and Robert, J.-L. 2000a. Structural transformation of 2:1 dioctahedral layer silicates during dehydroxylation-rehydroxylation reactions. *Clays and Clay Minerals.* **48** 572-585

Muller, F., Plançon, A. and Drits, V. A. 2000b. Studies of the dehydroxylated-rehydroxylated montmorillonite: structure of the layers and intercalation of water molecules. *Journal de Physique IV*. **10** 481-487.

Nakamura, T., Taniguchi, Y., Tsuji, S. and Oda, H. 2001. Radiocarbon dating of charred residues on the earliest pottery in Japan. *Radiocarbon.* **42** 1129-1138

Nodari, L., Marcuz, E., Maritan, L., Mazzoli, C. and Russo, U. 2007. Hematite nucleation and growth in the firing of carbonate-rich clay for pottery production. *Journal of the European Ceramic Society.* **27** 4665-4673

Norris, A. W., Baughn, F., Harrison, R. and Seabridge, K. C. J. 1958. Size changes of porous ceramics caused by water and soluble salts. *Transactions of the VIth International Ceramic Congress*. **6** 63-79

Norton, F. H. 1974. *Elements of Ceramics.* Addison-Wesley. Reading.

Numrich, M., Kutschera, W., Steier, P., Sterba, J.H. and Golser, R. 2015. On the effect of organic carbon on rehydroxylation (RHX) dating. *Journal of Archaeological Science.* doi: 10.1016/j.jas.2015.01.016.

Ó Baoill, R. 2008. *Carrickfergus. The Story of the Castle and Walled Town.* TSO Ireland for the Northern Ireland Environment Agency. Belfast.

Padowski, Z. and Mujumbar, A. S. 2006. Basic process calculations and simulations in drying. In Mujumbar, A. S. (Ed.) *Handbook of Industrial Drying (3rd Edition)*. CRC Press. Florida. p. 53

Pavía, S. 2006. The determination of brick provenance and technology using analytical techniques from the physical sciences. *Archaeometry*. **48** 201-218

Pavía, S. and Bolton, J. 2000. *Stone, Brick and Mortar: Historical Use, Decay and Conservation of Building Materials in Ireland.* Wordwell. Bray.

Pavía, S., Bolton, J., Walker, G., MacMahon, P. and Dunphy, P. 2000. The brick in Portumna Castle, County Galway, Ireland. *British Brick Society Bulletin.* **80** 5-10

Peters, T. and Iberg, R. 1978. Mineralogical changes during firing of calcium-rich brick clays. *American Ceramic Society Bulletin.* **57** 503-509

Philip, S., Martin, R. V., Pierce, J. R., Jimenez, J. L., Zhang, Q., Canagaratna, M. R., Spracklen, D. V., Nowlan, C. R., Lamsal, L. N., Cooper, M. J., and Krotkov, N. A. 2014. Spatially and seasonally resolved estimate of the ratio of organic matter to organic carbon. *Atmospheric Environment.* **87** 34-40

Potts, P. J. and West, M. 2008. *Portable X-ray Fluorescence Spectrometry: Capabilities for In Situ Analysis*. The Royal Society of Chemistry Publishing. Cambridge.

Prentice, J. E. 1990. *Geology of Construction Materials.* Chapman and Hall. London.

Pribyl, D. W. 2010. A critical review of the conventional SOC to SOM conversion factor. *Geoderma*. **156** 75-83

Quinn, P. S. 2013. *Ceramic Petrography: The Interpretation of Archaeological Pottery & Related Artefacts in Thin Section*. Archaeopress. Oxford.

Rasmussen, K. L., De La Fuente, F. A., Bond, A. D., Mathiesen, K. K. and Vera, S. D. 2012. Pottery firing temperatures: a new method for determining the firing temperature of ceramics and burnt clay. *Journal of Archaeological Science.* **39** 1705-1716

Rathossi, C. and Pontikes, Y. 2010. Effect of firing temperature and atmosphere on ceramics made of NW Peloponnese clay sediments. Part I: Reaction paths, crystalline phases, microstructure and colour. *Journal of European Ceramic Society.* **30** 1841-1851

Reimer, P. J., Bard, E., Bayliss, A., Beck, J. W., Blackwell, P. G., Bronk Ramsey, C., Buck, C. E., Cheng, H., Edwards, R. L., Friedrich, M., Grootes, P. M., Guilderson, T. P., Haflidason, H., Hajdas, I., Hatté, C., Heaton, T. J., Hoffmann, D. L., Hogg, A. G., Hughen, K. A., Kaiser, K. F., Kromer, B., Manning, S. W., Niu, M., Reimer, R. W., Richards, D. A., Scott, E. M., Southon, J. R., Staff, R. A., Turney, C. S. M. and van der Plicht, J. 2009. IntCal13 and Marine13 radiocarbon age calibration curves, 0-50,000 years cal BP. *Radiocarbon.* **55** 1869-1887

Reinders, J., Hambach, U., Krumsiek, K., Sanke, M. and Strack, N. 1999. An archaeomagnetic study of pottery kilns from Bruhl-Pingsdorf (Germany). *Archaeometry.* **41** 413-420

Renfrew, C. and Bahn, P. 2000. *Archaeology: Theories Methods and Practice (3rd Edition)*. Thames and Hudson. London.

Riccardi, M. P., Messiga, B. and Duminuco. 1999. An approach to the dynamics of clay firing. *Applied Clay Science.* **15** 393-409

Riisager, P., Abrahamsen, N. and Rytter, J. 2003. Research report: magnetic investigations and the age of a medieval kiln at Kungahälla (south-west Sweden). *Archaeometry.* **45** 675-684

Rocha, J. and Klinowski, J. 1991. The rehydration of metakaolinite to kaolinite. *Journal of the Chemical Society, Chemical Communications.* 582-584

Rocha, J., Adams, J. M. and Klinowski, J. 1990. The rehydration of metakaolinite to kaolinite: evidence from solid-state NMR and cognate techniques. *Journal of Solid State Chemistry.* **89** 260-274

Roosevelt, A. C. 1995. Early pottery in the Amazon: twenty years of scholarly obscurity. In Barnett, W. K. and Hoopes, J. W. (eds.). *The Emergence of Pottery: Technology and Innovation in Ancient Societies.* Smithsonian Institution Press. Washington. 115-132

Roy, R. 1949. Decomposition and resynthesis of the micas. *Journal Am. Cer. Soc.* **32.** 202-210

Roy, R. and Brindley, G. W. 1956. A study of the hydrothermal reconstruction of the kaolin minerals. *National Acad. Sci. publ.* **456** 125-132

Rice, P. M. 1987. *Pottery Analysis: a Sourcebook.* University of Chicago Press. Chicago.

Russell, J. D. and Fraser, A. R. 1994. Infrared methods. In Wilson, M. J. (ed.) 1994. *Clay Mineralogy: Spectroscopic and Chemical Determinative Methods.* Chapman and Hall. London. 11-67

Ruthenburg, T. C., Perlin, P. C., Liu, V., McDade, C. E. and Dillner, A. M. 2014. Determination of organic matter and organic matter to organic carbon ratios by infrared spectroscopy with application to selected sites in the improved network. *Atmospheric Environment.* **86** 47-57

Saalfeld, H. 1955. The hydrothermal formation of clay minerals from metakaolin. *Berichte der Deutschen Keramischen Gesellschaft.* **32** 150

Savage, S. D., Wilson, M. A., Carter, M. A., Hoff, W. D., Hall, C. and McKay, B. 2008a. Moisture expansion and mass gain in fired clay ceramics: a two-stage $(\text{time})^{1/4}$ process. *Journal of Physics D: Applied Physics.* **41** 055402

Savage, S. D., Wilson, M. A., Carter, M. A., McKay, B., Hall, W. D. and Hall, C. 2008b. Mass gain due to the chemical recombination of water in fired clay brick. *Journal of the American Ceramic Society.* **91** 3396-3398

Schachtschabel, P. 1930. Dehydration and rehydration of kaolin. *Chemie der Erde*. **4** 395-419

Schurect, H. G. 1928. Methods for testing crazing of glazes caused by increases in size of ceramic bodies. *Journal of the American Ceramic Society.* **11** 271-277

Sheridan, A. 1995. Irish Neolithic Pottery: the story in 1995. In Kinnes, I. and Varndell, G. (eds.). *Unbaked Urns of Rudely Shape: Essays on British and Irish Pottery for Ian Longworth. Oxbow monograph.* **55** 3-23

Shoval, S. 2003. Using FT-IR spectroscopy for study of calcareous ancient ceramics. *Optical Materials.* **24** 117-122

Shoval, S. and Beck, P. 2005. Thermo-FTIR spectroscopy analysis as a method of characterizing ancient ceramic technology. *Journal of Thermal Analysis and Calorimetry.* **82** 609-616

Shoval, S. and Paz, Y. 2013. A study of the mass-gain of ancient pottery in relation to archaeological ages using thermal analysis. *Applied Clay Science*. **82** 113-120

Shoval, S., Gaft, M., Beck, P. and Kirsh, Y. 1993. The thermal behaviour of limestone and monocrystalline calcite tempers during firing and their use in ancient vessels. *Journal of Thermal Analysis.* **40** 263-267

Shoval, S., Beck, P., Kirsch, Y., Levy, D., Gaft, M. and Yadin, E. 1991. Rehydroxylation of clay minerals and hydration in ancient pottery from the 'Land of Geshur' . *Journal of Thermal Analysis.* **37** 1579-1592

Smith, A. N. 1955. Investigations on moisture expansion of porous ceramic bodies. *Transactions of the British Ceramic Society*. **54** 300-318

Smith, R. G. 1993. Moisture expansion of structural ceramics. V: 28 years of expansion. *British Ceramic Transactions*. **92** 233-8

Smith B. J., Gomez-Heras M. and McCabe S. 2008. Understanding the decay of stone-built cultural heritage. *Progress in Physical Geography.* **32** 439-461

Sternberg, R. S. 2008. Archaeomagnetism in archaeometry – a semi-centennial review. *Archaeometry.* **50** 983-998

Stott, A. W., Berstan, R., Evershed, R. P., Hedges, R. E. M., Bronk Ramsey, C. and Humm, M. J. 2001. Radiocarbon dating of single compounds isolated from pottery cooking vessel residue. *Radiocarbon.* **43** 191-197

Stott, A. W., Berstan, R., Evershed, R. P., Bronk Ramsey, C., Hedges, R. E. M. and Humm, M. J. 2003. Direct dating of archaeological pottery by compound-specific ^{14}C analysis of preserved lipids. *Analytical Chemistry.* **75** 5037-5045

Tite, M. S. 1975. Determination of the firing temperature of ancient ceramics by measurement of thermal expansion. *Nature.* **222** 81-181

Tite, M. S. and Manianis, Y. 1975. Examination of ancient pottery using the scanning electron microscopy. *Nature.* **257** 122-123

Tite, M. S. 1995. Firing temperature determinations- how and why? *KVHAA Konferenser, Stockholm*. **34** 37-42

Tite, M. S. 1999. Pottery production, distribution, and consumption – the contribution of the physical science. *Journal of Archaeological Method and Theory.* **6** 181-233

Tite, M. S. 2008. Ceramic production, provenance and use – a review. *Archaeometry.* **50** 216-231

Toledo, T., dos Santos, D. R., Faria Jr., R. T., Carrio, J. G., Auler, L. T. and Vargas, H. 2004. Gas release during clay firing and evolution of ceramic properties. *Applied Clay Science.* **27** 151-157

Tosheva, L., Mihailova, B., Wilson, M. A. and Carter, M. A. 2010. Gravimetric and spectroscopic studies of the chemical combination of moisture by as-fired and reheated terracotta. *Journal of the European Ceramic Society.* **30** 1867-1872

Turpin, B. J. and Lim, H. J. 2001. Species contributions to PM2.5 mass concentrations: revisiting common assumptions for estimating organic mass. *Aerosol Science and Technology.* **35** 602-610

Vandiver, P. B., Soffer, O., Klima, B. and Svoboda, J. 1989. The origins of ceramic technology at Dolni Věstonice, Czechoslovakia. *Science.* **246** 1002-1008

Van der Marel, H. W. and Beutelspacher, H. 1976. *Atlas of Infrared Spectroscopy of Clay Minerals and their Admixtures.* Elsevier. Amsterdam.

Van Nieuwenberg, C. J. and Pieters, H. A. J. 1929. Rehydration of metakaolin and the synthesis of kaolin. *Berichte der Deutschen Keramischen Gesellschaft*. **10** 260-263

Velde, B. 1992. *Introduction to Clay Minerals: Chemistry, Origins, Uses and Environmental Significance.* Chapman & Hall. London.

Walker, M. 2008. *Quaternary Dating Methods.* John Wiley & Sons. Chichester. UK. 215-219

Wang, L., Zhang, M., Redfern, S.A.T. and Zhang, Z. 2002. Dehydroxylation and transformation of the 2:1 phyllosilicate pyrophyllite at elevated temperatures: an infrared spectroscopic study. *Clays and Clay Minerals*. **50** 272-283

Warke P. A. and Smith B. J. 2000. Salt distribution in clay-rich weathered sandstone. *Earth Surface Processes and Landforms*. **25** 1333–1342

Washburn, E. W. and Footitt, F. F. 1921. Porosity: III. Water as an absorption liquid. *Journal of the American Ceramic Society.* **4** 527-537

Waters, E. H. Hosking, J. S. and Hueber, H. V. 1960. Test for potential and past moisture expansion of ceramic building units. *American Society for Testing and Materials Bulletin*. **245** 55-59

West, H. W. H. 1969. *The Establishment of the Brick and Tile Industry in Developing Countries.* United Nations Industrial Development Organization Report. United Nations. New York.

Wheeler, D. and Mayes, J. 1997. *Regional Climates of the British Isles.* Routledge. London.

Wilson, M. J. 1994. *Clay Mineralogy: Spectroscopic and Chemical Determinative Methods.* Chapman and Hall. London.

Wilson, M. A., Hoff, W. D., Hall, C., McKay, B. and Hiley, A. 2003. Kinetics of moisture expansion in fired clay ceramics: a $(time)^{1/4}$ law. *Physical Review Letters*. **90** (12) 125503-(1-4)

Wilson, M. A., Carter, M. A., Hall, C., Hoff, W. D., Ince, C., Savage, S. D., McKay, B. and Betts, I. M. 2009. Dating fired-clay ceramics using long-term power law rehydroxylation kinetics. *Proceedings of the Royal Society A.* **465** 2407-2415

Wilson, M. A., Hamilton, A., Ince, C., Carter, M. A. and Hall, C. 2012. Rehydroxylation (RHX) dating of archaeological pottery. *Proceedings of the Royal Society A.* **468** 3476-3493

Wilson, M. A., Clelland, S., Carter, M. A., Ince, C., Hall, C., Hamilton, A. and Batt. C.M. 2014. Rehydroxylation of fired-clay ceramics: factors affecting early-stage mass gain in dating experiments. *Archaeometry*. **56** 689-702

Wintle, A. G. 2008. Fifty years of luminescence dating. *Archaeometry.* **50** 276-312

Worrall, W. E. 1956. The organic matter in clays. *Transactions of the British Ceramic Society.* **55** 689-705

Worrall, W. E. 1986. *Clays and Ceramics Raw Materials.* 2nd Edition. Elsevier Applied Science Publishers Ltd. Essex. UK.

Wu, X., Zhang, C., Goldberg, P., Cohen, D., Pan, Y., Arpin, T. and Bar-Yosef, O. 2012. Early pottery at 20,000 years ago in Xianrendong Cave, China. *Science.* **336** 1696-1700

Yang, Y., Yu, S., Zhu, Z. and Shao, J. 2014. The making of fired clay bricks in China some 5000 years ago. *Archaeometry.* **56** 220-227

Young, J. E. and Brownell, W. E. 1959. Moisture expansion of clay products. *Journal of the American Ceramic Society.* **42** 571-581

Zsembery, S., Waechter, R. T. and McNeilly, T. H. 2004. The expansion of clay bricks after 30 years and a method for its prediction. *Proceedings of the Seventh Australian Masonry Conference.* Newcastle. 182-191

Appendix A

XRD Results

This appendix presents, for each sample, the XRD spectra of dating samples following no heating and reheating at 500°C. These spectra are superimposed on one another for comparison. Plots with magnified regions are provided to highlight high temperature mineral phases where relevant. Together with this, a table of peaks and mineral interpretations is also provided for each sample.

Ann

Table A.1: XRD peak position and associated mineral interpretation for Annadale non-reheated sample.

No.	Pos. [°2Th.]	Height [cts]	Mineral
1	8.7445	158.31	Mica
2	13.1474	144.27	Microcline
3	13.6267	374.38	Microcline; Augite
4	14.9242	77.26	Microcline; Albite
5	17.5733	134.02	Mica
6	18.778	119.24	Albite
7	19.6872	107.15	Mica
8	20.7897	10495.64	Quartz; Mica
9	21.0694	1740.43	Microcline
10	21.9515	1079.09	Albite; Enstatite
11	22.331	452.61	Microcline; Enstatite; Mica
12	23.2059	444.46	Microcline
13	23.4838	1220.03	Mica
14	23.9672	1962.82	Microcline; Albite
15	25.245	332.55	Mica
16	25.6696	2140.97	Microcline
17	26.5788	59954.31	Quartz; Microcline; Albite; Augite; Mica
18	27.1212	4260.2	Microcline; Enstatite
19	27.4422	7909.44	Microcline; Mica
20	27.856	5539.9	Albite; Augite; Enstatite
21	28.3728	620.03	Albite; Enstatite; Mica
22	29.4465	1236.42	Microcline; Enstatite; Mica
23	29.8512	2221.67	Albite; Augite
24	30.2209	2054.53	Microcline; Albite
25	30.7777	2237.39	Microcline; Augite; Mica

26	31.0859	1963.36	Microcline; Enstatite; Mica; Spinel
27	32.3064	397.59	Microcline; Albite
28	32.4934	506.44	Microcline
29	33.1544	4719.82	Hematite; Albite; Enstatite; Mica
30	34.2191	394.79	Microcline; Mica
31	34.5334	442.43	Microcline; Enstatite; Mica
32	34.7884	520.27	Microcline; Enstatite; Mica
33	34.9244	654.64	Microcline; Augite; Enstatite; Mica
34	35.1488	1219.77	Microcline; Augite; Enstatite
35	35.6306	6749.38	Hematite; Microcline; Albite; Augite; Enstatite; Mica
36	36.4932	8029.41	Quartz; Albite; Enstatite; Mica
37	37.2148	431.95	Microcline; Albite; Mica
38	37.8109	221.97	Microcline; Albite; Augite; Enstatite; Mica
39	38.6551	242.73	Microcline; Albite; Augite; Spinel
40	39.4092	4654.53	Quartz; Hematite; Albite; Augite; Enstatite; Mica
41	40.2536	2867.16	Quartz; Microcline; Albite; Enstatite; Mica
42	40.8644	1322.58	Hematite; Albite; Augite; Enstatite; Mica
43	41.797	1262.14	Microcline; Albite; Mica
44	42.3987	5225.29	Quartz; Albite; Augite
45	42.8804	320.93	Microcline; Albite; Augite; Enstatite
46	44.7393	607.76	Microcline; Albite; Augite; Enstatite; Mica; Spinel
47	45.7293	2666.71	Quartz; Microcline; Albite; Enstatite; Mica
48	47.1834	735.54	Microcline; Enstatite
49	47.3854	981.12	Microcline; Albite; Enstatite; Mica
50	47.5894	571.41	Microcline; Albite; Enstatite; Mica
51	49.5013	2710.81	Hematite; Albite; Augite; Enstatite; Mica
52	50.0832	9508.47	Quartz; Microcline; Albite; Augite
53	50.6196	769.05	Quartz; Microcline; Albite; Augite; Enstatite; Mica
54	51.4237	393.31	Albite; Enstatite; Mica
55	52.293	282.2	Microcline; Albite; Mica
56	54.1494	2668.29	Hematite; Microcline; Albite; Enstatite; Mica
57	54.8208	3160.24	Quartz; Microcline; Albite; Augite; Enstatite; Mica
58	55.2594	771.18	Quartz; Microcline; Enstatite; Mica
59	55.4094	612.11	
60	56.6711	164.41	Microcline; Albite; Mica
61	57.1885	403.86	Quartz; Microcline; Albite; Enstatite; Mica
62	57.6969	209.78	Hematite; Microcline; Albite; Enstatite; Mica
63	58.7212	223.61	Microcline; Albite; Augite; Enstatite; Mica
64	59.9114	10697.61	Quartz; Microcline; Albite; Augite; Mica
65	60.0958	4794.48	
66	61.2465	383.05	Microcline; Albite; Augite; Enstatite; Mica
67	62.4346	1797.23	Hematite; Microcline; Albite; Augite; Enstatite; Mica
68	62.7447	656.34	Microcline; Albite; Augite; Enstatite; Mica

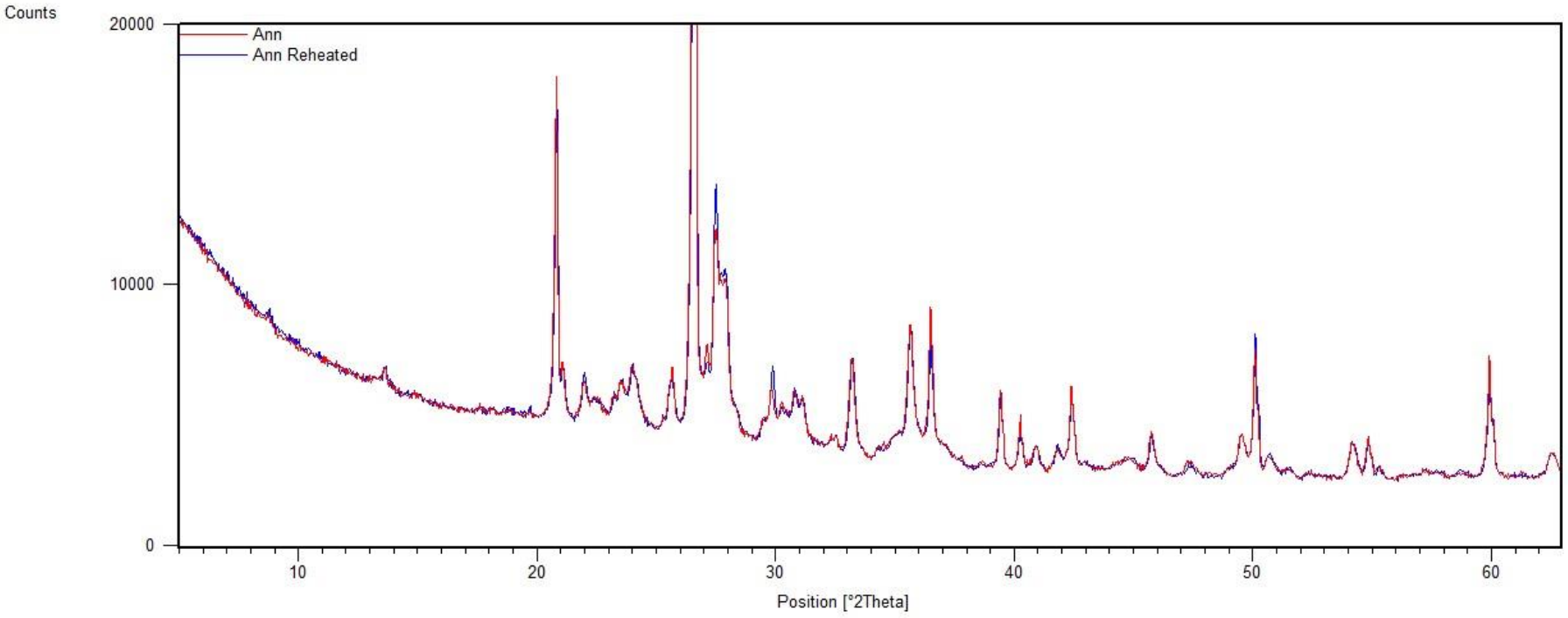

Figure A.1: XRD spectra of *Ann* sample without (red) and with (blue) reheating at 500°C.

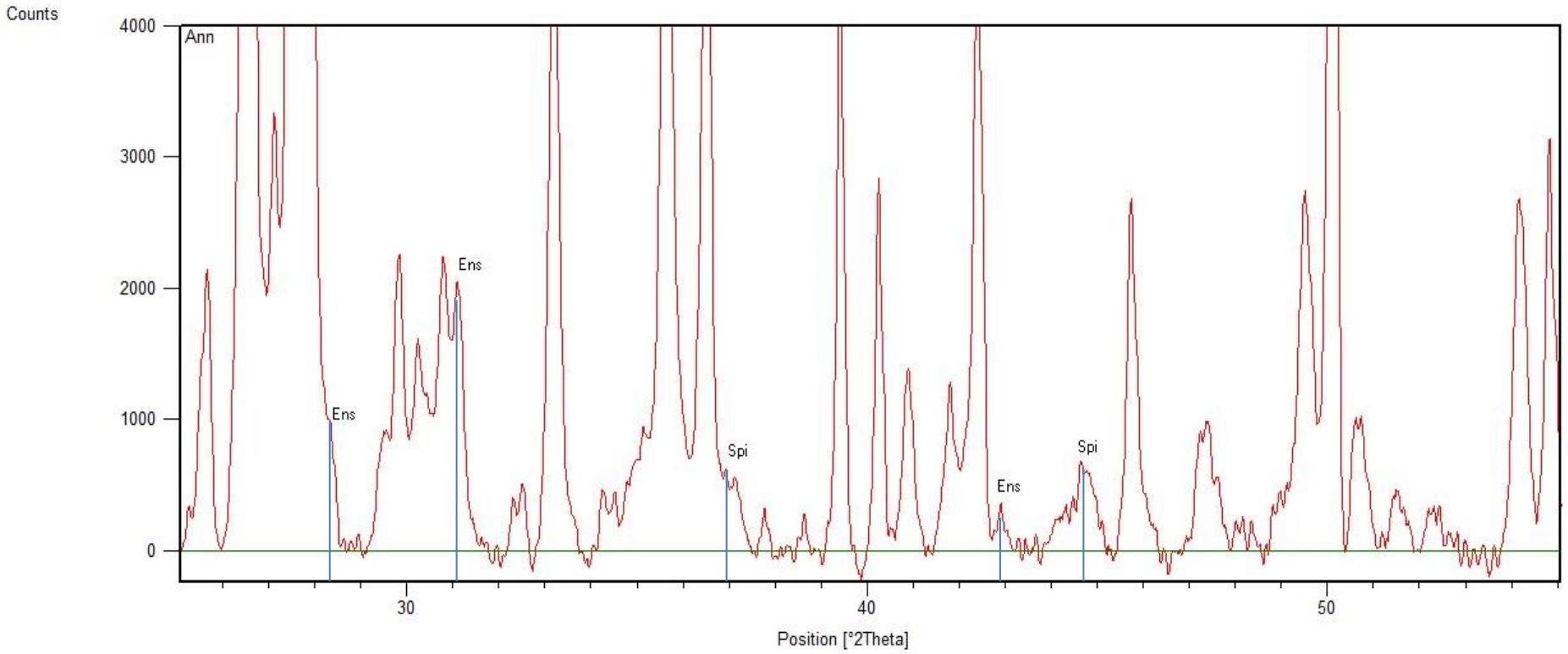

Figure A.2: XRD spectrum of Annadale non-reheated sample highlighting peaks attributed to minerals associated with high temperature firing. Spi = Spinel; Ens = Enstatite.

Esp

Table A.2: XRD peak position and associated mineral interpretation for *Esp* non-reheated sample.

No.	Pos. [°2Th.]	Height [cts]	Mineral
1	8.7784	537.53	Mica
2	13.328	151.01	Orthoclase; Microcline
3	13.6516	457.58	Orthoclase; Anorthite; Microcline
4	13.838	247.06	Orthoclase; Anorthite; Microcline; Enstatite
5	16.6512	120.65	
6	17.374	125.13	Forsterite; Mica
7	17.6183	248.65	Mica
8	18.1644	68.11	
9	18.9185	177.3	Anorthite
10	19.6751	308.97	Enstatite; Mica
11	20.8636	9236.18	Quartz; Orthoclase; Microcline; Mica
12	21.1196	1127.34	Orthoclase; Microcline
13	21.9748	1640.22	Anorthite; Enstatite
14	22.3632	383.66	Orthoclase; Microcline; Enstatite; Mica
15	22.7873	351.51	Forsterite; Anorthite; Microcline; Mica
16	23.2644	854.61	Orthoclase; Microcline
17	23.6024	1681.79	Orthoclase; Forsterite; Anorthite; Mica
18	23.9922	2062.6	Hematite; Forsterite; Microcline; Mica
19	24.4661	367.51	Orthoclase; Anorthite; Microcline
20	25.6282	1400.14	Orthoclase; Forsterite; Anorthite; Microcline; Mica
21	26.6358	50902.25	Quartz; Augite; Anorthite; Microcline; Mica
22	27.1564	3021.4	Orthoclase; Microcline; Enstatite
23	27.5155	11710.08	Augite; Orthoclase; Anorthite; Microcline
24	27.8889	13679.51	Rutile; Anorthite; Enstatite; Mica
25	28.4808	890.29	Anorthite; Enstatite; Mica
26	29.8125	5651.04	Augite; Orthoclase; Forsterite; Mica
27	30.2843	2765.4	Augite; Orthoclase; Anorthite; Microcline; Enstatite
28	30.8284	3070.41	Augite; Orthoclase; Anorthite; Microcline
29	32.4249	518.29	Orthoclase; Forsterite; Microcline
30	33.164	3211.14	Hematite; Anorthite; Enstatite; Mica
31	34.4946	215.64	Orthoclase; Forsterite; Microcline; Enstatite; Mica
32	35.1463	2684.21	Augite; Orthoclase; Anorthite; Microcline; Enstatite; Mica
33	35.6097	6513.77	Hematite; Orthoclase; Forsterite; Anorthite; Microcline; Enstatite; Mica
34	36.5473	5702.77	Quartz; Forsterite; Rutile; Anorthite; Enstatite; Mica
35	37.2637	186.29	Orthoclase; Anorthite; Microcline; Enstatite; Mica
36	38.6064	86.19	Orthoclase; Forsterite; Anorthite; Microcline; Mica
37	39.4519	4444.46	Quartz; Hematite; Orthoclase; Forsterite; Anorthite; Microcline; Enstatite; Mica

38	40.273	2309.75	Quartz; Augite; Orthoclase; Anorthite; Microcline; Enstatite; Mica
39	40.8982	1125.57	Hematite; Orthoclase; Anorthite; Enstatite; Mica
40	41.771	1298.15	Augite; Orthoclase; Forsterite; Rutile; Anorthite; Microcline; Mica
41	42.4366	5123.59	Quartz; Augite; Orthoclase; Anorthite; Mica
42	42.9113	632.17	Augite; Orthoclase; Forsterite; Anorthite; Microcline; Enstatite; Mica
43	44.7971	1022.47	Forsterite; Rutile; Anorthite; Microcline; Enstatite; Mica
44	45.7942	2626.77	Quartz; Orthoclase; Anorthite; Microcline; Enstatite; Mica
45	47.2051	643.74	Orthoclase; Anorthite; Microcline; Enstatite
46	48.4342	236.82	Orthoclase; Forsterite; Anorthite; Microcline; Enstatite; Mica
47	49.4427	2151.28	Hematite; Augite; Orthoclase; Forsterite; Anorthite; Microcline; Enstatite; Mica
48	50.1231	10816.58	Quartz; Orthoclase; Forsterite; Anorthite; Microcline
49	50.743	985.63	Quartz; Orthoclase; Forsterite; Anorthite; Microcline; Enstatite; Mica
50	51.5113	451.86	Orthoclase; Anorthite; Microcline; Enstatite; Mica
51	52.3012	869.96	Augite; Orthoclase; Forsterite; Anorthite; Microcline; Mica
52	54.0614	1607.86	Hematite; Orthoclase; Anorthite; Microcline; Enstatite; Mica
53	54.8435	3169.95	Quartz; Augite; Orthoclase; Forsterite; Anorthite; Microcline; Enstatite; Mica
54	55.2904	1146.42	Quartz; Orthoclase; Rutile; Anorthite; Microcline; Enstatite; Mica
55	56.138	345.7	Hematite; Orthoclase; Forsterite; Anorthite; Microcline; Enstatite; Mica
56	56.726	777.98	Augite; Orthoclase; Forsterite; Anorthite; Microcline; Enstatite; Mica
57	57.6784	224.06	Hematite; Orthoclase; Forsterite; Rutile; Anorthite; Microcline; Enstatite; Mica
58	58.6869	179.86	Augite; Orthoclase; Forsterite; Anorthite; Microcline; Enstatite; Mica
59	59.0175	228.98	Augite; Orthoclase; Forsterite; Anorthite; Enstatite; Mica
60	59.9295	8528.81	Quartz; Augite; Anorthite; Microcline; Enstatite; Mica
61	61.2975	389.5	Augite; Orthoclase; Forsterite; Anorthite; Microcline; Enstatite; Mica
62	62.4428	535.85	Hematite; Forsterite; Anorthite; Microcline; Enstatite; Mica

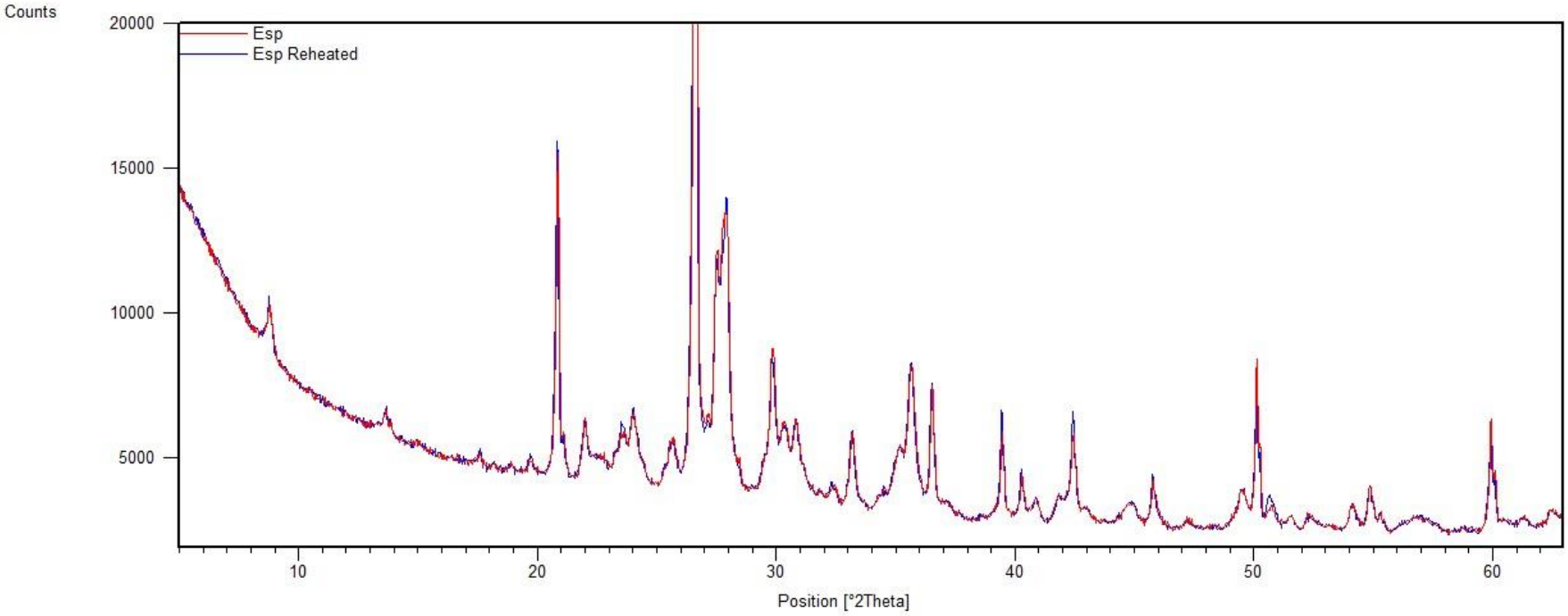

Figure A.3: XRD spectra of *Esp* sample without (red) and with (blue) reheating at 500°C.

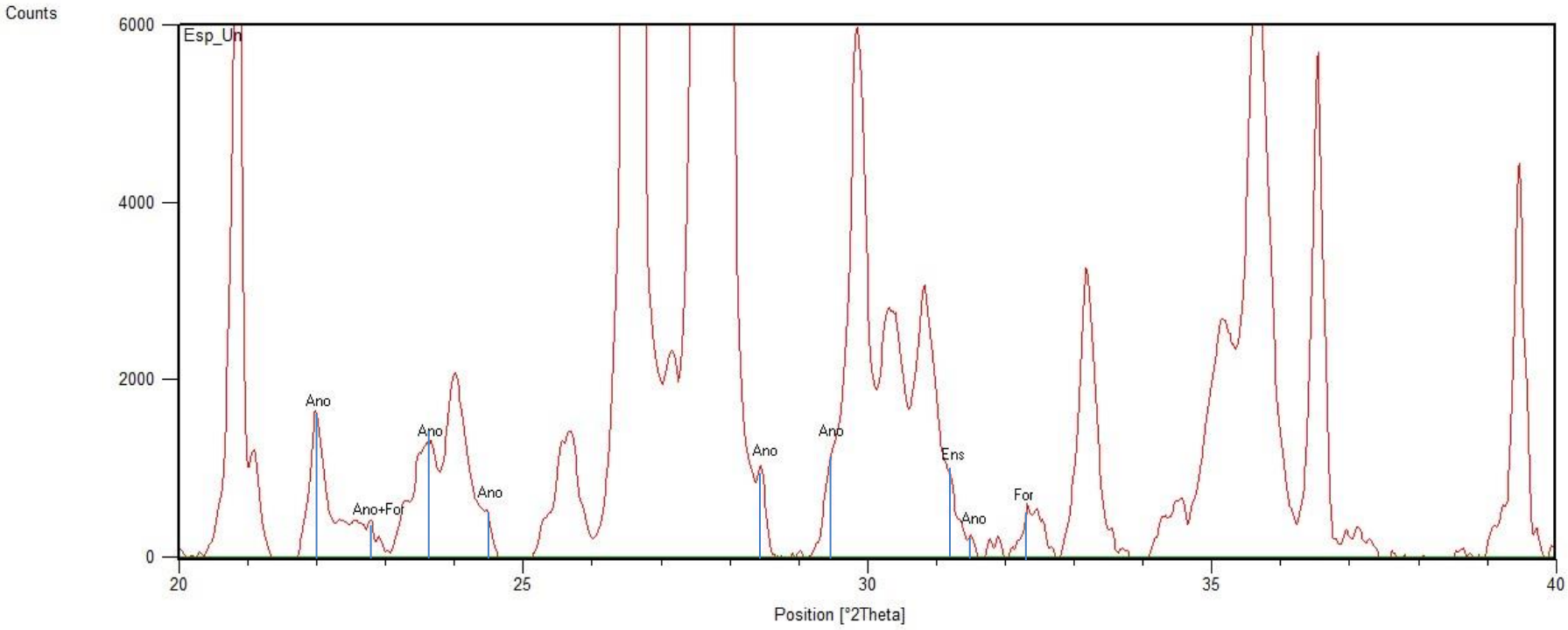

Figure A.4: XRD spectrum of Castle Espie non-reheated sample highlighting peaks attributed to minerals associated with high temperature firing. Ano = Anorthite; Ens = Enstatite; For=Forsterite.

Nic

Table A.3: XRD peak position and associated mineral interpretation for *Nic* non-reheated sample.

No.	Pos. [°2Th.]	Height [cts]	Mineral
1	13.5632	454.02	Anorthite; Diopside; Microcline
2	15.1085	94.59	Anorthite; Microcline; Albite
3	15.8131	942.47	Anorthite; Albite
4	16.3976	633.64	Anorthite; Gehlenite; Mullite
5	17.3912	205.77	Forsterite; Anorthite; Gehlenite
6	18.9149	441.86	Anorthite; Diopside; Spinel; Albite
7	19.8824	177.05	Anorthite; Diopside; Enstatite
8	20.8335	4894.51	Quartz; Anorthite; Gehlenite
9	21.949	3043.82	Anorthite; Cristobalite; Albite
10	22.8668	1673.19	Forsterite; Anorthite; Calcite
11	23.5836	2210.13	Anorthite; Mullite; Albite
12	23.8816	1535.97	Forsterite; Anorthite; Gehlenite; Enstatite; Microcline
13	24.1239	1760.37	Hematite; Anorthite; Diopside; Gehlenite; Enstatite; Microcline; Albite
14	24.4809	1293.58	Anorthite; Microcline; Albite
15	25.5097	1399.47	Forsterite; Microcline; Albite
16	25.9165	2589.05	Anorthite; Gehlenite; Mullite; Albite
17	26.6136	28687.52	Quartz; Diopside; Enstatite; Microcline; Albite
18	27.4237	7104.87	Anorthite; Diopside; Microcline
19	27.9618	9161.6	Anorthite; Enstatite; Rutile; Albite
20	28.4328	1596.86	Anorthite; Cristobalite; Albite
21	29.3301	2574.23	Anorthite; Gehlenite; Calcite; Microcline
22	29.8175	10892.54	Forsterite; Anorthite; Diopside; Enstatite
23	30.3245	5570.73	Anorthite; Diopside; Microcline; Albite
24	30.8183	4705.5	Anorthite; Diopside; Enstatite; Microcline; Mullite
25	31.49	1312.14	Anorthite; Diopside; Gehlenite; Calcite; Enstatite; Cristobalite; Albite
26	32.3068	2501.53	Forsterite; Enstatite; Microcline; Albite
27	33.1354	6662.88	Hematite; Anorthite; Gehlenite; Mullite
28	33.7077	788.85	Anorthite; Albite
29	34.9125	2331.25	Forsterite; Anorthite; Diopside; Enstatite; Microcline; Albite
30	35.7051	12662.6	Hematite; Forsterite; Anorthite; Diopside; Enstatite; Microcline; Albite
31	36.5021	6462.29	Quartz; Forsterite; Anorthite; Enstatite; Rutile; Spinel; Albite
32	38.3087	126.98	Forsterite; Anorthite; Diopside; Enstatite; Spinel; Cristobalite; Albite
33	38.8261	726.39	Forsterite; Anorthite; Diopside; Enstatite; Albite
34	39.418	3151.87	Quartz; Forsterite; Anorthite; Gehlenite; Calcite; Microcline; Albite
35	39.6899	1965.42	Forsterite; Anorthite; Microcline; Albite
36	40.0446	1126.13	Quartz; Forsterite; Enstatite; Rutile; Microcline; Albite

37	40.2438	1478.35	Quartz; Anorthite; Diopside; Enstatite; Microcline; Albite
38	40.822	2536.83	Hematite; Anorthite; Diopside; Enstatite; Mullite
39	41.7497	1731.55	Forsterite; Anorthite; Diopside; Enstatite; Rutile; Microcline; Albite
40	42.4085	5182.18	Quartz; Anorthite; Diopside; Gehlenite; Enstatite; Mullite; Albite
41	42.8607	1148.5	Anorthite; Diopside; Gehlenite; Enstatite; Microcline; Cristobalite; Mullite; Albite
42	44.4839	669.12	Forsterite; Anorthite; Gehlenite; Enstatite; Spinel; Microcline; Albite
43	44.8135	1962.91	Anorthite; Diopside; Rutile; Microcline; Cristobalite; Albite
44	45.7583	2635.34	Quartz; Enstatite; Microcline; Albite
45	47.0782	415.04	Calcite; Enstatite; Microcline; Cristobalite; Mullite; Albite
46	48.4415	862.34	Forsterite; Calcite; Microcline; Cristobalite
47	49.4386	4145.09	Hematite; Forsterite; Diopside; Mullite; Albite
48	50.0982	5902.65	Quartz; Forsterite; Diopside; Enstatite; Microcline; Albite
49	50.7149	817.01	Forsterite; Gehlenite; Enstatite; Microcline; Mullite; Albite
50	51.6085	1167.18	Enstatite; Microcline; Albite
51	52.2457	3835.74	Forsterite; Gehlenite; Enstatite; Microcline; Albite
52	54.0587	3513.08	Hematite; Enstatite; Microcline; Cristobalite; Albite
53	54.848	3707.76	Quartz; Forsterite; Diopside; Enstatite; Microcline; Albite
54	56.2782	1126.5	Hematite; Forsterite; Diopside; Gehlenite; Microcline; Albite
55	56.7579	2140.51	Forsterite; Diopside; Enstatite; Microcline; Albite
56	57.3447	739.97	Hematite; Forsterite; Calcite; Enstatite; Microcline; Cristobalite; Albite
57	58.7572	272.24	Forsterite; Diopside; Enstatite; Spinel; Microcline; Cristobalite; Mullite; Albite
58	59.9111	4179.38	Quartz; Diopside; Gehlenite; Enstatite; Microcline; Albite
59	60.3892	450.15	Forsterite; Diopside; Gehlenite; Enstatite; Microcline; Cristobalite; Mullite; Albite
60	61.5293	270.27	Forsterite; Diopside; Enstatite; Microcline; Mullite; Albite
61	61.9845	656.56	Forsterite; Diopside; Microcline; Cristobalite; Albite
62	62.3888	1674.9	Hematite; Forsterite; Enstatite; Microcline; Mullite; Albite

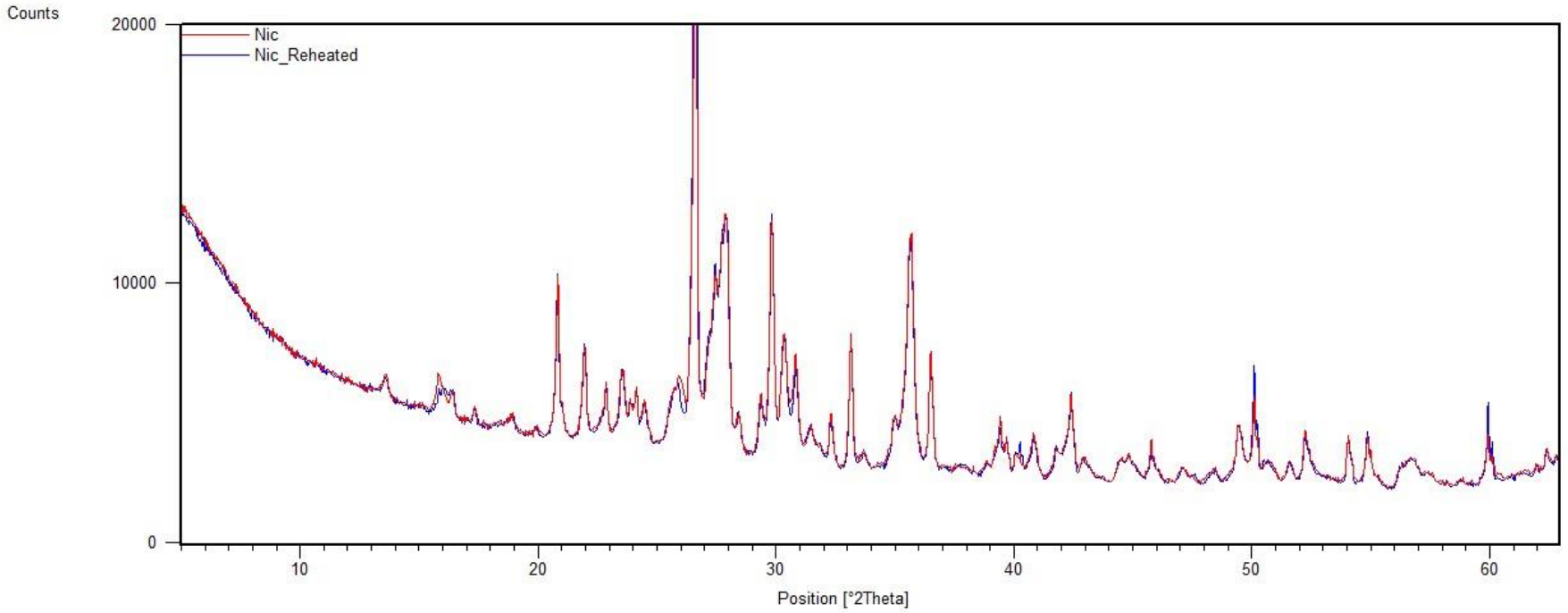

Figure A.5: XRD spectra of *Nic* sample without (red) and with (blue) reheating at 500°C. Differences are considered insignificant and due to inhomogeneity in samples and minor differences in composition of subsamples used.

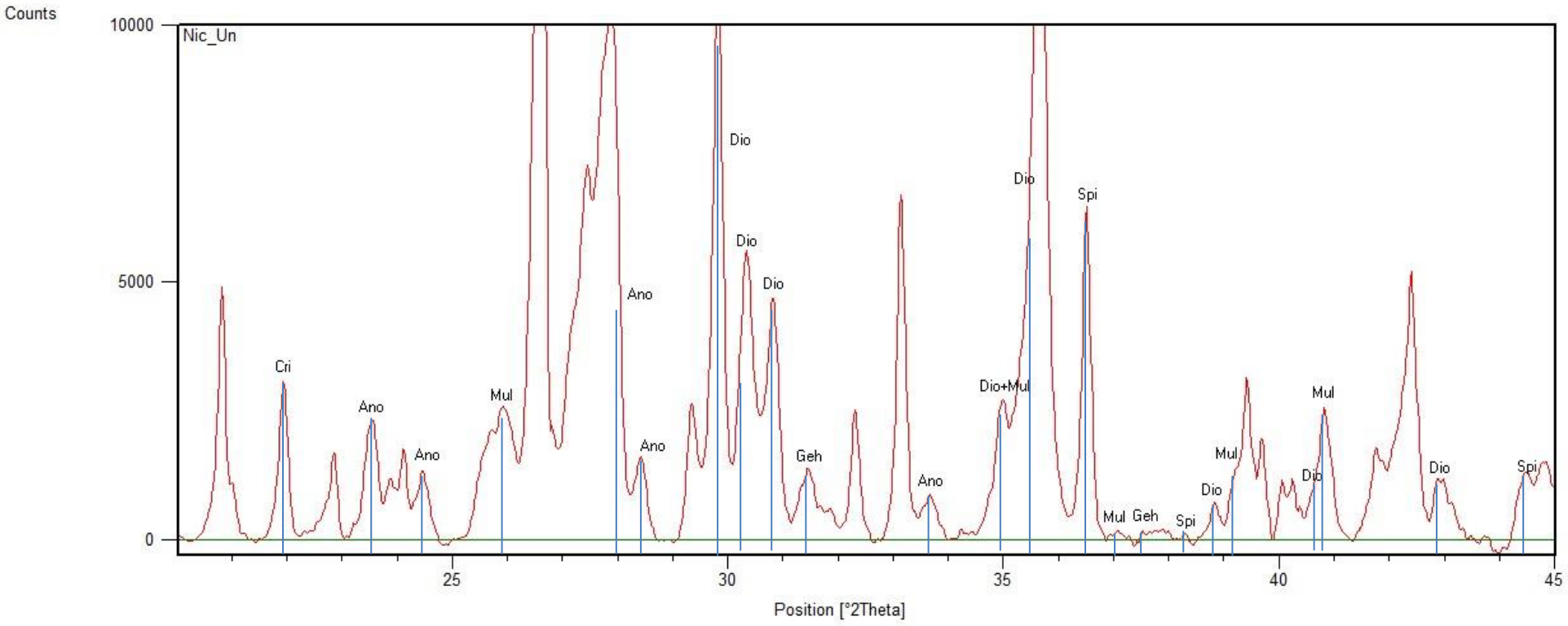

Figure A.6: XRD spectrum of non-reheated *Nic*, highlighting peaks attributed to high temperature related mineral phases. Mul=Mullite; Spi=Spinel; Cri=Cristobalite; Geh=Gehlenite; Dio=Diopside; Ano=Anorthite.

Mac

Table A.4: XRD peak position and associated mineral interpretation for *Mac* non-reheated sample.

No.	Pos. [°2Th.]	Height [cts]	Mineral
1	13.6668	175.76	Sanidine; Albite; Microcline
2	14.711	997.13	Bassanite
3	18.1531	200.08	Tridymite
4	18.9113	625.34	Spinel; Albite; Tridymite
5	20.813	12993.27	Quartz; Fayalite/Olivine; Tridymite; Bassanite
6	21.1758	427.11	Sanidine; Tridymite; Microcline
7	21.928	1345.01	Cristobalite; Dolomite; Albite
8	22.4124	138.53	Sanidine; Tridymite; Microcline; Bassanite
9	22.6674	176.56	Sanidine; Albite; Tridymite; Microcline
10	22.847	225.13	Albite; Tridymite
11	23.3076	285.94	Sanidine; Albite; Tridymite; Microcline; Bassanite
12	23.6249	1114.08	Sanidine; Albite
13	24.1673	1542.96	Hematite; Dolomite; Albite; Tridymite; Microcline
14	25.6013	1800.87	Sanidine; Albite; Fayalite/Olivine; Tridymite; Microcline; Bassanite
15	26.6106	89520.65	Quartz; Tridymite; Microcline
16	27.1767	936.66	Sanidine; Tridymite; Microcline
17	27.4924	3314.21	Rutile; Sanidine; Albite; Tridymite; Microcline; Bassanite
18	27.7299	4017.09	Sanidine; Albite; Tridymite; Bassanite
19	27.9849	2085.52	Albite; Tridymite
20	28.4061	476.32	Cristobalite; Tridymite
21	28.9044	71.18	Tridymite
22	29.6814	2225.79	Sanidine; Albite; Tridymite; Bassanite
23	30.2453	454	Albite; Tridymite; Microcline
24	30.8602	630.68	Dolomite; Sanidine; Tridymite; Microcline
25	31.1092	1532.25	Spinel; Sanidine; Albite; Tridymite
26	31.854	1780.2	Sanidine; Albite; Tridymite; Microcline; Bassanite
27	32.5568	441.44	Sanidine; Fayalite/Olivine; Tridymite; Microcline
28	33.2659	6201.72	Hematite; Dolomite; Albite; Tridymite
29	33.6766	216.17	Albite; Tridymite
30	34.3217	266.46	Tridymite; Microcline; Bassanite
31	35.6682	5185.62	Hematite; Sanidine; Albite; Fayalite/Olivine; Tridymite; Microcline
32	36.507	8962.16	Quartz; Albite; Fayalite/Olivine; Tridymite; Cristobalite
33	38.5989	204.43	Spinel; Albite; Fayalite/Olivine; Microcline; Bassanite
34	39.4235	6268.74	Quartz; Hematite; Sanidine; Albite; Microcline; Bassanite
35	40.2366	2781.28	Quartz; Albite; Microcline
36	40.9137	1567.72	Hematite; Dolomite; Sanidine; Albite; Bassanite
37	41.8031	308.36	Sanidine; Albite; Fayalite/Olivine; Microcline
38	42.4256	6658.34	Quartz; Cristobalite; Sanidine; Albite; Cristobalite; Bassanite

39	43.5697	135.28	Hematite; Dolomite; Sanidine; Albite; Microcline
40	44.5934	2443.33	Spinel; Cristobalite; Albite; Fayalite/Olivine; Cristobalite; Microcline
41	45.7468	3170.57	Quartz; Albite; Microcline
42	47.1545	111.71	Sanidine; Albite; Fayalite/Olivine; Microcline
43	47.5725	250.77	Sanidine; Albite; Microcline; Bassanite
44	48.4287	166.69	Cristobalite; Sanidine; Albite; Cristobalite; Microcline
45	49.5561	2653.92	Hematite; Sanidine; Albite; Fayalite/Olivine; Bassanite
46	50.0976	11940.34	Quartz; Dolomite; Sanidine; Albite; Microcline
47	50.6965	377.84	Quartz; Dolomite; Sanidine; Albite; Microcline
48	51.4075	281.83	Albite; Fayalite/Olivine; Microcline
49	52.3765	378.66	Cristobalite; Dolomite; Sanidine; Albite; Fayalite/Olivine
50	53.394	86.09	Sanidine; Albite; Microcline
51	54.2379	3463.93	Hematite; Rutile; Sanidine; Albite; Cristobalite; Microcline; Bassanite
52	54.8353	4526.46	Quartz; Sanidine; Albite; Microcline
53	55.2802	1637.97	Quartz; Spinel; Sanidine; Albite; Fayalite/Olivine; Microcline; Bassanite
54	56.2873	118.21	Hematite; Sanidine; Albite; Fayalite/Olivine; Microcline
55	57.1074	289.73	Quartz; Cristobalite; Sanidine; Albite; Fayalite/Olivine+D26; Microcline
56	57.8692	553.76	Hematite; Sanidine; Albite; Microcline
57	59.1234	1739.88	Spinel; Cristobalite; Sanidine; Albite; Fayalite/Olivine; Microcline
58	59.9092	10755.65	Quartz; Dolomite; Albite; Fayalite/Olivine; Microcline; Bassanite
59	61.4408	326.41	Dolomite; Sanidine; Albite; Fayalite/Olivine; Microcline
60	62.6542	1670.55	Hematite; Albite; Microcline; Bassanite

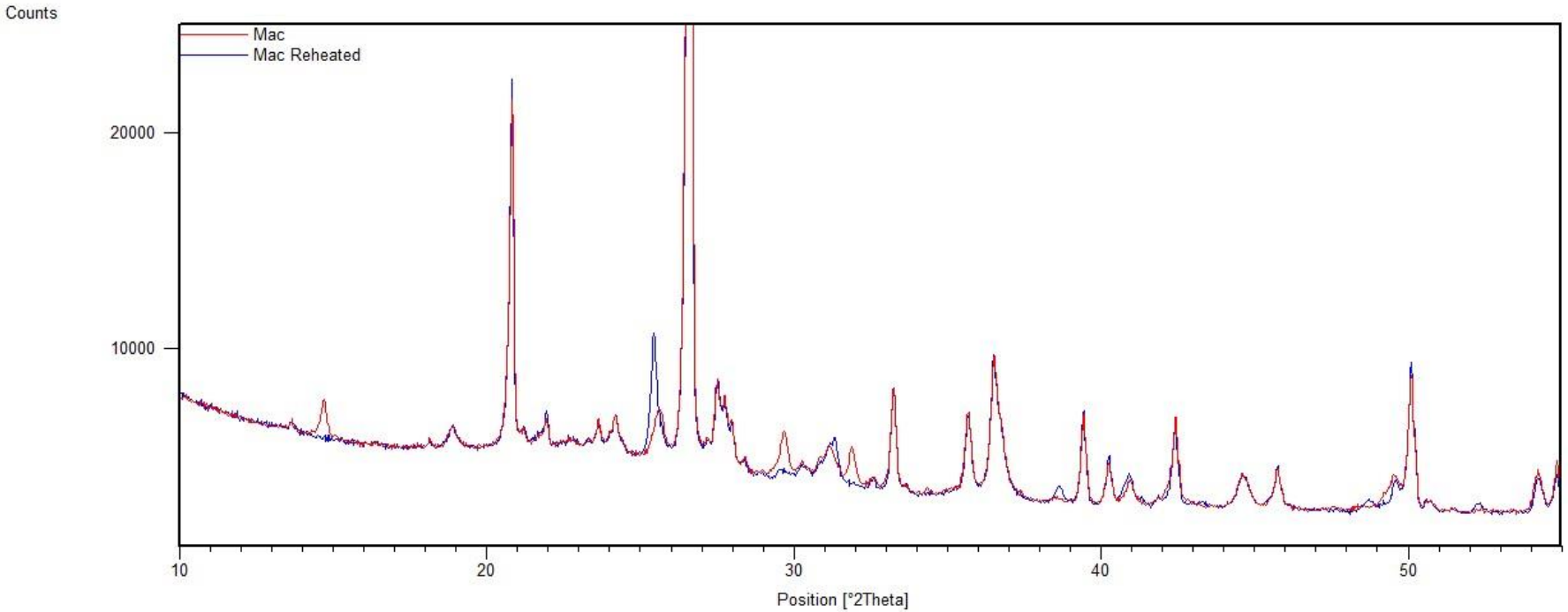

Figure A.7: XRD spectra of *Mac* sample without (red) and with (blue) reheating at 500°C. Region constrained to 10-55° (2θ).

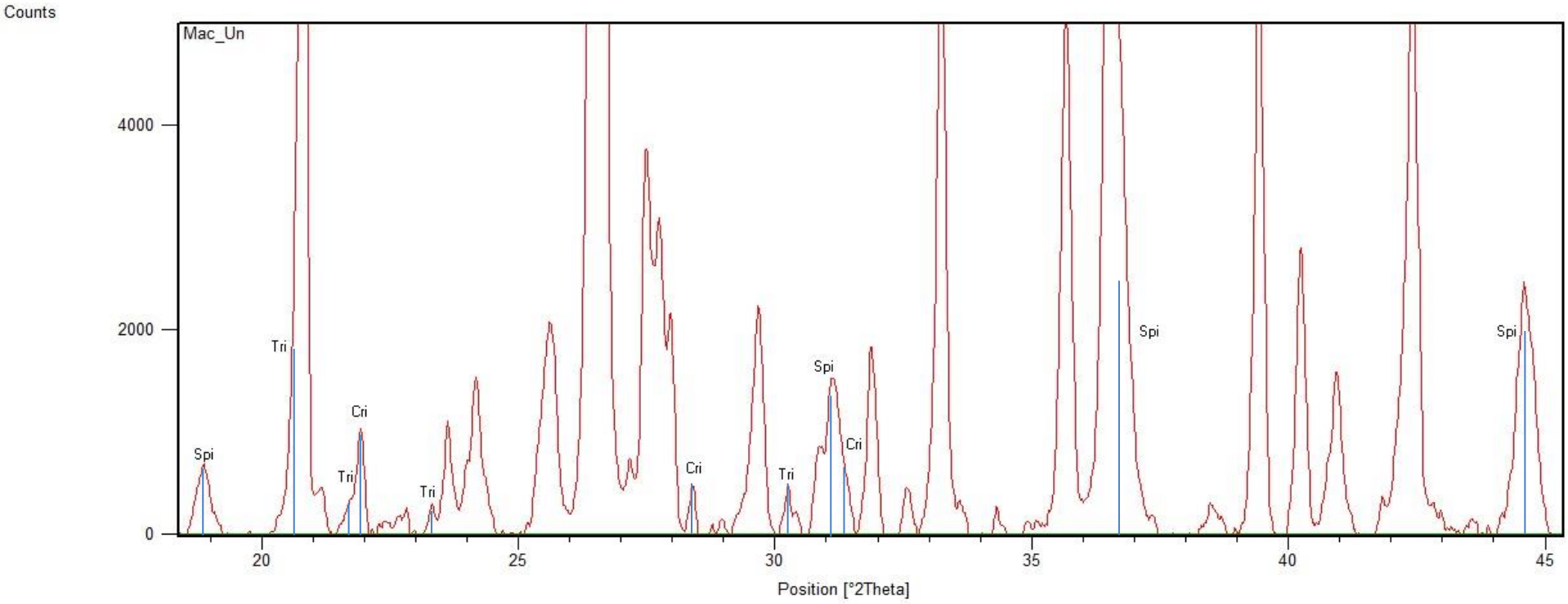

Figure A.8: XRD spectrum of non-reheated *Mac*, highlighting peaks attributed to high temperature related mineral phases. Spi=Spinel; Cri=Cristobalite; Tri=Tridymite.

Ria

Table A.5: XRD peak position and associated mineral interpretation for *Ria* non-reheated sample.

No.	Pos. [°2Th.]	Height [cts]	Mineral
1	13.345	73.74	Sanidine
2	13.6431	230.11	Anorthite; Microcline; Sanidine; Diopside; Albite; Enstatite
3	16.3864	195.29	Anorthite; Mullite; Gehlenite
4	18.1619	138.14	Anorthite
5	18.8151	365.11	Spinel; Anorthite
6	20.813	12472.65	Quartz; Anorthite; Sanidine
7	21.9524	486.5	Anorthite; Cristobalite; Albite
8	22.4469	373.77	Anorthite; Microcline; Sanidine
9	22.7184	228.13	Anorthite; Microcline; Albite
10	23.3365	341.19	Microcline; Sanidine; Mullite; Albite
11	23.5004	432.7	Anorthite; Sanidine; Mullite
12	23.6364	403.3	Albite
13	24.1857	1592.64	Hematite; Albite
14	24.9131	142.74	Microcline; Sanidine
15	25.5087	495.58	Microcline; Albite
16	25.724	1003.16	Anorthite; Microcline; Sanidine; Albite
17	26.6007	77468.37	Quartz; Diopside; Enstatite
18	27.2229	1432.18	Anorthite; Microcline; Sanidine
19	27.5105	4687.05	Microcline; Sanidine; Diopside; Albite; Enstatite
20	27.9197	1277.42	Anorthite; Albite; Enstatite
21	28.378	194.6	Anorthite; Cristobalite
22	29.0052	86.36	Enstatite
23	29.3478	396.47	Anorthite; Microcline; Calcite
24	29.7564	352.73	Anorthite; Sanidine; Diopside; Albite
25	29.8924	458.36	Anorthite; Sanidine; Diopside; Albite; Enstatite
26	30.2235	778.6	Anorthite; Microcline
27	30.8526	1019.54	Anorthite; Microcline; Sanidine; Mullite; Diopside; Albite; Enstatite
28	31.1059	1671.02	Spinel; Albite; Enstatite
29	31.4332	572.9	Anorthite; Gehlenite; Cristobalite; Calcite; Albite
30	32.5464	314.63	Anorthite; Microcline; Enstatite
31	33.2479	5657.7	Hematite; Anorthite; Mullite; Albite
32	34.3157	93.64	Anorthite; Microcline; Sanidine; Enstatite
33	35.2037	505.31	Anorthite; Microcline; Sanidine; Mullite; Albite; Enstatite
34	35.6787	4658.74	Hematite; Anorthite; Microcline; Diopside; Albite; Enstatite
35	36.4983	9048.42	Quartz; Spinel; Anorthite; Cristobalite; Albite
36	39.4246	5961.99	Quartz; Hematite; Anorthite; Gehlenite; Calcite; Enstatite
37	40.2451	3306.66	Quartz; Anorthite; Microcline; Albite; Enstatite
38	40.9611	1455.01	Hematite; Anorthite; Sanidine; Mullite; Diopside; Albite

39	41.8184	398.76	Microcline; Albite
40	42.4134	7029	Quartz; Anorthite; Sanidine; Mullite; Diopside; Gehlenite; Albite; Enstatite
41	44.4444	814.62	Spinel; Anorthite; Sanidine; Diopside; Gehlenite; Albite
42	44.6502	1679.64	Spinel; Microcline; Cristobalite; Albite
43	44.8864	932.05	Sanidine; Diopside; Cristobalite; Albite; Enstatite
44	45.7633	3929.85	Quartz; Microcline; Albite; Enstatite
45	49.5894	2070.05	Hematite; Sanidine; Mullite; Diopside; Albite
46	50.1046	14264.62	Quartz; Microcline; Albite; Enstatite
47	50.5952	367.53	Quartz; Microcline; Sanidine; Mullite; Gehlenite; Albite; Enstatite
48	54.2644	2879.25	Hematite; Microcline; Gehlenite; Cristobalite; Albite; Enstatite
49	54.8299	3595.63	Quartz; Microcline; Sanidine; Diopside; Albite; Enstatite
50	55.2865	1797.76	Quartz; Spinel; Microcline; Sanidine; Diopside; Albite; Enstatite
51	56.5654	324.64	Microcline; Diopside; Gehlenite; Calcite; Albite; Enstatite
52	56.9394	255.91	Microcline; Sanidine; Diopside; Gehlenite; Cristobalite; Albite; Enstatite
53	57.0414	273.79	Quartz; Microcline; Sanidine; Diopside; Gehlenite; Cristobalite; Albite; Enstatite
54	57.1659	448.55	Quartz; Microcline; Sanidine; Diopside; Gehlenite; Cristobalite; Albite; Enstatite
55	57.3134	467.81	Microcline; Sanidine; Cristobalite; Calcite; Enstatite
56	57.5174	476.44	Hematite; Microcline; Sanidine; Mullite; Cristobalite; Calcite; Albite
57	57.7214	519.68	Hematite; Microcline; Sanidine; Albite; Enstatite
58	57.8404	475.38	Microcline; Sanidine; Albite; Enstatite
59	58.7414	491.87	Microcline; Sanidine; Cristobalite; Albite; Enstatite
60	58.9284	593.65	Spinel; Microcline; Sanidine; Mullite; Cristobalite; Albite; Enstatite
61	59.1834	828.63	Sanidine; Diopside; Albite; Enstatite
62	59.9242	9692.8	Quartz; Microcline; Gehlenite; Albite; Enstatite
63	61.5788	133.12	Sanidine; Mullite; Diopside; Albite; Enstatite
64	62.6005	1388.38	Hematite; Microcline; Sanidine; Diopside; Albite

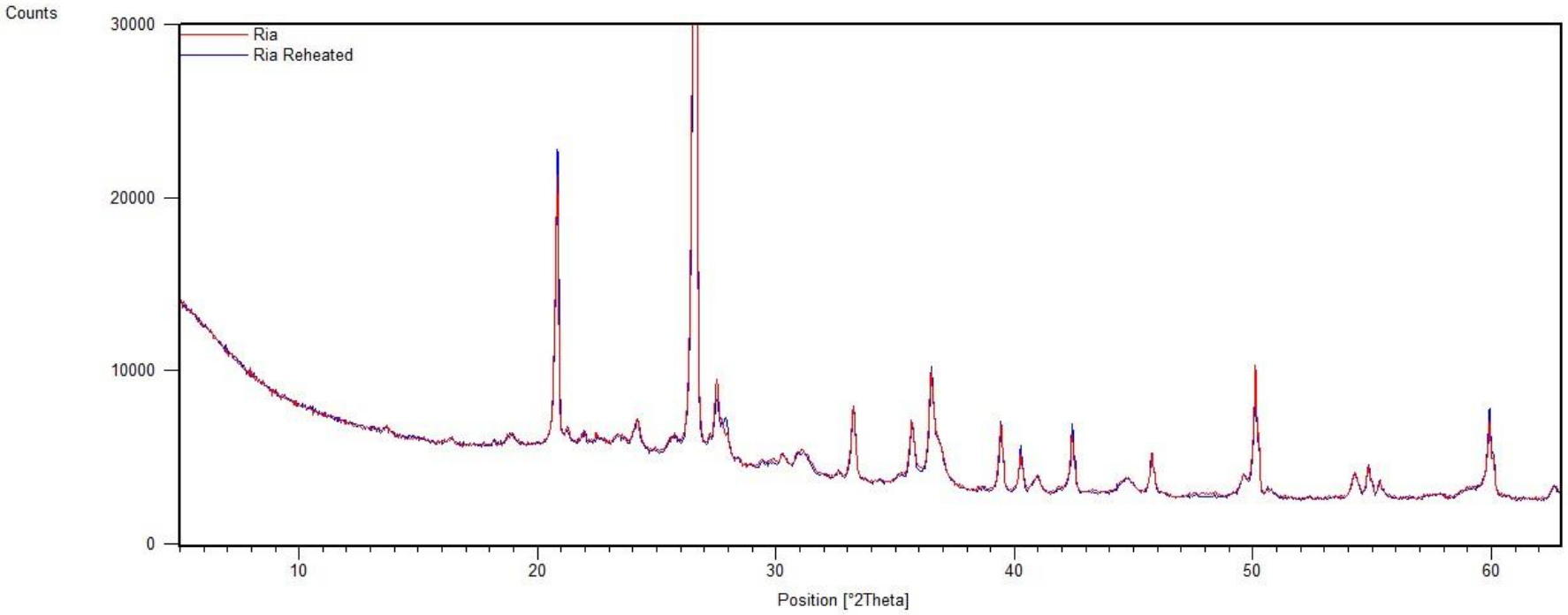

Figure A.9: XRD spectra of *Ria* sample without (red) and with (blue) reheating at 500°C.

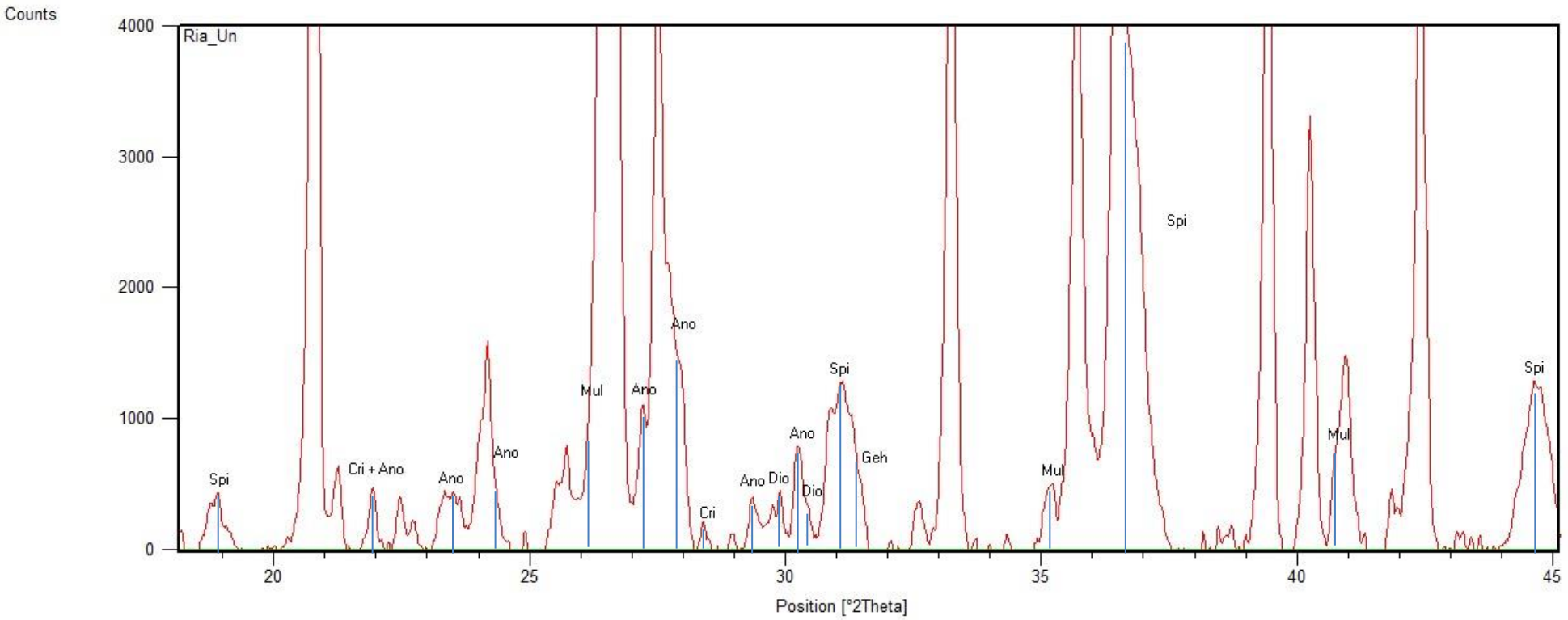

Figure A.10: XRD spectrum of non-reheated *Ria*, highlighting peaks attributed to high temperature related mineral phases. Spi=Spinel; Mul=Mullite; Geh=Gehlenite; Cri=Cristobalite; Dio=Diopside; Ano=Anorthite

Etr

Table A.6: XRD peak position and associated mineral interpretation for *Etr* non-reheated sample.

No.	Pos. [°2Th.]	Height [cts]	Mineral
1	8.7616	861.72	Mica (musc)
2	13.634	255.01	Microcline; Sanidine
3	13.867	249.53	Albite; Augite
4	14.9399	90.27	Microcline; Albite; Sanidine
5	17.6156	780.08	Mica (musc)
6	19.6838	1702.87	Mica (musc)
7	20.835	11452.78	Quartz; Mica (musc); Sanidine
8	21.9713	387.63	Albite
9	22.5144	121.7	Microcline; Sanidine
10	22.6844	215.34	Microcline; Olivine; Mica (musc); Sanidine
11	23.0771	841.74	Microcline; Calcite
12	23.4834	1777.23	Mica (musc); Sanidine
13	23.5998	1154	Albite; Mica (musc); Sanidine
14	24.0169	791.63	Microcline; Albite
15	24.2795	718.92	Microcline; Hematite; Albite
16	25.2853	878.27	Anatase; Olivine; Mica (musc)
17	25.4894	523.9	Microcline; Albite; Anatase; Olivine
18	25.6764	489.06	Microcline; Sanidine
19	26.6199	88124.8	Quartz; Microcline; Augite; Sanidine
20	27.5166	3967.59	Microcline; Mica (musc); Sanidine
21	27.93	4762.12	Albite; Augite
22	29.4161	13492.27	Calcite; Microcline; Olivine; Mica (musc)
23	29.8413	1176.66	Albite; Augite; Olivine; Sanidine
24	30.4656	213.22	Albite; Augite; Sanidine
25	30.8253	348.48	Microcline; Augite; Mica (musc); Calcite; Sanidine
26	31.3787	414.26	Albite; Sanidine
27	31.8319	88.49	Microcline; Albite; Augite; Mica (musc); Sanidine
28	32.2048	75.11	Microcline; Albite; Olivine; Sanidine
29	33.2238	404.03	Hematite; Albite; Mica (musc)
30	34.634	1013.02	Microcline; Olivine; Mica (musc); Sanidine
31	35.658	1741.04	Microcline; Hematite; Albite; Augite; Olivine; Mica (musc)
32	35.9983	2245.36	Microcline; Albite; Augite; Mica (musc); Calcite; Sanidine
33	36.5096	7677.38	Quartz; Albite; Olivine; Mica (musc); Sanidine
34	37.3523	210.08	Albite; Mica (musc); Sanidine
35	38.707	100.97	Microcline; Albite; Augite; Anatase; Olivine; Sanidine
36	39.4476	13138.41	Quartz; Hematite; Albite; Olivine; Mica (musc); Calcite; Sanidine
37	40.2534	2967.91	Quartz; Microcline; Albite; Augite; Mica (musc); Sanidine
38	40.684	106.41	Microcline; Albite; Mica (musc); Sanidine

39	40.9663	173.93	Albite; Augite; Mica (musc); Sanidine
40	41.7887	243.28	Microcline; Albite; Olivine; Mica (musc); Sanidine
41	42.409	4838.75	Quartz; Albite; Augite; Sanidine
42	43.1776	2549.89	Microcline; Albite; Augite; Mica (musc); Calcite; Sanidine
43	44.5154	116.82	Microcline; Sanidine
44	44.9912	996.51	Albite; Mica (musc)
45	45.7627	3915.02	Quartz; Microcline; Albite; Augite; Mica (musc); Sanidine
46	47.5406	2478.05	Calcite; Microcline; Albite; Mica (musc); Sanidine
47	48.4923	2366.38	Calcite; Microcline; Albite; Mica (musc); Sanidine
48	50.1076	16185.72	Quartz; Microcline; Albite; Augite; Olivine
49	50.5273	892.08	Quartz; Microcline; Augite; Olivine; Mica (musc); Sanidine
50	51.2919	3288.34	Microcline; Albite; Augite; Mica (musc); Sanidine
51	52.3891	110.06	Microcline; Albite; Augite; Olivine; Mica (musc); Sanidine
52	53.1747	254.76	Albite; Sanidine
53	54.8457	5633.67	Quartz; Microcline; Albite; Augite; Anatase; Olivine; Mica (musc); Sanidine
55	55.3041	2286.03	Quartz; Microcline; Augite; Mica (musc)
56	56.5157	147	Calcite; Microcline; Hematite; Albite; Augite; Olivine; Mica (musc); Sanidine
57	57.4679	1097.62	Calcite; Microcline; Hematite; Albite; Augite; Olivine; Mica (musc)
58	58.6737	156.89	Microcline; Albite; Augite; Olivine; Mica (musc); Sanidine
59	59.9183	9079.62	Quartz; Microcline; Albite; Augite; Mica (musc); Sanidine
60	60.6852	780.3	Calcite; Microcline; Albite; Mica (musc); Sanidine
61	62.2757	186.05	Microcline; Albite; Augite; Olivine; Mica (musc); Sanidine

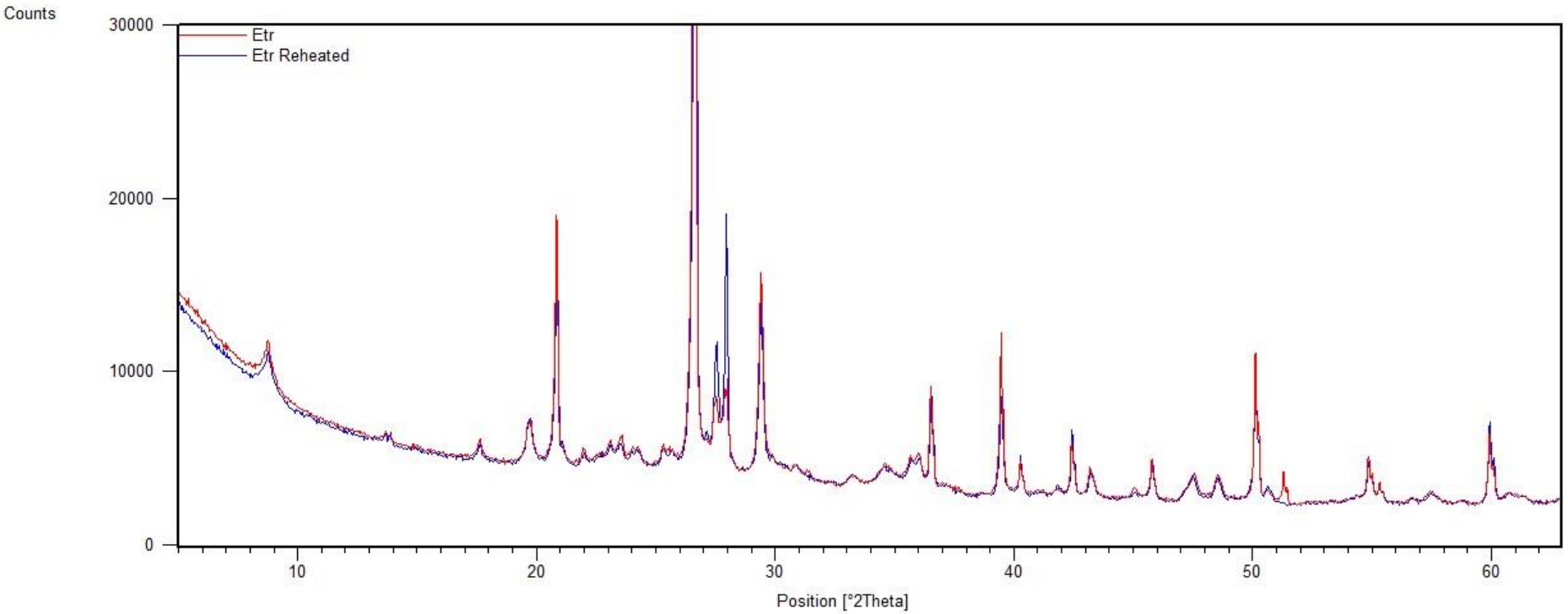

Figure A.11: XRD spectra of *Etr* sample without (red) and with (blue) reheating at 500°C.

Rom

Table A.7: XRD peak position and associated mineral interpretation for *Rom* non-reheated sample.

No.	Pos. [°2Th.]	Height [cts]	Mineral
1	8.7425	1823.01	Mica(Musc/Bio)
2	13.2154	134	Microcline; Orthoclase
3	13.6152	691.02	Microcline; Augite; Orthoclase
4	13.8425	399.6	Albite; Augite
5	14.9848	117.86	Albite; Microcline; Orthoclase
6	17.5997	795.41	Mica(Musc/Bio)
7	19.6435	2090.52	Mica(Musc/Bio)
8	20.8123	15291.33	Quartz; Mica(Musc/Bio)
9	21.9893	848.2	Albite
10	22.6742	318.99	Microcline; Mica(Musc/Bio); Orthoclase
11	23.5137	1711.49	Albite; Mica(Musc/Bio); Orthoclase
12	24.0155	1234.86	Albite; Microcline; Calcite
13	24.2617	901.41	Albite; Microcline; Augite; Calcite
14	25.2618	796.14	Albite; Mica(Musc/Bio); Orthoclase
15	25.6676	419.48	Albite; Microcline; Orthoclase
16	26.5987	82163.11	Quartz; Microcline; Mica(Musc/Bio); Augite
17	27.4171	6998.63	Microcline; Mica(Musc/Bio); Augite; Orthoclase
18	27.5401	8328.6	Microcline; Mica(Musc/Bio); Augite; Orthoclase
19	27.8716	4892.04	Albite
20	29.3563	3237.1	Calcite; Microcline
21	29.8543	457.06	Augite; Orthoclase
22	30.1914	286.45	Albite; Microcline; Augite
23	30.5025	167.63	Albite; Orthoclase
24	30.7551	423.59	Microcline; Mica(Musc/Bio); Augite; Orthoclase
25	31.2713	453.63	Calcite; Albite
26	33.1599	631.97	Mica(Musc/Bio); Calcite
27	34.4133	514.02	Microcline; Mica(Musc/Bio); Orthoclase
28	34.7884	573.03	Microcline; Mica(Musc/Bio); Augite; Orthoclase
29	34.9637	482.09	Albite; Microcline; Mica(Musc/Bio); Augite; Orthoclase
30	35.6276	1123.78	Albite; Microcline; Mica(Musc/Bio); Augite; Orthoclase; Calcite
31	35.9186	645.91	Calcite; Albite; Microcline; Mica(Musc/Bio)
32	36.4832	4241.05	Quartz; Albite; Mica(Musc/Bio); Orthoclase
33	37.2489	141.55	Albite; Microcline; Mica(Musc/Bio); Orthoclase
34	38.6963	138.21	Albite; Microcline; Orthoclase
35	39.4167	4468.85	Quartz; Calcite; Albite; Mica(Musc/Bio); Calcite
36	40.2337	2017.95	Quartz; Microcline; Mica(Musc/Bio)
37	40.9585	206.43	Mica(Musc/Bio); Augite; Orthoclase; Calcite

38	41.7788	229.33	Microcline; Mica(Musc/Bio); Augite; Orthoclase
39	42.396	3114.08	Quartz; Albite; Augite; Orthoclase
40	43.1021	284.32	Calcite; Microcline
41	44.1121	43.66	Microcline; Mica(Musc/Bio); Orthoclase
42	44.7844	130.75	Microcline; Mica(Musc/Bio); Augite
43	44.9881	354.61	Mica(Musc/Bio); Augite
44	45.2944	162	Albite; Mica(Musc/Bio); Augite; Orthoclase
45	45.7284	2401.16	Quartz; Albite; Microcline; Mica(Musc/Bio)
46	47.4519	462.36	Calcite; Microcline; Mica(Musc/Bio); Orthoclase
47	48.4344	281.07	Calcite; Microcline; Mica(Musc/Bio); Orthoclase
48	50.0844	8369.73	Quartz; Albite; Microcline; Orthoclase
49	50.5824	532.2	Quartz; Albite; Microcline; Mica(Musc/Bio); Augite; Orthoclase
50	52.1932	70.05	Microcline; Mica(Musc/Bio); Augite
51	53.2419	77.12	Microcline; Mica(Musc/Bio); Augite; Orthoclase
52	54.8227	2930.86	Quartz; Microcline; Mica(Musc/Bio); Augite; Orthoclase
53	55.272	947.57	Quartz; Microcline; Mica(Musc/Bio); Augite
54	56.5543	69.18	Calcite; Microcline; Mica(Musc/Bio); Augite; Orthoclase
55	57.4211	142.91	Calcite; Microcline; Mica(Musc/Bio); Orthoclase; Calcite
56	58.6771	469.6	Microcline; Mica(Musc/Bio); Augite; Orthoclase
57	59.9032	5212.07	Quartz; Microcline; Mica(Musc/Bio)
58	61.3825	138.73	Calcite; Microcline; Mica(Musc/Bio); Augite; Orthoclase

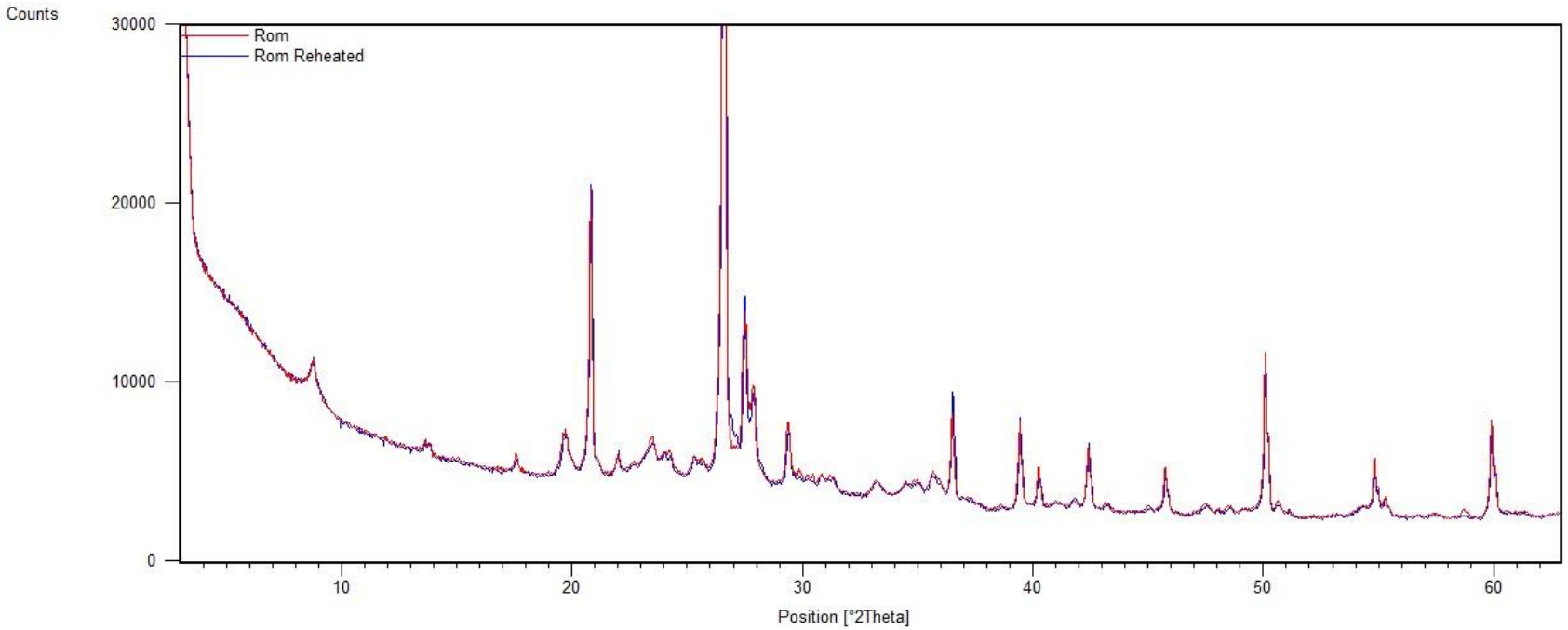

Figure A.12: XRD spectra of *Rom* sample without (red) and with (blue) reheating at 500°C.

Por

Table A.8: XRD peak position and associated mineral interpretation for *Por* non-reheated sample.

No.	Pos. [°2Th.]	Height [cts]	Mineral
1	13.6714	125.87	Diopside; Microcline; Anorthite; Diopside; Sanidine
2	15.1266	53.23	Microcline; Anorthite; Sanidine
3	16.1452	124.8	Gehlenite; Wollastonite
4	17.4695	155.46	Gehlenite; Wollastonite
5	19.0109	133.46	Spinel; Diopside; Anorthite; Diopside; Wollastonite
6	19.9516	94.27	Diopside; Diopside; Wollastonite
7	20.8104	12581.37	Quartz; Olivine(Fayalite)
8	21.8901	460.26	Cristobalite; Anorthite; Wollastonite
9	23.0584	397.01	Calcite; Gehlenite; Microcline; Wollastonite; Sanidine
10	23.2211	461.58	Calcite; Microcline; Wollastonite; Sanidine; Olivine(Fayalite)
11	23.6024	287.42	Anorthite; Wollastonite; Sanidine
12	23.9789	1343.99	Gehlenite; Microcline; Olivine(Fayalite)
13	24.2314	187.33	Diopside; Microcline; Diopside
14	24.3504	156.04	Diopside; Microcline
15	25.3024	270.59	Cristobalite; Wollastonite; Sanidine
16	25.3874	294.48	Cristobalite; Microcline; Wollastonite
17	25.5574	538.08	Gehlenite; Microcline; Anorthite; Sanidine; Olivine(Fayalite)
18	25.7054	938.63	Gehlenite; Microcline; Anorthite; Sanidine; Olivine(Fayalite)
19	26.6014	83068.71	Quartz; Diopside; Microcline; Anorthite; Diopside
20	27.4769	2560.14	Rutile; Microcline; Anorthite; Diopside; Wollastonite; Sanidine
21	27.845	2629	Diopside; Anorthite; Wollastonite
22	29.0396	883.91	Gehlenite; Wollastonite
23	29.4119	4691.74	Calcite; Microcline; Anorthite
24	29.9579	2821.47	Diopside; Wollastonite; Sanidine; Olivine(Fayalite)
25	30.763	433.8	Microcline; Anorthite; Diopside; Wollastonite; Sanidine
26	31.3515	5552.95	Calcite; Spinel; Gehlenite; Cristobalite; Marcasite
27	32.7484	305.94	Gehlenite; Wollastonite
28	33.1976	532.12	Wollastonite; Olivine(Fayalite); Marcasite
29	34.1652	161.66	Microcline
30	35.0993	1489.41	Diopside; Microcline; Anorthite; Diopside; Wollastonite; Sanidine; Olivine(Fayalite)
31	35.6315	1427.94	Gehlenite; Diopside; Microcline; Anorthite; Diopside; Wollastonite; Sanidine
32	36.5194	7369.82	Quartz; Gehlenite; Wollastonite; Olivine(Fayalite)
33	36.9162	1882.2	Spinel; Microcline; Anorthite; Wollastonite
34	37.4002	438.26	Gehlenite; Anorthite; Diopside; Marcasite
35	38.222	132.73	Cristobalite; Anorthite; Diopside; Wollastonite
36	39.4467	8656.71	Quartz; Calcite; Gehlenite; Wollastonite; Sanidine; Olivine(Fayalite)
37	40.2671	3138.48	Quartz; Cristobalite; Microcline; Anorthite; Diopside; Wollastonite;

			Sanidine
38	40.8921	123.51	Gehlenite; Diopside; Diopside; Wollastonite; Sanidine
39	42.4186	5391.27	Quartz; Diopside; Cristobalite; Diopside; Wollastonite; Sanidine; Olivine(Fayalite)
40	43.193	784.21	Calcite; Diopside; Microcline; Anorthite
41	44.3367	647.36	Gehlenite; Diopside; Microcline; Diopside; Wollastonite
42	44.5311	616.34	Gehlenite; Diopside; Cristobalite; Microcline; Diopside; Wollastonite
43	44.8252	798.76	Spinel; Cristobalite; Microcline; Anorthite; Diopside; Wollastonite
44	45.7668	3587.48	Quartz; Gehlenite; Microcline; Anorthite; Diopside; Wollastonite
45	47.0713	651.35	Calcite; Gehlenite; Microcline; Anorthite; Wollastonite; Sanidine; Olivine(Fayalite)
46	47.4891	1039.78	Calcite; Microcline; Wollastonite; Sanidine; Olivine(Fayalite); Marcasite
47	48.5051	474.84	Calcite; Gehlenite; Cristobalite; Microcline; Anorthite; Wollastonite; Sanidine
48	50.12	15122.62	Quartz; Gehlenite; Diopside; Microcline; Diopside; Wollastonite
49	50.5492	825.21	Quartz; Gehlenite; Diopside; Microcline; Diopside; Wollastonite; Sanidine; Olivine(Fayalite)
50	51.3124	127.59	Microcline; Diopside; Wollastonite
51	51.4994	205.44	Diopside; Microcline; Anorthite; Wollastonite; Sanidine; Olivine(Fayalite)
52	52.0152	1617.75	Gehlenite; Cristobalite; Microcline; Anorthite; Diopside; Wollastonite; Marcasite
53	53.1334	148.6	Microcline; Anorthite; Diopside; Wollastonite; Sanidine; Olivine(Fayalite)
54	54.2874	470.87	Rutile; Microcline; Diopside; Wollastonite; Sanidine; Marcasite
55	54.8416	4300.01	Quartz; Diopside; Microcline; Diopside; Wollastonite; Sanidine; Marcasite
56	55.3302	1821.74	Quartz; Diopside; Microcline; Wollastonite
57	56.2373	134.18	Gehlenite; Microcline; Diopside; Sanidine
58	56.5994	302.56	Calcite; Diopside; Rutile; Microcline; Diopside; Wollastonite; Sanidine
59	57.0924	457.85	Quartz; Gehlenite; Diopside; Cristobalite; Microcline; Wollastonite; Sanidine
60	57.3496	723.97	Quartz; Calcite; Gehlenite; Diopside; Cristobalite; Microcline; Anorthite; Diopside; Wollastonite; Sanidine; Olivine(Fayalite)
61	59.9285	10267.77	Quartz; Gehlenite; Diopside; Cristobalite; Microcline; Anorthite; Diopside; Wollastonite
62	61.1679	850.71	Calcite; Gehlenite; Microcline; Diopside; Wollastonite; Sanidine; Olivine(Fayalite); Marcasite

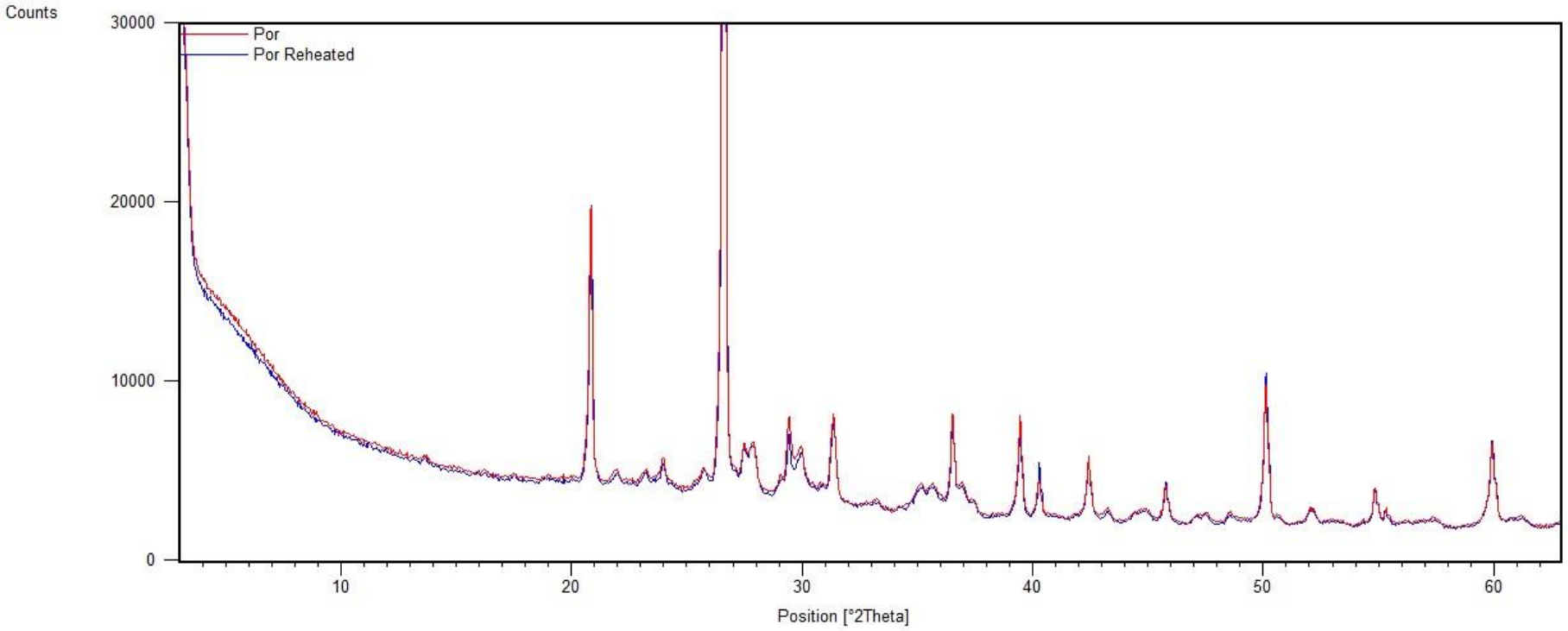

Figure A.13: XRD spectra of *Por* sample without (red) and with (blue) reheating at 500°C.

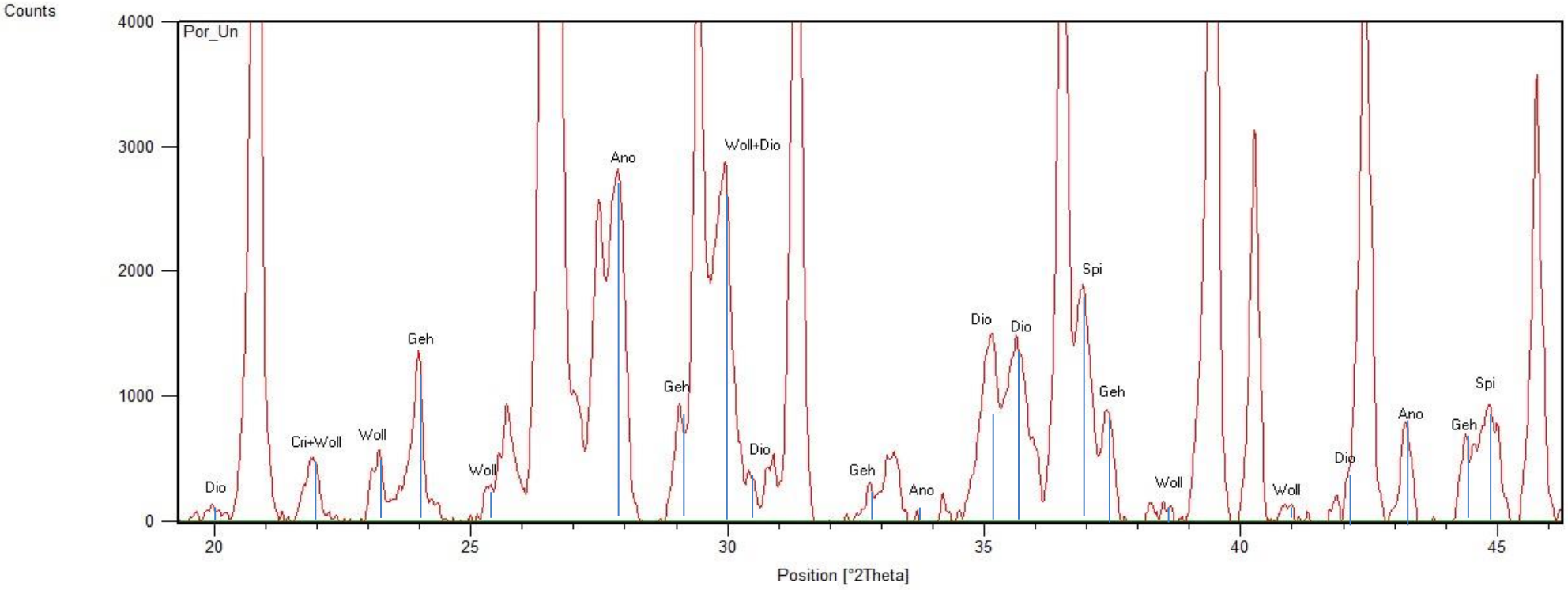

Figure A.14: XRD spectrum of non-reheated *Por*, highlighting peaks attributed to high temperature related mineral phases. Spi=Spinel; Woll=Wollastonite; Geh=Gehlenite; Cri=Cristobalite; Dio=Diopside; Ano=Anorthite

Rat

Table A.9: XRD peak position and associated mineral interpretation for *Rat* non-reheated sample.

No.	Pos. [°2Th.]	Height [cts]	Mineral
1	10.3531	114.83	Cordierite
2	13.6574	144.81	Anorthite; Diopside; Albite; Orthoclase
3	14.1478	33.39	Cordierite
4	18.1033	109.2	Cordierite
5	18.8808	535.61	Anorthite; Diopside; Spinel; Cordierite
6	20.8018	17095.01	Quartz; Orthoclase
7	21.6418	1270.05	Albite; Cordierite; Enstatite
8	21.958	1449.86	Anorthite; Cristobalite; Enstatite
9	22.8494	149.47	Anorthite; Albite; Orthoclase; Gehlenite
10	23.5624	693.17	Anorthite; Orthoclase
11	23.9764	554.63	Albite; Gehlenite; Enstatite
12	24.2076	1466.61	Hematite; Diopside; Enstatite
13	25.6302	349.29	Anorthite; Orthoclase; Gehlenite
14	26.538	115976.1	Quartz; Anorthite; Diopside; Cordierite; Enstatite
15	27.4894	1841.26	Anorthite; Diopside; Albite; Rutile; Orthoclase
16	27.7515	4776.47	Anorthite; Diopside; Albite; Cordierite; Rutile; Enstatite
17	27.9919	6093.65	Anorthite; Cordierite; Enstatite
18	28.3406	559.39	Anorthite; Cordierite; Cristobalite
19	29.368	471.34	Anorthite; Cordierite
20	29.8083	305.9	Diopside; Cordierite; Orthoclase; Enstatite
21	30.3032	551.04	Anorthite; Diopside; Albite; Orthoclase
22	31.1405	967.05	Spinel; Albite; Cristobalite; Gehlenite
23	32.5748	225.63	Albite; Gehlenite
24	33.2624	5362.52	Hematite; Albite; Cordierite
25	33.6653	662.34	Anorthite; Cordierite
26	34.98	128.73	Diopside; Orthoclase; Enstatite
27	35.6996	4540.05	Hematite; Anorthite; Diopside; Albite; Cordierite; Orthoclase; Gehlenite
28	36.488	10603.94	Quartz; Orthoclase; Enstatite
29	38.8707	89.21	Albite; Enstatite
30	39.4125	8307.1	Quartz; Hematite; Anorthite; Albite; Cordierite; Rutile; Gehlenite; Enstatite
31	40.2469	3984.16	Quartz; Anorthite; Diopside; Cordierite; Orthoclase; Cristobalite; Enstatite
32	40.9418	1335.39	Hematite; Diopside; Albite; Orthoclase; Gehlenite; Enstatite
33	41.8111	664.59	Diopside; Albite; Cordierite; Orthoclase; Enstatite
34	42.4006	6388.37	Quartz; Anorthite; Diopside; Albite; Cordierite; Orthoclase; Cristobalite; Enstatite
35	43.7099	86.05	Hematite; Diopside; Albite; Orthoclase

36	44.7887	1323.54	Anorthite; Diopside; Spinel; Albite; Orthoclase; Cristobalite; Enstatite
37	45.7533	4289.84	Quartz; Anorthite; Orthoclase; Gehlenite; Enstatite
38	47.1989	181.83	Anorthite; Albite; Cordierite; Orthoclase; Enstatite
39	48.3796	245.51	Anorthite; Albite; Cordierite; Cristobalite; Gehlenite
40	49.5786	2296.74	Hematite; Anorthite; Diopside; Albite; Cordierite; Orthoclase
41	50.0882	19202.87	Quartz; Anorthite; Diopside; Cordierite; Gehlenite; Enstatite
42	51.4599	583.78	Anorthite; Diopside; Albite; Cordierite; Orthoclase; Enstatite
43	54.2673	2381.45	Hematite; Albite; Cordierite; Enstatite
44	54.8294	5989.11	Quartz; Diopside; Rutile; Orthoclase; Enstatite
45	55.2774	1757.73	Quartz; Diopside; Spinel; Albite; Orthoclase; Enstatite
46	56.3516	320.9	Hematite; Diopside; Albite; Cordierite; Orthoclase; Gehlenite
47	57.8642	179.66	Hematite; Diopside; Cordierite; Enstatite
48	59.9063	13320.3	Quartz; Albite; Cordierite; Gehlenite; Enstatite
49	62.6227	1572.61	Hematite; Diopside; Albite; Cordierite; Orthoclase; Gehlenite; Enstatite
50	50.5492	825.21	Gehlenite
51	52.0152	1617.75	Gehlenite

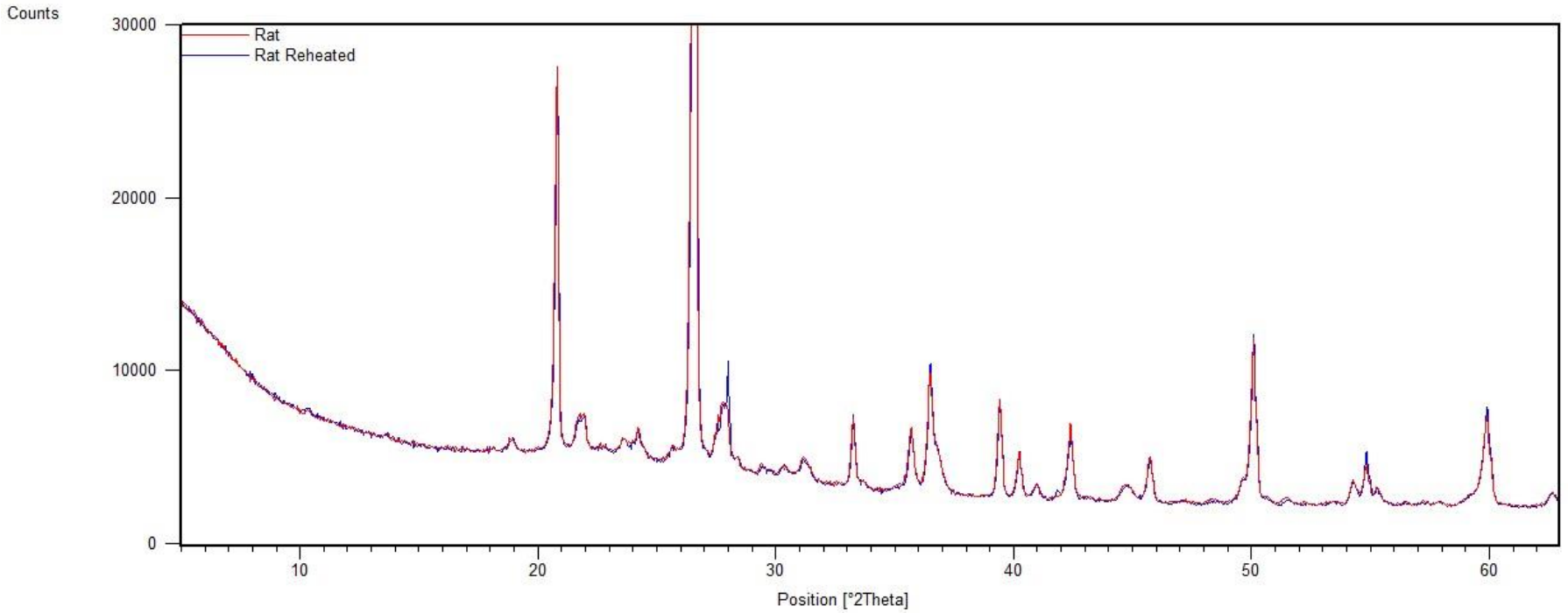

Figure A.15: XRD spectra of *Rat* sample without (red) and with (blue) reheating at 500°C.

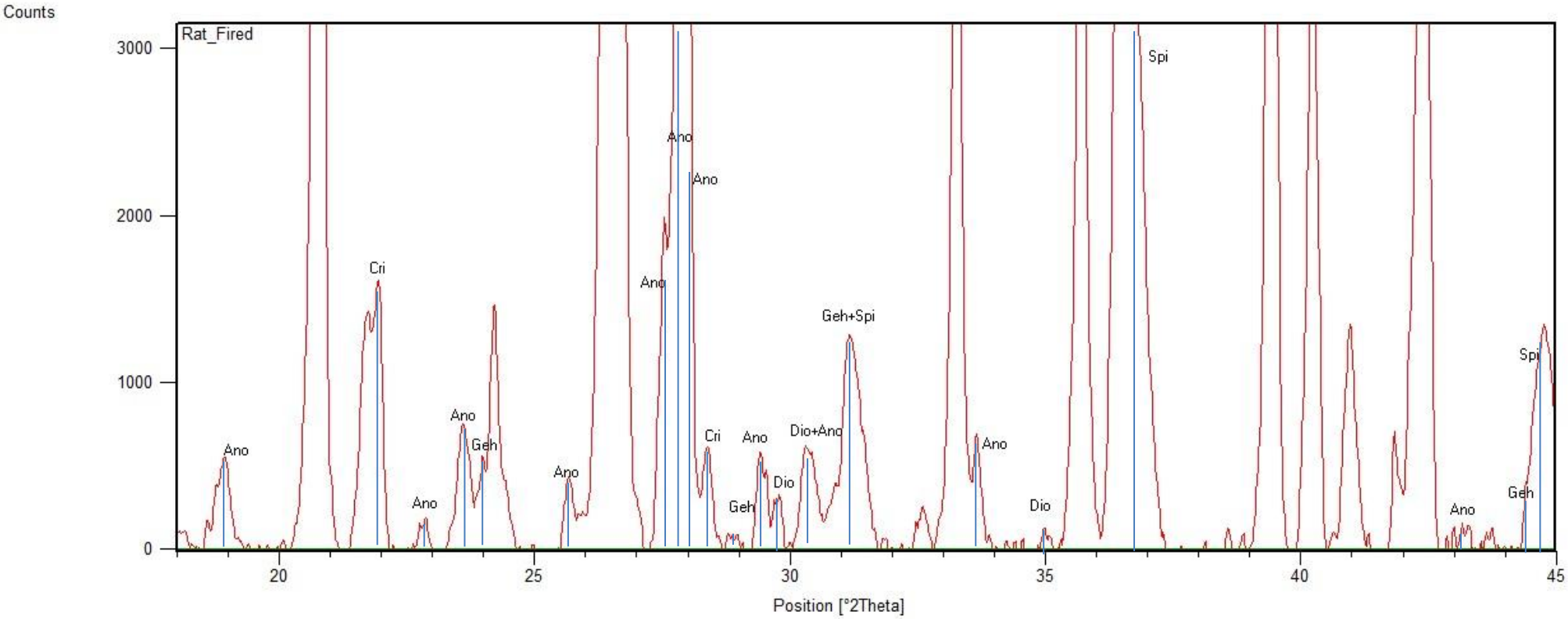

Figure A.16: XRD spectrum of non-reheated *Rat*, highlighting peaks attributed to high temperature related mineral phases. Spi=Spinel; Geh=Gehlenite; Cri=Cristobalite; Dio=Diopside; Ano=Anorthite

Cal

Table A.10: XRD peak position and associated mineral interpretation for *Cal* non-reheated sample.

No.	Pos. [°2Th.]	Height [cts]	Mineral
1	10.3851	238.65	Cordierite
2	13.6338	276.25	Anorthite; Orthoclase; Albite; Microcline
3	18.8603	611.13	Anorthite; Spinel; Cordierite
4	20.8484	12119.72	Quartz; Gehlenite
5	21.9533	3927.65	Anorthite; Enstatite; Cristobalite
6	22.7116	446.78	Anorthite; Orthoclase; Microcline
7	23.5934	1954.19	Anorthite; Orthoclase; Wollastonite
8	24.1401	1944.29	Hematite; Microcline; Wollastonite; Gehlenite
9	24.4486	1247.41	Anorthite; Orthoclase; Microcline
10	25.6786	909.56	Anorthite; Orthoclase; Albite; Microcline; Wollastonite
11	26.5968	84411.91	Quartz; Anorthite; Enstatite; Cordierite; Microcline
12	27.4577	10920.44	Anorthite; Orthoclase; Albite; Microcline
13	27.9239	11159.34	Anorthite; Albite; Enstatite; Cordierite; Wollastonite
14	28.404	2029.44	Anorthite; Enstatite; Cordierite; Cristobalite
15	29.3737	1369.49	Anorthite; Enstatite; Cordierite; Microcline; Calcite; Wollastonite
16	29.7734	392.73	Orthoclase; Cordierite
17	30.2636	1415.06	Anorthite; Albite; Enstatite; Microcline; Wollastonite
18	30.7594	516.59	Orthoclase; Albite; Microcline
19	31.0449	632.66	Spinel; Orthoclase; Albite; Enstatite; Microcline
20	31.4605	540.09	Anorthite; Enstatite; Cordierite; Calcite; Cristobalite; Gehlenite
21	31.8847	204.3	Orthoclase; Enstatite; Cordierite; Microcline
22	32.5588	150.13	Albite; Microcline; Wollastonite
23	33.1806	5995.74	Hematite; Albite; Enstatite; Cordierite; Wollastonite
24	33.6662	946.57	Anorthite; Cordierite
25	34.9754	226.72	Orthoclase; Enstatite; Microcline; Wollastonite
26	35.6163	7059.54	Anorthite; Hematite; Orthoclase; Albite; Enstatite; Microcline; Wollastonite; Gehlenite
27	36.5162	7549.02	Quartz; Spinel; Orthoclase; Enstatite; Cordierite; Cristobalite
28	37.5919	88.56	Orthoclase; Enstatite; Microcline; Gehlenite
29	38.8055	199.49	Orthoclase; Albite; Wollastonite
30	39.4362	5431.07	Quartz; Anorthite; Hematite; Albite; Enstatite; Cordierite; Calcite; Gehlenite
31	40.2663	3372.98	Quartz; Anorthite; Orthoclase; Enstatite; Cordierite; Microcline
32	40.866	1590.56	Hematite; Orthoclase; Albite
33	41.7074	371.6	Orthoclase; Albite; Cordierite; Microcline; Wollastonite
34	42.4072	8743.27	Quartz; Orthoclase; Albite; Cordierite; Gehlenite
36	43.1486	202.24	Anorthite; Albite; Enstatite; Cordierite; Microcline; Calcite; Cristobalite
37	44.4	271.92	Spinel; Albite; Enstatite; Microcline; Gehlenite

38	44.8409	320.85	Anorthite; Albite; Enstatite; Cristobalite
39	45.7605	4102.57	Quartz; Anorthite; Enstatite; Microcline
40	47.0731	1073.47	Anorthite; Orthoclase; Albite; Enstatite; Microcline; Calcite; Cristobalite
41	48.3063	776.07	Anorthite; Orthoclase; Albite; Enstatite; Cordierite; Microcline
42	49.4875	3947.36	Anorthite; Hematite; Orthoclase; Albite; Enstatite; Wollastonite
43	50.1134	13540.02	Quartz; Anorthite; Orthoclase; Cordierite; Microcline
45	50.6405	455.99	Quartz; Anorthite; Orthoclase; Albite; Enstatite; Cordierite; Microcline; Wollastonite; Gehlenite
46	51.5324	1924.85	Anorthite; Orthoclase; Enstatite; Cordierite; Microcline; Wollastonite
47	52.8201	248.26	Anorthite; Orthoclase; Albite; Enstatite; Microcline; Cristobalite; Wollastonite
48	53.4065	187.9	Anorthite; Orthoclase; Albite; Enstatite; Cordierite; Microcline; Gehlenite
49	54.0866	2778.32	Hematite; Orthoclase; Albite; Enstatite; Cordierite; Microcline; Cristobalite; Wollastonite
50	54.8554	4924.43	Quartz; Orthoclase; Enstatite; Microcline; Wollastonite
52	55.2885	2426.74	Quartz; Spinel; Orthoclase; Albite; Microcline; Wollastonite
53	56.2927	265.15	Hematite; Orthoclase; Albite; Enstatite; Cordierite; Microcline; Cristobalite; Wollastonite; Gehlenite
54	57.2286	504.57	Quartz; Anorthite; Orthoclase; Albite; Enstatite; Cordierite; Microcline; Calcite; Cristobalite; Wollastonite; Gehlenite
55	57.7081	455.49	Hematite; Orthoclase; Albite; Enstatite; Cordierite; Microcline; Cristobalite; Wollastonite
56	58.8015	364.16	Spinel; Orthoclase; Albite; Enstatite; Microcline; Cristobalite
57	59.9332	13640.15	Quartz; Albite; Enstatite; Cordierite; Microcline; Wollastonite; Gehlenite
59	62.4033	2020.17	Anorthite; Hematite; Albite; Enstatite; Cordierite; Microcline

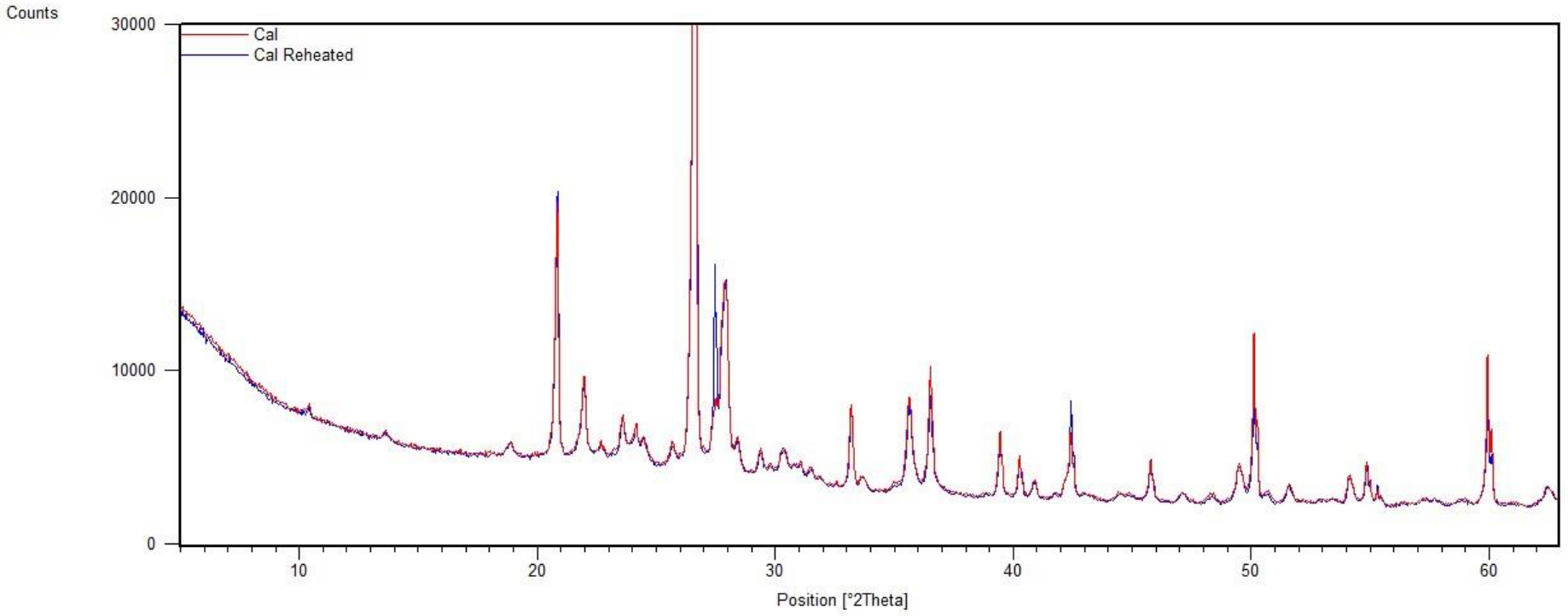

Figure 117: XRD spectra of *Cal* sample without (red) and with (blue) reheating at 500°C.

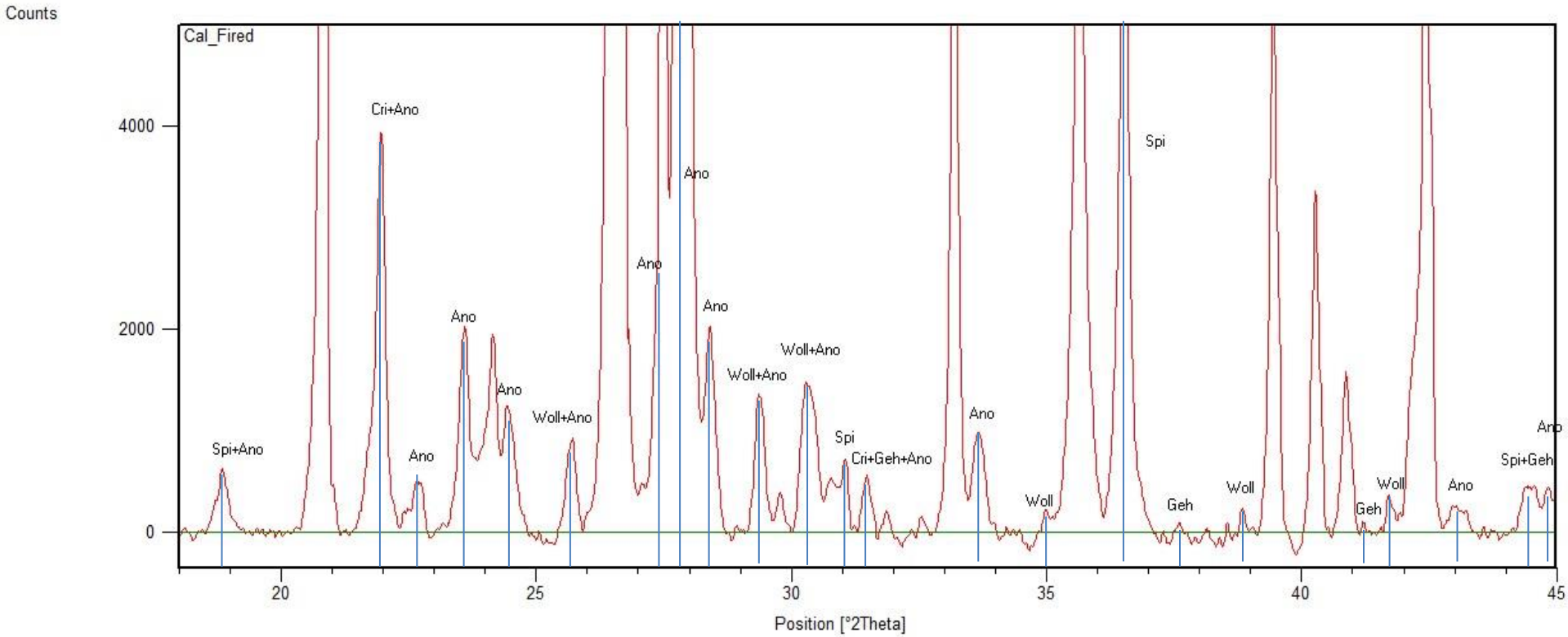

Figure A.18: XRD spectrum of reheated *Cal*, highlighting peaks attributed to high temperature related mineral phases. Spi=Spinel; Geh=Gehlenite; Cri=Cristobalite; Woll=Wollastonite; Ano=Anorthite

Lan

Table A.11: XRD peak position and associated mineral interpretation for *Lan* non-reheated sample.

No.	Pos. [°2Th.]	FWHM [°2Th.]	Mineral
1	8.7797	0.1004	Mica (Musc)
2	13.5997	0.1171	Orthoclase; Anorthite; Microcline; Enstatite; Diopside
3	15.1479	0.1673	Orthoclase; Anorthite; Microcline; Albite
4	17.6323	0.1338	Anorthite; Mica (Musc); Gehlenite
5	19.6657	0.2007	Mica (Musc); Enstatite
6	20.8418	0.1171	Quartz; Anorthite; Mica (Musc); Gehlenite
7	21.0722	0.1171	Orthoclase; Anorthite; Microcline; Gehlenite
8	21.9955	0.1171	Anorthite; Dolomite; Enstatite; Wollastonite; Albite; Cristobalite
9	22.6469	0.2342	Orthoclase; Anorthite; Mica (Musc); Microcline; Enstatite
10	23.4877	0.1171	Orthoclase; Anorthite; Mica (Musc); Enstatite; Albite
11	24.0116	0.1673	Hematite; Anorthite; Dolomite; Microcline; Gehlenite; Albite
12	25.3122	0.2175	Orthoclase; Anorthite; Mica (Musc); Wollastonite; Albite; Cristobalite
13	25.6913	0.1673	Orthoclase; Anorthite; Microcline; Enstatite; Gehlenite; Albite
14	26.5609	0.1171	Quartz; Anorthite; Mica (Musc); Microcline; Enstatite; Diopside; Albite
15	27.1429	0.3282	Orthoclase; Microcline
16	27.4222	0.1506	Orthoclase; Anorthite; Mica (Musc); Microcline; Diopside
17	27.9123	0.1673	Anorthite; Wollastonite; Albite
18	29.3816	0.184	Calcite; Anorthite; Microcline; Enstatite
19	29.803	0.1338	Orthoclase; Anorthite; Enstatite; Diopside
20	30.25	0.0395	Anorthite; Microcline; Wollastonite; Diopside; Albite
21	30.4154	0.1298	Orthoclase; Anorthite; Enstatite; Diopside; Albite
22	30.8255	0.1826	Orthoclase; Anorthite; Dolomite; Mica (Musc); Microcline; Wollastonite; Diopside
23	32.3376	0.1338	Orthoclase; Anorthite; Enstatite; Wollastonite
24	33.1572	0.368	Hematite; Anorthite; Dolomite; Mica (Musc); Enstatite; Albite
25	34.486	0.2007	Orthoclase; Anorthite; Mica (Musc); Microcline; Enstatite; Wollastonite
26	34.7908	0.0426	Orthoclase; Anorthite; Mica (Musc); Microcline; Enstatite
27	34.9294	0.0258	Orthoclase; Anorthite; Mica (Musc); Microcline; Enstatite; Diopside; Albite
28	35.648	0.2342	Hematite; Orthoclase; Anorthite; Mica (Musc); Microcline; Enstatite; Wollastonite; Diopside; Gehlenite; Albite
29	35.9831	0.01	Orthoclase; Calcite; Anorthite; Mica (Musc); Microcline; Enstatite; Albite; Cristobalite
30	36.5159	0.0836	Quartz; Anorthite; Mica (Musc); Enstatite; Wollastonite; Albite; Cristobalite; Spinel
31	37.1744	0.2007	Orthoclase; Anorthite; Dolomite; Mica (Musc); Microcline; Enstatite; Wollastonite; Albite
32	38.9999	0.0836	Anorthite; Microcline; Enstatite; Wollastonite; Diopside; Albite

33	39.4315	0.1004	Quartz; Hematite; Orthoclase; Calcite; Anorthite; Mica (Musc); Microcline; Enstatite; Wollastonite; Gehlenite; Albite
34	40.2475	0.1004	Quartz; Orthoclase; Anorthite; Mica (Musc); Microcline; Enstatite; Wollastonite; Albite
35	40.9192	0.3346	Hematite; Orthoclase; Anorthite; Dolomite; Mica (Musc); Enstatite; Wollastonite; Diopside; Gehlenite
36	41.736	0.2007	Orthoclase; Anorthite; Mica (Musc); Microcline; Enstatite; Wollastonite; Diopside
37	42.4124	0.0836	Quartz; Orthoclase; Enstatite; Diopside; Albite
38	43.1816	0.1338	Calcite; Anorthite; Mica (Musc); Microcline; Enstatite; Wollastonite; Albite; Cristobalite
39	44.9761	0.1673	Anorthite; Dolomite; Mica (Musc); Wollastonite; Diopside; Albite; Cristobalite
40	45.7483	0.1004	Quartz; Anorthite; Mica (Musc); Microcline; Enstatite; Wollastonite; Gehlenite; Albite
41	46.3019	0.1673	Orthoclase; Mica (Musc); Microcline; Enstatite; Wollastonite; Albite
42	47.4877	0.3011	Orthoclase; Calcite; Mica (Musc); Microcline; Enstatite; Wollastonite
43	48.1073	0.2342	Orthoclase; Mica (Musc); Microcline; Enstatite; Wollastonite; Diopside; Albite
44	48.4996	0.1673	Orthoclase; Calcite; Mica (Musc); Microcline; Enstatite; Wollastonite; Gehlenite; Cristobalite
45	49.5138	0.4684	Hematite; Orthoclase; Enstatite; Wollastonite; Diopside; Albite
46	50.1001	0.1224	Quartz; Orthoclase; Dolomite; Microcline; Enstatite; Wollastonite; Diopside; Gehlenite; Albite
47	50.6013	0.035	Quartz; Orthoclase; Mica (Musc); Microcline; Wollastonite; Diopside; Gehlenite; Albite
48	50.7454	0.102	Orthoclase; Dolomite; Mica (Musc); Microcline; Wollastonite; Diopside; Gehlenite; Albite
49	52.304	0.408	Orthoclase; Dolomite; Mica (Musc); Microcline; Wollastonite; Diopside; Albite
50	53.3023	0.408	Orthoclase; Mica (Musc); Microcline; Wollastonite; Diopside; Gehlenite; Albite
51	54.186	0.4896	Hematite; Orthoclase; Mica (Musc); Microcline; Wollastonite; Cristobalite
52	54.8321	0.1428	Quartz; Orthoclase; Mica (Musc); Microcline; Wollastonite; Diopside; Albite
53	55.2746	0.0223	Quartz; Orthoclase; Mica (Musc); Microcline; Wollastonite; Diopside; Spinel
54	56.7701	0.3264	Orthoclase; Calcite; Mica (Musc); Microcline; Wollastonite; Diopside; Albite
55	57.509	0.204	Hematite; Orthoclase; Calcite; Mica (Musc); Microcline; Wollastonite; Albite; Cristobalite
56	59.9276	0.1224	Quartz; Dolomite; Mica (Musc); Microcline; Wollastonite; Diopside; Gehlenite; Albite

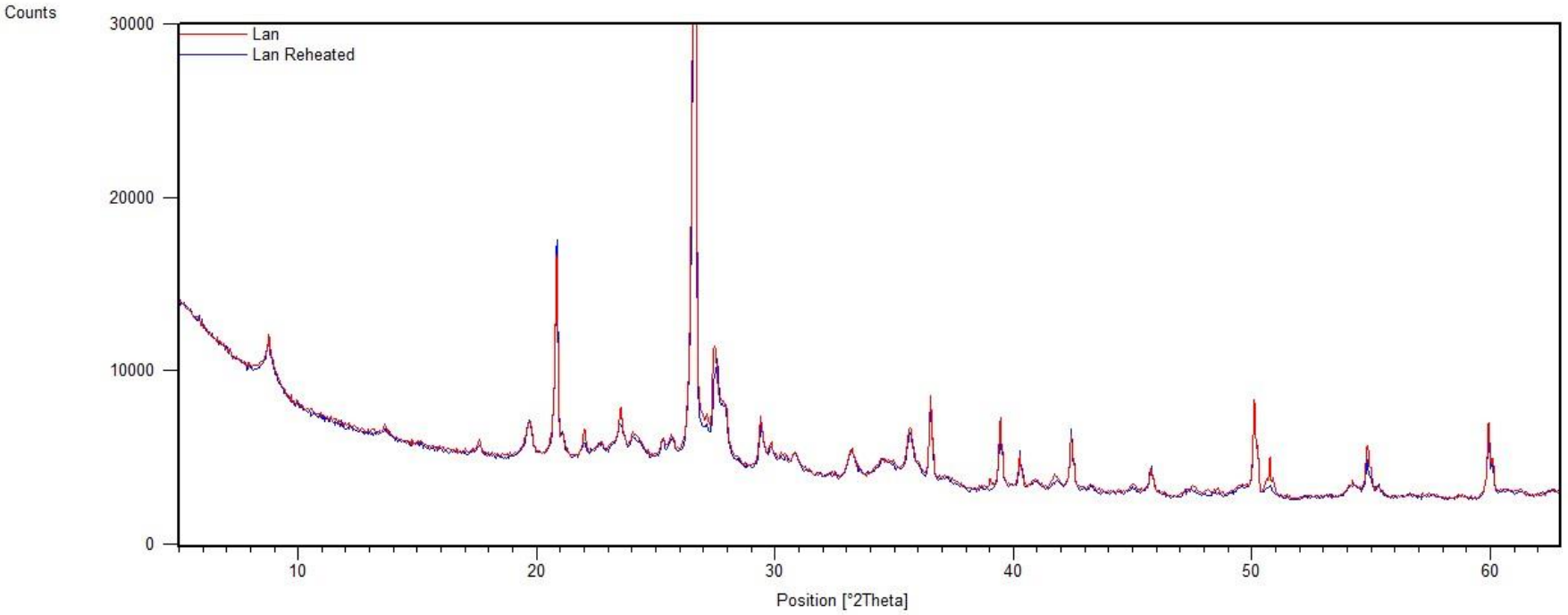

Figure A.19: XRD spectra of *Lan* sample without (red) and with (blue) reheating at 500°C.

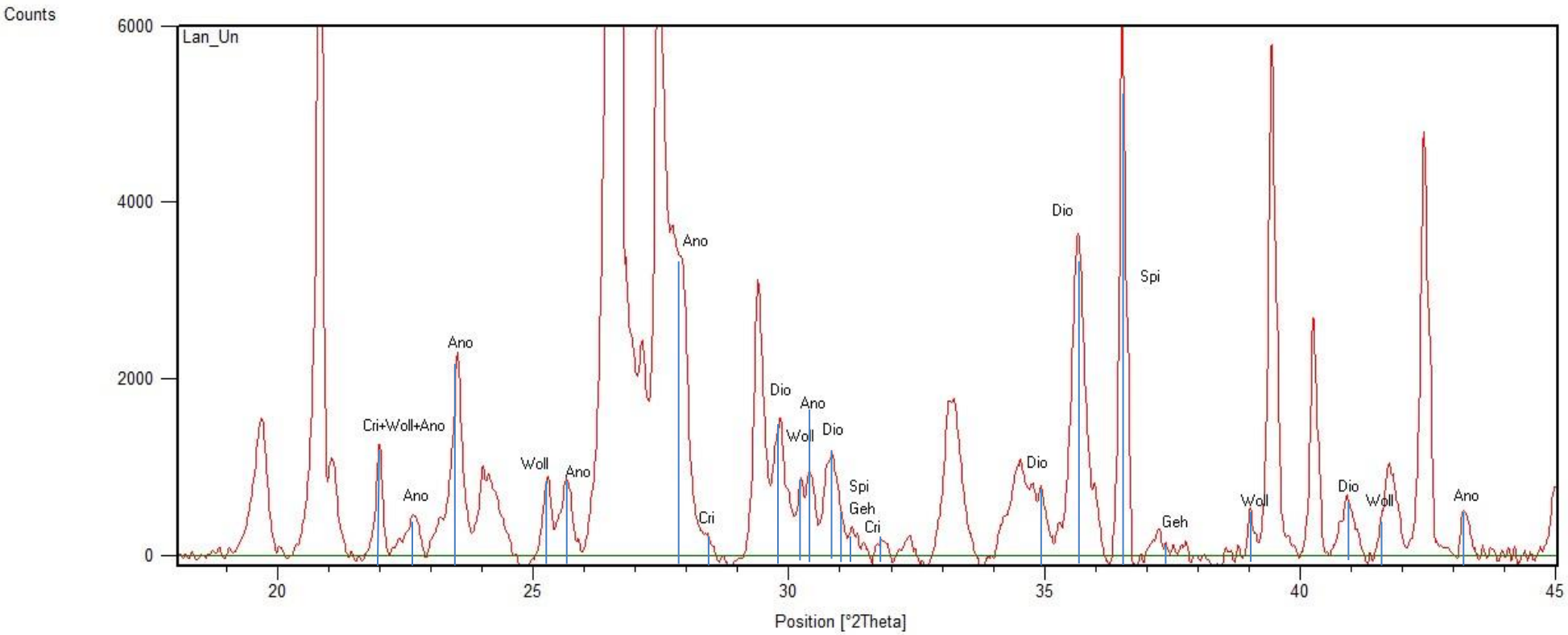

Figure A.20: XRD spectrum of non-reheated Lanyon, highlighting peaks attributed to high temperature related mineral phases. Spi=Spinel; Geh=Gehlenite; Cri=Cristobalite; Woll=Wollastonite; Ano=Anorthite; Dio=Diopside.

Joy

Table A.12: XRD peak position and associated mineral interpretation for *Joy* non-reheated sample.

No.	Pos. [°2Th.]	Height [cts]	Mineral
1	13.6152	173.06	Anorthite; Microcline; Albite
2	16.3554	117.38	Gehlenite; Mullite; Wollastonite
3	18.1478	176.19	Albite
4	18.9708	116.73	Spinel; Anorthite; Wollastonite
5	20.8155	15924.43	Quartz
6	21.1776	1159.09	Forsterite; Microcline
7	21.6151	1973.99	Enstatite
8	22.401	165.5	Microcline
9	22.621	157.32	Microcline
10	23.2824	346.59	Mullite; Microcline; Wollastonite; Albite
11	23.5954	489.13	Forsterite; Anorthite; Albite
12	24.0202	1263.51	Gehlenite; Enstatite; Microcline; Albite
13	24.1986	1923.37	Hematite
14	25.2854	292.2	Wollastonite; Albite
15	25.5281	1351.9	Anorthite; Microcline
16	25.6705	1234.51	Mullite; Anorthite; Microcline; Albite
17	26.5883	92092.38	Quartz; Enstatite; Anorthite; Microcline; Albite
18	27.1826	1669.01	Microcline; Albite
19	27.4553	5527.28	Microcline; Wollastonite
20	27.9884	604.38	Enstatite; Anorthite; Wollastonite; Albite
21	29.5746	156.42	Enstatite; Anorthite; Microcline; Albite
22	30.2183	284.39	Anorthite; Microcline; Wollastonite
23	30.8359	817.61	Enstatite; Microcline; Albite
24	31.0994	250.81	Albite
25	31.3204	411.28	Gehlenite; Spinel; Anorthite
26	31.4451	407.9	Gehlenite; Anorthite; Albite
27	31.7964	59.26	Anorthite; Microcline
28	32.473	451.18	Microcline; Albite
29	32.5784	614.76	Microcline; Albite
30	32.6804	603.86	Albite
31	33.2655	6025.79	Hematite; Forsterite; Anorthite
32	33.6664	364.43	Anorthite
33	34.782	257.23	Mullite; Microcline; Albite
34	34.9754	283.3	Mullite; Enstatite; Microcline; Albite
35	35.0604	293.18	Enstatite; Microcline; Albite
36	35.1794	280.83	Enstatite; Microcline; Wollastonite; Albite
37	35.6962	5026.97	Hematite; Forsterite; Microcline; Wollastonite; Albite
38	36.5005	11014.74	Quartz; Anorthite; Wollastonite; Albite

39	36.8536	2144.89	Gehlenite; Spinel; Mullite; Forsterite; Enstatite; Anorthite; Microcline; Albite
40	37.4189	320.78	Gehlenite; Mullite; Forsterite; Enstatite; Anorthite; Albite
41	39.4255	8293.94	Quartz; Hematite; Gehlenite; Anorthite; Wollastonite; Albite
42	40.2426	3899.64	Quartz; Anorthite; Microcline; Wollastonite; Albite
43	40.6831	474.49	Mullite; Forsterite; Enstatite; Anorthite; Microcline; Wollastonite; Albite
44	40.9871	1650.55	Hematite; Wollastonite; Albite
45	41.8205	136.66	Enstatite; Anorthite; Microcline; Wollastonite; Albite
46	42.4071	6855.42	Quartz; Gehlenite; Mullite; Enstatite; Albite
47	42.8634	220.29	Gehlenite; Forsterite; Enstatite; Anorthite; Microcline
48	43.074	202.95	Anorthite; Microcline
49	44.0704	189.15	Anorthite; Microcline; Albite
50	44.9005	557.63	Spinel; Anorthite; Wollastonite; Albite
51	45.7357	4030.68	Quartz; Mullite; Forsterite; Enstatite; Anorthite; Microcline; Albite
52	46.1614	280.62	Gehlenite; Anorthite; Microcline; Wollastonite
53	46.7554	115.76	Anorthite; Wollastonite; Albite
54	47.7391	160.28	Mullite; Forsterite; Enstatite; Anorthite; Microcline; Wollastonite; Albite
55	49.1704	520.53	Gehlenite; Spinel; Mullite; Enstatite; Anorthite; Microcline; Wollastonite; Albite
56	49.6067	2368.9	Hematite; Anorthite; Albite
57	50.0675	15396.56	Quartz; Forsterite; Enstatite; Anorthite; Microcline; Wollastonite; Albite
58	50.671	620.2	Quartz; Gehlenite; Forsterite; Enstatite; Anorthite; Microcline; Wollastonite; Albite
59	53.287	200.47	Gehlenite; Enstatite; Anorthite; Microcline; Wollastonite
60	54.2902	3264.23	Hematite; Gehlenite; Forsterite; Enstatite; Anorthite; Microcline; Wollastonite; Albite
61	54.8241	4798.01	Quartz; Enstatite; Rutile; Anorthite; Microcline; Wollastonite; Albite
62	55.2869	1645.06	Quartz; Enstatite; Microcline; Wollastonite; Albite
63	56.5824	277.6	Gehlenite; Forsterite; Enstatite; Anorthite; Microcline; Wollastonite; Albite
64	59.9054	14015.04	Quartz; Gehlenite; Forsterite; Enstatite; Anorthite; Microcline; Wollastonite; Albite
65	62.6732	1974.92	Hematite; Mullite; Forsterite; Anorthite; Microcline; Albite

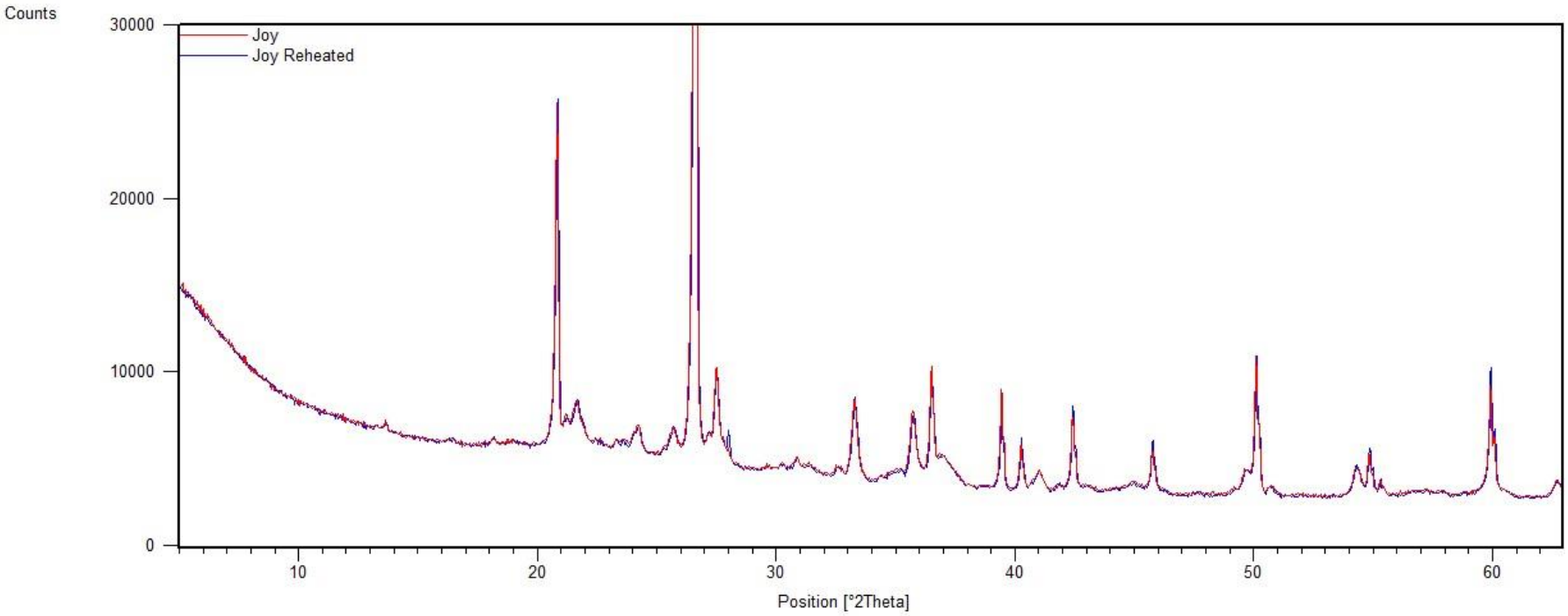

Figure A.21: XRD spectra of *Joy* sample without (red) and with (blue) reheating at 500°C.

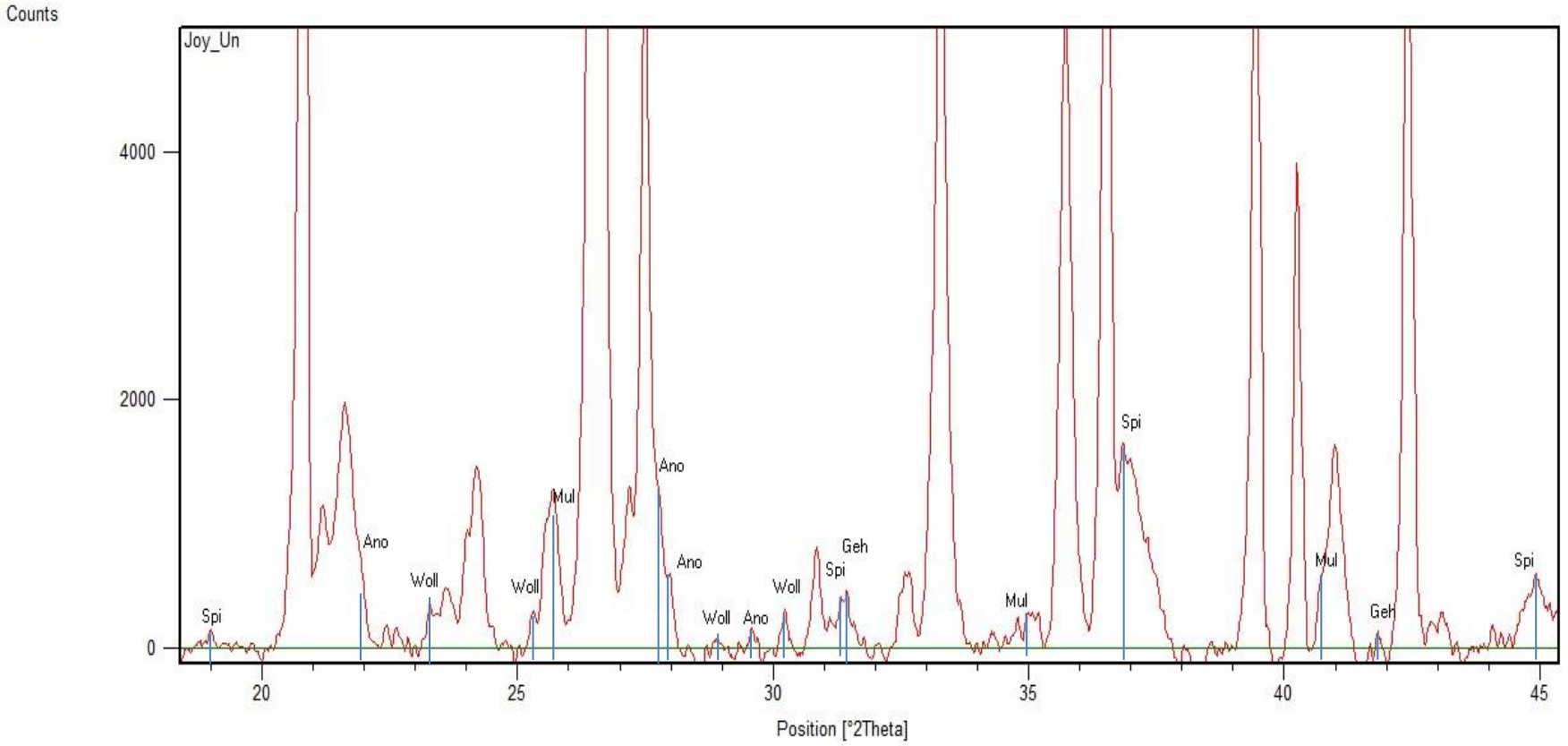

Figure 2: XRD spectrum of non-reheated *Joy*, highlighting peaks attributed to high temperature related mineral phases. Spi=Spinel; Mul=Mullite; Geh=Gehlenite; Woll=Wollastonite; Ano=Anorthite.

Cau

Table A.13: XRD peak position and associated mineral interpretation for *Cau* non-reheated sample.

No.	Pos. [°2Th.]	Height [cts]	Mineral
1	8.7708	254.45	Tridymite; Mica (Musc); Mica (Bio)
2	13.6447	147.56	Microcline; Albite
3	17.5552	263.19	Tridymite; Mica (Bio)
4	19.6924	499.17	Mica (Musc)
5	20.8331	23050.31	Quartz; Forsterite; Tridymite; Mica (Musc)
6	21.1971	584.63	Microcline; Tridymite; Mica (Musc); Mica (Bio)
7	21.909	87.28	Albite
8	22.2764	113.89	Microcline; Cristobalite; Tridymite; Mica (Musc)
9	22.3965	209.23	Microcline; Cristobalite; Tridymite; Mica (Musc); Mica (Bio)
10	22.6772	344.08	Microcline; Albite; Tridymite; Mica (Bio)
11	23.0924	181.1	Microcline; Calcite; Mica (Musc)
12	23.2572	357.53	Microcline; Albite; Tridymite
13	23.4817	456.31	Forsterite; Tridymite
14	24.0067	1017.15	Microcline; Albite
15	24.2431	1060.28	Microcline; Hematite; Forsterite; Tridymite; Mica (Bio)
16	24.463	217.02	Albite; Hematite; Tridymite
17	25.2433	1020.97	Anatase
18	25.7056	473.92	Microcline; Albite; Cristobalite; Tridymite; Mica (Musc)
19	26.5794	164216.8	Quartz; Microcline; Tridymite; Mica (Musc); Mica (Bio)
20	27.5169	6154.26	Rutile; Microcline; Albite; Tridymite
21	28.9076	140.14	Cristobalite; Tridymite
22	29.3385	952.64	Microcline; Calcite; Spinel
23	30.2065	195.27	Microcline; Forsterite; Tridymite
24	30.7973	500.3	Microcline; Albite; Tridymite
25	31.423	39.85	Albite; Tridymite
26	33.2091	3205.83	Albite; Hematite; Forsterite; Tridymite
27	34.4658	296.02	Spinel; Tridymite; Mica (Musc)
28	35.6523	2706.84	Microcline; Albite; Hematite; Forsterite; Tridymite; Mica (Bio)
29	36.4931	14804.27	Quartz; Albite; Cristobalite; Forsterite; Tridymite; Mica (Musc)
30	37.261	195.53	Albite; Forsterite; Tridymite
31	38.5674	76.41	Microcline; Anatase
32	39.4217	10656.15	Quartz; Albite; Hematite; Calcite; Forsterite; Mica (Bio)
33	40.2426	6012.39	Quartz; Microcline; Albite; Mica (Musc)
34	40.9254	866.1	Albite; Hematite; Mica (Musc); Mica (Bio)
35	41.1185	336.42	Albite; Hematite; Cristobalite; Forsterite; Mica (Musc)
36	41.8195	346.67	Microcline; Albite; Spinel; Mica (Bio)

37	42.4023	10555.53	Quartz; Albite; Forsterite; Mica (Musc)
38	42.8319	98.84	Microcline; Albite; Mica (Bio)
39	43.116	248.92	Microcline; Calcite; Mica (Bio)
40	45.0063	454.8	Mica (Bio)
41	45.1754	286.85	Albite; Mica (Bio)
42	45.7406	6274.91	Quartz; Microcline; Albite; Cristobalite; Spinel; Forsterite; Mica (Musc)
43	47.1627	91.37	Microcline; Calcite; Mica (Musc)
44	47.4635	295.06	Microcline; Albite; Forsterite; Mica (Bio)
45	47.9765	232.85	Microcline; Cristobalite; Forsterite; Anatase
46	48.4162	196.81	Microcline; Albite; Calcite; Mica (Musc)
47	50.0929	27700.21	Quartz; Microcline; Albite; Forsterite; Mica (Musc)
48	50.5727	1024.76	Quartz; Microcline; Albite; Forsterite
49	54.2936	1947.44	Rutile; Microcline; Albite; Hematite; Mica (Musc)
50	54.8356	12219.03	Quartz; Microcline; Albite; Anatase; Mica (Musc); Mica (Bio)
51	55.2877	2656.48	Quartz; Microcline; Albite; Cristobalite; Spinel; Mica (Musc)
52	56.5525	395.03	Rutile; Microcline; Albite; Calcite; Mica (Musc)
53	57.2137	340.38	Quartz; Microcline; Mica (Musc)
54	58.6824	65.86	Microcline; Albite; Cristobalite; Mica (Bio)
55	59.9153	23469.79	Quartz; Microcline; Albite; Cristobalite; Forsterite; Mica (Bio)
56	61.2579	217.11	Microcline; Albite; Cristobalite; Forsterite; Mica (Musc); Mica (Bio)

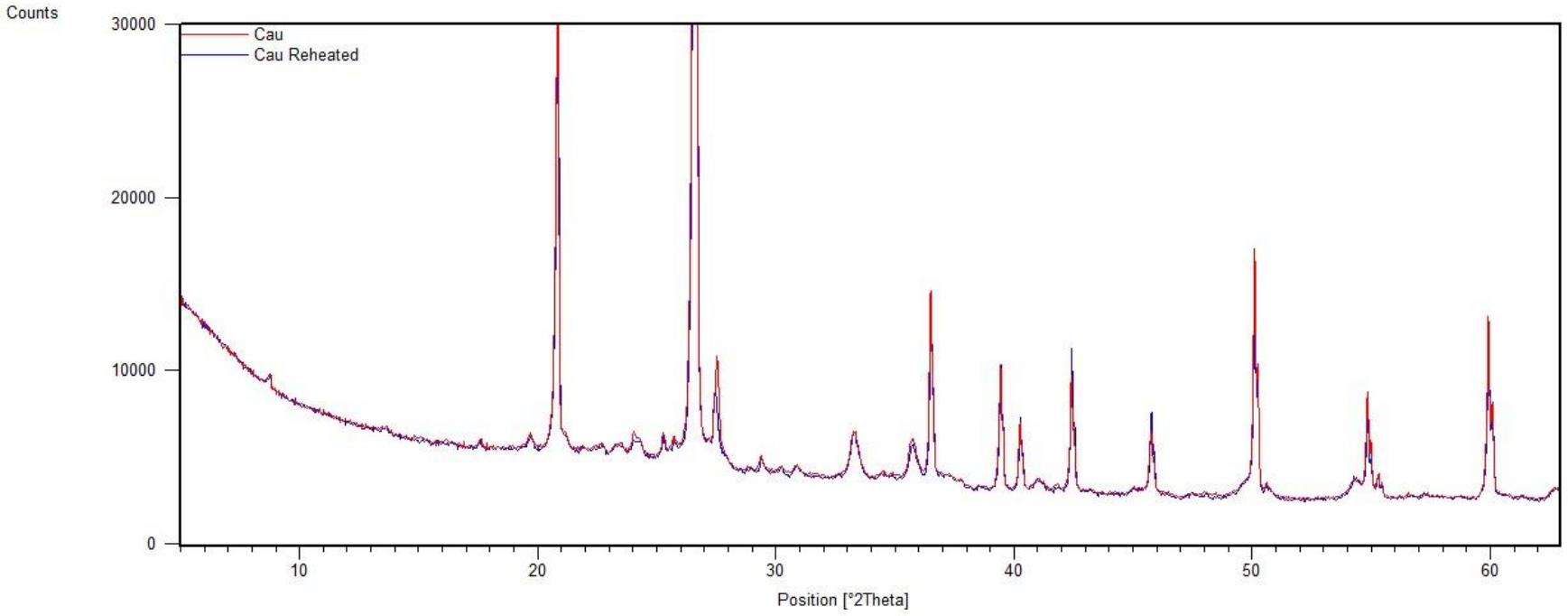

FigureA.23: XRD spectra of *Cau* sample without (red) and with (blue) reheating at 500°C.

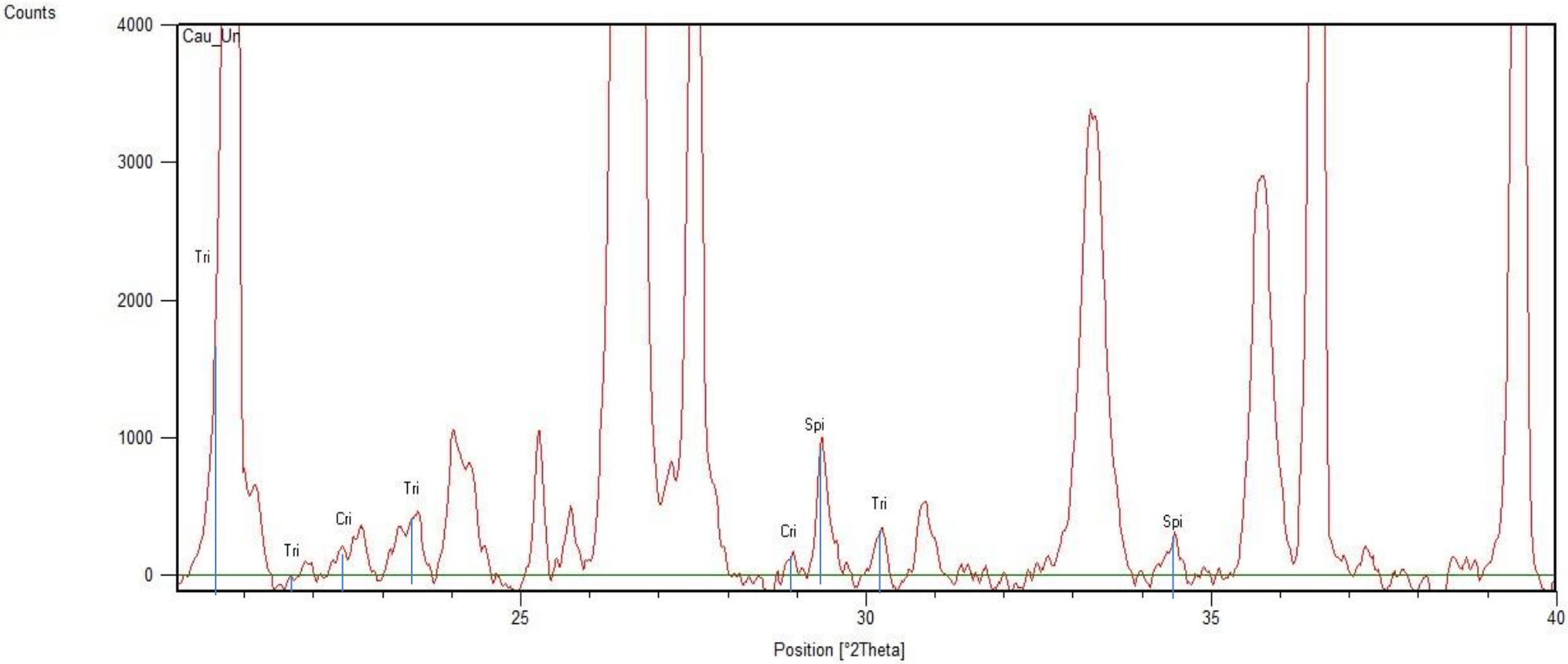

Figure A.24: XRD spectrum of non-reheated *Cau* highlighting peaks attributed to high temperature related mineral phases. Spi=Spinel; Cri=Cristobalite; Tri-Tridymite

Bel

Table A.14: XRD peak position and associated mineral interpretation for *Bel* non-reheated sample.

No.	Pos. [°2Th.]	Height [cts]	Mineral
1	8.7483	172.2	Biotite
2	13.6264	186.53	Microcline
3	14.7042	548.31	Bassanite
4	15.0816	76.01	Microcline; Albite
5	17.6124	170.77	Biotite
6	19.6866	438.49	Biotite
7	20.8201	15639.86	Quartz; Bassanite
8	21.1391	796.96	Microcline; Biotite
9	21.9057	128.56	Albite
10	22.3689	146.68	Bassanite; Microcline
11	22.6545	259.8	Microcline; Biotite
12	23.3151	330.88	Bassanite; Microcline; Spinel
13	23.545	386.74	Albite; Spinel
14	23.9396	595.4	Microcline; Albite
15	24.191	652.31	Hematite; Microcline; Biotite
16	25.2646	923.38	Anatase
17	25.6851	1381.73	Bassanite; Microcline; Albite
18	26.5973	118109.5	Quartz; Microcline; Albite
19	27.4286	7317.37	Microcline; Spinel
20	27.8522	1559.65	Bassanite; Albite
21	28.8173	149.85	Spinel
22	29.6475	1617	Bassanite; Albite
23	30.1579	303.86	Microcline; Albite
24	30.8632	568.22	Microcline
25	31.8505	1256.57	Bassanite; Microcline; Albite
26	33.2397	2154.03	Hematite; Albite; Spinel
27	34.433	280.7	Bassanite; Microcline; Biotite
28	34.9178	243	Microcline
29	35.6598	2600.41	Hematite; Microcline; Albite
30	36.4659	13985.42	Quartz; Albite; Spinel
31	36.9474	460.79	Microcline; Albite; Anatase; Biotite
32	37.2348	364.98	Microcline; Albite
33	38.5546	298.24	Bassanite; Microcline; Albite; Anatase
34	39.4137	9803.37	Quartz; Hematite; Albite; Biotite
35	40.2487	5344.56	Quartz; Microcline; Albite; Biotite
36	41.0001	466.76	Hematite; Albite; Biotite; Spinel
37	41.8084	406.58	Microcline; Albite
38	42.4002	6993.08	Quartz; Bassanite; Albite
39	43.1599	58.38	Microcline; Albite; Biotite

40	44.5705	78.6	Microcline; Biotite
41	45.7365	4800.71	Quartz; Microcline; Albite
42	47.5327	197.33	Bassanite; Microcline; Albite; Biotite
43	47.9555	282.96	Microcline; Anatase; Biotite; Spinel
44	49.2202	780.97	Bassanite; Microcline; Albite; Biotite
45	50.0892	22576.51	Quartz; Microcline; Albite; Spinel
46	50.5717	1183.3	Quartz; Microcline; Albite
47	54.2183	1611.16	Hematite; Bassanite; Microcline; Albite; Biotite
48	54.8223	8611.65	Quartz; Microcline; Albite; Anatase; Biotite
49	55.2858	2852.91	Quartz; Bassanite; Microcline; Biotite
50	57.1529	256.43	Quartz; Microcline; Albite; Biotite
51	59.9153	21694.46	Quartz; Bassanite; Microcline; Albite; Biotite

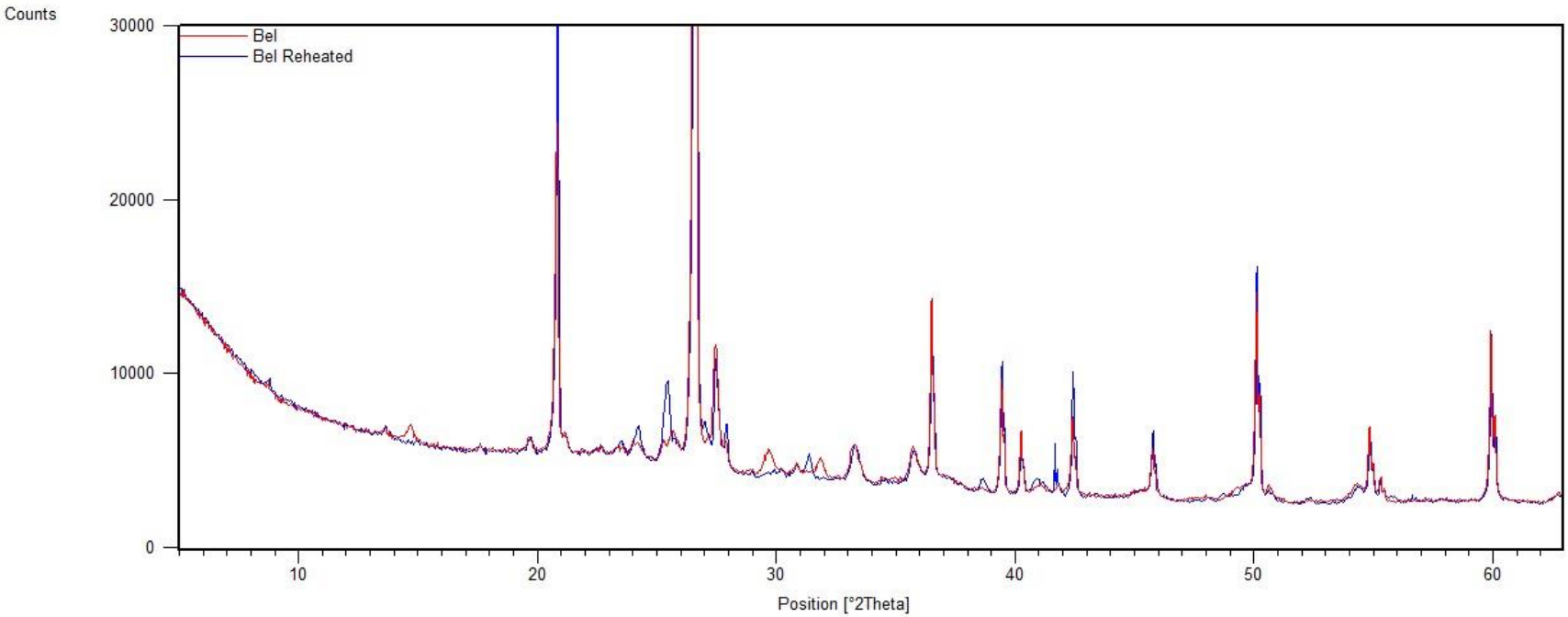

Figure A.25: XRD spectra of *Bel* sample without (red) and with (blue) reheating at 500°C.

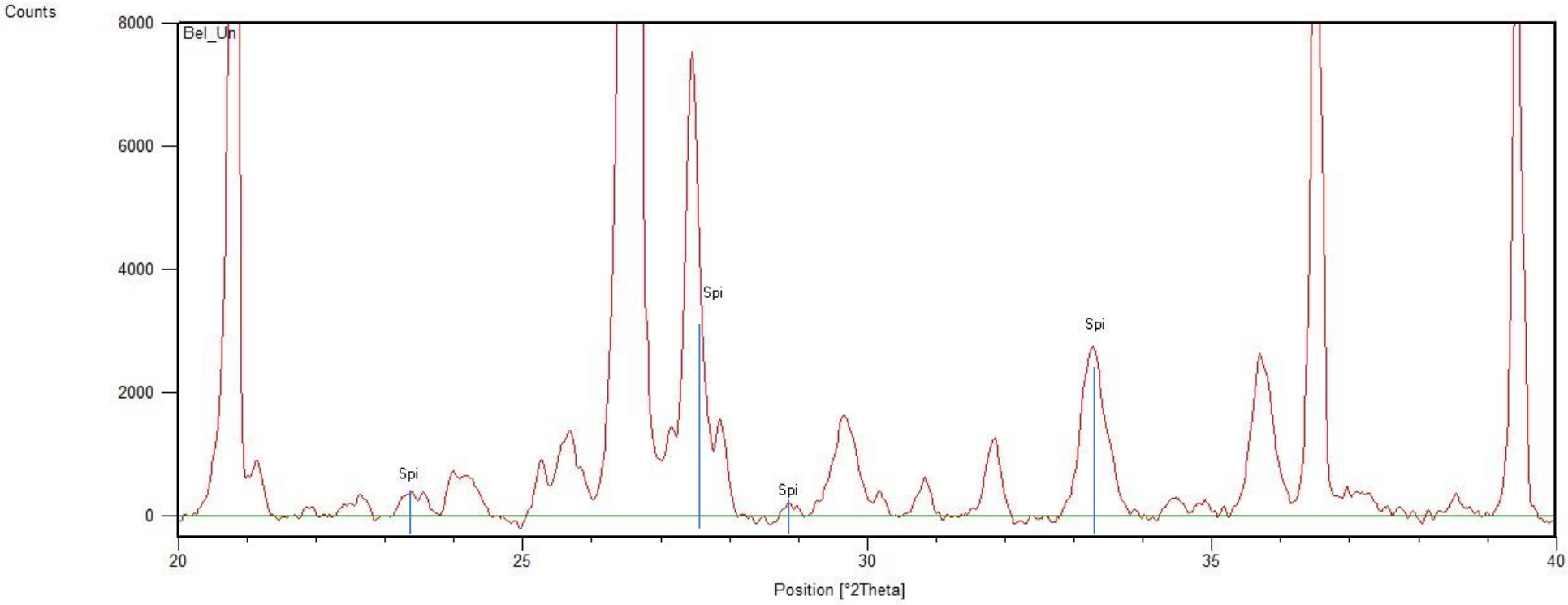

Figure A.26: XRD spectrum of non-reheated *Bel*, highlighting peaks attributed to high temperature related mineral phases. Spi=Spinel.

Dow1

Table A.15: XRD peak position and associated mineral interpretation for *Dow1* non-reheated sample.

No.	Pos. [°2Th.]	Height [cts]	Mineral
1	8.8115	172.96	Mica
2	14.973	74.98	Wollastonite
3	16.1793	84.52	Gehlenite; Wollastonite
4	17.2893	370.16	Forsterite; Gehlenite
5	18.898	175.26	Diopside; Wollastonite
6	20.0324	204.21	Diopside; Mica; Enstatite; Wollastonite
7	20.8124	3338.86	Quartz; Gehlenite; Mica; Enstatite
8	21.8992	117.06	Dolomite; Mica; Enstatite; Wollastonite
9	22.8323	1348.54	Forsterite; Mica
10	23.1389	1165.8	Calcite; Gehlenite; Wollastonite
11	23.419	1092.64	Mica; Wollastonite
12	23.9742	786.57	Dolomite; Forsterite; Gehlenite; Enstatite
13	24.2502	74.88	Diopside; Mica; Enstatite
14	25.3229	230.17	Forsterite; Mica; Enstatite; Wollastonite
15	25.6456	490.88	Forsterite
16	26.5909	22888.89	Quartz; Diopside; Mica; Enstatite
17	27.0474	2111.65	Enstatite; Wollastonite
18	27.463	2853.43	Mica; Wollastonite
19	27.7104	2274.47	Diopside; Wollastonite
20	28.6724	1859	Wollastonite
21	29.4576	7711.98	Calcite; Forsterite; Mica; Enstatite
22	29.8753	10482.19	Forsterite; Diopside; Enstatite; Wollastonite
23	30.4627	2983.07	Diopside; Mica; Wollastonite
24	30.8581	3647.45	Dolomite; Diopside; Enstatite
25	31.3298	3285.9	Calcite; Gehlenite
26	32.2602	1824.14	Forsterite; Enstatite
27	33.1311	437.46	Dolomite; Mica; Wollastonite
28	34.3805	1316.44	Mica; Enstatite; Wollastonite
29	35.1945	5941.98	Dolomite; Forsterite; Diopside; Gehlenite; Mica; Enstatite; Wollastonite
30	35.6786	6609.24	Forsterite; Diopside; Mica; Enstatite; Wollastonite
31	36.4804	5691.09	Quartz; Forsterite; Enstatite; Wollastonite
32	37.4062	265.58	Dolomite; Gehlenite; Mica
33	38.2583	275.98	Forsterite; Diopside; Mica; Enstatite; Wollastonite
34	39.4299	3446.8	Quartz; Calcite; Gehlenite; Mica; Enstatite; Wollastonite
35	39.6451	2901.64	Calcite; Forsterite; Mica; Wollastonite
36	40.0164	1486.3	Quartz; Forsterite; Mica; Wollastonite

37	40.2315	1727.53	Quartz; Forsterite; Enstatite; Wollastonite
38	40.5498	1376.34	Diopside; Mica; Enstatite; Wollastonite
39	40.8358	459.3	Dolomite; Diopside; Mica; Enstatite; Wollastonite
40	41.7715	1226	Forsterite; Mica; Enstatite; Wollastonite
41	42.4012	2787.06	Quartz; Diopside; Gehlenite; Mica; Enstatite; Wollastonite
42	42.9484	873.74	Diopside; Enstatite
43	43.3247	1361.02	Calcite; Mica; Enstatite; Wollastonite
44	44.691	2899.48	Dolomite; Forsterite; Diopside; Mica; Enstatite; Wollastonite
45	45.7685	1442.63	Quartz; Enstatite; Wollastonite
46	46.8509	230.26	Forsterite; Diopside; Enstatite; Wollastonite
47	47.6506	1194.14	Calcite; Mica
48	48.7081	1216.07	Calcite; Forsterite; Gehlenite; Mica
49	50.0841	4310.31	Quartz; Dolomite; Forsterite; Diopside; Gehlenite; Enstatite; Wollastonite
50	50.6154	546.79	Quartz; Forsterite; Gehlenite; Mica; Wollastonite
51	52.1993	3051.5	Dolomite; Forsterite; Gehlenite; Mica; Wollastonite
52	54.8064	2915.74	Quartz; Forsterite; Diopside; Mica; Enstatite; Wollastonite
53	56.2071	2133.48	Forsterite; Diopside; Gehlenite; Mica; Enstatite
54	56.8223	2368.94	Forsterite; Diopside; Gehlenite; Enstatite; Wollastonite
55	57.6194	737.98	Calcite; Forsterite; Mica; Enstatite; Wollastonite
56	58.7619	226.3	Dolomite; Forsterite; Mica; Enstatite; Wollastonite
57	59.9016	2725.73	Quartz; Dolomite; Diopside; Gehlenite; Mica; Enstatite; Wollastonite
58	60.4244	799.69	Forsterite; Diopside; Gehlenite; Mica; Enstatite; Wollastonite
59	61.2376	1770.11	Calcite; Forsterite; Diopside; Gehlenite; Mica; Enstatite; Wollastonite
60	61.8909	488.98	Forsterite; Diopside; Gehlenite; Mica; Enstatite
61	62.7364	787.35	Forsterite; Diopside; Gehlenite; Mica; Enstatite; Wollastonite

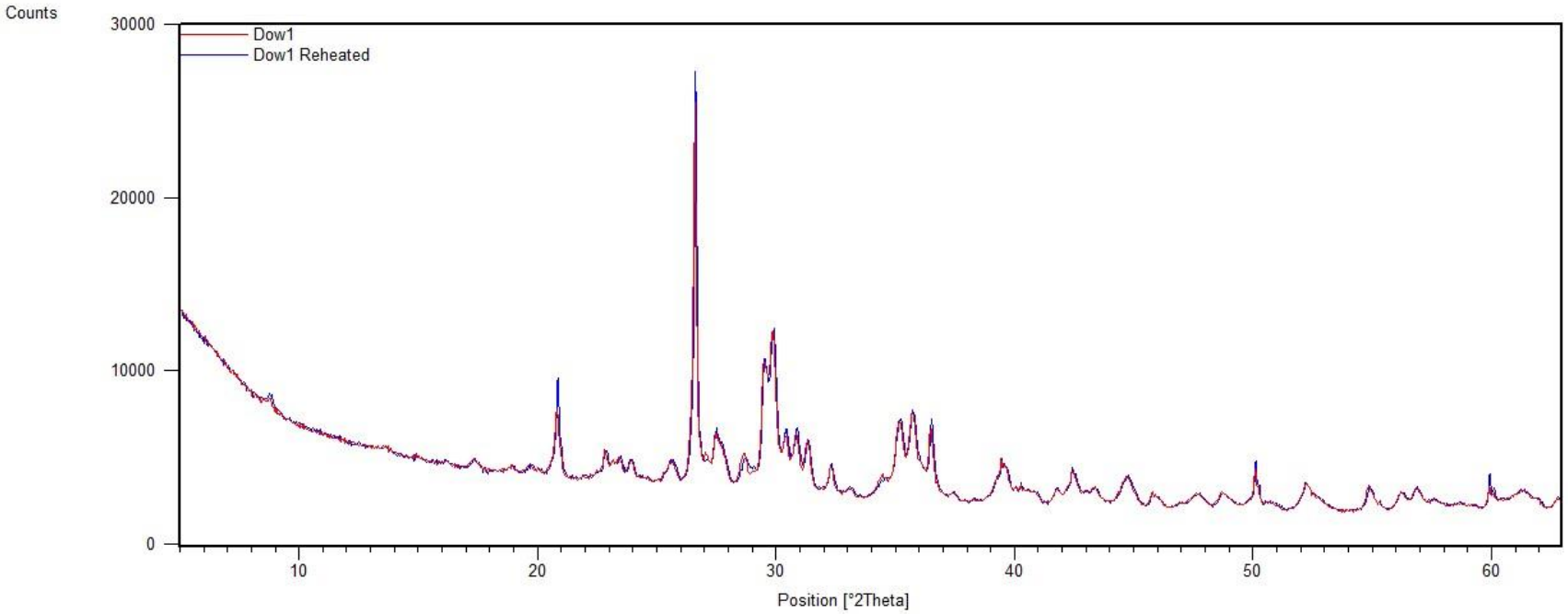

Figure 3: XRD spectra of *Dow1* sample without (red) and with (blue) reheating at 500°C.

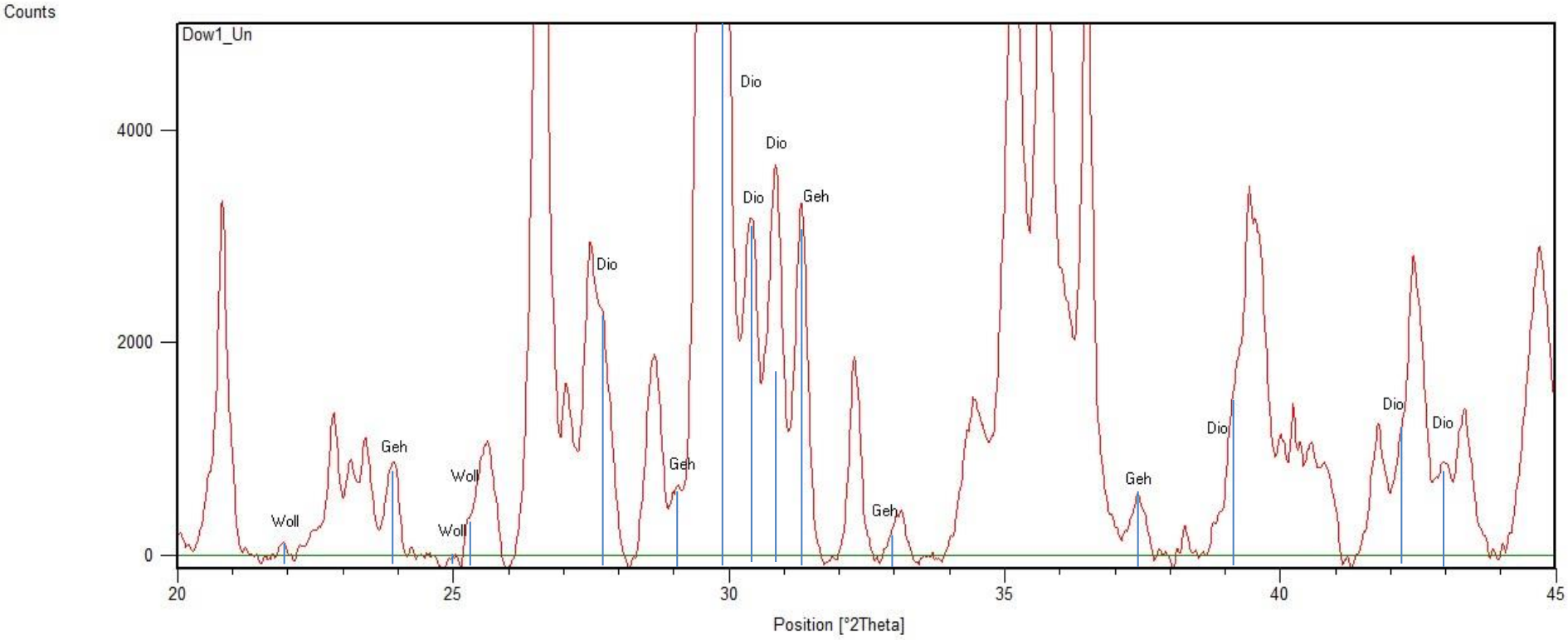

Figure A.28: XRD spectrum of non-reheated *Dow1*, highlighting peaks attributed to high temperature related mineral phases. Wol=Wollastonite; Geh=Gehlenite; Dio=Diopside.

Dow2

Table A.16: XRD peak position and associated mineral interpretation for *Dow2* non-reheated sample.

No.	Pos. [°2Th.]	Height [cts]	Mineral
1	13.6067	133.27	Diopside; Anorthite; Orthoclase; Microcline
2	17.5588	235.68	Forsterite; Spinel
3	19.0594	60.2	Diopside; Anorthite; Microcline
4	19.7075	899.59	Diopside
5	20.8187	4898.72	Quartz; Forsterite; Microcline
6	21.9085	312.42	Anorthite; Cristobalite
7	22.5516	258.61	Anorthite; Orthoclase; Microcline
8	23.5055	1372.87	Anorthite; Orthoclase
9	23.9336	674.22	Anorthite; Forsterite; Microcline
10	25.3074	703.72	Forsterite; Orthoclase; Cristobalite; Microcline
11	25.6571	1350.07	Anatase; Anorthite; Forsterite; Orthoclase; Microcline
12	26.5973	31083.69	Quartz; Diopside; Anorthite; Microcline
13	27.1026	2356.8	Orthoclase; Microcline
14	27.4368	3144.48	Diopside; Anorthite; Orthoclase; Microcline
15	27.8933	2865.43	Anorthite
16	29.5491	8172.92	Calcite; Anorthite; Forsterite; Microcline
17	29.841	9277.19	Diopside; Forsterite; Orthoclase
18	30.3941	3027.94	Diopside; Anorthite; Orthoclase; Microcline
19	30.8701	2305.26	Diopside; Anorthite; Orthoclase; Microcline
20	31.3155	784.24	Diopside; Cristobalite
21	31.7649	276.3	Diopside; Calcite; Anorthite; Microcline
22	32.2933	785.37	Forsterite; Orthoclase; Microcline
23	34.4131	1291.46	Orthoclase; Microcline; Spinel
24	35.2025	3171.45	Diopside; Anorthite; Forsterite; Orthoclase; Microcline
25	35.611	3268.13	Diopside; Anorthite; Forsterite; Orthoclase; Microcline
26	36.483	3135.22	Quartz; Forsterite; Orthoclase
27	37.2051	331.62	Anorthite; Orthoclase; Microcline
28	37.7689	263.79	Diopside; Anatase; Anorthite; Forsterite; Orthoclase; Microcline
29	38.531	132.98	Diopside; Anatase; Anorthite; Forsterite; Orthoclase; Cristobalite; Microcline
30	39.4255	3615.21	Quartz; Calcite; Orthoclase; Microcline
31	39.7084	2488.43	Anorthite; Forsterite; Orthoclase; Microcline
32	40.2492	1589.1	Quartz; Diopside; Anorthite; Forsterite; Orthoclase; Cristobalite; Microcline
33	40.8234	482.01	Diopside; Orthoclase
34	41.7181	732.15	Diopside; Anorthite; Forsterite; Orthoclase; Microcline; Spinel

35	42.3951	2798.71	Quartz; Diopside; Anorthite; Orthoclase; Cristobalite
36	43.4663	993.75	Diopside; Orthoclase; Microcline
37	44.7122	1194.17	Diopside; Anorthite; Forsterite; Cristobalite; Microcline
38	45.7416	1954.89	Quartz; Anorthite; Microcline; Spinel
39	46.9579	200.01	Calcite; Anorthite; Forsterite; Orthoclase; Cristobalite; Microcline
40	48.0073	1057.74	Diopside; Calcite; Orthoclase; Microcline
41	49.0224	1171.78	Diopside; Anatase; Forsterite; Orthoclase; Microcline
42	50.0907	10160.6	Quartz; Diopside; Orthoclase; Microcline
43	51.4484	128.22	Diopside; Anorthite; Orthoclase; Microcline
44	52.3506	614.84	Diopside; Forsterite; Orthoclase; Cristobalite; Microcline
45	54.179	389.75	Orthoclase; Microcline
46	54.8182	2593.61	Quartz; Diopside; Anatase; Forsterite; Orthoclase; Microcline
47	55.221	594.8	Quartz; Diopside; Orthoclase; Microcline; Spinel
48	56.2006	729.17	Anatase; Forsterite; Orthoclase; Microcline
49	56.8088	765.39	Diopside; Forsterite; Orthoclase; Cristobalite; Microcline
50	57.7761	310.32	Diopside; Anorthite; Forsterite; Orthoclase; Microcline
51	58.6054	160.95	Diopside; Calcite; Anorthite; Forsterite; Orthoclase; Cristobalite; Microcline
52	59.9026	3936.41	Quartz; Diopside; Anorthite; Cristobalite; Microcline
53	60.4074	1028.73	Diopside; Anorthite; Forsterite; Orthoclase; Microcline; Spinel
54	61.2794	1266.65	Diopside; Calcite; Forsterite; Orthoclase; Microcline

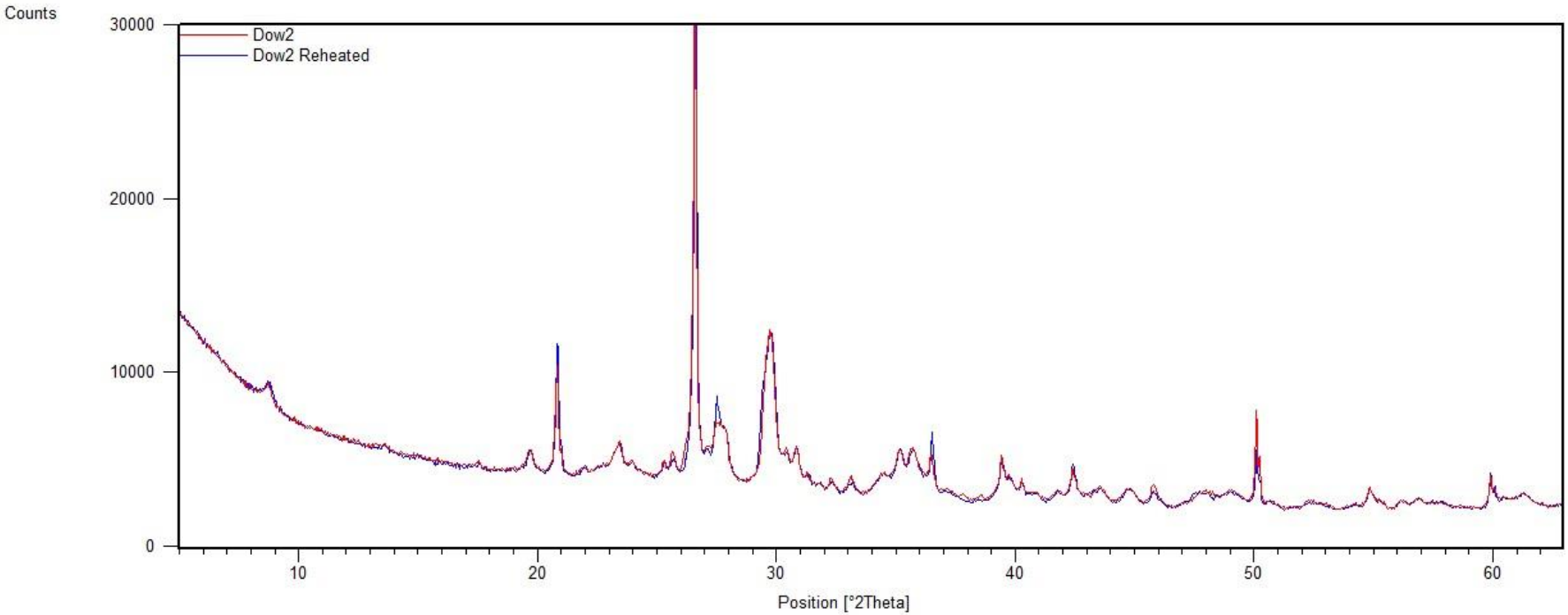

Figure A.29: XRD spectra of *Dow2* sample without (red) and with (blue) reheating at 500°C.

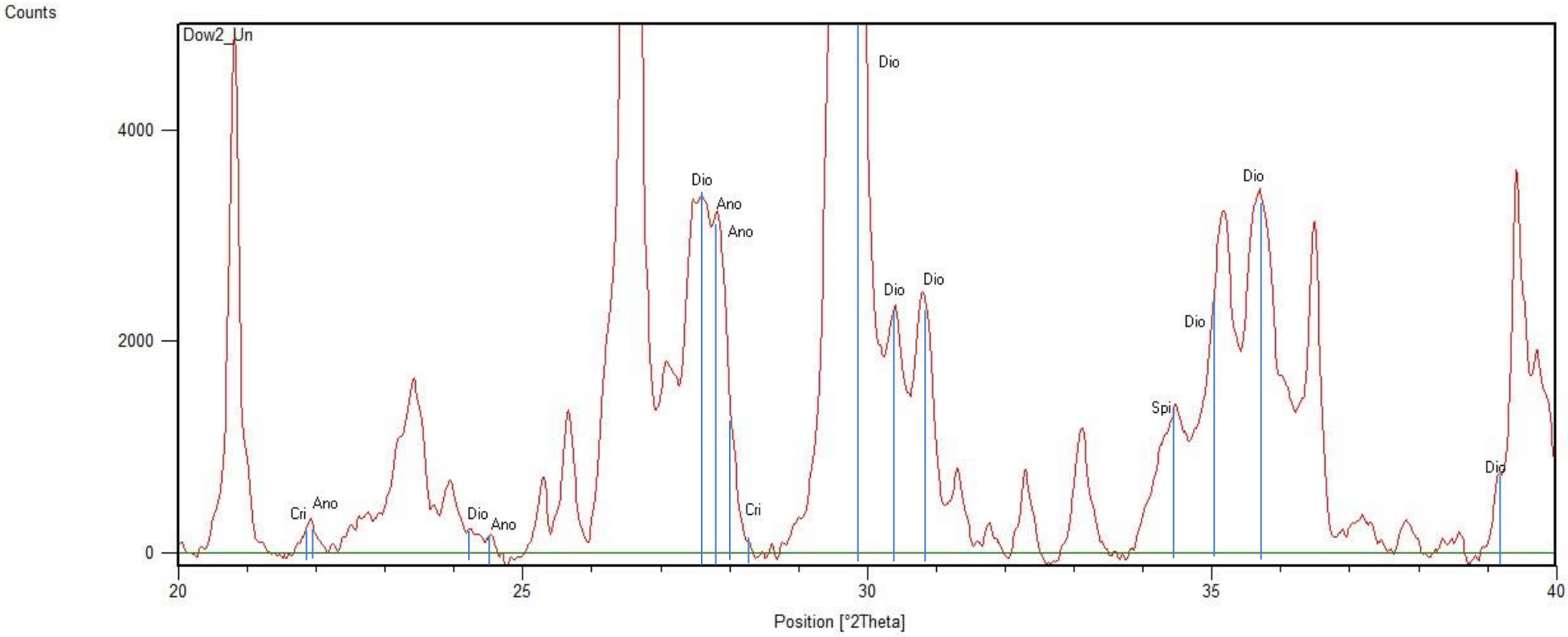

Figure A.30: XRD spectrum of non-reheated *Dow2*, highlighting peaks attributed to high temperature related mineral phases. Ano=Anorthite; Dio=Diopside; Spi=Spinel

Tur

Table A.17: XRD peak position and associated mineral interpretation for *Tur* non-reheated sample.

No.	Pos. [°2Th.]	Height [cts]	Matched by
1	13.6406	328.01	Microcline
2	18.7404	160.17	Spinel
3	18.9334	132.46	Spinel
4	20.839	19744.74	Quartz
5	21.1482	1110.78	Microcline
6	21.9243	95.36	Cristobalite
7	22.383	497.18	Microcline
8	22.677	177.92	Microcline
9	23.2838	763.85	Microcline
10	23.9845	999	Microcline
11	24.2367	726.53	Microcline; Hematite
12	24.791	82.59	Microcline
13	24.9454	101.31	Microcline
14	25.3534	215.1	Microcline; Anatase; Cristobalite
15	25.5321	1209.31	Microcline
16	25.7292	1248.76	Microcline
17	26.6085	121426.7	Quartz
18	27.1542	2316.01	Microcline
19	27.4806	7603.88	Microcline
20	29.0084	116.19	Calcite
21	29.511	238.72	Microcline
22	30.1898	579.97	Microcline
23	30.82	800.03	Microcline; Calcite; Spinel
24	31.3626	610.11	Cristobalite; Spinel
25	32.0679	114.63	Microcline
26	32.5712	346.98	Microcline
27	33.305	2438.06	Hematite
28	34.3093	249.2	Microcline
29	34.9466	421.6	Microcline
30	35.7363	1806.37	Microcline; Hematite
31	36.5114	10497.64	Quartz
32	36.9556	2451.31	Microcline; Anatase; Spinel
33	38.1204	15.36	Spinel
34	38.5302	236.24	Microcline; Anatase; Spinel
35	39.4253	10199.27	Quartz; Microcline; Calcite; Hematite
36	40.2412	4477.29	Quartz; Microcline; Cristobalite
37	40.9914	580.43	Hematite
38	41.815	798.89	Microcline
39	42.4178	8042.74	Quartz; Cristobalite

40	43.1073	552.16	Microcline; Calcite
41	44.1894	36.37	Microcline; Spinel
42	44.9204	908.88	Spinel
43	45.7465	4892.29	Quartz; Microcline
44	46.4291	110.23	Microcline; Calcite
45	47.5718	348.62	Microcline
46	48.307	134.47	Microcline; Cristobalite; Spinel
47	49.0098	200.6	Microcline; Spinel
48	49.2554	249	Microcline; Spinel
49	50.1	19583.53	Quartz; Microcline
50	50.5965	1383.53	Quartz; Microcline
51	53.3976	181.7	Microcline; Cristobalite
52	54.2972	1186.9	Microcline; Hematite
53	54.8273	5821.89	Quartz; Microcline; Spinel
54	55.2759	2011.22	Quartz; Microcline; Anatase
55	56.8034	389.48	Microcline; Cristobalite; Calcite
56	57.1299	654.31	Quartz; Microcline; Cristobalite
57	57.8234	261.61	Microcline; Hematite
58	59.9055	13965.19	Quartz; Microcline; Cristobalite
59	61.3543	461.79	Microcline
60	62.7024	594.14	Microcline; Anatase; Calcite

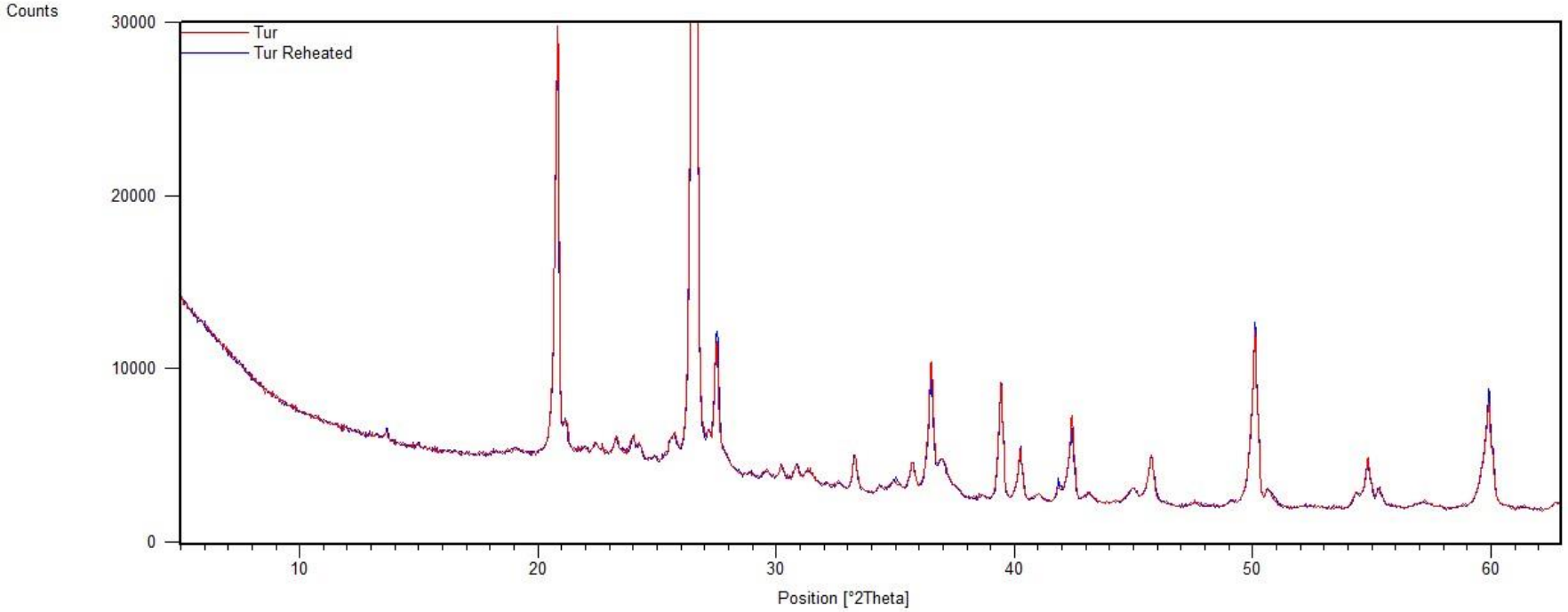

Figure A.31: XRD spectra of *Tur* sample without (red) and with (blue) reheating at 500°C.

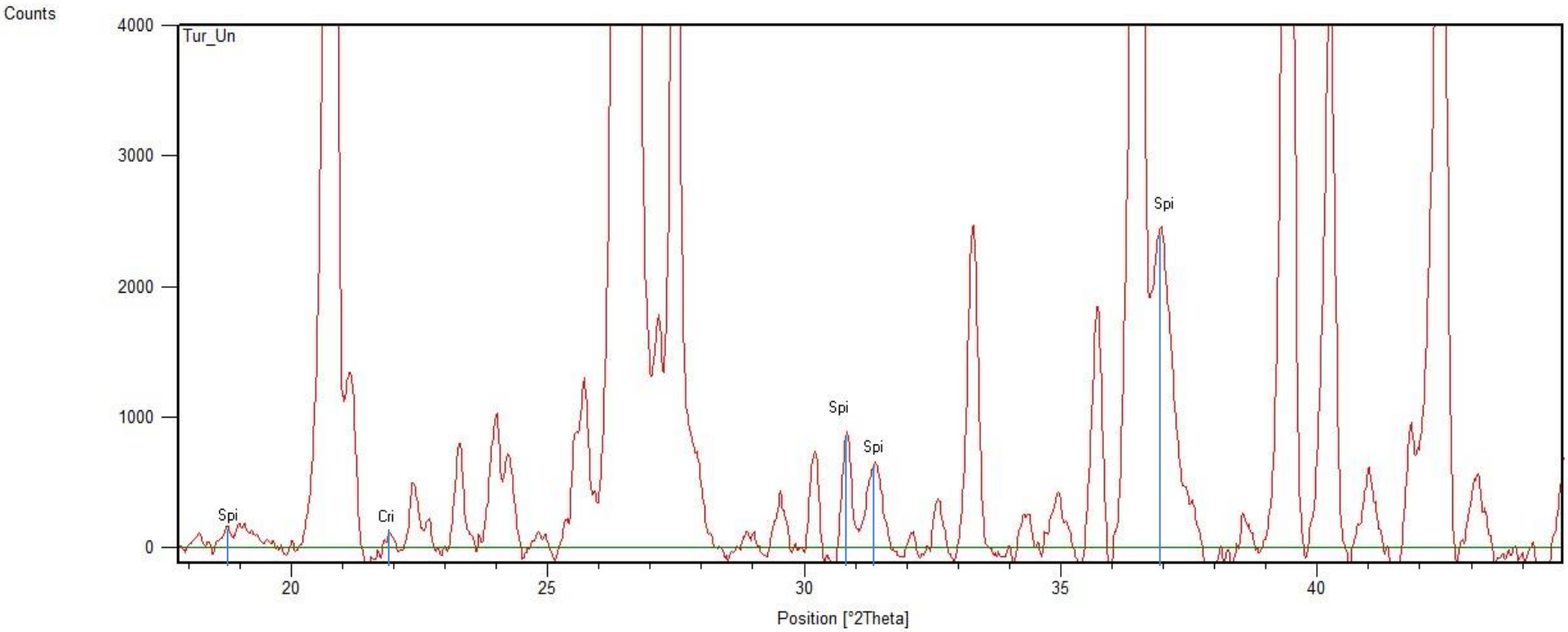

Figure 4: XRD spectrum of non-reheated *Tur* sample, highlighting peaks attributed to high temperature related mineral phases. Cri=Cristobalite; Spi=Spinel.

Ted

Table A.18: XRD peak position and associated mineral interpretation for *Tur* non-reheated sample.

No.	Pos. [°2Th.]	Height [cts]	Mineral
1	13.6004	98.31	Microcline; Orthoclase; Albite; Diopside
2	15.0186	59.82	Microcline; Orthoclase; Anorthite
3	16.3591	107.43	Mullite; Wollastonite; Gehlenite
4	18.1352	132.37	Wollastonite
5	20.8339	16112.53	Quartz; Anorthite
6	21.1345	1295.52	Microcline; Orthoclase; Gehlenite
7	21.6515	330.07	Anorthite; Albite
8	22.3878	387.54	Microcline; Orthoclase; Anorthite; Albite
9	22.6496	189.49	Microcline; Orthoclase; Anorthite
10	23.2385	700.76	Microcline; Orthoclase; Mullite; Anorthite; Albite; Olivine; Gehlenite
11	23.5416	558.88	Orthoclase; Anorthite; Olivine; Wollastonite
12	24.0227	1313.62	Microcline; Anorthite; Albite; Gehlenite
13	24.2162	1376.4	Hematite; Microcline; Anorthite; Albite; Wollastonite; Diopside
14	24.5736	173.78	Microcline; Orthoclase; Anorthite
15	24.7924	81.61	Microcline; Anorthite
16	25.2854	441.15	Anatase; Orthoclase; Anorthite; Wollastonite
17	25.7107	1604.25	Microcline; Orthoclase; Mullite; Anorthite; Wollastonite
18	26.6037	99044.36	Quartz; Microcline; Anorthite; Diopside
19	27.145	2559.16	Microcline; Orthoclase; Anorthite; Albite; Olivine; Wollastonite
20	27.4869	5301.72	Microcline; Orthoclase; Albite; Diopside
21	28.9008	154.31	Anorthite; Wollastonite
22	29.3654	565.08	Microcline; Calcite; Anorthite; Albite; Wollastonite
23	29.5325	794.39	Microcline; Calcite; Albite; Olivine
24	29.8074	353.41	Orthoclase; Anorthite; Albite; Olivine; Diopside
25	30.2045	208.83	Microcline; Wollastonite; Diopside
26	30.7602	680.12	Microcline; Orthoclase; Mullite; Anorthite; Albite; Olivine; Diopside
27	31.4663	288	Calcite; Anorthite; Gehlenite; Diopside
28	32.5976	490.39	Microcline; Anorthite; Albite; Olivine; Wollastonite
29	33.2609	5408.91	Hematite; Anorthite; Albite; Wollastonite
30	34.8024	377.83	Microcline; Orthoclase; Mullite; Anorthite; Albite; Wollastonite; Diopside
31	35.7351	3868.33	Hematite; Microcline; Orthoclase; Anorthite; Albite; Olivine; Wollastonite; Diopside
32	36.4921	8933.75	Quartz; Orthoclase; Anorthite; Albite; Olivine
33	37.6006	417.83	Microcline; Anatase; Anorthite; Albite; Gehlenite; Diopside
34	38.6432	274.65	Microcline; Anatase; Orthoclase; Mullite; Anorthite;

			Albite; Olivine; Wollastonite
35	39.4221	8581.57	Quartz; Hematite; Calcite; Anorthite; Albite; Gehlenite
36	40.2409	4184.59	Quartz; Microcline; Orthoclase; Anorthite; Olivine
37	40.9935	1462.22	Orthoclase; Anorthite; Albite; Diopside
38	41.7887	333.76	Microcline; Anorthite; Albite; Olivine; Wollastonite; Diopside
39	42.4067	8539.1	Quartz; Orthoclase; Mullite; Anorthite; Albite; Gehlenite; Diopside
40	43.0635	323.28	Microcline; Orthoclase; Calcite; Anorthite; Olivine
41	43.4618	261.51	Microcline; Orthoclase; Anorthite; Diopside
42	44.917	249.49	Anorthite; Albite; Diopside
43	45.7491	4873.38	Quartz; Microcline; Mullite; Anorthite; Olivine
44	46.1274	231	Microcline; Orthoclase; Anorthite; Albite; Olivine; Gehlenite; Diopside
45	46.3144	362.09	Microcline; Orthoclase; Anorthite; Albite; Olivine; Wollastonite; Gehlenite; Diopside
46	47.499	1050.68	Microcline; Orthoclase; Calcite; Albite; Olivine; Wollastonite; Gehlenite
47	48.0314	218.93	Microcline; Anatase; Orthoclase; Albite; Wollastonite; Diopside
48	48.3986	128.96	Microcline; Orthoclase; Calcite; Mullite; Albite; Olivine
49	49.6294	2080.01	Hematite; Orthoclase; Albite; Wollastonite; Diopside
50	50.0958	17558.48	Quartz; Microcline; Orthoclase; Albite; Olivine; Diopside
51	50.5572	1048.6	Quartz; Microcline; Orthoclase; Mullite; Albite; Olivine; Wollastonite; Gehlenite; Diopside
52	51.8026	119.91	Microcline; Orthoclase; Albite; Wollastonite
53	52.5027	149.12	Microcline; Orthoclase; Albite
54	54.2749	2832.62	Hematite; Microcline; Orthoclase; Olivine; Gehlenite; Diopside
55	54.8283	5072.54	Quartz; Microcline; Anatase; Orthoclase; Albite; Olivine; Wollastonite; Diopside
56	55.2844	1621.19	Quartz; Microcline; Albite; Olivine; Wollastonite; Diopside
57	56.4475	351.64	Hematite; Microcline; Orthoclase; Calcite; Olivine; Wollastonite; Gehlenite; Diopside
58	57.1944	312.9	Quartz; Microcline; Orthoclase; Calcite; Mullite; Albite; Olivine; Wollastonite; Gehlenite
59	57.8846	198.81	Microcline; Orthoclase; Calcite; Mullite; Albite; Olivine
60	58.7033	172.45	Microcline; Orthoclase; Albite; Olivine; Diopside
61	59.9155	15442.27	Quartz; Microcline; Albite; Olivine; Wollastonite; Gehlenite; Diopside
62	61.2631	160.31	Microcline; Orthoclase; Calcite; Albite; Wollastonite; Gehlenite; Diopside
63	62.6842	1574.17	Hematite; Microcline; Anatase; Mullite; Albite

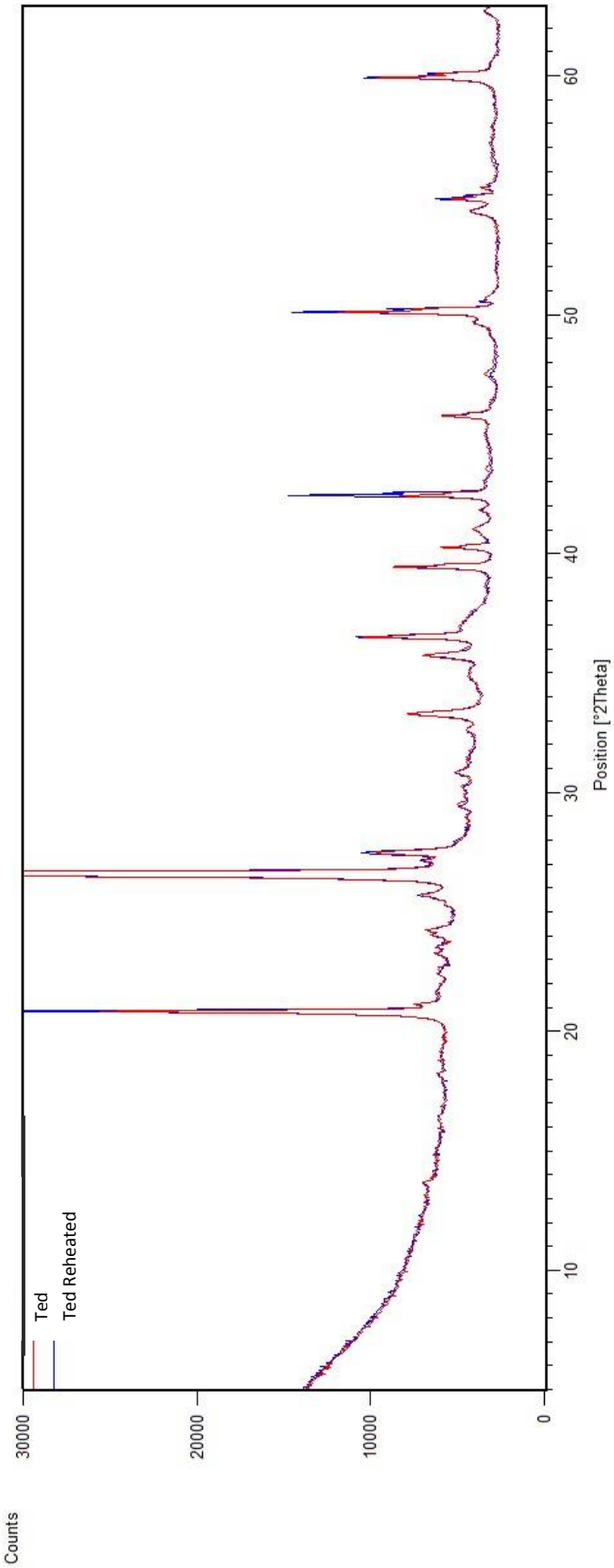

Figure A.33: XRD spectra of *Ted* sample without (red) and with (blue) reheating at 500°C.

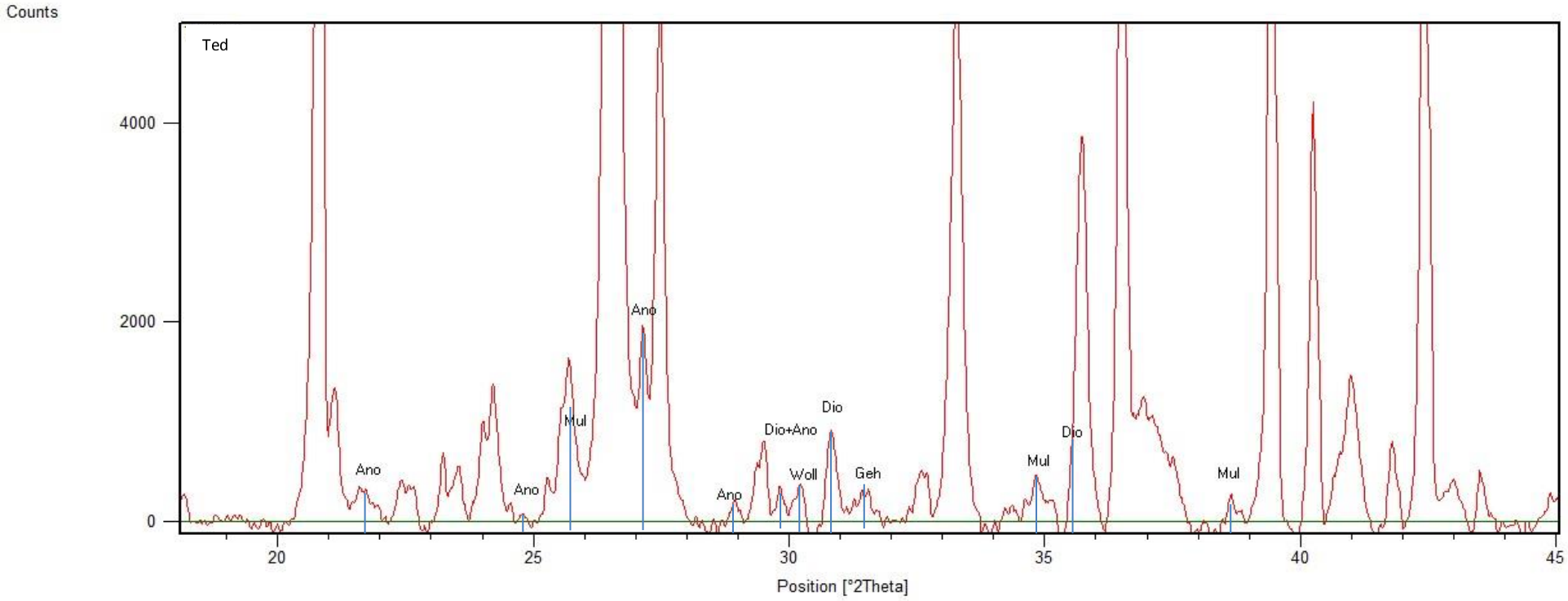

Figure A.34: XRD spectrum of non-reheated *Ted* sample, highlighting peaks attributed to high temperature related mineral phases. Ano=Anorthite; Dio=Diopside; Mul=Mullite; Geh=Gehlenite; Wol=Wollastonite.

Appendix B

FTIR Results

This appendix presents the FTIR spectra of non-reheated and reheated dating material subsamples. For each sample, a plot will be presented of the FTIR spectra across the entire scanned region 450-4000cm^{-1}, across the principle regions of mineral identification, 450-900cm^{-1} and 450-1500cm^{-1} (together with 2nd derivative plots used to aid peak identification), and across the region of organics identification 2800-3000cm^{-1}. Along with this, a table of peaks and their associated mineral interpretations will be presented. The organic region peak results are presented in full in *Chapter 5*.

Ann

Table B.1: Mineral identification of diagnostic FTIR peaks for *Ann*. Aug=Augite, Mic=Microcline, Qtz=Qtz, Spi=Spinel, Bio=Biotite, Mus=Muscovite, Ens=Enstatite, Hem=Hematite, Alb=Albite.

Peak At (1/cm)	ID
468.0000	Aug,Mic
507.0000	Aug
515.0000	Qtz
539.0000	Mic
568.0000	Mic
579.0000	Mic,Spi
607.0000	Mic,Bio
647.0000	Mic,Ens,Hem,Alb
694.0000	Qtz
730.0000	Mic,Bio
876.0000	Aug,Mus
988.0000	Mus
1013.0000	Mic,Alb
1056.0000	Mic
1078.0000	Ens,Mic
1139.0000	Mic

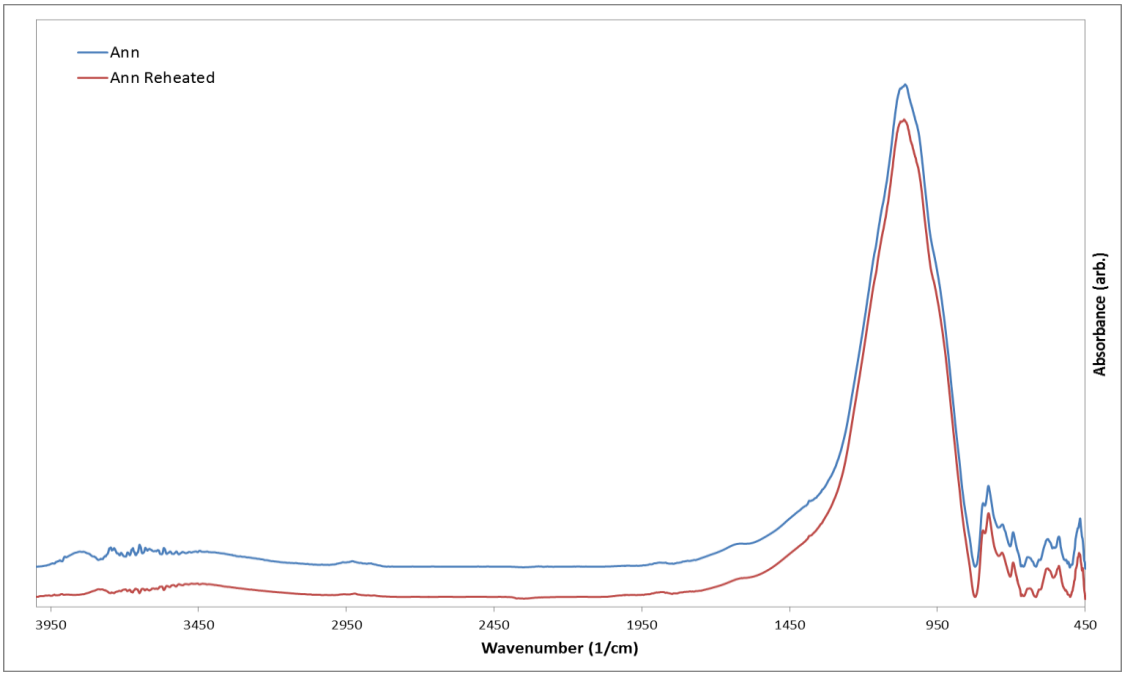

Figure B.1: FTIR Spectra of non-reheated (blue) and reheated (red) *Ann* sample.

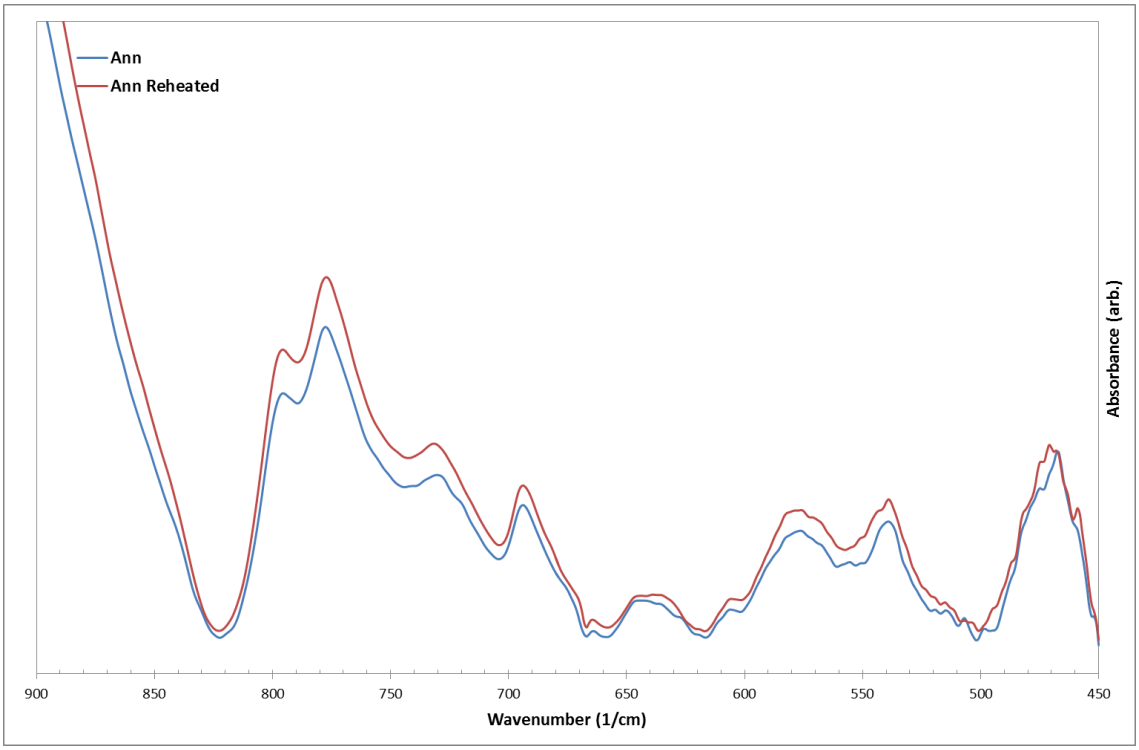

Figure B.2: FTIR spectra of non-reheated (blue) and reheated (red) *Ann* sample over the region 450-900(1/cm).

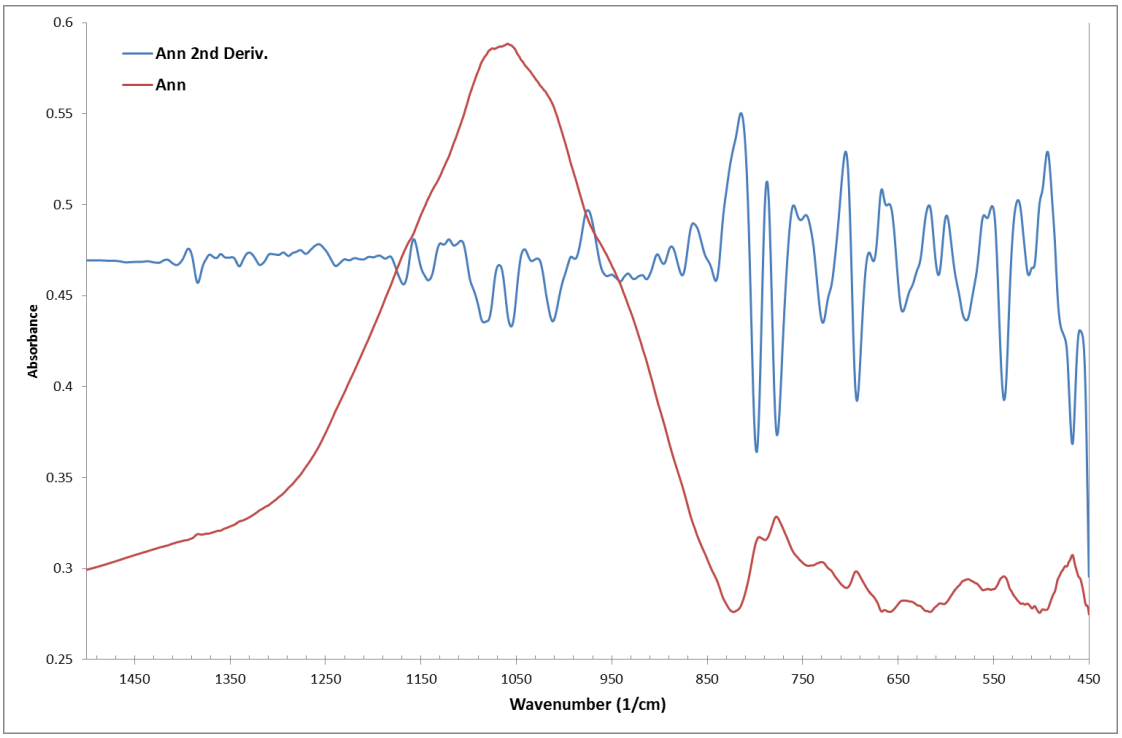

Figure B.3: FTIR spectrum of non-reheated *Ann* sample over region 450-1500 (1/cm) with smoothed second derivative overlaid.

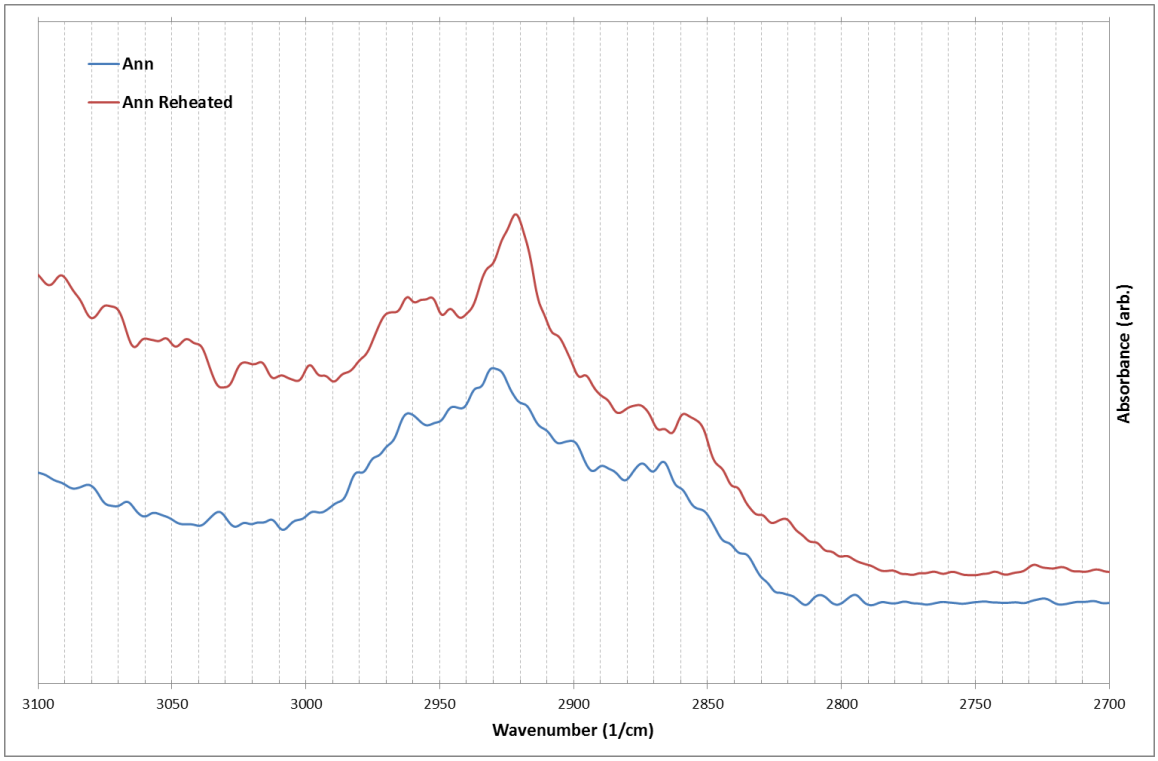

Figure B.4: FTIR spectra across region of interest in organic identification for *Ann* (non-reheated and reheated).

Esp

Table B.2: Mineral identification of diagnostic FTIR peaks for *Esp* samples. Ano=Anorthite, Dio=Diopside, Oli=Olivine, For=Forsterite, Fay=Fayalite, Aug=Augite, Ort=Orthoclase, Rut=Rutile, Mic=Microcline, Qtz=Qtz.

Peak At (1/cm)	ID
462.0000	Qtz
473.0000	Water
513.0000	Qtz
539.0000	Ano,Rut,Mic
579.0000	Mic
608.0000	Oli,For,Mic
633.0000	Dio
647.0000	Mic,Ort
730.0000	Ano,Ort,Mic
778.0000	Qtz
798.0000	Qtz
841.0000	For
876.0000	Aug
918.0000	Fay,Dio
961.0000	Aug
985.0000	For, Ano,Oli
1011.0000	Mic
1057.0000	Mic
1077.0000	Ano
1092.0000	Mic,Ano
1138.0000	Mic,Ano

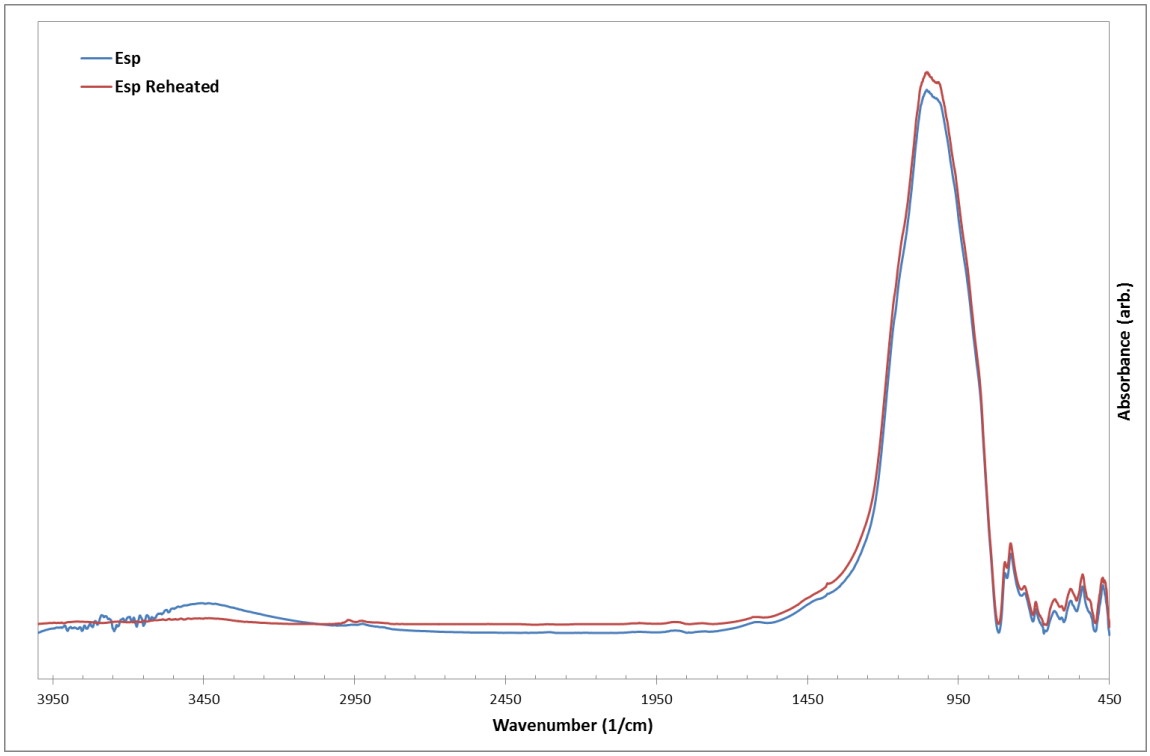

Figure B.5: FTIR Spectra of non-reheated (blue) and reheated (red) *Esp* sample.

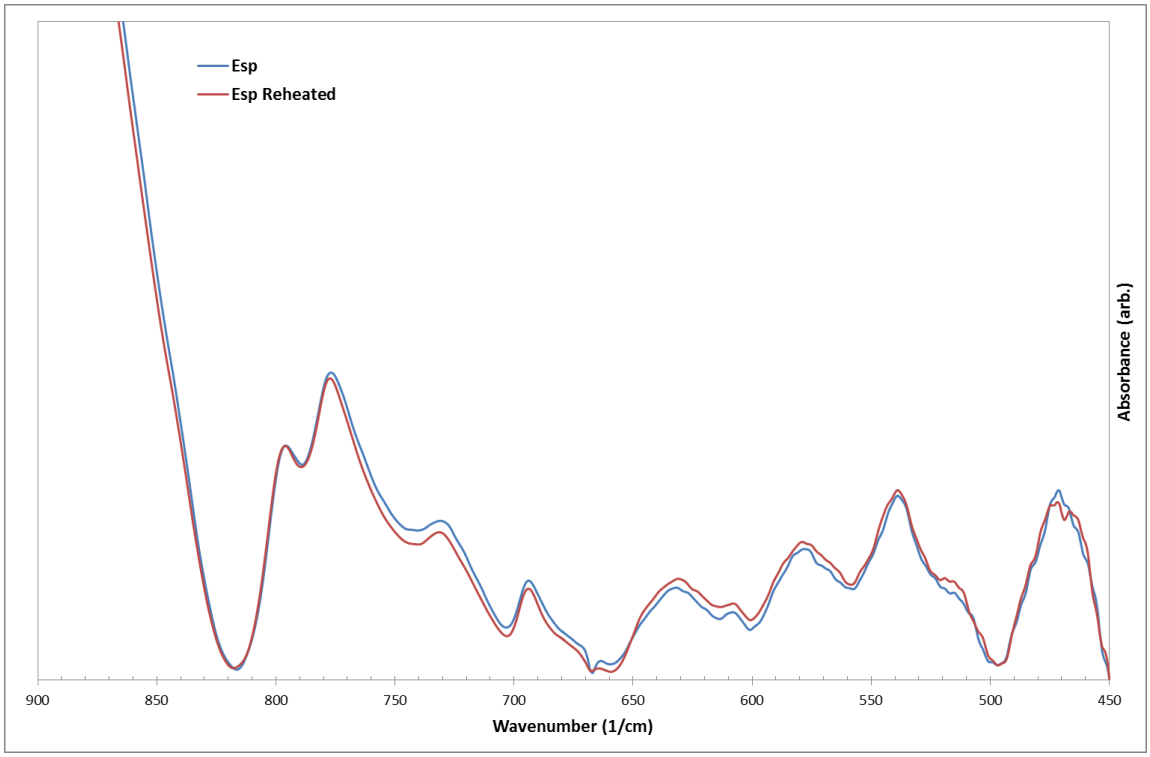

Figure B.6: FTIR spectra of non-reheated (blue) and reheated (red) *Esp* samples over the region 450-900(1/cm).

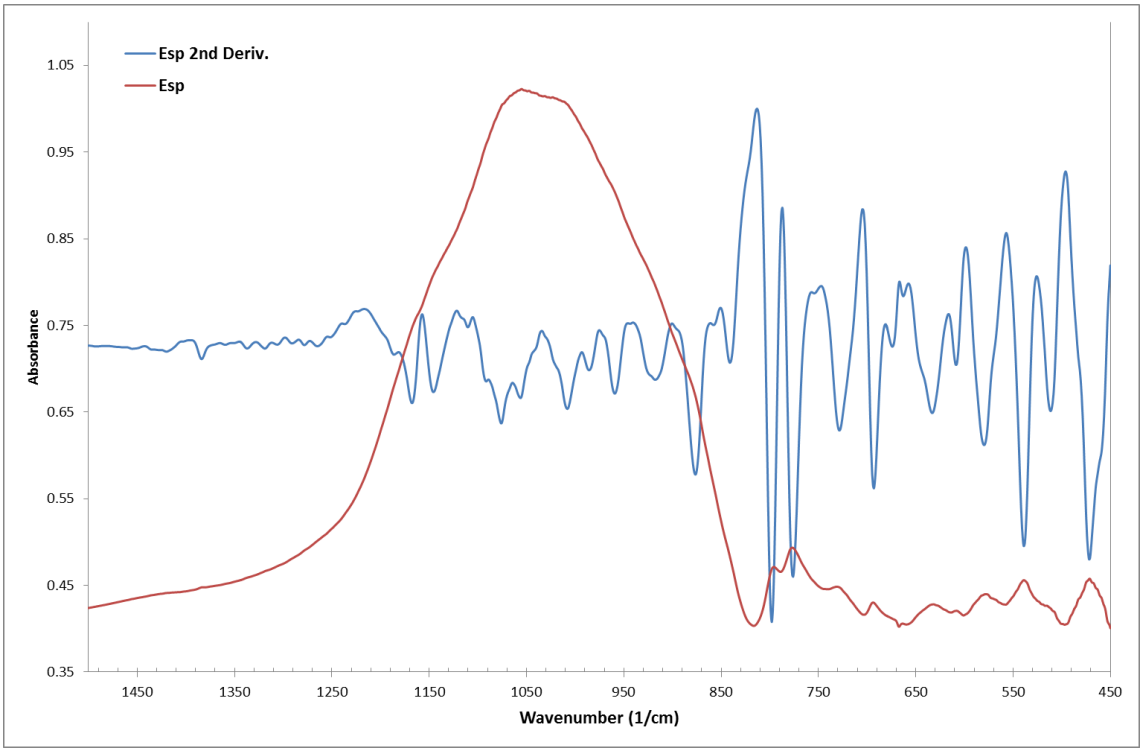

Figure B.7: FTIR spectrum of non-reheated *Esp* sample over region 450-1500 (1/cm) with smoothed second derivative overlaid.

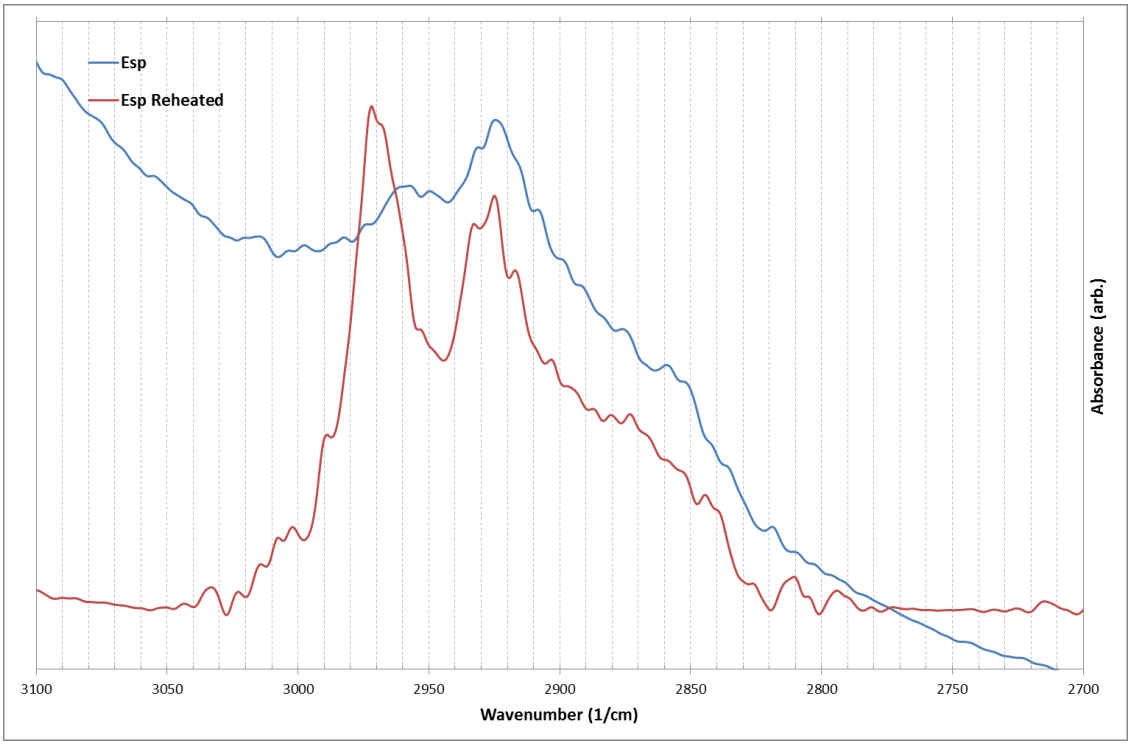

Figure B.8: FTIR spectra across region of interest in organic identification for *Esp* (non-reheated and reheated).

Nic

Table B.3: Mineral identification of diagnostic FTIR peaks for *Nic* samples. Ano=Anorthite, Dio=Diopside, For=Forsterite, Aug=Augite, Rut=Rutile, Mic=Microcline, Qtz=Qtz, Hem=Hematite, Cri=Cristobalite, Alb=Albite, Spi=Spinel, Geh=Gehlenite, Cal=Calcite, Mul=Mullite, Wol=Wollastonite.

Peak At (1/cm)	ID
465.0000	Hem,Mic, For,Aug
482.0000	Ano,Cri,Ano,Mul
515.0000	Qtz,Cri
539.0000	Ano,Mic,Rut
568.0000	Mic
579.0000	Mic,Spi
589.0000	Mic,Alb
609.0000	For,Mic,Alb
623.0000	Cri,Ano
634.0000	Geh,Dio
694.0000	Qtz
714.0000	Cal,Spi
731.0000	Mul
759.0000	Alb
775.0000	Qtz
796.0000	Qtz
841.0000	For
855.0000	Geh
875.0000	Cal,Aug
886.0000	For,Hem
895.0000	Mul
918.0000	Woll,Dio
961.0000	Aug,Ens
985.0000	Geh,Ano,For,Oli
1056.0000	Geh
1094.0000	Woll,Cri,Ano,Alb
1150.0000	Alb
1421.0000	Cal
2516.0000	Cal

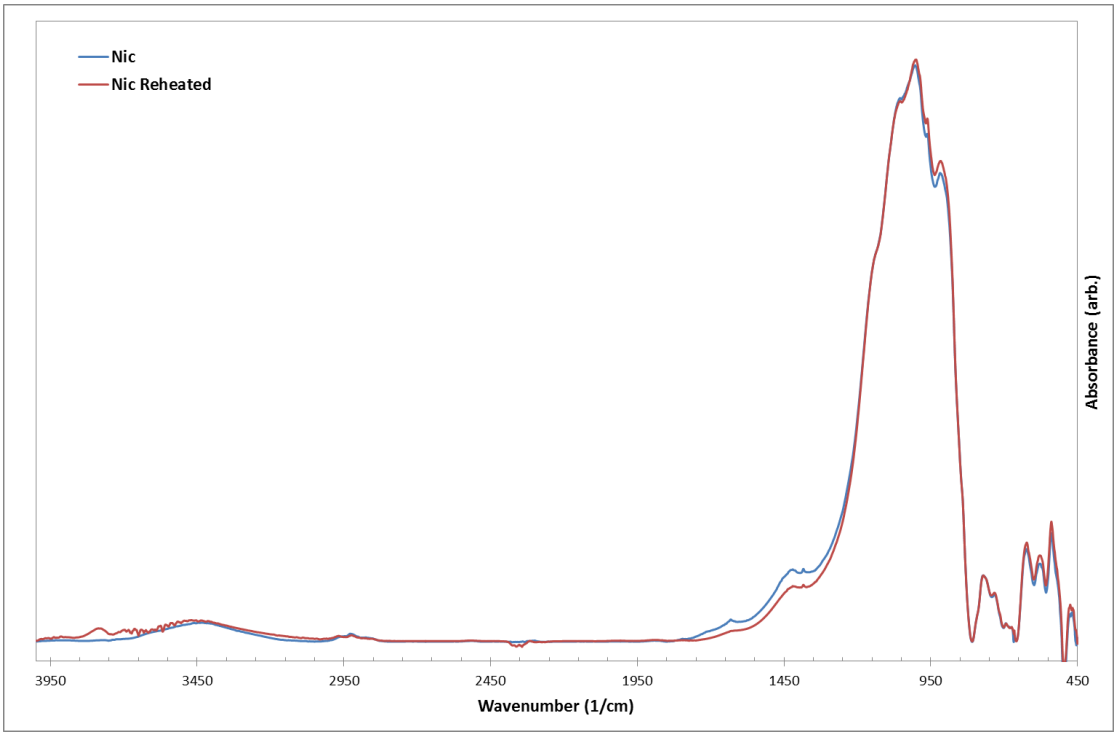

Figure B.9: FTIR Spectra of non-reheated (blue) and reheated (red) *Nic* sample.

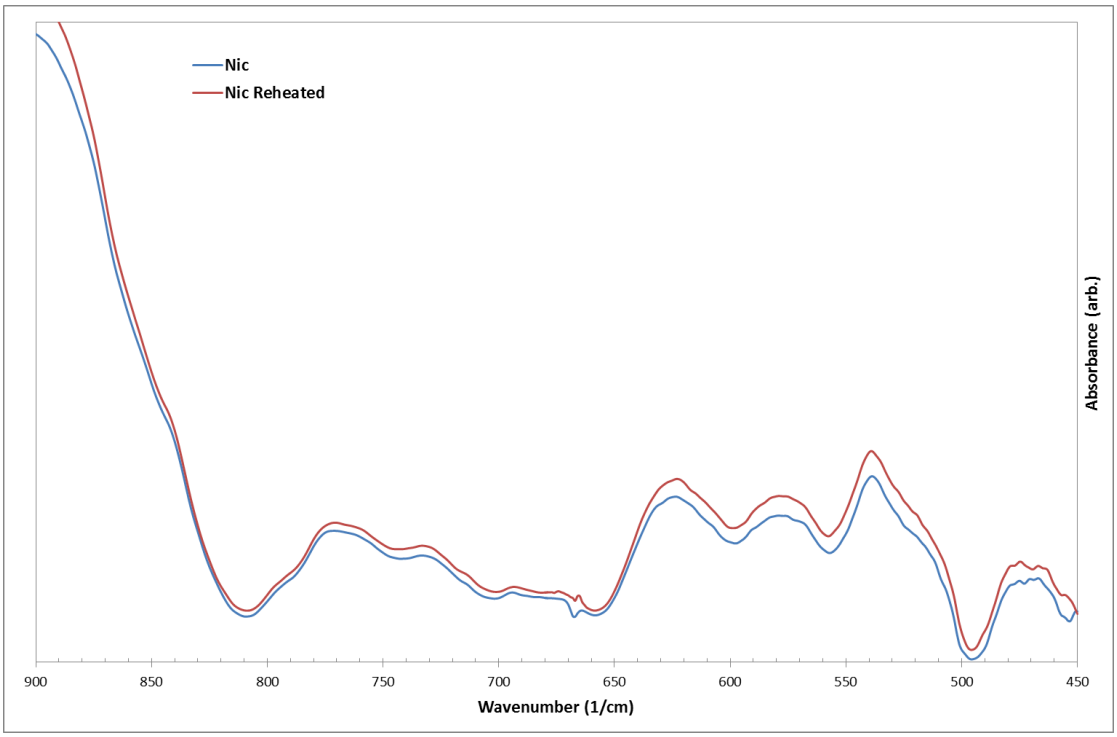

Figure B.10: FTIR spectra of non-reheated (blue) and reheated (red) *Nic* samples over the region 450-900(1/cm).

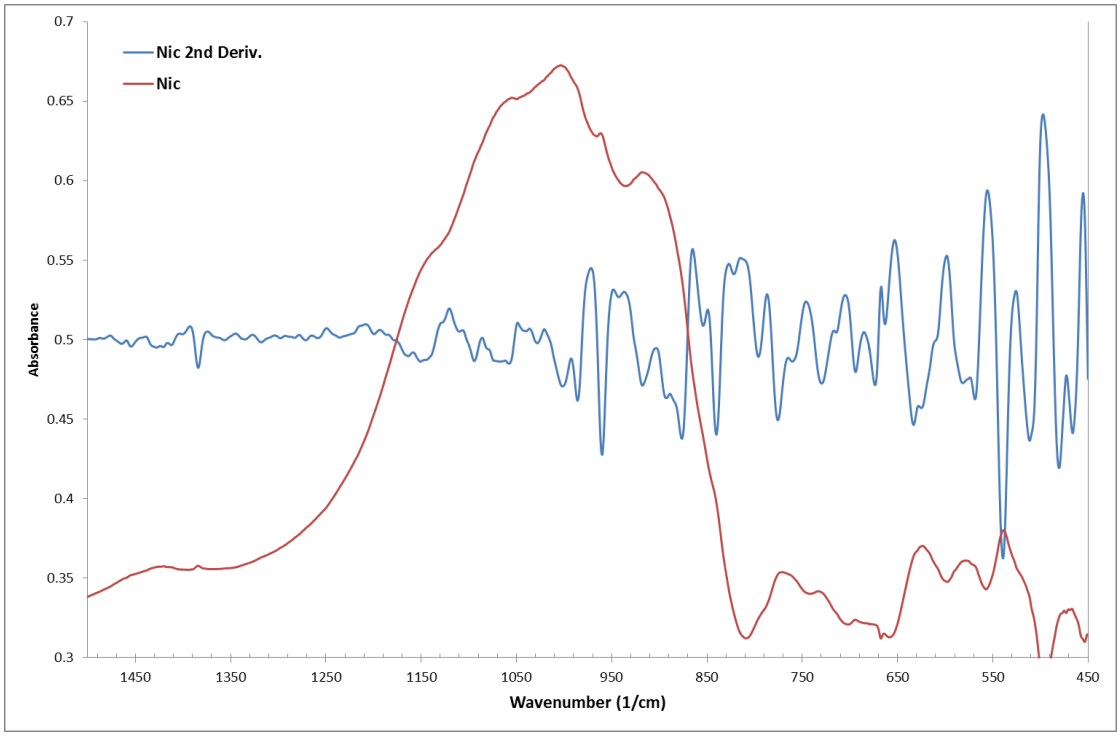

Figure B.11: FTIR spectrum of non-reheated *Nic* sample over region 450-1500 (1/cm) with smoothed second derivative overlaid.

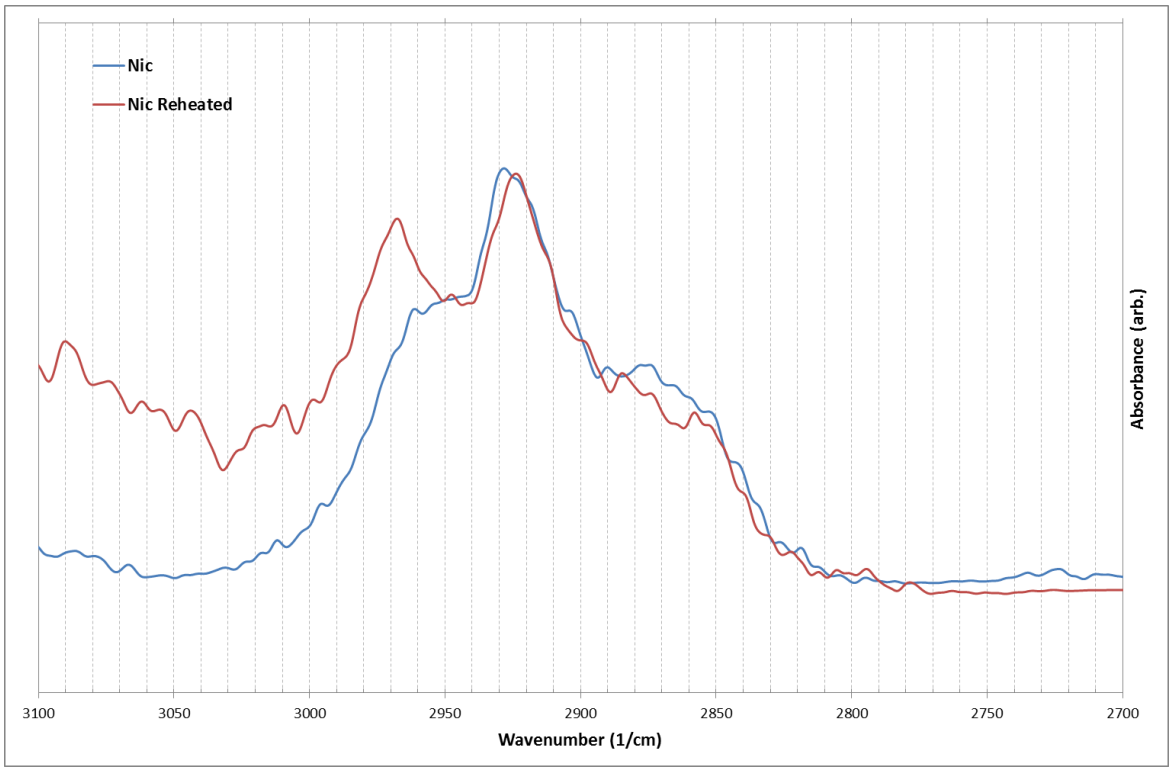

Figure B.12: FTIR spectra across region of interest in organic identification for *Nic* (non-reheated and reheated).

Mac

Table B.4: Mineral identification of diagnostic FTIR peaks for *Mac* samples. Ano=Anorthite, Rut=Rutile, Mic=Microcline, Qtz=Qtz, Hem=Hematite, Alb=Albite, Tri=Tridymite, Cri=Cristobalite, Mul=Mullite, San=Sanidine, Ana=Anatase, Ano=Anorthite, Mus=Muscovite, Anh=Anhydrite, Bas=Bassanite, Oli=Olivine.

Peak At (1/cm)	ID
461.0000	Qtz
470.0000	Mic
480.0000	Hem,Tri,Mul,Alb
517.0000	Qtz
527.0000	Rut
539.0000	Tri,Rut,San,Mic,Ana
576.0000	Ano
594.0000	Anh,Alb,Rut
596.0000	Anh
614.0000	Anh,Cri,Mus
617.0000	Anh
633.0000	Bas,San
673.0000	Anh
678.0000	Anh
694.0000	Qtz
778.0000	Qtz
798.0000	Qtz
953.0000	Oli
1009.0000	Bas,Mic
1082.0000	Qtz
1101.0000	Tri
1122.0000	San
1154.0000	Bas,Anh

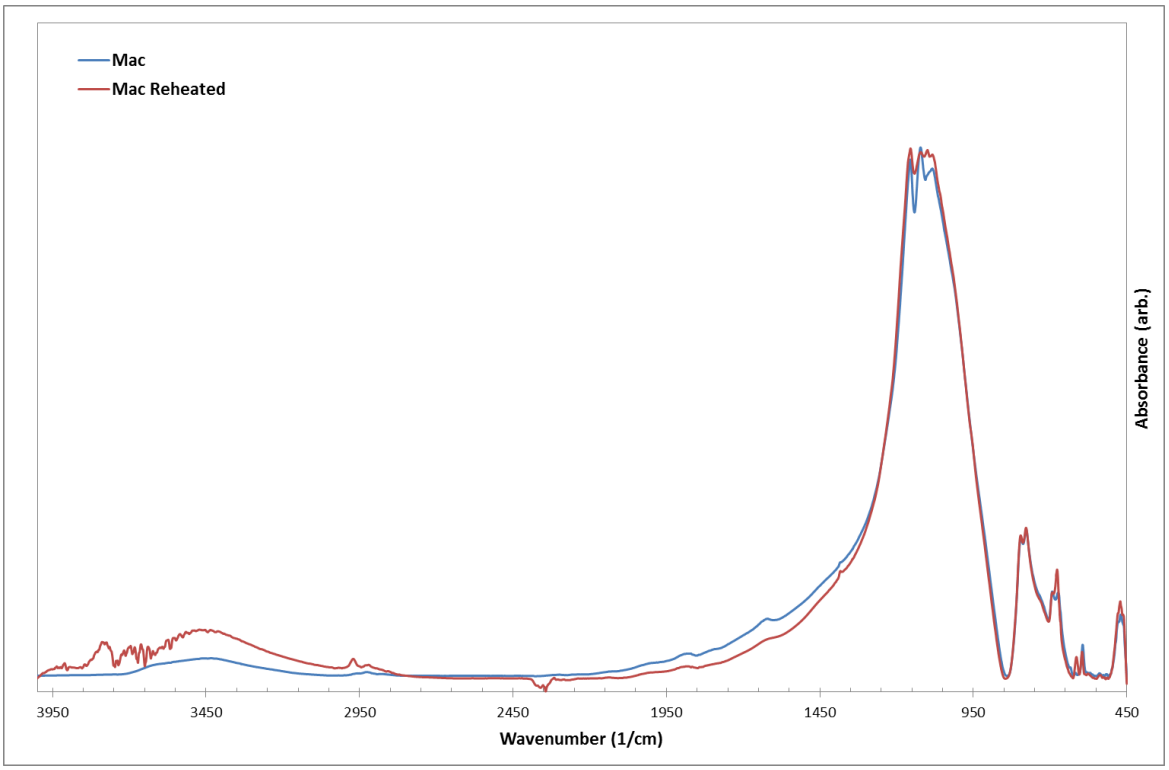

Figure B.13: FTIR Spectra of non-reheated (blue) and reheated (red) *Mac* sample.

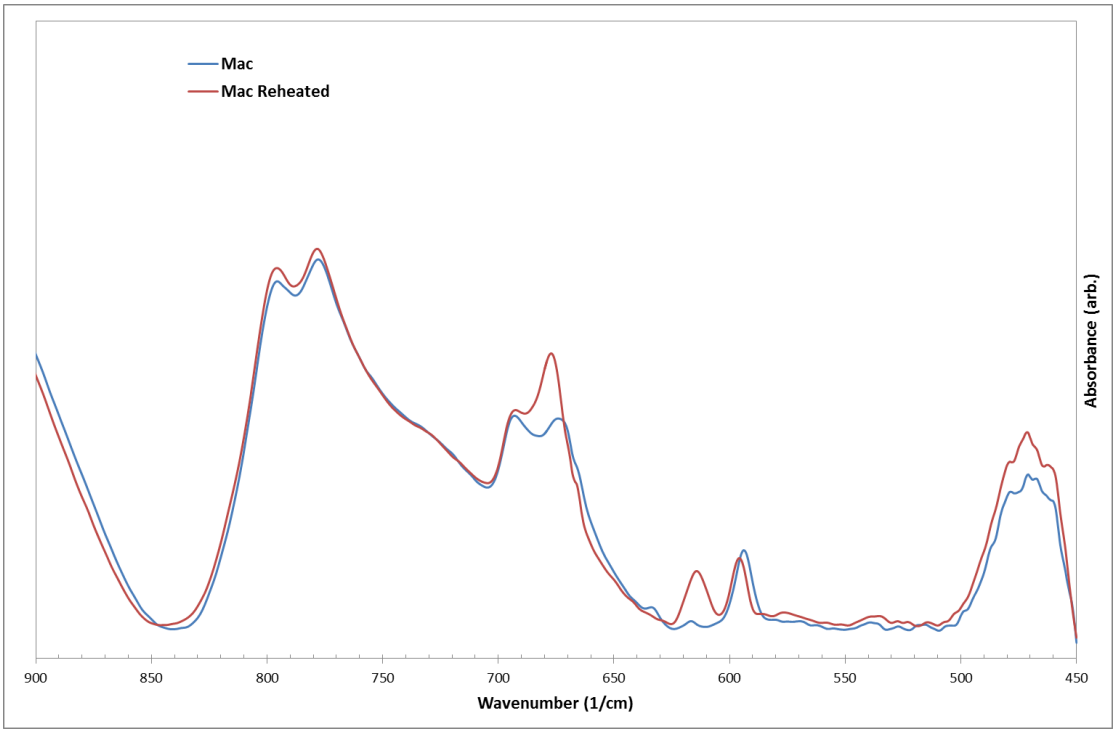

Figure B.14: FTIR spectra of non-reheated (blue) and reheated (red) *Mac* samples over the region 450-900(1/cm).

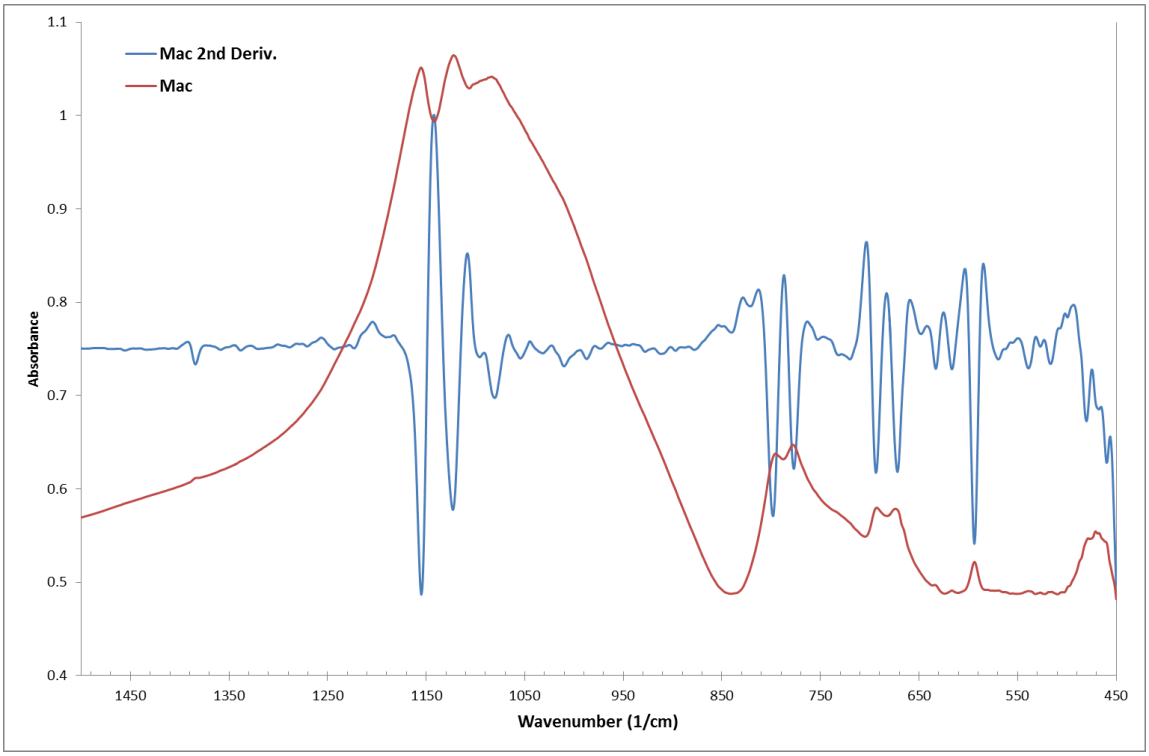

Figure B.15: FTIR spectrum of non-reheated *Mac* sample over region 450-1500 (1/cm) with smoothed second derivative overlaid.

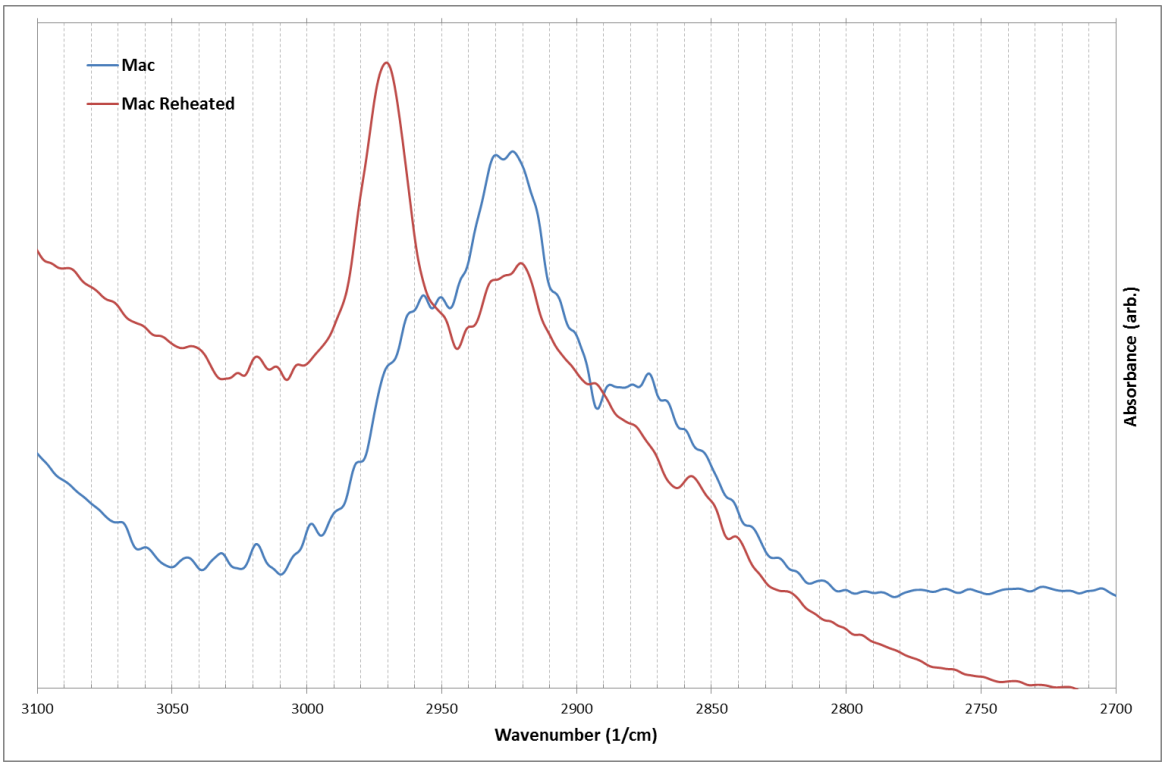

Figure B.16: FTIR spectra across region of interest in organic identification for *Mac* (non-reheated and reheated).

Ria

Table B.5: Mineral identification of diagnostic FTIR peaks for *Ria* samples. Ano=Anorthite, Rut=Rutile, Mic=Microcline, Qtz=Qtz, Hem=Hematite, Alb=Albite, San=Sanidine, Ana=Anatase, Mus=Muscovite, Ens=Enstatite, Fay=Fayalite, Wol=Wollastonite, Cor=Cordierite, Anh=Anhydrite, Geh=Gehlenite, Cal=Calcite, Dio=Diopside.

Peak At (1/cm)	ID
455.0000	Hem
468.0000	Ano,Mic
493.0000?	Rut
515.0000	Qtz
537.0000	Mic,Ens
549.0000	San
553.0000	Mus
567.0000	Fay,Wol
572.0000	Mic,Ano
580.0000	Mic,San
595.0000	Alb,Rut
606.0000	Mic
617.0000	Anh,Cor
647.0000	Mic,Ens,San,Hem,Alb
661.0000	Ano
674.0000	Geh
694.0000	Qtz
778.0000	Qtz
798.0000	Qtz
875.0000	Cal,Rut,Mus
975.0000	Geh,Dio
987.0000	Ano,Mus
1035.0000	Alb,San
1049.0000	Hem,Mic
1059.0000	San,Wol,Cal,Ens
1080.0000	Mic
1793.0000	Cal

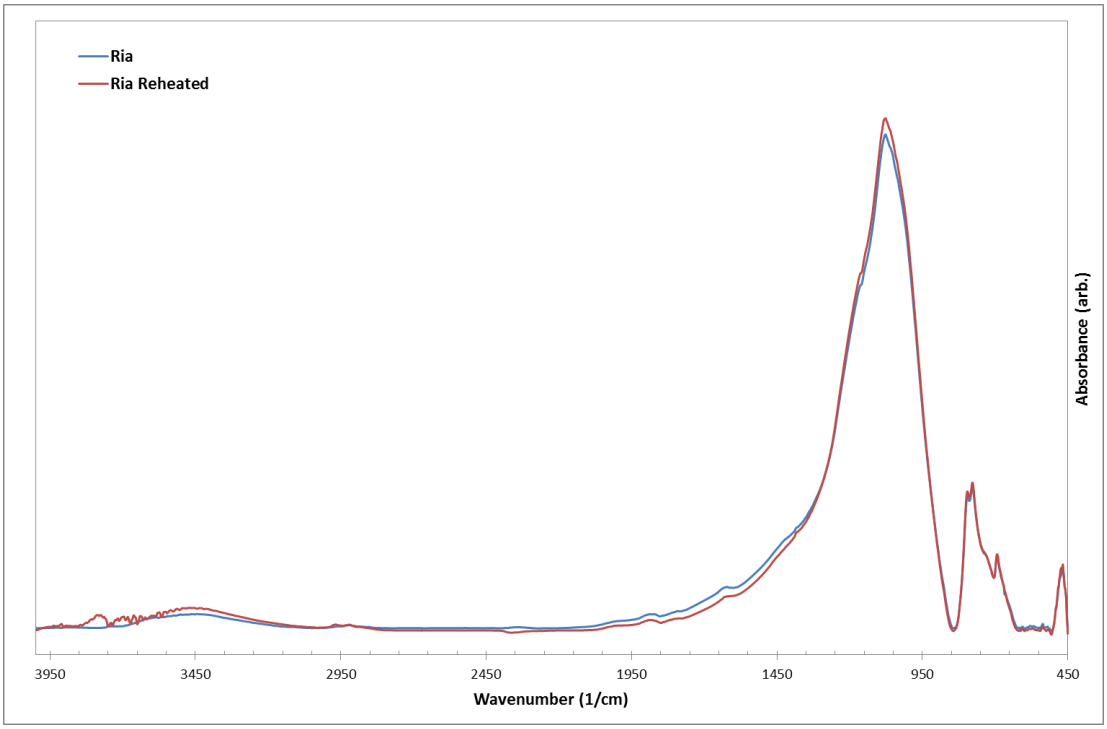

Figure B.17: FTIR Spectra of non-reheated (blue) and reheated (red) *Ria* sample.

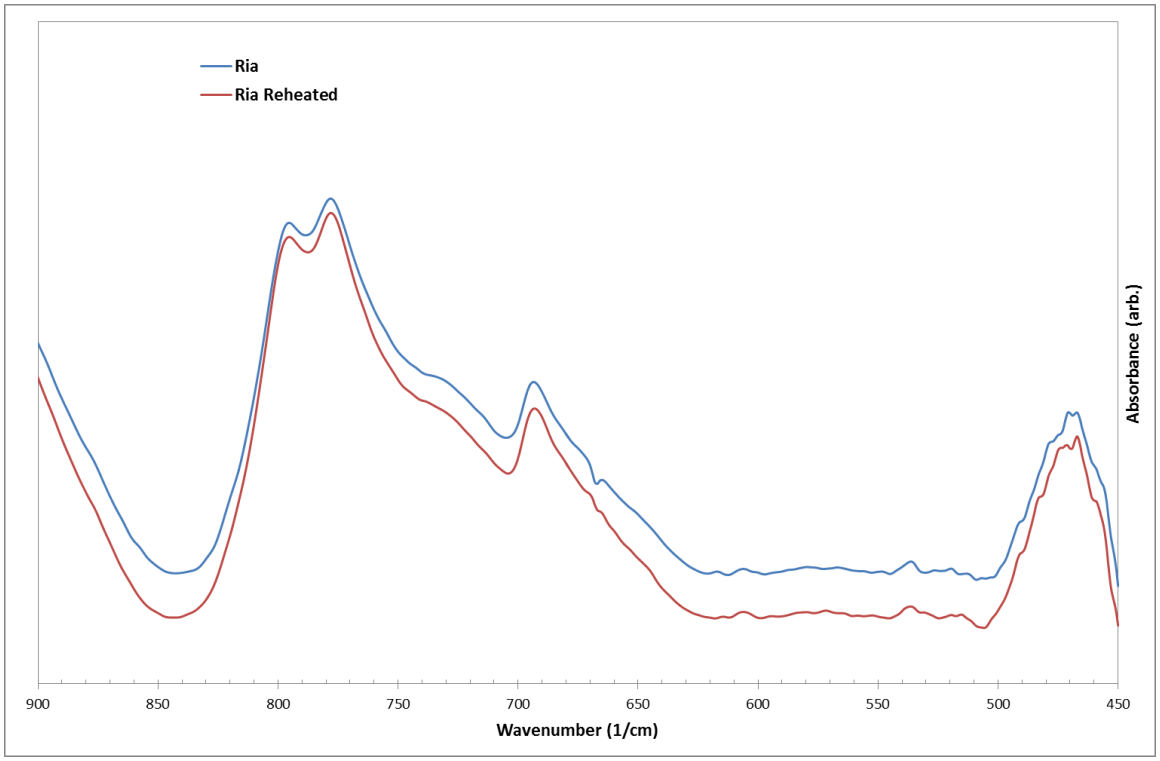

Figure B.18: FTIR spectra of non-reheated (blue) and reheated (red) *Ria* samples over the region 450-900(1/cm).

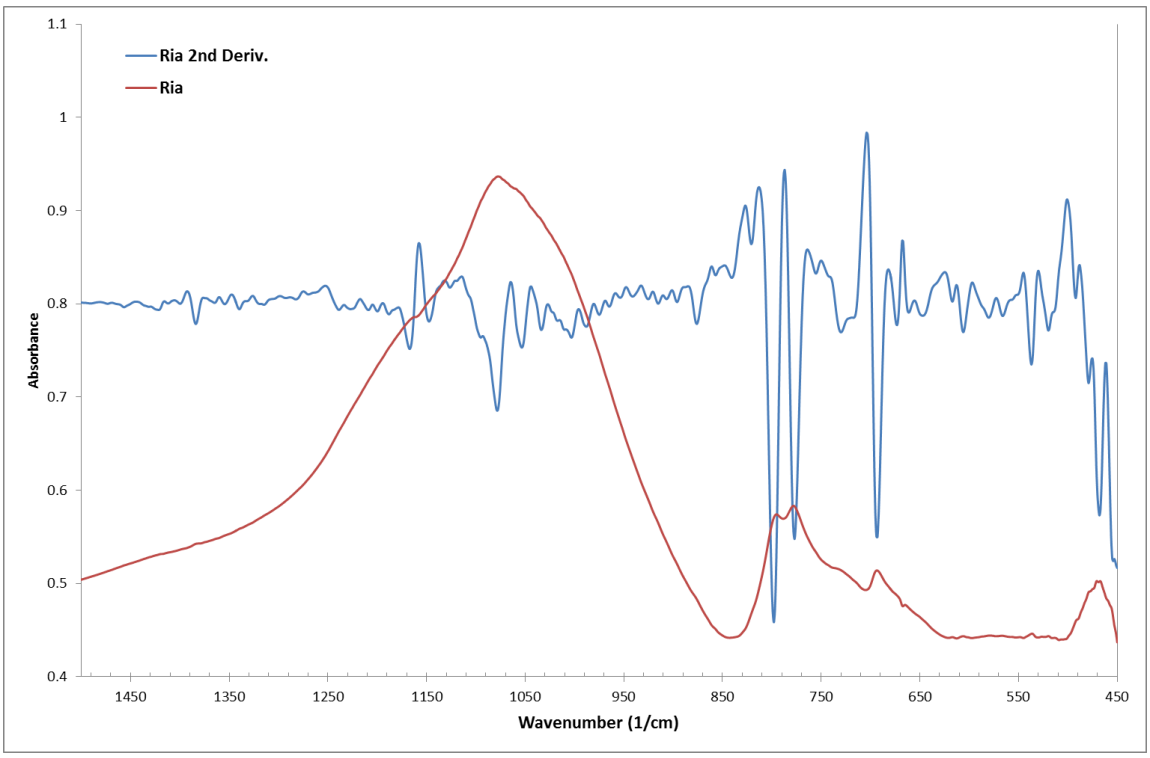

Figure B.19: FTIR spectrum of non-reheated *Ria* sample over region 450-1500 (1/cm) with smoothed second derivative overlaid.

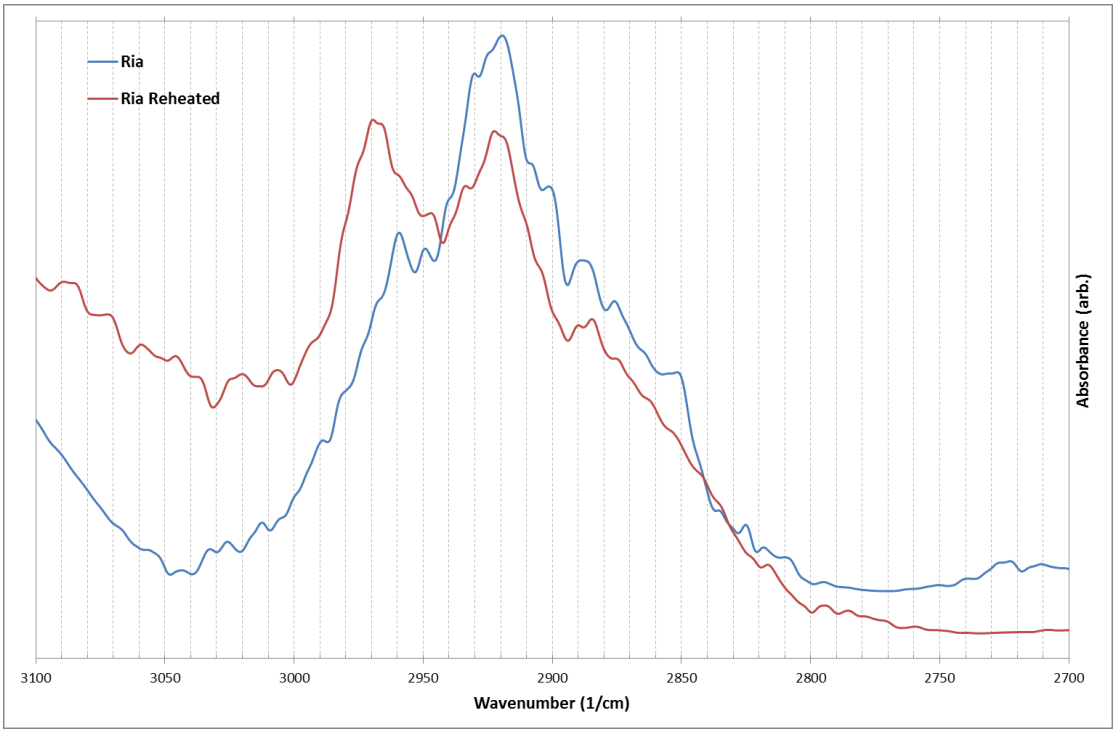

Figure B.20: FTIR spectra across region of interest in organic identification for *Ria* (non-reheated and reheated).

Etr

Table B.6: Mineral identification of diagnostic FTIR peaks for Etruscan samples. Qtz=Quartz, Aug=Augite, Mic=Microcline, Mus=Muscovite, Hem=Hematite, Oli=Olivine, Cal=Calcite, Fel=Feldspar, San=Sanidine.

Peak At (1/cm)	ID
461.0000	Qtz
472.0000	Water
478.0000	Qtz
484.0000	Water
506.0000	Aug
515.0000	Qtz
538.0000	Mic
553.0000	Mus
562.0000	Hem
567.0000	Oli
607.0000	Mic,Oli
647.0000	Mic
695.0000	Qtz
713.0000	Cal
778.0000	Qtz
799.0000	Qtz
848.0000	Cal
875.0000	Cal
1043.0000	Fel
1056.0000	Mic,San
1082.0000	Qtz
1093.0000	Mic
1106.0000	Fel
1116.0000	Mic
1412.0000	Cal
1422.0000	Cal
1454.0000	Cal
1471.0000	Cal
1797.0000	Cal
2516.0000	Cal

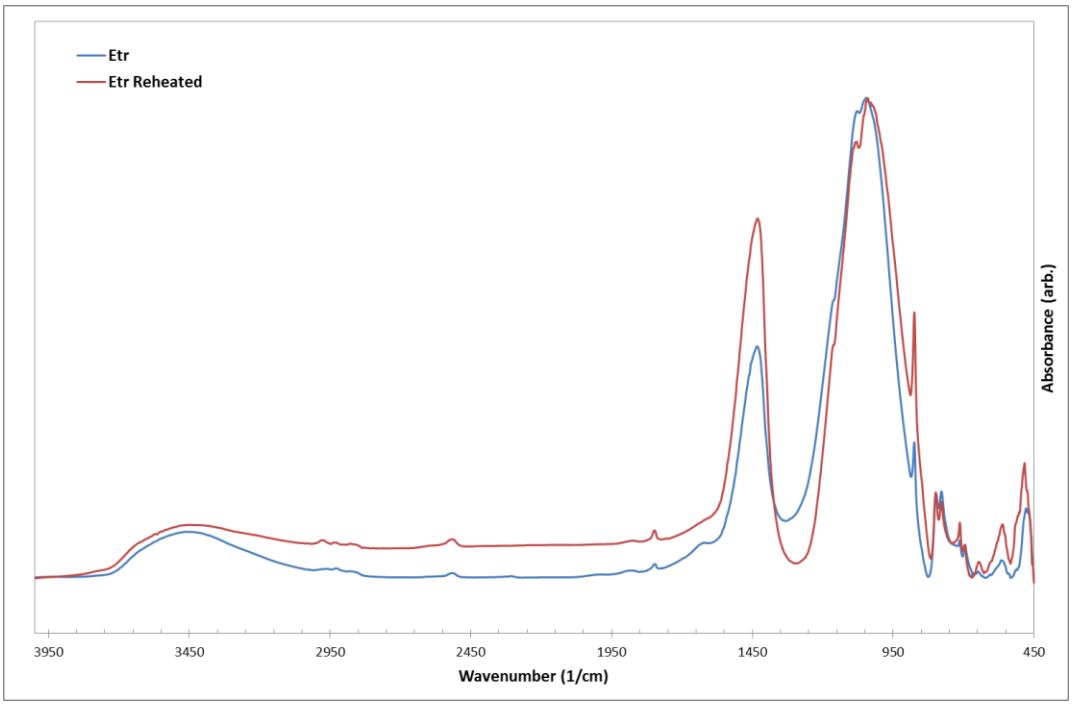

Figure B.21: FTIR Spectra of non-reheated (blue) and reheated (red) *Etr* sample.

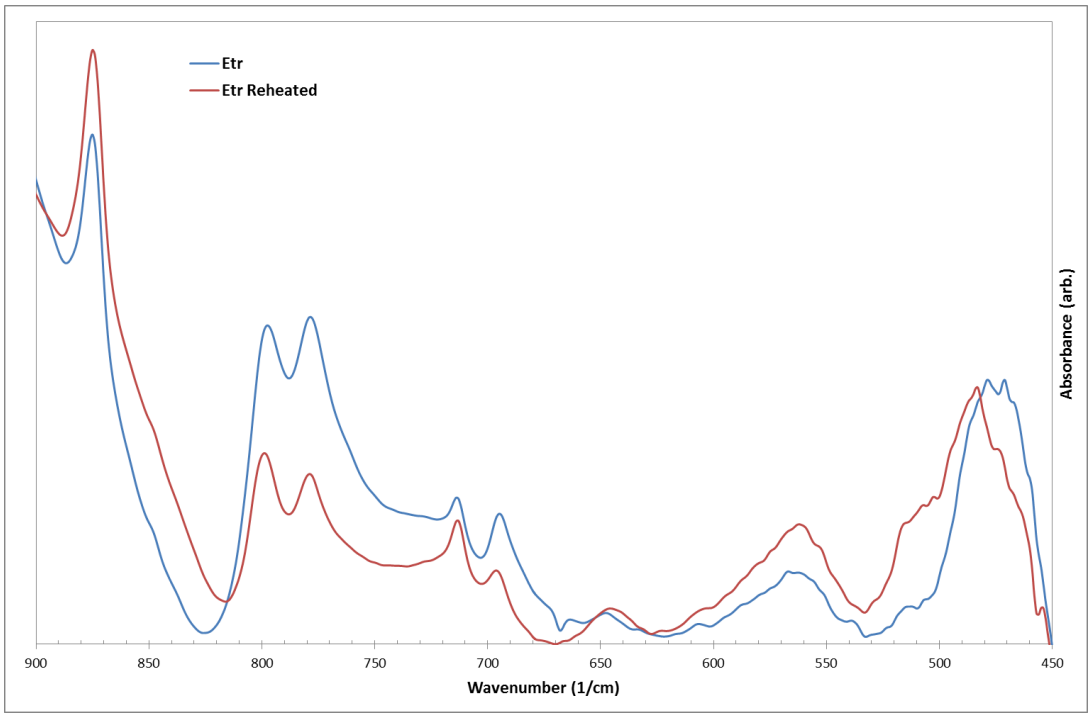

Figure B.22: FTIR spectra of non-reheated (blue) and reheated (red) *Etr* samples over the region 450-900(1/cm).

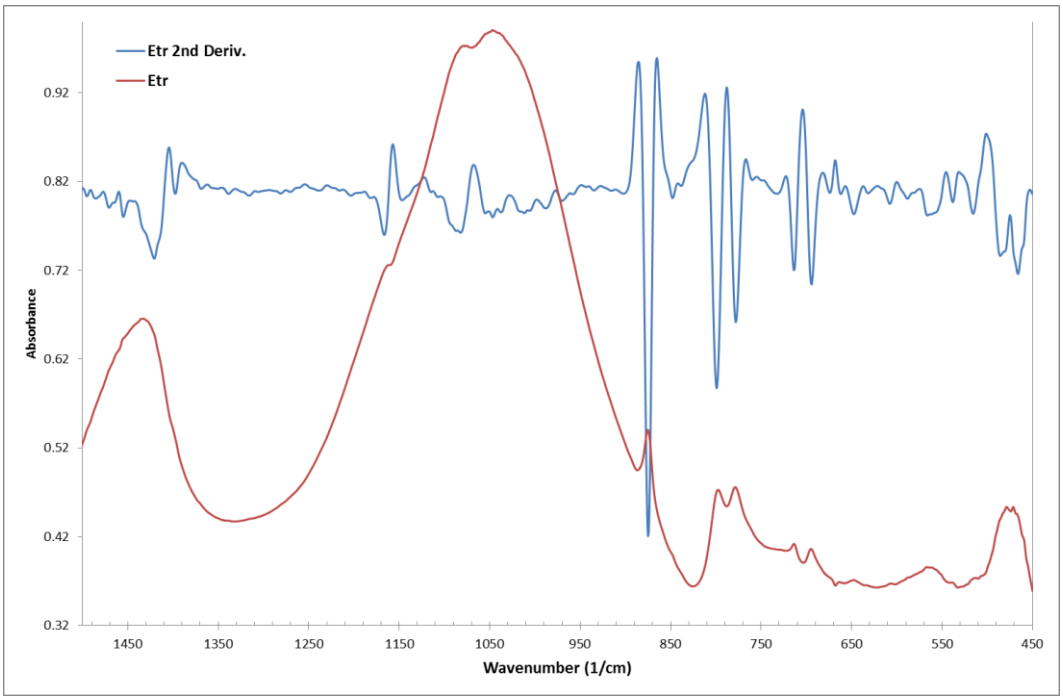

Figure B.23: FTIR spectrum of non-reheated *Etr* sample over region 450-1500 (1/cm) with smoothed second derivative overlaid.

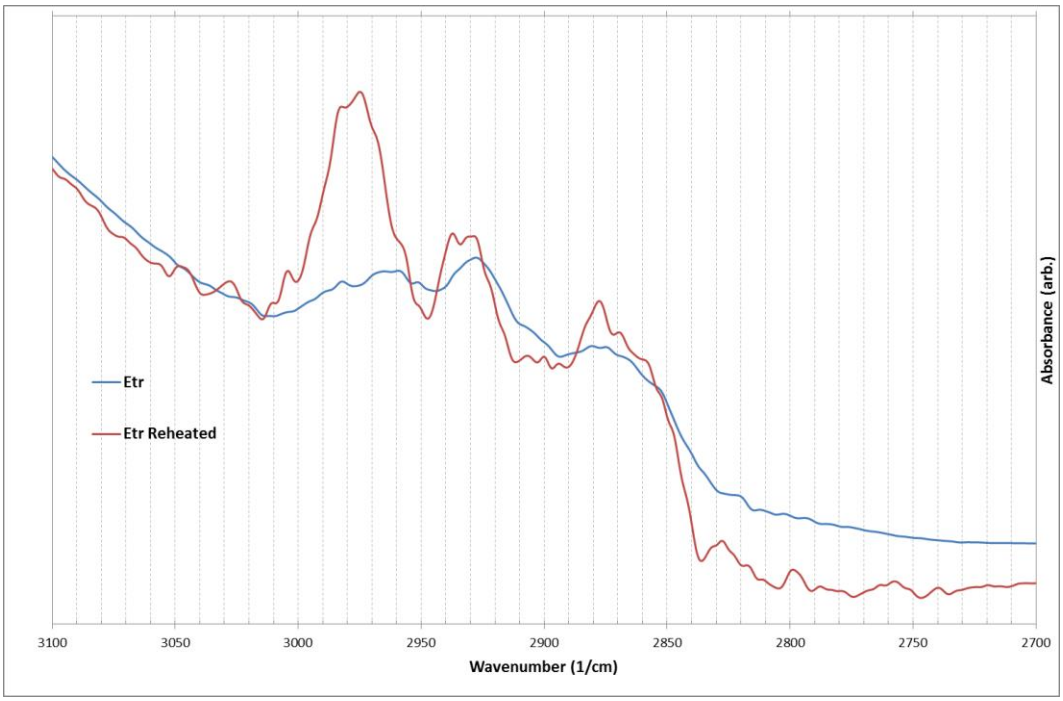

Figure B.24: FTIR spectra across region of interest in organic identification for *Etr* (non-reheated and reheated).

Rom

Table B.7: Mineral identification of diagnostic FTIR peaks for *Rom* samples. Qtz=Quartz, Hem=Hematite, Mic=Microcline, Aug=Augite, Mus=Muscovite, Fay=Fayalite, Alb=Albite, Ort=Orthoclase, Cal=Calcite, For=Forsterite, Oli=Olivine, Fel=Feldspar, Dol=Dolomite.

Peak At (1/cm)	ID
461.0000	Qtz
465.0000	Hem, Mic, Aug
473.0000	Water
483.0000	Water
514.0000	Qtz
518.0000	Qtz
537.0000	Mic
559.0000	Mus
565.0000	Fay
578.0000	Mic
607.0000	Mic
650.0000	Mic, Alb, Ort
695.0000	Qtz
729.0000	Mic, Ort
742.0000	Mic, Ort
779.0000	Qtz
798.0000	Qtz
875.0000	Cal
929.0000	Mus
951.0000	For,Oli
1007.0000	Mic
1046.0000	Mic
1059.0000	Cal
1077.0000	Dol
1107.0000	Fel
1118.0000	Fel
1414.0000	Cal
1424.0000	Cal
1432.0000	Cal,Dol
1798.0000	Cal
2514.0000	Cal

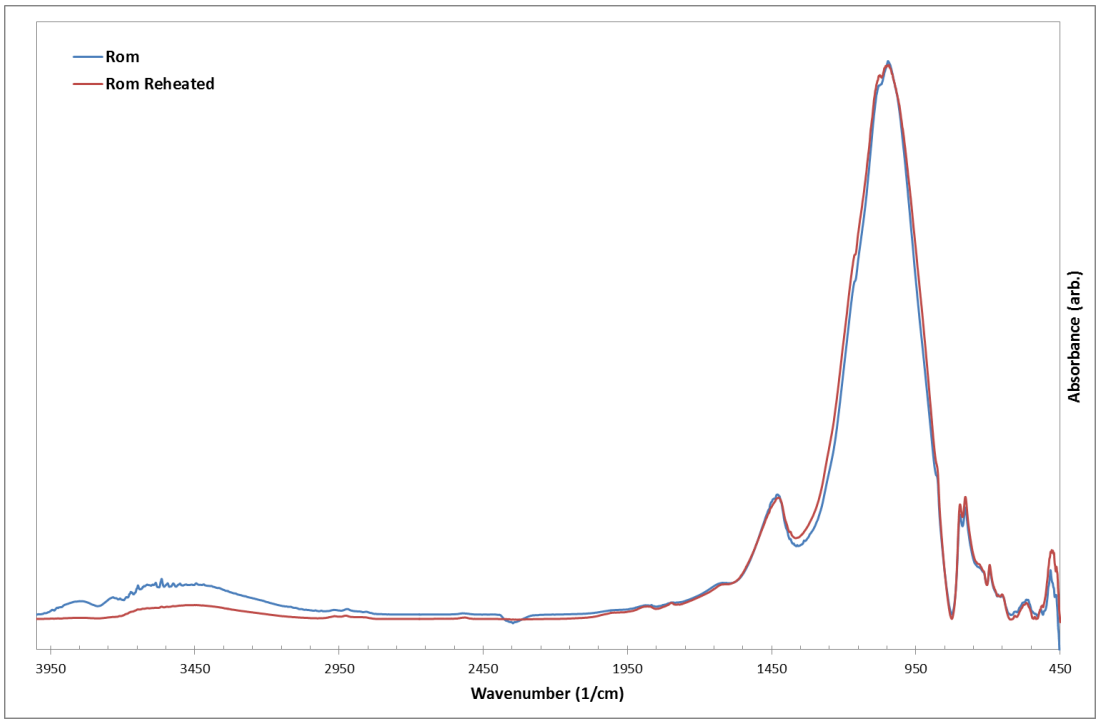

Figure B.25: FTIR Spectra of non-reheated (blue) and reheated (red) *Rom* sample.

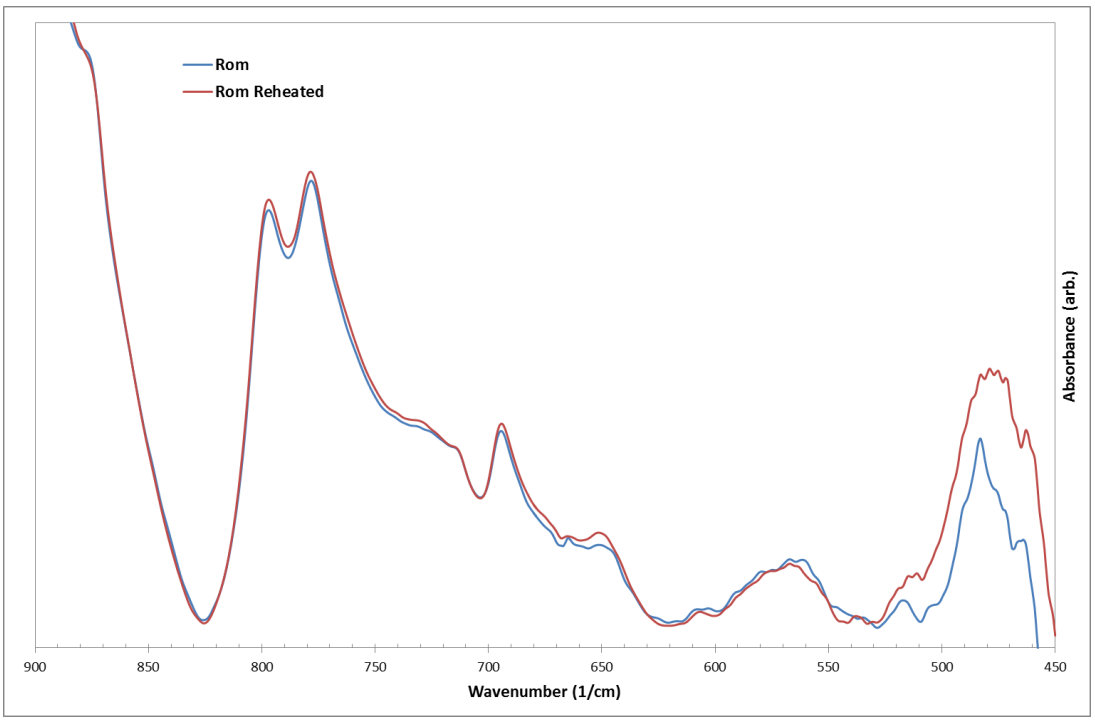

Figure B.26: FTIR spectra of non-reheated (blue) and reheated (red) *Rom* samples over the region 450-900(1/cm).

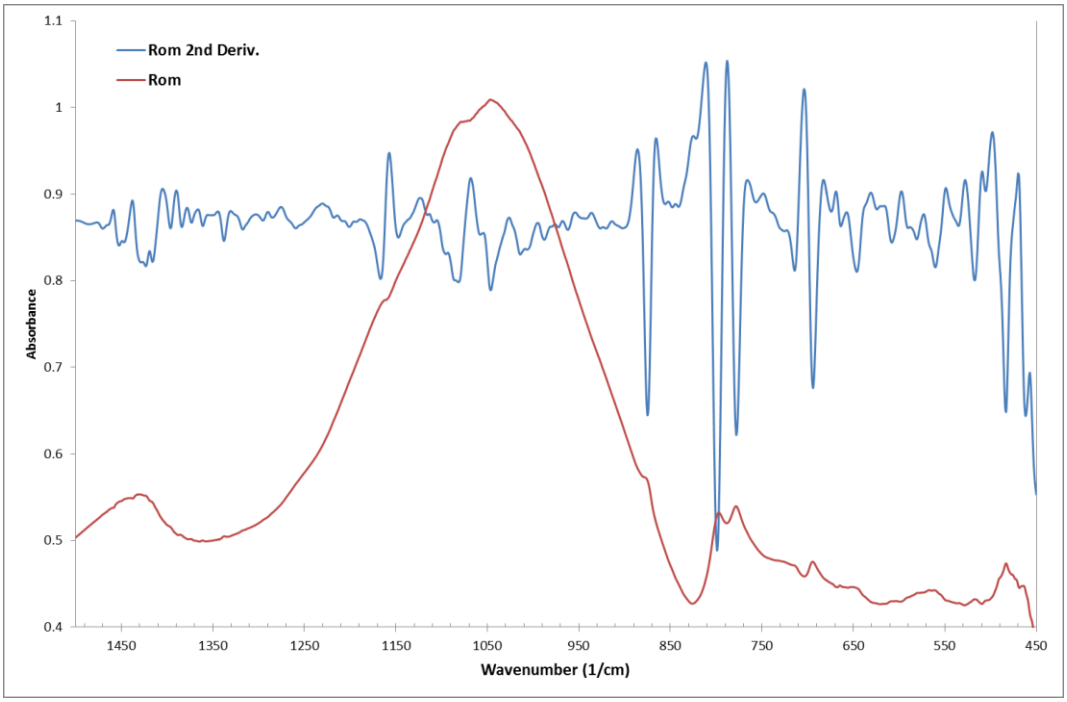

Figure B.27: FTIR spectrum of non-reheated *Rom* sample over region 450-1500 (1/cm) with smoothed second derivative overlaid.

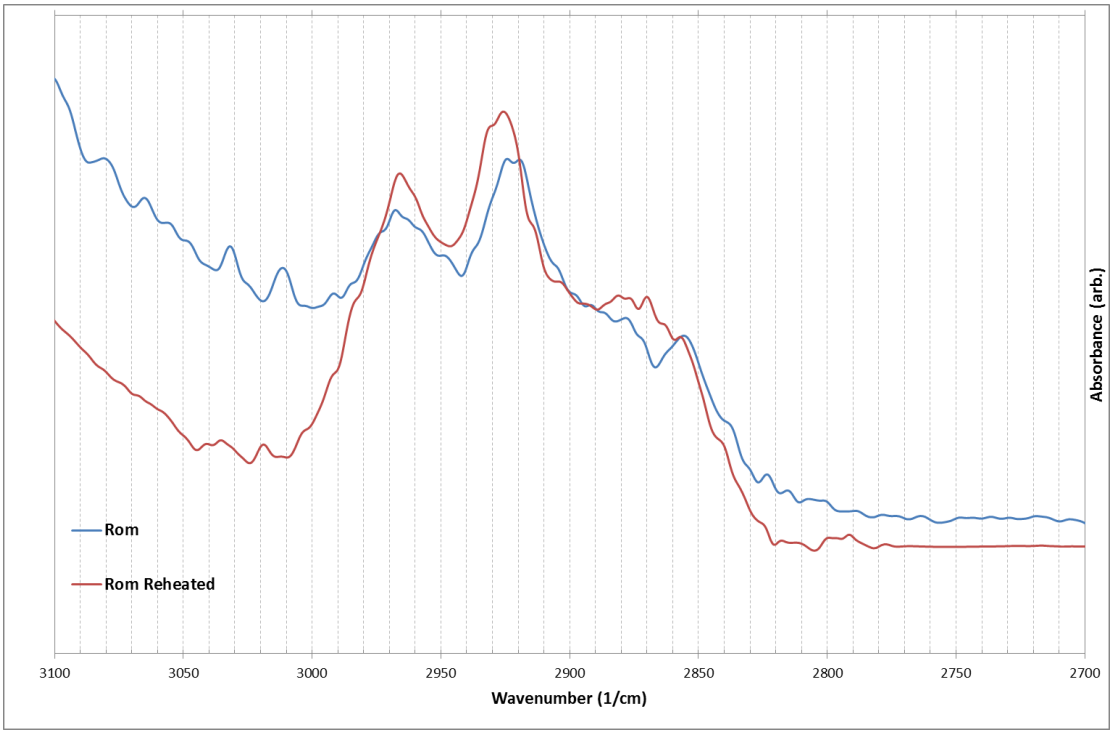

Figure B.28: FTIR spectra across region of interest in organic identification for *Rom* (non-reheated and reheated).

Por

Table B.8: Mineral identification of diagnostic FTIR peaks for *Por* samples. Qtz=Quartz, Ano=Anorthite, Rut=Rutile, Mic=Microcline, For=Forsterite, Wol=Wollastonite, Ens=Enstatite, Cal=Calcite, Geh=Gehlenite, Mus=Muscovite, Alb=Albite, Ort=Orthoclase.

Peak At (1/cm)	ID
461.0000	Qtz
472.0000	Water
516.0000	Qtz
539.0000	Ano,Rut
571.0000	Mic,Ano
584.0000	Mic
607.0000	Mic,For
645.0000	Mic,Wol,Ens
667.0000	Ano
694.0000	Qtz
714.0000	Cal
731.0000	Ano
778.0000	Qtz
799.0000	Qtz
875.0000	Cal
906.0000	Wol,Geh,Mus
939.0000	Ano
972.0000	Geh
1015.0000	Alb,Ort
1030.0000	Alb,Woll
1058.0000	Wol,Cal,Ens
1078.0000	Ano,Woll,Ens
1338.0000	Ana
1421.0000	Cal
1432.0000	Cal
1471.0000	Cal
1798.0000	Cal

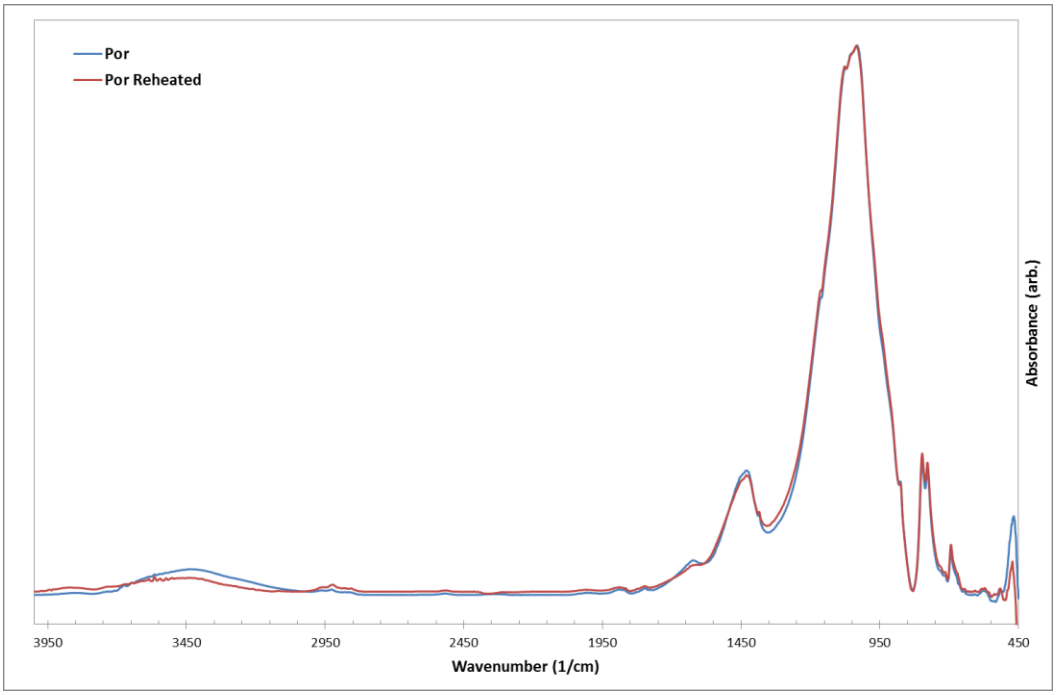

Figure B.29: FTIR Spectra of non-reheated (blue) and reheated (red) *Por* sample.

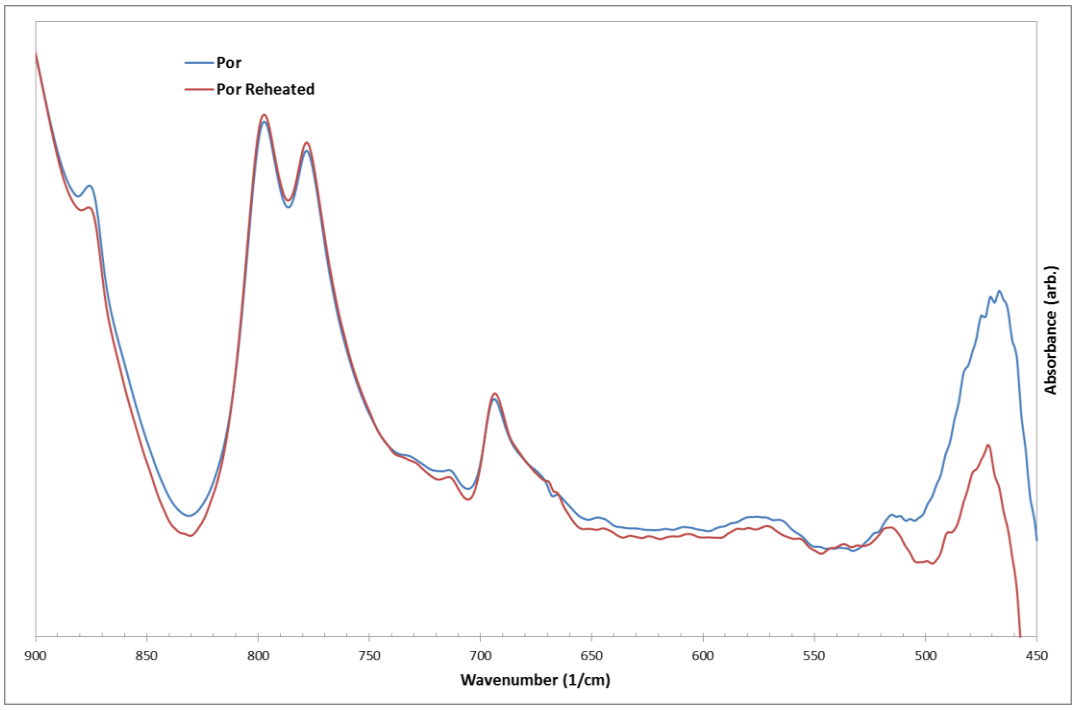

Figure B.30: FTIR spectra of non-reheated (blue) and reheated (red) *Por* samples over the region 450-900(1/cm).

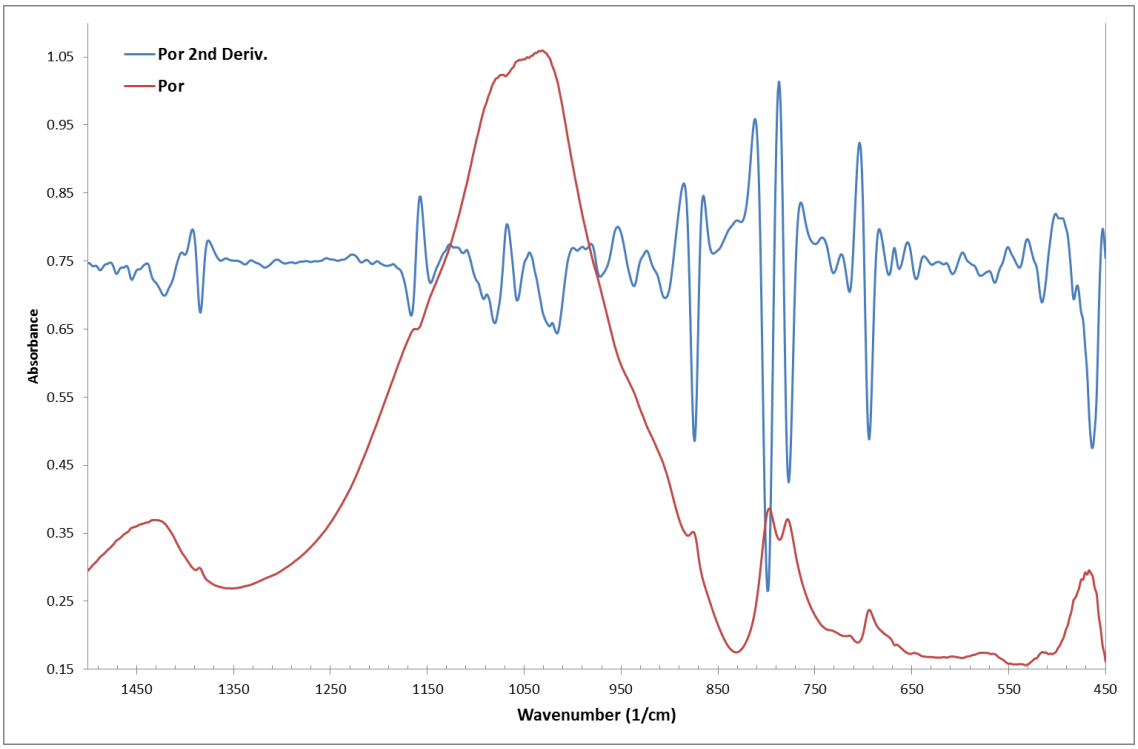

Figure B.31: FTIR spectrum of non-reheated *Por* sample over region 450-1500 (1/cm) with smoothed second derivative overlaid.

Figure B.32: FTIR spectra across region of interest in organic identification for *Por* (non-reheated and reheated).

Rat

Table B.9: Mineral identification of diagnostic FTIR peaks for *Rat* samples. Qtz=Quartz, For=Forsterite, Ano=Anorthite, Hem=Hematite, Ens=Enstatite, Ort=Orthoclase, Cor=Cordierite, Spi=Spinel, Dio=Diopside, Alb=Albite, Cal=Calcite, Cri=Cristobalite.

Peak At (1/cm)	ID
462.0000	Qtz
473.0000	Water
485.0000	Water
496.0000	For
518.0000	Qtz
540.0000	Ano
562.0000	Hem, Ens
572.0000	Ano
580.0000	Ort,Cor,Spi
631.0000	Ano,Dio
647.0000	Ort,Ens,Hem
660.0000	Ano
672.0000	Dio
694.0000	Qtz
724.0000	Alb,Ort
777.0000	Qtz
798.0000	Qtz
874.0000	Cal
1059.0000	Cal,Ens
1079.0000	Qtz
1090.0000	Dio,Ano,Cri
1100.0000	Alb
1131.0000	Ort
1166.0000	Qtz

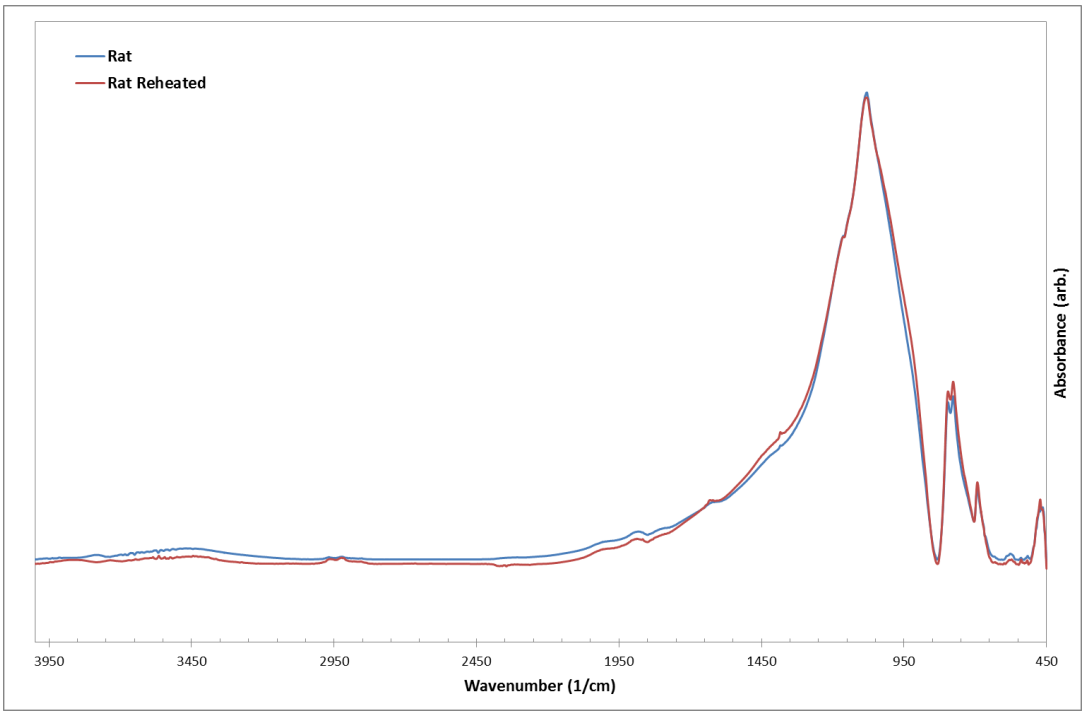

Figure B.33: FTIR Spectra of non-reheated (blue) and reheated (red) *Rat* sample.

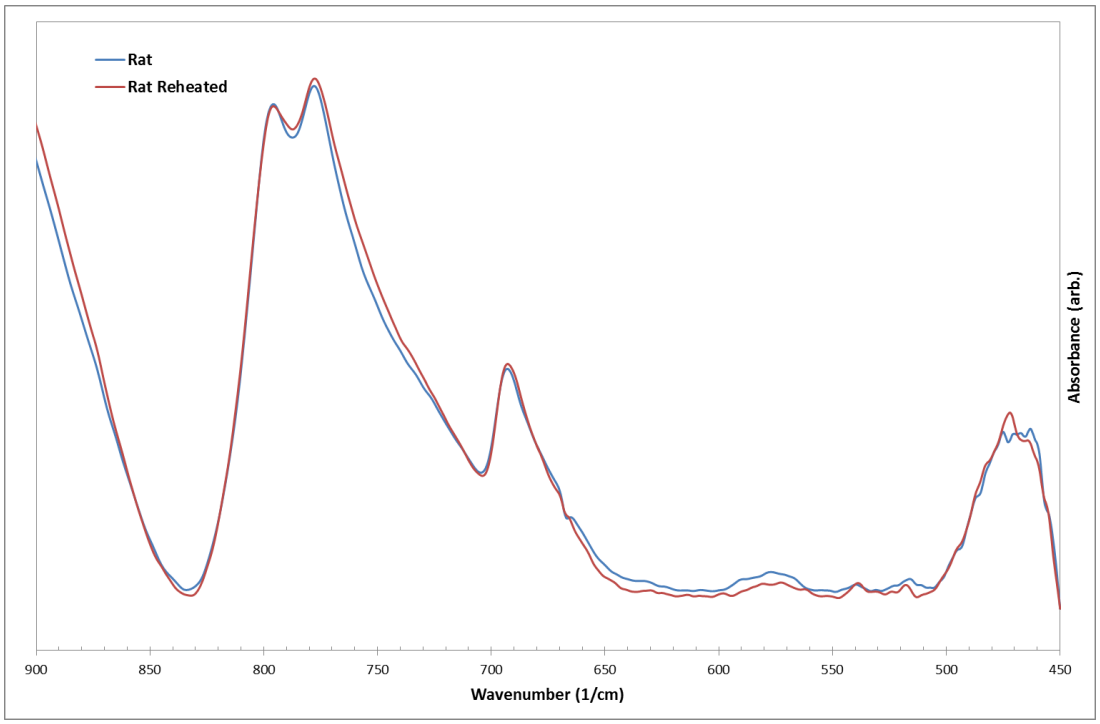

Figure B.34: FTIR spectra of non-reheated (blue) and reheated (red) *Rat* samples over the region 450-900(1/cm).

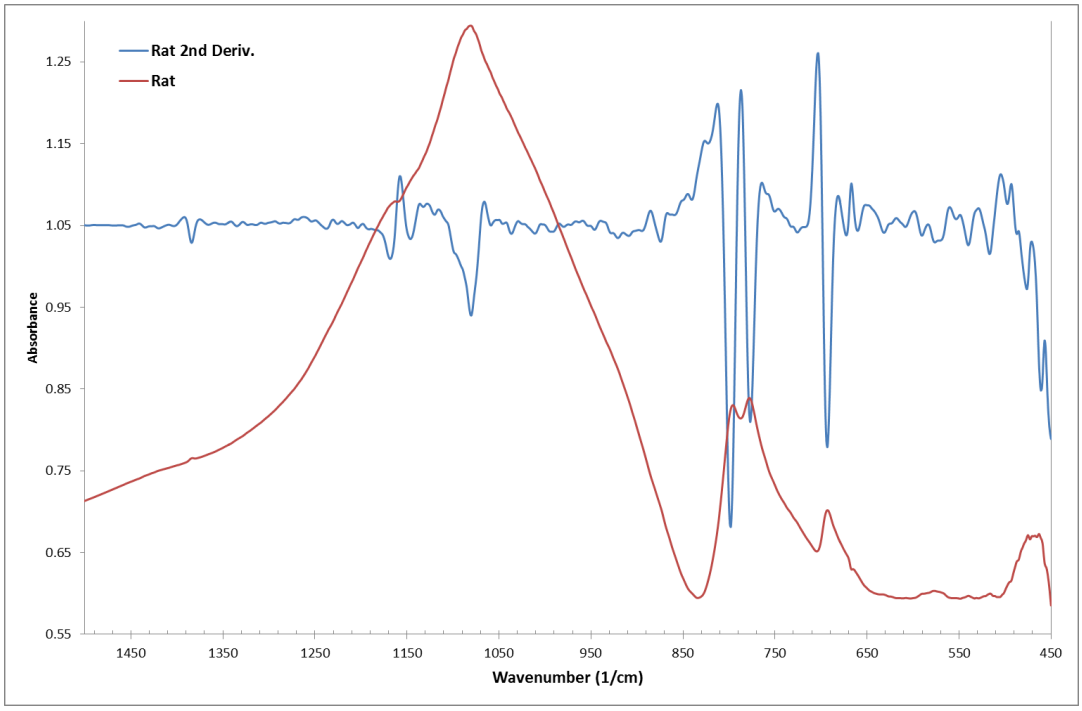

Figure B.35: FTIR spectrum of non-reheated *Por* sample over region 450-1500 (1/cm) with smoothed second derivative overlaid.

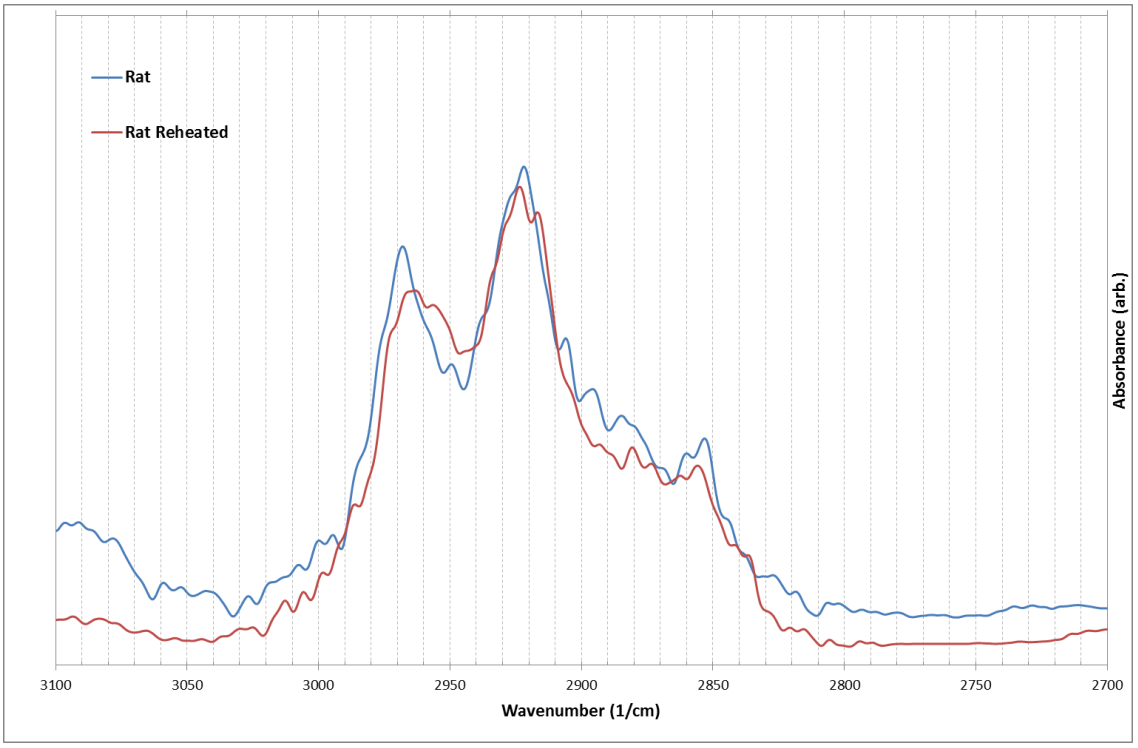

Figure B.36: FTIR spectra across region of interest in organic identification for *Rat* (non-reheated and reheated).

Cal

Table B.10: Mineral identification of diagnostic FTIR peaks for *Cal* samples. Qtz=Quartz, Ano=Anorthite, Cri=Cristobalite, Mul=Mullite, For=Forsterite, Wol=Wollastonite, Mic=Microcline, Enst=Enstatite, Geh=Gehlenite, Ort=Orthoclase, Cal=Calcite, Oli=Olivine, Dol=Dolomite.

Peak At (1/cm)	ID
469.0000	Ort,Ano
482.0000	Ano,Cri,Mul
496.0000	For
508.0000	For,Wol
514.0000	Qtz
518.0000	Cri
538.0000	Mic,Enst
567.0000	Wol,Mic
577.0000	Ano,Mic
580.0000	Ort,Mic
584.0000	Mic,Ort
625.0000	Ano
663.0000	Ano
674.0000	Geh
695.0000	Qtz
728.0000	Mic,Ort,Ano
757.0000	Ano
874.0000	Cal
916.0000	Wol,Geh
932.0000	Wol,Ano,Geh,Ens
953.0000	Oli
1079.0000	Qtz
1097.0000	Alb
1423.0000	Cal
1431.0000	Dol

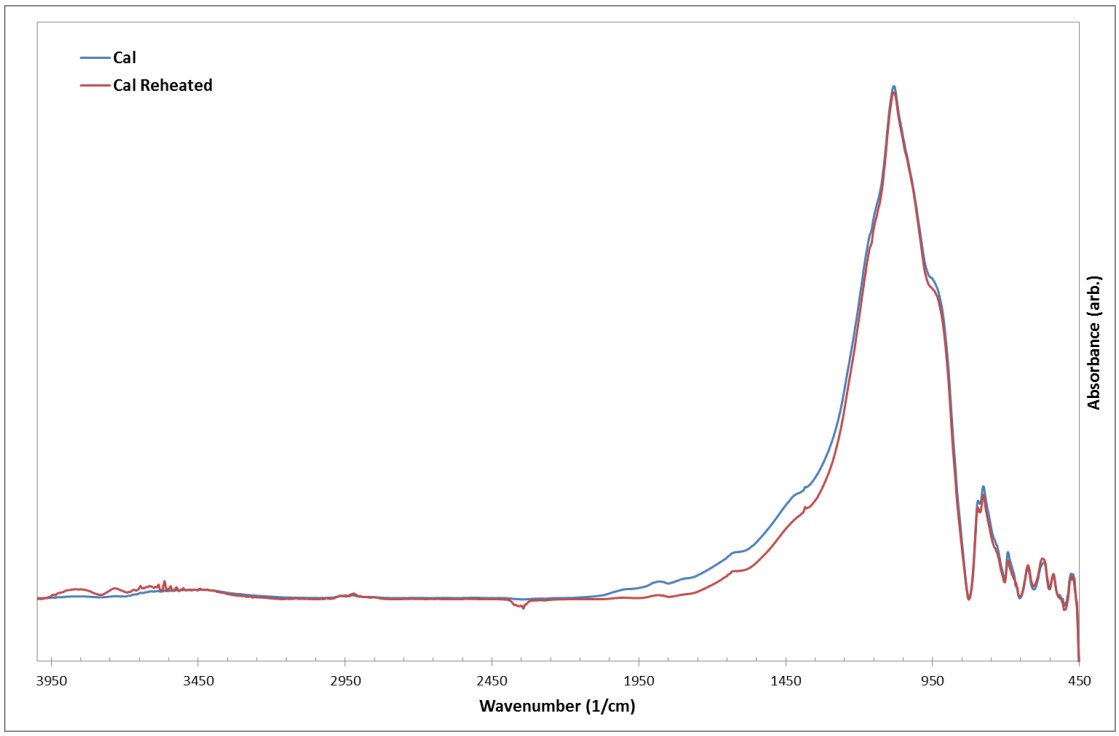

Figure B.37: FTIR Spectra of non-reheated (blue) and reheated (red) *Cal* sample.

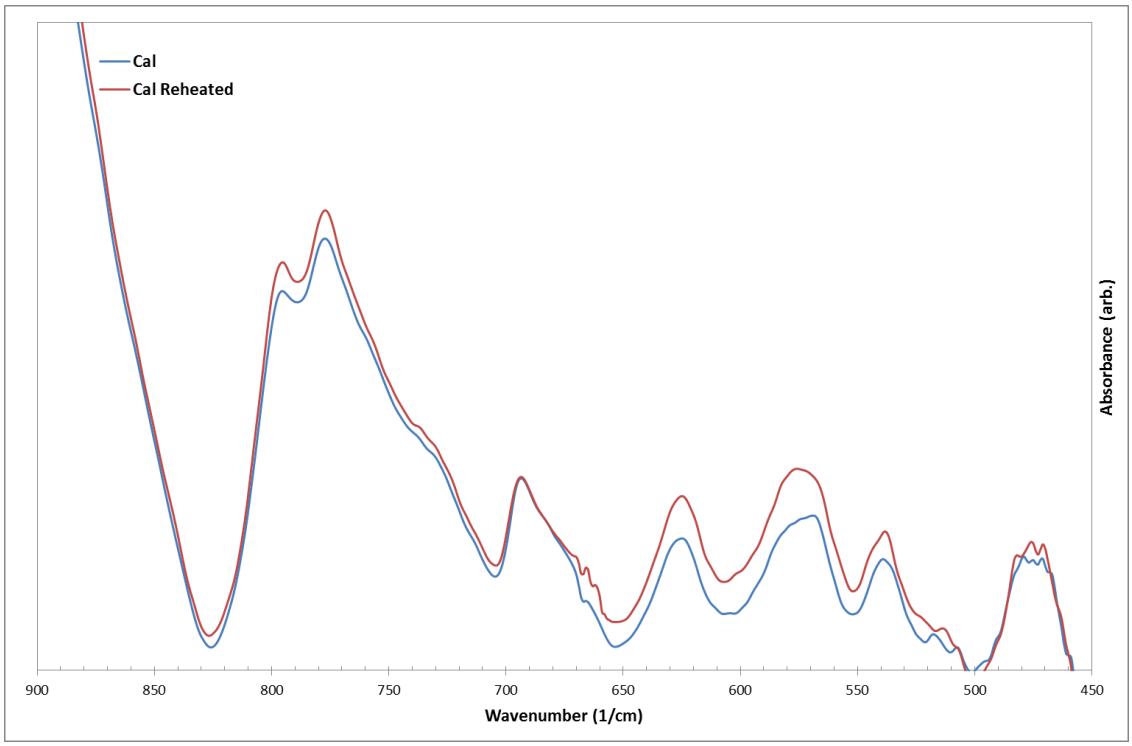

Figure B.38: FTIR spectra of non-reheated (blue) and reheated (red) *Cal* samples over the region 450-900(1/cm).

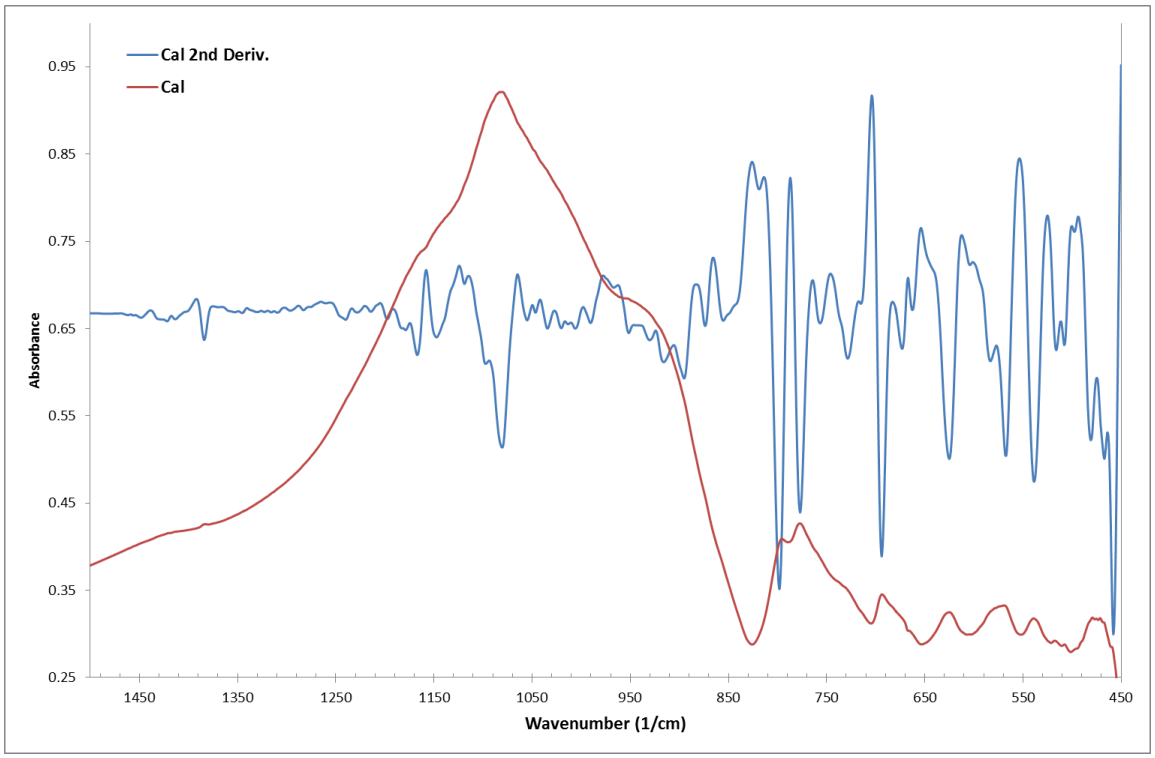

Figure B.39: FTIR spectrum of non-reheated *Cal* sample over region 450-1500 (1/cm) with smoothed second derivative overlaid.

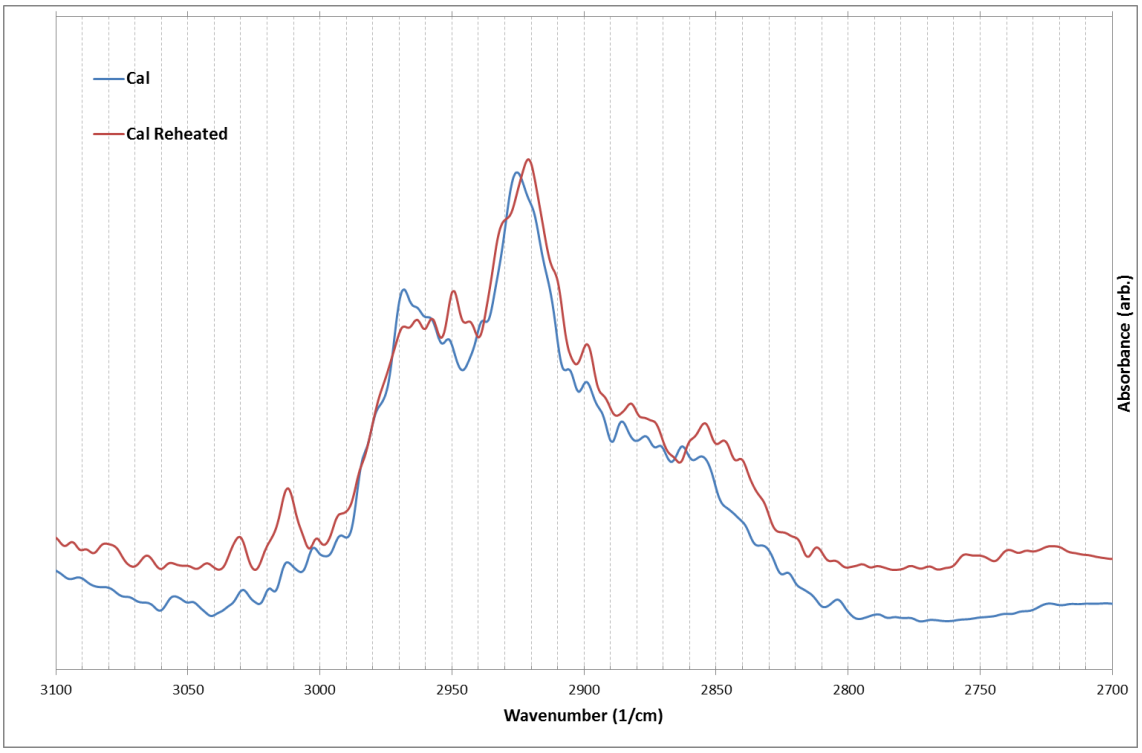

Figure B.40: FTIR spectra across region of interest in organic identification for *Cal* (non-reheated and reheated).

Lan

Table B.11: Mineral identification of diagnostic FTIR peaks for *Lan* samples. Ens=Enstatite, Hem=Hematite, Mic=Microcline, Alb=Albite, Wol=Wollastonite, Qtz=Quartz, Rut=Rutile, Ort=Orthoclase, Ano=Anorthite, Cri=Cristobalite, Geh=Gehlenite, Cal=Calcite, Mul=Mullite, Dol=Dolomite, Oli=Olivine, For=Forsterite, Mus=Muscovite, Bio=Biotite.

Peak At (1/cm)	ID
464.0000	Enst, Hem,Mic,Alb
506.0000	Wol
514.0000	Qtz
525.0000	Rut
536.0000	Hem,Mic,Alb
546.0000	Ort
565.0000	Wol
586.0000	Ort,Mic
606.0000	Mic
619.0000	Ano,Cri
626.0000	Ano
639.0000	Qtz
650.0000	Alb,Ort,Mic
662.0000	Ano
674.0000	Geh
714.0000	Cal
730.0000	Dol,Mul
757.0000	Ano
843.0000	Dol
875.0000	Cal
901.0000	Ens, Wol
952.0000	Oli,For
988.0000	Mus
1000.0000	Bio,For
1011.0000	Mic,Geh
1039.0000	Ort
1048.0000	Mic,Hem
1081.0000	Qtz
1098.0000	Alb,Cri
1128.0000	Ort
1138.0000	Ano

1420.0000	Cal
1798.0000	Cal
2516.0000	Cal

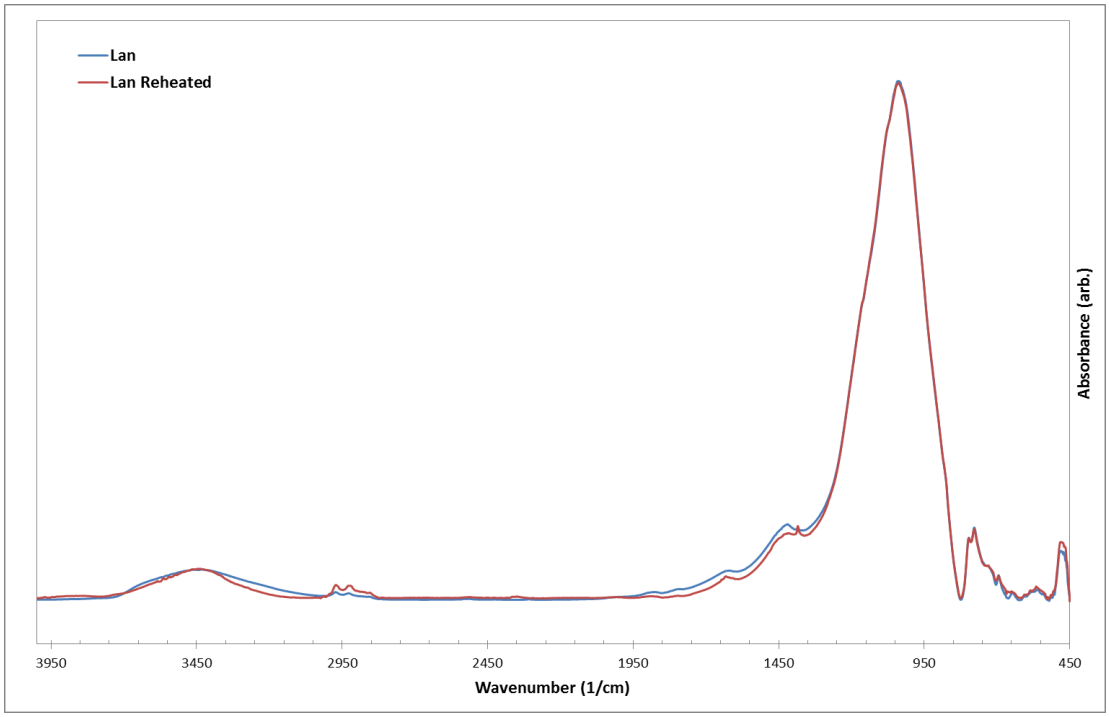

Figure B.41: FTIR Spectra of non-reheated (blue) and reheated (red) *Lan* sample.

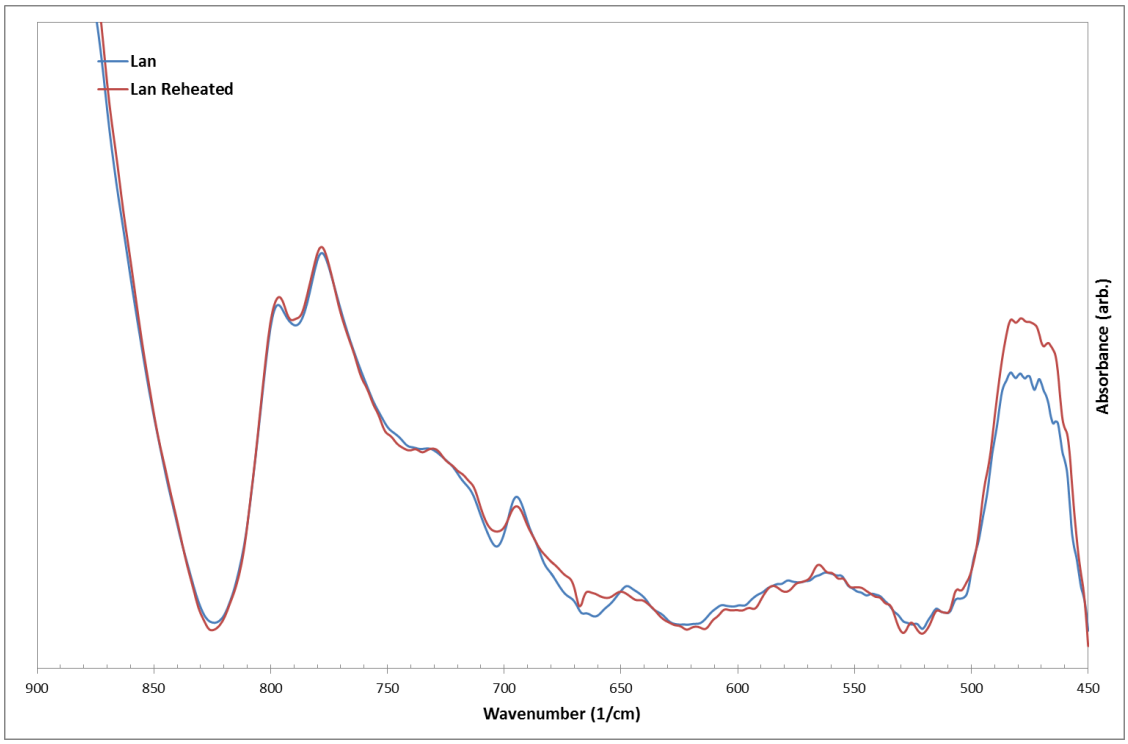

Figure B.42: FTIR spectra of non-reheated (blue) and reheated (red) *Lan* samples over the region 450-900(1/cm).

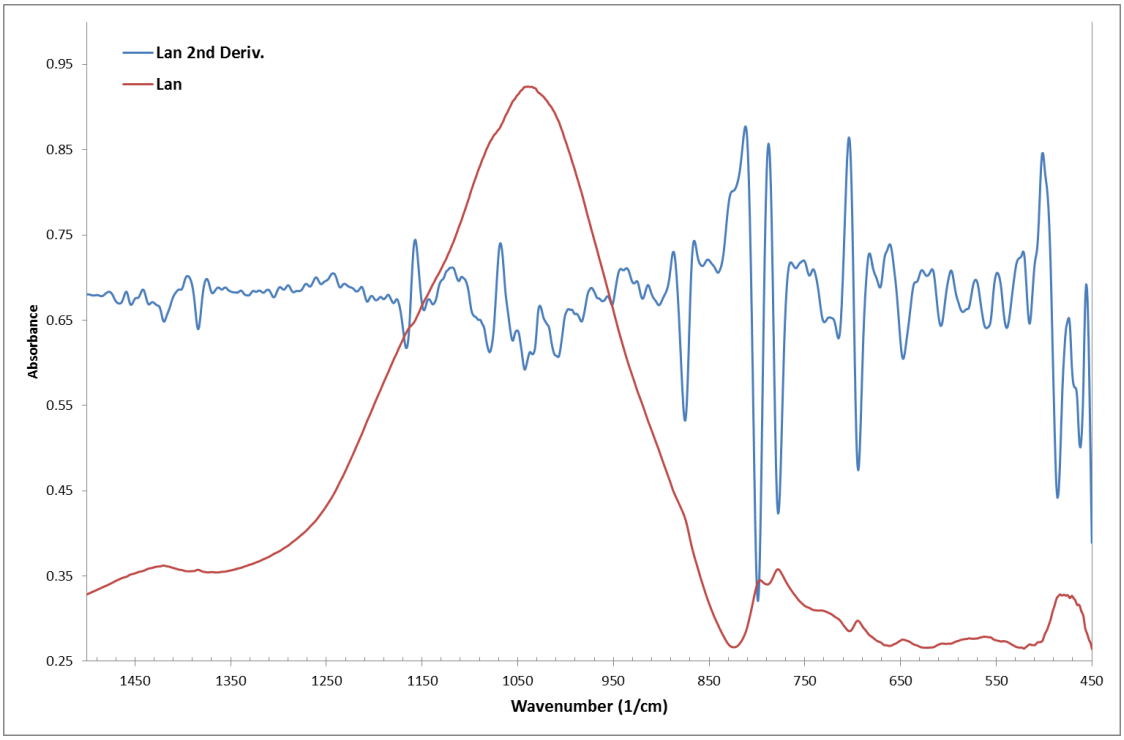

Figure B.43: FTIR spectrum of non-reheated *Lan* sample over region 450-1500 (1/cm) with smoothed second derivative overlaid.

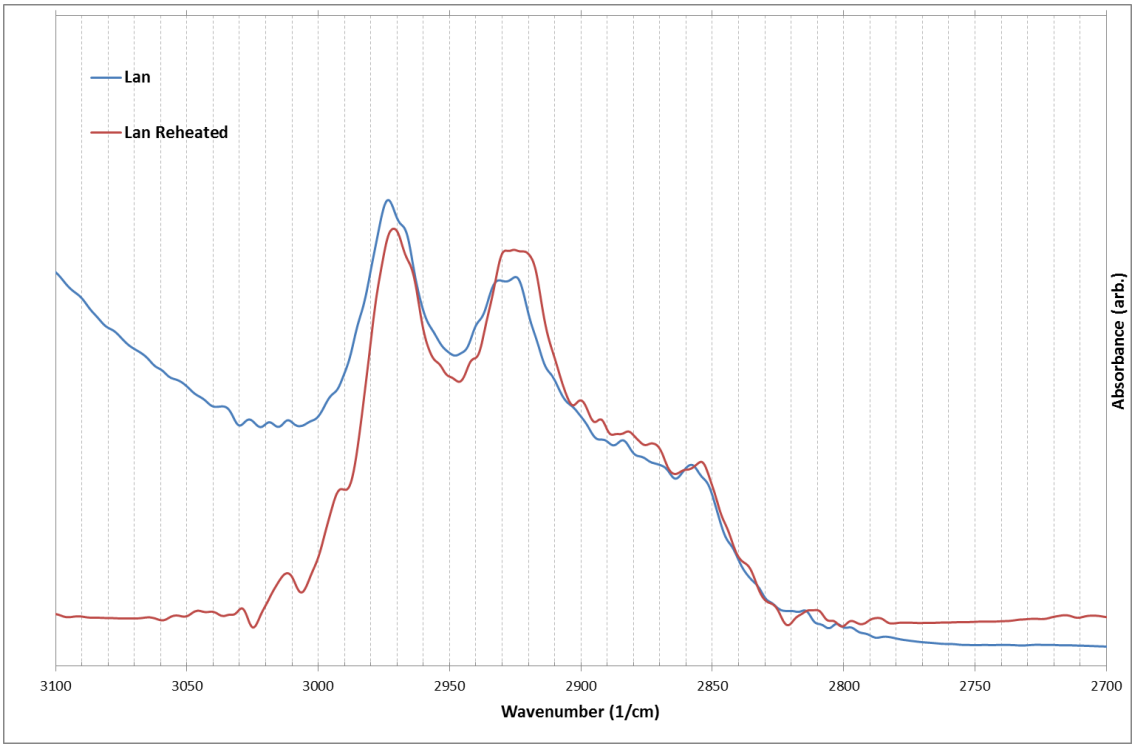

Figure B.44: FTIR spectra across region of interest in organic identification for *Lan* (non-reheated and reheated).

Joy

Table B.12 Mineral identification of diagnostic FTIR peaks for *Joy* samples. Qtz=Quartz, Ano=Anorthite, Mul=Mullite, Ens=Enstatite, Mul=Mullite, For=Forsterite, Hem=Hematite, Wol=Wollastonite, Mic=Microcline, Geh=Gehlenite, Rut=Rutile.

Peak At (1/cm)	ID
458.0000	Qtz
482.0000	Ano,Mul
502.0000	Ens,For
518.0000	Qtz
563.0000	Hem,Ens,Woll
570.0000	Mic
581-582	Mic
605.0000	Mic,For
633-634	Geh,Hem
647.0000	Woll, Mic,Ens,Hem
662.0000	Ano
674.0000	Geh
695.0000	Qtz
729-731	Rut,Mul
778.0000	Qtz
799.0000	Qtz
930.000	Wol,Ano, Geh
1037.0000	Alb,Geh
1052.0000	Mic
1062.0000	Mus,Ano
1078.0000	Ano,Ens,Woll
1086.0000	Qtz
1091.0000	Mic,Ano,Woll

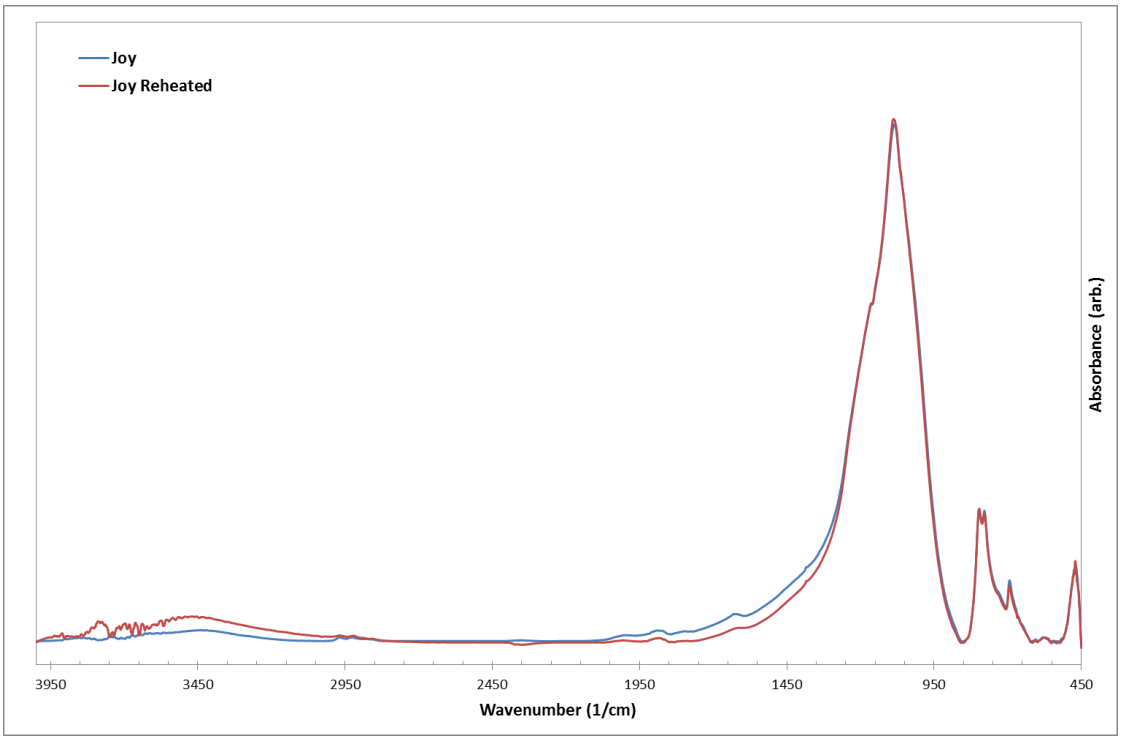

Figure B.45: FTIR Spectra of non-reheated (blue) and reheated (red) *Joy* sample.

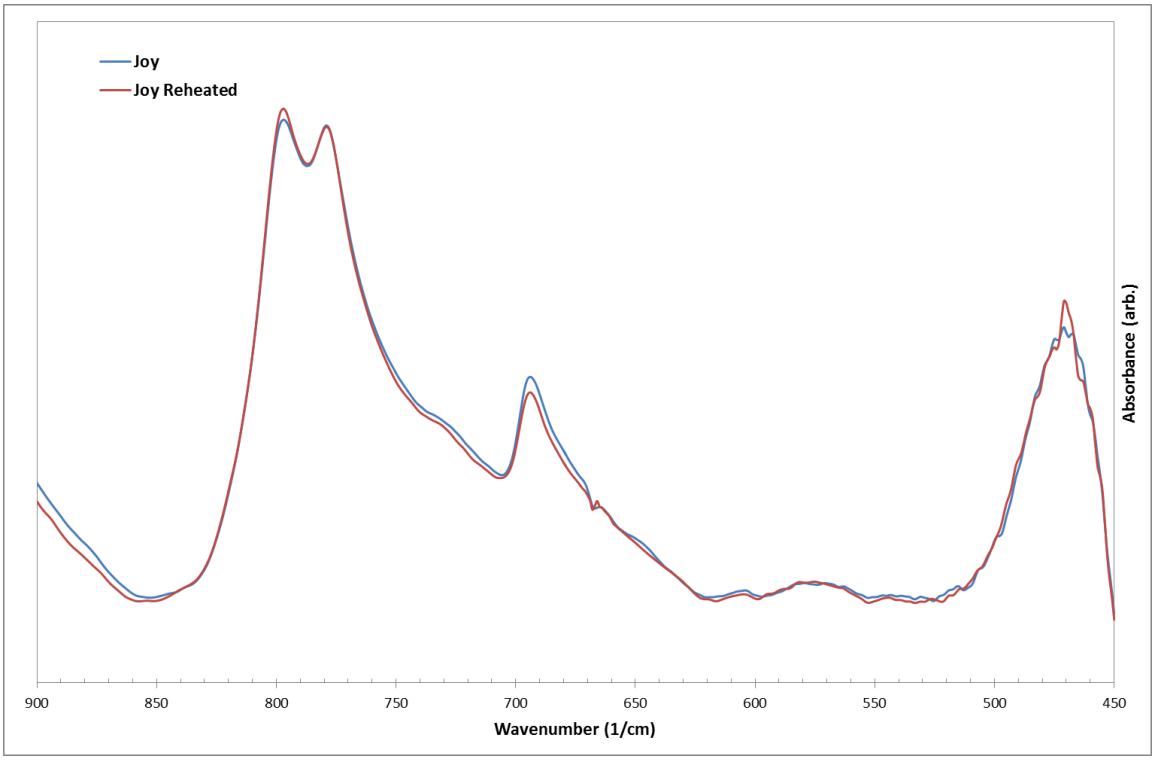

Figure B.46: FTIR spectra of non-reheated (blue) and reheated (red) *Joy* samples over the region 450-900(1/cm).

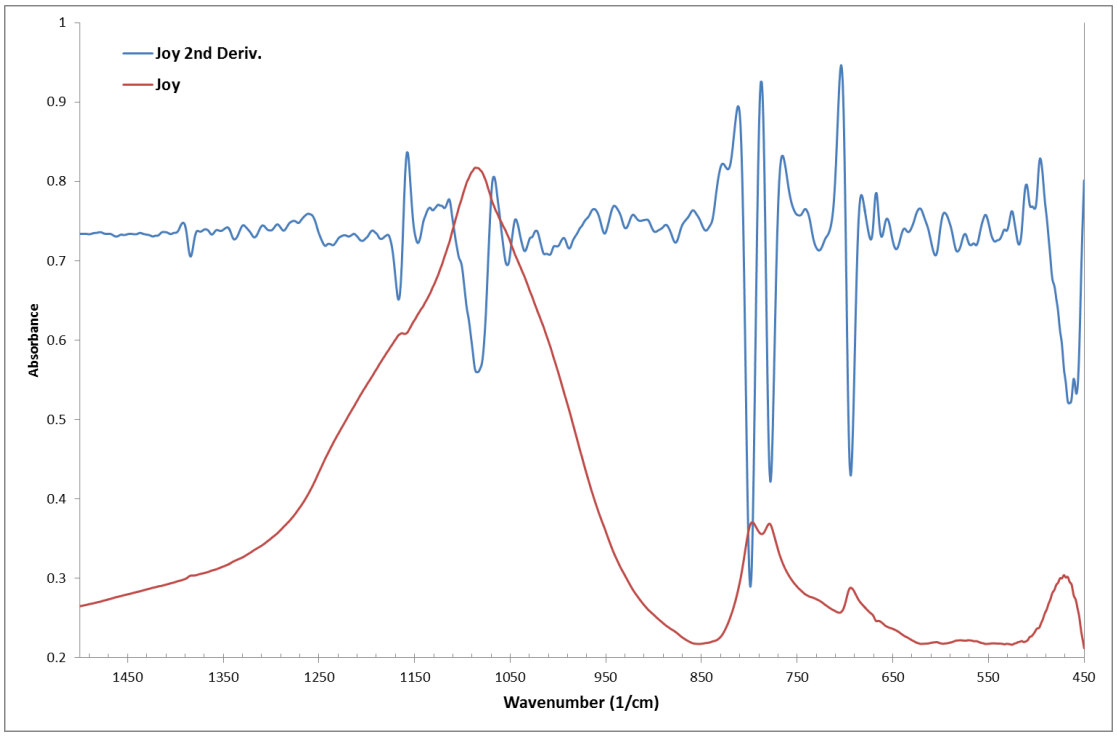

Figure B.47: FTIR spectrum of non-reheated *Joy* sample over region 450-1500 (1/cm) with smoothed second derivative overlaid.

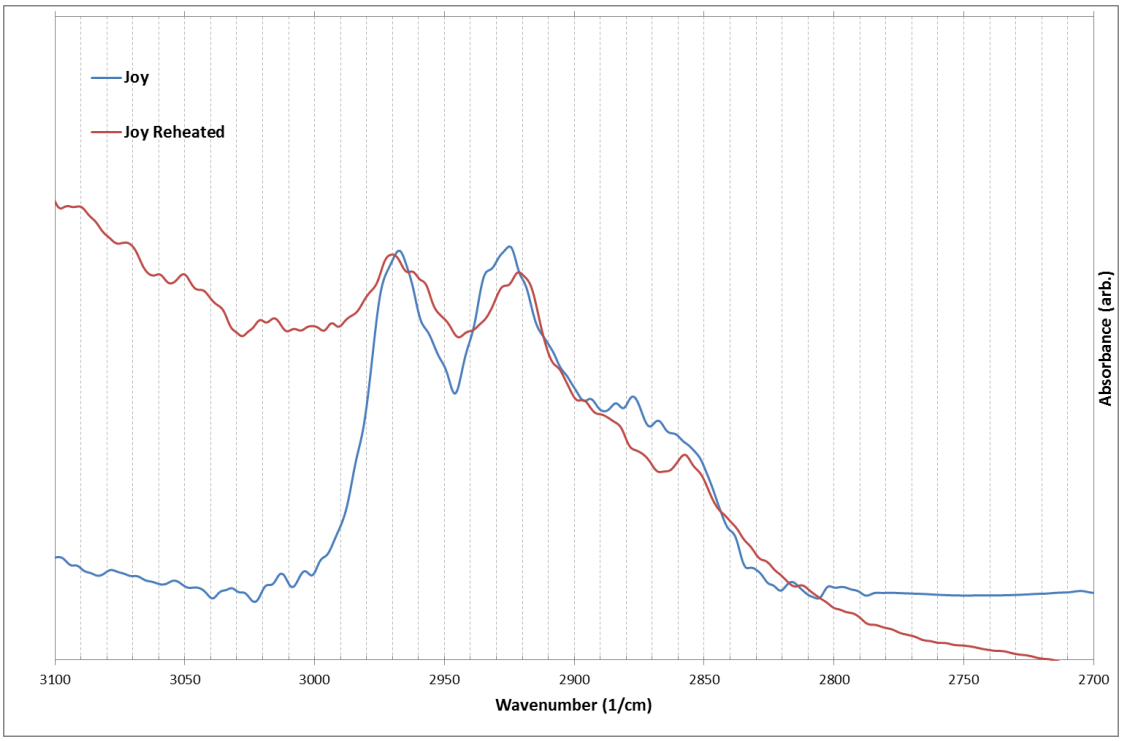

Figure B.48: FTIR spectra across region of interest in organic identification for *Joy* (non-reheated and reheated).

Cau

Table B.13: Mineral identification of diagnostic FTIR peaks for *Cau* samples. Qtz=Quartz, Hem=Hematite, Alb=Albite, Mic=Microcline, Bio=Biotite, Cal=Calcite, Aug=Augite, Ens=Enstatite, Org=Organic.

Peak At (1/cm)	ID
461.0000	Qtz
472.0000	Water
514.0000	Qtz
563.0000	Hem
650.0000	Alb,Mic,Bio
694.0000	Qtz
779.0000	Qtz
799.0000	Qtz
876.0000	Cal,Aug
1049.0000	Hem, Mic
1059.0000	Org,Cal,Ens
1080.0000	Mic

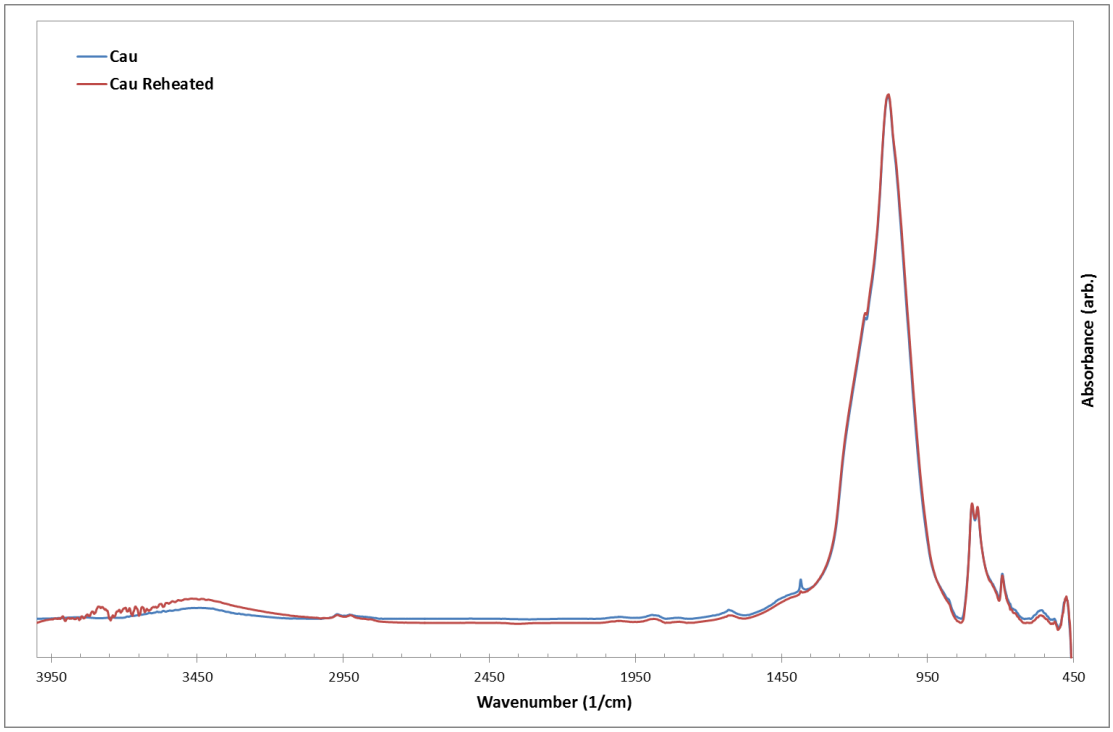

Figure B.49: FTIR Spectra of non-reheated (blue) and reheated (red) *Cau* sample.

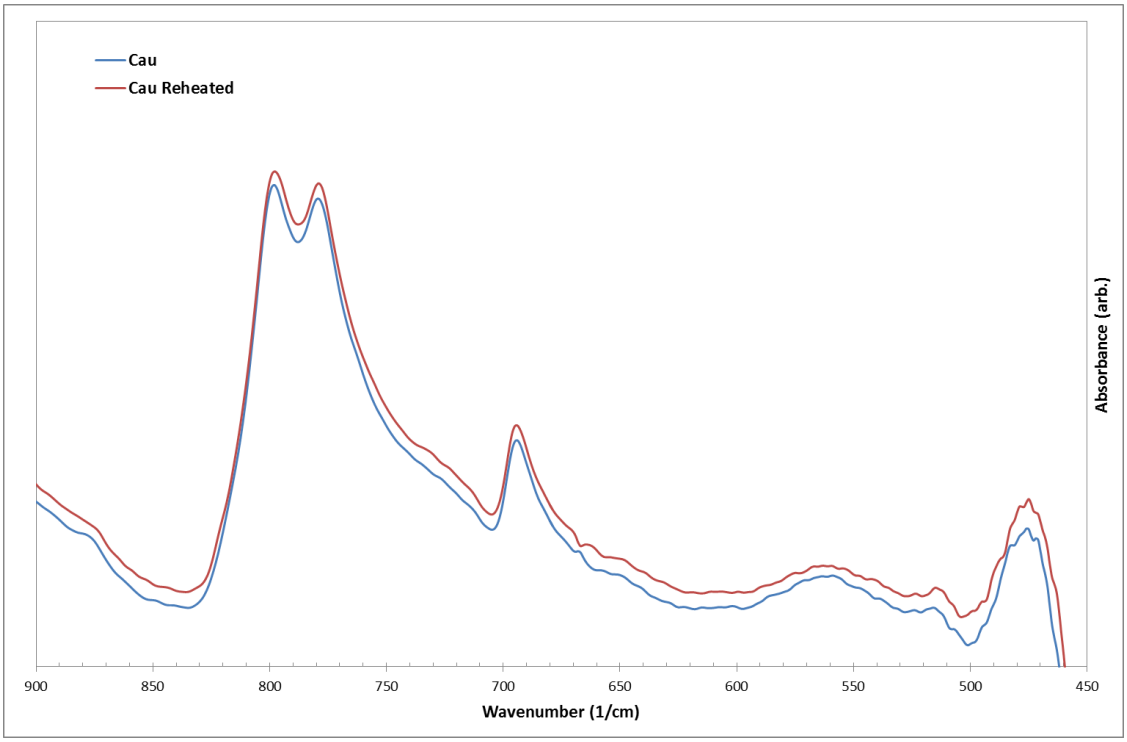

Figure B.50: FTIR spectra of non-reheated (blue) and reheated (red) *Cau* samples over the region 450-900(1/cm).

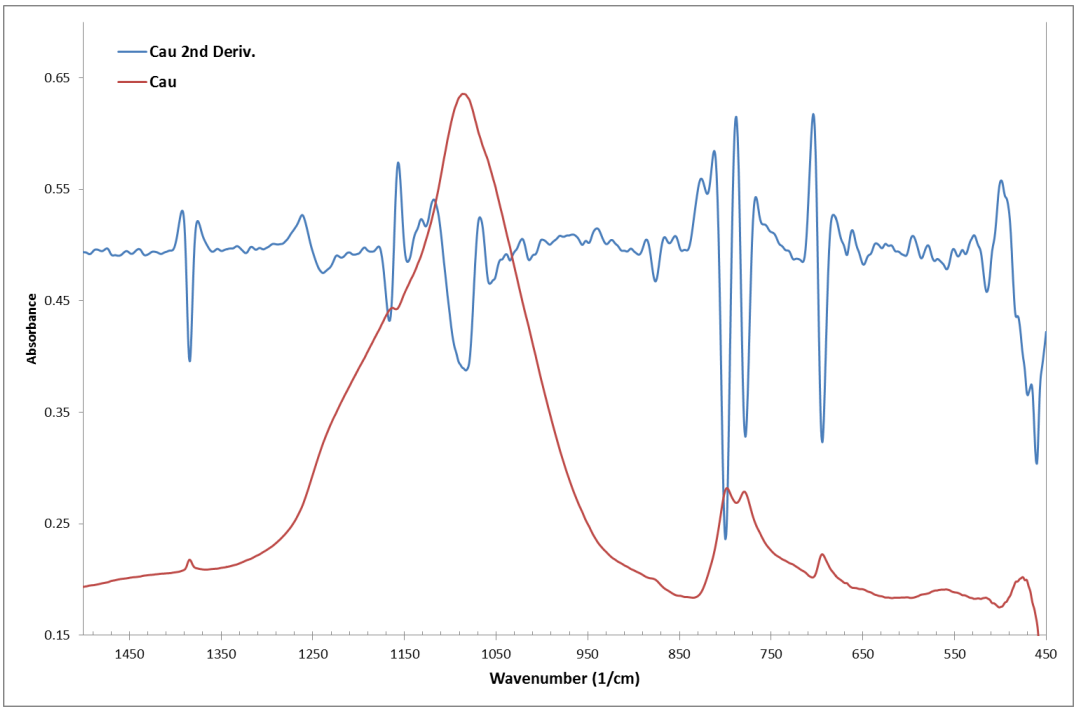

Figure B.51: FTIR spectrum of non-reheated *Cau* sample over region 450-1500 (1/cm) with smoothed second derivative overlaid.

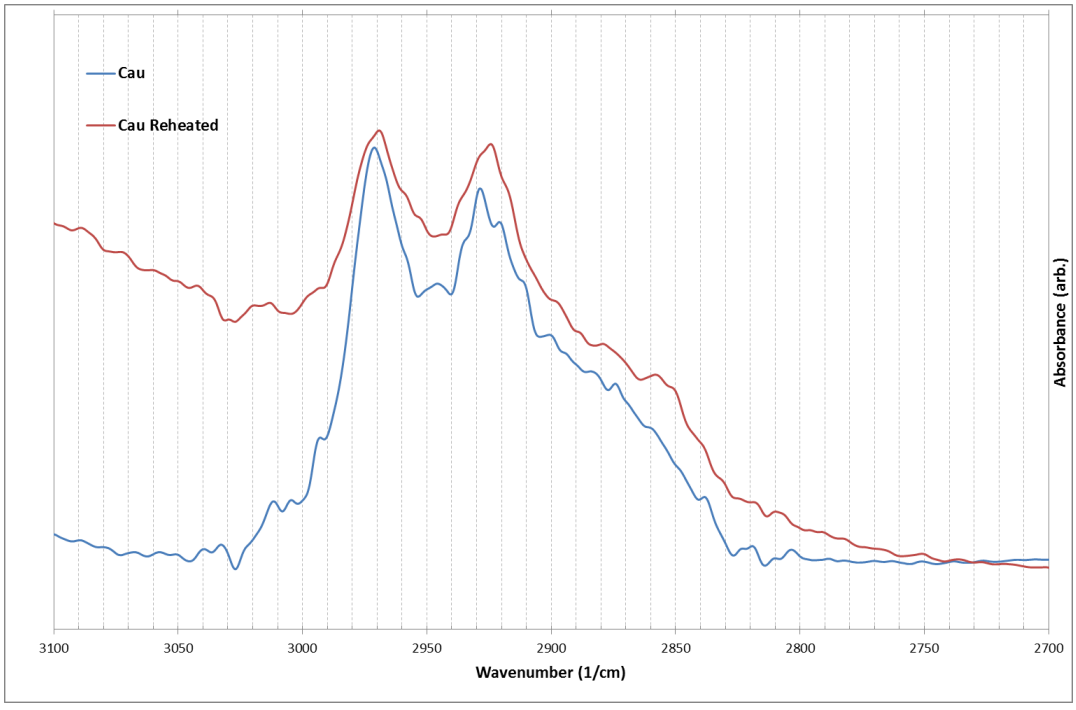

Figure B.52: FTIR spectra across region of interest in organic identification for *Cau* (non-reheated and reheated).

Bel

Table B.14: Mineral identification of diagnostic FTIR peaks for *Bel* samples. Hem=Hematite, Alb=Albite, Qtz=Quartz, Mic=Microcline, Anh=Anhydrite, Bas=Bassanite, Gyp=Gypsum, Spi=Spinel, Bio=Biotite.

Peak At	ID
473.0000	Water
480.0000	Hem,Alb
513.0000	Qtz
538.0000	Mic
594.0000	Anh,Alb
596.0000	Anh
614.0000	Anh,Alb
633.0000	Bas
649.0000	Mic, Alb
669.0000	Gyp
680.0000	Spi
694.0000	Qtz
729.0000	Mic, Bio
778.0000	Qtz
799.0000	Qtz
1014.0000	Alb
1037.0000	Alb
1056.0000	Mic
1076.0000	Ens
1085.0000	Qtz
1099.0000	Alb
1121.0000	Mic,Hem,Anh
1137.0000	Mic
1151-1154	Bas, Anh
1165.0000	Qtz
1619.0000	Bas

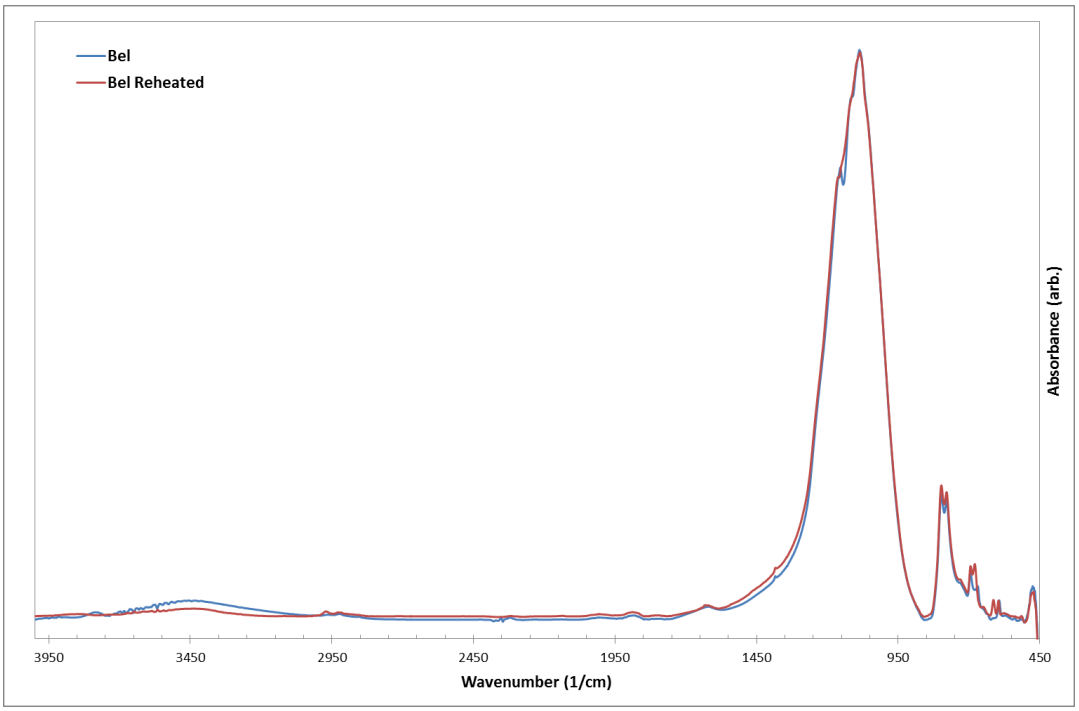

Figure B.53: FTIR Spectra of non-reheated (blue) and reheated (red) *Bel* sample.

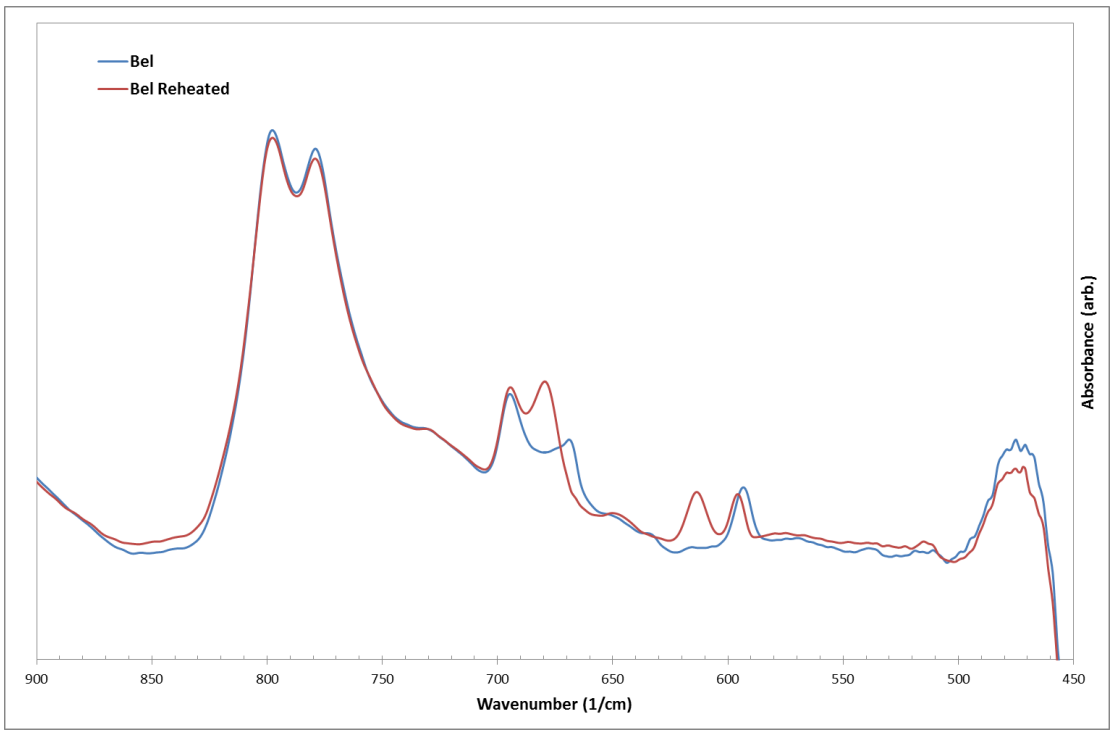

Figure B.54: FTIR spectra of non-reheated (blue) and reheated (red) *Bel* samples over the region 450-900(1/cm).

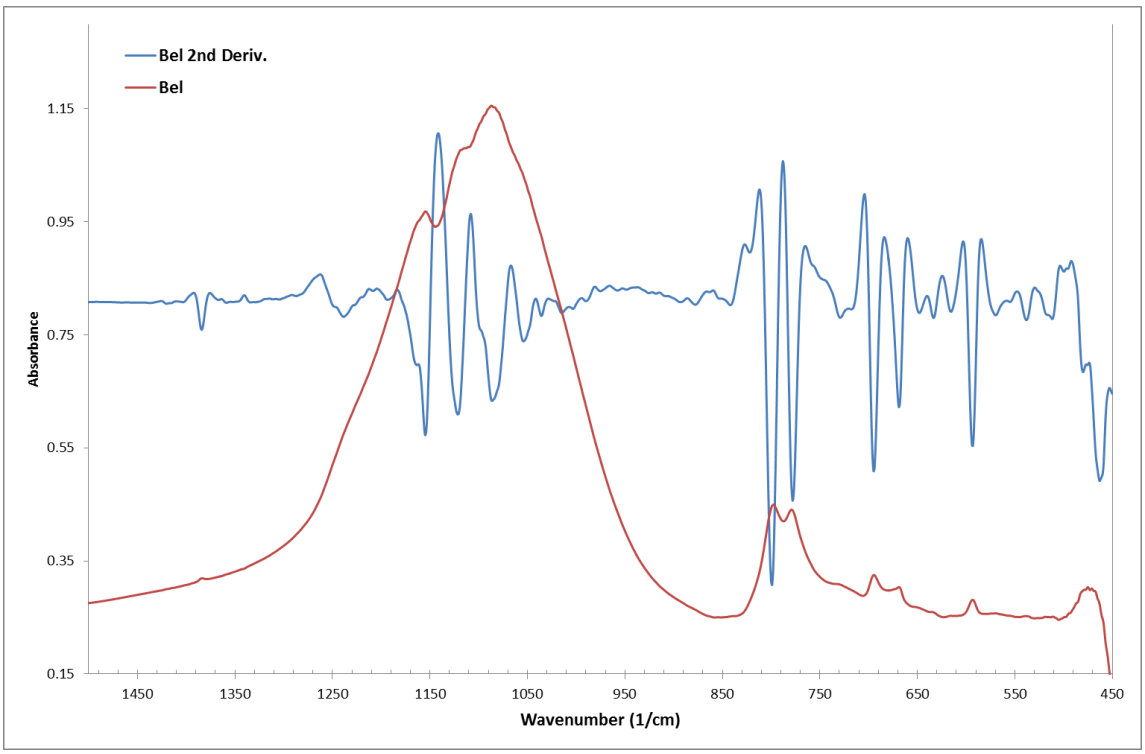

Figure B.55: FTIR spectrum of non-reheated *Bel* sample over region 450-1500 (1/cm) with smoothed second derivative overlaid.

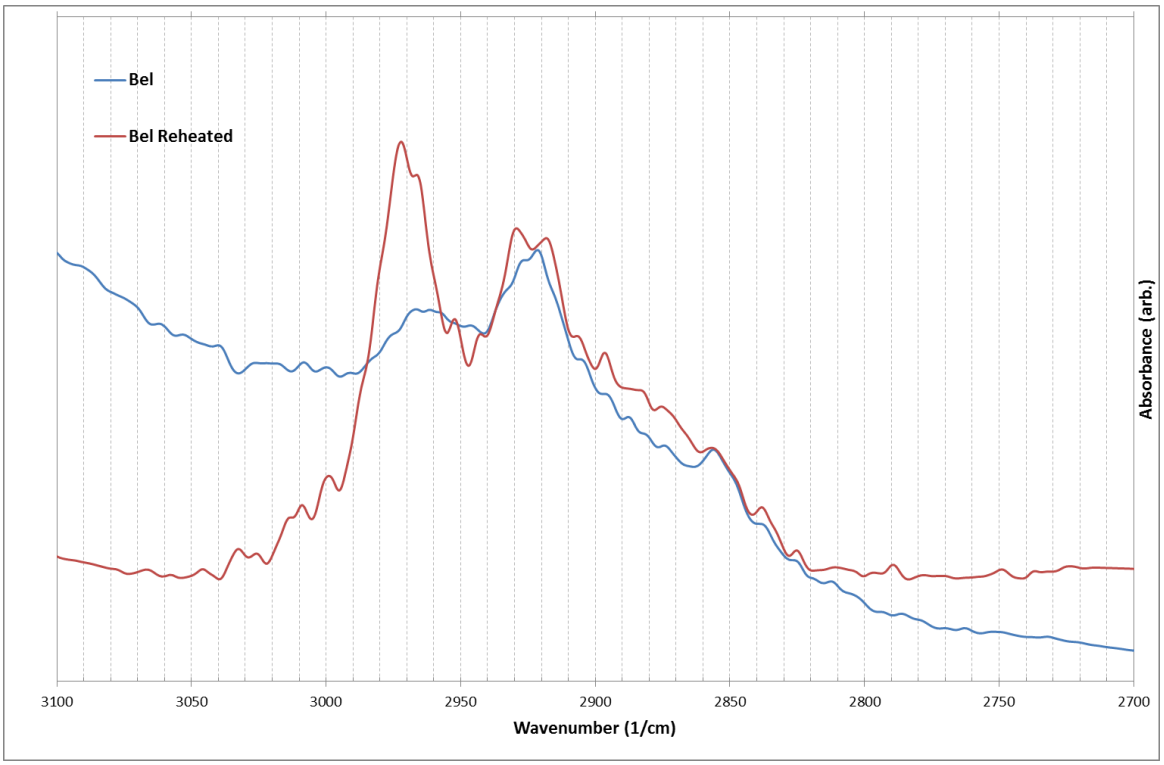

Figure B.56: FTIR spectra across region of interest in organic identification for *Bel* (non-reheated and reheated).

Dow1

Table B.15: Mineral identification of diagnostic FTIR peaks for *Dow1* samples. Qtz=Quartz, Ano=Anorthite, Cri=Cristobalite, Geh=Gehlenite, Cal=Calcite, Dol=Dolomite, For=Forsterite, Ens=Enstatite, Oli=Olivine, Mic=Microcline.

Peak At	ID
474.0000	Water
508-510	Qtz
538.0000	Ano
614.0000	Cri
663.0000	Ano
674.0000	Geh
695.0000	Qtz
714.0000	Cal
731.0000	Dol
778.0000	Qtz
799.0000	Qtz
841.0000	For,Dol
860.0000	Ens
876-877	Cal
961.0000	Enst
986.0000	For,Oli
1010.0000	Mic
1059.0000	Cal
1096.0000	Cri
1165.0000	Qtz
1422.0000	Cal
1454.0000	Cal
1799.0000	Cal
2515.0000	Cal

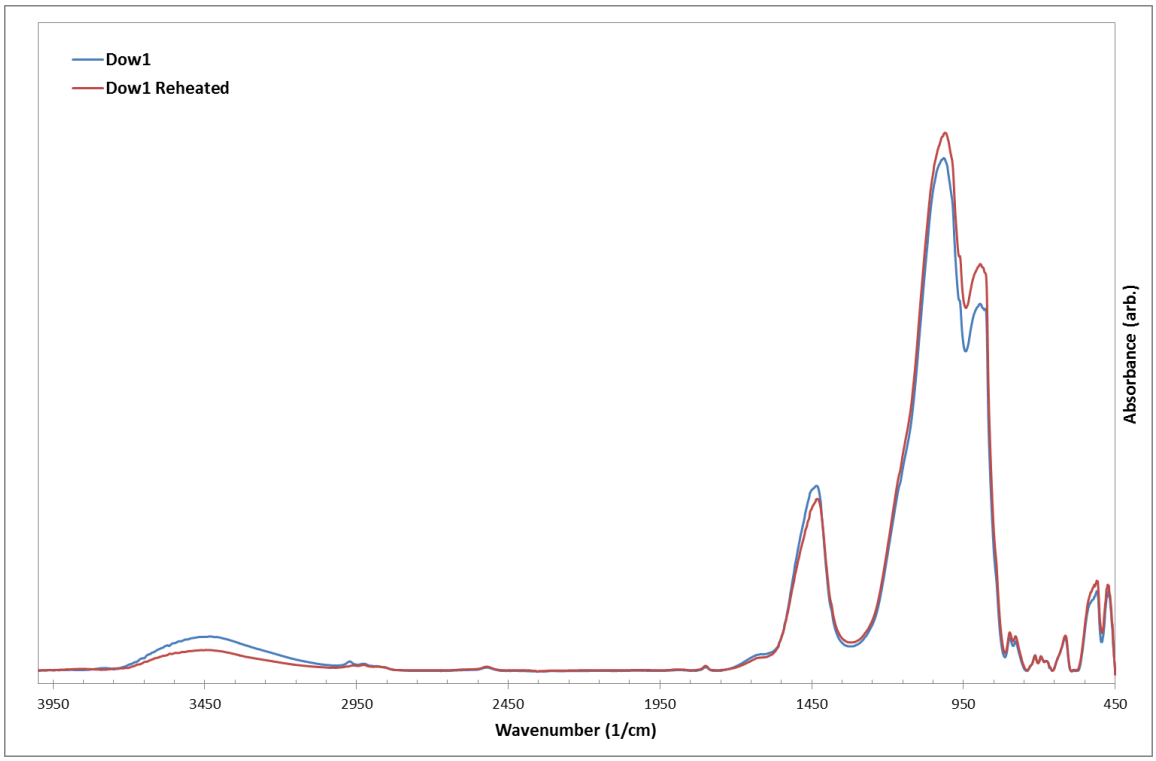

Figure B.57: FTIR Spectra of non-reheated (blue) and reheated (red) *Dow1* sample.

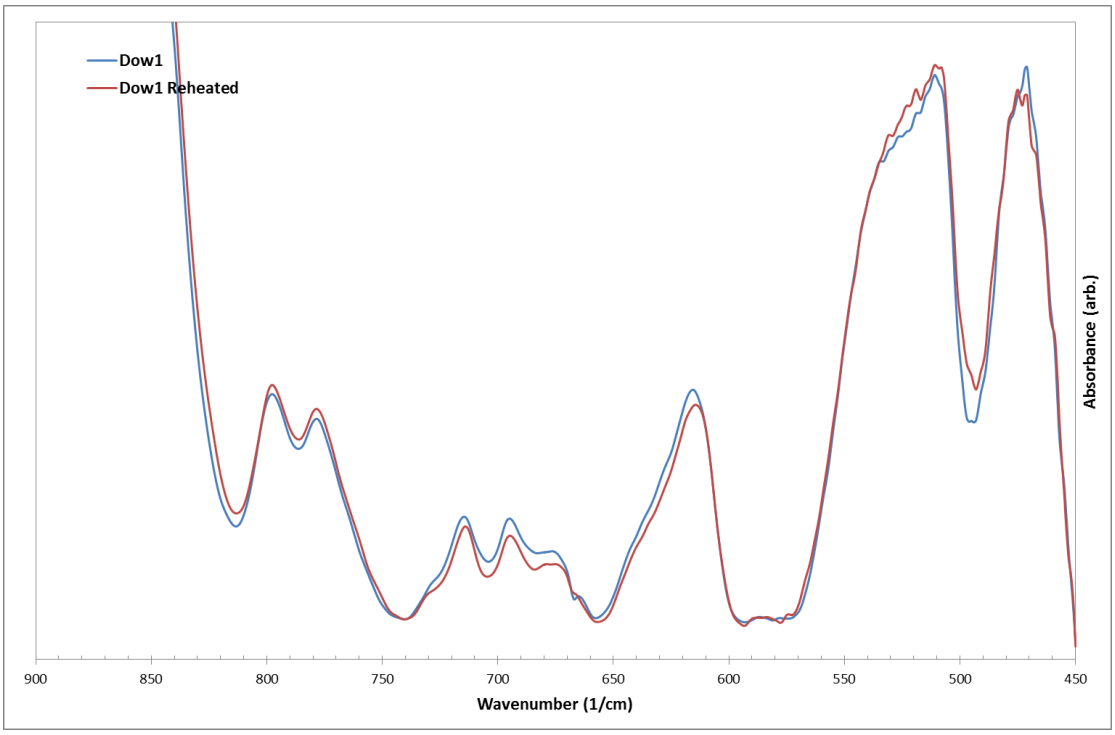

Figure B.58: FTIR spectra of non-reheated (blue) and reheated (red) Dow1 samples over the region 450-900(1/cm).

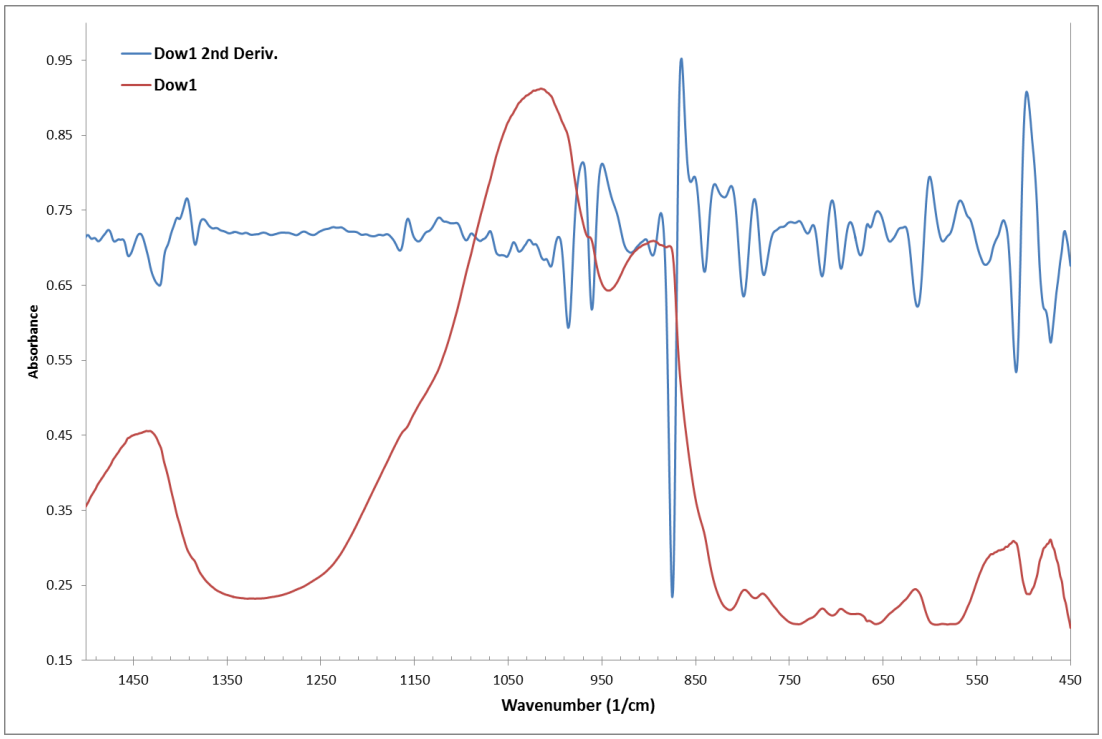

Figure B.59: FTIR spectrum of non-reheated *Dow1* sample over region 450-1500 (1/cm) with smoothed second derivative overlaid.

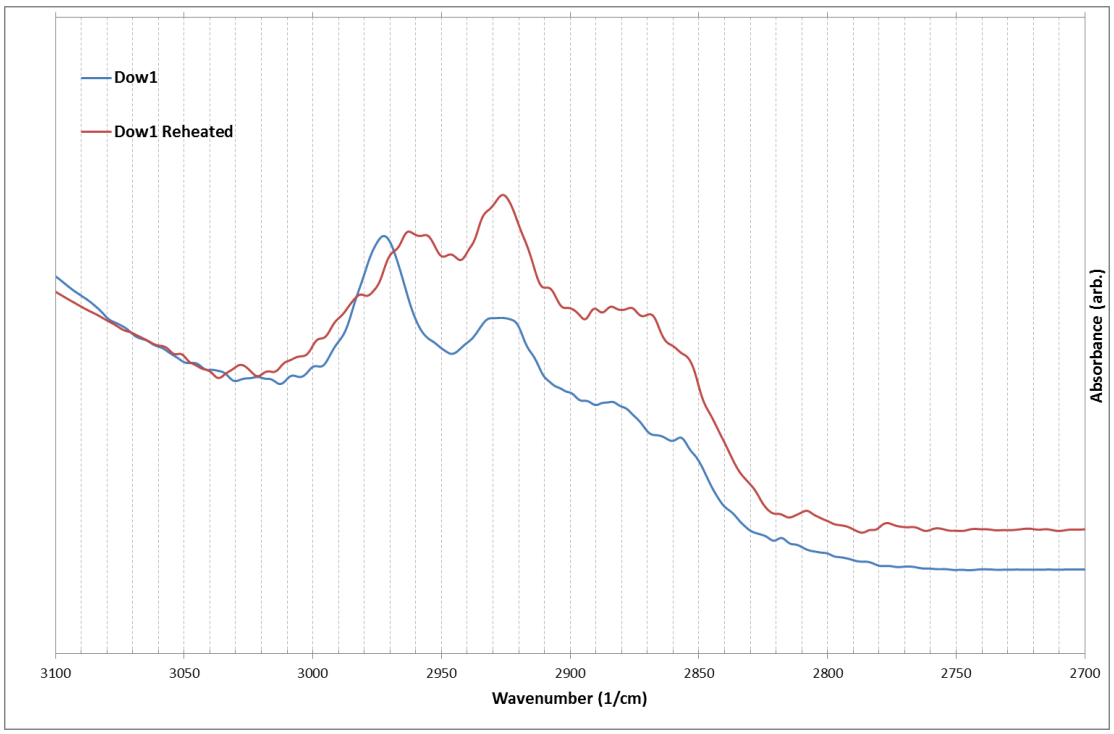

Figure B.60: FTIR spectra across region of interest in organic identification for *Dow1* (non-reheated and reheated).

Dow2

Table B.16: Mineral identification of diagnostic FTIR peaks for *Dow2* samples. Qtz=Quartz, Mul=Mullite, Ano=Anorthite, Mic=Microline, For=Forsterite, Alb=Albite, Wol=Wollastonite, Cri=Cristobalite, Ill=Illite, Ana=Anatase, Ort=Orthoclase, Dio=Diopside, Geh=Gehlenite, Cal=Calcite, Dol=Dolomite, Ens=Enstatite, Bio=Biotite.

Peak At (1/cm)	ID
460.0000	Qtz
467.0000	Mul,Ano,Mic,For
481.0000	Mul,Alb,Wol,Ano,Cri
507.0000	For,Mul
511.0000	Qtz
515.0000	Qtz
527.0000	Ill
541.0000	Ano,Mic,Ana,Mul,Ort
552.0000	Ana
560.0000	Mul,Ill
581.0000	Ort,Mic
587-590.0000	Mic,Ort
610.0000	Mic, Ana
633.0000	Dio
646.0000	Mic,Ort
662.0000	Ano
674.0000	Dio,Geh
683.0000	Ano,Woll
695.0000	Qtz
715.0000	Cal
731.0000	Mul
757.0000	Ano
777.0000	Qtz
797.0000	Qtz
859.0000	Geh
876.0000	Cal
960.0000	Ens
972.0000	Bio,Geh
985.0000	For,Geh,Ano
1004.0000	Ort,For

1015.0000	Ort
1033-1036	Ort
1055-1056	Geh
1073-1075	Dio
1084.0000	Qtz
1149.0000	Alb
1166.0000	Qtz
1422.0000	Cal
1459.0000	Cal,Dol
1790.0000	Cal
1799.0000	Cal
1806.0000	Dol
1827.0000	Dol
2511.0000	Cal
2522.0000	Dol
2530.0000	Dol
2879.0000	Cal

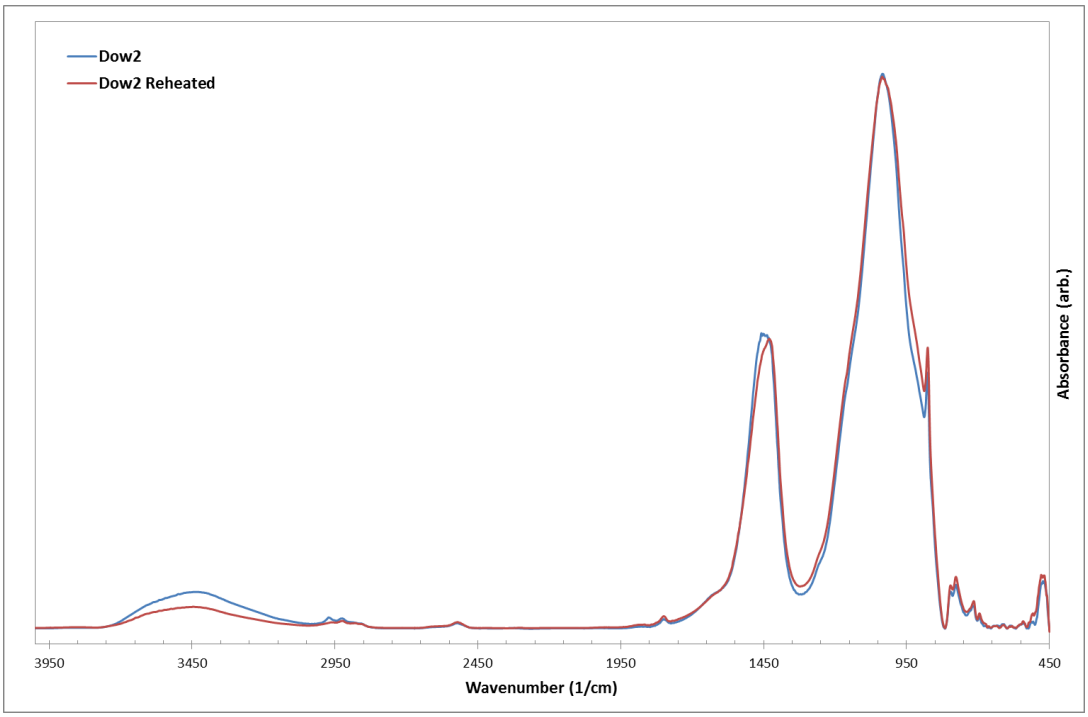

Figure B.61: FTIR Spectra of non-reheated (blue) and reheated (red) *Dow2* sample.

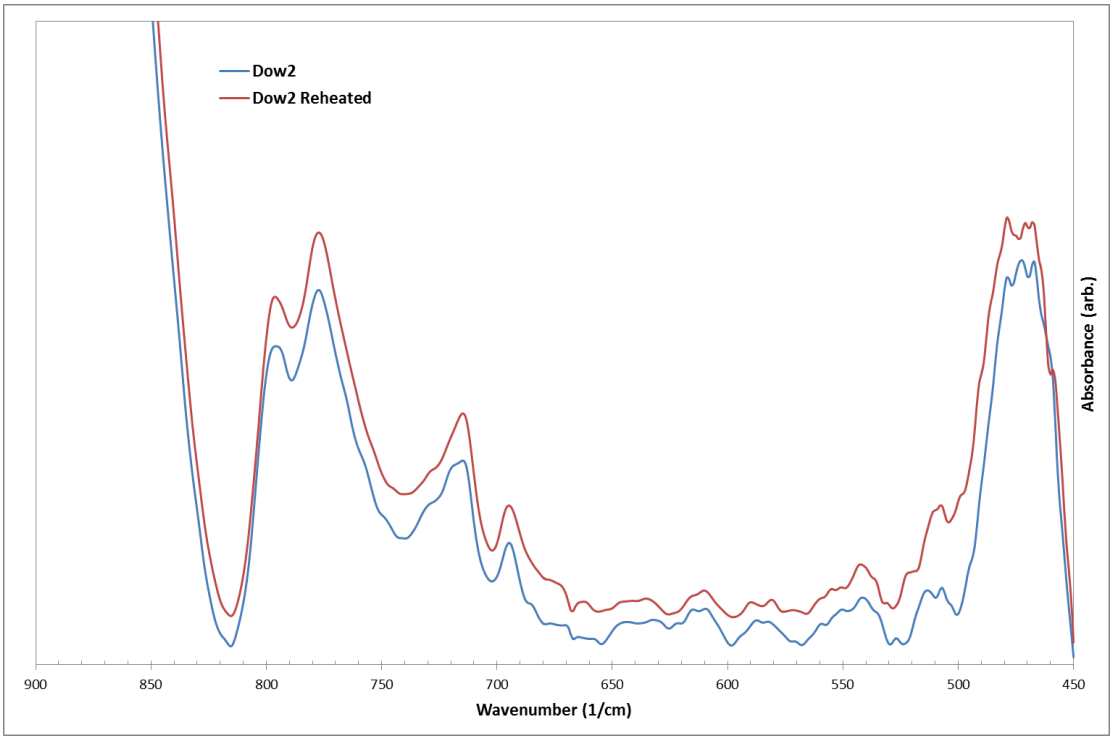

Figure B.62: FTIR spectra of non-reheated (blue) and reheated (red) *Dow2* samples over the region 450-900(1/cm).

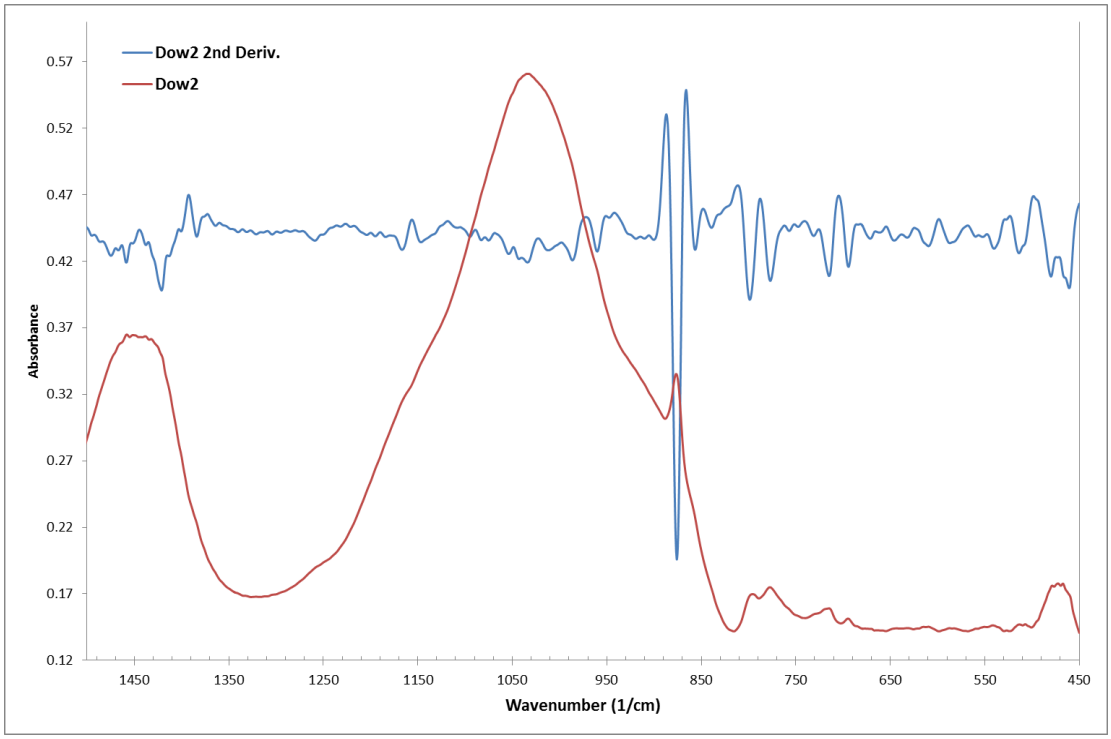

Figure B.63: FTIR spectrum of non-reheated *Dow2* sample over region 450-1500 (1/cm) with smoothed second derivative overlaid.

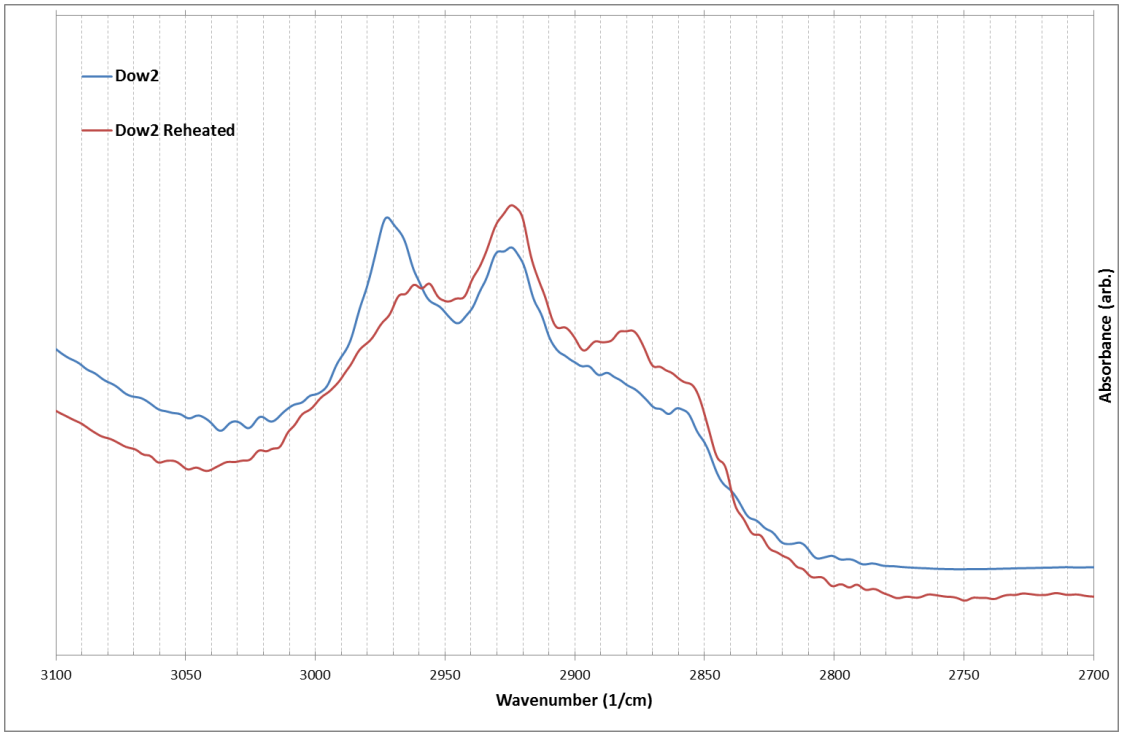

Figure B.64: FTIR spectra across region of interest in organic identification for *Dow2* (non-reheated and reheated).

Tur

Table B.17: Mineral identification of diagnostic FTIR peaks for *Tur* samples. Qtz=Quartz, Mic=Microcline, Mul=Mullite, Spi=Spinel, Wol=Wollastonite, Ort=Orthoclase, Cri=Cristobalite, Cal=Calcite.

Peak At (1/cm)	ID
461.0000	Qtz
471.0000	Mic
517.0000	Qtz
539.0000	Mic,Mul
578.0000	Mic,Spi
589.0000	Mic
607.0000	Mic
649.0000	Mic,Wol
694.0000	Qtz
731.0000	Mul,Mic
778.0000	Qtz
798.0000	Qtz
998.0000	Mic
1038.0000	Ort
1058.0000	Wol
1078.0000	Wol
1088.0000	Mic,Cri,Wol
1114.0000	Mic
1135.0000	Mic
1166.0000	Qtz
1453.0000	Cal
1469.0000	Cal

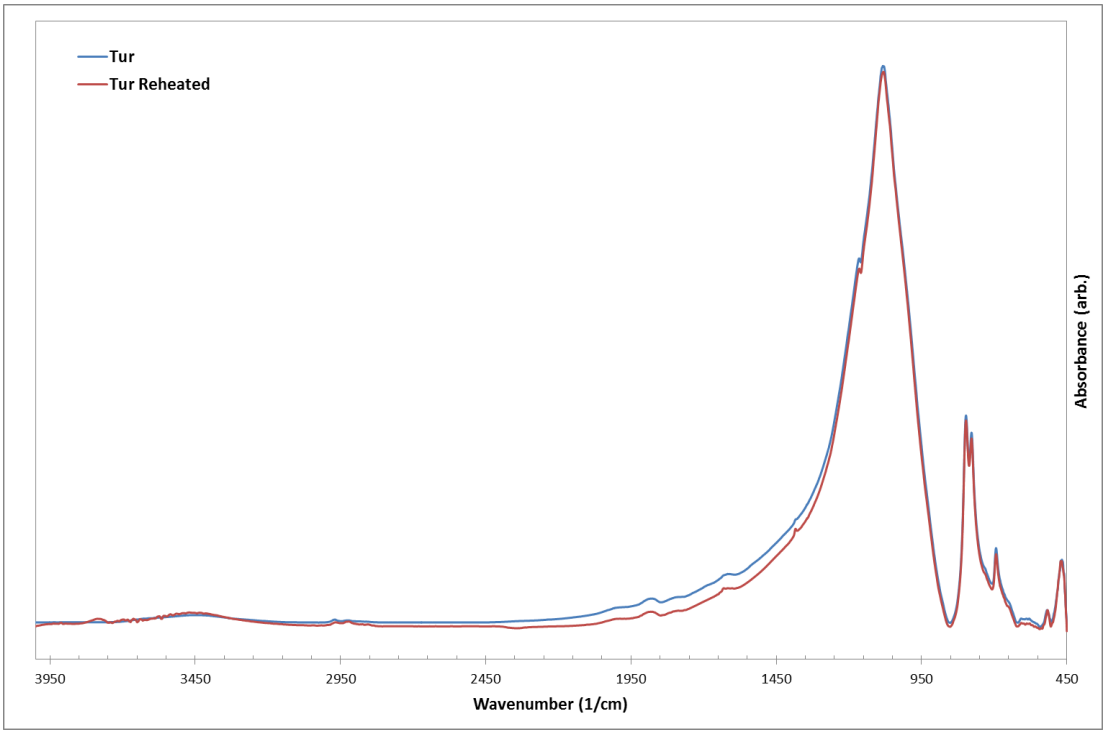

Figure B.65: FTIR Spectra of non-reheated (blue) and reheated (red) *Tur* sample.

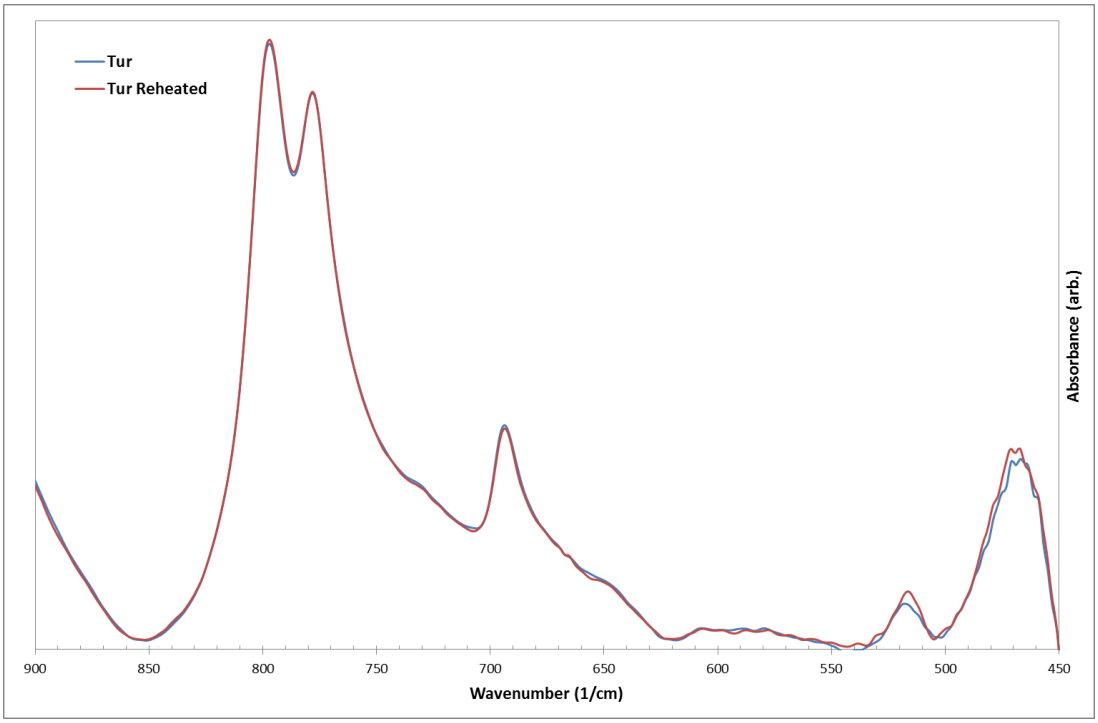

Figure B.66: FTIR spectra of non-reheated (blue) and reheated (red) *Tur* samples over the region 450-900(1/cm).

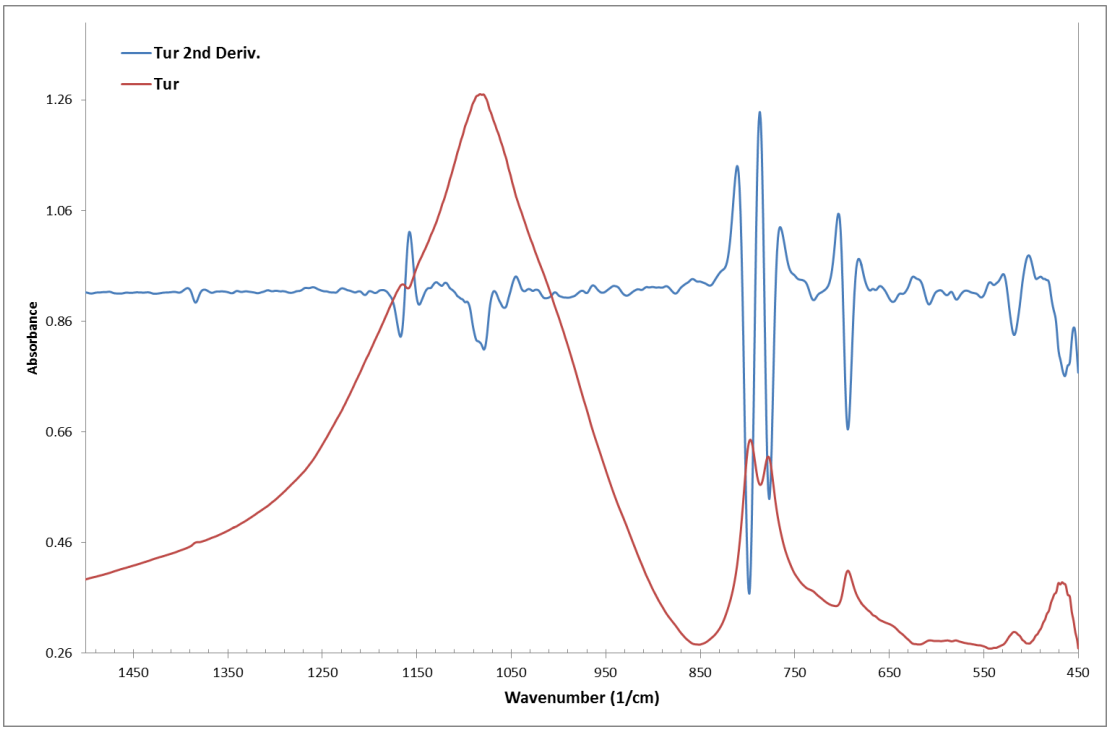

Figure B.67: FTIR spectrum of non-reheated *Tur* sample over region 450-1500 (1/cm) with smoothed second derivative overlaid.

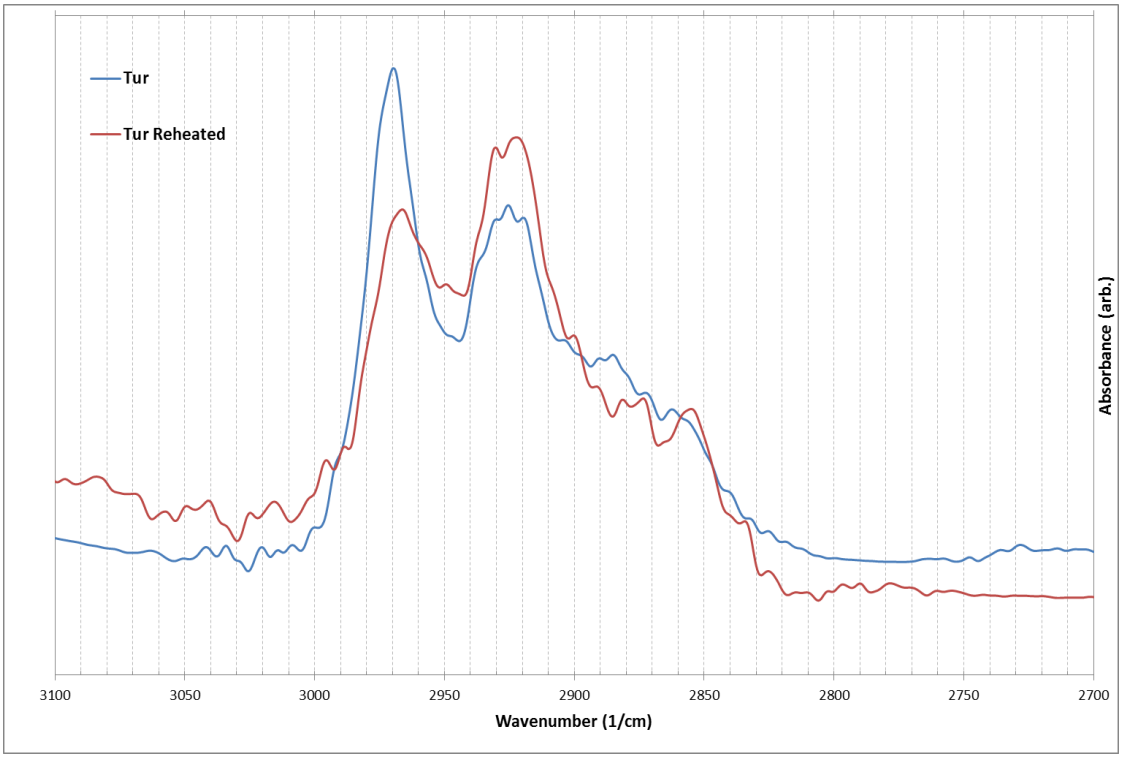

Figure B.68: FTIR spectra across region of interest in organic identification for *Tur* (non-reheated and reheated).

Ted

Table B.18: Mineral identification of diagnostic FTIR peaks for *Ted* samples. Qtz=Quartz, Mic=Microcline, Ort=Orthoclase, Dio=Diopside, Ana=Anatase, Cri=Cristobalite, Ano=Anorthite, Mul=Mullite, Hem=Hematite, Alb=Albite, Oli=Olivine, San=Sanidine, For=Forsterite, Cal=Calcite, Wol=Wollastonite, Mus= Muscovite, Geh=Gehlenite, Aug=Augite.

Peak At	ID
460.0000	Qtz
470.0000	Mic,Ort,Dio, Ana
477.0000	Qtz
483.0000	Cri, Ano, Mul
489.0000	Cri,Ana,Ano
512.0000	Qtz
540.0000	Ano,Mic,Ana,Mul
563.0000	Hem
572.0000	Ano
582.0000	Mic
606.0000	Mic,For
632.0000	Dio,Ano
648.0000	Alb,Mic
694.0000	Qtz
730.0000	Mul
745.0000	Alb,
756.0000	Ano
779.0000	Qtz
798.0000	Qtz
840.0000	Oli,San,For
875.0000	Cal,Aug
1013.0000	Mic,San,Alb
1023.0000	Wol,Mus
1036.0000	Alb,Geh
1051.0000	Mic
1060.0000	Wol,Cal,Ens
1080.0000	Qtz
1091.0000	Dio,Mic,Cri,Ano,Wol
1103.0000	Mul
1120.0000	Ort,Hem,Mic,Mul
1132.0000	Ort

1150.0000	Alb
1166.0000	Qtz
1183.0000	Hem
1422.0000	Cal

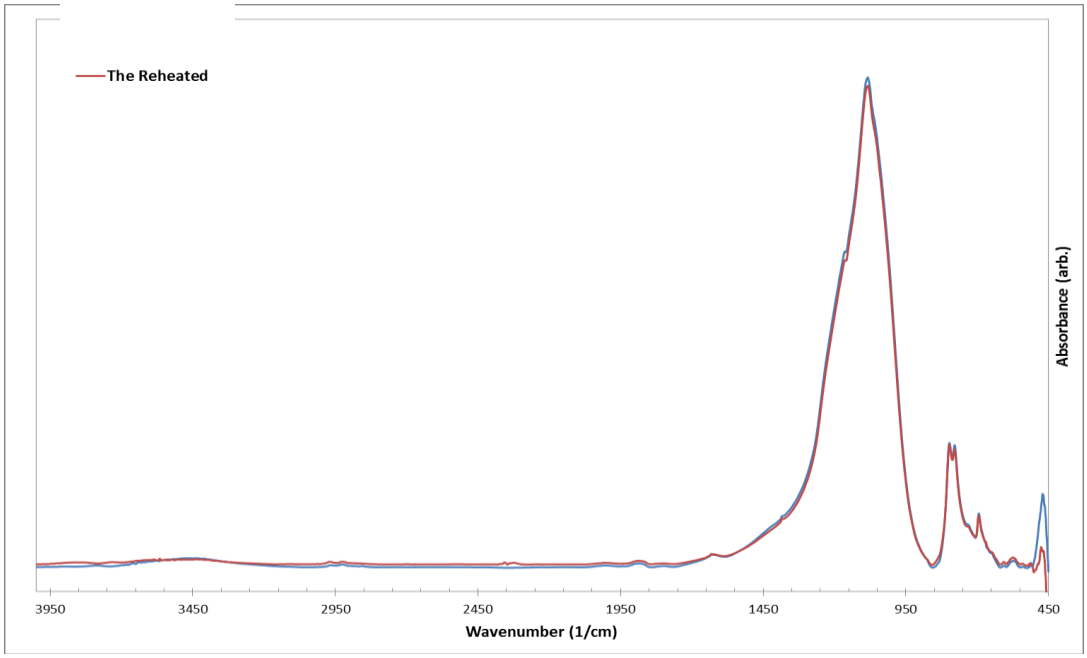

Figure B.69: FTIR Spectra of non-reheated (blue) and reheated (red) *Ted* sample.

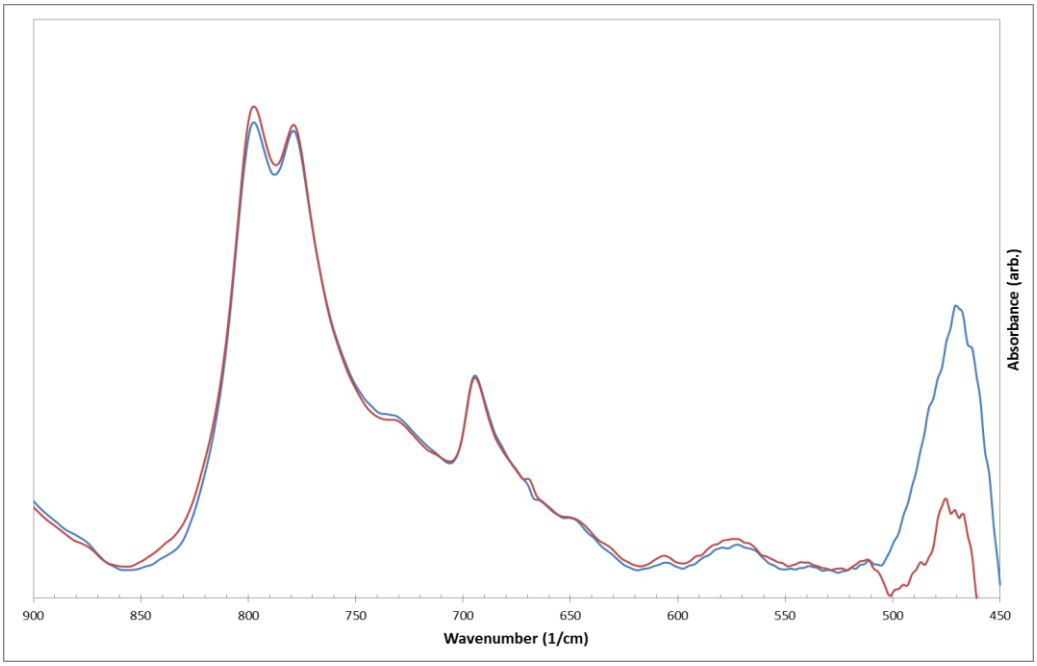

Figure B.70: FTIR spectra of non-reheated (blue) and reheated (red) *Ted* samples over the region 450-900(1/cm).

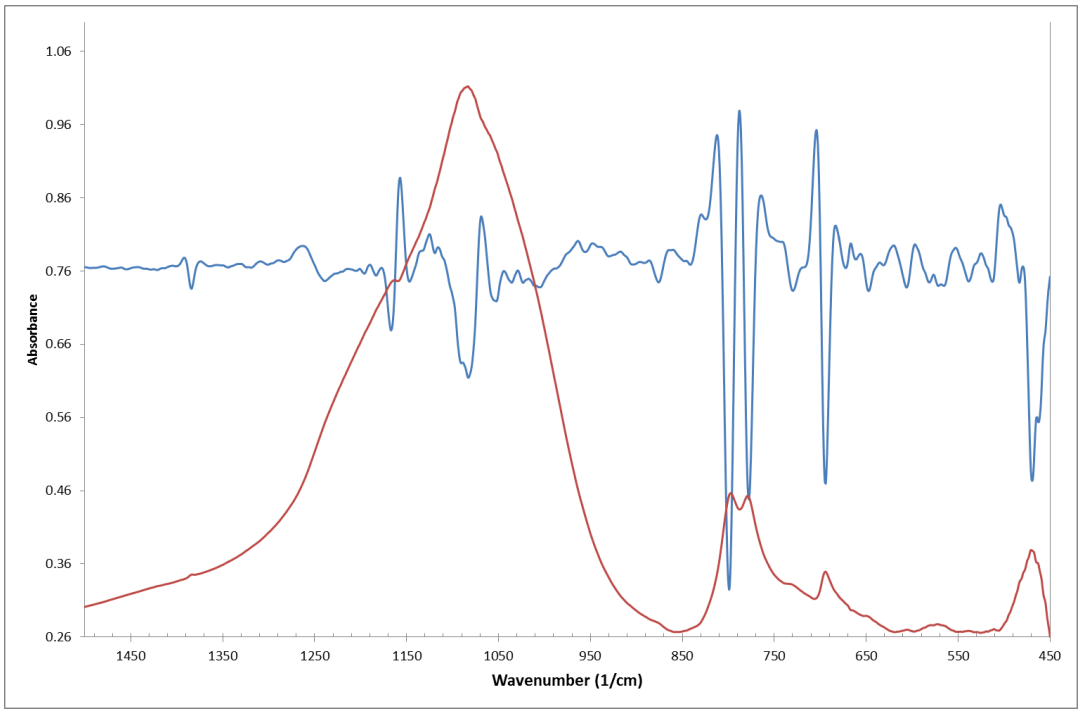

Figure B.71: FTIR spectrum of non-reheated *Ted* sample over region 450-1500 (1/cm) with smoothed second derivative overlaid.

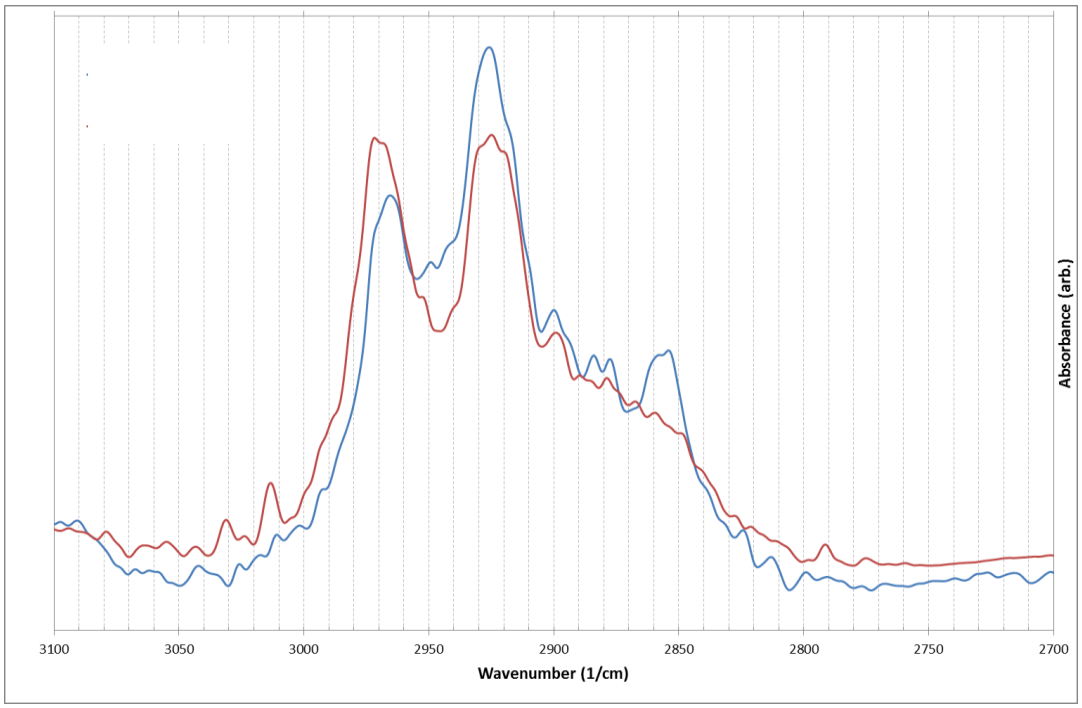

Figure B.72: FTIR spectra across region of interest in organic identification for *Ted* (non-reheated and reheated).

Appendix C

TG-MS Curves

This appendix will present the TG-MS data recorded for each sample. This includes a TG mass loss curve and its first derivative, a TG mass loss curve and mass 18 (H_2O proxy) mass spectrometry curve (ion current), a TG mass loss curve and mass 44 (CO_2 proxy) mass spectrometry curve (ion current), and a TG mass loss curve and mass 64 (SO_2 proxy) mass spectrometry curve (ion current). The last of these is only presented for *Mac* and *Bel,* where *SO_2* activity was detected.

Ann

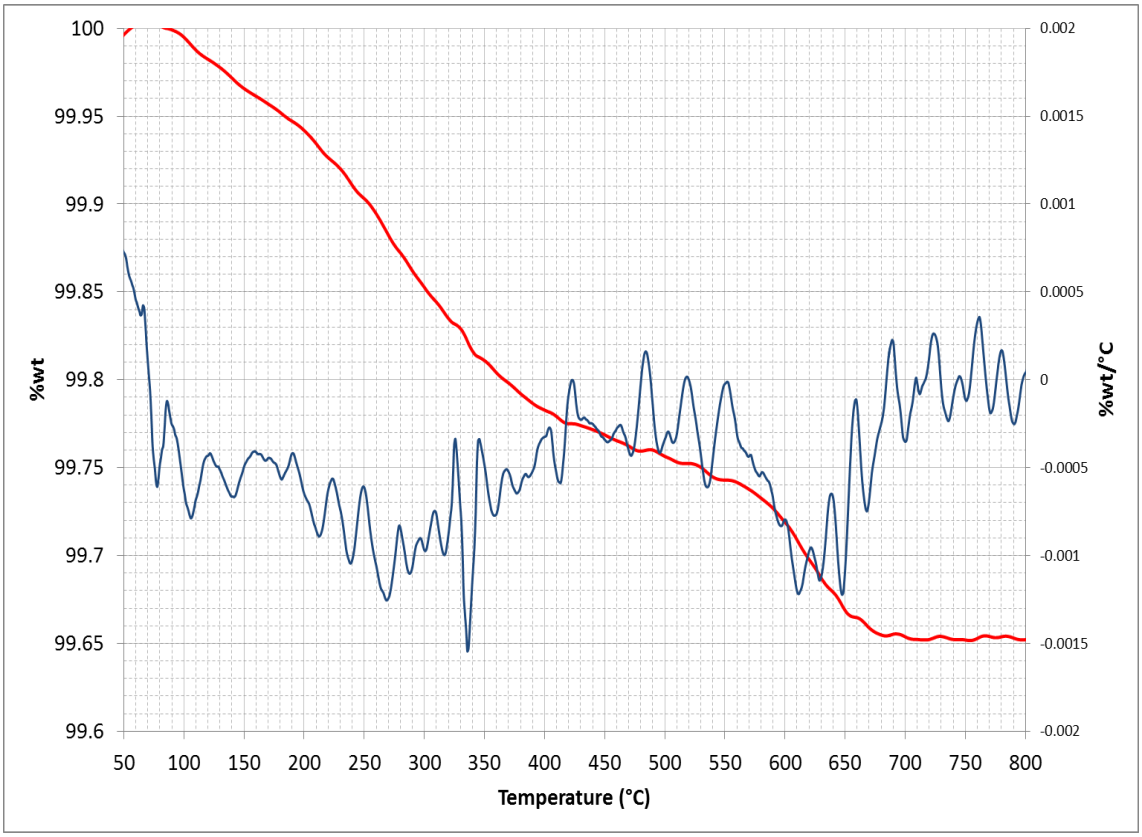

Figure C.1: TG mass loss curve (red) and first derivative curve (blue) for *Ann*.

Figure C.2: TG mass loss curve (red) and mass 18 (H_2O) mass spectrometry curve (blue) for *Ann*.

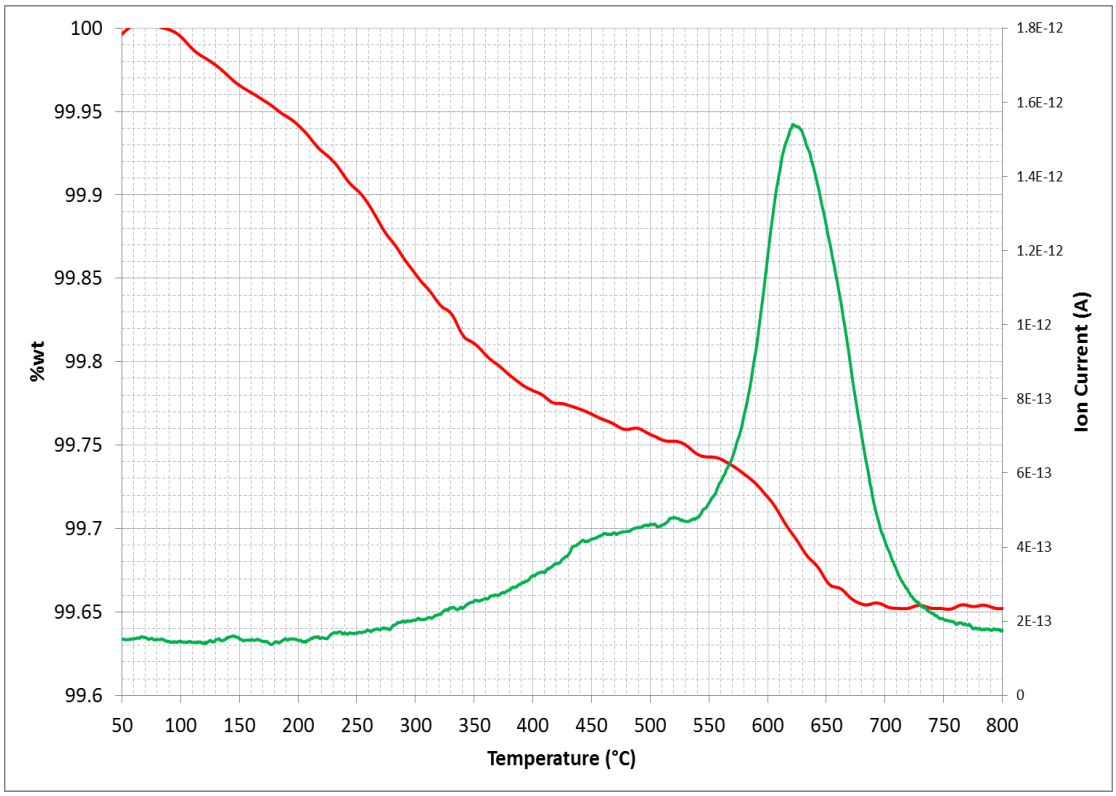

Figure C.3: TG mass loss curve (red) and mass 44 (CO_2) mass spectrometry curve (green) for *Ann*.

Esp

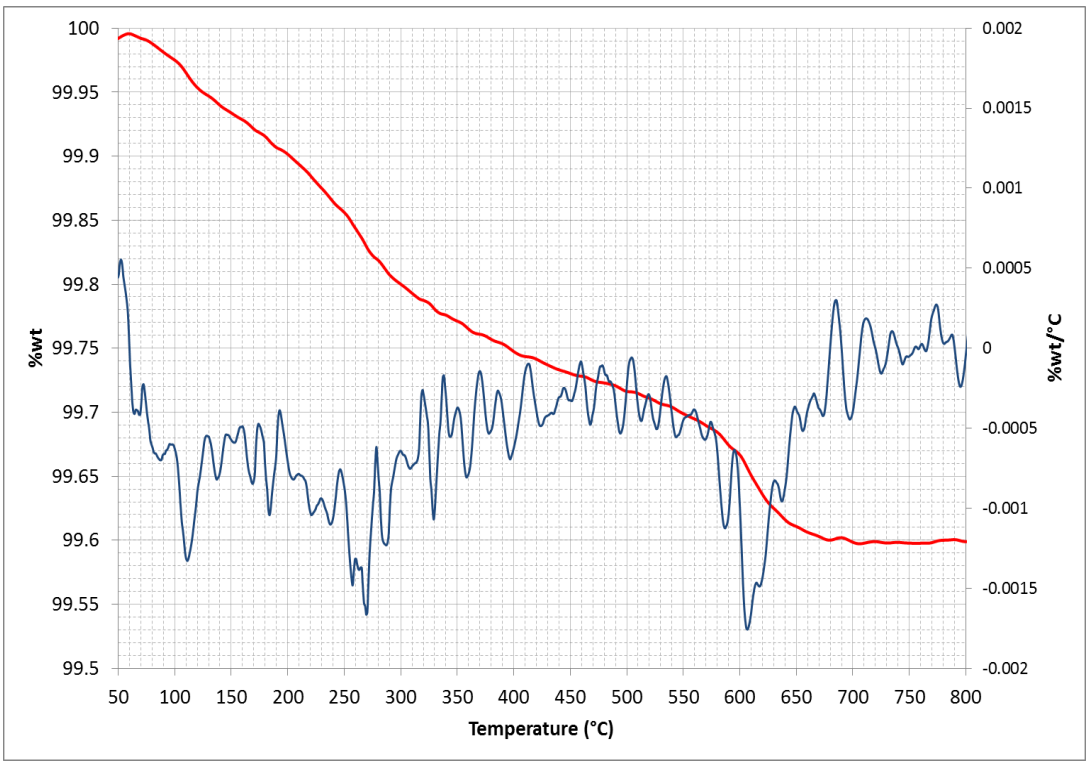

Figure C.4: TG mass loss curve (red) and first derivative curve (blue) for *Esp*.

Figure C.5: TG mass loss curve (red) and mass 18 (H_2O) mass spectrometry curve (blue) for *Esp*.

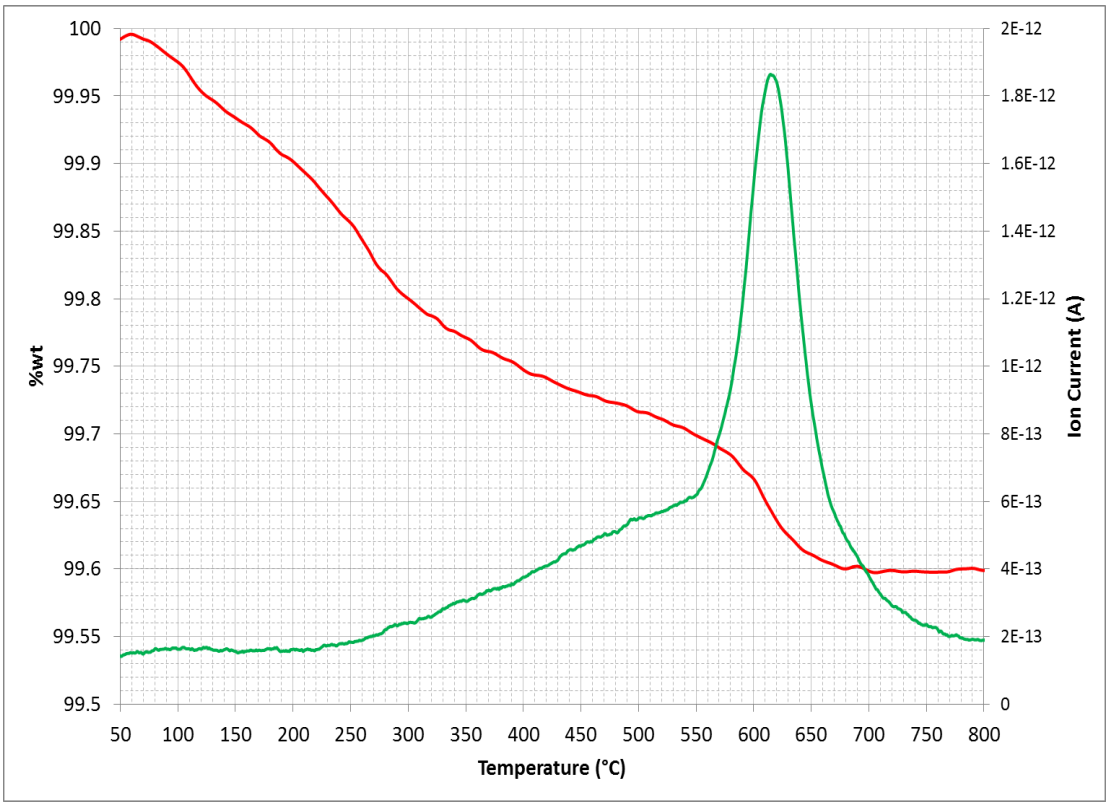

Figure C.6: TG mass loss curve (red) and mass 44 (CO_2) mass spectrometry curve (green) for *Esp*.

Nic

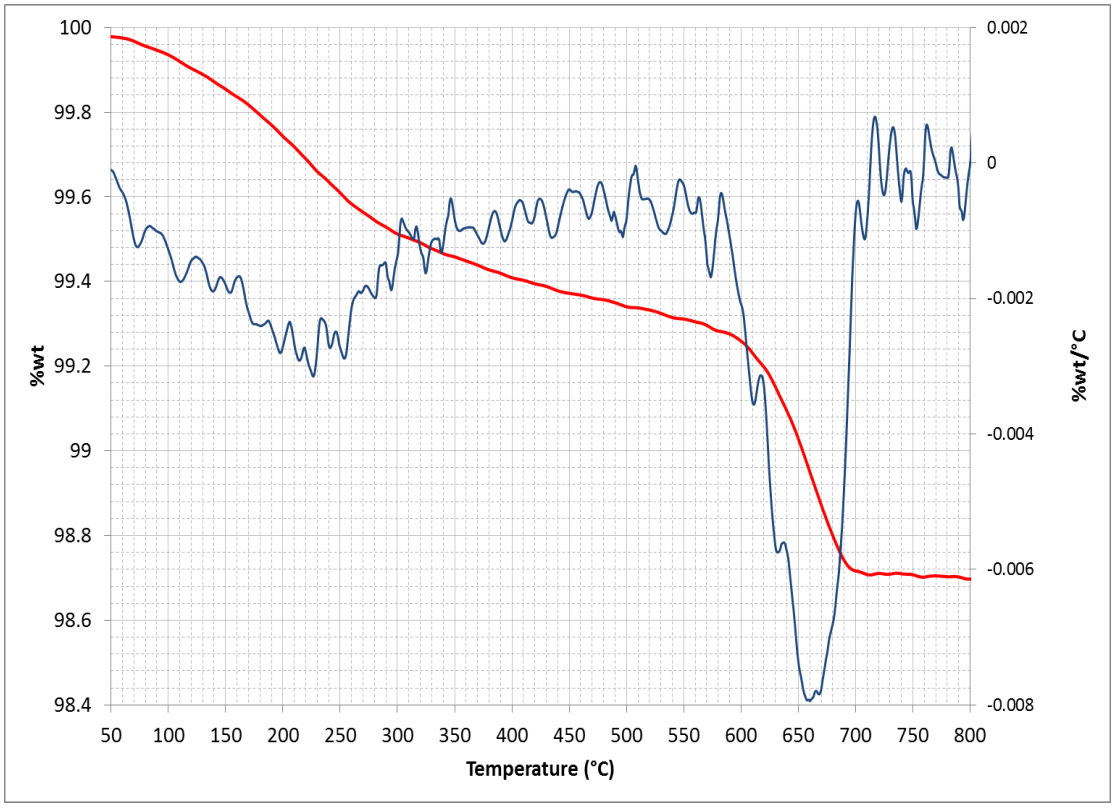

Figure C.7: TG mass loss curve (red) and first derivative curve (blue) for *Nic*.

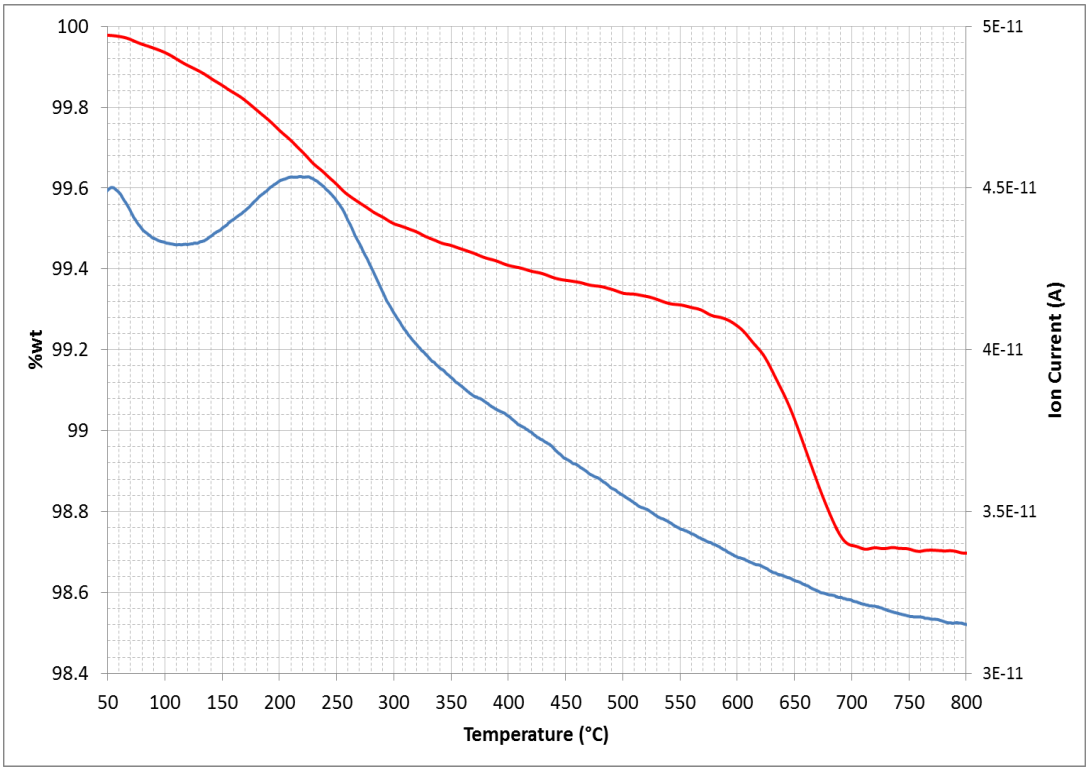

Figure C.8: TG mass loss curve (red) and mass 18 (H_2O) mass spectrometry curve (blue) for *Nic*.

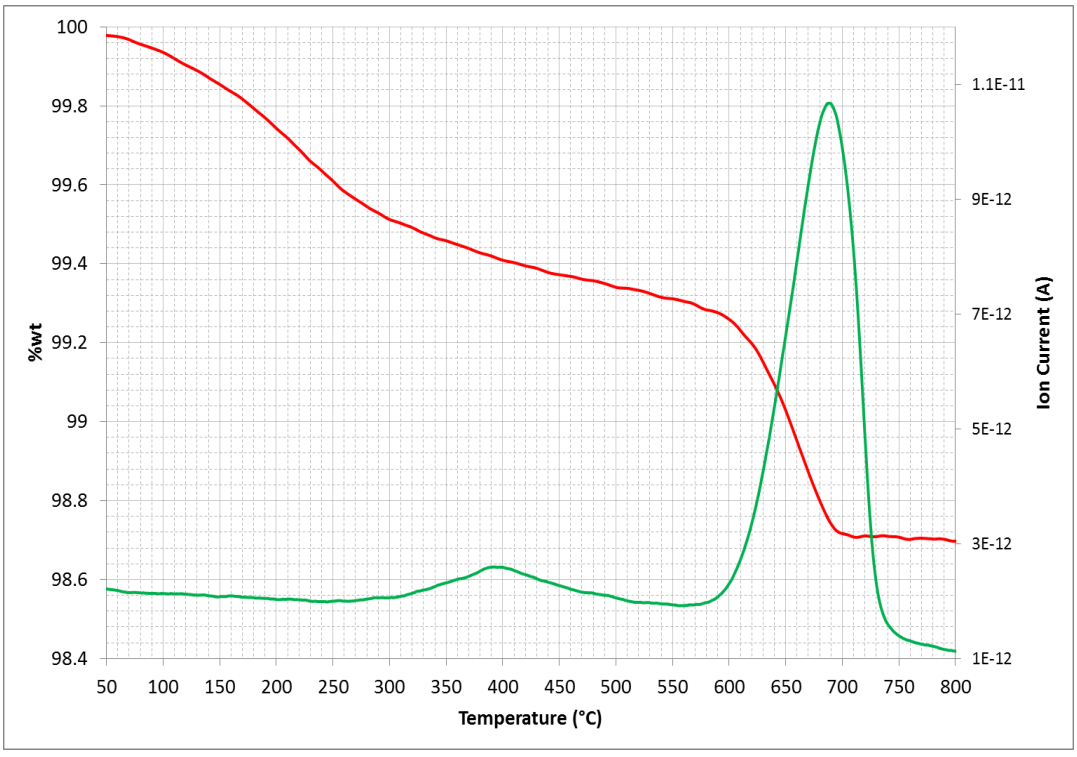

Figure C.9: TG mass loss curve (red) and mass 44 (CO_2) mass spectrometry curve (green) for *Nic*.

Mac

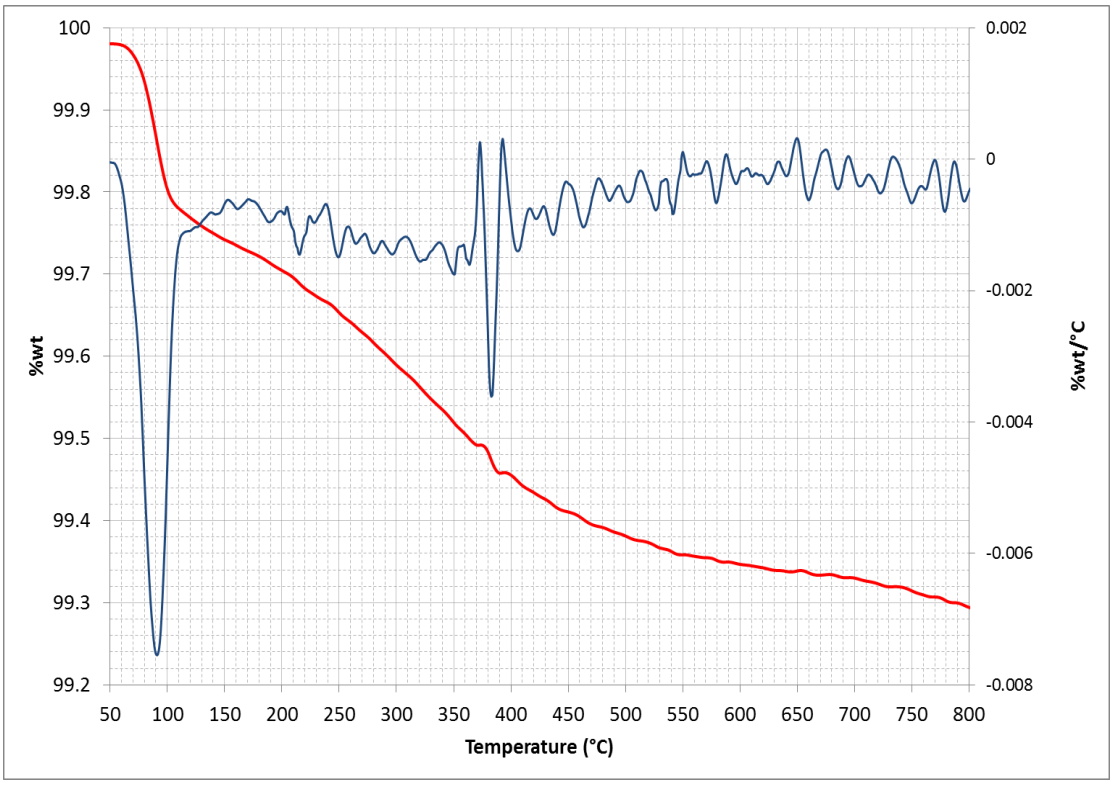

Figure C.10: TG mass loss curve (red) and first derivative curve (blue) for *Mac*.

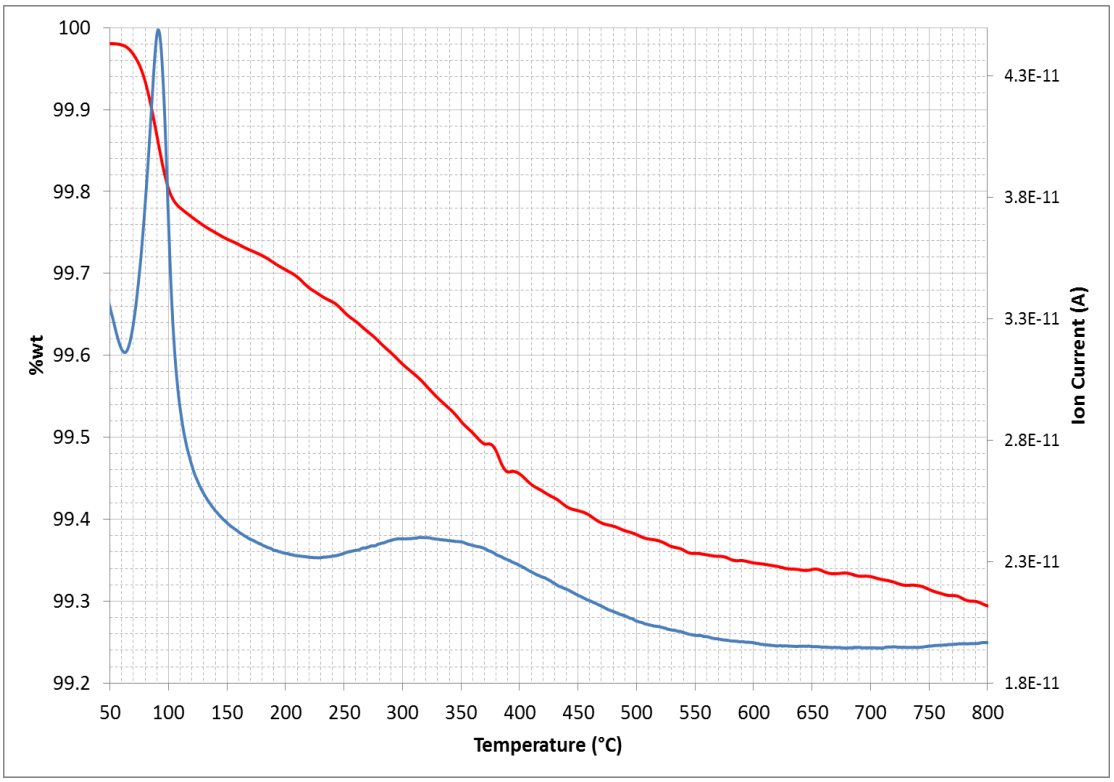

Figure C.11: TG mass loss curve (red) and mass 18 (H_2O) mass spectrometry curve (blue) for *Mac*.

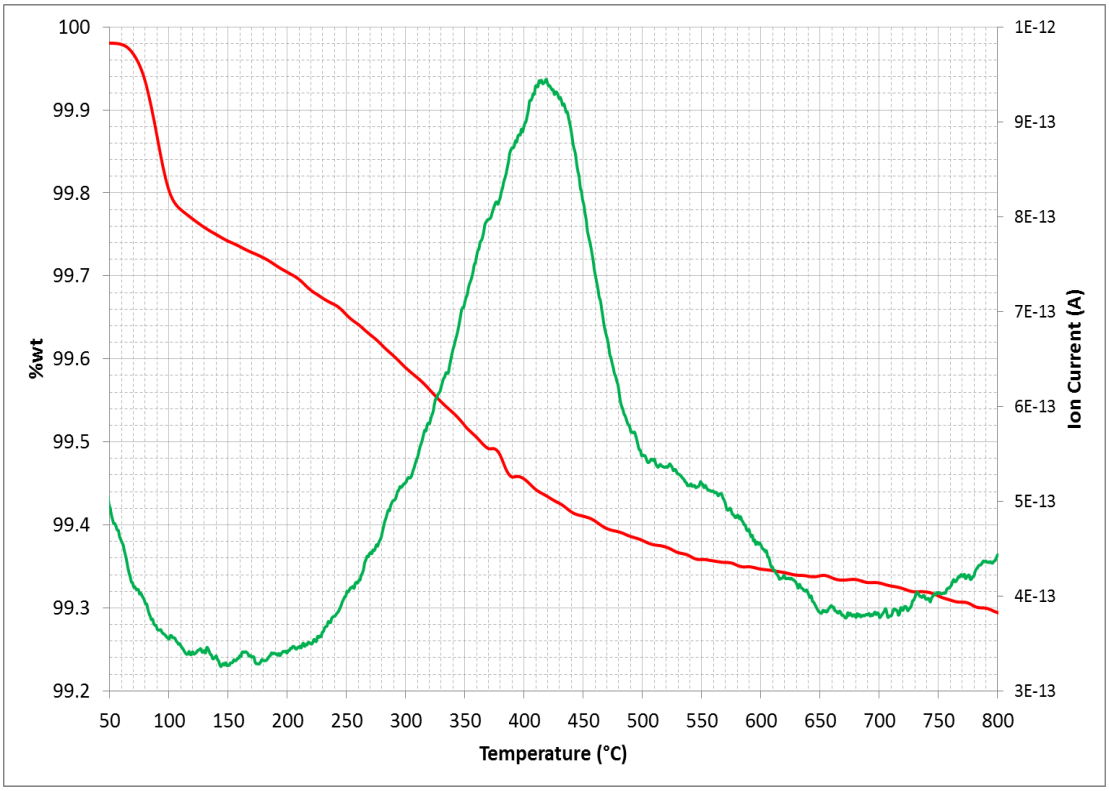

Figure C.12: TG mass loss curve (red) and mass 44 (CO_2) mass spectrometry curve (green) for *Mac*.

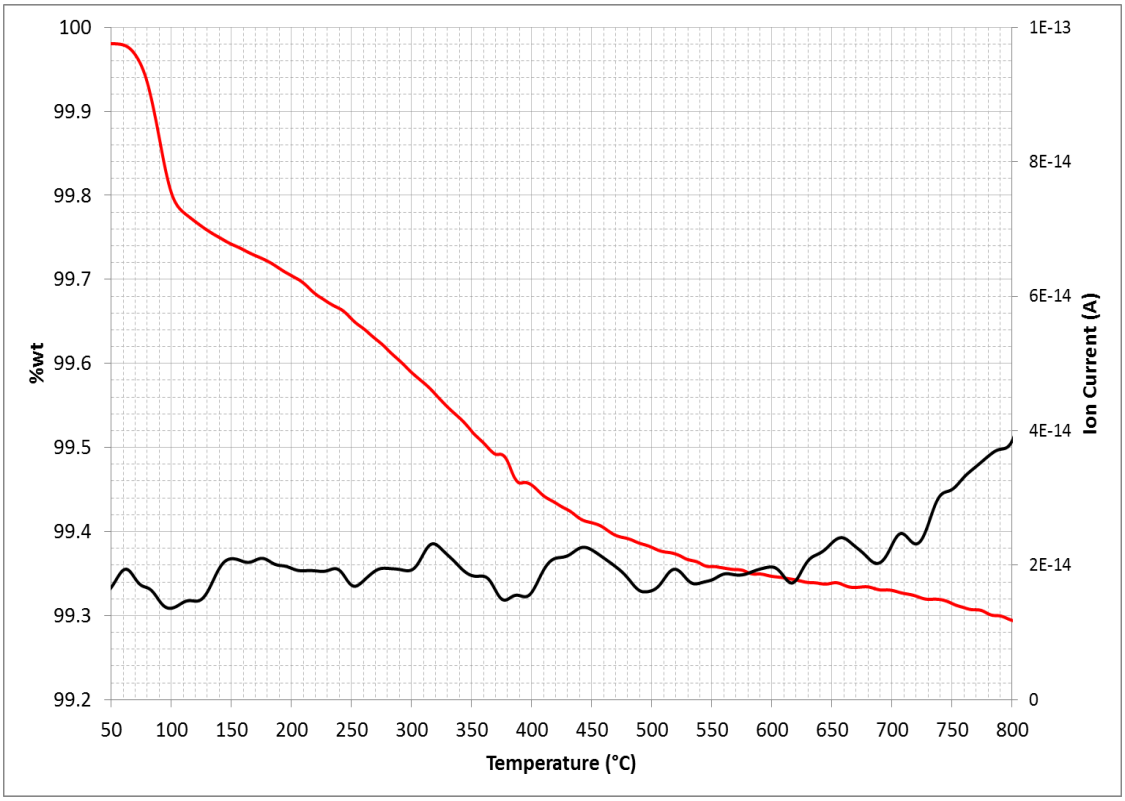

Figure C.13: TG mass loss curve (red) and mass 64 (SO_2) mass spectrometry curve (black) for *Mac*.

Ria

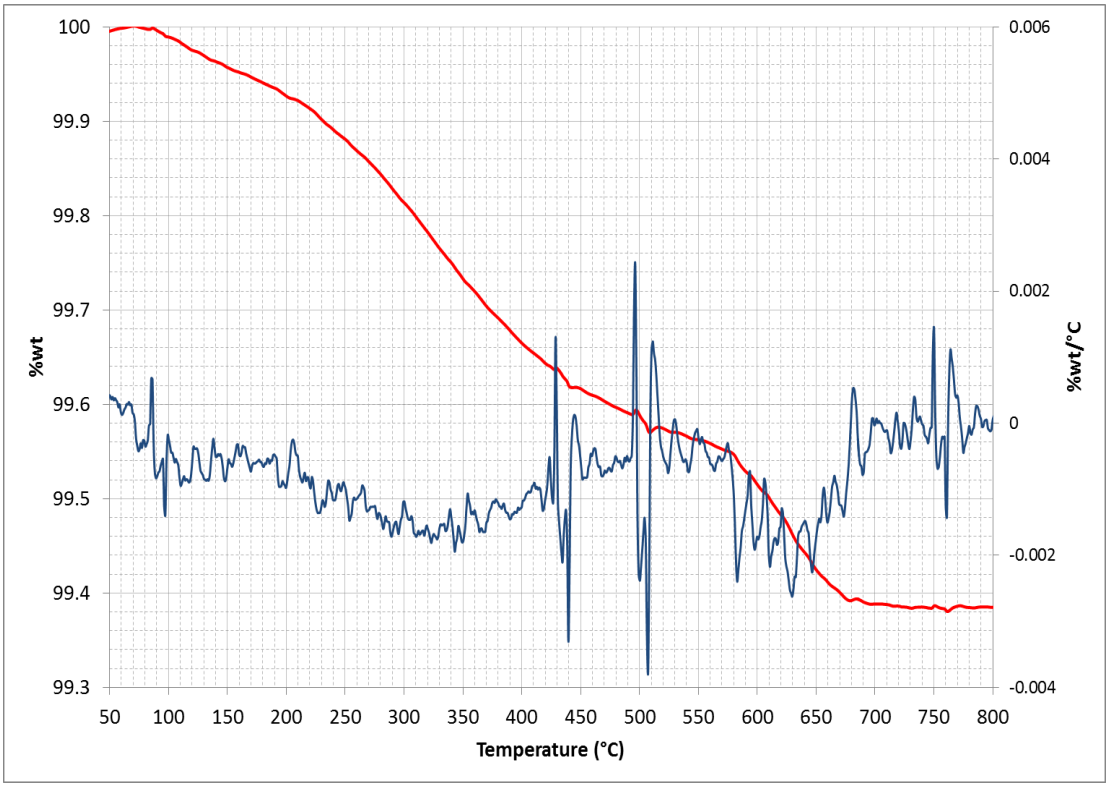

Figure C.14: TG mass loss curve (red) and first derivative curve (blue) for *Ria*.

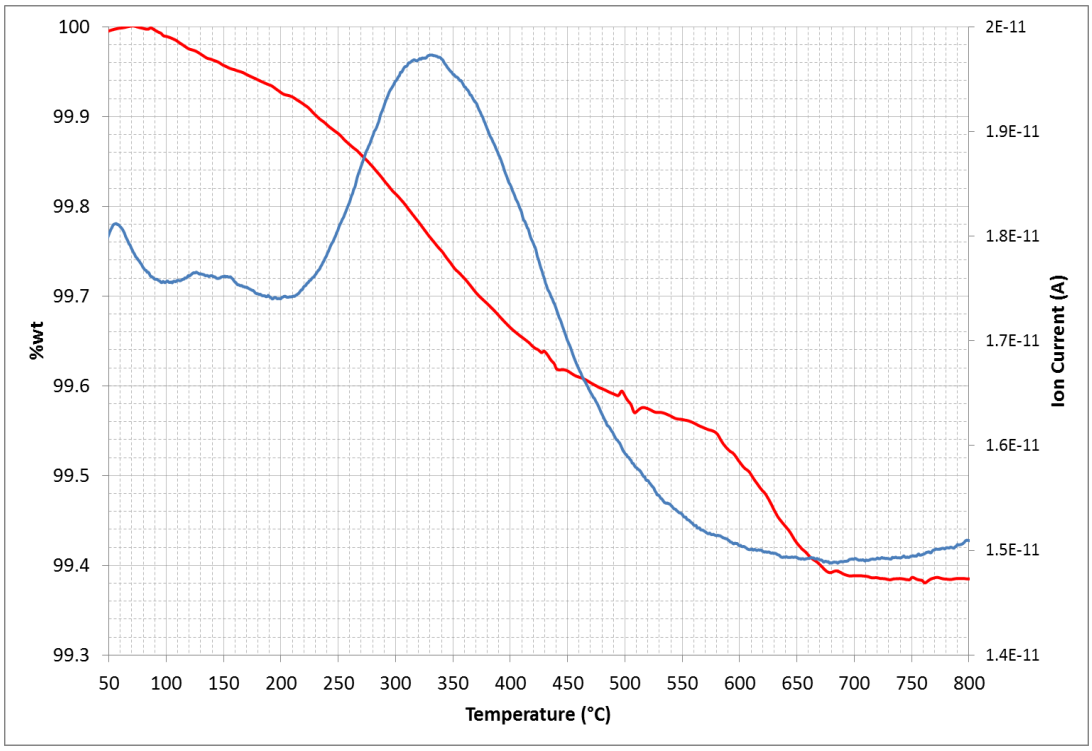

Figure C.15: TG mass loss curve (red) and mass 18 (H_2O) mass spectrometry curve (blue) for *Ria*.

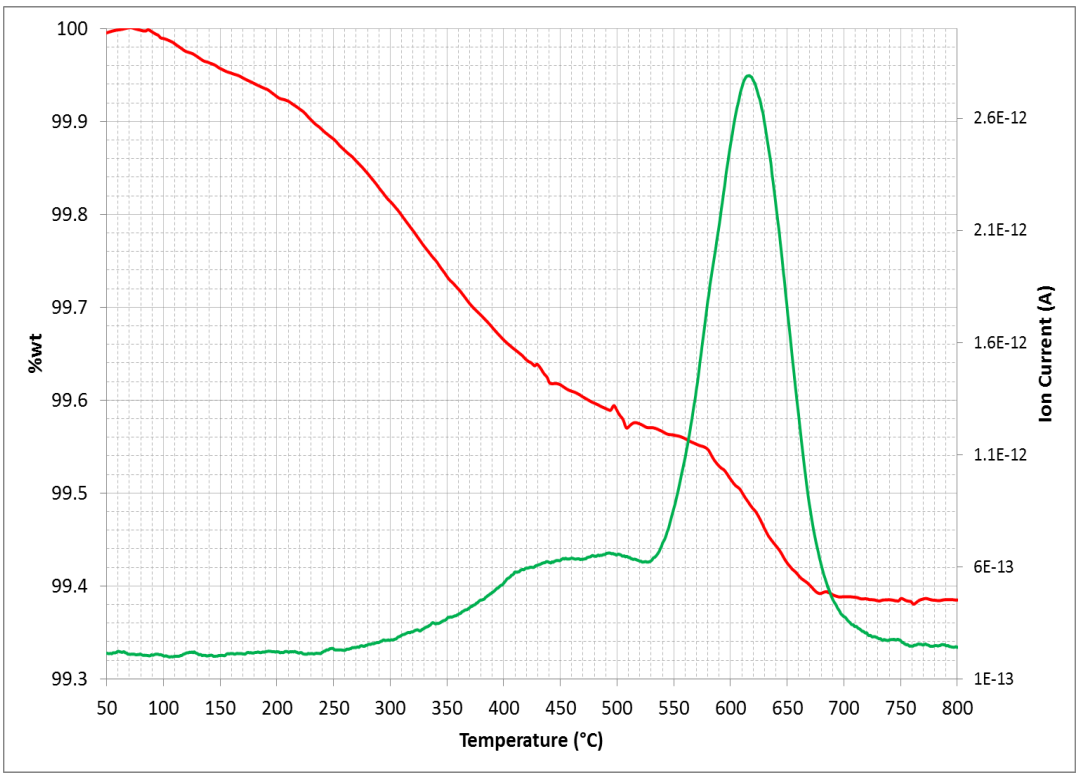

Figure C.16: TG mass loss curve (red) and mass 44 (CO_2) mass spectrometry curve (green) for *Ria*.

Etr

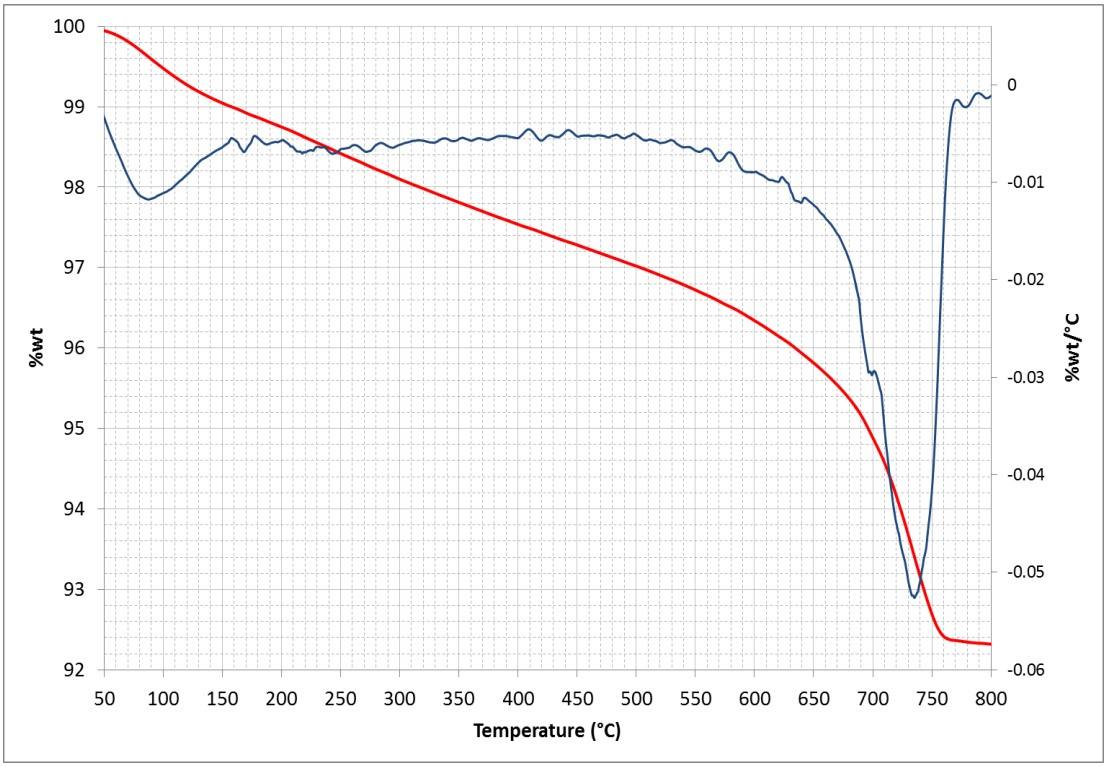

Figure C.17: TG mass loss curve (red) and first derivative curve (blue) for *Etr*.

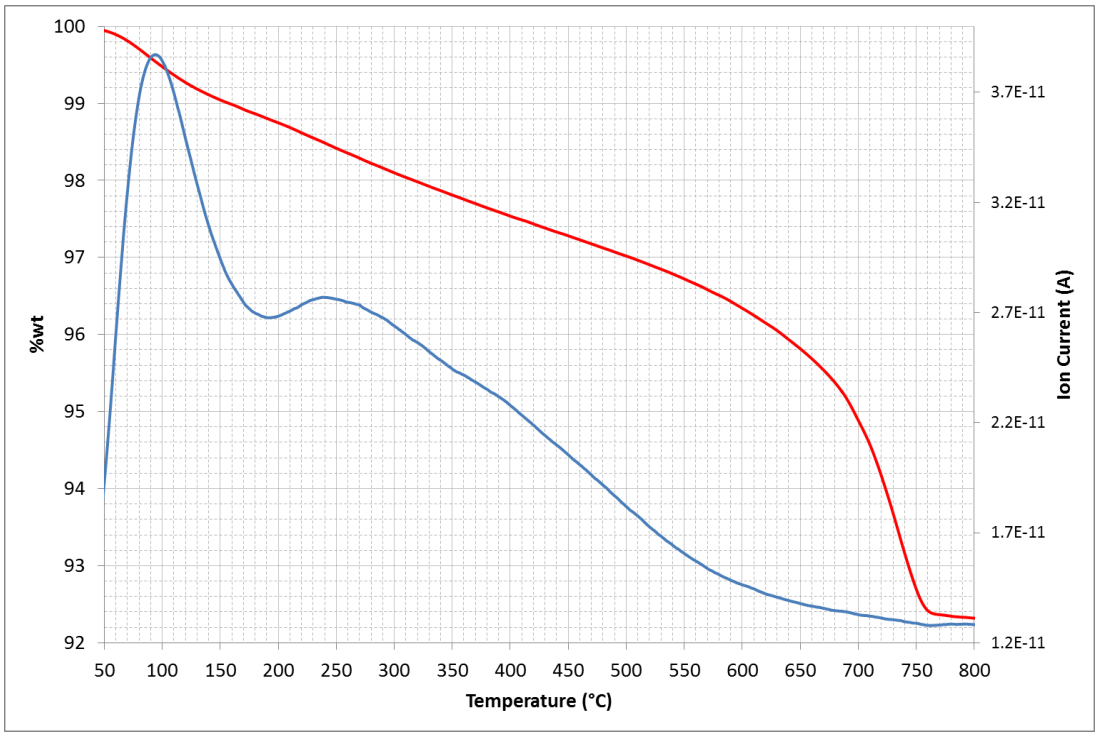

Figure C.18: TG mass loss curve (red) and mass 18 (H_2O) mass spectrometry curve (blue) for *Etr*.

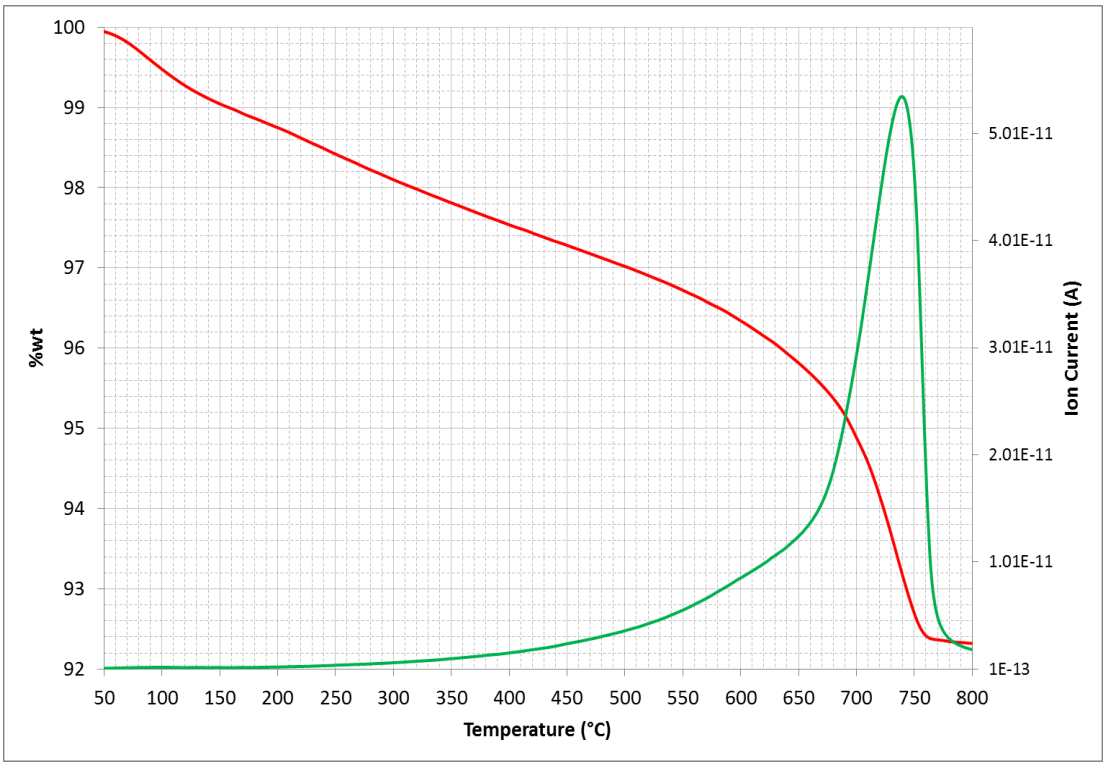

Figure C.19: TG mass loss curve (red) and mass 44 (CO_2) mass spectrometry curve (green) for *Etr*.

Rom

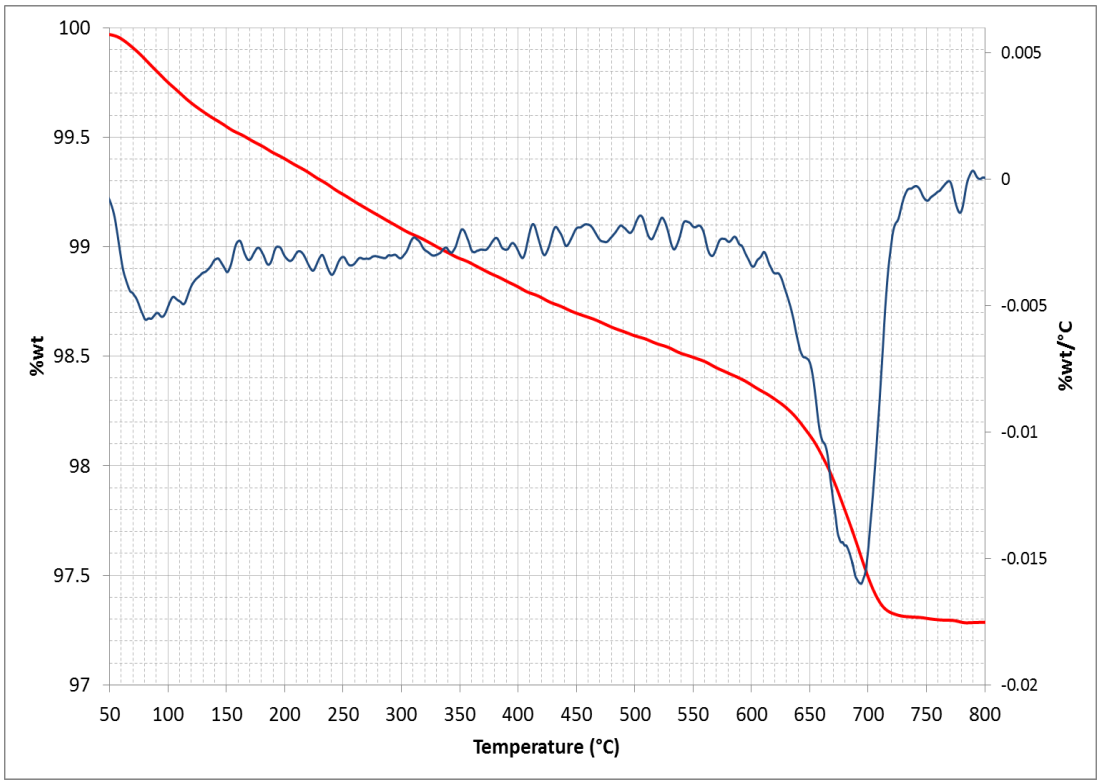

Figure C.20: TG mass loss curve (red) and first derivative curve (blue) for *Rom*.

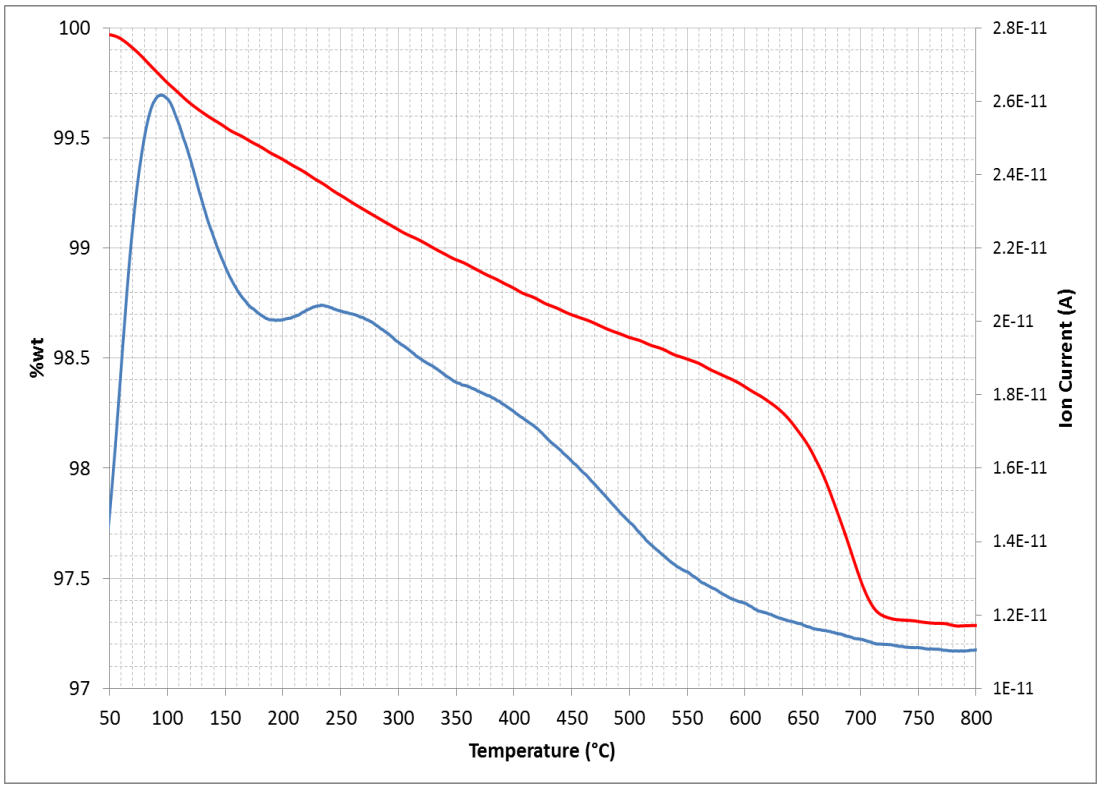

Figure C.21: TG mass loss curve (red) and mass 18 (H_2O) mass spectrometry curve (blue) for *Rom*.

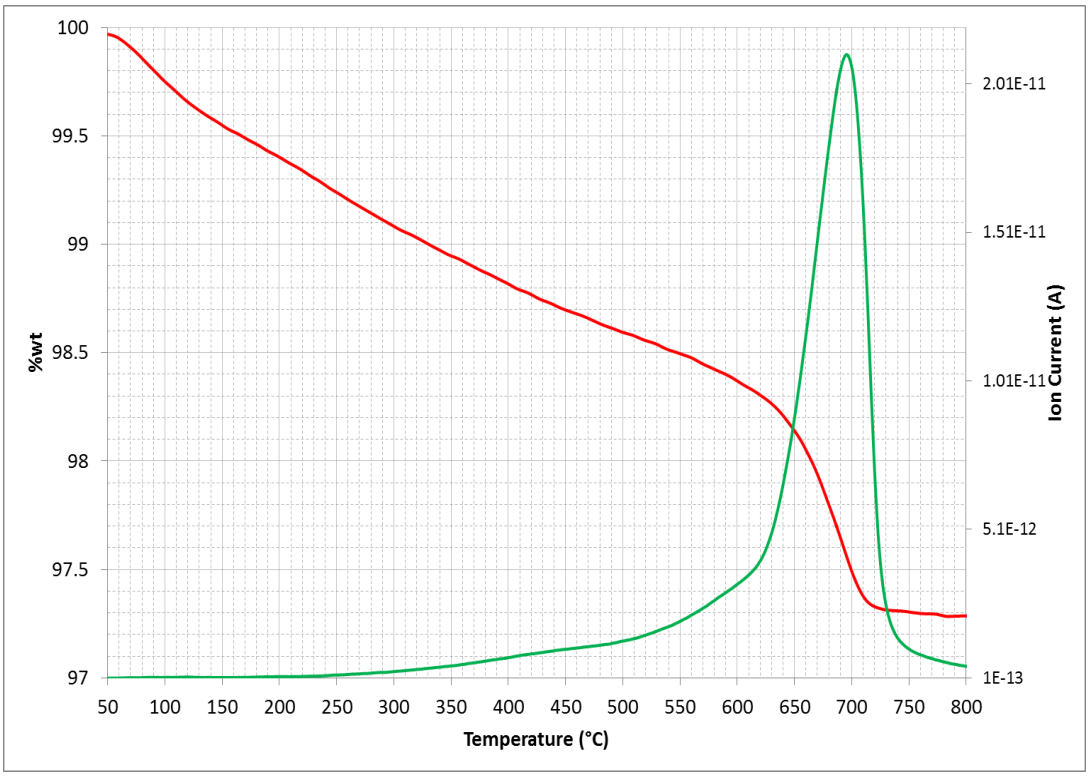

Figure C.22: TG mass loss curve (red) and mass 44 (CO_2) mass spectrometry curve (green) for *Rom*.

Por

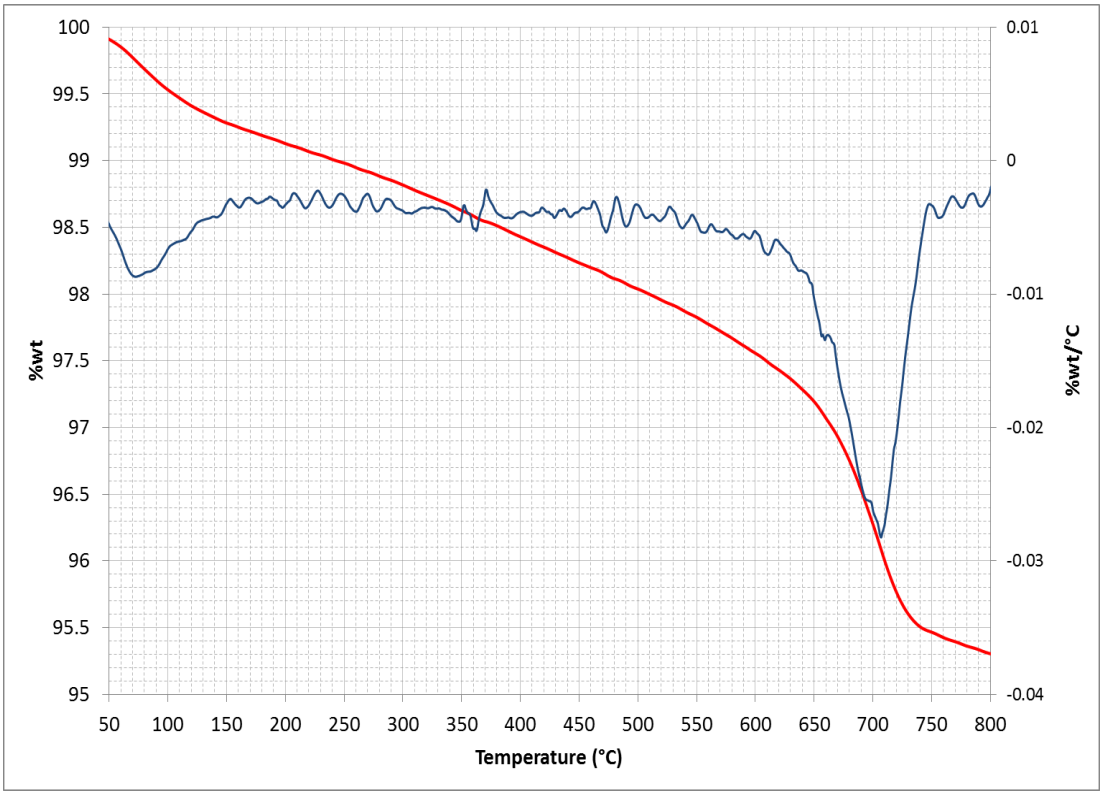

Figure C.23: TG mass loss curve (red) and first derivative curve (blue) for *Por*.

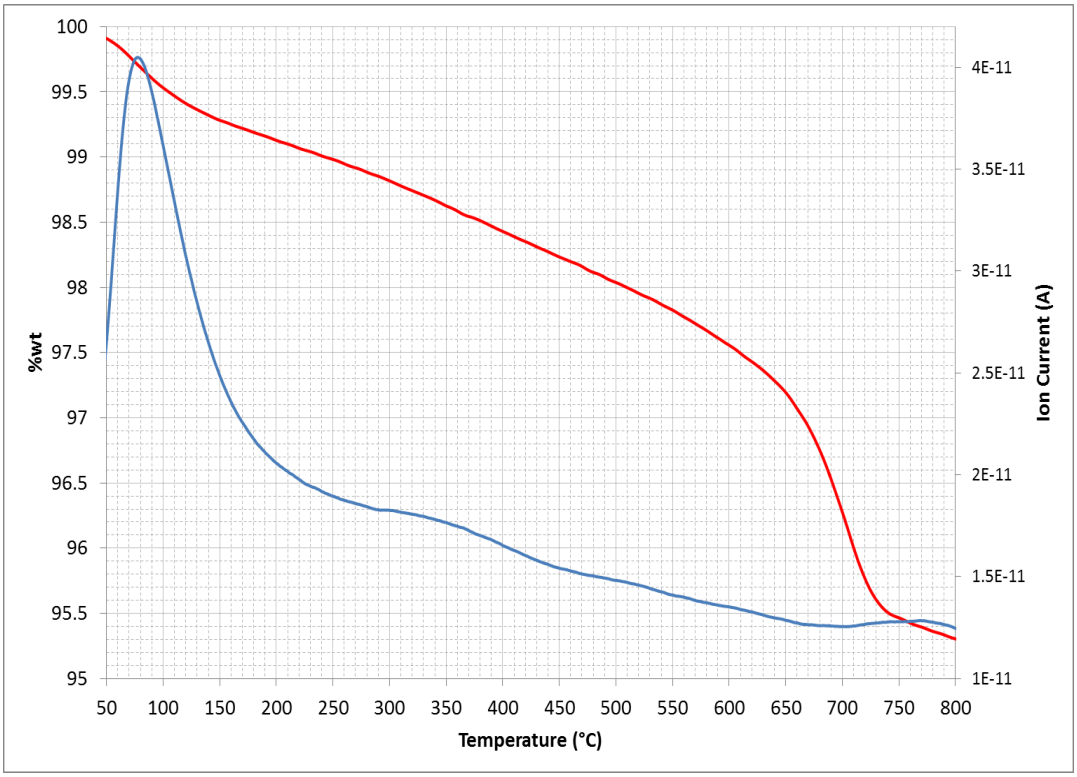

Figure C.24: TG mass loss curve (red) and mass 18 (H_2O) mass spectrometry curve (blue) for *Por*.

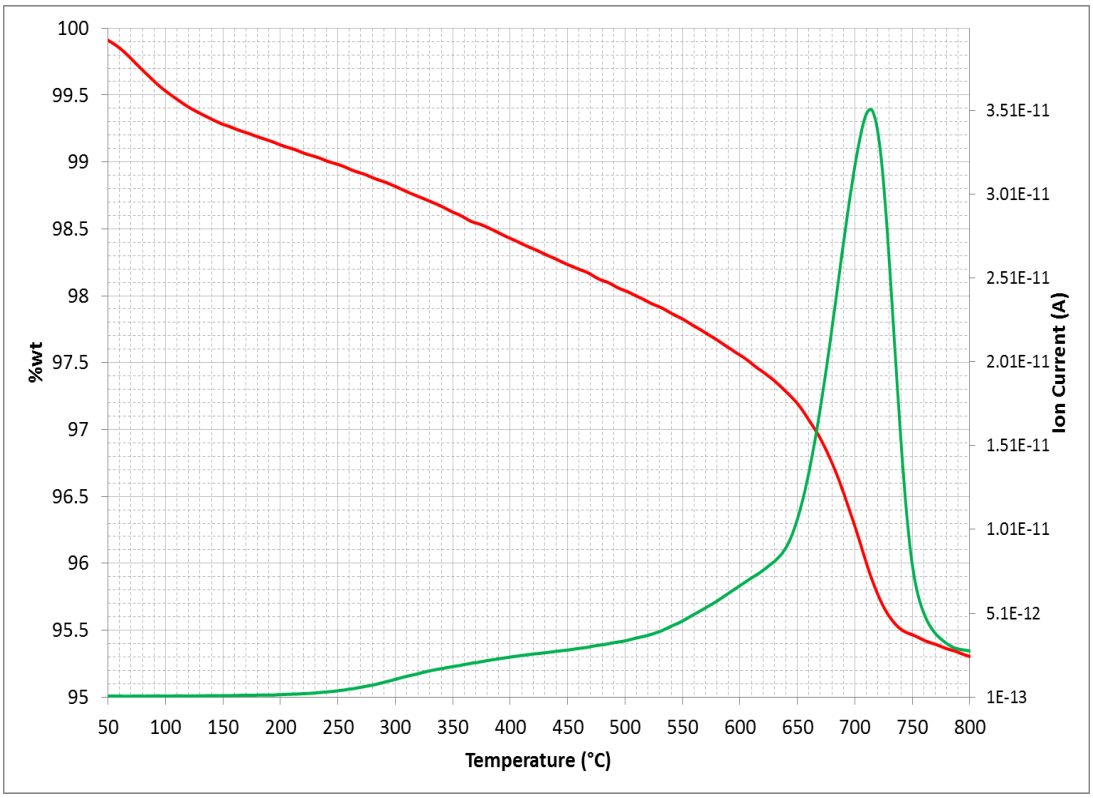

Figure C.25: TG mass loss curve (red) and mass 44 (CO_2) mass spectrometry curve (green) for *Por*.

Rat

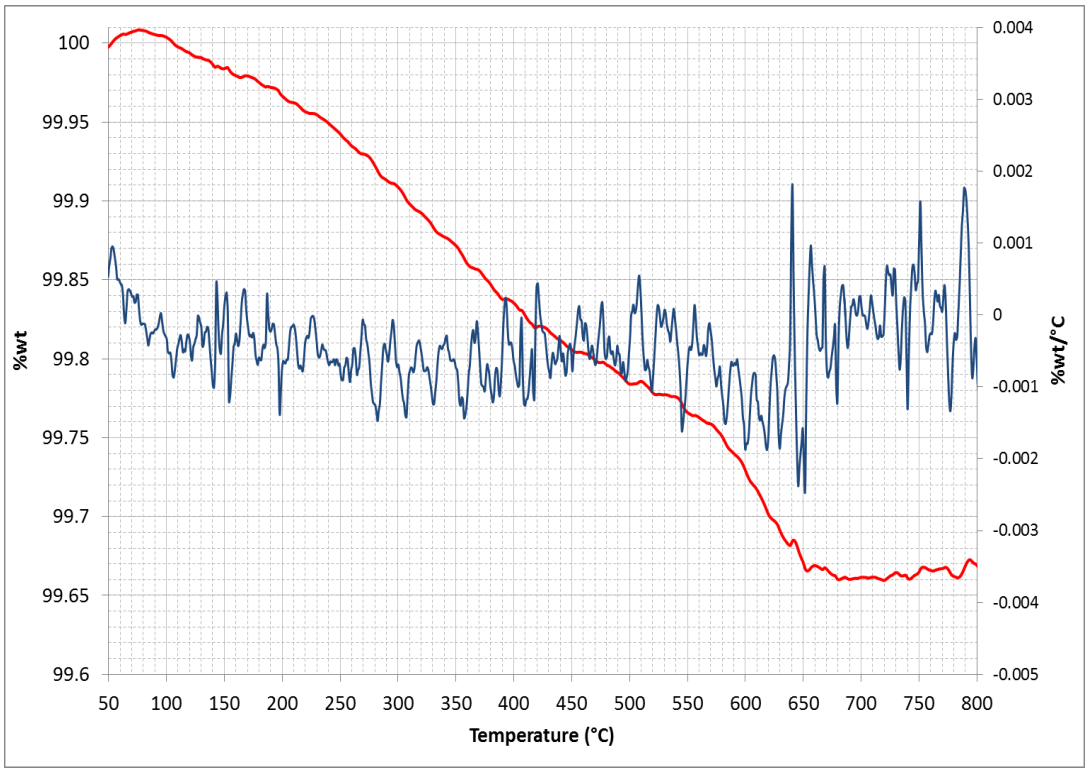

Figure C.26: TG mass loss curve (red) and first derivative curve (blue) for *Rat*.

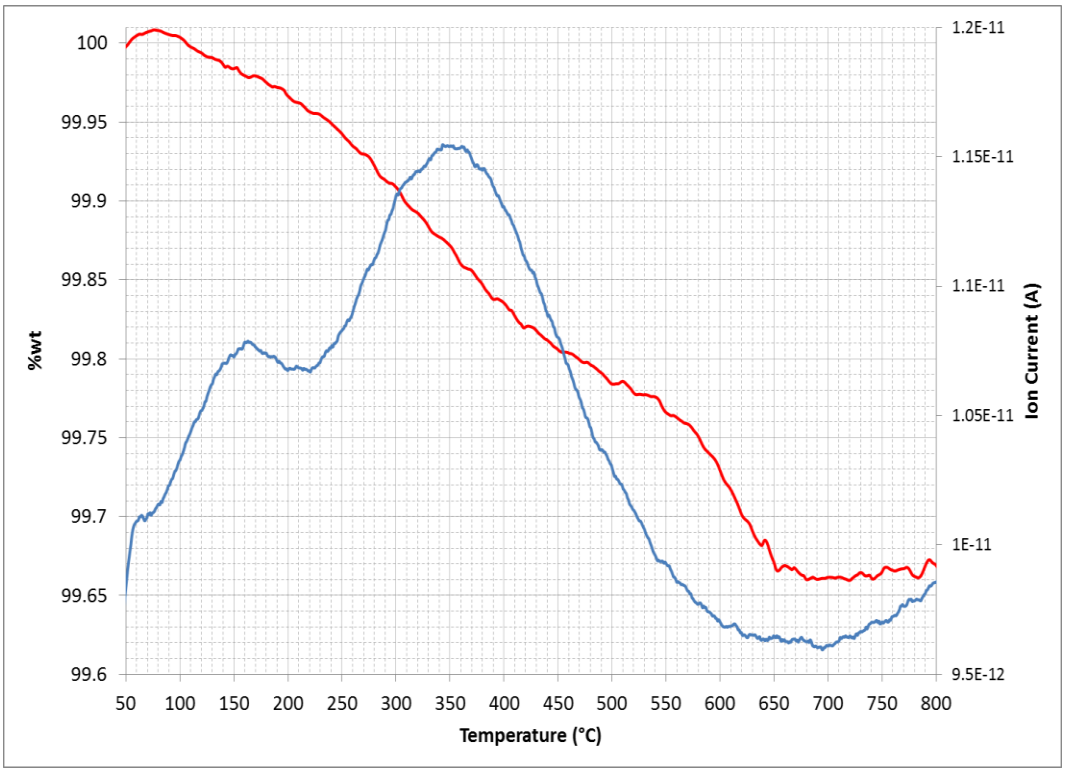

Figure C.27: TG mass loss curve (red) and mass 18 (H_2O) mass spectrometry curve (blue) for *Rat*.

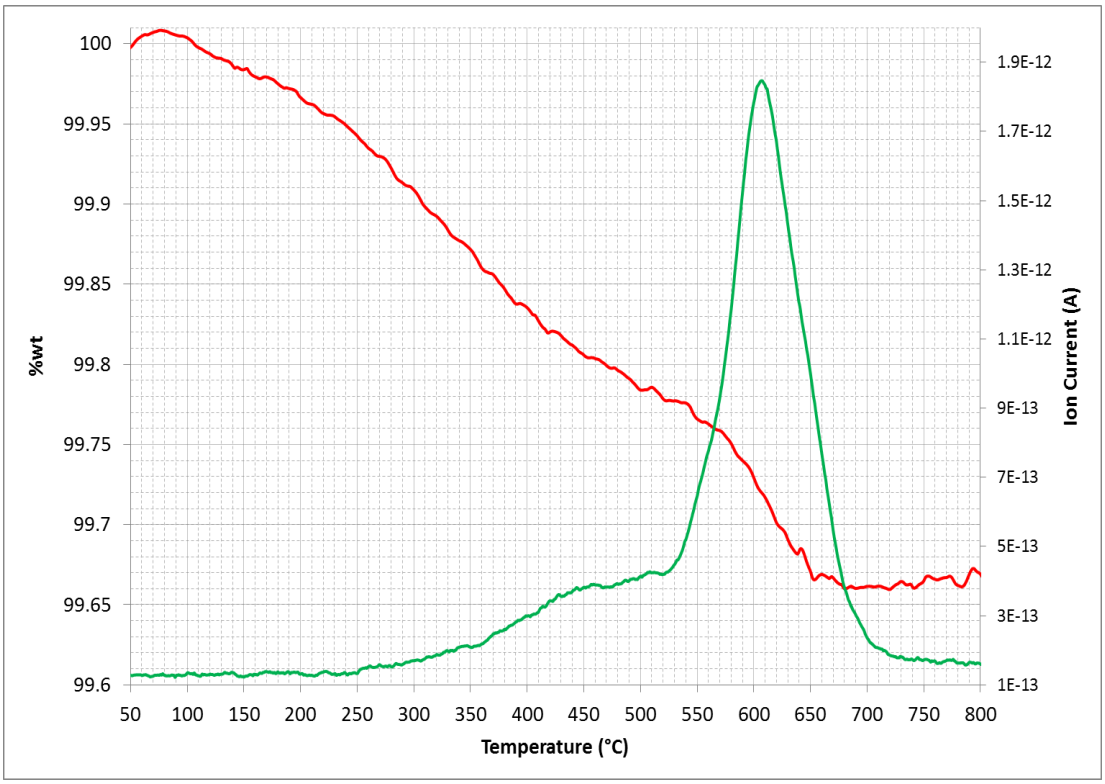

Figure C.28: TG mass loss curve (red) and mass 44 (CO_2) mass spectrometry curve (green) for *Rat*.

Cal

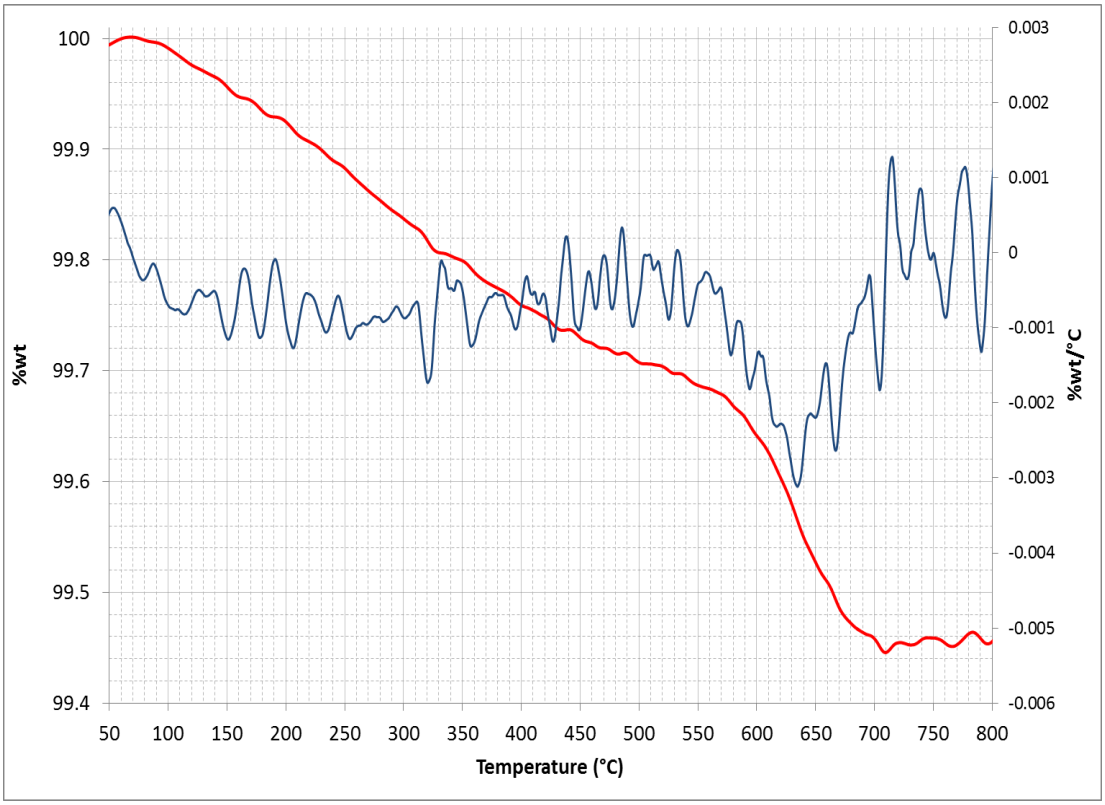

Figure C.29: TG mass loss curve (red) and first derivative curve (blue) for *Cal*.

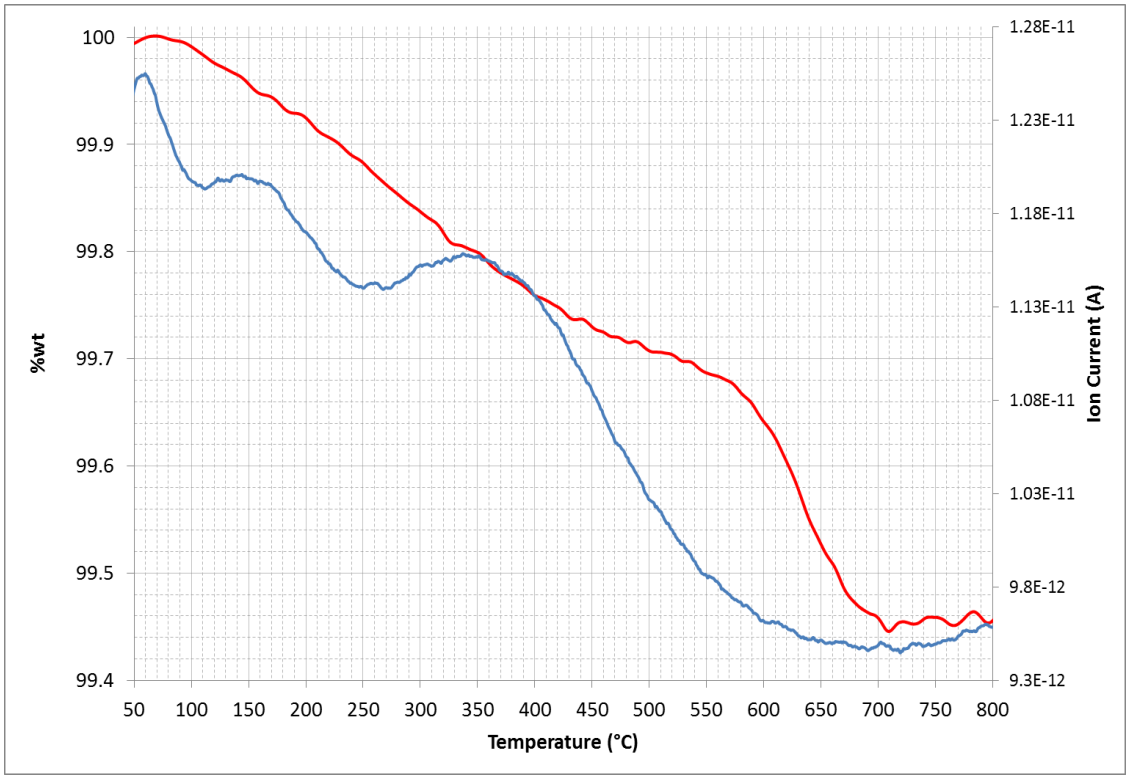

Figure C.30: TG mass loss curve (red) and mass 18 (H_2O) mass spectrometry curve (blue) for *Cal*.

Figure C.31: TG mass loss curve (red) and mass 44 (CO_2) mass spectrometry curve (green) for *Cal*.

Lan

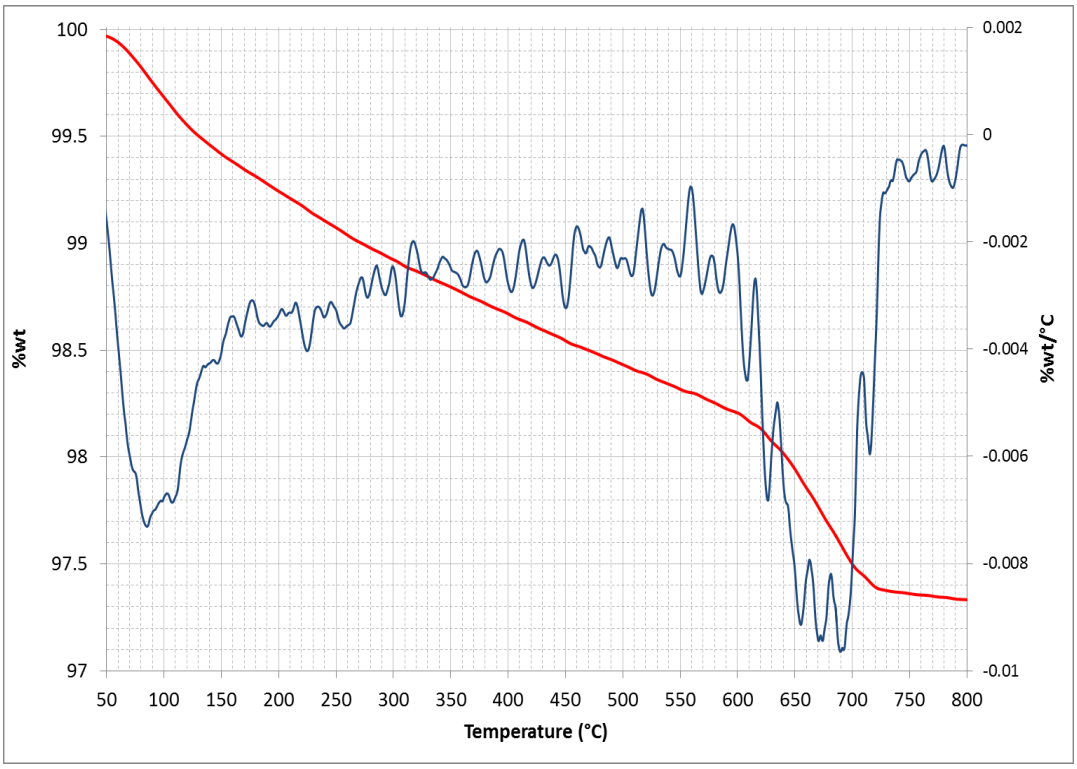

Figure C.32: TG mass loss curve (red) and first derivative curve (blue) for *Lan*.

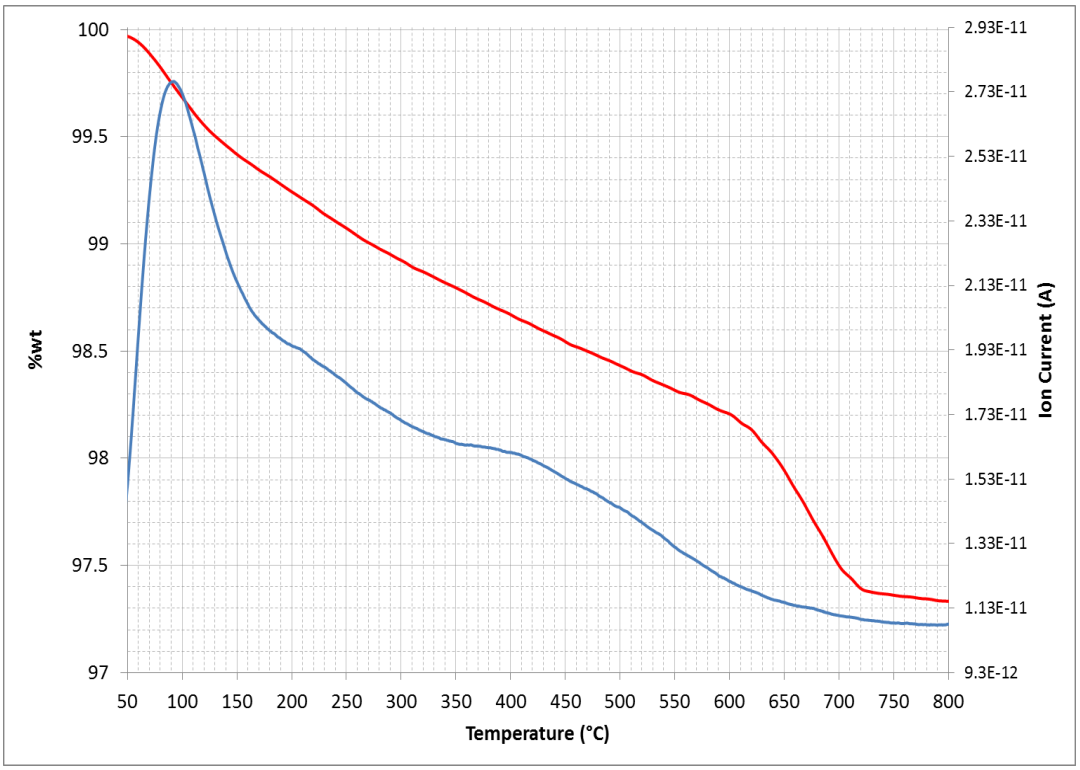

Figure C.33: TG mass loss curve (red) and mass 18 (H_2O) mass spectrometry curve (blue) for *Lan*.

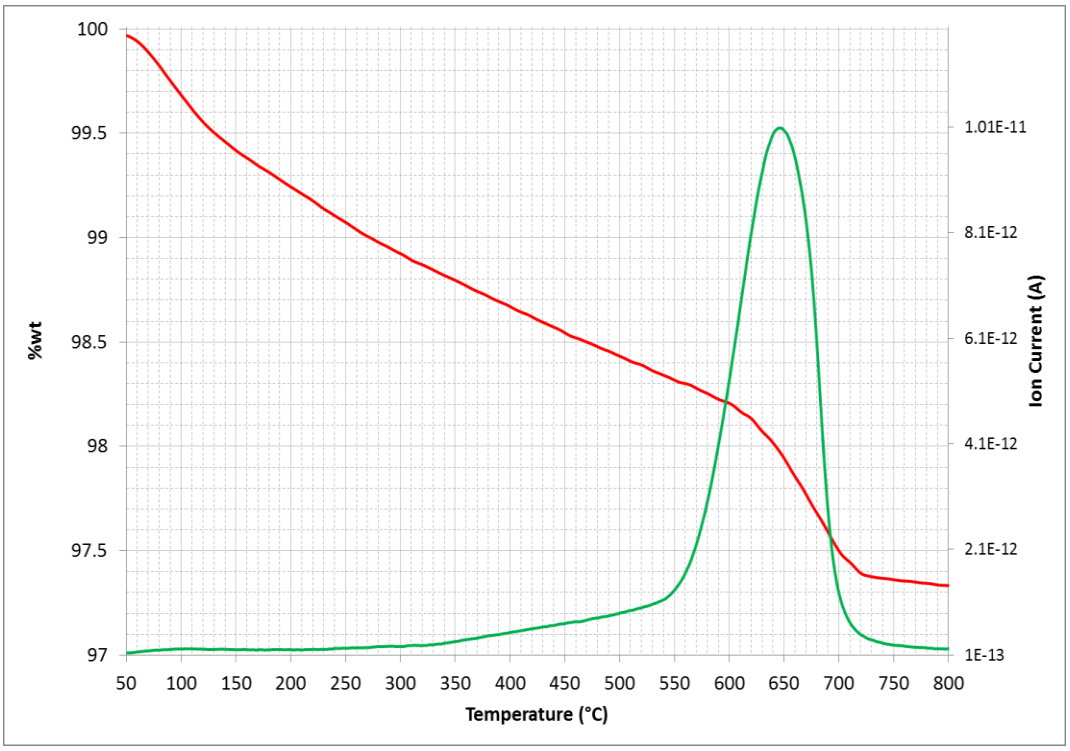

Figure C.34: TG mass loss curve (red) and mass 44 (CO_2) mass spectrometry curve (green) for *Lan*.

Joy

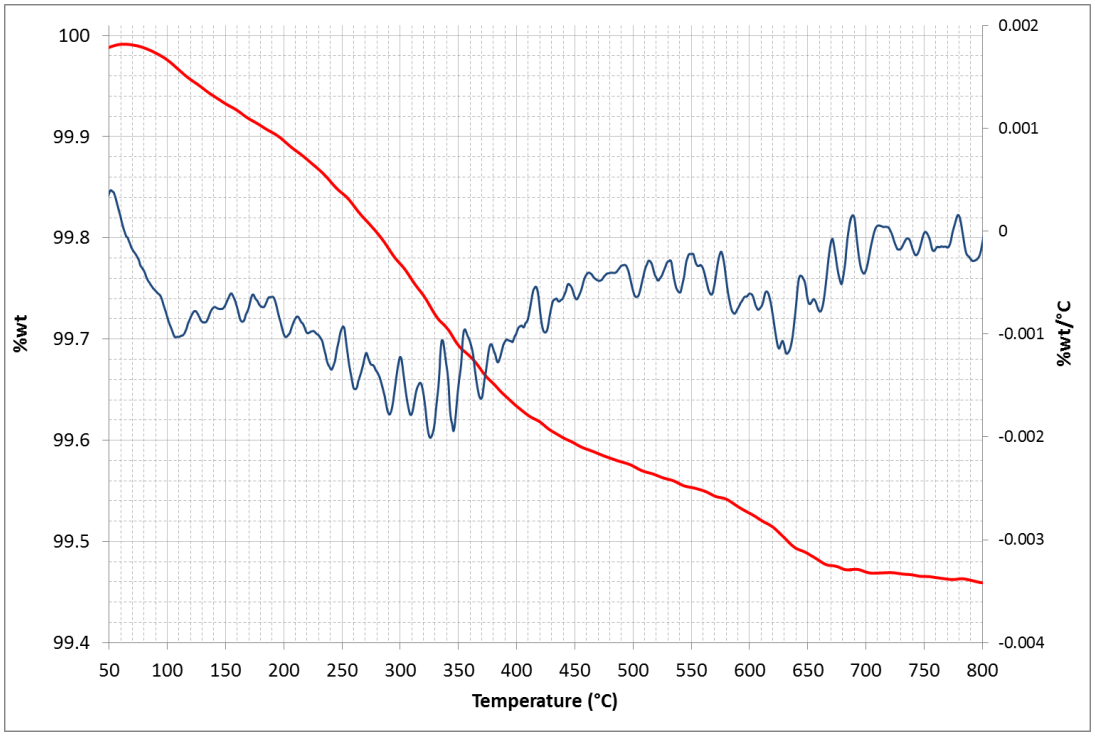

Figure C.35: TG mass loss curve (red) and first derivative curve (blue) for *Joy*.

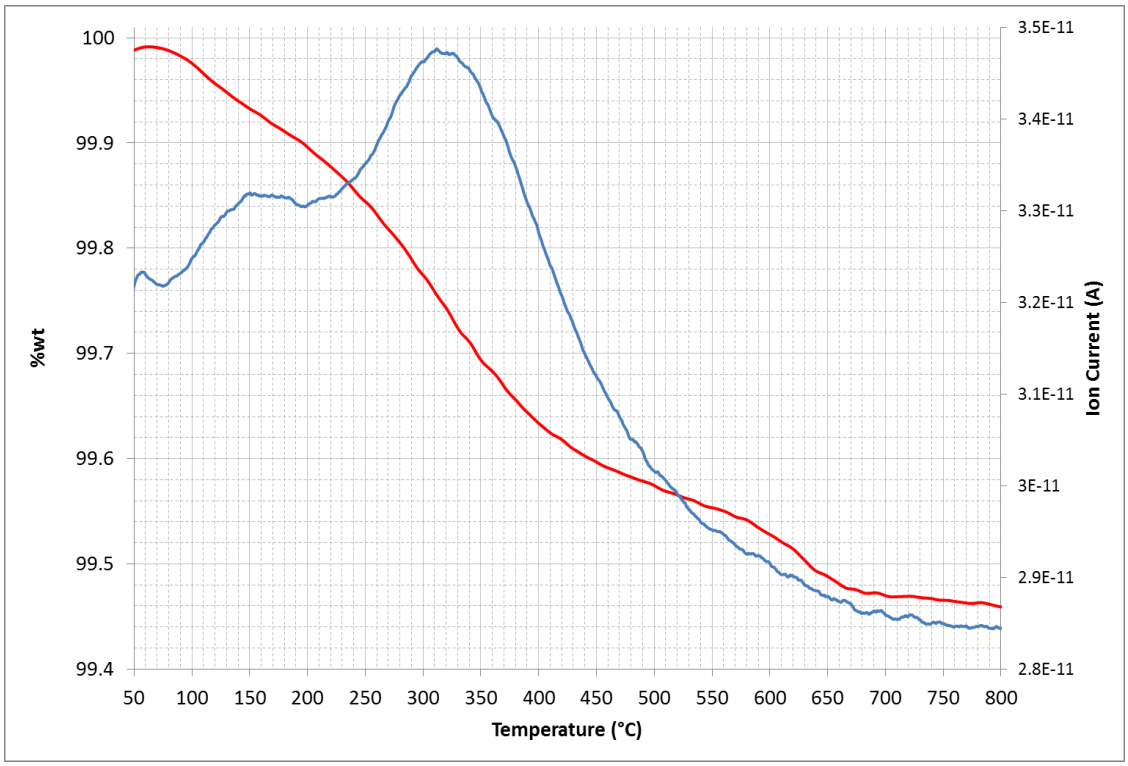

Figure C.36: TG mass loss curve (red) and mass 18 (H_2O) mass spectrometry curve (blue) for *Joy*.

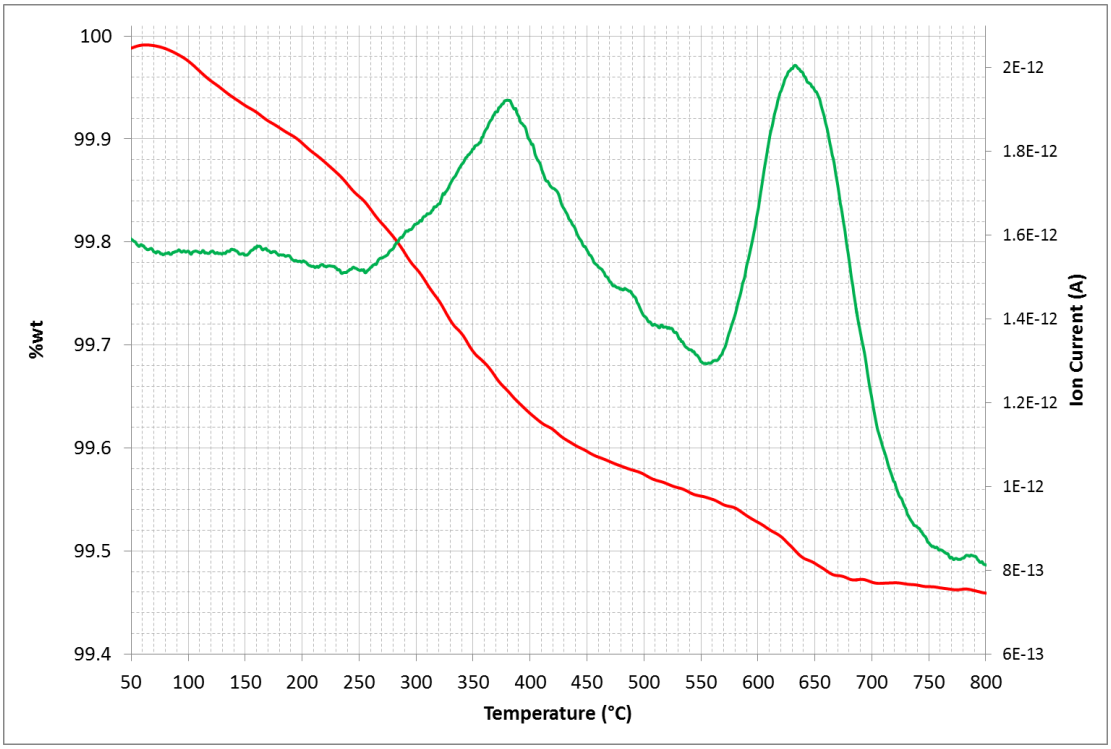

Figure C.37: TG mass loss curve (red) and mass 44 (CO_2) mass spectrometry curve (green) for *Joy*. Triangular hump between 250-450°C was caused by instrumental issues.

Cau

Figure C.38: TG mass loss curve (red) and first derivative curve (blue) for *Cau*.

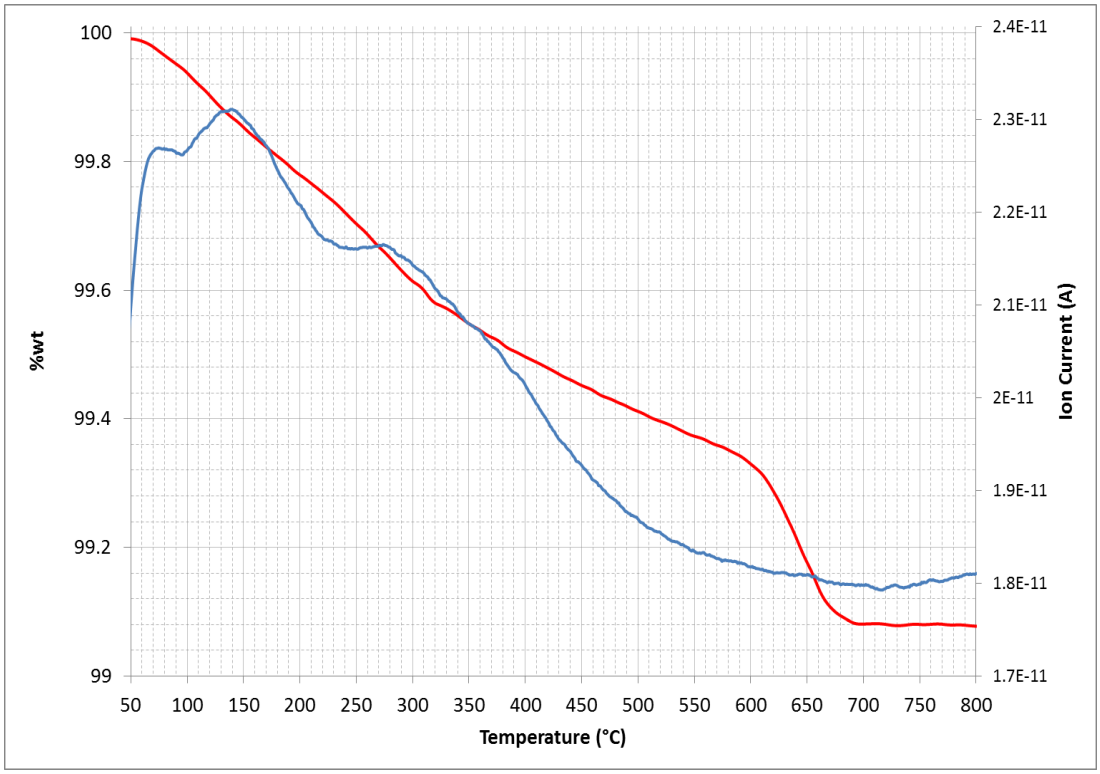

Figure C.39: TG mass loss curve (red) and mass 18 (H_2O) mass spectrometry curve (blue) for *Cau*.

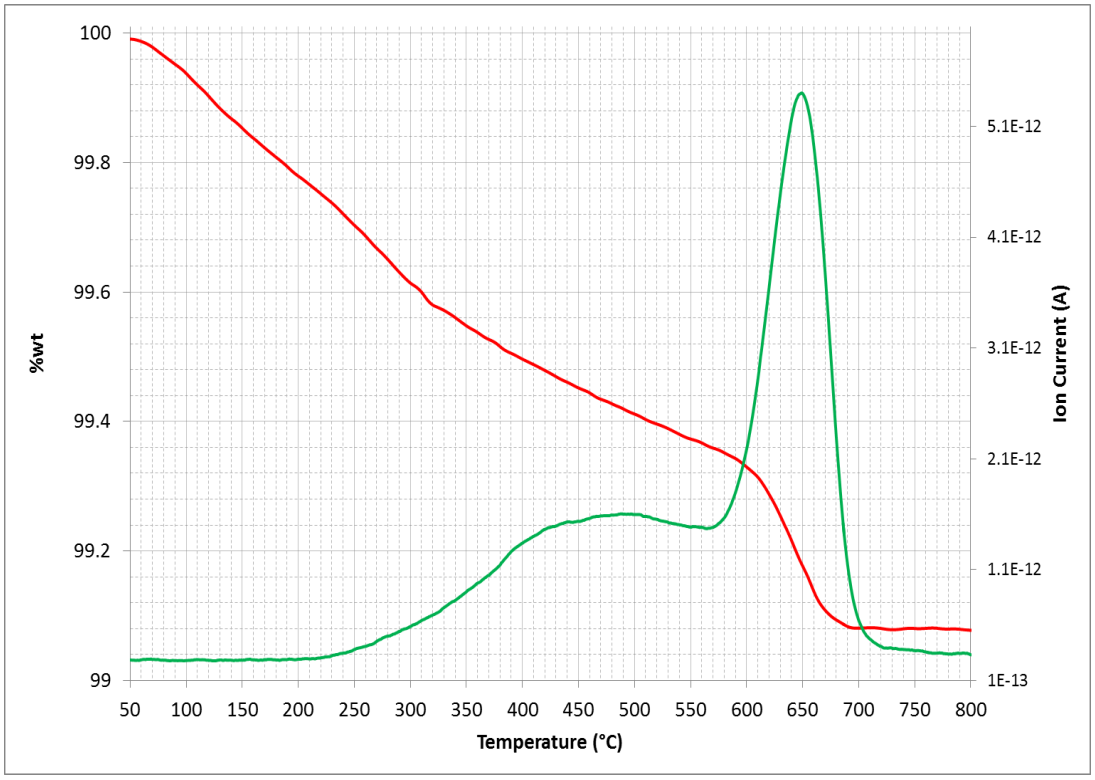

Figure C.40: TG mass loss curve (red) and mass 44 (CO_2) mass spectrometry curve (green) for *Cau*.

Bel

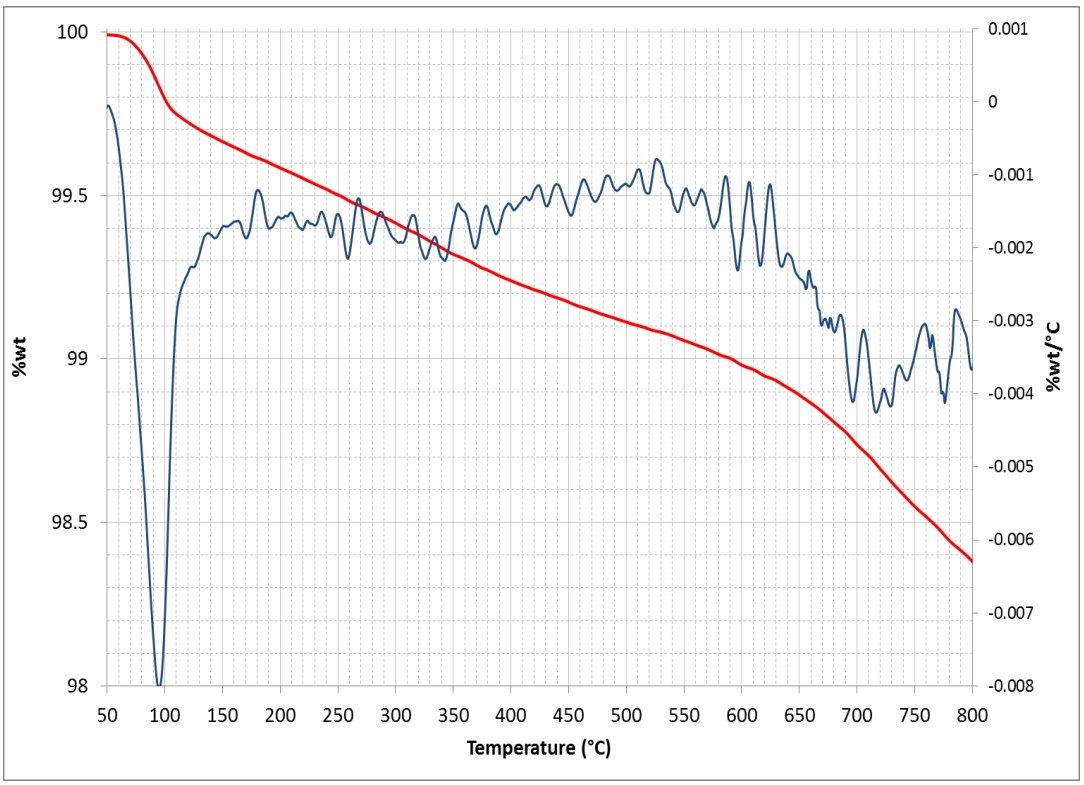

Figure C.41: TG mass loss curve (red) and first derivative curve (blue) for *Bel*.

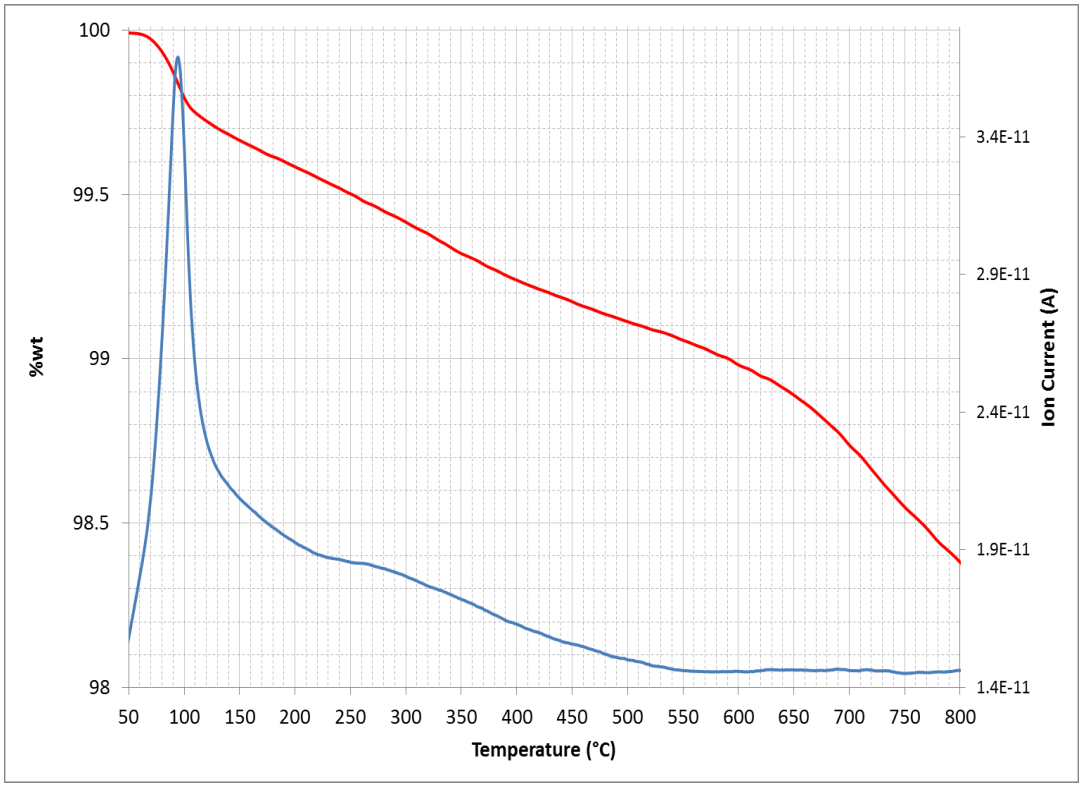

Figure C.42: TG mass loss curve (red) and mass 18 (H_2O) mass spectrometry curve (blue) for *Bel*.

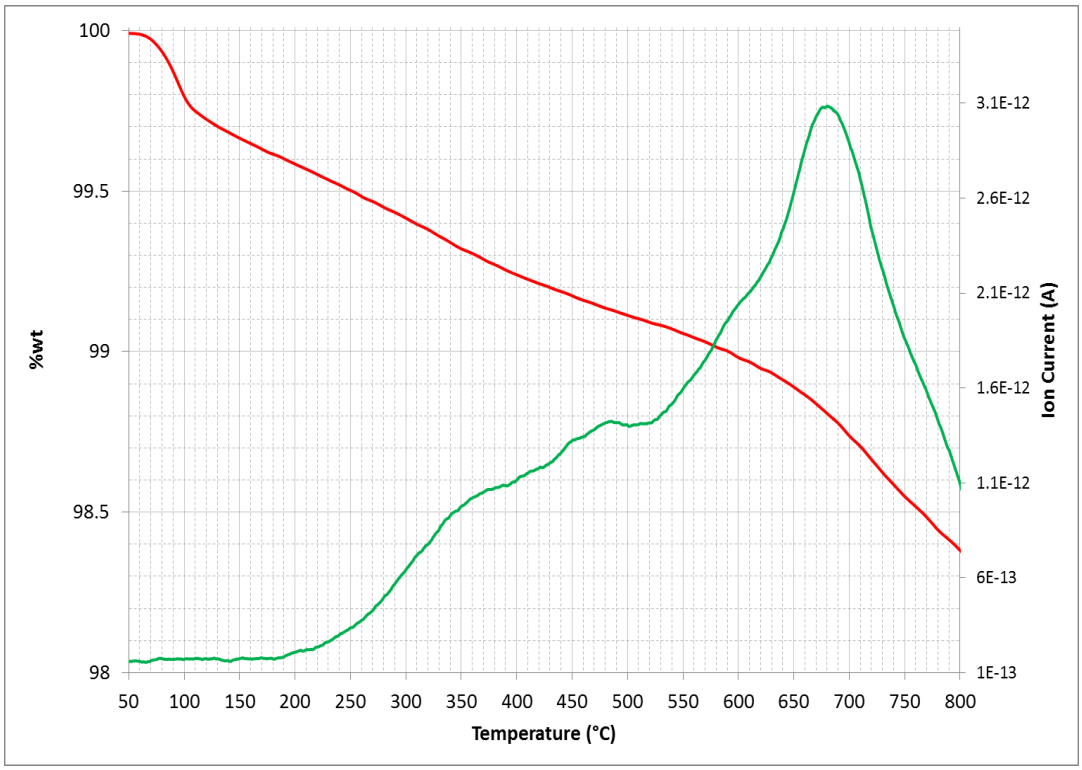

Figure C.43: TG mass loss curve (red) and mass 44 (CO_2) mass spectrometry curve (green) for *Bel*.

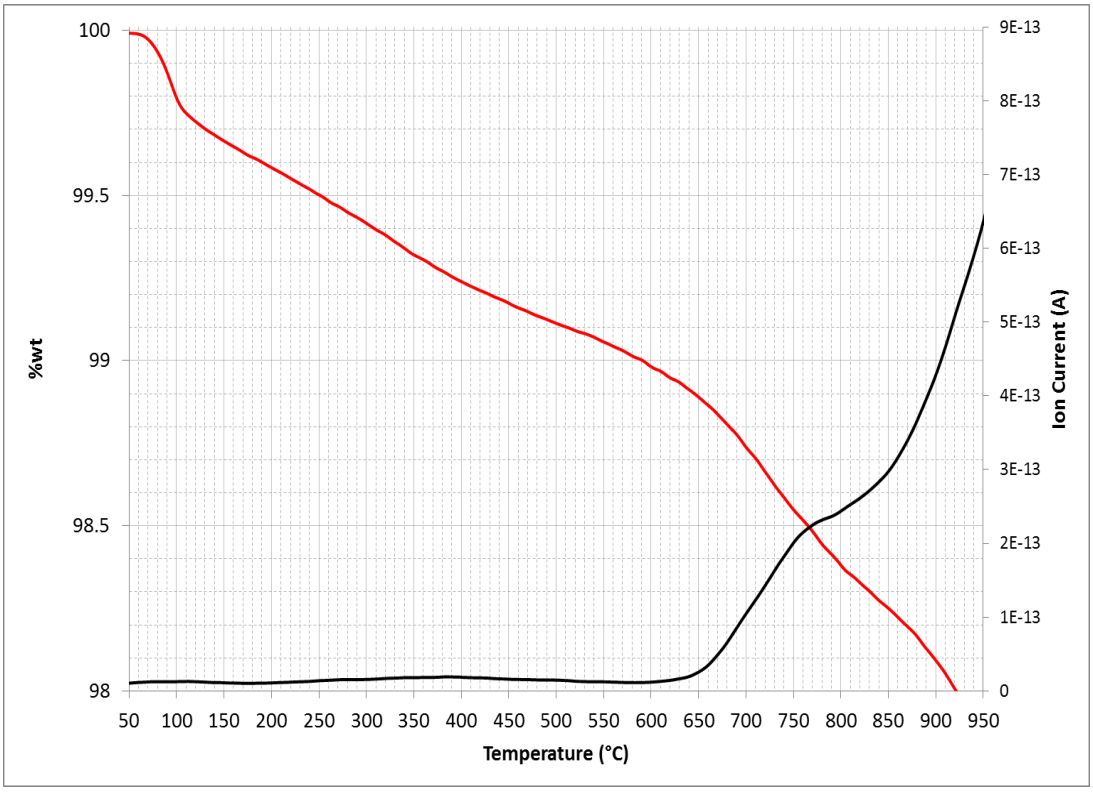

Figure C.44: TG mass loss curve (red) and mass 64 (SO_2) mass spectrometry curve (black) for *Bel*.

Dow1

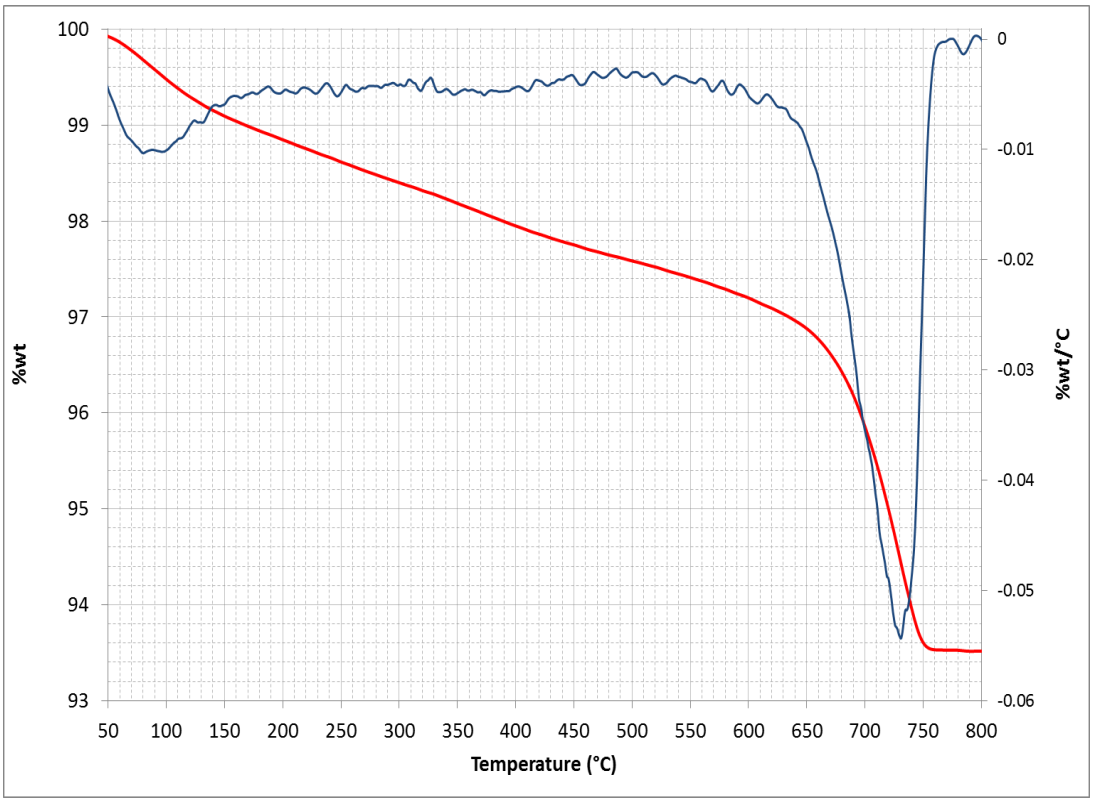

Figure C.45: TG mass loss curve (red) and first derivative curve (blue) for *Dow1*.

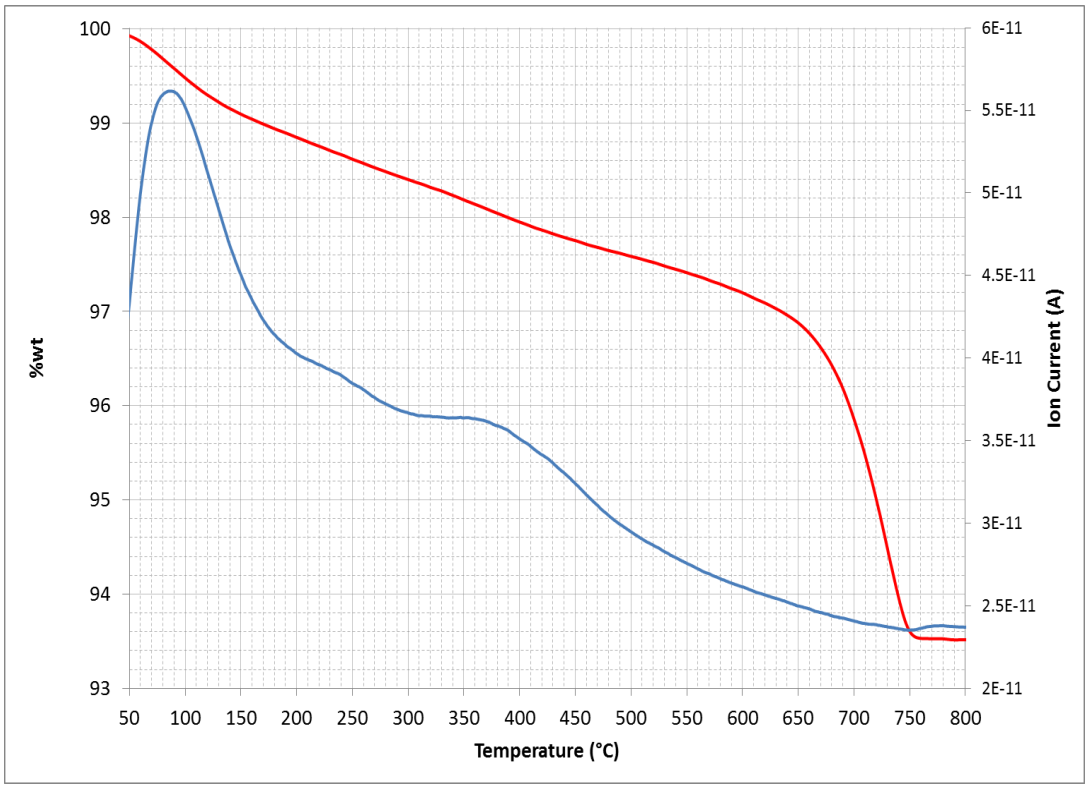

Figure C.46: TG mass loss curve (red) and mass 18 (H_2O) mass spectrometry curve (blue) for *Dow1*.

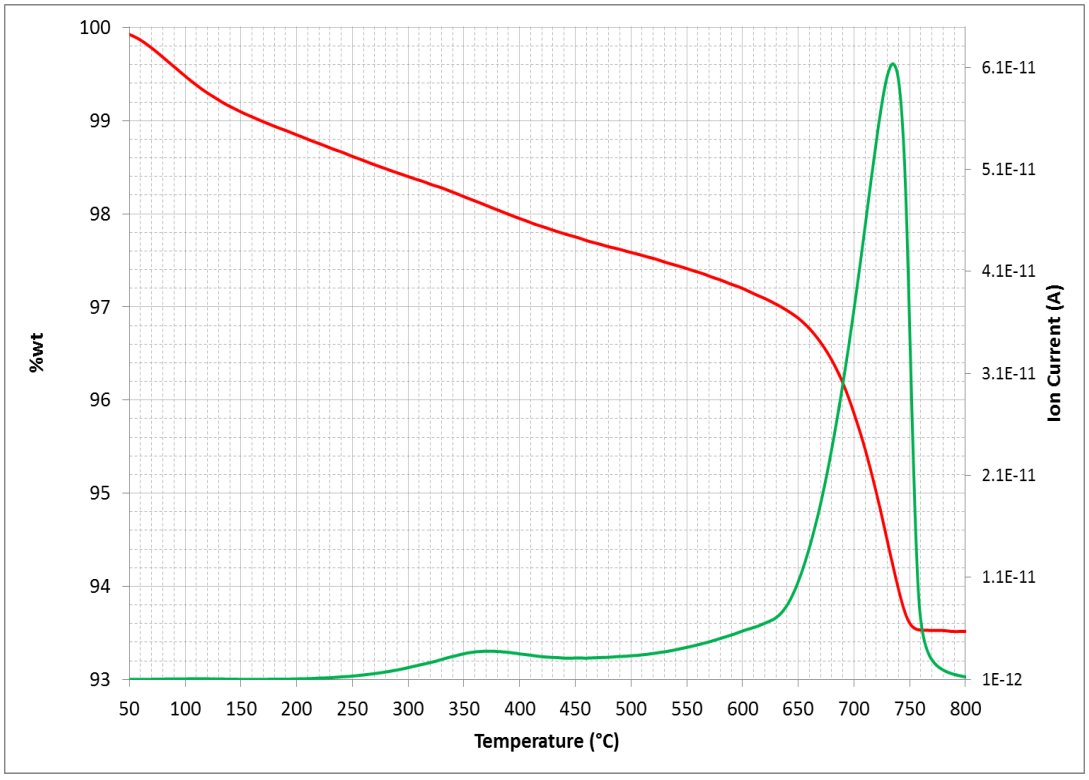

Figure C.47: TG mass loss curve (red) and mass 44 (CO_2) mass spectrometry curve (green) for *Dow1*

Dow2

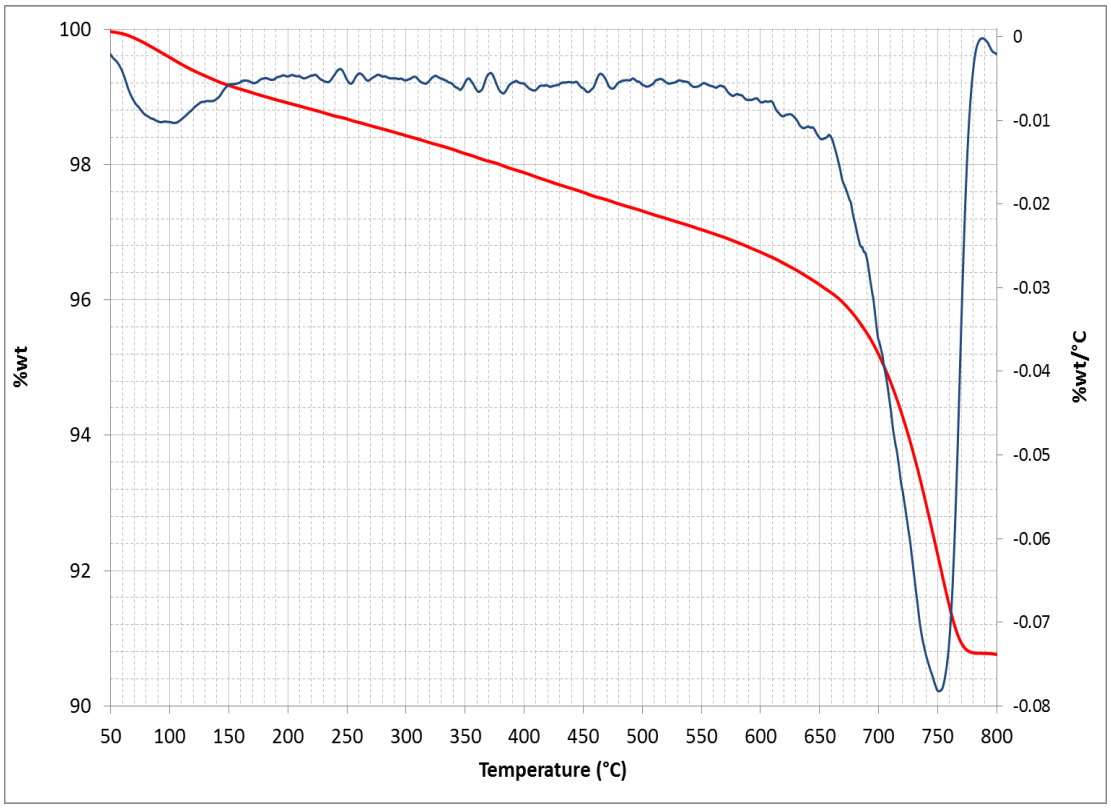

Figure C.48: TG mass loss curve (red) and first derivative curve (blue) for *Dow2*.

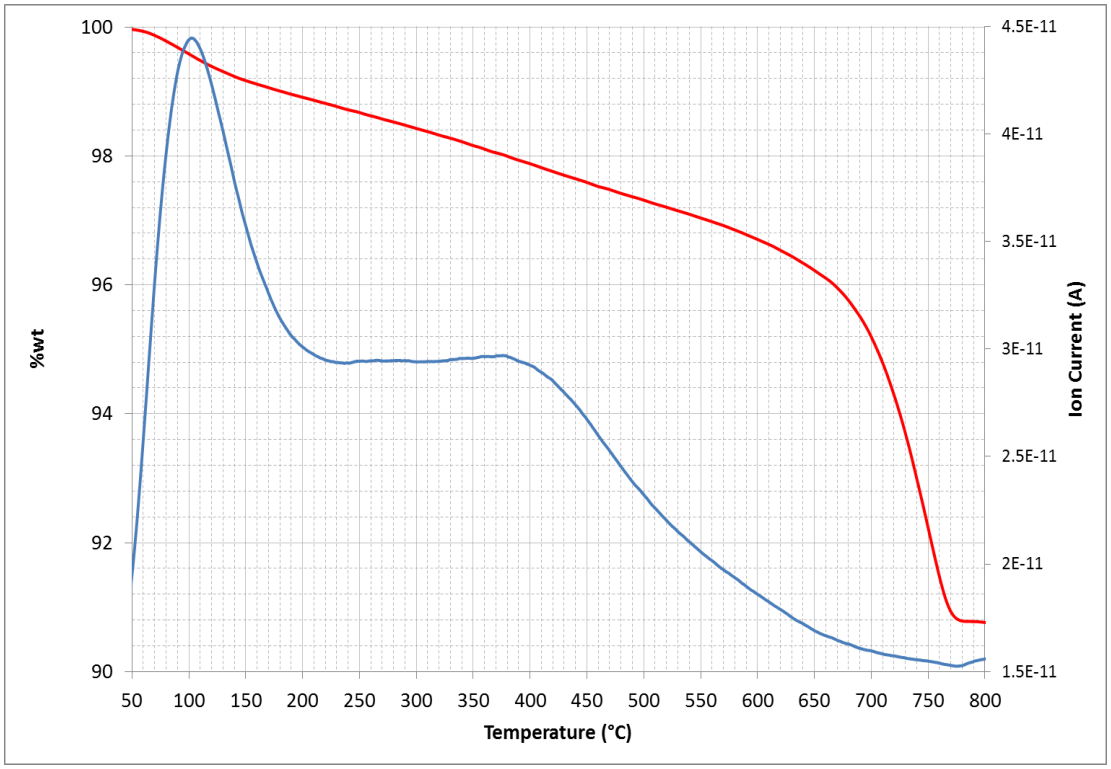

Figure C.49: TG mass loss curve (red) and mass 18 (H_2O) mass spectrometry curve (blue) for *Dow2*.

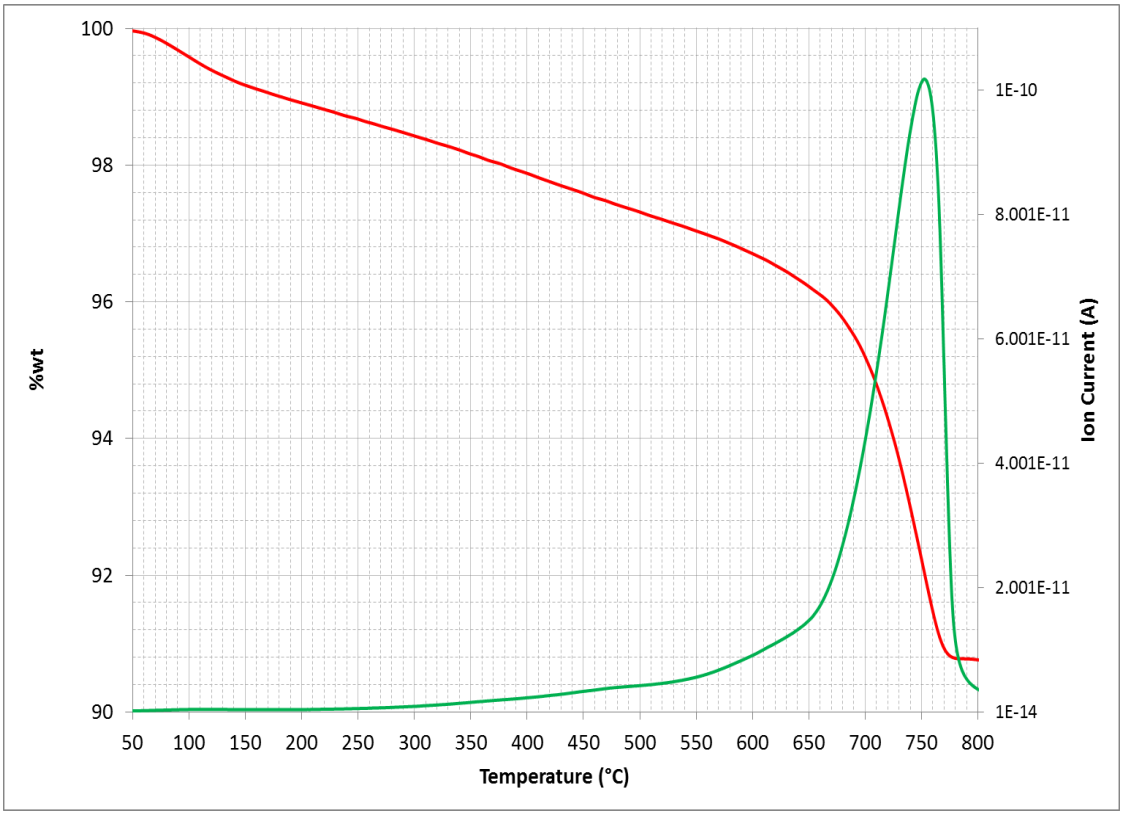

Figure C.50: TG mass loss curve (red) and mass 44 (CO_2) mass spectrometry curve (green) for *Dow2*.

Tur

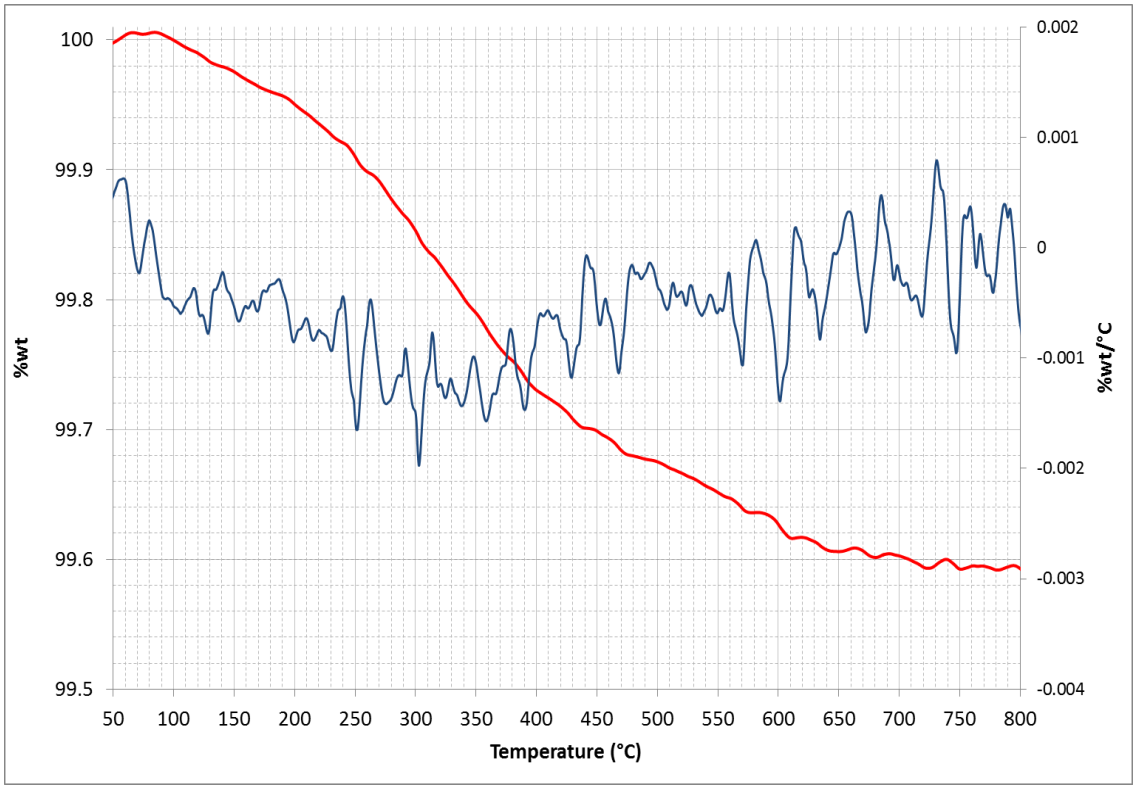

Figure C.51: TG mass loss curve (red) and first derivative curve (blue) for *Tur*.

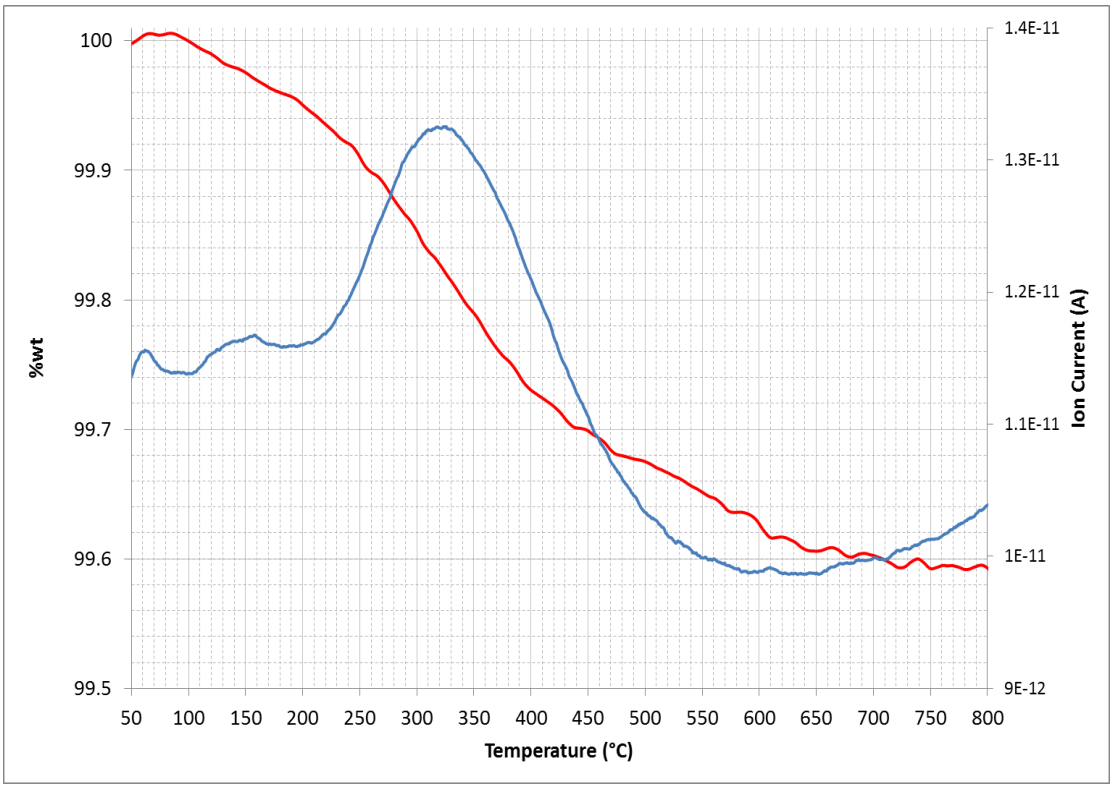

Figure C.52: TG mass loss curve (red) and mass 18 (H_2O) mass spectrometry curve (blue) for *Tur*.

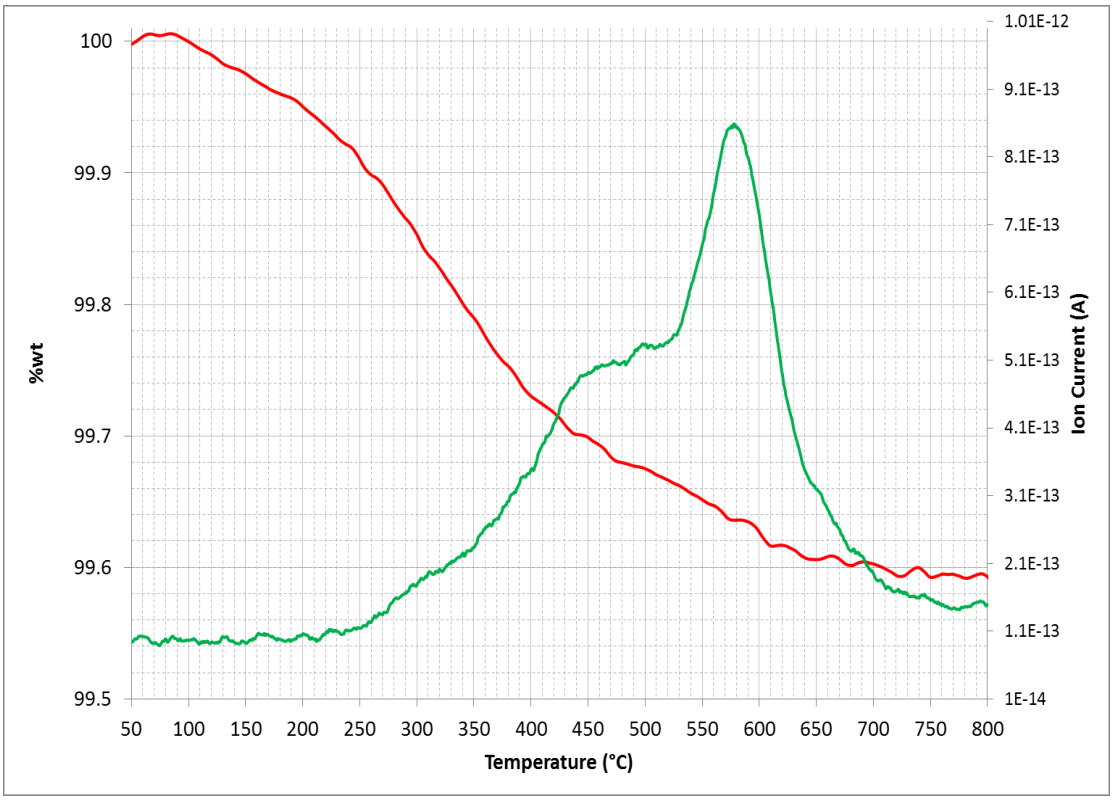

Figure C.53: TG mass loss curve (red) and mass 44 (CO_2) mass spectrometry curve (green) for *Tur*.

Ted

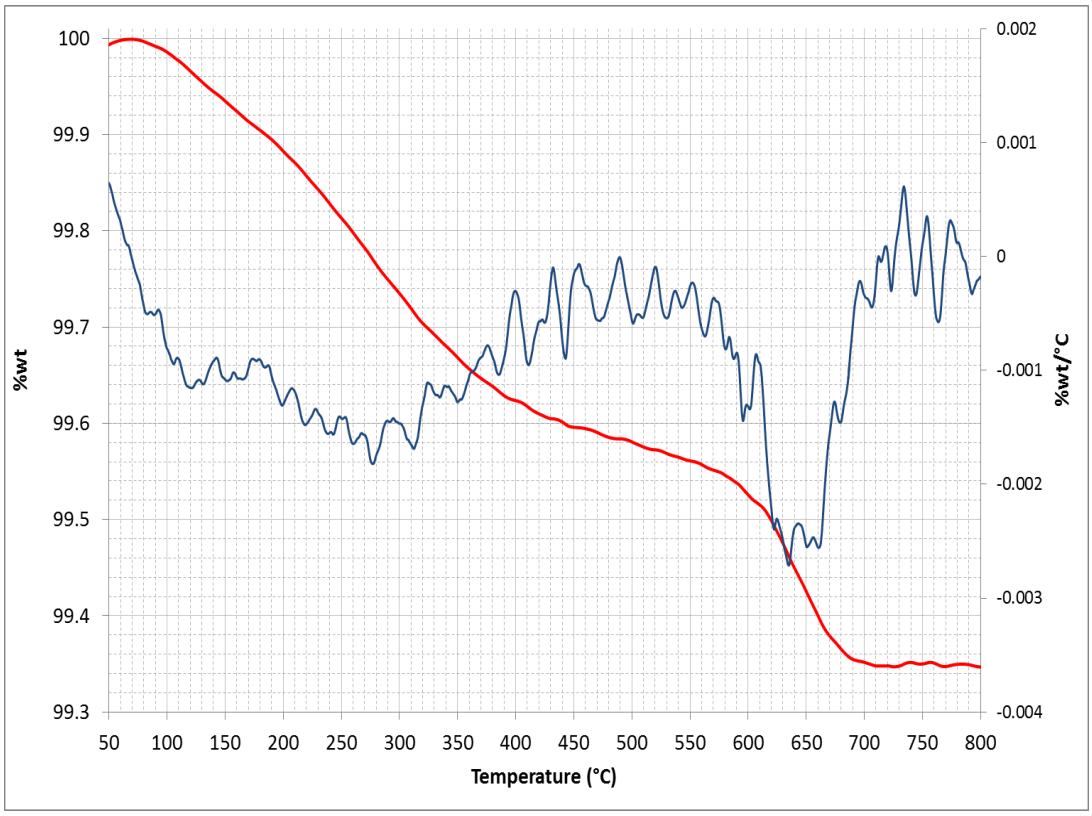

Figure C.54: TG mass loss curve (red) and first derivative curve (blue) for *Ted*.

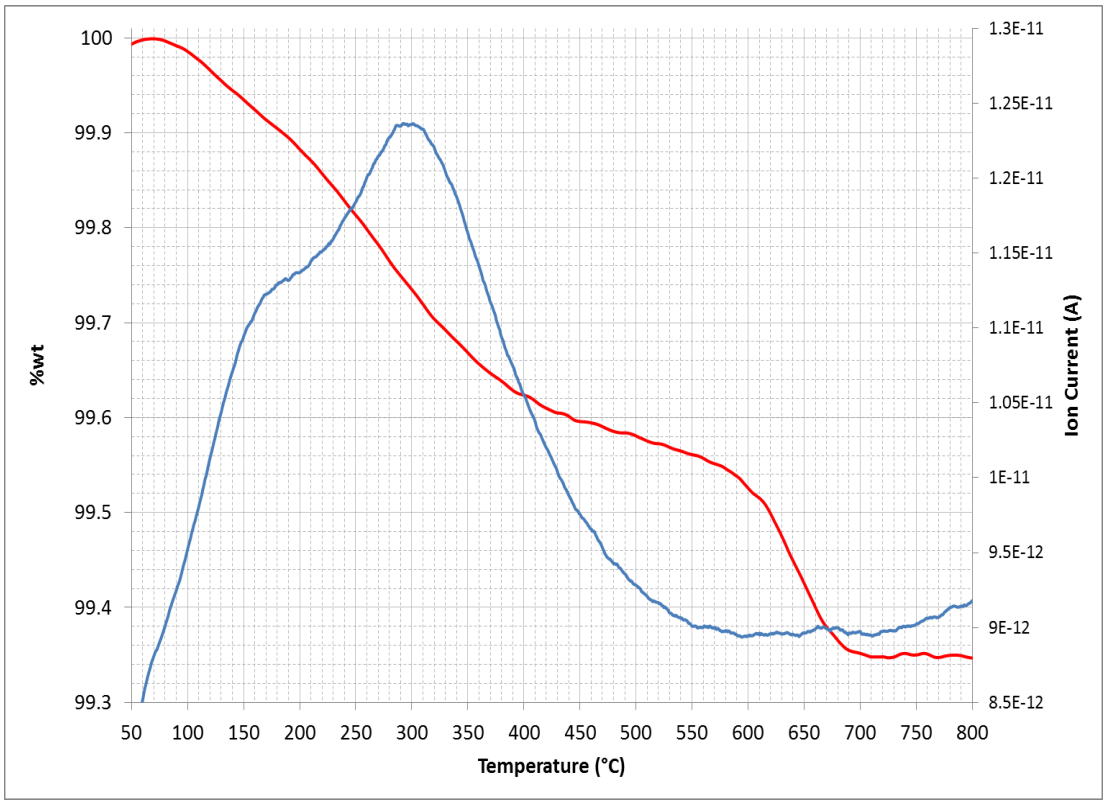

Figure C.55: TG mass loss curve (red) and mass 18 (H_2O) mass spectrometry curve (blue) for *Ted*.

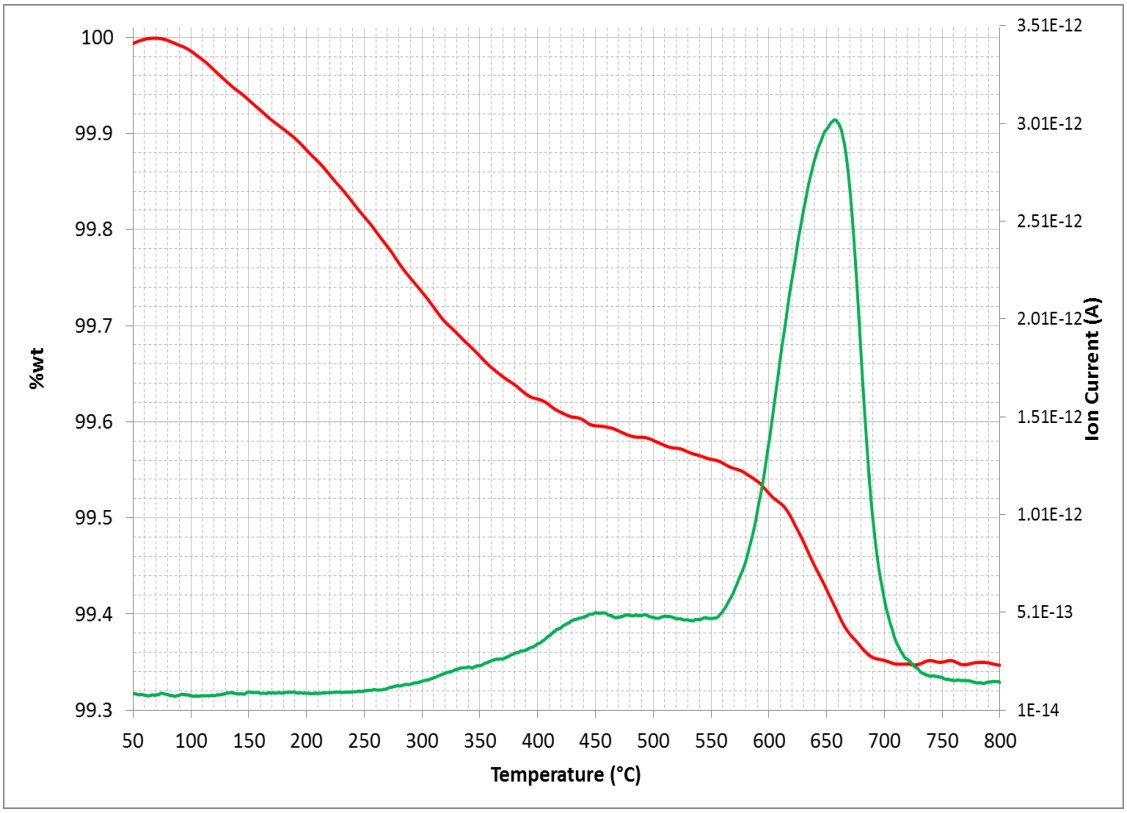

Figure C.56: TG mass loss curve (red) and mass 44 (CO_2) mass spectrometry curve (green) for *Ted*.

Appendix D

Arrhenius (Activation Energy) Plots

This appendix presents the Arrhenius plots for all samples (where previous curve modelling permitted), consisting of a plot for the 130C and 500C components together with the RHX component (labelled as 500C-130C). Plots are presented for both $t^{1/4}$ and $t^{1/n}$ models. The uncertainties are presented at the 2σ confidence level.

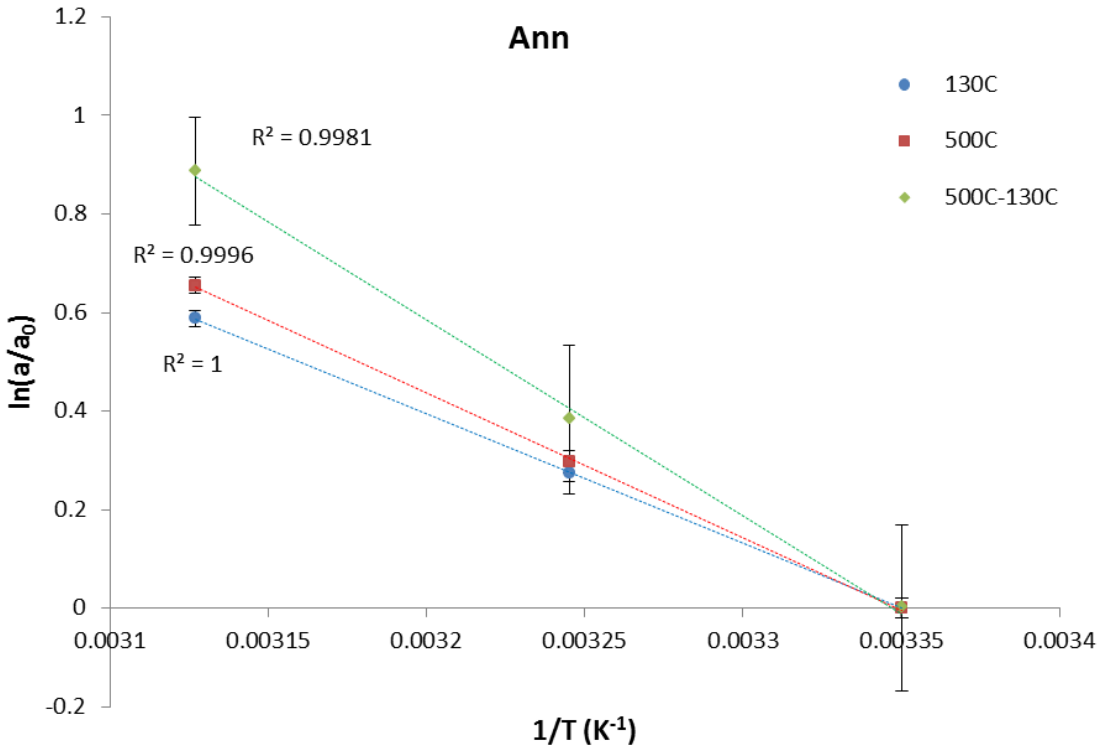

Figure D.1: Arrhenius plot ($t^{1/4}$ model) for 130°C (blue), 500°C (red) and 500-130°C (green, RHX component) components of mass gain rates for *Ann* sample. Uncertainties are at 2σ.

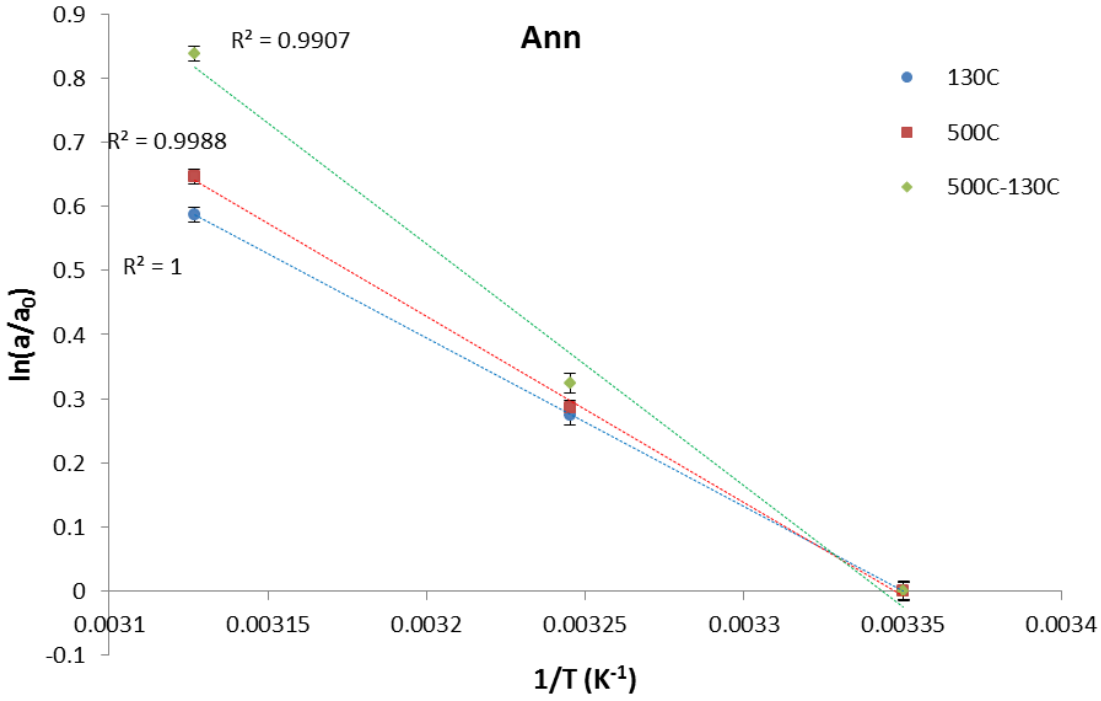

Figure D.2: Arrhenius plot ($t^{1/n}$ model) for 130°C (blue), 500°C (red) and 500-130°C (green, RHX component) components of mass gain rates for *Ann* sample. Uncertainties are at 2σ.

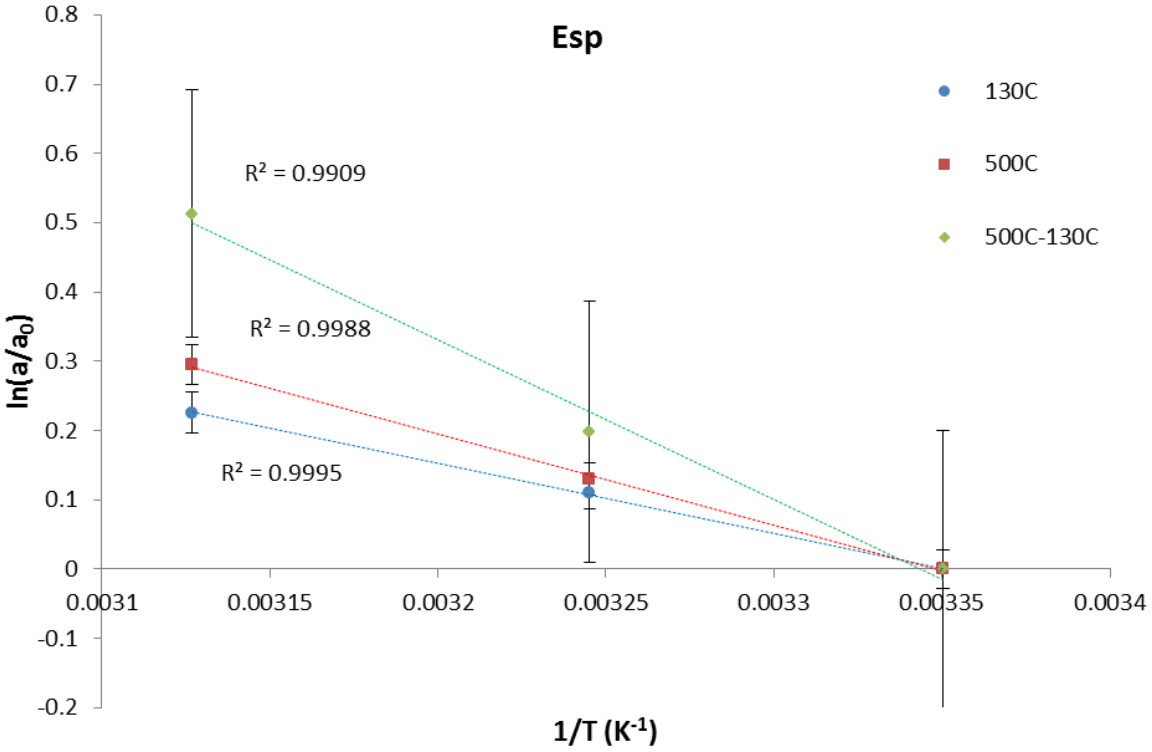

Figure D.3: Arrhenius plot ($t^{1/4}$ model) for 130°C (blue), 500°C (red) and 500-130°C (green, RHX component) components of mass gain rates for *Esp* sample. Uncertainties are at 2σ.

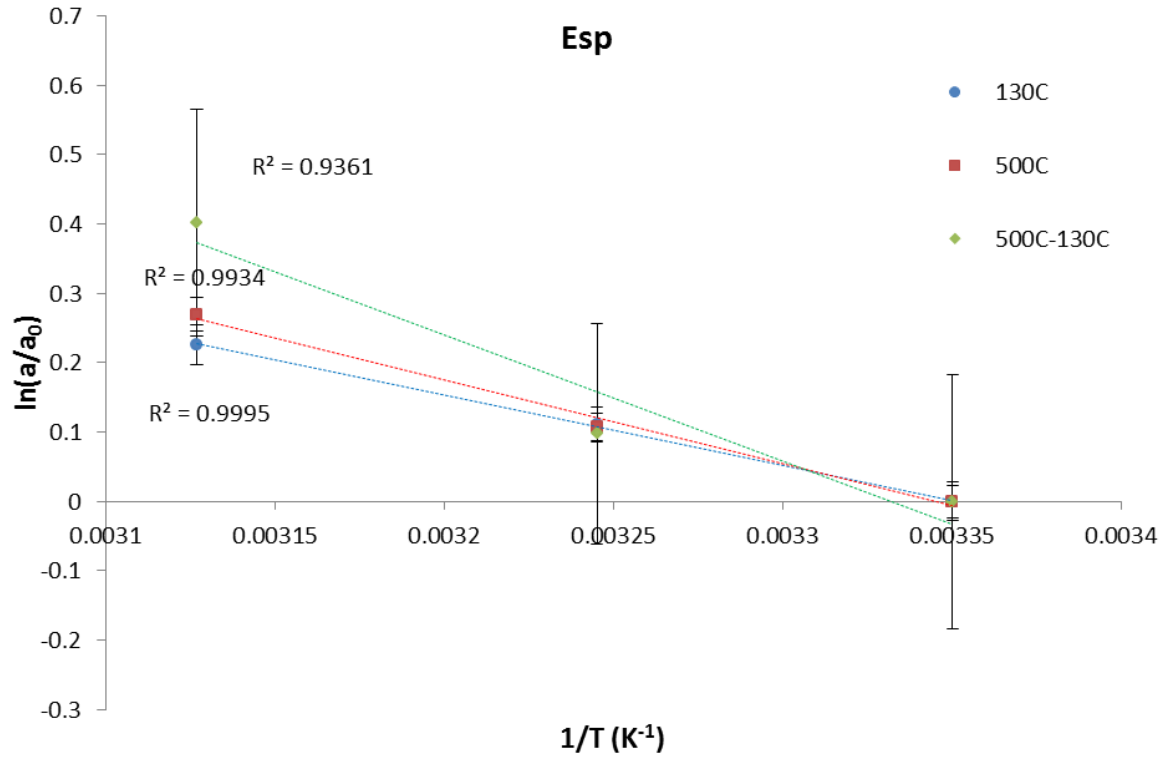

Figure D.4: Arrhenius plot ($t^{1/n}$ model) for 130°C (blue), 500°C (red) and 500-130°C (green, RHX component) components of mass gain rates for *Esp* sample. Uncertainties are at 2σ.

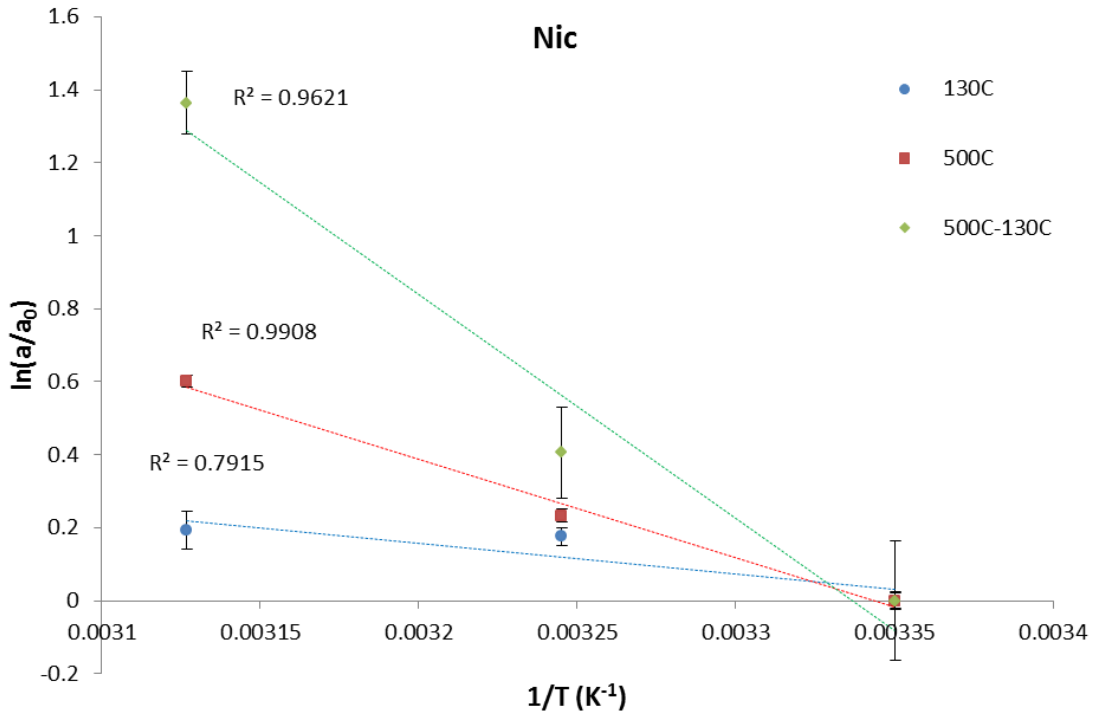

Figure D.5: Arrhenius plot ($t^{1/4}$ model) for 130°C (blue), 500°C (red) and 500-130°C (green, RHX component) components of mass gain rates for *Nic* sample. Uncertainties are at 2σ.

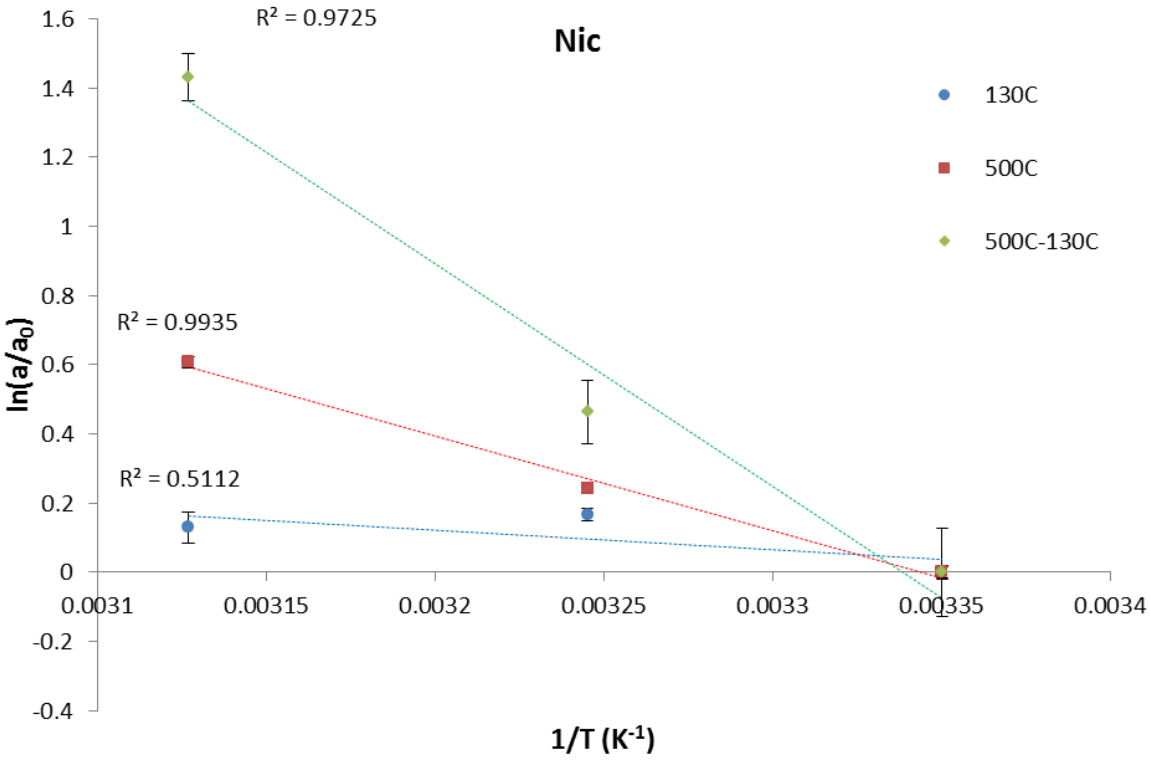

Figure D.6: Arrhenius plot ($t^{1/n}$ model) for 130°C (blue), 500°C (red) and 500-130°C (green, RHX component) components of mass gain rates for *Nic* sample. Uncertainties are at 2σ.

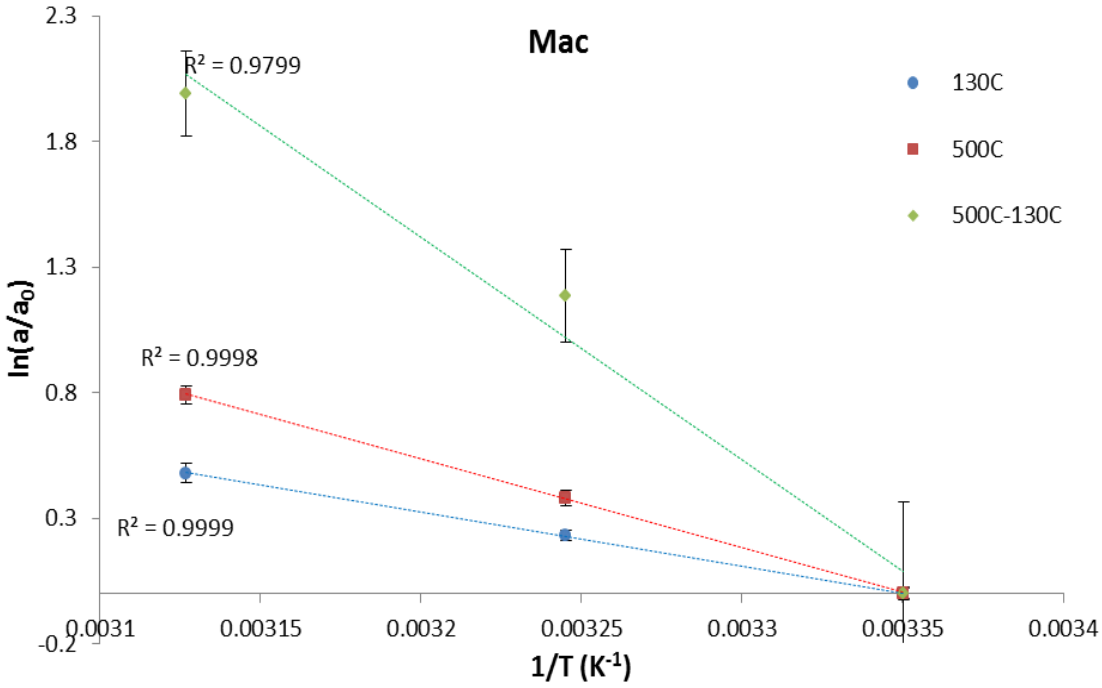

Figure D.7: Arrhenius plot ($t^{1/4}$ model) for 130°C (blue), 500°C (red) and 500-130°C (green, RHX component) components of mass gain rates for *Mac* sample. Uncertainties are at 2σ.

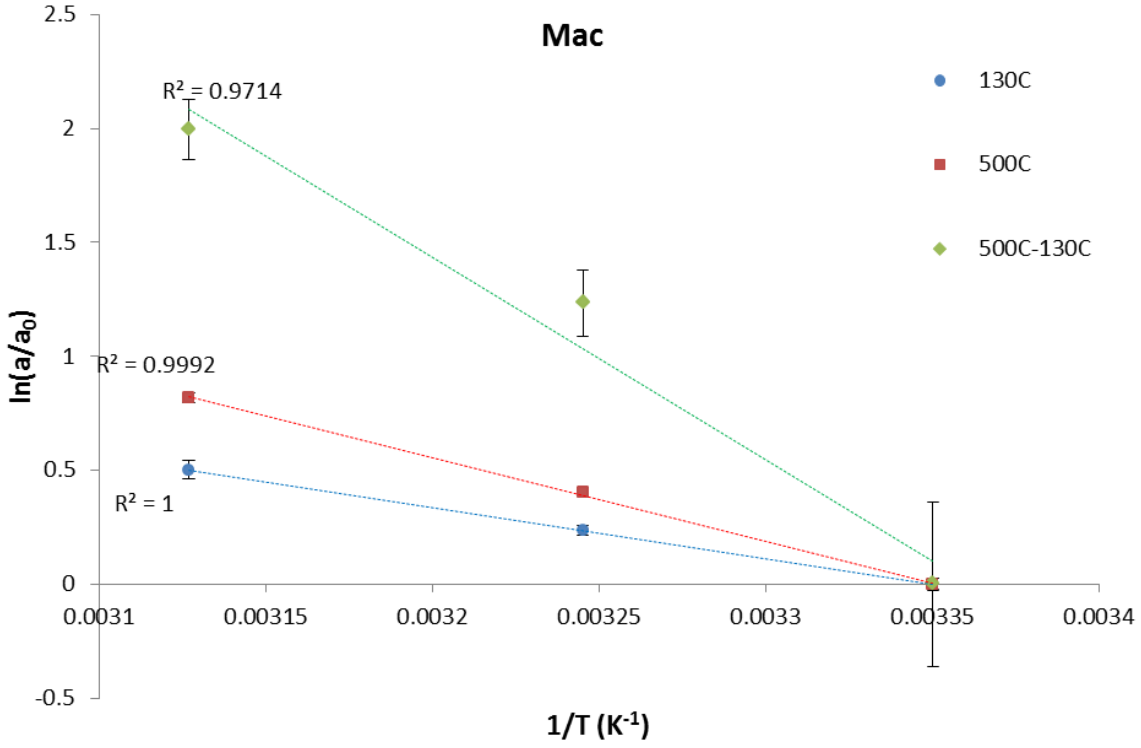

Figure D.8: Arrhenius plot ($t^{1/n}$ model) for 130°C (blue), 500°C (red) and 500-130°C (green, RHX component) components of mass gain rates for *Mac* sample. Uncertainties are at 2σ.

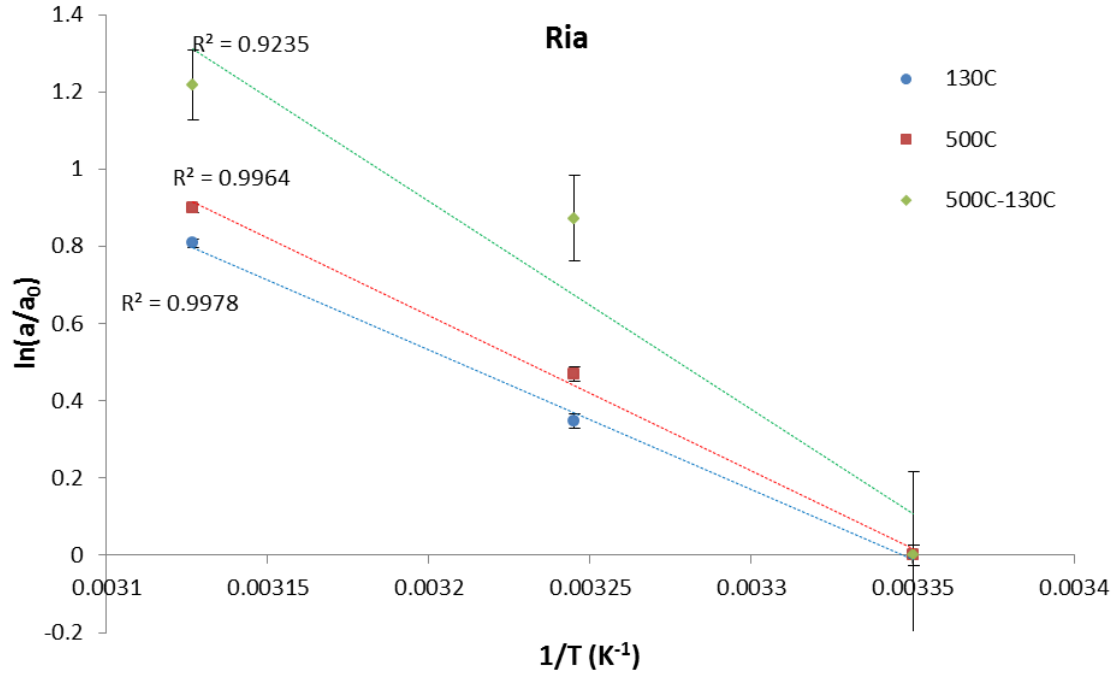

Figure D.9: Arrhenius plot ($t^{1/4}$ model) for 130°C (blue), 500°C (red) and 500-130°C (green, RHX component) components of mass gain rates for *Ria* sample. Uncertainties are at 2σ.

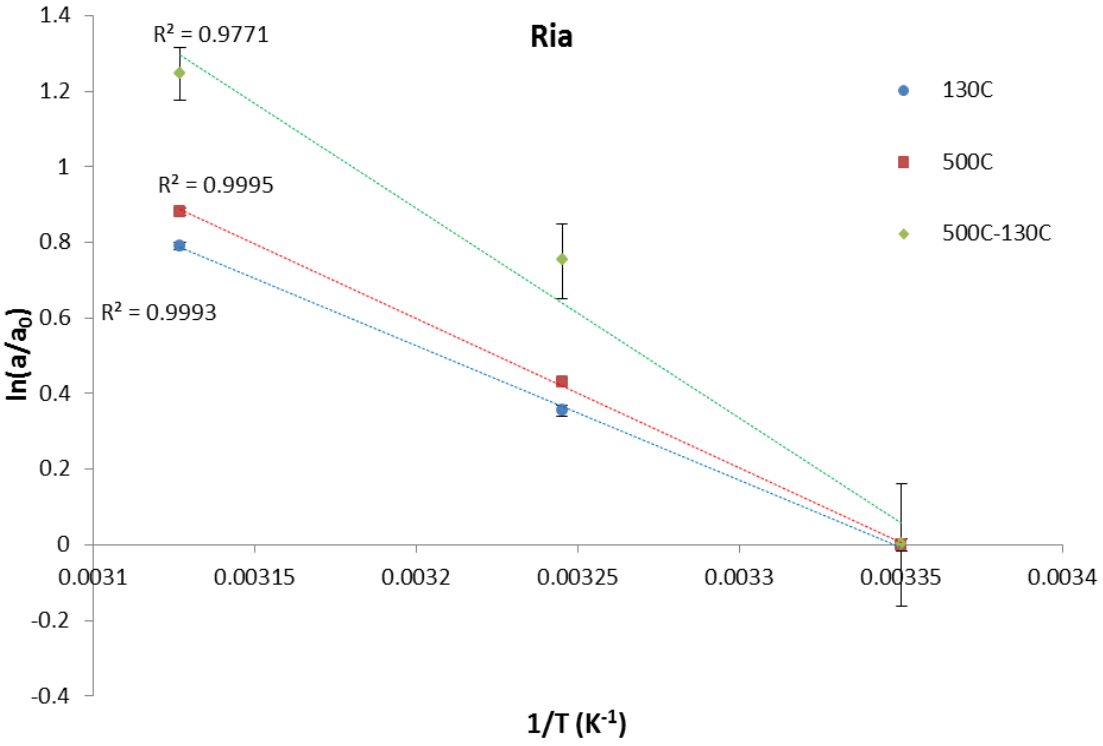

Figure D.10: Arrhenius plot ($t^{1/n}$ model) for 130°C (blue), 500°C (red) and 500-130°C (green, RHX component) components of mass gain rates for *Ria* sample. Uncertainties are at 2σ.

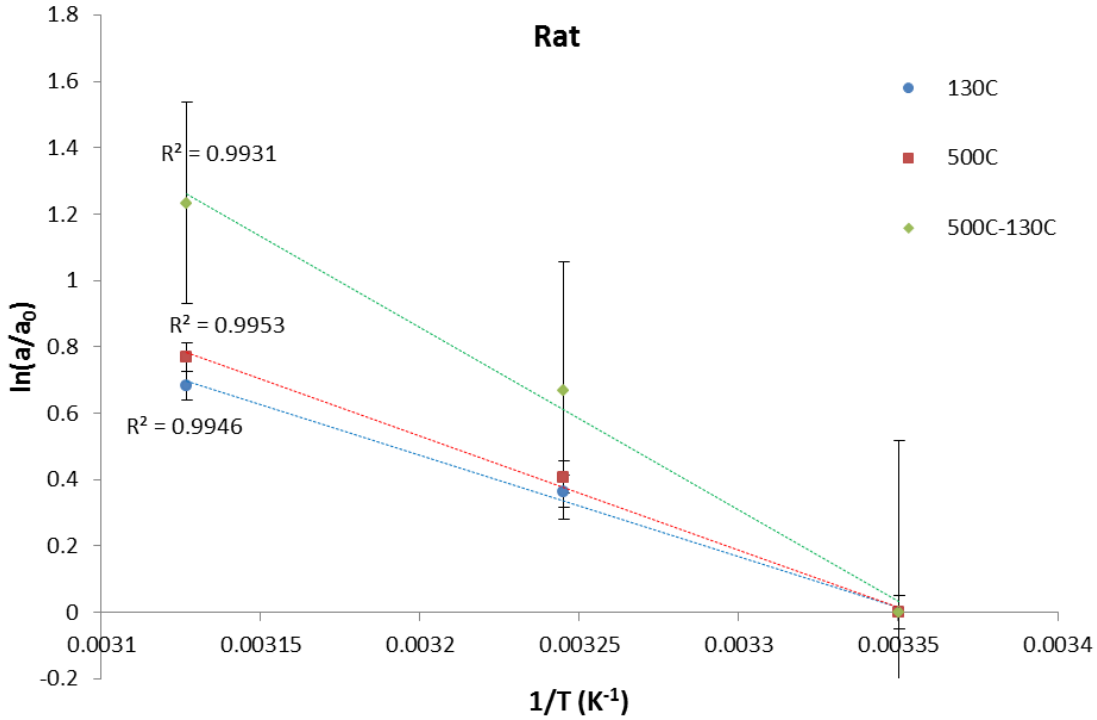

Figure D.11: Arrhenius plot ($t^{1/4}$ model) for 130°C (blue), 500°C (red) and 500-130°C (green, RHX component) components of mass gain rates for *Rat* sample. Uncertainties are to 2σ.

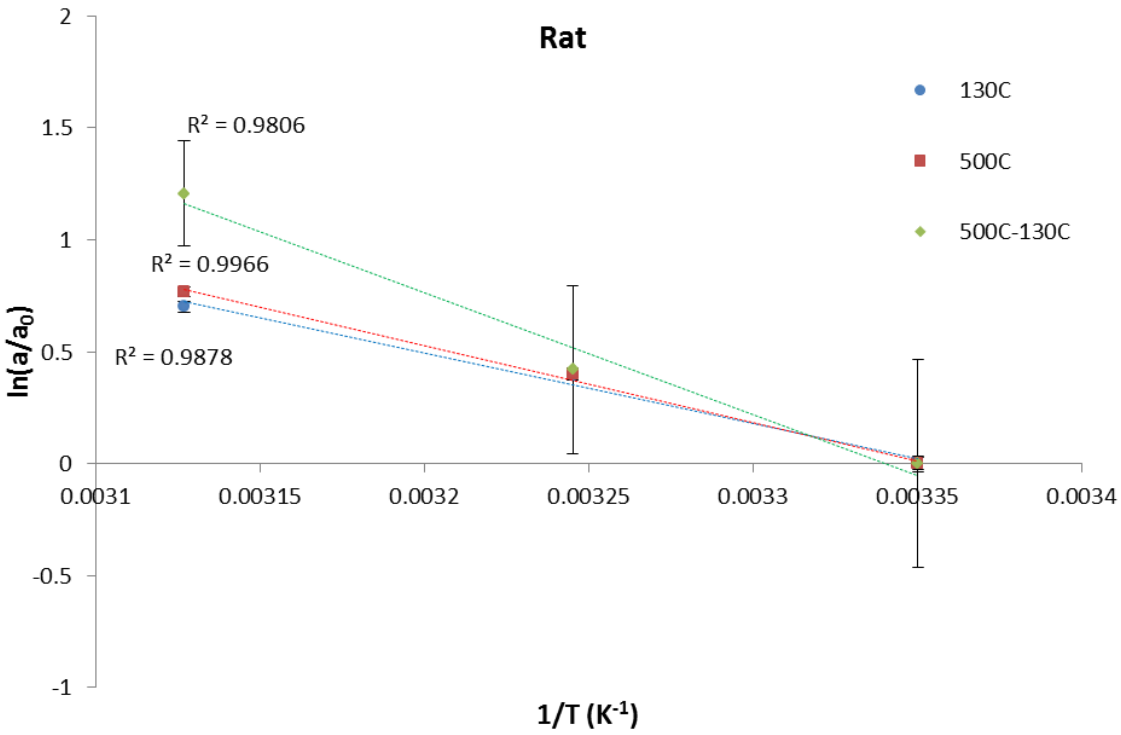

Figure D.12: Arrhenius plot ($t^{1/n}$ model) for 130°C (blue), 500°C (red) and 500-130°C (green, RHX component) components of mass gain rates for *Rat* sample. Uncertainties are to 2σ.

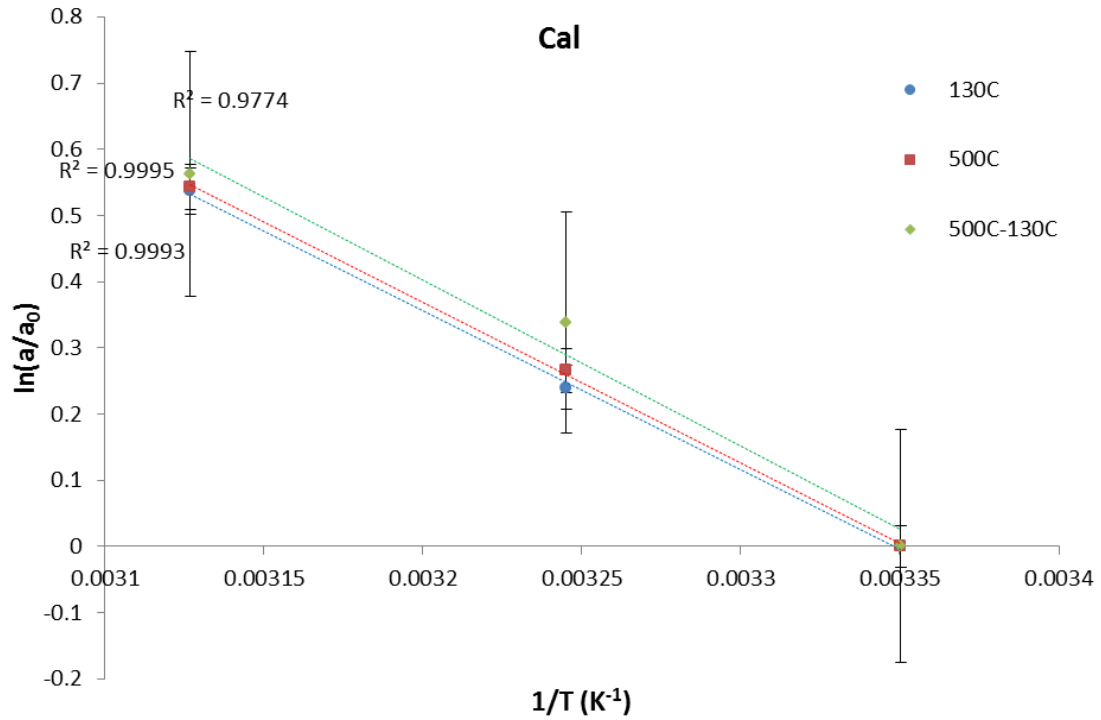

Figure D.13: Arrhenius plot ($t^{1/4}$ model) for 130°C (blue), 500°C (red) and 500-130°C (green, RHX component) components of mass gain rates for *Cal* sample. Uncertainties are to 2σ.

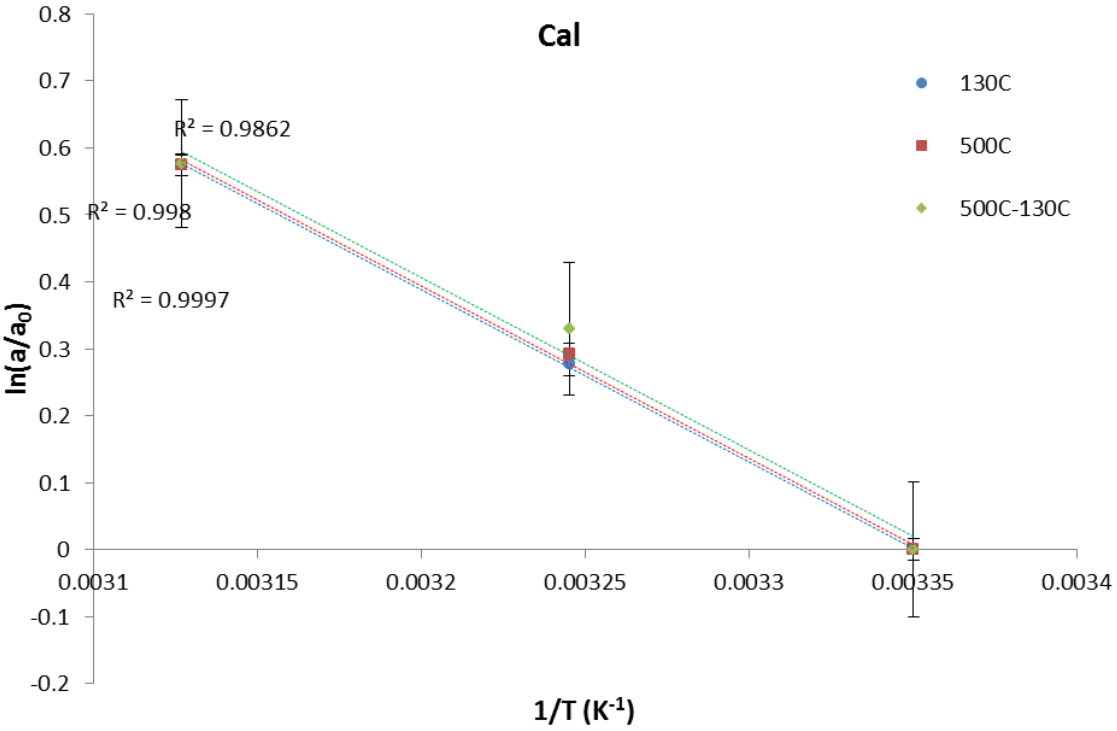

Figure D.14: Arrhenius plot ($t^{1/n}$ model) for 130°C (blue), 500°C (red) and 500-130°C (green, RHX component) components of mass gain rates for *Cal* sample. Uncertainties are to 2σ.

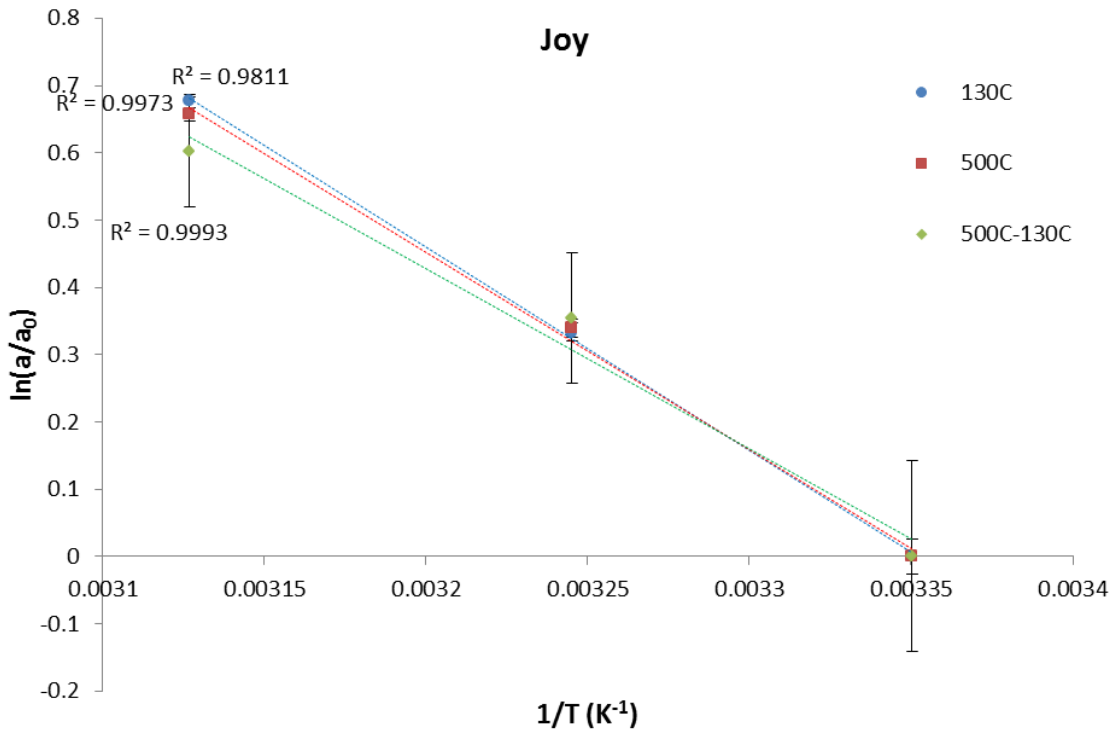

Figure D.15: Arrhenius plot ($t^{1/4}$ model) for 130°C (blue), 500°C (red) and 500-130°C (green, RHX component) components of mass gain rates for *Joy* sample. Uncertainties are to 2σ.

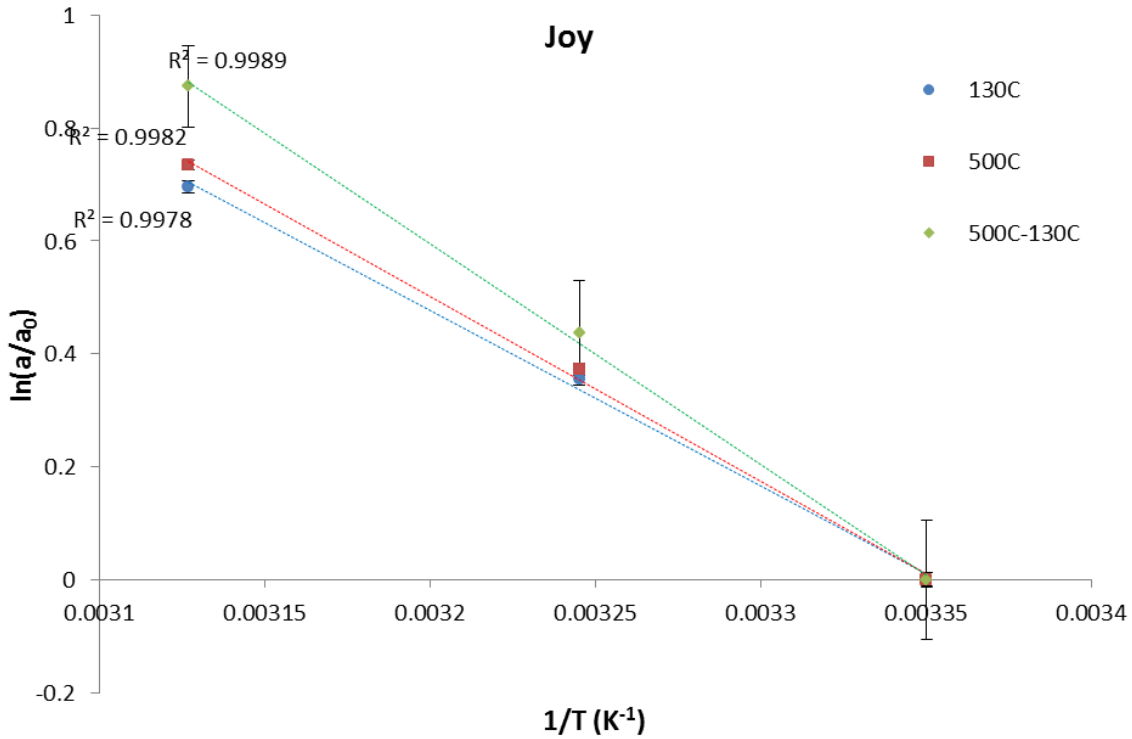

Figure D.16: Arrhenius plot ($t^{1/n}$ model) for 130°C (blue), 500°C (red) and 500-130°C (green, RHX component) components of mass gain rates for *Joy* sample. Uncertainties are to 2σ.

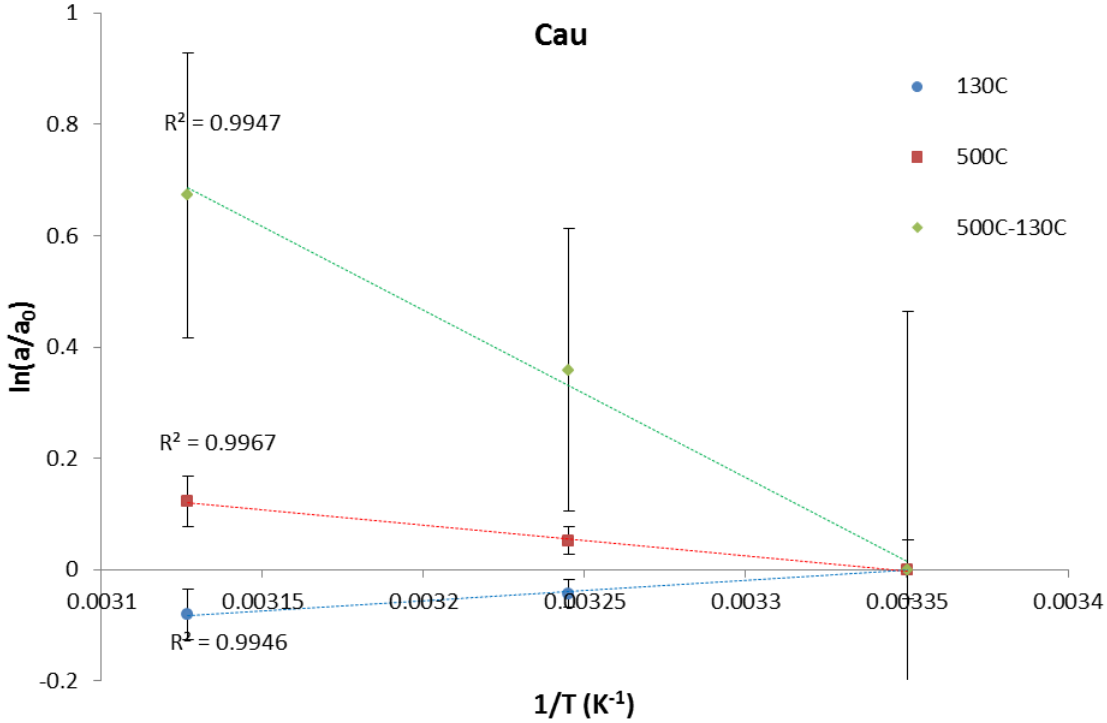

Figure D.17: Arrhenius plot ($t^{1/4}$ model) for 130°C (blue), 500°C (red) and 500-130°C (green, RHX component) components of mass gain rates for *Cau* sample. Uncertainties are to 2σ.

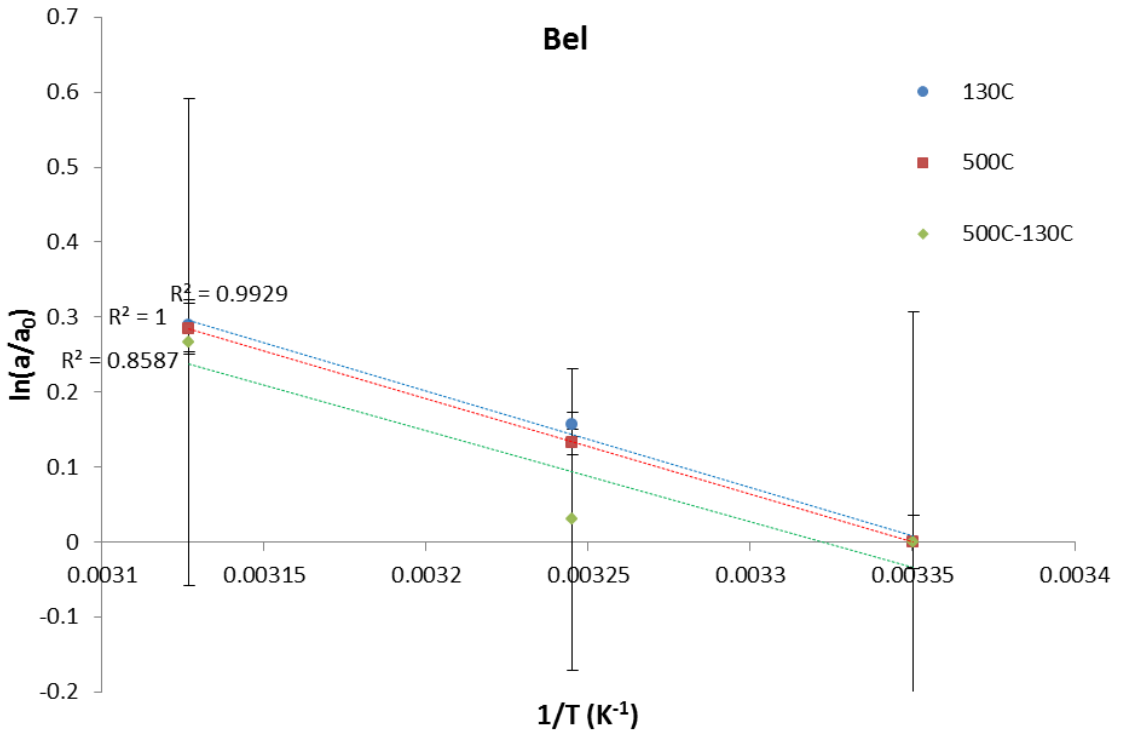

Figure D.18: Arrhenius plot ($t^{1/4}$ model) for 130°C (blue), 500°C (red) and 500-130°C (green, RHX component) components of mass gain rates for *Bel* sample. Uncertainties are to 2σ.

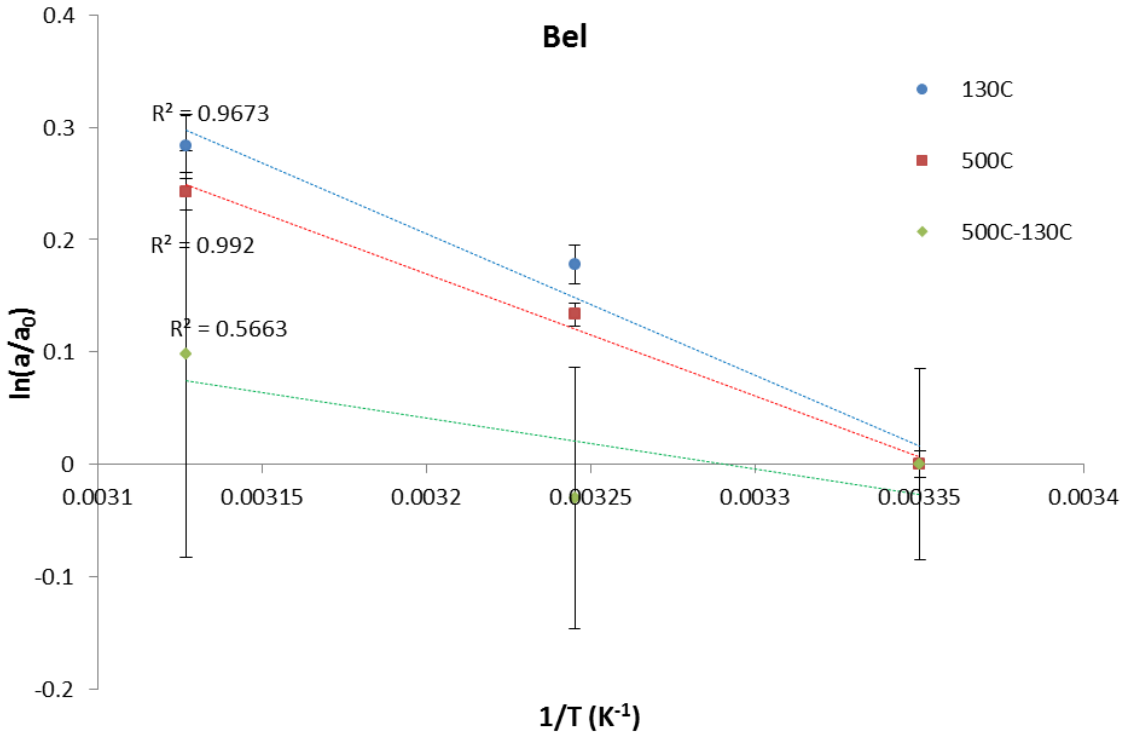

Figure D.19: Arrhenius plot ($t^{1/n}$ model) for 130°C (blue), 500°C (red) and 500-130°C (green, RHX component) components of mass gain rates for *Bel* sample. Uncertainties are to 2σ.

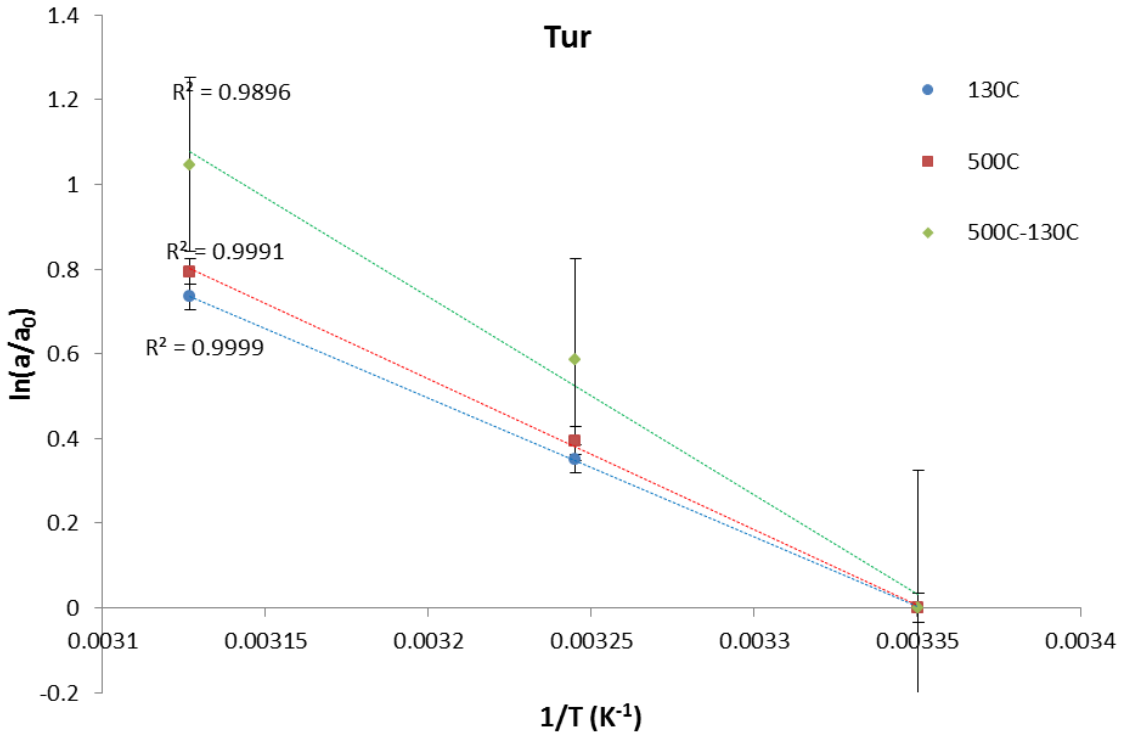

Figure D.20: Arrhenius plot ($t^{1/4}$ model) for 130°C (blue), 500°C (red) and 500-130°C (green, RHX component) components of mass gain rates for *Tur* sample. Uncertainties are to 2σ.

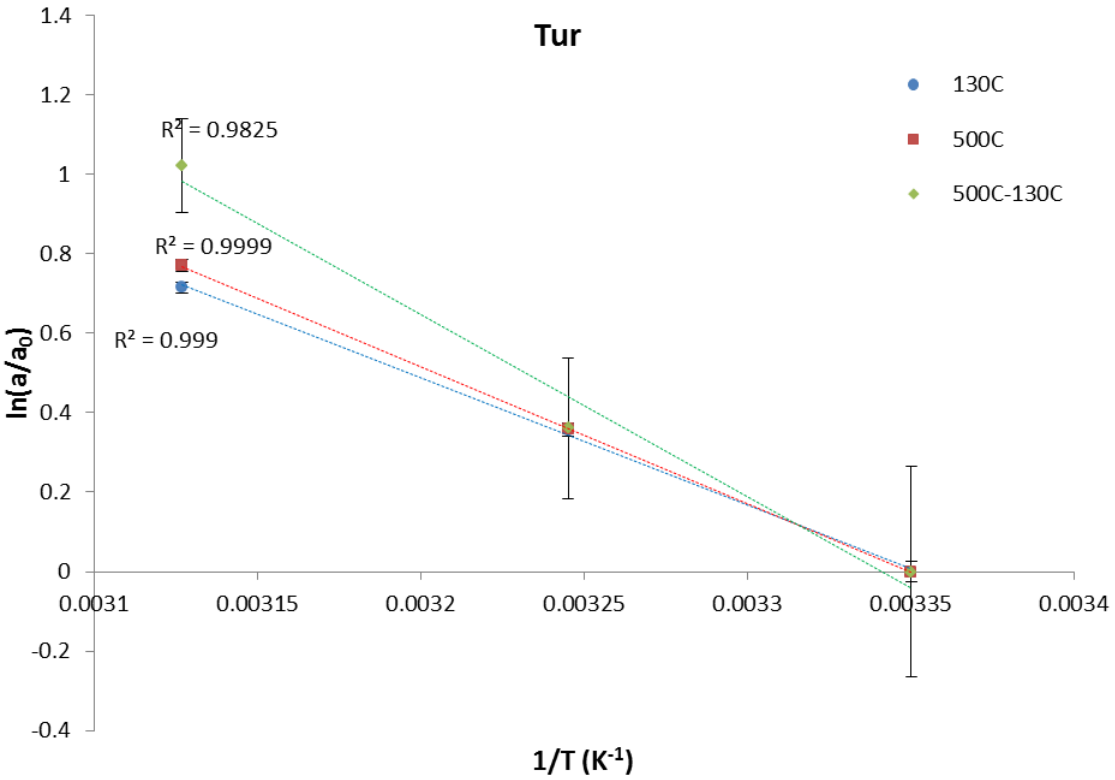

Figure D.21: Arrhenius plot ($t^{1/n}$ model) for 130°C (blue), 500°C (red) and 500-130°C (green, RHX component) components of mass gain rates for *Tur* sample. Uncertainties are to 2σ.

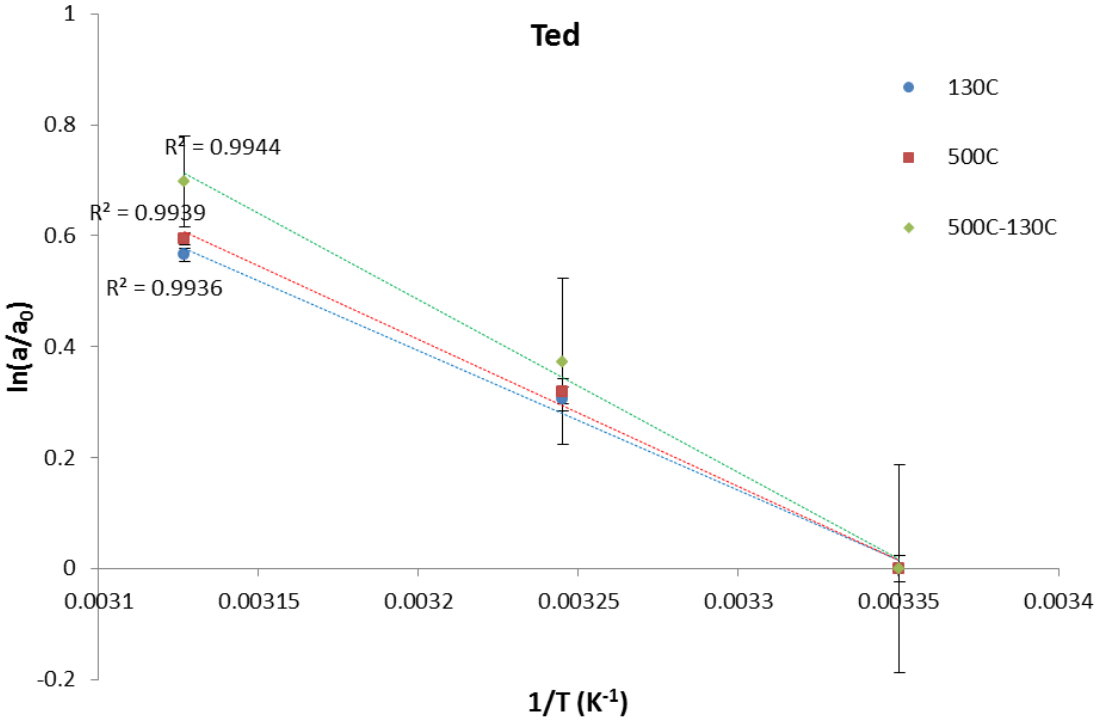

Figure D.22: Arrhenius plot ($t^{1/4}$ model) for 130°C (blue), 500°C (red) and 500-130°C (green, RHX component) components of mass gain rates for *Ted* sample. Uncertainties are to 2σ.

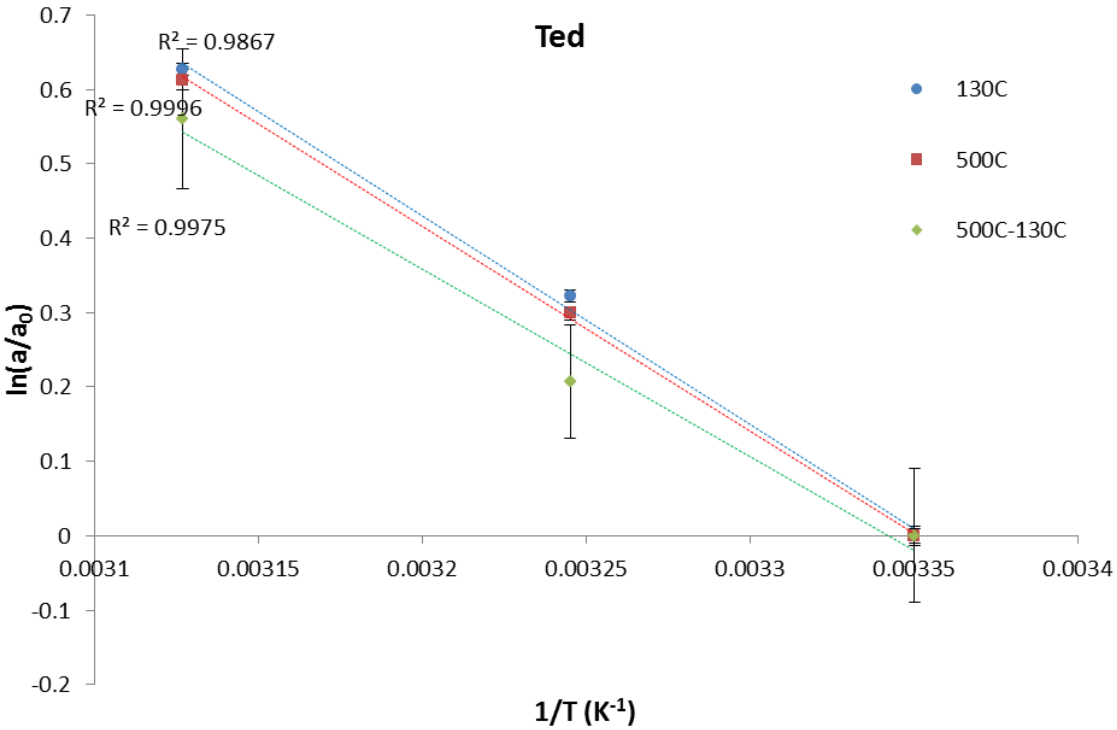

Figure D.23: Arrhenius plot ($t^{1/n}$ model) for 130°C (blue), 500°C (red) and 500-130°C (green, RHX component) components of mass gain rates for *Ted* sample. Uncertainties are to 2σ.

Appendix E

Stage 1 Curves

The mass gain curves covering *Stage 1* (25°C aging) are displayed in this appendix for all samples. The curves have been normalised with respect to m_0 obtained from modelling using the $t^{1/4}$ approach on the *Stage 2* of each curve (i.e. $m_{130\text{-}25}$ and $m_{500\text{-}25}$).

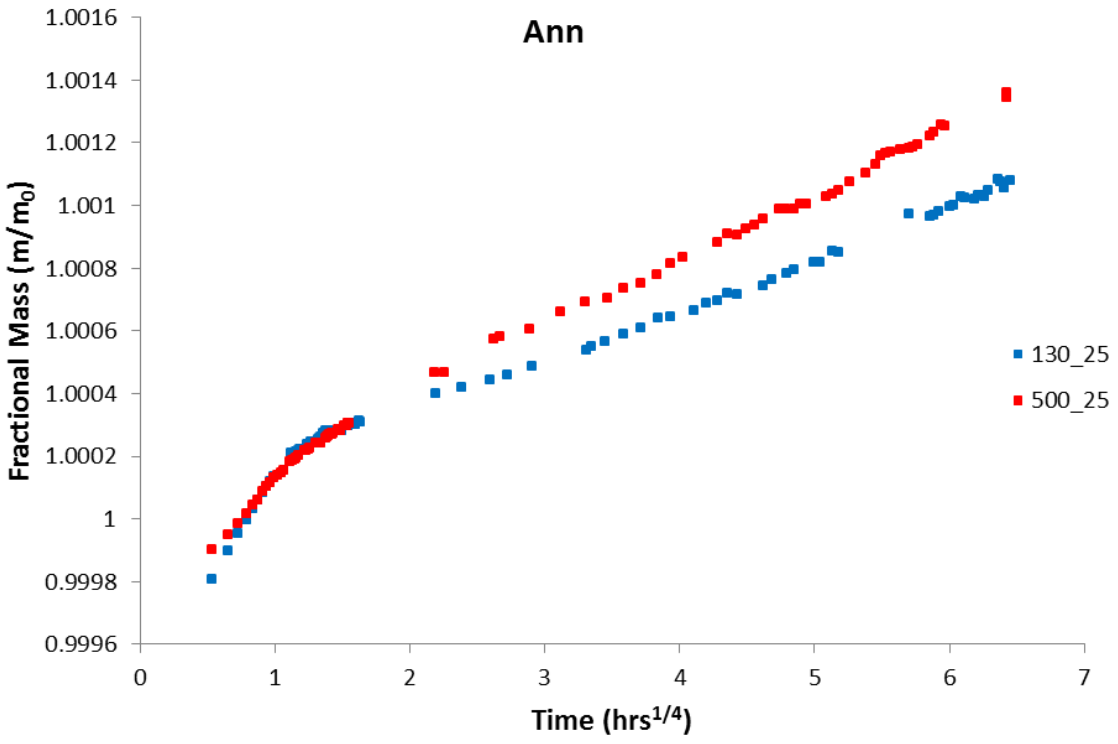

Figure E.1: Mass gain curves, displaying the *Stage 1* region, of *Ann* sample. Sample aging at 25°C following heating at 130°C (blue) and 500°C (red).

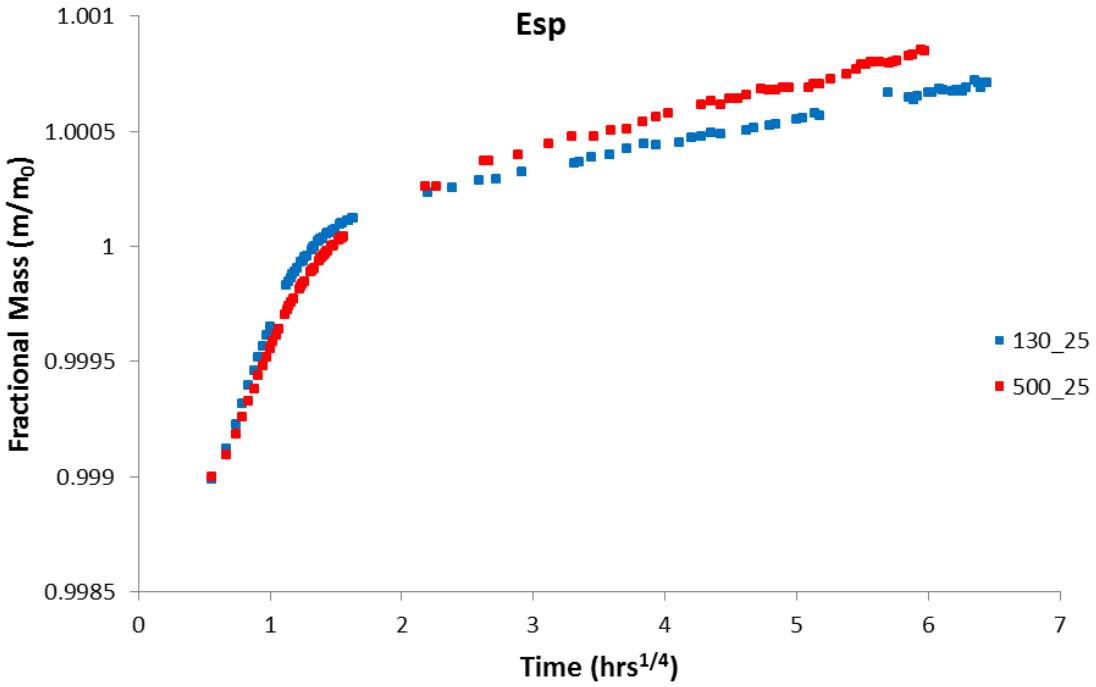

Figure E.2: Mass gain curves, displaying the *Stage 1* region, of *Esp* sample. Sample aging at 25°C following heating at 130°C (blue) and 500°C (red).

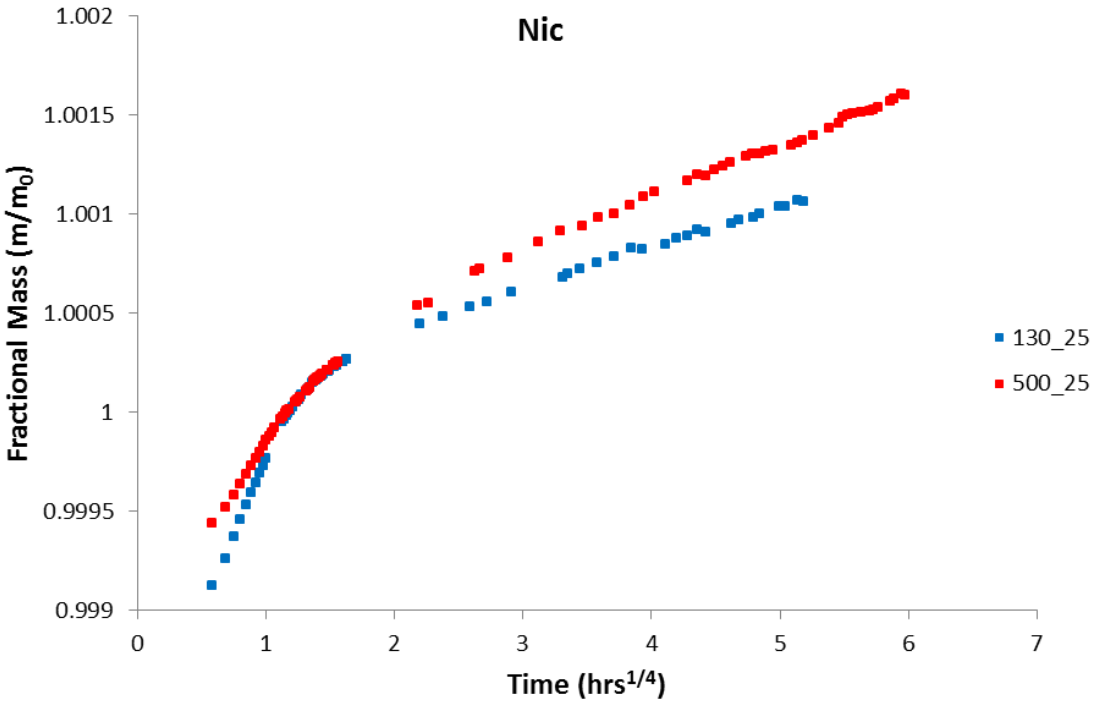

Figure E.3: Mass gain curves, displaying the *Stage 1* region, of *Nic* sample. Sample aging at 25°C following heating at 130°C (blue) and 500°C (red).

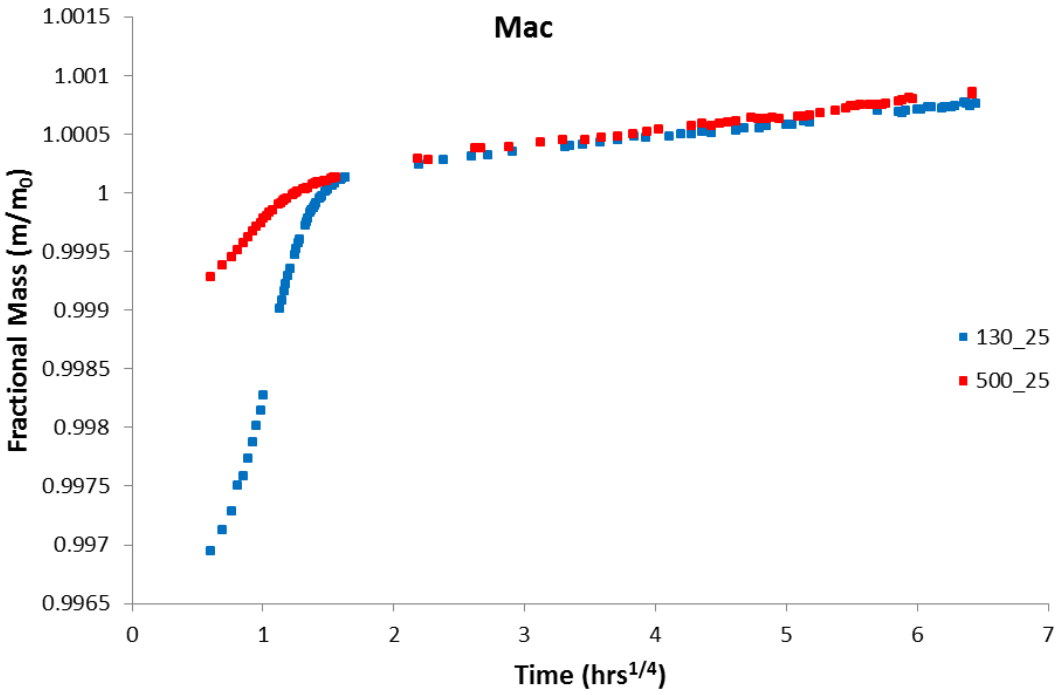

Figure E.4: Mass gain curves, displaying the *Stage 1* region, of *Mac* sample. Sample aging at 25°C following heating at 130°C (blue) and 500°C (red).

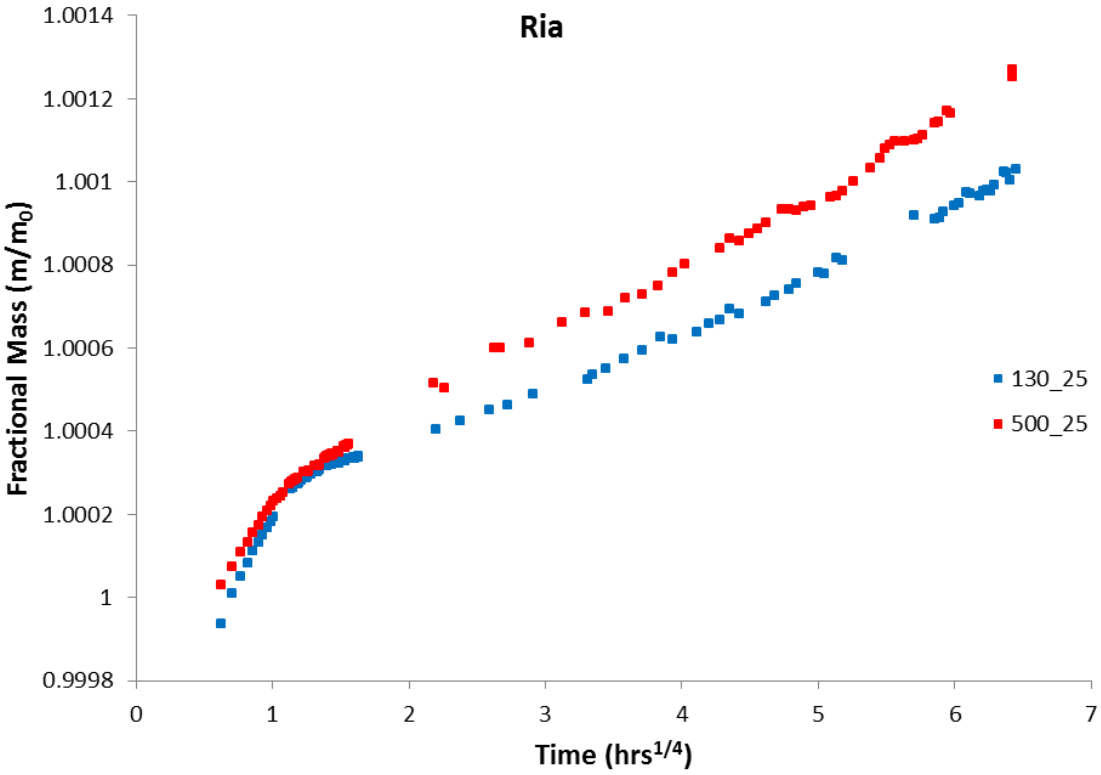

Figure E.5: Mass gain curves, displaying the *Stage 1* region, of *Ria* sample. Sample aging at 25°C following heating at 130°C (blue) and 500°C (red).

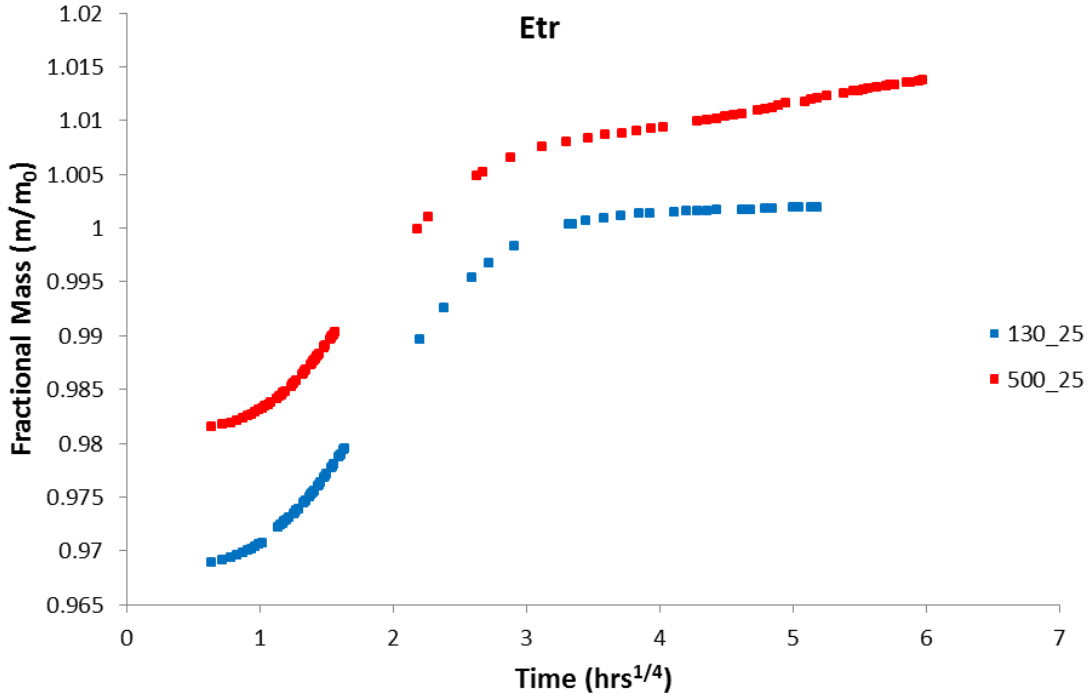

Figure E.6: Mass gain curves, displaying the *Stage 1* region, of *Etr* sample. Sample aging at 25°C following heating at 130°C (blue) and 500°C (red).

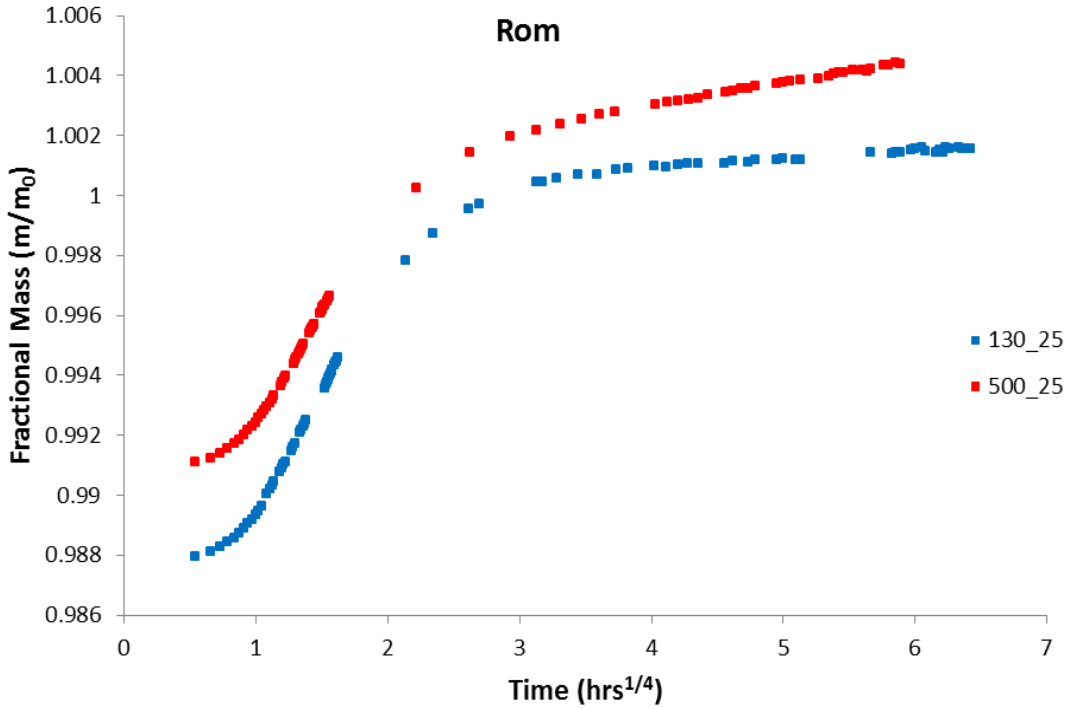

Figure E.7: Mass gain curves, displaying the *Stage 1* region, of *Rom* sample. Sample aging at 25°C following heating at 130°C (blue) and 500°C (red).

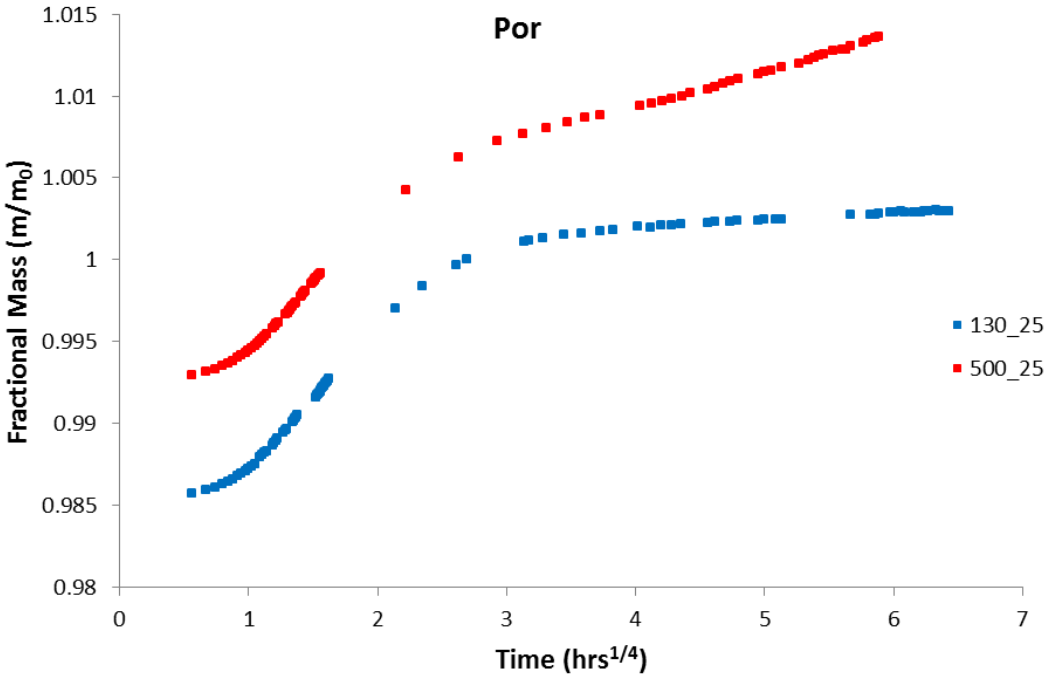

Figure E.8: Mass gain curves, displaying the *Stage 1* region, of *Por* sample. Sample aging at 25°C following heating at 130°C (blue) and 500°C (red).

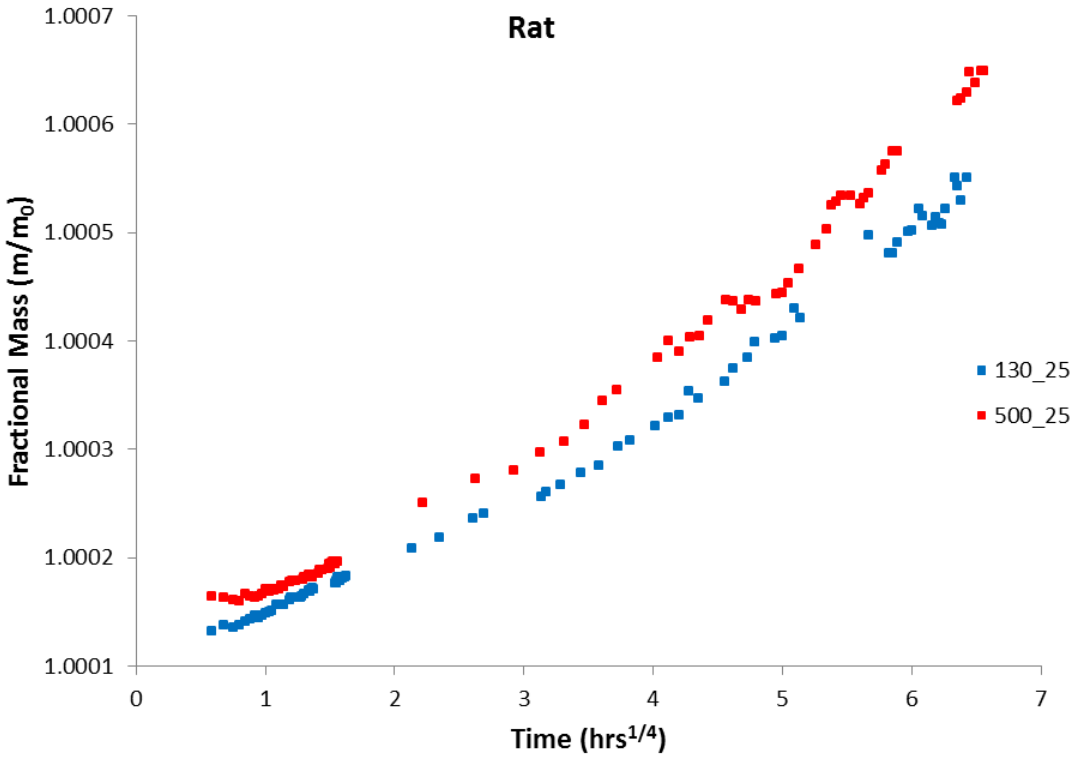

Figure E.9: Mass gain curves, displaying the *Stage 1* region, of *Rat* sample. Sample aging at 25°C following heating at 130°C (blue) and 500°C (red).

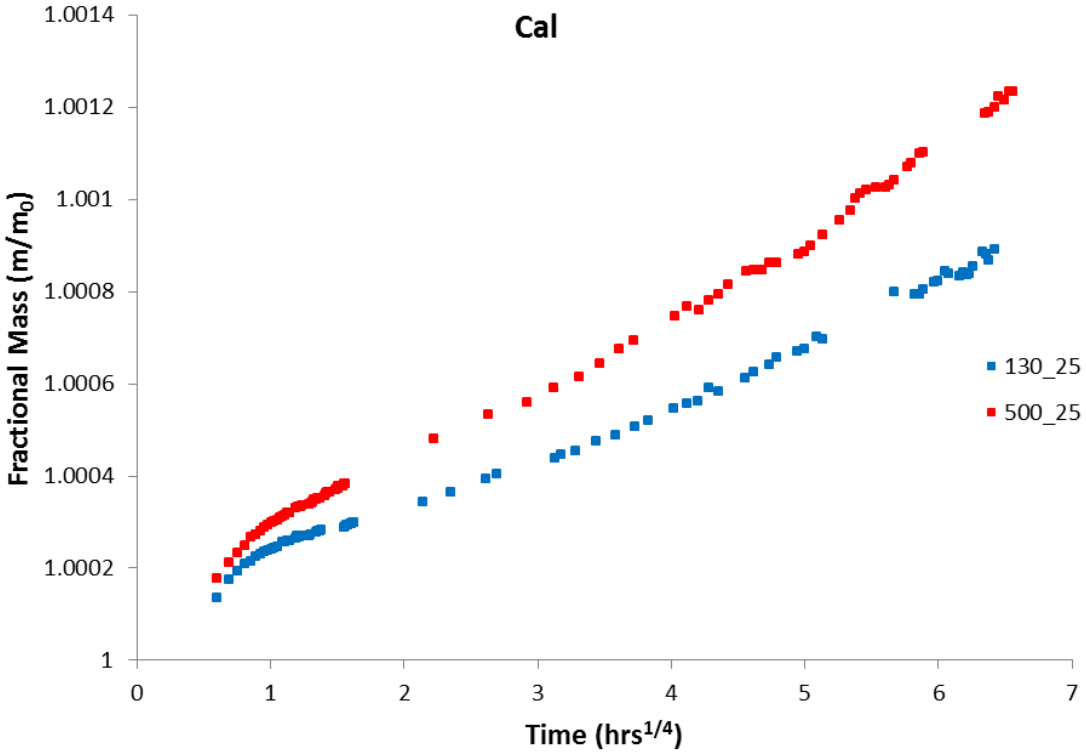

Figure E.10: Mass gain curves, displaying the *Stage 1* region, of *Cal* sample. Sample aging at 25°C following heating at 130°C (blue) and 500°C (red).

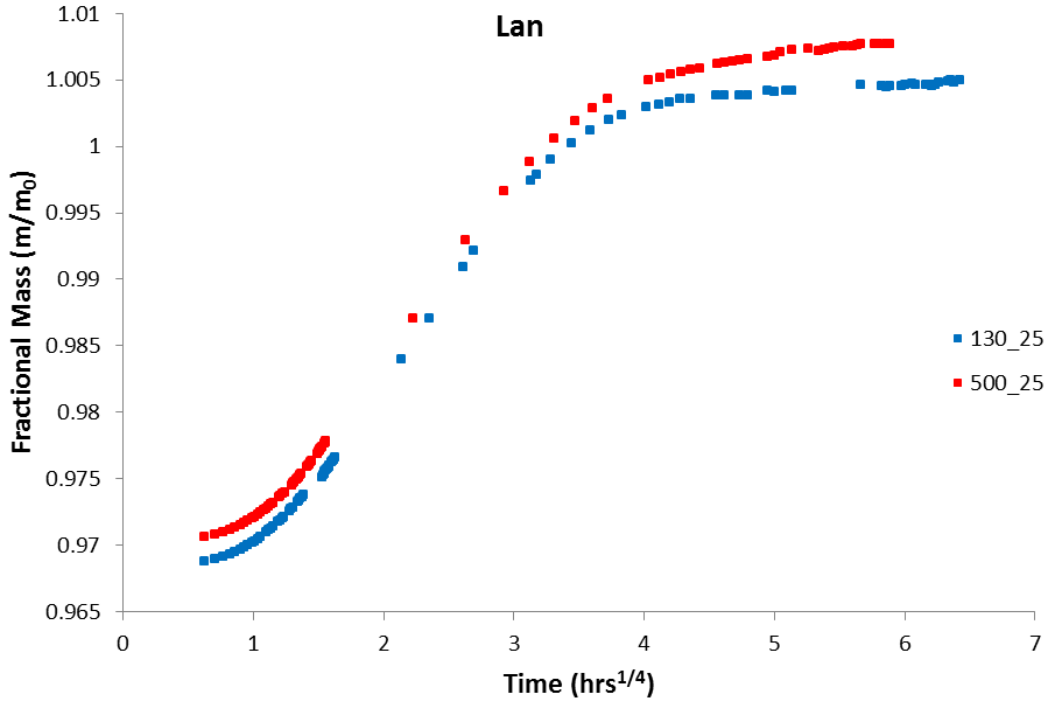

Figure E.11: Mass gain curves, displaying the *Stage 1* region, of *Lan* sample. Sample aging at 25°C following heating at 130°C (blue) and 500°C (red).

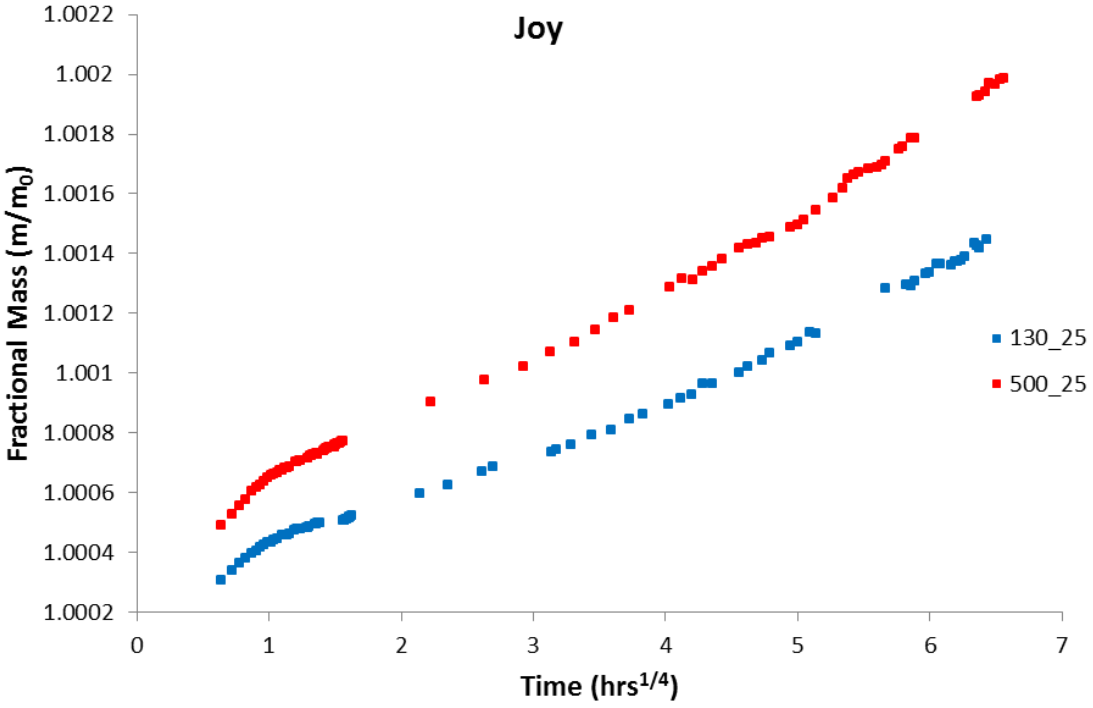

Figure E.12: Mass gain curves, displaying the *Stage 1* region, of *Joy* sample. Sample aging at 25°C following heating at 130°C (blue) and 500°C (red).

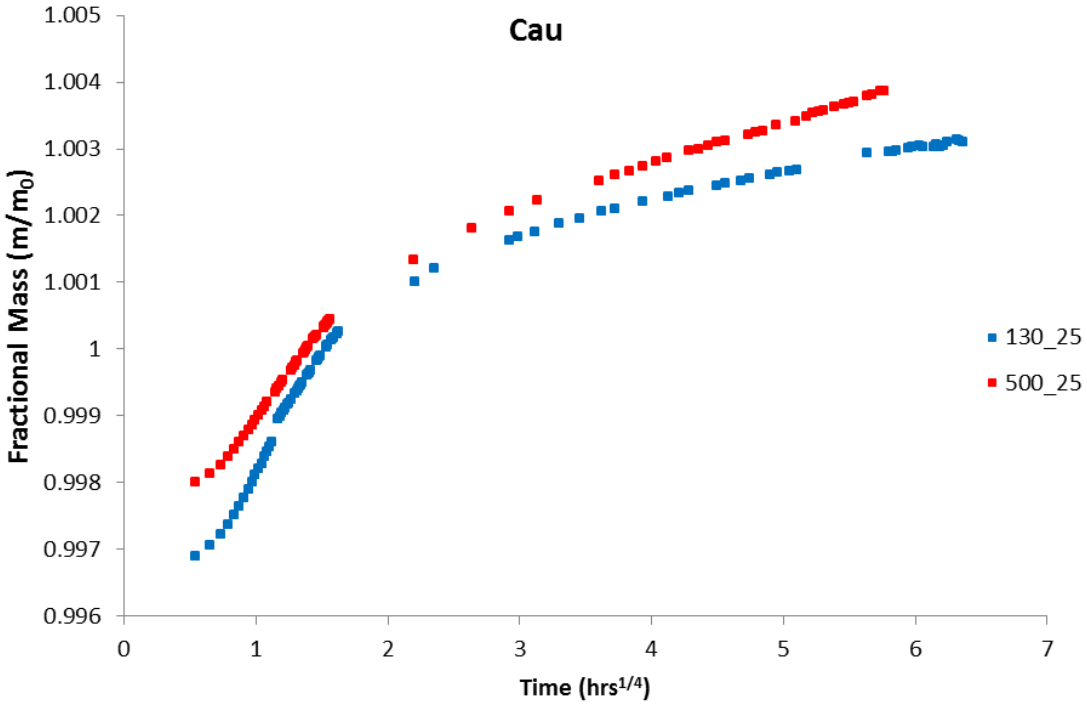

Figure E.13: Mass gain curves, displaying the *Stage 1* region, of *Cau* sample. Sample aging at 25°C following heating at 130°C (blue) and 500°C (red).

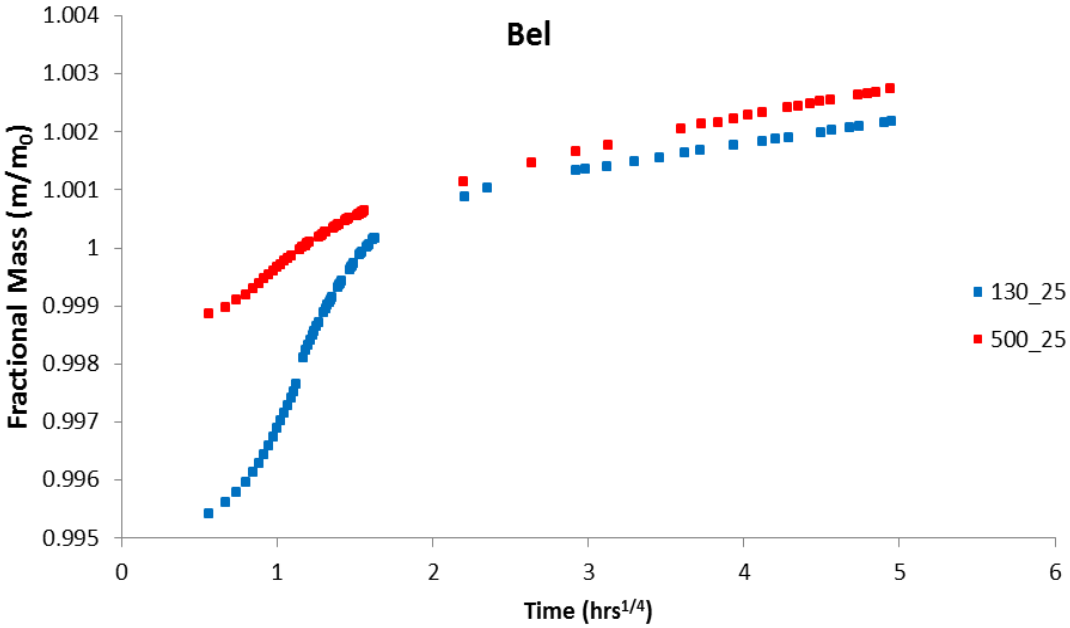

Figure E.14: Mass gain curves, displaying the *Stage 1* region, of *Bel* sample. Sample aging at 25°C following heating at 130°C (blue) and 500°C (red).

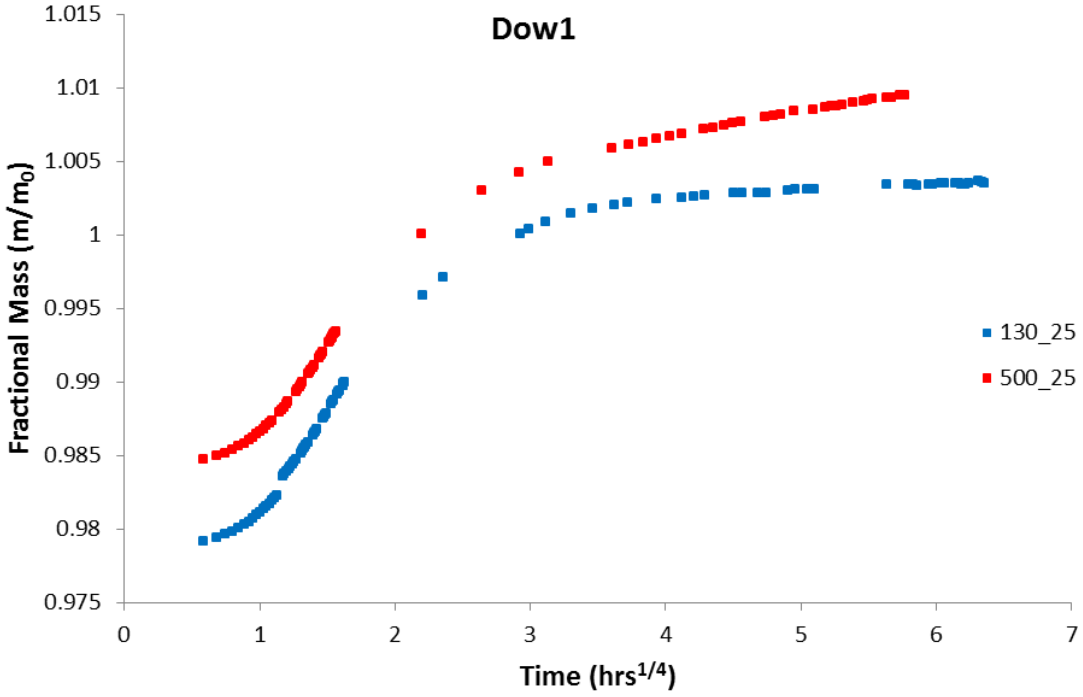

Figure E.15: Mass gain curves, displaying the *Stage 1* region, of *Dow1* sample. Sample aging at 25°C following heating at 130°C (blue) and 500°C (red).

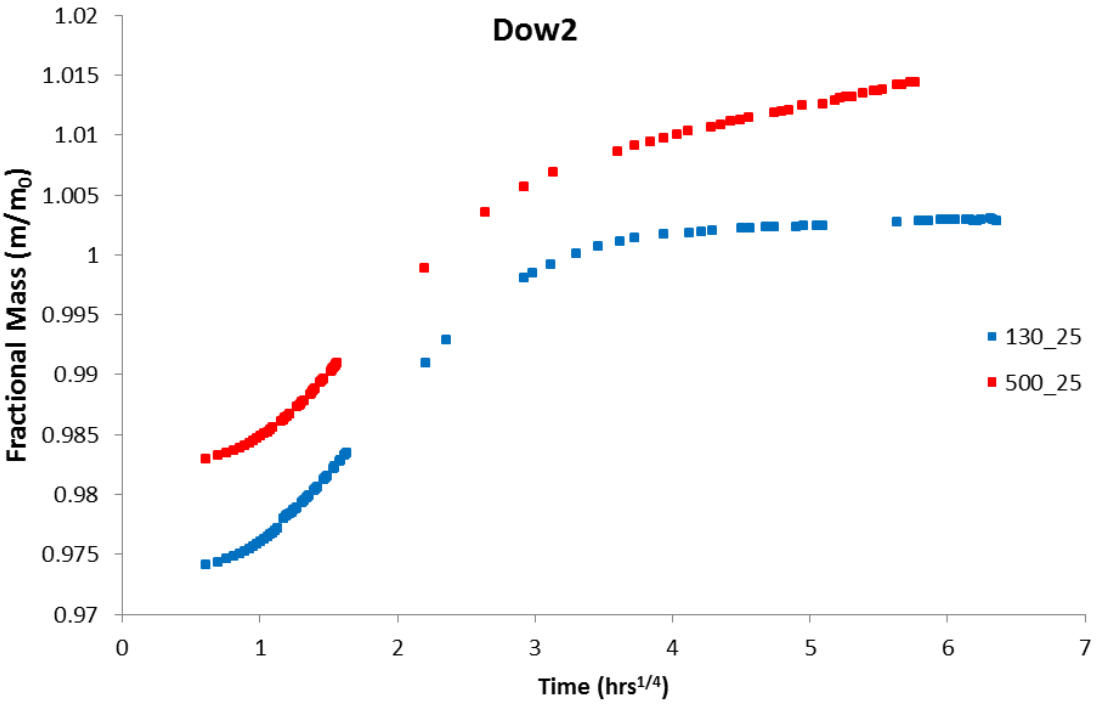

Figure E.16: Mass gain curves, displaying the *Stage 1* region, of *Dow2* sample. Sample aging at 25°C following heating at 130°C (blue) and 500°C (red).

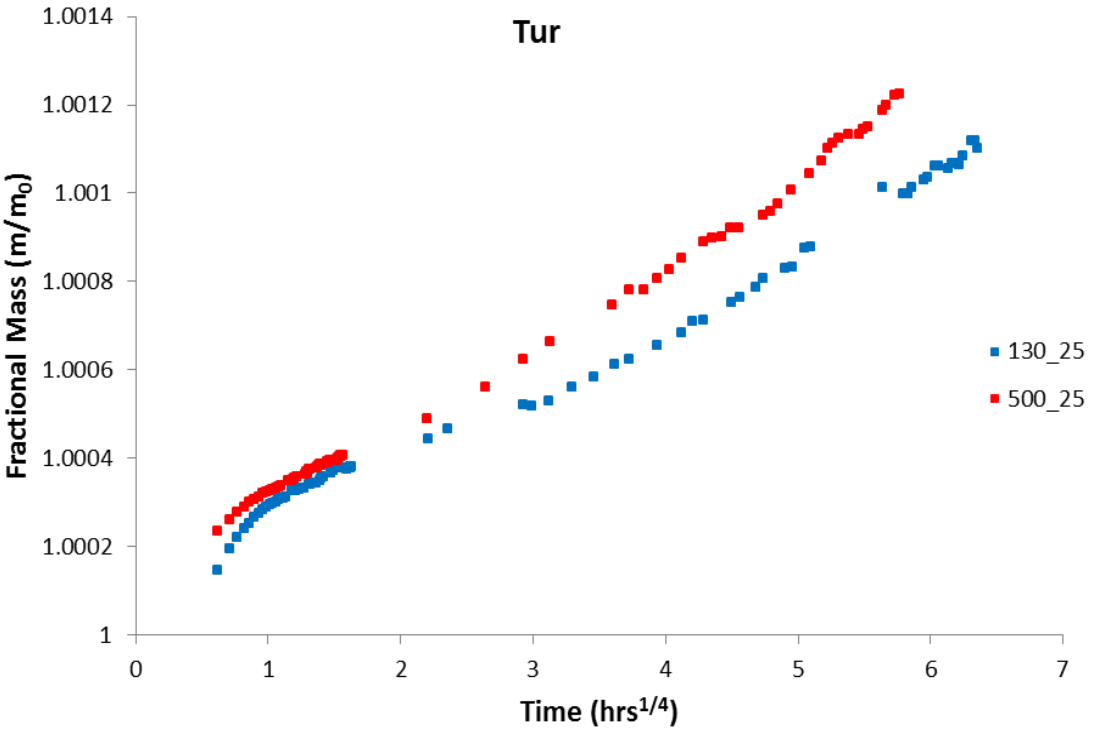

Figure E.17: Mass gain curves, displaying the *Stage 1* region, of *Tur* sample. Sample aging at 25°C following heating at 130°C (blue) and 500°C (red).

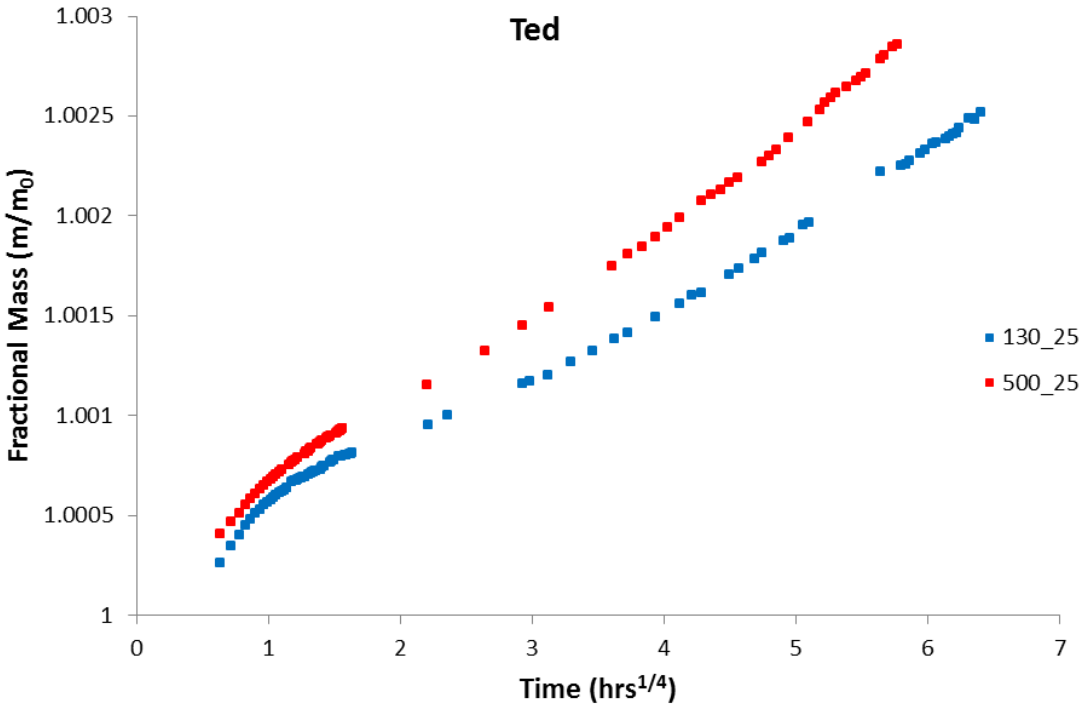

Figure E.18: Mass gain curves, displaying the *Stage 1* region, of *Ted* sample. Sample aging at 25°C following heating at 130°C (blue) and 500°C (red).

Appendix F

Nitrogen Sorption Curves: BET Analysis

The BET analysis sorption (nitrogen) curves are presented below for all samples, excluding *Rat* for which insufficiently low levels of adsorption occurred.

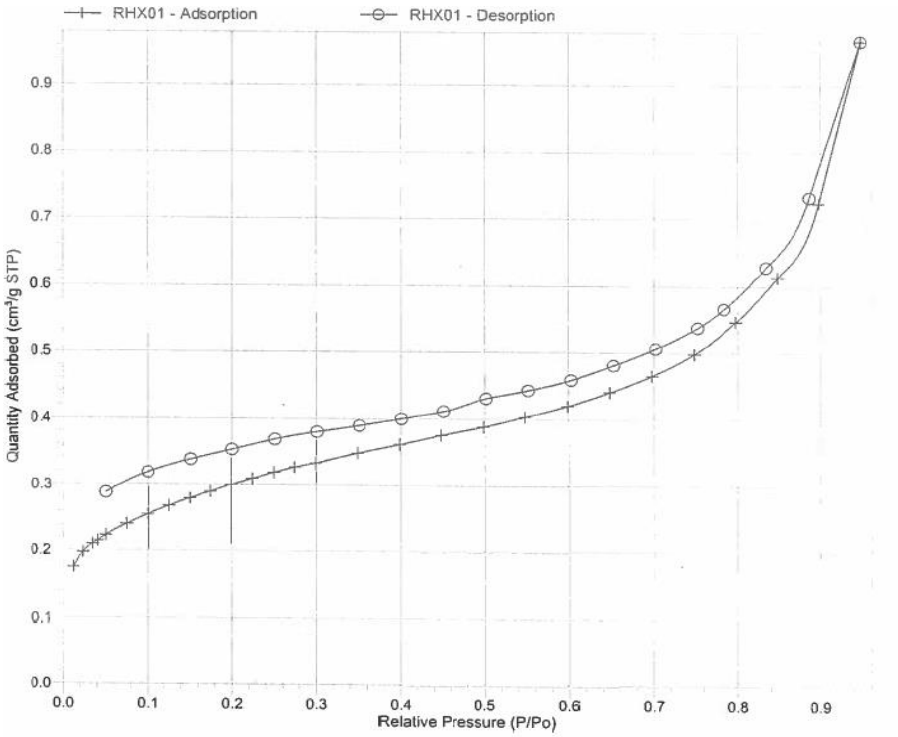

Figure F.1: Adsorption and desorption of nitrogen curves from BET analysis of *Ann.*

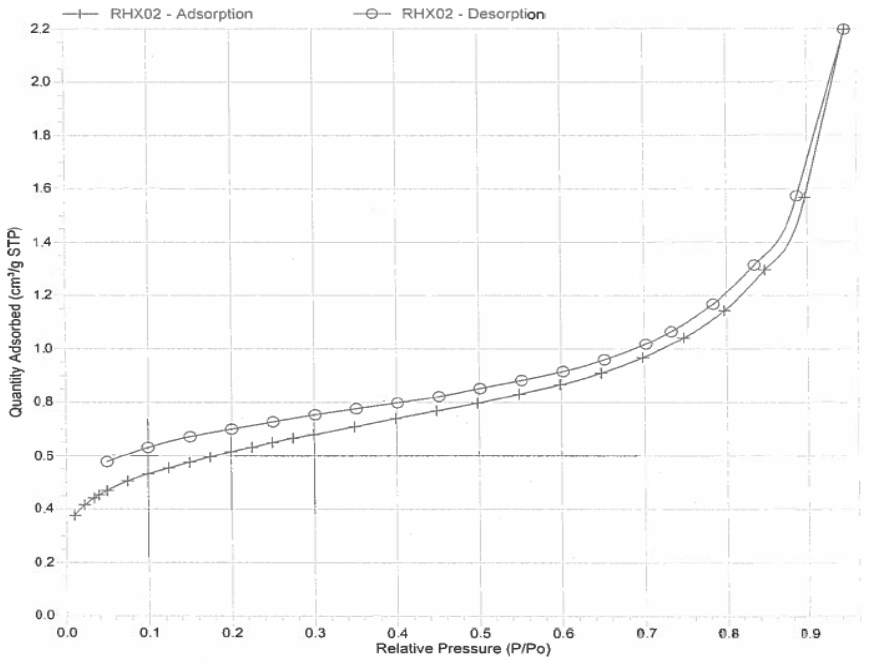

Figure F.2: Adsorption and desorption of nitrogen curves from BET analysis of *Esp.*

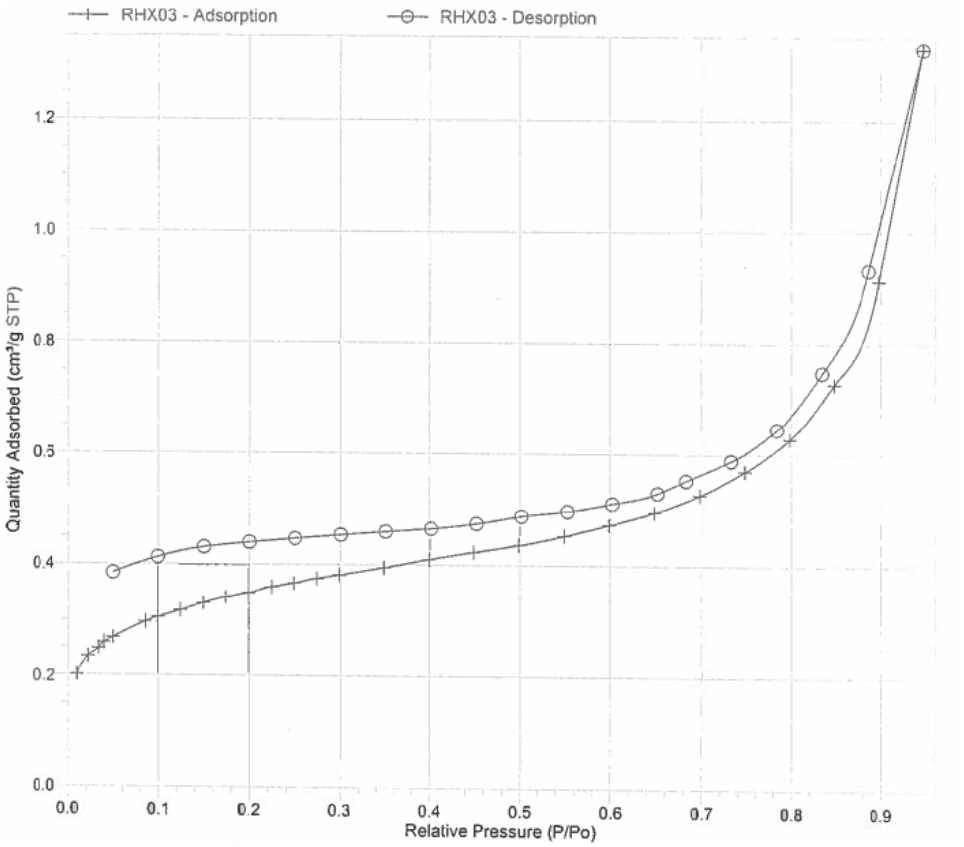

Figure F.3: Adsorption and desorption of nitrogen curves from BET analysis of *Nic.*

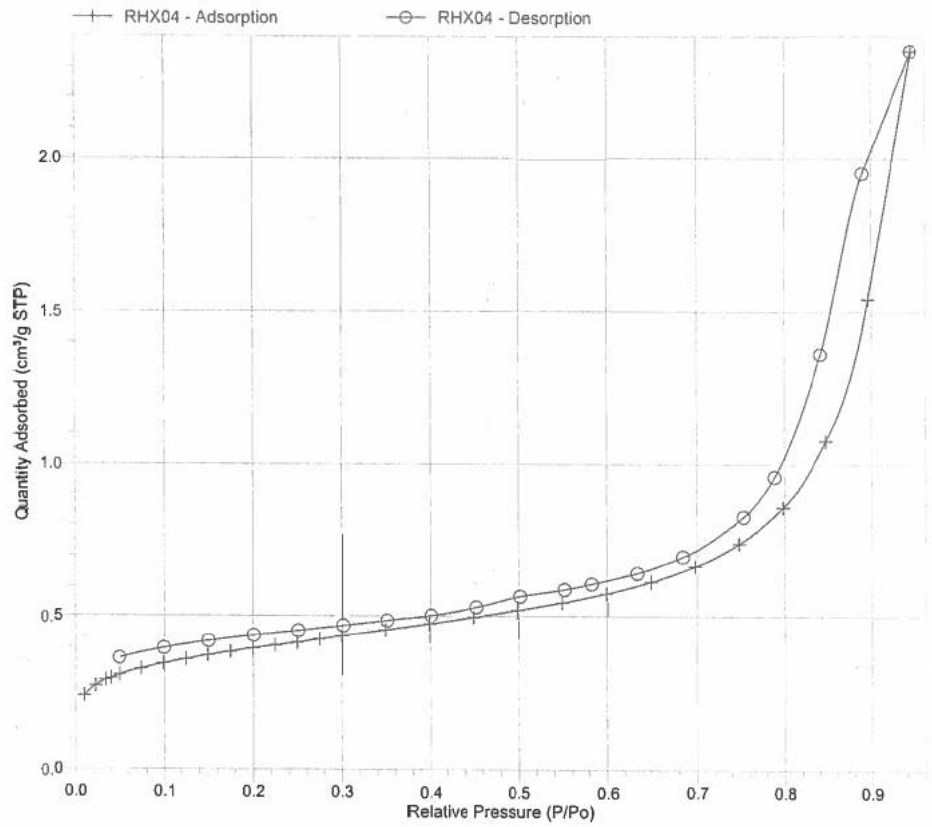

Figure F.4: Adsorption and desorption of nitrogen curves from BET analysis of *Mac.*

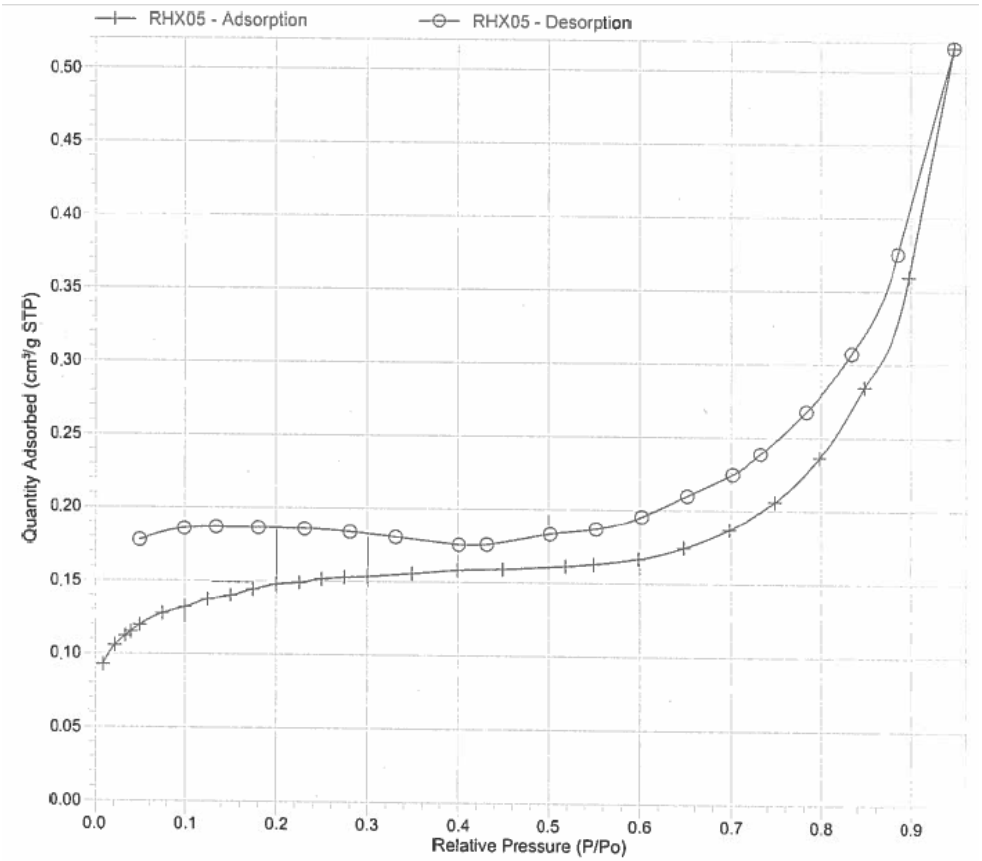

Figure F.5: Adsorption and desorption of nitrogen curves from BET analysis of *Ria.*

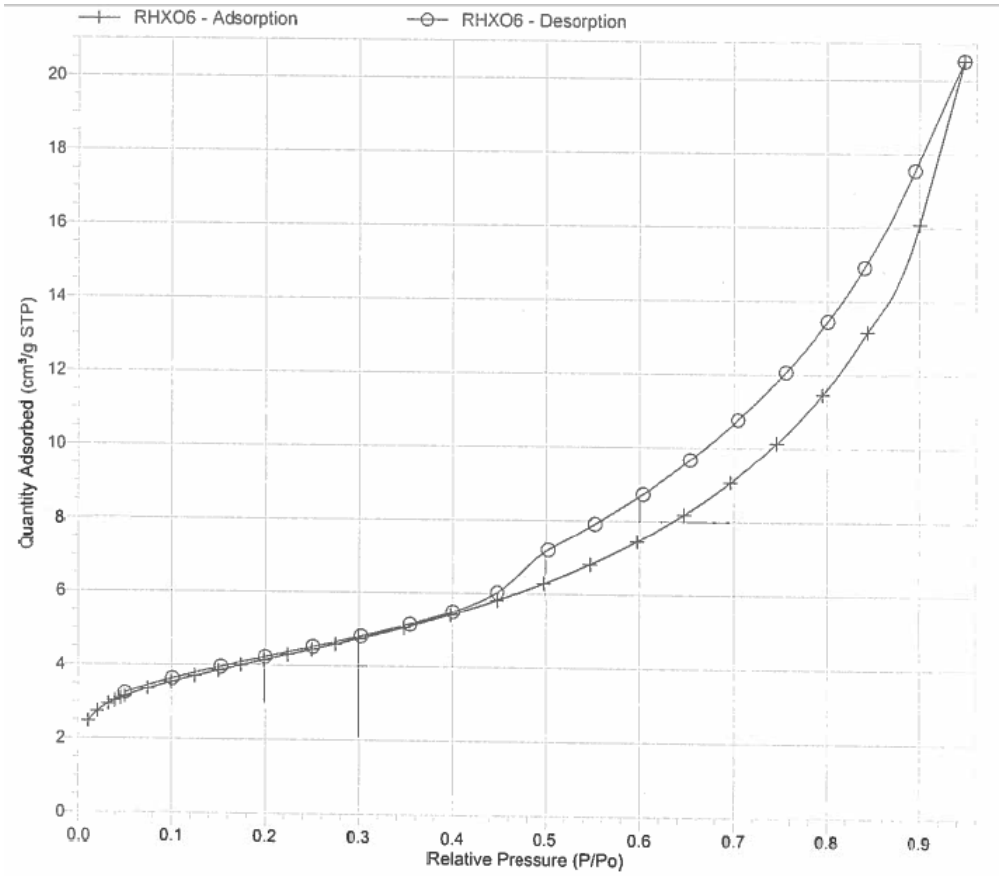

Figure F.6: Adsorption and desorption of nitrogen curves from BET analysis of *Etr.*

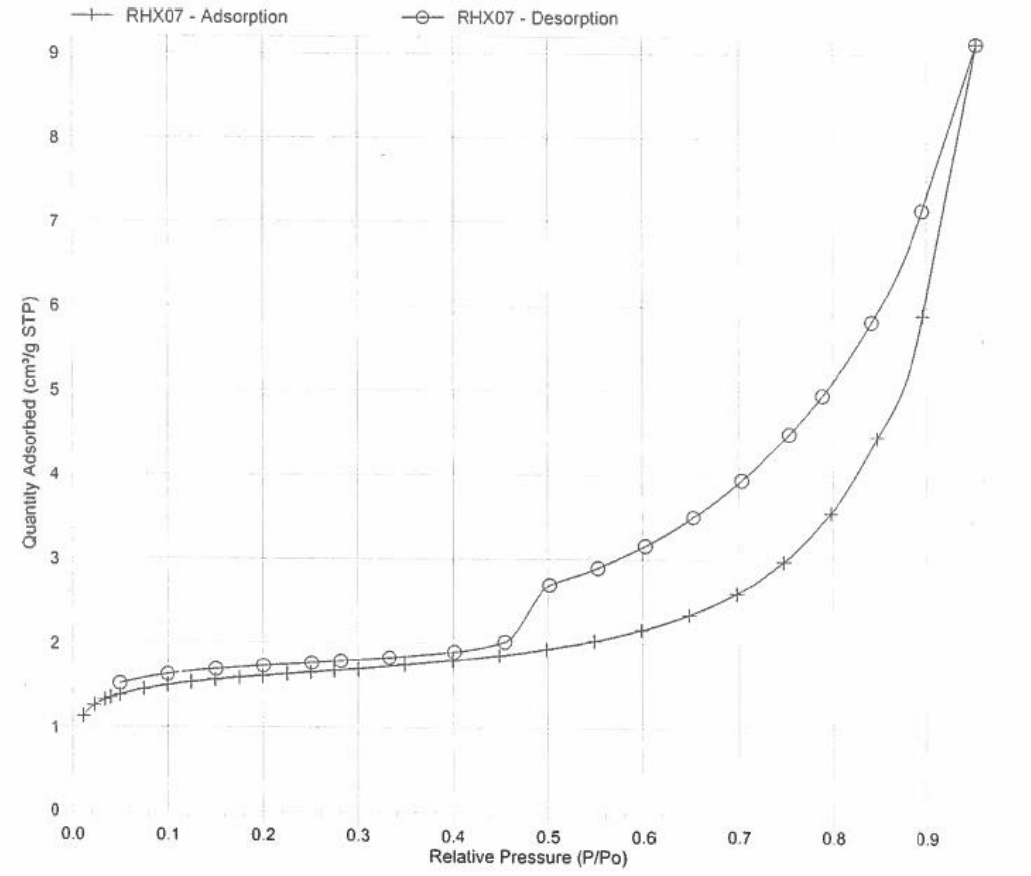

Figure F.7: Adsorption and desorption of nitrogen curves from BET analysis of *Rom.*

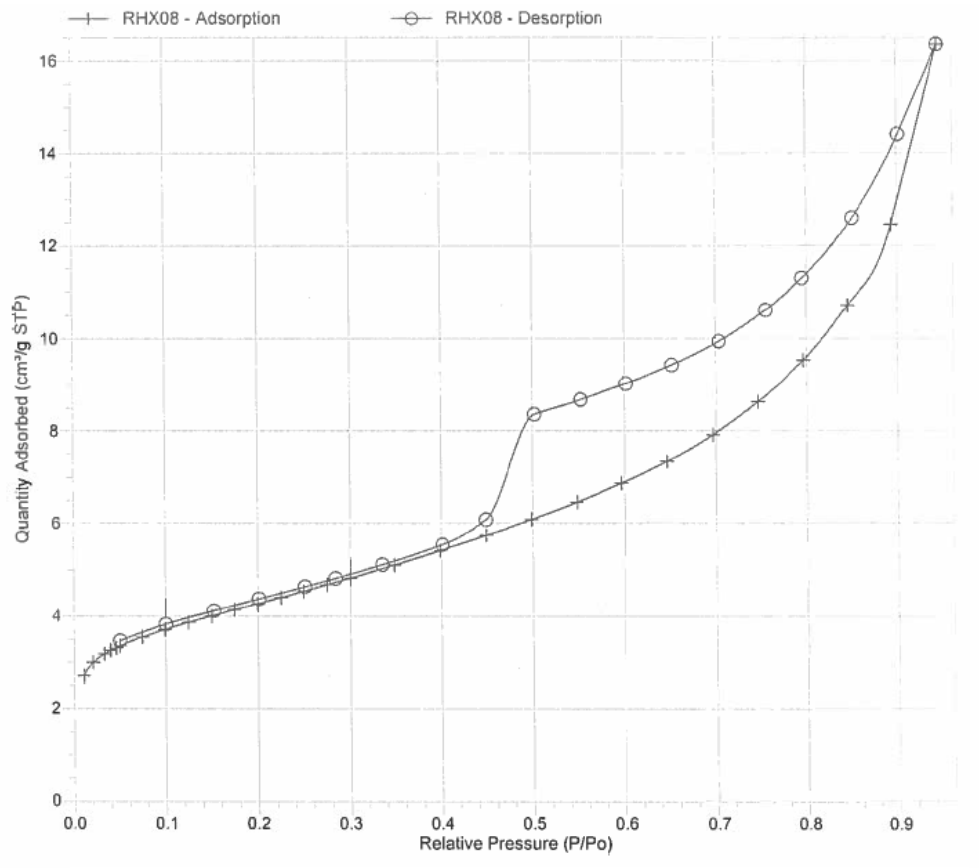

Figure F.8: Adsorption and desorption of nitrogen curves from BET analysis of *Por.*

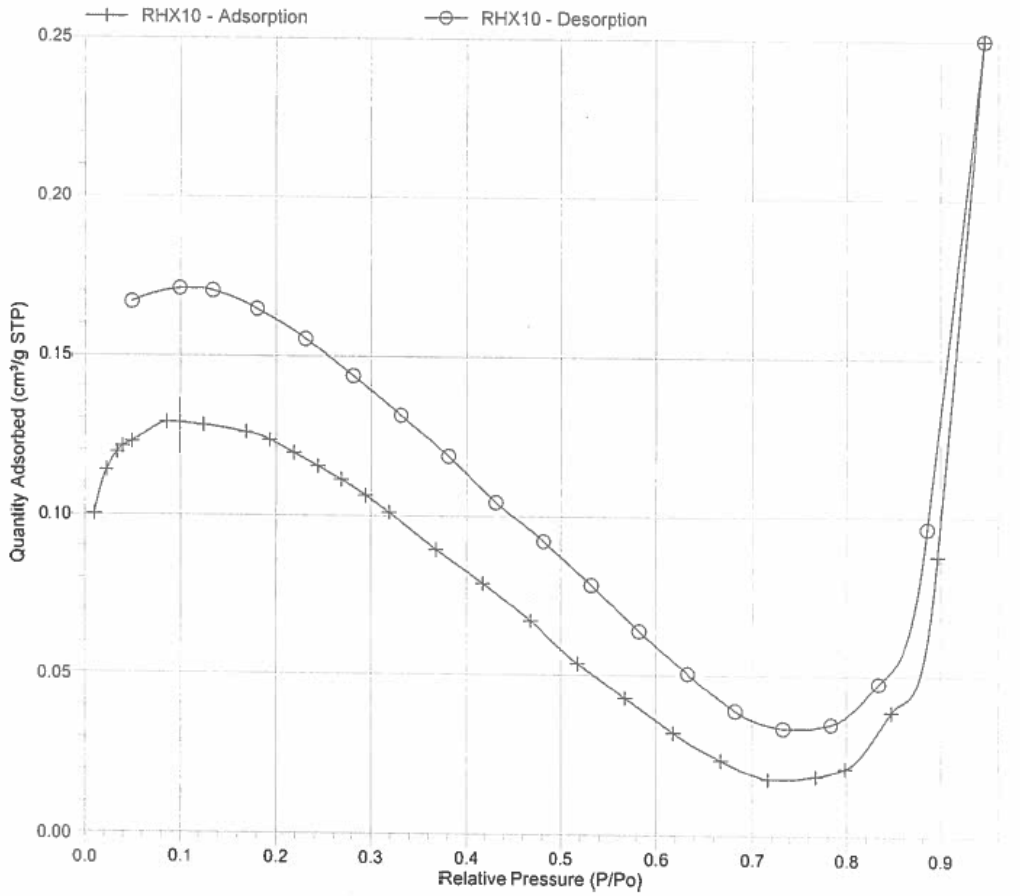

Figure F.9: Adsorption and desorption of nitrogen curves from BET analysis of *Cal.*

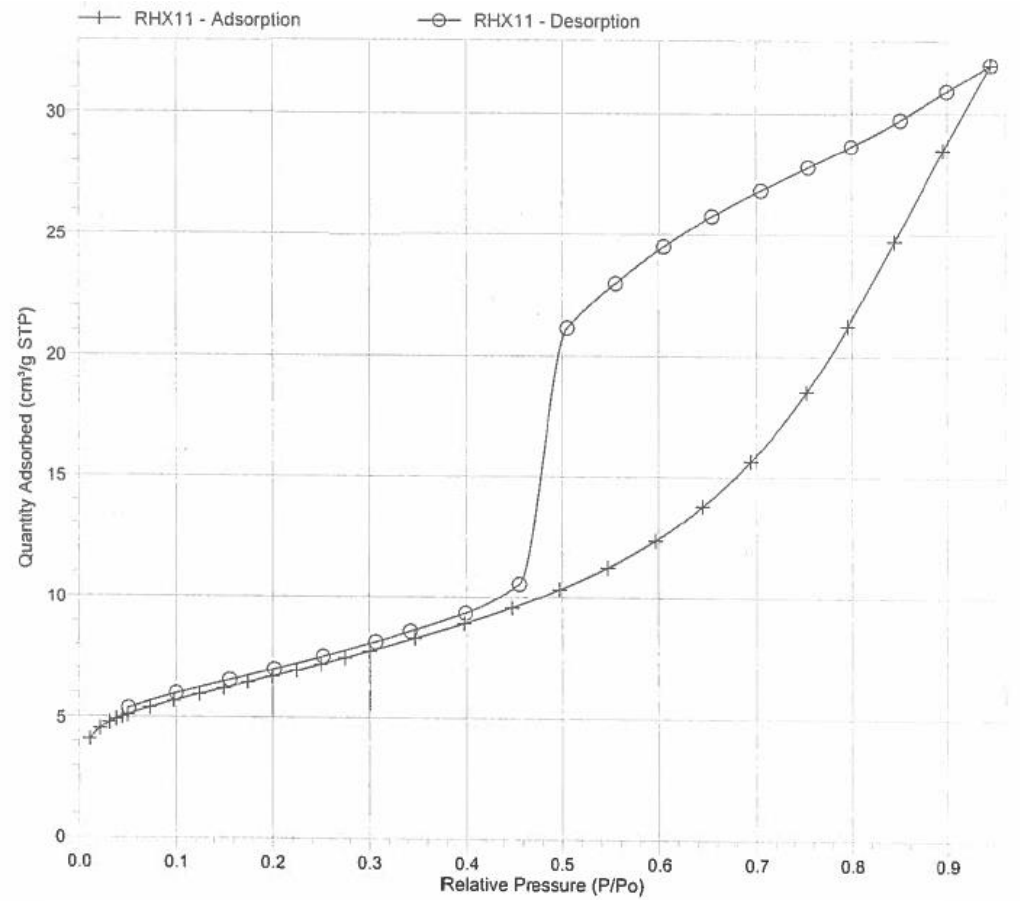

Figure F.10: Adsorption and desorption of nitrogen curves from BET analysis of *Lan.*

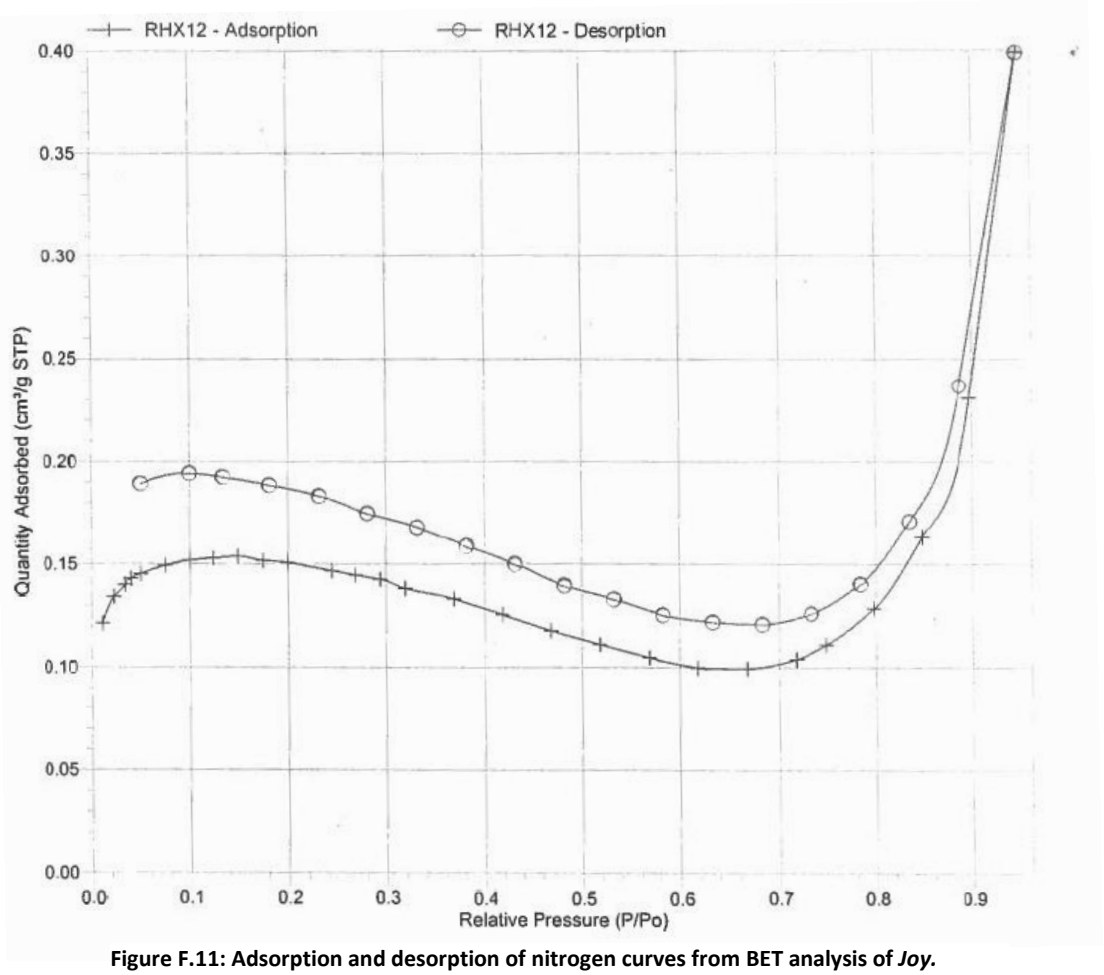

Figure F.11: Adsorption and desorption of nitrogen curves from BET analysis of *Joy.*

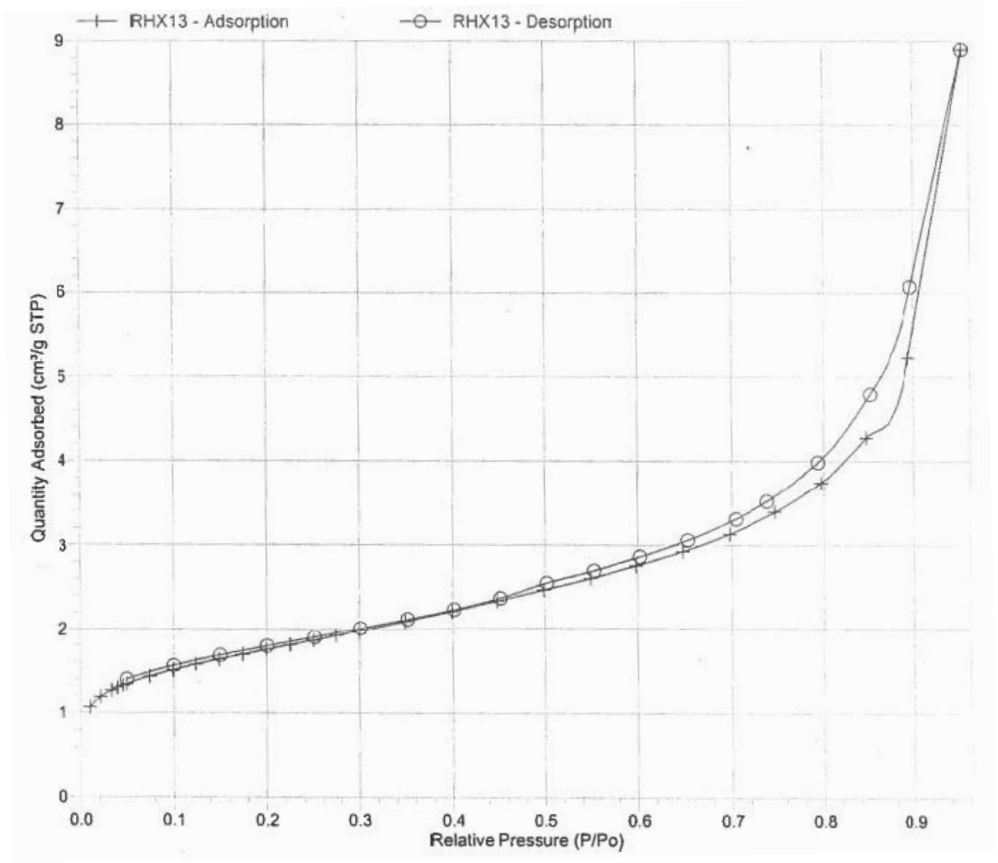

Figure F.12: Adsorption and desorption of nitrogen curves from BET analysis of *Cau.*

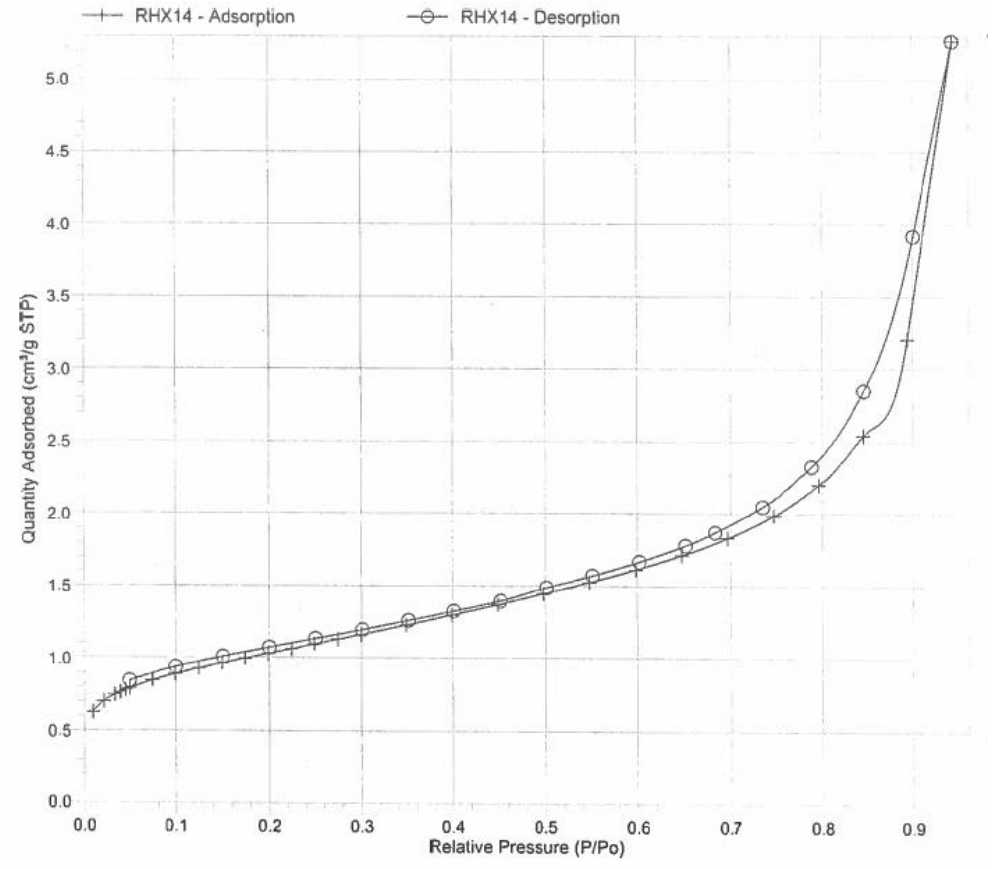

Figure F.13: Adsorption and desorption of nitrogen curves from BET analysis of *Bel.*

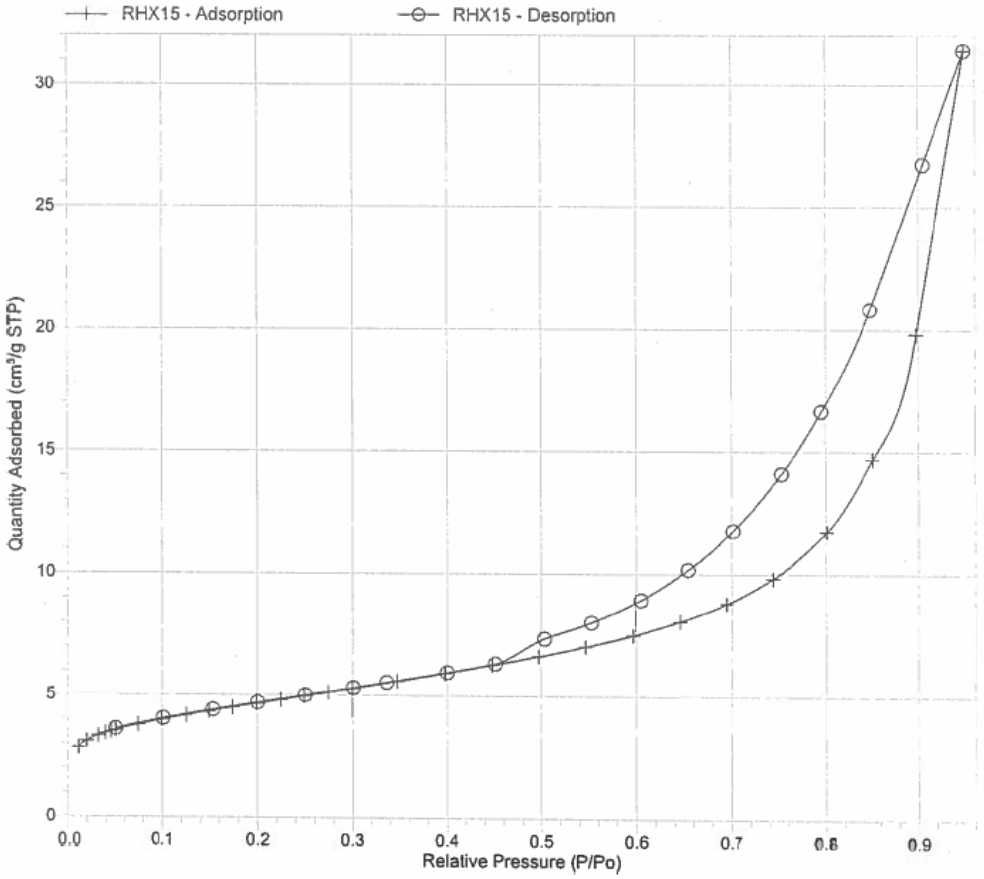

Figure F.14: Adsorption and desorption of nitrogen curves from BET analysis of *Dow1.*

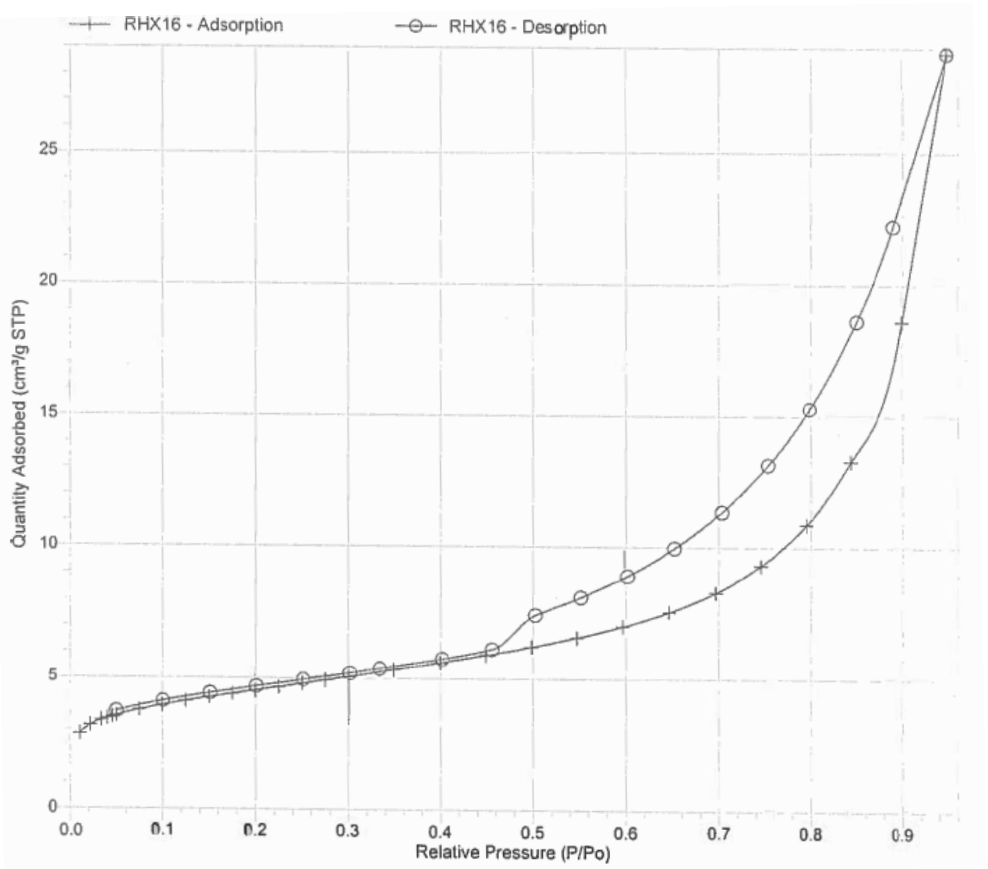

Figure F.15: Adsorption and desorption of nitrogen curves from BET analysis of *Dow2.*

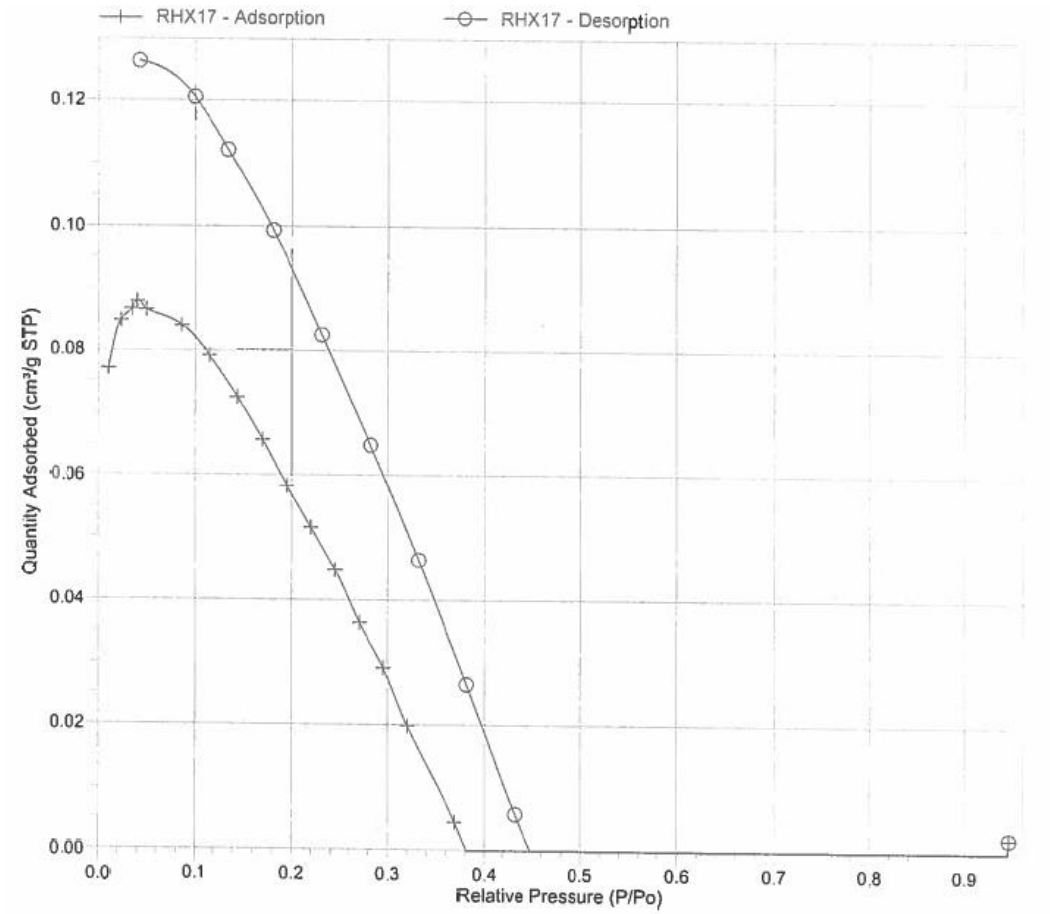

Figure F.16: Adsorption and desorption of nitrogen curves from BET analysis of *Tur.*

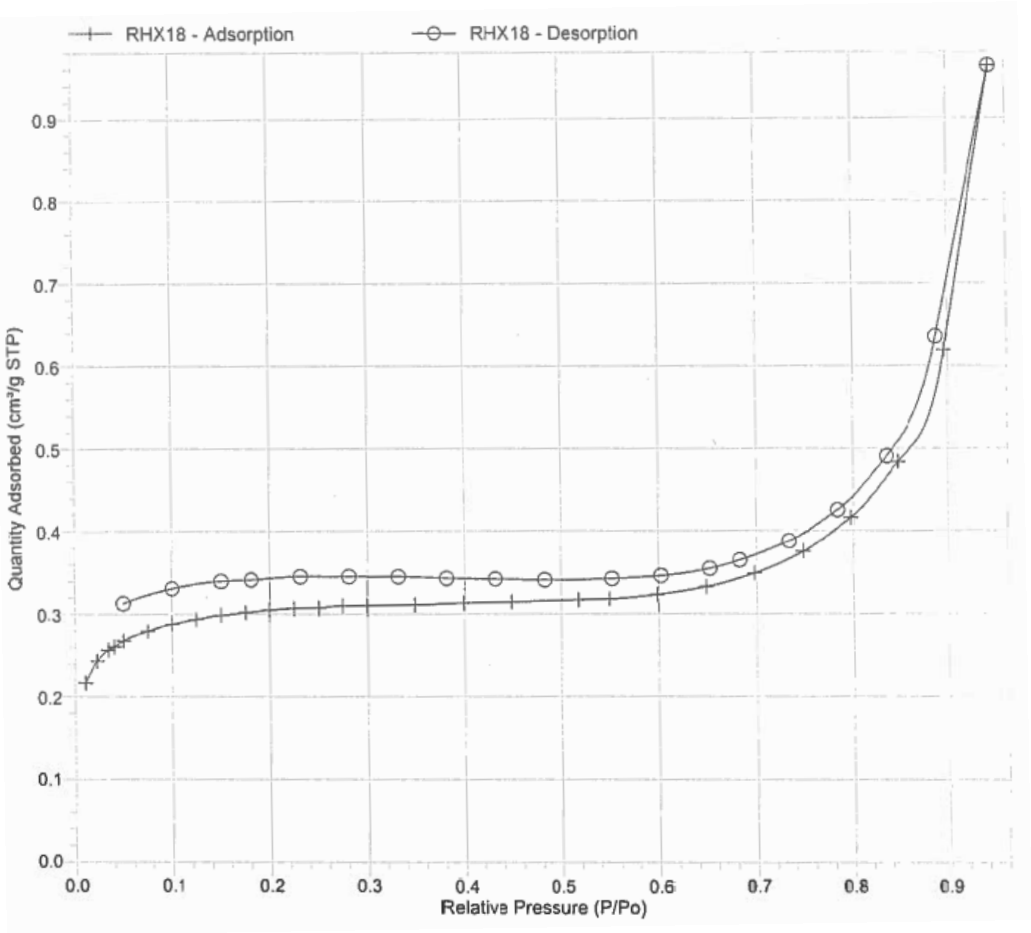

Figure F.17: Adsorption and desorption of nitrogen curves from BET analysis of *Ted.*

Appendix G

MATLAB Code: *bestfit*, *bestfitn*, *AETH5*

bestfit

```
function [adjR2,RMSE,coeff_m_b,conf_m,conf_b,results]=bestfit(time,mass,k)

l=size(mass);       %the number of datapoints in the dataseries
d=size(mass)-k;    %running algorithm up to l-k data points from end
adjR2=zeros(d,1);
RMSE=zeros(d,1);
coeff_m_b=zeros(d,2);   %for storing the fitting coefficients of y=mx+b
conf_m=zeros(d,2);      %split the confidence intervals into a matrix for
the confidence intervals of m(slope) and b(intercept)
conf_b=zeros(d,2);
results=zeros(9,1);     %for storing the results corresponding to the best
R2 value

for(i=1:d);
[fitobject,gof]=fit(time(i:l),mass(i:l),'poly1');   %carries out a
regression on the data of type 'poly'
adjR2(i,1)=gof.adjrsquare;   %extracts the adjusted R2 from the structure
RMSE(i,1)=gof.rmse;         %extracts the RMSE from the structure
coeff=coeffvalues(fitobject);   %gets the coefficients from the cfit object
conf=confint(fitobject);        %gets the confidence intervals of the cfit
object
coeff_m_b(i,1)=coeff(1,1);
coeff_m_b(i,2)=coeff(1,2);
conf_m(i,1)=conf(1,1);
conf_m(i,2)=conf(2,1);
conf_b(i,1)=conf(1,2);
conf_b(i,2)=conf(2,2);
end

[best,p]=max(adjR2);     %gets the best value of adjR2 and the corresponding
index

results(1,1)=p;
results(2,1)=best;
results(3,1)=RMSE(p,1);
results(4,1)=coeff_m_b(p,1);  %obtains the slope value corresponding to the
maximum adjR2
results(5,1)=conf_m(p,1);     %obtains the confidence intervals of this
slope value
results(6,1)=conf_m(p,2);     %obtains the confidence intervals of this
slope value
results(7,1)=coeff_m_b(p,2);
results(8,1)=conf_b(p,1);
results(9,1)=conf_b(p,2);

[bestfitted]=fit(time(p:l),mass(p:l),'poly1');  %an object defining the best
regression based on maximum R2 of all regression
j=max(time);

close all

%PLOTTING CODE
% Create figure for bestfit, i.e. the regression corresponding to best R2
figure1 = figure;
```

```
% Create axes
axes1 = axes('Parent',figure1,'FontSize',12,'FontName','Times New Roman');
box(axes1,'on');
hold(axes1,'all');

% Create plot
plot((0:j+1),bestfitted(0:j+1),'LineWidth',1,'LineStyle','--','Color',[1 0
0]);

% Create xlabel
xlabel({'Time^1^/^4 (hrs^1^/^4)'},'FontSize',14,...
    'FontName','Times New Roman');

% Create ylabel
ylabel({'Mass (g)'},'FontSize',14,'FontName','Times New Roman');

% Create plot
plot(time,mass,'Marker','.','LineStyle','none');



% Create figure for adjR2
figure1 = figure;

% Create axes
axes1 = axes('Parent',figure1,'FontSize',12);
%% Uncomment the following line to preserve the Y-limits of the axes
ylim(axes1,[0.95 1]);
box(axes1,'on');
hold(axes1,'all');

% Create plot
plot(time(1:d),adjR2,'MarkerFaceColor',[0 0
1],'Marker','.','LineStyle',':',...
    'Color',[0 0 1]);

% Create xlabel
xlabel({'Time^1^/^4 of initial data point (hrs^1^/^4)'},'FontSize',14,...
    'FontName','Times New Roman');

% Create ylabel
ylabel({'R^2 (adjusted)'},'FontSize',14,'FontName','Times New Roman');


%creating plot for RMSE
figure1 = figure;

% Create axes
axes1 = axes('Parent',figure1,'FontSize',12);
%% Uncomment the following line to preserve the Y-limits of the axes
% ylim(axes1,[0.95 1]);
box(axes1,'on');
hold(axes1,'all');

% Create plot
plot(time(1:d),RMSE,'MarkerFaceColor',[1 0
0],'Marker','.','LineStyle',':',...
    'Color',[1 0 0]);

% Create xlabel
xlabel({'Time^1^/^4 of initial data point (hrs^1^/^4)'},'FontSize',14,...
    'FontName','Times New Roman');

% Create ylabel
ylabel({'RMSE (g)'},'FontSize',14,'FontName','Times New Roman');


%creating plot for intercept and uncertainties
```

```
figure1 = figure;

% Create axes
axes1 = axes('Parent',figure1,'FontSize',12);
%% Uncomment the following line to preserve the Y-limits of the axes
% ylim(axes1,[0.95 1]);
box(axes1,'on');
hold(axes1,'all');

% Create plot
plot(time(1:d),coeff_m_b(:,2),'MarkerFaceColor',[0 0
1],'Marker','.','MarkerSize',6,'LineStyle',':',...
    'Color',[0 0 1]);

% Create xlabel
xlabel({'Time^1^/^4 of initial data point (hrs^1^/^4)'},'FontSize',14,...
    'FontName','Times New Roman');

% Create ylabel
ylabel({'Intercept Mass (g)'},'FontSize',14,'FontName','Times New Roman');

hold on

% Create plot
plot(time(1:d),conf_b,'MarkerFaceColor',[1 0
0],'Marker','.','MarkerSize',6,'LineStyle','--',...
    'Color',[1 0 0]);



%creating plot for slope and uncertainties
figure1 = figure;

% Create axes
axes1 = axes('Parent',figure1,'FontSize',12);
%% Uncomment the following line to preserve the Y-limits of the axes
% ylim(axes1,[0.95 1]);
box(axes1,'on');
hold(axes1,'all');

% Create plot
plot(time(1:d),coeff_m_b(:,1),'MarkerFaceColor',[0 0
1],'Marker','.','MarkerSize',6,'LineStyle',':',...
    'Color',[0 0 1]);

% Create xlabel
xlabel({'Time^1^/^4 of initial data point (hrs^1^/^4)'},'FontSize',14,...
    'FontName','Times New Roman');

% Create ylabel
ylabel({'slope (g/hrs^1^/^4)'},'FontSize',14,'FontName','Times New Roman');

hold on

% Create plot
plot(time(1:d),conf_m,'MarkerFaceColor',[1 0
0],'Marker','.','MarkerSize',6,'LineStyle','--',...
    'Color',[1 0 0]);

end
```

bestfitn

```
function
[adjR2,RMSE,coeff_a_b_c,conf_a,conf_b,conf_c,results]=bestfitn(time,mass,k)

l=length(mass);      %the number of datapoints in the dataseries
d=length(mass)-k;    %running algorithm up to l-k data points from end
adjR2=zeros(d,1);
RMSE=zeros(d,1);
coeff_a_b_c=zeros(d,3);   %for storing the fitting coefficients of y=mx+b
conf_a=zeros(d,2);      %split the confidence intervals into a matrix for
the confidence intervals of m(slope) and b(intercept)
conf_b=zeros(d,2);
conf_c=zeros(d,2);
results=zeros(12,1);


for(i=1:d);
[fitobject,gof]=fit(time(i:l),mass(i:l),'power2');  %carries out a
regression on the data of type 'power2'
adjR2(i,1)=gof.adjrsquare;   %extracts the adjusted R2 from the structure
RMSE(i,1)=gof.rmse;         %extracts the RMSE from the structure
coeff=coeffvalues(fitobject);   %gets the coefficients from the cfit object
conf=confint(fitobject);        %gets the confidence intervals of the cfit
object
coeff_a_b_c(i,1)=coeff(1,1);
coeff_a_b_c(i,2)=coeff(1,2);
coeff_a_b_c(i,3)=coeff(1,3);
conf_a(i,1)=conf(1,1);
conf_a(i,2)=conf(2,1);
conf_b(i,1)=conf(1,2);
conf_b(i,2)=conf(2,2);
conf_c(i,1)=conf(1,3);
conf_c(i,2)=conf(2,3);
end

[best,p]=max(adjR2);     %gets the best value of adjR2 and the corresponding
index

results(1,1)=p;
results(2,1)=best;
results(3,1)=RMSE(p,1);
results(7,1)=coeff_a_b_c(p,1);  %obtains the slope value corresponding to
the maximum adjR2
results(8,1)=conf_a(p,1);     %obtains the confidence intervals of this
slope value
results(9,1)=conf_a(p,2);     %obtains the confidence intervals of this
slope value
results(4,1)=coeff_a_b_c(p,2);
results(5,1)=conf_b(p,1);
results(6,1)=conf_b(p,2);
results(10,1)=coeff_a_b_c(p,3);
results(11,1)=conf_c(p,1);
results(12,1)=conf_c(p,2);

[bestfitted]=fit(time(p:l),mass(p:l),'power2');
j=max(time);

close all

%The following is code for creating plots of the results
% Create figure for bestfit
figure1 = figure;

% Create axes
axes1 = axes('Parent',figure1,'FontSize',12,'FontName','Times New Roman');
box(axes1,'on');
```

```
hold(axes1,'all');

% Create plot
plot((1:j),bestfitted(1:j),'LineWidth',1,'LineStyle','--','Color',[1 0 0]);

% Create xlabel
xlabel({'Time(hrs)'},'FontSize',14,...
    'FontName','Times New Roman');

% Create ylabel
ylabel({'Mass (g)'},'FontSize',14,'FontName','Times New Roman');

% Create plot
plot(time,mass,'Marker','.','LineStyle','none');


% Create figure for adjR2
figure1 = figure;

% Create axes
axes1 = axes('Parent',figure1,'FontSize',12);
%% Uncomment the following line to preserve the Y-limits of the axes
ylim(axes1,[0.95 1]);
box(axes1,'on');
hold(axes1,'all');

% Create plot
plot(time(1:d),adjR2,'MarkerFaceColor',[0 0
1],'Marker','.','LineStyle',':',...
    'Color',[0 0 1]);

% Create xlabel
xlabel({'Time of initial data point (hrs)'},'FontSize',14,...
    'FontName','Times New Roman');

% Create ylabel
ylabel({'R^2 (adjusted)'},'FontSize',14,'FontName','Times New Roman');


%creating second plot for RMSE
figure1 = figure;

% Create axes
axes1 = axes('Parent',figure1,'FontSize',12);
%% Uncomment the following line to preserve the Y-limits of the axes
% ylim(axes1,[0.95 1]);
box(axes1,'on');
hold(axes1,'all');

% Create plot
plot(time(1:d),RMSE,'MarkerFaceColor',[1 0
0],'Marker','.','LineStyle',':',...
    'Color',[1 0 0]);

% Create xlabel
xlabel({'Time of initial data point (hrs)'},'FontSize',14,...
    'FontName','Times New Roman');

% Create ylabel
ylabel({'RMSE (g)'},'FontSize',14,'FontName','Times New Roman');


%creating plot for intercept and uncertainties
figure1 = figure;

% Create axes
axes1 = axes('Parent',figure1,'FontSize',12);
%% Uncomment the following line to preserve the Y-limits of the axes
```

```
 %ylim(axes1,[0.95 1]);
box(axes1,'on');
hold(axes1,'all');

% Create plot
plot(time(1:d),coeff_a_b_c(:,2),'MarkerFaceColor',[0 0
1],'Marker','.','MarkerSize',6,'LineStyle',':',...
    'Color',[0 0 1]);

% Create xlabel
xlabel({'Time of initial data point (hrs)'},'FontSize',14,...
    'FontName','Times New Roman');

% Create ylabel
ylabel({'1/n'},'FontSize',14,'FontName','Times New Roman');

hold on

% Create plot
plot(time(1:d),conf_b,'MarkerFaceColor',[1 0
0],'Marker','.','MarkerSize',6,'LineStyle','--',...
    'Color',[1 0 0]);


%creating plot for slope and uncertainties
figure1 = figure;

% Create axes
axes1 = axes('Parent',figure1,'FontSize',12);
%% Uncomment the following line to preserve the Y-limits of the axes
%L=min(coeff_a_b_c(1:10,1));
%H=max(coeff_a_b_c(1:10,1));
%L1=L-(0.1*L);
%H1=H+(0.1*H);

%ylim(axes1,[L1 H1]);
box(axes1,'on');
hold(axes1,'all');

% Create plot
plot(time(1:d),coeff_a_b_c(:,1),'MarkerFaceColor',[0 0
1],'Marker','.','MarkerSize',6,'LineStyle',':',...
    'Color',[0 0 1]);

% Create xlabel
xlabel({'Time of initial data point (hrs)'},'FontSize',14,...
    'FontName','Times New Roman');

% Create ylabel
ylabel({'Mass Gain Rate (g/hrs^1^/^n)'},'FontSize',14,'FontName','Times New
Roman');

hold on

% Create plot
plot(time(1:d),conf_a,'MarkerFaceColor',[1 0
0],'Marker','.','MarkerSize',6,'LineStyle','--',...
    'Color',[1 0 0]);

%creating plot for slope and uncertainties
figure1 = figure;

% Create axes
axes1 = axes('Parent',figure1,'FontSize',12);
%% Uncomment the following line to preserve the Y-limits of the axes
% ylim(axes1,[0.95 1]);
box(axes1,'on');
hold(axes1,'all');
```

```
% Create plot
plot(time(1:d),coeff_a_b_c(:,3),'MarkerFaceColor',[0 0
1],'Marker','.','MarkerSize',6,'LineStyle',':',...
    'Color',[0 0 1]);

% Create xlabel
xlabel({'Time of initial data point (hrs)'},'FontSize',14,...
    'FontName','Times New Roman');

% Create ylabel
ylabel({'Intercept Mass (g)'},'FontSize',14,'FontName','Times New Roman');

hold on

% Create plot
plot(time(1:d),conf_c,'MarkerFaceColor',[1 0
0],'Marker','.','MarkerSize',6,'LineStyle','--',...
    'Color',[1 0 0]);

end
```

AETH5

```
function
[mass,LongELT]=AETH5(curve,AE,unc,intercept,a25,invn,strtyr,gap,per,index)

%AETH is used to calculate the mass gain as a function of temperature
history for a
%given AE (activation energy) and mass gain rate at 25.33C. Also invn (1/n
from the mass gain model)
%can be set. Calculated as fractional mass gain.

%This version carries out AETH from a starting year to a finishing year
%strtyr is the initial year (1500 say), gap the number of years between the
%runs (20 years say) and per is the period (200 years say). Keep gap and per
%to multiples of 5

%This version also calculates the mass gain using upper and lower
uncertainty ranges (1SE of the
%AE and temperature uncertainties). The upper activation energy is used with
the lower temperature curve
%(because it relates to lower mass gains at lower temperatures) with the
%lower activation energy used with the upper temperature curve

%Also carries out calculations for the upper and lower bounds of the
%temperature uncertainties (2 standard deviation for luterbacher) and the
%instrumental error in the long temperature series
%Armagh=1796-2002, Galway=1861-2000, Phoenix=1881-2005, Luterbacher =
%1500-start of these.

%The uncertainties from Luterbacher (2004) are not provided on a gridded
%basis - a best estimate is obtained from the paper, particularly figure 1
%and some of the text.  These only talk about the uncertainties over the
%winter and summer periods. The following estimates are used and are chosen
likely an overestimate instead of an underestimate.
%Winter 1500-1750=1.3degC, 1750-1880=0.6degC
%Summer 1500-1750=0.7degC, 1750-1880=0.3degC (note that these are
%considered optimistic by Luterbacher)
%Based on these it was decided that a suitable estimated of the standard
uncertainty (2SE) across
%the year would be of the order of 1degC over the period 1500-1750 and
%0.5degC over the period 1750-1880



ActEn=AE*1000;  %converts form kJ/mol to J/mol
UpActEn=(AE+unc)*1000;
DoActEn=(AE-unc)*1000;

R=8.3145;    %J/mol
m=invn;     %instead of 0.25 can be any value
n=1/m;
d=24.016;    %no of hours in a day see line below for how this was reached

slope=(ActEn/(n*R));
T0=slope/intercept; %this bit makes it compatible with excel by using slope
to estimate T0

%no of days in year is 365.25, whereas my data has only 365 days per hear,
%therefore 365.25*24 is number of hours in year. Divide whit by 365 to find
%additional amount (0.016hrs) required per day

a0=a25; %this is provided in hours^-0.25
%T0=298.48;  %273.15+25.33

yr0=strtyr-1500;    %using temperature records that start at 1500, yr0 will
be used to work out the start of the temperature record, ie, 1600-
1500=100,so start running on the 101th data point
```

```
v=length(curve);
w=per/gap;  %number of starting years
endyr=strtyr+per-gap;   %endyr is last run starting date, not end of
temperature history
yrs=[strtyr:gap:endyr];

mass=zeros(w,1);    %for store total mass gain (AETH approach) for each
starting year
uppermass=zeros(w,1);   %for storing total mass gain using upper temperature
curve
lowermass=zeros(w,1);   %for storing total mass gain using lower temperature
curve

massbad=zeros(w,1); %for storing total mass gain (mean temp) for each
starting year
lowermassbad=zeros(w,1);
uppermassbad=zeros(w,1);

LongELT=zeros(w,1); %for storing the ELT for each starting year run
upperLongELT=zeros(w,1);
lowerLongELT=zeros(w,1);

meantemp=zeros(w,1);%for storing the mean temp over each starting year run
uppermeantemp=zeros(w,1);
lowermeantemp=zeros(w,1);

offage=zeros(w,1);  %for storing the badage calculated using mean temp
upperoffage=zeros(w,1);
loweroffage=zeros(w,1);

uppercurve=zeros(v,1);  %for storing the upper and lower temp curves
lowercurve=zeros(v,1);


%INDEX 1=ARMAGH, 2=GALWAY, 3=PHOENIX
%TO CREATE UPPER AND lOWER TEMPERATURE CURVES

if index==1

uppercurve(1:91615)=curve(1:91615)+0.5;   %1500-1750
uppercurve(91616:108040)=curve(91616:108040)+0.25;   %1751-1795
uppercurve(108041:v)=curve(108041:v)+0.1;              %1796-end
lowercurve(1:91615)=curve(1:91615)-0.5;   %1500-1750
lowercurve(91616:108040)=curve(91616:108040)-0.25;   %1751-1795
lowercurve(108041:v)=curve(108041:v)-0.1;              %1796-end

elseif index==2

uppercurve(1:91615)=curve(1:91615)+0.5;   %1500-1750
uppercurve(91616:131765)=curve(91616:131765)+0.25;   %1750-1860
uppercurve(131766:v)=curve(131766:v)+0.1;              %1861-end
lowercurve(1:91615)=curve(1:91615)-0.5;   %1500-1750
lowercurve(91616:131765)=curve(91616:131765)-0.25;   %1751-1795
lowercurve(131766:v)=curve(131766:v)-0.1;              %1796-end

else
   %if its no 1 or 2 it is assumed to be phoenix

uppercurve(1:91615)=curve(1:91615)+0.5;   %1500-1750
uppercurve(91616:139065)=curve(91616:139065)+0.25;   %1750-1880
uppercurve(139066:v)=curve(139066:v)+0.1;              %1880-end
lowercurve(1:91615)=curve(1:91615)-0.5;   %1500-1750
lowercurve(91616:139065)=curve(91616:139065)-0.25;   %1751-1795
lowercurve(139066:v)=curve(139066:v)-0.1;              %1796-end
end


%METHOD OF MASS GAIN CALCULATION (AETH APPROACH)
```

```
%calculate mgain rate for initial step
%T=tempcurve(1);
%a=PreExp*exp(-ActEn/4*R*T);
%calculate frac mass gain up to change in temp
%y=a*(t^0.25);
%change in temp - calculate new rate and adjusted time at change point
%T=tempcurve(2);
%a=PreExp*exp(-ActEn/4*R*T);
%t=(y/a)^4;
%calculate new mass at end of this temperature phase
%y=a*(t^0.25);
% now to algorithm it
% in steps of 1 minute
% tempcurve will have a temperature for every interval


%SETTING UP CURVE INITIAL YEAR AND CALCULATING MASS GAIN AND ELT FOR CURVE
for j=1:w

    s=1+((yr0+((j-1)*gap))*365);    %+1 is to account fot the initial 00
year
    tempcurve=curve(s:v);

    l=length(tempcurve);
    t=[1:l];
    tyr=t/365;
    y=zeros(l,1);
    ymean=zeros(l,1);    %used for the mass gain using the mean temperature
between start and calculation time
    AdjTime=zeros(l,1);
    a=zeros(l,1);
    TmeanC=zeros(l,1);  %keep in celsius for plotting etc but as kelvin for
calculations
    ELT=zeros(l,1);
    badage=zeros(l,1);
    %initial step
    T=tempcurve(1,1)+273.15;
    a(1,1)=a0*exp(-(ActEn/(n*R))*((1/T)-(1/T0)));

    y(1,1)=a(1,1)*(d^m);
    ymean(1,1)=y(1,1);
    TmeanC(1,1)=tempcurve(1,1);
    ELT(1,1)=tempcurve(1,1);
    badage(1,1)=1;  %expressing in days

    %SUBSEQUENT STEPS
    %mass gain and ELT calculations
for i=2:l;
    T=tempcurve(i,1)+273.15;
    a(i,1)=a0*exp(-(ActEn/(n*R))*((1/T)-(1/T0)));

    AdjTime(i,1)=((y(i-1,1)/a(i,1))^n);
    y(i,1)=a(i,1)*((AdjTime(i,1)+d)^m);

    temp=tempcurve(1:i);
    TmeanC(i,1)=mean(temp);
    Tmean=mean(temp)+273.15;
    b=a0*exp(-(ActEn/(n*R))*((1/Tmean)-(1/T0)));

    ymean(i,1)=b*((i*d)^m);
    %temp=[];

    aELT=y(i,1)/((i*d)^m);  %effective lifetime rate needed to work out ELT
    invELT=(1/T0)-((n*R/ActEn)*log(aELT/a0));

    ELT(i,1)=(1/invELT)-273.15;
```

```
    %to calculate the age of the ceramic if the mean temperature, not ELT
was used
    badage(i,1)=((y(i,1)/b)^n)/(24.016*365);

end

mass(j,1)=y(l,1);
massbad(j,1)=ymean(l,1);
LongELT(j,1)=ELT(l,1);
meantemp(j,1)=TmeanC(l,1);
offage(j,1)=badage(l,1);
end


%SETTING UP CURVE INITIAL YEAR AND CALCULATING MASS GAIN AND ELT FOR UPPER
CURVE
for j=1:w

    s=1+((yr0+((j-1)*gap))*365);    %+1 is to account fot the initial 00
year
    tempcurve=uppercurve(s:v);

    l=length(tempcurve);
    t=[1:l];
    tyr=t/365;
    y=zeros(l,1);
    ymean=zeros(l,1);    %used for the mass gain using the mean temperature
between start and calculation time
    AdjTime=zeros(l,1);
    a=zeros(l,1);
    TmeanC=zeros(l,1);  %keep in celsius for plotting etc but as kelvin for
calculations
    ELT=zeros(l,1);
    badage=zeros(l,1);
    %initial step
    T=tempcurve(1,1)+273.15;
    a(1,1)=a0*exp(-(DoActEn/(n*R))*((1/T)-(1/T0)));

    y(1,1)=a(1,1)*(d^m);
    ymean(1,1)=y(1,1);
    TmeanC(1,1)=tempcurve(1,1);
    ELT(1,1)=tempcurve(1,1);
    badage(1,1)=1;  %expressing in days

    %subsequent steps
    %mass gain and ELT calculations

for i=2:l;
    T=tempcurve(i,1)+273.15;
    a(i,1)=a0*exp(-(DoActEn/(n*R))*((1/T)-(1/T0)));

    AdjTime(i,1)=((y(i-1,1)/a(i,1))^n);
    y(i,1)=a(i,1)*((AdjTime(i,1)+d)^m);


    temp=tempcurve(1:i);
    TmeanC(i,1)=mean(temp);
    Tmean=mean(temp)+273.15;
    b=a0*exp(-(DoActEn/(n*R))*((1/Tmean)-(1/T0)));

    ymean(i,1)=b*((i*d)^m);
    %temp=[];

    aELT=y(i,1)/((i*d)^m);  %effective lifetime rate needed to work out ELT
    invELT=(1/T0)-((n*R/DoActEn)*log(aELT/a0));

    ELT(i,1)=(1/invELT)-273.15;
```

```
    %to calculate the age of the ceramic if the mean temperature, not ELT
was used
    badage(i,1)=((y(i,1)/b)^n)/(24.016*365);

end

uppermass(j,1)=y(l,1);
uppermassbad(j,1)=ymean(l,1);
upperLongELT(j,1)=ELT(l,1);
uppermeantemp(j,1)=TmeanC(l,1);
upperoffage(j,1)=badage(l,1);
end


%SETTING UP CURVE INITIAL YEAR AND CALCULATING MASS GAIN AND ELT FOR LOWER
CURVE
for j=1:w

    s=1+((yr0+((j-1)*gap))*365);    %+1 is to account fot the initial 00
year
    tempcurve=lowercurve(s:v);

    l=length(tempcurve);
    t=[1:l];
    tyr=t/365;
    y=zeros(l,1);
    ymean=zeros(l,1);    %used for the mass gain using the mean temperature
between start and calculation time
    AdjTime=zeros(l,1);
    a=zeros(l,1);
    TmeanC=zeros(l,1);  %keep in celsius for plotting etc but as kelvin for
calculations
    ELT=zeros(l,1);
    badage=zeros(l,1);
    %initial step
    T=tempcurve(1,1)+273.15;
    a(1,1)=a0*exp(-(UpActEn/(n*R))*((1/T)-(1/T0)));

    y(1,1)=a(1,1)*(d^m);
    ymean(1,1)=y(1,1);
    TmeanC(1,1)=tempcurve(1,1);
    ELT(1,1)=tempcurve(1,1);
    badage(1,1)=1;  %expressing in days

    %subsequent steps
    %mass gain and ELT calculations

for i=2:l;
    T=tempcurve(i,1)+273.15;
    a(i,1)=a0*exp(-(UpActEn/(n*R))*((1/T)-(1/T0)));

    AdjTime(i,1)=((y(i-1,1)/a(i,1))^n);
    y(i,1)=a(i,1)*((AdjTime(i,1)+d)^m);


    temp=tempcurve(1:i);
    TmeanC(i,1)=mean(temp);
    Tmean=mean(temp)+273.15;
    b=a0*exp(-(UpActEn/(n*R))*((1/Tmean)-(1/T0)));

    ymean(i,1)=b*((i*d)^m);
    %temp=[];

    aELT=y(i,1)/((i*d)^m);  %effective lifetime rate needed to work out ELT
    invELT=(1/T0)-((n*R/UpActEn)*log(aELT/a0));

    ELT(i,1)=(1/invELT)-273.15;
```

```
    %to calculate the age of the ceramic if the mean temperature, not ELT
was used
    badage(i,1)=((y(i,1)/b)^n)/(24.016*365);

end

lowermass(j,1)=y(l,1);
lowermassbad(j,1)=ymean(l,1);
lowerLongELT(j,1)=ELT(l,1);
lowermeantemp(j,1)=TmeanC(l,1);
loweroffage(j,1)=badage(l,1);
end


%CREATING ALL FIGURES

% Create figure
figure1 = figure;

% Create axes
axes1 = axes('Parent',figure1,'FontSize',14);
%% Uncomment the following line to preserve the X-limits of the axes
% xlim(axes1,[0 200]);
box(axes1,'on');
hold(axes1,'all');

% Create multiple lines using matrix input to plot
plot1 =
plot(yrs,mass,yrs,massbad,yrs,uppermass,yrs,lowermass,yrs,uppermassbad,yrs,l
owermassbad);
set(plot1(1),'DisplayName','AETH','Color',[0 0 0]);
set(plot1(2),'Color',[0 0 1],'DisplayName','Mean');
set(plot1(3),'LineStyle',':','DisplayName','AETH (1 sigma)');
set(plot1(4),'LineStyle',':','Color',[1 0 0],'DisplayName','AETH (1
sigma)');
set(plot1(5),'LineStyle','--',...
    'Color',[0.749019622802734 0 0.749019622802734],...
    'DisplayName','Mean (1sigma)');
set(plot1(6),'LineStyle','--',...
    'Color',[0.749019622802734 0 0.749019622802734],...
    'DisplayName','Mean (1sigma)');

% Create xlabel
xlabel('Time (years)','FontSize',14);

% Create ylabel
ylabel('Fract Mass Gain','FontSize',14);
% Create legend
legend1 = legend(axes1,'show');
set(legend1,'EdgeColor',[1 1 1],'Location','SouthEast','YColor',[1 1 1],...
    'XColor',[1 1 1]);

%figure;
%plot(tyr,y);
%hold on
%plot(tyr,ymean);
%figure;
%plot(tyr,AdjTime);

% Create figure
figure1 = figure;

% Create axes
axes1 = axes('Parent',figure1,'FontSize',14);
%% Uncomment the following line to preserve the X-limits of the axes
% xlim(axes1,[0 200]);
box(axes1,'on');
hold(axes1,'all');
```

```
% Create multiple lines using matrix input to plot
plot1 =
plot(yrs,LongELT,yrs,meantemp,yrs,upperLongELT,yrs,lowerLongELT,yrs,uppermea
ntemp,yrs,lowermeantemp);
set(plot1(1),'LineWidth',1,'Color',[1 0 0],'DisplayName','ELT');
set(plot1(2),'DisplayName','Mean T');
set(plot1(3),'LineStyle',':','DisplayName','ELT (1 sigma)');
set(plot1(4),'LineStyle',':','Color',[1 0 0],'DisplayName','ELT (1 sigma)');
set(plot1(5),'LineStyle','--',...
    'Color',[0.749019622802734 0 0.749019622802734],...
    'DisplayName','Mean T (1sigma)');
set(plot1(6),'LineStyle','--',...
    'Color',[0.749019622802734 0 0.749019622802734],...
    'DisplayName','Mean T (1sigma)');

% Create xlabel
xlabel('Time (years)','FontSize',14);

% Create ylabel
ylabel('Temperature (deg.C)','FontSize',14);
% Create legend
legend1 = legend(axes1,'show');
set(legend1,'EdgeColor',[1 1 1],'Location','SouthEast','YColor',[1 1 1],...
    'XColor',[1 1 1]);


figure;
plot(yrs,offage,yrs,upperoffage,yrs,loweroffage);


end
```